RECEIVED BY TIC APR 1 0 1978

13th BIENNIAL CONFERENCE ON CARBON

EXTENDED ABSTRACTS and PROGRAM

July 18-22, 1977
Irvine, California

Co-sponsored by
THE AMERICAN CARBON SOCIETY
THE AEROSPACE CORPORATION
and
TRW INC.

DISTRIBUTION OF THIS

13th BIENNIAL CONFERENCE ON CARBON

EXTENDED ABSTRACTS and PROGRAM

July 18-22, 1977
Irvine, California

Co-sponsored by
THE AMERICAN CARBON SOCIETY
THE AEROSPACE CORPORATION
and
TRW INC.

DISTRIBUTION

FOREWORD

This document contains extended abstracts of all contributed papers for presentation at the 13th Biennial Conference on Carbon. The abstracts were prepared by the authors and have not been edited. The papers are arranged in the scheduled order of presentation, with the exception that there are three concurrent sessions for all the contributed papers.

The plenary papers and the award lectures are included in the Table of Contents for completeness. However, abstracts for these invited papers were not requested.

The Local Conference Committees would like to express appreciation to all those whose efforts went into making this conference possible. The financial assistance in support of this publication from the Energy Research and Development Administration, Division of Nuclear Research and Applications, is gratefully acknowledged.

The present conference includes some changes in format from previous conferences. In addition to providing this volume of extended abstracts in advance to all attendees and limiting the oral presentations to ten minutes and five minutes discussion, in-depth group discussions have been arranged by the Technical Area Chairmen to stimulate the exchange of information and ideas. This has entailed considerable effort on the part of the Technical Area Chairmen and those who have agreed to act as Discussion Leaders; their cooperation is especially appreciated.

Finally, the Local Conference Committees wish to express their special thanks to Mrs. Florence Rucker for her skillful management of the many details involved in preparing this volume of abstracts for printing.

The Local Conference Committees

LOCAL CONFERENCE COMMITTEES

Arrangements

Dr. W. V. Kotlensky
TRW, Inc.
(Chairman)

Dr. W. E. Duggins
Collier Carbon and Chemical Corporation
(Treasurer)

Mr. G. M. Studdert
HITCO
(Registrar)

Mr. L. F. Harrigan
American Automated Engineering, Inc.
(Housing)

Mr. D. W. Gibson
Morganite-Modmor Incorporated
(Catalina Outing)

Mr. C. E. Northway
HAVEG
(Wine Tasting Party)

Mr. D. A. Eitman
Science Applications, Inc.
(Cocktail Party and Barbecue)

Mr. G. B. Engle
General Atomic Company
(San Diego/Sea World Outing)

Technical Program

Dr. R. A. Meyer
The Aerospace Corporation
(Chairman)

Dr. J. L. White
The Aerospace Corporation
(Assistant Technical Program Chairman)

Mr. M. Buechler
The Aerospace Corporation
(Session Coordinator)

Mr. R. J. Larsen
SUPER-TEMP Company
(Session Coordinator)

TECHNICAL AREA CHAIRMEN

"ACTIVATED CARBON AND ADSORPTION"

Professor P. J. Reucroft
University of Kentucky

"ADVANCES IN CARBON CHARACTERIZATION"

Dr. D. B. Fischbach
University of Washington

"INDUSTRIAL APPLICATIONS"

Mr. R. K. Carlson
POCO Graphite, Inc.

"AEROSPACE APPLICATIONS"

Major H. E. Keck
Defense Systems Management College

"BIOMATERIALS APPLICATIONS"

Dr. J. C. Bokros
General Atomic Company

"CHEMICAL REACTIVITY AND SURFACES"

Professor J. G. Hooley
The University of British Columbia

"ELECTRICAL AND THERMAL PROPERTIES"

Dr. J. A. Woollam
National Aeronautics and Space Administration

"FIBERS AND COMPOSITES"

Professor R. J. Diefendorf
Rensselaer Polytechnic Institute

"MECHANICAL AND FRICTIONAL PROPERTIES"

Dr. J. L. Kaae
General Atomic Company

"MESOPHASE, CARBONIZATION AND GRAPHITIZATION"

Dr. J. L. White
The Aerospace Corporation

"MICROMECHANICS AND MODELING"

Dr. B. W. Rosen
Material Sciences Corporation

"NUCLEAR APPLICATIONS"

Mr. C. R. Kennedy
Oak Ridge National Laboratory

AMERICAN CARBON SOCIETY COMMITTEES

Executive

Dr. J. T. Meers, Chairman
Union Carbide Corporation

Dr. J. C. Bokros
General Atomic Company

Dr. V. R. Deitz
U. S. Naval Research Laboratory

Professor S. Mrozowski, Editor-in-Chief of CARBON
Ball State University

Professor P. L. Walker, Jr., Secretary-Treasurer
The Pennsylvania State University

Advisory

Mr. R. K. Carlson
POCO Graphite, Inc.

Professor R. J. Diefendorf
Rensselaer Polytechnic Institute

Dr. D. B. Fischbach
University of Washington

Dr. L. A. Joo'
Great Lakes Carbon Corporation

Dr. W. V. Kotlensky
TRW, Inc.

Dr. D. W. McKee
General Electric Company

Dr. W. A. Nystrom
Stackpole Carbon Company

Mr. C. A. Pratt
Air Force Materials Laboratory

Dr. D. Rivin
Cabot Corporation

Dr. F. Rusinko, Jr.
Edimax, Inc.

Dr. P. A. Thrower
The Pennsylvania State University

Dr. L. L. Winter
Union Carbide Corporation

	MONDAY	TUESDAY	WEDNESDAY	THURSDAY	FRIDAY
8:30 → 9:30	Opening Announcements Plenary Session (S)	Plenary Session (S)	Plenary Session (S)	MM-1 (1) | AC-3 (S) | CC-3 (4)	Plenary Session (S)
9:45 → 10:30	MF-1 (1) | CR-1 (S) | Ia-1 (4)	F-2 (1) | CR-3 (S) | MF-2 (4)	E-4 (S) | AC-2 (1) | MF-3 (4)	MM-2 (1) | CR-5 (S) | N-4 (4)	CR-6 (S) | I-4 (1) | MF-4 (4)
10:30 → 10:45	BREAK				
10:45 → 12:15	MG-1 (1) | CR-2 (S) | I-1 (4)	F-3 (1) | B-2 (4) | E-2 (S)	E-4 (S) | CC-1 (1) | CR-4 (4)	MM-2 (1) | MG-4 (S) | N-4 (4) Ia-3 (1)	CR-7 (S) | MG-5 (1) | MF-4 (4)
11:45 → 1:00	LUNCH				
1:30 → 3:30	E-1 (S) | Ia-2 (1) | B-1 (4)	B-3 (1) | I-2 (4) | MG-2 (S)	F-4 (1) | MG-3 (S) | I-3 (4)	Awards Lectures (F)	
3:30 → 3:45	BREAK				
3:45 → 5:15	F-1 (1) | N-1 (S) | AC-1 (4)	B-4 (1) | E-3 (S) | N-2 (4)	N-3 (1) | MG-3 (S) | CC-2 (4) ** Group Discussion	Business Meeting (F)	
DINNER	6:30 *	5:00 – 6:30	5:00 – 6:30	Cocktail Party (5:00 – 6:30)	
7:30 → 9:30	Group Discussions and/or Free Time			Banquet (6:30)	

* Wine tasting party prior to dinner (5:00 - 6:30).

** Group Discussion (4:15 - 5:15).

SESSION CODES:

AC = Activated Carbon and Adsorption
CC = Advances in Carbon Characterization
I = Industrial Applications
Ia = Aerospace Applications
B = Biomaterials Applications
CR = Chemical Reactivity and Surfaces
E = Electrical and Thermal Properties
F = Fibers and Composites
MF = Mechanical and Frictional Properties
MG = Mesophase, Carbonization and Graphitization
MM = Micromechanics and Modeling
N = Nuclear Applications

LOCATION CODES:

S = Science Lecture Hall
1 = Physical Sciences, Room 101
4 = Physical Sciences, Room 104
F = Fine Arts Theatre

TABLE OF CONTENTS

Page

FOREWORD ii

PROGRAM SUMMARY vi

PROGRAM

8:30 am, Monday, July 18

Welcome: W. V. Kotlensky and R. A. Meyer, Conference Chairmen

OPENING REMARKS

8:45 am, Monday, July 18

PLENARY SESSION

"Carbon Black Properties and Applications"

Dr. A. I. Medalia
Cabot Corporation, Billerica, Massachusetts

9:45 am, Monday, July 18

MECHANICAL AND FRICTIONAL PROPERTIES

Session MF-1

Mr. M. J. Bullock, presiding

MF-1(1) Effects of Oxygen and Moisture on Carbon-Composite Frictional Behavior

N. A. Hooton and A. L. Courtney 1

MF-1(2) Adsorptive Properties of CDE Charcoal Cloth

F. A. P. Maggs, M. E. Smith, and G. A. Robins 3

MF-1(3) Measurement of Long-Term Stress-Relaxation in Carbon-Carbon Composites

R. S. Pickering. 5

9:45 am, Monday, July 18

CHEMICAL REACTIVITY AND SURFACES

Session CR-1

Dr. J. G. Hooley, presiding

CR-1(1) Graphite Lamellar Compounds with Thallium (III) Chloride and the Bromides of Thallium (III), Cadmium, Mercury, Iron (II) and Uranium (V)

E. Stumpp and R. Niess 7

CR-1(2) The State of Water on Pure and Silicon-Alloyed LTI-Carbons

T-H. Chiu, E. Nyilas and F. J. Micale 9

CR-1(3) Diffusion Coefficients of Br_2, HNO_3, and $PdCl_2$ in Graphite

M. B. Dowell 11

9:45 am, Monday, July 18

AEROSPACE APPLICATIONS

Session Ia-1

Major H. E. Keck, Ph. D., presiding

Page

Ia-1(1) Diagnosis of Matrix Quality in CVD Infiltrated Carbon-Carbon by In-Process Monitoring and Nondestructive Evaluation

E. R. Stover and J. A. Roetling 13

Ia-1(2) Effect of Substrate Fiber Orientation on Chemical Vapor Deposited (CVD) Needled Felt Carbon-Carbon Composites

J. L. Irwin 15

Ia-1(3) Processing Scale-Up Studies on Carbon-Carbon Composites

P. N. Bolinger 17

10:45 am, Monday, July 18

MESOPHASE, CARBONIZATION AND GRAPHITIZATION

Session MG-1

Dr. L. S. Singer, presiding

MG-1(1) ESR Study of the Kinetics of Carbonization

L. S. Singer and I. C. Lewis 19

MG-1(2) Carbonization of 3.5-Dimethylphenol-Formaldehyde Resin and its Chemical Structure at Mesophase Appearance

Y. Yamashita and K. Ouchi 21

MG-1(3) The Role of Free Radicals and Molecular Size in Mesophase Pitch

I. C. Lewis and C. A. Kovac 23

MG-1(4) Study of Carbonaceous Mesophase through the ESR Spectra of Vanadyl Chelates

Y. Yamada, K. Ouchi, Y. Sanada and J. Sohma. 25

MG-1(5) A Rheological Investigation in the Mesophase Region

G. W. Collett and B. Rand. 27

MG-1(6) Carbon Formation During Pyrolysis in the Presence of Hydrogen

A. LaCava and D. L. Trimm 29

10:45 am, Monday, July 18

INDUSTRIAL APPLICATIONS

Session I-1

Dr. F. Rusinko, presiding

I-1(1) Solar Selective Carbon Coatings

C. R. Schmitt, J. M. Schreyer, J. M. Googin and H. D. Whitehead 31

I-1(2) The Relationship of Physical Properties of Graphite to EDM Performance

C. L. Greatorex 32

I-1(3) Casting Cores Made from Porous Carbon

G. Gistinger and G. Hochegger. 33

I-1(4) New Application for Flexible Graphite Sheet

H. Eicher and E. Winkler 35

I-1(5) Formation of Divided Particles from Carbon Vapor

J. LaHaye, P. Kappler, P. Ehrburger and J. B. Donnet 37

I-1(6) Applications of Carbon in the Sodium-Sulfur Battery

F. A. Ludwig. 39

Page

10:45 am, Monday, July 18

CHEMICAL REACTIVITY AND SURFACES

Session CR-2

Dr. V. Deitz, presiding

CR-2(1) The Oxidation of Graphite Under Compressive Stress
P. A. Thrower and D. R. Marx 41

CR-2(2) Superficial Reaction of Carbon Black with Oxygen
D. Rivin and J. H. Atkins 43

CR-2(3) Catalysis of Water Vapour Gasification of Coke by Iron
R. Hahn and K. J. Hüttinger 44

CR-2(4) Kinetics of the Gasification by Oxygen of a Graphitizing Carbon Catalyzed by Transition Metal Impurities
H. Marsh and D. W. Taylor 46

CR-2(5) Corrosive Effects of Pyrolytic Carbon in Gas Turbines
D. W. McKee and D. Chatterji 48

CR-2(6) The Effect of Natural Coal Impurities on Carbon Gasification
K. Otto and M. Shelef 50

1:30 pm, Monday, July 18

ELECTRICAL AND THERMAL PROPERTIES

Session E-1

Dr. J. W. McClure, presiding

E-1(1) On a Special Effect of Y3 on the Electronic Equienergy Surfaces of Graphite
C. Ayache 52

E-1(2) Theory of the Galvanomagnetic Properties of Graphite — Consequences of Trigonal Warping of the Constant Energy Surfaces
R. O. Dillon and I. L. Spain 54

E-1(3) Impurity State of Graphite in the Quantum Limit
K. Sugihara 56

E-1(4) Galvanomagnetic Properties of Graphite from 10 to 23T
W. H. Lowrey and I. L. Spain 58

E-1(5) Anisotropy of the Magnetic-Field-Induced Anomaly in the Resistance Versus Temperature Curve of Graphite
C. Ayache and A. de Combarieu 60

E-1(6) Temperature and Field Dependencies of Galvanomagnetic Effects in Graphite
L. W. Kreps and J. A. Woollam 62

E-1(7) Anomalous Phonon Drag Effect in Graphite
K. Sugihara, H. Ohshima, K. Kawamura and T. Tsuzuku 64

E-1(8) Electrical Conduction in C-Direction of Graphite
K. Kawamura, Y. Ohuchi, H. Ohshima and T. Tsuzuku 66

1:30 pm, Monday, July 18

AEROSPACE APPLICATIONS

Session Ia-2

Major H. E. Keck, Ph.D., presiding

Page

Ia-2(1) Densification of Carbon-Carbon Composites at 30 KSI

G. W. Weber, K. R. Young, A. J. Taylor and T. J. Curci 68

Ia-2(2) Analysis of Dimensional Changes and Fiber-Matrix Interactions During Processing of 3D Carbon-Carbon Composites

L. B. Greszczuk 70

Ia-2(3) Mechanical Properties of Pitch Fiber Carbon-Carbon Composites

C. R. Rowe and L. L. Lander 72

Ia-2(4) Carbon/Carbon Material Application to Solid Rocket Motor Nozzles

R. Laramee, G. Lamere, B. Prescott, R. Mitchell, P. Sottosanti and D. Dahle 74

Ia-2(5) Influence of Pyrolysis Pressure on Microstructure of Carbon-Carbon Composites

J. S. Evangelides 76

Ia-2(6) Carbon - Carbon for Nozzles

G. W. Driggers and H. S. Starrett 78

1:30 pm, Monday, July 18

BIOMATERIALS APPLICATIONS

Session B-1

Dr. S. F. Hulbert, presiding

B-1(1) Use of Carbons in Dental and Orthopaedic Implants

S. F. Hulbert and J. C. Bokros 79

B-1(2) Factors Affecting the Biological Properties of Various Carbons in the Physiological Environment

S. D. Bruck 81

B-1(3) Interaction of Human Fibrinogen with Pure LTI-Carbon

T-H. Chiu and E. Nyilas 83

B-1(4) Adsorptive Properties of Human Y-Globulin on Pure and Silicon Alloyed LTI-Carbons

E. Nyilas and T-H. Chiu 85

B-1(5) Diamond-Like Carbon Films -- Factors Leading to Improved Biocompatibility

S. Aisenberg 87

B-1(6) Investigations of Vitreous and Pyrolytic Carbon-Metallic Alloy Surgical Biomaterials

J. E. Lemons, R. A. Buchanan, I. L. Baswell and N. G. Thompson 89

B-1(7) LTI Carbon Surfaces

A. D. Haubold, J. D. Andrade, H. S. Shim and R. King 91

B-1(8) Tissue Response to Charcoal Cloth Implanted Subcutaneously in the Rat and the Guinea Pig

N. H. Creasey and F.A.P. Maggs 93

3:45 pm, Monday, July 18

FIBERS AND COMPOSITES

Session F-1

Dr. R. J. Diefendorf, presiding

Page

F-1(1) Production of Carbon Fibres from Char Tars
I. Romey 94

F-1(2) High Strength Carbon Fibers from Mesophase Pitch
J. B. Barr, S. Chwastiak and R. Didchenko 96

F-1(3) Structure and Properties of Fibers Derived from Pitch
A. Johnson and W. Bradshaw 98

F-1(4) Electronic and Structural Characteristics of Carbon Fibers from Mesophase Pitch
A. A. Bright and L. S. Singer 100

F-1(5) Neutron Diffraction Studies on some Carbon Fibre Reinforced Carbon Composites and Their Precursor Materials
L. F. Pain and P. B. Roscoe 102

3:45 pm, Monday, July 18
NUCLEAR APPLICATIONS
Session N-1
Dr. R. J. Price, presiding

N-1(1) The Theory of Irradiation Damage in Graphite
B. T. Kelly 104

N-1(2) The Application of Chemical Rate Theory to Fast Neutron Irradiation Damage in Graphite
II. The effect of thermal annealing and thermal equilibrium defect concentrations
B. T. Kelly 105

N-1(3) The Structure of Graphite Resulting from He-Ion Injection
A. S. Rao and D. J. Bacon 107

N-1(4) Experiments on the Concentration Dependence of Strontium Diffusion in Graphite
L. R. Zumwalt and P. T. Williams 109

N-1(5) Inert Gas Permeability of Pyrocarbon Coatings
C. S. Morgan, W. P. Eatherly and G. L. Powell 111

N-1(6) B_4C/Graphite Pellets for Nuclear Reactor Shutdown Systems
W. K. Alexander, A. E. Goldman and H. D. Schlesselman 113

3:45 pm, Monday, July 18
ACTIVATED CARBON AND ADSORPTION
Session AC-1
Dr. V. R. Deitz, presiding

AC-1(1) Dependence of Gas Adsorption Rates on Carbon Granule Size and Linear Flow Velocity
J. A. Rehrmann and L. A. Jonas 115

AC-1(2) Reaction Steps in Gas Sorption by Impregnated Carbon
L. A. Jonas 117

AC-1(3) Effect of Continued Activation on Activated Carbon Pore Structure
A. J. Juhola 119

AC-1(4) Chemisorption of Hydrocarbons on Graphitized Carbon Blacks at 300°C
W. P. Hoffman, F. J. Vastola and P. L. Walker, Jr. 121

Page

AC-1(5) Use of Carbons for Removal of Ammonia from Water
O. P. Mahajan, A. Youssef and P. L. Walker, Jr. 123

AC-1(6) Dissociative Storage of Hydrogen on Modified Carbon Surfaces
R. K. Sinha and N. J. Wagner 125

8:30 am, Tuesday, July 19

PLENARY SESSION

"High Resolution Microscopy"

Professor J. M. Thomas
Edward Davies Chemical Laboratories
University College of Wales, UK

9:45 am, Tuesday, July 19

FIBERS AND COMPOSITES

Session F-2

Dr. E. R. Stover, presiding

F-2(1) Correlation Between Structure and Properties of Chopped-Fiber Carbon-Carbon Composites
W. G. Bradshaw, P. C. Pinoli and R. F. Karlak 126

F-2(2) Carbon Fibre Reinforced Composites for Applications at Elevated Temperatures
E. Fitzer and M. Heym 128

F-2(3) Oxidation Behavior of Some Carbon/Carbon Composites
D. B. Fischbach and D. R. Uptegrove 130

9:45 am, Tuesday, July 19

CHEMICAL REACTIVITY AND SURFACES

Session CR-3

Dr. P. T. Hough, presiding

CR-3(1) A Temperature-Programmed Desorption Study of Surface Oxygen Complexes Formed on Carbons from Atomic Oxygen
H. Marsh and D. W. Taylor 132

CR-3(2) The Reactivity to Atomic Oxygen and Carbon Dioxide of Anisotropic Carbons of Different Optical Texture
H. Marsh, M. French, J. Smith and J. L. White 134

CR-3(3) A New Substrate for Surface Studies
M. B. Dowell 136

9:45 am, Tuesday, July 19

MECHANICAL AND FRICTIONAL PROPERTIES

Session MF-2

Dr. R. J. Price, presiding

MF-2(1) Friction Characteristics of Some Graphites and Carbon Composites Sliding Against Themselves
E. M. Tatarzycki 138

MF-2(2) The Fatigue Behavior of Thin Carbon Films
H. S. Shim, N. K. Agarwal and A. D. Haubold 140

Page

MF-2(3) Size Effects on Strengths of Glassy Carbon
R. E. Bullock and J. L. Kaae 141

10:45 am, Tuesday, July 19
ELECTRICAL AND THERMAL PROPERTIES
Session E-2
Dr. J. A. Woollam, presiding

E-2(1) The Effects of Fast Neutron Irradiation on the Galvanomagnetic Properties of Graphite
R. O. Dillon, I. L. Spain and J. W. McClure 143

E-2(2) Study of the Elastic Constant C_{44} of Pyrolytic Graphite After Low Temperature Irradiation (4 K)
J. B. Ayasse and E. Bonjour 145

E-2(3) Effect of Chemical Impurities on the Galvanomagnetic Properties of Carbons
T. Kimura and K. Yazawa 147

E-2(4) Electronic Processes in Boron-Doped Turbostratic Carbons
K. Kawamura, T. Emori and T. Tsuzuku 149

E-2(5) Electrical Resistivity of Graphite Nitrates
F. L. Vogel, C. Zeller and W. C. Forsman 151

E-2(6) Mechanism for Formation of Graphite "Acceptor Compounds"
W. C. Forsman 153

10:45 am, Tuesday, July 19
BIOMATERIALS APPLICATIONS
Session B-2
A. N. Cranin, DDS, presiding

B-2(1) Two Year Freestanding Vitreous Carbon Implants in Baboons
L. Shulman, P. Schnitman, R. Feingold, L. Gettleman, P. Kalis and M. Woolfson 155

B-2(2) The Effect of Surface Texture and Bacterial Plaque on the Tissues Surrounding Vitreous Carbon Implants
M. Samida, R. A. James, J. M. Whittaker and R. L. Schultz 156

B-2(3) Clinical Evaluation of Functional LTI Pyrolite Carbon Blade Implants in Primates with Design Considerations
J. Kent, C. Farrell, S. Hulbert and J. Bokros 157

B-2(4) Histology of LTI Pyrolite Carbon Dental Implant-Tissue Interface in Primates
C. Farrell, J. Kent, J. Klawitter, J. Bokros, S. Hulbert and R. Carr 159

B-2(5) Scanning Electron Microscopy of LTI Carbon Dental Implant-Tissue Interface
J. J. Klawitter, S. F. Hulbert, J. Kent, C. Farrell and J. Bokros 161

B-2(6) An Ultrastructural Study of Baboon Tissue Interfacing with Pyrolytic Carbon Dental Implants
R. A. James, J. M. Whittaker and R. L. Schultz 163

10:45 am, Tuesday, July 19

FIBERS AND COMPOSITES

Session F-3

Dr. R. Didchenko, presiding

F-3(1) C. V. D. Carbon Composites: Preparation, Electronic and Thermal Properties

A. Pacault, P. Loll and P. Delhaes 164

F-3(2) Development of Interfilament Matrix Structures in CVD-Infiltrated Carbon-Carbon

E. R. Stover, J. F. D'Andrea, P. N. Bolinger and J. J. Gebhardt 166

F-3(3) Unidirectionally Reinforced Carbon/Carbon-Composites with Polyimide and Phenolic Resin as Matrix Precursor

E. Fitzer, K.-H. Geigl and M. Heym 168

F-3(4) High Temperature Properties of Carbon Fibers

C. R. Rowe and D. L. Lowe 170

F-3(5) Fracture Behavior of Carbon Fiber-Glassy Carbon Composite

S. Kimura, H. Tanaka and E. Yasuda 172

F-3(6) Acoustic Emission from Carbon Fibre Reinforced Carbon Composites

M. J. Fry 174

1:30 pm, Tuesday, July 19

BIOMATERIALS APPLICATIONS

Session B-3

Dr. J. J. Klawitter, presiding

B-3(1) Design Considerations for LTI-Carbon Heart Valves

M. C. Huffstutler, Jr. 176

B-3(2) Experimental and Clinical Application of Carbon Fibre as an Implant in Orthopaedics

D. H. R. Jenkins 178

B-3(3) Preparation of Pyrocarbon Coated Carbon Fibres for Use in Ligament Replacement

E. Fitzer, W. Hüttner and D. Wolter 180

B-3(4) Development of Carbon Materials for Endoprosthetics

H. Brückmann, K. J. Hüttinger and U. Rosenblatt 182

B-3(5) Graphite Fiber/TPE Polymer Porous Composites in Reconstructive Surgery

C. A. Homsy and J. N. Kent 184

1:30 pm, Tuesday, July 19

INDUSTRIAL APPLICATIONS

Session I-2

Dr. M. J. Block, presiding

I-2(1) Rheological Properties of Coal-Tar Pitch Binders

R. W. Wallouch, H. N. Murty and E. A. Heintz 186

I-2(2) Physical Properties and Composition of the Green Mix

S. Mrozowski 188

Page

I-2(3) Effect of Raw Materials on Lampblack Grade Graphite Properties

G. W. Morelli and J. F. Rakszawski 189

I-2(4) Puffing of Electrode Stock as Influenced by Sulfur Content and Heating Rate

E. W. Tucker, L. D. Loch, G. Stecker and L. A. Joo' 191

I-2(5) Effect of Coke-Sizing on Puffing Characteristics of Baked Stock

L. D. Loch, E. W. Tucker and L. A. Joo' 193

I-2(6) The Use of Sulfur to Control Physical Properties in Graphite

C. R. Kennedy 195

I-2(7) Occupational Exposure to Fugitive Emissions from a Graphite Production Operation

W. H. Griest, H. Kubota and W. P. Eatherly 197

1:30 pm, Tuesday, July 19

MESOPHASE, CARBONIZATION AND GRAPHITIZATION

Session MG-2

Mr. J. E. Zimmer, presiding

MG-2(1) Magnetic Orientation Studies of Synthetic Mesophase Pitches

C. A. Kovac and I. C. Lewis 199

MG-2(2) Influence of a Magnetic Field on the Molecular Arrangement of Mesophase Spherules

S. Matsumoto, S. Oi, T. Imamura, N. Nakamizo, Y. Yamada and H. Honda 201

MG-2(3) Disclination Structures in Coke and Graphite

J. L. White and J. E. Zimmer 203

MG-2(4) Structural Characterization of Fine Morphology in Carbon Using High Resolution Electron Microscopy

H. Marsh and D. Crawford 205

MG-2(5) A Phase-Contrast Electron Microscope and Optical Microscope Study of Anisotropic Carbons of Different Optical Texture

R. A. Forrest, M. French, H. Marsh, J. A. Griffiths and J. L. White 207

MG-2(6) Structure of Coke Formed During Thermal Hydrocracking of Athabasca Bitumen

B. N. Nandi, K. Belinko and J. M. Denis 209

MG-2(7) Carbon Microstructural Development at High Pressures

W. Chard and H. Keck 212

MG-2(8) Thermal and Electrical Properties of Petroleum Cokes

E. G. Morris and J. M. Faircloth 214

3:45 pm, Tuesday, July 19

BIOMATERIALS APPLICATIONS

Session B-4

L. B. Shulman, DMD. presiding

B-4(1) L. T. I. Carbon Permucosal Dental Implants

A. N. Cranin, M. F. Rabkin, H. Silverbrand, S. Unger, J. E. Armitage and M. Meenaghan 216

Page

B-4(2) Carbon Materials for Oral Implantation: A Preliminary Report
D. Leake, S. Michieli, S. Freeman, J. Bokros and A. Haubold 218

B-4(3) Vapor Deposited Carbon Coated Tooth Root Replicas
S. Michieli, D. Leake, S. Freeman, J. Bokros, A. Haubold and A. Pizzoferrato 220

B-4(4) Various Applications of Pyrolytic Carbon in Alveolar Bone to Retard Resorption and Stimulate Osteogenic Activity. A Preliminary Report
J. Warrens 222

B-4(5) Experience with Biocompatible Carbon at Rancho Los Amigos Hospital
J. Reswick, V. Mooney, D. McNeal and M. Quigley 224

3:45 pm, Tuesday, July 19
ELECTRICAL AND THERMAL PROPERTIES
Session E-3
Dr. L. Singer, presiding

E-3(1) The Low Current Carbon Arc and the Properties of Graphite Near the Sublimation Temperature
W. W. Lozier and M. R. Null 226

E-3(2) Perpendicular Electric Field Effect on the Electric Resistivity of Thin Graphite Crystals
Y. F. Ohashi and S. Mizushima 228

E-3(3) Esaki Kink Effect in Graphite
S. Mizushima and Y. Fujibayashi 229

E-3(4) Two Types of Broadening of the ESR Line in the Transition Region, Effects of Oxydizing Atmosphere
S. Mrozowski 231

E-3(5) Relationship Between Preferred Orientation, Thermal Expansion, and Coke Preparation Temperature of Some Experimental Graphites
O. J. Horne and C. R. Kennedy 232

E-3(6) Relationship Between Preferred Orientation, Thermal Expansion, and Molding Pressure of Some Experimental Graphites
O. J. Horne and C. R. Kennedy 234

3:45 pm, Tuesday, July 19
NUCLEAR APPLICATIONS
Session N-2
Dr. J. C. Bowman, presiding

N-2(1) Nuclear Graphites Based on Coal Tar Pitch Behaviour Under Neutron Irradiation Between 400 and 1400°C
P. Mottet, A. Fillatre, R. Schill, G. Micaud, J. Lore and P. Cornuault 236

N-2(2) Isotropic Nuclear Graphites - The Effect of Neutron Irradiation
J. Lore, A. Buscailhon, P. Mottet and G. Micaud 238

N-2(3) Properties and Behaviour Under Irradiation of Isotropic Fine Grained Graphites
J. Maire, J. Fourre and A. Pernollet 240

Page

N-2(4) Tensile Properties of Neutron-Irradiated Graphites
R. J. Price 242

N-2(5) Fatigue of Near-Isotropic Graphite: Influence of Stress Cycle
R. J. Price 244

8:30 am, Wednesday, July 20

PLENARY SESSION

"Carbon/Fiber Composites"

Professor R. J. Diefendorf
Rensselaer Polytechnic Institute
Troy, New York

9:45 am, Wednesday, July 20

ELECTRICAL AND THERMAL PROPERTIES

Session E-4

Dr. J. A. Woollam, presiding

E-4(1) Negative Magnetoresistance and Electrical Conduction in Glassy Carbon
S. Ho, R. Saxena and R. H. Bragg 246

E-4(2) Magnetoresistance of Disordered Carbons at Low Temperature
Y. Hishiyama, Y. Kaburagi and A. Ono 248

E-4(3) Band Theory of Pyrocarbons and Cokes
O. Gonzalez and A. Charlier 250

E-4(4) Low Temperature Magnetic and Thermal Properties of an Amorphous Carbon
F. Carmona, P. Delhaes, J. L. Tholence and J. C. Lasjaunias 252

E-4(5) Lattice Defects and Low Temperature Specific Heat Peaks in Soft Carbon and Polycrystalline Graphite
S. Mrozowski and A. S. Vagh 254

E-4(6) Magnetic Field Dependence of Specific Heat Peaks in Neutron Irradiated Polycrystalline Graphite
A. S. Vagh and S. Mrozowski 255

E-4(7) Specific Heat of Neutron Irradiated Glassy Carbon (GC 30) in the Intermediate Range of Temperatures 3-78°K
E. Michael, B. Myers and S. Mrozowski 256

9:45 am, Wednesday, July 20

ACTIVATED CARBON AND ADSORPTION

Session AC-2

Dr. P. L. Walker, Jr., presiding

AC-2(1) Saran Carbon--A Superior Adsorbent for Volatile Compounds
D. D. Schmidt and R. G. Melcher 257

AC-2(2) Charcoals as Catalyst Supports in the Trapping of Methylradioiodide (131)
V. R. Deitz 259

9:45 am, Wednesday, July 20

MECHANICAL AND FRICTIONAL PROPERTIES

Session MF-3

Dr. J. L. Kaae, presiding

MF-3(1) Correlation of Strength with Physical Properties
W. C. Morgan and F. L. Becker 261

MF-3(2) Effects of Oxidation on the Mechanical Properties of Carbon/Graphite
T. C. Peng 263

MF-3(3) The Effect of Oxidation on the Compressive Strength of Graphite
P. A. Thrower and J. C. Bognet 265

10:45 am, Wednesday, July 20

ADVANCES IN CARBON CHARACTERIZATION

Session CC-1

Dr. M. Inagaki, presiding

CC-1(1) Application of X-ray Measurements for Characterization of Artificial Carbons
E. Fitzer, K.-H. Köchling and G. Schwarz 267

CC-1(2) Raman Spectrum of Ground Natural Graphite
M. Nakamizo, M. Inagaki, H. Kakiyama and H. Honda 269

CC-1(3) Raman Spectra of Carbons and Their Intercalation Residue Compounds
A. Marchand and C. Garrigou-LaGrange 271

CC-1(4) Raman Spectra and Characterization of Carbon Materials
R. Vidano and D. B. Fischbach 272

CC-1(5) Raman Spectra, Effective Debye Parameter and Magnetoresistance
M. Nakamizo, M. Inagaki and Y. Hishiyama 274

CC-1(6) Force Constants for the Graphite Lattice
A. P. P. Nicholson and D. J. Bacon 276

10:45 am, Wednesday, July 20

CHEMICAL REACTIVITY AND SURFACES

Session CR-4

Dr. J. G. Hooley, presiding

CR-4(1) The Adsorption of Alcohols on Several Graphite Oxides
J. de D. López-González, A. Martín-Rodríguez, A. Martín-Pozuelo and F. Rodríguez-Reinoso 278

CR-4(2) The Kinetic Dependence of Iron Catalyzed Graphite Oxidation on Oxygen Potential
H. S. Isaacs 280

CR-4(3) The Behaviour of Hydrogen and Carbon Monoxide with Graphite Ferric Chloride
S. Parkash, S. K. Chakrabartty and J. G. Hooley 282

CR-4(4) Adsorption of Benzene on Exfoliated Graphite Between -70°C and -5°C
M. Coulon, Y. Khatir and L. Bonnetain 284

Page

N-2(4) Tensile Properties of Neutron-Irradiated Graphites
R. J. Price 242

N-2(5) Fatigue of Near-Isotropic Graphite: Influence of Stress Cycle
R. J. Price 244

8:30 am, Wednesday, July 20

PLENARY SESSION

"Carbon/Fiber Composites"

Professor R. J. Diefendorf
Rensselaer Polytechnic Institute
Troy, New York

9:45 am, Wednesday, July 20

ELECTRICAL AND THERMAL PROPERTIES

Session E-4

Dr. J. A. Woollam, presiding

E-4(1) Negative Magnetoresistance and Electrical Conduction in Glassy Carbon
S. Ho, R. Saxena and R. H. Bragg 246

E-4(2) Magnetoresistance of Disordered Carbons at Low Temperature
Y. Hishiyama, Y. Kaburagi and A. Ono 248

E-4(3) Band Theory of Pyrocarbons and Cokes
O. Gonzalez and A. Charlier 250

E-4(4) Low Temperature Magnetic and Thermal Properties of an Amorphous Carbon
F. Carmona, P. Delhaes, J. L. Tholence and J. C. Lasjaunias 252

E-4(5) Lattice Defects and Low Temperature Specific Heat Peaks in Soft Carbon and Polycrystalline Graphite
S. Mrozowski and A. S. Vagh 254

E-4(6) Magnetic Field Dependence of Specific Heat Peaks in Neutron Irradiated Polycrystalline Graphite
A. S. Vagh and S. Mrozowski 255

E-4(7) Specific Heat of Neutron Irradiated Glassy Carbon (GC 30) in the Intermediate Range of Temperatures 3-78°K
E. Michael, B. Myers and S. Mrozowski 256

9:45 am, Wednesday, July 20

ACTIVATED CARBON AND ADSORPTION

Session AC-2

Dr. P. L. Walker, Jr., presiding

AC-2(1) Saran Carbon--A Superior Adsorbent for Volatile Compounds
D. D. Schmidt and R. G. Melcher 257

AC-2(2) Charcoals as Catalyst Supports in the Trapping of Methylradioiodide (131)
V. R. Deitz 259

Page

9:45 am, Wednesday, July 20

MECHANICAL AND FRICTIONAL PROPERTIES

Session MF-3

Dr. J. L. Kaae, presiding

MF-3(1) Correlation of Strength with Physical Properties
W. C. Morgan and F. L. Becker 261

MF-3(2) Effects of Oxidation on the Mechanical Properties of Carbon/Graphite
T. C. Peng 263

MF-3(3) The Effect of Oxidation on the Compressive Strength of Graphite
P. A. Thrower and J. C. Bognet 265

10:45 am, Wednesday, July 20

ADVANCES IN CARBON CHARACTERIZATION

Session CC-1

Dr. M. Inagaki, presiding

CC-1(1) Application of X-ray Measurements for Characterization of Artificial Carbons
E. Fitzer, K.-H. Köchling and G. Schwarz 267

CC-1(2) Raman Spectrum of Ground Natural Graphite
M. Nakamizo, M. Inagaki, H. Kakiyama and H. Honda 269

CC-1(3) Raman Spectra of Carbons and Their Intercalation Residue Compounds
A. Marchand and C. Garrigou-LaGrange 271

CC-1(4) Raman Spectra and Characterization of Carbon Materials
R. Vidano and D. B. Fischbach 272

CC-1(5) Raman Spectra, Effective Debye Parameter and Magnetoresistance
M. Nakamizo, M. Inagaki and Y. Hishiyama 274

CC-1(6) Force Constants for the Graphite Lattice
A. P. P. Nicholson and D. J. Bacon 276

10:45 am, Wednesday, July 20

CHEMICAL REACTIVITY AND SURFACES

Session CR-4

Dr. J. G. Hooley, presiding

CR-4(1) The Adsorption of Alcohols on Several Graphite Oxides
J. de D. López-González, A. Martín-Rodríguez, A. Martín-Pozuelo and F. Rodríguez-Reinoso 278

CR-4(2) The Kinetic Dependence of Iron Catalyzed Graphite Oxidation on Oxygen Potential
H. S. Isaacs 280

CR-4(3) The Behaviour of Hydrogen and Carbon Monoxide with Graphite Ferric Chloride
S. Parkash, S. K. Chakrabartty and J. G. Hooley 282

CR-4(4) Adsorption of Benzene on Exfoliated Graphite Between -70°C and -5°C
M. Coulon, Y. Khatir and L. Bonnetain 284

Page

N-2(4) Tensile Properties of Neutron-Irradiated Graphites
R. J. Price 242

N-2(5) Fatigue of Near-Isotropic Graphite: Influence of Stress Cycle
R. J. Price 244

8:30 am, Wednesday, July 20

PLENARY SESSION

"Carbon/Fiber Composites"

Professor R. J. Diefendorf
Rensselaer Polytechnic Institute
Troy, New York

9:45 am, Wednesday, July 20

ELECTRICAL AND THERMAL PROPERTIES

Session E-4

Dr. J. A. Woollam, presiding

E-4(1) Negative Magnetoresistance and Electrical Conduction in Glassy Carbon
S. Ho, R. Saxena and R. H. Bragg 246

E-4(2) Magnetoresistance of Disordered Carbons at Low Temperature
Y. Hishiyama, Y. Kaburagi and A. Ono 248

E-4(3) Band Theory of Pyrocarbons and Cokes
O. Gonzalez and A. Charlier 250

E-4(4) Low Temperature Magnetic and Thermal Properties of an Amorphous Carbon
F. Carmona, P. Delhaes, J. L. Tholence and J. C. Lasjaunias 252

E-4(5) Lattice Defects and Low Temperature Specific Heat Peaks in Soft Carbon and Polycrystalline Graphite
S. Mrozowski and A. S. Vagh 254

E-4(6) Magnetic Field Dependence of Specific Heat Peaks in Neutron Irradiated Polycrystalline Graphite
A. S. Vagh and S. Mrozowski 255

E-4(7) Specific Heat of Neutron Irradiated Glassy Carbon (GC 30) in the Intermediate Range of Temperatures 3-78°K
E. Michael, B. Myers and S. Mrozowski 256

9:45 am, Wednesday, July 20

ACTIVATED CARBON AND ADSORPTION

Session AC-2

Dr. P. L. Walker, Jr., presiding

AC-2(1) Saran Carbon--A Superior Adsorbent for Volatile Compounds
D. D. Schmidt and R. G. Melcher 257

AC-2(2) Charcoals as Catalyst Supports in the Trapping of Methylradioiodide (131)
V. R. Deitz 259

9:45 am, Wednesday, July 20

MECHANICAL AND FRICTIONAL PROPERTIES

Session MF-3

Dr. J. L. Kaae, presiding

MF-3(1) Correlation of Strength with Physical Properties
W. C. Morgan and F. L. Becker 261

MF-3(2) Effects of Oxidation on the Mechanical Properties of Carbon/Graphite
T. C. Peng 263

MF-3(3) The Effect of Oxidation on the Compressive Strength of Graphite
P. A. Thrower and J. C. Bognet 265

10:45 am, Wednesday, July 20

ADVANCES IN CARBON CHARACTERIZATION

Session CC-1

Dr. M. Inagaki, presiding

CC-1(1) Application of X-ray Measurements for Characterization of Artificial Carbons
E. Fitzer, K.-H. Köchling and G. Schwarz 267

CC-1(2) Raman Spectrum of Ground Natural Graphite
M. Nakamizo, M. Inagaki, H. Kakiyama and H. Honda 269

CC-1(3) Raman Spectra of Carbons and Their Intercalation Residue Compounds
A. Marchand and C. Garrigou-LaGrange 271

CC-1(4) Raman Spectra and Characterization of Carbon Materials
R. Vidano and D. B. Fischbach 272

CC-1(5) Raman Spectra, Effective Debye Parameter and Magnetoresistance
M. Nakamizo, M. Inagaki and Y. Hishiyama 274

CC-1(6) Force Constants for the Graphite Lattice
A. P. P. Nicholson and D. J. Bacon 276

10:45 am, Wednesday, July 20

CHEMICAL REACTIVITY AND SURFACES

Session CR-4

Dr. J. G. Hooley, presiding

CR-4(1) The Adsorption of Alcohols on Several Graphite Oxides
J. de D. López-González, A. Martín-Rodríguez, A. Martín-Pozuelo and F. Rodríguez-Reinoso 278

CR-4(2) The Kinetic Dependence of Iron Catalyzed Graphite Oxidation on Oxygen Potential
H. S. Isaacs 280

CR-4(3) The Behaviour of Hydrogen and Carbon Monoxide with Graphite Ferric Chloride
S. Parkash, S. K. Chakrabartty and J. G. Hooley 282

CR-4(4) Adsorption of Benzene on Exfoliated Graphite Between -70°C and -5°C
M. Coulon, Y. Khatir and L. Bonnetain 284

Page

CR-4(5) Adsorption of Long Chain Electrolytes on Carbons
R. C. Bansal 286

1:30 pm, Wednesday, July 20
FIBERS AND COMPOSITES
Session F-4
Dr. R. Prescott, presiding

F-4(1) Surface Study of Carbon Fibres with Auger Electron Spectroscopy
F. Hopfgarten 288

F-4(2) Surface Characteristics of Pan Based Carbon Fibres
B. Rand and R. Robinson 290

F-4(3) Fiber Density Analysis by Density Gradient Technique
P. C. Pinoli and A. Ambrosio 292

F-4(4) Pore Analysis of Carbon Fabric by Density Gradient Technique
P. C. Pinoli and A. C. Johnson 294

F-4(5) Current Conduction Experiments with Single Carbon Fibers
I. R. McNab 296

F-4(6) Piezoresistance of Carbon Fibers
D. B. Fischbach and K. Komaki 298

F-4(7) Preparation and Electrical Properties of Graphite Fiber Nitrate
M. Endo, T. Koyama and M. Inagaki 299

F-4(8) The Mechanism of the Addition and Removal of Br_2 in a Carbon Fiber
J. G. Hooley and V. R. Deitz 301

1:30 pm, Wednesday, July 20
MESOPHASE, CARBONIZATION AND GRAPHITIZATION
Session MG-3
Dr. H. Marsh, presiding

MG-3(1) Aspects of Formation of Graphitizable Carbons from Blends of Pitch-Like Substances
H. Marsh, I. Macefield and J. Smith 304

MG-3(2) Compatibility of Pitch Fractions in Their Cocarbonization Process
I. Mochida, K. Amamoto, K. Maeda and K. Takeshita 306

MG-3(3) Relationships Between the Characteristics of Petroleum Feedstocks and the Graphitizability of Their Petroleum Cokes
M. Kakuta, M. Kooriki and Y. Sanada 308

MG-3(4) Influence of Sulfur and Metals on Mesophase Formation
S. Oi, T. Imamura, M. Komatsu, Y. Yamada, M. Nakamizo and H. Honda 310

MG-3(5) *Isotropic Coke Based on Reactive Tar from Coal Pressure Vaporisation*
H. Tillmanns and G. Pietzka 312

MG-3(6) Coke Formation Mechanisms in Selected Slurry Oils
H. C. Fritz, H. L. Hsu, L. I. Grindstaff and M. P. Whittaker 314

Page

MG-3(7) Graphitising Carbons from Coal via Solvent Extraction: Effects of Processing Conditions on Product Quality
G. M. Kimber 316

MG-3(8) Thermal Expansion of Microconstituents of Coke
J. E. Zimmer and J. L. White 318

MG-3(9) Thermogravimetric Investigation of the Carbonization of Some Pitches
G. W. Collett and B. Rand 320

MG-3(10) Structural Aspects of Mesophase Materials from Petroleum, Coal and Oil Shale
T. F. Yen 322

1:30 pm, Wednesday, July 20

INDUSTRIAL APPLICATIONS

Session I-3

Dr. W. A. Nystrom, presiding

I-3(1) Effect of Boron Carbide Addition on Some Properties of Hot-Pressed Polycrystalline Graphite Made from Coke Powder
K. Miyazaki, T. Hagio, K. Kobayashi and H. Honda 324

I-3(2) Effect of Hot-Pressing Temperature on Sintered Polycrystalline Graphite Made from Pitch Coke with B_2O_3 Addition
T. Hagio, Y. Matsushita, K. Kobayashi and H. Honda 326

I-3(3) Effect of B_2O_3 Addition on Sintering and Graphitization of Carbon Materials
K. Kobayashi, T. Hagio, K. Miyazaki, Y. Matsushita, S. Kondo, K. Iwata and H. Honda 328

I-3(4) Various Vibration Methods for the Forming of Carbon Products
S. Wilkening 330

I-3(5) The Influence of Quinoline Insoluble Pitch Constituents on the Impregnation Behavior
H. Tillmanns and G. Pietzka 332

I-3(6) Wettability of Carbon and Graphite by Metal Melts
B. Goetze and U. Rosenblatt 334

I-3(7) Calculation of Steady State Temperatures in Graphite Electrodes in an Electric Arc Steel Furnace
T.-L. Weng and E. J. Seldin 336

I-3(8) Adhesion Characteristics of Thin Vacuum Deposited Carbon Films
N. K. Agarwal, H. S. Shim and A. D. Haubold 338

3:45 pm, Wednesday, July 20

NUCLEAR APPLICATIONS

Session N-3

Mr. C. R. Kennedy, presiding

N-3(1) Design and Operation of a Graphite Creep Irradiation Experiment
R. L. Senn, W. H. Cook, J. A. Conlin and W. P. Eatherly. 340

N-3(2) Results of Irradiation Creep Testing Graphite at 900°C
C. R. Kennedy, W. H. Cook and W. P. Eatherly 342

Page

N-3(3) Irradiation Creep and its Flux Dependence on Near Isotropic Graphite at 850°C

H. Veringa and M. R. Cundy 344

3:45 pm, Wednesday, July 20

ADVANCES IN CARBON CHARACTERIZATION

Session CC-2

Dr. D. B. Fischbach, presiding

CC-2(1) Nondestructive Testing I: Correlation of Detectable Flaw Size with Grain Structure by Ultrasonic Techniques in Graphite

J. F. Rosendahl, J. T. Gill and L. D. Fiel 346

CC-2(2) Nondestructive Testing II: X-Ray Imaging of Graphite Precursors

J. T. Gill, J. F. Rosendahl and L. D. Fiel 348

8:30 am, Thursday, July 21

MICROMECHANICS AND MODELING

Session MM-1

Dr. B. W. Rosen, presiding

MM-1(1) The Effect of Aligned Matrix Material on the Mechanics of Cracked Fibers

E. L. Stanton 349

MM-1(2) A Physically Based Analytical Tensile Model for the Carbon-Carbon Composites

J. S. Evangelides 351

MM-1(3) Application of Fracture Mechanics for C/C-Composites

E. Fitzer and K. Karlisch 353

MM-1(4) Correlation of a Physically Based Statistical Theory of Fracture with Full Scale Ground Tests of Reentry Nosetips

J. D. Buch, J. G. Crose, R. L. Holman and T. E. Mack 355

8:30 am, Thursday, July 21

ACTIVATED CARBON AND ADSORPTION

Session AC-3

Dr. L. A. Jonas, presiding

AC-3(1) Compared Adsorptive Properties of Active Carbons from Olive Stones and Almond Shells

C. Berenguer, J. de D. López-González, F. M. Velchez and F. Rodriguez-Reinoso 357

AC-3(2) Retention of 2,4-Dichlorophenoxiacetic Acid by an Activated Carbon

A. Jiménez-López, J. de D. López-González and C. Valenzuela-Calahorro 359

AC-3(3) Adsorption of HCN and H_2O Vapor Mixtures by Activated and Impregnated Carbons

G. B. Freeman, P. J. Reucroft and C. T. Chiou 361

AC-3(4) Interaction of Ozonised Oxygen with Microcrystalline Carbons

B. R. Puri and V. M. Arora 363

Page

8:30 am, Thursday, July 21

ADVANCES IN CARBON CHARACTERIZATION

Session CC-3

Dr. D. B. Fischbach, presiding

CC-3(1) An Examination of Five Preferred Orientation Functions

W. S. Horton 365

CC-3(2) A Comparison of Optical Methods for Determining Preferred Orientation in Nearly Isotropic Pyrocarbon

D. W. Stevens 367

CC-3(3) X-Ray Studies of Graphitization of Glassy Carbon

S. Bose, R. Saxena and R. H. Bragg 369

CC-3(4) High Resolution Dark-Field EM Applied to Carbon Characterization Pan Fiber Microtexture

A. Oberlin, F. Molleyre and M. Bastick 371

9:45 am, Thursday, July 21

MICROMECHANICS AND MODELING

Session MM-2

Dr. B. W. Rosen, presiding

MM-2(1) Effects of Fiber Choice and Weave Geometry upon Cylindrical Weave Carbon/Carbon

J. J. Kibler 373

MM-2(2) Nonlinear Finite Element Analyses of Reentry Vehicle Graphite Nosetips

T. E. Mack and J. G. Crose 375

MM-2(3) Analytical Relationships Between Bulk Density and Pore Size in 3D Carbon-Carbon Composites

J. Jortner 377

MM-2(4) Application of the Jones/Nelson Nonlinear Stress-Strain Law to Reentry Graphite Survival Predictions

R. L. Holman, J. G. Crose and J. D. Buch 379

MM-2(5) Characterization of Carbon/Carbon Composites

R. J. Diefendorf 381

9:45 am, Thursday, July 21

CHEMICAL REACTIVITY AND SURFACES

Session CR-5

Dr. J. G. Hooley, presiding

CR-5(1) Glassy Carbon as a Catalyst Support

P. L. Walker, Jr., A. Oya and O. P. Mahajan 382

CR-5(2) Viscose Carbons: Modification of Thermal Decomposition of Viscose by Inorganic Additives

A. Capon and F. A. P. Maggs 384

CR-5(3) Activation of Fibrous Chars

F. A. P. Maggs, A. Capon and M. E. Smith 386

Page

9:45 am, Thursday, July 21

NUCLEAR APPLICATIONS

Session N-4

Mr. M. S. T. Price, presiding

N-4(1) Towards Density Determination of Pyrolytic Carbon Layers Deposited on Nuclear Fuel Microspheres
W. Delle, K. Koizlik, H. Nickel and E. Wallura 388

N-4(2) Structure of Pyrocarbon Coatings for Nuclear Fuel and Implications for Quality Assurance
M. S. T. Price 390

N-4(3) Improved Graphite Matrix for Coated Particle Fuel
D. Schell, K. Davidson, C. Hollabaugh, R. Reiswig and P. Wagner 392

N-4(4) Properties of Extruded Fuel Rods for HTGR Applications
R. L. Hammer, J. M. Robbins and W. P. Eatherly 394

N-4(5) Thermal Conductivity and Electrical Resistivity of Simulated Fuel Elements
J. P. Moore, R. S. Graves and W. P. Eatherly 396

N-4(6) Fabrication of Graphite Matrix Fuel for Pulsed Reactors
K. V. Davidson, D. H. Schell, C. H. Karnes and R. H. Marion 398

N-4(7) Thermal Treatment of HTGR Fuel
G. W. Weber and R. L. Beatty 400

N-4(8) Progress in the Irradiation of Carbon-Carbon Composites
E. J. Walker, L. F. Pain and P. B. Roscoe 402

10:45 am, Thursday, July 21

AEROSPACE APPLICATIONS

Session Ia-3

LtCol. J. M. McCormack, presiding

Ia-3(1) Effects of Matrix and Process Variations on Properties of 3-D Carbon-Carbon Composites
R. W. Seibold 404

Ia-3(2) Permeability, Porosimetry, and Microstructure of 3D Carbon-Carbon Composites
J. Jortner 406

Ia-3(3) Microstructural Features Which Influence the Ablation Performance of Carbon-Carbon Composites
D. A. Eitman 408

Ia-3(4) Influence of Carbon Polymorphs on Ablation of Graphitic Materials
A. G. Whittaker and J. S. Evangelides 410

Ia-3(5) Ablative Recession of 3D Carbon-Carbon Composites
J. Jortner, F. I. Clayton and R. W. Seibold 411

10:45 am, Thursday, July 21

MESOPHASE, CARBONIZATION AND GRAPHITIZATION

Session MG-4

Dr. K. J. Hüttinger, presiding

Page

MG-4(1) A Kinetic Study of the Transformation Graphite ⇌ Linear Carbon Forms by X-Ray Diffraction
A. G. Whittaker 413

MG-4(2) The Effect of Microporosity on Graphitizability of Glassy Carbon
J. L. Kaae 414

MG-4(3) Relation Between Sulfur Content and X-Ray Profile of Coke
Y. Yamada, S. Oi, M. Tsuchitani, M. Honda, K. Shibata, M. Nakamizo and H. Honda 416

MG-4(4) Graphitizability of Carbons Under 5 kbars Pressure
M. Inagaki and S. Naka 418

MG-4(5) Apparent Catalysis of Graphitization. IV. Effect of Titanium
H. N. Murty, D. L. Biederman and E. A. Heintz 420

MG-4(6) Graphitization of Thin Carbon Films
M. Oberlin, J. Goma and A. Oberlin 422

1:30 pm, Thursday, July 21

AWARD LECTURES

George Skakel Memorial Award:

Prof. Dr. E. Fitzer
Institut für Chemische Technik
der Universität Karlsruhe

Lecture: "From Silicon to Carbon"

Charles E. Pettinos Award:

Dr. L. S. Singer
Parma Technical Center
Union Carbide Corporation

Lecture: "The Mesophase and High-Modulus Carbon Fibers from Pitch"

3:45 pm, Thursday, July 21

BUSINESS MEETING

American Conference on Carbon

8:30 am, Friday, July 22

PLENARY SESSION

"Behavior of Metal Particles on Carbon in Various Gas Atmospheres"

Dr. R. T. K. Baker
Exxon Research & Engineering
Corporate Research Laboratory
Linden, New Jersey

9:45 am, Friday, July 22

INDUSTRIAL APPLICATIONS

Session I-4

Dr. W. E. Duggins, presiding

I-4(1) CERAPHITE, A Hard and High Strength New Carbon Material
C. Nakayama, M. Okawa and H. Nagashima 424

I-4(2) Production Scale Up of the GRAPHNOL N Process
P. G. Ruopp, L. D. Loch and L. A. Joo' 426

Page

I-4(3) The Microstructure of Vapor Deposited Carbon Films
H. S. Shim, N. K. Agarwal and A. D. Haubold 428

9:45 am, Friday, July 22
CHEMICAL REACTIVITY AND SURFACES
Session CR-6
Dr. J. G. Hooley, presiding

CR-6(1) Studies of the Rate of Oxidation of ATJ Graphite by Steam
R. D. Burnette, C. Velasquez, G. Hightower and K. Koyama. 429

CR-6(2) The Kinetics of the Carbon-Oxygen Reaction in Pyrolytic Graphites and Its Relation to the Degree of Orientation
J. de D. López-González, M. Rodríguez-Gallego, F. Rodríguez-Reinoso and L. Zurita-Herrera 431

CR-6(3) The Rate of Oxidation of Carbon Fibers in Air
B. H. Eckstein 433

9:45 am, Friday, July 22
MECHANICAL AND FRICTIONAL PROPERTIES
Session MF-4
Dr. J. L. Kaae, presiding

MF-4(1) Tensile Properties of AXF-5Q Graphite
L. D. Fiel, J. T. Gill, J. F. Rosendahl, R. A. McCormack and H. S. Starrett 435

MF-4(2) Elastic Constants of Graphite
C. R. Kennedy. 437

MF-4(3) The Room-Temperature Mechanical Properties of Boron-Doped Graphite
M. Eslick and D. J. Bacon 439

MF-4(4) Physical Properties of CDE Charcoal Cloth
F. A. P. Maggs, G. A. Robins and M. E. Smith 441

MF-4(5) Shear Deformation of 3D Carbon-Carbon Composites
J. Jortner. 443

MF-4(6) A Study of the Dependence of Physical Properties on Particle Size in Graphite
E. P. Kennedy and C. R. Kennedy 445

MF-4(7) The Temperature Dependence of Elastic Constants of Polycrystalline Graphite
J. D. Buch 447

10:45 am, Friday, July 22
CHEMICAL REACTIVITY AND SURFACES
Session CR-7
Dr. J. G. Hooley, presiding

CR-7(1) Oxidation Mechanisms of Carbon-Carbon Composites
H. W. Chang and R. M. Rusnak 449

CR-7(2) Activated Carbon Textiles
R. N. MacNair 451

Page

CR-7(3) Evaluation of Gasification Reactivities of Coals by Differential Thermal Analysis

C. Chow, H. M. Hawthorne, E. Peters and I. H. Warren 452

CR-7(4) Intercalation Properties of the Carbon Liners of Aluminum Reduction Cells

J. G. Hooley and P. T. Hough 454

CR-7(5) Kinetics of Pyrolytic Carbon Deposition at High Temperatures and Low Pressures

A. Wehrer, P. Wehrer and X. Duval 456

10:45 am, Friday, July 22

MESOPHASE, CARBONIZATION AND GRAPHITIZATION

Session MG-5

Dr. G. M. Kimber, presiding

MG-5(1) The Influence of the Type of Quinoline Insolubles on the Quality of Coal Tar Binder Pitch

D. R. Ball 457

MG-5(2) Use of Petroleum Residues as Binder Pitches - Relation of Fixed Carbon and Softening Point of Pitch with Component Properties and Correlation of Binding Power with Fixed Carbon of Its Components

H. Tanaka, T. Tano, E. Kitajima, Y. Yamada and H. Honda 458

MG-5(3) Chemical Changes during the Mild Air Oxidation of Pitch

J. Barr and I. C. Lewis. 460

MG-5(4) Pyrolysis Mechanism as Studied by Electron Microscopy, DTA, IR and ESR

A. Oberlin, M. Villey, A. Combaz, P. Rouxhet and R. Setton 462

MG-5(5) The Process of Carbonization and Graphitization of Petrographic Components of Hard Coals
Part I. Properties and Structure and the Coking Process of Petrographic Components of Hard Coals

S. Jasienko and H. Kidawa 464

MG-5(6) The Process of Carbonization and Graphitization of Petrographic Components of Hard Coals
Part II. The Changes of Properties and Structure of Cokes from Petrographic Components in the Process of Graphitization

S. Jasienko and H. Kidawa 466

EXTENDED ABSTRACTS

EFFECTS OF OXYGEN AND MOISTURE ON CARBON-COMPOSITE FRICTIONAL BEHAVIOR

N. A. Hooton and A. L. Courtney
The Bendix Corporation
Aircraft Brake & Strut Division, South Bend, Indiana

Introduction

Carbon-composite friction materials are state-of-the-art in aircraft brakes. They have demonstrated their ability to provide light weight, smoothly operating, long life systems which are capable of absorbing large quantities of energy while maintaining safe braking characteristics. Carbon materials also exhibit several unique properties which require specific consideration during the design of an integrated braking system. Among these are the tendency to show oxidation degradation at higher operating temperature, the susceptibility to friction reduction in the presence of moisture, and a slow speed (or static) friction coefficient which is sensitive to both temperature and the environment. These properties have been found to some degree in all of the carbon-composites evaluated at Bendix, including those fabricated by suppliers other than Bendix. The slow speed (static) behavior is of particular interest for aircraft with high residual thrust or those operating on aircraft carrier decks. This paper discusses the first phase of an investigation of such slow speed and static friction phenomena, and the role played by the environment in modifying such behavior.

Experimental

Testing was conducted on a small shaft dynamometer containing a specimen environmental chamber constructed so that a fixed flow rate of a chosen gas could be maintained around the friction specimens. The flowing also assisted in cooling the specimens between simulated braking engagements. The test specimens were carbon-composite rings 2-3/16 in. (5.56 cm) O.D. by 1-3/8 in. (3.49 cm) I.D. and 0.25 in. (0.64 cm) thick. For a given test, both rings were of the same composition. During this investigation the kinetic energy absorbed during a dynamic braking engagement (mass loading) was varied over the range of 130,000-1,000,000 ft.lb./lb. and the normal force was varied over the range of 30-540 psi. Initial sliding velocity of dynamic engagements was in the range of 20-60 ft./sec. A thermocouple for bulk temperature indications was imbedded in the stationary ring.

Increased moisture content in the atmospheres was obtained by blending dry gas with gas passed through a bed of distilled water. For each dynamic brake stop, records were made of generated torque, bulk temperature and time to complete the stop.

The test technique consisted of exposing the test rings to a series of identical simulated braking engagements in a chosen atmosphere, continuing until the dynamic friction coefficient was stable. At the completion of the stop, the normal force was allowed to remain applied, and as the cooling friction discs reached the desired temperature, sufficient force was exerted on a lever arm attached to the flywheel to initiate sliding and to continue relative motion through a circular arc of approximately 1 cm. Recordings of the generated torque were used to calculate the friction coefficients.

While results from the small dynamometer are qualitatively transferable to a full-scale brake system, the specific values for friction coefficient are not identical. Therefore, data on friction in this paper will be presented in relative terms to amply define the observed phenomena without inferring specific values to any brake system.

Results and Discussion

Carbon exhibits a dome shaped curve of static friction coefficient vs. temperature. Values for static friction at both high (+ 400°C) and low (< 150°C) temperatures are most frequently below the average dynamic friction generated during the immediately preceding stop. At all but the lowest temperatures there is no significant difference (independent of temperature) between the force required to initiate sliding and that required to sustain slow relative motion, and even near room temperature where an initial "spike" may occur in the torque measurement. The peak is almost always below the dynamic value. Further, the same temperature dependence of friction is observed if a continuous relative motion (~1 cm/sec.) is maintained during the complete cooling cycle. Repeated measurements taken at approximately 5 second intervals at 66°C gave no variation in friction, tending to rule out the effect of sliding distance.

The result of changing the atmosphere in the test chamber from air to nitrogen is shown in Figure 1. Little increase in friction at high temperatures is seen but the low temperature drop is completely eliminated. Figure 2 shows the effect on a different specimen of increasing the moisture content of a nitrogen atmosphere. A small but significant drop in friction at both high and low temperatures is seen. The effect of moist air is much greater as shown by the test presented in Figure 3. A moderately humid atmosphere results in the complete elimination of the dome effect. Also shown in Figure 3 is a static friction test on a specimen run in dry air but which followed the soaking of the specimen surfaces in liquid water for one minute prior to the dynamic stop. Sufficient water was contained in the specimens to reduce the maximum temperature obtained

during the dynamic stop. It is possible that sufficient moisture was still present in the sample tested at wet bulb 20°C for it to act in a similar fashion. The strong effect that the degree of prior work at the surface has on static friction near room temperature is shown in Figure 4. Here, a good relationship is found between static friction at 66°C and the product of mass loading and surface loading (average horsepower per square inch).

The mechanism of static friction is essentially mechanical in character. The drop in friction is related to conditions which ease the shearing of carbon or graphite platelets at the sliding interface. Although the reason for the high temperature drop is not understood, the reduction at lower temperatures appears to be clearly related to moisture. It is most enhanced by the presence of oxygen, generally accepted to be a requirement for any significant adsorption of water. The reduction in the presence of moist nitrogen is thought to be related to small amounts of oxygen being desorbed from the substrate during the high temperature portion of the braking engagement, although the interaction of water with possible nitrogen complexes is not ruled out. The decreasing value of room temperature static friction with increasing energy loading suggests that higher temperatures and longer cooling times in air increases moisture pickup.

This work is continuing with particular interest in separating the surface condition effects from moisture adsorption effects, and with further definition of the conditions responsible for the high temperature drop in static friction.

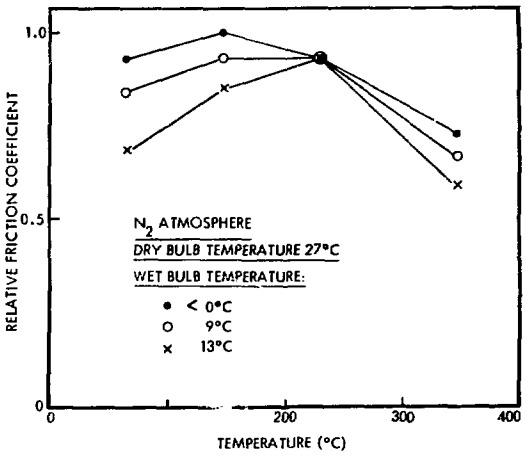


Fig. 2. Effect of Moist N_2 on Static Friction. Prior Dynamic Mass Loading - 580,000 Ft. Lb./Lb.

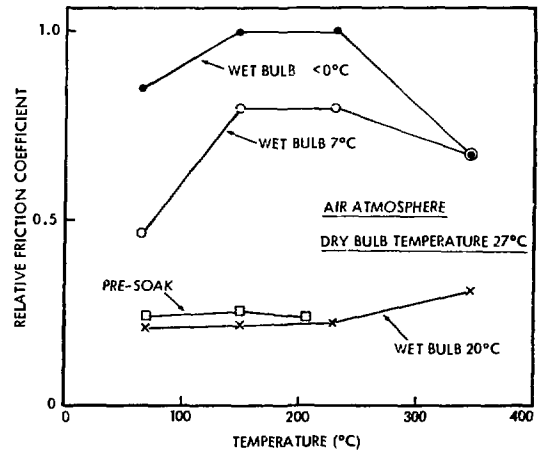


Fig. 3. Effect of Moist Air on Static Friction. Prior Dynamic Mass Loading - 580,000 Ft. Lb./Lb.

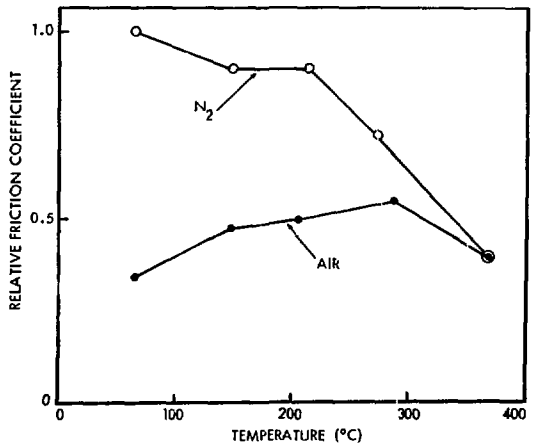


Fig. 1. Effect of Excluding O_2 on Static Friction. Prior Dynamic Mass Loading - 580,000 Ft. Lb./Lb.

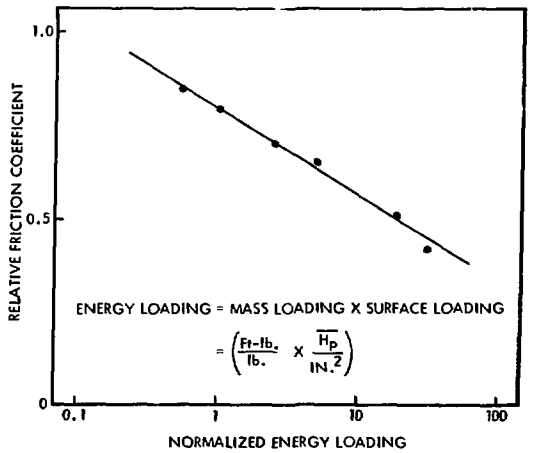


Fig. 4. Effect of Prior Energy Loading on Static Friction at 66°C.

ADSORPTIVE PROPERTIES OF CDE CHARCOAL CLOTH

By F.A.P. Maggs, M.E. Smith, and G.A. Robins
Chemical Defence Establishment, Porton Down, Salisbury, Wiltshire, UK

Summary

Data are reported for the adsorption of vapours and solutes on to charcoal cloth, under both dynamic and equilibrium conditions. BET N_2 areas are in the range 900 to 1660 m^2/g and saturation capacities are high, varying with the activity. In dynamic adsorption larger capacity at penetration is attributed to a rapid rate of adsorbate/solid interaction.

Introduction

CDE charcoal cloth is a new, high activity adsorbent in the form of a robust, flexible woven cloth composed entirely of charcoal (1, 2). It is produced in the form of 60 cm wide rolls in the CDE experimental plant, the degree of activation being varied to suit the requirement. This paper summarises the results of measurements of the adsorptive properties both under equilibrium and dynamic conditions. Physical properties are described in a further paper to this Conference.

Charcoal Activity

The adsorptive activity of the charcoal cloth may be varied as required during manufacture, and a range of samples are reported on here. To provide an assessment of activity, heats of wetting (3) in benzene and silicone fluid (2 cP) have been measured and are quoted for comparative purposes. Such data provide a measurement of not only the accessible surface area of carbons but also of molecular sieving (4), silicone fluid (molar vol. 433) being a much larger molecule than benzene (molar volume 80).

In practical situations, adsorbed moisture will influence adsorption behaviour; in certain cases measurements have therefore been made both with dry charcoal and with charcoal equilibrated with air at 80% RH (for brevity, "moist" charcoal). Where comparative data for granular charcoal is included, the results refer to two high quality nutshell charcoals (graded 14 x 25 BSS) of medium and high activity, referred to here as "granular" A and B.

Equilibrium Adsorption

Surface Areas

BET surface areas derived from $N_2/77^oK$ isotherms on numerous cloth samples taken from the experimental production runs gave BET areas in the range 900 - 1660 m^2/g. Typical examples are shown below.

Sample	Sil.2 HOW	BET Surface Area
Charcoal Cloth 1	113 j/g	1660 m^2/g
Charcoal Cloth 2	44 j/g	1350 m^2/g
Granular A	80 j/g	870 m^2/g

Pore Size

The heats of wetting (Table 1) showed the molecular sieve effect usually observed with charcoals (5). The increase in pore size arising from further activation was also clear, Cloth 146 having been subjected to the greater activation.

TABLE 1. Molecular Sieve Properties

Wetting liquid	Molar Volume ml mol^{-1}	Heat of Wetting j/g Cloth	
		107	146
Methanol	40.5	84	86
Chlorobenzene	101.7	67	72
Dekalin	154	42	60
Sil.1 cP	288	12	54
Sil.2 cP	433	5	43

Vapour Adsorption at Saturation Vapour Pressure

The adsorption of benzene, chlorobenzene and carbon tetrachloride at saturation vapour pressure have been measured by exposing dried, weighed samples to the respective liquids in an enclosure until equilibrium was observed. The results, given in Table 2, show that substantial amounts of vapour are adsorbed, spanning the range of good commercial charcoals. The Gurvitsch rule is followed, and volumes adsorbed rise with increasing activity.

Vapour Adsorption under Dynamic Adsorption Conditions

Vapour concentrations in the 1 to 10 mg/l range in air, set up by standard methods, were passed through layers of charcoal cloth held in a suitable jig. Effluent concentrations were measured by use of a calibrated CDE halogen detector or by an FID equipment. Experiments were made with both dry and moist air over an air velocity range of 0.5 - 8.0 cm/s.

In all cases the usual linear variation of penetration time T (and hence weight adsorbed w at penetration) with the weight of charcoal cloth W (or number of layers) was observed. It was found that $w = FCT = N_o(W - W_c)$ where F = volume flow, c = influent concentration, W_c = critical bed and N_o = equilibrium uptake.

For the adsorption of chlorobenzene, styrene, halothane and carbon tetrachloride on dry cloth W_c was small, corresponding to less than one layer (0.5 mm) of cloth. Increase in the moisture content of the cloth led to an increase in the critical bed to 2 to 4 layers, depending on the system. The value of N_o was unchanged for the strongly adsorbed chlorobenzene (b.p. 132°C), but was reduced for halothane (b.p. 56°C). Critical flow rate and critical concentration were also small, being nearly zero for dry cloth. In consequence, beds consisting of more than 5 layers (0.25 cm deep) showed a notable constancy of the amount adsorbed when flow and concentration are varied. Change in cloth activity around the average had only a minor influence on the general behaviour.

Experiments with only 1 and 2 layers show that appreciable removal of vapour occurred even in such shallow beds. Thus for the system 0.5 mg/l styrene, velocity 2 cm/s, 2 layers (1 mm) moist charcoal cloth, penetration times of 24 and 68 min were recorded at penetration levels of 1% and 10% respectively.

TABLE 2. Vapour Adsorption at Saturation Vapour Pressure

Charcoal	Heat of Wetting joule/g		% Vapour adsorbed w/w			Vapour adsorbed cc/g		
	Benzene	Sil.2 cP	Benzene	Carbon Tet.	Chloro-benzene	Benzene	Carbon Tet.	Chloro-benzene
Cloth P57 (1)	105	19	35.4	62.2	43.1	0.404	0.391	0.390
Cloth P57 (4)	120	123	67.3	127.8	86.9	0.767	0.804	0.786
Cloth P66	96	88	45.8	81.7	57.0	0.522	0.514	0.514
Cloth P68	69	10	29.2	52.9	36.8	0.333	0.333	0.333
Cloth P69	69	72	44.7	75.9	55.0	0.510	0.477	0.499
Granular A	130	80	-	63.5	47	-	0.40	0.43
Granular B	155	125	-	101.0	68	-	0.63	0.62

Comparison with Granular Charcoal

Experiments measuring the penetration times of chlorobenzene with granular charcoal and charcoal cloth show that under identical conditions (concentration 9 mg/l, velocity 8 cm/s, 80% RH) the main difference lay in the critical bed depth, which was in the weight ratio of 1:5. Thus the weight of granules required to give T = 10 min was 250% greater, and for T = 30 min 175% greater, than that of charcoal cloth of similar activity.

In experiments with the anaesthetic halothane (6) (concentration 43 mg/l), a 3.7 cm depth of dry granules gave the same penetration time as 1 cm (20 layers) of dry charcoal cloth at flow rates of 1 to 4 cm/s. With moist charcoal, at a linear velocity of 1 cm/s the % uptake on charcoal cloth was 300% greater, and at a linear velocity of 4 cm/s 200% greater than on granules.

Adsorption from Aqueous Solution

(a) Equilibrium uptake

The adsorption isotherms for adsorption of phenol, acetic acid and dimethoate (an insecticide) from aqueous solution were measured for both charcoal cloth and a granular charcoal. The isotherms for the two charcoals were very similar, showing that the charcoal activities were the same. Rates of adsorption were also measured and a first order rate constant (K) calculated. With both phenol and acetic acid, K was 1.6 min^{-1} for the charcoal cloth, but only 0.1 min^{-1} for the granules. For the larger dimethoate molecule, K for cloth was 0.012 min^{-1} and 0.0011 min^{-1} for the granules. Thus the rate of adsorption on charcoal cloth was more than an order of magnitude the greater.

(b) Dynamic adsorption

The removal of phenol (concentration 50 g/l) from a solution flowing through a 2 cm diameter column of charcoal was measured by following the change in effluent concentration with time (7). Experiments were made with 2 g charcoal cloth, 2 g and 7 g granular charcoal. When the effluent concentration had risen to 1/1000 of the influent concentration, the weights adsorbed by the three columns were calculated as: 2 g charcoal cloth column: 37% w/w; 2 g granular column: zero; 7 g granular column: 17% w/w.

In experiments at two further influent concentrations, equilibrium adsorption on charcoal cloth was also calculated from extended experiments: these values corresponded closely with those determined in the earlier equilibrium experiments.

Discussion

Under equilibrium conditions CDE charcoal cloth has the properties of an adsorptive carbon, exhibiting molecular sieving and capacity depending on the extent of activation. The capacity of high activity charcoal cloth exceeds that of good commercial granular charcoals. However, the small critical bed for charcoal cloth found in all dynamic adsorption experiments indicates a high rate of adsorption in comparison with granular charcoals, a conclusion borne out by rate measurements in solution. To this is attributed the large adsorptions observed at initial penetration of test vapour or solutes. In dynamic adsorption the influence of pre-adsorbed moisture is notably less than with granular charcoal.

References

(1) UK Patent 1,301,101.

(2) USA Patent 3,849,332.

(3) Maggs F.A.P., Schwabe P.H., and Williams J.H., J.Sc.Inst., 39, 364-366, 1962.

(4) Bond R. and Maggs F.A.P., Fuel, 28, 172-175, 949.

(5) Maggs F.A.P., "Manufactured Carbons", Chapter 4, 81-101, Pergamon Press, 1968.

(6) Maggs F.A.P. and Smith M.E., Anaesthesia, 30, 30-40, 1975.

(7) Maggs F.A.P. and Smith M.E., Shirley Institute Conference on Fibrous Materials for the Filtration of Liquids, 1975.

MEASUREMENT OF LONG-TERM STRESS-RELAXATION IN CARBON-CARBON COMPOSITES

R S Pickering, MOD(PE), AWRE, Aldermaston, Reading RG7 4PR, England

Introduction

The factors which contribute to the phenomena of creep and stress-relaxation in carbon/carbon composites are not fully understood but it is reasonable to assume that such processes as fibre fracture, fibre/matrix debonding and matrix cracking are involved. Knowledge of creep and stress-relaxation behaviour is important in any long term engineering uses of these relatively new materials.

The measurement of flexural stress-relaxation in thin carbon composites is more complex than the related measurement of creep, due to absence of easily measured stress-dependent parameters. In particular the condition of constant strain prohibits the measurement of non-elastic movement, and methods of detecting stress-relaxation depend on either (a) measuring the change in some other physical property which varies with internal stress or (b) the direct measurement of internal stress, keeping the change in strain to as small a value as possible.

A number of possible methods of measuring stress-relaxation are described and reviewed.

Methods Using the Instron Universal Testing Machine

The specimen is stressed in flexure, either directly or by use of a removable jig in which the specimen can be locked at a pre-determined stress. Both methods enable a stress history of the specimen to be obtained, but the first monopolises the Instron and the second involves handling difficulties which gave rise to unacceptable errors. Neither method involves appreciable creep, but both are dependent on the stability of the Instron load-cell.

Direct Loading Method

The specimen is stressed in flexure by means of a weight hung at its mid-point and the deflection is measured by means of a micrometer mounted above the specimen. To measure stress-relaxation, small increments are periodically removed from the original weight, sufficient to bring the deflection of the specimen back to its original value. Equipment requirements are minimal, but removal of weights is difficult without disturbing the assembly. Automated versions are expensive and elaborate. The specimen is also subject to unlimited creep between stress checks.

Cantilever Method

The specimen is contained in a special jig in which it is stressed in flexure by means of a load hung on a cantilever acting on the specimen at its mid-point. At a pre-determined load, the specimen can be locked in position by means of screws operating an electrical circuit, and the load can be removed. When a stress reading is taken, one screw is unlocked slightly and a load is gradually applied until contact with the second screw is broken. The difference in the two loads gives the stress-relaxation.

Development of this method is still proceeding, but precision construction may be necessary for the production of accurate data.

Electrical Resistance Method

This method depends on the assumption that the electrical resistance of a material varies with its internal stress. Periodic resistance measurements are made on a specimen locked at a pre-determined stress.

Experiments have shown that any resistance changes are comparable with errors in measurement, and therefore assessment of stress changes by this method is not feasible.

Hydraulic Method

In this method stress is applied to the specimen by means of a hydraulically operated piston. Any relaxation of stress in the specimen will be communicated to the hydraulic fluid and can therefore be measured. The main disadvantages are (1) the possibility of fluid leakage (2) the possibility of creep of the specimen. In addition, a pressure gauge would be required, capable of measuring very small pressure changes at the standing pressure changes at the standing pressure in the fluid.

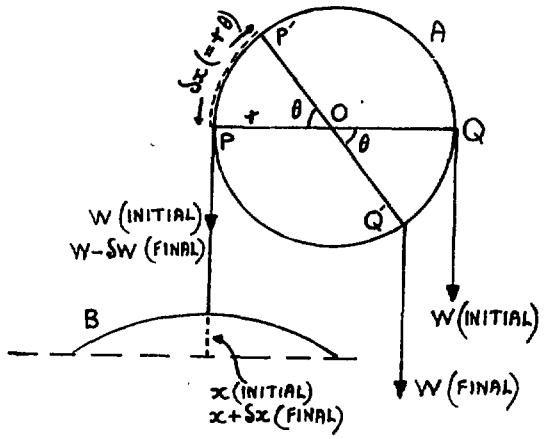
Piezoelectric Method

Stress is applied to the composite via a piece of piezoelectric material in compression, and is measured by a voltage generated in the piezoelectric. The charge on the piezoelectric leaks away after a short time, however, and thus the method has no long-term value. Use of the piezoelectric material in a capacitative mode offers no advantages over other capacitative systems. Stray capacitance in the vicinity would obscure small changes in stress-related capacitance.

The resonant frequency of piezoelectric material is lowered if the material is suitably loaded. Use of the material to stress composites might be considered to constitute such a loading, enabling the applied stress to be measured from the resonant frequency, and hence loss of stress to be found from the subsequent rise in resonant frequency.

Simultaneous Measurement of Creep and Stress-Relaxation

Stress-relaxation may be regarded as creep occurring under variable stress. Thus a material under stress, free of any constraint which would restrict changes either in its internal stress or in strain, is assumed to undergo simultaneous creep and stress-relaxation. This situation is partially obtained in the arrangement shown below:



In the diagram, A is a weightless disc of radius r, pivoted at its centre O on frictionless bearings. Initially, the specimen B, of modulus E, is flexurally strained by a load W to a deflection x. W is initially attached to the circumference of the disc at Q and can move to any point Q' on the circumference as the disc turns. B is attached to the circumference by a theoretical string initially at P. As the disc turns, the point of attachment of the string moves round the circumference to P' in such a way as to always apply the stress to the specimen from P.

Free of constraint, the specimen will undergo simultaneous creep and stress-relaxation. At time t, the point of attachment of the string moves to P' such that PP' (and QQ') both subtend an angle θ at O. The modulus of the specimen B is now E_t. The stress in the specimen falls by δW (load equivalent) and the deflection increases by δx. The following equations can be derived for δW and δx:

Setting δx = 0 (the stress-relaxation condition of constant strain)

$$\delta W = W\left(1 - \frac{E_t}{E}\right) + W\left(1 - \frac{x \cos\theta}{x + r\theta}\right)$$

Setting δW = 0 (the creep condition of constant stress) gives:

$$\delta x = x\frac{E}{E_t} - 1 = x\frac{x + r\theta}{x\cos\theta} - 1$$

Thus the only quantity which is required to be measured at time t is the angle θ, which would be probably $< 1^0$. The practical realisation of the arrangement is likely to be difficult. A degree of constraint exists on the free movement of stress and strain (ie if δx = rθ then δW = W(1 - cos θ), but it is possible to calculate either (1) stress-relaxation at zero creep, or (2) creep at zero stress-relaxation.

Acoustic Transducer Method

Stress is applied to a carbon composite specimen in flexure, by means of a thin steel wire in longitudinal tension. The stress in the wire is related to that in the carbon and can be measured by means of the acoustic frequency emitted when the wire is suitably excited. Since the system must always be in equilibrium, any loss of stress in the carbon will be accompanied by a loss of stress in the wire (assumed to be behaving elastically), and hence by a lowering of the emitted frequency. Since the longitudinal extension of the wire is very much less than the flexural extension of the carbon, small losses of stress of the carbon-wire system will result in very small contractions of the wire. The system thus exhibits a close approximation of that of zero creep of the carbon.

This is the principle method which is being used at the present time. Excitation of the wire is carried out by means of short electromagnetic pulses, causing the wire to vibrate in its fundamental mode and generate a current of identical frequency in the sensing/excitation head. The frequency is given as a digital read-out of the period of 100 oscillations. Stress-relaxation of the wire is minimised by prior heat-treatment under tension. It has been found that readings of frequency tend to vary with atmospheric conditions ie temperature and humidity. The precise relationships and the reasons for them have not yet been established.

Direct Acoustic Method

This method depends on the possibility that the frequency emitted by a flexurally strained bar is related to the internal stress in the bar. Excitation would probably be carried out by passing a variable frequency alternating current through the bar, which would be located between the poles of a permanent magnet. The main attraction of this method would be the elimination of the wire transducer.

Conclusions

(a) An acoustic method, using a wire transducer (Sect 9), has been adopted for the measurement of flexural stress-relaxation in carbon-carbon composites.

(b) A mechanical method using cantilever loading is under development with a view to adoption as a standard means of measurement.

(c) A piezoelectric method is under consideration for development.

(d) A method of simultaneous measurement of creep and stress-relaxation appears promising theoretically, but is likely to be very difficult to realise in practice.

GRAPHITE LAMELLAR COMPOUNDS WITH THALLIUM(III) CHLORIDE AND THE BROMIDES OF THALLIUM(III), CADMIUM, MERCURY, IRON(II) AND URANIUM(V)

E. Stumpp and R. Nicss
Technische Universität Clausthal, Anorganisch-chemisches Institut
Clausthal-Zellerfeld, Federal Republic of Germany

Introduction

In contrast to the extensive studies of the intercalation of metal chlorides the reaction of graphite with metal bromides has received scant attention.

At present more than thirty metal chlorides are known to intercalate into the graphite lattice but only few graphite/metal bromide compounds have been reported until now.

CROFT claimed to have prepared $AlBr_3$-graphite [1]. Recently SASA et al. [2] have investigated the reactivity of graphite with $AlBr_3$ in detail. The formation of ternary compounds was observed with a maximum composition of $C_9AlBr_3 \cdot Br_2$ and a lamellar structure of the 1st stage. Independently BALESTRERI [3] has obtained similar results. She investigated also the system graphite $GaBr_3$-Br_2 and succeeded in obtaining ternary compounds analogous to the graphite/$AlBr_3$ compounds. $AuBr_3$ is reported to give a 1st stage compound in which planar Au_2Br_6 molecules are located in the center between the carbon layers [4]. HEROLD et al. have tried unsuccessfully to intercalate graphite with other metal bromides [4]. In commenting on their results they expressed the opinion that it may be possible to prepare other graphite/metal bromide compounds under proper conditions.

In fact we have revealed that $TlBr_3$, $CdBr_2$, $HgBr_2$, $FeBr_2$ and UBr_5 do form intercalation compounds. The present paper gives some experimental and structural details of the new compounds. In order to draw a comparision with graphite/metal chloride compounds we have done a detailed study of the system graphite-$TlCl_3$-Cl_2. Results obtained from these investigations are given first. Apart from CROFT's report [1] of the occurance of a graphite/$TlCl_3$ compound there is no information concerning its composition or structure.

Graphite/$TlCl_3$. Experimental

Purified natural graphite (flakes) from Passau, Germany, was used. Anhydrous $TlCl_3$ was prepared by dehydrating $TlCl_3 \cdot 4H_2O$ using $SOCl_2$. Several methods were explored to synthesize $TlCl_3$-graphite:
I heating graphite and $TlCl_3$ or TlCl in sealed tubes filled with chlorine vapour (table 1, samples 1-5);
II before sealing liquid chlorine (2 ml) have been condensed onto the reaction mixture (sample 6);
III refluxing a solution of $TlCl_3$ in $SOCl_2$ with graphite with or without bubbling chlorine through the solution (sample 7); IV heating $TlCl_3$ and graphite with $SOCl_2$ in sealed tubes (sample 8). The samples were washed with a solution of chlorine in methanol in which $TlCl_3$ and TlCl are soluble. With sample 6 $TlCl_3$ and graphite were separated by flotation in liquid chlorine. Sample 6a is the same as 6 but washed with chlorine-methanol solution. 6b has been obtained from 6a by keeping several weeks in an evacuated vessel.

Results

It is shown from table I that the amount of intercalated $TlCl_3$ and the chlorine to thallium ratio is dependent on the procedure employed. The intercalated $TlCl_3$ is considerably more stable than the free $TlCl_3$ which decomposes above 100 °C. For the 1st stage I_c was determind to be 977 pm and for the 2nd stage 1311 pm.

Table 1.

Compositions of Graphite/$TlCl_3$ Compounds

Sample	Reaction temp. °C	Reaction time (h)	Composition	Stage
1	80	15	no reaction	
2	120	44	$C_{18.7}TlCl_{3.4}$	1+2
3	120	80	$C_{12.1}TlCl_{4.1}$	1
4	120	110	$C_{11.8}TlCl_{3.4}$	1
5	150	30	$C_{15.1}TlCl_{3.8}$	1
6	150	140	$C_{8.7}TlCl_{4.1}$	1
6a			$C_{11.6}TlCl_{4.4}$	1
6b			$C_{11.7}TlCl_{3.4}$	1
7	75	24	$C_{10.9}TlCl_{3.2}$	1
8	140	30	$C_{8.2}TlCl_{3.1}$	1
9	60	48	$C_{25.3}TlBr_{5.2}$	
9a			$C_{25.3}TlBr_{3.4}$	
10	60	100	$C_{21.8}TlBr_{5.3}$	
11	120	10 d	$C_{19.5}TlBr_{3.5}$	
12	150	48	$C_{18.6}TlBr_{3.4}$	

Graphite/$TlBr_3$. Experimental

TlBr and graphite were given into bromine. This mixture was heated in sealed tubes. The samples were washed with a solution of bromine in methanol.

Results and Discussion

The compositions of some samples are given in table 1. $TlBr_3$-graphite resembles $AlBr_3$- and $GaBr_3$-graphite in forming ternary compounds. The composition of sample 9 may be formulated as $C_{25.3}TlBr_{3.2} \cdot Br_2$. When kept in a vacuum it released bromine and a substance with the composition $C_{25.3}TlBr_{3.4}$ remained. All listed compounds are of the 2nd stage type but with slightly different I_c values: 1358 pm (sample 9), 1358 (10), 1343 (11), 1340 (12). For compound 9 the

carbon layer spacing containing $TlBr_3$ is 1358 - 335 = 1023 pm. This is exactly the same value reported by SASA [2] for $C_9AlBr_3 \cdot Br_2$. It was found to be 1000 pm for $C_{24}AlBr_{3,3}$ and our X-ray studies give a value of 1005 pm for sample 12. These similarities indicate that the structures of the two intercalated metal bromides closely resemble one another. It is likely that $AlBr_3$ and $TlBr_3$ are isomorphous. The structure of $TlBr_3$ is unknown.

$TlBr_3$-graphite has an unexpected high thermal sta[illegible]ty. Free $TlBr_3$ decomposes at room temperature to in[illegible]-mediate compounds and finely to TlBr. As op[illegible] to this $TlBr_3$-graphite can be heated to 12[illegible] without decomposition. Obviously $TlBr_3$ is st[illegible]ized by intercalation.

Graphite/$TlCl_3$/$TlBr_3$

By treating a 2nd stage graphite/$TlBr_3$ compound with $TlCl_3$ in refluxing $SOCl_2$ a 1st stage compound with the composition $C_{12,5}TlCl_{1,8}Br_{1,6}$ was obtained. As X-ray studies confirmed there is a regular sequence of $TlCl_3$-carbon-$TlBr_3$-carbon layers. Similar compounds with two different metal chlorides have been prepared previously [5].

Graphite/$CdBr_2$ and Graphite/$HgBr_2$

Intercalation compounds with $CdCl_2$ and $HgCl_2$ have been prepared by RÜDORFF et al. [5]. Since $CdBr_2$ and $HgBr_2$ have layer lattice structures resembling the $CdCl_2$ structure it was to be expected that this bromides can form graphite lamellar compounds. Indeed, we succeeded in obtaining graphite/$CdBr_2$ and graphite/$HgBr_2$ compounds by heating the anhydrous metal bromides with graphite in the presence of bromine. Attempts to intercalate these metal bromides in the absence of bromine were unsuccessful. The products were washed with dilute HNO_3 to remove excess $CdBr_2$ and with acetone to remove $HgBr_2$.

Only a representative compound is mentioned: $C_{15,5}CdBr_{2,06}$, prepared at 500 °C, I_c = 1330 pm, 2nd stage. $C_{23,8}HgBr_2$, prepared at 100 °C, I_c = 1684 pm, 3rd stage. $CdBr_2$ and $HgBr_2$ can also be intercalated in refluxing nitromethan. Products with the compositions $C_{28,6}CdBr_{2,2}$ and $C_{25}HgBr_{2,1}$ were obtained. They have both a 3rd stage structure I_c = 1662 pm and I_c = 1688 pm.

Graphite/$FeBr_2$

Heating of $FeBr_3$ or $FeBr_2$ with graphite in the presence of bromine results in various compounds depending on the experimental conditions. Mixed compounds with $FeBr_3$ and $FeBr_2$ can be prepared. A product with the composition $C_{18}FeBr_{2,0}$ was obtained by heating anhydrous $FeBr_2$ with graphite in a sealed tube filled with bromine vapour up to 350 °C. It was identified to be a 2nd stage with I_c = 1328 pm.

It is generally said that a metal halide can only react with graphite in its highest oxidation state. This example demonstrates that this is not a necessary condition.

Graphite/UBr_5

Like other bromides with the metal in a high formal oxidation state UBr_5 has a low stability. Although UBr_5 is soluble in liquid bromine we did not succeed in intercalating UBr_5 in refluxing bromine. Positive results were obtained by heating UBr_5 with graphite under a high bromine pressure at 300 °C. The compound with the highest UBr_5 amount had the composition $C_{38}UBr_{5,1}$. This compound was a mixture of a 2nd and 3rd stage (I_c = 1328 and 1645 pm).

Conclusion

The present investigations have shown that there is a great similarity between graphite/metal chloride and graphite/metal bromide compounds. It is likely that many other metal bromides can react with graphite. However, the total number of the members of this class of graphite lamellar compounds will be always smaller than the number of graphite/metal chloride compounds. This would be expected because the electronegativities of chlorine and bromine are different and because the metal bromides are thermal less stable than the chlorides. More metal chlorides are known than metal bromides.

For intercalation of metal halides the presence of halogen is a necessary condition. The intercalation reaction can be interpreted in terms of an electron-transfer process, the graphite acting as an electron donor the halogen and in certain cases the metal halide as an electron acceptor. For intercalation of metal chlorides chlorine or bromine may be used, for bromides, of course, only bromine is applicable.

We have investigated the intercalation of many metal chlorides in the presence of bromine. Always only the 2nd stage has been obtained with such metal chlorides which form the 1st stage if the intercalation occurs in a chlorine atmosphere at the same temperature. Therefore, we suppose that genuine graphite/metal bromide compounds can form at best the 2nd stage structure. There is a close relationship between the intercalates of acids and metal chlorides [6,7]. If sulphuric acid is intercalated using chlorine as oxidising agent the 2nd stage in obtained, with bromine only the 3rd stage is formed [8]. SASA et al. concluded that the 1st stage graphite/$AlBr_3$ compound may be bromine graphite stabilized by $AlBr_3$.

References

1. R.C.CROFT, Austral. J. Chem. 9 201 (1956)
2. T.SASA, Y.TAKAHASHI and T.MUKAIBO Bull. Chem. Soc. Japan 45 2250 (1972)
3. C.BALESTRERI, Thèse, Nancy 1973
4. C.BALESTRERI, R.VANGELISTI, J.MELIN, A.HEROLD C.R. Acad. Sc. Paris, Ser.C, 279 279 (1974)
5. W.RÜDORFF, E.STUMPP, W.SPRIESSLER, F.W.SIECKE Angew. Chemie 75 130 (1963)
6. A.BOECK and W.RÜDORFF, Z.anorg.allg.Chem. 392 236 (1972)
7. E.STUMPP and K.D.WAGERINGEL, Carbon Conf. 1976 Baden-Baden, Extended Abstracts p. 147
8. W.RÜDORFF and U.HOFMANN Z.anorg.allg.Chem. 238 1 (1938)

THE STATE OF WATER ON PURE AND SILICON-ALLOYED LTI-CARBONS*

T-H. Chiu and E. Nyilas
Avco Everett Research Laboratory, Inc.
Everett, MA 02149

and

F. J. Micale
Center for Surface and Coatings Research, Lehigh University
Bethlehem, PA 18015

The state of water attached to surfaces assumes an important role when, among others, these materials are placed in contact with a biological environment. This is particularly true for a low temperature isotropic (LTI) or silicon-alloyed (SLTI) carbon surface contacting blood in devices implanted in humans. Under these conditions, the adsorption of flexible macromolecules such as native proteins takes place, and the mechanism as well as the energetics of protein sorption is affected by the degree to which water is structured on those surfaces.

Microparticulate adsorbents composed of either 97.3% pure LTI-carbon or, 96.7% pure SLTI-carbon containing on the order of 10% by weight silicon, were obtained from discs which were prepared at the Medical Products Div., General Atomic Co. by deposition of the corresponding types of carbon on ultrathin graphitic substrates. The pulverization of both types of discs, which was carried out over extended periods of time, was performed in non-metallic equipment to avoid any contamination.

Both LTI- and the SLTI-carbon adsorbents were polydisperse particles measuring $\leq 1\mu$ in the SEM. Specific surface area (Σ) determinations performed by B.E.T. multipoint N_2 adsorption at -195°C gave 109.2 m^2/g for the pure LTI-carbon and 52.8 m^2/g for SLTI-carbon. In both cases, these Σ's have been disproportionately greater than the specific surface area that can be estimated (viz., 10-20 m^2/g) based on the particle sizes observed and the density of the materials. This has indicated the presence of internal porosity in both types of adsorbents, which, in the case of LTI-carbon, is consistent with the established internal micromorphology of that substance.[1] The value of Σ obtained for the SLTI-carbon, indicating of a smaller degree of porosity, is consistent with the known effects of silicon-alloying on pyrolytic carbon microstructure. To determine the pore size and shape distributions of both adsorbents, (a) the measured hysteresis between their 25°C water vapor adsorption and desorption isotherms, and (b) the pressurized mercury penetration technique[2] were utilized. Analyses of these data revealed that, in both powders, their porosity is constituted by "ink-bottle" pores. The same analyses gave 27.7 and 17.8 m^2/g, respectively, for the LTI- and SLTI-carbon adsorbents as their surface areas which are exclusive of the internal surface area associated with the "ink-bottle" pores. The relatively greater degree of internal porosity in the LTI-carbon adsorbent is substantiated by the fact that its ratio between its B.E.T. surface area and "pore-free" area (3.9) is greater than that obtained for SLTI-carbon powder (3.0).

For each of the 2 microparticulate adsorbents, the 0°, 25° and 37°C water vapor adsorption isotherms were determined using a vacuum quartz-spring balance described elsewhere.[3]

For both the LTI- and SLTI-carbon adsorbents, their 25° and 37°C heats of immersion were also determined in (a) pure water, $h_I(SLW)_T$, and (b) a sodium acetate/HCl buffer, $h_I(SLB)_T$, having a pH= 7.4 and an ionic strength of 0.05. These heats were measured using a custom-built, isothermal-jacketed thermistorized microcalorimeter system having a sensitivity of $\pm$ 1 x 10^{-5}°C when charged with 100 ml of liquid volume. Details of the design, specifications and operation of this instrument have been described elsewhere.[4]

The 25° and 37° microelectrophoretic mobilities of each of the 2 adsorbents were determined in the buffer specified above. These experiments were performed in a calibrated precision-bore glass capillary cell having a ground optical polished flat. For each adsorbent, the mobilities of an average of 12-14 particles were individually determined, after all particles > 1μ were allowed to settle out. All mobility values obtained at 37°C have been corrected to 25°C according to standard methods.

All water vapor adsorption isotherms which have been obtained at the 3 specified temperatures, are of Type II for both the microparticulate LTI- and SLTI-carbon adsorbents. Consistent with the internal porosity found in both materials, determination of their heats of water vapor adsorption in the first statistical monolayer can not be performed according to the B.E.T. method. For both adsorbents, every isotherm plotted in terms of the B.E.T. function vs. relative pressure deviates from linearity at values of $p_T/p_T^o \geq 0.1$. In fact, when plotted up to $p_T/p_T^o = 0.3$, the B.E.T. isotherm of SLTI-carbon appears to be parabolic.

Comparison of the water vapor adsorption and desorption isotherms of the LTI-carbon powder did not indicate hysteresis up to $p_T/p_T^o \simeq 0.3$, and those of the SLTI-carbon up to $p_T/p_T^o \simeq 0.4$. Thus, the application of standard thermodynamic functions which imply equilibrium conditions is justified in the range up to those relative pressures. Differential isosteric heats of adsorption have been computed using $q_{st} = (RT_2T_1/T_2 - T_1) \ln (p_1/p_2)$ where T_2 is taken as either 310.1°K or 298.1°K, with T_1 = 273.1°K, and p_1 and p_2 denote the measured equilibrium pressures at the respective temperatures. With this set of q_{st} values and the computable free

*This work was performed with support from the Biomaterials Program, Devices and Technology Branch, Division of Heart and Vascular Diseases, National Heart, Lung, and Blood Institute, under Contract NIH-N01-HV-3-2917.

energies of sorption, changes in entropy, and the entropy of sorbed layers have been determined.

Within the relative pressure range specified above, each of the isosteric heat curves of LTI-carbon powder adsorbents which were activated either at 25° or 37°C, display 2 peaks as a function of surface coverage. The first peak is quite sharp, and is centered at a coverage of 2×10^{13} molec/cm^2, with a maximum heat of adsorption that is about 1.5 Kcal/mole greater than Q (~ 10.5 Kcal/mole), the latent heat of condensation of water vapor. The second peak which is flatter but more broad, is centered at 2.5×10^{14} molec/cm^2, with a maximum ~ 1.2 Kcal/mole > Q. The peaks indicate the presence of 2 types of heterogeneous (viz., non-carbon) active sites on the LTI-carbon surface, which are capable of binding water in an ordered state. In the domain of these peaks, the differential and integral entropies of water sorbed onto LTI-carbon are significantly below the entropy value of bulk liquid water at the corresponding temperatures. At surface coverages > 4×10^{14} molec/cm^2, q_{st} rapidly approaches the value of Q indicating the absence of interaction between water and the LTI-carbon surface.

The microcalorimetrically-determined 25° and 37°C heats of immersion of the LTI-carbon powder into pure water are, respectively, -60.7 ± 4.7 erg/cm^2, and -62.6 ± 4.7 erg/cm^2, which are statistically indistinguishable indicating no temperature-dependence. As compared to Graphon, which is a graphitized carbon black with a comparable B.E.T. N_2 surface area of 95.0 m^2/g and an $h_I(SLW)_{25°}$ -32.4 ± 4.0 erg/cm^2,[5] the LTI-carbon surface is more polar. After conversion into the appropriate units, the integral of the q_{st} function of LTI-carbon corresponds to about 85% of the measured heat of immersion values of that adsorbent. In view of the fact that q_{st} and $h_I(SLW)$ have been determined by entirely different methods, the correspondence is satisfactory.

The 25° and 37°C electrophoretic mobilities of LTI-carbon particles are $u_e(25°) = -1.63 \pm 0.17$ and $u_e(37°$ corr. to 25°$) = -1.45 \pm 0.24 \mu$-sec^{-1}-V^{-1}cm. Since prior to these measurements all particles < 1μ were allowed to settle, the mean radius of those whose mobility has been determined, a ~ 2.5×10^{-5}cm. It can be shown that, in the buffer used, the thickness of the Debye-Hückel double layer, 1/K ~ 12.5×10^{-8} cm indicating that the ionic atmosphere surrounding these particles ≪ a. This justifies application of the Helmholtz-Smoluchowski equation to compute the charge density of LTI-carbon particles, $\sigma^e \simeq 1.1 \mu$Coul/cm^2 which converts to 6.9×10^{12} sites/cm^2. Taking that water vapor interacts with all potential binding sites regardless of whether these are on the particle surface or inside of "ink-bottle" pores, but charged sites inside of these pores can not contribute to electrophoretic mobility, the ratio between 2×10^{13} cm^{-2}, the surface number density of active sites binding water with the relatively greatest energy, and the computed charged site density given above is 2.9. This value compares favorably with 3.9, which is the ratio between the total B.E.T. and "pore-free" surface areas noted earlier for LTI-carbon. Based on these data, it can be assumed that the sites on the LTI-carbon surface, which are binding water with energies equal to that of an H-bond and indicate the negative charge of these particles, are of the carboxylic acid type.

The differential isosteric heat curves of water vapor sorption on the SLTI-carbon powder which was activated at either 25° or 37°C, also display 2 peaks. The first of these is centered at a coverage ~ 2×10^{13} molec/cm^2 with a maximum energy of about 1 Kcal/mole > Q and the second at ~ 2×10^{14} molec/cm^2 with 2 Kcal/mole in excess of Q. At coverages > 5×10^{14} molec/cm^2, q_{st} falls below the value of Q, and the integral entropy of sorbed water becomes greater than that of the bulk liquid at corresponding temperatures. This indicates that, except for a relatively low surface number density of hydrophilic sites, the rest of an SLTI-carbon surface is "hydrophobic" as compared to that of pure LTI-carbon. This is substantiated by the fact that both heat of immersion values of SLTI-carbon into pure water, $h_I(SLW)_{25°} = -1.48 \pm 3.50$ and $h_I(SLW)_{37°} = -52.55 \pm 3.54$ erg/cm^2, are smaller than those of pure LTI carbon.

Since the state of silicon atoms in LTI-carbon has not been clarified, only the following information can be derived about the type of functional groups present on SLTI-carbon surfaces. The absence of temperature-dependence in the $h_I(SLW)$'s of SLTI carbon implies that the mechanism of water attachment to the binding sites of this surface could be similar to that exhibited by the active sites of pure LTI-carbon. However, the calorimetrically-determined difference, $h_I(SLB)_T - h_I(SLW)_T$ measures the energy of attachment of Na^+ counterions from the buffer to the adsorbent particles. For the SLTI-carbon, these differences are -8.9 and -13.2 erg/cm^2 at 25° and 37°C, respectively, whereas for LTI-carbon they are greater, by a factor ~ 2, viz., -16.8 and -25.1 erg/cm^2 at the corresponding temperatures. The electrophoretic mobilities of SLTI-carbon particles are $u_e(25°) = -1.40 \pm 0.2$ and $u_e(37°$ corr. to 25°$) = -1.58 \pm 0.15 \mu$-sec^{-1}-V^{-1}cm, which are statistically indistinguishable from those of pure LTI-carbon particles, indicating approximately equal charge densities. In this case, the smaller values of $h_I(SLB)_T - h_I(SLW)_T$ obtained for the Na^+ binding of SLTI-carbon, imply smaller binding energies per site which, in turn, suggests that the type of its functional groups may not be identical to those on the pure LTI-carbon. This is corroborated by the fact that the heats of sorption of native human γ-(7S)-globulin which have been microcalorimetrically measured as presented in a companion paper,[6] are smaller on the SLTI surface under identical conditions.

REFERENCES

1. Kaae, J. L., J. Biomed. Mater. Res., 6, 279 (1972).
2. Orr, C. Jr., Powder Technol., 3, 117 (1970).
3. Nyilas, E., Chiu, T-H., Lederman, D. M., and Micale, F. J., "The State of Water Adjacent to Glass," in "Colloid and Interface Science," Vol. III., pp. 471-484, M. Kerker, editor, Academic Press, Inc., New York, NY (1976).
4. Nyilas, E., Chiu, T-H., and Herzlinger, G. A., Trans. Amer. Soc. Artif. Int. Organs, 20, 480 (1974).
5. Lavell, J. A., and Zettlemoyer, A. C., J. Phys. Chem., 71, 414 (1967).
6. Nyilas, E., and Chiu, T-H., "Adsorptive Properties of Human γ-Globulin on Pure and Silicon-Alloyed LTI-Carbons," paper presented at the 13th Carbon Conference, Irvine, CA, July 1977.

DIFFUSION COEFFICIENTS OF Br_2, HNO_3, and $PdCl_2$ IN GRAPHITE

M. B. Dowell
Union Carbide Corporation, Carbon Products Division
Parma Technical Center, Parma, Ohio 44130

Bromine, nitric acid, and palladium dichloride react, at sufficiently high vapor pressures, with graphite to form second stage $C_{16}Br_2$ [1], second stage $C_{48}{}^{+}NO_3{}^{-}\cdot 3HNO_3$ [2] and third stage $C_{18}{}_{.7}PdCl_2$ [3]. Kinetics of bromination of graphite have been studied in some detail [4-6], but rates of intercalation of HNO_3 and $PdCl_2$ have not yet been studied from the same kinetic point of view. Comparative studies of rates of intercalation might be expected to clarify mechanisms of intercalation and to permit useful generalizations. Nitric acid, palladium chloride, and bromine were chosen for study because they intercalate respectively as a two dimensional liquid-like layer [6], a disordered two dimensional solid, and an ordered solid[1]. Higher stage intercalates of bromine and nitric acid are also known, and it is of interest to know whether changes in rate of diffusion attribute to the formation of discrete stages can be observed.

Cylindrical wafers of stress annealed, highly oriented pyrolytic graphite used in these experiments have mosaic spreads (FWHM) ≤ 2 deg. Weight gains of graphite wafers suspended in HNO_3 and Br_2 vapors are monitored continuously by a recording microbalance, and rates of weight gain in HNO_3 vapor are monitored using a derivative computer. Temperature of the wafer is maintained $\sim$3 deg higher than that of the intercalant reservoir by which the vapor pressure of intercalant is fixed. Graphite wafers are exposed to $PdCl_2$ vapor by packing them in $PdCl_2$ powder in a quartz boat and heating in flowing Cl_2.

Weight gains M_t at time, t, during intercalation are plotted as fractions of the ultimate weight gain M_∞ corresponding to formation of the lowest stage compound for Br_2 and $PdCl_2$ in Figure 1 and for HNO_3 in Figure 2. Figure 1 shows an initial "induction period" during which little weight gain occurs, and a region in which M_t/M_∞ increases linearly with $t^{\frac{1}{2}}$ as expected for a diffusion process. The "induction period" region has been omitted for clarity's sake from Figure 2, which shows a third region, during which M_t/M_∞ increases more slowly with time than in the second region. Diffusion coefficients, D, calculated from the expression[5]

$$(1)\quad \frac{M}{M_\infty} = \frac{4}{\pi^{\frac{1}{2}}}\left(\frac{Dt}{r^2}\right)^{\frac{1}{2}} - \frac{Dt}{r^2} - \frac{1}{3\pi^{\frac{1}{2}}}\left(\frac{Dt}{r^2}\right)^{3/2}$$

where r is the radius of the wafer, are shown in Table I. Rates of intercalation increase linearly with $t^{-\frac{1}{2}}$ when the contribution of $t^{\frac{1}{2}}$ is small, as expected from the time derivative of Equation 1 and as shown in Figure 3 for a typical bromination reaction. Nitration can thus be attributed to a process characterized by a single diffusion coefficient up to $M_t/M_\infty = 0.50$, a weight gain corresponding to formation of Stage III graphite nitrate, and bromination can be characterized by a single diffusion coefficient at least up to $M_t/M_\infty = 0.25$.

X ray diffraction scans of graphite wafers exposed to $PdCl_2$ vapor until $M_t/M_\infty \approx 0.5$ and then quenched show only the (00ℓ) reflections of Stage III $C_{18}{}_{.7}PdCl_2$. No higher stage compound is observed; indeed, none is known. Electron microprobe analysis of the cleavage surface of such a wafer yields the plot of Cl_2 intensity versus radial distance shown in Figure 4. The pronounced reaction front and absence of lower-stage compounds shown here, and the linearity of M_t/M_∞ shown in Figure 1, are expected for a process characterized by a single diffusion coefficient.

The diffusion coefficient of HNO_3 in graphite at 30°C increases with increasing HNO_3 vapor pressure as shown in Table I, and seems in fact to be proportional to vapor pressure. The diffusion coefficient of $PdCl_2$ increases with increasing vapor pressure of $PdCl_2$ and with increasing temperature. Values of log D_{PdCl_2} fall closely on a straight line when plotted versus 1/T. The activation energy for diffusion calculated from the slope of this line is approximately 35 kcal/mole. For comparison, the activation energy for diffusion of Br_2 in graphite is approximately 6 kcal/mole. [7]

References

1. T. Sasa, Y. Takahashi and T. Mukaibo, Carbon 9, 407 (1971).
2. A. R. Ubbelohde, Proc. Roy. Soc. (London) A304, 25 (1968).
3. Yu. N. Novikov, V. A. Postnikov, Ya. V. Salyn, V. I. Nefedov and M. E. Volpin, Izv. Akad. Nauk. SSSR, Ser. Khim (1973) 1689. [Bull. Acad. Sci. SSSR, Ser. Chem. (1973) 1653.]
4. J. G. Hooley, Canadian J. Chem. 40, 749 (1962).
5. J. G. Hooley and J. L. Smee, Carbon 2, 135 (1964).
6. J. G. Hooley, W. P. Garby and J. Valentin, Carbon 3, 7 (1965).
7. T. Mukaibo and Y. Takahashi, Bull. Chem. Soc. Japan 36, 625 (1963).
8. D. E. Dixon, G. S. Parry, and A. R. Ubbelohde, Proc. Roy Soc. 291A, 324 (1966).

Table I

Diffusion of Intercalants into Highly-Oriented Pyrolytic Graphite

Intercalant	Vapor Pressure, Torr	Intercalation Temperature °C	D, cm²/min.
Br_2	258	30	1.47×10^{-6}
HNO_3	81	30	203×10^{-6}
	81	40	133×10^{-6}
	37	30	85×10^{-6}
$PdCl_2$	2.10×10^{-4}	416	0.16×10^{-6}
	1.04×10^{-3}	450	0.52×10^{-6}
	8.82×10^{-3}	500	2.46×10^{-6}

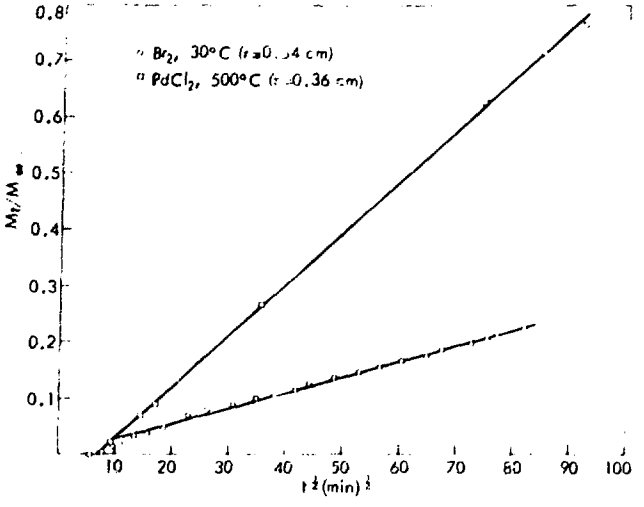


Figure 1. Increases of Br_2 and $PdCl_2$ with $t^{\frac{1}{2}}$.

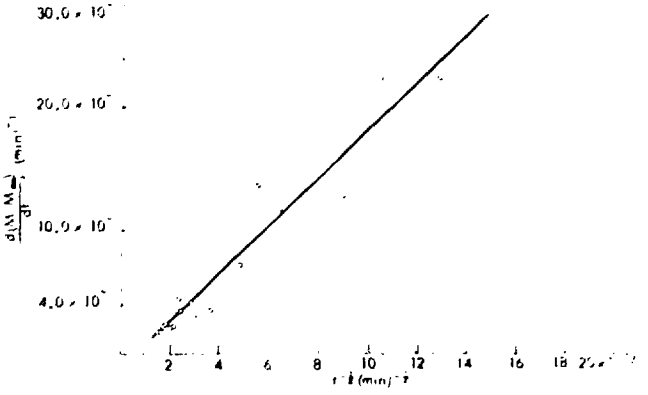


Figure 3. Rate of bromination at 30°C as a function of $t^{\frac{1}{2}}$.

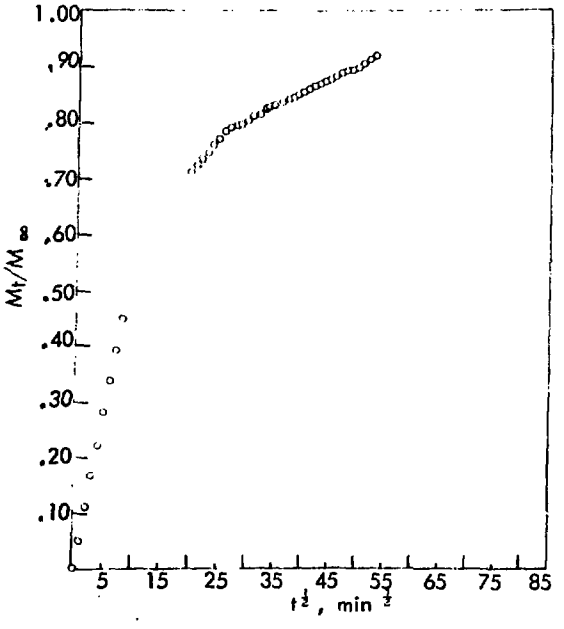


Figure 2. Increases of HNO_3 with $t^{\frac{1}{2}}$.

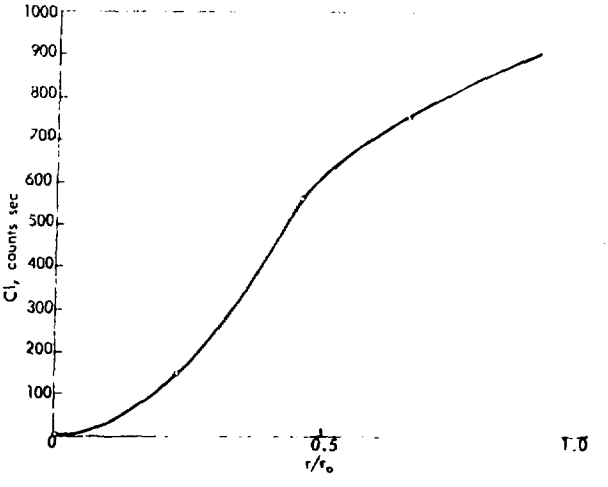


Figure 4. Chlorine concentration of a graphite wafer exposed to $PdCl_2$ until $M_t/M_\infty \approx 0.50$ then quenched, as a function of fractional distance r/r_o from the center of the wafer.

DIAGNOSIS OF MATRIX QUALITY IN CVD INFILTRATED CARBON-CARBON BY IN-PROCESS MONITORING AND NONDESTRUCTIVE EVALUATION

E. R. Stover and J. A. Roetling
General Electric Company, Re-Entry and Environmental Systems Division
Philadelphia, Pa. 19101

Introduction

A carbon-carbon composite material developed for re-entry applications utilizes a 3-D orthogonal preform, comprising about one-half of the volume, which is initially CVD infiltrated and surface ground before adding a graphite matrix. Impregnation with pitch and carbonization above 600°C at 100 MPa, followed by graphitization to 2750°C, provides adequate densification in 4 to 6 cycles. Ablation tests have shown that performance varies with matrix quality, particularly residual porosity, which can vary due to thermal history during the pressure bake. Procedures were developed to monitor the material during successive process cycles and to evaluate porosity distribution in the finished billets nondestructively.

Gradients in Density and Porosity

The isothermal CVD infiltration of the preforms (typically 10x10x20 cm) results in an initially high density at the surface, which develops a lower final density compared with the billet core, because CVD films on the filaments block penetration of pores in the fiber bundles by the pitch. Figure 1 illustrates porosity data obtained on samples cut from different locations in billets, using either liquid or gas permeation. Normally, open porosity as well as density is lower near the surface. However, in some samples (upper left in Fig. 1), low density in the core was associated with high open porosity, apparently as a result of bubble formation in the impregnant within the billets during the autoclave processing.

Measurements during Processing

Most of the processing discussed here was conducted at the Y-12 Plant, Union Carbide Corp. Nuclear Div., Oak Ridge, Tenn., where the cycles were first developed, and at the Battelle Columbus Laboratories. Later cycles at GE-RESD were accomplished with thermocouples placed within billets or adjacent pitch; these data showed a significant thermal lag compared with autoclave chamber temperatures, which had been used to control the pressure-impregnation-carbonization cycles in earlier processing.

Weight and dimension data on each billet, provided to GE-RESD after each process step, provided a basis for evaluating the adequacy of autoclave heating in the absence of accurate material temperature data. The density increase in each cycle followed a consistent trend with the available open porosity, as illustrated by Figure 2. The billets in one run had abnormally high densities, shown in the figure, because of a heater failure, and weight loss during subsequent graphitization was high. The "coke" lost in graphitization, calculated by dividing the weight lost during graphitization by the weight gained in the preceding autoclave cycle is shown as % CLIG in the figure. Even in normal runs, this factor varied with location of billets in the autoclave and with the size of the load, indicating differences in maximum temperature in the material even though cycles were nominally the same. When the cycle was modified to provide additional time at maximum temperature and pressure, lower "CLIG" values confirmed that billets had reached higher temperatures.

Work sponsored by the Air Force Materials Laboratory, Wright-Patterson Air Force Base, Ohio.

3-Dimensional Radiometry

Unusual heating conditions in one autoclave resulted in abnormalities not adequately detected by changes in weight and density. Subsequent studies with many thermocouples in a can have shown that significant temperature gradients can occur. In one set of runs the top half of billets set on end in the can contained a porous core, but the pitch displaced remained in outer portions of the billet, leaving the average bulk density unaffected. This condition was first identified by precision radiometric density apparatus and a 3-dimensional analysis of the data.

Figure 3 illustrates the normal density gradient found in blocks cut from a slab through a billet. "Core" and "edge" average densities represent this gradient. Such densities were calculated from the relative absorption of radiation in a well-collimated 0.64 cm diameter beam, centered at stations representing the centers of equal-sized prisms in the billet, equated to the measured bulk density (Figure 4). For the 10x10 cm section billets, 4 rows on both "X" and "Y" faces were normally used, although 8 rows combined with "Z" direction data have been used to establish the gradients with better precision. The reproducibility of the procedure and adequacy of the counting statistics at each station have been established by evaluating billets without CVD in which the true gradients are small. A simple analysis of the in-line density gradients to evaluate core vs. edge density has been refined by an iterative computer program which provides the best set of densities for all of the internal prism positions (usually cubes) matching the measured absorptions at each station.

Figure 5 illustrates core vs. edge density averages down the length of both normal and abnormal billets, which also provided samples for some of the density and porosity comparisons in Figure 1. Good agreement has been found between measured densities of core samples and those predicted from the radiometry, providing confidence in the nondestructive evaluation of porosity gradients in this material.

Acknowledgments: W. Mueller, A. E. Oaks, T. M. Hollenbeck and D. G. Breskman, G. E.; Maj. H. E. Keck, AFML; R. Paluzelle, Y-12, UCCND, and W. Chard, Battelle Columbus Laboratories, made particularly significant contributions to this work.

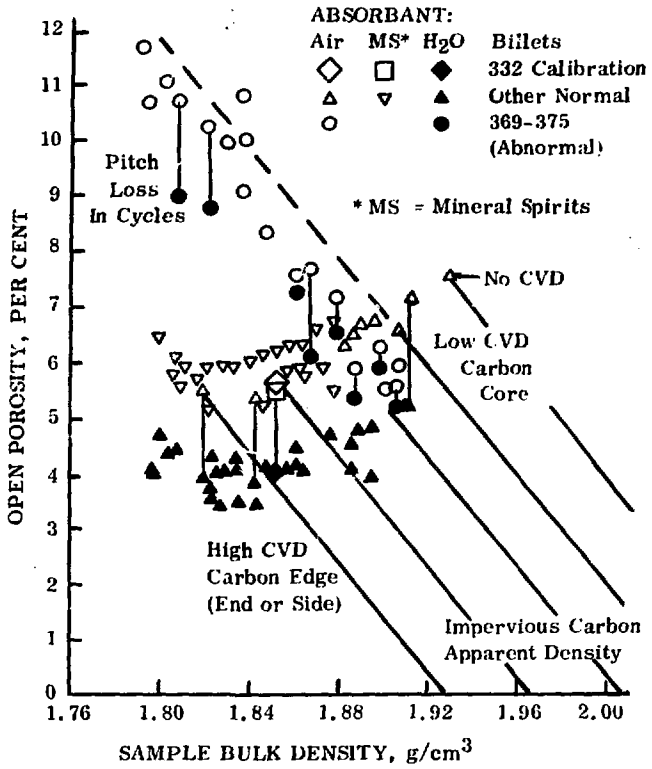


Fig. 1. Comparative Open Porosity Data Obtained by Different Methods, and Densities in Different Billet Locations. (MS Data provided by H. Littleton, Southern Research Institute.)

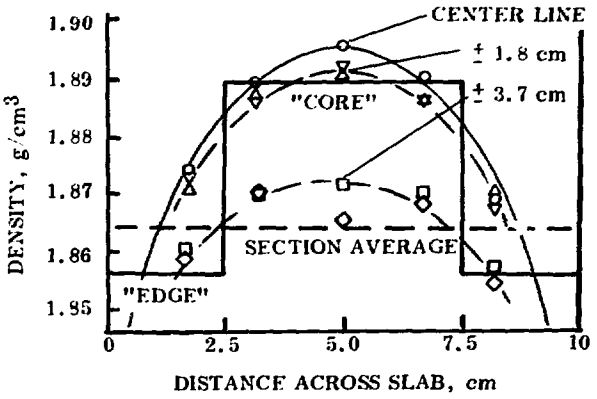


Fig. 3. Bulk Density of 25 (5x5) Blocks in a Slab, and Average "Edge" and "Core" Densities.

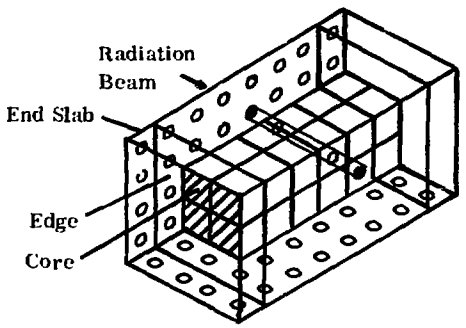


Fig. 4. Typical Stations for Radiometric Analysis Showing Calculated "Core".

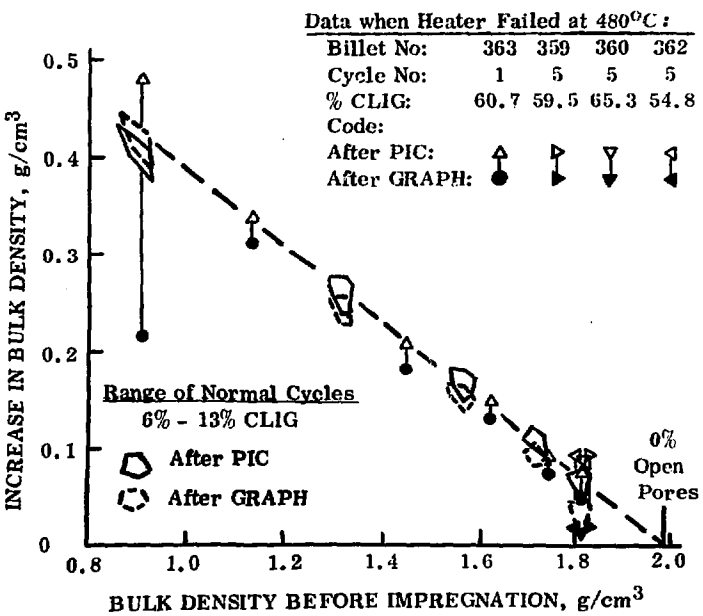


Fig. 2. Densification in Normal and Abnormal Cycles.

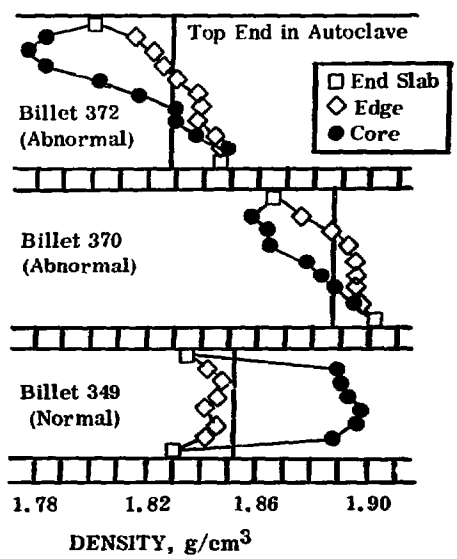


Fig. 5. Radiometric Edge and Core Densities at 2.54 cm Stations along the Length of Billets. Bar is Billet Average.

EFFECT OF SUBSTRATE FIBER ORIENTATION ON CHEMICAL VAPOR DEPOSITED (CVD) NEEDLED FELT CARBON-CARBON COMPOSITES*

J. L. Irwin
Sandia Laboratories
Albuquerque, New Mexico 87115

Introduction

Previous material development conducted by Sandia with chemical vapor deposited (CVD) composites has resulted in successful atmospheric reentry of carbonized felt/carbon matrix heatshields.[1,2] CVD/felt conical shapes are made by first fabricating a needled rayon felt substrate, which is subsequently carbonized and CVD infiltrated to the desired density.

Conical shapes had previously been fabricated in two separate rayon fiber orientations as illustrated in Figure 1. The two configurations were placed for cutting conical batts with or across the fiber orientation as shown in the figure. The preferential alignment of short rayon fibers in the two different fiber orientations resulted in strength differences as noted in Table I. The type 2 configuration has been used for all later reentry testing.

Thermal stresses produced during reentry are a critical parameter for CVD/felt materials. The factors of safety of the type 2 cone during a typical reentry are shown in Figure 2. As noted, the factor of safety for the circumferential direction is lower than the longitudinal direction. If the circumferential strength of the type 2 cone could be improved by combining the fiber orientations shown in Figure 1, it was theorized that the circumferential factor of safety could be increased. This paper describes an experimental study that was accomplished to investigate the effect of different fiber orientations on the carbon-carbon composite properties.

Experimental

Conical shapes were fabricated for this study because it had been found from previous studies [3] that CVD/felt flat plates do not produce representative properties of conical shapes. The seamless rayon felt cones were produced by applying batts of carded felt material over a mandrel and needling each applied batt until the desired thickness and density were obtained. The felt cones having an average bulk density of 208 to 240 kg/m^3 (.208 to .240 gm/cc) were fabricated from 5.5 denier, 0.038 meter (1.5 inch) long viscose rayon fibers. Conical rayon shapes were fabricated to represent types 1 and 2 of Figure 1, and a combination of these two types using alternate plies of types 1 and 2. The cones were subsequently carbonized and infiltrated to an approximate density of 1810 kg/m^3 (1.81 gm/cc) by the isothermal CVD technique. Heat treatment to 3273°K for two hours followed the infiltration. One each of the type 1 and type 2 cones and two of the combination types were used in this evaluation.

Samples were cut from the finished shapes for evaluation and destructive tests. In addition to non-destructive evaluation (NDE) of the cones, evaluation and testing included metalurgical examination of the CVD matrix, x-ray diffraction, ablation testing, tensile and compressive testing, and thermal conductivity and thermal expansion measurements. Mechanical properties and thermal expansion measurements for the longitudinal and circumferential directions and thermal conductivity for the perpendicular (radial) direction were obtained at room and elevated temperatures.

Results and Discussion

The three different types of cones had similar physical properties (metallurgical, x-ray diffraction density, NDE).

Figure 3 shows the tensile strength in the longitudinal direction for the cones as a function of temperature. The longitudinal strengths of the combination type cones are approximately equal to the strength of the type 2 cone. The type 1 cone, although having a lower longitudinal strength than the other two cone types evaluated in this study, had approximately seventy percent greater strength than cones made previously as type 1 (Table I). The reason for this anomaly is being studied. The room temperature circumferential strengths of type 1 and the two combination cones were approximately the same (28.6-29.4 MN/m^2), and the type 2 strength was, as expected, lower (24.8 MN/m^2).

Figure 4 shows the thermal expansion of types 1 and 2 construction and one of the combination type cones for the longitudinal and circumferential directions. The types 1 and 2 construction have thermal expansions in the longitudinal and circumferential directions which are the reverse of each other, whereas the thermal expansion for the combination type of construction is between these values.

Ablation results from arc plasma tests indicated that all materials were similar in ablation performance. No significant differences in thermal conductivity were noted.

While detailed thermal stress calculations (as accomplished for the data presented in Figure 2) must be performed to fully assess the thermal stress capability of the CVD/felt material, a thermal stress figure of merit value is a useful technique for comparing different types of the same material. This figure of merit can be defined as:

$$FOM = \frac{(\text{Tensile Strength})(\text{Thermal Conductivity})}{(\text{Modulus})(\text{Coef. of Thermal Expansion})}$$

Increasing values of this parameter are a measure of increasing thermal stress resistance. The figure of merit values shown in Figure 5 for the longitudinal and circumferential directions were obtained for properties at 2200°K. The figures of merit in each direction for the combination type of cone construction are more equal than for the type 2 construction and are higher than for either the type 1 or type 2 cones. The higher figures of merit for the combination type cones indicate that the higher circumferential stress would be lowered without raising the stress in the other direction.

*This work was supported by the U. S. Air Force and U. S. Energy Research and Development Administration.

Conclusion

CVD/felt cones were successfully fabricated with two different fiber orientations (types 1 and 2) and with a combination of types 1 and 2. Similar physical properties were obtained for all infiltrated cones. The properties obtained from the combination type of cone construction indicate that the calculated thermal stresses were lower than in the types 1 and 2.

References

1. Schmitt, H. W., Paper FC-57A, Tenth Biennial Conference on Carbon, Lehigh University (1971)
2. Stoller, H. M., Irwin, J. L., Wright, G. F., Granoff, B., and Gieske, J. H., Paper FC-57, Tenth Biennial Conference on Carbon, Lehigh University (1971)
3. Irwin, J. L., Proceedings of the 16th National SAMPE Symposium, Los Angeles (1971)

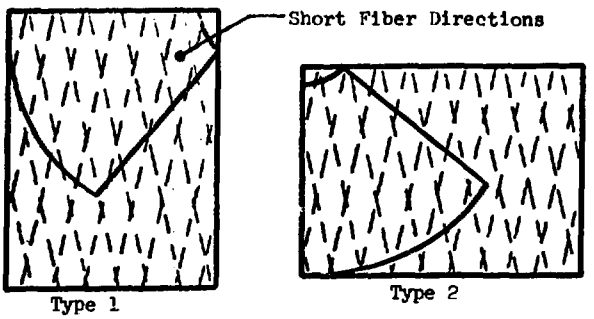


FIGURE 1. RAYON FIBER ORIENTATION

TABLE I. STRENGTH OF TYPES 1 & 2 CVD/FELT CONES

Cone	Long.Strength, MN/m^2	Circum.Strength, MN/m^2
Type 1	16.9	32.6
Type 2	34.5	23.4

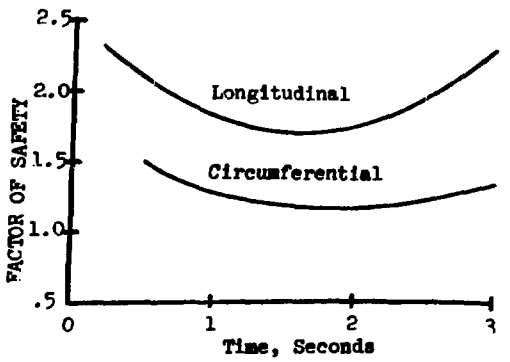


FIGURE 2. FACTOR OF SAFETY TYPE 2 CVD/FELT CONE

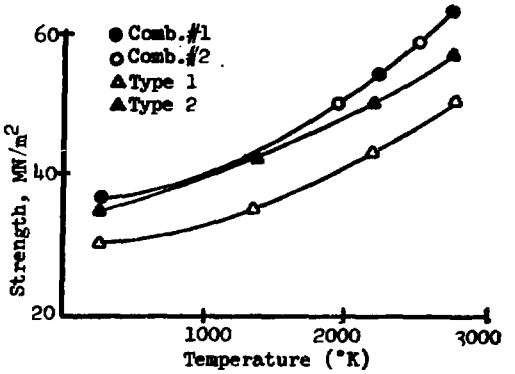


FIGURE 3. LONGITUDINAL TENSILE STRENGTH OF CVD/FELT CONES

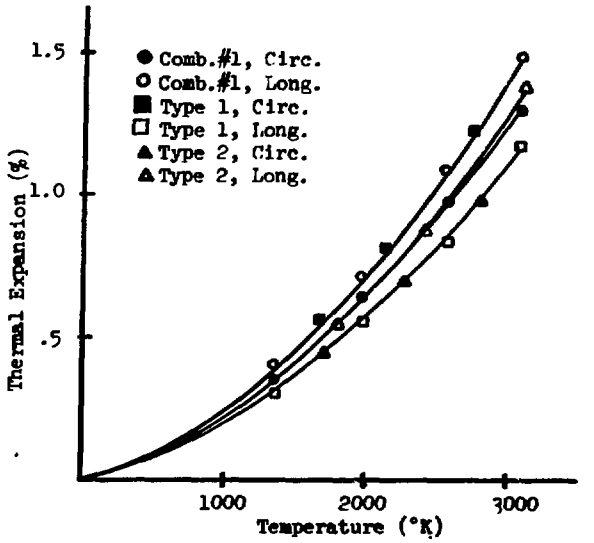


FIGURE 4. THERMAL EXPANSION OF CVD/FELT CONES

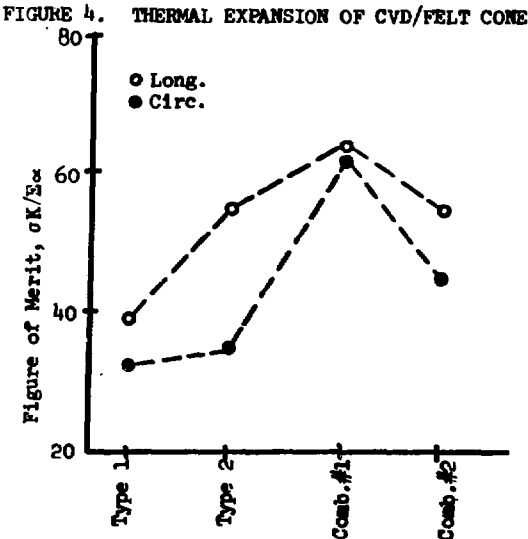


FIGURE 5. FIGURE OF MERIT FOR CVD/FELT CONES

PROCESSING SCALE-UP STUDIES ON CARBON-CARBON COMPOSITES

Phillip N. Bolinger
General Electric Company, Re-Entry & Environmental Systems Division
Philadelphia, Pa. 19101

Introduction

Larger carbon/carbon components will be required for future applications. Procedures are being developed for processing carbon/carbon composites up to (20 cm x 20 cm x 30 cm) which exhibit the same favorable performance characteristics as has been obtained with smaller composites (10 cm x 10 cm x 20 cm). The scale-up processes being studied on this program include an initial chemical vapor deposition of carbon within a woven carbon preform and the subsequent impregnation, carbonization and graphitization of this composite. Mechanical and thermal test results are being obtained.

Chemical Vapor Deposition (CVD)

The woven graphite preforms are rigidized using a CVD infiltration procedure which consists of a heat-treatment to clean the carbon fiber bundles followed by a CVD infiltration which coats the fibers and rigidizes the preform. For 10 cm x 10 cm x 20 cm preforms, the infiltration time required is 80 hours. Process parameters were developed to infiltrate the 20 cm x 20 cm x 30 cm preforms to achieve similar density gradients and fiber coating thicknesses in these larger preforms as was previously achieved in 10 cm x 10 cm cross-section preforms. The major changes to the process included a slightly lower deposition pressure, an increased deposition time, and a redesign of the preform support. Figure 1 shows the typical coating thicknesses on T-50 fibers, and Figure 2 shows the coating thickness on individual fibers as a function of location within the preform.

Densification

The densification process consists of an impregnation/encapsulation of the CVD infiltrated preform, followed by a high pressure (100 MPa) carbonization at 650°C, and then a graphitization at 2750°C. These steps are repeated for five cycles. The density increase in these five cycles is typically 0.98-1.03 gms/cm^3 (from 0.86 to 1.88 gm/cm^3). The major change which had to be made to the standard process was a "pre-impregnation" step which is required for the first impregnation. This process consists of applying a pressure up to 3 MPa on the liquid pitch (~230°C) during the encapsulation operation. This added step is to insure the pitch has penetrated into the core of the preform before the pitch is allowed to solidify. Figure 3 compares the impregnation process used for the larger billets to the process used for 10 cm x 10 cm cross-section billets.

In addition to scaling up the process for larger carbon/carbon composites, a secondary objective is to establish if the standard process is acceptable for an alternate weave construction. The standard size preforms and larger preforms are all orthogonal weaves. The alternate construction is fabricated from stacks of woven graphite cloth which are pierced on 1.3 mm centers perpendicular to the cloth. Carbon fibers are then inserted into these sites. It was found that the standard process can be used to densify the alternate weave construction preforms without any changes. These types of preforms were densified to bulk densities of ~1.95 gm/cm^3. Figure 4 illustrates the densification behavior of the different types and sizes of billets processed on this program.

Characterization

The characterization of these carbon/carbon composites consists of detailed NDE at three stages, namely (1) of the as-received preform, (2) after the CVD infiltration, and (3) after final densification. The NDE consists of radiography, radiometric density, ultrasonic velocity measurements, visual inspection, layer spacing counts and fiber deficiency maps.

Many of the composites have also been destructively tested to determine mechanical/thermal properties and physical properties as a function of location within the billet. Table 1 lists typical properties for these carbon/carbon composites.

Conclusions

Process conditions have been established for fabricating carbon/carbon composites in sizes up to 20 cm x 20 cm x 30 cm. The larger sizes require additional CVD infiltration time and modified conditions to achieve similar density gradients and fiber coating thicknesses as was achieved with smaller billets. The densification process appears to be insensitive to sizes up to 20 cm x 20 cm x 30 cm. The only modification required was to apply a pressure of 3 MPa on the pitch before allowing it to cool during the initial pitch encapsulation process.

Acknowledgments

This work was sponsored by the Manufacturing Technology Division of the Air Force Materials Laboratory. Mr. Harry P. Materne was AFML Project Engineer. The author is Program Manager and Principal Investigator. The suggestions and assistance of Dr. E. Stover, Dr. J. Gebhardt, Mr. W. Mueller, Mr. J. Roetling and Mr. J. D'Andrea of the General Electric Co; Dr. D. VanWagoner of Southern Research Institute, and Dr. Gary Weber of Union Carbide Corp. (Nuclear Division), is gratefully acknowledged.

TABLE 1

TYPICAL PROPERTIES OF 223 CARBON/CARBONS	
Density, gm/cm^3	1.880
Open Porosity, % (air)	6.5
Tensile Strength, ksi (RT)	
"X" Direction	20.
"Z" Direction	44.
Tensile Modulus, 10^6 psi (RT)	
"X" Direction	8.
"Z" Direction	14.
Strain, % (RT)	
"X" Direction	.25
"Z" Direction	.32
Compressive Strength, ksi (RT)	
"X" Direction	16.
"Z" Direction	22.
Thermal Expansion ($\Delta L/L \times 10^{-3}$)	
"X" Direction: RT to 4000°F	3.43
"Z" Direction: RT to 4000°F	3.19



FIG. 1. Typical CVD Coatings on T50 Fibers. Left--Fiber at ~ 0.6 cm. from outer surface. Right--Fiber Taken at ~ 3 cm. from Outer Surface. (Original SEM @ 10,000X)

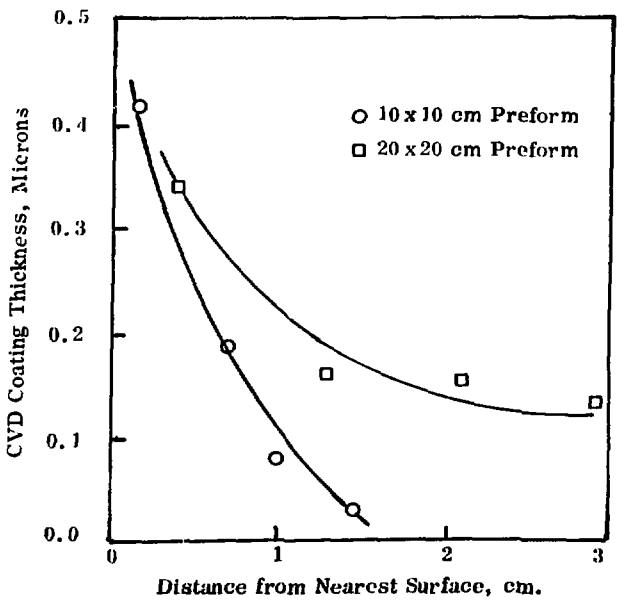


FIG. 2. Coating Thickness of Fibers at Various Depths in 10x10 cm. and 20x20 cm. Preforms. (From SEM Measurements)

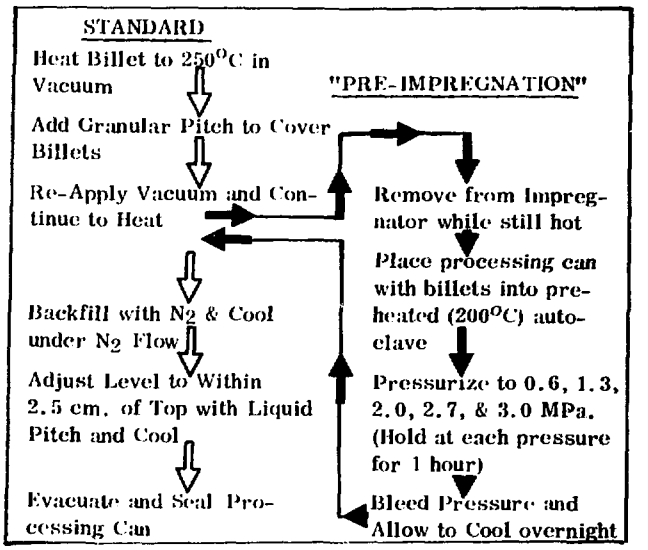


FIG. 3. Procedure for Impregnation of Preforms. Left side--Conventional Procedure. Right side--Additional Steps used in "Pre-Impregnation" Procedure of Larger Preforms.

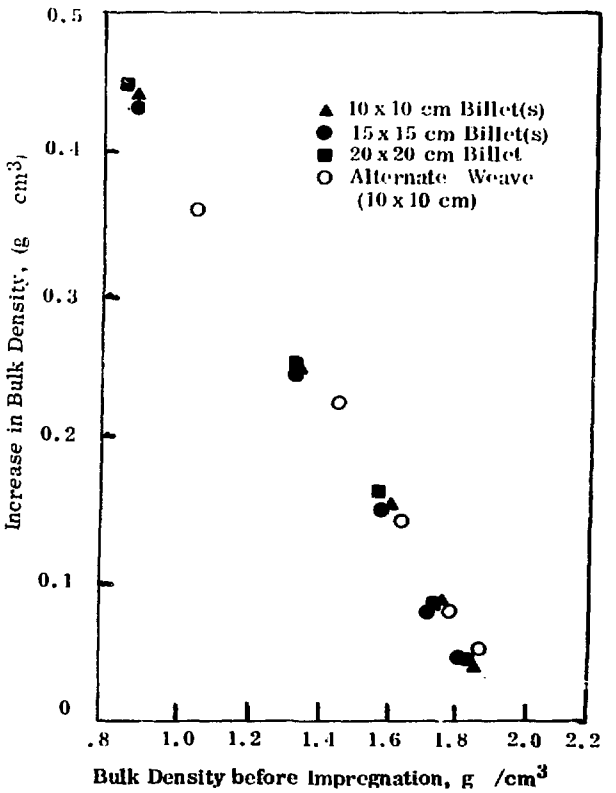


FIG. 4. Densification of 3 sizes of an Orthogonal Preform and One Alternate Weave Construction Preform. There is Little Difference between the Different Sizes. The Alternate Type was not Infiltrated Prior to Densification.

ESR STUDY OF THE KINETICS OF CARBONIZATION

L. S. Singer and I. C. Lewis
Union Carbide Corporation, Carbon Products Division
Parma Technical Center, Parma, Ohio 44130

I. Introduction

There have been a number of attempts to relate the stable free radicals observed by electron spin resonance (ESR) to the mechanism of the thermal transformation of organic materials to pitch, coke, and carbon. For example, ESR has been measured as a function of heat treatment temperature (HTT) for many materials, and efforts have been made to correlate the data with the ultimate carbonization behavior.[1] Specific radical intermediates which are suggestive of different types of thermal reactions have also been identified.[2] However, none of the previous work has tried to utilize the ESR technique to study the kinetics of the transformation of pitch to coke. The purpose of this study was to determine the free radical concentration and characteristics as a function of time at various heat-treatment temperatures, and to relate the data to both kinetic and constitutional parameters for both a well-graphitizing and a poorly-graphitizing material.

II. Experimental

A. Sample Preparation

The two starting materials used were a well-graphitizing petroleum pitch derived from catalytic cracking and a poorly-graphitizing ethylene tar pitch. The heat treatments were performed in an inert atmosphere using three to four gram samples of pitch in ceramic boats. The heat-treatment temperature was accurately monitored by a thermocouple placed at a fixed position in a specially constructed aluminum sample-boat holder.

B. ESR Measurements

Weighed, evacuated samples (1-10 mg) were measured in a 10 GHz superheterodyne spectrometer at room temperature. Power levels were kept below 100 microwatts to avoid saturation. All the signals were assumed to be Lorentz-shaped and "effective" spin concentrations, N_{eff}, were calculated from $S_F{}^2D$, where S_F is the peak-to-peak linewidth and D is the peak-to-peak amplitude of the derivative curve. A ruby crystal was used as a secondary standard, $CuSO_4 \cdot 5H_2O$ as a primary standard, and Curie's law was assumed.

III. Experimental Results

A. Spin Concentrations (N_{eff})

Spin concentrations were measured for the petroleum pitch samples as a function of time at heat-treatment temperatures of 400°C, 430°C, 460°C, and 490°C and for the ethylene tar pitch at 400°C, 430°C, and 460°C. The experimental results obtained for the 400°C heat-treated materials are plotted in Figure 1. The N_{eff} values are seen to increase regularly with increasing heat-treatment time for each material. The poorly graphitizing pitch, however, shows a more rapid rate of free radical development than the well-graphitizing pitch. Similar differences in rate were found for each of the subsequent heat-treatment temperatures. The data do not seem to obey simple first order kinetics.

B. Linewidth (S_F)

Figure 2 shows plots of the variation of ESR linewidth with heat-treatment time for the petroleum pitch at each of the four reaction temperatures. The decrease in linewidth with time is consistent with a line-narrowing mechanism which is related to an increase in both free radical size and concentration.

C. Correlation of ESR Data with Molecular Constitutional Parameters

In Figure 3, the N_{eff} data at all temperatures are plotted versus the atomic C/H ratios measured for each material. It is significant that all of the data for a given material fall on a single curve. Of equal significance are the different relationships between N_{eff} and C/H ratio for the two materials. The higher free radical content for a given C/H ratio in the ethylene tar pitch is consistent with a higher average molecular weight and a lower degree of ring fusion in this more poorly-graphitizing pitch.

D. Free Radical Kinetics During Mesophase Formation

There has been some question about the importance of dehydrogenation during the formation of mesophase in pitch. Figure 4 contains plots of both C/H ratio and N_{eff} versus the pyridine insolubles content during mesophase development at both 400°C and 430°C for the petroleum pitch. The results show that the change in solubility is due to an increase in molecular weight resulting from aromatic dehydrogenation. The correlation between N_{eff} and P.I. content indicates that the stable free radicals are concentrated in the higher molecular weight components of the mesophase pitch.

IV. Conclusions

Our results are consistent with the following conclusions concerning the role of free radicals in carbonization.

(1) The free radical characteristics as measured by ESR, (N_{eff} and S_F) correlate with the changes in molecular constitution which accompany the dehydro-

genative polymerization process during carbonization.

(2) The ESR kinetic results obtained for the stable free radicals in carbonization appear to be related to the ease of graphitizability of the starting material.

(3) The concentration of stable free radicals during carbonization seems to be a direct function of molecular weight.

(4) The correlation of all of the free radical parameters with chemical kinetic data for the carbonization reactions, supports the contention that free radical formation is the rate-controlling step in the carbonization process.

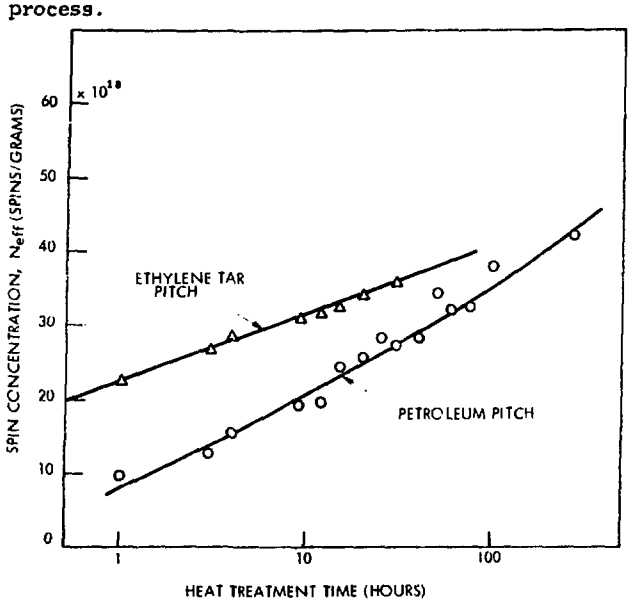


Figure 1. Effective Spin Concentration (N_{eff}) vs. Heat Treatment Time at 400°C; △ Ethylene Tar Pitch, and ○ Petroleum Pitch.

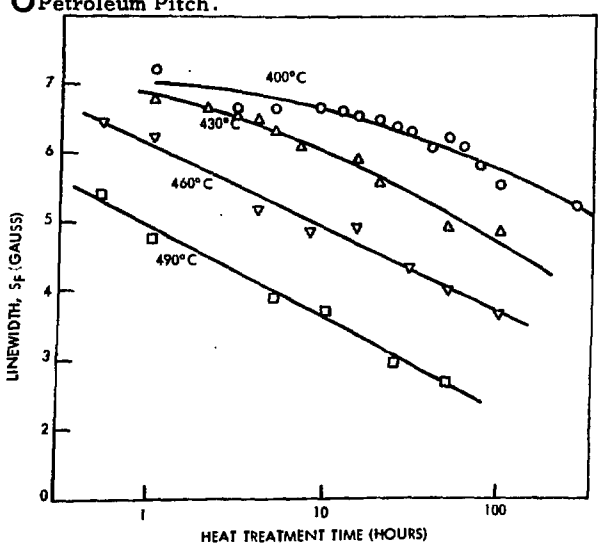


Figure 2. Linewidth (S_F) vs. Heat Treatment Time at 400°C, 430°C, 460°C, and 490°C for the Petroleum Pitch.

V. Acknowledgments

The authors wish to thank Mr. G. W. Gifford for preparing the samples and Mr. D. T. Orient for performing the ESR measurements.

References

1. L. S. Singer, Proceedings of the Fifth Carbon Conference, Volume II (1963).

2. I. C. Lewis and L. S. Singer, Carbon 7, 93 (1969).

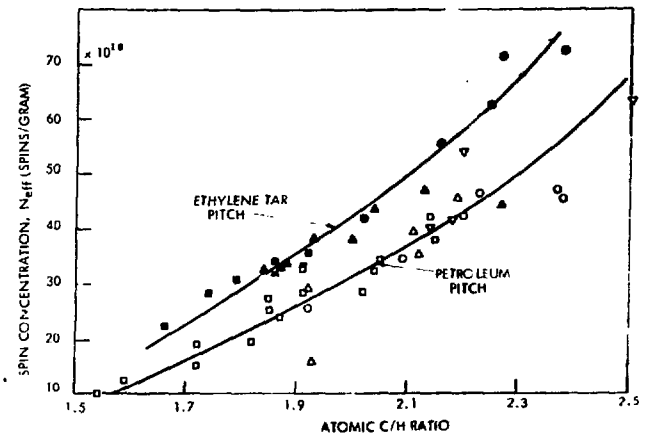


Figure 3. Effective Spin Concentration (N_{eff}) vs. Atomic C/H Ratio for Ethylene Tar Pitch and Petroleum Pitch Heat Treated at Various Temperatures. Petroleum pitch: □ 400°C, △ 430°C, ○ 460°C, and ▽ 490°C; Ethylene Tar Pitch: ■ 400°C, ▲ 430°C, and ● 460°C.

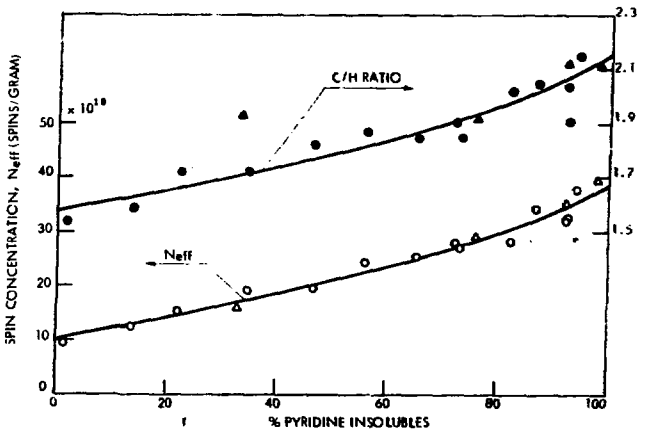


Figure 4. Effective Spin Concentration (N_{eff}) and Atomic C/H Ratio vs. % Pyridine Insolubles for the Petroleum Pitch Heat Treated at 400°C and 430°C; ○ ● 400°C; △ ▲ 430°C.

Carbonization of 3.5-dimethylphenol-formaldehyde resin and its chemical structure at mesophase appearence

Y. Yamashita, National Research Institute for Pollution and Resources
K. Ouchi, Faculty of Engineering, Hokkaido University

(Introduction)

Some type of pitches such as PVC pitch, petroleum pitch or coal tar pitch which become graphitizable carbon at high temperature, generally forms mesophase during the heat treatment of 400~450°C and the mechanism of its formation was studied by many workers which was well reviewed by Books-Taylor[1] or White[2]. So far it is tacitly recognized generally that mesophase consists of large polycondensed aromatic compounds orienting nearly in parallel each other and still remaining as liquid state. In most of the cases this view may be true but it was not yet chemically confirmed.

This report pursued the change of chemical structure of 3.5-dimethylphenol-formaldehyde resin during its heat treatment, which shows mesophase formation as fine mosaic structure at 430°C, and estimated the chemical structure of mesophase.

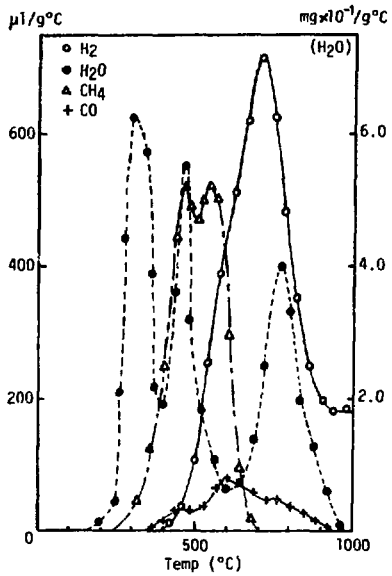
(Experimentals)

The resin has been prepared from 1:1 mol ratio of 3.5-dimethylphenol and formaldehyde (36% aqueous solution) using 10ml of ammonia (23% aqueous solution) per 1 mol of phenol as catalyst and reacting at 90~98°C for 3 hours under nitrogen atmosphere. Then it was cured at 130~140°C on oil bath for 10 hours.

This sample was carbonized with 3°C/min and evolving gases were analysed by gaschromatography every 20°C employing active charcoal for CO and CO_2 and molecular sieve 5A for another gases. Water was decomposed by zinc metal heated at 400°C and produced hydrogen was analysed[3]. The amount of distilled low molecular weight substance was obtained from the difference of weight decrease measured by thermobalance and the weight of evolved gases analysed by gaschromatography mentioned above.

The infrared spectra was measured by KBr pellet with the sample concentration of about 1%.

Fig.1 Gas evolution curves



NMR was measured in D-pyridine employing TMS as reference. Mesophase was observed by microscope using polarized light with the magnification of 250 times.

(Results and discussion)

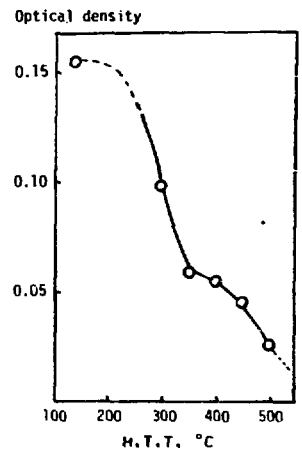
The gas evolution during carbonization is illustrated in fig.1 in the differential curve (ml volume or mg weight of evolved gases/1gr sample/1°C). All the amount is corrected for the loss of low molecular weight substance under the assumption that the low molecular weight substance has the same elemental composition as the original sample.

Firstly dewater reaction starts from 200°C, then methane evolves from 300°C making first peak at about 450°C and second peak at about 520°C. From 400°C second dewater reaction starts and a little later hydrogen begins to evolve reaching to maximum at about 700°C. Third dewater starts from 600°C making a maximum at about 750°C. Evolution of CO makes the maxima at 450°C, 600°C and 750°C.

The decreasing curve of OH absorption intensity in IR spectrum shows two steps divided at about 350°C (fig.2) which corresponds very well to the evolution curve of water. Moreover the absorption at 1200cm^{-1} which means diphenyl ether type oxygen shows a maximum at about 350°C (fig.3). From these results it is concluded that the first dewater reaction should be dewater from two OH groups leaving ether linkages.

The first peak of demethanation may result from the evolution of methane from two neighbouring methyl groups forming naphthene ring between two benzene nuclei, because phenol-formaldehyde resin which has not methyl groups shows a peak of demethanation at the temperature exactly corresponding to the second demethanation peak of 3.5-dimethylphenol-

Fig.2 Change of OH absorption at 3400 cm^{-1}



formaldehyde resin[3].

The sample carbonized at 400°C can dissolve into pyridine up to 92.2% and its molecular weight measured by VPO was 1380. Structural indices of this soluble part calculated from NMR chart are shown in table 1. In this calculation the following procedure was taken. Namely one-third of oxygen is calculated as OH group (from fig.2) and the others ether type between two benzene nuclei. The number of hydrogen substituted as methylene bridges were corrected as to the polymeric type of this resin, that is to say twice of the value was used for the calculation of Hau.

From these results the change of chemical structure when carbonized at 400°C may be estimated as shown in fig.4.

At 400°C mesophase doesn't appear yet, but at 430°C fine mosaic structure suddenly develops over all the faces. The evolution of gases from 400°C to 430°C was as follows. H_2O:0.52mol/MW, CH_4:0.55mol/MW, H_2:0.02mol/MW, CO:0.04mol/MW (MW is assumed to be 1380). That is to say only a very small amount of evolved gases could be observed, indicating that total feature of the molecular structure of 430°C carbonized sample is nearly same as that carbonized at 400°C except a little increase of ether linkage and of ring formation with demethanation. The large aromatic condensed ring structure does not develop at all at 430°C, nevertheless mesophase develops all over the sample. Namely the formation of mesophase doesn't necessitate the existance of large aromatic condensed ring structure, but it can be formed from rather planer large molecules.

(References)

1) Brooks, J.D., Taylor, G.H., Chem. and Phys. of Carbon, vol.4, 243 (1968)
2) White, J.L., AirForce Report, No.SAMSO-TR-74-93 (1974)
3) Yamashita, Y., Ouchi, K., Nenryokyokaishi (J. Fuel Soc. Japan), 53, 1064 (1974)

Fig.3 Change of diphenylether type oxygen at 1200 cm^{-1}

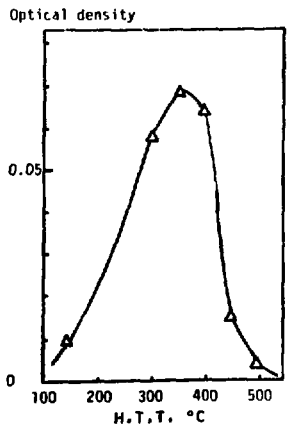


Fig.4 Model of carbonization up to 400 C

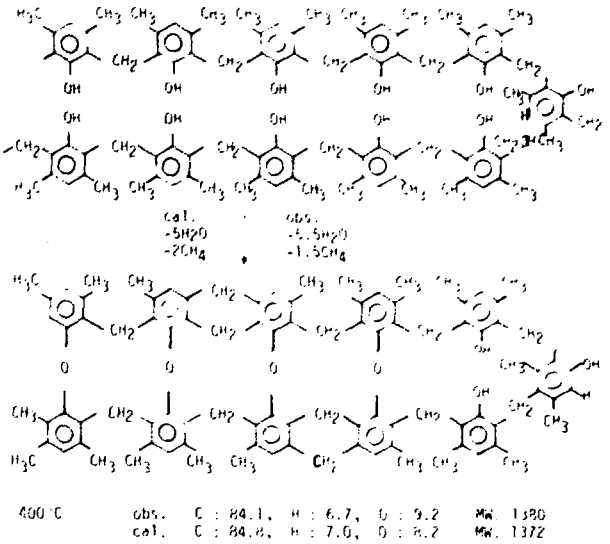


Table 1 Structural indices of pyridine soluble part of carbonized sample at 400°C

	C	H	O	MW	fa	Hau/Ca	σ
Observed	96.8	91.9	7.9	1372	0.71	0.94	0.78
Model	97	96	7	1380	0.67	1.00	0.83

	Ca	Cal	Ca (us)	Cal (us)	polym. degree	Ra	R_T	R_h
Observed	68.9	27.9	6.9	2.8	10.0	9.2	17.4	8.1
Model	66	31	6	2.9	11	11	17	6

fa : Ca/C
Hau/Ca : ring condensation index
σ : substitution index
Ca : aromatic carbon number
Cal : aliphatic carbon number
Ca(us) : aromatic carbon number per unit structure
Cal(us) : aliphatic carbon number per unit structure
Ra : aromatic ring number
R_T : total ring number
R_h : ring number except aromatic one

THE ROLE OF FREE RADICALS AND MOLECULAR SIZE IN MESOPHASE PITCH

I. C. Lewis and C. A. Kovac
Union Carbide Corporation, Carbon Products Division
Parma Technical Center, Parma, Ohio 44130

I. Introduction

It is now apparent that the mesophase in pitch can be classified as a nematic liquid crystalline phase.[1,2,3] Most conventional liquid crystals consist of rod like molecules often containing polar functional groups. Shape factors and polarizability are thought to play a dominant role in liquid crystal formation in such molecules.[4] Since pitch largely contains nonpolar aromatic hydrocarbons and heterocyclics which are flat and disc-shaped, the mechanism for liquid crystal formation in pitch is not understood. Various proposals have been made concerning the liquid crystal interactions in pitch including the involvement of free radicals.[5]

In this paper, we have studied the melting behavior of model compounds which are prototypes of the components of pitch in an attempt to clarify the molecular requirements for mesophase formation.

II. Experimental Procedure

A. Aromatic Compounds - The aromatic compounds, coronene, 1, 2, 8, 9 - dibenzpentacene, decacyclene, 13, 13' - dibenzanthronyl and anthraceno (2',1':1,2) - anthracene were obtained from commercial sources and purified by vacuum sublimation. The hydrocarbon 9,9'-bianthryl was synthesized by the reduction of anthraquinone with Sn and HCl in acetic acid.[6] The compounds 1,14,7,8 - dibenzoperopyrene and terrylene were separated in liquid chromatographic fractions of pitches prepared from pyrene and naphthalene respectively. UV - visible absorption spectroscopy showed that these compounds were the main components of the specific chromatographic fractions.

B. Stable Aromatic Hydrocarbon Free Radical Precursors - Benzanthrene and naphthanthrene were synthesized by reduction of benzanthrone and naphthanthrone tosylhydrazones respectively.

C. Melting Determination - The melting behavior of the compounds and mixtures were studied using a Koefler micro-hot stage in combination with a Leitz polarizing microscope.

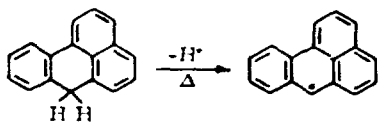
III. Experimental Results

A. Melting Behavior of Individual Compounds

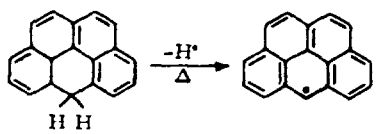
The individual compounds and their melting points are listed in Table I. Several of the materials melted over a temperature range as a result of the presence of impurities. This was particularly true of the chromatographically separated products, terrylene and dibenzoperopyrene. The most important point, however, is that in no instance was a liquid crystal transition observed during the melting of any of the compounds in Table I.

B. Melting Behavior of Terrylene in the Presence of Aromatic Free Radicals

Benzanthrene and naphthanthrene thermally dissociate on melting to form stable free radicals.[7,8]



Benzanthrene



Naphthanthrene

Examination of these compounds on the hot stage showed that their melting occurred without exhibiting any liquid crystal transition. Mixtures of the hydrocarbon terrylene with approximately equal amounts of the free radical formers were then heated on the hot stage through the melting range and at temperatures up to 400°C. The results are shown in Table II.

Terrylene was found to react rapidly at a low temperature of 350°C to give directly a liquid crystal phase. Mixtures of terrylene with the free radical precursors did not show any liquid crystal transition in the temperature range of free radical formation. In fact, the presence of the free radicals seemed to inhibit the liquid crystal development in terrylene.

IV. Conclusions

From the results of these studies we conclude that:

1. Large aromatic molecules, even those containing nine condensed rings did not form a liquid crystal phase on melting.
2. Aromatic free radicals do not induce liquid crystal formation for such compounds.
3. Molecular size appears to be a key requirement for development of mesophase from aromatic hydrocarbons.

References

1. J. D. Brooks and G. H. Taylor, Chemistry and Physics of Carbon, edited by P. L. Walker, Volume 4, p. 243, Dekker, New York, 1968.

2. J. Nehring and A. Saupe, Trans. Far. Soc. II, I I(1972).

3. H. Marsh, Fuel 52, 205 (1973).

4. G. W. Gray, Advances in Liquid Crystals, edited by G. H. Brown, Volume 2, (1976).

5. I. C. Lewis and L. S. Singer, Proceedings of the 12th Biennial Conference on Carbon, p. 265 (1975).

6. F. Bell and D. H. Waring, J. Chem. Soc. 267 (1949).

7. I. C. Lewis and L. S. Singer, Carbon 7, 93 (1969).

8. I. C Lewis and C. A. Kovac Unpublished results.

Table I

Melting of Aromatic Compounds

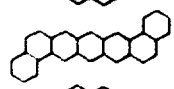
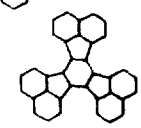
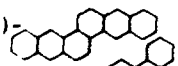
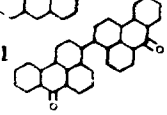
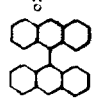
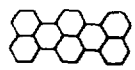
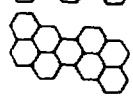
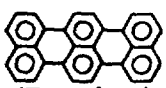
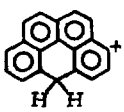
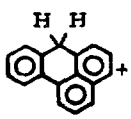
Compound	Structure	Melting Range °C (Hot Stage)
Coronene		415-427
1,2,8,9-Dibenzo pentacene		435
Decacyclene		391-401
Anthraceno (2',1':1,2)-anthracene		413-421
13' 13'-Dibenzanthronyl		355
9,9'-Bianthryl		300
Terrylene		155-210
1,14,7,8,-Dibenzo peropyrene		400-440

Table II

Melting Behavior of Terrylene with Free Radical Formers

Sample Composition	Melting Range(°C)	Mesophase Formation Temperature (°C)
 (Terrylene)	155-210	350
 + Terrylene	100-130	400
 + Terrylene	80-150	375

STUDY OF CARBONACEOUS MESOPHASE THROUGH THE ESR SPECTRA OF VANADYL CHELATES

Y. Yamada*, K. Ouchi**, Y. Sanada**, J. Sohma**
*National Research Institute for Pollution and Resources, Kawaguchi, Saitama, Japan
**Faculty of Engineering, Hokkaido University, Sapporo, Japan

Introduction

Orientation of optically anisotropic mesophase spheres in the magnetic field has been investigated by means of the polarized-light microscopy[1-3]. Our study was initiated to draw information from a different point of view on the mesophase conversion and on the behaviors in the magnetic field on the basis of the ESR spectra of paramagnetic vanadyl chelates in the mesophase. Also, from the spectra observed at elevated temperatures rotational correlation times of the chelates were estimated as a kind of the fluidity during the carbonization process and the activation energy obtained from the temperature dependence of the correlation times was discussed in relation to the size of the mesophase.

Experimental

Iranian heavy oil(IH) was used as one of petroleum heavy oils with high vanadium content(306 ppm as vanadium metal). On the other hand, vanadyl tetraphenylporphyrin which is similar to vanadyl chelates existing in the heavy oils, was doped to Ethylene tar pitch(ET) free from vanadium.

In order to heat the sample in the magnetic field and to measure the ESR spectra in situ the samples were heat-treated in nitrogen atmosphere in the cavity, which had been specially designed for this experiment. By this cavity it was possible to make such a heat-treatment and observation of spectral changes at higher temperatures to about 500°C: for a temperature variation experiment, temperature of a sample in the cavity was controlled by hot air passing through a spiral silicon-carbide heater installed just under the cavity.

Results and Discussion

When the original IH sample was heated to 430°C, remarkable spectral changes were observed near ca. 300 and 430°C. The typical spectra are represented in Figs. 1(a)-(c). The anisotropic structure at room temperature is similar to that previously reported and the ESR parameters are comparable to those of pure vanadyl porphyrin complexes[4]. Therefore, the spectrum is considered to be due to vanadyl chelate complexes coordinating to porphyrin rings.

The conversion of the anisotropic spectrum into the isotropic one appeared at the temperature near 300°C. However, an anisotropic structure emerged again in the vicinity of 430°C. Appearance of the anisotropy by heating was found to be irreversible: once the anisotropic pattern was formed, no isotropic spectrum was observed in the range between 430°C and room temperature. It suggests that some change in the structure was induced by such heating of the sample and that the molecular motion was so hindered on the changed structure as not to produce sufficient averaging of anisotropy.

The spectral changes similar to those of IH were observed also in the case of ET doped vanadyl tetraphenylporphyrin. However, the spectrum gave only isotropic structure in the range of about 250-400°C. The anisotropic spectrum occurred with the treatment at 400°C for 2 hr.

The IH sample was treated at 450°C for 30 min in the various magnetic fields and then frozen to room temperature. Thus, one can obtain information on the orientation by magnetic field at such higher temperature like 450°C, since the vanadyl chelates are reasonably assumed to be involved into the formed mesophase[5] and to behave in the same manner to the mesophase. According to Schwerdtfeger and Diehl[6], the intensity ratio is related to an ordering parameter, s, which is a measure of the arrangement of the mesophase:

$$s = \langle 3\cos^2\phi - 1\rangle/2$$

where ϕ is the angle between the symmetry axis and the optical axis of the liquid crystal. It is apparent that the ordering parameter increases linearly with the magnetic field(Fig. 2), but the value at 10 Kgauss, -0.09, is considerably small, compared with that of pure liquid crystals.

The IH sample in the cavity was heated in the field of 10 Kgauss at 350 and 450°C for 30 min and then cooled to room temperature. The spectra were recorded in situ by rotating the sample tube from 0 to 90° around the axis perpendicular to the magnetic field. As can be seen in Fig. 3, the sample treated at 450°C represents the large angular dependence, while the spectrum is little affected by the rotation for the sample heat-treated at 350°C. On the other hand, the intensity ratio of the parallel part to the perpendicular one for ET treated at 400°C for 2 hr also changes with the rotation, although the angular dependence is smaller than that of IH treated at 430°C for 30 min. The mesophase has a stacking texture of the lamellae which consist of large aromatic molecules. Accordingly, when the magnetic field is applied, c-axis of the mesophase is considered to be aligned perpendicular to the field because of diamagnetism due to aromatic sheets. If the chelates are incorporated between and/or in the lamellae, one can explain reasonably the high value of perpendicular component at 0°. In addition, the increase of $I_{M/\!/}$ with the rotation can be interpreted as follows: since the c-axis of the mesophase is allowed to take any directions in the plane perpendicular to the field, the chelates in the mesophase whose c-axis is vertical to both the field and the sample tube make positive contribution, for example $I_{M/\!/}$ with the rotation of the sample tube.

In liquid, in which Brownian motion is sufficiently rapid, the anisotropy of the ESR spectrum is averaged out and appears isotropic. For this case the Kivelson's theory[7] is the most convenient for the analysis of the experimental results. The correlation time τ_c is estimated by using the theory from the line widths and the heights at each temperature at which the isotropic spectrum appears. Fig. 4 shows the changes of τ_c with the reduced temperature. The correlation time of each sample decreased with rising temperature, but it increased drastically

near 370-390°C. From the fact that no sphere is observed micrographically at these temperatures, one can say that the mesophase precursors presumably begin to grow in the matrix.

The activation energy was estimated to 15.8 Kcal/mol for IH and 4.8 Kcal/mol for ET from the slope of streight line at the range of lower temperature. The optical micrograph of IH treated at 430°C for 30 min shows the very small spheres of 1-5 μm, while tha large size of mesophase appeared in the matrix of ET treated at 400°C for 2 hr. The relation between the sizes of the mesophase spheres and the activation energy of the vanadyl chelates in IH and ET suggests that the high activation energy accompanied by the drastic appearance of the mesophase results in the formation of the small spherulites.

References

1. Sanada, Y., Furuta, T., Kimura, H. and Honda, H., Carbon, 10, 644 (1972).
2. Singer, L. S. and Lewis, R. T., 11th Biennial Conference on Carbon, 1973, p. 207.
3. Imamura, T., Honda, H. and Kakiyama, H., Tanso, No. 76, 17 (1974).
4. Assour, J. M., J. Chem. Phys., 43, 2477 (1965).
5. Imamura, T., Yamada, Y., Honda, H., Kitajima, E. and Tsuchitani, M., Sekiyu Gakkaishi, 18, 776 (1975).
6. Schwerdtfeger, C. F. and Diehl, P., Mol. Phys., 17, 417 (1969).
7. Kivelson, D., J. Chem. Phys., 33, 1094 (1960).

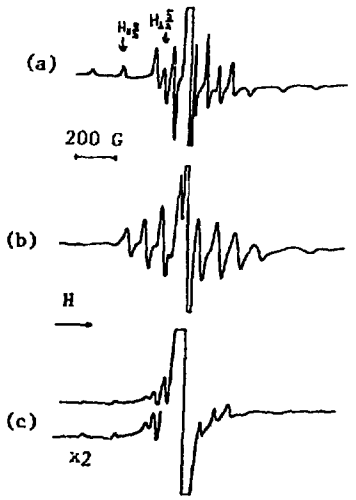


Fig. 1 ESR spectra of IH at (a) room temperature, (b) 360 and (c) 430°C.

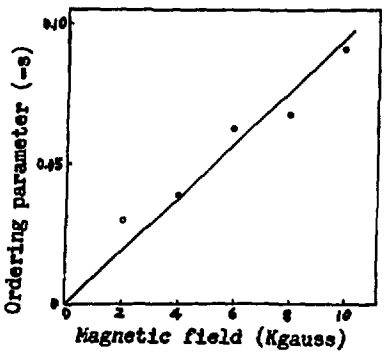


Fig. 2 Variation of ordering parameter for IH with the magnetic field.

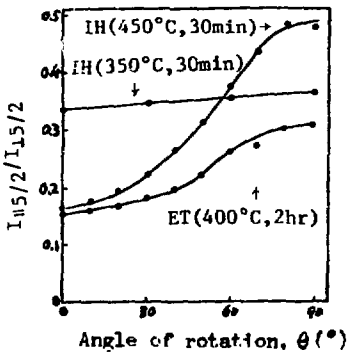


Fig. 3 Angular dependence of the intensity ratio, $I_{\parallel 5/2}/I_{\perp 5/2}$, for IH and ET heat-treated in the field of 10 Kgauss.

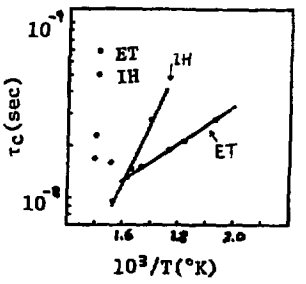


Fig. 4 Variation of correlation time for IH and ET with temperature.

A RHEOLOGICAL INVESTIGATION IN THE MESOPHASE REGION

G.W. Collett and B. Rand

Department of Ceramics, Glasses and Polymers, University of Sheffield, Sheffield S10 2TZ, UK

Introduction

The rheological behaviour of pitches during heat treatment is of considerable technological significance, both in the low temperature region where pitch/coke mixtures are formed and extruded and at higher temperatures where the mesophase grows and coalesces. The characteristic anisotropy of needle coke is a result of deformation of the mesophase during delayed coking and such structural orientation is also important in the initial stages of the manufacture of carbon fibres from pitch (1). It has also been suggested that internal reaction and rearrangement within the mesophase spheres themselves alters their rheological behaviour, which in turn is considered to influence the degree of coalescence (2). Didchenko et al (1) investigated the 'viscosities' of pitches containing mesophase and observed a peak in the 'viscosity'-temperature curves which appeared to be related to the mesophase content of the pitches. However, no explanation of this phenomenon has appeared in the literature. Didchenko et al (1) also reported that mesophase systems could be thixotropic or plastic, depending upon the temperature of measurement and molecular weight distribution of the pyridine soluble and insoluble fractions.

As a contribution to the understanding of the rheological properties of pitches containing mesophase, a rheological investigation has been undertaken using a concentric cylinder measuring system.

Experimental

All rheological observations were made with the Contraves Rheomat-30 viscometer which has a range of rotational speeds of 0.05-350 rev min^{-1} and a rapid response to changes in torque in the measured system. Speed selection can be carried out manually and the torque signal fed to a recorder to follow time dependent phenomena, or with a programmed X-Y recorder attachment which enables flow curves to be determined automatically at predetermined rates of change of speed. Since only a fixed range of torque can be detected, measuring systems of different geometry must be designed for fluids of widely different viscosities.

Co-axial cylinder measuring systems were constructed in stainless steel. A flowing nitrogen atmosphere was maintained over the sample and the whole unit was heated electrically. Most experiments were carried out with a gap width of 1 mm as follows. The system containing the pitch was heated at 0.4°C min^{-1} with the inner cylinder rotating continuously at a constant speed whilst the torque and temperature were displayed continuously on a two pen recorder. In selected experiments heating was arrested at certain temperatures and flow curves measured, and in others samples were removed from the fluid above the rotating bob. These samples had not been sheared during the heat treatment but gave an indication of the mesophase development. They were subjected to quinoline and toluene extraction and examined microscopically.

Orgreave binder and impregnation pitches were examined principally along with an Ashland petroleum pitch and Gilsonite. A thermogravimetric study of the pyrolysis of these materials is described elsewhere in the abstracts of this conference.

Results and Discussion

At temperatures below 250°C the coal tar pitches are Newtonian. Heating and cooling curves on the binder pitch established that below 240°C the apparent viscosity-temperature curve was reversible but above this temperature higher viscosities were obtained on cooling, indicating the onset of polymerisation. Volatilisation in this system was first observed at about 185°C.

At high temperatures the apparent viscosity increases markedly with temperature as the mesophase grows and coalesces. However, there are maxima in the apparent viscosity-temperature curves of the coal tar pitches but not the petroleum pitch (Fig.1). It is clear also that in this temperature region the system is shear thinning and the positions and magnitudes of the two peaks are influenced by the rate of shear. At a speed 1.03 rev min^{-1} the largest peak occurs at a quinoline insoluble content of 65% and the smaller one at 57%, whilst at the faster speed both peaks are closer together occurring at QI levels of 50-53%. Microscopic examination of samples shows that the first signs of mesophase coalescence are at a QI of 53% and at the 65% value there are substantial areas of coalesced mesophase.

Nematic liquid crystals are known to be shear thinning due to the orientation of the molecules in the shear field (3) and maxima are often observed in one component systems at the transformation temperature because of the lower viscosity of the oriented phase. Hermans (4) showed that the apparent viscosities of solutions of poly-γ-benzyl-L-glutamate in m-cresol, measured at low shear stresses, exhibited maxima at a critical concentration above which the solution was birefringent. At higher shear stresses the effect was absent. The anisotropic phase was considered to be more easily oriented than the isotropic phase at low shear stresses, but in the high shear Newtonian region both phases could be oriented.

The behaviour of liquid crystals offers a possible explanation of the rheological properties of the carbonaceous mesophase in coal tar pitches. At temperatures above 400°C, shear thinning behaviour is apparent because the mesophase spheres can be elongated and partially oriented in the shear field along with the high molecular weight aromatic molecules in the isotropic liquid. Initially the mesophase probably remains as discrete particles because of surface tension effects. Hence, as the amount increases so does the apparent viscosity. An increase in the average molecular weight of the isotropic phase is also a possible contributory factor to the apparent viscosity. When coalescence sets in and the mesophase becomes the major phase, however, it can be

oriented more easily than the isotropic liquid at low rates of shear and the apparent viscosity at low rates decreases. Presumably the subsequent increase again at higher mesophase contents is a result of stronger intermolecular forces between the lamellar molecules restricting their motion.

The Ashland petroleum pitch has not yet been extensively investigated and it is not clear why no maxima are seen in the rheological behaviour of this pitch.

Optical micrographs of the 420°C impregnation pitch sample, cooled under shear, show elongated mesophase units oriented in a particular direction. On heating, they do not revert to spherical shape until a temperature of 300°C, indicating that this is the temperature at which the molecules within the mesophase of this particular sample become mobile. The sample which received a similar heat treatment but no shear, when examined rheologically at temperatures between 250 and 300°C, exhibited flow curves of the type shown in Fig. 2. After heating to a particular temperature under continuous shear conditions a Newtonian flow curve was obtained (A in Fig. 2), but on aging the sample at this temperature for various periods, flow curves of type B were observed, and the position of the 'bulge' shifted to higher values of shear stress with time. A second flow curve measured immediately after the first was Newtonian. This response is typical of a thixotropic material and since the mesophase in this temperature region has been shown to be 'solid-like', it is tentatively suggested that this thixotropic effect is due to a reversible sol-gel transformation.

These and other results will be presented in more detail at the conference.

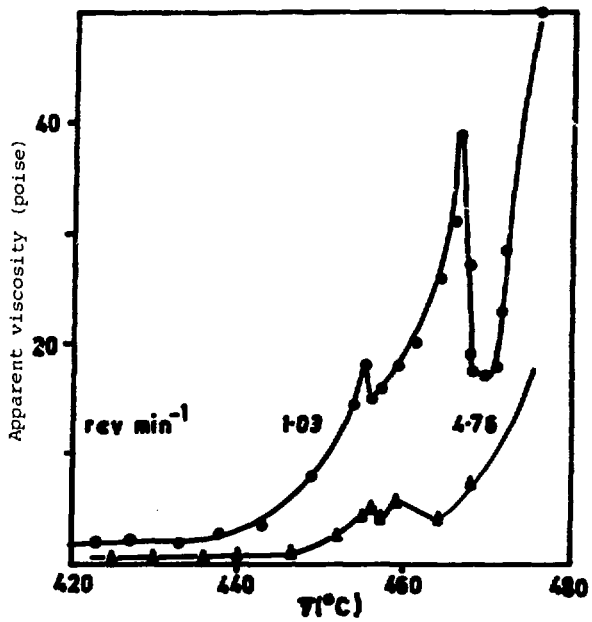


Fig.1 Rheological changes during mesophase growth in an Orgreave impregnation pitch

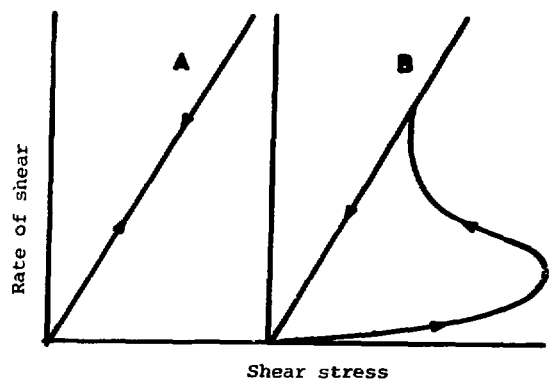


Fig.2 Flow curves in region 250-300°C of a 420°C Orgreave impregnation pitch
A - immediately after shearing
B - after time t under isothermal conditions

References

1. Didchenko, R., Barr, J.B., Chwastiak, S., Lewis, I.C., Lewis, I.T. and Singer, L.S. 12th Biennial Conference on Carbon; extended abstracts p. 329.

2. Marsh, H. and Cornford, C., 'Petroleum Derived Carbons', Daviney and O'Grady (eds), ACS Symposium Series 21 (1976).

3. Porter, R.S. and Johnson, J.F., "Rheology", ed. F.R. Eirich, Vol.4, p. 317, Academic Press (1967).

4. Hermans, J.Jr., J. Colloid Sci., 17, 638 (1962).

CARBON FORMATION DURING PYROLYSIS IN THE PRESENCE OF HYDROGEN

A. La Cava and D. L. Trimm
Imperial College Univ. of Trondheim,NTH
Dept.Chem.Eng. & Chem.Tech. Lab. Ind. Chem.

Recent interest has been focused on the conversion of heavy hydrocarbons to more amenable feedstocks, by using reactions such as hydrogasification (1), the pyrolysis of hydrocarbons in the presence of hydrogen. Although such reactions may be industrially feasible, they tend to lose efficiency as a result of carbon formation on the reactor walls. The present studies were designed to investigate this phenomenon in the context of hydrogasification of butane.

Experiments were carried out with a flow system involving a tubular reactor in which metal liners could be placed. A sample of copper (an inert metal) was hung in the reactor from one arm of a C.I. Mark 2B microbalance. A continuous record of carbon formation on the copper was obtained, and the exit gases and liquids were analysed gas chromatographically.

As shown in figure 1, variation of the metal liner had a significant effect on carbon formation on copper, inferring that the metal liner affected the composition of the gases responsible for carbon formation on copper. In general carbon formation involved an induction preiod, followed eventually by a reproducible rate of deposition (figure 1). The variation of gaseous, liquid and solid products was studied as a function of operating variables. Typical plots of yields vs. residence time are shown in figures 2 and 3.

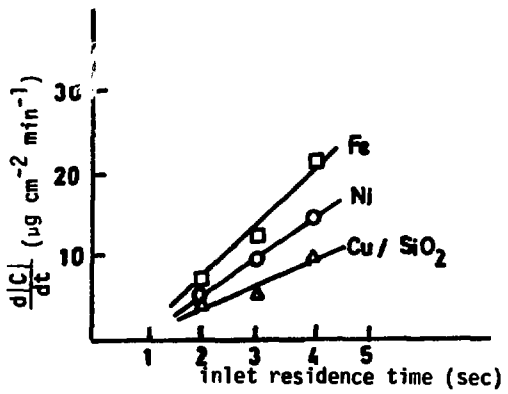


Figure 1. Carbon deposition vs metal liner

Butane: 800 °C

The presence of the induction period supported the concept of carbon formation involving intermediates such as polycyclic aromatics (2). Assuming a simple first order reaction

$$\alpha RH \rightarrow I \qquad 1$$

the integrated kinetic expression would be

$$|I| = \alpha|RH_o|(1-e^{-k_1\tau}) \qquad a$$

where τ is the residence time.
If the intermediate adsorbs and dehydrogenates

$$I + S \rightleftarrows IS + H_2 \qquad 2$$

and this reacts to give carbon

$$IS \rightarrow \text{carbon} + S \qquad 3$$

Then the sequence of reactions can be shown to predict the kinetics, at the steady state:

$$\frac{d|C|}{dt} = \frac{k_2k_1|I|}{k_1 (1+\frac{k_{-2}}{k_2}|I|+\frac{k_{-2}}{k_3}|H_2|)} \qquad b$$

This equation may be tested against experimental results. Thus, for example, if $|RH_o|$, τ and T are held constant, the variation of carbon deposition with hydrogen can be expected to be

$$\frac{dt}{dC} = A_1 + A_2|H_2| \qquad c$$

Experimental results agreed with this prediction for A_1 = 500 mg^{-1}cm^{-2}min, A_2 = 62.5 mole percent^{-1} mg^{-1}cm^{-2}min. Similarly, the variation of carbon deposition with butane concentration should take the form

$$|RH_o|\frac{dt}{dC} = A_3+A_4|RH_o| \qquad d$$

Again experimental results agreed with this prediction for A_3 = 200 mg^{-1}cm^{2}min^{-1}, A_4 = 500 mg^{-1} cm^{-2}min^{-1} mole fraction^{-1} for $|RH_o|$ expressed as mole fraction of butane in the feed.

When considering relatively short residence times, equation a can be expanded in a Taylor series to give, considering only the first power.

$$|I| = \alpha|RH_o|k_1\tau \qquad e$$

Substitution in equation b for constant inlet compositions and temperature gives

$$\tau\frac{dt}{dC} = A_5 + A_6\tau \qquad f$$

Application to results such as those summarised in figures 2 and 3 gives good agreement except at low temperatures and very low residence times. At 800°C, A_5 = 200 sec mg^{-1} min cm^2 and A_6 = 50 mg^{-1} min cm^2.

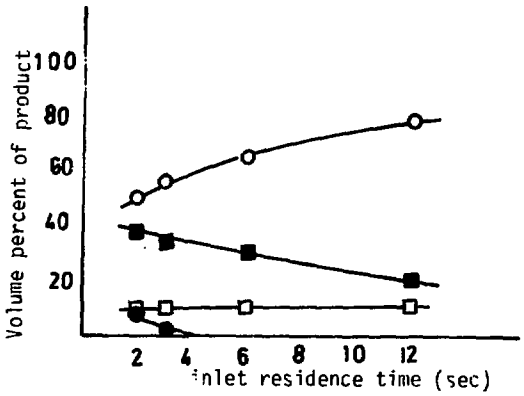


Figure 2. Effect of residence time on gas phase products
T = 800 °C
50 % Butane: 50 % Hydrogen

□ Ethane ■ Ethylene
○ Methane ● Propylene

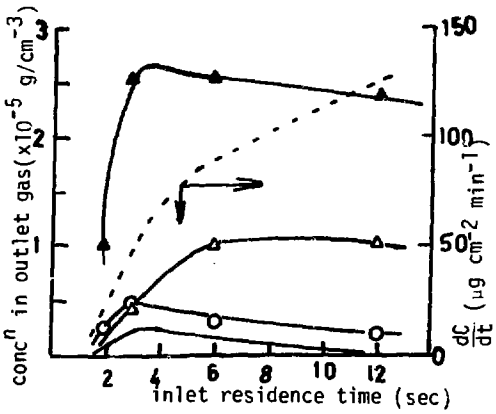


Fig. 3. Effect of residence time on the formation of aromatics and carbon. T = 800°C
50% Butane: 50% Hydrogen

▲ Benzene
△ Naphthalene
○ Toluene
- - - - Carbon
——— Ethylbenzene + Acenaphthylene + Anthracene + Phenanthrene

Substitution of equation f in equation b gives

$$\frac{dC}{dt} = \frac{k_3 k_2 k_1 \alpha |RH_0| \tau}{(1 + \frac{k_2}{k_3} k_1 \alpha |RH_0| \tau + \frac{k_{-2}}{k_3} |H_2|)} \quad g$$

which predicts a complicated dependence of rate upon temperature. However, if the rate of carbon formation is compared in the presence and absence of hydrogen at differing temperatures, this equation can be reaaranged to give

$$\left|\frac{dt}{dC}\right)_{+H_2} - \left.\frac{dt}{dC}\right)_{-H_2}| = \frac{A_2}{A_3 A_2 A_1} \exp \frac{(2E_3 + E_2 + E_1 - E_2)}{RT} \frac{H_{2o}}{\alpha\, RH_o} \quad h$$

where A_i is the pre-exponential factor of reaction i.
Experimental runs were carried out to study this prediction, which was found to hold over T = 800-950 °C, with $(2E_3 + E_2 + E_1 - E_{-2})$ = 22.6 kcal/mole.

It is also possible to extend the predictions of the model to include the effect of surface. volume ratio (figure 4)

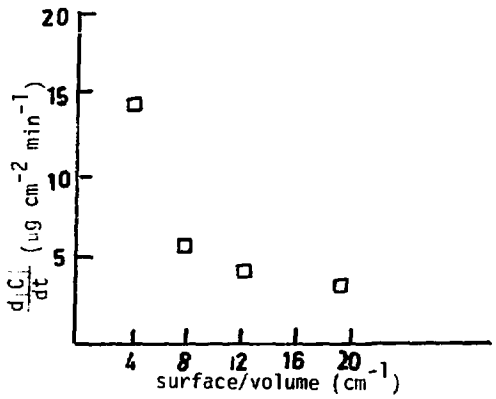


Figure 4. Carbon deposition as a function of S/V
τ = 3 sec T = 800°C
Butane 50%: Hydrogen 50%

At large ratios, the model predicts that the rate of carbon formation should be inversely related to the surface: volume ratio, in close agreement with the experimental results.

Although the model is obviously very simplified, the predictions are thus seen to be in good agreement with experimental results. On the basis of results similar to those presented in figures 2 and 3, attempts were made to identify the intermediates. This showed that polycyclic aromatics did appear to be important, but it was not possible to characterize the reactivity of individual molecules.

References

1) Dent, F.J., Edge, R.F., Hebden, D., Wood. F.C. & Yarwood, T.A.: Trans. Inst.Gas Eng. 106, 194 (1956-57)

2) Brooks, C.T., Cunnings, C.P.R. & Peacock, S.J.: Trans. Farad.Soc. 67, 3265 (1971)

SOLAR SELECTIVE CARBON COATINGS

C. R. Schmitt, J. M. Schreyer, J. M. Googin, H. D. Whitehead
Oak Ridge Y-12 Plant, Nuclear Division
Union Carbide Corporation, Oak Ridge, TN 37830

A carbon coating, having a high absorption capability for solar energy, has been developed and demonstrated. The coating consists of carbon particles of a selective size range, bonded to a metal plate with an appropriate inorganic or organic binder. The carbons and graphites used in this demonstration are those with a particle size near the wavelengths of the infrared/visible light boundary.

The heat-treated (2800° C) spherical Thermax powder used in our work with an acrylic resin binder had an average particle diameter of 0.57 micrometers and is shown in Figure 1. A larger diameter microspheroidal carbon powder (approximately 150 micrometers) having a selective absorbing surface was also used and its surface morphology is shown in Figure 2.

Two commercial flat-plate solar collectors (10 square feet each) were used to compare a selective carbon coating with black velvet paint. One collector was sprayed with a microspherical Thermax carbon powder/acrylic resin/mixed solvent formulation and the other collector was sprayed by the manufacturer with a commercial black velvet paint.

The microspheroidal-carbon solar collector coating consisted of a fluid mixture of 16.0 wt.% carbon powder, 0.5 wt.% acrylic resin, and 83.5 wt.% mixed solvents comprising equal volumes of xylene, methyl ethyl ketone, and methylene chloride. Five ounces of the fluid mixture were used to obtain a uniform coating having a thickness of approximately 1/3 mil over the 10 square feet of collecting metal surface. Estimated material cost of the black coating presently used by the panel manufacturer is $4.50 per 2' by 5' (10 sq. ft.) collector surface; the estimated material cost for the proposed solar selective carbon coating is approximately $0.20 per collector. A statistical evaluation of the outlet water temperature from the two collectors, measured at equal water flow rates, showed that the total heat collected by the selective-carbon-coated collector was significantly higher than that of the heat collected by the black velvet paint-coated collector.

A typical experimental efficiency of the carbon-coated collector was calculated to be 62.4%, and for the black velvet-coated collector, it was 57.4%. These efficiencies would be somewhat higher if the solar panels had been at an optimum angle of orientation with respect to the sun's incident radiation instead of being horizontal. A solar-absorbing coating capable of withstanding higher temperatures would result by using selective carbon particle fractions with a high-temperature binder.

Report Y/DA-6701, "Selective Absorptivity of Carbon Coatings," by J. M. Schreyer, C. R. Schmitt, J. M. Googin, and H. D. Whitehead is available upon request.

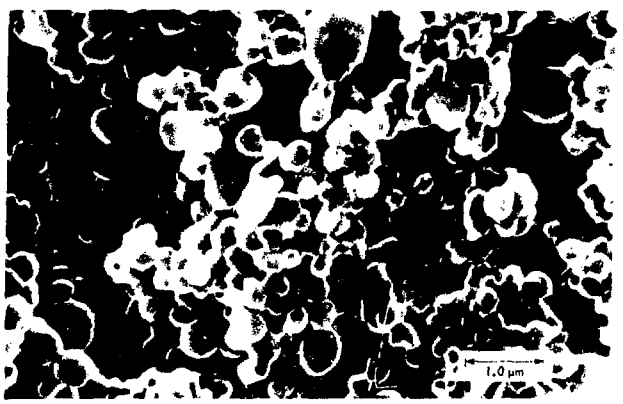


Fig. 1: The Heat-Treated, Thermax/Acrylic Coatings Contain Small, Spherical Particles

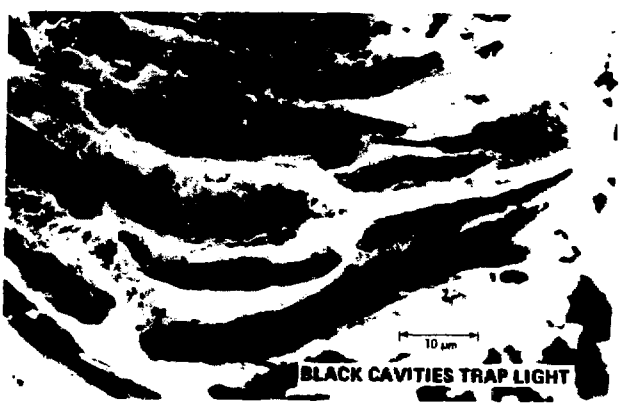


Fig. 2: Selective Absorbing Surfaces May be Formed by Controlling the Surface Morphology

ENDORSEMENT NOTICE: Reference to a company or product name does not imply approval or recommendation of the product by Union Carbide Corporation or the U. S. Energy Research And Development Administration to the exclusion of others that may meet specifications.

THE RELATIONSHIP OF PHYSICAL PROPERTIES OF GRAPHITE TO EDM PERFORMANCE

Clive L. Greatorex
POCO Graphite, Inc.
Decatur, Texas 76234

Introduction

EDM (Electrical Discharge Machining) is a process that removes metal by utilizing the damaging effects of electric sparks, in a closely-controlled manner, between two conducting surfaces immersed in a dielectric medium.

Although EDM is considered a modern means of nonconventional metal removal, relatively few people realize that it has been employed in its present form since the mid-nineteen fifties. In fact, the process was first recognized during the Second World War by Lazarenko, a Soviet scientist. Lazarenko and his colleagues developed and designed the original circuitry for EDM, comprising of a condenser charged via a resistor and coupled across the gap between two electrodes. The Relaxation circuit, as this original design is known, is still found in some present day machines.

At the end of the War, the process was taken to the U. S., U. K. and Switzerland, where development continued and the manufacturing of EDM began. At this writing, there are some thirty-plus original equipment manufacturers supplying EDM, the majority featuring solid state technology in the generation of pulsed machining energy.

EDM applications have continued to grow as more and more exotic, difficult-to-machine materials are introduced to meet today's stringent demands on component life and reliability. These Space Age alloys and other materials must meet a basic condition for successful EDMing. They must be electrically conductive.

One of the most important component in an EDM operation is the electrode and the material from which it is manufactured. In the United States, the most versatile and widely used material is synthetic graphite readily available from a number of prominent manufacturers. This electrode material varies from coarse grain, low strength graphite to fine grain, high strength graphite.

Graphite as an Electrode Material

The acceptance of graphite as an electrode material was mainly due to the development of the pulse generator. The versatility of the control units enabled the EDM operator to select a wider range of machine parameters some of which particulary enhance the electrode characteristics of graphite when compared to metallic electrode materials.

One such characteristic of graphite is the ability to resist wear. The EDM process is explosive in nature and the temperature at the point of discharge is extremely high, in excess of 3000°C, high enough to vapourise most workpiece materials and unfortunately most electrode materials. Graphite, as a metalloid, sublimes at approximately 3,350°C; therefore, the spark temperature will not erode graphite at a rate even approaching that of metal.

Other EDM performance criteria are classified under the following headings.

Metal Removal Rate
Fine Finish Reproducibility
Machinability (Ease of Fabrication)

Conclusion

Experimentation has shown that all electrode materials have different optimum machining parameters for meeting these critrea and obtaining maximum performance. These optimum condition variances also occur between different grades of graphite electrodes material and can generally be related to the physical properties of the material.

CASTING CORES MADE FROM POROUS CARBON

G. Gistinger and G. Hochegger (Sigri Elektrographit GmbH, 8901 Meitingen, Germany)

Introduction

Highly porous carbon prepared by carbonizing foams of cross-linked thermosetting resin, e.g. phenol-formaldehyd, is an excellent thermal insulating material (1, 2). Suitable high-temperature insulating materials can also be made from hollow carbon microspheres which are produced from small pitch droplets (3). A normally disadvantageous property of these highly porous carbons is their high oxidation rate.

Porous carbon for casting cores

Sand cores are used for the manufacture of castings containing cavities and in special cases, cores are made of water soluable salts for cavities which are not easily accessible. Removal of the core material from the finished casting is not always easy and residues of this material may cause severe corrosion or even catastrophic wear. These difficulties may be avoided by using porous carbon casting cores (4, 5). The specification of a suitable porous carbon grade is presented in Table I. Casting cores can be easily machined by sawing, cutting or turning in useable range of tolerances. Owing to the low CTE of porous carbon the dimensional changes during pouring are insignificant. Usually the casting core has to be fixed within the mould to avoid floating in the molten metal. Casting cores used to form cooling channels are shown in Fig. 1 and 2. After solidification of the metal the casting core is ignited and burnt out. The burning rate can be accelerated by blowing oxygen onto the core. Only a very small amount of ash particles are retained which can be removed by washing.

Carbon fabric for casting cores

Instead from porous carbon the burnable casting cores can also be made from carbon fabric or felt (6). In this case the fabric would be wound on a mandrel and impregnated with a resin to strengthen the material and is afterwards machined to the final shape. This material is especially suitable for torus- or tube-shaped casting cores. As the burning rate is not as high as for porous carbon the fabric should be impregnated with suitable catalysts, e.g. alcali metal compounds or lead oxide.

Conclusions

Casting cores made from porous carbon and fabric are equally suited for the casting of aluminum, aluminum alloys and other non-ferrous metals. In contrast to other core materials the porous carbon can be removed without any residue from cavities which are not easily accessible.

References

1) Nobrac Carbon Ltd., Brit. Pat. 1 016 449 (1966)

2) Hochegger G., O. Vohler and H. Ernst, CVA 51 (1973)

3) Kureha Kagaku Kogyo K.K., Germ. Offenlegungsschrift 2 126 262 (1971)

4) Wischnack, W., Aluminium 50, 229 (1974)

5) Alcan Aluminiumwerk GmbH, Germ. Pat. 2 123 732 (1972)

6) Sigri Elektrographit GmbH, Germ. Offenlegungsschrift 2 418 070 (1975)

Table I

Specification of a porous carbon grade

bulk density kg/m^3	60
porosity %	95
compressive strength N/cm^2	70
thermal conductivity W/mK	0,05
CTE 1/K · 10^6	2,7
ash content %	0,2



Fig. 1 Diesel piston with cooling channel, and torus-shaped casting core; outer diameter 220 mm

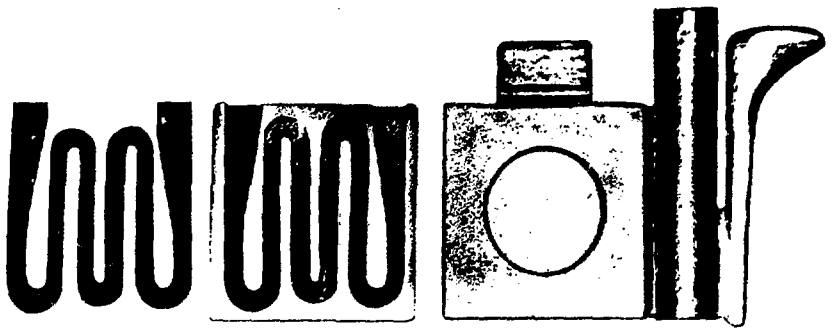


Fig. 2 Cooler with meander-shaped cooling channel

NEW APPLICATION FOR FLEXIBLE GRAPHITE SHEET

H. Eicher and E. Winkler (Sigri Elektrographit GmbH, 8901 Meitingen, Germany)

Introduction

In recent years, flexible graphite sheets made by compacting exfoliated or expanded graphite particles has become useful for a wide range of applications (1). The outstanding properties of flexible graphite were recognized at a very early stage (2). Sheets of flexible graphite having the same chemical and thermal stability as other graphite grades are well suited to protect other materials against chemical and thermal corrosion. Their flexibility enable their adaption to nearly every contour and their low permeability provides a good seal against fluids. A valuable property for some applications is also the anisotropy of the sheet (Table I).

Thermal insulation

Flexible graphite sheets are especially suited for radiation shields (3, 4). The radiation shields shown in Fig. 1 are efficient high temperature insulators. In comparison with heating shields made from molybdenum graphite sheets are cheaper, easy to handle and its weight is comparatively low. For the insulation of vessels carrying a cyrogenic fluid it is advantageous to provide the graphite sheet with a thin, highly reflective metal coating, such as aluminum, gold, silver or copper (3).

Surprisingly, flexible graphite sheets are very suitable for irradiation shielding against continuous and pulsed laser radiation. Perforating a 0,1 mm thick sheet with a continuous carbon dioxid laser takes about 3 seconds for instance. Sheets of 2 mm thickness could not be perforated with the same laser equipment the power output of which was 100 W with a focal point diameter of about 1 mm. Even a ruby laser furnishing a pulsed energy of 40 kW could not perforate sheets of 5 mm thickness. After irradiation only small bubble shaped bulges were observed at the surface of the sheet (5). Obviously the incident radiation energy is dissipated within the sheet, predominantly parallel to its surface whereby the density of the energy decreases below the vaporizing energy of carbon.

Chemical and metallurgical applications

Electrostatic precipitators used for the purification of gases containing acids, are often destroyed by corrosion especially the precipitating electrodes. By cladding the structural parts as well as the electrodes, any corrosion attack can be prevented. Fig. 2 shows the cross section of an electrostatic filter containing precipitating electrodes, which are clad with flexible graphite sheets (6). To avoid the corrosion of the discharge wire it is advantageous to make the wires from carbon or graphite threads (7). These electrostatic precipitators are used in plants for the combustion of garbage and in aluminum foundries in which the metal is refined using chlorine.

In foundries flexible graphite sheets are also used instead of black washes (8) and as liners for both pressing and casting moulds (9). The sheets are hardly wetted and therefore metal adherence does not occur. For hot pressing, flexible graphite sheets can be used simultaneously as heating elements and as liners. At high temperatures, normal cements are not suited for bonding the sheets to the mould and also carbonizeable binders are not always effective. In another method the sheet is welded with the aid of stainless steel welding rods (Fig. 3) (10). The most suitable method has to be established for each individual case, however.

Conclusion

Flexible graphite sheets are a valuable material in the chemical and metallurgical field and for thermal insulation.

References

1) Dowell, M.B., 11th Biennal Conference on Carbon, 31, 35 (1975)

2) Aylsworth, J.W., US-Patent 1 137 373 (1915)

3) Union Carbide Corp., US-Patent 3 404 061 (1968)

4) Sigri Elektrographit GmbH, Germ. Pat. 1 814 052 (1970)

5) Sigri Elektrographit GmbH, US-Pat. 3 720 836 (1972)

6) Aluminium-Hütte Rheinfelden GmbH, Germ. Offenlegungsschrift 2 500 888 (1976)

7) Schunk & Ebe GmbH, Germ. Offenlegungsschrift 2 311 468 (1974)

8) Race, B., Gießerei-Praxis, 160 (1974)

9) Vohler, O., H. Ernst and G. Hochegger, VII. Congr. on Electroheat, Warsaw 1972, Paper No. 424 (Warsaw Int. Union for Electroheat and Polish National Committee, 1973)

10) Sigri Elektrographit GmbH, Germ. Offenlegungsschrift 2 406 902 (1975)

Table 1

Properties of graphite sheets

bulk density g/cm^3	0,9 - 1,1
spec. electr. resistivity	
parallel to the surface $\Omega \cdot mm^2/m$	8
perpendicular to the surface $\Omega \cdot mm^2/m$	$4 \cdot 10^{-4}$
coefficient of anisotropy	5000
thermal conductivity	
parallel to the surface W/mK	175
perpendicular to the surface W/mK	3,5
coefficient of anisotropy	50
permeability (air) cm^2/s	$< 10^{-6}$
ash content %	0,002

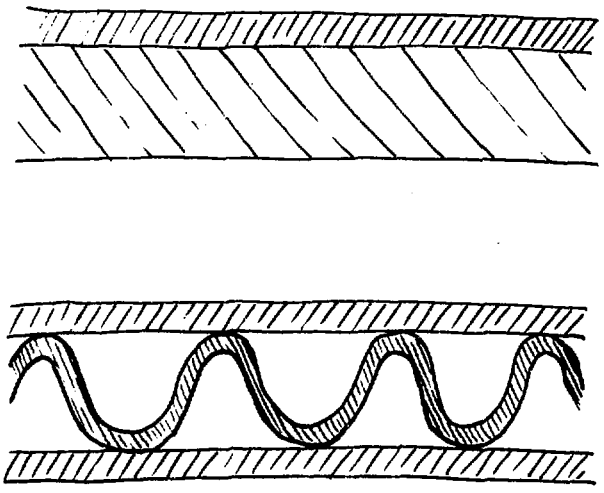


Fig. 1 Radiation shields

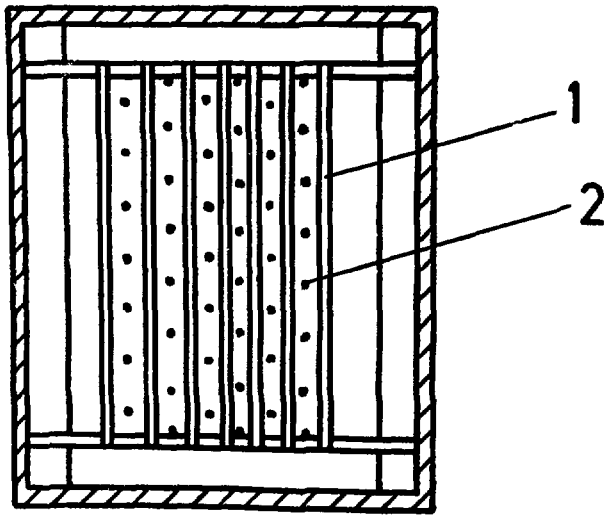


Fig. 2 Electrostatic precipitator;
1 - precipitating electrodes,
2 - discharge wires

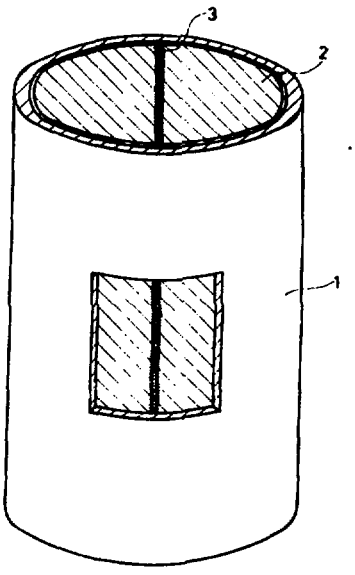


Fig. 3 Flexible graphite liner with welding seam;
1 - steel tube,
2 - flexible graphite sheet
3 - welding seam

FORMATION OF DIVIDED PARTICLES FROM CARBON VAPOR

J. LAHAYE, P. KAPPLER, P. EHRBURGER and J.B. DONNET
Centre de Recherches sur la Physico-Chimie des Surfaces Solides
24, Avenue du Président Kennedy 68200 MULHOUSE (FRANCE)

Introduction. In previous work, the mechanism of finely divided carbons in hydrocarbon pyrolysis has been established (1). In particular, it has been shown, that the chemical processes occuring during the pyrolysis are based on the transformation of the starting hydrocarbon, methane or benzene, into polyaromatic hydrocarbons with molecular weights of several hundred units (2). Those hydrocarbons are then condensed into liquid droplets (phase change) which are transformed into solid particles mainly through dehydrogenation. The chemical reactions taking place during the phase change, gas to liquid, are very complex and thus hinder a better understanding of the physical processes involved. Therefore, we investigated a system of particles formation rather simple from a chemical stand point, i.e. the vaporization of graphite and the subsequent condensation of the carbon vapor. Depending on the experimental conditions of the vapor condensation, carbon films or carbon particles may be produced (3). When the condensation of carbon takes place in an atmosphere of inert gas, fine carbon particles can be obtained.

In the present study, we investigated mainly the size of the produced carbon particle as a function of the experimental conditions (evaporation rate, pressure of inert gas). A mechanism for the particle formation has been suggested.

Experimental. Carbon vapor is produced by electrically heating (10-14 V ; 100-140 A) of a spectroscopically pure graphite rod (length 20 mm, diameter 3 mm) placed in a cylindrical Pyrex vessel (80 mm diameter). The graphite rod is outgassed for five hours at 20°C under 10^{-5} torr and then for 15 min. at 2000°C. After cooling in vacuum the inert gas (argon) is introduced to a known pressure. The evaporation takes place during 2 min. heating cycles followed by cooling periods of about 20 min.

The weight loss of graphite rod is determined accurately and the evaporation rate is calculated by dividing the weight loss by the total evaporation time.

The carbon deposits may be recovered from the pyrex walls or from metallic supports set at known distances from the source. Grids for electron microscopy covered with a thin film of carbon are also used. The temperature of the carbon source is measured with an optical pyrometer. Thermocouples shielded with a refractory cap to prevent radiation disturbance from the source are used to measure the temperature at different points inside the evaporation chamber.

Thermal profiles (temperature as a function to the distance from the source) determined after 1 mn of evaporation do not show any marked variation with changes in experimental conditions (evaporation rate, argon pressure).

The carbon particles are observed under a Jeol 100B microscope. Their size is measured with a particle analyzer TGZ3 Zeiss. The carbon samples are characterized by the most frequent diameter D_f of their size distribution.

Results. The morphology of the carbon deposits has been studied as a function of the three following parameters in these ranges :

- P_A : pressure of argon (10^{-3} to 30 torrs)
- V_e : evaporation rate of carbon (0.5 to 4.5 mg/min)
- z : distance from the source (10 to 40 mm).

It appears that for $P_A < 1$ torr, the carbon deposits is mainly a film which may be smooth or rough. For $1 < P_A < 5$ torrs, particles appear at distances between 30 and 10 mm for evaporation rate higher than 1 mg/min.

Finally, when $P_A \geq 5$ torrs, particles are formed at any evaporation rate between 0.5 and 4.5 mg/min. This experimental range $5 \leq P_A \leq 30$ torrs has been especially investigated. The particles diameters (D_f) versus distance from the source (z) are indicated on figure 1 for different conditions. It is seen that for a given P_A, D_f increases with the evaporation rate V_e. Also, for given V_e and P_A values, D_f increases when $z < 20$ mm and remains constant for $z > 20$ mm.

Discussion. The results indicate clearly that the particles are formed in the gas phase. The shape of the particles, the presence of aggregates, the increase of the particle diameter with distance and the independence of the particle size of the nature of their support are strong indications of a gas phase formation of the particles.

Therefore the following mechanism may be postulated : the carbon snecies migrate from the source to the walls and collide with each other in the gas phase. The collision frequency is proportional to the residence time of the carbon species in the gas phase. It increases with the argon pressure and with the evaporation rate of carbon.

Estimations of the radius of the critical nucleus show no significant differences for film or particles formation. Moreover, a tremendously high thermal gradient ($\sim 10^7$ K/m) exits on our system and therefore classical nucleation thermodynamics involving equilibrium may not be applicable. We consider another approach based on collisions between two carbon species yielding a single one.

Assuming for simplification that the carbon vapor is composed only of C_3, we postulate a stepwise growth mechanism.

The first step is $C_3 + C_3 \rightarrow C_6$ and the pth step :

$$C_{3x2^{p-1}} + C_{3x2^{p-1}} \rightarrow C_{3x2^p} \quad (1)$$

At the end of each step, the number of particles is divided by two and the distance z_p is calculated after which the pth step is terminated. The diameter of C_{3x2^p} may be determined assuming a spherical shape and a density of 1.9 g/cm^3.

Kinetic theory of gases show that the number of particle N per unit volume may be calculated as a function of z by the equation

$$\frac{dN}{dz} = -\frac{c\sqrt{\pi}}{v} D^2 N^2 \left(\frac{4kT}{m}\right)^{1/2} \quad (2)$$

D : diameter of the particle
m : mass of the particle
v : migration velocity of the particles in the z direction

c : efficiency factor < 1

The number of C_3 per unit volume at the source may be calculated knowing the partial pressure of C_3, $(P_{c3})s$. From the evaporation rates in vacuum and in argon atmosphere, it is possible to compute the $(P_{c3})s$ values.

Assuming that the migration along the z axis is generated by a thermophoresis mechanism, the velocity is given by

$$v = 3.1\ 10^{-4}\ \frac{\nabla T}{P_A}^{1/2} \quad (3) \text{ (SI units).}$$

∇T is the thermal gradient, experimentally determined.

Substituting (3) into (2), it is possible to calculate, after integration, the particle diameter. The theoretical curves fit the experimental points well when taking $c = 10^{-2}$ for $3 < 20$ mm and $c = 0$ for $3 > 20$ mm (figure 1). Indeed for particles large enough, collisions do not lead to single particles but to the aggregation of two individual spheres and thus there is no more growth.

The assumptions are obsiously over simplified, the efficiency factor c depending certainly on the particle size and the temperature. Nevertheless, it should be pointed out that a unique value allows a fit for all sets of experiments. Thus, the satisfactory agreement between theory and experimental values supports strongly the irreversible association of carbon species as being the fundamental process in formation of the carbon particles in our system. A generalization of the proposed mechanism may be found by investigating metal vaporization.

References.

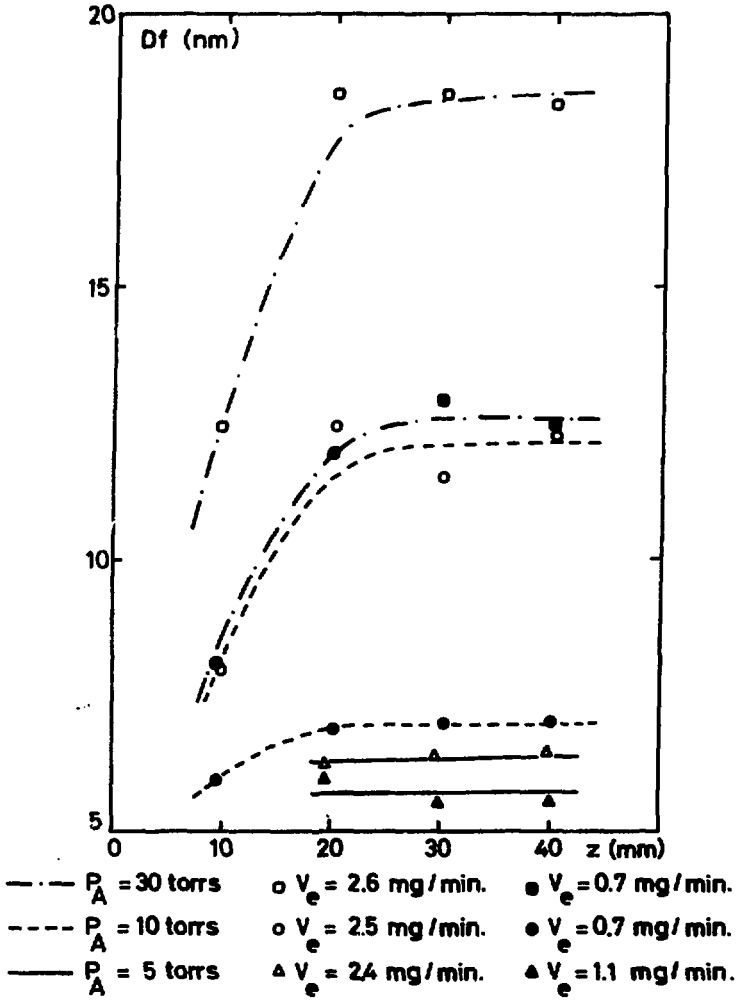
(1) J. Lahaye, G. Prado and J.B. Donnet, Carbon 12, 27, (1974)

(2) H.B. Palmer, A. Voet and J. Lahaye, Carbon 6 (1) 65, (1968)

(3) D.E. Bradley, Brit. J. Apply. Phys. 5, 65, (1954)

(4) I.S. McLiniock and J.R. Orr Chemistry and Physics of Carbon 11, 243, P.L. Walker and P.A. Thrower Ed. Marcel Dekker Inc. New York 1973.

Figure 1 : Particle diameter as function of distance to carbon source.



APPLICATIONS OF CARBON IN THE SODIUM-SULFUR BATTERY

Frank A. Ludwig, Fuels and Lubricants Department, Research Staff
Ford Motor Company, P. O. Box 2053, Dearborn, Michigan 48121

A brief description of the sodium-sulfur battery will serve as a basis for a more detailed discussion of the use of graphite as a current collector and inert electrode. The battery operates in the range of 300-400°C, liquid sodium being oxidized at the negative electrode and liquid sulfur being reduced at the positive graphite electrode. The liquids are separated by β or β"-alumina solid electrolyte which is highly selective to the passage of sodium ions. The sodium ions passing through the solid electrolyte combine with reduced sulfur to form a continuous solution of sodium polysulfide compounds, Na_2S_x, the nominal value of x varying from 5.2 to 2.7 as the reduction proceeds. A miscibility gap occurs between sulfur and $Na_2S_{5.2}$, polysulfide being virtually insoluble in the sulfur phase. The end of discharge is signaled by the precipitation of Na_2S_2. Thus discharge may be viewed as the two phase reduction of sulfur to $Na_2S_{5.2}$, followed by the one phase reduction of $Na_2S_{5.2}$ to $Na_2S_{2.7}$. The battery is reversible and may be recharged to about 90% of the original amount of sulfur.

Materials problems in the battery are due to the corrosiveness of the sulfur-polysulfide system. The container as well as the inert electrode needs to be considered. Most metals corrode, at least to the extent that the corrosion products cause a gradual decrease in battery efficiency and capacity. Some metals, such as Mo, are protected to a degree by metal sulfide film formation, while others, such as Al and Cr are protected by their oxides. Oxides generally are stable in molten polysulfides; e.g., Cr_2O_3, ZrO_2, $La_{0.84}Sr_{0.16}CrO_3$, Ta doped TiO_2, Fe doped $CaTiO_3$, and glass such as the borosilicate glasses. Some carbides and nitrides have been found to be stable under certain test conditions; e.g., SiC. Carbon is stable, and, as we shall see, carbon is the only readily available material which meets most of the requirements for the inert sulfur electrode. (The materials problems related to the container for the sulfur-polysulfide system will not be discussed.)

One desirable structure for the sulfur electrode is a graphite felt. The properties of the felt which relate to the performance of the electrode are: pore volume or felt density, surface area, compressibility, two-dimensional resistivity, nature of surface adsorption sites, and structural integrity. In order to understand the relationship of these properties to electrode performance, a more detailed description of the electrode reaction is required.

A typical sodium-sulfur cell consists of a β"-alumina tube filled with sodium. Graphite felt surrounds the outside of the tube and a protected metal container surrounds the graphite felt so that the β"-alumina tube and the metal container are concentric. The sulfur is stored in the porous graphite felt. The graphite surface in close proximity to the β"-alumina is the electrochemical reaction site; the remainder of the graphite felt serves as a storage and supply bed for sulfur and polysulfide, and as a radial current collector from the reaction site to the conductive container wall. The container serves as an axial current collector. The rationale for this structure may be perceived through an examination of the relevant resistivities. Both the β"-alumina and the polysulfide melt have resistivities of about 4 ohm·cm at operating temperatures. The β"-alumina is thin (0.1-0.3cm); therefore, the ohmic loss is kept small. For most applications the amount of sulfur and polysulfide stored in the felt requires a felt thickness of about one cm. The resistivity of a typical graphite felt is 0.3 ohm·cm; this is low enough to provide satisfactory radial conductivity over the one cm distance. Furthermore, it constrains the electrochemical reaction to the close proximity of the β"-alumina since the electronic conduction through the felt is much greater than the ionic conduction through the polysulfide melt.

The details of the chemical reaction have been given previously (1). In summary, the discharge reaction is diffusion controlled in the one phase region and under mixed kinetic and diffusion control in the two phase region. The cathodic reaction may be generalized as:

$$S_4^{=} + 2e^{-} = 2S_2^{=} \qquad \text{(A)}$$

$$4S + 2S_2^{=} = 2S_4^{=} \qquad \text{(B)}$$

$$4S + 2e^{-} = S_4^{=} \qquad \text{Net Reaction}$$

If any $S_3^{=}$ ions are formed, they disproportionate to $S_2^{=}$ and $S_4^{=}$. In the sequence: S, $S_5^{=}$, $S_4^{=}$, $S_2^{=}$, a mixture of two separated species will chemically react to form the intermediate species.

In the two phase region the polysulfide is electrochemically reduced by (A), but regenerated by the chemical reaction (B). In the one phase region the net reaction is reaction (A) by itself. The consequence of these reactions is that a counter diffusion of the polysulfide ions exists at the electrode; e.g., $S_2^{=}$ and $S_4^{=}$ in reaction (A). Mass transport polarization occurs. This polarization has been measured in actual cells and can be the largest contribution to the lowering of the cell voltage. It has been found that the cell voltage can be increased (mass transport polarization decreased) by increasing the surface area of graphite felt in the region adjacent to the β"-alumina tube. The increased electrode area

permits a decrease in the diffusional flux and in the concentration gradients of reactants and products. In the two phase region, the sulfur phase must be brought into contact with the polysulfide phase in order to facilitate reaction (B). Since sulfur is very viscous at the temperature of cell operation (sulfur, ~ 20 poise; polysulfide ~ 20 centipoise), it is desirable to have open regions in the storage and supply regions of the felt. It has been experimentally demonstrated that the lighter sulfur will rise in open vertical channels and the heavier polysulfide will fall at rates in excess of the supply requirements of the reaction. Thus natural convection can be an aid to the transport of electrode reactants and products. The open regions in the felt have several other influences. First, graphite is preferentially wettable by sulfur, having an advancing contact angle of about 25°, whereas polysulfide has an angle of about 90° (1). Thus if the cathode space is underfilled with sulfur, the sulfur will wick into the felt. Vapor transport of sulfur can then occur in the open regions. Also the open regions can fill with polysulfide as discharge progresses. Thus preferential wicking can be an effective means of enhancing a counterflow of reactant and product. The importance of wicking is especially relevant during charging of the battery. On charging, at the transition from the one phase to the two phase melt (at 40% of full charge) sulfur is formed at the electrode. The sulfur is an insulator and halts further charging, unless special means are used. One such means is to coat the graphite with an oxide such as Al_2O_3. The graphite becomes wettable by polysulfide, and the sulfur is expelled from the electrode surface. At $350^{\circ}C$ and at currents of $100mA/cm^2$ the utilization (% of capacity for total conversion of Na_2S_3 to sulfur) for a cell with open regions and Al_2O_3 coated felts was 82%, while an identical cell except with untreated felts yielded 34%. On charging during the two phase regime, the polysulfide is oxidized directly to sulfur, and since reactant and product are essentially immiscible, very little diffusion occurs. Means to improve performance must rely on other modes of mass transport, such as differential wicking or convection.

The density or pore volume of the porous electrode will affect mass transport by wicking, convection and diffusion within the porous body. Cells using vitreous carbon foam electrodes of different pore size (but equal bulk void volume) gave nearly identical performance.

The compressibility and elasticity of the electrode material are relevant in terms of the electronic contact of the porous electrode with the axial current collector or container. It has been found that the contact resistance is low, even when the electrode is not tightly compressed or cemented against the container. Apparently ionic bridging through the melt between slightly separated electronic contacts provides low impedance connections.

In summary, porous carbon or graphite structures in tubular cells provide:

1. good radial conductivity
2. adequate structural integrity for incorporating open regions
3. adequate elasticity for good electrical contact to the container
4. adsorption characteristics conducive to mass transport by differential wicking
5. surface area high enough to minimize mass transport polarization
6. density and pore size within a range which permits adequate storage capacity and adequate mass transport.

1. Tischer R. P. and Ludwig F.A., In Advances in Electrochemistry and Electrochemical Engineering (Edited by H. Gerischer and C. W. Tobias), Vol. 10, pp. 391-482. John Wiley & Sons, New York (1977).

THE OXIDATION OF GRAPHITE UNDER COMPRESSIVE STRESS*

P. A. THROWER, D. R. MARX

Material Sciences Department
The Pennsylvania State University
University Park, PA 16802

Introduction

In recent years data has been published showing a large effect of tensile stress on the oxidation rate of graphite in argon with small additions of water vapor (1,2). This work was undertaken primarily to determine the effect of compressive stress on such a reaction. In the course of the work, other factors affecting gasification rate, such as temperature, flow rate and concentrations of inhibiting species are also being investigated.

Experimental

Graphite samples in the form of right cylinders 0.75" diameter and 1.50" long were cut from blocks of Stackpole 2020 and Great Lakes H440 graphite and were held between an alumina anvil and ram. The load was applied via a lever arm by a simple dead weight loading technique. The sample was placed in a vertical tube furnace with a bellows arrangement at the top to allow load to be transmitted to the sample. The load was measured using a Tyco 1000 pound load cell.

He-CO and He-CO_2 gas mixtures were obtained by combining gas from cylinders of He, He + 1000 ppm CO and He + 1000 ppm CO_2. Water vapor was added to the gas stream by passing it over ice in a refrigerated bath whose temperature was varied to change H_2O concentration. During any run six parameters were continuously monitored viz., furnace and sample temperatures, compressive load, and the concentrations of CO_2, CO and H_2O in either the inflowing or outflowing gas stream. H_2O concentration was measured using a Beckman trace moisture analyzer and CO and CO_2 concentrations were measured using Beckman infrared gas analyzers. The respective accuracies were ± 5% and ± 1%. The data collected were recorded using a six point recorder.

Effect of Compressive Loading

In no case investigated so far has there been the slightest hint of any effect of compressive loading on reaction rate. A summary of some of the data obtained using Stackpole 2020 graphite is given in Table 1. Gas concentrations are given to the nearest 5 ppm but in most cases the accuracy of measurement was slightly better than that. In all cases in which a He-CO_2 reactant gas mixture was used there was conservation of oxygen.

The compressive strength (σ_c) of Stackpole 2020 graphite is around 12,000 psi so that the loads applied here are $<\sigma_c/20$, however even when the experimenter's own weight was added to the load to give a stress of $\sim\sigma_c/7$ there was still no effect on reaction rate!

A typical data output for the C-H_2O reaction is shown in Figure 1. There are very slight variations in gas concentrations during the run but no sign of any effect of stress. The original Euratom Petten work on this effect by Krefeld et al., [1,2] differed from our investigations in that tensile stresses were used. Effects were observed at 1000°C with only 20 ppm H_2O present and stresses of 350 psi were sufficient to produce the maximum effect, which consisted of a 2-7 fold increase in the concentrations of reaction products.

Duplication of Krefeld's work (3) has been attempted by other workers using an identical apparatus and the same graphite material as that for which Krefeld found the largest effect, in addition to other materials. In no case was any effect of tensile stress on oxidation found.

No model which can qualitatively explain Krefeld et al.'s results (viz. pore opening or impurity migration due to the stress field) would predict zero effect for compressive stress. Our results are obviously inconsistent with those of Krefeld et al. In addition to the different mode of stress there is a major difference in the gas flow rates (33,000 - 55,000 ml/hr vs 200 ml/hr). Lower flow rates cannot be used in our apparatus because of the requirements of the infrared gas analyzers.

Table 1

Sample Temp. (°C)	Stress Comp. (psi)	$X^{in}_{CO_2}$ (ppm)	$X^{in}_{H_2O}$ (ppm)	$X^{out}_{CO_2}$ (ppm)	X^{out}_{CO} (ppm)
888	0	85	-	60	45
	267	85	-	60	45
	362	85	-	60	45
888	0	175	-	135	80
	267	175	-	135	80
	362	175	-	135	80
893	0	-	885	75	125
	267	-	885	75	125
	362	-	885	75	125
	456	-	885	75	125
908	0	115	-	85	60
	456	115	-	85	60
	650	115	-	85	60
908	0	-	125	15	30
	362	-	125	15	30
	456	-	125	15	30

Effect of Gas Flow Rate on Oxidation

Using the apparatus designed for examining oxidation under stress it has been possible to commence investigations into the effect of gas flow rate on

oxidation rate. The exact flow rates used were 9.2, 13.8 and 15.3 ml/sec corresponding to velocities of 2.1, 3.2 and 3.6 mm/sec past the sample.

Reaction rates are calculated using the first order rate equation given by Hedden and Löwe[4] for their "open circuit" oxidation experiments. For the graphite - CO_2 reaction the rate is given by

$$-\frac{dr_c}{dt} = V_{in}(X^{in}_{CO_2} - X^{out}_{CO_2})\ \frac{P_{total}}{82.05\ T_{room}\ (K)}$$

where $-dr_c/dt$ is the number of moles of carbon consumed per second, V_{in} is the gas flow rate in cm^3/sec and $X^{in}_{CO_2}$ and $X^{out}_{CO_2}$ are the inlet and outlet mole fractions of CO_2. P_{total} is one atmosphere.

For the graphite $-H_2O$ reaction the rate is

$$-\frac{dr_c}{dt} = V_{in}(X^{out}_{CO_2} + X^{out}_{CO})\ \frac{P_{total}}{82.05\ T_{room}\ (K)}$$

where X^{out}_{CO} is the mole fraction of CO in the outlet gas.

Reaction rates as defined in the above equations are plotted as functions of the inlet CO_2 and H_2O partial pressures (mm Hg) in Figures 2 and 3. The three curves on each figure correspond to the three flow rates used. It can be seen that for any given partial pressure the rates increase on increasing the flow rate from 9.2 ml/sec to 13.8 ml/sec but decrease when the flow rate is further increased to 15.3 ml/sec. These results are somewhat mysterious and further investigation is necessary. However the same effect is found for both the $C-H_2O$ and $C-CO_2$ reactions and there is no reason to doubt its validity at present.

*Sponsored by the U.S. ERDA under Contract No. EY-76-S-02-2712.*000

References

1. R. Krefeld, G. Linkenheil, Ph. Glaude and W. Karcher, Carbon '72, Baden-Baden, p. 216 (1972).
2. R. Krefeld, G. Linkenheil, and W. Karcher, ORNL-CONF-730601, p. 88 (1973).
3. Heinrich and Weimann, (HRB, Mannheim) private communication.
4. K. Hedden and A. Löwe, Dragon Project Report #205 (1963).

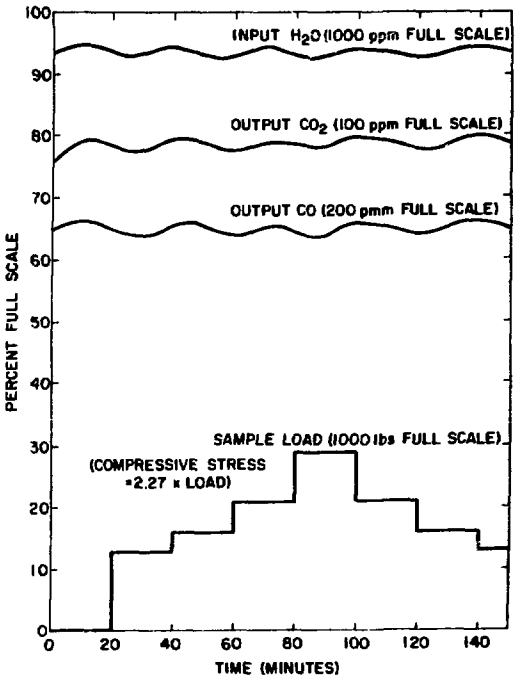


Fig. 1 Typical data output for Stackpole 2020 graphite oxidized in helium containing 930 ppm H_2O under different compressive loads.

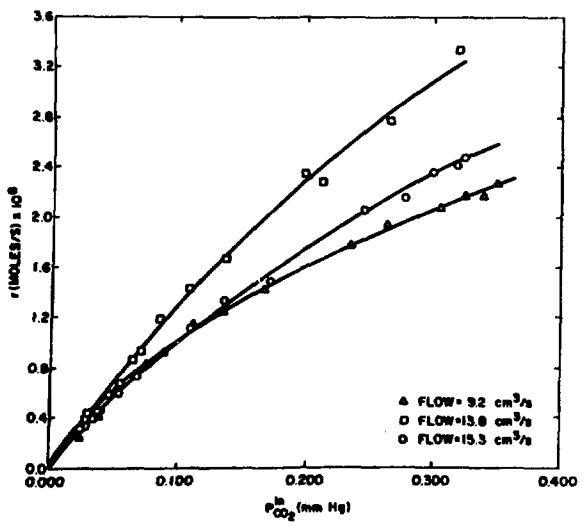


Fig. 2 Reaction rate of Stackpole 2020 graphite versus partial pressure of CO_2 in the inlet gas at 893°C for different flow rates.

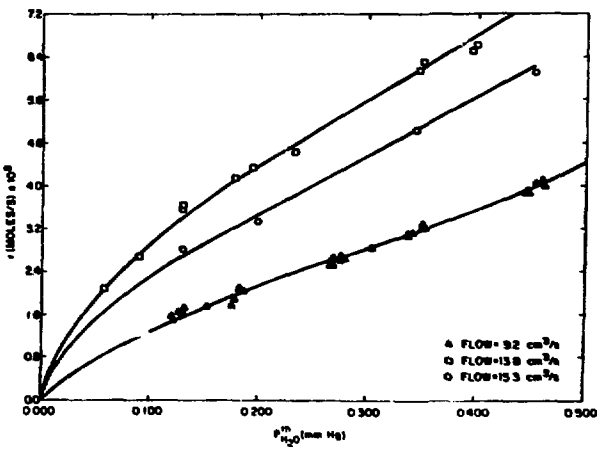


Fig. 3 Reaction rate of Stackpole 2020 graphite versus partial pressure of H_2O in the inlet gas at 893°C for different flow rates.

SUPERFICIAL REACTION OF CARBON BLACK WITH OXYGEN

D. Rivin and J. H. Atkins
Cabot Corporation
Concord Road
Billerica, Massachusetts 01821

Combined thermal and gas analyses are employed to investigate the kinetics of carbon black oxidation at temperatures $\geq 100^{\circ}C$. Relative reactivities have been determined as a function of surface properties (i.e., area, microstructure, chemistry) and impurity levels. Critical autoignition parameters are estimated using a computer modeling technique which corrects for variations in sample geometry and heat transfer.

CATALYSIS OF WATER VAPOUR GASIFICATION OF COKE BY IRON

R. HAHN, K. J. HÜTTINGER

Institut für Chemische Technik
Universität Karlsruhe,W.-Germany

Introduction

Gasification of carbonaceous materials like coal or coke with pure water vapour offers a possibility for producing clean fuel gases, synthesis or reduction gases.
As reaction rate is rather small the use of catalysts becomes of interest. Alkali metals and earth alkali metals are known as being potential catalysts (G. WOYKE, 1975). Among the transition metals iron has shown to be very effective (D.McKEE, 1974), provided that is exists in reduced metallic state under reaction conditions. It was chosen for this study, because iron-sulfate or -chloride are available in waste acids of chemical industry. The coke used was a calcined, needle-like petroleum coke of low ash (o,o3 wt-%) and low sulfur (o,46 wt-%).

Experimental

The coke particles, one to two mm in diameter, were vacuum impregnated with iron-sulfate solutions of different concentrations and then vacuum dried at 50°C. Iron-sulfate was present as tetrahydrate. Iron concentrations were in the range 0,05 up to 1,8 wt-%. Electron microprobe analysis showed homogeneous distribution of iron on the walls of the pores.

The reaction was studied in a fixed bed reactor at temperatures between 890 and 1000°C using N_2/H_2O-gas mixtures and one bar total pressure. Besides temperature and partial pressure the influence of time, feed rate, bed depth and catalyst concentration on coke and water vapour conversion were investigated. Coke conversion was in the range up to 50% and water vapour conversion up to 100%.

Results

In the following, some selected results will be given in order to demonstrate the extent and the limits of iron catalysis. The rate of coke gasification was measured under various conditions up to 50% and found to be constant, i.e. independent of burn-off. Fig. 1 shows the corresponding constant water vapour conversion. Fig. 2 gives the BET-surface increasing linearly with time.
Variations of water vapour partial pressure and feed rate had the most dramatic effect on gasification rate, as shown in fig.3 and 4, respectively. Stationary water vapour conversion decreases with increasing partial pressure and increasing feed rate in two distinct ranges with different intensity. In any case the rate of the catalized reaction is higher than that with pure coke.

Fig. 5 shows the reaction rate for various catalyst concentrations. Maximum rates are already obtained with low iron concentrations. Temperature dependence is finally given in Fig. 6 by an ARRHENIUS plot. The starting temperature of catalysis is around 900°C. The apparent activation energy for the catalyzed reaction varies between 19 and 29 kcal/mol as compared to 43 kcal/mol for the uncatalyzed coke gasification.

Discussion

Gasification rates,which are constant and independent of burn-off, although BET-surface increases strongly , seem to be surprising. De facto, it can be suggested, that the reaction only occurs at carbon surfaces covered with catalyst. Electron microprobe analysis showing agglomeration of iron with burn-off and, combined with the observation, that increasing catalyst concentrations beyond o,5% don't accelerate the reaction, confirm this suggestion.

The two ranges found with increasing water vapour pressure and feed rate show that the reaction is well catalyzed by metallic iron and less catalyzed by iron oxide.

The temperature range in which catalysis starts coincides with the transition of α-iron to β-iron at 910°C. It can be the supposed that the higher carbon solubility of β-iron is of influence on the catalysis by iron.

Literature

G. WOYKE, "Zur katalytischen Wasserdampfvergasung von Kohle bei hohen Drücken", Diss. Universität Erlangen, 1975

D. McKEE, Carbon 12 (1974), 453

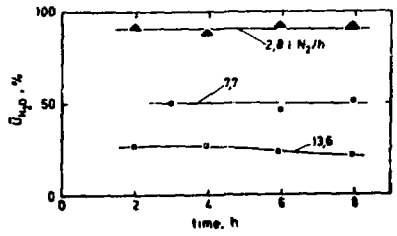


Fig.1-Water vapour conversion with time at 935°C; catalyst concentration 1,8 wt-%; p_{H_2O} = 0,055 bar

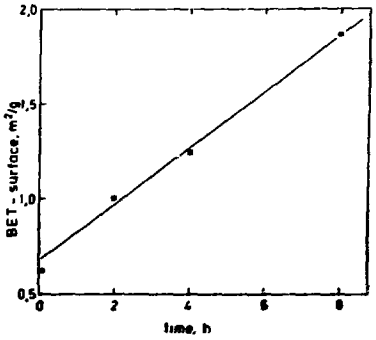


Fig.2-BET-surface with reaction time at 935°C; catalyst concentration 1,8 wt-%; p_{H_2O} = 0,055 bar

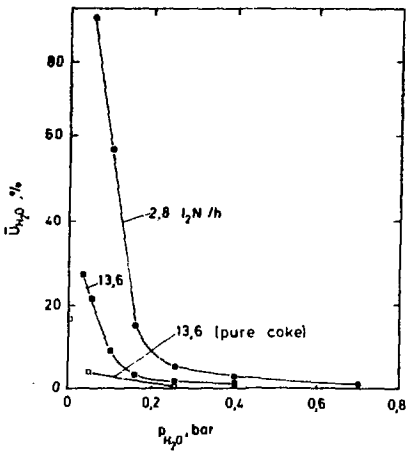


Fig.3-Water vapour conversion with partial pressure at 935°C; catalyst concentration 0 and 1,8 wt-%

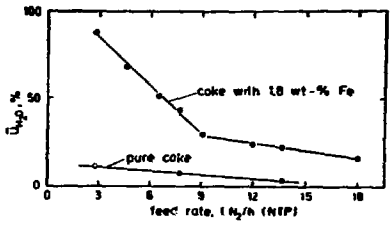


Fig.4-Water vapour conversion with feed rate at 935°C; catalyst concentration 0 and 1,8 wt-% p_{H_2O} = 0,055 bar

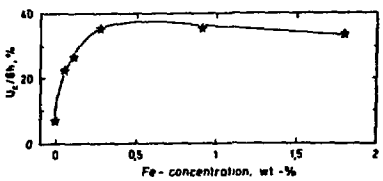


Fig.5-Coke conversion with catalyst concentration at 935°C; p_{H_2O} = 0,055 bar

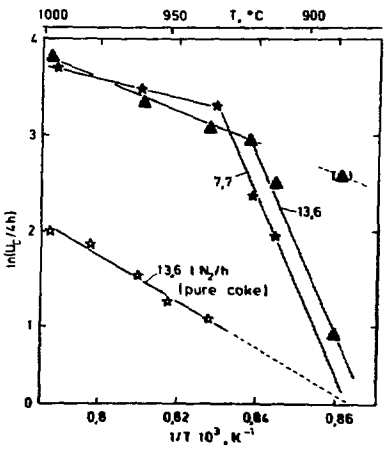


Fig.6-Arrhenius-plot, catalyst concentration 0 and 1,8 wt-%; p_{H_2O} = 0,055 bar

KINETICS OF THE GASIFICATION BY OXYGEN OF A GRAPHITIZING CARBON CATALYZED BY TRANSITION METAL IMPURITIES

H. Marsh, D.W. Taylor
Northern Carbon Research Laboratories, School of Chemistry,
The University of Newcastle upon Tyne, Newcastle upon Tyne NE1 7RU, U.K.

Introduction

In a previous communication (Ref. 1) we discussed variations in the kinetics of gasification by molecular oxygen, as a function of the heat-treatment temperature (in the range 1200 K to 3200 K) of a graphitizing carbon prepared from polyvinyl acetate (PVA). The results of that study showed that with the samples of lowest HTT (1200 K to 1800 K) the reaction is catalyzed by the presence of residual hydrogen in the carbon. This is manifest by significantly higher rates of reaction (one to two orders of magnitude higher than for the PVA carbon, HTT 3200 K, depending on the HTT and the reaction temperature) and lower activation energies for the reaction (126 kJ mol^{-1} for PVA 1200 K; 240 kJ mol^{-1} for PVA 3200 K). This paper is concerned with an extension of these studies in which the effect is investigated on the reaction with oxygen of incorporating transition metal impurities (which are generally known to catalyze the carbon-oxygen reaction) into these anisotropic PVA carbons of HTT 1200 K.

The Experimental Approach

The 'pure' polyvinyl acetate carbon, HTT 1200 K, was prepared according to the method described previously (Ref. 1). Carbons doped with transition metals were prepared by dissolving a coordination compound (with the acetylacetonate ion) of the appropriate metal (e.g. for iron, $Fe(C_5H_7O_2)_3$) in the vinyl acetate, prior to polymerization and subsequent carbonization (to a final temperature of 1200 K heating at a rate of 5 K min^{-1}). This method of incorporation of metal into carbon is known (Ref. 2) to lead to a very fine dispersion of metal particles (~3-100 nm in diameter) distributed evenly through the carbon. The metal concentrations of the carbons studied (expressed as p.p.m. on at atomic basis i.e. number of metal atoms per 10^6 carbon atoms) as determined by atomic absorption, are summarized in Table 1.

Table 1
Metal content of doped PVA 1200 K carbons (p.p.m.)

Metal added	Sample series A (7 p.p.m. in polymer)	B(20 p.p.m.)	C(200 p.p.m.)
V	-	160	-
Cr	-	~300	-
Mn	-	520	-
Fe	-	105	-
Co	55	235	3150

Rates of gasification were measured gravimetrically (under conditions where the reaction rate is controlled by chemical processes only) by a vacuum microbalance(C.I. Electronics Mk. 2B; sensitivity ± 4 μg), following outgassing for 3 hours at 1150 K, on 50 mg samples of the carbon at an oxygen pressure of 1.33 kPa (10 torr). Further details of the experimental procedure can be found in reference 1.

Results

The kinetic results for the metal-doped carbons gave linear Arrhenius plots. The corresponding activation energies for the reaction are in Table 2.

Table 2
Activation Energy (E) for $C-O_2$ reaction (kJ mol^{-1})

Metal added	Sample series A	B	C
V	-	126	-
Cr	-	119	-
Mn	-	142	-
Fe	-	126	-
Co	157	141	148

cf for 'pure' PVA 1200 K sample E=126 kJ mol^{-1}

Discussion

One of the principal features of the results of Tables 1 and 2 is that three of the five metals studied (V, Co, and Fe), apparently do not influence the activation energy of the reaction of oxygen with these anisotropic carbons to any appreciable extent when compared with the undoped carbon of HTT 1200 K (E = 126 kJ mol^{-1}), although with chromium there is a small reduction to 119 kJ mol^{-1}. The reaction of oxygen with carbons doped with manganese proceeds with a higher activation energy (142 kJ mol^{-1}) than that of reaction with pure carbons. Also the rates of oxidation are not changed as dramatically as observed in other metal-carbon systems (Ref. 3). With the manganese-doped carbons the rate, compared to pure carbon, is only about 2.5 times faster. This is a rather unexpected result, perhaps associated with the use of a high density, anisotropic carbon of low surface area and almost total lack of internal porosity.

The cobalt-doped carbons are much more reactive than those carbons doped with comparable amounts of the other metals. The data in Table 3 show the temperatures which would correspond to rates of gasification of 1 x 10^{-6} s^{-1}. Again, the reaction proceeds with an increased energy of activation for the three carbons doped with different concentrations of cobalt. Rates of reaction are enhanced however, by factors between 10^2 and 10^3 more in keeping with previous experience (Ref. 3).

A possible explanation for inactivity in the present case is felt to be associated with the mode of dispersion of the metal within the carbons.

Table 3

Carbon		Temperature/K
Pure:		805
Cr	300 p.p.m.	794
Fe	105 p.p.m.	779
V	160 p.p.m.	775
Mn	520 p.p.m.	775
Co	55 p.p.m.	754
Co	235 p.p.m.	703
Co	3150 p.p.m.	648

It has already been mentioned that in these samples the metal is present as a very fine dispersion of particles distributed throughout the bulk of the material. In such circumstances only a very small fraction of the metal can be present at the surface of the carbon and therefore able to catalyze the reaction via the currently favoured oxygen-transfer mechanism (Ref. 3, 4). By contrast, most previous work has involved addition of the catalyst by direct deposition on to the carbon surface, or has used carbons of high internal surface areas.

Overall, the metal additions to these anisotropic carbons produce similar effects, differences being one of extent. Either the activation energy is unchanged or it is increased. Each of the metal additions produces a positive catalytic effect. The rates are not enhanced spectacularly except for those resulting from the additions of cobalt.

To understand this aspect of catalytic gasification, the exact state of dispersion of the metals in these carbons will have to be ascertained. It is still an open question if there has to be a minimum size of crystallite of metal or metal oxide before such a unit can become an effective catalyst. Also, if the efficiency of agglomeration of the metal in the carbon is high, there may be only a few effective units of catalyst available to the oxidizing gas. Cobalt may form suitably sized units. The other metals could be either too small or too big.

It could be suggested that the cobalt, in these partially graphitic anisotropic carbons, is able to catalyze the reaction via the alternative electron-transfer mechanism (Ref. 5) but this is difficult to prove.

The enhanced rates of oxidation, apparently, are brought about by the enhanced values of the pre-exponential values of the Arrhenius equation, rather than by a lowering of activation energies.

References

1. Taylor D.W. and Marsh H.
Carbon '76. Deutsche Keramische Gesellschaft pp. 101-104 (1976).

2. Crawford D., Marsh H. and Taylor D.W.,
Carbon '76. Deutsche Keramische Gesellschaft. pp. 243-246. (1976).

3. Walker P.L., Shelef M. and Anderson R.A.,
"Chemistry and Physics of Carbon", 4, 287 (1968).

4. McKee D.W.,
Carbon 8, 131 (1970); 13, 381 (1975).

5. Long F.J. and Sykes K.W.,
Proc. Roy. Soc., (London) A215, 100 (1952).

Acknowledgements

We express our thanks to the British Carbonization Research Association for financial support (H.M.) and a Research Fellowship (D.T.).

CORROSIVE EFFECTS OF PYROLYTIC CARBON IN GAS TURBINES

D. W. McKee and D. Chatterji
Research and Development Center, General Electric Company, Schenectady, New York 12301

In the gas turbine air is compressed to 10-20 atm., mixed with a hydrocarbon fuel, which is then burnt to form combustion gases thereby producing the thrust or shaft horsepower of the engine. A major materials problem associated with gas turbines is corrosion of alloy parts at high temperatures by salts, particularly Na_2SO_4, resulting from reactions involving sulfur in the fuel and NaCl in the ingested air. This form of corrosion, which is most severe in the 800-1000°C range, is characterized by the formation of porous oxide scales and internal sulfides which can penetrate deep into the alloys and drastically reduce their useful life [1]. Hot salt corrosion is accelerated by the presence of particulate carbon which promotes local reducing conditions in the salt deposit and increases the sulfur activity at the alloy-salt interface. Carbon particles may arise from incomplete combustion of a liquid fuel or by catalytic decomposition of gaseous hydrocarbons and CO on the hot alloy surfaces. Even though such carbon deposits tend to burn off in the oxidizing combustion gases, the corrosive effects of pyrolytic carbon may persist for long periods [2]. In the present study the deposition, burn-off and corrosive effects of carbon on turbine superalloys have been investigated as a function of the size of the carbon particles.

The rates of deposition of pyrolytic carbon on polished metal and alloy specimens from a 10%CH_4-N_2 stream were measured in a Mettler thermobalance, using a gas flow rate of 100 ml/min and a linear temperature rise rate of 2°C/min. After heating the specimens to 1050°C in contact with the gaseous hydrocarbon, the morphology of the resulting carbon deposit was examined by SEM. Metallic materials included Ni, Co and the Ni-base superalloys U 700, IN 713C and IN 738. The effect of alloy preoxidation on the kinetics of carbon deposition was not investigated. Previous studies have shown that alloys which form NiO scales are more active in promoting pyrolytic carbon formation following preoxidation [3].

Experiments on the behavior of carbon in Na_2SO_4 deposits were also carried out in the thermobalance by heating mixtures of powdered salt and graphite in flowing streams of air or N_2 at a linearly increasing temperature of 2°C/min. Weight changes of the mixtures were measured in both gaseous environments as functions of temperature for graphite samples in the 1μ-2 mm size range.

Corrosion measurements were made by heating polished coupons of IN 738 (½ x ¼ x 1/16 in) in contact with Na_2SO_4-graphite mixtures for 6 hours in flowing air at 950°C, after which time the alloy specimens were cooled and the corrosion products were examined by metallographic and electron microprobe techniques. The influence of graphite particle size on the extent and morphology of the resulting corrosion was investigated.

Even though a large excess of oxygen is normally present in the combustion gases in a gas turbine, carbon deposits are often observed to form on hot path components during engine operation. Particularly during startup fuel-oxidant mixing may be incomplete so that carbonized unconbusted fuel droplets or particulate carbon may deposit along with salt on the hot surfaces of blades and vanes. Also high stationary concentrations of gaseous hydrocarbons or CO may be present in the combustion gases even when high air/fuel ratios are employed [4]. As much as 3 percent by weight of the inlet fuel to the gas turbine may be emitted in the exhaust as unburnt hydrocarbons.

Turbine alloys, especially those containing Ni and Co, may catalyze the decomposition of such gaseous species to give pyrolytic carbon deposits which may be only slowly burnt away in the oxidizing combustion gases. Fig. 1 shows the results of TGA measurements of the rate of pyrolytic carbon formation, from a gas containing methane, on a series of metals and turbine alloys. Both Ni and Co showed high rates of carbon deposition at temperatures above 900°C, with Co exhibiting some evidence of reversible carbide formation at lower temperatures. Although deposition rates on the Ni-base superalloys were slower than on the pure metals, appreciable carbon deposition occurred at temperatures of 950°C and above for all three alloys studied. The morphology of the deposited carbon varied widely depending on the substrate material. Ni gave a granular crystalline deposit composed of columnar stacks of graphite flakes. Co gave a compact rope-like structure of tangled filaments. A fibrous matte of fine carbon threads was formed on U 700, whereas IN 738 and IN 713C developed both globular amorphous carbon masses and filamentary or whisker growth. The crystallinity, particle size and morphology of a pyrolytic carbon deposit will influence its reactivity towards oxidizing combustion gases and towards a codeposited salt phase. In particular the accelerating effect of carbon in hot salt corrosion has been shown to be strongly dependent on the particle size in the case of graphite.

Fig. 2 shows TGA data obtained in flowing air for mixtures of powdered graphite with Na_2SO_4. A strong dependence of oxidation rate on graphite particle size is evident, with burnoff proceeding slowly over a period of hours as the temperature increased from 600 to 1000°C. With the largest particles, oxidation was still incomplete at the highest temperature. Fig. 3 shows weight changes obtained on heating graphite-Na_2SO_4 mixtures in a nitrogen atmosphere. In this case, reduction of the sulfate to sulfide,

$$Na_2SO_4 + 2C = Na_2S + 2CO_2$$

began at temperatures close to the melting point of Na_2SO_4 (884°C) and proceeded rapidly at higher temperatures. A less marked graphite particle size effect was evident in this case, the 75 μm (325 mesh) material showing the greatest reactivity. This

pattern of behavior was mirrored by the results of corrosion experiments with the IN 738 alloys (Table I). Exposure of alloy coupons to pure Na_2SO_4 in flowing air for 6 hours at 950°C produced a thin corrosion layer consisting of an outer porous oxide scale and an inner sulfide band, the total depth of the corroded layer being about 12 μm. By contrast, addition of 25 wt. percent graphite powder to the initial salt resulted in a very marked increase in extent of corrosion even though the bulk of the graphite burnt off below 950°C. As in the TGA experiments, the 75 μm (325 mesh) graphite showed the greatest effect with resulting sulfide penetrations of up to 140 μm.

Table I
Effects of Graphite on IN 738 Salt Corrosion
1g Na_2SO_4 + 250 mg. graphite
950°C 6 hours in air

Graphite	Oxide/sulfide penetration μm
- (Na_2SO_4 alone)	8/12
1 μm	50/100
75 μm (325 mesh)	60/140
250 μm (100 mesh)	30/60
1-2 mm	20/40

Although these experiments were not intended to simulate conditions in an actual gas turbine, it is clear that the presence of solid carbon particles can have an important influence on the magnitude of high temperature salt-induced corrosion of turbine structural materials. The corrosive effects of carbon depend on the structure and particle size of the deposit and in general the burnoff of carbonaceous material may be slow enough for local reducing conditions to persist for extended periods in a salt condensate, leading to accelerated sulfidation of turbine alloys. Every precaution should therefore be taken to minimize carbon formation in the engine by improving combustor efficiency and by utilizing inert protective coatings on hot path components.

1. Beltran, A.M. and Shores, D.A., "The Superalloys", C.T. Sims and W.C. Hagel, eds., J. Wiley, New York, Chap. 11 (1972).

2. McKee, D.W. and Romeo, G. Met. trans. 6A, 101 (1975).

3. McKee, D.W. and Romeo, G., ibid 5A, 1127 (1974).

4. Starkman, E.S., Mizutani, Y., Sawyer, R.F., and Teixeira, D.P., J. Eng. for Power A93, 333 (1971).

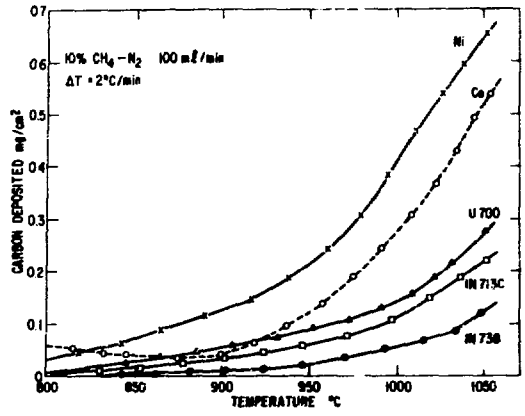


Fig. 1 Pyrolytic carbon formation on metals and alloys from 10%CH_4-N_2. Weight deposited vs. temperature.

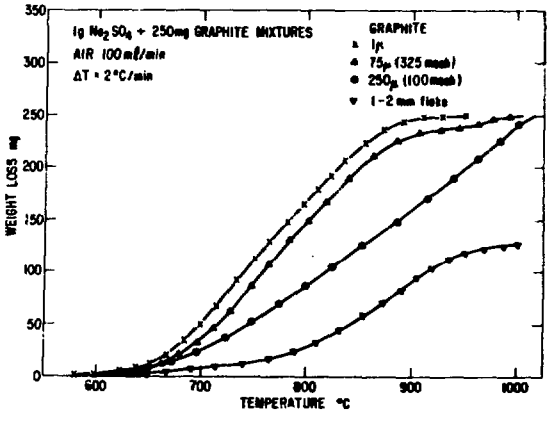


Fig. 2 Burnoff of graphite in air from Na_2SO_4-graphite mixtures. Effect of graphite particle size.

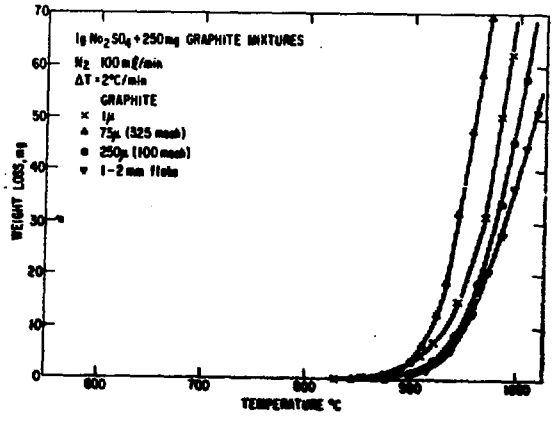


Fig. 3 Reduction of Na_2SO_4 by graphite as a function of temperature and graphite particle size.

THE EFFECT OF NATURAL COAL IMPURITIES ON CARBON GASIFICATION

K. Otto and M. Shelef, Chemistry Department, Research Staff
Ford Motor Company, P.O.Box 2053, Dearborn, MI 48121

In an earlier study, steam-gasification kinetics of 6 chars, prepared from coals of U.S. and German origin, and pure graphite were compared. The gasification was followed gravimetrically in a recirculation system at a water pressure of 2.67 kPa. Rates were evaluated per unit surface area, obtained in situ, from carbon dioxide adsorption at the temperature of dry ice. Five of the six chars yielded specific gasification rates less than a factor of 4 higher (at 850 C) than that of pure graphite. The sixth char, prepared from a German lignite, Braunkohle (BK), yielded a 20-fold rate increase over graphite. At the same time, the activation energy of gasification of this char was lower (59 kcal/mol) than the corresponding values of the other chars (65-82 kcal/mol). It was of interest to study with the same experimental arrangement, whether the reactivity of BK char was higher due to a true catalytic action of its impurities, or to an increase in the number of gasification sites.

Three approaches were selected to study the effects of natural coal impurities on the steam gasification of chars: (a) addition of coal ash to graphite, (b) addition of ash to a less reactive coal, and (c) removal of noncarbonaceous matter from the lignite by acid-leaching.

Metals, such as Fe, Co, Ni, Ru, Rh, Pd and Pt can increase steam gasification of graphite by several orders of magnitude. The results obtained for 3% of BK ash in graphite are shown in the table below. Rates, taken at 850 C, remain constant up to almost 80% burn-off. A 12- to 16-fold enhancement is observed compared to pure graphite, as the table shows, accompanied by a decrease in activation energy. Addition of ash from a Pittsburgh seam coal (PSC) to graphite did not cause such changes.

Nickel and other catalysts, which are quite active in graphite gasification, influence the reaction of chars much less. Furthermore, activity in chars is often lost quickly, while it persists in graphite. These discrepancies can be explained by structural differences. Thus, electron micrographs show extensive channel formations in graphite, indicating preservation of contact between metal particles and graphite surface, while contact loss in chars can be deduced from the agglomeration and isolation of catalyst particles in craters of the char structure. In addition, the much larger surface areas of chars require a 100-fold increase in catalyst concentration per unit weight, compared to graphite, to achieve the same ratio of catalyst weight to carbon-surface area.

T A B L E

Activation Energies and
Specific Gasification Rates

Burn-off %	BET Area m^2/g	Activ. Energy kcal/mol	Rate at 850°C $\mu g/(m^2 \times min)$
A. Pure SP1-Graphite			
13	3.6	80.5	0.3
B. Graphite + 3% BK Ash			
0	2.5	61.9	4.4
14	3.4	60.1	4.8
28	4.3	61.9	4.3
40	5.3	61.4	4.5
80	7.9	64.5	3.6
C. PSC Char, untreated			
19	407	66.3	0.7
D. BK Char, untreated			
24	436	59.5	4.7
E. PSC + 3% BK Ash			
0	318	58.7	4.3
17	293	64.7	2.1
48	276	72.8	1.9
F. BK, leached by $HF+HCl+HNO_3$			
25	625	67.1	1.5
G. BK, leached by HF+HCl			
24	592	58.3	2.0
H. BK, leached by HNO_3			
30	629	59.6	2.1

With these facts in mind, the effect of 3% BK ash, added to PSC, a coal of low reactivity, was examined. For comparable surface areas and stages of burn-off, the specific gasification rate of BK char exceeds that of PSC char more than 6-fold. Of the two chars, BK shows the lower apparent activation energy. Addition of 3% BK ash to PSC produced a marked enhancement in the rate of char gasification. The rate decrease with burn-off indicates some contact loss between the active ash particles and the char surface. At 17% burn-off, the kinetic data fall about halfway between the corresponding values of the untreated chars of BK and PSC. PSC char containing nickel or potassium carbonate showed a much steeper loss of catalytic activity. It is remarkable that the sample pellet containing BK ash could be reacted completely while suspended by a quartz-glass fiber; in fact, the surface of the remaining ash could be measured in situ. These results suggest that the added ash has the ability to preserve contact with the carbon surface, possibly by incipient melting and wetting, or by redistribution through the vapor phase.

Analyses of the ashes of BK and PSC by x-ray fluorescence showed the same elements to be present, the main elements being Fe, Ca, Ti, Si, Al, K and S. However, there was a distinct difference in the distribution of these elements. Quantitatively, one would have expected an advantage of the higher ash content of PSC (6%) over that of BK (4%). When BK was leached by a mixture of HNO_3, HF and HCl, elements found in the solution by atomic adsorption were Fe, Ca, Ti, Si, Al, B and Mg.

A comparison of the gasification rates of BK char, after the acid leachings, is listed in the table. The simultaneous leaching by the three acids caused a decrease of the specific rate by a factor of three, and an increase in the apparent activation energy. It is not known, whether the higher activation energy results from a loss in catalytic action, or from an increase in pore size, which appears possible in view of the increased surface area. The two other leachings caused smaller decreases in the reaction rates, as shown in the table. Differences are also noticeable in the micrographs of leached and unleached BK char.

A parallel study was performed with a lignite of North Dakota origin; it was found to be even more reactive than BK when exposed to steam. The kinetic results obtained from the leaching and ash-impregnation experiments on the two lignites, which show distinct similarities, are compared in considerable detail.

Ash transfer from a reactive to an unreactive coal is an interesting possibility for improving gasification of a particular coal, or for equalizing gasification characteristics when blending coals of different sources.

ON A SPECIAL EFFECT OF γ_3 ON THE ELECTRONIC EQUIENERGY SURFACES OF GRAPHITE

C. AYACHE
Centre d'Etudes Nucléaires de Grenoble
Service des Basses Températures

Within the framework of SLONCZEWSKI-WEISS one-electron theory of graphite the secular equation reads [1].

$$F(r,\alpha) \equiv Ar^4 + B\cos 3\alpha\, r^3 + Cr^2 + D = 0 \quad (1)$$

where r, α are the polar radius and angle measured from the zone edge and A,B,C,D, are polynomials versus the energy ε (of degree 4,2,1 and 0 respectively) with coefficients depending on k_z ($= 2\pi/c_0$).

(1) may be transformed into :

$$F(r,r_X) \equiv A r^4 + (C-3B r_X) r^2 + (D+4B r_X^3) = 0 \quad (2)$$

(2) is an implicite equation of r versus r_X which is solved in a straight-forward way. For fixed values of k_z and ε it represents the *exact form* of the k_z-cross-section of the ε-equienergy surface and we can study the effect of γ_3 on the actual form of this surface. Numerical calculus has been performed for the following parameter set :

$\gamma_0 = 3$ eV $\quad \gamma_1 = 0.3$ eV $\quad \gamma_2 = -0.018$ eV
$\gamma_4 = 0.2$ eV $\quad \gamma_5 = 0$ eV $\quad \Delta = 0.02$ eV

Figs.1 and 2 show the two general shapes of interest obtained for $\gamma_3 = 0.3$ eV and for values of ε of the same order or magnitude as the usually adopted Fermi level.

The major feature is the possibility of *a change of topology* consisting in the connection of the three off-edge "legs" of the two hole-pockets, besides the mere change of form ("trigonal warping") of the equienergy surfaces, we may also notice the consecutive disappearance of the electron-off-edge "legs" and the reduced dimensions of the electron pocket compared with those of the hole one(s).

Many consequences arise from this γ_3-effect. We particularly remark that an anomaly in the electronic density of states is expected from the *change* of topology and that the topology of Fig.2 enables the presence of *open hole-orbits*. Also, in the evaluation of the parameter set from experimental results one must eventually take account for the new topology. However no *immediate* conclusion can be drawn for the behaviour of the carriers under an applied magnetic field because of the interconnection of the γ_3 - and field - effects as shown by the work of NAKAO [2].

1. SPAIN I.L., *Chem.Phys.Carbon*, 6, 1 (1973)

2. NAKAO K., *J.Phys.Soc.Japan*, 40, 761 (1976)

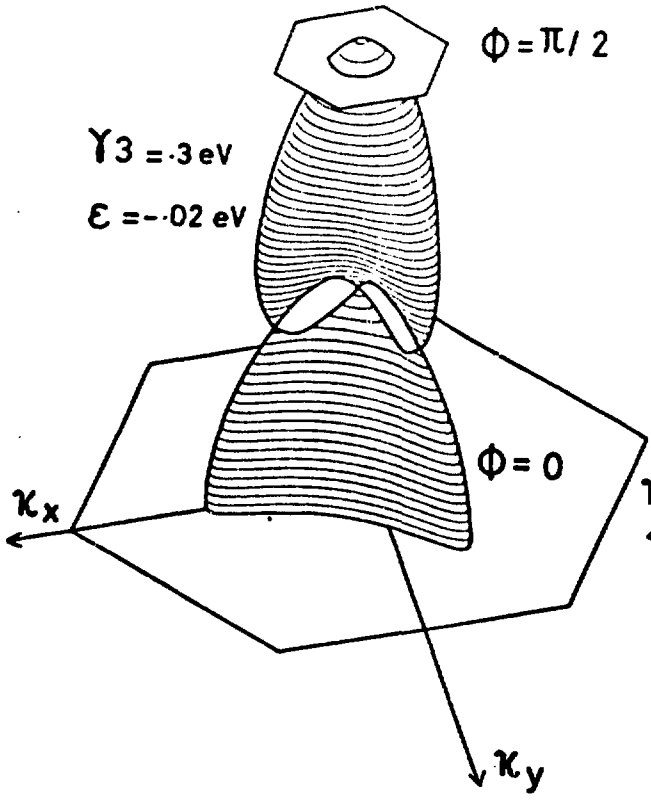


FIG. 1

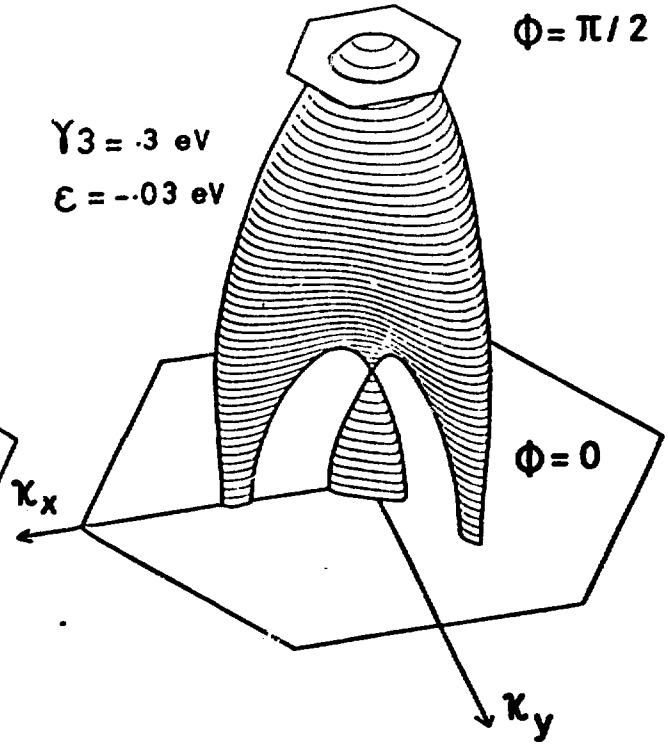


FIG. 2

THEORY OF THE GALVANOMAGNETIC PROPERTIES OF GRAPHITE - CONSEQUENCES OF TRIGONAL WARPING OF THE CONSTANT ENERGY SURFACES*

R.O. Dillon** and I.L. Spain, Dept. of Chemical Engineering, University of Maryland, University Park, MD 20740

The out-of-plane electronic overlap parameter, γ_3, appearing in the band theory of Slonczewski and Weiss, introduces many complexities into the electronic structure of graphite. The most striking effect is that the constant energy surfaces become warped with three-fold symmetry about the vertical edges of the Brillouin zone. Using a simplified model of the energy surfaces and taking $\gamma_3 = 0.29$ eV, the effect of this trigonal warping on the conductivity tensor components σ_{xx} and σ_{xy} was calculated[1,2]. Based on this calculation, the present paper discusses the effect of trigonal warping on: 1.) the field dependence of the low temperature Hall coefficient, 2.) low field conductivity data and carrier densities derived from such data, 3.) carrier densities derived from an integral of σ_{xx} over the field, and 4.) the pressure dependence of the basal conductivity of graphite.

Hall Coefficient

Warping of an energy suface can exert strong effects on the Hall coefficient at weak and intermediate fields. At strong fields warping never affects the Hall coefficient and it asymptotes to the value of $R_\infty = 1/(P-N)e$. For graphite, the model results indicate that trigonal warping will have only a small effect on the Hall coefficient at weak fields. However, it can have a large effect at intermediate fields tending to make the Hall coefficient become positive (for the model calculation, the intermediate field range is $.02 \lesssim \omega\tau \lesssim 2$). This positive-going tendency may cause a sign reversal at intermediate fields. The reason this tendency occurs is that portions of negative curvature on the cross section in Figure 1 become important in determining the Hall coefficient.

A tendency for the Hall coefficient to become positive at intermediate fields is, in fact, observed at 4K and 77K as illustrated in Figure 2. At 293K thermal broadening reduces the effect of trigonal warping. Previous workers have tried to explain the field dependencies shown in Figure 2 in terms of mobile minority carriers dominating the weak-field behavior. However, the following difficulties arise with this interpretation: 1.) the graphite band model predicts the existance of minority holes , but the weak-field data in Figure 2 cannot be explained without both minority electrons and holes 2.) the switch from a minority electron to a minority hole at 77K as the specimen is changed from pyrolytic to natural graphite cannot be explained and 3.) the pressure dependence of the weak-field Hall coefficient predicts extremal area changes of the minority pocket which are quite different than the pressure dependence of minority carrier de Haas Van Alphen oscillations.

A consistent explanation of the data in Figure 2 is reached if the positive excursions at intermediate fields are interpreted in terms of trigonal warping. The weak field behaviors are explained in terms majority carriers, and the change between pyrolytic and natural graphite at 77K is explained by differences in scattering mechanisms.

Low Field Conductivity

The trigonal warping modulates the velocity of carriers on the Fermi surface, such that their average velocity increases. This causes a conductivity enhancement as represented by the factor ξ in,

$$\sigma = (N+P)e\bar{\mu}\xi(\gamma_3, B) \qquad (1)$$

where N and P are carrier densities, $\bar{\mu}$ is an average mobility without trigonal warping, and the average on β denotes a Fermi surface average. As illustrated in Figure 3 for the part of the model calculation dealing with the electrons, ξ is large at weak fields and then asymptotes to a strong field limit somewhat greater than unity. The model uses non-warped hole cross sections and thus minimizes the enhancement of σ_{xx} due to warping of the hole Fermi surface. Even so the model yields a 60% enhancement of $\sigma_{xx}(o)$, indicating that trigonal warping strongly influences the weak field conductivity behavior. Figure 4 shows the observed behavior using the slope, n, of a log-log plot of $[\sigma_{xx}(o)/\sigma_{xx}(B)] - 1$ versus $\bar{\mu}B$. The anomolous weak field behavior has previously been interpreted in terms of mobile minority carriers. However, the estimated density of minority carriers is too low for them to be strongly affecting σ_{xx}.

Figure 4 also shows the prediction of the model calculation. Although the magnitudes are different, this shows that trigonal warping can produce a minimum in n at the same field region as the observed minimum.

The effect of warping on σ_{xx} at low fields indicates that use of equation

$$N + P = \sigma_{xx}(o)/e\bar{\mu} \qquad (2)$$

to calculate carrier densities will result in error. Trigonal warping tends to increase both $\sigma_{xx}(o)$ and $\bar{\mu}$. Since these increases oppose each other in calculating N+P, the net result is very sensitive to the exact form of the warping. The model calculation yielded an over-estimation of N+P on the order of 10%. The major effect of warping in using equation (2) is then not this error, but the variation on n at weak fields shown in Figure 4. This variation of n makes it impossible to define $\bar{\mu}$ without arbitrariness[3].

Carrier Densities Based on Field Integrals

An alternative to equation (2) which has been used to derive carrier densities is based on

$$N + P = \frac{2}{\pi e}\int_0^\infty \sigma_{xx} dB \qquad (3)$$

The enhancement of σ_{xx} caused by warping indicates that N+P will be overestimated with this formula. The model calculation yields an overestimation of 22%. However, a more serious problem associated with the application of (3) is that σ_{xx} does not asymptote to a B^{-2} dependence at high fields as required in derivation of (3). Evidence of this problem is indicated in Fig. 4 where at $\bar{\mu}B = 8$, $n = 1.6$ instead of a value near 2. Figure 4 also indicates that this high field behavior is not caused by trigonal warping. At higher fields σ_{xx} asymptotes to approximately a B^{-1} dependence. Because of this, equation (3) cannot presently be meaningfully applied to graphite.

*This research was supported by the Atomic Energy Commission.

**Now at Dept. of Material Science, 6532 Boelter Hall, University of California, L.A., CA 90024

Pressure Dependence of Conductivity

Equation (1) shows that trigonal warping introduces a term $(d\ln\bar{r}^2/d\ln\gamma_3)(d\ln\gamma_3/dp)$ in the logarithmic derivative of the conductivity with pressure. The calculation of this term is difficult because both $\bar{r}$ and $d\ln\bar{r}^2/d\ln\gamma_3$ vary along the vertical edge of the Brillouin zone. The model calculations show that $d\ln\bar{r}^2/d\ln\gamma_3 \gg 1$. This result indicates that the variation of conductivity with pressure cannot be satisfactorily interpreted without the γ_3 term because $d\ln\bar{r}^2/dp$ is on the order of $d\ln N/dp$.

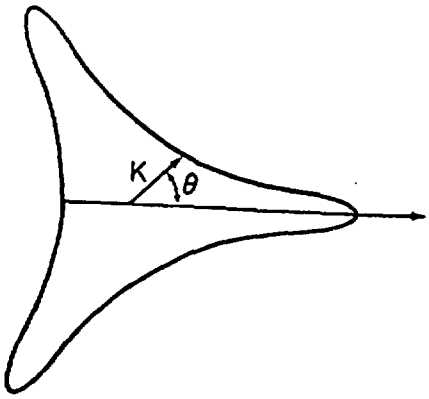


Figure 1. Cross section of the electron Fermi surface, based on $\gamma_3 = 0.29$ eV. The vector K points to a region of negative curvature.

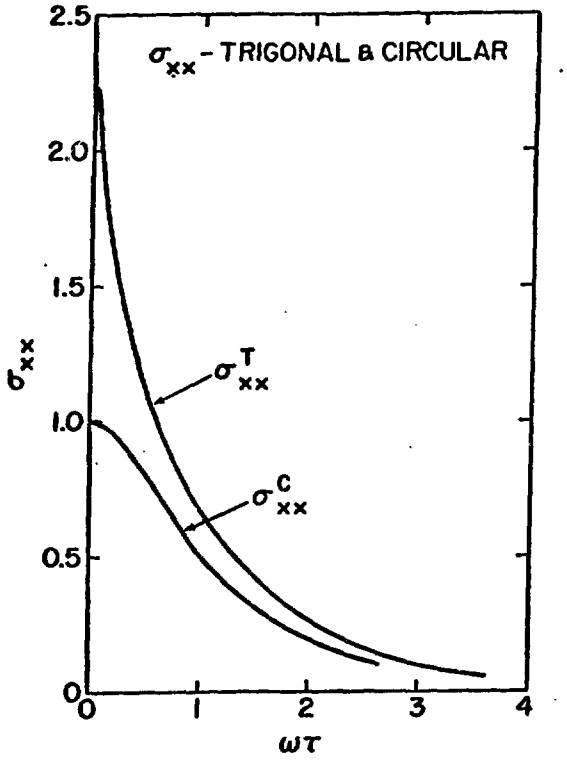


Figure 3. The normalized conductivity for the electron Fermi surfaces for circular, σ_{xx}^C, and trigonally warped, σ_{xx}^T, energy surfaces.

References

1. Dillon, R.O., Ph.D Thesis, University of Maryland (1974).
2. Dillon, R.O. and Spain, I.L, J.Phys.Chem.Solids, in press.
3. Spain, I.L. and Dillon, R.O., Carbon 14, p.23, (1976).

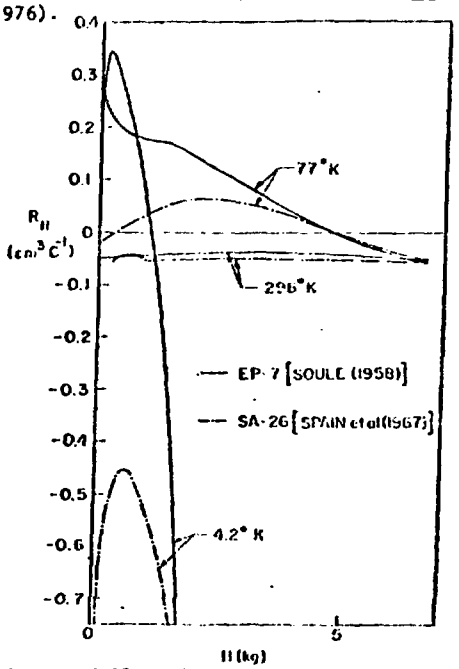


Figure 2. The Hall coefficients of graphite for pyrolytic (---) and natural (-) specimens.

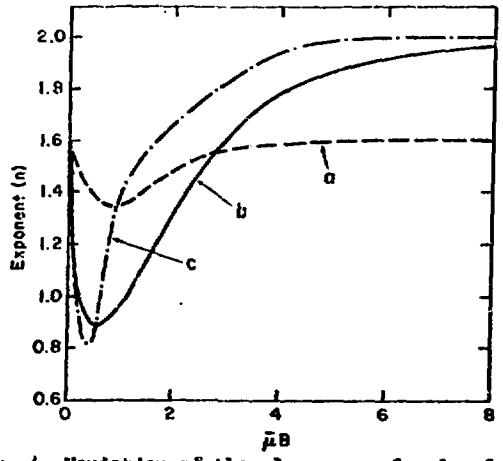


Figure 4. Variation of the slope, n, of a log-log plot of $[\sigma_{xx}(o)/\sigma_{xx}(B)] - 1$ versus $\bar{\mu}B$. Curves are for experimental data for pyrolytic graphite at 4.2K (a), and model calculation results, electron surface only (b) and both surfaces (c).

IMPURITY STATE OF GRAPHITE IN THE QUANTUM LIMIT

Ko Sugihara

Central Research Laboratory, Matsushita Electric Industrial Co., Ltd. Moriguchi, Osaka, Japan

§1. Introduction

Brandt et al have carried out detailed experiments on the galvanomagnetic properties of graphite in magnetic field ranged from 200 Oe to 500 kOe. (1) They observed that in fields $H > 200$ kOe $|\sigma_{xy}H|$ decreases sharply with H. (see Fig.1) In strong magnetic field $\sigma_{xy}H$ is given by

$$\sigma_{xy}H = ec(p - n), \quad (e > 0), \qquad (1.1)$$

where p and n denote hole and electron concentrations, respectively. Charge neutrality needs the following condition:

$$p - n = \sum_i \left(\frac{e_i}{e}\right) z_i N_i , \qquad (1.2)$$

where z_i denotes the valence of the i-th impurity and N_i its concentration.

Brandt et al ascribed the decrease of $|\sigma_{xy}H|$ to the freeze-out of carriers. They conjectured that the similar effect predicted by YKA theory in semiconductors (2), can occur in graphite. Namely, $a_B^* < r_s$ holds, where a_B^* denotes the Bohr radius of an impurity electron and r_s is the screening radius of current carriers. In graphite the condition $a_B^* < r_s$ is not satisfied in zero magnetic field, then bound states are not formed, but intense magnetic field changes the condition necessary for occurance of magnetic freeze-out. As H increases, the effective Bohr radius a_B decreases and the binding energy E_B increases, accordingly the bound states, which trap current carriers, are formed.

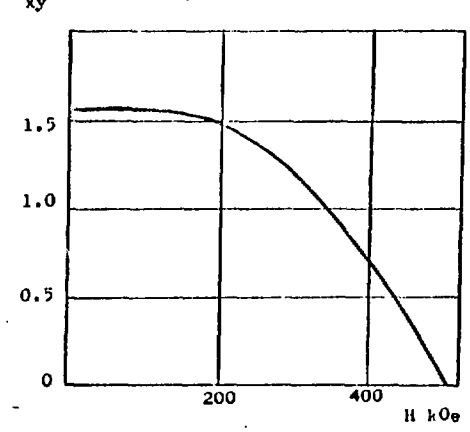


Fig.1 $\sigma_{xy}H$ vs H curve in graphite (T = 4.2 K)

However, it seems to be doubtful to apply the theory of the freeze-out effect in semiconductors to semimetallic graphite. In this article we present a theory describing an impurity state in graphite in the quantum limit by extending the theories of Koster-Slater, Koster, Wolf, and Clogston. (3~6) As will be stated later, we can show that feature of the Landau states in graphite make appearance of the bound states possible for $H > H_c$, where H_c ($\cong 70$ kOe) correspond to the quantum limit field strength.

§2. Scattering of Landau Electrons

In a field of an impurity potential V(r) an incoming state Ψ_λ is related to an outgoing scattered wave as follows:

$$\Psi = \Psi_\lambda + (\epsilon - \mathcal{H}_0 + i\eta)^{-1} V\Psi , \qquad (2.1)$$

where λ indicates a Landau state and $\mathcal{H}_0$ is the unperturbed Hamiltonian. (7) Let us expand Ψ by the Wannier function (3~6),

$$\Psi = N^{-1/2} \sum_{t=1}^{4} \sum_n U_t(R_n) w_t(r-R_n), \qquad (2.2)$$

where t = 1~4 corresponds to the bands E_1, E_2, E_3, and E_3' (8), and N is a number of the unit cell.

By neglecting γ_3 the Landau state Ψ_λ is given by

$$\Psi_\lambda = \sum_{t=1}^{4} c(\lambda_t) u_{N_t}(x-X) e^{ik_y y} \phi_{k_z}^{(t)} , \qquad (2.3)$$

where

$$X = \frac{k_y}{s} , \quad s = \frac{eH}{\hbar c} ,$$

and $\phi_{k_z}^{(t)}$ is the Bloch function at $k_x = k_y = 0$.

By expanding $V\Psi$ into the Landau states and operating

$$\int d\tau\, \overline{w_t(r-R_n)} \ \ldots ,$$

we get

$$U_t(K_0) \cong A(\lambda_t) + N^{-1}\sum_{\mu}|c(\mu_t)|^2(\varepsilon-\varepsilon_\mu+i\eta)^{-1}\times$$

$$\sum_s V_{ts}U_s(K_0)\ , \qquad (2.4)$$

where

$$\begin{cases} A(\lambda_t) = c(\lambda_t)u_{\lambda_t}(\lambda_0-x)e^{ik_yY_0}e^{-ik_zZ_0}, \\ \int d\tau\ \overline{w_s(r-R_m)}V(r)w_{s'}(r-R_n) \cong V_{ss'}\delta_{mn}. \end{cases}$$

In deriving (2.4) we assumed that $V(r)$ is well localized around $R_0(X_0,Y_0,Z_0)$. Due to the presence of $C(\mu_t)$ it is difficult to solve the simultaneous equation (2.4). To obtain the condition of the bound state formation is eqivalent to find in what situation $U_t(R_0)$ becomes infinite.

§3. Bound state in graphite

It is more easier to treat $U(R_0) = \sum_t U_t(R_0)$ instead of $U_t(R_0)$. For simplicity we put

$$\sum_s V_{ts}U_s(K_0) = V_0\sum_s U_s(K_0) = V_0U(K_0), \qquad (3.1)$$

and assume V_0 as a constant. Thus, we get

$$U(K_0) = \frac{A_\lambda}{D(\varepsilon)},\quad A_\lambda = \sum_t A(\lambda_t). \qquad (3.2)$$

Introducing a quantity

$$\varphi = \frac{1}{2}c_0k_z,\ c_0\text{: unit cell height}, \qquad (3.3)$$

$D(\varepsilon)$ is represented by

$$D(\varepsilon) = 1 - V_0\left\{\sum_\mu \frac{\Omega s}{2\pi^2c_0}\int d\varphi\ P\left(\frac{1}{\varepsilon-\varepsilon_\mu(\varphi)}\right)\right.$$

$$\left. - i\pi\Omega\sum_\mu g_\mu(\varepsilon)\right\}, \qquad (3.4)$$

$\begin{cases} g_\mu(\varepsilon)\text{: density of state related to } \mu\text{-th level}, \\ \Omega\text{: unit cell volume.} \end{cases}$

The condition of the bound state formation is given by

$$\mathrm{Re}D(\varepsilon) = 0,\ g(\varepsilon) = \sum_\mu g_\mu(\varepsilon) = 0. \qquad (3.5)$$

Carriers enter into the quantum limit at H = 70 kOe. (9,10) Landau levels at H = 70 kOe is shown in Fig.2, which indicates that any energy ε does not satisfy $g(\varepsilon) = 0$. Since $\varepsilon_0^{-1}(1) = E_3$ is a level which is independent of H, with increasing H $\varepsilon_1^{-1}(1)$ goes down, and we can find ε satisfying $g(\varepsilon) = 0$ between $\varepsilon_0^{-1}(1)$ and $\varepsilon_1^{-1}(1)$.

In strong magnetic field the quantity $\alpha = |\mathrm{Re}D(\varepsilon) - 1|$ decreases with H. Then, if

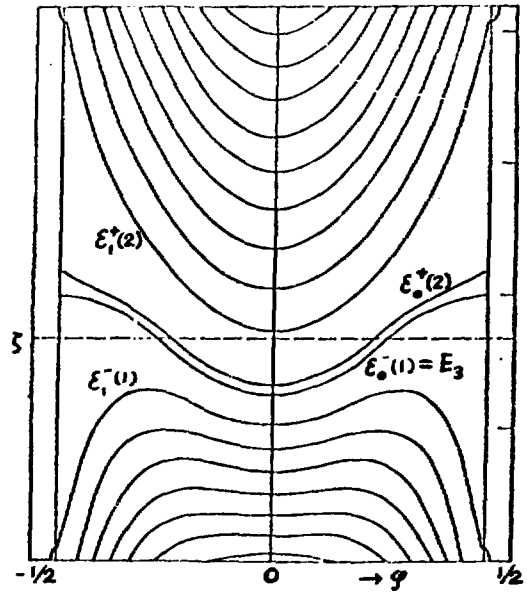


Fig.2 Landau levels for H = 70 kOe.

α is larger than unity for H < 200 kOe, the condition of $\mathrm{Re}D(\varepsilon) = 0$ can be realized with further increase of H. The consideration stated above provide a possibility of decrease of $|\sigma_{xy}H|$ in strong magnetic field.

REFERENCES

1. Brandt N. B., Kapustin G. A., Karavaev V. G., Kotosonov A. S., and Svistra E. A., Soviet Phys. - JETP 40, 564 (1975).
2. Yafet Y., Keyes R. W., and Adams E. N., J. Phys. Chem. Solids 1, 137 (1956).
3. Koster G. F., and Slater J. C., Phys. Rev. 95, 1167 (1954).
4. Koster G. F., Phys. Rev. 95, 1436 (1954).
5. Wolf P. A., Phys. Rev. 124, 1030 (1961).
6. Clogston A. M., Phys. Rev. 125, 439 (1962).
7. Lippmann B. A., and Schwinger J., Phys. Rev. 79, 469 (1950).
8. Slonczewski J. C., and Weiss P. R., Phys. Rev. 109, 272 (1958).
9. Sugihara K., and Ono. S., J. Phys. Soc. Japan 21, 631 (1966).
10. Woollam J. A., Phys. Rev. Letters 25, 810 (1970); Phys. Rev. B3, 1148 (1971).

GALVANOMAGNETIC PROPERTIES OF GRAPHITE FROM 1.1K TO 23T*

W.H. Lowrey†
Naval Research Laboratory
Washington, D.C.

&

I.L. Spain
University of Maryland
College Park, Md.

1. Introduction

Measurements of the magnetoresistance ($\rho xx(Bz)$ and $\rho zz(B_z)$) and Hall resistivity ($\rho yx(B_z)$) of highly oriented pyrolytic graphite have been made in steady magnetic fields up to 23T. The starting material (supplied by Dr. A.W. Moore of Union Carbide) is the best quality pyrolytic graphite reported to date, as evidenced by the similarity of its electronic properties to those of natural single crystals. Details of measurements on the material for B 10T will be found elsewhere (1,2). We report here the first work on graphite in the field range at 300K, and the first at 77K other than pulsed-field work (3). Also, new results at 4.2K and 1.1K are reported.

While the experimentally measured quantities are resistivities, the conductivities are needed for comparison with theory. We use the standard transformation and calculate $\sigma xx(B_z)$, $\sigma yx(B_z)$ and $\sigma zz(B_z)$.

2. $\sigma xx(B_z)$.

Classical theory predicts σxxB^2 saturates in the high field limit. However McClure and Spry (4) found $\sigma xx \propto B^{-1}$ at 4.2K in (pulsed) fields up to 16T. Later, Woollam et al(5,6) showed σxx increases more slowly than B in the high-field region. Our results are shown in Fig. 1 in the form σxxB vs. B. At 298K σxxB decreases and seems to have reached a constant value of ~160kT/Ωm at 23T. The data at 4.2K and 77K are remarkably similar, both showing a minimum at ~13-14T and the 4.2K data shows some structure at higher fields. The data at 4.2K agree with Woollam's observation, and we see a continuing approach to saturation in ρxx at high fields. We also note $\sigma xx(B,T=4.2K) \approx \sigma xx(BT=1.1K)$, in accord with earlier results below 12T (7).

3. σxy

In simple theory $\sigma xyB = (P-N)|e|$ in the high-field limit. McClure and Spry [4] found σxyB to be constant above about 8T. We find (Fig. 2) that $\sigma xyB(T=4.2K)$ shows a maximum at ~12T then decreases with decreasing slope out to 23T. Deviations from a smooth curve are seen at this temperature and at 1.1K. The curve at 1.1K has pronounced "bumps" at ~18T and ~20.5T. A maximum is also seen at ~11.5T but it is much weaker. At 77K, σxyB shows a general increase with a large "bump" at ~15.5T, and possibly a smaller one at ~21T. At 298K, σxyB increases uniformly with decreasing slope.

4. ρzz

Earlier work on longitudinal magnetoristance in graphite up to 8T [8] indicated saturation for temperature of 77K and below. Our results show not saturation, but a maximum in ρzz(Fig. 3). At 298K this maximum occurs at 16.5T. At 77K, the maximum occurs below 10T. At this temperature ρzz falls linearly with B above 15T. The data at 1.1K show a weak maximum at ~20T. No maximum is seen in the 4.2K data up to 23T.

5. Anisotropy

In measuring the conductivity anisotropy $\sigma xx/\sigma zz$ as a function of field, we have used the approximation $\sigma xx=\rho zz^{-1}$, which is a good approximation in this field range. The results at 298K and 77K (Fig. 4) are remarkably similar in light of the vast difference between $\sigma xx(298K)$ and $\sigma xx(77K)$ and between $\rho zz(77K)$;note that at 23T the anisotropy changes by less than 5% in going from 298K to 77K. The results for 4.2K and 1.1K are qualitively similar, both showing anisotropy which is decreasing with decreasing slope. The anisotropy at 1.1K is larger than at 4.2K (~50% larger at 22T). This increase in anisotropy as the temperature is lowered from 4.2K to 1.1K follows from our observation that while $\sigma xx(B,T=4.2K) \approx \sigma xx(B,T=1.1K)$, $\sigma zz(B,T=4.2K) \approx \sigma zz(B,T=1.1K)$.

Conclusions

The present results show structure in the galvanomagnetic properties above the quantum limit. It is possible that this is related to magnetophonon oscillations. A measurement of the variation of the amplitude of oscillation with temperature would be helpful in determining if this surmise is correct. This would require an A-C technique.

The behavior of σxx and σxy in very high fields is of great interest, particularly the approximately linear dependence at 1.1 and 4.2K. A revised calculation of the conductivity in this regime is called for.

Finally, the conductivity anisotropies reported here are smaller than any reported for highly oriented graphite (either natural or synthetic) and suggest that defects are not responsible for the high values of $\sigma xx/\sigma zz$ found at low field in pyrolytic materials (The anisotropy of the present samples was ~ 3,000 at 298K rising to ~10^5 at 1.1K.).

References

1. W.H. Lowrey and I.L. Spain, to be published in Physics Letters.
2. R.O. Dillon, I.L. Spain, J.A. Woollam and W.H. Lowrey to be published in J. Phys. Chem. Solids
3. N.B. Brandt, G.A. Kapustin, V.G. Karavaev, A.S. Kotosonov and E.A. Svistova, Zh. Eksp. Teor. Fiz. 67, 1136 (1974) [Eng. Trans. Sov. Phys. JETP 40, (3) 564 (1975).
4. J.W. McClure and W.J. Spry, Phys. Rev. 165 (3), 809 (1963).
5. J.A. Woollam, Physics Letters, 32A (6), 371(1970).
6. J.A. Woollam, D.J. Sellinger, R.O. Dillon & I.L. Spain, Low Temp Physics, LT13, Vol 4, p. 358 (ed K.D. Timmerhaus, W.J. O'Sullivan, & E.F. Hammel (Plenum Press, 1971).
7. L. Kreps, R. Devaty, J.A. Woollam, Abstracts of 12th Biennial Conference on Carbon, p 9 (1975)
8. I.L. Spain and J.A. Woollam, Solid State Comm. 9, 1581 (1971).

* Work performed at National Magnet Laboratory supported at MIT by NSF

† NRC Resident Research Associate

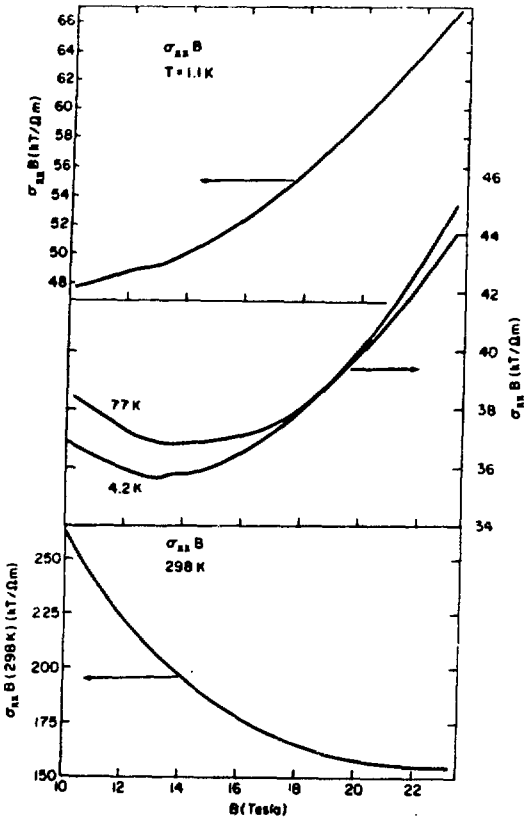


Fig. 1. σxx.B at 1.1, 4.2, 77 and 298K.

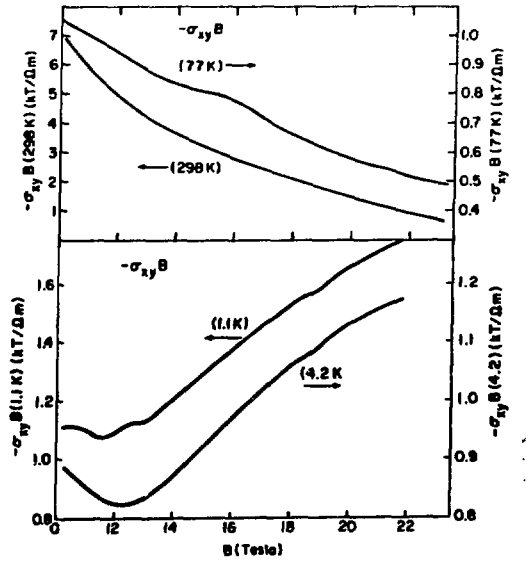


Fig. 2. σxy.B at 1.1, 4.2, 77 and 4.2K.

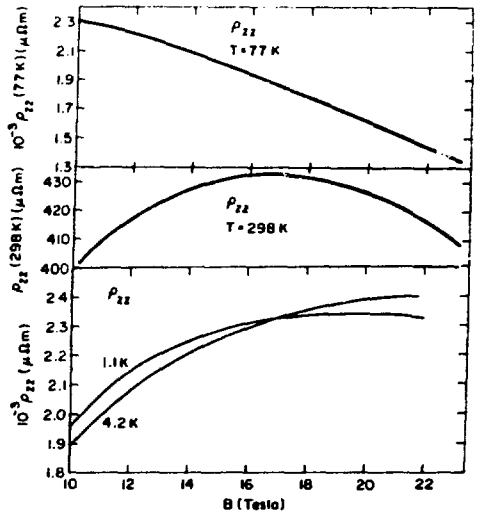


Fig. 3. ρzz at 1.1, 4.2, 77 and 298K.

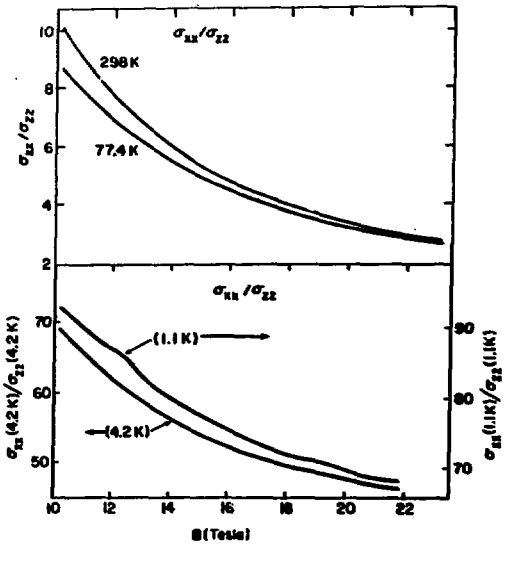


Fig. 4. The conductivity anisotropy ratio as a function of field (σxx/σzz) at 1.1, 4.2, 77 and 298K.

ANISOTROPY OF THE MAGNETIC-FIELD-INDUCED ANOMALY IN THE RESISTANCE VERSUS TEMPERATURE CURVE OF GRAPHITE

AYACHE C. and de COMBARIEU A.

Centre d'Etudes Nucléaires de Grenoble
Service des Basses Températures

The basal magnetoresistance of a highly oriented pyrolitic graphite has been measured as a function of temperature for the two configurations H // C and H $\perp$ C - H // J. In both cases the anomaly previously observed [1] [2] is present but is very anisotropic.

As regard to the first configuration and when we consider the resistance variation versus magnetic field at a fixed temperature (see Fig.1a) we can distinguish essentially two regimes. In the first one -below 4 Teslas - we get a nearly H^2 law but there is as usually a neat departure from it and the results cannot be fitted to a H^n law with $1.5 < n < 2$. The second regime - above 4 Teslas - is nearly described by a H law but yet with a departure from the exact law. If we compare these results (valuable at any temperatures) with the low-temperatures ones where the quantum effects are sensitive, the separation between the two regimes seems to be closely correlated with the oscillation usually attributed to the n = 1 hole - level crossing. Let us notice too that, below a determined temperatures, the isotherms all cross on the same range of temperature and magnetic field (about 250 oersteds). Considering now the temperature variations at fixed magnetic field (see Fig.1b) we observe the already mentionned anomaly which consist in an important enhancement of resistance at low temperatures (about 2000 at 4.2 K and 7.3 T) and the appearance of a maximum. As the magnetic field is increased the maximum temperature raises up to a limit of about 27 K for magnetic fields above a value comprised between 3 and 4 Teslas.

In the second experimental configuration and for the same range of magnetic fields (see Fig.2a) there is only one regime corresponding to the nearly H^2 law. The departure from the exact law is not exactly the same as in the first configuration. Below a certain temperature all the isotherms still cross in the same magnetic field range but this range is quantitatively different from the previous one (about 7000 oersteds).

The low-temperature enhancement (see Fig.2b) is much lower than in the former case (about 90 at 4.2 K and 7.3 T) and there is no evidence for any maximum.

However from this differences (different range of isotherms crossing, different enhancement) we have been able to evaluate a scaling factor for the magnetic field (about 25-30) between the behaviour of the second configuration and the the first regime of the first one.

1. KREPS L., DEVATY R. and WOOLLAM J.A. *12th Biennal Conference on Carbon (Extended Abstracts and Program)* p9 (1965)

2. WOOLLAM J.A., KREPS L.W., ROJESKI M., VOLD T. and DEVATY R., *Technical paper presented at the March 1976 Meeting of the America Physical Society, Atlanta, Georgia, March 29-April 1* (1976).

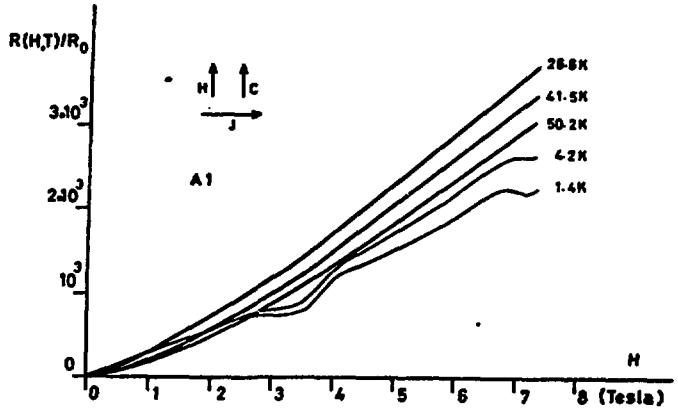


FIG. 1a

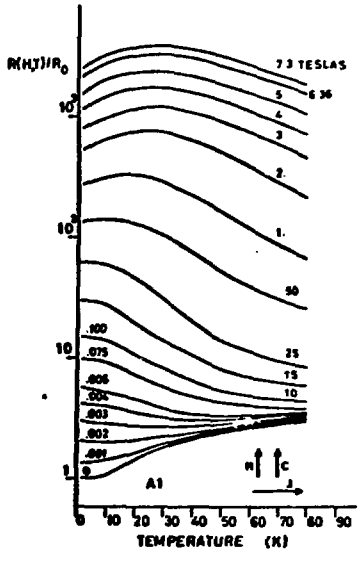


FIG. 1b

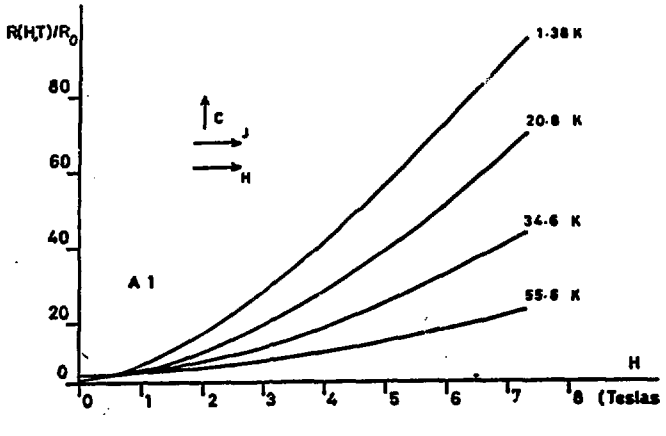


FIG. 2a

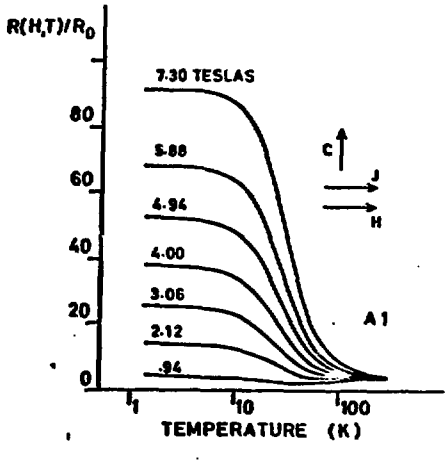


FIG. 2b

TEMPERATURE AND FIELD DEPENDENCIES OF GALVANOMAGNETIC EFFECTS IN GRAPHITE

L. W. KREPS* AND J. A. WOOLLAM
NASA Lewis Research Center, Cleveland, Ohio 44135

At the twelfth biennial conference on carbon, we reported that highly oriented pyrolytic graphite (HOPG) had an anomolous temperature dependent magnetoresistivity.[1] In zero field, B, the electrical resistivity, $\rho_{xx}(0,T)$, decreased monotonically with decreasing temperature, T, becoming nearly constant below 4 Kelvin. However, in an applied field B_z the transverse resistivity component $\rho_{xx}(B_z,T)$ went through a maximum as a function of temperature at about 25 degrees Kelvin. We now have data on a single crystal (figure 1) which is very similar to the data for HOPG. That is, the resistivity in high field goes through a maximum as a function of temperature, the maximum is more pronounced at high B, and the maximum is at roughly the same temperature as for HOPG. The data in figure 1 are "modulated" by the presence of Shubnikov deHaas (SdH) oscillations which are more pronounced at lower temperatures. The last SdH oscillation as a function of field is near 8 tesla, so the data from 10 to 13.5 tesla in figure 1 illustrate the maximum, unmodulated by the SdH effect. Since we now find maxima for both HOPG and single crystal graphite, we must conclude that the effect is intrinsic to graphite.

As a second set of experiments, we measured the B dependence of $\rho_{xx}(B_z,T)$ at a series of fixed T's from 1 to 300°K. According to the simple two-band model for a compensated material

$$(1)\quad \frac{\Delta\rho}{\rho} \equiv \frac{\rho_{xx}(B_z,T)-\rho_{xx}(0,T)}{\rho_{xx}(0,T)} = \overline{\mu(T)}^2 B_z^2 \text{, where}$$

$\overline{\mu}$ (T) is a suitably defined average carrier mobility. However, we find, as have others,[2-5] that the exponent of B_z in equation (1) is generally less than two and is a function of temperature and field strength, indicating that the simple theory is inadequate. We present results which better define the temperature and field dependence of the exponent for several HOPG samples and a natural single crystal. We have determined an "effective" exponent, n(T), relating $\Delta\rho/\rho$ to $B_z^{n(T)}$ from plots of log ρ_{xx} vs. log B_z. We find, in HOPG for example, that at 1 Tesla $n \simeq 1.8$ at 300 Kelvin, decreases to 1.4 at 40 Kelvin, then drops rapidly to 1.2 at 4.2 Kelvin. The mobility, $\mu(T)$, as estimated from plots of ρ_{xx} vs. B_z at low fields, is roughly constant at low temperatures, but decreases rapidly at higher temperatures. Qualitatively, then, the maximum in ρ_{xx} result because $n(T)$ decreases at low temperatures while $\overline{\mu}$ (T) decreases at high temperatures, so the product goes through a maximum. However, since the data associated with $n<1.8$ are in or near the quantum limit regime, calculations including the effects of the quantization of electronic motion are needed.

We conclude that: 1) the maxima are present in both HOPG and natural single crystals, and, therefore, seem to be intrinsic to graphite; and 2) The maxima are related to the field dependence of ρ_{xx} at low temperatures; and 3) calculations are needed of the field dependence of $\sigma_{xx} \simeq 1/\rho_{xx}$ in graphite as a function of temperature just below and in the quantum limit for phonon and boundary scattering.

1. Lawrence Kreps, Robert Devaty, and John A. Woollam; "Anomalous Temperature Dependent Magnetoresistivity in Pyrolytic Graphite" in Extended Abstracts and Program, 12th Biennial Conference on Carbon, July 28-Aug. 1, 1975, p.9.

2. John A. Woollam, Physics Letters 32A, 371 (1970)

3. John A. Woollam, David J. Sellmyer, Rodney O. Dillon, and Ian L. Spain, Low Temperature Physics-LT13, 4 (1975) p. 358.

4. Joel W. McClure, W. J. Spry, Physical Review 165 809 (1968).

5. Rodney O. Dillon and Ian L. Spain, Carbon, 14, 23 (1976).

*Visiting Scientist: now at 4216 W 227th Street, Fairview Park, Ohio

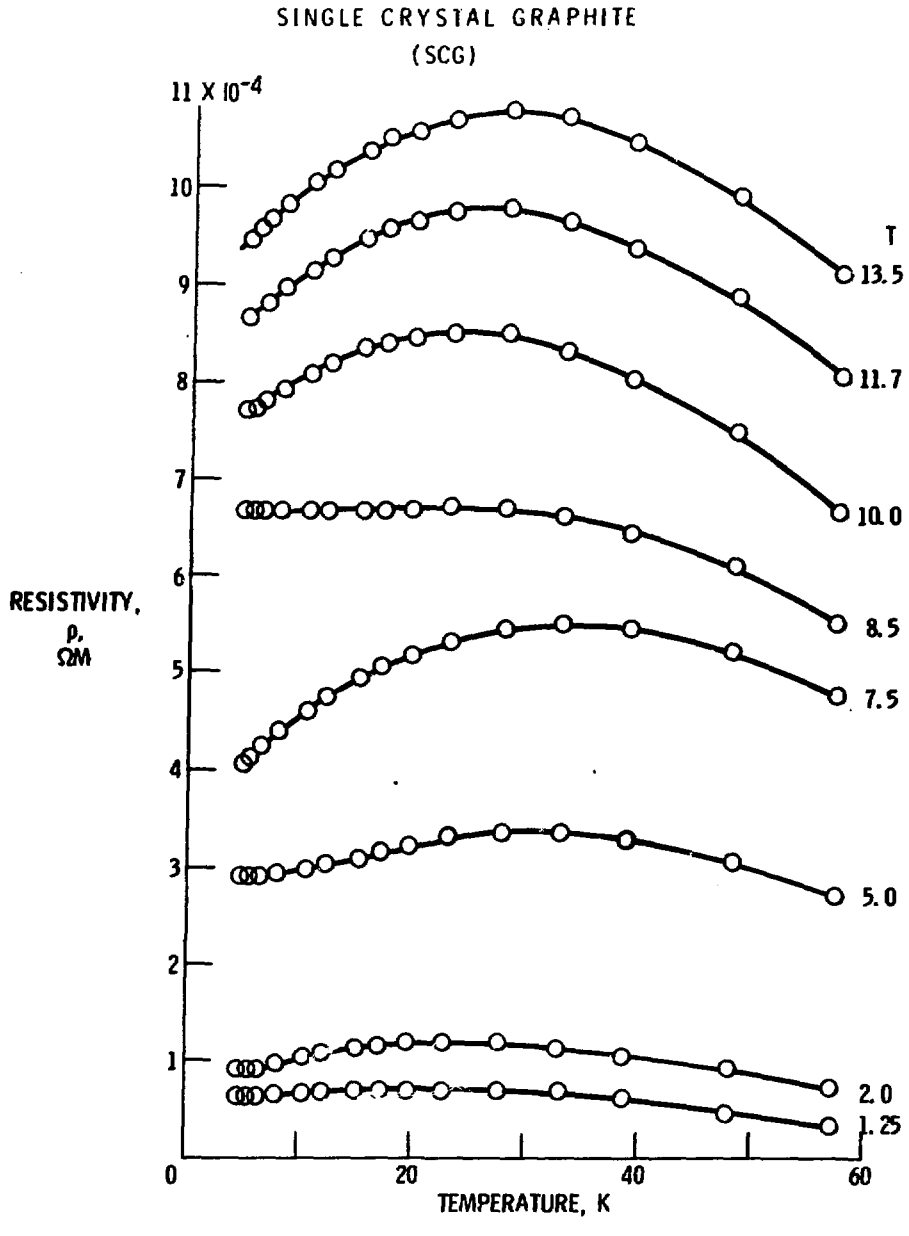


FIGURE 1 Electrical Resistivity vs. Temperature for a purified natural single crystal in a series of magnetic fields (in units of Tesla)

ANOMALOUS PHONON DRAG EFFECT IN GRAPHITE

K. Sugihara*, H. Ohshima+, K. Kawamura+, and T. Tsuzuku+

* Central Research Laboratory, Matushita Electric Industrial Co., Ltd. Moriguchi, Osaka, Japan

+ Nihon University at Ochanomizu, Tokyo, Japan

§1. Introduction

Detailed investigations on the thermoelectric and thermomagnetic effects of graphite, revealed the appearance of negative dip of the thermopower (S) and the Nernst-Ettingshausen coefficient (A_{NE}) around 35~40K. (1~5) These anomalies are related to the phonon drag effect. (6~9)

Recently, we have ascertained that well-crystallized kish graphite exhibits a sharp peak of β_{xx} below 20K beside a dip around 35K, where β is related to a current density $\underline{j} = \sigma \underline{E} - \underline{\beta} \nabla T$. Under the condition of $H \parallel z$, and $\nabla_x T \neq 0$, S is given by

$$S(H) = \frac{E_x}{\nabla_x T} = \frac{\sigma_{yy}\beta_{xx} - \sigma_{xy}\beta_{yx}}{\sigma_{xx}\sigma_{yy} - \sigma_{xy}\sigma_{yx}}. \qquad (1.1)$$

The dip is associated with the normal phonon drag effect, while the peak can be ascribed to the two-stage drag effect. (10~13) Observed results of $\beta_{xx}(0)$, $\beta_{xx}(H)$ and $\beta_{xy}(H)$ in kish graphite are given in Fig.1.

In the normal phonon drag effect the "electron phonon" which interact with carriers come to a stationary state mainly through the scattering by carriers and short wave phonons. In this case short wave phonons are assumed to be in thermal equilibrium, and so

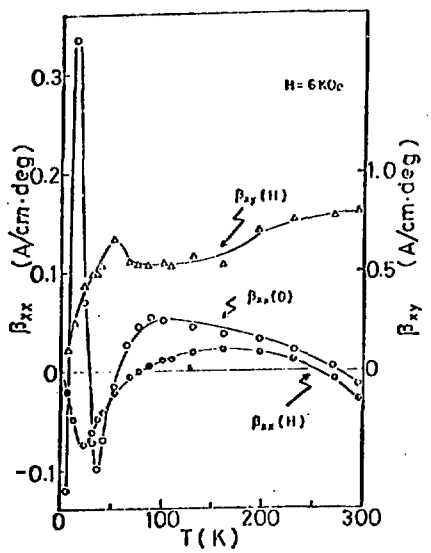


Fig.1 Temperature dependence of $\underline{\beta}$ in kish graphite.

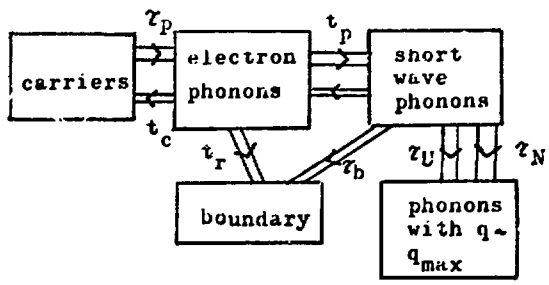


Fig.2 Momentum relaxation processes in carrier- and phonon-systems.

they do not explicitly participate in the kinetic equation. However, with decreasing temperatures the short wave phonons deviate from the thermal equilibrium because the Umklapprocess (U-process) becomes inactive as compared with the Normal process(N-process). Accordingly, the short wave phonons can drag carriers via the electron phonons. This two-stage drag induces the extra anomaly of $\beta_{xx}(0)$ in Fig.1.

By solving the coupled Boltzmann equation of carriers and phonons, an expression of the two-stage drag effect is given in §2.

§2. Two-stage drag effect in graphite

Main assumptions made in our calculation are as follows:

1) The Fermi surface is approximated by the ellipsoid model. (6~9)

2) Electron-phonon interaction is limited to the coupling with the in-plane vibration. (6~9)

3) As we consider a case of $\tau_U \gg \tau_N$, where τ_U and τ_N correspond to relaxation times of the short wave phonons and U and N indicate the U- and N-processes, their distribution functions are assumed to be

$$F_q \cong \left[\exp \beta(\hbar\omega_q - \hbar \underline{u}\cdot\underline{q}) - 1\right]^{-1}. \qquad (2.1)$$

$\underline{u}$ is a quantity to be determined by use of the coupled Boltzmann equation.

To get β, it is more convenient to calculate the heat flux $\underline{w}$ subjected to an electric field $\underline{E}$ and without temperature gradient ∇T. In this case we have

$$\underline{w} = \underline{\chi}\,\underline{E}, \quad T\beta_{ij}(H) = \chi_{ji}(-H). \qquad (2.2)$$

Along the similar line to the procedure

of Kozlov and Kozlov et al (10~12), we get an expression of w due to the two-stage drag effect as follows:

$$\underline{w} = \sum_q \hbar\omega_q \underline{v}_s \left(\frac{\tau_0}{t_p(q)}\right) (\delta N_q)_{\text{normal drag}}. \quad (2.3)$$

v_s: phonon velocity,
$t_p(q)$: relaxation time of the electron phonon q related to the scattering by the short wave phonons (see Fig.2),
$(\delta N_q)_{\text{normal drag}}$: electron phonon deviation in the normal phonon drag process.

According to the theory of the normal phonon drag effect in graphite (6,8,9), $(\delta N_q)_{\text{normal drag}}$ takes the form:

$$(\delta N_q)_{\text{normal drag}} = -\varphi_q \frac{\partial N_q^0}{\partial \hbar\omega_q}, \quad (2.4)$$

$$\varphi_q \cong \sum_{\lambda,\mu} R_{\lambda\mu}(q)(\underline{v}^{(\mu)} \cdot \hbar\underline{q}),$$

$R_{\lambda\mu}(q) = t(q)/t_{\lambda\mu}(q)$,
$t(q)$: total relaxation time of the electron phonon q,
$t_{\lambda\mu}(q)$: relaxation time of the electron phonon q in the scattering process by carriers,
λ, μ: indicies specifying carriers,
$\underline{v}^{(\mu)}$: drift velocity of μ-th carrier.

Inserting (2.4) into (2.3), we get

$$\underline{w} = \beta \sum_q \hbar\omega_q (\underline{v}_s \cdot \underline{q}) \left(\frac{\tau_0}{t_p(q)}\right) \left\{ \left[R_{ee}(q) + 2R_{eh}(q)\right] \underline{v}^{(e)} + 2\left[R_{hh}(q) + R_{eh}(q) + R_{hh'}(q)\right] \underline{v}^{(h)} \right\} \times N_q^0(1 + N_q^0), \quad \beta = 1/k_0 T. \quad (2.5)$$

In (2.5) contributions of electron and hole cancel each other.

At low temperatures τ_0 increases rapidly as $\exp(\alpha\Theta/T)$ ($\alpha \sim 1$). With further decrease of temperatures boundary scattering plays an important role in the relaxation process of the short wave phonons. Then, we should replace τ by

$$\tau_U^* = \tau_U / (1 + \tau_U/\tau_b). \quad (2.6)$$

(see Fig.2)

If a condition of $t_p \gg \tau_b$, $\tau_0 \gg \tau_b$ is satisfied, two-stage drag effect becomes negligible. This explains the feature of Fig.1 qualitatively. In the presence of a magnetic field β_{zz} decreases due to the cyclotron motion of carriers. (see Fig.1)

Clear indication of the two-stage drag effect was observed in good samples of bismuth at helium temperatures. (13)

REFERENCES

1. Tamarin P. V., Shalyt S. S., and Volga V. I., Soviet Phys.-Solid State 11, 1399 (1969).
2. Takezawa T., Tsuzuku T., Ono A., and Hishiyama Y., Phil. Mag. 19, 623 (1969).
3. Takezawa T., Thesis for the Degree of Science (in Japanese) Nihon University 1971.
4. Mangez J. H., private communication.
5. de Combarieu A., Jay-Gerin J. P., and Maynard R., J. Phys. Chem. Solids 34, 189 (1973).
6. Sugihara K., J. Phys. Soc. Japan 29, 1465 (1970).
7. Jay-Gerin J. P., and Maynard R., J. Low Temp. Phys. 3, 337 (1970).
8. Sugihara K., Takezawa T., Tsuzuku T., Hishiyama Y., and Ono A., J. Phys. Chem. Solids 33, 1475 (1972).
9. Tsuzuku T., and Sugihara K., Chemistry and Physics of Carbon (ed. by Walker P. L. Jr., and Thrower P. A., Marcell Dekker Inc. New York and Basel, 1975) vol. 12.
10. Kozlov V. A., and Nagaev E. L., JETP Letters 13, 455 (1971).
11. Kozlov V. A., Soviet Phys.-Solid State 16, 1413 (1975).
12. Kozlov V. A., and Lakhno L. D., Soviet Phys.-Solid State 18, 790 (1976).
13. Kopylov V. N. and Mezhov-Deglin L. P., JETP Letters 18, 188 (1972).

ELECTRICAL CONDUCTION IN C-DIRECTION OF GRAPHITE

K. Kawamura, Y. Ouchi, H. Ohshima and T. Tsuzuku
College of Science and Technology, Nihon University, Tokyo, Japan

§1. Introduction

Electronic conduction along the c-axis of graphite has not been sufficiently understood. For instance, experimental results of the absolute value as well as temperature dependence of the c-axis resistivity have been widely scattered from author to author and also from sample to sample, intrinsic nature of the c-axis resistivity having been not established. The present work reveals both absolute value and temperature dependence of the c-axis electrical resistivity of highly crystalline graphite in relation to the structural perfection evaluated from temperature dependence of the basal plane resistivity.

§2. Experimentals and results

Graphite specimens used in the present work were kish graphite (KG) prepared by Toshiba Ceramic Company, Japan and compression annealed pyrolytic graphite (CAPG) manufactured by Union Carbide Corporation, America. The resistivity measurements were made by means of a phase sensitive detection technique, being confirmed to agree well with those of a usual DC amplification method for the specimens immersed directly in liquid nitrogen. The specimen thickness was calculated by making use of the results of mass measurements and the theoretical density (2.26 g/cm^3).

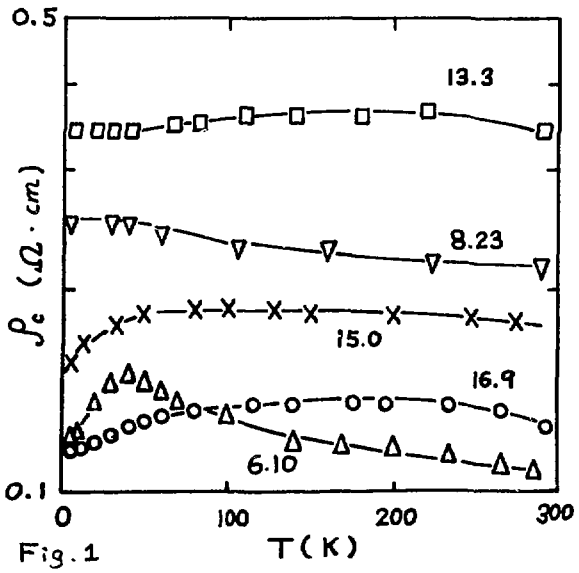


Fig.1

Fig. 1 illustrates temperature dependence of the c-axis resistivity (ρ_c) of kish graphite specimens. The parameter indicated shows ratio of the basal plane resistivity at 300 K to that at 4.2 K [$\rho_a(300)/\rho_a(4.2) = R_T$]. In the specimens having R_T smaller than 10, ρ_c has a maximum around 50 K and shows a semi-conductor-like temperature dependence above it. With further increase of R_T, the maximum of ρ_c around 50 K disappears and its temperature dependence becomes gradually metallic-like, though a marked metallic-like behaviour similar to those obtained by Primak and Fuchs(1) in natural crystals, and by Tsang and Dresselhaus(2) in other kish graphite is not observed in the present specimens.

A maximum of ρ_c around 50 K is often observed in variour highly oriented pyrolytic graphites and may possibly related to the presence of such defects as microcracks. In the present work, therefore, the thickness of CAPG specimen is varied by slicing the original specimen, and the effect of specimen thickness on ρ_c is examined.

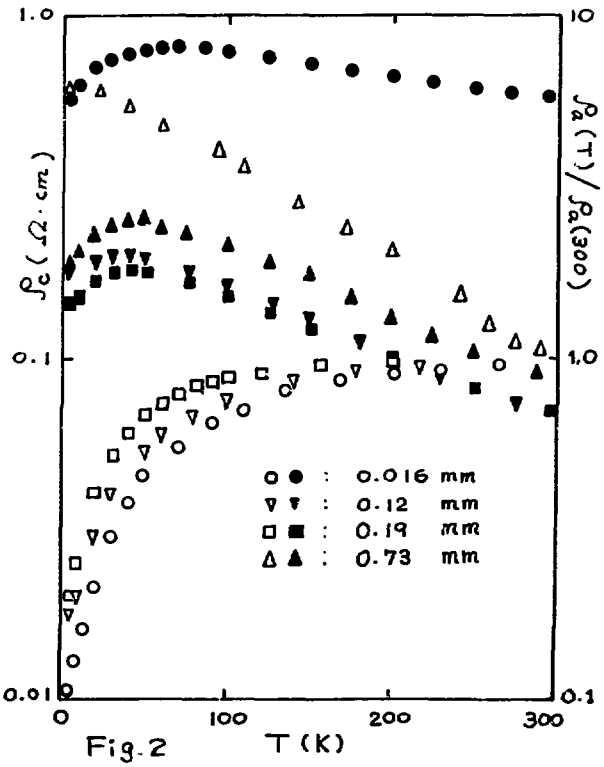


Fig.2

Fig. 2 summarized the effect of specimen thickness on both ρ_a and ρ_c of CAPG. The thickness of the originally selected specimen is 0.73 mm and is stepwise reduced down to 0.016 mm. It should be noted that originally semiconductor-like temperature dependence of ρ_a becomes metallic-like after being sliced to 0.19 mm and, moreover, the metallic-like behaviour is enhanced with the decrease in thickness. Furthermore, the thinnest specimen has

the highest value of ρ_c throughout the temperature range examined and its semiconductor-like temperature dependence becomes less marked than those of the thicker specimens.

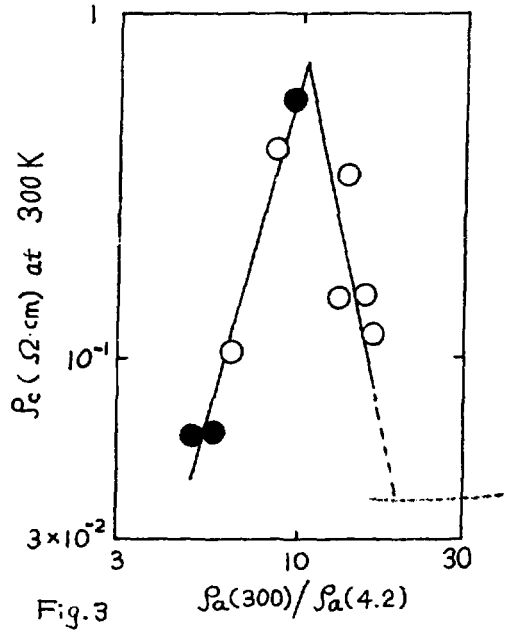


Fig.3

Fig. 3 reveals ρ_c of CAPG (solid circle) and KG (open circle) at 300 K as a function of R_T, indicating that ρ_c has a maximum at R_T of about 10. The result suggests the following items:

(i) If such a highly crystalline graphite specimen having R_T larger than 30 as EP-14 of Soule(3) is obtained, ρ_c could be as low as 10^{-3} Ω·cm at 300 K as is shown by the dotted line in Fig. 3.

(ii) The statement describing that ρ_c / ρ_a of an ideal graphite would be infinity is obviously a wrong one (4), which might be mislead if only such relatively poor specimens as those having R_T smaller than 10 are examined.

§3. Concluding remarks

ρ_c of an ideal graphite could be as low as 10^{-3} Ω·cm at room temperature and its temperature dependence should be metallic-like at least below room temperature. The value obtained by Primak and Fuchs(1), however, seems too low because R_T of their natural crystals does not exceed 20. A similar low value observed by Tsang and Dresselhaus(2) in other kish graphite is not easy to be discussed in detail since they have not examined temperature dependence of ρ_a of the same specimen.

Electronic conduction in c-direction of graphite should be interpreted not in terms of hopping conduction but on the basis of the band theory.

It should be emphasized that the thickness of PG specimen is a critical factor in determining the c-axis as well as basal plane transport phenomena in graphite.

References

(1) W. Primak and L. H. Fuchs
Phys. Rev. 95, 22 (1954)

(2) D. Z. Tsang and M. S. Dresselhaus
Carbon 14, 43 (1976)

(3) D. E. Soule
Phys. Rev. 112, 698 (1958)

(4) I. L. Spain, A. R. Ubbelohde and D. A. Young
Phil. Trans. Roy. Soc. London A262, 345 (1967)

Ddensification of carbon-carbon composites at 30 ksi

G. W. Weber
K. R. Young
A. J. Taylor
Oak Ridge, Tennessee
and
T. J. Curci
Air Force Materials Laboratory
Wright-Patterson Air Force Base, Ohio

Introduction

The high-pressure-impregnation-carbonization (HPIC) cycle, developed at Y-12, was designed to densify carbon-carbon composites by impregnating with pitch and carbonizing at ∿ 100 MPa in a hot-gas autoclave. The 100 MPa pressure was utilized since this was the maximum operating pressure of the existing vessel. Considerable discussion has developed as to the effect of pressure during impregnation and carbonization. Comparison of densification at 100 MPa with low-pressure impregnation (3 MPa) and atmospheric pressure carbonization indicated a doubling of the coking yield. A corresponding decrease in the number of cycles needed to obtain the desired composite density was observed.

A hot-gas autoclave with capabilities to 200 MPa at 650°C has recently been made operational at Y-12. This new vessel is designed to evaluate the effects of pressure on the densification of carbon-carbon composites.

The first stage in this investigation was to provide a direct comparison of identical billets processed at 100 and 200 MPa. Porous carbon billets were employed to determine project feasibility before more expensive 3-D woven billets were processed.

Presentation of Experimental Work

The HPIC cycle has been used to densify woven, 3-D carbon-carbon composites for several years. The standard cycle (shown in Figure 1) uses a pressure of ∿ 100 MPa for impregnation and carbonization purposes. There has been much discussion as to the necessity of using 100 MPa in this cycle. Low-pressure impregnation (∿ 3 MPa) with carbonization at atmospheric pressure will yield a part of approximately the same final density but will require 2-3 times the number of cycles. The effect of using higher pressures has not yet been analyzed.

The initial stage of this project was to investigate the effects of 200 MPa impregnation and carbonization on the densification of carbon-carbon composites. The first stage was to use porous carbon as the sample material to approximate the amount of porosity of woven billets. Six porous carbon billets (130 mm dia. x 180 mm long) were procured with small pieces of stock to serve as samples. All six billets were labeled, indexed, measured, and weighed before being heat treated to ∿ 2900°C. This step assured that all billets had been heated to a temperature higher than the highest temperature to be used in the densification process. The bulk densities measured after this heat treatment ranged from 1.13 to 1.26 gm/cm^3. For the first comparison test with 15-V pitch, two billets which had approximately the same bulk density were chosen. One billet (HP-5) was to be densified using the standard HPIC cycle (Figure 1) and the other (HP-2) using the ultra-high-pressure impregnation and carbonization (UPIC) cycle (Figure 2). The UPIC cycle closely approximates the HPIC cycle except that the pressure was doubled.

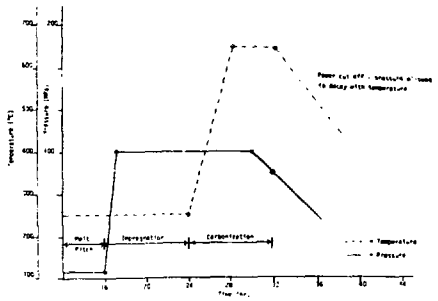


Figure 1. HPIC CYCLE.

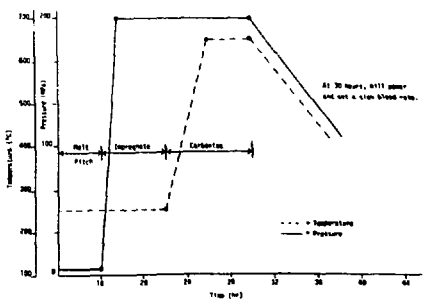


Figure 2. UPIC CYCLE.

The graphitization cycle was the standard cycle used for nose-tip preforms (Figure 3). Although there is reason to believe the porous carbon billets would not survive several of these graphitization cycles, this cycle was employed for comparison purposes.

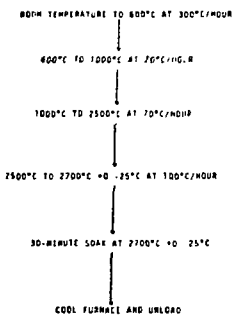


Figure 3. HEAT-TREATMENT CYCLE, TOTAL TIME—46 HOURS.

Note: Furnace atmosphere is argon flowing at rate of 1.0 scfm.

For the initial phase of the program, two impregnants were used—Allied Chemical's CP-277-15V (coal tar pitch) and Ashland's A-240 (petroleum base pitch). The base-line impregnant for the Air Force nose-tip densification program is 15-V pitch. The A-240 pitch has a higher sulfur content and a lower coking yield. The billets were to be densified with each pitch in each type of cycle.

The data derived from measurements of the billets are given in Table 1. It should be noted that the coke yield in the can was approximately the same for both the HPIC and UPIC cycles for the same type of pitch. The A-240 coke yield was ~ 6 wt % less than that of 15-V. From these data, the UPIC cycle gave a slightly higher weight gain than the HPIC cycle. The slight compaction of the billet in the UPIC cycle, which is alleviated in the graphitization cycle, is not apparent from Table 1.

Table 1

Physical Measurement Data for the Densification of Porous Carbon

Billet	After Original Graphitization	After 1st Cycle Densification	Percent Change	After 2nd Cycle Densification	Percent Change
HP-2					
15-V Pitch - Vol (cc)	2124.370	2123.486	-0.041	2135.195	+0.51
HPIC Cycle - Wt (g)	2604.381	3488.389	+33.9	4002.968	+53.70
Density (g/cc)	1.226	1.643	+34.0	1.875	+52.94
HP-5					
15-V Pitch - Vol (cc)	2132.403	2130.392	-0.091	2149.774	+0.81
HPIC Cycle - Wt (g)	2706.171	3474.053	+28.4	3950.176	+46.02
Density (g/cc)	1.268	1.631	+28.1	1.837	+44.76
HP-3					
A-240 Pitch - Vol (cc)	2129.980	2129.281	-0.03	2149.133	+0.71
UPIC Cycle - Wt (g)	2908.088	3319.552	+32.23	3837.632	+53.0
Density (g/cc)	1.370	1.559	+32.76	1.799	+51.9
HP-6					
A-240 Pitch - Vol (cc)	2118.667	2117.872	-0.03	2136.033	+0.86
UPIC Cycle - Wt (g)	2692.007	3197.572	+28.31	3674.799	+47.86
Density (g/cc)	1.376	1.510	+29.40	1.795	+48.68

Note: All percentages are based on original graphitization.

As shown in Figures 4 and 5, carbonization at 200 MPa appears to inhibit mesophase coalescence. This phenomena has been observed on both porous carbon and very fine porosity chopped fiber materials using Allied 15-V pitch as the impregnant. However, uncoalesced mesophase spheroids were not observed in the porous carbon billets after the second UPIC cycle using 15-V pitch and in any runs using Ashland A-240 pitch. Experiments will be reported which were done at 200 MPa with four identical porous carbon billets

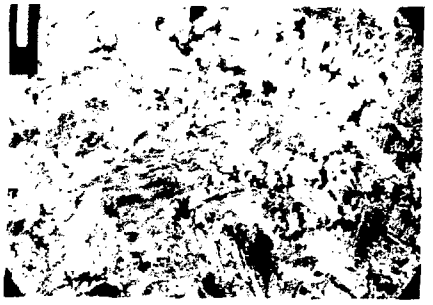


Figure 4. HP-2 AFTER FIRST CYCLE UPIC.

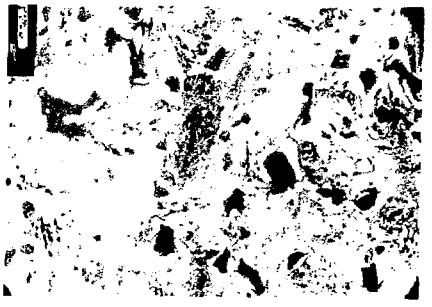


Figure 5. HP-5 AFTER FIRST CYCLE HPIC.

with four different pitch types; A-240, Allied 15-V, 30M and Koppers pitch made to 15-V specification. This approach will determine the reproducibility of this phenomena and its dependence on pitch properties.

The effects of the 200 MPa process on densification of typical woven three-dimensional orthogonal (3-D) composites will also be reported. The program includes densification of several 3-D billets and comparison of the microstructure obtained in each cycle with matching billets processed in the standard 100 MPa process. The effect of significantly increased pore size of the 3-D billets as compared to the porous carbon billets will therefore be determined. This will provide the first real microstructural examination of sequential densification of carbon-carbon composites at these pressures.

The development of small spheroids in the normally large porosity offers an attractive option for tailoring the composite microstructure. The current densification process attempts to fill the pore from the pore wall inward with sequential deposits. This process results in a distribution of partially filled large pores. Inhibiting mesophase coalescence to retain spheroids which break up the large porosity into a number of small pores would provide not only improved densification possibilities resulting in higher densities with fewer cycles but also improved ablation performance. As ablation is controlled by porosity size and distribution rather than density per se, the fine evenly distributed porosity demonstrated in the 200 MPa results may significantly improve performance, particularly transition behavior, in aerospace applications. The fact that the second cycle microstructure does not show this behavior may indicate a process composed of decreasing pressures with subsequent cycles. A process of this type could optimize performance, densification, and cycle cost.

ANALYSIS OF DIMENSIONAL CHANGES AND FIBER-MATRIX INTERACTIONS DURING PROCESSING OF 3D CARBON-CARBON COMPOSITES

L. B. Greszczuk
McDonnell Douglas Astronautics Company-West
5301 Bolsa Avenue
Huntington Beach, California 92647

Introduction

The 3-D carbon-carbon composites undergo dimensional changes [1] during the multiple carbondization/graphitization cycles, as shown in Fig. 1a. For the particular material shown, all dimensions decrease initially. Subsequent processing cycles cause little change in the Z dimension and significant increases in X, Y dimensions. Other pertinent changes that occur in the material and are related to the growth phenomena are shown in Fig. 1b.

Analysis and Results

To establish the mechanism that causes dimensional changes during processing, an approximate analysis was conducted using a mathematical model shown in Fig. 2. Starting with the temperature-dependent properties of constituents (fibers and matrix), the elastic and thermal properties in the axial and transverse directions of yarn bundles were calculated using equations (modified to account for fiber orthotropy) of [2 and 3]. The matrix within the yarn bundles and matrix pockets was assumed to have temperature-dependent mechanical and thermal properties similar to ATJS graphite. The fibers were assumed to be orthotropic. The ambient in situ Thornel 50 fiber Young's modulus in the axial direction was determined using the results of [4]. Variations of fiber axial modulus and axial coefficient of thermal expansion with temperature were taken as shown in [5]. The room-temperature Young's modulus and coefficient of thermal expansion of the fibers in the transverse direction were calculated using equations of [2 and 3] in combination with test data on transverse Young's modulus and transverse thermal expansion data for graphite/epoxy composites. Once the room-temperature properties of the fibers in the transverse direction were determined, the variation of these properties with temperature was assumed to be similar to pyrolytic graphite in the c-direction. The final results for the typical properties of unidirectional carbon-carbon yarn bundles are given in [1].

To determine the elastic and thermal properties and the internal stress state in the 3-D carbon-carbon composites as the latter undergo exposure to elevated temperatures, analytical techniques similar to those described in [2], were used. The nominal void content of 3-D material was assumed to be 8%, of which 2% of the voids were estimated to be within the yarn bundles. The effective fiber content (including sheath of highly oriented material) within the yarn bundle was taken as 68%, which is representative of the values observed in various composites. The dimensions of the yarn bundles in the X, Y, and Z directions were taken as shown later in Fig. 5. Typical theoretical results as well as limited experimental data on the mechanical and thermal properties of 3-D carbon-carbon composites are shown in Figs. 3 and 4, whereas Fig. 5 shows the final results on the stress state of various locations within the 3-D carbon-carbon composites. The stresses shown were based on elastic analysis. If the influence of plasticity (both fibers and matrix undergo elastic deformations at high temperatures) were taken into account, the stresses would be somewhat lower than shown in Fig. 5. It is these stresses that cause the changes in the dimensions of the 3-D carbon-carbon blocks as well as internal cracks within the yarn bundles and at the bundle crossovers. The compressive stresses at locations shown in Fig. 5 cause the yarn bundles to undergo necking and billowing, as well as cracking within the yarns as shown in Fig. 6. As the yarns undergo necking and cracking due to compressive stresses, the tensile stresses in the direction of yarn axis are relieved. The net result is that during the initial processing cycles, only necking and interyarn cracking takes place. Such deformations would cause initial decrease in the dimensions of 3-D carbon-carbon composites blocks. Upon exposure to additional processing cycles, the necking ceases when the fiber compaction at the yarn crossovers is stablized. High tensile stresses then arise in the direction of yarns (see Fig. 5). The tensile stresses would be somewhat lower than shown in Fig. 5 because of relief due to plastic fiber deformations at high temperatures. On cooldown, the high tensile stresses would be relieved; however, a permanent set and cracking at theyarn crossovers would take place because of the plastic deformations noted above. It is this permanent set which causes the increase in the dimensions of 3-D carbon-carbon blocks. Because the stresses are higher in the X and Y directions than in the Z direction, the increase in X and Y dimensions should be higher than the increase in the Z dimension. The experimental results shown in Fig. 1 and [1] confirm the behavior postulated on the basis of theoretical results. As is readily seen, the various blocks initially undergo decrease in dimensions and on subsequent carbonization/graphitization cycles the dimensions of the blocks increase, the increases being greater in the X and Y directions than in the Z direction. Work is now underway to obtain quantitative results on the dimensional changes of 3D C-C composites during the multiple processing cycles.

Acknowledgements

This work was sponsored by Naval Surface Weapons Center, Silver Spring, Md under contract N60921-74-C-0241.

References

1. R. W. Seibold, J. Jortner and L. B. Greszczuk; Final Report, NSWC Contract N60921-74-C-0241, Dec. 1976.

2. L. B. Greszczuk; AIAA Journal, Vol 9, No. 7, 1971.

3. L. B. Greszczuk; Proc. 6th AIAA Struct. and Matl's Conf., Apr. 1965.

4. D. A. Eitman, L. B. Greszczuk, and J. Jortner; Final Report, NSWC Contract N60921-72-C-0290, July 1973.

5. D. L. Lowe; Final Report, NSWC Contract N60921-75-C-0060, July 1976.

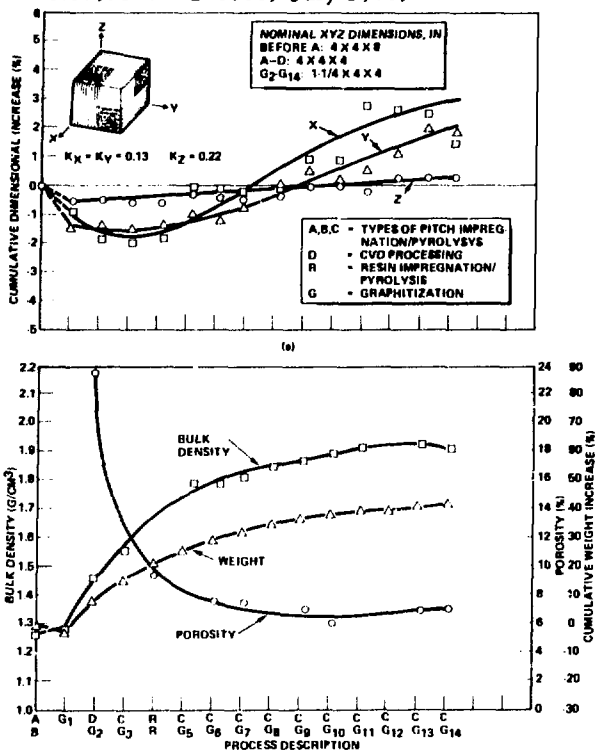


Figure 1

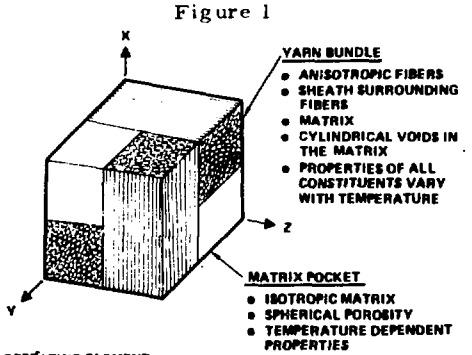


Figure 2

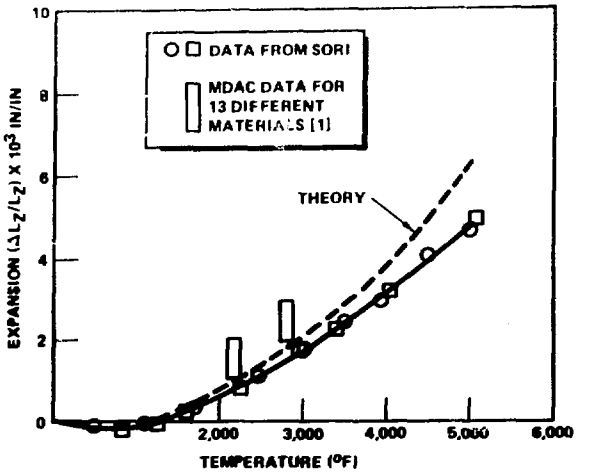


Figure 3

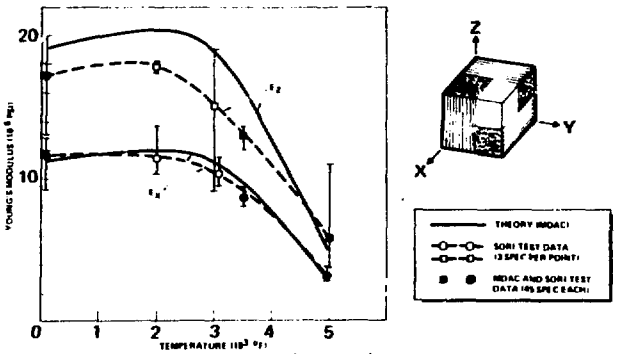


Figure 4

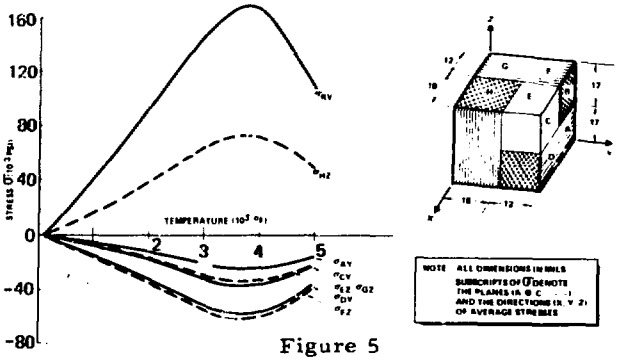


Figure 5

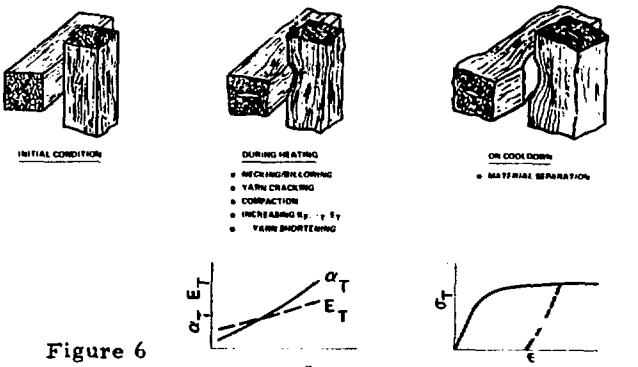


Figure 6

MECHANICAL PROPERTIES OF PITCH FIBER CARBON-CARBON COMPOSITES

Charles R. Rowe (Naval Surface Weapons Center, Silver Spring, MD)
Louis L. Lander (Fiber Materials, Inc., Biddeford, ME)

Introduction

A new class of carbon fiber reinforced carbon composites utilizing pitch-based carbon fibers are being developed for applications that require high strength at temperatures greater than 3000°C. These applications, such as rocket nozzles, aircraft brakes, and reentry vehicle nosetips, have depended upon rayon-based carbon fibers, but with uncertainty of future rayon supply, alternate fibers are needed. Pitch-based carbon fiber is one alternative.

The knowledge of processing and weaving variables on the properties of carbon-carbon composites has advanced substantially in the past few years. However, because the broad base of knowledge about carbon-carbon composites was developed for rayon-based fibrous reinforcement, it does not necessarily apply to pitch-based composites. Therefore, it is the purpose of this work to determine the effects of carbonization and graphitization temperatures, pyrolysis pressure, and type of carbon matrix on the mechanical properties of pitch fiber composites.

Experimental

Union Carbide Corp. (Parma, Ohio) manufactured the fiber used for the composites for this study.

The fiber was woven into twelve three-dimensional performs in which the fiber was arranged in three mutually orthogonal directions designated X, Y, and Z. Figure 1 shows the dimensions of a unit cell of the preforms in which the distances between fiber bundles are indicated. The preforms, woven by Fiber Materials, Inc. (Biddeford, Maine), were 5cm x 5cm x 13cm.

To determine the effect of process variables on the mechanical properties of pitch fiber composites, a baseline process and eleven variations were selected to isolate process effects. The baseline process involved impregnation with pertroleum pitch, A240 (Ashland Oil Co., Ashland, KY) followed by initial carbonization up to 900°C and graphitization to 2600°C in an inert atmosphere. This was followed by repeated impregnation, carbonization to 535°C at 34.5 MPa (5,000 psi), and graphitization to 2600°C. Approximately six such cycles were required to reach a density 1.95 g/cc. Table 1 summarizes the composites that were fabricated.

The mechanical properties determined on each composite included tensile, compressive, and flexure strength, modulus and strain. These measurements were made at room temperature in the Energy Materials Testing Laboratory (Fiber Materials, Inc.).

Results

Mechanical data for the composites are summarized on Table 2 which list the maximum, minimum, average, standard deviation, coefficient of variation, and number of data points for each type of test. Results indicate there are wide ranges of some properties such as X/Y flexure modulus, 26.3 to 120 GPA (3.81 to 17.4 msi, Cv = 0.39). However, some properties, such as tensile strength, varied a small amount, 154 to 197 MPa (22.4 to 28.6 ksi, Cv = 0.06) for all process variations.

Discussion

In order that the effect of each process variables on the mechanical properties, two parameters were selected to compare the composites for their resistance to thermal stress and impact. A thermal stress parameter, $T = \frac{\sigma \cdot K}{E \cdot \alpha}$ where

σ = strength
E = modulus
K = thermal conductivity
α = coefficient of thermal expansion

has been used to rank graphites. If the assumption is made that the conductivity and expansion of these materials are independent of process variables, then $T = \sigma/E$.

Impact resistance is approximately equal to the area under the stress strain curve, $I = \sigma(\varepsilon/2)$, where ε = total strain. For brittle materials $\varepsilon = \sigma/e$, hence $I = \frac{\sigma^2}{2E}$.

Each parameter was calculated for all composites at the various test conditions. The effect of each process variable was determined by comparing the parameters for that process variable with the mean and standard deviation of all composites by the equations: $T' = \frac{\sum\left(\frac{T - \bar{T}}{s}\right)}{N}$ $I' = \frac{\sum\left(\frac{I - \bar{I}}{s}\right)}{N}$.

In both equations a positive number indicates a composite better than the average of all the composites.

The effect of each processing variable on the mechanical properties of pitch fiber composites is shown by plotting R, the average of T′ and I′, as a function of the process variables. Figure 2 shows the effect of the type of matrix on the properties of the composites. Petroleum pitch (A240) and coal tar pitch (15V) are approximately equal but the low sulfur petroleum pitch (LS24) is much worse. Also, the composites with CVD carbon are better than those without it. CVD carbon gave the composites essentially the same tensile strength as the composites without CVD carbon (7% less for LS24 and 6% more for A240), but lower moduli (-41% for LS24 and -16% for A240).

The importance of the initial carbonization temperature is shown in Figure 3, which indicates that low temperature is better than high initial carbonization temperature.

Figure 4 shows that there is a slight upward trend of R for graphitization temperatures above 2600°C (27% higher than the baseline). However, lower graphitization temperatures has a definite adverse affect. Higher graphitization temperatures gives better alignment of graphite crystallites.

The effect of pyrolysis temperature pressure is shown in Figure 5. It is apparent that pyrolysis at pressure less than 34.5 MPa (5000 psi) yield composite properties worse than the average. On the other

hand, for pressures greater than 34.5 MPa there is little difference up to 103 MPa (15,000 psi).

Summary and Conclusions

It has been found that carbon-carbon composites reinforced with pitch-based carbon fibers can be fabricated with wide variations of processing conditions. The trends in thermal stress and impact resistance indicate that composites with CVD carbon are better than those composites without it. The CVD carbon appears to affect the alignment of graphite layer planes; that is, the presence of a small amount (V_f= 0.11) causes less formation of highly aligned graphite or "sheath" along the fiber axis. The initial carbonization temperature, although only used once during the fabrication of the composites, ..as a similiar effect on graphite alignment: lower carbonization temperatures cause less fiber damage. For example the tensile strengths for the 600°C, 900°C and the 1200°C composites were the same (±2%) whereas the 1200°C composite is 32% stiffer than the 600°C composite.

There appears to be a threshold graphitization temperature (2600°C) and a threshold pyrolysis pressure (34.5 MPa; 5,000 psi) above which little change in thermal stress and impact resistance is apparent. Below those thresholds there are strong adverse effects.

COMPOSITE NO.	CVD CARBON	PITCH	INITIAL CARB. TEMP. (°C)	GRAPH. TEMP. (°C)	PYROLYSIS PRESSURE (MPa)	FINAL DENSITY (g/cc)
P-1	NO	A240	900	2800	36.5	1.98
P-2	YES	•	•	•	•	1.93
P-3	•	15V	•	•	•	1.96
P-4	•	LS24	•	•	•	1.96
P-5	YES	LS24	•	•	•	1.94
P-6	•	•	600	•	•	1.97
P-7	•	•	1200	•	•	1.98
P-8	•	•	•	2400	•	1.96
P-9	•	•	•	2800	•	1.94
P-10	•	•	•	•	6.9	1.87**
P-11	•	•	•	•	20.7	1.96
P-12	•	•	•	•	103.4	1.94

*SAME A P-1

**OPEN POROSITY >10%; NOT TESTED

Table 1 - Composite Summary

TEST TYPE	PROPERTY	UNITS	MINIMUM X	MAXIMUM X	X̄	S	Cv	n
Z DIRECTION TENSILE	MODULUS	MPa	125	210	178	25	0.14	18
	STRENGTH	MPa	154	197	172	10	0.06	18
	STRAIN	%	0.08	0.15	0.11	0.02	0.17	18
Z DIRECTION COMPRESSION	MODULUS	MPa	97.2	23.4	146	34	0.23	25
	STRENGTH	MPa	86.2	82.7	89.8	7.8	0.10	25
	STRAIN	%	0.04	0.14	0.07	0.02	0.33	24
Z DIRECTION FLEXURE	MODULUS	MPa	114	182	161	23	0.14	11
	STRENGTH	MPa	157	283	170	18	0.09	11
	STRAIN	%	0.16	0.33	0.22	0.06	0.26	11
X/Y DIRECTION FLEXURE	MODULUS	MPa	20.3	120	63.2	24.0	0.38	16
	STRENGTH	MPa	36.8	117	73.1	22.2	0.30	16
	STRAIN	%	0.17	0.40	0.31	0.10	0.32	16
45°X/Y DIRECTION COMPRESSION	MODULUS	MPa	4.96	0.31	5.86	1.30	0.24	22
	STRESS AT 0.2% YIELD	MPa	0.41	20.0	14.6	4.2	0.28	22
	STRESS AT 1% YIELD	MPa	11.4	28.1	18.9	3.7	0.20	22
	STRENGTH	MPa	29.0	48.7	34.3	3.6	0.10	22

Table 2 - Mechanical Property Summary

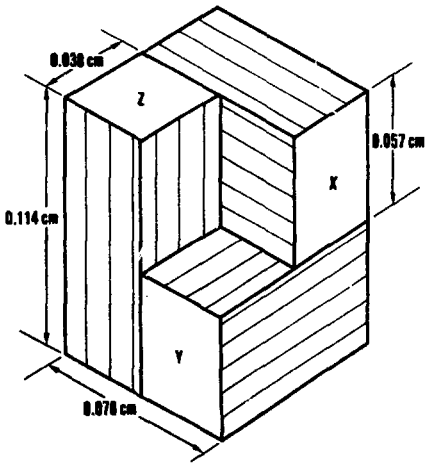


Fig. 1 - Composite Unit Cell

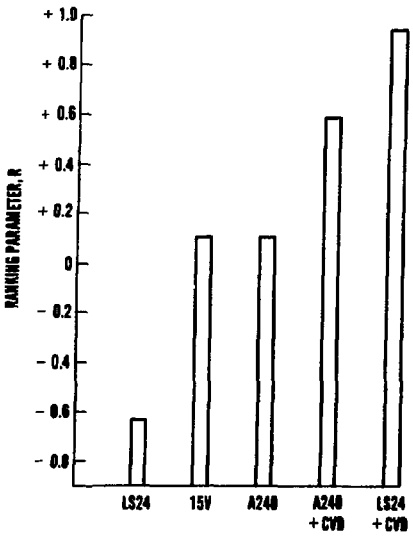


Fig. 2 - R vs Matrix Type

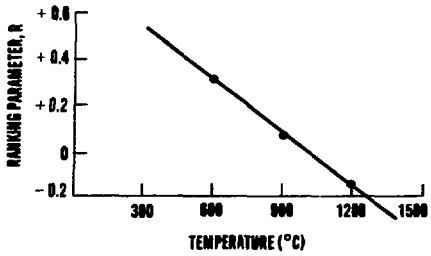


Fig. 3 - R vs Pyrolysis Temp.

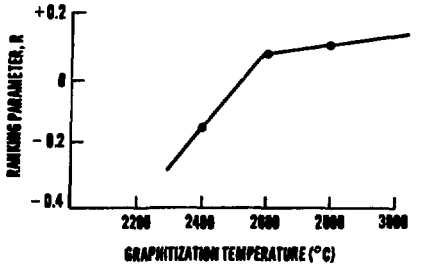


Fig. 4 - R vs Graphitization Temp.

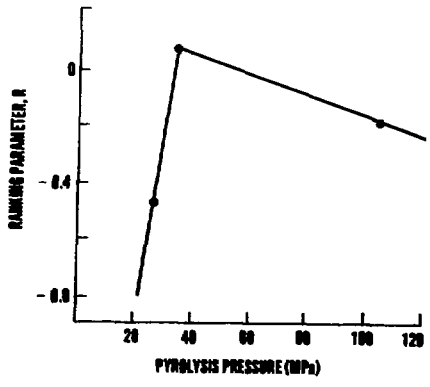


Fig. 5 - R vs Pyrolysis Pressure

CARBON/CARBON MATERIAL APPLICATION TO SOLID ROCKET MOTOR NOZZLES

R. Laramee, G. Lamere, B. Prescott,
R. Mitchell, P. Sottosanti, D. Dahle

Thiokol/Wasatch Division
A Division of Thiokol Corporation
P.O. Box 524, Brigham City, Utah 84302

Current design requirements for Solid Rocket Motor (SRM) nozzles drive the nozzle volume envelope, cost, throat erosion and weight to the smallest reliable number and the exit cone thrust level to the highest reliable number.

In addition, the nozzle must support the highest SRM chamber gas pressure and temperature, and the lowest gas, surface wall material erosion and charring.

To successfully apply C/C composite billets to production missile programs the design and manufacturing engineer must know the following five major design application factors:

1. Fabrication and Processing

First, what is a 2-D or 3-D billet? A 2-D square block is a series of alternating layers of graphite cloth (composed of warp and fill graphite fiber yarn bundles) and an impregnating resin. The square block is subsequently cured (325° F and 200/1,000 psi), carbonized (1,500° F), and graphitized (4,500° F). No axial (Z) graphite fibers are used.

The graphite fiber cloth is processed by graphitizing rayon, polyacrylonitrile (PAN) or pitch cloth. The resin is an epoxy, phenolic or pitch material.

Other methods used to fabricate 2-D cones include tape wrapping or rosette layup.

A 3-D C/C square block is a woven, flexible grid of (X) warp - (Y) fill - (Z) axial graphite fiber, yarn bundles.

Fabricating the 3-D block flexible fiber grid is a manual operation. The axial graphite epoxy rods are in place in a holding jig, with the X (warp) and Y (fill) graphite fiber bundle layers manually inserted by hand and packed down for tight fiber layer spacing.

The 3-D cone mandrel is filled with manually inserted radial (Y) fill graphite-epoxy rods and the automated graphite is placed by hoop (X) warp helix winding and the axial (Z) polar winding by machine. The spacing between fiber bundles may vary from 0.040 to 0.125 inch.

An impregnating resin (epoxy - phenolic - pitch) fills the voids between fiber bundles and is subsequently carbonized and graphitized (similar to the 2-D block), rigidizing the block.

Densification of billets with resin char is done at 200 to 15,000 psi. For both the 2-D and 3-D blocks, the number of impregnating resin - curing - carbonization - graphitization cycles will determine billet density and porosity. The range of billet density is 1.45 to 2.05 gr/cc, with a goal of 10% porosity or less at 1.85-1.95 gr/cc density.

The 2-D and 3-D billet process parameters for fiber percent by weight in the finished block and the fiber distribution in the three planes is shown below:

C/C Type	Billet Fiber Weight-Percent		Percent Fiber Distribution X-Warp	Y-Fill	Z-Axial
2-D	50 - 60%		55%	45%	0%
3-D	40 - 50%	1	35%	10%	55%
		2	55%	10%	35%

2. Cost-Schedule-Size

The cost and delivery time for C/C billets will depend on:

1. Min-max diameter, length and radial thickness
2. Type of graphite fiber - high or low modulus
3. Spacing between fiber bundles in X-Y-Z directions.
4. Density of finished billet
5. Specification testing requirements

A cost, schedule and a current billet size limitation for 2-D and 3-D billets is listed in Table I.

Generally the 2-D C/C billets are used in nozzles as short inlet and throat rings and long exit cones, while 3-D C/C billets are used as a short one piece nose-inlet-throat (ITE) cone. Figure 1 shows typical submerged nozzles with design application areas - (nose-exit cone) listed.

3. Material Properties

A comparison of 2-D and 3-D material properties from cylinder or cone tag ends or blocks at room and elevated temperatures is listed in Table II. The 2-D billet is fabricated with low modulus/strength graphite fiber, while the 3-D billets are processed with a higher strength/modulus graphite fiber.

Quality control of the billets is achieved by density and X-ray inspection of the cured 2-D preform and 3-D woven fiber grid preform and after each 2-D/3-D impregnation-graphitization cycle. In addition, the billet is tested for mechanical-thermal properties to compare to specification requirements.

4. Design Application Examples

The material design application has been achieved by two routes.

1. Design and test of a complete 2-D C/C fixed submerged nozzle (Figure 1) with the ablative, insulative, and structural shells combined into a single function

material using rosette, flat laminate and tape wrap cloth processing.

2. Redesign of a current movable submerged nozzle for a 3-D C/C Integrated Throat-Exit (ITE) short cone and a standard tape wrapped carbon cloth phenolic reinforced plastic throat support, forward exit cone and submerged liner (Figure 2).

Both designs allow the design and manufacturing engineers to assess C/C nozzle costs, weight, reliability and erosion-char depth performance.

As for machining, bonding, aging and handling characteristics, the C/C composites act like reinforced plastics. For bonding C/C materials to RFP or metals, use an EA934 HySol epoxy. To bond C/C to itself, use C-34 Union Carbide carbon cement.

5. Static Test Performance

The static test performance of 3-D C/C material, while limited to cylinders or rings in the nose-inlet-throat area of nozzles in approximately 22 motor tests, has been 100% successful. No motor failures have been attributed to the 3-D C/C material. The erosion rates have been zero mils/sec minimum to a 9.0 mils/sec maximum. In addition, no delaminations or cracks have been noted in the postfired billets.

Considering 2-D C/C experience on more than 100 motor tests of approximately 200 2-D C/C rings tested as inlets, throats and exit cones - at least two inlet-throat rings and two exit cones have failed in static test. More 3-D C/C test experience is required to make an equal assessment of 2-D vs 3-D C/C future potential in all areas of the nozzle design.

A comparison of the 3-D C/C erosion performance in the inlet and throat vs 2-D C/C and PG and 2-D C/C vs carbon phenolic in the forward exit cone is given in Table III.

Summary

The application of extensive C/C composites to SRM nozzles will be easier with the five design application factors. The C/C design is lighter, simpler, and has smoother post-test wall surface and better structural integrity. However, C/Cs do cost more, need more tests, properties fabrication history, and lead purchase time.

The final decision to extensively use C/C composites in a production SRM missile program will be made by each manufacturer on the basis of the following items:

- Available development time and funding
- Design criteria requirements
- Design and manufacturing state-of-the-art
- SRM risk priority assessment

TABLE I

COST, SCHEDULE, SIZE LIMITATIONS

C/C Type	Max Dia (in.)	Max Length (in.)	Max Radial Thickness (in.)	Cost Range $/lb	Mfg Delivery Time (Months)
2-D Billets					
Blocks-Rings	40.0	2.0	2.0	100/500	4/6
Cylinders-Cones	72.0	96.0	1.5		
Suppliers - Carborundum - Kaiser - Polycarbon - Hitco					
3-D Billets					
Blocks-Rings	12.0	48.0	6.0	400+	6/8
Cylinders-Cones	30.0	50.0	6.0	1,400	
Suppliers - Avco - FMI - General Electric - McDonnell Douglas					

TABLE II

3-D/2-D C/C MATERIAL PROPERTIES

	Type	Tensile Strength and Modulus X Warp	Y Fill	Z Axial	Compressive Strength and Modulus X Warp	Y Fill	Z Axial	Shear Strength and Modulus X Warp	Y Fill	Z Axial	Compression Poisson's Ratio XY/Z	Z/XY	Coeff of Thermal Expansion X Warp	Y Fill	Z Axial	K Thermal Conductivity X Warp	Y Fill	Z Axial
1.	2-D C/C Ring SG = 1.55 T-50 Fiber Phenolic Resin RT	5,750 psi 1.68 x 10^6 psi		100 psi 0.47 x 10^6 psi	5,800 psi 1.30 x 10^6 psi		15,500 psi 6.25 x 10^6 psi	1,200 psi 0.74 x 10^6 psi		3,500 psi N/A	0.25	0.08	RT to 250°F 0.30		1.12	RT 31.0		23.4
	3,000°F	7,750 psi 1.85 x 10^6 psi		650 psi 0.45 x 10^6 psi	5,000 psi 1.20 x 10^6 psi		22,300 psi 6.25 x 10^6 psi	1,200 psi N/A		N/A	0.25	0.08	RT to 1,800°F 1.12		1.95	at 1,500°F 27.0		12.2
		X-Hoop	Y-Radial	Z-Axial	X-Hoop	Y-Radial	Z-Axial	X-Hoop	Y-Radial	Z-Axial			X Hoop	Y Radial	Z Axial	X Hoop	Y Radial	Z Axial
2.	3-D C/C Rings-Blocks T-50 Fiber Pitch Resin SG = 1.90 RT	N/A	N/A	25,806 psi 19.53 x 10^6 psi	6,172 psi 6.65 x 10^6 psi	8,467 psi 6.56 x 10^6 psi	16,866 psi 16.36 x 10^6 psi	2,790 psi N/A	N/A	4,040 psi N/A	N/A	N/A	RT to 250°F -0.50	N/A		RT 117.0		99.0
	3,000°F	N/A	N/A	23,600 psi 11.50 x 10^6 psi	N/A	N/A	15,500 psi N/A	N/A	N/A	N/A	N/A	N/A	RT to 1,800°F -0.35	N/A		at 1,500°F 52.5		46.0

NOTES: 1. CTE Terms in./in.-°F x 10^{-6}
2. K terms BTU/ft-hr-°F

TABLE III

EROSION PERFORMANCE COMPARISON

Mtl	Inlet Erosion (mils/sec)	Throat Erosion	Forward Exit Erosion	Forward Exit Cone
2-D C/C	ϵ = 1.26 - 1.50 p = 685 - 1,100 psi 9.44 in/s	ϵ = 1.0 p = 550 - 1,100 psi 7.80 m/s avg 3 rings	ϵ = 1.10 - 1.17 4.05 m/s	ϵ = 2.0 1.31 m/s
3-D C/C	5.48 m/s avg 3 tests	3.87 m/s	2.30 m/s	--
PG	--	2.98 m/s	--	--
CCP/CCP	16.32 m/s	15.61 m/s	7.60 m/s	2.89 m/s

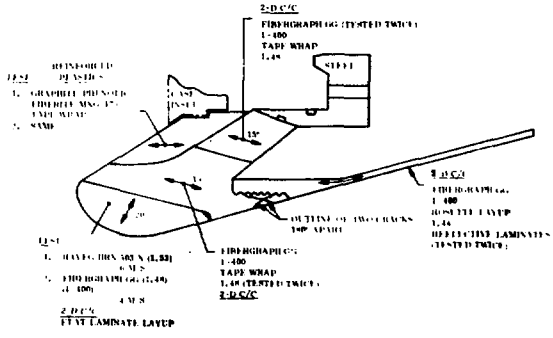


Figure 1. 2-D C/C Fixed Submerged Nozzle

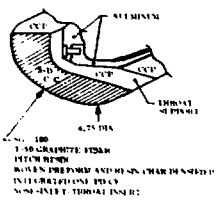


Figure 2. Reinforced Plastic - 2-D/CC - PG Redesign for 3-D C/C

INFLUENCE OF PYROLYSIS PRESSURE ON MICROSTRUCTURE OF CARBON-CARBON COMPOSITES

J. S. Evangelides
The Ivan A. Getting Laboratories
The Aerospace Corporation
P.O. Box 92957, Los Angeles, California 90009

Carbon-carbon composites are finding increasing use in thermostructural applications such as reentry vehicles and rocket nozzles. Although some increases in composite properties have been achieved, the development of advanced materials with improved performance and uniform properties will require a basic understanding of the macro/microstructural characteristics that control properties. A first step toward this goal is the description of the characteristics and changes that occur as a result of processing. The aerospace community has concentrated on the use of various pyrolysis pressures (6.9 to 103 Mpa) and filament coatings (with and without chemical-vapor-deposited carbon, CVD) as a means of improving performance. The objective of this experimental program was to study the effect of pyrolysis pressure and filament surface treatment on the resulting matrix structure. The description of the microstructural characteristics and thermal and physical properties of the constituents is essential to an understanding of processing stresses and is a vital part of the input data to analytical processing models. Ultimately, the correlation of performance to properties and structural characteristics can aid in establishing the optimum processing procedure.

The experimental approach has been to examine composites and bulk matrix after selected processing steps. After appropriate metallographic preparation and ion etching, the methods of optical and scanning electron microscopy were utilized to characterize microstructure. The xenon ion etching provided a simple means of observing the orientation of the graphitic layer planes with respect to the filament surfaces (Fig. 1). A well-defined etched lamellar structure in the matrix phase occurs when the graphitic basal planes were oriented within approximately 30 deg of the polished surface [1-4]. If the planes were parallel to the surface, a flat planar appearance was obtained while intermediate orientations yielded a fish-scale appearance.

The majority of the carbon-carbon composite samples were fabricated with Union Carbide Thornel 50 fibers and either Allied Chemical CP277 15V or Ashland A240 pitch. In order to supplement these specimens and represent extremes in processing pressure, miniature unidirectional samples were fabricated by low- (6.9 Mpa) and high-pressure (103 Mpa) procedures.

The effect of impregnation and pyrolysis pressure on matrix microstructure was most striking between individual filaments of a fiber bundle. Composites fabricated by the pyrolysis of coal tar (15V) or petroleum (A240) pitches under pressures of less than 6.9 Mpa resulted in the graphitic layer planes of the matrix being aligned parallel to the filament surface (Fig. 2). This highly aligned sheath of graphite basal planes formed irrespective of the type of filament (high- or low-modulus rayon, pitch, or polyacrylonitrile) or whether or not the filament had a CVD coating. Progressing away from the filament and sheath, the matrix structure became more complex or intertwined and, as such, more isotropic.

The pitch microstructure developed under high-pressure procedures (103 Mpa) was found to be significantly different. In the interfilament regions of a composite that had received an initial CVD coating, the graphite basal planes were randomly oriented to the filament surface (Fig. 3). Although regions of parallel orientation existed, the transverse orientation predominated. This random matrix had a characteristic structure indicative of inhibited mesophase spherule coalescence. In addition, this structure did not possess the long-range order of the composites fabricated by low-pressure procedures. Immediately at the CVD pitch interface, the basal planes were aligned at angles of 0 to 90 deg with the 0 deg or parallel alignment occurring the majority of the time. Examination of transverse sections of this composite indicated that the pitch matrix had penetrated those regions where the CVD coating had separated from the Thornel 50 filament [5].

The unidirectional composites fabricated by high-pressure impregnation procedures without an initial CVD coating also had the random basal plane orientation with respect to filament surface (Fig. 4). However, a qualitative assessment of the amount of random or transversely oriented matrix suggested that a slighly less random structure was obtained than when a CVD coating was present.

Since the pitch matrix microstructure is established during the mesophase pyrolysis occurring below 600°C and the interior of filament bundles density early in liquid impregnation procedures, the alignment of the graphite basal planes between filaments will be determined by the pyrolysis pressure employed during the initial densification cycles. Therefore, in those composites where initial low-pressure pyrolysis procedures are followed by high-pressure procedures, the graphite basal planes will be aligned parallel to the filament surfaces within the fiber bundles.

These microstructural observations indicated that high-pressure impregnation and pyrolysis results in a random orientation of botryoidal spheres, as was discussed by Marsh [6]. The effect of this pressure, then, appears to be to inhibit the coalescence of the mesophase spherules. Under low-pressure procedures, this coalescence results in a highly anisotropic sheath.

Although pressure was primarily responsible for imparting the random structure, it appears that the CVD coating increases the amount of random spherules or decreases the amount of coalescence. Since fiber surfaces promote parallel alignment between planes, the effect of the CVD coating may be to reduce the pitch wetting of filaments, thereby reducing coalescence [7].

Acknowledgments

The author acknowledges the valuable assistance of A. L. Ealy in these experiments. This work was supported by the Naval Surface Weapons Center under Air Force Contract No. F04701-76-C-0077.

References

[1] J. S. Evangelides, et al., TOR-0076(6726-01)-1, The Aerospace Corporation (30 September 1976).

[2] J. L. White and J. E. Zimmer, Surface and Defect Properties of Solids 5, 16 (1976).

[3] R. D. Reiswig, et al., Carbon 5, 603 (1967).

[4] J. S. Evangelides, 12th Conference on Carbon, Extended Abstracts, p. 93 (1975).

[5] J. E. Zimmer, et al., TOR-0076(6726-02)-2, Vol. I, The Aerospace Corporation (September 1975).

[6] H. Marsh, et al., Carbon 9, 159 (1971).

[7] J. S. Evangelides, High Pressure Working Group (1976).

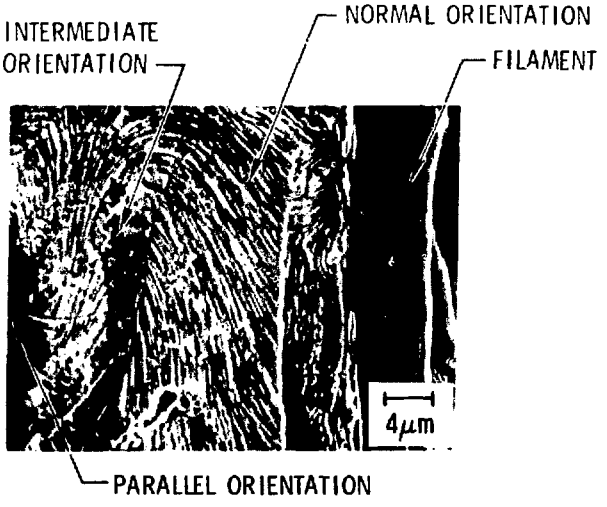


Fig. 1. Scanning electron micrograph of etch pattern orientations.

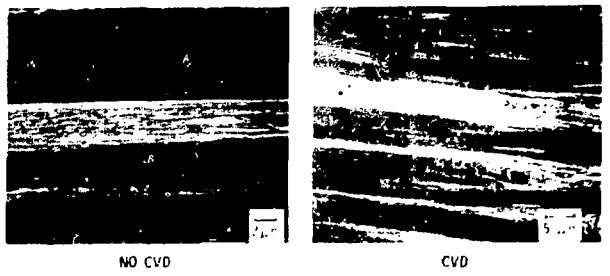


Fig. 2. Scanning electron micrographs of matrix structure due to low-pressure processing.

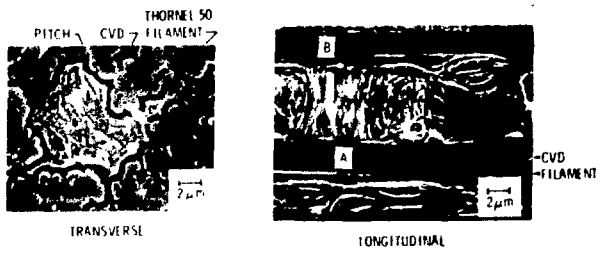


Fig. 3. Scanning electron micrographs of matrix structure due to high-pressure processing.

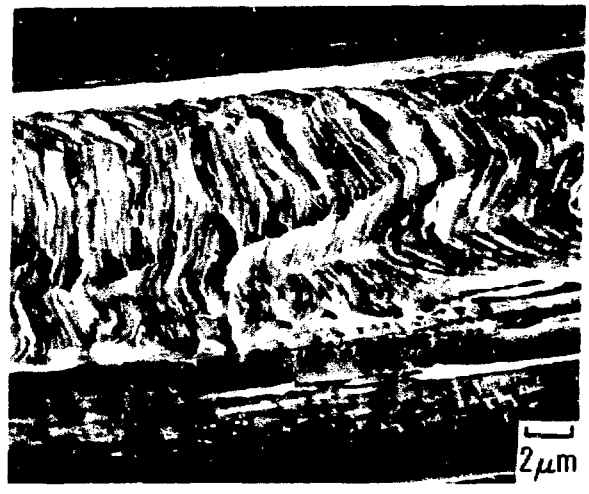


Fig. 4. Scanning electron micrograph of matrix structure due to high-pressure processing. No CVD.

CARBON - CARBON FOR NOZZLES

G. W. Driggers and B. S. Starrett
Southern Research Institute
Birmingham, Alabama 35205

Application Environment

Missile and space launch systems using solid propellants are setting demanding new requirements on materials to be used in nozzles. Missile systems are projected to use propellants with gas stagnation temperatures exceeding 6000°F and highly reducing constituency. Design chamber pressures of 1000 to 3000 psi are common in advanced systems. At the other extreme, the Space Shuttle Interim Upper Stage and various solid propellant space motors are incorporating relatively benign propellants with long burn times. The current premium on reliability, weight savings and potential performance gains is substantial.

Carbon-Carbon Nozzle Programs

It has been suggested by Ellis (1974) that a carbon or graphite reinforcement in a carbonaceous matrix (carbon-carbon composite) could provide a near optimum nozzle material. The tailorability, potential ablation resistance and probable higher reliability of a one piece c-c nozzle compared to complex multi-piece nozzles made the proposal attractive.

A subsequent program, sponsored by the Naval Surface Weapons Center, (NSWC), was conducted by Chemical Systems Division (CSD) of United Technologies, Inc. to investigate the c-c Integral Throat and Entrance (ITE) concept experimentally. The four c-c ITE's were examined at the micro- and macro-structure level to determine what material and surface characteristics potentially affected ablation performance. Additionally, mechanical and thermal properties were determined to the extent possible considering material quantity limitations. These investigations were conducted at Aerospace Corporation and Southern Research Institute.

Current efforts in carbon-carbon nozzle components and ITEs are in progress under the sponsorship of both NSWC and the Air Force through a series of joint AFML/AFRPL programs. The Carbon Nozzle Opportunities (CNO) program is firing both multipiece and ITE nozzles with a nominal seven inch I.D. throat section. The NSWC program and USAF C/CAN efforts will fire a variety of nominal 1.96 inch throat diameter subscale nozzles. Selected mechanical, thermal and surface removal phenomena characterizations are in progress on the CNO and C/CAN programs with similar efforts planned for the new NSWC program.

Observations to Date

The amount of characterization to date has been limited due to the small number of firings and the availability of materials and funds. Sufficient work has been done, however, to develop a series of observations and hypotheses on relationships between construction parameters and process characteristics (such as nature of porosity, permeability, etc.) and thermo-mechanical or ablation performance. In addition, work in recent years on c-c materials for nose tips and heat shields has yielded data and information on the impact of construction anomalies relative to mechanical and thermal behavior. The strength of a c-c in a given direction, for example, can be tied to the extent and type of damage experienced by the reinforcement during weave and process. Filament breaks and kinks, yarn waviness and maladjustment as well as matrix to filament bonding have correlated to modulus, strength and thermal expansion anomalies.

On axis tensile and compressive properties are directly related to the properties of the reinforcement for the three-dimensional orthogonal constructions. Therefore construction anomalies of any extent can affect the on axis properties. For example, initial compressive failure at low temperatures occurs as a result of local buckling of yarn bundles. This buckle precedes shear failure and occurs at nominal stress levels less than one-half those where tensile failure normally occurs. If these are bowed, wavy, or kinked reinforcements, then the stress levels are further reduced. This could become an important consideration in materials with cylindrical weaves where the successful manufacture of parts without wavy circumferential yarn bundles is difficult.

The wavy circumferential yarn bundles in cylindrical weaves can also have a pronounced affect on the hoop tensile strength of these materials. Recent data have shown tensile strength reductions of 75% and greater on cylindrical materials with weave distortions versus material with relatively straight yarns.

Ref. [1]Ellis, R.A., "Nozzle Efficiency Improvement With Advanced Materials", Presented JANNAF Propulsion Meeting San Diego, October, 1974

USE OF CARBONS IN DENTAL AND ORTHOPAEDIC IMPLANTS

S. F. Hulbert J. C. Bokros

LTI carbon is a clinically accepted material for use in prosthetic devices Its unique combination of properties makes LTI carbon especially useful in the construction of artificial heart valves and other cardiovascular devices. It is:

- Thromboresistant
- Compatible with plasma proteins and cellular components of blood
- Non-biodegradable
- Wear resistant
- Immune to fatigue

The physiologically inert nature of LTI carbon allows it to survive in the difficult transcutaneous situation and can provide access to the circulatory and nervous systems for a broad spectrum of applications.

The ability to survive in the transcutaneous situation and its mechanical similarity to bone make LTI carbon a logical artificial tooth root material. Long-term animal tests are confirming the use of LTI carbon as a dental implant to support a bridge or single tooth.

Because of the wear resistance of LTI carbon it is a potential material for use in prosthetic joints.

The biocompatibility of LTI carbon has been established through investigations of many groups. Bruck, in a recent review, has summarized the results (Table 1). As shown in the table, the thromboresistance of LTI carbon is very good to excellent in both the canine vena cava test of Gott and the renal embolus test of Kesserow. In in-vitro tests the calcium replacement clotting time is not affected by prolonged exposure to LTI carbon surfaces. The material had no effect on the plasma proteins tested by Halbert and no significant effect on the activity of plasma enzymes.

LTI carbon has been in use clinically since 1969; there have been no contraindications

Table 1 Biological Properties of LTI Carbons

In Vivo	
Vena cava	
2 hr	Excellent
2 weeks	Excellent
Renal embolus	Very good
In Vitro	
Effect on plasma proteins	None
Effect on plasma enzymes	None to slight
Calcium replacement clotting time	Not prolonged
Adherence of erythrocytes (WB)	Light
leucocytes (WB)	None
platelets (PRP)	Moderate
Platelet aggregation and activation	Slight
Cell growth (amnion)	Near 100%
Zeta potential (Krebs)	Negative
Critical surface tension	50 dynes/cm

attributable to the material. Problems of long-term biodegradation in the body, such as those often encountered when polymers are implanted for long periods, have not been observed with chemically inert LTI carbons.

LTI carbon may be cleaned by detergent washing and sterilized either by steam auto-claving or with ethylene oxide.

The mechanical properties of LTI carbon may be tailored for specific applications. The fracture strength varies from about 50,000 psi to 100,000

psi depending on density and alloy content. The modulus of elasticity can also be adjusted through processing and falls in the range of the values reported for that of bone.

Wear studies have been shown LTI carbon-LTI carbon bearing surfaces to have a lower wear rate than any other combination of surfaces presently being used in total hip prostheses.

Shim has reported that LTI carbon is not susceptible to fatigue. Repeated stressing up to near the fracture stress will not cause failure. The endurance limit coincides with the single cycle fracture stress.

In comparative tests, the endurance limit of alloyed LTI carbons was more than double that of vitreous carbon.

Applications of LTI Carbon

1. Cardiovascular

LTI carbon was introduced clinically in early 1969; more than 170,000 parts for prosthetic heart valves have been delivered for clinical use. The wear rates predicted by in-vitro or in-vivo animal tests suggest that significant wear will not occur even during the lifetime of a young patient. The wear resistance together with the fact that the material is not subject to fatigue or biodegradation makes it the material of choice for long-term implantation either in valves or as the components of cardiac assist devices.

2. Transcutaneous Leads

The ability to have a continuous, long-term access through the skin allows for diagnostic and treatment procedures not previously possible. Applications of LTI carbon transcutaneous leads in humans include those for skeletal attachment of prosthetic limbs, and lead-throughs for electrical stimulation of the nervous system. Other applications, still in animal testing, include devices that provide access to the blood for renal dialysis and ports for the controlled administration of drugs.

3. Dental Implants

The biocompatibility of LTI carbon, its strength and ability to perform transcutaneously, and its elastic match with bone make it especially suitable for use as an artificial tooth root. Tests in primates that were begun in 1971 confirm the viability of the approach. Encouraged by further animal tests, human tests were begun in 1975.

4. Orthopedic

Its biocompatibility, high strength and resistance to wear make LTI carbon an attractive material for use in orthopedic applications, particularly in total joint reconstruction.

Summation

Because of the very encouraging results obtained with LTI carbon in such applications as cardiovascular devices, transcutaneous leads, and dental implants, expanded efforts are being directed toward other applications in bioengineering. It is anticipated that LTI carbon and other new carbons will be instrumental in advancing the science and technology of prosthetics.

FACTORS AFFECTING THE BIOLOGICAL PROPERTIES OF VARIOUS CARBONS IN THE PHYSIOLOGICAL ENVIRONMENT

Stephen D. Bruck, Ph.D.
National Institutes of Health, Bethesda, Maryland 20014

Introduction

The biocompatibility and blood compatibility of materials may be enhanced by various surface modifications, including the chemical attachment of suitable macromolecules, biologically active agents, hydrogels, or by the deposition of thin, essentially impermeable surface coatings (1). Although LTI (low temperature isotropic) carbons have been successfully used in biomedical applications for several years, their deposition parameters bestow limitations. Guided by the biocompatible properties of LTI carbons, vacuum processes are being applied for the deposition of thin, carbon films onto a variety of substrates, including polymers (2). In addition, investigations are being also conducted with ion-beam deposited carbons (3). The ultimate biological properties of these carbons will be influenced by their structural parameters and by the substrates on which they are deposited (4).

Discussion

Diamond-polished LTI carbons are known to exhibit excellent blood and tissue compatible properties. This assessment is based on a variety of procedures including the in vivo (canine) vena cava and renal embolus tests, in vitro tests involving the effect on plasma proteins and enzymes, calcium replacement clotting time, adherence of the formed blood elements, platelet activation and aggregation and cell growth (5). LTI carbons have been evaluated in a variety of animals, and most importantly performed well in humans. This is significant because species-related hematological differences of experimental animals have received less than adequate attention in the past and is the subject of another paper by this author (6). LTI carbons are deposited on smooth, rigid surfaces, such as graphite (7). The porosity of the carbon coatings which may extend up to a depth of approximately 25 microns is eliminated by diamond-polishing, thus leaving a smooth surface which is essentially impermeable to gases and liquids. LTI carbons are turbostratic and the microcrystallites (10 to 30 Å) form aggregates that contain large fractions of disorganized carbon. Although the properties of the individual crystallites are anisotropic, when they are randomly oriented in the aggregates, the anisotropy is averaged and the aggregate structures display isotropic properties (7).

Despite the good biological performance of LTI carbons, the relatively high temperature required for deposition represents limitations for certain biomedical applications. Consequently, vacuum deposition processes are being studied with a variety of polymeric and non-polymeric substrates requiring temperatures of less than 100°C to yield carbon coatings in the thickness range of 500 to 1250 Å (2). The vacuum deposited carbons exhibit isotropicity, crystallinity, and density (1.8 gm/cm^2) similar to LTI carbons (2). The preliminary biological data underline the importance of substrate effects. These become especially important when either impermeable or permeable coatings are attached to appropriate materials to enhance their blood compatibility and are discussed in more detail elsewhere by this author (4). Both diamond-polished LTI carbons (deposited on graphite substrates) and carbons deposited in a vacuum onto smooth stainless steel substrates exhibit low levels of hemolysis under shear stresses below 100 dyne/cm^2 with human blood, although LTI carbons performed somewhat better (8). Rotating disk experiments using blood of heparinized shunted dogs show low level of platelet adhesion with both diamond-polished LTI carbons on graphite substrates and polished vacuum deposited carbons on glass, in comparison to the control polyurethanes (9). Canine ex vivo studies with a rotating shaft device show significantly less thrombotic deposit for vacuum deposited carbons on smooth stainless steel shafts than for control silicone rubber (10). Although the data are preliminary, canine vena cava tests (10) conducted with vacuum deposited carbons using stainless steel substrate rings showed no clots on two rings after two weeks of implantation.

In the case of ion-beam deposited carbons (11), preliminary studies thus far involved carbons deposited on "as machined" polypropylene and solution cast segmented polyether-urethanes. The thickness of the ion-beam deposited carbons is in the order of 500 Å with a density of 2.36 gm/cm^2, and differ from LTI carbons. Preliminary biological evaluations thus far involved mainly the canine in vivo vena cava (10) and renal embolus tests (12). The former yielded mixed results, whereas the latter showed various degrees of renal infarctions despite the relative absence of clots on the rings themselves. The scatter of the available data probably reflects, at least in part, substrate irregularities which apparently have a dominant effect on the thin carbon coatings. It remains to be seen how the structural differences between ion-beam deposited carbons and vacuum deposited carbons affect their respective overall biological properties.

In any case, smooth substrates seem to be needed with ion-beam deposited and vacuum deposited carbon coatings. Although both types of carbons adhere well to polymeric substrates, their potential biomedical applications should find greatest usefulness with non-elastomeric substrates to avoid surface cracks.

References

1. Bruck S. D., Blood Compatible Synthetic Polymers - An Introduction, C. C. Thomas Publisher, Springfield, Illinois (1974).
2. Haubold A. D., Shim H. S. and Agarwal N. K., Contract No. NIH-NO1-HV-4-2928, Annual Report, March 1976, PB 254 201/AS.

3. Aisenberg S. and Chabot R. W., Contract No. NIH-NO1-HV-3-2919, Annual Report, February 1976, PB 253 089/AS.

4. Bruck S. D., paper in press.

5. Bruck S. D., Rabin S. and Ferguson R. J., Biomat., Med. Dev., Art. Org., 1, 191-222 (1973), and references therein.

6. Bruck S. D., Biomat., Med. Dev., Art. Org., (in press); see also, Bruck S. D., in Abstract of Papers, 3rd Annual Meeting of the Biomaterials Society, New Orleans, Louisiana, April 15-19, 1977.

7. Bokros J.C. and Akins R. J., in Proceeding of the Fourth Buhl International Conference on Materials, Pittsburgh, Pennsylvania, November 16-18, 1971, Carnegie Press, Pittsburgh (1971).

8. Williams M. C., Contract No. NIH-NO1-HV-3-2952, Annual Report, August 1976, PB 259 119/AS.

9. Leonard E. F., Kochwa S, Litwak R. S. and Rosenfield R. E., Contract No. NIH-NO1-HV-3-2910, Annual Report, May 1976, PB 255 113/AS.

10. Schultz J.S., Ciarkowski A. A., Goddard J. D., Lindenauer S. M. and Penner J. S., Contract No. NIH-NO1-HV-4-2962, Annual Report, July 1976, PB 257 219/AS.

11. Daniels A. U. and Mortensen J. D., Contract No. NIH-NO1-HV-4-2979, Annual Report, November 1975, PB 248 222/AS.

12. Kusserow B. K. and Larrow R. W., Contract No. Contract No. NIH-NO1-HV-5-2939, Annual Report, August 1976, PB 259 118/AS.

(The views expressed in this paper are those of the author and do not necessarily reflect those of the National Heart, Lung, and Blood Institute, the NIH or the DHEW.)

INTERACTION OF HUMAN FIBRINOGEN WITH PURE LTI-CARBON*

T-H. Chiu and E. Nyilas
Avco Everett Research Laboratory, Inc.
Everett, MA 02149

Low temperature isotropic (LTI) carbon surfaces which have been diamond-polished according to specified tolerances, display a favorable degree of nonthrombogenicity not only in vitro and ex vivo but, most importantly, in vivo as parts of various prosthetic devices chronically implanted in man. As the primary event of their interaction with native blood, foreign surfaces acquire within very short periods of time a "conditioning" layer that is a few hundred Å's thick and composed of sorbed plasma proteins. This layer mitigates the effects of the original contact surface on other blood components and hence, the state of protein molecules in it (viz., native, partially or irreversibly denatured) can influence the incidence of potentially ensuing thromboembolic phenomena. Based on experimental evidence [1] consistent with diffusion kinetic theory, [2] fibrinogen (FGN) which has been strongly implicated in thromboembolic phenomena, can be expected to be a major constituent of the "conditioning" protein layer. With respect of these factors, the studies reported here have been undertaken to elucidate the specifics of the mechanism and energetics of interaction between native FGN and LTI-carbon surfaces.

Microparticulate LTI-carbon adsorbent was obtained from discs, prepared at the Medical Products Div., General Atomic Co., by the deposition of this type of carbon on ultrathin graphite substrates. After the grinding of these discs in nonmetallic equipment over extended periods of time, the powder collected consisted of polydisperse particles which $\leq 1\mu$, contained 97.3% pure LTI-carbon, and gave a specific surface area of 109.2 m^2/g as determined by B.E.T. multipoint N_2 adsorption at -195°C. This area was inconsistent with the particle size observed in SEM's, and indicated the presence of porosity which was consistent with the established internal micromorphology of LTI-carbon.[3] Using (a) the measured hysteresis between the 25°C water vapor adsorption and desorption isotherms of the LTI-carbon adsorbent, and (b) the pressurized mercury penetration technique,[4] the pore size and shape distribution was determined revealing the presence of "ink-bottle" type pores. Analysis of these data gave 27.7 m^2/g as the specific surface area of the LTI-carbon adsorbent, which is exclusive of the internal surface area constituted by "ink-bottle" pores and is unrestrictedly accessible to all types of molecules, regardless of their size and shape. This area is commensurate with the particle size observed, and has been taken as the effective specific surface area for protein sorption. As described in a companion paper[5] the LTI-carbon adsorbent was also characterized by its (a) 25° and 37°C heats of immersion into a standard buffer, $h_I(SLB)_T$, whose composition is specified below, and (b) electrophoretic mobilities determined in the same buffer at the same temperature.

All FGN used in these experiments was freshly purified according to the method of Laki,[6] had a clottability of $\geq 92\%$; and displayed upon sodium dodecyl sulfate (SDS)/polyacrylamide gel electrophoresis only 3 bands, as required, corresponding to the α-, β- and γ-chains of the molecule which were detectable by staining with Coomassie-blue. In all experiments reported here, FGN was (a) adsorbed from a standardized sodium acetate/HCl buffer having a pH= 7.4 which simulated plasma conditions, and a low ionic strength of 0.05; and (b) at a fixed ratio of total available adsorbent surface area to total protein solution volume, $\Sigma'/V = 277\ cm^2/ml$.

The 25° and 37°C adsorption isotherms of FGN on the microparticulate LTI-carbon adsorbent were determined according to experimental protocols described elsewhere.[2, 7] Both isotherms have indicated multilayer sorption with FGN adsorptivities at the completion of first monolayer coverage, which were found to be identical within the error of the measurement at both temperatures. Based on the specific protein sorption area given above, the first monolayer coverages obtained convert to $\sigma_1(25°) \simeq \sigma_1(37°) \simeq 0.52 \mu g/cm^2$.

In another series of experiments also employing the experimental conditions specified earlier, the 25° and 37°C heats of FGN sorption on the LTI-carbon powder adsorbent were directly measured as a function of increasing bulk protein concentrations. This was performed with a custom-made, isothermal-jacketed, thermistorized microcalorimeter system routinely capable of resolving $\pm 1 \times 10^{-5}$°C in 100 ml of liquid volume.[2, 7] As a function of increasing surface coverages, the 25°C integral net heats released per mole of sorbed FGN have remained approximately constant whereas those obtained at 37°C have shown a moderate decrease within the concentration range studied. At the completion of first monolayer coverages, the integral net heats of FGN sorption on the microparticulate LTI-carbon are -3.6×10^3 and -2.4×10^3 Kcal/mole at 25° and 37°C, respectively. These quantities are smaller, by a factor of about 5, than the integral net heats of sorption of FGN reported elsewhere,[8] which have been determined under identical conditions but on a microparticulate glass adsorbent. In addition, the inverse holds for the FGN/glass system inasmuch as its 37°C integral net heats of sorption are greater than those obtained at 25°C. Thus, the different trends in the temperature-dependence of FGN sorption as well as the large difference between the magnitudes of the heats of sorption of that protein at comparable surface coverages indicate an entirely different structuring and interaction mechanism of FGN sorbed onto LTI-carbon surfaces.

The 25° and 37°C electrophoretic mobilities of LTI-carbon adsorbent particles were measured, which were coated with known amounts of FGN adsorbed at the corresponding temperatures under the conditions specified earlier. At both temperatures, these mobilities have remained practically

*This work was performed with support from the Biomaterials Program, Devices and Technology Branch, Division of Heart and Vascular Diseases, National Heart, Lung, and Blood Institute, under Contract NIH-N01-HV-3-2917.

constant, at about $-1.5\mu\text{-sec}^{-1}\text{-V}^{-1}\text{cm}$, up to a relative surface coverage, $\theta \sim 0.7$, and levelled off to a steady-state value at about first monolayer completion. This trend of change in the mobilities of FGN-coated LTI-carbon particles is in sharp contrast to that displayed by particles of the strongly procoagulant glass,[8] which were also coated with the same protein under identical conditions but rapidly shifted their mobilities in a positive direction with increasing θ's. The rapid positive shift indicates that sorbed FGN molecules effectively cancel negative charges on the glass surface. This, in turn, implies that FGN molecules undergo restructuring on glass, in contrast to that observed on LTI-carbon on which the original charge is preserved suggesting, at least, a less severe restructuring of the sorbed protein. Thus, the electrophoretic mobility data of FGN-coated LTI-carbon particles are in concert with the trend shown by the integral net heats of sorption of that protein on the same adsorbent.

The intensity of interaction arising between a native protein and an adsorbent, as measured in terms of the integral net heat of protein sorption, is generally a function of the mean number of binding sites established per sorbed protein molecule, and the mean net binding energy per site. Relatively smaller integral net heats of sorption of a given protein at submonolayer coverages indicate, as a minimum, either a relatively smaller number of attachment sites or smaller mean binding energies per site, or both. According to the working hypothesis underlying these studies, which was put forward earlier,[2] native plasma proteins may retain their conformation or, undergo relatively less extensive adsorption-induced structural rearrangements on nonthrombogenic surfaces than on thrombogenic ones. This implies that, under identical experimental conditions, the calorimetrically determinable interaction energy between a given native protein and different surfaces should be smaller for the less thrombogenic materials. In comparison to the FGN/glass system,[8] both the microcalorimetric and electrophoretic mobility data described above consistently indicate that native FGN undergoes, at least at submonolayer coverages, a considerably less intense interaction with the relatively nonthrombogenic surface of LTI-carbon. The data obtained for the microparticulate LTI-carbon and glass adsorption systems also indicate that, at least these 2 systems, support the postulations of our working hypothesis and imply a significantly smaller degree of adsorption-induced restructuring of native FGN on LTI-carbon surfaces. The same data which pertain to interactions occurring at the molecular level, appear to be consistent with the nonthrombogenic properties of LTI-carbon surfaces displayed on a macroscopic scale.

REFERENCES

1. Vroman, L., and Adams, A.L., J. Biomed. Mater. Res., 3, 43 (1969).

2. Nyilas, E., Chiu, T-H., and Herzlinger, G.A., Trans. Amer. Soc. Artif. Int. Organs, 20, 480 (1974).

3. Kaae, J.L., J. Biomed. Mater. Res., 6, 279 (1972).

4. Orr, C. Jr., Powder Technol., 3, 117 (1970).

5. Chiu, T-H., Nyilas, E., and Mical, F.J., "The State of Water on Pure and Silicon-Alloyed LTI-Carbon," paper presented at 13th Carbon Conference, Irvine, CA, July 1977.

6. Laki, K., Arch. Biochem. Biophys., 32, 317 (1951).

7. Nyilas, E., Chiu, T-H., and Lederman, D.M., "Thermodynamics of Native Protein/Foreign Surface Interactions. II. Calorimetric and Electrophoretic Mobility Studies on the Human γ-Globulin/Glass System," in "Colloid and Interface Science," Vol. V., pp. 77-89, M. Kerker, editor, Academic Press, Inc., New York, NY (1976).

8. Chiu, T-H., Nyilas, E., and Lederman, D.M., Trans. Amer. Soc. Artif. Int. Organs, 22, 498 (1976).

ADSORPTIVE PROPERTIES OF HUMAN γ-GLOBULIN ON PURE AND SILICON ALLOYED LTI-CARBONS*

E. Nyilas and T-H. Chiu
Avco Everett Research Laboratory, Inc.

As part of a study employing model systems to elucidate the energetics and mechanisms of native plasma protein sorption, the adsorptive properties of human γ-(7S)-globulin (γ-GLB) were investigated earlier with glass, one of the strongest known procoagulants.[1,2] This work has been extended to low temperature isotropic (LTI) and silicon-alloyed (SLTI) carbons, both of which are relevant biomaterials.

Microparticulate adsorbents composed of either 97.3% pure LTI-carbon or, 96.7% pure SLTI-carbon containing on the order of 10% by wt. silicon, were obtained from discs which were prepared at the Medical Products Div., General Atomic Co. by deposition of the corresponding types of carbon on ultrathin graphitic substrates. After grinding over extended periods of time in nonmetallic equipment to avoid any contamination, both types of discs yielded polydisperse particles measuring $\leq 1\mu$ in the SEM. For both adsorbents, B.E.T. multipoint N_2 adsorption at -195°C gave specific surface areas (Σ_{BET}) listed in Table I. These values are disproportionately greater than the specific surface areas which can be estimated from the particle sizes observed, indicating the presence of internal porosity. For LTI-carbon adsorbent, this is consistent with its established internal micromorphology.[3] Based on the (a) hysteresis between its 25°C water vapor adsorption and desorption isotherm, and (b) mercury penetration volume technique,[4] the pore size and shape distribution of each adsorbent has been determined. Analyses of these data revealed that both powders contain "ink-bottle" pores, and yielded the values, denoted as Σ_{eff} in Table I, as the specific surface areas exclusive of the internal surface areas of "ink-bottle" pores. These have been taken as the areas effective in protein sorption. Both the LTI- and SLTI-carbon adsorbents have been characterized, at T = 25° or 37°C, by their (a) heats of immersion into pure water, $h_I(SLW)_T$; (b) heats of immersion into a standardized sodium acetate/HCl buffer whose composition is given below, $h_I(SLB)_T$; and (c) electrophoretic mobilities, $u_e(25^o)$ and $u_e(37^o)$, with the 37°C data corrected to 25°C, $u_e'(37^o)$. For both adsorbents, these data are given in Table I.

TABLE I

$\Sigma_{BET}(m^2/g)$	109.2	52.8
$\Sigma_{eff}(m^2/g)$	27.7	17.8
$\Sigma_{BET}/\Sigma_{eff}$	3.9	3.0
$h_I(SLW)_{25}$ (erg/cm^2)*	-66.7±12.3	-51.5±3.5
$h_I(SLW)_{35}$ (erg/cm^2)*	-62.6±4.7	-52.6±3.5
$h_I(SLB)_{25}$ (erg/cm^2)*	-83.5±11.1	-60.4±2.3
$h_I(SLB)_{37}$ (erg/cm^2)*	-87.7±3.5	-65.8±1.8
$u_e(25^o)$ (μ-sec^{-1}-V^{-1}cm)	-1.63±.17	-1.46±.20
$u_e'(37^o)$ (μ-sec^{-1}-V^{-1}cm)	-1.45±.24	-1.58±.15

*Values are based on the corresponding Σ_{BET}.

All γ-GLB used was the highest commercially available grade 95% pure by electrophoresis. In all experiments, γ-GLB was always exposed to the adsorbents in a standardized sodium acetate/HCl buffer having a pH = 7.4 which simulated plasma conditions, and a low ionic strength of 0.05. In each protein adsorption, a fixed ratio of total available surface area to total protein solution volume, Σ'/V was used for each of the adsorbents. This was 277 cm^2/ml for the LTI-carbon, and 178 cm^2/ml for SLTI-carbon. The ratio given for LTI-carbon is identical to that used in human fibrinogen adsorption studies on that material, which have been reported in a companion paper.[5]

Determination of the 25° and 37°C γ-GLB adsorption isotherms of the microparticulate LTI- and SLTI-carbons was performed according to established protocols described elsewhere.[1,2] All enthalpy changes, including $h_I(SLW)_T$'s, $h_I(SLB)_T$'s and the 25° and 37°C heats of immersion of each of the adsorbents into γ-GLB solutions containing known amounts of the protein, i.e., $h_I(SLP)_T$'s were directly measured using a custom-made, isothermal-jacketed, thermistorized microcalorimeter system which, as reported elsewhere,[1,2] is routinely capable of resolving $\pm$ 1 x 10^{-5}°C in 100 ml of liquid volume. All electrophoretic mobility determinations were performed in the standard buffer, using a calibrated precision-bore glass capillary cell with a ground optical published flat. In each of these measurements, the mobilities of an average of 12-14 particles were recorded in both directions. All mobility values obtained at 37°C have been corrected to 25°C.

In the concentration range (0 - 2.0 mg/ml) studied, both the 25° and 37°C adsorption isotherms of γ-GLB on the microparticulate LTI-carbon indicate multilayer sorption. This is confirmed by the fact that a Langmuir plot of each of these isotherms splits into 2 linear segments having different slopes and intercepts. Both isotherms display well-defined "knee" points which are indistinguishable within the error of the measurement, and correspond to the completion of first monolayer coverages. Using the Σ_{eff} of LTI-carbon, these coverages convert to $\bar{\sigma}_1(25^o) \simeq \bar{\sigma}_1(37^o) \simeq 0.23\mu g/cm^2$. On the microparticulate SLTI-carbon, the shape of the 25°C isotherm of γ-GLB clearly displays multilayer sorption easily confirmed by the corresponding Langmuir plot. In contrast, the 37°C isotherm does not exhibit a well-defined "knee" point but the corresponding Langmuir plot verifies the incidence of multilayer sorption at that temperature as well. Based on the Σ_{eff} of SLTI-carbon, adsorbances at the completion of first γ-GLB monolayers are $\bar{\sigma}_1(25^o) \simeq 0.28\mu g/cm^2$ and $\bar{\sigma}_1(37^o) \simeq 0.24\mu g/cm^2$, which are indistinguishable from each other as well

*This work was performed with support from the Biomaterials Program, Devices and Technology Branch, Division of Heart and Vascular Diseases, National Heart, Lung, and Blood Institute, under Contract NIH-N01-HV-3-2917.

as from the $\bar{\sigma}_1$'s obtained for the pure LTI-carbon. Thus, no appreciable differences in γ-GLB adsorptivity appear between the LTI- and SLTI-carbons.

A measure of the intensity of interaction between a native protein and a given adsorbent is the integral net heat of protein sorption which, at a T temperature, is $\overline{\Delta H}' = h_I(SLP)_T - h_I(SLB)_T$. In general, $\overline{\Delta H}'$ is a function of the mean number of binding sites established per sorbed protein molecule, and the mean net binding energy per site. Since the term $h_I(SLP)_T$ measures the enthalpy change of protein attachment in the presence of buffer ions and since $h_I(SLB)_T$ measures that of the buffer alone, both processes are exothermic and hence, the sign of both quantities is negative. If $|h_I(SLP)_T| > |h_I(SLB)_T|$, $\overline{\Delta H}'$ is also negative.

For both microparticulate LTI- and SLTI-carbons, the calorimetrically measured values of $|h_I(SLP)_T| < |h_I(SLB)_T|$ when these adsorbents are exposed, at either 25° or 37°C, to γ-GLB solutions which have bulk protein concentrations (C_o) up to 0.10 mg/ml and give rise to coverages ranging up to ~ 0.20 μg/cm^2 (or relative γ-GLB surface coverages up to $\theta \sim 0.75$). Under these conditions, positive $\overline{\Delta H}'$ values are obtained which would seemingly indicate that the protein attachment in itself would be endothermic. However, direct attachment of the protein involves the displacement of water and ions from the surface, and the enthalpy change associated with protein attachment can, in certain cases, be smaller than the enthalpy change that is associated with the water and ion displacement. In these cases, attachment of protein molecules is attained if the entropy change of the overall adsorption process is positive. It can be shown that, in cases where nominally positive of $\overline{\Delta H}'$ have been obtained at submonolayer coverages on both LTI- and SLTI-carbons, the integral net heats of γ-GLB sorption are negative (i.e., exothermic), and can be computed using $\overline{\Delta H}' = h_I(SLP)_T - h_I(SLB)_T\ (1-\theta\Sigma_{eff}/\Sigma_{BET})$.

At C_o's > 0.10 mg/ml, $|h_I(SLP)_T| > |h_I(SLB)_T|$ and hence, all $\overline{\Delta H}'$ values are negative for both adsorbents. Within the entire concentration range studied, the magnitude of all integral net heats of sorption are in the range of -(2-4) x 10^2 Kcal/per mole of sorbed γ-GLB. At $\theta=1$, the 37°C integral net heats of γ-GLB sorption on the LTI- and SLTI-carbons are, respectively, -356 and -328 Kcal/mole. At comparable surface coverages, these heats are somewhat smaller for the SLTI-carbon, consistent with the fact that, as described in a companion paper,[6] the SLTI surface is relatively "hydrophobic" as compared to that of the LTI-carbon. This is also reflected by their respective $h_I(SLW)_T$ values listed in Table I.

The adsorptive properties displayed by γ-GLB on LTI- and SLTI-carbons are in sharp contrast to those displayed by the same protein under identical conditions but on a microparticulate glass. As described elsewhere,[1,2] the 25° and 37° integral net heats of γ-GLB on the glass adsorbent are respectively, -1,700 and -1,200 Kcal/mole at completion of first monolayer coverages, which are an order of magnitude greater than those obtained on the LTI- and SLTI-carbons. This indicates, at least, that γ-GLB undergoes an entirely different interaction mechanism with glass.

The electrophoretic mobilities of LTI- and SLTI-carbon particles were measured at 25° and 37°C after they were coated with known amounts of γ-GLB adsorbed under the conditions specified earlier. The mobilities of both types of protein-coated carbon particles remained equal to those of the corresponding uncoated particles up to $\theta \sim 0.85$, and levelled off to a steady-state value at $\theta=1$. In contrast, particles of the strongly procoagulant glass, which were also coated with γ-GLB under identical conditions, rapidly changed their mobilities in a positive direction at relatively small surface coverages ($\theta \leq 0.1$), indicating that small amounts of the sorbed protein are already sufficient to neutralize negative charges on the glass surface.

The trend of change in the mobilities of γ-GLB-coated LTI- and SLTI-carbon particles as well as the comparatively small values of the integral net heats of γ-GLB sorption on these carbons are consistent with each other. In addition, both sets of data indicate that, at least at submonolayer coverages, γ-GLB undergoes a significantly smaller degree of adsorption-induced restructuring on both carbon surfaces. With respect to the definition of the integral net heat of protein sorption, relatively smaller values of this enthalpy quantity are indicative of less intense interactions which occur between a particular native protein and various adsorbents. As described earlier,[1,2] the working hypothesis of the studies reported here holds that, in contrast to procoagulants, nonthrombogenic surfaces give rise to less severe adsorption-induced structural alterations in sorbed plasma proteins. As characterized in terms of the microcalorimetric and electrophoretic mobility data given above, the adsorptive properties of γ-GLB on LTI- and SLTI surfaces are in concert with the established nonthrombogenic properties of these carbons, and support our working hypothesis.

REFERENCES

1. Nyilas, E., Chiu, T-H., and Herziinger, G. A. Trans. Amer. Soc. Artif. Int. Organs, 20, 480 (1974).
2. Nyilas, E., Chiu, T-H., and Lederman, D. M., "Thermodynamics of Native Protein/Foreign Surface Interactions. II. Calorimetric and Electrophoretic Mobility Studies on the Human γ-Globulin/Glass System," in "Colloid and Interface Science," Vol. V., pp. 77-89, M. Kerker, editor, Academic Press, Inc., New York, NY (1976).
3. Kaae, J. L., Carbon, 9, 291 (1971).
4. Orr, C., Jr., Powder Technol., 3, 117 (1970).
5. Chiu, T-H., and Nyilas, E., "Interaction of Human Fibrinogen with Pure LTI-Carbon," paper presented at the 13th Carbon Conference, Irvine, CA, July 1977.
6. Chiu, T-H., Nyilas, E., and Micale, F. J., "The State of Water on Pure and Silicon-Alloyed LTI-Carbon," paper presented at the 13th Carbon Conference, Irvine, CA, July 1977.

DIAMOND-LIKE CARBON FILMS--FACTORS LEADING TO IMPROVED BIOCOMPATIBILITY*

S. Aisenberg, Ph.D.
Gulf + Western Applied Science Laboratories
(formerly Space Sciences Division of Whittaker Corporation)

The various physical and chemical properties of Ion Beam Deposited diamond-like carbon were studied in order to determine the factors related to improved blood compatibility. The insight gained can contribute to the development of a "unified theory of blood compatibility."

Ion Beam Deposited Carbon (IBDC) is produced by means of an energetic beam of carbon ions derived from a plasma of inert gas and carbon atoms (1,2). This carbon ion beam is extracted into a low pressure deposition chamber and accelerated to the deposition substrate with an energy of 50-100 electron volts.

As a result of the high ion energy the carbon film grows with many properties similar to that of diamond. During the ion beam deposition, simultaneous ion beam etching occurs so that impurity atoms and atoms with weaker bonds are removed giving a film with a composition of atoms having the strongest bonds. Typical of the properties measured (3) are the following:

1. Essentially amorphous in structure with grain size in the range of 5-30 (X-ray diffraction).
2. Smooth surface, closely conforming to substrate as observed with scanning electron microscope.
3. Good adhesion to polymeric and other substrates, typically 700 psi (as high as 5,000 psi on metal substrates).
4. Typical coating thickness 500-1000Å.
5. High critical surface tension, 40 dynes/cm.
6. Low gas permeability.
7. Transparent.
8. Surface charge is low, less than 10^{-11} coul/cm^2 (vibrating capacitor measurements).
9. Density of 2.36 gm/cm^3.
10. Good performance in vena cava and renal embolus tests.
11. Dielectic constant is approximately 16.
12. Insulating, with a high resistivity of 10^{11} ohm-cm.

Bell Telephone Laboratories reported using procedures similar to that of Aisenberg and Chabot (1,2) to also obtain Ion-Beam-Deposited polycrystalline diamond-like films. The characteristics they reported include:

1. Films are insoluble in all common inorganic acids (as well as numerous inorganic and organic solvents) including HF, HNO_3, HCl, H_2SO_4, HCOOH, Acetone, Trichloroethane, Chloroform, Ethyl Acetate and others.
2. Films are optically transparent (either pale yellow or water clear with bright colored interference rings for thicker films).
3. The thin films have a smooth surface.
4. DC and AC resistivities are about 10^{12} ohm/cm.
5. The index of refraction is about 2.
6. All thin free standing films were quite flexible.
7. Film curling was not observed for stripped films indicating the essential absence of strain.
8. X-ray diffraction studies showed that "in many cases definite, but usually very weak lines assignable to diamond were recorded." The average grain size was 50-100Å according to line broadening.

Hard carbon films have been reported for plasma glow discharge deposition (5) but the film properties have not been characterized.

In reviewing the results of biocompatibility tests such as the vena cava and renal embolus tests for our IBD carbon and for other materials that are also blood compatible, it became apparent that a "unified theory of biocompatibility" is needed to guide future development and testing.

The unified theory should be consistent with the results reported for the better biocompatible material such as:

1. Collagen
2. Hydrogels
3. Natural endothelium
4. Various forms of carbon (pyrolytic, ion beam deposited, plasma deposited)
5. Glow discharge polymers
6. Heparinized polymers
7. Fluroesters of ethyl cellulose
8. Various polymers (such as Avcothane which is a compound of polyurethane and silioxyane).

It is proposed (3) that if surfaces are going to form clots in varying degrees, the best surfaces will be those that release the emboli while they are in the early, seed, or juvenile stage. There are two reasons for this. First, the mass release rate of the clots increases approximately as the square of the clot diameter at release so that the sooner the clots are released the smaller the total mass of clots released per nucleation site. For example, if the material and test conditions permit the clot release at a size of 100 microns rather than 1,000 microns, then the total rate of clot mass throw-off is reduced by a factor of 100 and has a better chance of quickly being reabsorbed by the body before prohibitive damage is caused.

Second, small clots are less likely to close off an important artery, but instead will lodge in the smaller arteries and/or capillaries so the necessary blood is more likely to be supplied by collateral circulation with less chance of severe necrosis. The

* This work was supported by Contract No. NIH-NOI-HB-3-2919, National Heart and Lung Institute.

damage to tissue downstream is thus less serious in the case of early shedding of seed clots.

Third, the smaller the size of the necrosis (if present), the better chance of being reabsorbed before irreversible damage is produced.

Thus, it appears logical that a figure of merit for a blood compatible surface is the release radius, R_R, of typical blood clots released from the surface. The smaller R_R, the better it is for the subject.

As an extreme example of the above argument, it is better for a subject to continuously release large numbers of small thrombi that can be reabsorbed quickly and safely, than one large thrombus one year later. Note also that the body is able to cope with small thrombi expected to result from long term atherosclerotic deposits frequently present in people.

In addition to the basic fabrication properties of blood compatible materials (fabrication ease, flexibility, flex life, and stability) it is postulated that the following factors will be important for blood compatibility:

1. Smooth surface, free of defects, or inclusions to aid early release of thrombi and to reduce thrombi formation caused by local stagnation due to defects.

2. Fast flow to give greater removal forces and earlier release (small sizes).

3. Fast flow to increase removal of clotting factors at surface.

4. Smooth surfaces also prevent local trapping of clotting factors due to stasis.

5. The use of heparinized polymers and blood will aid the early release of any thrombi that form.

6. Ability to flex without permanent damage such as development of cracks and loss of protective coatings.

7. Non molecular structure of IBD carbon film can avoid the configuration change of protein molecules that can occur with polymer substrates encouraging protein change.

8. Absence of impurities to migrate to surface (such as plasticizers, catalysts, fillers, stabilizers, additives).

9. An impermeable barrier to substrate impurity migration (such as IBD carbon with its tight lattice structure). Even if there are micro cracks in film due to flexing, the micro crack area will be many orders of magnitude smaller than the geometric area and the out migration of substrate impurities will be much smaller than for uncoated substrates.

10. No impurities in coating itself--this is true for the case of IBD carbon because of the use of vacuum and sputtering techniques. This is true for other vacuum-plasma deposited films as well as for pyrolytic carbon formed under high temperature.

11. The coating must also be chemically inert (as well as the substrate).

12. Critical surface tension in correct range.

13. Stability of physical strength in contact with blood.

14. Uniformity of surface properties. Patches of bad materials will make the whole surface act bad from the observers view.

15. Surface charge (slightly negative) and uniformity.

16. Surface is contamination free--otherwise growth and adhesion of thrombi are encouraged.

Some of the problems of more efficient development and use of blood compatible materials are:

a. Lack of reproducibility of tests from same source and same testing groups.

b. Long time involved for tests resulting in slow feedback.

c. Few data points--usually at the end of test.

d. Contradictory data and interpretations are frequently found in literature.

There is a need for in vitro, ex vivo, and in vivo tests that can give data continuously during each test.

There is also a need for a simple test for the reproducibility of the materials surface, both for uniformity within a batch, and for different batches. We have a vibrating capacitor electrode test system that can determine the surface potential to within a few millivolts. For example, this system can easily detect a fingerprint on the surface and has a detection limit of the surface potential corresponding to one hundredth of a fingerprint. Use of such techniques can be of help in comparing IBD carbon films and other blood-compatible surfaces.

REFERENCES

1. S. Aisenberg, R.W. Chabot, J. Appl. Phys., 42, 2953, (1971).

2. S. Aisenberg, R.W. Chabot, J. Vac. Sci. Technol. 10, 104, (1973).

3. S. Aisenberg, R.W. Chabot, Ion Beam Deposited Carbon Coatings for Bio-Compatible Materials, Ann. Rep., February 1976, Contract NIH-NOI-HB-3-2919, Whittaker Corporation, Space Sciences Division, Document No. SSD-P-860.

4. E.G. Spencer, P.H. Schmidt, D.C. Joy and F. H. Sansalone, Appl. Phys. Letter, 29, No. 2, 118 (1976).

5. L. Holland, J. Vac. Sci. Technol., 14, 5, (1977).

INVESTIGATIONS OF VITREOUS AND PYROLYTIC CARBON-METALLIC ALLOY SURGICAL BIOMATERIALS

J.E. Lemons, R.A. Buchanan, I.L. Baswell and N.G. Thompson
Department of Biomaterials and School of
Engineering, University of Alabama in Birmingham 35294 USA

Vitreous and pyrolytic forms of carbon have been used extensively as synthetic biomaterials for the replacement of, augmentation of, and attachment to biological tissues.[1,2] One such device involving the integrated use of carbon and metallic alloys, the vitreous carbon tooth root replacement system, is schematically illustrated in Figure 1. The biocarbons, in general, have demonstrated very acceptable biocompatibility and the prognosis for expanding clinical applications is quite good.

Biomaterial Analyses

Vitreous and pyrolytic carbon specimens received for limited clinical trials were subjected to laboratory examination. A number of the vitreous carbon devices,* when examined stereomicroscopically and radiographically, showed irregular surface and internal features. Many of these features appeared as cracks with some extending from the external carbon surface to the stainless steel core. Metallographic analyses of transverse and longitudinal sections showed surface to core interconnected features.[3]

To establish basic data on possible electrochemical influences of co-exposure of carbon and metallic alloy materials to biological environments, in vitro laboratory corrosion experiments were initiated.[4] Mixed-potential corrosion theory and accompanying potentiostatic polarization data were used to determine corrosion rates of carbon-metal ** couples, and then compare these corrosion rates with those of the individual alloys. Anodic and cathodic polarization curves were generated in isotonic saline (0.9% NaCl) solution at a pH of 7.0 and a temperature of 37.0°C. The anodic dissolution curves of stainless steel (316L) and Tivanium (Ti-6Al-4V) alloys were measured in nitrogen-saturated solution. The cathodic polarization curves of the two alloys and pyrolytic carbon were determined in oxygen-saturated solution. Extrapolation of the Tafel regions of the cathodic polarization curves to their respective intersections with the anodic dissolution curves allowed corrosion rates to be graphically determined.

Results and Discussion

The number of vitreous carbon devices examined and the irregular features found are summarized in Table I. The first three groups were examined prior to the general release of this implant system. The last group examined stereomicroscopically, Group 10 showed no significant irregular features. In our opinion, this number of irregular features represents a significant statistic. It was previously proposed[5] that these type features could influence electrochemical (biodegradation) and mechanical (strength and fracture) properties.

The potentiostatic polarization curves for passivated Ti-6Al-4V and 316L stainless steel with pyrolytic carbon are shown in Figures 2 and 3 respectively. With these results and by application of mixed-potential theory, the effect of carbon-to-metal area ratio on corrosion rate was evaluated.

The investigation indicated that the Ti-6Al-4V alloy in a pyrolytic carbon-metal couple would not undergo corrosion at a significantly more rapid rate than the alloy alone in simulated body fluids, even if the carbon-to-metal area ratio was quite large. This result is taken from inspection of Figure 2 where it is noted that all curve intersections are located far below the apparent transpassive potential of Ti-6Al-4V. In the case of stainless steel, however, the results indicate that the presence of pyrolytic carbon would accelerate the corrosion rate through the pitting corrosion mechanism, and that the detrimental effect of carbon would grow worse as the carbon-to-metal area ratio increased. This result is drawn from inspection of igure 3 where it is noted that the curve intersections are very close to or in the transpassive region of 316L stainless steel. Furthermore, pitting corrosion was observed on the sample surfaces at noble potentials as low as +0.1 volt.

The post clinical implantation vitreous carbon stereomicroscopic evaluations, Group 11 of Table I, showed two devices with irregular features. One device had fractured in vivo and showed pitting

corrosion of the stainless steel core. The relative area ratio of carbon to metal was high in this situation. In our opinion, this example provides some support for previous predictions that certain types of carbon-to-metal alloy couples in biological environments can compromise biocompatibility criteria.

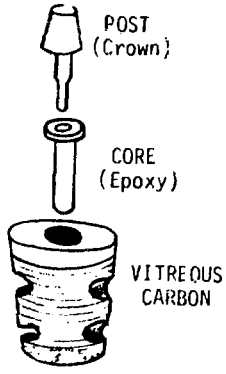


FIGURE 1. Schematic Drawing of Vitredent Tooth Root Replacement System.

GROUP	NUMBER OF SPECIMENS	IRREGULAR FEATURES	COMMENTS
1	85	5	Early design-no big grooves
2	71	7	Early design-no big grooves
3	48	10	Clinical design
4-7	85	18	Receiv. for clinic. place.
8-10	72	6	Receiv. for clinic. place.
11	9	2	Post clinical placement specimens(rec.from dentists)
1-3	47	8	3 view radiographic evalua.

TABLE I. Nondestructive Stereomicroscopic and Radiographic Examinations of Vitreous Carbon Tooth Root Replacement Systems.

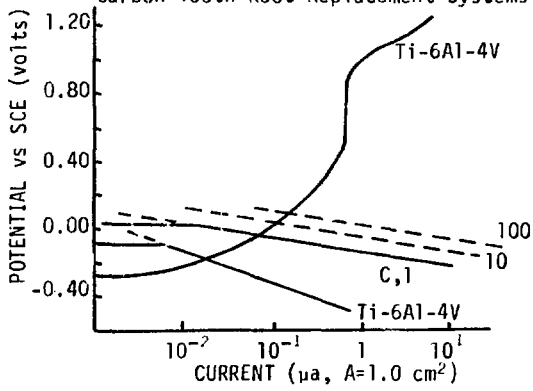


FIGURE 2. POLARIZATION RESULTS FOR Ti-6Al-4V and Pyrolytic Carbon.

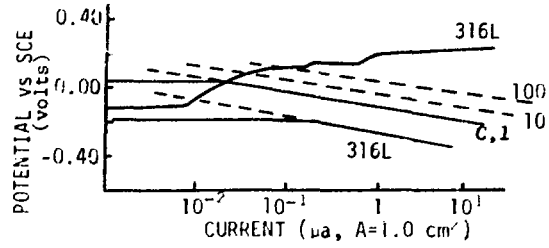


FIGURE 3. POLARIZATION RESULTS FOR Type 316L Stainless Steel and Pyrolytic Carbon.

References

(1) D.E. GRENOBLE and R. VOSS, Analysis of Five Years of Study of Vitreous Carbon Endosseous Implants in Humans, Oral Implantology, 6, 509-525 (1977).

(2) J.C. BOKROS, R.J. AKINS, H.S. SHIM, A.D. HAUBOLD and N.K. AGARWAL, Prostheses Made of Carbon, Chemtech., January, 40-49 (1977).

(3) J.E. LEMONS, Biomaterials Science Protocols for Clinical Investigations of Porous Alumina Ceramic and Vitreous Carbon Implants, J. Biomed. Mater. Res. Symp., 6, 9-16 (1975).

(4) N.G. THOMPSON, R.A. BUCHANAN, and J.E. LEMONS, In Vitro Corrosion of Carbon-Metal Galvanic Couples, Abst. No. 116, Society for Biomaterials Symp., 27 (1977).

* Samples furnished by Vitredent Corporation, Los Angeles, CA., USA.

**Pyrolytic carbon samples supplied by Medical Products Division, Gulf General Atomics, San Diego, CA., USA.

LTI CARBON SURFACES

A.D. Haubold,* J.D. Andrade,** H.S. Shim* and R. King**
*General Atomic Company
P.O. Box 81608
San Diego, Calif. 92138
**Dept. of Materials Science and Eng.
University of Utah
Salt Lake City, Utah 84112

Background

LTI carbon is one of the very few synthetic materials generally recognized as suitable for long term blood contact applications (1). Although a large number of hypotheses have been formulated with respect to the blood tolerability of materials, a general theory or mechanism is not yet available. It is known that in certain situations the local hemodynamics can play a predominant role (2) and in most cases the solid-blood interfacial properties can play a predominant role (2,3). It is assumed that understanding the plasma protein adsorption process onto solids used for blood-contact applications will lead a better understanding of solid-blood interactions (1-3).

A number of preliminary studies of plasma protein adsorption onto LTI carbon surfaces are available (4-7). Radioiodinated -(I^{125})-proteins have been utilized by Kim, et al. (4) to measure adsorption of individual proteins and protein mixtures on LTI carbon. His results indicate the carbon very rapidly adsorbs albumin. This is consistent with Kim's model of blood interactions via a platelet-adhesion mechanism (8). Microcalorimetric and electrophoretic mobility studies of proteins onto LTI carbon have been done by Nyilas, et al. (5). The extension of the adsorbed layers have been measured directly using ellipsometry by Fenstermaker et al. at NBS (6,7).

Characterization of surface properties of LTI carbons has been rather limited. Baier, utilizing contact angles and infrared spectroscopy (9, 10),and Schoen, utilizing scanning electron microscopy (11), have studied such surfaces before and after blood exposure. Epstein et al. have utilized electrochemical methods to study the LTI carbon-aqueous solution interface (12, 13).

Extensive measurements have been made on the bulk, composition and structure of LTI carbons and experiments with modified surfaces have been reported (15). Direct measurement of the composition of LTI carbon surfaces by modern surface analytical tools however are not available. Here we report Auger and X-ray photoelectron spectroscopy studies of such surfaces. It is expected that such data, coupled with electrochemical and protein adsorption data, may aid in understanding why LTI carbon is relatively blood compatible.

Materials and Methods

Unalloyed LTI carbon samples were prepared in the conventional manner (14). For the photoelectron studies, three lots of samples (A, B, C) from the same coating run were prepared. Specimens from a different coating run (Lot D) were used for Auger studies.

Lot A was placed in clean glass vials immediately after coating and examined without any subsequent handling or treatment. Lot B was ultrasonically cleaned in isopropyl alcohol, air dried, and stored in glass vials prior to study. Lots C and D were ground and polished in several steps and contacted metal oxides, silicon carbide, diamond, water, detergent, isopropyl alcohol, and ethyl alcohol. The final cleaning was done in ethyl alcohol. The samples of Lot C were packaged in a soft blue foam and are representative of the surface which is normally delivered to medical device manufacturers for further processing. Lots A and B have very rough porous surfaces. Lot C and D are highly polished yet still shows some porosity and microscratches at 100X magnification.

X-ray photoelectron spectorscopy was done on a Hewlett-Packard 595B ESCA utilizing monochromatic $A\ell K\alpha_{1,2}$ radiation. The samples were mounted in air, inserted into the spectrometer and analyzed in a 10^{-9} torr vacuum at ambient temperature utilizing 800 watts of x-ray power (at the x-ray anode, not at the sample). The instrument resolution was normally 0.8 eV measured as the full width at half maximum of the C-1s line from graphite. All spectra are charge referenced to the C-1s line at 284.0 eV. Wide scans (0 to 600 eV) were performed for surface elemental analyses as well as detailed 20 eV scans of the C-1s (275 to 295 eV) and O-1s (520 to 540 eV) regions. The spectra were not resolution "enhanced" or curve resolved.

Auger electron spectroscopy was done on a Physical Electronics Industries Auger microprobe Model 541. Surface analyses were carried out at 10^{-9} torr. Depth profiling was performed using the in-situ ion beam sputtering gun at 10^{-5} torr. Scan speeds used were on the order of 2-5 eV per second. The primary beam voltage was generally maintained at 3KV while the modulating voltage was 3V at low energies (<600 eV) and 6V for higher energies.

Please note that the ESCA and Auger studies were not obtained on identical lots. Auger studies were performed at the General Atomic Co. in Oct. 1976, the ESCA studies were done at the University of Utah in February, 1977.

Results and Conclusions

Lot A had a highly porous surface with carbon particulate matter on the surface. The surface composition as determined by ESCA is given in Table 1. Note the low oxygen content, which appears to be part of a carbon-oxygen bond. No other elements are evident on the surface.

Lot B had finer carbon particulates on the surface but otherwise is identical to A, including the ESCA results (Table 1).

The as received Lot C shows a much higher oxygen concentration and substantial quantities of silicon (Table I). Other elements present in the surface include traces of sulphur, phosphorous, chlorine and possibly aluminum.

Lot C prewashed in methanol shows no evidence of silicon. The carbon/oxygen ratio is ca. 10:1. Traces of chlorine were present on the surface. The fact that the silicon lines were readily removed by a brief ultrasonic methanol wash suggests a surface contaminant as the source of silicon, perhaps a silicone release agent. The only likely source of such a contaminant is the blue foam in which the samples were packaged. ESCA examination of the foam revealed relatively high concentrations of silicon on the surface as well as nitrogen and chlorine suggesting a polyurethane foam with a silicone anti-stick or release agent and traces of possible NaCl from handling. Thus we tentatively identify the silicon on the as received Lot C as silicone material transferred from the foam packing material. Studies of methanol-cleaned Lot C material (Silicon-free) contacted with the foam confirmed that the silicon (silicone) on the foam readily transfers to the carbon.

Auger analysis of Lot D confirm the ESCA results obtained on C. Oxygen was found on the surface at a level on the order of 10 atomic percent. A trace amount (< 1 percent) of sorbed nitrogen was also generally detected. Depth profiling showed that both the oxygen and nitrogen are found only on the surface. At a depth of approximately 30-50 Å into the carbon, the oxygen signal had dropped by a factor of 10; nitrogen was no longer detected. Since Lot D was not packaged for shipment, these specimens did not contact the polyurethane foam.

Table I

Surface Elemental Ratios for Various LTI Carbon Samples

C:O:N:Si Ratio (Normalized to 100 Carbon Atoms)

LTI Lot Code	Ratio
A	100:1.8:0:0
A	100:1.2:0:0
B	100:1.4:0:0
C	100:8.5:0:1.9
C	100:11.0:1.0:1.5
C"Methanol Cleaned"	100:8.2:0:0
Foam Packing Material	100:39.3:2.8:12.3
D	100:10: <1:0
D (50Å)	100:1:0:0

These initial results from direct measurements of the composition of LTI surfaces confirm previous conclusions (15). The history of a biomaterial surface is important. Variability in test surfaces can be unintentionally produced by very subtle means. The fact that the impurities found on the LTI carbon surfaces could be readily removed shows that the material is inert but leaves open the question in the case of less inert materials. Furthermore, the role of tightly bound surface impurities in activating the clotting mechanism should be investigated. Similar studies on alloyed LTI carbons will be performed in the future.

References

1. J.D. Bruck, et al., Biomat., Med. Dev. Art. Org., 1 (1973) 191.
2. E. Nyilas, et al., Trans. Amer. Soc. Artif. Int. Organs, 21 (1975) 55.
3. J.D. Andrade, Med. Inst. 7 (1973) 119.
4. S.W. Kim, Personal Communication.
5. T.H. Chin, et al., Trans. Amer. Soc. Artif. Int. Organs, 22 (1976) 498.
6. C.A. Fenstermaker, et al., Nat. Bur. Standards Internal Report NBSIR 74-470, 3/22/74.
7. R.R. Stromberg, et al., Nat. Bur. Standards Internal Report NBSIR 75-667, 1/15/75.
8. S.W. Kim, et al., Trans. Amer. Soc. Artif. Int. Organs, 20 (1974) 449.
9. R.E. Baier, et al., Trans. Amer. Soc. Artif. Int. Organs, 16 (1970) 50.
10. V.L. Gott, et al., U.S. Gov't. Report PB-213110, Sept., 1972, pp 93ff.
11. F.J. Schoen, in Proceedings of 4th Annual Scanning Electron Microscope Symposium, Part I, p. 385, IIT Research Institute, Chicago (1971).
12. B.D. Epstein and E. Dalle-Molle, Trans. Amer. Soc. Artif. Int. Organs, 17 (1971) 14.
13. B.D. Epstein, et al., Carbon 9 (1971) 609.
14. R.J. Akins and J.C. Bokros, Carbon 12 (1974) 439.
15. J.C. Bokros, et al., in Chemistry and Physics of Carbon, Vol. 9 (P.L. Walker, Jr. and P.A. Thrower, eds.), pp 103-171, Dekker, New York, 1972.

TISSUE RESPONSE TO CHARCOAL CLOTH IMPLANTED SUBCUTANEOUSLY IN THE RAT AND THE GUINEA PIG

By N.H. Greasey and F.A.P. Maggs
Chemical Defence Establishment, Porton Down, Salisbury, Wiltshire, UK

Introduction

The utilisation of the adsorptive properties of CDE charcoal cloth (1, 2) - a woven, flexible cloth composed entirely of charcoal - have already been examined in one medical application (3). Other potential uses in this sphere may involve the tissue compatibility of charcoal cloth, and this aspect is reported upon here.

Technique and Observations

Rats or guinea pigs were anaesthetised with ether, clipped over the flank and the implantation site washed with ethanol (70%). A 15 mm incision was made with a scalpel as far as the areola connective tissue beneath the panniculus carnosus. A small pocket was opened up between the skin and the body wall by means of a probe and the charcoal cloth, 10 x 5 mm, inserted with sterile forceps. The incision was closed with a dumb-bell adhesive plaster suture. The animals made an uneventful recovery and there were no rejections or infections.

Animals were sacrificed for gross and histological examination for tissue responses to the implants at 2, 6, 14 and 22 weeks.

The implantation site was visible from the lower side of the skin as a slight thickening of the connective tissue. No other gross abnormalities were observed.

The skin was fixed in Bouin's solution, washed, dehydrated, embedded in paraffin wax and 8 µm sections stained with haemotoxylin and eosin and with Masson's Trichrome stain.

The histological appearance of the skin plus the implanted cloth remained almost unchanged from 2 to 22 weeks and in both species amounted to only a very mild response: between and along the fibres of cloth there was a moderate accumulation of macrophages, giant cells, fibroblasts and new collagen fibres, the whole being inserted into and surrounded by the normal subcutaneous connective tissue. There were no lymphocytes, polymorphonuclear leucocytes or eosinophils, and there were no abnormalities in the adjacent muscle layers. These observations will be continued at intervals for a total of two years.

Conclusion

Implantation of CDE charcoal cloth subcutaneously in the rat or the guinea pig has caused no adverse tissue responses over a period of 5½ months.

References

(1) Adsorptive Properties of CDE Charcoal Cloth, Maggs F.A.P., Smith M.E., and Robins G.A. This Conference.

(2) Physical Properties of CDE Charcoal Cloth, Maggs F.A.P., Smith M.E., and Robins G.A. This Conference.

(3) 29th ACEMB; Boston, Mass.; Nov. 1976. Gaylor J.D.S., Maggs F.A.P., Park G.B., and Smith, E.M.

PRODUCTION OF CARBON FIBRES FROM CHAR TARS

I. PÖTTY

Bergbau-Forschung GmbH, Frillendorfer Str. 351,

D-4300 Essen-Fray

Introduction

During the pressure gasification of coals, char tars with high contents of solids are obtained in the temperature range of about 500 to 600° C which, after separation of the constituents insoluble in chinoline, are suitable as base products for the making of carbon fibres. In the following, these tars are called "HDV-tars".

In the same way, tars obtained during the charring of hard coals, e.g. according to the Lurgi-Ruhrgas process, in the temperature range from 500 to 600° C, so-called LR-tars, can be used. The cleaning of such tars is done, without adding any solvents, in a pressure filter at temperatures from 150 to 250° C and filtration pressures from 2 to 6 bar. As filter tissue, metal tissues with a mesh size of about 60 µm are used[1].

Due to the high solid contents in the tars, it is necessary to add 2 to 3 % filtering aids on the basis of diatomaceous earth in order to obtain a filter cake as permeable as possible even with larger cake thicknesses.

Despite of the low particle size (1 to 80 µm) of the solids to be separated, the solid contents could be reduced, by pressure filtration, from about 15 to 20 % in the base tar to < 0.1 % in the final product. In order to increase the softening point to about 130 to 150° C, the purified tars were either subsequently treated by distilling or blasted by air.

Similarly, the purification of the tars was tested in a centrifuge[2] after adding a suitable solvent. Due to the high solid contents in the tar, however, higher degrees of purity were obtained by the pressure filtration.

Spinning Process

In a plant where the fibres are spun above the smelting point, endless fibres with a diameter of 5 to 20 µm were produced at a spinning temperature of about 230° C. In order to avoid a sticking together of the individual fibres during the thermal secondary treatment, the fibres were dusted with an activated carbon impregnated by H_2SO_4. In order to shorten the oxidative secondary treatment with air, an additional short treatment of the fibres (from 1 to 5 minutes) in bromine proved well. The fibres were pushed in a spinning machine by piston pressure through a perforated plate with apertures of 0.3 mm Ø and stretched, via a smoothing mechanism, to the desired Ø between 5 and 20 µm. The fibres were then wound up crosswise on coils and could be wound off the coil continuously during the thermal secondary treatment[3].

Thermal Secondary Treatment

The secondary treatment was carried out in two stages, viz. by oxidation of the fibres in air up to about 400° C in a tubular oven and the subsequent carbonization of the primarily treated carbons under inert gas (N_2). As far as possible, the oxidation time during the various tests was fixed to 60 minutes and the subsequent carbonization to 55 minutes in order to obtain better comparison values with previously measured carbons made from high-temperature tar pitch. The shortest possible oxidation time was taken for samples which could not be oxidized within 60 minutes without sticking together. The activated carbon prepared with oxidizing agents prevents a sticking together of the individual fibres during oxidation. Beyond that, H_2SO_4 is purposively liberated during higher temperatures and accelerates the oxidation of the pitch fibres. With temperatures above 300° C, an increased outlet of low-molecular pitch constituents from the surface of the fibres can be observed, and these very sticky constituents are absorbed by the activated carbon. However, the activated carbon sticks only loosely to the surface of the fibres and does not enter into a connection with the pitch fibres. After the carbonization stage, the activated carbon can be recovered and can be used again after a corresponding impregnation with H_2SO_4.

Results

Very thin fibres with diameters up to 5 µm can be made from LR- and HDV-tar pitches by spinning above the smelting point. Similarly to fibres made from high-temperature tar pitch, the tensile strength increases with smaller diameters of the fibres.

The attainable tensile strengths are plotted in the Figs. 1 and 2 as a function of the diameter of the fibres. For the sake of comparison, the strength curves for high-temperature tar pitches are shown, too[4].

It can be seen from these curves that char pitches are suitable as a base product for making fibres of a high tensile strength. Char tar

pitches blasted by air have a higher tensile strength than pitches secondarily treated by destilling.

Mixtures of high-temperature tar pitch and char tar pitch are not suitable for making fibres of a high tensile strength.

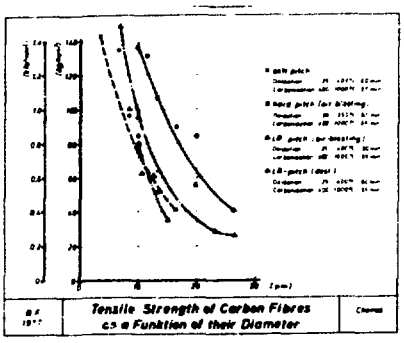


Fig. 1

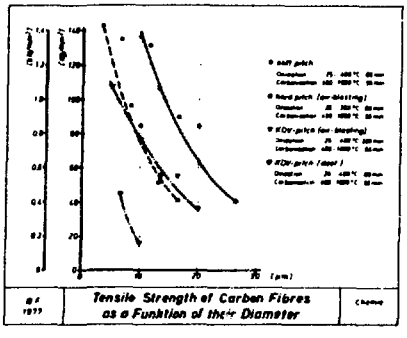


Fig. 2

Summary

With the gasification and charring of coal, char tars are obtained in the temperature range from about 500 to 600° C which, after the separation of constituents insoluble in chinoline and a further secondary treatment, are suitable for the production of carbon fibres by distilling or blasted with air. Char tar pitches with a softening point of about 130 to 150° C can be spun, above the smelting point, at a temperature of 230° C to raw fibres with a diameter of 5 to 20 µm and are then secondarily treated by oxidation in air up to 400° C and carbonization in a nitrogen atmosphere. The tensile strengths then reached depend on the primary treatment of the char tars: they are, for air-blasted char tars, in the range of the tensile strengths of fibres made, according to the same process, from high-temperature tar pitches.

References

1. Romey, I.
   Model tests for the purification of coal oils
   4. Gemeinschaftstagung der ÖGEW/DGMK,
   Salzburg, Austria,
   4 - 6 Oct. 1976

2. Romey, I.
   Carbon from Purified Coal Tar Pitch
   12th Biennial Carbon Conference,
   Pittsburgh, USA,
   28-7 to 1-8-1975

3. DBP 24 19 659
   US Patent 3.997.654

4. Romey, I.
   Production of Carbon Fibres from coal tar pitch
   International Carbon Conference "Carbon 1976",
   Baden-Baden, Germany,
   28-6 to 2-7-1976

HIGH STRENGTH CARBON FIBERS FROM MESOPHASE PITCH

J.B. Barr, S. Chwastiak, and R. Didchenko
Union Carbide Corporation, Carbon Products Division
Parma Technical Center, Parma, Ohio 44130

Introduction

It has been demonstrated in the past that carbon fibers from mesophase pitch are capable of reaching a tensile strength of 3.5-4.0 GPa[1,2]. So far, such high strengths have been obtained only in selected, thin monofilaments spun from a mesophase pitch that was prepared from a carefully processed commercial precursor material. The purpose of the present study was to confirm the initial results and to analyze the data statistically as a means of estimating the intrinsic strength of these carbon fibers.

Experimental

Additional monofilaments have been spun from a mesophase pitch prepared from a processed precursor. After thermosetting and carbonizing, the filaments had round cross-sections with diameters between 7.3 and 8.5 μm. Most filament in one sample were free of voids that could be seen at 1000X magnification, but the filaments in another sample had a large number of voids. These two samples were compared to determine the effect of voids on tensile strength.

Filaments were mounted on perforated cardboard tabs and broken in tension routinely at gauge lengths of 1.4 to 40 mm on an Instron testing machine. A perfect vertical alignment of very short filaments was difficult to achieve, particularly at the gauge length of 1.4 mm.

Results and Discussion

The average tensile strength and Young's modulus, along with the frequency of break histogram, at each gauge length, are shown in Figures 1 and 2 for weak and strong filaments, respectively. Clearly, most weak filaments broke under a stress of 1.0-2.0 GPa. This level of strength, attributed to the presence of holes, occurs in the strong filaments with a relatively low frequency which decreases with decreasing gauge length and practically disappears at and below 3.2 mm.

The probability of failure and the fiber strength can be correlated analytically by means of the Weibull function[3]. Figure 3 shows the tensile strength of the strong filaments at 3.2 mm length plotted on the Weibull probability chart. The Weibull plot allows one to identify and eliminate "stray" values that do not fall on the straight line whose slope is the flaw dispersion parameter m, a characterisitc constant for the material. Table I shows the values of m at various gauge lengths calculated from the two-parameter form of the Weibull equation. Calculations of the mean strength $\bar{\sigma}$ from the Weibull data was performed in the manner described by Street and Ferte[4].

Table I

Weibull Dispersion Parameter m at Different Gauge Lengths

Gauge length (mm)	Weibull Slope m	
	Strong filaments	Weak filaments
1.4	8.2	3.1
3.2	5.2	3.2
10	4.1 Avg.=5.0	3.7 Avg.=3.7
20	5.6	4.2
40	2.8	2.4

The relationship between $\bar{\sigma}$ and the gauge length, L, for a particular m can be represented as $\ln \bar{\sigma} = -(1/m) \ln L + \text{constant}$. Figure 4 shows the double logarithm plots of $\bar{\sigma}$ vs. L for weak and strong filaments. The average tensile strength derived from simple sample statistics (see histograms) are also included in the plot. With one exception, the results are almost identical. The solid lines were drawn through the points, using -1/m as the slope where m is the average value shown in Table I. The points at L = 1.4 mm are excluded because of the poor reliability of measurements at low gauge lengths[4,5]. The values of m at L = 40 mm are excluded because the Weibull distribution plots indicated failure due to a secondary flaw population, probably caused by surface damage.

A tensile strength of 7 GPa is obtained for the strong filaments by extrapolation to a length just below 0.1 mm. Thorne estimates from the loop test at an effective length of 0.1 mm that the strength is greater than 6 GPa for PAN-based carbon fibers[6]. Others have made estimates of strength for PAN-based carbon fibers at even smaller lengths. Diefendorf and Tokarsky report a strength of 8 GPa at 0.02 mm length[7]. Watt cites a strength value of 7 GPa by extrapolation to near zero length[8]. Obviously, carbon fibers made from mesophase pitch are capable of reaching at least equivalent levels of strength.

In terms of the potential performance of fibers in composites, it is more practical to consider only fiber lengths larger than the load transfer length as defined by Kelly[9]. This length is estimated to be about 0.2 mm for the fibers in this study. Morita et al. reported good agreement between strand results and single filament data extrapolated to a length of 0.6 mm, using Weibull statistical analysis[10]. At this gauge length, our strong fibers have a tensile strength of 4.7 GPa, while the fibers with voids are 30% weaker.

Acknowledgments: This work was supported in part by the Air Force Materials Laboratory, Wright-Patterson Air Force Base, Ohio. The authors are grateful to J. D. Grigsby for fiber test measurements and to M. B. Carter for assistance with the Weibull calculations.

1. R. Didchenko, J. B. Barr, S. Chwastiak, I.C. Lewis, R. T. Lewis, and L. S. Singer, Extended Abstracts, Am. Carbon Soc. 12th Biennial Conf. on Carbon, University of Pittsburgh, PA, July 28 to Aug. 1, 1975, pp. 329-332.
2. J.B. Barr, S. Chwastiak, R. Didchenko, I.C. Lewis, R. T. Lewis, and L. S. Singer, Appl. Poly. Sym., 29, 161 (1976).
3. E.V. Robinson, Calif. Inst. Tech., Jet Propulsion Lab., Tech. Memorandum, JPL-TM-33-580, Dec. 15, 1972 (N73-17650).
4. K.N. Street and J.P. Ferte in E. Scala Ed., Proceedings of the 1975 Int. Conf. on Composite Materials, Metallurgical Soc. AIME, N.Y., N.Y., 1976.
5. S. L. Phoenix and R.G. Sexsmith, J. Comp. Mat., 6, 322 (1972).
6. D.J. Thorne, Nature, 248, 754 (1974).
7. R.J. Diefendorf and E. Tokarsky, Poly. Eng. and Sci., 15, 150 (1975).
8. W. Watt, Carbon, 10, 121 (1972).
9. A. Kelley, Strong Solids, 2nd Edition, Clarendon Press, Oxford, 1973.
10. K. Morita, H. Meyachi, K. Kobori, and I.Matsubara, Extended Abstracts, "Carbon '76" Conference, Deutsche Keramische Gesellschaft, Baden-Baden, Germany, June 27 to July 2, 1976, p. 479.

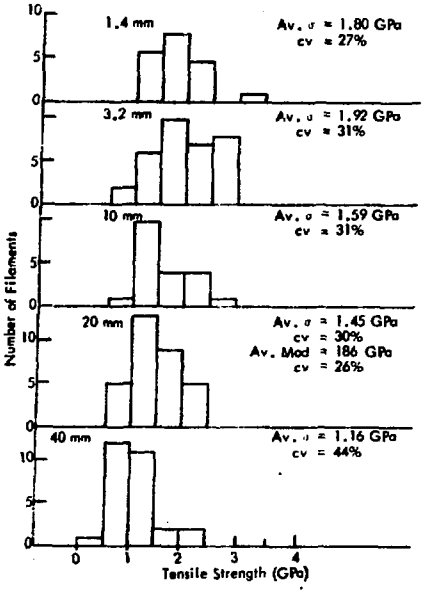


Figure 1. Tensile Strength Distribution for Various Gauge Lengths of Weak Filaments.

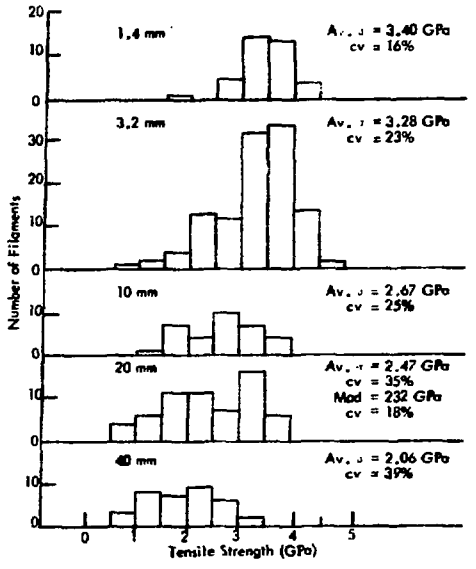


Figure 2. Tensile Strength Distribution for Various Gauge Lengths of Strong Filaments.

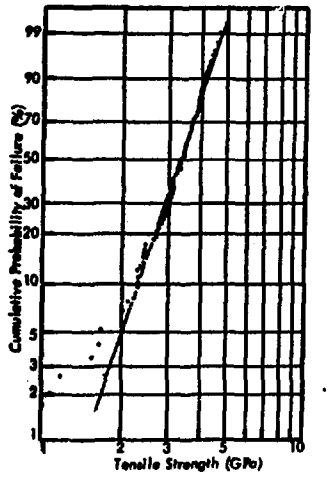


Figure 3. Weibull Strength Distribution of Strong Filaments at 3.2 mm Gauge Length.

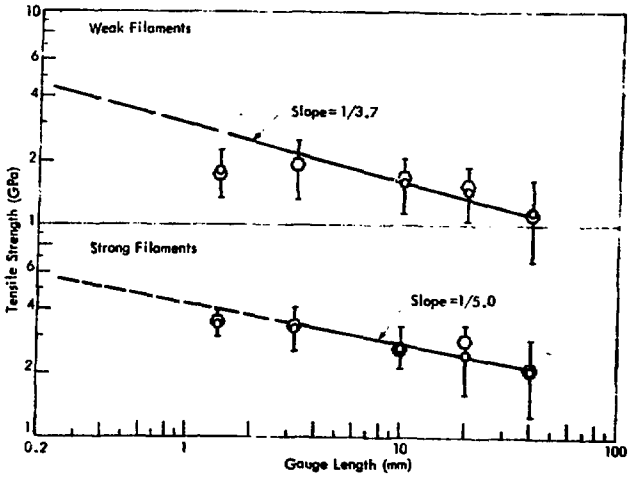


Figure 4. Tensile Strength as a Function of Gauge Length ○Av. Strength ○Calc. Strength $\bar{\sigma}$.

STRUCTURE AND PROPERTIES OF FIBERS DERIVED FROM PITCH

by A. Johnson and W. Bradshaw
Lockheed Missiles & Space Co., Inc.
P. O. Box 504, Sunnyvale, Calif.

Introduction

The primary objective of this study was to evaluate various available pitch-base fibers as a practical replacement for carbon fibers derived from continuous filament rayon precursors for use in advanced carbon composites, such as carbon phenolic for heat-shield application and 3-D carbon-carbon composites for nosetip application. On the basis of cost and projected utilization, such fibers will replace the present generation of fibers produced from rayon. The purpose of this study was to evaluate the characteristics of the various grades of pitch fiber available and to fabricate composite hardware for comparison of properties with reference fibers scheduled to be phased out because of pending unavailability.

Fiber and Composite Evaluation

The fibers were evaluated for density by a density gradient technique, for moisture pickup at 100% relative humidity as an indication of pore accessibility, for microstructure by optical and scanning electron microscopy, and for crystallite size and d-spacing by x-ray diffraction. Measured composite tensile properties consisted of tensile strength, modulus, and elongation.

Results of Fiber Evaluation

At the present time there is considerable variation in fiber morphology and physical properties. Filaments may vary in shape, size, density, and hygroscopicity depending upon heat-treatment condition and lot. Split or crescent-shaped fibers appear randomly throughout the various types of pitch fiber studied. This effect is reportedly related to the spinning operation and is independent of heat-treatment condition. The internal texture of the fibers as inferred from phase contrast microscopy and scanning electron microscopy of tensile fracture surfaces is radial; i.e., the basal planes radiate from the fiber center.

Two types of pitch fiber were studied: (a) high-fired pitch fibers for nosetip applications, and (b) low-fired pitch fibers for heat-shield application. The high-fired pitch fibers exhibited high densities of 2.002 to 2.024 g/cc. The moisture adsorption was low, from 0.27 to 2.27%, indicating a low intrinsic pore structure. The crystallite size, L_c, ranged from 112.0 to 144.0 Å with a d-spacing of 3.43 to 3.44 Å.

The low-fired pitch fibers were heat-treated to varying temperatures, cycles A, B and C. With increasing temperature, the density increased from 1.614 to 1.773 g/cc, the moisture pickup decreased from 7.44 to 0.92%, the fiber diameter decreased from 13.22 to 11.22 microns, the crystallite size increased from 14.59 to 17.44 Å, while the interlayer distance remained invariant at 3.53 Å. Clearly, with increasing temperature, the fiber is shrinking and pore closure takes place.

Nosetip Composites

Four 3-D preforms (2 in. × 2 in. × 5 in.) using Union Carbide VS-0022 high-fired pitch were woven by Fiber Materials Incorporated (FMI). Two preforms were densified at FMI using the high pressure (10,000 psi) process, and two were densified at Union Carbide (UCC) using both low pressure, 500 psi autoclave, and medium pressure, 5000 psi. Preliminary data as summarized in Table 1 indicate that the composite densities are greater with pitch fiber and that the strengths approach the standard T-50 value. Lower pressures can be used to achieve values comparable to those obtained with high-pressure impregnation.

Table 1

NOSETIP COMPOSITE PROPERTIES

Type	Specific Gravity (g/cc)	Ultimate Tensile Strength (psi)	Modulus (psi × 10^6)
T-50 (Standard)	1.91	31,000 ±1,800	19
Pitch UCC (Low Pressure	1.95	25,000	28
Pitch UCC (Med Pressure) 5000 psi	2.04	23,500	23
Pitch FMI (High Pressure) 10,000 psi	1.95	27,600	23

Heat-Shield Composites

One each (1), 12 in. × 12 in. × 0.3 in. flat panels were fabricated by Hitco for the following systems: (a) UCC pitch fiber A/SC-1008, (b) UCC pitch fiber B/SC-1008, (c) UCC pitch fiber C/SC-1008, and (d) Hitco staple rayon /91-LD. Systems (a) through (c) were prepregged by Fiberite, and system (d) was prepregged by U.S. Polymeric. Table 2 shows preliminary tag end data in comparison with standard rayon material. These data indicate that the A system looks very promising; the density approaches that of the rayon base material, the ultimate tensile strength is higher, and the elongation is greater.

Conclusions

The highlights of these data are: (a) high-fired pitch fibers have been used to produce 3-D composites with properties comparable to those obtained with T-50; (b) densities of 3-D composite structures using pitch fibers have increased without using high-pressure impregnation; and (c) low-fired pitch-base fibers have been used in carbon phenolic to achieve properties that compare favorably with the reference rayon base material.

Table 2

HEAT-SHIELD COMPOSITE PROPERTIES

Type	Specific Gravity (g/cc)	Ultimate Tensile Strength (psi)	Elongation (%)
(Standard) CCA-3-1641 Rayon	1.43	7,500	0.35
Staple Rayon	1.405	9,600	0.71
Pitch A/SC-1008	1.465	10,946	0.59
Pitch B/SC-1008	1.519	9,993	0.63
Pitch C/SC-1008	1.521	6,861	0.47

ELECTRONIC AND STRUCTURAL CHARACTERISTICS OF CARBON FIBERS FROM MESOPHASE PITCH*

A. A. Bright and L. S. Singer
Union Carbide Corporation, Carbon Products Division
Parma Technical Center, Parma, Ohio 44130

Electronic properties have long been used as a means for studying the structure of carbons. A recent series of studies of PAN-based carbon fibers[1] showed that all of the electronic and structural properties could be correlated with processing conditions. A single parameter, such as the resistivity ratio, was found to be a good indicator of the structural evolution of the fibers with processing. The present work is an attempt to apply the same principles to the study of mesophase pitch-based carbon and graphite fibers. The purpose is two-fold: first, to provide a better understanding of the structure of these fibers and its relation to the fiber properties; and second, to clarify the differences in structure and properties between pitch-based and PAN-based carbon fibers.

Several series of fibers were studied, each processed at various temperatures up to 3000°C. Fibers having both radial and random microstructures were included. Resistivity and magnetoresistance measurements were made on single filaments by four-contact ac and dc methods at temperatures between room temperature and 4.2K. Standard ESR techniques were used to measure the g-anisotropy, linewidth, and effective spin concentration of strands of fibers.

The resistivity ratio is defined as $\rho(300°K)/\rho(4.2°K)$. For fibers heat treated to 1000°C, this parameter has a value of about 0.4, increasing to 0.93 for HTT = 1700°C. Above 1700°C, the resistivity ratio decreases again, reaching values around 0.4 for HTT = 3000°C. Radial structure fibers have lower resistivity ratios (above 1700°C) than random structure fibers processed at the same temperature.

Figure 1 shows the transverse magnetoresistance at 4.2K for selected fibers. At low HTT's, the magnetoresistance (MR) is very small, becoming larger and negative as HTT increases to around 2000°C to 2500°C. At higher HTT's, the MR becomes positive at high fields, but remains negative at low fields until the highest HTT's. Radial fibers show a stronger tendency toward positive MR than equally processed random structure fibers. The results of Ingram and coworkers[1] on PAN fibers show a negative MR (at 77K) even for samples heat treated up to 3000°C.

The above results are illustrated more dramatically in Figure 2, where the transverse MR at 14kG is plotted against resistivity ratio. All samples fall precisely on the same curve. Two distinct regions are evident, corresponding approximately to HTT's below and above 2500°C. The low-temperature region is characterized by negative MR and larger resistivity ratios. The high-temperature region, in which the MR is positive, corresponds to the onset of three-dimensional ordering as evidenced by the appearance of three-dimensional X-ray diffraction lines. The results of Ingram and coworkers[1] for PAN fibers cannot be compared directly since they were measured at a different temperature, but they fall roughly in the low-HTT region for all samples.

Figure 3 shows the crystallite size in the c-axis direction, L_c, plotted against resistivity ratio. Again, all samples fall on a single curve. The results for PAN fibers[1] fall on a separate curve. Presumably, this is due to the fact that the resistivity ratio is more closely related to L_a than to L_c and reflects the difference between PAN and pitch in their crystallization behavior.

Crystallite size (L_c) and interlayer d-spacing results show similar correlation with electronic properties and offer further confirmation that radial structure fibers are capable of a higher degree of graphitic order than random structure fibers.

From ESR, the "effective spin concentration," calculated assuming no skin effect and Curie's law, was similar to that obtained by Robson et al.[1] for heat treated PAN fibers viz., a decrease from ~15 to ~10 x 10^{18}/g over an HTT range from 1800°C to 3000°C.

The linewidth is sensitive to impurities and narrows by as much as a factor of five when the sample is purified with chlorine. The effect is reversible when one diffuses impurities back into these same samples. The purification process has no effect on any of the other electrical or ESR properties, indicating the phenomenon is purely one of relaxation. The broad linewidths observed by Robson et al.[1] are most likely due to impurities.

In Figure 4, the fiber g-anisotropy is plotted against HTT. The dashed line indicates that the anisotropy was so large that the spread in g-values broadened the signal in the perpendicular orientation beyond detection. The g-anisotropy of the PAN derived fibers[1] saturates at high HTT's at a value equal to that of pitch-based fibers heat treated in the 2000°C to 2300°C range. This finding is consistent with the fact that mesophase pitch-based fibers are graphitizable whereas PAN-based fibers are not.

This study has shown that reproducible correlations exist between various electrical, mechanical, and structural properties of mesophase pitch-based carbon fibers. Radial fibers are more graphitic than random fibers at a given HTT above 1700°C and reach a higher ultimate degree of graphitization at the highest HTT. These observations strongly imply that the graphitization process is inhibited from proceeding beyond a certain stage in the random fibers. The most likely explanation for this is that the random structure is more highly defected and grain growth is inhibited at an earlier stage than in the radial structure.

The exploratory ESR experiments described here

*Work supported in part by AFML, Wright Patterson Air Force Base, Ohio, Contract No. F33615-75-C-5109.

demonstrate that effects of preferred orientation, degree of graphitic character, nature of the unpaired spins, and impurity and other defects are all apparent and seem to have interpretable effects on the observed ESR spectra.

Finally, the electrical measurements suggest that mesophase pitch fibers are very similar to pyrolytic carbons treated in the same temperature range. This is consistent with the high degree of graphitization attainable by these fibers. On the other hand, PAN-based fibers have been found[1] to exhibit a much lower ultimate degree of crystalline order, comparable to pitch fibers treated in the 1700°C to 2300°C range.

Reference

1. D. Robson, F.Y.I. Assabghy, and DJE Ingram, J. Phys. D: Appl. Phys. 4, 1426 (1971); 5, 169 (1972); 6, 1822 (1973).

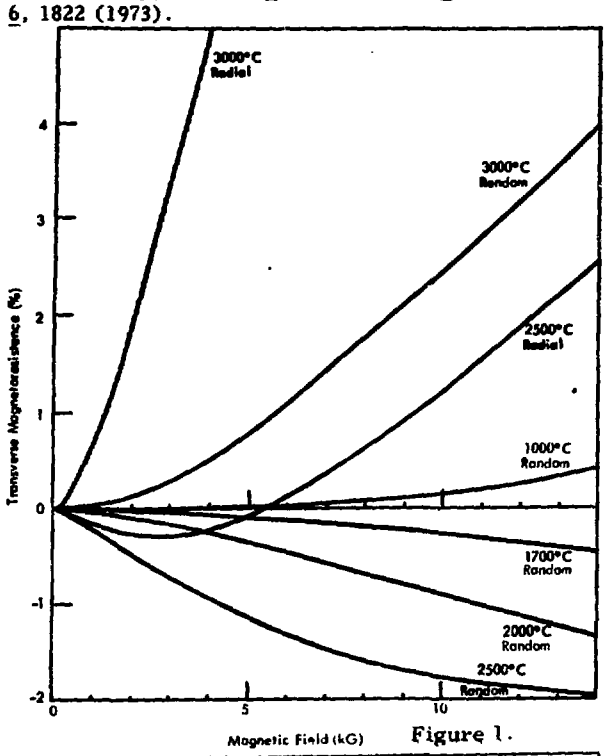


Figure 1.

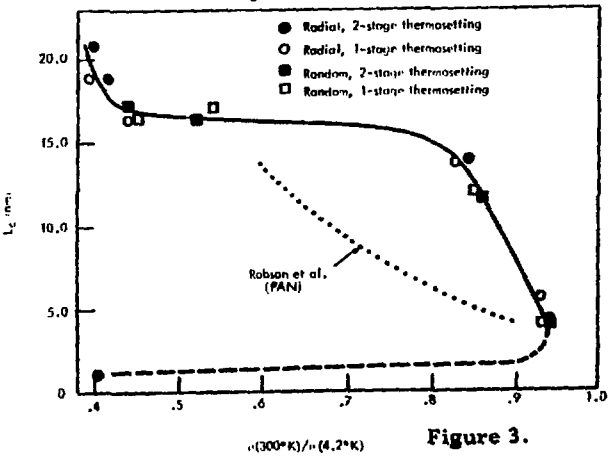


Figure 3.

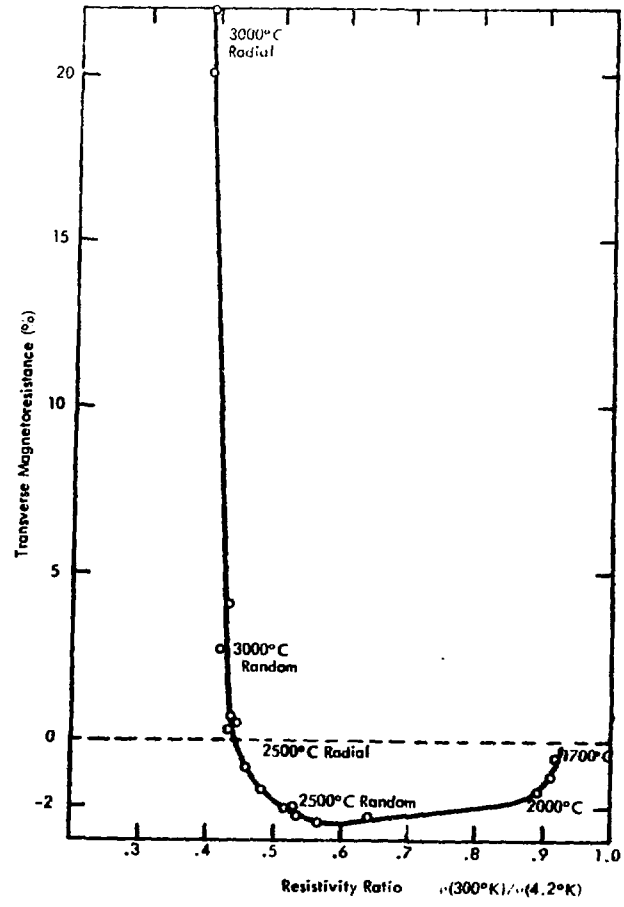


Figure 2.

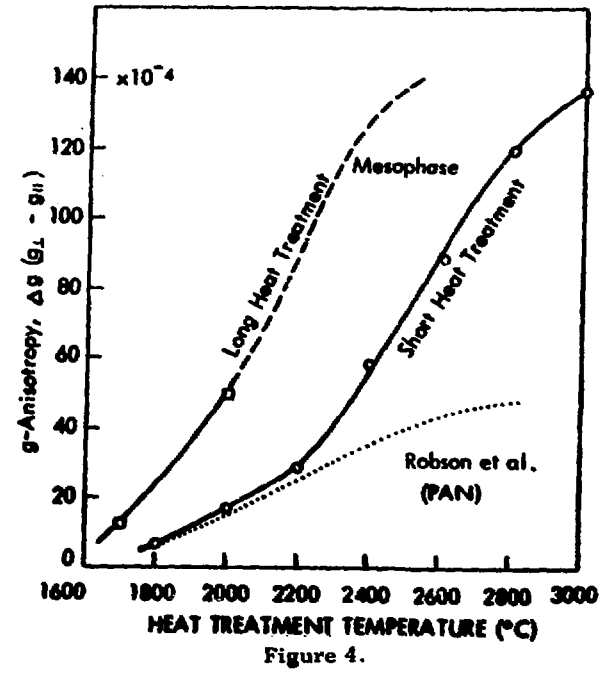


Figure 4.

NEUTRON DIFFRACTION STUDIES ON SOME CARBON FIBRE REINFORCED CARBON COMPOSITES AND THEIR PRECURSOR MATERIALS

L F PAIN, P B ROSCOE
Atomic Weapons Research Establishment, M.O.D.(P.E.),
Aldermaston, Reading RG7 4PR England

1. Introduction

The properties and processing steps in making uni-directional carbon fibre re-inforced composites (CFRC) have been described previously (1,2,3).

This paper reports on some preliminary studies made to assess the uses of neutron diffraction in characterising the production method and quantifying some of the changes taking place.

Although carbon fibres on their own have been extensively studied using electron microscopy and X-ray diffraction and some agreement reached on the crystal structure (4), little structure work has been done on the CFRC system. One of the problems in doing this work by diffraction is that both the fibre and matrix material are carbon and have similar diffraction patterns. Thus the addition of a matrix material during the processing stage mainly alters the absolute intensity of the diffraction peaks and only produces very subtle changes in the profile. In order therefore, to measure quantitatively the changes taking place during processing, it is necessary to know accurately the mass and volume of the samples in the beam. The diffraction scans, normalised to volume or mass, can then be subtracted to quantify the differences.

Neutron diffraction has some advantages over X-rays in this respect. Apart from having an isotropic form factor there are no polarization or Compton scattering effects. Thus there are fewer corrections to make to the data. However one of the most important advantages for this work is the very low absorption of neutrons. The neutron linear absorption co-efficient (μ) for carbon is 0.0005 compared with 1.3 for X-rays. This makes it possible to measure the bulk properties of large samples for which it is easy to measure accurately the mass and volume.

2. Experimental

The neutron diffraction work was done on the HERALD 5 MW reactor at AWRE using monochromatic 0.11 nm (1.1 Å) neutrons.

CFRC materials using both High Strength (HT) (Surface treated - S) and HT (untreated - U) fibres were investigated (i) at the cured resin (green) stage, (ii) after carbonising in an inert gas and (iii) after the chemical vapour densification (CVD) process. In addition studies were made on matrix materials on their own.

Large samples 8x8x40 mm were used so that the weight and volume in the neutron beam could be accurately measured.

As the carbon in the samples is oriented at least two measurements were required on each sample, one looking for carbon with its layer planes parallel to the fibre axis and one looking for the layer planes lying perpendicular to the axis.

3. Results and discussion

The diffraction patterns produced by the step scan diffractometer were typical for those of a turbostratic poorly graphitised carbon. From these diffraction scans, done at different production stages, we calculated or made deductions on:-

(1) The build up of carbon (i) with layer planes parallel to the fibre axis and (ii) perpendicular to the fibre axis. These results were calculated from the integrated intensity of the diffraction peaks.

(2) Spacing of the (001) and (hk) planes.

(3) Mean crystallite size and elastic strain

(4) Distribution of (002) plane spacing (interlayer distances)

(5) Concentrations of small defects, from diffuse background measurements.

The results obtained do of course represent the mean value for the whole sample.

3.1 HTU system

Table 1 shows the way the carbon built up during processing. It should be noticed that the CVD process also produced carbon with its layer planes oriented perpendicular to the fibre axis.

Further investigation of the CVD process showed that a low temperature xylene source gas did not lay down carbon oriented perpendicular to the fibre carbon layers, but a higher temperature CVD process did.

Although the spacings of the layer planes calculated from the peaks showed little difference during processing, there were changes in peak profile. All the (001) peaks were asymmetric in shape and showed that the interlayer spacing varied significantly about the turbostratic value, probably with a continuous variation.

From this initial study only a simple analysis of the mean crystallite size and elastic strain was undertaken and the results are of most use in comparing changes taking place.

Using Fourdeux's concept of crystallite size (4) the mean height of the stacked layer planes (Lc) was about 2.7 nm and varied little during processing.

The strain in this direction for the HTU fibre was 1.45% rising in the green stage to 2.2%. After the carbonising and CVD process it fell to 1.56%.

The flat length of the layer plane La was about 8.6 nm and the strain in this direction 0.9%. Neither of these parameters showed much variation during processing.

These results indicate that the curing of the resin causes a considerable increase in elastic strain perpendicular to the axis of the fibre. This strain is reduced by the carbonising and CVD process, although it never falls to the original HT fibre value.

The results for the HTU glassy matrix material showed that the carbon laid down by this process had a much lower mean crystallite size than that for the CVD densifying process.

Small defects in materials are frequently one of the major factors affecting their strength. The diffuse background, that is the slowly varying background between Bragg peaks, can give information on these defects.

For the HTU green material the background was relatively high, partly due to the incoherent scattering fron the hydrogen in the resin and partly from the amorphous nature of the resin. After carbonising the background fell considerable. As C^{12} is a coherent scatterer for neutrons, the background is now mainly due to defects in the system.

After the CVD densifying process the background had halved showing that a large number of defects had been removed by this process.

Further measurements on the effect of changes of temperature of the CVD process indicated a critical temperature about 1150°C, above which the diffuse background fell even more. As this seemed to be accompanied by a fall in strength it showed that a certain number of defects may have a beneficial effect.

3.2 HTS system

It has been shown that HTU fibre gives an improved impact performance over HTS fibre in CFRC materials. However as HTU fibre become surface treated inadvertently some studies were done on CFRC materials made with HTS fibre.

The main difference noted in the HTS system was a much higher elastic strain and a lower mean crystallite size then for the HTU system. These effects are presumably due to the matrix not being able to shrink away from the fibre during carbonisation. As a result the carbon layers are much more wrinkled and strained. It is easy to detect the presence of these surface treated fibres in the carbonised materials using neutron diffraction.

4. Conclusion

The results from this study have shown that neutron diffraction can be used for the quantitative characterisation of the CFRC manufacturing process in terms of, changes in the amount of layered carbon, mean crystallite size and elastic strain. Also because of the low absorption of neutrons the measurements can be done non-destructively on actual components.

Diffuse background measurements can provide information on the very small defects in the structure, which can affect the strength. This work would be easier to do using cold neutrons of greater than 0.8 nm (8 Å) wavelengths to eliminate Bragg reflections.

Material	002 plane direction to fibre axis	
	Parallel	Perpendicular
HTU Green	-26.0 (-20.8)	None
HTU Carbonised	0 0	None
HTU CVD	13.9 (23.4)	4.6 (5.0)
HTU Glassy-matrix	21.7 (25.4)	None
HTS Carbonised	-11.6 (5.8)	None
HTU Fibre	- -	None

Table 1: Percentage changes in integrated peak intensity during manufacture. Normalised to volume. Note: Figures in brackets allow for changes in processing volumes.

References

1. Newling D O, and Walker E J, Proc 1st International Carbon Fibres Conf, London 1971, (Paper 37).
2. Boyne L, Cook D, Hill J, and Turner K, SCI 4th London International Carbon and Graphite Conf, 1974 (Paper 128).
3. Hill J, Thomas C R and Walker E J, Proc 2nd International Conf on Carbon Fibres (Paper 19) London 1974.
4. Fourdeux A, Perret R and Ruland W, Proc 1st International Carbon Fibres Conf, London 1971 (Paper 9).

THE THEORY OF IRRADIATION DAMAGE IN GRAPHITE

B T Kelly
UKAEA Reactor Fuel Element Laboratories, Springfields, Salwick, Preston, Lancashire, UK

Introduction

The low atomic weight of carbon and the open crystal structure of graphite simplifies the irradiation damage process in that atomic displacements may be considered to take place at random at a rate G atoms/atom/sec in a neutron flux ϕ. A number of models of the damage process have been based on this feature, but none have attempted to account for detailed crystal dimensional change data at high doses.

In this paper, a full diffusion theory of the growth of interstitial clusters in graphite is developed based on an earlier model due to Kelly et al.[1]

Theory

It is assumed that N_ℓ interstitial dislocation loops are nucleated at a very small dose ($\sim 10^{19}$ n/cm^2(EDN)) which then proceed to grow by two dimensional diffusion of newly created interstitials through a field of single vacancies, concentration C_v. Vacancies disappear by the formation and growth of collapsed vacancy lines, density N_L cm^{-3}. It is postulated that the density of these lines cannot increase beyond a definite value N_m in the crystal lattice which is independent of irradiation temperature and determined by overlap of anharmonic forces. Vacancies are also allowed to diffuse in the basal planes and disappear at collapsed lines or crystallite boundaries defining a crystallite size L_a. These assumptions lead to the following equations for the interstitial concentration C_i and the single vacancy concentration C_v.

$$C_i \quad (G/\phi)^2 \frac{\Delta^2}{4} \frac{N_\ell}{R} \left[\int_0^\gamma C_v^{-\frac{1}{2}} . d\gamma\right]^2 \qquad \ldots(1)$$

where R is the interstitial-vacancy recombination probability/collision, Δ is a constant and γ is the fast neutron dose.

$$\frac{dC_v}{d\gamma} \quad \frac{G}{\phi}\left\{\frac{G}{\phi}\frac{\Delta^2}{2R}\frac{N_\ell}{C_v^{\frac{1}{2}}}\left[\int_0^\gamma C_v^{-\frac{1}{2}} . d\gamma\right] - \varkappa C_v - \frac{2\varkappa N_m}{N_o}\right.$$

$$\left[1-\exp\left(-\frac{G}{\phi}\frac{N_o}{N_m}\varkappa\int_0^\gamma C_v . d\gamma\right)\right]\Bigg\} - \left\{\frac{8 D_{ov} \exp(-E_{mv}/kT)}{\phi}\right.$$

$$\left[\frac{Z_v N_m}{a^2 N_o}\left(1-\exp\left(-\frac{G}{\phi}\frac{N_o}{N_m}\varkappa\int_0^\gamma C_v . d\gamma\right)\right) + \frac{1}{L_a}\left(\frac{2Z_v}{\Pi a^2}N_m\right)^{\frac{1}{2}}\right.$$

$$\left.\left(1-\exp\left(-\frac{G}{\phi}\frac{N_o}{N_m}\varkappa\int_0^\gamma C_v . d\gamma\right)\right)^{\frac{1}{2}}\right]\Bigg\} C_v \qquad \ldots(2)$$

where N_o is the number of atoms/cm^3, $\varkappa \simeq 3$, a is the defect jump distance, L_a the crystallite size, D_{ov} the vacancy diffusion constant and E_{mv} the vacancy activation energy.

The crystal dimensional changes due to defects are calculated from

$$e_{zz} = C_i$$

$$e_{zz} = -\frac{G}{\phi}\frac{\varkappa}{N_o}\int_0^\gamma N_L . d\gamma - \frac{1}{2}\int_0^\gamma\left[\left(\frac{dC_v}{d\gamma}\right)_{line} + \left(\frac{dC_v}{d\gamma}\right)_{boundaries}\right] . d\gamma \qquad \ldots(3)$$

where N_L is the number of vacancy lines/cm^3.

$(dC_v/d\gamma)_{line}$ is the rate of vacancy loss at lines due to diffusion.

$(dC_v/d\gamma)_{boundaries}$ is the rate of vacancy loss at boundaries due to diffusion.

Comparison of Theory and Experiment

A detailed comparison of theory and experiment is made over the range 300°C to 1200°C using data obtained in irradiations in DFR and the DIDO-PLUTO Materials Testing Reactors. The theory, using appropriate values of the parameters gives good agreement with the crystal dimensional change up to doses $\sim 10^{22}$ n/cm (EDN) and also gives concentrations of uncollapsed vacancies quite close to experimental measurement. At higher doses it is found that there are far too many uncollapsed vacancies and it is clear that recombination with interstitials with a low probability is necessary to improve agreement at very high doses.

The theory has also been compared with crystal dimensional changes in boron doped (B^{11} to avoid additional displacement damage) polycrystalline and pyrolytic samples irradiated at 450°C and 600°C in DIDO/PLUTO. The general behaviour is predicted quite accurately using loop densities taken from electron microscope studies.

References

(1) Kelly B T, Martin W H, Prince A and Bland J T. Phil. Mag. Vol 14, No. 128, p.343. (1966).

THE APPLICATION OF CHEMICAL RATE THEORY TO FAST NEUTRON IRRADIATION DAMAGE IN GRAPHITE
II. The effect of thermal annealing and thermal equilibrium defect concentrations

B T Kelly
(UKAEA Reactor Fuel Element Laboratories, Springfields, Salwick, Nr Preston, Lancashire, England)

1. Introduction

A simple chemical rate theory of fast neutron irradiation damage in graphite has been presented[1] and shown to give reasonable accord with experiment.[2] It was noted in the presentation of the theory that it possessed a number of deficiencies including

(1) The neglect of the effect of vacancy mobility parallel to the hexagonal axis.
(2) The neglect of thermal annealing of non-saturable sinks and point defects by the equilibrium defect concenctration.

The purpose of this paper is to consider the modifications necessary in the theory to accommodate these processes.

2. Theory

The simple chemical rate theory of irradiation damage in graphite assumes that it is sufficiently accurate to distribute the sources and sinks for the point defects homogeneously throughout the solid. The particular sinks for point defects (other than the mutual annihilation of interstitial atoms and vacancies) which are assumed to be present in the solid at constant concentration are:

(a) For interstitial atoms, the interstitial loop with density N_ℓ cm^{-3}.
(b) For vacancies, the vacancy line, density N_L cm^{-3}, and the crystal boundaries defining the crystallite size L_a parallel to the basal plane.

The uniform interstitial and vacancy concentrations denoted by x_i and C_v are obtained as solutions of the equations:-

$$\left.\begin{aligned} G_i - K_i^2 D_i x_i - Z\nu_i R x_i C_v &= 0 \\ G_i\left[1 - 2x'\frac{N_L}{N_o}\right] - K_v^2 D_v C_v - Z\nu_i R x_i C_v &= 0 \end{aligned}\right\} \quad (1)$$

(valid for temperatures where thermal defect concentrations are not significant). Where G_i is the atomic displacement rate in atoms/atom/sec, in a neutron flux ϕ (measured in Equivalent DIDO nickel units), R is the repulsive barrier to interstitial - vacancy recombinations, Z is the number of neighbours from a vacancy from which recombination occurs, and x' is the number of sites adjacent to the end of a vacancy line, D_i and D_v are the diffusion coefficients for interstitials and vacancies respectively, parallel to the basal planes. K_i^2 and K_v^2 are the terms defined in (I) related to the mean free paths for interstitials and vacancies respectively, given in terms of the defects by

$$\left.\begin{aligned} K_i^2 &= 2\pi r Z_i N_\ell \\ K_v^2 &= \frac{4Z_v}{dL_a} + \frac{8N_L}{N_o a^2} \end{aligned}\right\} \quad (2)$$

where r is the interstitial loop radius, d the interlayer spacing, a the basal jump distance and Z_i, Z_v are small numbers allowing for the effects of stress fields.[1]

The motion of vacancies parallel to the hexagonal axis enables them to annihilate interstitial atoms in the loops. This process has been analysed by Reynolds and Thrower[2] and Baker and Kelly.[3] The rate of change of the radius of a single loop r in a crystal with uniform vacancy concentration C_v due to movement parallel to the hexagonal axis is

$$\frac{dr}{dt} = xy/\alpha\ \nu_c\left\{\exp\left[\frac{-F_c\alpha - E_{fv} - E_{mc}}{kT}\right] - C_v \exp\left[\frac{-E_{mc}}{kT}\right]\right\} \quad (3)$$

where x is the fraction of edge sites on the loop which can absorb vacancies, y is the co-ordination number of an edge atom (6 or 7), α is the area/atom in the loop, ν_c is the atomic vibration frequency parallel to the hexagonal axis, E_{fv} is the formation energy of a vacancy, E_{mc} is the activation energy for vacancy movement parallel to the c-axis, k is Boltzmann's constant and T is the absolute temperature.

The parameter F_c is defined by

$$F_c = -\frac{1}{2\pi r}\left(\frac{dE}{dr}\right) \quad (4)$$

where E is the energy of the dislocation loop. The term $\exp(-E_{fv}/kT)$ is small up to a temperature 2500°K while for loops of reasonable size $\exp(-F_c\alpha/kT)$ is less than unity, when (3) may be approximated by

$$\frac{dr}{dt} = -xy/\alpha\ \nu_c \exp(-E_{mc}/kT)\ C_v \quad (5)$$

Inclusion of the interstitial loops as sinks for vacancies in the second of Eqn (2) modifies it to

$$K_v^2 = 4Z/dL_a + 8N_L/N_o a^2 + \frac{2\pi x y \nu_c}{D_{o_v} d\alpha} \exp\left[-\frac{(E_{mc} - E_{ma})}{kT}\right] \quad (6)$$

where $D_v = D_{o_v} \exp(-E_{ma}/kT)$

without modifying the equation for K_i^2.

The growth rate of a graphite crystal parallel to the c-axis, $X_c^{-1}(dX_c/dv)$ in the usual notation[1] is

$$\frac{1}{X_c}\cdot\frac{dX_c}{dv} = \frac{D_i}{\phi} K_i^2 x_i - \frac{2\pi r}{\alpha\phi}\left(\frac{N_\ell}{N_o}\right)\left(\frac{dr}{dt}\right) \quad (7)$$

Defining as before, (1), $\eta = 4Z_i G_i / D_i D_v K_i^2 K_v^2$ (8)

and $\mu = -\frac{N_L}{N_o}\frac{Z_i}{2}\eta$ (9)

then the solution of Eqn (1) is, as before:

$$\left.\begin{aligned} x_i &= \frac{D_v K_v^2}{2\nu_i RZ}\left\{\left[(1+\mu)^2 + \eta\right]^{\frac{1}{2}} - [1+\mu]\right\} \\ C_v &= \frac{D_i K_i^2}{2\nu_i RZ}\left\{\left[(1+\mu)^2 + \eta\right]^{\frac{1}{2}} - [1-\mu]\right\} \end{aligned}\right\} \quad (10)$$

where ℓ is the average length of the i_1 vacancy disks, $(dr/dt)_i$ is the rate of growth of i_1 radii due to interstitial annihilation.

The pair of Eqs (14) are now linked, and the complexities of the solution obscure the behaviour and many of the numerical parameters are not known. Consider the most likely case, that $x_v \ll x_i$, $(dr/dt)_i \to 0$, and eventually $C_o \gg C_v$, then Eqs (14) can be written:

$$\frac{dC_o}{dt} = D_i K_i^2 x_i - \nu_i R x_i C_o \qquad (15)$$

$$\frac{dC_v}{dt} = D_v K_v^2 C_v - \nu_i R x_i C_o \qquad (15)$$

with the solutions

$$x_i = \frac{G_o}{D_i K_i^2 + \nu_i R C_o} \qquad (16)$$

and

$$C_v = \frac{G_v}{D_v K_v^2} + \nu_i \frac{R C_o}{D_v K_v^2}\left[\frac{G_o}{D_i K_i^2 + \nu_i R C_o}\right] \qquad (17)$$

The crystal growth rate parallel to the hexagonal axis is

$$\frac{1}{X_c}\frac{dX_c}{dv} = \frac{D_i K_1^2 x_i}{\phi} - \frac{2\pi r}{\phi v}\left(\frac{N_\ell}{N_o}\right)\left(\frac{dr}{dt}\right) \qquad (18)$$

where the last term is due to the annealing of the interstitial loops by the equilibrium vacancy concentration.

Substituting for K_1^2 and x_i in the first term gives

$$N_a = \frac{\ell}{\pi r^2} = f/\pi r^2$$

$$\frac{dr}{dt} = x_i \nu_i \left[\frac{\nu_i R C_o}{D_i K_i^2 + \nu_i R C_o}\right] - f/\pi r^2$$

$$\frac{dr}{dt} = \frac{\nu_i R C_o}{D_i K_i^2 + \nu_i R C_o}\left[\frac{D_i K_i^2}{\nu_i R C_o}\right] - \frac{f}{\pi r^2}$$

$$\frac{dr}{dt} = \frac{D_i K_i^2}{\nu_i R C_o} - \frac{f}{\pi r^2}$$

The effect of the annealing term is to limit r to the value

$$r_{max} = \left(\frac{f \nu_i R C_o}{\pi D_i K_i^2}\right)^{1/2}$$

and the rate of growth is then given by

$$\frac{1}{X_c}\frac{dX_c}{dv} = \frac{D_i K_i^2 x_i}{\phi} - \frac{2f}{\phi v}$$

3. Discussion

The second term in Eqn (20) was calculated for reasonable approximations of values and is found to be of the order 10^{-4} to 10^{-5}. Even in the case $C_v \to C_o$ it was negligible. Physically the annihilation sink $2\pi r\ell$ for all vacancies has disappeared at crystal boundaries before a significant concentration can form parallel to the hexagonal axis. This could be reversed for very large L_a values.

Eqn (20) is very transparent, the second term is found to be very small, while the first term shows the damage to be temperature independent until the term in the square brackets reduces below unity. Evaluating the bracketed term indicates that this does not occur until $\sim 4000^{\circ}$C for the case $C_v \ll C_o$.

It would be interesting to observe the results of irradiation of pyrographites at very high temperatures.

4. References

1. KELLY B T. Carbon. Unpublished.
2. REYNOLDS W N and THROWER P A. Phil. Mag 12, p.573 (1965).
3. BAKER C and KELLY A. (Phil Mag 9, p.927 (1964)) (Phil Mag 11, p.729 (1965))
4. KELLY B T. Chemistry and Physics of Carbon Vol. p.119, Ed. by P L Walker Jr, Marcel Dekken (NY)(1

Department of Metallurgy and Materials Science, The University,
P.O. Box 147, Liverpool L69 3BX, England.

1. Introduction

The use of graphite for components in nuclear-fission reactors has resulted in a large number of studies of the effects of neutron irradiation in this material. (For review see [1]. More recent suggestions [2] that graphitic materials could be used in a controlled thermonuclear reactor now require that additional studies of particle injection be made. In particular, the effects of helium atoms within graphite, which could result from either ion injection or the transmutation of fast neutrons and carbon atoms, should be investigated. In contrast to the extensive studies of metals in this area (see [3] for example), very little work has been reported on graphite. Mazey and Barnes [4] bombarded single-crystal flakes with various ions, and showed that twinning occurs. Ekern et al. [5] irradiated graphite-fibre cloths with 100 keV He^+ ions to a dose of 3×10^{16} ions/cm^2 at various temperatures. Scanning-electron microscope observations revealed flaking on room-temperature irradiated samples, but no damage was detected for irradiations at 400 and 800°C.

Transmission electron microscopy is a more sensitive technique for revealing damage, and the aim of the present work is to study by means of optical and T.E. microscopy the effects in graphite of He-ion bombardment for a range of bombardment temperatures, ion energies and ion doses. Damage effects have been observed, and this note presents a preliminary report of the observations made to date; it will be expanded upon at the conference.

2. Experimental Procedure

Both natural, single-crystal and pyrolytic-graphite (supplied by Union Carbide) specimens were used. The former were bombarded in an unthinned state for observation of surface features using optical microscopy. Transmission electron microscopy (at 100 kV) was undertaken on single crystal specimens repeatedly cleaved after injection and on pyrolytic samples which were cleaved, mounted on supporting grids and studied in the TEM prior to injection. The latter treatment ensured that any structural effects observed were due to the ion bombardment.

The specimens were injected with $^4He^+$ ions in the Heavy Ion Accelerator at AERE, Harwell, for ion energies in the range 70 to 100 keV and injection temperatures between 20 and 700°C. No noticeable ion-induced features were observed for ion doses $\simeq 10^{16}$ ions/cm^2, and heavy erosion occurred for doses $\geq 5 \times 10^{18}$ ions/cm^2. Accordingly, only doses in the range 5×10^{17} to 10^{18} ions/cm^2 have been used for this study.

3. Results

An optical micrograph of a single crystal injected at 20°C with 100 keV ions to a dose of 10^{18} ions cm^{-2} is shown in Fig.1. This unpolished surface was free of imperfections before irradiation, and it can be seen that the ions have resulted in twinning on a fine scale, as reported earlier in [4]. Twinning of this form was observed for all injection temperatures, but contrast associated with bulging of the surface between the twins was apparent for temperatures $\geq$ 300°C. The effect is more marked for higher doses and energies, and an example for 100 keV ions at 500°C and a dose of 10^{18} ions/cm^2 is shown in Fig.2. Numerous observations suggest that increasing the energy and dose widens the twins, and that an increase in the injection temperature increases the twin density, up to 300°C but marginally decreases it above 300°C. These trends are very weak, however, and are not yet supported by quantitative measurements. TEM analysis of the twins shows that most twins intersect the basal plane along either the $\langle 10\bar{1}0 \rangle$ or $\langle 11\bar{2}0 \rangle$ directions, as expected [6].

In the pyrolytic samples cleaved before ion injection, the density of twins produced by ion bombardment is much less than in the unthinned, single crystals, and twins are almost absent from very thin areas. At high irradiation temperatures, large blisters are formed. An example of a pyrolytic specimen injected at 700°C with 70 keV ions to a dose of 10^{18} ions/cm^2 is shown in Fig.3. The blisters take the form of well-defined domes which produce characteristic bend-contour patterns. In addition to the large blisters, ion-induced damage on a much finer scale can be seen in the matrix and blister dome, and this is currently being analysed [7]. Blistering effects are observed at lower bombardment temperatures, but as the temperature is reduced, the blisters become smaller and are less well defined. There is a good correlation between the surface bulging seen in the optical microscope (Fig.2) and the contrast observed in the TEM. An example for a natural-crystal sample bombarded at 500°C with 100 keV ions to a dose of 10^{18} ions/cm^2 is shown in Fig.4; the bend contours between the twins are clearly seen and they correspond to irregularly-shaped domes. It is not yet known if these are actually blisters, nor is it known to what extent twins and blisters are related or how they affect each other. In some areas at 700°C, blisters are observed at twin intersections and twins are seen around the perimeter of individual blisters.

4. Conclusion

The important new result reported here is that blisters are produced in graphite by the injection of the ions; a result now well-established for metals. The blisters are particularly well defined at high

injection temperatures and are accompanied by defects distributed on a fine scale. Further analysis of these, the damage produced at low temperatures and the possible inter-relation between gas content, twinning and blister formation is in progress and will be reported at a later date.

Acknowledgements

The authors acknowledge valuable discussions with Drs. D.G. Martin, D.J. Mazey and D. Vesely, and the assistance of Mr. P. Copp with the ion injection. The work is supported by the UKAEA, Harwell.

References

1. P.A. Thrower, 'Chemistry and Physics of Carbon', vol. 5, p.217, Marcel R. Decker, N.Y., (1969).
2. G. Kulcinski and R. Conn, Nucl. Fusion, 15, 327 (1975).
3. Proc. Conf. on Surface Effects in Controlled Fusion Devices, J. Nucl. Mat., 53 (1974).
4. D.J. Mazey and R.S. Barnes, 6th Int. Congress for Electron Microscopy, Kyoto, vol.1, p.365, Maruzen, Tokyo (1966).
5. R.Ekern, S.K. Das and M. Kaminsky, Proc. 6th Sympos. on Engineering Problems of Fusion Research, San Diego, IEEE (1975).
6. E.J. Friese and A. Kelly, Proc. Roy. Soc. (Lond.), A264, 269 (1961).
7. D.J. Bacon, A.S. Rao and D. Vesely, unpublished work.

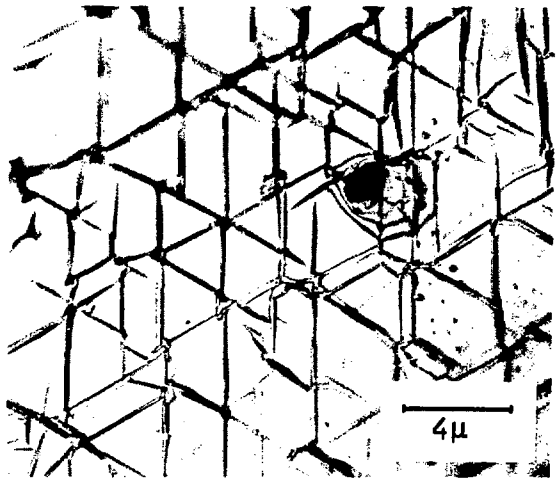


Fig.1

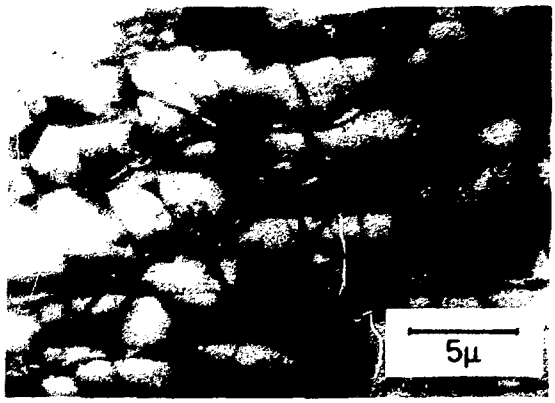


Fig.2

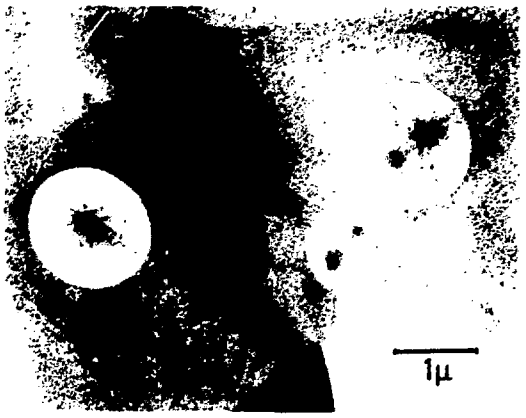


Fig.3

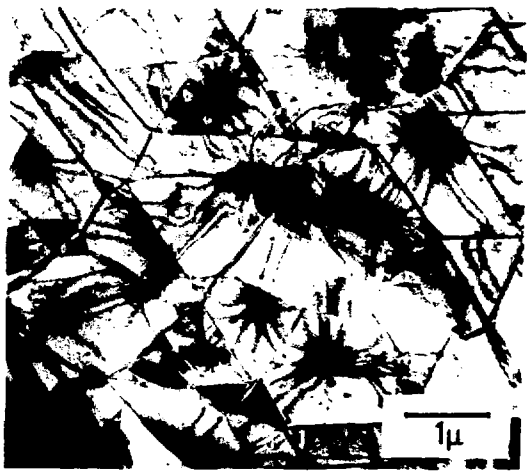


Fig.4

EXPERIMENTS IN THE [illegible] OF [illegible]

L. R. Zumwalt and P. T. Williams
North Carolina State University

A number of studies indicate volatile metals such as cesium, barium and strontium show concentration dependent diffusion in graphite (1, 2, 3). In connection with a study of the effect of strontium concentration on cesium sorption in H-451 nuclear grade graphite, the diffusion of Sr-85 traces was studied in samples preloaded with ordinary stable strontium at several selected concentrations. The experimental technique involved the determination of tracer activity profiles in rod-shaped samples after they had been annealed in contact with a source disk of the same diameter. The method is similar to that of the classical study of "self-diffusion" in metals where the diffusion is at a constant chemical potential.

The source disk and sample rods, of H-451 graphite, were of diameter, 0.794 cm, and of lengths L = 0.1 cm and S = 1.9 cm respectively. Strontium was originally added as the nitrate dissolved in a water-acetone mixture. After a series of processes of impregnation, evaporation, baking and finally annealing at 1400°C in a graphite tube (King) furnace uniform impregnations of stable strontium at nominal concentrations of 10,100,300 and 1000 μg Sr/g C were obtained. The source disks were then further impregnated with strontium-85 (and annealed) which added 18 ± 4 μg Sr-85 to the source disk depending on the experiment. The manipulations involving the impregnated and annealed strontium-graphite samples were carried out in a dry, inert gas (argon) atmosphere. After adding the Sr-85, the source disk and rod sample faces, which had been lapped to a good fit before the impregnations, were put together and placed inside a molybdenum container provided with a tantalum spring which pressed the graphite source-rod couple together in an axial direction through pressure applied by the screw-top closure of the container. This assembly was transferred to the King Furnace and then diffusion runs were carried out at 1300°C for two hours in an argon atmosphere.

After the diffusion runs the source disk was counted to determine the amount (using a calibrated reference source) of strontium-85 remaining in the disk, C_s. Successive axial sections of the graphite rod were taken using the lathe and a vacuum collection rig whereby the graphite cuttings of each section were collected on a 9 mm diameter filter paper. These papers were folded, weighed and counted to determine the amount of Sr-85 and mass of graphite in each section. In this manner strontium-85 concentration profiles were obtained. These were integrated to find the average concentration $\bar{C}$. From a plot of Sr-85 concentration C(x) versus distance along the rod axis (x), the extrapolated boundary concentration C(0) was obtained from a curve fit so as to avoid any perturbations, which occurred in some cases, of concentrations for sections taken very near the surface ($x \approx 0$).

Plots of C(x)/C(0) vs x, i.e. normalized concentration profiles, all for 2.0 hour diffusion anneals at 1300 ± 10°C but for different initial preloaded strontium concentrations are given in Figure 1. The profile curves which are the result of an "eyeball fit" of the data points show the data to have little scatter and indicate a monatonically increasing rate of diffusion with increasing strontium concentration.

To obtain a first approximation of the diffusion coefficients it was assumed that the first portion of the curves would approximately correspond to the diffusion equation solution for constant Sr-85 concentration at x = o. Then at time t at the end of the anneal

$$C(x)/C(0) = \text{erfc}\,(x/2\sqrt{Dt}) \qquad (1)$$

Figure 2 is a plot of the diffusion coefficients, D_{Sr} (obtained from a curve fit using Equation 1) versus the approximately uniform total strontium concentration of the graphite-rods.

The plot shows the diffusion coefficient to vary approximately as the square-root of concentration. The empirical equation corresponding to the straight line fit is,

$$D\left(\frac{cm^2}{sec}\right) = 1.3 \times 10^{-6}\left[C\left(\frac{\mu gSr}{gc}\right)\right]^{0.47}$$

This relationship is substantially different than the variation of D with strontium concentration reported by Sandalls and Walford (1) for AGL-9 graphite at 1000°C. They give

$$D\left(\frac{cm^2}{sec}\right) = 4.42 \times 10^{-16}\left[C\left(\frac{\mu gSr}{gc}\right)\right]^{3.15}$$

where C must exceed 62 μg/g.

Once the necessary computer programing is complete it is planned to revaluate the diffusion coefficients obtained in our experiments by a more precise analysis which takes account of the depletion of the source and employs a boundary condition of the third kind which takes into account the resistance to mass transfer due to the small gap at the source disk - graphite rod interface.

The solution, obtained using the method of the integral transform (4) is

$$C(x)/C_{so} = \frac{L}{S+L} + H_1\sum_{m=1}^{\infty} K\left(\beta m,0\right) K\left(\beta m,x\right) \frac{S}{S+L}\,\frac{\exp(-kt)}{\beta m^2 - k/D}$$

$$- H_1\sum_{m=1}^{\infty} K\left(\beta m,0\right) K\left(\beta m,x\right) \exp\left(-\beta m^2 Dt\right)\left[\frac{L}{(S+L)\beta m^2} + \frac{S}{(S+L)(\beta m^2 - k/D)}\right] \qquad (2)$$

where

$$K\left(\beta m,x\right) = \sqrt{2}\left[\frac{\beta m^2 + H_1^2}{S(\beta m^2 + H_1^2) + H_1}\right]\cos \beta m(S-x) \qquad (3)$$

βm are roots of $\beta \tan(\beta S) = H_1$ (4)

$$H_1 = \frac{-\left(\frac{dC}{dx}\right)_{x=o}}{C_s - C(0)} \qquad (5)$$

The concentration of its source disk at time t is,

$$C_s = C_{so}\left[\frac{S}{S+L}\right]\exp\left(-kt\right) + C_{so}\left[\frac{L}{S+L}\right], \qquad (6)$$

where

C_{so} = the initial source concentration.

All boundaries, excepting the source-graphite interface, are taken as of the second kind - i.e. $dC/dx = 0$.

References

1. Sandalls, F. J., and M. R. Walford, "Laboratory Determinations of Strontium Diffusion Coefficients in Graphite," Report AERE R-6911, Atomic Energy Research Establishment, Harwell, Berkshire, 1972.

2. Besenbruch, G. D., et al., "Diffusional Behavior of Strontium in Graphite, "Trans. Amer. Nucl. Soc. 12, 81 (1969).

3. Zumwalt, L. R., "The Concentration Dependence of the Diffusion Coefficient of Volatile Fission Product Metals in Graphite,"Trans. Amer. Nucl. Soc. 13-2, 566-568 (1970).

4. Ozisik, M. N., Boundary Value Problems of Heat Conduction, International Textbook Co., Scranton, Pa. (1968).

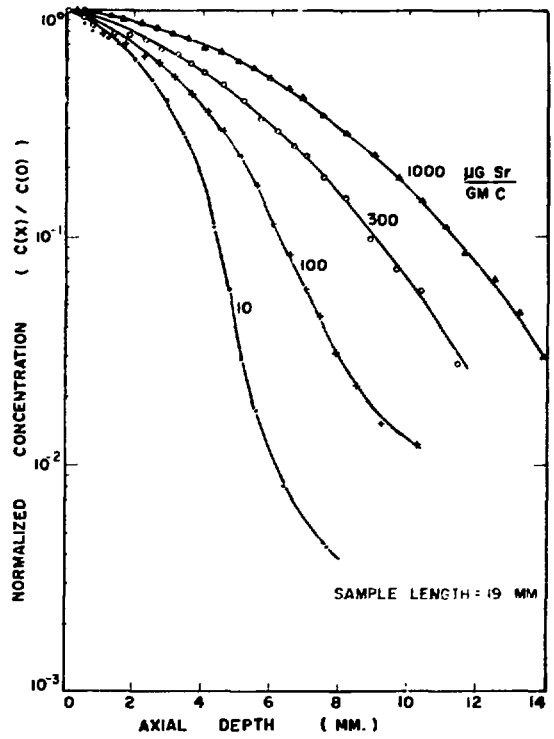


Figure 1. Normalized Concentration Profiles

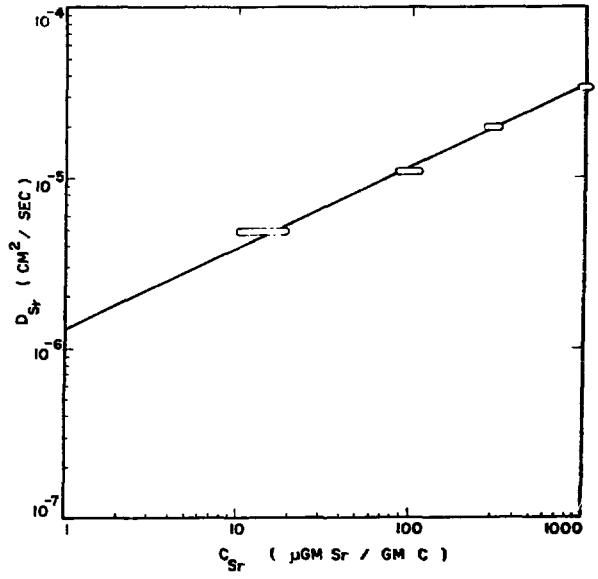


Figure 2. Diffusion Coefficient vs. Concentration

INERT GAS PERMEABILITY OF PYROCARBON COATINGS*

C. S. Morgan and W. P. Eatherly, Metals and Ceramics Division, Oak Ridge National Laboratory
and
G. L. Powell, Development Division, Oak Ridge Y-12 Plant

Pyrocarbon coatings are used to retain fission products produced in thorium- or uranium-containing kernels during irradiation of fuel particles in gas-cooled reactors. The extent of inert gas permeability of pyrocarbon coatings, which can be varied extensively by adjusting deposition parameters, is important for this purpose. Permeability values may bear a correlation with other pyrocarbon properties such as strength, density, crystal structure, or growth feature size. Thus, inert gas permeability measurements can be useful in evaluating pyrocarbon coating techniques.

Gas contents of fuel particles have been measured by cracking the particle in a chamber connected to a mass spectrometer by Bildstein and Strigl[1] and Clough *et al.*[2] This method afforded a measure of internal pressure when the volume occupied by the gas was estimated from geometrical measurements. Lindemer and Pearson have obtained similar results without use of a mass spectrometer.[3] In the present work the high-temperature inert gas permeabilities of the pyrocarbon coatings of HTGR Biso fuel particles have been measured. Fuel particles were annealed in an atmosphere of the inert gas or gases, then broken individually in a dynamically pumped chamber containing a mass spectrometer and the inert gas pressure transient was monitored and integrated. The mass spectrometer was calibrated using known amounts of gas and was sensitive to 1×10^{-14} mol of an inert gas. The composition of gas evolving from the fuel particle could be determined qualitatively by operating the mass spectrometer in a scanning mode or an individual gas could be determined quantitatively by monitoring a single mass number. The particle crushing gas measurement technique and data on helium permeability of Biso fuel particles have been previously reported.[4]

Extensive measurements of helium permeability of the pyrocarbon coating were made on one fairly typical batch of fuel particles (OR 2261-T). Process helium was first removed from these fuel particles by a vacuum anneal for 1 hr at 1800°C.[4] Lots of fuel particles were then annealed under isothermal and isobaric conditions for fixed time intervals. Twenty samples from each lot were analyzed individually to determine the average helium content. Results for samples exposed to 98 kPa He under isothermal conditions at either 450, 550, 650, 750, 850, 1000, 1200, or 1425°C for various time intervals were used to construct permeation isotherms. An inflection in the permeation curve at early times characteristic of a nonsteady state diffusion process was observed.[5] At long times the helium content data approach a saturation value at a rate that is first order. Empirically, the asymptotic gas content, n_∞, is dependent on the absolute temperature according to

$$n_\infty = 3.95 \times 10^{-7}/T \text{ mol He/particle} \qquad (1)$$

in agreement with the perfect gas law. The coefficient in Eq. (1) yields a standard deviation of 4% indicating that samples of 20 particles are adequate. The helium permeation curves had essentially the same shape at all temperatures. All isotherms were well fitted by first-order kinetic equations beyond the point of inflection. The inverse of the calculated characteristic time (*i.e.*, the permeation coefficient) was found to obey

$$k_{He} = 43.6 \exp\{-14175/T\} \text{ sec}^{-1} \qquad (2)$$

where the standard deviation of the pre-exponential term is 5.5 sec^{-1} and 122 K for the activation temperature. Equation (2) indicates an activation energy for permeation of 118 kJ mol^{-1} (28 kcal mol^{-1})

A solution to the mathematical aspects of the problem of transient diffusion through a spherical shell into a finite reservoir has been developed by Reeves and Tolliver[6] and will be used for a more rigorous evaluation of the permeation isotherm data.[5]

Pyrocarbon coatings are permeable to neon and the preliminary rate constant data from permeation isotherms at 850 to 1500°C for batch OR 2261-T could be expressed as Eq. (3)

$$k_{Ne} = 21.8 \exp\{-20264/T\} \text{ sec}^{-1} \qquad (3)$$

indicating an activation energy for permeation of 166 kJ mol^{-1} (40 kcal mol^{-1}). At 1000°C the neon content was a linear function of neon pressure for 48-hr anneals. Insufficient data were available to give a reliable standard deviation, but the saturation neon content at 1000 and 1200°C agrees well with Eq. (1). As $T \to \infty$, $k_{He}/k_{Ne} = 2.0$. If the permeation rates were inversely related to the square root of the molecular weights of the permeating species, k_{He}/k_{Ne} would have the value 2.2.

Inert gas permeabilities of the pyrocarbon coatings of many fuel particle preparations were screened using a dual-gas technique. The fuel particles were annealed at 1375°C for 1 hr in a 96 kPa atmosphere composed of He–50% Ne. The gas content of the particles was determined individually, one gas at a time. Usually 15 particles were broken for the determination of each gas and the results averaged. The ratio of moles neon:helium in the fuel particle represents a measure of the permeability which is relatively independent of particle size. Also, the use of two gases enables differentiation between a very impermeable compact and one which is so highly permeable that the gases leak out before the particle is broken. The permeability values obtained for selected fuel particle batches are given in Table I along with standard deviations determined from the measurements. Table I also contains deposition conditions and geometric parameters of the pyrocarbon coatings. The results show that pyrocarbon coating permeability

*Research sponsored by the U.S. Energy Research and Development Administration under contract with the Union Carbide Corporation.

Table I. Pyrocarbon Coating Permeabilities

Batch Number	Gas Content[a] (moles·particle^{-1} × 10^{10}) Helium	Neon	Ratio Ne/He	Particle Geometry, μm Diameter	LTI Thickness	Deposition Conditions Temperature (°C)	Gas[b] Composition (mol %)	Coating Rate (μm·sec^{-1})
OR-1978-T	0.66±0.03	0.02±0.003	0.03	819	84	1240	50 propylene	0.013
OR-2263-T	1.51±0.17	0.19±0.03	0.13	874	91	1325	25 MAPP[c]	0.060
OR-2276-T	1.95±0.39	0.25±0.02	0.13	865	85	1275	15 MAPP	0.052
OR-2262-T	1.66±0.38	0.33±0.04	0.20	872	85	1275	50 MAPP	0.108
OR-2261-T	1.62±0.39	0.38±0.04	0.23	875	89	1325	50 MAPP	0.123
OR-2265-T	1.67±0.24	0.54±0.10	0.32	888	94	1325	100 MAPP	0.262
OR-2269-T	1.81±0.32	0.74±0.10	0.41	847	81	1325	50 MAPP	0.208
OR-2274-T	2.03±0.31	1.02±0.16	0.50	889	91	1325	100 MAPP	0.465

[a]Immersed 1 hr at 1375°C in Ne–50% He at 720 torr. [b]Remaining gas component argon.

[c]MAPP gas is marketed by Airco, Inc., and consists primarily of methylacetylene and propadiene with alkanes as stabilizers.

increases with increasing rate of deposition and, to a lesser extent, with increasing deposition temperature.

Void volumes obtained from helium content data are in good agreement with values obtained by mercury porosimetry at a pressure of 103 MPa on cracked fuel particles, *e.g.*,

Batch Number	Volume, m^3 per fuel particle By Helium Content	By Mercury Porosimetry
	× 10^{-11}	× 10^{-11}
OR-2013-T	1.70	1.77
OR-1972-T	1.54	1.59
OR-2010-T	4.25	4.14

The extent of void volume present in small pores not opened when the pyrocarbon coating is cracked has not been determined.

Tests of the permeability of pyrocarbon coatings for higher molecular weight inert gases were initiated using argon. Significant argon permeability at 1800°C was evident only in more permeable pyrocarbon coatings such as in batch OR-2274-T. Argon permeability was unmeasurably low in pyrocarbon coatings with typical Ne/He ratios. In these fuel particles process argon remaining from preparation was not removed by 4-hr vacuum anneal at 1800°C. The decrease in permeability in the He, Ne, Ar series indicates that typical, unirradiated, uncracked pyrocarbon coatings have no measurable permeability to krypton or xenon at 1800°C.

The permeability of irradiated fuel particles with inert kernels measured on two batches is shown in Table II. The permeability decreases with small doses of radiation but increases sharply with fluence approaching HTGR design. The significance of irradiation temperature is not clearly defined from this limited number of tests.

The extensive variation of permeability with pyrocarbon preparation may indicate that defects in the coating are important rather than lattice spacing. The sharp increase of permeability with higher fluences shows that structural defects resulting from the neutron bombardment increase permeability.

Table II. Permeability of Irradiated Inert Fuel Particles

Batch Number	Fluence (neutrons/m^2) (E > 0.18 MeV) × 10^{25}	Design Temperature (°C)	Ne/He
OR-2294-T	0		0.22
OR-2294-T	4.0	950	0.12
OR-2291-T	0		0.27
OR-2291-T	3.5	900	0.23
OR-2291-T	7.5	1250	0.89
OR-2291-T	8.6	1250	1.26

References

(1) A. Strigl and H. Bildstein, *Determination of Free Volumes in Coated Fuel Particles*, D. P. Report 854 (October 1973).

(2) D. J. Clough *et al.*, *Proceedings of the European Conference Organized by the British Nuclear Energy Society*, University of Reading, March 1972.

(3) T. B. Lindemer and R. L. Pearson, *J. Nucl. Mater.* 25, 359 (1975).

(4) C. S. Morgan and G. L. Powell, Special Issue of *Nuclear Technology* (to be published).

(5) R. C. Jenkins, P. M. Nelson, and L. Spirer, *Trans. Faraday Soc.* 66, 1391–1401 (1970).

(6) M. Reeves and J. S. Tolliver, ORNL Report (to be published).

B_4C/GRAPHITE PELLETS FOR NUCLEAR REACTOR SHUTDOWN SYSTEMS

W. K. Alexander, United Nuclear Industries
A. E. Goldman, Union Carbide Corporation
H. D. Schlesselman, Union Carbide Corporation

An economical procedure has been developed for producing large quantities of boronated graphite pellets for use in nuclear reactor emergency control systems. The pellets were formed by tumble abrading right cylindrical sections cut from extruded rod stock.

Boronated graphite pellets were selected for this application since boron produces no radioactive products nor is gamma radiation emitted under neutron bombardment. In addition the boronated graphite pellets flow by gravity and are thermally and chemically stable in the reactor environment.

The nominal 7/16" diameter pellets produced met all required physical, mechanical, and chemical specification requirements.

The current material used for emergency control of the graphite moderated Hanford N reactor is a dispersion of natural samarium oxide in 3/8" diameter aluminum oxide (Sm_2O_3/Al_2O_3) ceramic pellets. Samarium oxide was chosen because of its large neutron capture cross section and "assumed" fast burn out. These pellets have been used from start-up of the Hanford N reactor in 1964 until the summer of 1977. The pellets are stored in hoppers above the reactor core. In the event that the control rods cannot be inserted into the core to shut the reactor down, the pellets are dropped into the core to serve the same purpose. The control channels are filled with pellets during routine testing of the emergency control system and the pellets are retrieved and returned to the hoppers. Problems have arisen in the use of these pellets since some pellets have remained in the graphite moderator causing reactivity losses which are more or less permanent since samarium transmutation daughter products have neutron capture cross-sections similar to samarium. Also, samarium and other rare earth elements normally found as impurities in the samarium become extremely radioactive when irradiated causing gross radiation and contamination problems. For example, one Sm_2O_3/Al_2O_3 pellet may read as much as 500 Rem after irradiation in the N reactor.

For this reason it was decided to replace the Sm_2O_3/Al_2O_3 pellets during a convenient reactor outage. Boronated graphite pellets, as natural B in the form of B_4C in graphite, were selected since the effective boron isotope, B^{10}, undergoes the following reaction when bombarded with neutrons:

$$_0N^1 + {}_5B^{10} \longrightarrow {}_3Li^7 + {}_2He^4$$

Thus no radioactive products are formed nor is gamma radiation emitted.

The boronated graphite pellets must be thermally stable when dropped into the reactor core operating at 750°C. They must be shaped such that they will flow and must not wear nor break excessively when dropped. The pellets must, of course, shut the reactor down, be "burnable" to eliminate radioactivity loss if pellets remain in the graphite moderator, and must not become highly radioactive in the event they are inadvertently irradiated.

The boronated graphite pellets were produced from (1) minus 60 mesh nuclear grade B_4C, (2) high purity, low ash petroleum coke based graphite flour, and (3) a coal tar pitch binder.

Previous attempts to mold boron carbide loaded graphite spheres proved uneconomical because of excessive tooling costs. The extreme abrasiveness of the boron carbide in the soft graphite matrix caused rapid punch and die wear. In addition, the large number of pellets required for this application would have necessitated long processing times because of the capacity restrictions of conventional molding equipment.

Alternate methods of achieving a suitable "spherical" form were investigated. The extrusion of rods of boronated graphite had been demonstrated in the prior production of "burnable poison" rods. It was felt that such rods could be reduced to right cylindrical pellets with length equal to diameter and the pellets then either warm tumbled as "green" pellets or tumble abraded as heat treated pellets.

Experiments conducted with small lots of trial material indicated that the baked boronated graphite rod stock could be accurately reduced to the desired pellet configuration at the production rates required. Attempts to form pellets from the green, pitch bonded rod stock were generally unsuccessful because of distortion and structural cracking.

After demonstrating the feasibility of the basic processing procedures, several small test lots were produced. Pellets capable of meeting the proposed specification were obtained using the process procedures developed. The production lot of material was produced by preparing a primary blend of boron carbide and graphite. Cross blending procedures were used to ensure uniform distribution of the boron carbide. The coal tar pitch binder was added and the boronated graphite rods were formed by extrusion. The rods were thermally processed to carbonize the pitch binder and to provide the necessary thermal stability for the service environment. Following the baking operation, the boronated graphite rods were sawed to right cylindrical pellets. The pellets were then dry tumbled to abrade the sharp pellet edges and achieve the final, acceptable quasi-spherical configuration.

A boron content of 65 to 105 grams of natural boron per foot of 3" ID channel was specified to provide adequate poisoning of the core without prolonging "burnout". A density of not less than 1.50 g/cc was required to assure pellet flow from the hoppers and thru the core. A weight loss

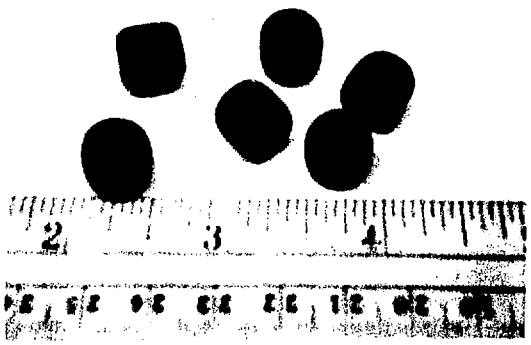
specification of no more than 1% when heated to 850°C was imposed to prevent property changes during repetitive testing of the emergency control system. It was required that not more than 1 pellet per thousand be broken and not more than 0.5 wg't percent of the pellets be lost after ten drops of 30 feet to assure that usage will not cause deterioration, since broken pellets tend to slow pellet flow and "dusting" of the pellets might cause contamination problems.

Finished pellets were measured for boron content using a modification of the ASTM method for ferroborons (ASTM E-31). A boron level of 81 + 5 grams B/foot of 3" I.D. channel was determined. Physical property tests on the finished pellets results in an apparent density of 1.50 g/cc or greater. Thermal stability was verified by measuring pellet weights before and after thermal treating to 850°C for 12 hours in an inert atmosphere. Wear and breakage were determined by dropping pellets thirty feet into a graphite crucible ten times. Pellet sizing was determined by passing the pellets thru a perforated plate onto a plate with perforations smaller than the pellet dimensions. In all cases the pellets met or exceeded material requirements when MIL-STD-105D inspection standards were applied.

In addition, irradiation and activation analysis of sample pellets by United Nuclear Industries (UNI) personnel indicated that activity and contamination levels were better by a factor of 10^3 when compared to the present Sm_2O_3/Al_2O_3 pellets. Thus activity levels will be measured in millirems rather than in Rems, as at present.

Flow tests carried out at UNI indicated that the boronated graphite pellets will flow from the storage hoppers well within the allowable time limits. However, since they are neither as spherical nor as dense as the current Sm_2O_3/Al_2O_3 pellets, they do not flow as readily in the return troughs.

A photograph of sample pellets is shown below as Figure 1.



These sample pellets were taken from the finished lot of ten tons of pellets which were produced on schedule, met or exceeded all requirements, and provide a satisfactory replacement for the previously used Sm_2O_3/Al_2O_3 material.

DEPENDENCE OF GAS ADSORPTION RATES ON CARBON GRANULE SIZE AND LINEAR FLOW VELOCITY

JOSEPH A. REHRMANN, LEONARD A. JONAS
Edgewood Arsenal, Aberdeen Proving Ground, Maryland 21010

1. INTRODUCTION

The modified Wheeler adsorption kinetics equation (1), initially derived from a continuity equation of mass balance between the gas entering an adsorbent bed and the sum of the gas adsorbed by plus that penetrating through the bed, shown in the polynomial form

$$t_b = \frac{W W_e}{C_0 Q} - \frac{W \rho_\beta}{C_0 k_v} \ln\left(C_x/C_0\right) \qquad (1)$$

has been successfully used by Jonas and Rehrmann (2) in studies on the kinetic adsorption of gases by activated carbons. In this equation, t_b is the gas breakthrough time in minutes at which the concentration C_x appears in the exit stream, C_0 the inlet concentration in g/cm^3, Q the volumetric flow rate in cm^3/min, ρ_β the bulk density of the packed bed in g/cm^3, k_v the pseudo first order adsorption rate constant in min^{-1}, W the adsorbent weight in g, and W_e the kinetic adsorption capacity in g/g at the arbitrarily chosen ratio of C_x/C_0. In Eq (1), ρ_β is determined as a property of the granular size and shape of the adsorbent when filled by gravity settling in a container column, and the parameters C_0, C_x, and Q are set by the conditions of test. A plot t_b vs W, for any fixed flow rate and temperature, yields a straight line curve from whose slope and intercept the parameters W_e and k_v can be respectively calculated. Eq (1), in its derivation, assumed constant temperature, a single effective carbon granule diameter, an invariant adsorption capacity (obtained by choosing the challenge concentration to be large enough to assure being on the plateau of the adsorption isotherm) and the absence of other parametric interrelationships.

The pseudo first order adsorption rate constant k_v in Eq (1) has recently been shown (1), in the case of benzene vapor adsorption by 12-30 mesh activated carbon granules (weighted mean diameter of 0.104 cm), to be a function of the superficial linear velocity V_g of the gas-air flow into the carbon bed. The mathematical relationship found, which exhibited a 0.999 correlation coefficient with the experimental data over a 120 to 4000 cm/min (2 to 50 cm/sec) velocity range was

$$k_v = \frac{a+b}{1+(a/b)\exp[-(a+b)cV_g]} \qquad (2)$$

where a, b, and c were constants of the system. It is expected that one or more of these constants includes the effect of carbon granule size. Equation (2) describes a sigmoidal curve of k_v versus V_g, showing a minimum value of b for k_v at low V_g and a maximum value for k_v of $a+b$ at high V_g.

The purpose of this paper (in which we used dimethyl methylphosphonate) was to extend the study by investigating the dependence of the adsorption rate constant on both carbon granule size and superficial linear velocity. The granule size effect was studied over a 7-fold range from 0.019 to 0.144 cm diameter, and the superficial linear velocity was varied over a 30-fold range from 2 to 60 cm/sec, for each discrete granule size.

2. EXPERIMENTAL

The vapor used as an adsorbate was dimethyl methylphosphonate (DMMP), and the activated carbon adsorbent was a BPL grade, lot 7502, from PAC Co, Pittsburgh, PA, having a surface area of 1000 m^2/g. The carbon was sieved and ground into the discrete mesh fractions of 12-16, 16-20, 20-30, 30-40, 40-50, 50-60, 60-70, and 70-80, having mean granule diameters of 0.144, 0.102, 0.072, 0.051, 0.036, 0.027, 0.021, and 0.019 cm respectively. The kinetic adsorption tests were carried out with a gas adsorption test apparatus described in detail by Jonas and Svirbely (4). The inlet or challenge concentration was set at 2×10^{-6} g/cm^3. The vapor penetration of the bed was detected by an F&M 5750 gas chromatograph with a flame ionization detector and used a 12-ft length column of 1/16 in. diameter stainless steel tubing packed with 1% Dow-Corning silicone on a Chromosorb T support. The exit air stream was monitored continually by passage into 25 cm^3 gas sampling valve of the gas chromatograph. The breakthrough time t_b was denoted as the time when the exit stream showed the presence of a gas concentration of 2×10^{-8} g/cm^3, equal to an exit to inlet concentration ratio (C_x/C_0) of 0.01.

3. RESULTS AND DISCUSSION

Each of the eight mesh fractions was tested with DMMP vapor at five linear velocities, ranging from 2 to 60 cm/sec. For each test condition the breakthrough time t_b was determined for a minimum of four different carbon weights W. Plots of t_b vs. W resulted in straight line curves, in accordance with Eq (1). The regression equations obtained from the t_b vs W data points had correlation coefficients (r) ranging from 0.917 to 0.999, indicating a high degree of confidence for the linear dependence of t_b on W. Values for the adsorption capacity W_e and the adsorption rate constant k_v were calculated from the slope and intercept of the regression analysis equations, in the polynomial form of Eq (1), for each velocity and carbon granule size tested. The adsorption capacity was independent of both the flow velocity and the carbon particle size, the mean capacity for the forty test conditions being 0.345 g DMMP/g carbon with a standard deviation of ± 0.040 and a coefficient of variation of ± 11.6%. The adsorption rate constant, however, was a function both of the carbon particle size and the superficial linear velocity, increasing nonlinearly with increase in velocity and decrease in particle size to a limiting value of approximately 2600 reciprocal seconds. The data for the eight carbon mesh fractions each tested at superficial linear velocities of 2, 4, 10, 30, and 60 cm/sec are shown in Table 1. A plot of adsorption rate constant vs superficial linear velocity, for the eight carbon granule

diameters tested, is shown in Fig. 1. The curves indicate that the rate constant, at least over the carbon granule diameter range 0.144 to 0.027 cm, appears to exhibit the type of nonlinear dependence shown by Eq (2). However, the k_V vs V_ℓ curve for the 0.023, and especially that for the 0.019 cm diameter granule, approach independence of linear velocity, indicating a change in the rate controlling step for the overall adsorption process. A plot of adsorption rate constant vs the reciprocal of the carbon granule diameter, for the five superficial linear velocities, is shown in Fig. 2. In this plot it can readily be seen that all curves converge to the limiting value of 2600 reciprocal seconds for the adsorption rate constant, an apparent basic characteristic of this activated carbon for DMMP vapor.

In accord with the concept of a first order heterogeneous reaction we perceive that a limit of 2600 volumes of a gas-air mixture (containing 2×10^{-6} g DMMP/cm^3), each volume equal to the volume of the carbon granular bed, can be reacted with or adsorbed by the carbon per second. Therefore, the DMMP in each such volume of DMMP-air mixture was adsorbed by the carbon in 0.00038 seconds.

TABLE 1. DMMP ADSORPTION RATE CONSTANT AT VARIOUS PARTICLE DIAMETERS AND LINEAR VELOCITIES

Mean Carbon Part. Diam. d_p (cm)	Reciprocal Carbon Diam. $1/d_p$ (cm^{-1})	Ads. Rate Constant, k_V (sec^{-1}) at Sup. Linear Vel., V_ℓ (cm/sec)				
		2	4	10	30	60
0.144	6.94	70	101	117	187	354
0.102	9.80	92	138	188	302	421
0.072	13.89	165	244	309	401	605
0.051	19.61	211	371	485	760	805
0.036	27.78	461	619	758	1287	1430
0.027	37.04	813	974	1034	1485	1949
0.023	43.48	1509	1548	1635	1671	2313
0.019	52.63	2405	2477	2577	2628	2595

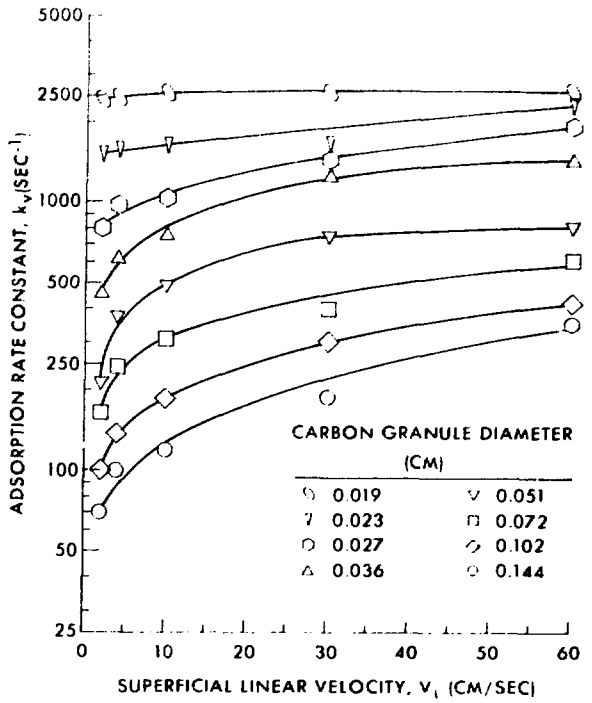


Fig. 1. DMMP adsorption rate constant as a function of linear velocity for various carbon granule diameters.

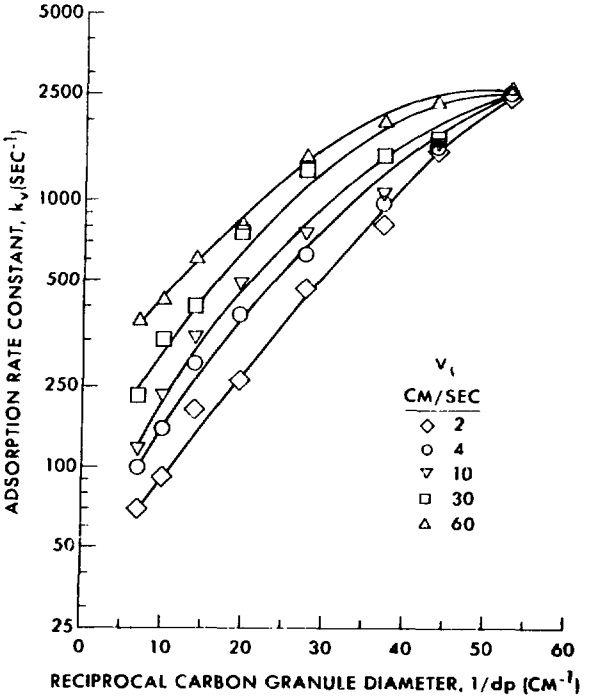


Fig. 2. DMMP adsorption rate constant as a function of carbon granule diameter for various linear velocities.

4. REFERENCES

1. Wheeler, A. and Robell, A. J., J. Catal. 13, 299 (1969).

2. Jonas, L. A. and Rehrmann, J. A., CARBON (Oxford) 10, 657 (1972); 11, 59 (1973).

3. Jonas, L. A. and Rehrmann, J. A., CARBON (Oxford) 12, 95 (1974).

4. Jonas, L. A. and Svirbely, W. J., J. Catal. 24, 446 (1972).

5. Hoel, P. G., "Introduction to Mathematical Statistics", p. 120, John Wiley and Sons, New York, N. Y., 1954.

REACTION STEPS IN GAS SORPTION BY IMPREGNATED CARBON

by

LEONARD A. JONAS
Chemical Laboratory, Edgewood Arsenal,
Aberdeen Proving Ground, MD 21010

1. INTRODUCTION

The removal of a gas or vapor from a flowing stream by a bed of chemically impregnated activated carbon granules, in which both physical adsorption and chemical reaction occur, is represented as a series of seven consecutive steps. This sequence of seven steps in gas removal, initiated when the flowing gas-air stream approaches the first layer of carbon granules in the bed, is shown to be (1) mass transfer, (2) surface diffusion, (3) intragranular diffusion, (4) physical adsorption, (5) gas desorption (6) chemical reaction, and (7) surface renewal. The first four steps describe the sequence involved in the physical adsorption of a gas by an activated carbon. Since it is believed that physical adsorption occurs prior to any chemical reaction between the gas and the impregnants on the carbon steps (5) through (7) apply only to a chemically impregnated activated carbon. Some authors (1) have combined steps (2) and (3) into one, identifying it as an internal diffusion step. The overall rate of physical gas adsorption will be determined by which one of these steps, or combination of steps, is the slowest and therefore rate controlling.

Under dynamic flow conditions, wherein the mean residence time of a gas flowing through a carbon bed is a fraction of a second, gas removal from the flowing air stream by the activated carbon, due to physical adsorption processes alone, may not be efficient enough to produce the desired concentration attenuation. To increase the overall gas removal efficiency activated carbons may be impregnated with certain metals and/or metal salts which permit and induce chemical reaction between the impregnants and the initially adsorbed gas.

It is the intent of this paper to study the mechanism and kinetics of this dual approach to gas sorption by impregnated activated carbons and to devise a method of data analysis which will identify the rate controlling step.

2. EXPERIMENTAL

The activated carbon adsorbent was a 12-30 mesh BPL grade, lot 7502, from Pittsburgh Activated Carbon Company, Pittsburgh, Pennsylvania, having an internal surface area of 1000 m^2/g. The weighted mean granule diameter was 0.104 cm. When pulverized to a 70-80 mesh fraction the mean diameter was 0.019 cm. The carbon when impregnated with an aqueous solution (12% NH_3) buffered by 10.9% carbonate ion and containing 8.5% copper, 4.1% chromate ion, and 0.3% silver nitrate was termed ASC whetlerite. The adsorbate vapor was 98% pure cyanogen chloride. Cyanogen chloride penetration of the bed was detected by the decolorization of a starch-iodine bubbler in a gas test apparatus similar in design to that described in detail by Jonas and Rehrmann (2).

3. THEORY

The general hypothesis on reaction steps taking place in gas removal by impregnated carbons is that physical adsorption of the gas on the surface must precede any catalytic or reactive process. The proposed sequence of reaction steps in the removal of cyanogen chloride from an air mixture, flowing into a bed of impregnated carbon granules, is as follows:

1. Mass Transfer (bulk or external diffusion). The gas molecules are transported from a vicinity of neighboring air molecules to a vicinity of the adsorbent granule outer surface. The transport is characterized by mass flow if a pressure gradient exists or by mass diffusion if a concentration gradient exists in the absence of a pressure gradient. For molecular diffusion the transfer can be quantified by Fick's 2nd Law of Diffusion which indicates that the rate of gas movement is a function of several parameters, most especially the concentration gradient. The simple form of Fick's Law for one-dimensional flow is shown as

$$-\frac{dm}{dt} = DA\frac{\partial C}{\partial X} \qquad (1)$$

where dm/dt is the rate of mass decrease ($g\ sec^{-1}$) over a boundary of area A (cm^2), $\partial C/\partial X$ the concentration gradient across the boundary thickness ($g\ cm^{-4}$), and D the diffusivity or diffusion coefficient of the gas ($cm^2\ sec^{-1}$).

The diffusivity D is normally dependent upon the 3/2 power of T°K and can be calculated using Gilliland's equation (3).

2. Surface Diffusion. The rate of surface migration of gas molecules from their initial contact point on the surface of a sorbent granule to a pore opening is normally considered rapid when compared to the intragranular diffusion step, although a rigorous treatment of the mathematics has not been developed. However, if the surface migration step were the slowest step, and therefore rate controlling, the differential rate of gas adsorption would be independent of linear velocity, nearly independent of inlet gas concentration, and vary inversely with the square of the sorbent particle size (4).

3. Intragranular Diffusion. Intragranular or Knudsen diffusion, also called pore or molecular diffusion, should prevail when the mean free path between intermolecular collisions is large compared to the pore diameter. In general, Knudsen diffusion occurs for gas phase reactions at one atmosphere pressure on surfaces whose pores are 20 nm in radius or smaller (5). Molecular flow due to Knudsen diffusion is independent of total pressure differences occurring in an adsorbent pellet as a result of reaction.

4. Physical Adsorption. For the study of the adsorption kinetics of a bed of carbon granules exposed to an inlet gas concentration at a finite volumetric flowrate, and for which the breakthrough time represents the first trace of gas found in the bed exit stream, pseudo first order kinetics should pertain. The kinetic equation, applicable to the study of gas adsorption by a carbon bed, was originally

derived by Wheeler (4) from a continuity equation of mass balance between the gas entering an adsorbent bed and the sum of the gas adsorbed by plus that penetrating the bed. The equation can be shown in the form of

$$t_b = \frac{W_e}{Q\rho}\left[W - \frac{\rho_p \rho}{k_v} \ln(C_o/C_x)\right] \qquad (2)$$

where t_b is the gas breakthrough time in minutes at which the concentration C_x appears in the exit stream, C_o the inlet concentration in g/cm³, Q the volumetric flow rate in cm³/min, ρ_p the bulk density of the packed bed in g/cm³, k_v the pseudo first order adsorption rate constant in min⁻¹, W the adsorbent weight in g, and W_e the kinetic saturation capacity in g/g at the arbitrarily chosen ratio of C_x/C_o. Values of t_b plotted as a function of W yield a straight line curve from whose slope and x-axis intercept the properties W_e and k_v can be respectively calculated.

5. Gas Desorption. The study of gas desorption from a bed of carbon granules can be approached in terms of a regeneration of the bed, no desorption resulting in no regeneration and complete desorption resulting in 100% regeneration. The theoretical basis for the approximate solution of the desorption equations was accomplished by Wheeler (7) in the form

$$t_R = \frac{W-W_r}{Q(C_e-C_o)}\left[W + \frac{\rho_p \rho}{k_d} \ln(1/1-f)\right] \qquad (3)$$

where t_R is the time for regeneration to obtain the fractional regeneration f, k_d is the desorption (or regeneration) rate constant, and W_o-W_r and C_e-C_o are modified capacity and concentration terms. The form of equation (3) follows closely that of the adsorption equation (2), an important difference being that the terms within the brackets are added to rather than subtracted from one another.

Independent calculations by Jonas and Svirbely (8) have shown that the adsorption rate constant k_v for carbon tetrachloride was approximately 780 times larger than the desorption rate constant k_d, that for chloroform was 1285 larger.

6. Chemical Reaction. A logical consequence of the fact that with activated carbons the adsorption rate constant was approximately 10^3 larger than the desorption constant is that the slower desorption step should permit a longer residence time for passage of the gas over those areas onto which the chemical impregnants were deposited. Thus, regardless of the actual reaction order of the gas with respect to the reacting chemical species a longer residence time indicates higher probabilities for reaction to occur. The postulated reaction of the cyanogen chloride with the chromate brochantite (believed to be the most active form of the chemical impregnants on the carbon) is catalyzed hydrolysis, shown as

$$CNCl + HOH \xrightarrow{Cu^{2+}} HOCN + HCl$$

and forming cyanic acid and hydrogen chloride.

7. Surface Renewal. The surfaces of the activated carbon, in the case of sorption of cyanogen chloride, are renewed by the further reaction or second hydrolysis step of the cyanogen chloride. For example, the cyanic acid is believed to react with another mole of water

$$HOCN + HOH \xrightarrow{HCr_2O_4^-} CO_2 + NH_3$$

forming the volatile and poorly adsorbed carbon dioxide and ammonia, thus renewing the carbon surface and making it available for continuation of the reaction mechanism.

4. ANALYSIS

A series of gas tests has been devised using cyanogen chloride as the adsorbate and activated and impregnated carbons as the adsorbents. The tests will encompass the following conditions: invariant inlet concentration and temperature (4×10^{-6}g/cm³ at 25°C); variable carbon weight (1 to 9 g); variable flowrate corresponding to superficial linear velocities of 2, 10, and 60 cm/sec and covering the range 0.30 to 0.007 seconds residence time; variable mesh size (12-30 and 70-80); and three relative humidities (0, 50, and 80%). The values of W_e and k_v are calculated from a plot of t_b vs W in accord with equation (2). The calculated values are then tabulated in the following matrix shown below in generalized alphabetic row and column notation.

Rel Hum %	Sup Lin Vel V_s (cm/sec)	Ads Cap W_e (g/g)				Ads Rate Const k_v (sec^{-1})			
		Act Carb		Imp Carb		Act Carb		Imp Carb	
		12-30 Mesh	70-80 Mesh	12-30 Mesh	70-80 Mesh	12-30 Mesh	70-80 Mesh	12-30 Mesh	70-80 Mesh
0	2	AA	AB	AC	AD	AE	AF	AG	AH
	10	BA	BB	BC	BD	BE	BF	BG	BH
	60	CA	CB	CC	CD	CE	CF	CG	CH
50	2	DA	DB	DC	DD	DE	DF	DG	DH
	10	EA	EB	EC	ED	EE	EF	EG	EH
	60	FA	FB	FC	FD	FE	FF	FG	FH
80	2	GA	GB	GC	GD	GE	GF	GG	GH
	10	HA	HB	HC	HD	HE	HF	HG	HH
	60	IA	IB	IC	ID	IE	IF	IG	IH

A proper analysis of the data so charted should permit the determination of which of the seven consecutive reaction steps is rate controlling.

5. REFERENCES

1. (a) Schneider P. & Smith J.M., A.I. Ch. E.J. 14, 762 (1968). (b) Masamune, S. & Smith J.M., A.I. Ch. E.J. 11, 34 (1965).

2. Jonas L.A. & Rehrmann J.A., CARBON, 10, 657 (1972).

3. Knudsen J.G. & Katz D.L., "Fluid Dynamics & Heat Transfer", p18, McGraw-Hill Book Co, N.Y. 1958.

4. Wheeler A., 10th Progress Report(1966), p22, AiResearch Mfg. Co., LA, CA, under Army Contract DA-18-035-AMC-279(A).

5. Wheeler A. (edited by Emmett P.H.), Catalysis, Vol II, 127, Reinhold Publishing Co., N.Y. 1955.

6. Wheeler A. & Robell A., J. Catal. 13, 299 (1969).

7. Wheeler A., 6th Progress Report, (1965), p85, AiResearch Mfg Co., LA, CA, under Contract DA18-035-AMC-279(A).

8. Jonas L.A. & Svirbely W.J., J. Catal. 24, 454 (1972).

EFFECT OF CONTINUED ACTIVATION ON ACTIVATED CARBON PORE STRUCTURE

A. J. JUHOLA
MSA Research Corporation, Evans City, Pa. 16033 U.S.A.

Introduction

The adsorptive characteristics of activated carbons change with continued activation. In a general way these changes have been associated with changes in pore structure and surface area. In this paper a closer investigation is made of the actual changes taking place in the pore structure and its effect on adsorptive characteristics.

Experimental Procedure

Three activation series were studied wherein the base or starting materials were coconut, bituminous coal and lignite. The water isotherm method (1,2) was used to determine the pore structures; the adsorption branch of the isotherm was used to calculate the pore cavity diameter distribution and the desorption branch to determine the pore constriction diameter distribution. This method covered the diameter range from ~7Å to ~2,000Å. Total pore volumes, corresponding to 100,000A pore diameter, were determined by measuring the carbon volume by helium and mercury displacements (1). Pore size distributions between 2,000Å and 100,000Å, normally measured by mercury penetrometry, were estimated in this study since they did not enter into the calculation in a significant manner. Pore structure determinations were further supported by vapor and aqueous phase iodine adsorption data (2). Effect of pore structure on acetone, carbon tetrachloride and benzene vapor adsorption was done according to procedures described in reference 3.

Experimental Results

Figures 1, 2 and 3 show families of complete pore size distribution curves for each of the base materials. The base material has a very predominating effect on the relative micro- and macropore volumes. In coconut carbons 64% of the total pore volume is micropore, while the percentage drops to about 50 for the coal base and about 20 for the lignite base. Common to all, continued activation increases the total pore volume and increases the micropore diameters, with the cavity diameters increasing at a faster rate than the constriction diameters. Table I presents calculated areas based on the constriction and cavity diameters; calculations were made by the method described in reference 2. The last column shows a decrease in cavity area/constriction area ratios for each group of carbons as activation is continued. This decrease in ratios further supports the above observation that the cavity diameters enlarge at a faster rate than the constriction diameters.

Iodine vapors adsorb in micropores, pores <30Å dia., by pore filling accompanied by monolayer coverage of the macropores during or after the pore filling process. Figure 4 presents correlations of the theoretical adsorbed weights as a function of experimentally observed weights. The good agreement between the calculated points and the solid line, which represents a perfect correlation, supports the micropore volume measurements as derived from water adsorption data.

Iodine in aqueous phase is adsorbed by monolayer surface coverage, hence, it is a means for determining the portion of surface area associated with pore constrictions and cavities. Figure 5 shows correlations of theoretical amount adsorbed as calculated from the constriction and cavity diameter curves when plotted as function of actual amount adsorbed. The points calculated from the cavity-diameter distribution curves are close to the solid line, representing perfect correlation. Points calculated from the constriction-diameter distribution curves deviate from the solid line with increasing divergence for carbons of increased activity. These test results show that as activation continues, the surface associated with cavities becomes the major part of the total surface area. Referring to Table I, the surface areas calculated for the cavities are then closer to the true surface area than those calculated for the constrictions.

Table I. Surface areas from pore constriction- and cavity-diameter distribution curves

Carbon	Surface area, m^2/g		Area ratio,
	Constrictions	Cavities	Cavity/Const.
1	1250	1000	0.80
2	2050	1290	0.63
3	2140	1170	0.55
4	680	640	0.94
5	940	810	0.86
6	1280	1040	0.81
7	1470	1170	0.80
8	1020	770	0.75
9	1030	790	0.77
10	1500	1080	0.72
11	1580	1090	0.69

The effect of pore structure on the carbon's ability to adsorb carbon tetrachloride, benzene and acetone is shown in Figure 6. Two sets of test results are shown, one at low relative vapor pressures and one at high relative vapor pressures, as given below:

Vapor	p/p_o	Pore dia., Å
Carbon tetrachloride	0.0005	18.6
Carbon tetrachloride	0.30	50.
Benzene	0.001	12.6
Benzene	0.25	37.3
Acetone	0.0005	14.6
Acetone	0.30	35.

In pores of the diameter being considered, adsorption proceeds by pore filling, hence, at the given p/p_o pores will fill with adsorbed liquid to the diameter given in the last column. The procedures for making these calculations are given in reference 3. As shown in the figure, adsorption at the higher p/p_o fills the micropores, while adsorption at the lower p/p_o fills only the smallest micropores. With continued activation the ability of the carbon to adsorb at low p/p_o decreases while at the higher p/p_o it increases.

References

1. Juhola, A. J. and Wiig, E. O., J. Am. Chem. Soc. 71, 561, 2069 and 2078 (1949)
2. Juhola, A. J., Carbon 13, 437-442 (1975)
3. Juhola, A. J., Paper submitted November 8, 1976 for publication in the Carbon journal.

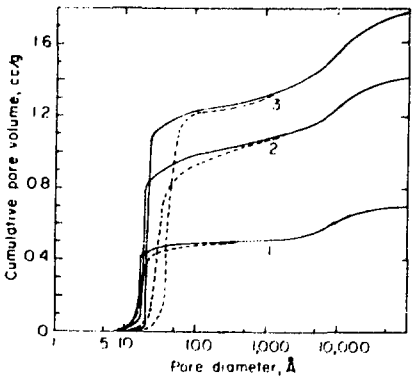


Fig. 1. Pore size distribution, coconut carbons, constrictions ——, cavities ---.

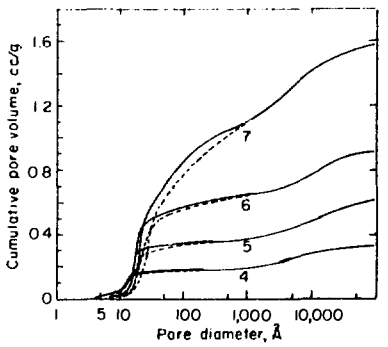


Fig. 2. Pore size distribution, coal carbons, constrictions ——, cavities ---.

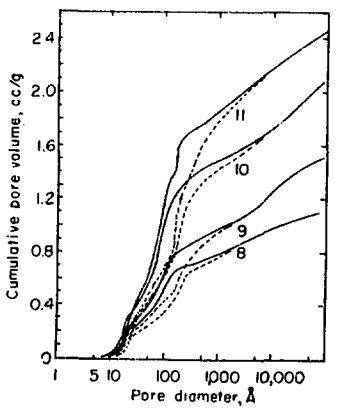


Fig. 3. Pore size distribution, lignite carbons, constrictions ——, cavities ---.

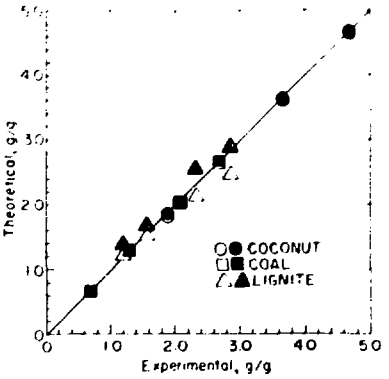


Fig. 4. Iodine vapor adsorption, constrictions-solid points, cavities-open points.

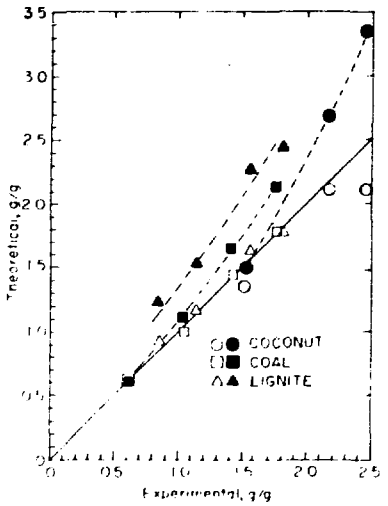


Fig. 5. Aqueous phase iodine adsorption, constrictions-solid points, cavities-open points.

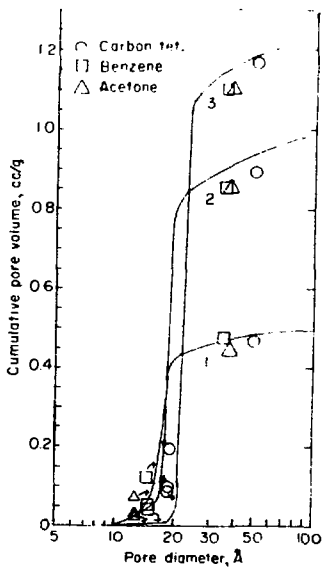


Fig. 6. Distribution of pore constriction diameters, coconut carbons.

CHEMISORPTION OF HYDROCARBONS ON GRAPHITIZED CARBON BLACKS AT 300°C*

W. P. Hoffman, F. J. Vastola and P. L. Walker, Jr.
Department of Material Sciences
The Pennsylvania State University
University Park, PA 16802

Introduction

The physical adsorption of hydrocarbons on graphitized carbon blacks has been studied under various conditions (1-3). However, there is virtually no literature on the chemisorption of hydrocarbons on these materials or on any carbon other than evaporated carbon films (4). This might be due, in part, to the rather small active surface area (<0.6% of the total area) that chemisorbed hydrocarbons will occupy on a graphitized carbon black. This surface area that is active for hydrocarbon chemisorption is analogous to the oxygen active surface area (ASA), as measured by Laine et al. (5), on the same material.

The purpose of this study is not to undertake the difficult task of determining how hydrocarbons bond to the surface but rather to determine the "reactivity" of various hydrocarbons to the surface and what factors have the greatest effect on their adsorption. The gases used were C_1 to C_4 alkanes and alkenes.

Experimental

The graphitized carbon black used in this study was Graphon, supplied by the Cabot Corp. Samples were burned off to 5-15% weight loss in air at 450°C. The samples were subsequently treated in 1 atm of Cl_2 at 900°C to remove metallic surface impurities. After pumping to 10^{-8} Torr with the temperature again at 900°C, the samples were treated with H_2 at a starting pressure of .05 Torr to remove chemisorbed chlorine. Finally, the samples were pumped to 10^{-8} Torr and the temperature was raised to 950°C to remove chemisorbed H_2.

The BET area of the prepared samples ranged between 80-90 m^2/g, while the oxygen active surface area, as determined by Laine (5), ranged between 0.8-1.8 m^2/g.

Adsorption was carried out at 300°C in a volumetric apparatus with a total volume of 17.9ℓ. Adsorption was followed using a Baratron electronic differential manometer with a sensitivity of 1×10^{-5} Torr.

The rate of chemisorption of all the gases except methane decreased to a negligible value in 1 hr. In order to determine the amount chemisorbed, gas was introduced at 12 mTorr and the quantity of gas adsorbed in 1 hr recorded. The sample was then pumped to 10^{-8} Torr with the temperature held constant, and gas was reintroduced at 12 mTorr for 1 hr. Using this approach, the amount adsorbed during the second cycle was taken as equal to the gas physically adsorbed, while the difference in the amount adsorbed in the two cycles was taken as the amount chemisorbed.

After completion of the two adsorption cycles, the samples were pumped to 10^{-8} Torr at adsorption temperature. The temperature was then raised stepwise to 900°C in a closed system and products of desorption measured. The samples were cleaned by heating at 950°C until the pressure dropped to 10^{-8} Torr, prior to commencing a new adsorption run.

A CEC Model 21-614 residual gas analyzer was used to check the purity of each gas (>99.9%) and to monitor the gas phase during adsorption and desorption. A Vacion pump was used in conjunction with an oil diffusion pump and a rotary floor pump to obtain a pressure of 10^{-8} Torr.

Results and Discussion

Chemisorbed species cannot be removed at adsorption temperature but desorb only at elevated temperatures. Isotherms for these adsorptions are of the Langmuir type, with saturation being reached at a pressure <5 mT. The amount of each gas chemisorbed increased with burn-off of the Graphon.

All gases studied are listed in order of decreasing surface coverage in the first column of Table 1. The surface area covered by each adsorbate (m^2/g) is placed in square brackets, the numbers running diagonally down the table from left to right, that is from butadiene to methane. The numbers represent average areas covered during the series of runs. These areas were calculated from the product of the number of molecules adsorbed and the surface area that each molecule occupies. Estimated molecular surface areas (A^2) are given in parenthesis in column 1 of Table 1. The calculation of these molecular areas for the hydrocarbons consisted of constructing each molecule, considering both ionic and van der Waals radii, and measuring the surface area covered by their projection. Since extensive work has been done on the dissociative chemisorption of oxygen and hydrogen on Graphon (5,6), these molecules were included for comparison and the molecular areas calculated by the previous workers were used for these gases.

For all but the most active gases, the surface had to be very clean for chemisorption to take place. Times for the rate of chemisorption to decrease to a negligible value ranged from <15 min for n-butane and butadiene to several hours for methane. During adsorption of each gas, the gas phase was monitored. In each case, only the adsorbate could be detected. No hydrogen was seen in the gas phase so if C-H bonds were broken during chemisorption, the hydrogen also chemisorbed.

In order to determine what factors affect chemisorption, a series of blockage runs was made for each pair of gases. These runs involve adsorbing a gas and pumping off the physically adsorbed portion. (This is the gas shown as preadsorbed in Table 1.) Then a second, different gas

*Supported, in part, by a Gulf Oil Company Fellowship.

was adsorbed (shown as blocked gas in Table 1) without desorbing the chemisorbed portion of the first gas. Another adsorption was then performed to determine what portion of the blocked gas was physically adsorbed so that the amount of blocked gas chemisorbed could be determined. As is seen in Table 1, the preadsorbed gas blocked chemisorption of the second gas to a varying degree. The percentages given are those of sites blocked; for example ethylene, which occupies 0.46 m^2/g, blocks 90% of the 0.57 m^2/g area that propylene would normally occupy on a clean surface. Where two different percentages are given for a single pair of gases, the top one was determined early in the series; and the bottom values were determined near the end of the series.

The type and distribution of the sites has the greatest effect on the chemisorption of hydrocarbons on Graphon. On each hydrocarbon adsorption-desorption cycle, the surface is slightly changed. However, the greatest change comes with the first hydrocarbon cycle on each new sample of Graphon, resulting in approximately a 40% decrease in the amount of any gas that can subsequently be chemisorbed. All the data presented here were taken after the first hydrocarbon cycle. The structure and orientation of the adsorbate have less of an effect on adsorption than do surface changes. Adsorption is greater for double bonds and larger molecules. However, with increasing molecular length (>3 carbon atoms), the factor of size may come into play to decrease adsorption. Blockage by the preadsorbed gas depends on these factors, in addition to the percentage of common sites they occupy.

The fact that the surface changes slightly with each hydrocarbon cycle is attributed to carbon deposition. That is, during desorption at elevated temperatures, most of the adsorbate carbon stays on the surface, as a result of cracking of the adsorbate and most of the hydrogen is desorbed as hydrogen gas.

The carbon left on the surface is probably on the sites active for hydrocarbon chemisorption. These new sites are still active. The cumulative effect is to gradually decrease the active area available to some of the molecules depending on their size and activity. After the initial hydrocarbon cycle, surface coverage and blockage is small for each subsequent cycle. For example, the chemisorption of n-butane decreased only 15% following more than 100 cycles. Thus the same sample can be used for numerous blockage runs with good reproducibility.

References

1. Hoory, S. E. and Prausnitz, J. M., Trans. Faraday Soc., 63, 455 (1966).

2. Friederich, R. O. and Mullins, J. C., Ind. Eng. Chem. Fund., 11, 439 (1972).

3. Stacy, T. D., Hough, E. W., and McCain, W. D., J. of Chem. and Eng. Data, 13, 74 (1968).

4. McLintock, I. S. and Orr, J. C., Third Conf. Ind. Carbon and Graphite, 201 (1970).

5. Laine, N. R., Vastola, F. J., and Walker, P. L., Jr., J. Phys. Chem., 67, 2030 (1963).

6. Bansal, R. C., Vastola, F. J. and Walker, P. L., Jr., Carbon, 9, 185 (1971).

TABLE 1

BLOCKING EXPERIMENTS AT 300°C ON 14% BURN-OFF GRAPHON

	Gas Preadsorbed										
Blocked Gas,%	C=C-C=C	C=C-C	O_2	C=C	C-C-C-C	C-C(C)-C	C-C-C	C-C	C-C(C)-C	H_2	CH_4
C=C-C=C (29.6)	[0.59]	81/83	71/64	79/72	74/81	64/76	67/68	67/65	57	22	14
C=C-C (23.4)	∿100	[0.57]	96	90	98	97	96	92	84	22	18
O_2 (16.6)	89/89	83/83	[0.52]	77/85	87	87	86	77	65	30	11/11
C=C (20.5)	∿100	99	97	[0.46]	99	98	98	93	88	22/26	18
C-C-C-C (27.7)	∿100	∿100	99	91	[0.33]	∿100	∿100	∿100	67	26	18
C-C(C)-C (25.1)	∿100	∿100	∿100	97	∿100	[0.30]	∿100	∿100	75	26	4
C-C-C (22.6)	∿100	∿100	∿100	98	∿100	∿100	[0.27]	∿100	87	26	5
C-C (19.7)	∿100	∿100	∿100	∿100	∿100	∿100	∿100	[0.16]	91	26	5
C-C(C) (20.2)	∿100	∿100	∿100	∿100	∿100	∿100	∿100	∿100	[0.16]	26	9
H_2 (16.6)	∿100	∿100	∿100	∿100	∿100	∿100	∿100	∿100	∿100	[0.09]	30
CH_4 (16.2)	∿100	∿100	∿100	∿100	∿100	∿100	∿100	∿100	∿100	∿100	[0.01]

USE OF CARBON FOR REMOVAL OF AMMONIA FROM WATER*

O. P. Mahajan, A. Youssef and P. L. Walker, Jr.
Department of Material Sciences
The Pennsylvania State University
University Park, PA 16802

Introduction

Ammonia is produced in waste water and sewage treatment plants. The presence of ammonia in water is undesirable because ultimately it gets converted into nitrites and nitrates which act as nutrients for algae growth. The present study describes the use of surface-modified carbons for the removal of ammonia.

Experimental

Activated carbons supplied by five different companies, namely A (12x40 mesh), B (4x10 mesh), C (8x30 mesh), D (6x8 mesh) and E (4x10 mesh) were used. These carbons had N_2 areas (77°K) in the range 750-830 m^2/g and CO_2 areas (298°K) in the range 540-825 m^2/g. Aqueous suspensions of the carbons had alkaline pH values in the range 7.1-9.1.

The as-received carbons were given oxidative treatments with dry and moist air at 285°C, HNO_3, 0.2N $(NH_4)_2S_2O_8$ (ammonium persulfate), and 2N H_2O_2. Moist air refers to an air-water vapor mixture at a total pressure of 1 atm containing water vapor at a partial pressure of 17 Torr. For treatment with HNO_3, carbon was heated with concentrated HNO_3 (10 cm^3 HNO_3/g carbon) to dryness at 80°C. For treatment with $(NH_4)_2S_2O_8$ and H_2O_2, 2g portions were mixed with 50 cm^3 of the oxidizing solution. The suspensions were shaken mechanically for 48 hr at room temperature. After oxidative treatment with different oxidizing solutions, the carbons were washed free of excess oxidants with water and dried at 110°C.

Neutralization of 0.1N solutions of NaOH, $NaHCO_3$, Na_2CO_3 and NH_4OH by carbons was determined by mixing 1g portions with 100 cm^3 of solution. After attainment of equilibrium, the fall in concentration of NaOH, $NaHCO_3$ and Na_2CO_3 solutions was determined by titration with HCl, whereas decrease in concentration of ammonia was determined using an Orion ammonia electrode.

The efficacy of carbons for removal of ammonia under dynamic (flow) conditions was studied in a Pyrex glass column of 2 in diameter. The carbon bed (height, 4 in) was held between two glass wool plugs (height, 2 in). During the runs, the level of ammonia in the column was always kept constant (about 2 in above the upper glass wool plug). Ammonia was passed through the bed at a constant flow rate. The concentration of ammonia in the effluent was followed as a function of time until the outlet concentration equalled the inlet concentration. The 'spent' carbon was regenerated with 0.1N HCl followed by washing with water until free from chloride ions.

Results and Discussion

The as-received carbons did not adsorb noticeable amounts of ammonia. However, following oxidation all the carbons adsorb significant amounts of ammonia (Table 1). The pH values of aqueous suspensions of various oxidized samples and the amounts of various bases neutralized by the carbons are listed in Table 1. The efficiency of various oxidative treatments to enhance ammonia uptake of a given carbon follows the order: HNO_3 > $(NH_4)_2S_2O_8$ > H_2O_2 > moist air > dry air. Amounts of $NaHCO_3$, Na_2CO_3 and NaOH neutralized by various samples follow the same trend as the adsorption of ammonia, whereas pH values of the aqueous suspensions decrease in the reverse order. For a given carbon, the amounts of different bases neutralized vary in the order

$$NaOH > Na_2CO_3 > NH_4OH > NaHCO_3$$

Various oxidative treatments had little or no effect on surface areas of carbons. Although for each oxidative treatment surface areas of samples derived from carbon C are lower than those of the other carbons, samples from carbon C have the highest ammonia removal capacities. The high surface area of activated carbon often determines its use in most industrial applications. However, in the present study the chemical nature of the surface, rather than the magnitude of the surface, determines ammonia removal capacity.

Boehm (1) has suggested a selective neutralization technique using $NaHCO_3$, Na_2CO_3 and NaOH for estimating the concentration of carboxylic, lactonic and phenolic acid groups. He has concluded that $NaHCO_3$ neutralizes carboxylic groups, Na_2CO_3 neutralizes carboxylic and lactonic groups, and NaOH neutralizes carboxylic, lactonic and phenolic groups. That is, NaOH gives a measure of total surface acidity of carbons. Boehm also found that for completely oxidized carbons twice as many acid groups were neutralized with Na_2CO_3 as with $NaHCO_3$, whereas with NaOH three times the $NaHCO_3$ neutralization was achieved.

In the present study when the amounts of $NaHCO_3$, Na_2CO_3 and NH_4OH neutralized by different samples were plotted against amounts of NaOH neutralized, the data points in each case fell more or less on straight lines passing through the origin. From the plots, ratios of $NaHCO_3$, NH_4OH and Na_2CO_3 neutralized relative to NaOH were found to be 0.36, 0.51 and 0.63, respectively. These results show that for a given carbon, irrespective of the organic precursor, amount and nature of inorganic impurities present, the activation process, the degree of activation and subsequent oxidative treatment, the concentration of acid groups of different strengths relative to the total surface acidity is more or less constant.

Since the amount of Na_2CO_3 neutralized by a carbon has been suggested to be a measure of the concentration of carboxyl and lactone groups (1), the amount of CO_2 evolved on outgassing a carbon at elevated temperatures should be theoretically equivalent to the Na_2CO_3 neutralization capacity.

*Supported by the Office of Water Research and Technology.

However, in this study amounts of CO_2 evolved were invariably greater than the Na_2CO_3 values.

Carbons A and C oxidized with HNO_3 were used in dynamic studies. Breakthrough times and bed capacities for different flow rates are listed in Table 2. Breakthrough times increase with decreasing flow rates, as expected. Capacities are independent of flow rate after the first cycle, indicating the presence of minimal external mass transport resistance to adsorption. Regeneration of the carbon beds between successive runs was conducted by treatment with HCl. Following the first ammonia adsorption run, about 95% of the ammonia adsorbed could be 'desorbed' with HCl. In subsequent runs, essentially all adsorbed ammonia could be desorbed. The irreversibly adsorbed ammonia has been suggested to be due to the presence of some, as yet unidentified, surface functional group (2).

In conclusion, the results of the present study suggest that oxidized carbons, preferably those oxidized with HNO_3, should be strong contenders for ammonia removal from waste waters.

References

1. Boehm, H. P. in "Advances in Catalysis", Vol. 16, Academic Press, New York, 1966, pp. 179-268.

2. Puri, B. R. and Mahajan, O. P., J. Indian Chem. Soc., 41, 586 (1964).

Table 1 - BASE NEUTRALIZATION CAPACITIES AND pH VALUES OF CARBONS

Oxidizing Agent	Carbon	pH	Base neutralization capacity, m-equiv/g			
			$NaHCO_3$	NH_4OH	Na_2CO_3	NaOH
HNO_3	A	4.40	1.40	1.80	2.30	3.60
	B	4.40	1.25	1.60	2.10	3.20
	C	4.02	2.15	2.80	3.55	5.55
	D	4.35	1.30	1.70	2.20	3.60
	E	4.35	1.35	1.80	2.25	3.65
$(NH_4)_2S_2O_8$	A	4.95	0.95	1.40	1.70	2.65
	B	4.95	0.90	1.40	1.70	2.65
	C	4.14	1.70	2.60	3.25	4.95
	D	4.92	1.65	1.60	1.95	3.00
	E	4.82	0.95	1.40	1.75	2.65
H_2O_2	A	5.25	0.60	0.90	1.05	1.60
	B	5.30	0.65	0.90	1.05	1.65
	C	4.28	0.80	1.20	1.40	2.20
	D	5.22	0.45	0.70	0.80	1.25
	E	5.11	0.60	0.90	1.05	1.65
Moist air	A	5.60	0.40	0.65	0.65	1.05
	B	5.27	0.40	0.65	0.70	1.15
	C	5.14	0.55	0.85	0.85	1.40
	D	5.28	0.40	0.65	0.60	1.00
	E	5.65	0.45	0.85	0.75	1.20
Dry air	A	5.81	0.20	0.40	0.45	0.70
	B	5.31	0.20	0.40	0.45	0.65
	C	5.15	0.35	0.70	0.85	1.25
	D	5.30	0.20	0.40	0.45	0.65
	E	5.65	0.32	0.60	0.75	1.10

Table 2 - BREAKTHROUGH TIMES AND BED CAPACITIES

Sample	Flow rate (cm^3/min)	Breakthrough time (min)	Bed capacity (m-equiv/g)
C	95	30	2.63
	95	30	2.48
	125	22	2.46
	165	16	2.46
	200	13	2.44
	280	10	2.42
A	90	20	1.68
	90	20	1.58
	130	14	1.59
	165	11	1.56
	200	9	1.56
	260	7	1.52

DISSOCIATIVE STORAGE OF HYDROGEN ON MODIFIED CARBON SURFACES

R. K. Sinha and N. J. Wagner

Interest in the use of hydrogen as a fuel prompted investigations into the use of activated carbon as a means of storing hydrogen. At 298°K in low pressure investigations, type PCB activated carbon irreversibly adsorbed 1.3 wt-% atomic hydrogen in contrast to type BPL activated carbon which reversibly adsorbed 0.59 wt-% atomic hydrogen.

At high pressures molecular hydrogen was dissociated in situ using impregnants known to dissociatively adsorb hydrogen. Previous work by others has suggested that suitable impregnants should promote hydrogen atom spillover onto the carbon surface resulting in enhanced capacities similar to those found for atomic hydrogen at low pressures. Adsorption isotherms were determined for a series of impregnants on type BPL activated carbon over the temperature range 195-423°K. At 122 atmospheres pressure and 298°K, a maximum of 0.60 wt-% hydrogen was adsorbed on a Pd impregnated carbon. A second carbon impregnated with Pt was able to adsorb 0.58 wt-% hydrogen under similar conditions. At 195°K the Pd and Pt impregnated type BPL activated carbons adsorbed 1.08 and 1.10 wt-% hydrogen, respectively. A series of other impregnants were tested; however, all displayed lower capacities. The effects of pressure, temperature and impregnant were investigated and will be reported.

CORRELATION BETWEEN STRUCTURE AND PROPERTIES OF CHOPPED-FIBER CARBON-CARBON COMPOSITES

W. G. Bradshaw, P. Pinoli, and R. F. Karlak

Department of Materials Sciences, Lockheed Palo Alto Research Laboratory
3251 Hanover Street, Palo Alto, California 94304

Introduction

Structure-property relationships were studied in random chopped-fiber, carbon-carbon composites. Flexural strength, strain-to-failure, and modulus were correlated with graphite crystallite size and lattice strain as affected by processing variations.

Experimental Method

Disc-shaped specimens were prepared from chopped, copolymer PAN-based fibers and 20- to 80-weight-percent high-char yield, p-polyphenylene-type, graphitizing resins, by dispersing the fibers in a solution of the resin, partially curing, attritioning, molding, and completely curing followed by pyrolysis to 1000°C (Ref. 1) and graphitization for 8 or 16 hours at 2600°C. Fibers were made from the oxidized precursor by heating to 1800°C (PAN-1800) or 2600°C (PAN-2600). Flexural properties were measured on a four-point bend device using specimens with a 10:1 length:thickness ratio strain gaged on the tension surface. Crystallite variations were determined from x-ray diffraction line profiles.

Experimental Results

Data on the effect of matrix concentration for PAN-1800 composites heat-treated 16 hours at 2600°C are plotted in Figure 1. Flexural strength reaches a maximum at an initial matrix concentration of 50 to 60% (Curve A). Similarly, strain-to-failure reaches a maximum at an initial matrix concentration of 60% (Curve B). The best combination of strength, 10,260 psi, and strain-to-failure, 0.60%, are obtained when the matrix concentration is 60%.

Discussion of Results

Flexural behavior was reconciled by analyzing x-ray diffraction-line broadening and the stresses developed by matrix contraction during carbonization. The former provides an indication of the crystallite size and strain distribution, whereas the latter provides a possible mechanism for the graphitization trends.

- X-ray line-broadening analyses of all samples show a linear relationship between matrix content and either crystallite size or lattice strain after carbonization and graphitization, as shown in Figure 2. A linear relationship exists in the range of matrix concentrations from 35 to 80%. Size and strain broadening occur simultaneously but separation was not possible with the simplified analysis used with most samples. For a limited number of samples, a more detailed calculation was made using the change in broadening with diffraction order and more precise corrections (Refs. 2 and 3). These results revealed that both factors are present, but mean crystallite size depends more upon the matrix concentration than does the strain parameter. The latter was thus disregarded.

- Crystallinity and mechanical behavior correlate well for all samples. Figure 3 shows that both the ultimate-flexural strength (F^{FU}) and strain (ϵ^{FU}) increase with crystallite size. This increase demonstrates the importance of lattice perfection for producing a composite with good mechanical properties, and together with preceding data shows that the best results are attained with an initial matrix precursor concentration of about 60 weight percent.

- Mechanisms responsible for the crystallinity changes with matrix content appear to be related to residual stresses in the matrix, induced by contraction of the matrix during carbonization. A theoretical analysis, assuming that each fiber is encased in a cylindrical sheath of matrix, shows that increasing the matrix content (sheath thickness) causes the hoop, radial, and longitudinal matrix-stresses to increase as do the hydrostatic stresses in the fiber. Microscopic evidence of matrix graphitization strongly suggests that this is where most of the observed effects are taking place. Also, since a nongraphitic, amorphous (glasslike carbon) matrix would be brittle regardless of fiber properties, improved mechanical properties would not be expected from crystalline changes in the fiber alone.

Conclusions

The flexural strength and strain-to-failure of random short-fiber, carbon-carbon composites are directly proportional to the matrix content (and are not the fiber content, as might be expected) in the range from 35 to 60 weight percent of initial precursor, and this results from stress-induced graphitization of the matrix that reduces its brittle behavior by increasing the crystallite size, by reducing lattice strains, or by both.

References

1. Bradshaw, W. G. and Pinoli, P. C., 12th Biennial Conference on Carbon, 297 (1975)

2. Ergun, S., Carbon, 14, 139 (1976)

3. Thrower, P. A. and Nagle, D. C., Carbon, 11, 663 (1973)

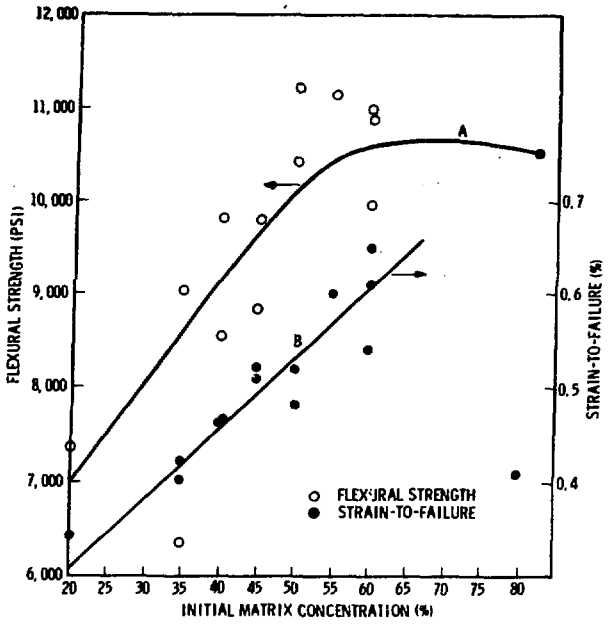


Fig. 1 Flexure Strength and Strain-to-Failure Versus Matrix Concentration for Pan 1800 Heat-Treated to 2600°C for 16 Hours

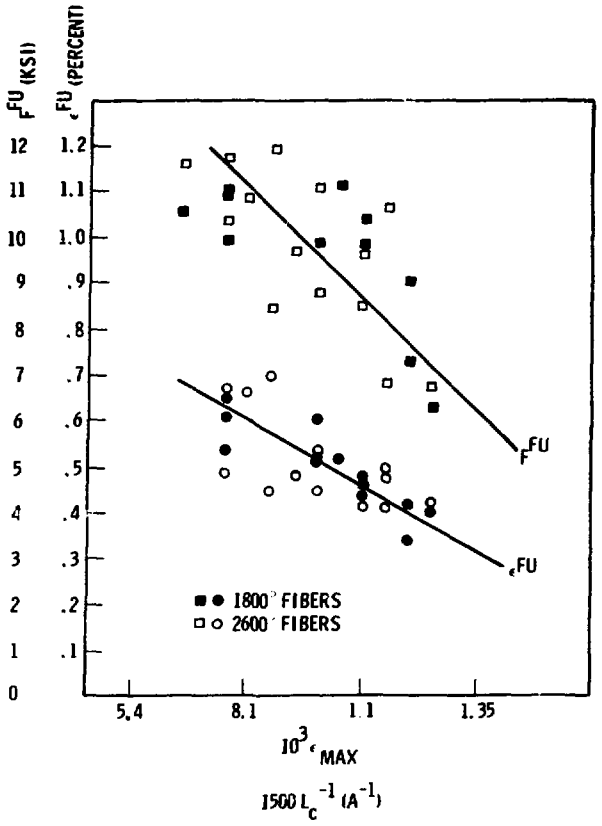


Fig. 3 Cumulative Plot of Flexural Strength (F^{FU}) and Strain-to-Failure (ϵ^{FU}) Versus Maximum Lattice Strain and/or Reciprocal Crystallite Size for Carbon-Carbon Random Fiber Composites With Initial Matrix Content Ranging From 30 to 60 Weight Percent

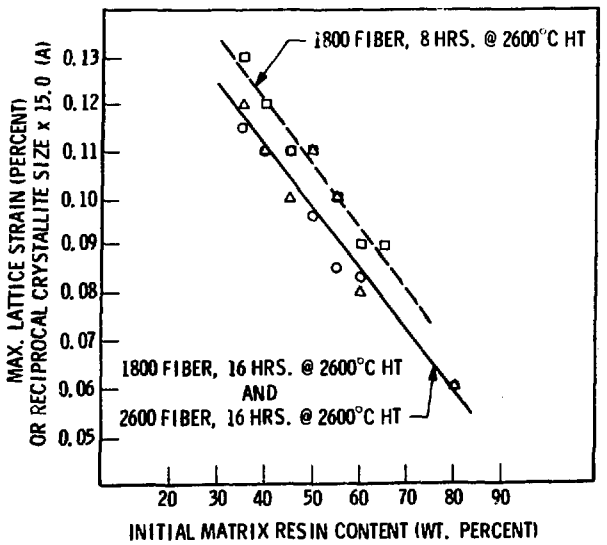


Fig. 2 Crystallographic Lattice Strain Normal to Basal Planes and/or Mean Reciprocal Crystallite Size in That Direction for Carbon-Carbon Composites With Initial Matrix Resin Content in Range From 30 to 80 Weight Percent

CARBON FIBRE REINFORCED COMPOSITES FOR APPLICATIONS AT ELEVATED TEMPERATURES

E. FITZER and M. HEYM

Institut für Chemische Technik
Universität Karlsruhe, W.-Germany

1. Introduction

The development of high strength continuous fibre materials from light weight elements enables us to fabricate high performance composites having mechanical properties similar to steel, but at the same time a density which is five times lower.

In fig.1 the tensile strength and YOUNG's modulus of commercially available continuous low density fibre materials is shown. The black areas correspond to the different varieties of carbon fibres. It can be recognized that carbon fibres with strength up to 4000 MN/m^2 or moduli above $50 \cdot 10^4$ MN/m^2 can be fabricated. For room temperature applications most of these fibre materials are already successfully used, mainly as reinforcing component in epoxy matrix. Boron fibres are also tested as reinforcement for aluminium. However at present there is no structural application of fibre reinforced composites at elevated temperature say above 150°C, because the true potential and applicability of temperature resistant fibre reinforced composites is not yet known sufficiently.

Therefore we studied the fabrication, the chemical stability and the mechanical properties of unidirectionally fibre reinforced composites with the most promising fibre/matrix combinations at ambient and especially at elevated temperatures, that means up to 500°C in air. The study includes carbon fibre reinforced phenolic resin and various polyimide resins, carbon fibre- and boron fibre reinforced aluminium and carbon-carbon (C/C)- composites. Carbon fibre reinforced epoxy composites prepared from a commercial C/Epoxy-prepreg (FIBREDUX 911) have been tested for comparison with composites with high temperature resistant polymer matrix.

2. Experimental

The polymer matrix composites have been fabricated by impregnating surface treated carbon fibre yarns with resin solutions and wet winding them into the shape of prepregs. The prepregs have been precured and subsequently hot molded to receive bars (2x5x160 mm) which have been postcured up to the final strength. Three different kinds of polyimide resins have been used: Resin 212 is a processable condensation polyimide which releases acetic acid during hardening; P 13 N is a prepolymer which undergoes imidization at curing temperatures between 210 - 260°C and crosslinkage of the nadic acid endgroups above 290°C, Kerimid 601 is a poly-bismaleinimide. The phenolic resin consists of a novolac, which has been hardened with hexamethylentetramine.

The C/C-composites which have been used for tests at elevated temperatures were prepared by liquid infiltration of the carbon fibre yarns with molten coal tar pitch (softening point 63°C) as carbon matrix precursor. The fibre content was controlled by hot pressing the infiltrated carbon fibres into laminates. The laminates were baked up to 550°C under elevated nitrogen pressure and subsequently upto 1400°C under atmospheric pressure. The porous carbon composite framework obtained after carbonization was reimpregnated with pitch and recarbonized four times which is sufficient to reach maximum strength. Further details on this technique have been published by FITZER et al.(1972).

Boron fibre reinforced aluminium samples have been prepared using commercially available tapes with B_4C-and SiC-coated boron fibres. In these tapes the fibres are held in position on an aluminium foil (6061) by plasma sprayed aluminium (6061). The tapes were combined in an eutectic bonding process.

Carbon fibre reinforced aluminium composites have been prepared by infiltration of carbon fibres which were coated with nickel or silver as wetting promoter with molten aluminium at temperatures of about 700°C. The influence of the different wetting agents on the composite fabrication process and the composite properties as well as the effect of SiC, TiN, TiC-coatings on the carbon fibres as diffusion barriers between carbon and aluminium during composite fabrication and especially during application at elevated temperatures will be discussed.

3. Results

In table 1 the room temperature properties of the different studied composite materials are compiled. It can be recognized that the fibre strength is almost completely utilized in the case of C/epoxy-, C/phenolic-,B/aluminium- and C/C-composites. The incomplete fibre strength yield for composites with polyimide matrices is caused by a residual porosity due to the release of condensation products or traces of the used high polar solvent during postcuring.

The interlaminar shear strength is very high in epoxy and phenolic matrix composites and comparatively low for polyimidematrix composites. In the case of aluminium matrix composites interlaminar shear strength is so high that the short beam test could not cause delamination. The given values there-

fore have to be regarded as minimum values, the real shear strength is lying higher.

The flexural strength of the composites as function of the test temperature is shown in fig.2. It can be recognized that C/epoxy composites loose their strength completely up to a test temperature of 200°C. C/Resin 212-composites show a better strength retention especially between 200 and 300°C. Most surprising is the excellent elevated temperature strength of C/phenolic-composites which is similar to that of B/aluminium-composites. As can be recognized the absolute room temperature strength of B/aluminium-composites exceeds that of C/aluminium-composites but the difference in strength vanishes at a test temperature of 450°C. The strength of C/C-composites does not decrease at all with increasing test temperature, thus being superior to all other composite materials at temperatures above 400°C. The fracture behaviour of the different composite materials at room temperature and at elevated temperature will be discussed.

Futhermore the behaviour of the composites during long time exposure in air at elevated temperatures under static flexural load will be shown. It turns out that improvements of the mechanical temperature resistance of B/aluminium composites can be realized by age hardening of the matrix. The chemically caused temperature limits will be pointed out by microscopic analysis of heat treated composites and the dependence of the composite strength on the barrier function of B_4C-and SiC-protective coatings on the boron fibres will be discussed.

Thermogravimetric measurements of the oxidation behaviour of C/C-composites at elevated temperatures in air have shown that these composites are sensitive against oxidation already at temperatures above 350°C. Methods for improving the oxidation resistance of C/C-composites have been studied which allow an application of C/C-composites in oxidizing atmosphere up to 500°C.

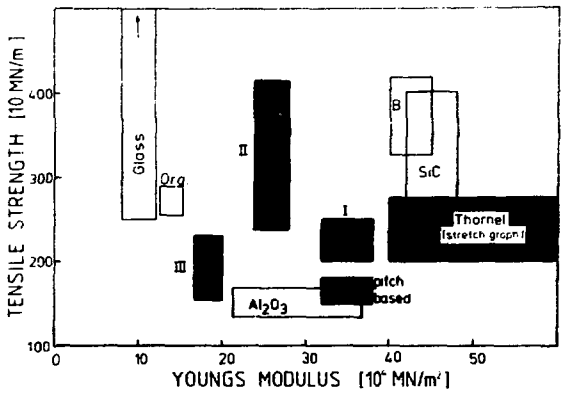


Fig.1: Tensile strength and YOUNG's modulus of high performance fibre materials

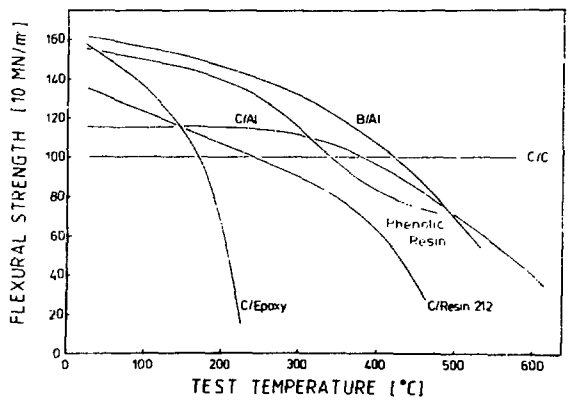


Fig.2: Flexural strength of unidirectionally fiber reinforced composites as function of test temperature

Reference:

E. FITZER, B. TERWIESCH, 1972 Carbon 10, p. 383

Tab.1: Mechanical room temperature properties of unidirectionally fibre reinforced composites

Matrix	Epoxy	Phenolic	Kerimid	P 13 N	Resin 212	Aluminium			Carbon
Fibre vol. fraction v/o	55	58	56	60	60	45	49	60	50
Fibretype	T 300 B	Mag.HTS	Mag.HTS	Mod.IIS	Mag.HTS	Graf.HM	B/B_4C	B/SiC	Mod.I
Flexural strength 10 MN/m²	158	155	127	112	135	115	163	172	95
Fibre strength yield %	96	99	84	78	83	78	82	96	100
Flexural modulus 10^4 MN/m²	11,5	12,4	12,6	11,4	13,0	24,0	16,8	20,0	15,4
Strain to failure %	1,5	1,2	1,1	1,1	1,1	0,45	1,0	0,9	0,6
Interlam. shear strength MN/m²	83	88	44	56	57	(55)	(75)	(75)	25
Bulk density 10³ kg/m³	1,45	1,50	1,45	1,45	1,42	2,16	2,5	2,55	1,65

OXIDATION BEHAVIOR OF SOME CARBON/CARBON COMPOSITES

D.B. Fischbach and D.P. Stegrove
Department of Mining, Metallurgical & Ceramic Engineering, University of Washington FB-10
Seattle, Wash. 98195

The oxidation behavior of a family of commercial carbon/carbon composite materials was studied with particular attention to microstructural aspects. The composites were characterized before oxidation by X-ray diffraction and porosimetry (1); and by ignition and isothermal burnoff behavior in dry air. The major emphasis was on scanning electron micrography of oxidized samples, and some results of these studies are described here.

Four commercial laminar carbon fiber cloth/carbon binder matrix composites (Carbitex P , Carborundum Co.) were studied: C-100, carbonized fiber and matrix; C-500, graphitized fiber, carbonized matrix; C-700, C-730, graphitized fiber and matrix (different cloth weaves). The fibers were ex-rayon. A plain weave cloth was used in C-100, 500, 700 and these composites were less anisotropic than C-730, made of a flatter satin weave. X-ray diffraction showed that the composites were more graphitic, d(004) $\cong$ 3.43A (C-100), 3.39 (500), 3.36 (700,730), than the fibers, d(004) $\cong$ 3.48A (C), 3.43 (G), indicating a graphitic primary binder. Micrography revealed a laminar, oriented primary binder and a "glassy" impregnant binder phase (see Fig. 3). Bulk and immersion (benzene/tetrabromethane) densities indicated that accesible porosity (volume %) increased in the order C-500 (7.4), C-730 (8.6-9.7), C-100 (10.1), C-700 (12.3-13.5). The low C-730 porosity is due to the denser cloth weave; the high C-100 value is attributable to a deficiency of binder. Mercury porosimetry, combined with CCl_4 adsorption porosimetry and BET surface area measurements, revealed a trimodal pore distribution with mean entrance-diameters $\geq$ 100 μm (unimpregnated weave interstices, etc.); 3-8 μm (interply and yarn gaps, larger for plain weave and after graphitization); and $\sim$0.4 μm (fiber/binder and primary/impregnant binder interfaces). Some additional porosity $\simeq$ 0.02 μm in C-500 was attributed to poor graphitized fiber/carbon matrix wetting and bonding. (2).

The ignition behavior (weight loss vs temperature at constant heating rate) in dry air of the composites is compared with that of some homogeneous carbon materials in Fig. 1. Oxidation resistance is poor relative to that of 2000 and 3000°C HTT glassy carbons and as-deposited and graphitized pyrolytic carbons; but it increases appreciably with graphitization for all of the materials, in agreement with other observations. Isothermal weight loss behavior in flowing dry air at 650°C is shown in Fig. 2 for the four composites. The samples were about $4 \times 6 \times 6$ mm^3 and weight loss has been normalized to unit initial external area. The small reactivity differences between C-700 and 730, and between C-100 and 500 correlate qualitatively with porosity differences; but fiber graphitization (C-500) and binder deficiency (C-100) may also contribute. The large difference between the C-100, 500 and the C-700, 730 composites results from two factors: Fall-off of unburned material may contribute to weight loss of the carbonized matrix composites; and graphitization increases purity and structural development, especially of the binder, reducing reactivity.

Sequential SEM observations on selected areas of interlaminar cleavage and polished cross section surfaces as a function of increasing 650°C burn-off revealed many details of the oxidation process. Figs. 3 and 4 illustrate some of the important features that were identified from studying a large number of micrographs. In general, the lateral surfaces of the fibers (about 8 μm initial diameter) are attacked first (even on polished cross sections), especially at the bottoms of the longitudinal grooves characteristic of ex-rayon fibers. The fiber cores remain after extensive burn off, due evidently to lower reactivity, aided by structural integrity. After the initial oxidation stages, the carbonized binder and fiber phases in C-100 are consumed at about the same rate; and the residual carbonized fiber cores are decorated with fine ash particles (Fig. 4). The average reactivity of the graphitized fibers in C-500 is lower than that of the carbonized matrix; but a strong pitting attack occurs at active sites (residual impurities or structural flaws) distributed randomly along the fiber length. The reactivity of the binder matrix is significantly reduced by graphitization in C-700, 730. Furthermore, the fiber surfaces in these composites are coated with wrinkled but oriented and adherent thin films of binder graphite. As shown in Fig. 4, these films have low reactivity and protect the fibers; oxidation attack initiates preferentially at points where the film is ruptured. Smooth oriented carbonized binder films coat the fibers in C-100, but provide less protection because they are poorly adherent and relatively reactive. The graphitized fibers in C-500 are not wet by the binder, and bare fibers are exposed on cleavage surfaces, in agreement with observations elsewhere (2).

In summary, relative apparent reactivities may be ranked as follows: laminar primary binder > glassy impregnant binder; fiber lateral surface > fiber core or binder; and for high burn off, binder $\sim$ fiber in C-100, binder > fiber in C-500, and binder < fiber in C-700,730. Oxidation resistance of these composites is improved by graphitization, despite increased open porosity. This results from reduced fiber and matrix phase reactivity (probably due to purification); and the protective effects of oriented, graphitic binder films on the fibers. The results obtained here complement those of a study of the oxidation behavior of PAN fiber/glassy carbon (PFA) matrix composites by Kimura, Shibusa, Tanaka, and Yasuda (3).

This research was supported by the National Aeronautics and Space Administration as part of work done under grants NGR 48-002-129 and NGL 48-002-004.

1. Fischbach D.B. & Kucheria C.S., 4th London Carbon and Graphite Conf., Imperial College, Sept. 1974
2. Fitzer E. & Terwiesch B., Carbon 10 (4) 383 (1972)
3. Kimura S., Shibusa Y., Tanaka H., and Yasuda F., Carbon '76 Conf. Abs., Baden-Baden, June, 1976; High Temp/High Pressure, to be publ.

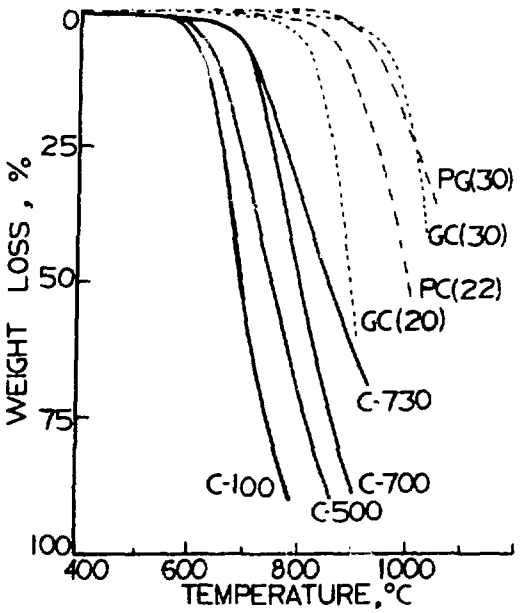


Fig. 1 Burnoff behavior at 10 C/min heating rate of the composites and some glassy and pyrolytic carbons. Numbers in brackets are HTT in 100 C.

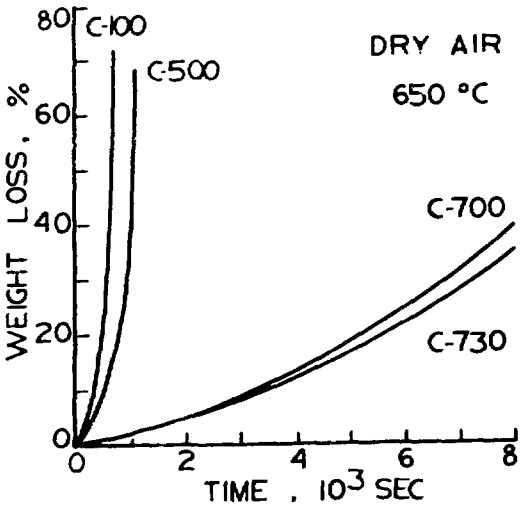


Fig. 2. Isothermal burnoff behavior of the carbon/carbon composites.

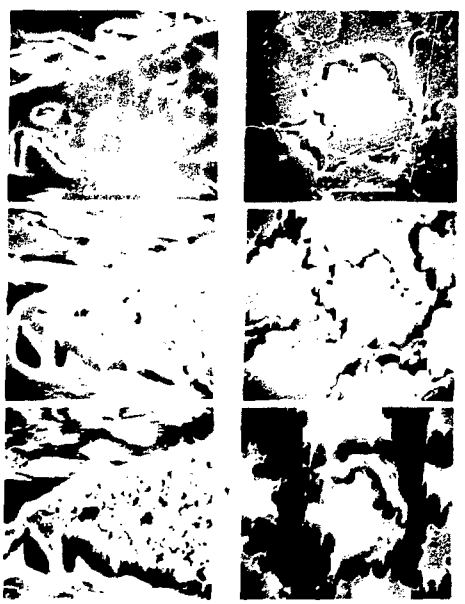


Fig. 3. Sequential SEM micrographs of selected areas of initially polished cross sections as a function of oxidation burnoff. From top to bottom, bulk sample weight loss is 0, 4, 12% for C-100; and 1, 4, 10% for C-500.



Fig. 4. Sequential SEM micrographs of individual fibers exposed on interlaminar cleavage surfaces. Bulk sample weight loss, from top to bottom, is 0, 2, 4% for C-100; and 0, 4, 8.5% for C-700.

A TEMPERATURE-PROGRAMMED DESORPTION STUDY OF SURFACE OXYGEN COMPLEXES FORMED ON CARBONS FROM ATOMIC OXYGEN

H. Marsh, D.W. Taylor
Northern Carbon Research Laboratories, School of Chemistry,
The University of Newcastle upon Tyne, Newcastle upon Tyne, NE1 7RU, U.K.

Introduction

A knowledge of the properties of surface oxygen complexes on carbons is important, not only for an understanding of their role in gasification reactions (Ref. 1) but also in determining the surface chemistry e.g. adsorptive properties, of the carbon (Ref. 2). A recent approach adopted by Marsh and co-workers (Refs. 3 to 6) involves the use of atomic oxygen to form surface oxygen complexes. This has the advantage that relatively large amounts of surface complex, approaching monolayer coverage (Ref. 3), are formed even at room temperature and below. In one study using atomic oxygen (Ref. 5), a linear-programmed increase in temperature was used to investigate the decomposition of the surface complex formed by the sequential adsorption of ^{16}O and ^{18}O atoms at 195 K. The isotopic content of the desorbed products (CO and CO_2) indicated that at some time during either their formation or decomposition the surface oxygen complexes were mobile over the carbon surface. This led Marsh and Foord (Ref. 6) to suggest a unified hypothesis (Ref. 6) explaining variations in the CO/CO_2 ratio in the products of the gasification reaction between carbons and oxygen. The desorption of CO_2 was considered to be governed by the likelihood of collision-interactions between mobile chemisorbed oxygen atoms (i.e. the surface oxygen complexes). Hence, increasing the concentration of surface oxygen complex or its mobility over the surface should result in an increased chance of collision-interaction and so a lower CO/CO_2 ratio should be found. Factors such as an increase in reaction temperature, a lower oxygen pressure, the presence of micropores in the carbon and the presence of surface imperfections would all be predicted to either lower the concentration of surface complex or impede its mobility. While the results of Foord (Ref. 5) confirm the identification of factors which impede surface complex mobility (e.g. the presence of microporosity, or increasing the extent of surface imperfection by lowering the HTT of the carbon) they do not indicate whether complex mobiliy occurs immediately following the initial interaction of an oxygen atom with the carbon surface, or immediately prior to desorption (the latter case is necessary for complex mobility to influence the CO/CO_2 ratio). The present study is concerned with a more detailed study of selected carbon samples in order to investigate further this possible relationship between surface oxygen complex mobility and reaction product ratio.

Experimental

The preparation of graphitizing carbons from polyvinyl acetate (PVA) is described elsewhere (Ref.7). Surface oxygen complex was formed by adsorption, at 195 K, of oxygen atoms prepared by a microwave discharge in (40 Pa) 0.3 torr of oxygen with a power adsorption of 55 watts. The sample, previously outgassed at 1175 K, was situated approximately 150 mm from the discharge zone. ^{16}O was adsorbed first for 30 minutes followed by ^{18}O for 2 hours. This gave a surface approximately equally covered by each isotope. The surface oxygen complex was decomposed by linear programmed heating from room temperature to 1175 K. The decomposition products were continuously pumped away (maintaining a vacuum over the sample of better than 133 Pa (10^{-6} torr) and analyzed by a mass spectrometer (Micromass 6).

Results and Discussion

The results to be discussed are those from two experiments performed on samples of a PVA carbon, HTT 1200 K. The experiments were identical except for the linear desorption heating rate which was 4.8 K min^{-1} in one experiment and 12 K min^{-1} in the other. The isotopic ratio in the desorbed carbon monoxide is plotted as a function of desorption temperature in Figure 1. That the CO is initially rich in the oxygen isotope that was adsorbed last indicates that some mobility of complex to the available sites of highest heat of adsorption has occurred immediately following the initial adsorption step (i.e. leading to a last-on, first-off process on desorption). Since the desorption of surface oxygen complex is a kinetically activated process, increasing the desorption heating rate will have the effect of increasing the amount of unstable complex (or mobile complex if mobility is a prerequisite of desorption) present on the surface at a particular desorption temperature. As shown in Figure 1 this also displaces the isotopic ratio curve to higher temperatures (as an increasing contribution from low temperature desorption is carried over to higher temperatures by a faster heating rate) although one is not able to conclude from this whether complex mobility immediately prior to desorption is occurring.

However, if the surface oxygen complex is mobile immediately prior to desorption, the increased chance of collision-interaction due to the higher concentration of mobile species present at the higher heating rate should, according to the hypothesis outlined earlier, lead to a lower CO/CO_2 ratio. That this is not the case is shown in Figure 2. One is led therefore to the conclusion, either that surface complex mobility does not play a part in governing reaction product ratio, or perhaps more likely that once adsorbed on a particular surface site the complex does not become mobile again before desorption. Carbon dioxide is then formed by the reaction between adjacent surface complexes.

Although these studies of adsorption and desorption processes related to surface oxygen complexes on carbons do help our understanding of their reaction with molecular oxygen, the latter reaction must always be considered as a dynamic changing (perhaps non-equilibrium) system so that the detail of the separate studies of complexes may not be directly applicable.

References

1. Phillips R., Vastola F.J. and Walker P.L. Jr., Carbon 7, 479 (1969); 8, 205 (1970).
2. Mattson J.S. and Mark H.B. Jr., "Surface Chemistry and Adsorption from Solution". Marcel Dekker, New York, 1971.
3. Marsh H., O'Hair T.E. and Lord Wynne-Jones, Carbon 7, 555 (1969).
4. Marsh H., Foord A.D., Mattson J.S., Thomas J.M. and Evans E.L., J. Coll. Int. Sci. 49, 368 (1974).
5. Foord A.D., Ph.D. thesis, University of Newcastle upon Tyne (1972).
6. Marsh H. and Foord A.D., Carbon 11, 421 (1973).
7. Taylor D.W. and Marsh H., "Carbon '76," *Deutsche Keramische Gesellschaft* (1976). pp. 101-104 (1976).

Acknowledgements

We express our thanks to the British Carbonization Research Association for financial support (H.M.) and a Research Fellowship (D.T.).

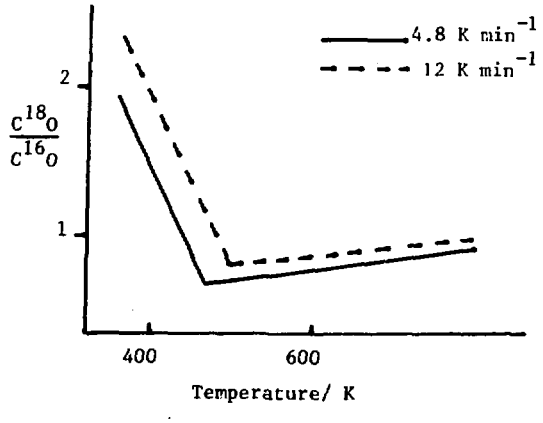


Figure 1. (Not drawn accurately to scale)

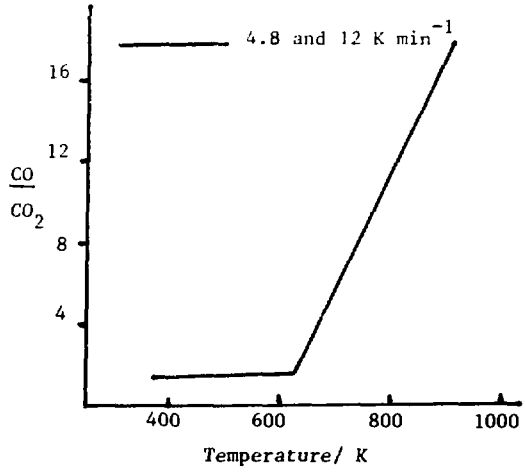


Figure 2. (Not drawn accurately to scale).

THE REACTIVITY TO ATOMIC OXYGEN AND CARBON DIOXIDE OF ANISOTROPIC CARBONS OF DIFFERENT OPTICAL TEXTURE

H. Marsh, Maggi French, Janet Smith and J.L. White*
Northern Carbon Research Laboratories, School of Chemistry,
University of Newcastle upon Tyne, Newcastle upon Tyne NE1 7RU, U.K.
*The Aerospace Corporation, P.O. Box 92957, Los Angeles, California

Introduction

The Northern Carbon Research Laboratories study aspects of the formation of graphite electrode material and metallurgical coke. If the electrode is to be used in steel manufacture, then like metallurgical coke, it is subject to extreme operating conditions of mechanical stress, of high temperature and of oxidation (gasification). The consequence of mechanical and thermal stress and of gasification is the development of fizzures, the propagation of which results in breakage of the graphite and coke and a serious diminution in operating performance. The origins and extent of development of deformation, shrinkage and gasification fizzures, therefore, are aspects of considerable practical importance and warrant investigation at the fundamental level.

Optical Texture

Polycrystalline, synthetic graphites and cokes are structurally heterogeneous materials with considerable porosity, some mesoporosity but mainly macroporosity. The structural heterogeneity is beautifully revealed by examination of polished sections in reflected polarized light using a half wave retarder-plate between the specimen and the analyzer to produce a range of interference colours (i.e. the optical texture). Isochromatic areas can be seen varying in size from <1.0 µm to >200 µm. These isochromatic areas owe their origin to the growth of nematic liquid crystals and mesophase from the fluid phase of the carbonization system (Ref. 1, 2).

An essential aspect of the formation of isochromatic areas of various sizes is the viscosity of the mesophase and its temperature dependence. A relatively low viscosity and an associated relatively long temperature zone of low viscosity permit the growth units of mesophase (when large enough to make contact), to coalesce together so that the identity of the original growth units is lost. This coalescence process is a complicated entwining of the flow-sheets of stacked lamellae (the mesophase), this process eventually establishing isochromatic areas of size, larger than the growth units as well as the various forms of 'disclination' as described by White (Ref. 3, 4). These disclinations are essentially zones of extensive deformation of stacked lamellae. A relatively high viscosity and a short temperature zone of high viscosity, apparently, do not permit the coalescence of the growth units (of smaller size). On making contact, these growth units fuse or adhere together and their identity is not lost. The resultant pattern of small, fused, isochromatic areas appears, under the optical microscope, as a mozaic. This is the characteristic feature of many metallurgical cokes.

Fizzuring and Optical Texture

A research theme of The Laboratories is an appraisal of the origins of mechanical, thermal and gasification fizzures in terms of the optical texture of the carbons. It is established that shrinkage cracks in the large isochromatic areas of carbons from selected grades of coal-tar and petroleum pitch are associated with cleavage parallel to basal planes, within the isochromatic areas, and also at positions of extensive deformation, i.e. the disclination (Ref. 3, 4). The situation with regard to optical textures of diminishing size is less clear, except for the knowledge that in metallurgical cokes the regions composed of small mozaics are not susceptible to cleavage. This raises the question as to the nature of the attachment between the small isochromatic mozaics.

The Experimental Approach

A programme of work was therefore initiated to prepare carbons, from known source materials, having different optical textures ranging from the large isochromatic areas of the needle-cokes to the fine mozaics in carbons prepared in the laboratory from Gilsonite pitch. Part of the programme was heat-treatment to temperatures >2300 K and the examination of carbons by optical and scanning electron microscopy. Polished surfaces can be prepared of low temperature carbons (HTT <1200 K) and the same area re-examined after progressive heating to the highest temperatures.

Another approach is to react the low temperature carbons with atomic oxygen at about 300 K and with carbon dioxide at about 1100 K. Atomic oxygen is known to react preferentially at defects in the graphite lattice (Ref. 5); it was therefore postulated that a similar reaction may occur with anisotropic carbons. Accordingly, carbons were prepared based upon A200 Ashland petroleum pitch, D112 coal extract (National Coal Board) and Gilsonite pitch. These carbons exhibited a range of optical texture. The atomic oxygen was generated using a "Microtron 200" micro-wave generator with an air-cooled resonant cavity, at an oxygen pressure of about 0.1 kPa. Reaction times were 3 minutes. Atomic hydrogen was also used for periods of about 15 minutes.

Discussion

It was found for carbons based on A200 Ashland petroleum pitch that both the atomic hydrogen and oxygen reacted preferentially with parts of polished surfaces to produce channels about 5 μm diameter. Using the colours of the optical texture, reaction occurred at positions of disclinations and within the isochromatic areas. The major part of the polished surface was hardly affected. No such preferential channelling was found using carbons of small mozaic texture. There was some non-uniform gasification of the surface, the non-uniformity being of the same size (SEM) as seen in optical microscopy (2 μm). The appearance resembled that of surfaces of cokes subject to argon-ion bombardment (Ref. 6).

Gasification by carbon dioxide of these carbons also produced quite different effects. With carbons of large isochromatic domains, deep gasification fizzures were a common feature; no comparable fizzures were produced in carbons with an optical texture of small mozaics, only a roughening of the surface resulted.

It is possible that selective etching by the atomic gases occurs at positions of extreme deformation or stress where micro-fizzures may already be in existence, but in size are beyond the limits of resolution of the optical microscope. Gasification by carbon dioxide may follow a similar mechanism. Etching by atomic gases may provide a useful method of assessing the shrinkage characteristics (in low HTT carbons) of graphitizable carbons. The processes of selective, structural etching by carbon dioxide remain intriguing.

References

1. Marsh H. and Cornford C., "Petroleum Derived Carbons", ACS Symposium Series, 21, pp. 266-281 (1976).
2. Marsh H., Proc. 4th Conf. on Industrial Carbon and Graphites, S.C.I. London, pp. 2-38 (1976).
3. White J.L., "Petroleum Derived Carbons", ACS Symposium Series, 21, pp. 282-314 (1976).
4. White J.L. and Zimmer J.E., "Surface and Defect Properties of Solids", Chem. Soc. London, 5, pp. 16-35 (1976).
5. Marsh H., O'Hair T.E. and Reed R., Trans. Far. Soc., 61, pp. 285-293, (1965).
6. Patrick J.W., Shaw F.H. and Willmers R.R., Fuel, London, 56, pp. 81-88 (1977).

Acknowledgement

We express our appreciation to the European Coal and Steel Community for financial support.

A NEW SUBSTRATE FOR SURFACE STUDIES

M. B. Dowell
Union Carbide Corporation, Carbon Products Division
Parma Technical Center, Parma, Ohio 44130

Expanded graphite foil is a novel substrate for studies of adsorbed films because its large surface, ~16 m^2/g, consists of homogeneous basal planes. ([1,2]) The accuracy of diffraction studies and heat capacity measurements of films adsorbed on graphite foil are often limited by the size of the basal plane regions ([3]) and by the orientation of basal planes with respect to the foil. ([4]) A substrate made by intercalating and expanding oriented pyrolytic graphite might be expected to exhibit improved basal plane size and orientation because pyrolytic graphite experiences little change in basal plane orientation when it is expanded, ([5]) and because it can be expanded and recompressed as a monolith rather than as an assembly of flakes. Expanded highly oriented pyrolytic graphite is now being offered as UCAR-ZYX*. Preparation of a highly oriented graphite substrate for adsorption, and an investigation of interlayer disorder resulting from intercalation, expansion, and recompression of highly ordered pyrolytic graphite, may thus be of interest to surface scientists.

Disorder introduced by intercalation is determined by comparing the full width at half maximum intensity of the (002) reflection of pyrolytic graphite specimens before intercalation with that of the comparable (00ℓ) reflection of the same specimens after intercalation. A specimen of UCAR-ZYA* stress annealed HOPG having a "mosaic spread" 0.24 to 0.31 deg (FWHM), exposed to HNO_3 vapor to form Stage II $C_{48}{}^{+}NO_3{}^{-}\cdot 3HNO_3$ and further exposed to air for 20 hours to form a stable "residue compound" consisting of a mixture of stages, exhibited a mosaic spread 0.52 to 0.80 deg of the (005) of $C_{98}{}^{+}NO_3{}^{-}\cdot 3HNO_3$ at 3.59Å. Another specimen of stress-annealed HOPG immersed in a hot mixture of sulfuric and nitric acids and rinsed in water to form a graphite bisulphate residue compound exhibited a reflection at 3.15Å having a mosaic spread 0.69 deg. Stress annealed pyrolytic graphites are thus disordered only slightly by intercalation and partial disintercalation.

Intercalated pyrolytic graphites are expanded by placing them in metal molds having closely fitting sides and heating them rapidly to 400°C to 600°C for a few minutes. Mosaic spreads of the expanded specimens of Figure 1 have a mean value 2.1 deg and appear to decrease as the density increases. Specimens recompressed to densities 0.8 to 1.4 g/cm^3 have mosaic spreads averaging 2.2 deg which appear to decrease with increasing density in the same way. Considerable interlayer disorder is thus introduced by expansion; little increase in mosaic spread results from recompression; and mosaic spreads reported here may be compared with values ~ 25 deg for "Grafoil"* flexible graphite.

Transmission diffraction studies of adsorbed monolayers require the fraction of substrate basal planes oriented nearly normal to the foil to be as small as possible. ([6]) The ratio of integrated intensity of the (002) peak in transmission to that in reflection is much smaller for expanded pyrolytic graphite than for "Grafoil"* as shown in Table I. This "transmission ratio", unlike the mosaic spread, can be increased by compression and is sensitive to the mechanical history of the specimen.

References

1. J. G. Dash, Films on Solid Surfaces, New York, Academic Press, 1975.

2. J. G. Daunt and E. Lerner, eds., Monolayer and Submonolayer Helium Films, New York, Plenum Press, 1973.

3. M. Bretz, J.G. Dash, D.C. Hickernell, E.O. McLean, and O.E. Vilches, Phys. Rev. A8, 1589 (1973).

4. J.K. Kjems, L. Passell, and H. Taub, Phys. Rev. Lett. 32, 724 (1974).

5. L.C. Olsen, S.E. Seeman, and H.W. Scott, Carbon 8, 85 (1970).

Table I

Surface and Structural Properties of Various Graphites

	Density g/cm³	N₂ Surface Area, m²/g	Mosaic Spread deg FWHM	Transmission ratio I(002)ₜ/I(002)ᵣ
Highly Oriented Pyrolytic Graphite	2.2	10[7]	0.1 0	~
Expanded HOPG	0.15-0.9	~	~2.1	~
Expanded HOPG	0.4-0.4	4	~2.2	0.1
"Grafoil"	1.0	20	~7	4

*"Grafoil" flexible graphite, UCAR Grade ZYA stress-annealed highly oriented pyrolytic graphite and UCAR Grade ZYX expanded pyrolytic graphite are products of Union Carbide Corporation, 270 Park Avenue, New York, N.Y. 10017. "Grafoil" is a registered trademark of Union Carbide Corporation.

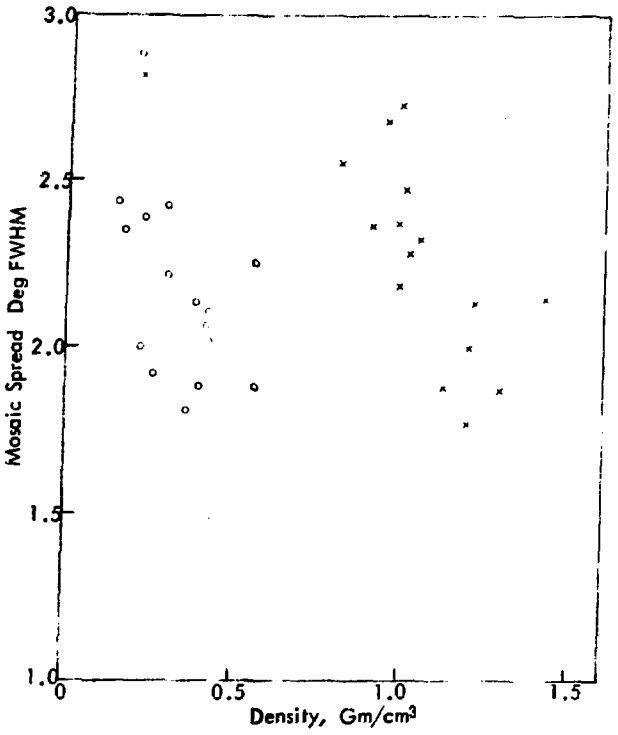


Figure 1. Mosaic spread of (O) expanded and (X) recompressed HOPG of different densities.

FRICTION CHARACTERISTICS OF SOME GRAPHITES AND CARBON COMPOSITES SLIDING AGAINST THEMSELVES

E. M. TATARZYCKI
The BFGoodrich Company Research and Development Center
Brecksville, Ohio 44141

Introduction

Researchers generally agree that the low coefficient of friction of graphite may be explained by its lamellar structure and the presence of a vapor film between these lamellar and other graphite debris. The concept of the lamellar theory is credited to Bragg[1] and later improvements to Holm[2]. Savage[3] showed that the low coefficient of friction of graphite depends upon adsorption films of water vapor. Later Rowl's[4] experiments showed that easily condensible gases(such as hydrogen, water vapor, oxygen and heptane) also resulted in low coefficients of friction. In more recent studies of carbons and graphites Lancaster[5] reported friction transients which he attributed to the desorption of water vapor. The purpose of this study is to describe the coefficient of friction-time-temperature relationships of some graphites and carbon composites and show that they are affected by the presence or absence of moisture.

Experimental Procedure

All the friction experiments were performed on a BFGoodrich developed machine called the Tribotester. This machine uses two identical disc type specimens rubbing against each other. One specimen rotates while the other remains stationary. Each specimen has an annular rubbing surface 6.35mm wide and a mean rubbing diameter of 5.08cm. Rubbing speed and load were maintained constant throughout each test at 0.69 m/s and 756 N respectively. Torque and interface temperature were recorded continuously as functions of time. Coefficient of friction was calculated. Duration of the test was limited to a rubbing distance of 2540m.

Three commercially purchased graphites, Pure Carbon PO-3, POCO AXF-5Q, and POCO AXF-90 were evaluated. In addition a BFG carbon/carbon composite(rayon based fiber in a pitch impregnated matrix) was studied.

All specimens were pre-conditioned in humid air,pre-heated in an oven or soaked in water. Test environment was ambient air, dry air, dry argon or moist air from a humidifier.

Results and Discussion

Because of the specimen geometry and design of the Tribotester a certain amount of heat buildup occurred in the specimens. At low speeds and light loads only a slight temperature increase was observed. For higher loads, higher temperatures occurred. At some point in the test an equilibrium condition was reached after which both the temperature and coefficient of friction remained constant.

Figures 1 and 2 show how the friction and temperature varied with time during the test. Figure 1 shows the behavior of carbon/carbon composite specimens which had been oven dried just prior to test. Thus, for all practical purposes the rubbing surfaces were void of moisture. Figure 1 shows a peaking of friction early in the test and before equilibrium was reached. Additional composite specimens were soaked overnight in water and then tested in the same manner. Results of these tests are shown in Figure 2. Peaking of the friction occurred just as it had with the dry specimens, but at the beginning of the test the friction was low. Other tests were run on specimens which had been pre-conditioned in humid air. Still others were tested with a moist air humidifier providing the ambient atmosphere. Results were identical to those of the water soaked specimens. Based on these results and the previous work of others it was hypothesized that the presence of water on the rubbing surface provided a lubricating effect as observed by the low friction. As rubbing proceeded, sufficient heat was eventually generated to evaporate the moisture from the surfaces and cause the sudden rise in friction which then caused the temperature to rise more quickly. Once the moisture evaporated the friction appeared to be temperature dependent as shown in Figure 3. Below a temperature of about 200°C the influence of moisture may be seen. At 200°C the friction peaks; beyond this temperature a single characteristic remains. Note that the friction decreases rapidly. At 400°C it has a value of 0.4. If rubbing is stopped at any time during the test(point A), the specimens permitted to cool down(point B) and the test restarted, the friction is determined by the surface temperatures at the initiation of rubbing(point C). Below 200°C(point D) the friction assumes the higher values if the surfaces are dry(point E). If, on the other hand, the surfaces are exposed to atmospheric air for a long period of time moisture is adsorbed and low friction results(point F). Many tests were performed to verify this reversibility of the friction-temperature relationship.

Being able to supply either a humid environment or wet surfaces was rather easy. To provide a dry surface was more difficult. Baking the specimens and cooling in a desicator was

fine. After removal from the desicator but before startup there was sufficient time to permit the adsorption of moisture from the air. As long as specimen temperatures were maintained higher than 120°C adsorption would not occur, but below 120°C that possibility always existed.

Consequently, it was decided to not only pre-dry the specimens but to supply a dry atmosphere as well. Thus moisture-free air was purchased in bottle form and piped into a rather loosely enclosed chamber surrounding the test specimens when mounted on the Tribotester. A specimen which had been initially soaked was tested in the dry air chamber. As expected, it exhibited the wet friction characteristic. The test was continued until the temperature was well above 200°C. At this point the surfaces were moisture free and the Tribotest chamber was engulfed in dry air. The specimens were cooled to room temperature and retained in the dry air for four hours ensuring sufficient time for any possible adsorption to take place. Then the test was restarted and the observed friction behavior was that of a dry material. The same procedure was repeated several times with the same results. When a pre-dried specimen was used, the typically dry friction characteristic was also observed.

In order to fully resolve the possibilty that neither oxygen nor nitrogen was causing the low coefficient of friction the above tests were repeated but with dry argon gas instead of the dry air. Results were identical with those of the dry air tests. It was quite apparent that moisture was being adsorbed onto the friction surfaces and producing a lubricating effect. In the absence of moisture the magnitude of friction was determined by magnitude of temperature.

All of the above tests were performed on the BFG carbon/carbon composite. Other materials evaluated were commercially purchased graphites PO-3, POCO AXF-5Q and AXF-90. The frictional behavior of these materials is identical to that of the carbon/carbon composite.

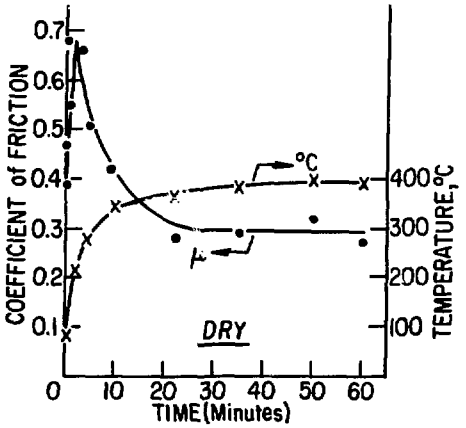


Fig. 1-Variation of friction and temperature with time for a dry carbon/carbon composite.

References

1. Bragg,W.L.,Introduction to Crystal Analysis, G. Bell & Son,Ltd.,London,1928,p.64.
2. Hohm,R.,Electrical Contacts,Hugo,Gerber, Forlog,Stockholm,1946,p.193.
3. Savage,R.H.,J. Appl. Physics,19,1 (1948).
4. Rowe,G.W., Wear 3, 274 (1960).
5. Lancaster,J.F., Wear 34,275 (1975).

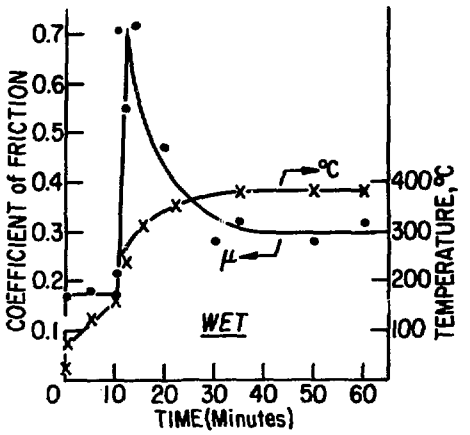


Fig. 2-Variation of friction and temperature with time for a wet carbon/carbon composite.

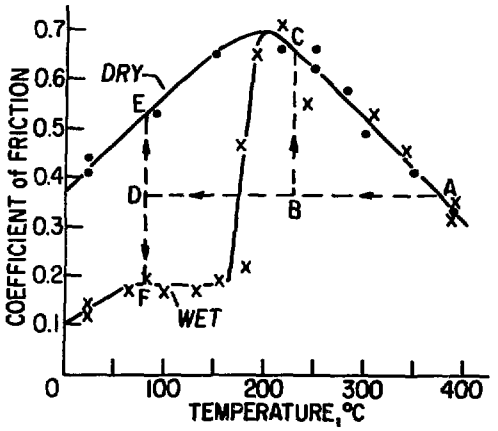


Fig.3-Friction-Temperature relationship showing reversibility of a carbon/carbon composite.

THE FATIGUE BEHAVIOR OF THIN CARBON FILMS

H.S. SHIM, N.K. AGARWAL, A.D. HAUBOLD
General Atomic Company
P.O. Box 81608
San Diego, California 92138

Composites made of vapor-deposited thin carbon film and appropriate substrate material (e.g., metals) are being considered for use in prosthetic devices such as artificial heart valve housings, fracture fixation plates and dental implants. A few of the most important properties required for these devices would be that the carbon films are structurally similar to LTI carbons* which are highly biocompatible, adequately adhere to the substrate, and do not undergo dynamic fatigue failure. The strucutre of the vapor-deposited carbon films and its bond strength to the metallic substrates have been characterized[1,2]. In this presentation, the fatigue behavior of thin carbon film on stainless steel (Type 304) is discussed.

Carbon film of about 4000-5000Å was deposited on tensile coupons cut from highly polished stainless steel sheet (0.005-inch thick). The composites were then uniaxially flexed with a cyclic rate of 60 cpm and various strain levels. During the test, carbon film surface was periodically monitored with a microscope and, at the end of each test, the final surface topography was examined in detail using a scanning electron microscope.

The results are summarized in Fig. 1. The calculation of film stress requires a knowledge of Young's modulus, which is very difficult to measure. The results are therefore expressed in terms of strain versus number of cycles to failure rather than stress versus number of cycles to failure.

It was found that the carbon film in composites would not fail if flexed below the elastic strain limit of the substrate. Above this strain level, the composites had fracture in the carbon film that always coincided with the onset of plastic deformation in the substrate. In other words, the carbon film fractured only and if the substrate has plastically deformed, and no carbon film failed first in fatigue before the substrate failed; i.e., the carbon films, like LTI carbons, are immune to dynamic fatigue. The strains at the elastic limit and the fracture were measured in independent tensile testing, and were 5.5×10^{-3} and 2.5×10^{-2}, respectively.

In conclusion, the carbon film in prostheses would remain as a protective coating so long as the metallic substrate in function flexes within its elastic strain limit. If exceeded, the prostheses would become inserviceable, not because of the carbon film fracture but because of the configurational distortion in the prostheses. Currently, the tests are being continued using carbon film/polymer composites.

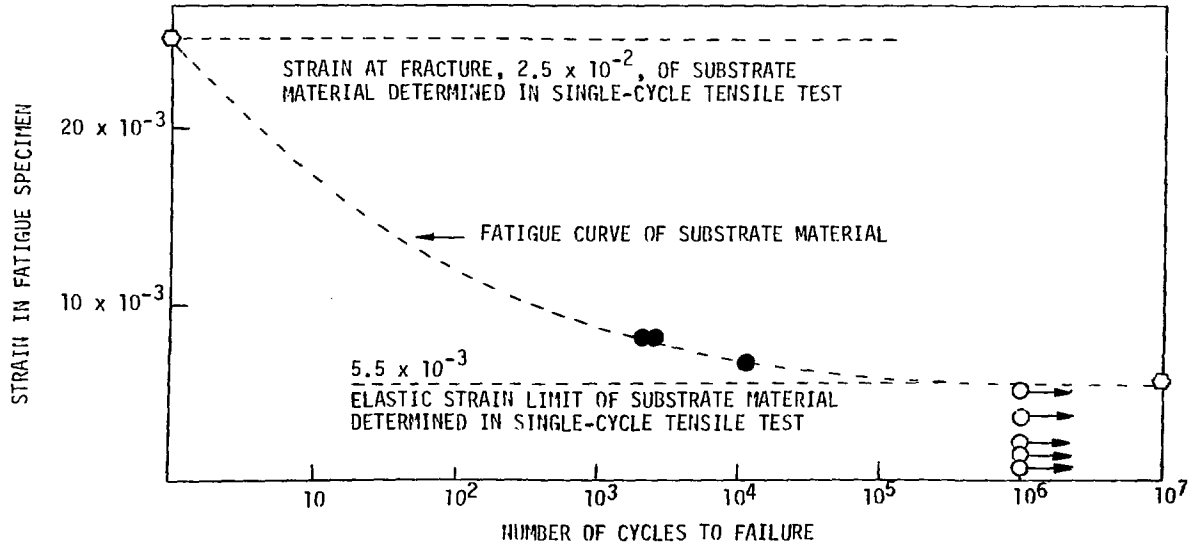
This work was supported in part by NHLI (S.D. Bruck, Program Manager).

* Commercially availalbe under a registered trade name of Pyrolite® Carbons.

References

(1) H.Shim, N. Agarwal, A. Haubold, "The Microstructure of Vapor Deposited Carbon Films", This Conference.

(2) N. Agarwal, H. Shim, A. Haubold, "The Adhesion of Thin Vacuum Deposited Carbon Films", This Conference.



SIZE EFFECTS ON STRENGTHS OF GLASSY CARBON

R. E. Bullock, J. L. Kaae - General Atomic Company, San Diego, California 92138

Introduction

Weibull predictions of strength ratios for brittle materials of different volumes that are evaluated under two different test conditions have the general form [1]

$$\frac{\sigma_1}{\sigma_2} = \left(\frac{V_2}{V_1}\right)^{1/m} \times \text{stress-distribution term(STD)}, \quad (1)$$

where

STD = $[2(m+1)^2]^{1/m}$ for the ratio of three-point bend strength to tensile strength,

= $[4(m+1)^2/(m+2)]^{1/m}$ for the ratio of four-point bend strength (quadrant loading) to tensile strenth,

= $[m/2+1]^{1/m}$ for the ratio of three-point bend strength to four-point bend strength,

with the Weibull modulus m providing a measure of the scatter found within experimental strength data.

These predictions have agreed reasonably well with experiment when graphite specimens of the same volume have been tested under different stress distributions [2], but the agreement has not usually been good when different volumes of graphite have been tested under the same conditions [3,4]. The theoretical volume term has generally been found to considerably overestimate the actual size effect for large-grained graphites [2-6], but it has been suggested that the agreement here would improve if test samples were made large in relation to their grain size [7,8]. Therefore, it is of interest to examine size effects on the strength of a glassy carbon that has an x-ray crystallite size of less than 20Å [9], as opposed to values for graphite that are often 10^6 times as large.

Experimental Details

The material tested was a commercial glassy carbon manufactured by Beckwith Carbon Corporation. This disc-shaped material was designated as 1800 grade, indicating heat treatment to 1800°C; it was 125 mils thick and had a bulk density of 1.39 g/cm^3. When thin strips taken from the surface were polished to a mirror finish and viewed in the microscope under the proper angle of incident light, a great many spherical pores were observed. While most of these pores were only 1 to 5μm in diameter, several were 10 to 15μm, and the largest observed was about 30μm. Pores larger than 1μm virtually disappear at depths greater than 8 mils into this particular material, however, as previously observed [10]. Therefore, a 10 mil thickness was removed from all outer surfaces in order to leave only the remaining bulk material; this is justified because it is possible to produce glassy carbon in the laboratory that does not have a porous surface layer [11]. Discs 4 mils thicker than the desired thickness of the bend specimens were longitudinally sliced from this bulk material with a mechanically controlled diamond section wheel; these thin sections were sealed between glass slides and then cut into strips 40 mils wide with the sectioning wheel. Finally, these strips were attached to an arbor and sanded down uniformly by 2 mils on each side to remove the small edge chips (<20μm) that almost inevitably result during cutting of this brittle material, particularly on the exit side of the cut. The final polishing compound was 3μm diamond powder, which produced test specimens with mirror-like surfaces.

The finished specimens were examined under a microscope to ensure that they were free from serious chips or scratches, and the surface that appeared best was selected to be the tension face in the three-point bend test. To ensure uniformity before testing, the width of each specimen was measured in a toolmaker's microscope to an accuracy of ±0.04 mils at three points, which corresponded roughly to the load points during subsequent testing, and the thickness was measured at about the same points to an accuracy of ±0.05 mils with a sharp-point micrometer. Then, after testing, dimensions of each fragment were measured adjacent to the fracture and averaged to get values for the failed section. Specimens were tested over a span width of 0.2 in. on a three-point bend fixture, which had been designed for use on pyrocarbon strips removed from graphite discs that were coated along with nuclear fuel particles [12]. Specimens were loaded with the use of a table-model Instron machine at a crosshead speed of 0.01 in./min, and the load and deflection were simultaneously recorded. Fracture stresses were calculated from expressions [13] that take into account large deflections and frictional effects at the knife edges [14]; these corrections were significant only for the thinnest specimens tested (3 mils), where the calculated fracture stresses exceeded those calculated from simple-beam theory by as much as 10%.

Results and Discussion

The test plan for this study eventually calls for three sample thicknesses to be tested under three-point bending at two different span widths to investigate size effects, with two of these specimen types also being tested under four-point bending to investigate stress-distribution effects. However, only interim results can be reported at this time. Three-point bend testing for a single span width has been completed to date for specimens with thicknesses of 12 and 6 mils, and partial results are available for 3-mil specimens. The experimental strength data are plotted in Fig. 1, and results of a Weibull analysis on these data are summarized in Table 1. Strength ratios for the three different test volumes are compared to Weibull predictions in Table 2. It is observed from Fig. 1 that the strength distributions for the 6-mil and 12-mil specimens have essentially the same shape, as verified by the closeness of their Weibull moduli (Table 1), but that the entire distribution for the thinner specimens is shifted upward in strength by an average amount that agrees well with the 4-ksi difference in mean values for the two distributions. The Weibull parameters which best characterize both of these curves are given by: m=6.0 and σ_0=2.9 ksi·in.$^{3/m}$, where these values have been determined to best fit

(in the sense of maximum likelihood estimates) the data of Fig. 1 with the three-point-bend survival probability $S=\exp[-V(\sigma/\sigma_0)^m/2(m+1)^2]$.

The partial data for the 3-mil specimens (Fig. 1) were not sufficient for use in these distribution determinations, but once such parameters were determined then the still higher mean strength (Table 1) for these thinnest specimens was useful for comparison with Weibull predictions of the various strength ratios (Table 2). It is observed from these comparisons that the Weibull volume term gives good agreement with experiment for glassy carbon, as was previously found to be the case for structural composites reinforced with carbon fibers having small crystallite sizes [15]. Finally, based on results of this study, Weibull theory was applied to calculate the tensile strength expected for a 1cm gauge length of 25μm glassy carbon fiber having the same modulus ($E=4\times10^6$psi) as the bulk material investigated, and the comparison with experiment [16] is very good (Fig. 2).

References

1. Weil, N. A. and Daniel, I. M., J. Amer. Ceram. Soc. 47, 268 (1964).
2. Marshall, P. and Priddle, E. K., Carbon 11, 627 (1973).
3. Brocklehurst, J. E. and Darby, M. I., Mater. Sci. Eng. 16, 91 (1974).
4. Price, R. J., Entended Abstracts of 12th Conf. on Carbon, 145 (1975).
5. Price, R. J. and Cobb, H. R. W., Proc. Conf. on Continuum Aspects of Graphite Design, 547 (1970).
6. Amesz, J., Donea, J. and Lanza, F., Extended Abstracts of 11th Conf. on Carbon, 221(1973).
7. Mason, I. B., Proc. 5th Conf. on Carbon, 597 (1963).
8. Lanza, F. and Burg, H.,Extended Abstracts of 11th Conf. on Carbon, 223(1973).
9. Kaae, J. L., J. Biomed. Mater. Res. 6, 279(1972).
10. Nadeau, J. S., J. Amer. Ceram. Soc. 56, 467 (1973).
11. Fitzer, E., Schaefer, W. and Yamada, S., Carbon 7, 643 (1969).
12. Bokros, J. C. and Price, R. J., Carbon 3, 503 (1966).
13. Conway, H. D., Phil. Mag. 36, 905 (1947).
14. Kaae, J. L., J. Nucl. Mater. 46, 121(1973).
15. Bullock, R. E., J. Comp. Mater. 8, 200 (1974).
16. Kawamura, K. and Jenkins G. M., J. Mat. Sci. 7, 1099 (1972).

Table 1. Three-Point Bend Data for Glassy Carbon

	Specimen Thickness		
	12 mil	6 mil	3 mil
Number Specimens	24	24	8
Mean Strength (ksi)	27.86	31.86	36.12
1 Stdard Deviation (ksi)	5.38	6.28	6.54
Test Volume (10^{-5} in.^{3})	9.90	4.58	2.40
Weibull Modulus (m)	6.00	5.90	6.46
σ_0 Parameter (ksi. in.$^{3/m}$)	2.93	2.85	3.60

Table 2. Weibull Predictions Versus Measurements

Strength Ratios	Theory	Experiment
σ(3 mil)/σ(6 mil)	1.11	1.13
σ(6 mil)/σ(12 mil)	1.14	1.14
σ(3 mil)/σ(12 mil)	1.27	1.30

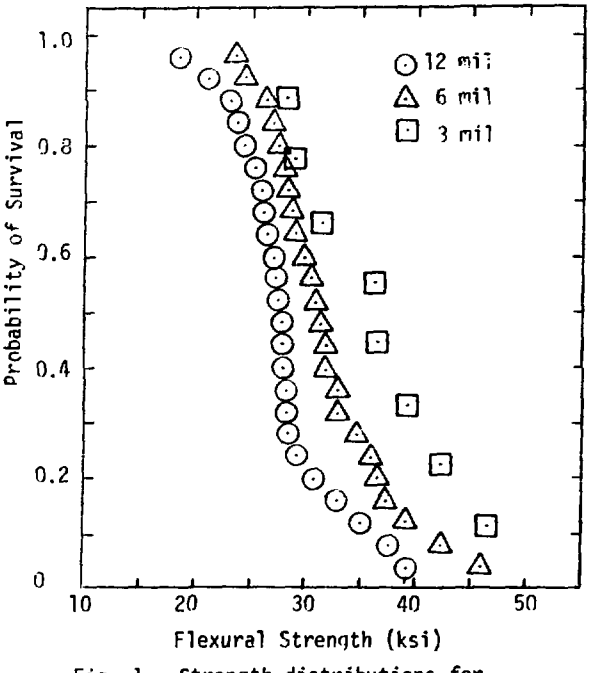


Fig. 1. Strength distributions for glassy carbon.

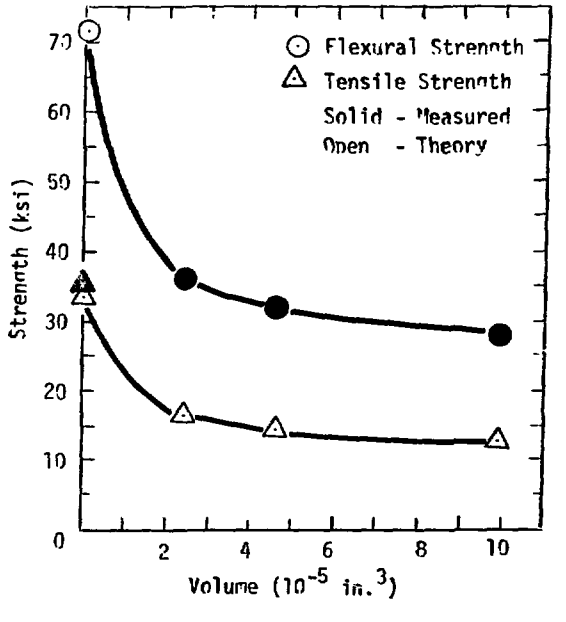


Fig. 2. Size effects on strengths of glassy carbon.

THE EFFECTS OF FAST NEUTRON IRRADIATION ON THE GALVANOMAGNETIC PROPERTIES OF GRAPHITE

R.O. Dillon & I.L. Spain
University of Maryland
College Park, Md. 20742

J.W. McClure
University of Oregon
Eugene, Ore. 97403

1. Introduction

Highly oriented pyrolytic graphite was irradiated with fast neutrons at ~90°C in the NBS reactor (Gaithersburg, Md) to doses 0.18-2.9x10^{17}nvt(E>1MeV) or 0.29-4.6x10^{17}nvt(E>1MeV). Galvanomagnetic effects (Hall resistivity, ρyx, and magnetoresistance, ρxx) were measured between 1.2 and 4.2K in the water-cooled solenoids at NRL (Washington, D.C.) in fields up to 9Tesla (90kg). Description of starting specimens used in the present work and detailed measurements of galvanomagnetic measurements are given elsewhere(1). From the resistivity ratio ($\rho 298/\rho 4.2K$ = 14.2) the present specimens are of high quality.

2. Results for σxx

From these data the conductivity components σxx and σxy were obtained. Classical Theory (2) predicts that $\sigma xx\ B^2$ should saturate in high fields, $B > B'_{\frac{1}{2}}$, where $B'_{\frac{1}{2}}$ is the field at which the resistivity is doubled. As seen in figure 1 this condition is satisfied for all specimens at 9Tesla but it is σxxB that saturates for all specimens. This behavior has been observed in pristine graphite by a number of workers in this temperature and field range (See ref 1 for discussion).

3. Results for σxy

Classical theory also predicts that σxyB should saturate and this behavior is observed (fig. 2). The limiting value of σxyB allows the number of acceptors NA to be calculated from the formulae:

$$(\sigma xyB)_{B>>B'_{\frac{1}{2}}} = (P-N)|e| \qquad [1]$$

$$NA = (P-N) \qquad [2]$$

where P,N are the densities of holes and electrons respectively.

It is noted that values of (P-N) should also be given from the limiting value of the Hall Parameter ($RH \cdot (\sigma xyB)^{-1}$ for $B>>B'_{\frac{1}{2}}$, according to theory). However, RH does not saturate at high fields because the limiting value of RH is predicted on the basis that $\rho xx << \rho xy$ or $\sigma xx << \sigma xy$ in high fields. Neither of these conditions is satisfied at high fields, and RH did not saturate. Earlier workers (3) had estimated (P-N) from Hall data at ambient temperature at relatively low fields (eg B~0.5T). Their estimates for the number of acceptors per unit dose level would be several times higher than that given here for the same data. For instance, using the value of RH at 9T, and comparing with data for σxyB, we obtain:

No. of acceptors per dose = (14±2)ppm/10^{17}nvt(E>1MeV)-σxy data
(30±10)ppm/10^{17}nvt(E>1MeV)-RH data.

If Hall data were used at lower field the calculated value of NA would be even higher.

4. Shift of Shubnikov de Haas Oscillations in the Quantum Limit

In figs 1 and 2 an oscillatory component of the conductivity components can be seen-the Shubnikov de Haas oscillations. As the number of acceptors increases the Fermi level should fall so that the extremal positions of these oscillations should shift. Cooper et al(4) measured these shifts in the field region up to ~25T for specimens irradiated to 1.2x10^{17}nvt(no criterion given for neutron energy). Since (i) the Shubnikov de Haas frequencies for hole and electrons in graphite differ only by a factor of ~1.5 (ii) irradiation increases the scattering of carriers and (iii) shifts of frequencies are small in this dose region, the present work concentrated on the shift of the quantum limit oscillations which can be observed more readily without recourse to complicated curve-fitting proceedures. (An analysis showing the difficulties inherent in Cooper et al's work is given in ref 5).

Data showing the quantum-limit oscillations for specimens used in the present work are given in fig. 3. At each of the extrema, the Fermi level is in coincidence with a magnetic energy level (Landau level). Since the c-axis lattice spacing is changed by less than 0.02% for doses less than 10^{18}nvt it is reasonable to assume initially that band overlap parameters do not change with irradiation. A calculation was made of the shift of the n=1,2 (electron) and n=1 (hole) extrema with acceptor level and comparison is made with the experimental data in fig. 4 using values of NA calculated from [1] and [2].

5. Conclusions

The following conclusions follow from the present work.

(1) The shift of the coincidence fields for electron levels generally follows the predictions of the rigid band model, but the shift of the hole level is much smaller than predicted. Agreement cannot be obtained by employing a scaling factor for the acceptor levels calculated using [1] and [2]. Thus a rigid band model does not appear to be appropriate.

(2) A calculation was made to assess the change of coincicence fields with band overlap parameters. The data could not be fitted with a reasonable set of parameter changes.

(3) The shifts of the coincidence levels are generally in agreement with a band model in which the parameter γ2 is negative.(6) This is in agreement with Cooper et al's results(4) but in disagreement with Soule's results on boron-doped graphite(7).

(4) In the low dose region the abrupt shift of the n=1 electron level with dose is difficult to explain unless changes occur in phase-shift parameters.

(5) The absolute increase in the amplitude of the n=1,2 (electron) oscillation for sample #2 is difficult to explain. Since the introduction of acceptors should increase the scattering probabilities absolutely, as shown by changes in conductivity, an absolute decrease in the amplitude of the Shubnikov de Haas oscillations should be observed.

Acknowledgements

This work was supported by a grant from the Atomic Energy Commission to the University of Maryland. Thanks are due to the staff of the Magnet Facility, Naval Research Laboratory and to the staff of the Reactor Facility, National Bureau of Standards. Dr. A.W. Moore kindly supplied the graphite samples.

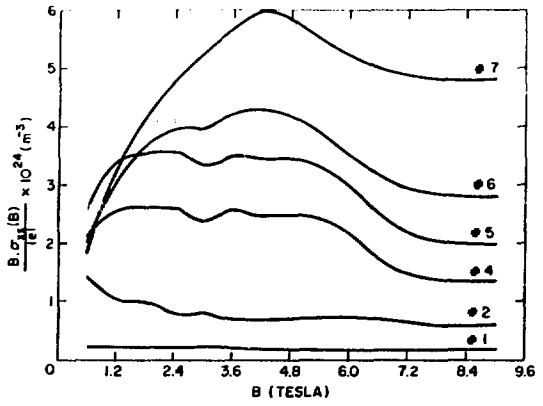


Fig. 1. σ_{xx}.B versus field plot. Hours in the reactor for these specimens are given in figure 3. Doses can be interpolated directly from exposure time and dose of specimen irradiated to 32 hours (#7) (2.9×10^{17}nvt(E>1MeV); 4.6×10^{17}nvt(E>.1MeV)).

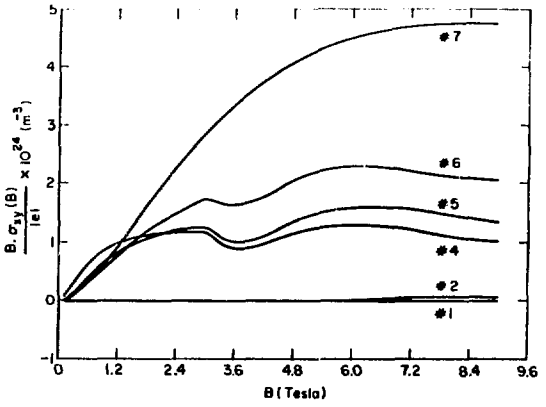


Fig. 2. σ_{xy}.B versus field plot.

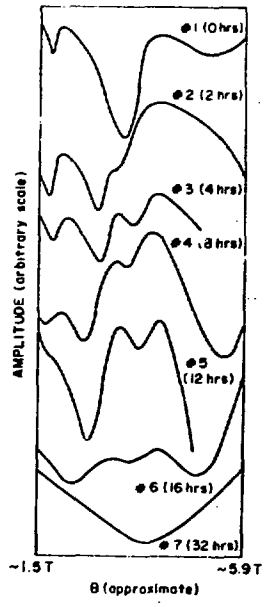


Fig. 3. Oscillatory components of σ_{xx} after midline drift subtracted with a bucking signal. In these data, small magnet calibration errors, which differ from sample to sample, are not corrected for. Values in brackets refer to hours in the reactor.

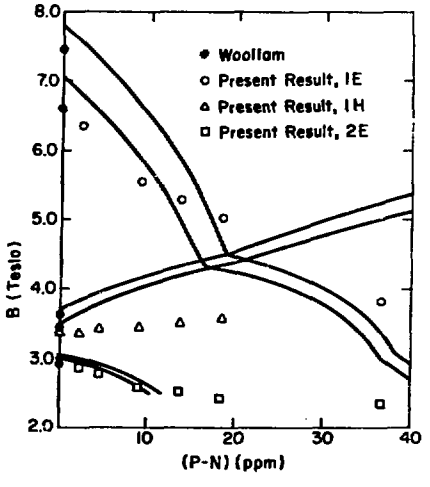


Fig. 4. Summary plot of the shift in the coincidence fields 1E, 2E, 2H (E and H refer to electron and hole) with (P-N) obtained from σ_{xy}B data. Theoretical curves based on the rigid band model are shown. Double curves refer to spin-splitting which can only be resolved experimentally for the pristine sample.

References

1. R.O. Dillon, I.L. Spain, J.A. Woollam & W.H. Lowrey (Submitted to J. Phys. Chem. Solids)
2. J.W. McClure, Phys Rev 112, 715 (1958).
3. L.C.F. Blackman, G. Saunders & A.R. Ubbelohde Proc. Phys. Soc.(London) 78, 1048 (1961).
4. J.D. Cooper, J.P. Smith, J. Woore & D.A. Young J. Phys. (London) C4, 442 (1971).
5. R.O. Dillon, I.L. Spain & J.W. McClure (J. Phys. Chem. Solids (in press)).
6. P.R. Schroeder, M.S. Dresselhaus and A. Javan Phys. Rev. Letters, 20, 1291 (1968).
7. D.E. Soule, IBM J. Res. Dev. 8, 268 (1964).

STUDY OF THE ELASTIC CONSTANT C_{44} OF PYROLYTIC GRAPHITE AFTER LOW TEMPERATURE IRRADIATION (4 K)

J.B. AYASSE and E. BONJOUR

Centre d'Etudes Nucléaires de Grenoble
Service des Basses Températures

Introduction :

The Granato-Lücke Theory [1] about the pinning of dislocations by the defects was successfully applied to metals [2]. With this theory, we tried to analyse experiments [3] of electron irradiation on pyrolytic graphite at liquid helium temperature. We have performed new experiments to study the irradiation effects on the shear modulus of the perfect lattice C_{44L}. We have irradiated under the same conditions that previously a pyrocarbon sample (H.T.T. ∿ 2400°C) where the effects of dislocations are supposed to be zero.

We also measured the specific heat of a pyrolytic graphite (U.C. grade ZYH) between 1.2 K and 5 K, after neutron irradiation at liquid nitrogen temperature and subsequent annealing at room temperature.

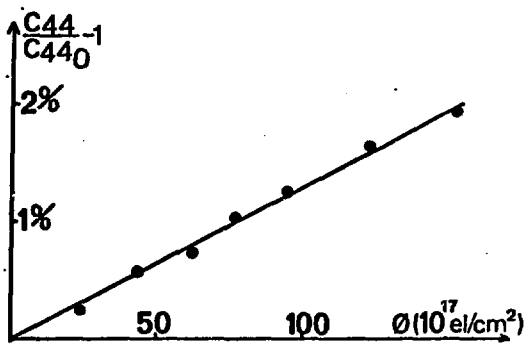


FIG. 1 - C_{44L} change for the pyrocarbon sample at 4 K. C_{44o} = 1.18 10^{10}dynes/cm^2

Experimental results :

The figure 1 presents the shear modulus change of a pyrocarbon sample which shows a linear dependance upon the dose.

The figure 2 shows the specific heat of pyrolytic graphite before and after irradiation for 2 doses (10^{17}-10^{18} neutrons/cm^2). The experimental data may be fitted on a linear law versus T^2, $C/T = \gamma + \beta T^2$ where the slope $\beta=(1/\Theta_D)^3$ and $\Theta_D^3 \alpha C_{44L} (C_{33})^{1/2}$ (Θ_D Debye temperature).

The relative changes $\Delta C_{44L}/C_{44oL}=-\Delta\beta/\beta_o$ are about + 6 % and + 26 % for 10^{17} and 10^{18} n/cm^2 respectively with β_o ∿ 30 μJ/M/K^4 [4]. These values are certainly overestimated because of the existence of a peak on the specific heat

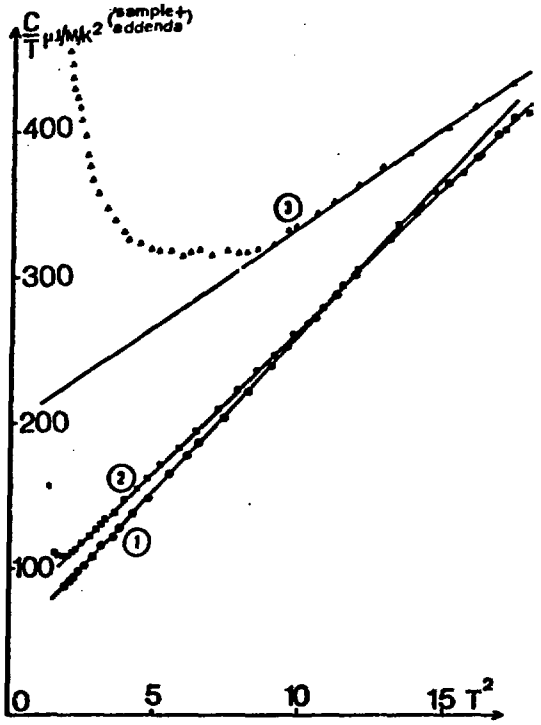


FIG. 2 - Specific heat data obtained in the range 1.2 - 4 K for the pyrolytic graphite : ① before irradiation ② 10^{17} n/cm^2 ③ 10^{18} n/cm^2

curves at low temperature already seen by other authors [5]. Nevertheless this 2 results show a large increase of the shear modulus C_{44L} with damage.

The figure 3 shows C_{44} changes versus dose Φ for a pyrolytic graphite sample (U.C. grade ZYA) irradiated at 4.2 K. The large C_{44} increase forbids certain approximations of the Granato-Lücke Theory ordinarily used for the metals which have variations of about a few per cent.

The final relation is :

$$\frac{(C_{44L}/C_{44}-1)\ \text{irrad.}}{(C_{44oL}/C_{44o}-1)\text{unirrad.}} = \frac{(C_{44L}/C_{44oL})^{1/2}}{(1 + n_r/n_o)^2}$$

where n_r/n_o is the ratio between the pinning points n_r created by irradiation and those n_o existing before ; let $n_r/n_o = p\Phi$ be linear with the dose Φ (p parameter). Two stages are required for the fit on

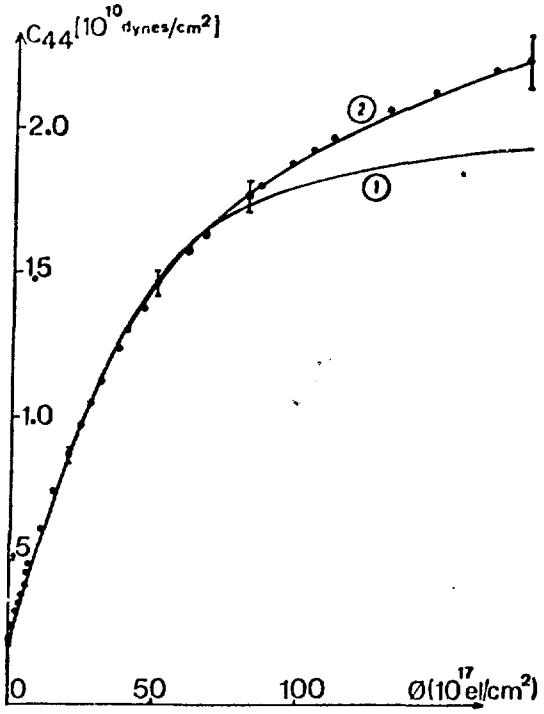


FIG.3 - C_{44} change for the pyrolytic graphite C_{44_O} = (.22 ±.02) 10^{10} dynes/cm^2

the experimental curve.

1) Assuming that the effect of the defects remains negligible on C_{44_L} : $C_{44_L} = C_{44_{oL}}$, we can fit the experimental points up to $\Phi \sim$ Imax/3 only. For higher doses the theoretical curve (1) is below the experimental curve. In this case the parameter values are : C_{44_L} = 2 10^{10} dynes/cm^2, p = 7.5 10^{-19}cm^2/$_{el}$

2) Taking into account a linear increase of C_{44_L} with the dose : $C_{44_L} = C_{44_{oL}}$ (1 + bΦ) we can fit, at about 5 %, the whole experimental curve 2. The new parameters are : $C_{44_{oL}}$ = 1.8 10^{10} dynes/cm^2 p = 7.5 10^{-19} cm^2/$_{el}$, b = .16 $.0^{-19}$ cm^2/$_{el}$

Discussion :

These results show the existence of both processes :

Pinning of dislocations by the defects and linear increase with the dose of the shear modulus of the lattice C_{44L}. The concentration of defects is about 10^{-3} for 10^{18} n/cm^2 [6]. The specific heat results $\Delta C_{44_L}/C_{44_{oL}} \sim$ + 6 % for 10^{-4} and + 26 % for 10^{-3} are the same order of magnitude than those for electron irradiation : $\Delta C_{44_L}/C_{44_{oL}}$ = b Φmax ~ 28 % for a concentration of defects about 4 10^{-4} [7].

On the other hand, the changes are smaller for the pyrocarbon, probably because of larger space between the planes. The lattice shear modulus deduced : $C_{44_{oL}}$ 1.8 10^{10} dynes/cm^2 is smaller than the usually accepted value (4 10^{10} dynes/cm^2).

References :

1. A. GRANATO, K. LÜCKE, J. *Appl. Phys.* 27, 583 (1956)

2. *Ultrasonic Methods in Solid State Physics* - R. TRUELL, C. ELBAUM, B.B. CHICK, Academic Press London p 190 (1969)

3. J.B. AYASSE, E. BONJOUR, R. LAGNIER *2nd International Carbon Conference Baden-Baden* (1976)

4. Jr. VAN DER HOEVEN, P.H. KEESOM, *Phys. Rev.* 130, 1318 (1963)

5. A.S. VAGH, S. MROZOWSKI, *Carbon* 13 N° 4 (1975)

6. L. BOCHIROL, E. BONJOUR, *Carbon* 6 pp 661-669 (1968)

7. T. IWATA, T. NIKIRA, *J. Phys. Soc. Japan*, 31 N° 6 pp 1761-1782 (1971)

EFFECT OF CHEMICAL IMPURITIES ON THE GALVANOMAGNETIC PROPERTIES OF CARBONS

T.KIMURA , K.YAZAWA
University of Electro-Communications,
Chofugaoka 1-5-1, Chofu-shi, Tokyo 182, Japan

It has been understood that boronation of carbons results in a change of the Hall coefficient(R_H) equivalent to a decrease in HTT. However, experiments show that R_H remains positive even for the highest doses and the maximum reached is much lower than the maximum attained in direct heattreatment of carbons or in neutron irradiation of graphite. As to chemical donors, it is shown that introduction of sodium or potassium changes R_H in a way inverse to that of boron-doping; R_H reaches a negative minimum and converges to a negative constant.

The magnitudes of maximum and minimum of R_H appearing in carbons doped with chemical impurities have been often discussed in connection with those of maximum attained in heattreatment of samples. However, what is the physical basis for that?

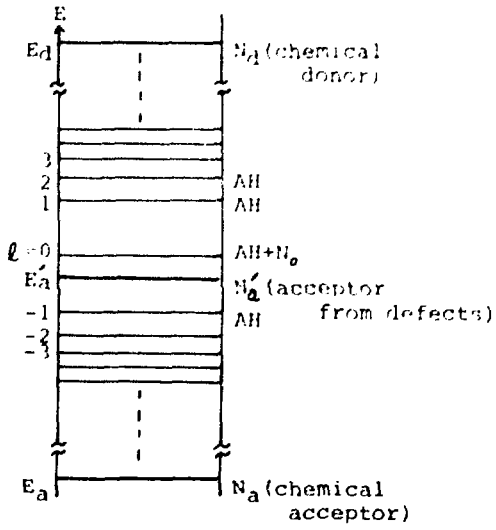
It is understood that the maximum in R_H appearing with heattreatment is due to variation of the carbon structure from turbostratic to graphitic one. However, it is shown by our analysis that the maximum appearing with doping can be explained in terms of our band model[1] by locating impurity levels deep below(for acceptor) or far above(for donor) the band edge.

Fig.1 shows our schematic energy diagram of a graphitic carbon in the presence of a magnetic field. Each Landau level has a state density proportional to a magnetic field(=AH,A:constant). At the band edge, a state density N_o is included as a simple expedient for the band overlap. An acceptor level(E_a') originating from structural defects is considered to be located at about 4meV below the band edge; their density denoted by N_a'. Whereas, we assume that the impurity levels are located deep from the band edge; for example, boron level is evaluated to be about 320meV below the band edge and potassium level to be 340meV above the band edge.

Using this band model, we have calculated the Hall coefficients of carbons doped with chemical impurities. The results are shown in Fig.2. At low temperatures($kT \ll E_a'$), an acceptor-doped carbon has a maximum in R_H ($=2/e(AH+N_o)$), and with increasing acceptor concentration R_H converges to a positive constant determined mainly by the acceptor level. With introducing chemical donors, R_H reaches a negative minimum($=-2/e(AH+N_o)$) and then converges to a negative constant determined by the donor level. At high temperatures($kT \gtrsim E_a'$), a maximum or a minimum is also obtained, but its magnitude decreases with increasing temperature. Therefore, theoretical magnitudes of maximum and minimum of R_H are smaller than those of maximum predicted in HTT dependence of undoped carbons and decrease with increasing HTT. The limiting value of R_H with high doses is independent of temperature(calculation is up to 300K).

Experiments made on the soft carbons by J.Bulawa et al.[2] and by S.Toyoda et al.[3] show that the theory is in semiquantitative agreement in both boron- and potassium-doped carbons heattreated above 2200C(Fig.3). The discrepancy in magnitude may be due to improper evaluation of the band parameters(E_a', N_a',N_o) for lack of precise data of R_H on the soft carbons. In terms of this band model, the effect of chemical impurities on the magnetoresistance of carbons can also be analyzed.

References
1)T.Kimura and K.Yazawa,Carbon 11,139(1973)
2)J.Bulawa,S.Mrozowski and A.S.Vagh,Carbon 10,207(1972)
3)S.Toyoda and S.Mrozowski,Carbon 7,239(1969)



$$E_\ell = \pm\left(\frac{3}{2}\right)^{1/2}\gamma_0 a\left(\frac{eH}{\hbar c}(\ell)\right)^{1/2}$$

$$W = \frac{4}{\pi c_0}\frac{eH}{\hbar c} = AH$$

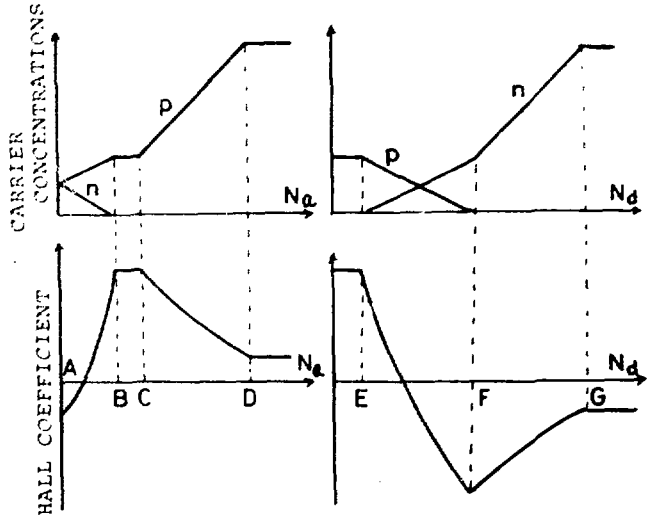
$\gamma_0 = 2.8eV$, $a = 2.64\text{Å}$

$e = 1.6\times10^{-19}$ C, c:light velocity

c_0: twice the interlayer spacing

$\hbar$: Planck constant

Fig.1 Schematic energy diagram of our band model for graphitic carbon



A:p=n=$(N_o+AH)/4$ E:p=$(N_o+AH)/2$,n=0

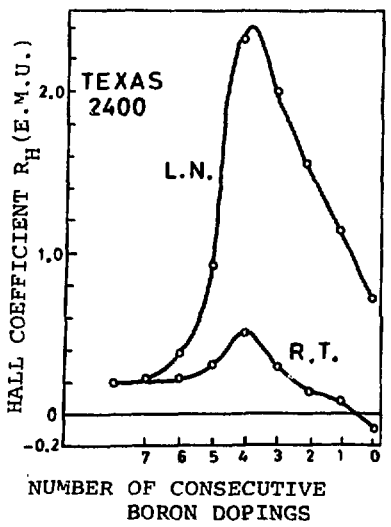
B:p=$(N_o+AH)/2$,n=0 F:n=$(N_o+AH)/2$,p=0

D:p=$N_o/2+W_{ao}$,n=0 G:n=$N_o/2+W_{do}$,p=0

W_{ao} :total state density between E=0 and E_a

W_{do} :total state density between E=0 and E_d

Fig.2 Schematic chemical acceptor (left) and donor(right)concentration dependences of carrier concentrations and Hall coefficients at low temperature.



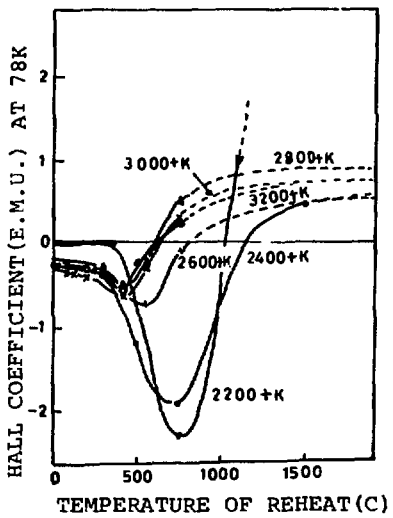


Fig.3(left) Changes in the Hall coefficient of a soft carbon heattreated to 2400C as boron is introduced in a number of consecutive operations. After J.Bulawa et al.[2]

(right) Changes in the Hall coefficient for soft carbons as the degree of potassium doping decreases with increasing temperature of reheat. The numbers in the figure indicate HTT. After S.Toyoda et al.[3]

K. Kawamura, T. Enoki and T. Tsuzuku
College of Science and Technology, Nihon University, Tokyo, Japan

§1. Introduction

Turbostratic carbon has been known to exhibit distinguished negative magnetoresistance at liquid nitrogen temperature(1) but its electronic structure as well as origin of the negative magnetoresistance has not been fully understood yet. In the present work, the effect of boronation on the galvanomagnetic properties and diamagnetic susceptibility of turbostratic carbon is investigated with a particular emphasis on the variation in magnitude of the negative magnetoresistance with boronation.

§2. Experimentals and results

A Texas coke heat treated at 2100°C for 10 min. was used as a turbostratic carbon specimen in the present work. Boronation was carried out at 1650 - 1800°C by using boric acid powder(2). Galvanomagnetic properties were measured at 77 K by a usual DC amplification technique and diamagnetic susceptibility was determined by Farady method using a Cahn electrobalance as a function of temperature between 77 K and 300 K.

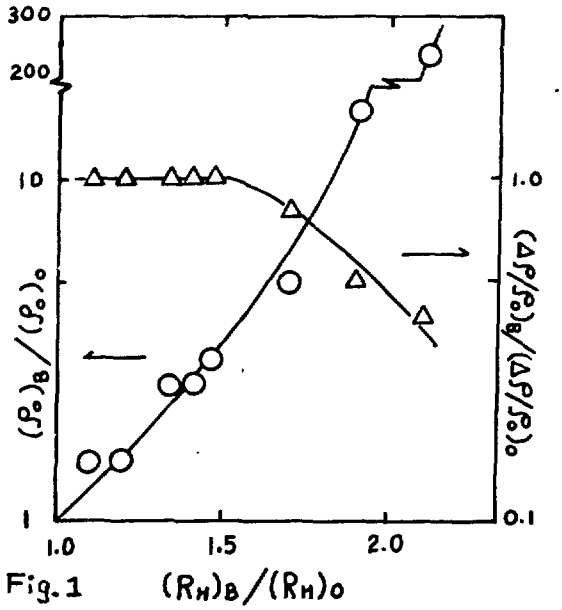


Fig. 1

Fig. 1 summarizes effects of boronation on the galvanomagnetic properties. The abscissa indicates ratio of the Hall coefficient after boronation $[(R_H)_B]$ to that before boronation $[(R_H)_0]$, showing a measure of effective concentration of substitutionally ionized boron. Each ordinate shows a similar ratio of the zero-field electrical resistivity and the magnetoresistance measured at 7 kOe respectively. The result reveals that the Hall coefficient ratio increases up to 2.2 and the resistivity ratio amounts even to 230. On the other hand, the magnitude of negative magnetoresistance is quite insensitive to boronation and, in particular, it does not vary at all when the Hall coefficient ratio is smaller than 1.5, suggesting that the negative magnetoresistance is a phenomenon insensitive to the position of Fermi level.

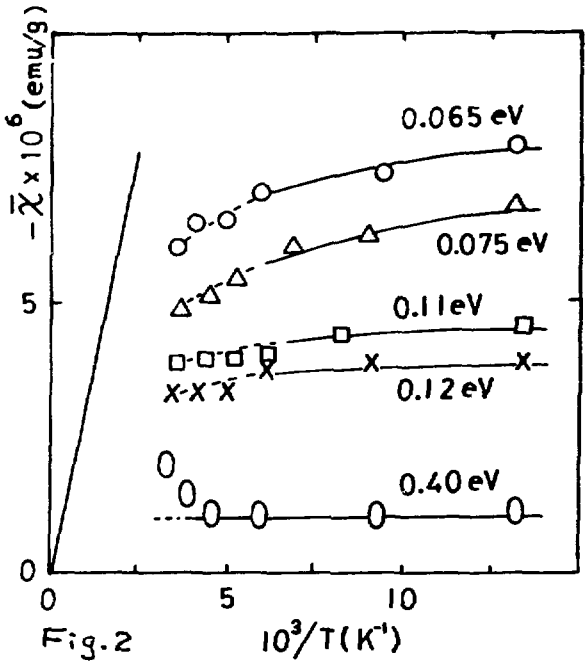


Fig. 2

Fig. 2 shows the average diamagnetic susceptibility as a function of the reciprocal of temperature. The solid lines are theoretical ones developed by Haering and Wallace(3) on the basis of a band model of two-dimensional graphite. The parameter indicates the Fermi level depression at 0K (Δ) which is estimated to be from 0.065 eV up to 0.40 eV for the present specimens.

The above-mentioned Fermi level depression is sufficiently large for one to regard electronic structure of the specimens as a one-carrier system at liquid nitrogen temperature.

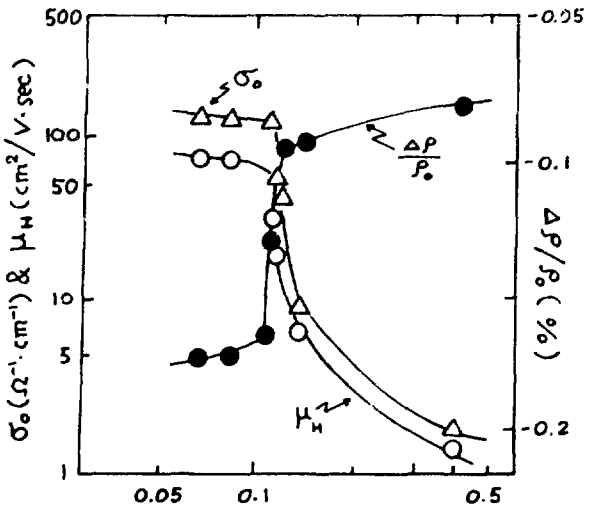


Fig. 3

Fig. 3 reveals variations as a function of Δ in the zero-field electrical conductivity (σ_0), the magnetoresistance ($\Delta\rho/\rho_0$) at 7 kOe and the Hall mobility (μ_H) calculated by conventional formulae for one-carrier system. These quantities are found to change in a drastic way at Δ of about 0.1 eV but they are quite insensitive to the change of Δ above and below 0.1 eV.

§3. Discussion

The mobility (μ_H) is expressed by

$$\mu_H = (e/m^*)\tau$$

where m^* denotes the effective mass and τ the relaxation time respectively. According to the uncertainty principle, the energy uncertainty (ΔE) is estimated by

$$\Delta E \sim \hbar/\tau = e\hbar/(m^*\cdot\mu_H).$$

To the first approximation, the effective mass can be related to the Fermi level depression as follows;

$$\Delta \simeq \hbar^2 k_F^2/2m^*$$

where k_F represents the Fermi wave number. Moreover, the Fermi wave length (λ_F) may roughly be correlated to crystallite size (L_a) of the present specimen as follows;

$$\lambda_F = 2\pi/k_F \lesssim \frac{1}{2} L_a \sim 50\,\text{Å}.$$

The estimation in conjunction with the numerical values for μ_H shown in Fig. 3 leads to the following results:

$\Delta E \lesssim \Delta$ for $\Delta \lesssim 0.1$ eV

$\Delta E > \Delta$ for $\Delta > 0.1$ eV

This indicates that the band model cannot be applied to the specimens having Δ larger than 0.1 eV and that Δ is merely a phenomenological parameter having no proper physical significance for these specimens. On the other hand, application of the band model seems fairly reasonable when Δ is smaller than 0.1 eV but the physical significance of Δ is still not so clear as is originally indicated by the model. Therefore, the electronic structure of turbostratic carbon before as well as after doping is not fully explained in terms of the rigid band model of two-dimensional graphite. The negative magnetoresistance peculiar to turbostratic carbon is considered closely related to disturbance of the band structure and should be interpreted by taking disturbed structure into account.

References

(1) S. Mrozowski and A. Chaberski
Phys. Rev. 104, 74 (1956)

(2) Y. Komatsu
Carbon 6, 204 (1968)

(3) P. R. Haering and P. R. Wallace
J. Phys. Chem. Solids 3, 253 (1957)

ELECTRICAL RESISTIVITY OF GRAPHITE NITRATES

F. Lincoln Vogel, Claude Zeller* and W.C. Forsman
College of Engineering and Applied Science and
Laboratory for Research on the Structure of Matter
University of Pennsylvania
Philadelphia, Pennsylvania 19104

Introduction

Intercalation of acid molecules into the grahite lattice produces a lamellar compound, which for the case of nitric acid has the formula $C_{6n}HNO_3$ where n=stage of the compound. The formation of the lamellar compound invariably results in a decrease in the "a" axis resistivity over that of pristine graphite. This change on intercalation of graphite has been examined in some detail by several groups all employing the same general method, that is, four point resistivity measurements on highly oriented pyrolytic graphite (HOPG) performed in situ. The generally accepted value for in-plane resistivity of pure graphite is $4x10^{-5}\Omega cm$(1) Ubbelohde (2) reported values of $4x10^{-6}\Omega cm$ for 1st and 2nd stage graphite in one series of experiments, and the same for stages 1 to 3 in another set of experiments (3). Fuzellier and Herold (4) reported lower values of $2.1x10^{-6}\Omega cm$ for stage 2 and $2.2x10^{-6}\Omega cm$ for stage 1. Since these are lower than any reported in the literature there is some reason to question them. Thompson,(5)using essentially the same techniques as the others reports $4.9x10^{-6}\Omega cm$ with stage 2 and 3 being indistinguishable.

Recent work on SbF_5- and AsF_5-intercalated graphite (6) revealed that the anistropy that develops in acid intercalated compounds and the difficulty in forming suitable electrical contacts leaves the four point resistivity method open to serious question. An adequate solution to this problem has been found in an r.f. induction method (7) of measuring in-plane resistivities and so it seems advisable to re-examine the graphite nitrates with this technique.

*Visting Scholar from University of Nancy, France.

Intercalation and Deintercalation Procedures

Graphite samples 0.2" x 0.2" x 0.01" thick were cut and cleaved from HOPG kindly supplied by Dr. Arthur Moore of Union Carbide Corporation. These were intercalated in vapor from 100% nitric acid made by distilling a mixture of KNO_3 and concentrated sulfuric acid. The apparatus was similar to that used by Ubbelohde having a reaction chamber containing a quartz spring balance and a means of controlling its temperature. It is connected by a manifold to the trapped vacuum pump or the temperature controlled nitric acid source or the purified nitrogen source. In operation, the sample is put in place on the pan of the balance, warmed in vacuum (10^{-3} torr) overnight. Intercalation takes place by admitting HNO_3 vapor to a

pressure determined by the temperature of the source and following the reaction by weight gain. Deintercalation is made to occur by first admitting N_2 to atmospheric pressure and then evacuating. Stage as determined by weight gain and x-ray diffraction agreed. It was possible, by means of a glove bag surrounding the reaction chamber, to transfer a sample to measurement vial without exposure to air.

Electrical Resistivity Measurements

Details of the measurement technique are given elsewhere (7). It consists of a ferrite core as part of a resonant circuit operating at 100 Khz. Inserting the sample into an air gap in the ferrite core produces a change in the resonant frequency which is a measure of the resistance of the sample. From the known geometry of the sample the resistivity can be calculated.

Results

In the work reported here only stage 2 and stage 4 compounds will be dealt with. The stage 2 compounds were made by direct intercalation only whereas the stage 4 compounds were made either by deintercalation of a stage 2 compound or by direct intercalation. The stage 2 compounds had in-plane resistivity values $\rho_a=3.0\times10^{-6}\Omega cm$ while the stage 4 compounds had in-plane resistivity values $\rho_a=2.9\times10^{-6}\Omega cm$. The stage 4 compounds were lamellar regardless of whether formed by intercalation or deintercalation.

Acknowledgement

We are grateful to Dr. Arthur Moore for supplying the HOPG material for this investigation.

References

1. I.L. Spain, Chemistry and Physics of Carbon 8, 1 (1973).
2. A.R. Ubbelohde, Proc. Roy. Soc. A304, 25-43 (1968).
3. A.R. Ubbelohde, Proc. Roy. Soc. A309, 297-311 (1969).
4. H. Fuzellier and A. Hérold, Proceedings of Fourth London International Conference on Carbon and Graphite (1974).
5. T.E. Thompson - Private Communication.
6. E.R. Falardeau, G.M.T. Foley, C. Zeller and F.L. Vogel, to be published in Chemical Communications.
7. C. Zeller and G.M.T. Foley, Submitted for publication in Review of Scientific Instruments.

MECHANISM FOR FORMATION OF GRAPHITE "ACCEPTOR COMPOUNDS"

W. C. Forsman
Department of Chemical & Biochemical Engineering
University of Pennsylvania, Philadelphia, Pennsylvania 19104

A review of the intercalation literature suggests that a single mechanism accounts for most known reactions that lead to so-called acceptor compounds. In many of the well documented cases, it is clear that before intercalation can take place, the graphite lattice must first be attacked by an electrophylic reagent. As the reagent removes electrons from the graphite, negative ions, accompanied by neutral molecules, diffuse into the lattice. This is undoubtedly the case in the formation of the aluminum chloride intercalation compound.

It has been established that, when acting separately, neither chlorine gas nor the vapor of $AlCl_3$ will intercalate the graphite lattice (1). A mixture of the two will, however, cause rapid intercalation (1). This is clearly an example of a Friedel-Crafts type process (2). Most probably, the complex $AlCl_4^-\cdots Cl^+$ is formed at the graphite-vapor interface by adsorbed $AlCl_3$ and Cl_2. It extracts electrons from the lattice and releases chlorine atoms, which couple to regenerate chlorine gas. The $AlCl_4^-$ then diffuses into the lattice along with neutral $AlCl_3$ molecules.

Although it has been reported that the Friedel-Crafts catalyst $FeCl_3$ can be intercalated without the addition of Cl_2 gas (3,4), Rüdorff, et al. (5) pointed out that at intercalation temperaures $FeCl_3$ decomposes to generate enough chlorine to effect intercalation by the mechanism described above. Although there is less detail given in the literature on either reaction conditions or characterization of products (6), the above comments on intercalation by $FeCl_3$ apply equally well to $ZnCl_2$, $BeCl_2$, $ZrCl_4$, $NbCl_5$ and $TaCl_5$ - all known to be Friedel-Crafts catalysts (2).

Although pure BF_3 does not intercalate, introducing small amounts of water into the reacting system effects rapid intercalation (7). This is readily explained by attack on the graphite by the highly electrophylic $\cdots H^+$ of the well known complex (2)

$$(BF_3OH)^-\cdots H^+$$

Ubbelohde (8) wrote a balanced reaction for the formation of graphite nitrate that gives NO_2 as a side product. This suggests that intercalation is effected by attack on graphite by nitronium ions, NO_2^+, which capture electrons and generate NO_2. In a series of experiments from this laboratory, we recently established that NO_2 is indeed generated during intercalation of highly oriented pyrolytic graphite by the vapor of 100% HNO_3. There is thus little doubt about the role played by nitromium ions in the formation of graphite nitrate.

It is important to note, however, that after formation of a 2nd stage compound, molecular HNO_3 could be moved in and out of the intercalated lattice by adjusting its partial pressure without concomitant oxidation or reduction of the graphite. Varying the HNO_3 content between apparent 2nd and 4th stages had little effect on electrical conductivity and lattice spacing (9).

Intercalation compounds based on AsF_5 and SbF_5 are of special interest because of conflicting evidence concerning their mechanism of formation. Opalovskii (10) reported that ClF was evolved when graphite was intercalated in a mixture of SbF_5 and ClF_3, which suggests the mechanism

$$SbF_5 + ClF_3 \rightleftharpoons SbF_6^-\cdots ClF_2^+$$

$$SbF_6^-\cdots ClF_2^+ + nC \rightarrow \underset{\text{intercalated}}{SbF_6^- + C_n^+} + \underset{\text{unstable intermediate}}{ClF_2}$$

$$2\,ClF_2 \rightarrow ClF + ClF_3$$

Graphite is also readily intercalated with liquid mixtures of SbF_5 and HF. The well-known electrophylic species in this mixture is H_2F^+ generated by the reaction (11)

$$SbF_5 + 2HF \rightleftharpoons SbF_6^- + H_2F^+$$

If graphite is oxidized by H_2F^+, however, either H_2 must be liberated or Sb^V must be reduced to Sb^{III}. We have established that no H_2 is formed during intercalation; although Sb^{III} was found in the reaction mixture, we have not satisfied ourselves that it could not have been formed by a side reaction. This must be done before its presence represents conclusive evidence for the proposed mechanism.

Both SbF_5 and AsF_5 intercalate graphite without addition of co-reagents, and there is evidence the intercalation involves only diffusion into the graphite lattice followed by electron transfer (12,13). An alternative mechanism involving electrophylic attack would be:

$$MF_5 + MF_5 \rightleftharpoons \underbrace{MF_6^- \cdot\cdot MF_4^+}_{\text{adsorbed complex}}$$

$$\underbrace{MF_6^- \cdot\cdot MF_4^+}_{\text{adsorbed complex}} + nC \rightarrow \underbrace{MF_6^-}_{\text{intercalated}} + \underbrace{C_n^+}_{\text{unstable intermediate}} + MF_4$$

$$2MF_4 \rightarrow MF_5 + MF_3$$

Lin (14) reports that AsF_3 is evolved during intercalation by pure AsF_5. In addition, we have identified substantial quantities of SbF_3 in the reaction mixture after liquid phase intercalation by SbF_5, but we have not yet established beyond doubt that it could not have been introduced by a side reaction. Consequently, at this writing it is still not established whether or not intercalation by AsF_5 and SbF_5 is by simple diffusion and electron transfer, or by oxidation of graphite by M^V, which is reduced to M^{III}, accompanied by diffusion of MF_6^- and MF_5 (and possibly MF_3) into the lattice.

*) Supported by the National Science Foundation, MRL Program under Grant No. DMR 76-00678.

References

1. Dzurus, M.L. and Hennig, G.R., J. American Chem. Soc., 79, 1051 (1957).
2. Olah, G.A. (Editor), "Friedel-Crafts and Related Reactions," Vol. 1, Interscience, New York, 1963.
3. Hooley, J.G. and Bartlett, M., Carbon, 5, 417 (1967).
4. Novikov, Y.N., et al., Zhurnal Strukturnoi Khimii, 11, 1039 (1970).
5. Rüdorff, W. et al., Angew. Chem. Internat. Edit., 2, 67 (1963).
6. Croft, R.C., Australian J. Chem., 9, 184 (1956).
7. Vogel, F.L., personal communications.
8. Ubbelohde, A.R., Proc. Roy. Soc. A., 304, 25 (1968).
9. Vogel, F.L., Zeller, C. and W. Forsman, presented at the 13th Biennial Conference on Carbon, University of California, Irvine, California, July 18-22, 1977.
10. Opalovskii, A.A., et al., Zhur. Neorg. Khim., 19, 1518 (1974).
11. Dean, P.A.W., et al., J. Chem. Soc. (A), p. 341 (1971).
12. Opalovskii, A.A., et al, Zhur. Neorg. Khim., 17, 1214 (1972).
13. Lalancette, et al., J. Chem. Soc. Comm., p. 815 (1973).
14. Lin, H.C., et al., Inorg. Nucl. Chem. Lettr., 11, 601 (1975).

TWO YEAR FREESTANDING VITREOUS CARBON IMPLANTS IN BABOONS

L. Shulman, P. Schnitman*, R. Feingold, L. Gettleman, P. Kalis, and M. Woolfson
Harvard Tooth Implant-Transplant Research Unit

Objective

The purpose of this project is to determine the long-term efficacy of vitreous carbon tooth-root implants [1] as self-supporting replacements for missing teeth.

Experimental Design

Forty-eight implants were inserted into fresh second premolar extraction sockets in 12 baboons. They were placed in functional occlusion and splinted for a 12-week healing period. At that time one half of the splints were removed and the associated implants left freestanding. The splints on the remaining implants were periodically removed to test mobility and replaced immediately. At two years, these splints were removed and all implants are now freestanding.

Results

In the first 2-year phase of this study half of the implants were splinted. Of the 24 which were freestanding, 6 were exfoliated and 2 were fractured. These losses all occurred within 28 weeks of splint removal: 4 by 4 weeks; 1 at 20 weeks; and 1 at 28 weeks. The fractures occurred at 12 and 20 weeks after splints were taken off. Of the 24 splinted implants all remained in place for 2 years. At 2 years, these splints were removed and left off for the duration of the study. Within 2 months of splint removal at 2 years, 5 of these implants were lost. Of the total 11 implants exfoliated in the study, only 3 were in the mandible. Throughout the study, the large majority of mobile implants were in the splinted group and these exfoliated soon after splints were removed at 2 years.

At this writing, of the 48 implants, 11 were exfoliated and 2 fractured. All remaining implants are in function, freestanding, and range from 2 to 2-1/2 years of age. Twenty-eight are immobile; and 7 have measurable buccolingual mobility (6 0.5 mm and 1 0.5 mm). Bone adaptation or its absence was apparent radiographically after 12 weeks. Radiographs delineated major bone changes and these occurred prior to 36 weeks. The ability of the radiograph to demonstrate minor bone changes taking place after 36 weeks was limited. Minor progressive bone loss was measurable, however, by periodontal probing to bone from a reference point and could be demonstrated in 35 of the 40 implants in place at 2 years. In addition, the reentry of some implant sites demonstrated bone saucerization and deep infraboney defects not evident on x-ray. After 2 years, there was radiographic evidence of change in some immobile implants in the appearance of the lamina dura like entity.

Conclusions

A high proportion of vitreous carbon implants can function without maintenance splinting for prolonged periods in baboons, even those with mobilities up to 0.5 mm. Prolonged splinting holds mobile implants in place that would otherwise be lost. There is gradual bone loss around even the most clinically successful implants which will ultimately limit their useful lifespan. Vitreous carbon implants survive best in the mandibular arch. Pocket probing to bone is the best criteria for assessing long-term bone adaptation and implant prognosis. The ability of vitreous carbon to function as a freestanding implant for 2 years appears to be determinable radiographically according to bone adaptation at 36 weeks. The long-term freestanding function of vitreous carbon implants with minimal bone loss warrants further investigation in humans.

1. Grenoble, D. E., Kim, R. L.: Progress in the evaluation of a vitreous carbon endosteal implant. Arizona State Dental Journal, 19:12-19, January - February 1973.

Supported by Grant No. RO1-DE03755 from the National Institute of Dental Research, NIH

* Co-Director with Dr. Shulman, Harvard Tooth Implant-Transplant Research Unit

THE EFFECT OF SURFACE TEXTURE AND BACTERIAL PLAQUE ON THE TISSUES SURROUNDING VITREOUS CARBON IMPLANTS

Samida, M. Loma Linda University School of Dentistry, Loma Linda
James, R.A.* Whittaker, J.M.* Schultz, R.L.**

While bacterial plaque is a widely recognized etiologic factor in periodontal disease and has been shown to contribute to the disease process commonly found around metal dental endosteal implant devices, several clinicians have denied it plays a significant role in chronic tissue destruction around vitreous carbon dental implants.

It is common clinical practice for the carbon surface in the area of the gingival sulcus to be textured either by sandblasting during fabrication or by instrumentation at the time of crown preparation. It seems reasonable that bacterial plaque retention should be related to surface texture. This study, therefore, involved both surface texture and bacterial plaque as variables in order to test if these factors were significant in affecting the tissue health around vitreous carbon implants. It also sought to ultrastructurally study the interface tissue.

Twenty-two vitreous carbon rods were implanted in a stump tail monkey (Macaca arctoides) and stabilized with gold splints.

One proximal side of each implant was textured by sandblasting, the other remained glazed. Clinical measurements were taken at regular intervals for (1) amount of crevicular fluid, (2) gingival recession and (3) sulcular depth.

After three months the animal was euthanized. Block sections were fixed either for transmission electron or light microscopy and embedded accordingly. The implant segments were carefully removed from the specimens to be studied by light microscopy prior to paraffin embedding.

TEM analysis illustrated (1) cords of epithelial cells close to surface, surrounded by connective tissue, (2) carbon particles adherant to junctional epithelium, (3) neutrophils amongst the fibroblasts, (4) interface contacting both connective tissue and epithelium in same area, (5) foreign body giant cells at the deep interface, and (6) bone and thin layer of osteoid close to implant at the deep layer.

Paraffin embedded specimens were sectioned and stained. Areas of inflammation and the distance from the gingival crest to the end of the junctional epithelium were measured and recorded.

Clinical data revealed a statistical significance showing increased pocket depth with plaque.

Considerable tearing occurred when the implant segments were removed from their tissue beds. This tearing made measurement difficult and inaccurate. No statistical significance was shown between tissue health (as measured by the microscopic parameters) and either surface texture or plaque, although definite trends were apparent.

* Loma Linda University
School of Dentistry
Department of Restorative Dentistry
Loma Linda, CA 92354

** Loma Linda University
School of Medicine
Anatomy Department
Loma Linda, CA 92354

This work was supported by Vitredent Marketing Corporation, 400 W. Florence Avenue, Inglewood, CA 90301.

CLINICAL EVALUATION OF FUNCTIONAL LTI PYROLITE CARBON BLADE IMPLANTS IN PRIMATES WITH DESIGN CONSIDERATIONS

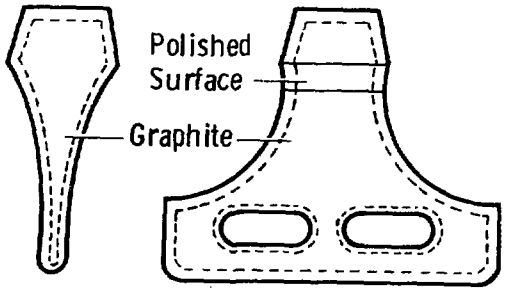
J. Kent*, C. Farrell*, S. Hulbert**, J. Bokros***

* LSU School of Dentistry
Department of Oral & Maxillofacial Surgery
New Orleans, Louisiana

** Rose-Hulman Institute of Technology
Terre Haute, Indiana

*** General Atomic Company
San Diego, California

Low temperature isotropic-silicon alloyed pyrolite carbon dental implants (endosseous blade type) (Figure 1) were placed in eight baboons (papio cynocephalus) for a period of 24 months to determine the clinical response. Mandibular second and third molar teeth were removed bilaterally and the tooth sockets allowed to heal for eight weeks. Conventional surgical techniques using Numbers 4 and 700 air driven high speed carbide burs with saline coolant were used for placement of the carbon blade. The shoulder of the implants were seated bilaterally to a depth of 7 mm placing the polished margin of the implant neck at the alveolar crest. (Figure 2) Insertion was completed with finger pressure. Tight mucosal closure around the neck of the implant was accomplished with polyglycolic acid sutures. An interocclusal distance of 2 mm was established with reduction of the opposing maxillary teeth and if necessary up to 1 mm reduction of the head of the implant. Bimonthly dental prophylaxis was accomplished along with clinical observation recording mobility, gingival sulcus depth, tissue texture, and contour. Periapical radiographs were taken at 6 month intervals. The animals were anesthetized with Phencyclidine hydrochloride and maintained on parenteral penicillin 12 postoperative days. All implants on the right side were free standing opposing the natural maxillary dentition. (Figure 3) All implants on the left side were restored with a three unit cast gold prosthesis utilizing the natural first molar as a single abutment two months postoperatively. (Figure 4) Centric vertical occlusion without lateral interference was established and maintained.



Silicon-alloyed LTI carbon on graphite substrate

Figure 1



Figure 2



Figure 3



Figure 4



Figure 5

Results

Mobility of the endosseous implant was utilized as chief criteria in the determination of a successful implant. The following mobility scale was utilized; 0 - no mobility, 1/2 - clinically perceptable mobility, 1 - 1/2 mm movement in buccal or lingual direction, 2 - 1 mm movement in buccal or lingual direction. Seven of eight right side free standing implants had a mobility of 0. One of eight right sided free standing implants had a mobility of 1. Seven of eight left side restored implants had a mobility of 0 and 1 of eight restored implants had a mobility of 1. The mobility of 1 in both the freestanding and restored implants were recorded in the same animal.

Gingival sulcus depth was measured at buccal, lingual, mesial and distal sites using a standard calibrated periodontal probe. Sulcus depth is a reflection of oral hygiene status. Satisfactory maintenance of oral hygiene is determined by proper implant design, fixed prosthesis construction and contour, and professional care. Increased sulcus depth may be due to either gingival inflammation and hypertrophy secondary to impaired oral hygiene or to apical epithelial migration. Increased sulcus depth recordings secondary to gingival hypertrophy are usually short term if local etiologic factors are corrected. Increased depth due to apical epithelial migration is usually associated with implant mobility and loss of supporting bone due to improper implant-bridge designs or abnormal occlusal forces. Gingival sulcus depth was recorded as less than 3 mm for seven of eight free standing implant and six of eight restored implants and greater than 3 mm in one of eight free standing and restored implants. The greater sulcus depth recordings were found in the same animal with mobility of 1.

Periapical radiographs demonstrated the formation of a sclerotic line along the neck of the implant along the alveolar crest to the shoulder of the blade at 3-6 months post insertion. This sclerotic line was quite distinct at 12 months. (Figure 5) There appeared to be an increased density of bone at the neck of the free standing implant when compared to the restored implants. (Figure 6) Only two of 16 implant sites showed any

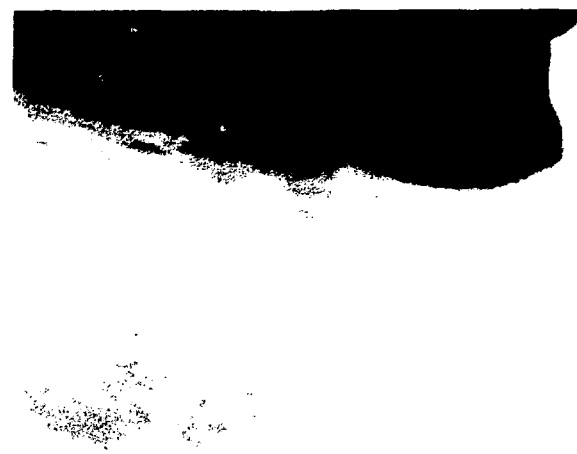


Figure 6

evidence of saucerization or vertical bone loss. This bone loss was observed in both the free standing and restored implant in the same animal with increased sulcus depth of mobility of 1.

Gingival texture and contour was essentially normal at all implant sites except two in which free mucosa rather than attached gingiva was present at the implant neck of the baboon with increased sulcus depth, mobility of 1, and vertical loss.

Clinical observations made during this study substantiate the impression that excellent results were obtained with properly designed prostheses, sanitary "high water" pontics, implants designed utilizing a flared neck (crown support), placement so that attached gingiva surrounds the implant neck, and maintenance of satisfactory hygiene with professional care.

HISTOLOGY OF [illegible] ARTIFICIAL IMPLANT-TISSUE INTERFACE IN PRIMATES

C. Farrell*, J. Kent*, J. Blawitter**, [illegible]***, [illegible]****, R. Carr*

* LSU School of Dentistry
Department of Oral & Maxillofacial Surgery
New Orleans, Louisiana

** Tulane University, Biomaterials Laboratory
New Orleans, Louisiana

*** General Atomic Company
San Diego, California

**** Rose-Hulman Institute of Technology
Terre Haute, Indiana

Low temperature isotropic - silicon alloyed pyrolite carbon dental implants (endosseous blade type) were placed in eight baboons (papio cynocephalus) for a period of 24 months to determine the histologic findings of the implant-tissue interface. Mandibular second and third molars were removed bilaterally and the tooth sockets allowed to heal eight weeks. Convertional surgical techniques were used to place the carbon implants to a shoulder depth at 7 mm placing the polished margin of the implant at the level of the alveolar crest. Tight mucosal closure was obtained with interrupted polyglycolic acid sutures. The animals were maintained on parenteral penicillin twelve postoperative days. Two months after insertion a fixed cast gold prosthesis was placed on the left implants using the natural first molar as a single abutment. Centric vertical occlusion without lateral interference was maintained. All right sided implants were left free standing opposing the natural maxillary dentition. Bimonthly dental prophylaxis and clinical observation of the implant was accomplished. Radiographs were taken at six month intervals.

At 24 months post insertion marginal mandibular resections were performed on six animals (12 implant sites). Two animals have been extended for long term evaluation. Immediately upon resection the implant-tissue interface was forcefully probed with a sharp instrument. The specimens were then placed in 10% formalin. The gingival tissue-bone-implant specimens were divided bucco-lingually through the center of the implant. (Figure 1) One half of the specimen was prepared in the undecalcified state with the implant in place. The specimen was dehydrated with ethyl alcohol and then infiltrated with methyl methacrylate monomer. The specimen was they polymerized by embedding in a hard plastic block. Bucco lingual sections 250 micra thick were prepared with a diamond saw. These sections were glued to a slide and ground to approximately 100 micra. Staining was accomplished with Paragon 1301. The remaining half of the original specimen was decalcified, the implant removed and tissue embedded in parafin. The sections obtained were routinely stained with hematoxylin and eosin.



Figure 1

Results

Histologic findings on 10 of the 12 specimens showed a complete absence of bone resorption of the alveolar crest and an absence of epithelial migration or fibrous tissue formation at the implant-tissue interface. (Figure 2) Two of the 12 specimens revealed a dense connective tissue capsule with fiber bundles paralleling the implant surface totally surrounding the implant. This capsule was of variable thickness at different areas of the implant. No epithelial migration could be found in either of these implants. In the successful implant no evidence of necrosis or inflammatory processes including foreign body type reactions were observed. At the epithelial junction of the neck of the implant a normal sulcus was observed which closely simulated the normal gingival sulcus. Sulcus depth also appeared normal. There was close adherence of the soft tissue to the implant surface. Normal bony architecture and constructive remodeling occurred throughout the cortical and cancellous bone adjacent to and distant from the implant. (Figure 3) Along the bone-implant interface extending from the neck of the implant to the midbody portion normal dense lamellated bone was seen with occasional marrow



Figure 2



Figure 3

spaces and Haversian canals approximating the implant. Inferiorly, along the body of the implant surface including the vent areas there was a normal increase in fatty marrow and dense bone which radiated from the implant in an apparent buttressing phenomenon secondary to functional stresses. High power views of the interface between dense bone and implant where artefactual separation occurred showed adherence of carbon particles to

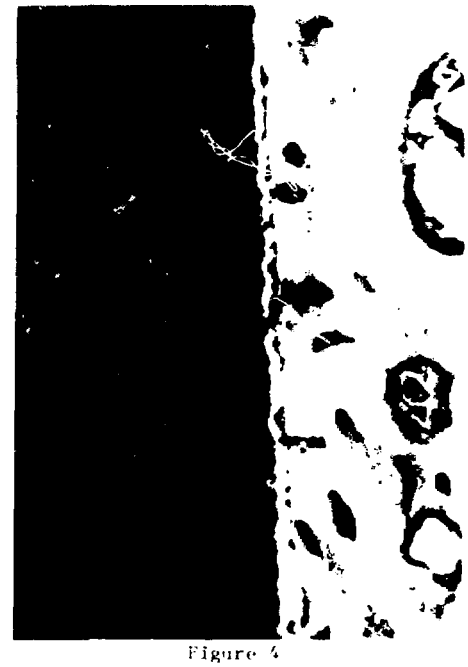


Figure 4

Conclusions

The histologic findings of this study correlated exactly with the clinical observations made with the same animals. Those implants which demonstrated clinical stability and histologic depth revealed a fibrous encapsulation of varying thickness surrounding the implant. Successful implants demonstrated an interdigitating mechanical bond between bone and the carbon surface. The Ti-silicon alloyed carbon dental implant appears to be extremely well tolerated in the primate experimental animal and provides a surface substrate capable of producing an effective mechanical interlock with surrounding bone.

[illegible]
[illegible]
[illegible]
[illegible] Center
Tulane University
New Orleans, La.
[illegible]
Rose-Hulman Institute of Technology
Terre Haute, Ind.
J. Kent, [illegible] Farrell
Louisiana State University
School of Dentistry
New Orleans, La.
J. [illegible]
General Atomic Corp.
San Diego, Calif.

Functional retention of a dental implant requires that the interface between tissue and implant is capable of transmitting service loads without causing adverse changes in the tissue structures adjacent to the device. Animal studies have [illegible] that LTI carbon blade type dental implants [illegible] [illegible] functional retention [illegible] [illegible] years. The objective of this [illegible] was to [illegible] the [illegible] interface between LTI carbon dental implants and bone.

Twelve LTI carbon blade type dental implants and surrounding tissues were removed together with surrounding tissues from the mandible [illegible] after an implant duration of 24 months. [illegible] half of the implants were fitted with three unit restorations and the other half were left unrestored and free standing. No adverse changes were observed clinically or radiographically in ten of twelve sites. The tissue blocks containing the implants were sectioned to provide specimens from each implant for histological, microradiographic and scanning electron microscopic (SEM) analyses. Histological evaluations were performed using decalcified and undecalcified sectioning techniques. The undecalcified sections containing the carbon implants were produced using polymethylmethacrylate embedding, diamond sawing and abrasive grinding and polishing techniques. The undecalcified procedure allowed for the preparation of microradiographs of the implant-mandibular bone sections.

An SEM analysis of the LTI carbon implant surface prior to implantation revealed a microporous surface layer was present on the otherwise dense carbon material. Examination of the undecalcified histological sections revealed that bone had formed so that it interdigitated with the microporous surface of the implants, Figure 1. Examination of the microradiographs revealed evidence that a mechanical bond had been formed by the interdigitation of bone with the microporous carbon surface. Figure 2 shows a microradiograph of an undecalcified section of a specimen in which the implant was mechanically dislodged from the bone during the sectioning procedure. The arrow in figure 2 points to a microradiographically detectable layer of bone left adherent to the carbon surface, indicating that a sufficiently strong bond had formed so that delamination of the bone in contact with the carbon had occurred. SEM examination of the corresponding surfaces of tissue and implant after mechanical separation revealed a distinctly different morphological appearance for the areas of bone contact as compared to areas of soft tissue contact. [illegible] always found to [illegible] the carbon surface. The areas corresponding to the bone-carbon interface [illegible] [illegible] different characteristics. [illegible] bone and carbon material separated at the interface [illegible] adherent to the carbon and [illegible] adherent to the bone. [illegible] type of behavior [illegible] shown in figure 3. The second type of bone-carbon interface behavior resulted in a delamination of the bone tissue leaving a layer of bone adherent to the carbon, as shown in figure 4. The delamination of bone observed with the SEM appears to be the same as that observed microradiographically as shown in figure 2.

It was concluded that a load transmitting interfacial bond between the microporous LTI carbon surface and bone had been formed and may have been a contributing factor to the successful performance of the dental implants.



Figure 1 Photomicrograph showing bone growth into the microporous LTI carbon surface, 180X.



Figure 2 Photomicrograph of microradiograph showing bone adherent to carbon (arrows) after mechanical separation of bone from implant, 75X.

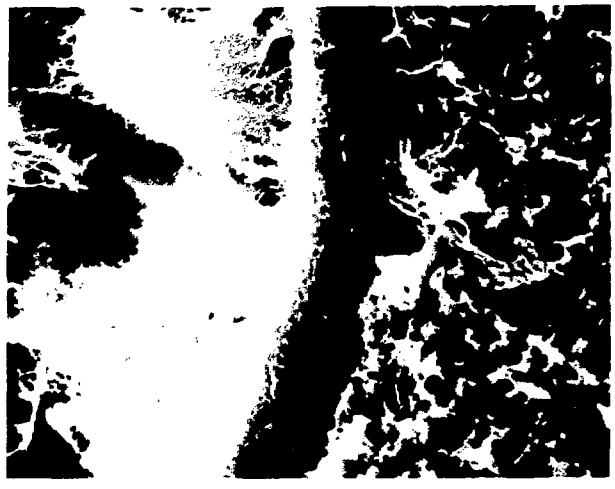


Figure 3b

Figure 3 Scanning electron micrograph of a) LTI carbon surface, and b) corresponding tissue surface. Left hand portion of figures show adherent soft tissue and right hand portion shows clean separation of bone from carbon, 3750X.

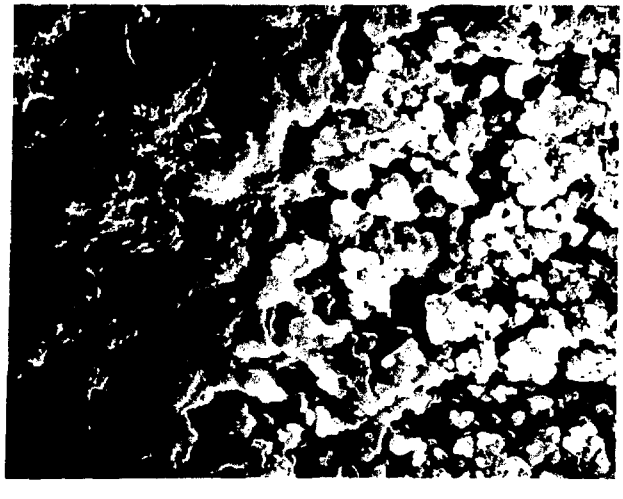


Figure 3a



Figure 4 Scanning electron micrograph of carbon surface showing a portion of adherent bone tissue, 1500X.

AN ULTRASTRUCTURAL STUDY OF BABOON TISSUE INTERFACING WITH PYROLYTIC CARBON DENTAL IMPLANTS

James, R.A. Loma Linda University School of Dentistry, Loma Linda
Whittaker, J.M.* Schultz, R.L.**

The science of dental implantology has advanced greatly in recent years both in materials development and knowledge of supporting tissue reaction. The ultrastructure of these tissues, however, has not as yet been extensively studied. The purpose of this investigation was to more thoroughly evaluate the ultrastructure of these tissues and to correlate the findings with light microscopic evaluation.

Four blade type endosteal dental implants fabricated of silicon-alloyed, low-temperature-isotropic, pyrolytic carbon (LTI-Si) were surgically placed interdentally between the canine and second molars in the jaw bones of a male baboon. The surgical sites had been edentulatized three months earlier. Each implant had a pergingival post which was stabilized with a cast gold splint which extended from the canine to the second molar. One rod of the same implant material was surgically placed endosteally in the symphysis area of the mandible and was completely buried.

Six months after placement, block sections containing the implants were removed. One half of the blade implants along with the buried rod were fixed for transmission electron microscopy, the other half of the blades for light microscopy. All specimens were embedded in epon. The epon blocks containing the specimens were sectioned into segments measuring approximately 1 mm thick and the implant removed by thermal stress fracturing.

Tissue specimens were then reembedded in epon, oriented and sectioned for either light microscopic or TEM analysis.

Findings: Foreign body giant cells were found at the interface at all levels. There was evidence of a direct bony interface in the areas remote from the pergingival site. There were also areas of considerable osteoblastic activity. An abundance of lymphocytes and plasma cells gave evidence of a chronic inflammatory gingivitis in the pergingival tissue.

* Loma Linda University
School of Dentistry
Department of Restorative Dentistry
Loma Linda, CA 92354

** Loma Linda University
School of Medicine
Anatomy Department
Loma Linda, CA 92354

This work was supported by Loma Linda University, Loma Linda, CA 92354.

C.V.D. CARBON COMPOSITES :
PREPARATION, ELECTRONIC AND THERMAL PROPERTIES

A. PACAULT, P. LOLL, P. DELHAES

Centre de Recherches Paul Pascal, Université de Bordeaux I, 33405 TALENCE (France)

and

A. PIERRE

S.N.E.C.M.A.-AQ, Centre d'Issac, 33162 SAINT-MEDARD-EN-JALLES

1 - Introduction

Carbon densification processing (1) of porous or fibrous substrates have been studied during these recent years because of the aerospace applications (2). We have prepared and investigated a family of carbon felt-carbon matrix composites. In relation with the different microstructures we have studied the electronic and thermal properties.

2 - Deposition technique and characterization

- *Experimental* : the isothermal process with a resistor-graphite furnace working between 1000 and 1300°C has been used. The hydrocarbons is methane diluted in nitrogen and sometimes with hydrogen additions. The substrate is a carbon felt.

- *Existence diagram* : the pyrolysis of methane occurs under conditions far from thermodynamical equilibrium. In order to describe such a process it is useful to distinguish (3).

The constraints : variables which might be controlled by the experimenter ; they are either fixed by the method (shape and size of the furnace, no thermal gradient because of the isothermal process, constant pressure of gases) or adjustable (deposit temperature T_D, composition and flow (D) of gases, time of deposit t_D).

The responses : variables measurable by the experimenter, all the observations and the physical properties which are involved in the study (see table I).

The system is the whole set of response and depending on the processing constraints an existence diagram can be established in the constraints space. In order to do that a response must be chosen as pertinent : this is the nature of the microstructure determined by optical microscopy under polarized light illumination (4). Differents microstructures have been characterized : rough laminar (R.R), smooth laminar (L.L), granular (G.G), isotropic (I) and mixture of them in agreement with previous investigations (5) except a difference quoted for the granular microstructure (4). For a quasi-constant flow a section of the existence diagram characteristic of the carbon felt is drawn with only 15 responses (figure 1).

- *Physical properties* : they are presented on table I for the CVD as deposited :

- the apparent and powder densities, the X-ray informations which are in agreement with results on similar composites (3)(5).

- the magnetic properties have been examined for the first time ; the EPR line widths are characteristic for each microstructure and the diamagnetism furnishes a very interesting result. There is significant differences between the characterized microstructures (see figure 1). Furthermore the relative diamagnetic anisotropy ($\Delta\chi$%) allows us to confirm quantitatively the optical anisotropy of the different samples.

- the electrical and thermal conductivities confirm the picture : the thermal variations of the thermal conductivity give further evidence of two classes of materials (figure 2).

- *Graphitization process* : after heat-treatment at 2500°C during 1 h 30 mn the studies of structural and physical properties confirm that only the rough laminar microstructure is graphitized the other ones behave as hard carbons.

3 - Conclusion

The model proposed by LIEBERMAN (6) which relates gas phase conditions to the structure of deposit is discussed in the frame of the established correlations between electronic properties and microstructu-

res. We show in this study that a graphitable microstructure (L.R) exists between the non-graphitable ones (see figure 1). This behavior could be correlated with the formation of a mesophase from the gas phase reaction processes which might occurs only for these constraint conditions.

The existence diagram shows up how to obtain the desired microstructures under defined conditions. They change with the fixed and adjustable constraints. Finally we proposed a method to analyze the parameters which define an evolution and to make possible a selection of a specific material for a given application.

(1) [illegible] - *Chemistry of Carbon*, vol. 2, p. [illegible] (ed. by P.L. WALKER, 1972).

(2) B. GRANOFF, H.O. PIERSON and D.M. SCHUSTER - *J. Composite Materials*, vol. [illegible], p. [illegible] (1972).

(3) A. PACAULT, P. HANUSSE, P. DE KEPPER, C. VIDAL and J. BOISSONADE - *Accounts of Chemical Research* p. 428 (1976).

(4) P. LOLL - *Ph. D Thesis, Bordeaux 1976.*

(5) B. GRANOFF - *Carbon, vol. 12, p. 681 (1974)(and previous publications from SANDIA Laboratories).*

(6) M.L. LIEBERMAN - *Proceedings of the 3rd Conference on Carbon vapor deposit, p. 25 (1972).*

Samples	Deposit conditions: Flow (l/h) H_2	Flow (l/h) H_2	% CH_4	T_D(°C)	time t(h)	micro-structure	dimensions: apparent d	dimensions: of powder	R.F. Structures L_c(Å)	L_a(Å)	d_{002}(Å)	Static magnetism χ_d(10^6cm CGS/g)	$\Delta\chi$	E.P.R. g-factor	E.P.R. S(gauss)	Conductivities electrical (Ωcm)$^{-1}$	Conductivities thermique K(Wcm^{-1}K^{-1})
PLB	30	367	8	1350	74		1.50	2.05				- 3.53	16				
PLD	15.5	347	4.7	1100	123		1.65	2.07	80	90	3.430	- 3.28	18		55		0.36
PLE	16.5	347	4.7	1050	178	L.R.	1.60	2.07	72		3.432	- 3.31	16	2.0005	65		
PLH	16.5	347	4.7	1210	281		1.73										
PLI	16.5	347	4.7	1135	105		1.65	2.07	87		3.424	- 3.42	21	2.0034	20	890	
PLL	16.5	347	4.7	1080	200		1.80	2.04	78	75	3.436	- 3.26	22	2.0026	34	840	0.36
PLC	[illegible]	[illegible]	[illegible]	1080	97		1.75	1.98	86	70	3.438	- 2.75	16	2.0027	27		0.34
PLG	54.6	305	15	1080	85	L.R.+L.L	1.75	1.98	57		3.447	- 2.47	15	2.0019	26		
* PLQ	36.4	327,6	10	1140	21		1.33	1.91	74		3.432				66	490	
PLJ	109	255	30	1080	59		1.70	1.87	42	<70	3.447	- 2.10	12	2.0031	6.8	555	0.145
PLN	73	291	20	1060	120	L.L.	1.88	1.95	43	<70	3.458	- 2.25	12	2.0030	12.5	570	
* PLK	7.3	357	2	1210	67		>1	1.51	48		3.433	- 3.75	7		> 55	230	
PLM	6	294	2	1150	100		1.25	1.67	68		3.428	- 3.66	8		46	290	0.16
PLO	4	296	2	1150	154	L.G.	1.19										
PLP	2	98	2	1150	205		1.20	1.52	50		3.428						
PLR	16.5	347	4.7	1150	69		1.30	1.51	85	75	3.426	- 3.65	8	2.0022	12	175	
PLS	2 + H_2=6	96	2	1225	116		1.05	1.51	58		3.440	- 4.35	5	2.0071	9.4	155	
PLT	2 + H_2=12	96	2	1230	257	1	1.22	1.46	52	90	3.440	- 4.42	2.5	2.0021	6	135	0.225

* These samples are not completly densified.

Table I : Structural and physical properties measured at 295 K of the C.V.D. composites.

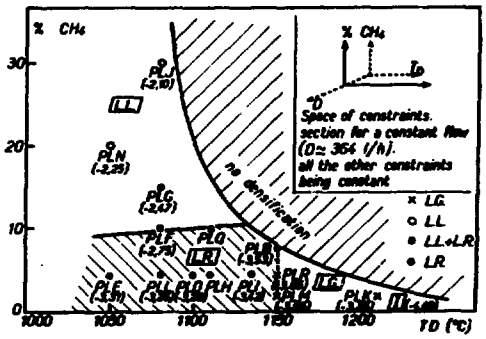


Fig. 1 : *Existence diagram in the constraint space. The dashed part represents the graphitable L.R microstructure zone and the numbers between brackets are the diamagnetic susceptibilies measured at room temperature.*

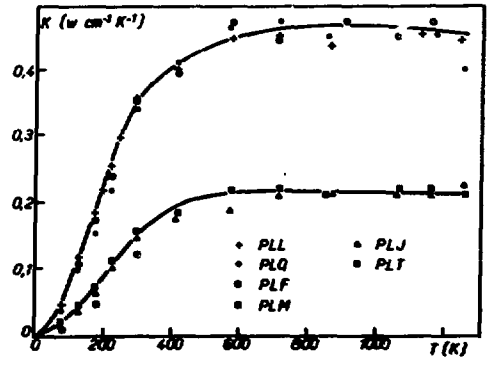


Fig. 2 : *Thermal conductivity versus temperature between 80 and 1300 K for several characteristic composites.*

DEVELOPMENT OF INTERFILAMENT MATRIX STRUCTURES IN CVD-INFILTRATED CARBON-CARBON

E. R. Stover, J. F. D'Andrea, P. N. Bolinger and J. J. Gebhardt
General Electric Company, Re-Entry & Environmental Systems Division
Philadelphia, Pa. 19101

Introduction

Some carbon-carbon composites have been processed by an initial infiltration with methane at low pressure to deposit pyrolytic (CVD) carbon on the fibers. When subsequently impregnated with coal tar pitch and baked at 100 MPa pressure, a graphite matrix is often formed within the bundles having basal planes perpendicular to the fiber direction. This structure, termed "transverse oriented graphite" (TOG)[1], provides an explanation for the lower values of thermal conductivity and elastic modulus in such composites, compared with identical materials in which the intrabundle matrix is primarily oriented with planes parallel to the fibers (POG). The TOG is readily identified by rotation of polished sections under plane polarized light, or by ion bombardment which etches cracks parallel to the basal planes. This presentation reviews observations made in connection with several programs relevant to the conditions required for TOG formation.

Origin of Transverse Oriented Graphite

The microstructures in several composites have been evaluated after the initial cycle of pitch impregnation and carbonization, using scanning electron microscopy and polarized light on polished sections. Supplementary information has been obtained from many billets after final processing. It has been observed that when a clean, high-modulus fiber preform is impregnated with pitch and carbonized under the same conditions as a CVD-infiltrated preform, TOG does not form next to the bare fibers. The pitch, and resulting mesophase, appear to wet the surfaces completely within the fiber bundles, and the primary matrix orientation is parallel to the filaments. Such composites, after final processing, may show some transverse structures in gaps filled in later cycles. Mesophase coating the broken ends of filaments can also develop planes transverse to the fiber bundle direction (parallel to the fractured surface).

When an isotropic CVD coating is applied, however, the only matrix in the bundles after the first cycle consists of nonwetting globules of mesophase, provided that fine particles present in the pitch have been filtered out by the preform; a fine-grained isotropic matrix may result if particles are present. The globules, characteristic of mesophase formation at high pressure, may contain a random orientation of planes in the final composite. This is more often the case if the gap between filaments is large, and if the CVD coating is relatively thick.

However, a standard CVD process has produced billets in which TOG has formed in the major portion of the initial globules within the fiber bundles. TOG formation frequently decreases near the surface, where the films are thicker,[1] and it may vary with location within some billets. Figure 1 illustrates such globules on the surface of coated bundles. Note that bladelike growths on the coated Thornel 50 have a transverse orientation, and appear to be wet by the droplets; most contact with the surface, however, has an angle greater than 90°. A variability in such "nucleating sites" in the coating is one hypothesis for the variability in TOG formation.

Changes during Successive Cycles

Several billets have been examined by excising samples after successive cycles. Figure 2 illustrates observations made on a 15-cm square section billet in which adjacent slabs were removed after each cycle at the Y-12 plant, Union Carbide Nuclear Division, Oak Ridge, Tenn. These were examined at GE-RESD. The amount of TOG present in the bundles increased, in subsequent cycles, with some variability due to exact differences in location.

The increase in TOG content is due primarily to filling cracks formed in the initial globules having the transverse orientation. Continuous TOG may be formed for long distances as a result. Parallel-oriented graphite, however, often develops on fibers which were not initially covered by the mesophase. The liquid in subsequent cycles wets these surfaces, in contrast to the first cycle.

Effects of Fiber and CVD Conditions

Minor changes in CVD conditions have not affected the amount of TOG formed in billets. However, changing conditions to produce a more anisotropic deposit resulted in no formation of TOG, and lower contact angles between the droplets and the surfaces. It has also been found that under similar deposition conditions, CVD coatings on fibers made from PAN (acrylic) or pitch precursors graphitize more readily than those on rayon-precursor Thornel 50, thus altering structure after the first graphitization.

Effects of Mesophase Formation Conditions

In autoclave runs where heater failures or other heating anomalies permitted the pressure to drop before the mesophase had stiffened, some of the matrix was removed from the material due to gas formation while the pitch was still liquid. Where a standard graphitization followed, involving a relatively high heating rate, the

Work sponsored by the Air Force Materials Laboratory, Wright-Patterson Air Force Base, Ohio, under the following contracts: F33615-71-C-1436, F33615-76-C-5134, F33615-75-C-5254, and F33615-76-C-5161.

residual pitch carbonized at one atmosphere. No TOG formed under these conditions within the bundles, even if subsequent cycles were normal; the absence of globular structures in the bundles indicated that the CVD coating had been affected so as to permit wetting.

Conclusions

Formation of TOG requires (a) thin, isotropic coatings on the fibers which inhibit wetting by the pitch (or mesophase), (b) formation of mesophase at high pressures to produce globules within the bundles, and (c) a nucleus or other mechanism for formation of transverse molecular orientations within the globules, rather than a random orientation.



Fig. 1. Carbonized Mesophase Globules on the Surface of Thornel 50 Coated with CVD for 35 Hours at 1100°C; Note Transverse Oriented "Blades" on the Fiber Surface.

References

(1)R. H. McSwain and C. F. Bates (Southern Research Institute), AFML-TR-77-26, to be published.

Acknowledgments

Dr. E. A. Feingold of the Space Sciences Laboratory, General Electric Company, provided electron microscopy and electron diffraction studies.

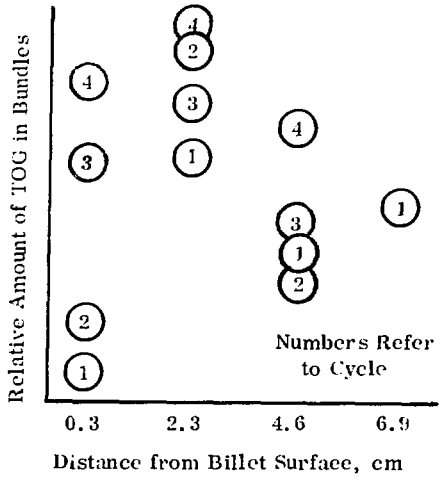


Fig. 2. Relative Amounts of TOG in Bundles of a 15 cm Square Section Billet after Successive Cycles of 100 MPa Carbonization to 650°C and Graphitization.

UNIDIRECTIONALLY REINFORCED CARBON/CARBON-COMPOSITES WITH POLYIMIDE AND PHENOLIC RESIN AS MATRIX PRECURSOR

E. FITZER, K.-H.GEIGL, M. HEYM

Institut für Chemische Technik
Universität Karlsruhe,West-Germany

Introduction

Carbon-Carbon-(C/C)-Composites are usually fabricated by infiltration of carbon fibres with a solution of a thermosetting resin, molding the resulting prepregs to the final shape of the composite and carbonizing the resin binder. Thus a skeletal composite with carbon bridges between the monofilaments is obtained which is densified subsequently by gas phase impregnation with pyrocarbon (HILL et al., 1974). FITZER et al.(1972,1974) succeeded to use coal tar pitch as primary binder precursor and to replace the CVD impregnation process by repeated reimpregnation/recarbonization cycles with pitch. Carbonizations of the pitch binder have been performed under elevated gas pressure up to temperatures of semicoke formation in order to provide high coke yield of the pitch and good adhesion between the fibres and the resulting carbon bridges. The final mechanical properties of C/C-composites prepared by the CVD and by the pitch process have been found to be equivalent and correspond to 100% utilisation of the fibre properties.

With the aim to make the C/C-composite fabrication technology more economic FITZER et al. (1976) have found recently that the elevated gas pressure during baking of pitch bonded carbon fibre composites can be avoided if the used binder pitch is modified by sulfur addition. The sulfur acts mainly as dehydration agent for low molecular aromatic constituents and therefore increases the coke yield of the pitch without preventing mesophase formation.

Thermosetting resins however which are highly crosslinked and show strong adhesion at the fibre surface have been found to be unsuitable as carbon matrix precursor for carbon/carbon-composites in spite of their high coke yield (FITZER et al., 1971). The anisotropic shrinkage of the resin matrix during carbonization caused cracks in the formed carbon matrix which partially run across the filaments.

In the present study we tried to overcome the shrinkage problems using polymers with linear aromatic molecular chains such as polyimide and phenolic novolacs with special chemical composition.

Experimental

C/C-composites have been prepared using three types of resins as matrix precursors:

a processable, condensation type polyimide, releasingacetic acid during curing (Resin 212 by Yorkshire Chemicals)

phenolic novolac with hexamethylentetramine as hardener (Resin A)

phenolic novolac with benzenesulfochloride as hardener (Resin B)

For the fabrication of C/C-composites prepregs have been made by impregnating the fibres with the molten resin(as in the case of the polyimide), with a 50%-solution of the resin (as in the case of Resin A) or with liquid prepolymer (as in the case of Resin B).The resulting prepregs have been precured, hot molded into laminates(3x5x160 mm) and hardened under pressure. Composites with phenolic resin have been postcured up to 250°C, those with polyimide resin up to 400°C. Subsequently the composites were carbonized in inert atmosphere with a heating rate of 1o-15°C/h.

Commercially available carbon fibres in the carbonized (MODMOR II, SIGRAFIL HF) as well as in the graphitized (MODMOR I, SIGRAFIL HM) state have been used as reinforcement. All fibres were non surface treated.

Results

On the left hand side of fig.1 the linear shrinkage of unreinforced bulk samples of the different resins during carbonization up to 1000°C is shown. It can be recognized that the unreinforced phenolic resin A and the polyimide resin have very similar shrinkage behaviour, the main part of shrinkage occuring in the temperature range between 400 and 600°C. On the right hand side of fig.1 the cross-section shrinkage of composites with the different resins as matrix precursors and various fibre types during carbonization is shown. No shrinkage has been detected parallel to the fibre direction. It can be recognized from the figure that polyimide matrix composites show higher shrinkage during carbonization than phenolic matrix composites and higher shrinkage than expected from shrinkage values of the unreinforced resin samples. This behaviour can be explained by preferred orientation of the linear aromatic ladder molecules of the polyimide precursor parallel to the fibre axis and fibre surface which results in preferred transverse contraction. Furthermore it can be seen that the amount of composite shrinkage depends on the type of fibre. Especially composites with phenolic resin A as matrix precursor and graphitized carbon fibres (SIGRAFIL HM) shrink only 6% whereas those with carbonized carbon fibres (SIGRAFIL HF) shrink at about 15%. The low carbonization shrinkage in the case of composites with graphitized fibres is a result of the poor ad-

hesion between graphitized fibres and the carbonizing matrix which causes shrinkage gaps at the fibre/matrix-interface and reduces the macroscopic shrinkage. Composite samples with phenolic resin B as matrix exhibit very low carbonization shrinkage because this resin forms a foam-like structure with closed spherical pores upon curing.

The effect of the carbonization shrinkage on the flexural strength of the composites during pyrolysis up to 1000°C is shown in fig.2. It can be reccgnized that C/C-composites with MODMOR I-and-II-fibres and polyimide resin as matrix precursor have strength as high as 700 MN/m^2 after carbonization up to 1000°C without any impregnation. C/C-composites with phenolic resin A and graphitized (HM)-fibres have strengths of only 50 MN/m^2 but the structure of these composites provides very effective impregnation. In C/C-composites with phenolic resin A as matrix precursor and carbonized fibres fibre breakage caused by shrinkage stresses has been observed by scanning electron microscopy. However, no fiber damage occured if phenolic resin B was used because the matrix shrinkage was reduced by the porosity.

The influence of 4 reimpregnations with resin or pitch respectively on the composite flexural strength is shown in table 1. Pitch impregnations have been found to be more effective in comparison with resin impregnations. The high strength of non-impregnated C/C-composites with polyimide as matrix precursor can be increased by 10 - 15% corresponding to a final value of 820 MN/m^2 after 2 pitch impregnations/recarbonization cycles. The highest final strength of 1100 MN/m^2 has been obtained in C/C-composites with phenolic resin A as matrix precursor, and graphitized(HM)-fibres although this fibre/matrix combination had the lowest strength before impregnation.

The influence of impregnations on the interlaminar shear strength and the influence of heat treatments up to graphitization temperatues will be discussed.

Furthermore it will be shown that the strength of C/C-composites with phenolic resins as matrix precursor can be increased if the carbonization shrinkage of the matrix is reduced by addition of graphitic fillers with suitable grain size.

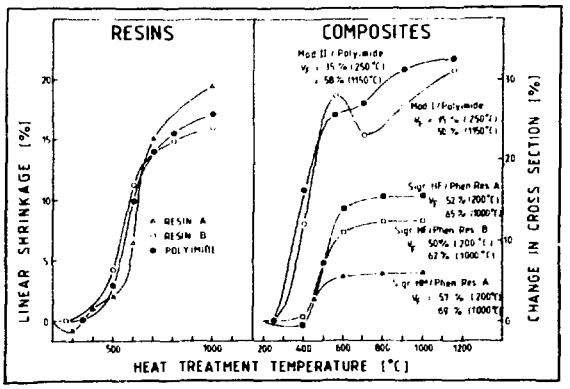


Fig.1: Linear shrinkage of resin bulk samples and cross-section shrinkage of UD-composites as function of HTT

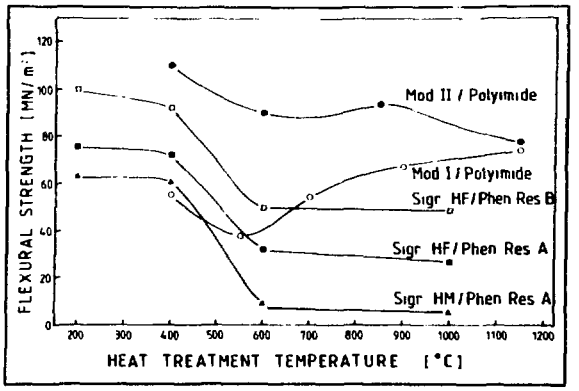


Fig.2: Room temperature flexural strength of UD-composites as function of the final HTT

RESIN	FIBRE	FIBRE CONTENT [%]	FLEXURAL STRENGTH [MN/m²]			YIELD OF FLEX STRENGTH [%]		
			0	4 RESIN IMPR	4 PITCH IMPR	0	4 RESIN IMPR	4 PITCH IMPR
RESIN A	Sigr. HF	65 %	270	490	520	18,9	34,3	36,4
	Sigr. HM	69 %	59	850	1100	4,3	61,6	80,0
RESIN B	Sigr. HF	62 %	490	-	920	36,0	-	67,5
POLYIMIDE	Mod. II	58 %	730	-	820*	52,4	-	59,0*

* reached after 2 impregnation cycles

Tab.1: Flexural strength of UD-C/C-composites (carbonized up to 1000°C) without and with reimpregnation/recarbonization-treatment using resin and pitch resp.

References:

E. FITZER, B. TERWIESCH, 1972, Carbon 1o, p. 383

E. FITZER, B. TERWIESCH, 1974, Z.f.Werkstofftechnik 5, p. 53

E. FITZER, E. HEYM, B. RHEE, 1976, High Temperatures-High Pressures 8,p.3o7

J. HILL, C.E.THOMAS, E.J.WALKER, 1974, Proc.2nd Int.Carbon Fibres Conference, London, paper 19, p. 122

HIGH TEMPERATURE PROPERTIES OF CARBON FIBERS

Charles R. Rowe (Naval Surface Weapons Center, Silver Spring, MD)
David L. Lowe (General Electric Co., Valley Forge, PA)

Introduction

The increased utilization of recently developed carbon fiber reinforced carbon composites, called carbon-carbons, has highlighted the need for physical, mechanical and thermal properties of carbon fibers at temperatures up to 2800°C. This work describes the experimental data collected on six carbon fibers.

Experimental

The fibers selected for this study were:

Thornel-50	(Union Carbide Corp.)
Thornel-75	(Union Carbide Corp.)
VSO022(Pitch)	(Union Carbide Corp.)
CX-2	(Polycarbon, Inc.)
HM-1000	(Hercules, Inc.)
HM-1000(2400°C)	(Hercules, Inc.)

Density, denier, acoustic modulus, and electrical resistivity were determined for each spool of fiber using standard techniques.

To determine the effect of gauge length on the tensile strength of the bare fiber (not coated with epoxy resin), twenty tensile tests were conducted for each yarn at gauge lengths of 1.3, 2.5, 5.1, 10.2, 20.3, 40.6, and 81.3 cm.

The effect of four thermal cycles up to 2800°C was determined by measuring the density (ρ) and denier (D) of three of the fibers after thermal cycling. The results were compared to the density (ρ_o) and denier (D_o) collected on fiber without heat treatment.

Tensile strength and modulus of the fibers at high temperatures were measured by conducting tensile tests on bare fiber inside a graphite tube furnace capable of 2800°C. Values at each test temperature were compared to the room temperature values for that fiber. Additional room temperature tests were conducted on fiber samples that were preconditioned by various numbers of 2800°C thermal cycles.

The longitudinal thermal expansion of the carbon fibers was determined by measuring the movement of flags attached to fiber samples heated in four consecutive cycles to 2800°C.

Results

Table 1 shows the results of the density, denier, acoustic modulus and resistivity measurements on the fibers. The wide range of values was in the modulus which was 37 GPa (5.4×10^6 pso) to 503 GPa (72.9×10^6 psi). Table 2 shows the effect of thermal cycling on the density and denier for three fibers. The density of Thornal 50 and 75 increased by 4.4% and CX-2 increased only 1%. Conversely the denier decreased by 4% and 7% for Thornel-50 and Thornel-75, respectively. The denier of CX-2 decreased by 35%.

It was found that the measured tensile strength of the fibers decreased as the gauge length of the test increased (Figure 1). HM-1000 was affected most by longer gauge length, -72% (1.27cm to 81.3cm) compared to -29% for VSO022. When the tensile strength of Thornel-50 was measured at elevated temperature (Figure 2), it was found that the strength dropped off by 10% at 1100°C but increased at 2200°C to 10% more than the room temperature value. After the maximum, the strength dropped to 45% of room temperature strength at 2800°C. The modulus of Thornel-50 (Figure 3) was a constantly decreasing function of test temperature with only 20% of the room temperature modulus remaining at 2800°C.

The tensile strength (at 24°C) of Thornel-50 was measured on fiber which had been heat treated by 1, 2, 3 and 4 cycles to 2800°C. Figure 4 shows that the modulus was unaffected by even four cycles. The tensile strength, however, decreased by 35% after four cycles. On similarly heat-treated fiber samples of Thornel-50 the thermal expansion along the fiber axis was measured. Figure 5 shows the thermal expansion of a fiber sample heated by four consecutive cycles to 2800°C. Thornel-50 shrinks sharply on the first cycle and then expanded normally for the second, third and fourth cycles.

Discussion

As was shown in Table 2 the density of Thornel-50 increased by 4.4% and the denier decreased by 4%. This corresponds to an 11% decrease in filament diameter and a 21% decrease in filament cross-sectional area after four 2800°C cycles. Table 2 showed that the density of CX-2 increased by 1% and the denier decreased by 35% which translates into an 18% decrease in filament diameter and a 32% decrease in filament cross-sectional area after four 2800°C cycles.

Figure 1 showed the effect of gauge length on the bare fiber tensile strength. As expected the tensile strength of each decreased as the gauge length increased; however, some fibers had a larger negative slope than others. HM fiber had the largest slope and Thornel-75 the smallest.

When the tensile strength of Thornel-50 was measured at various temperatures up to 2800°C, it was found that the maximum strength occurs at 2200°C. Above that temperature the strength drops sharply as the graphite crystallites become plastic. However in the case of the modulus, which is a constantly decreasing function of temperature, the slope of the line from 0° to 1950°C was -0.40 and -1.85 from 1950° to 2800°C.

It was seen in Table 2 that Thornel-50 experienced an increase in density after four cycles to 2800°C. Figure 5 indicates most of this increase occurs during the first cycle when the fiber undergoes shrinkage.

Summary

It can be concluded from this study that on heat treatment to 2800°C Thornel-50, Thornel-75 and CX-2 increase in density and decrease in denier. The tensile strength of all fibers tested decreased as the gauge length of the test increased. When the Thornel-50 was tested at temperatures up to 2800°C, it was found that the fiber was strongest at 2200°C.

Fiber modulus at 2800°C was only 20% of room temperature modulus. Thornel-50 strength decreased when repititiously cycled to 2800°C, whereas the modulus was unaffected. Any finally, it was found that Thornel-50 shrinks on the first cycle to 2800°C and then expands on the second, third and fourth cycles.

FIBER	DENSITY g/cc	DENIER g/9000m	ACOUSTIC MODULUS GPa	RESISTIVITY 10^{-4} ohm-cm
THORNEL 50	1.66	655	363	9.6
THORNEL 75	1.80	528	503	7.4
CX-2	1.47	1208	37	36.3
VSO022	1.92	2111	305	8.4
HM-1000	1.81	1350	337	9.0
HM-1000(24)	1.81	1308	322	8.8

Table 1 - Carbon Fiber Physical Properties

FIBER	ρ/ρ_0	D/D_0
THORNEL 50	1.044	0.958
THORNEL 75	1.044	0.932
CX-2	1.010	0.650

Table 2 - Density and Denier Ratios After four cycles

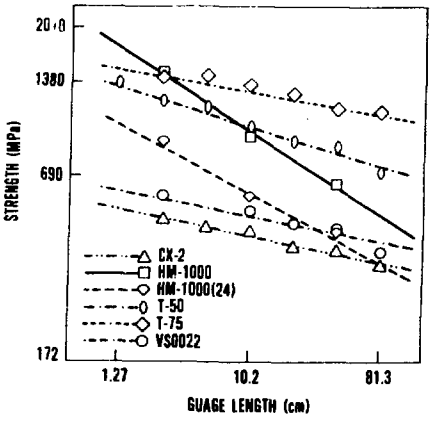


Fig 1 - Fiber Tensile Strength vs Gauge Length

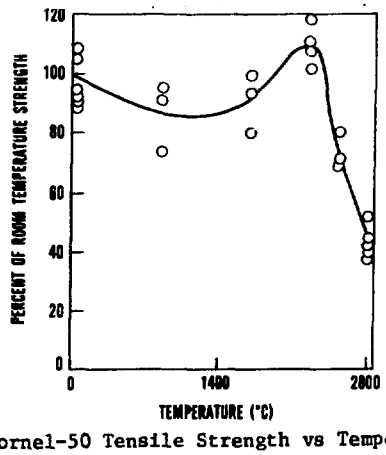


Fig 2 - Thornel-50 Tensile Strength vs Temperature

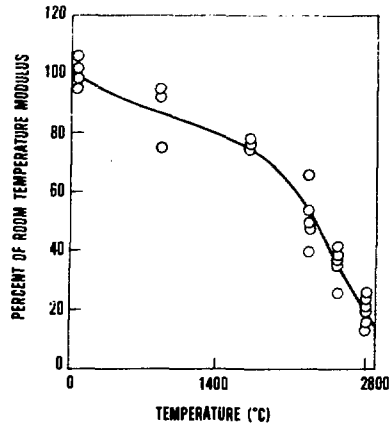


Fig 3 - Thornel-50 Modulus vs Temperature

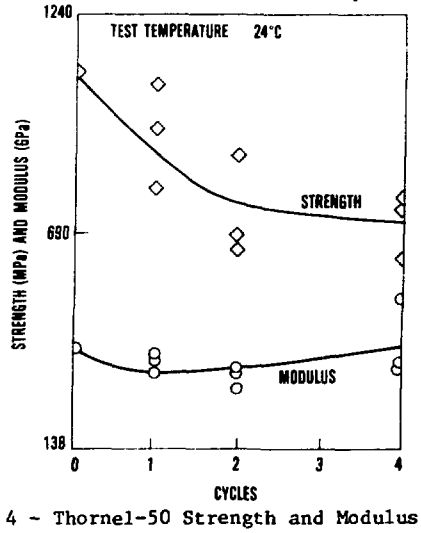


Fig 4 - Thornel-50 Strength and Modulus as a function of Thermal Cycles

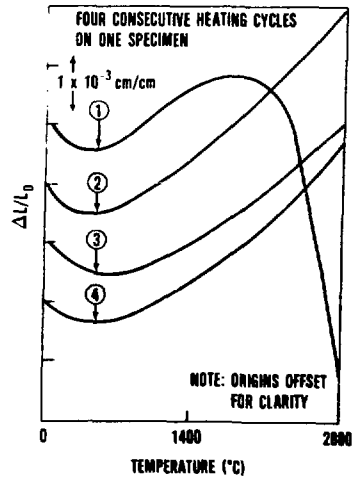


Fig 5 - Thornel-50 Thermal Expansion as a Function of Thermal Cycles

FRACTURE BEHAVIOR OF CARBON FIBER-GLASSY CARBON COMPOSITE

S.KIMURA, H.TANAKA, E.YASUDA
RESEARCH LABORATORY OF ENGINEERING MATERIALS
TOKYO INSTITUTE OF TECHNOLOGY
2-12-1 OOKAYAMA,MEGURO-KU,TOKYO

Introduction

The mechanical properties of carbon fiber-carbon composite are considered to be strongly dependent on material structure, ie., matrix, fiber or interface[1]. The fracture behavior of carbon fiber-glassy carbon composite was investigated and discussed in relation to the microstructure.

It was reported previously that the glassy carbon was graphitized to layer structure in the composite at about 2400 °C. The graphitization starts at the fiber-matrix interface and proceeds into the matrix[2]. The graphitic layer structure aligns its layers parallel to the fiber axis. The graphitization seems to be accelerated by the stress accumulated around fibers when the resin matrix shrinks by 47 wt% during carbonization.

In this study, it is found that the increase of strength accompanied the pseud-plastic fracture manner is measured by the graphitization of the matrix.

Experimental procedure

Unidirectionally reinforced composite were prepared by filament winding technique, using furfuryl alcohol condensate as matrix carbon precursor. Commercially available PAN based carbon fiber yarns (Torayca T200, Toray Industries, Inc.,) were employed. The strength and the young's modulus of the fibers are about 200 kg/mm^2 and 20×10^3 kg/mm^2 respectively.

Carbonization temperature was 1000 °C and graphitization was carried out up to 2800°C. The fiber content is about 50 vol% after carbonization treatment.

The testing bars were cut into $60\times10\times3$ mm orientating fibers parallel to longitudinal direction. The notch (0.25 mm width and 1 mm depth) was machined by a diamond blade.

The strength was determined by four point bending test with constant loading velocity. The dynamic young's modulus was calculated from the measurement of ultrasonic velocity.

Results and discussion

(1) Young's modulus

Fig.1 shows the dynamic young's moduli in the longitudinal (fiber) direction and the transverse (perpendicular to fiber axis) direction.

The longitudinal young's modulus increased from about 9 to 17×10^3 kg/mm^2 by the heat treatment. This modulus seems to be determined by the high modulus of PAN based carbon fiber, since fibers are continuous through the specimen in this direction.

The transverse young's modulus was in the range of $0.2\sim0.4\times10^3$ kg/mm^2. It inclined to reduce by the heat treatment. In the transverse direction, the young's modulus should be a reflection of low modulus carbon matrix. The pores induced in the matrix increasingly by the heat treatment might contribute to reduce the young's modulus.

(2) Strength

The structural change of matrix was influencing the strength and the fracture behavior.

Fig.2 shows that the strength increases by the increase of heat treatment temperature. The strength was calculated from a maximum load of bending test.

Typical load-deflection curves for specimens heat treated at temperature of 1000°$\sim$2800°C are shown in Fig.3. Specimen carbonized alone shows an elastic failure.

Carbonized composite (H.T.T. 1000°C) consists of carbon fiber and glassy carbon matrix. This composite was broken in a brittle manner, and gave relatively low strength of about 10 kg/mm^2 . Scanning electron microscopy has revealed the smooth fracture surfaces which opened perpendicular to fiber axis (Fig.4a). The fiber pull-out was not observed. The crack seems to propagate matrix crossing fibers in one direction. The reinforcement of fibers may not appear in the brittle fracture manner.

Fig.4b shows the fracture surface of the composite heat treated at 2800°C. The matrix has changed to graphitic layer structure. The fracture surface revealed a fibrous one with fiber pull-out. The crack did not propagate colinear to the machined notch, rather, but to the relatively weak

interfaces between fibers and matrix by a delamination process. The delamination blunts the crack and absorbs energy. In fact, the load-deflection curve deviated from the linear relation.

The anisotropic layer structure of matrix prevents the crack propagation, and results in high strength and large energy for failure.

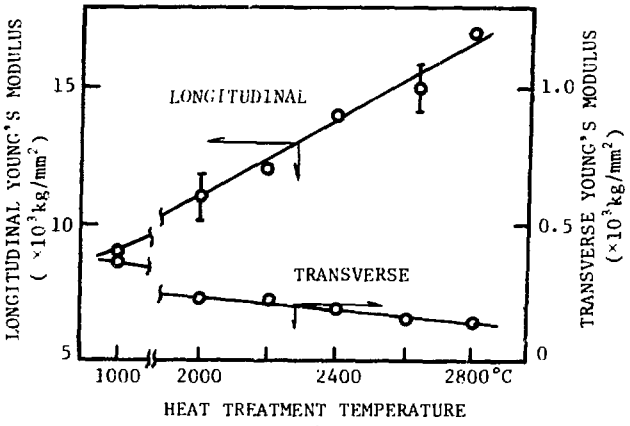


Fig.1 Dynamic young's modulus.

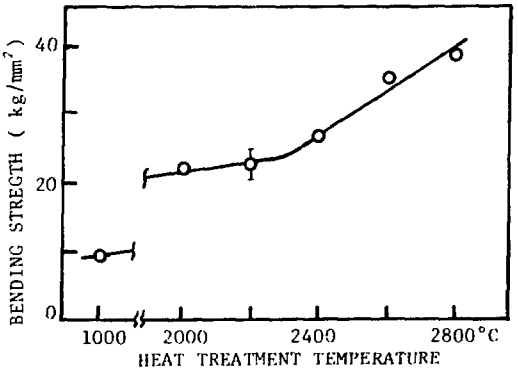


Fig.2 Strength of the composite.

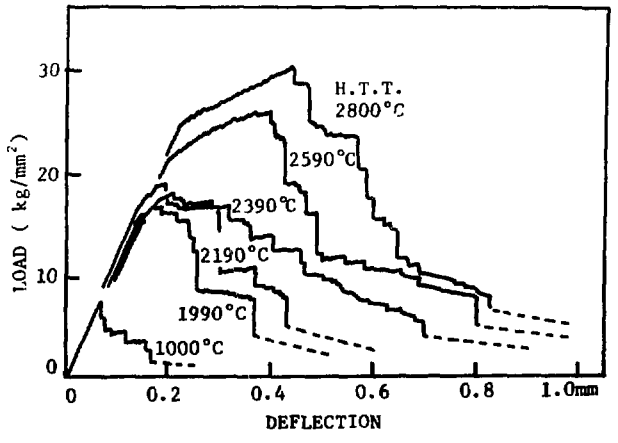
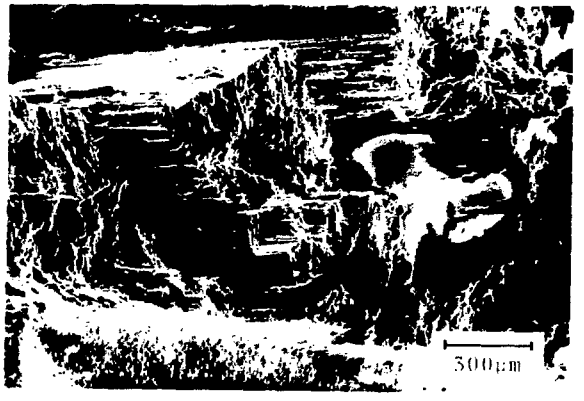


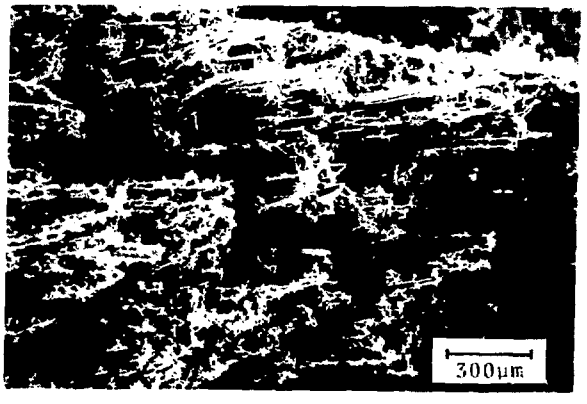
Fig.3 Fracture behavior on the four point bending test.

References

1) L.Boyne, D.Cook, J.Hill and K.Turner, SCI 4th London International Carbon and Graphite Conference, (1974) p50. T.R.Guess and W.R.Hoover, J. Composite Materials, 7,2 (1973).
2) Y.Hishiyama, M.Inagaki, S.Kimura and S.Yamada, Carbon, 12, 249 (1974). S.Kimura, E.Yasuda, H.Tanaka and Y.Yamada, J. Ceram. Soc. Japan, 83, 122(1975).



a) H.T.T. 1000°C



b) H.T.T. 2800°C

Fig.4 Fracture surface of carbon fiber-glassy carbon composite.

ACOUSTIC EMISSION FROM CARBON FIBRE REINFORCED CARBON COMPOSITES

M J Fry, MOD (PE), RARDE, Fluorocarbon, Reading RG7 4PR, England

Introduction

When a material is stressed localised deformations result in the release of strain energy, generating stress waves which can be detected by a sensor coupled to the material surface. These stress waves, or acoustic emissions (AE) are characteristic of the failure process and their study will lead to a greater understanding of fracture mechanisms occurring in materials.

In fibre reinforced composites sources of acoustic emission are fibre fracture, matrix cracking and debonding at the fibre-matrix interface. The most energetic failure process is expected to be associated with fibre breakage, and several authors (1,2,3,4) working on fibre reinforced plastic report this mechanism as the major source of emission in these composites.

Experimental Methods

Unidirectional carbon-carbon composites were fabricated from a precursor which consisted of sheets of high strength, non surface treated carbon fibre tow preimpregnated with a phenolic novolak resin. Layers of this prepreg material were hot pressed followed by carbonisation in an argon atmosphere. The specimens were then densified by the deposition of pyrocarbon using either an isothermal or thermal gradient technique.

All specimens were tested by three point bending on an Instron Universal Testing Instrument. The acoustic emission signals were processed by an AECL 105 Acoustic Emission System using a system gain of 80dB and a 100-300 KHz band pass filter.

Results

Figure 1 compares typical acoustic emission responses with stress for the green, carbonised and densified composites. The relatively high number of counts for the densified and carbonised composites at low stresses compared with the response of the green material can be attributed to cracking in the carbon matrix. The strain to failure of the densified composites is of the order of 1% compared to a matrix strain to failure of approximately 0.3% and consequently matrix damage is a significant contribution to the acoustic emission monitored at 80dB.

Matrix failure is also a probable explanation of the different behaviour of the two densified materials. The isothermally densified composites generally have a higher weight increase on densification than the thermal gradient composites (15-20% compared with 10-12%) and the former usually have a pyrocarbon surface coating. This pyrocarbon surface deposit is observed to crack at low stresses and strains and this will contribute towards the higher number of counts in the isothermally densified composites. Differences in the fine structure of the deposited pyrocarbon for each of the densification processes may also be a factor leading to the variation in the acoustic emission responses of carbon-carbon composites.

An indication of the energy of an emission can be obtained by measuring the transducer signal on an RMS voltmeter, since the energy output is proportional to the square of the voltage at the transducer terminal. Many specimens exhibited high energy peaks at stresses well below the failure level and each peak was associated with an increased rate of emission. The higher the stress at which the first significant energy peak occurred the greater was the failure stress of the composite.

Figure 2 shows the acoustic emission obtained for a selection of carbon-carbon composites during cycling between 0 and 0.4 GPa. There is clearly a relationship between the ultimate flexural strength of a composite and the slope of the acoustic emission trace after the first load cycle. Figure 3 shows this relationship. Above a threshold fracture stress of approximately 1GPa the total number of counts during 15 cycles is independent of the ultimate strength and is of the order 10^4 or less. For composites having a fracture strength significantly less than 1GPa the number of counts is at least an order of magnitude higher.

Conclusions

Acoustic emission can distinguish carbon-carbon composites manufactured by different process routes and also the precursor materials. Low strength composites are characterised by the emission of high energy events at low stress levels. The results obtained during cycling of carbon-carbon composites suggests the use of AE as a suitable NDT technique by which an upper limit can be set to the number of counts monitored during cycling after the first complete cycle, which will enable the identification of low strength composites.

References

1. Hamstad M A and Chiao T T. J Comp. Mat 7 (1973) p320.
2. Rotem A and Baruch J. J Mat Sci 9 (1974) p1789.
3. Fuwa M, Bunsell A R and Harris B. ibid 10 (1975) p2062.
4. Fitz-Randolph J, Phillips D C, Beaumont P W R and Tetelman A S. J Comp Mat 5 (1971) p 542.

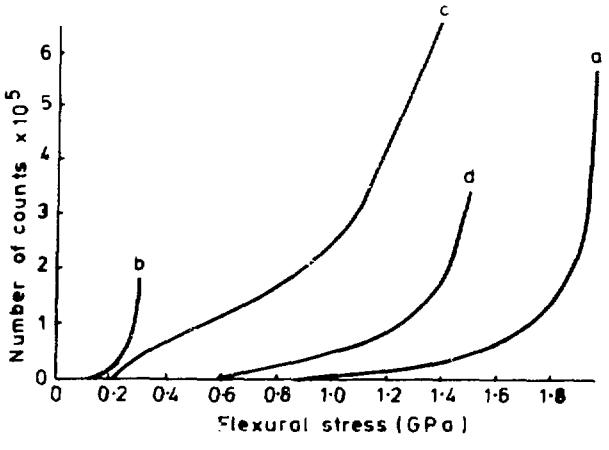


Figure 1 Acoustic emission responses of (a) green, (b) carbonised, (c) isothermal CVD and (d) thermal gradient CVD carbon–carbon composites

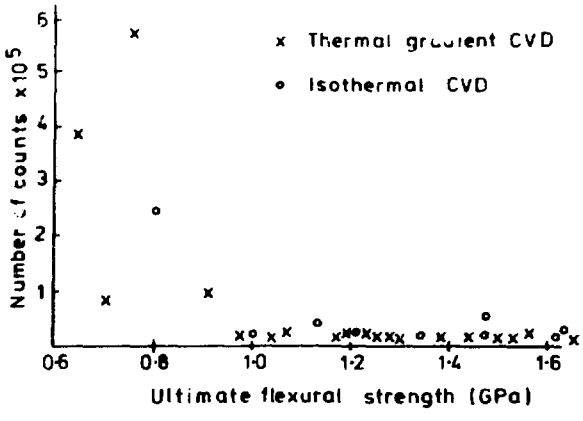


Figure 3 Relationship between the ultimate flexural strength and the acoustic emission monitored during flexural cycling between 0 and 0.4 GPa

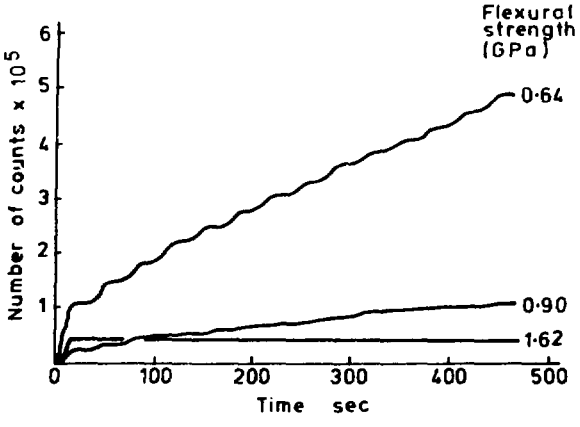


Figure 2 Acoustic emission from carbon–carbon composites during flexural cycling between 0 and 0.4 GPa

DESIGN CONSIDERATIONS FOR LTI CARBON HEART VALVES

M. Conrad Buffalotter, Jr.
Medical Incorporated
9605 W. Jefferson Trail
Inver Grove Heights, Minnesota 55075

Certain critical user needs for performance of prosthetic heart valves define the over-all design problem. These include:

a) non-thrombogenic surface throughout the entire useful life,
b) minimal lost work (over broad range of flow rates) due to fluid-friction effects,
c) minimal design-related flow turbulence (which produces blood trauma) or requirement for long-term anticoagulant therapy,
d) robust total design with demonstrated, long-term wear resistance, capable of providing a useful service life not less than projected patient life.
e) radio-opacity of fixed and moving elements needed for post-operative clinical cineangiography study.

In order to produce and certify such devices as being appropriate for implantation, several other problems must be solved, i.e.:

f) establishment of optimum mechanical tolerances,
g) development of manufacturing techniques,
h) validation of procedures/apparatus for accelerated tests of wear and fatigue.

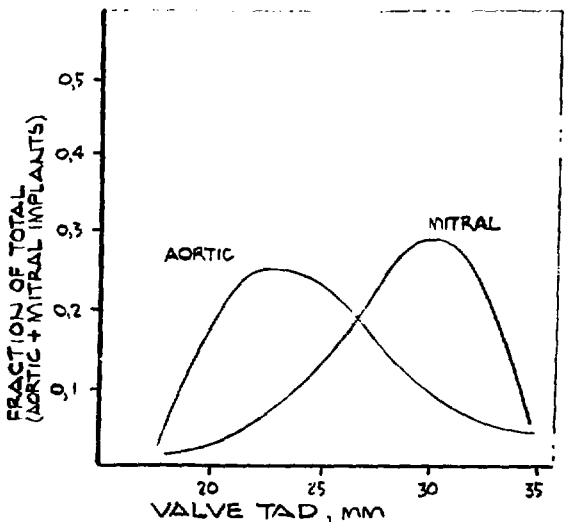
This review will examine, quantitatively, some of the unusual questions one faces in design of an all-carbon (Pyrolite-GAC) pivoting-disc heart valve.

Polished surfaces of LTI-carbon (Pyrolite) are well known to have long-term blood compatibility for heart valve occluders (both disc and ball types). Certain pivoting-and oscillating-disc heart valve body configurations involving bent-wire structural elements may pose significant technical barriers to established technology for LTI deposition on high-purity graphite preforms. Because of limitations of control of LTI deposition, certain valve body designs are inherently more feasible to produce in volume to close tolerances.

An optimum valve-mechanism design is essential to success of the prosthesis. For a pivoting disc configuration, there are a number of mechanical/fluid-mechanical variables which must be simultaneously optimized. These include opening angle, pivot-axis displacement, pivoting means (rolling/sliding bearings), and structure-elements which retain the disc within the valve and limit its travel. Analytic formalisms have been developed to calculate the true flow area as a function of open angle for pivoting-disc mechanisms.

In an actual patient, the total lost-work due to a prosthetic heart valve includes fluid and mechanical friction contributions from a number of sources. Quantitative, fundamental relationships are available for lost-work due to: (a) fluid turbulance related to flow area constriction, (b) growth of boundary layers during opening process, and (c) sliding/rolling friction between fixed and moving elements. Generally, these effects can be unambiguously demonstrated with a well-designed laboratory experiment. Optimum mechanical tolerances for various valve sizes and material combinations can be determined by precise measurements in a pulse duplicator (left-heart simulator). Recent advances in cine X ray technology permit accurate, dynamic observations and measurements of the valve movements and size/shape changes (heart chambers as well as major vessels). These data can be extremely helpful in developing and testing new models for heart valve pressure gradient (lost work) resulting from unusual elastic and volume change effects in the flow circuit. Radio-opaque occluders and valve bodies are helpful in this work.

In order to avoid non-sequitur conclusions about a specific heart-valve design implanted in the usual range of sizes, one must examine long-term performance in a rationally selected patient follow-up sample. Some current international statistics for both mitral-and aortic type prosthetic valves are shown below. Since small-sample statistics would require test groups of at least 30 to 50 patients, an investigator must carefully choose groups of individuals so that the resulting distribution of valve sizes [expressed as tissue annulus diameter (TAD)] closely parallels the actual demand pattern in world markets. A few exploratory observations without a null hypothesis cannot be evaluated by normal statistical methods.



Rational design of apparatus and procedures for significant accelerated testing of wear, fatigue, and performance degradation of heart valves is a topic of considerable interest (and some disagreement) to specialists. The major experimental problem areas include test-fluid properties, pressure-pulse shape, and elimination of spurious variables such as

vibration, wear debris, and cavitation. Although an Arrhenius plot may be an adequate method of presentation of some types of wear data, Weibull functions may be much more useful in predicting the probability of survival. Since "survival" of a prosthesis can be defined as a certain maximum pressure gradient under fixed test condition, reliability theory may be helpful in predicting "useful life". The concepts of step-stress aging can be used to stimulate certain modes of failure which would be difficult or impossible to observe otherwise.

Because of the hardness of LTI coatings, many manufacturing methods for heart-valve elements are generally similar to those used for ceramics. While certain simple geometries, such as flat discs, can be produced by conventional methods with selected abrasives, complex shapes represent a significant challenge.

EXPERIMENTAL AND CLINICAL APPLICATION OF CARBON FIBRE AS AN IMPLANT IN ORTHOPAEDICS

D.H.R. Jenkins, M.B., Ch.B., F.R.C.S., *Consultant Orthopaedic Surgeon/Senior Lecturer*

If any material is to replace another as an implant in orthopaedics it must not only demonstrate the advantages of the material it is to replace but must also show additional advantages; these may be either mechanical or biological. We feel that in theory at least, carbon may be such a material. It can be made in a number of shapes and forms. It can be manufactured to differing strengths and flexibility. Because of its very nature it is in theory at least, totally inert.

In the first series of experiments the tendo-Achilles in sheep was excised and replaced with a double plaited strand of flexible carbon fibre tow. In a controlled series of sheep the tendo-Achilles was excised and either replaced with nylon or not replaced at all. The control sheep never walked satisfactorily, whereas the sheep in which the carbon fibre tendo-Achilles had been inserted walked normally within two to three weeks. Examination of the carbon implant at six months showed that there was a massive fibrous reaction in the region of the implant which appeared to mimic both in shape and size a new tendon. It was virtually impossible to see any evidence of the implant at all because it had become enveloped in new tendon-like tissue.

A further series of experiments was carried out in rabbits in which the tendo-Achilles was replaced with filamentous carbon fibre. It was found that the breaking strain of the normal tendon on the opposite side was between 10 and 20 Kgms. Breaking strain of the replaced tendon rose from 2 Kgms at insertion. The new tendon did not actually snap but in fact tore out from the muscle at the proximal end. By six weeks however the tendon had become fully enveloped in what appeared to be new tendon-like tissue and the breaking strain had reached that of the other side.

A number of other experimental models have been tested. One such was to create large incisional hernias in the abdomens of sheep. These were repaired with carbon fibre woven in the form of a mat with satisfactory results. Another experiment was to replace one of the flexor tendons in a chicken. While this apparently functioned as a normal tendon for two to three weeks, it rapidly ceased to move. Histological examination showed ingrowth of new tissue, not only from the ends, but also from the sides and this suggests that carbon may not be suitable as a flexor tendon replacement in its present form.

In order to test the suggestion that the actual presence of the flexible carbon was somehow stimulating or inducing a new tendon to form we replaced the only tendon in the body which lies free from adjacent tissue. The anterior cruciate ligament in sheep was excised and replaced with carbon fibre. At six weeks the macroscopic appearance was that of a new but slightly thicker anterior cruciate ligament. Histological examination of the new tendon showed that while the carbon fibre was still present, the individual strands were widely separated by tissue which was histologically similar in every way to that of normal tendon.

Histological examination of soft tissues proximal to the implant showed heavy concentrations of carbon in the soft tissue adjacent to the regional nodes and the regional lymph nodes them-

selves were seen to have a black rim which contrasted strongly with the lymph nodes on the opposite sides. Cross section of one such lymph node taken from the para-aortic group on the carbon implantation side shows that there is a heavy concentration of carbon within the node. These nodes appear similar in every way to those found in coalminers and city dwellers in that the black appearance of the node clearly seen by naked eye is in fact due to the carbon. This appears to cause no detrimental effect. In other tissues taken from animals killed two years following implantation, there is no evidence of carbon either in lungs, spleen, liver or elsewhere. If carbon was found it is always found in the nearest major adjacent proximal lymph nodes.

It is our suggestion that flexible carbon fibre may act as the ideal implant material for the following reasons.

It is inert. This statement can be substantiated by histological examination of sections following implantation in which there is little more than the inflammatory reaction normally expected in any injury.

It is strong. This is demonstrated by the ability of the carbon to support a walking sheep within days of implantation.

Its strength increases. This is demonstrated by the experiments in which the strength was seen to increase as time went by. This increase in strength corresponds with the stimulation of an ingrowth of new tissue into the carbon fibre scaffold.

Lastly, it possibly begins to disappear from the site of implantation. We feel that the formation of new tendon-like tissue as opposed to primitive scar tissue is due to the comparatively early fragmentation of the individual carbon fibre filaments. This produces a stress reaction in the new tissue resulting in the formation of tendon of the type demonstrated.

In order to test the clinical application of this material we have so far reinforced the medial ligaments of an unstable knee and have similarly reinforced the capsule of a ruptured carpo-metacarpal joint. Early impressions are that this material behaves in the human in a manner similar to that in the animal experiments described.

PREPARATION OF PYROCARBON COATED CARBON FIBRES FOR USE IN LIGAMENT REPLACEMENT

E. FITZER, W. HÜTTNER, D. WOLTER [x]

Institut für Chemische Technik, Universität Karlsruhe, and
[x]Department für Chirurgie, Universität Ulm, West-Germany

Introduction

Successful experiments with carbon fibres as tendon and ligament replacement were first reported by H.R. Jenkins (1976). The biological inertness, the high specific tensile strength and the pliability of carbon filaments constitute this material to take charge of damaged or absent tendons. The implanted fibre tows act furthermore also as a scaffold for regenerating tissue, which is growing around, along and through the fibre bundle. But also a partial disintegration of the fibre is observed and the removed carbon particles are transported primarily into lymph ducts. Nevertheless it is not yet cleared up, where these particles are finally deposited. It can not be excluded, that the mechanical degradation of fibres occurs before the tissue is regenerated. The mechanical properties of implanted carbon fibres are not completely utilized. It is obvious to try to improve the fibre surface properties, e.g. its resistance against splitting and breaking. The aim of the present work was, to obtain such modifications of the carbon fibres by pyrocarbon depositions. The fibres then were tested "in vivo" in animals.

Principles of pyrocarbon deposition on the monofilaments of carbon fibre yarn

Carbon fibre yarn, consisting of several thousand monofilaments, are geometrically complicated systems with a large inner surface area. Figure 1 shows schematically the cross section of a part of fibre bundle after pyrocarbon deposition. The average slit width between the monofilaments can be assumed to be about 1/um. The overall deposition rate must be controlled by the chemical reaction and not by the diffusion of the gas molecules to and from the fibre surface in order to obtain uniform coatings (AGGOUR et al.1974; FITZER et al., 1973). Otherwise the carbon deposition will take place on the outer shell of the bundle, causing the formation of carbon bridges between the monofilaments, which will not only reduce the flexibility of the yarn, but may also prevent the ingrowth of fibrous tissue in implanted yarns. It was found experimentally, that these carbon bridges can be avoided only if the coating thickness does not exceed about o,3/um (FITZER et al., 1973; SAHEBKAR, 1973). From this result one can conclude, that a slit width of o.6/um seemed to be present between the filaments during deposition process. This value is confirmed by the average bundle diameter of about 1,o mm in the case of 1o.ooo and o,5 mm for 3ooo monofilaments. As a consequence the deposition gas must penetrate the bundle up to a depth of o,5 mm and o,25 mm respectively.

A deposition apparatus was developed basing on the experience in SiC deposition from methylchlorosilanes /hydrogen mixtures (AGGOUR et al., 1974). It was shown, that this penetration depth can be realized even in the case of pore diameters of 1/um. Theoretical calculations, using the THIELE modulus $\sqrt{k \cdot (L^2/D)}$, have confirmed this result (FITZER et al., 1973). The transfer of these experiments on pyrocarbon deposition from methane has shown, that hot wall arrangements must be used in that case. In cold wall arrangements with directly heated fibre bundles inhomogeneous deposition was found by SAHEBKAR (1973).

The deposition apparatus

The continous CVD of pyrocarbon from methane was performed in a tubular reactor with hot wall arrangement and inductive heating. The apparatus (fig. 2a) consists of an outer quartz glass shell, a graphite tube as susceptor of inductive heating and a device for fibre transport. The residence times of the fibres can be varied between 10 sec. and some minutes. The gaseous feed enters through whirl-nozzles, as shown in part b of fig.2, in order to separate somewhat the monofilaments and to avoid adhering during deposition.

Experiments

Commercially available PAN based carbon fibres type II, SIGRAFIL HF with 10000 filaments (fibre diameter: 8-9/um, tensile strength: 2200 MN/m^2) and TORAY T300 with 3000 filaments (fibre diameter: 7-8/um, tensile strength: 2560 MN/m^2) were used as substrates. Both fibre types have nearly circular cross sections of monofilaments. A deposition temperature of 1300°C, a methane feed of 10 l/h, and a residence time of the substrate of 180 sec. were applied.

Results

Carbon black formation was avoided by argon addition to the reaction gas. The optimal deposition conditions are indicated in fig. 3. It was found, that a minimum coating thickness of o,15/um was necessary in order to achieve homogeneous coatings on each monofilament. A coating thickness of more than o,3/um decreases the flexibility of the fibre bundle. The average coating thickness was

measured by weighing: 0,15/um for SIGRAFIL HF with 10 000 monofilaments and 0,35/um for TORAY T 300 with 3000 monofilaments.

Table 1 shows the mechanical properties of the fibres before and after coating. In the case of TORAY T 300 the coating resulted in a small increase of the tensile strength of 8%, in the case of SIGRAFIL HF of 4%. YOUNG's modulus and strain to failure are not influenced by deposition. These results are similar to former observations of FITZER at al.,(1973), who reported, that an improvement of the fibre strength by PC deposition can only be achieved in the case of low strength fibres, and here up to 30%.

Medical Investigations

Medical experiments were performed on 20 rabbits, aged 12 weeks. The medial collateral ligament of the knee joint of the animals was resected. Bone screws were placed into the point of origin and insertion of the medial collateral ligament in the tibia and femur. These screws were tied together with the carbon fibres in a figure 8 fashion.

Furthermore on 10 rabbits only the medial collateral ligament was resected and 10 rabbits were used as control group for the "only resected" and "carbon fibre replaced" animals. Histological investigations after 3 months have shown the incorporation of the fibres in the tissue.

Indications were found for some fibres being removed, which is a symptom, that breaking of the fibres could not be avoided completely. The full knee joint function was maintained (WOLTER et al., 1977). The animals are still under observation. It is expected that the final results of the present test will allow to draw some conclusions on the effect of the coatings.

References

L. AGGOUR, E. FITZER, E.IGNATOWITZ, M. SAHEBKAR, 1974 Carbon 12, pp.358 - 362

E. FITZER, D. KEHR, M.SAHEBKAR, 1973 Chemie-Ingenieur-Technik 21, pp 1244-125o

D.H.R. JENKINS, 1976 8th Annual International Biomaterials Symposium Philadelphia

M. SAHEBKAR, 1973 PhD-Thesis at Inst.f.Chem.Technik Univ. Karlsruhe

D. WOLTER, G. HELBING, E.FITZER, J.COLDEWAY, 1977 - 9th Annual International Biomaterials Symposium, New Orleans

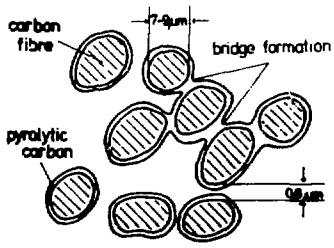


Fig.1: Schematic of a PC-coated carbon fibre bundle

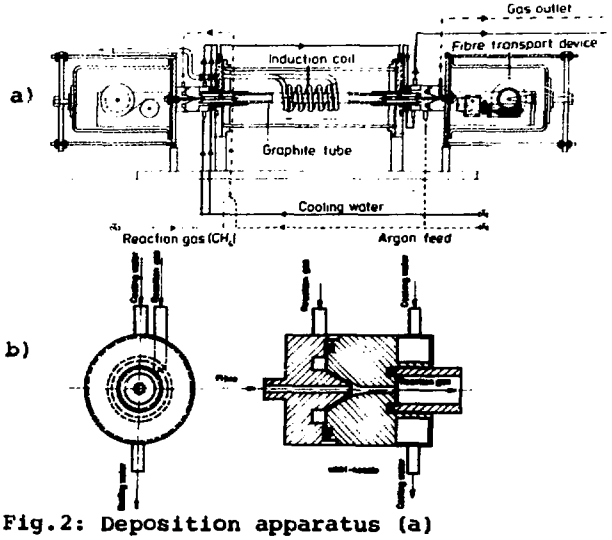


Fig.2: Deposition apparatus (a) Whirl-nozzle (b)

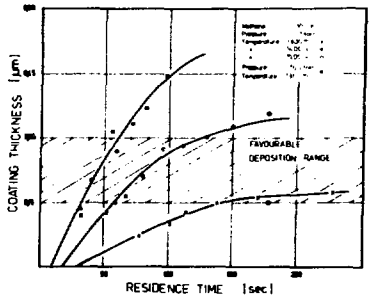


Fig.3: Coating thickness as function of temperature and residence time

Fibretype		TORAY T300/90A	SIGRAFIL HF
Tensile strength [MN/m²]	without coating	2560	2220
	with PyC coating	2760	2310
Youngs modulus [MN/m²10³]	without coating	218,8	185,4
	with PyC coating	224,6	186,6
Strain to failure [%]	without coating	1,17	1,27
	with PyC coating	1,23	1,18

Table 1: Mechanical properties of carbon fibres before and after deposition

DEVELOPMENT OF CARBON MATERIALS FOR ENDOPROSTHETICS

H. Brückmann, K. J. Hüttinger, U. Rosenblatt
Schunk & Ebe GmbH, D-6300 Giessen, W.-Germany

1. INTRODUCTION

In recent years, new materials for application in bioengineering are in development. For endoprosthetic application, especially Al_2O_3-ceramic has been developed to a high standard and hip joints are now under clinical testing (1). Carbon seems to be extremely promising according to its well known biocompatibility, friction and wear behaviour (2, 3). Mechanical properties of commercially available carbon materials are insufficient for endoprosthetic purposes. It is the aim of our development program to supply carbon materials with sufficient strength for joint replacements. Those materials must posses excellent gliding properties, wear resistance and perfect biocompatibility, the latter property being especially important for worn off particles.

When starting this project, we were convinced, that all these demands cannot be fullfilled by a single carbon material. Therefore the program includes the development of three different types of materials, namely

(1) high strength isotropic carbon
(2) carbon fibre reinforced carbon
(3) silicon impregnated carbon.

2. MATERIALS

2.1 High strength isotropic carbon

The development of such material was concentrated primarily on high strength combined with maximum hardness.

These demands are satisfied by a carbon grade based on a special raw coke, which is treated with coal tar pitch for several times with intermediate heat treatments. Thereby, the raw coke is reduced to a state comparable to mesophase (4). The mix is milled and formed to blocks. These are baked in an industrial ring furnace up to 1200°C. Final heat treatment includes gas-phase purification. The mechanical properties of the material are listed in table 1.

Table 1 - Properties of high strength isotropic carbon

Bulk density,	g/cm^3	1,8 - 1,9
Flexural strength,	N/mm^2	120 - 140
Compressive strength,	N/mm^2	300 - 400

2.2 Carbon fibre reinforced carbon

For the manufacture of carbon fibre reinforced composites we developed a new process. Carbon fibres, usually of the HT-type, are wound on a kernel, impregnated with coal tar pitch, and thermally pretreated before pressing and baking. The treatment of the matrix is similar to that used for the high strength isotropic carbon After baking up to 1200°C, the composites exhibit densities in the range of 1,6 to 1,7 g/cm^3 without any impregnation. We aim to produce C-C-composites of low Young's modulus and sufficient flexural strength.

Some properties of our unidirectionally reinforced composites are given in table 2.

Table 2 - Properties of unidirectionally reinforced carbon-carbon composites

Bulk density,	g/cm^3	1,6 - 1.7
Young's modulus,	KN/mm^2	120 - 150
Flexural strength, parallel to fibre axis	N/mm^2	600 - 800
Flexural strength, perpendicular to fibre axis	N/mm^2	30 - 35
Interlaminar shear strength,	N/mm^2	30 - 40

2.3 Silicon impregnated carbon

This material was developed based on our experience as manufacturer of metal impregnated carbons for a wide range of mechanical applications. Silicon has been chosen due to its ability of forming a chemically resistant carbide, the composite being a material with superiour gliding properties. Furthermore, test results with "silicon alloyed carbon" indicate the biocompatibility of a silicon-carbon composite (2). Carbon materials, especially suitable for impregnation with liquid silicon in a vacuum-pressure-process had to be developed. As expected and eludicated in our experiments, porosity and reactivity of the base carbon material strongly influence the properties of the Si-C-composite. Therefore the further development includes not only Optimizations of the impregnation process but also of the carbon material.

During the impregnation process silicon is completely transformed to SiC by consumption of carbon.

Properties of the materials developed are shown in table 3.

Table 3 - Properties of silicon impregnated carbon

Bulk density,	g/cm^3	2,6 - 2,7
Flexural strength,	N/mm^2	150 - 200
Brinell hardness		280 HB 2,5/30
Porosity,	%	0,1 - 0,5

3. APPLICATIONS

The material development program is accompanied by a clinical testing program. Test specimen of joint prosthesis for hips and knees were designed by taking into account the special properties of the materials. Their qualifications are being tested in vitro under standard conditions before animal tests will be started. Isotropic carbon and silicon impregnated carbon are of interest for gliding parts, whereas carbon fibre reinforced carbon shall be used for load-bearing parts.

4. REFERENCES

(1) D. Geduldig, E. Dörre, M. Happel, R. Lade, P. Prüssner, H.-G. Willert, L. Zichner, Med. Orthop. Techn., 6, 138, (1975)

(2) J. C. Bokros, L. D Lagrange, F. J. Schoen, Chem. and Phys. of Carbon, 9, 103, (1973)

(3) J. K. Lancaster, Proceed. 4th London Intern. Conf. on Carbon and Graphite, Soc. of the Chem. Industry, London 1974, p.663

(4) K. J. Hüttinger, Chem. Ing. Techn, 21, 1145, (1971)

Acknowledgement

This research program is supported by the Federal Minister for Research and Technology under Grant MT 267.

GRAPHITE FIBER/TFE POLYMER POROUS COMPOSITES IN RECONSTRUCTIVE SURGERY

C.A. Homsy
Prosthesis Research Laboratory, The Methodist Hospital
Houston, Texas 77030

J.N. Kent
Department of Oral Surgery, Dental School, LSU Medical Center
New Orleans, Louisiana 70119

Graphite fiber and TFE polymer were combined to produce a porous low modulus composite intended for medical implant use.* The specific methodology for preparation of this novel composite structure has been published elsewhere.[1] The microstructure of this composite is illustrated in Figure 1 at 300X magnification. The structure is an isotropic matrix of polytetrafluoroethylene polymer upon which is superimposed graphite fibers in the range of 50 to 100 micra in length. The composite is approximately 80% void, with average pore diameter of about 300 micra. The open pore structure also exhibits dendritic interpore connections of between 100-200 micra. The bulk physical appearance of the material is that of a stiff sponge of Yaung's modulus--40 Kg/cm^2 and an ultimate tensile strength--10 Kg/cm^2.

The creatian of the composite was premised on 3 requirements: (1) ingredient biocompatibility; (2) bio-functionality through the selection of a modulus close to that of soft tissue and spongey bone; and (3) maximum porosity and interpore connections consistent with appropriate bulk mechanical properties. Initial studies evaluated biocompatibility,[2] tissue ingrowth kinetics and performance of the material as a bulk implant or as a coating on metallic endoprostheses whereby stabilization of the prostheses was provided by tissue ingrowth.[3,4,5]

Very rapid fibrous tissue ingrowth into the material was observed at rates of 600 micra per week for loose immature collagen and 80 micra per week for dense mature collagen. These rates are approximately 5 times those observed with open pore polytetrafluorothylene exhibiting the same porosity and pore architecture as the composite. This difference is now attributed to the surface energy character of the graphite fiber ingredient and specific surface area of the composite which results from the inclusion of that ingredient.

Implant stabilization is directly related to the surface area and geometry of an implant and the interfacial reaction of the implant withadjacent tissue. More area disposed perpendicular to stress direction would decrease the unit loads supporting tissue must sustain and thereby enhance stability. The microporosity of the Proplast composite develops very large surface interaction areas. Although porosity of biologically inert materialsis generally known to engender tissue ingrowth,[2] lang-term fixation between the implant and tissue has been seen to depend on appropriate selection of modulus for the porous implant; newly forming fibrous tissue within the porosity of the Proplast is not irreversibly traumatized by micro-motion that necessarily must take place between an implant and the implantation site.[6,7]

Proplast composite exhibits a low modulus in order to provide an interface of gradual conversion from the structure and property of the opposed tissue to that of the bulk material of an implant. Under such conditions, stress vectors can be supported by the omnidirectional interlocking of tissue with implant. Moreover, stress would tend to be uniformly dispersed to low unit values. In addition to implant fixation, a viable ingrowth interlocking between implant and adjacent tissue may also serve to prevent extrusion of percutaneous and permucosal implants secondary to epithelial encapsulation.

Histological preparations of composite implants placed in dogs, rabbits, and primates, showed that tissue morphology and rate of organization depend upon the implantation site.[8] Specimens recovered from long bone, femoral head prostheses coatings, and alveolar ridge augmentation, show rapid collagenous ingrowth with some bone formation usually limited to the interface with bone. Multinucleated giant cells or other remarkable cell populations are absent. Implants from mobile soft tissue locations show less rapid collagenization associated with transient presence of giant cells. The latter appear to have no

---

* Proplast® implant biomaterial, Vitek, Inc., Houston, Texas 77054.

deleterious effect other than to reduce the rate of collagenation.

Both porous and non-porous forms of the composite were compared with USP Plastic Negative Standard material in long bone of Beagle dogs for 2 years. No findings of toxicological significance were evident in the general observations, opthalmology, body weight, hemotology, and clinical chemistry data, or in the necropsy and histopathological examinations. Implant prototype studies have been reported in 20 publications involving both soft tissue and bone in the rat, cat, rabbit, dog, monkey, and baboon.

The composite was first used in humans in 1970. Pre-commercial clinical studies were carried on through 1974 in more than 190 patients with success rates in excess of 90% for applications involving contour and boney reconstruction of the chin, nose, zygoma, malar, orbit, and mastoid defect. Those cases of failure were assaciated with the learning curve of operative technique and the usual hospital rates of operative sepsis. Alveolar ridge augmentation with Proplast has been notably less successful (60-70%) with early and late losses from sepsis. The procedure involves extensive intra-oral manipulation in proximity to mucosal tissue. Late losses from mucosal perforation can be minimized by good patient cooperation in oral hygiene and routine denture adjustment. Optimal surgical instructions have been developed to reduce losses. Notwithstanding the occurrence of losses, alternative procedures such as bone grafting are less successful and satisfying to both patient and surgeon.

Clinical publications document efficacy of the composite in Tenon's capsule of the eye, middle ear, facial contour reconstruction, mastoid obliteration, alveolar ridge, TMJ prosthesis stabilization, pectus excavatum repair, and treatment of atrophic rhinitis.[9-15] Prospective studies have been underway for over 3 years in the clinical use of the composite for stabilization of orthopedic joint prostheses, knee ligament prostheses, and hand tendon prostheses. Current research studies in animals involve the use of the composite for reversible sterilization, peridontal pocket obliteration, herniation defect repair, and prostheses for the bladder, trachea, mandible, and endosseous denture support.

[1] U.S. Patent 3,992, 725
[2] C.A. HOMSY, JADA, 86, 817, (1973).
[3] C.A. HOMSY, et al., Clin. Orthop. Rel. Res., 89, 220, (1972).
[4] E.C. HINDS, et al., O. Surg., O. Med., O. Path., 38, 512, (1974).
[5] J.N. KENT, et al., JADA, 89, 1142, (1974).
[6] C.A. HOMSY, Orthop. Clin. N. Amer., 2, 295, (1973).
[7] F.W. RHINELANDER et C.L. NELSON, Acta Orthop. Belg., 40, 771, (1974).
[8] C.A. HOMSY et M.S. ANDERSON, Chapter 10, Biocompatibility of Implant Materials, Sector Publishing, London, England, (1976).
[9] M.G. LYALL, Trans. Opthal. Soc. U.K., 96, 79, (1976).
[10] J.J. SHEA et C.A. HOMSY, Laryngoscope, 84, 1835, (1974).
[11] J.B. JANEKE et J.J.SHEA, S. African Med. J., 50, 781, (1976).
[12] B.S. FREEMAN, Brit. J. Plast. Surg., 29, 158, (1976).
[13] H. VENO et R.G. MERRILL, Shikai Tembo, 4, (1973).
[14] C.D. FARRELL et J.N. KENT, Alpha Omegan, December, 21, (1975).
[15] E. WHITEHEAD, Can. J. Otol., 4, (1975).

Figure 1



Proplast® Implant Material, SEM 300X

RHEOLOGICAL PROPERTIES OF COAL-TAR PITCH BINDERS

R. W. Wallouch, H. N. Murty, and E. A. Heintz
Technical Department
Airco Speer Carbon-Graphite
P. O. Box 828
Niagara Falls, New York 14302

Summary

It is found that the viscosity-temperature relation of various pitches can be approximated from the softening point. At the respective softening point, the viscosity is the same to a first order of approximation, for all the pitches studied. The viscosity-temperature relation obeys Duhring's rule which can be advantageously used in intrapolating and extrapolating viscosity data to temperatures of practical interest. The conclusions given for "pure" pitches are also valid for binary mixtures of miscible pitches.

Experimental

The softening points of six coal-tar pitches and their mixtures were determined by the ASTM cube-in-air method.[1] The viscosity was measured using a Brookfield, Model RVT, Synchro-Lectric Viscometer.[2]

Theory and Results

Plots of the logarithm of the measured viscosities versus temperature are linear and nearly parallel for the family of pitches studied. Each of these straight lines is represented by the relation

$$\log (\log \eta) = R - b \log T \qquad (1)$$

where η is the viscosity, R is a material constant and b is a universal constant. The values of R and b were calculated and are summarized in Table I. The slope, b, is nearly the same for all the pitches. In consequence, the family of parallel lines can be made to coincide by a translation parallel to the temperature axis. Figure 1 is such a translation and shows a plot of $\log \eta$ versus reduced temperature (T/T_s) where T_s is the softening point of the pitch and T is the temperature of a particular viscosity. The straight line in Figure 1 is described by the relation

$$\log (\log \eta) = \log \eta_o - b' \log (T/T_s) \qquad (2)$$

Since b and b' were found to be the same, equation (2) takes the form

$$\log (\log \eta) = \log \eta_o - b \log (T/T_s) \qquad (3)$$

TABLE I

Values of R, b, η_o and b' for Various Coal-Tar Pitches

Pitch	Softening Point, T_s °C	Softening Point, T_s °K	R	b	η_o	b'	%BI	%QI	%TI
1	96.8	369.8	2.7×10^{23}	8.9	3.7	8.9	15.0	5.6	17.0
2	102.9	375.9	7.0×10^{22}	8.7	4.3	8.7	30.1	11.0	29.7
3	116.4	389.4	5.2×10^{22}	8.5	4.2	8.5	34.5	13.3	32.0
4	132.4	405.4	3.9×10^{21}	8.4	4.1	8.4	40.1	15.6	26.5
5	145.9	418.9	5.3×10^{21}	8.1	4.1	8.2	35.9	13.7	36.5
6	170.3	443.3	1.3×10^{21}	7.8	4.4	7.7	45.1	19.0	42.5

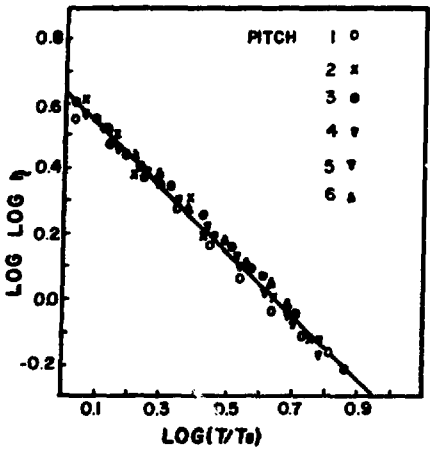


Figure 1. Log Log Viscosity Versus Log (T/T_S) for Various Coal-Tar Pitches

where η_o and b are considered to be the same for the family of pitches. Thus, equation (3) suggests that:

(a) The viscosity is the same for all the pitches at the respective softening points ($T=T_S$), i.e., $\log (\log \eta)_{(T=T_S)} = \log \eta_o$.

(b) The viscosity-temperature relationship can be described by a single characteristic parameter - the softening point, T_S.

(c) The viscosity-temperature relationship obeys Duhring's rule which is useful in intrapolating the viscosity data to temperatures of practical interest such as the temperatures of mixing and forming of carbon artifacts.

Using the technique employed for pure pitches, values of η_o and b were calculated for pitch mixtures. The values of R and b of mixtures suggest that all the generalized relations derived for individual pitches are applicable to mixtures. This confirms the concept that the softening point, T_S, can be used to describe the viscosity-temperature relation of any pitch.

References

1. ASTM Method, D-2319-66, Vol. 11 (1969).
2. A. Roeger, M.S. Thesis, The Pennsylvania State University (1969).

PHYSICAL PROPERTIES AND COMPOSITION OF THE GREEN MIX

S. Mrozowski
Department of Physics and Astronomy, Ball State University
Muncie, Indiana 47306

In extension of an old paper under the same title the dependence of various physical properties of molded and extruded carbon products is analyzed in terms of a filler-binder system. It will be shown how the weight proportions and size ratios optimizing the density can be predicted for binary filler mixtures on the basis of a simple model. The dual role of carbon black additive as a filler and as a binder component will be discussed.

EFFECT OF RAW MATERIALS ON LAMPBLACK GRADE GRAPHITE PROPERTIES

G. W. Morelli and J. F. Rakszawski
Technical Department, Airco Speer Carbon-Graphite
A Division of Airco, Inc., St. Marys, Pennsylvania 15857

Introduction

Artificial graphite grades based on lampblack are used for motor and generator brushes, rings and seals and other applications where a fine-grained material is required. The lampblack is "calcined" to reduce binder demand so the material can be baked without excessive shrinkage and breakage. Calcining is accomplished by hot mixing the lampblack with either tar or pitch, forming into suitable shapes for handling ease and baking to carbonize the binder. After carbonization, the calcine is milled to a fine powder and hot mixed with pitch and other additives. The mix is molded into plates or other shapes, baked and finally graphitized.

Each manufacturer uses a grade (or grades) of lampblack that satisfies the processing requirements of his production techniques and results in final grades having the appropriate properties required for each application. As with all industries, raw material costs and property changes force the evaluation of cheaper and different raw materials to determine if cost savings or property improvements can be obtained. This work describes the evaluation of a lower cost thermal black in lampblack brush grades. In addition, the use of a resin modified coal tar pitch binder was investigated to determine its effect on physical properties.

Raw Materials and Processing

Two blacks were used in this work as shown in Table 1. Black B, a lampblack typical of the kind used in brush grades, had an oil absorption of 12.7 gallons/100 lbs. Tar level, used in making the calcine mix, was 109 pph. The thermal black, Black A, had an oil absorption of 4.8 gallons/100 lbs. The tar level was 43 pph. The tar and black were mixed in a heated sigma blade mixer and formed into rods. The rods were heated rapidly to carbonize the binder. After calcining, the material was milled to a nominal 200 mesh size. Three pitch mixes were prepared from the two calcines. Calcine A was hot mixed with 48 pph #30 Medium pitch to form Mix M1. Two mixes were made from calcine B. Mix M2 was made with 70 pph #30 Medium pitch. In Mix M3, one-half of the pitch was replaced by a phenolic-furfural resin mixture. Total binder level in Mix M3 was virtually the same as Mix M2.

TABLE 1
BINDER LEVELS

Calcine	Black	Oil Absorption of Black gal/100 lbs	Tar Level, pph
A	A	4.8	43
B	B	12.7	109

Mix	Calcine	Pitch Level pph	Resin Level pph
M1	A	48	0
M2	B	70	0
M3	B	35	34.4

After mixing, the three mixes were cooled to room temperature, milled to 48 mesh size and blended. Each blended mix was molded to 10" x 4" x 2-1/2" plates at a variety of molding pressures to obtain a series of green densities. The green plates were packed into saggers with sand as the supporting medium and baked. They were finally graphitized in an Acheson furnace and tested for graphite properties.

Experimental Results

Graphite apparent density is shown as a function of green apparent density in Figure 1.

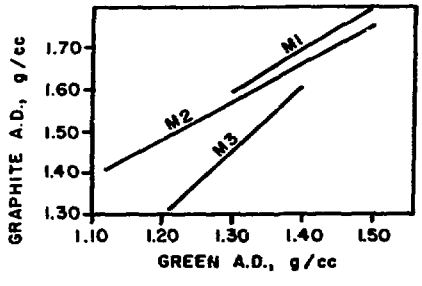


Fig 1. Effect of Raw Materials on A. D.

Black B produces graphites having the highest apparent densities. When resin is substituted for a portion of the pitch binder, the graphite apparent density decreases. These effects are due primarily to the weight loss during baking as shown in Table 2. The plates made from Mix M1 experienced the lowest weight loss during baking because of their lower pitch level. When resin is substituted for a portion of the pitch, weight loss during baking increases because of the

lower coking value of the resin. These effects are reinforced by the volume changes during baking and graphitizing as shown in Figure 2.

TABLE 2

WEIGHT LOSS DURING BAKING AND GRAPHITIZATION

Mix	% Weight Loss		
	Green-Baked	Baked Graphitized	Green-Graphitized
M1	10.1	2.3	12.4
M2	12.5	2.1	14.6
M3	14.5	2.7	17.2

Volume shrinkage is comparable for Mixes M1 and M2. However, M3, containing resin in place of a portion of the pitch, does not shrink as much.

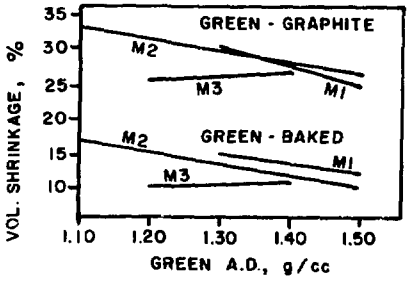


Fig. 2 Effect of Raw Materials on Vol. Shrinkage

When pitch is used along as a binder, volume shrinkage generally decreases at higher densities and the slope of the curve is negative. As resin is substituted for a portion of the pitch, the slope of the shrinkage-density line changes from a negative value to zero and, as shown for very high substitutions, to a positive value.

Electrical resistivity is strongly controlled by the amount and type of binder used in the mix as shown in Figure 3. As binder level increases (M1 versus M2) electrical resistivity decreases, presumably because binder carbon is a better conductor of electricity than the black. Substitution of resin for pitch increases resistivity (M2 versus M3). Since resin carbon does not graphitize as well as pitch carbon, its resistivity is higher.

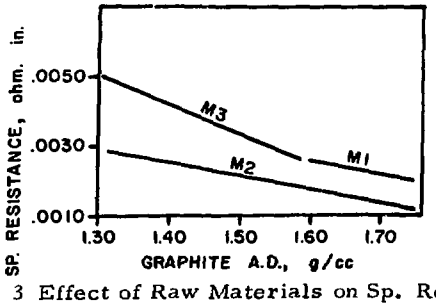


Fig. 3 Effect of Raw Materials on Sp. Resistance

Flexural strength is also affected by amount of binder as shown in Figure 4. Higher pitch levels (M1 versus M2) result in higher strengths. Substituting resin for pitch (M2 versus M3) decreases strength.

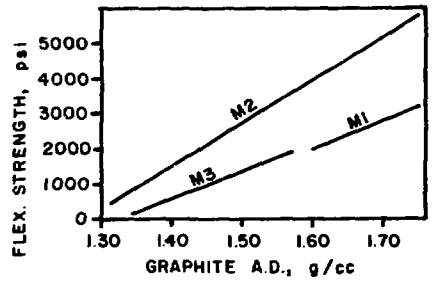


Fig. 4 Effect of Raw Materials on Flex Strength

Increasing binder level in the mix increases the scleroscope hardness (M1 versus M2) as does the substitution of resin for a portion of the pitch (M2 versus M3), as shown in Figure 5. Upon graphitization, resins form glassy carbons which are very hard. This is reflected in the results obtained from M3.

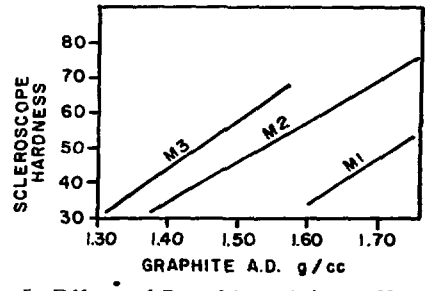


Fig. 5 Effect of Raw Materials on Hardness

Conclusions

The results of the work presented here show that one can produce lampblack grades with a variety of properties by varying the type of black and the ratio of resin/pitch used as binder. Thus, it is possible to design a mix to produce a graphite with specified levels of physical properties.

PUFFING OF ELECTRODE STOCK AS INFLUENCED BY SULFUR CONTENT AND HEATING RATE

K. W. Tucker, L. D. Loch, G. Stecker, L. A. Joo'
Great Lakes Research Corporation, Elizabethton, TN.

The relationships among acicular petroleum coke sulfur level, upheat rate during graphitization and puffing test characteristics of typical electrode type mixes have been evaluated in detail. Also, other physical properties have been measured on the 1"øx1" long puffing plugs after graphitization to determine whether these properties can be correlated to puffing behavior. Baked electrode type stock (all with the same coke-sizing, the largest coke particle size 6.7mm) from four different cokes were evaluated for puffing behavior through the temperature range 1200°C to 2900°C at 3°C/min., 5°C/min., 10°C/min., and 14°C/min. upheat rates.

Cokes with the following S contents were evaluated:

Coke A %S = 0.5, non puffer
Coke B %S = 0.8, low to moderate puffer
Coke C %S = 1.15, high puffer
Coke D %S = 1.25, very high puffer

Whittaker and Grindstaff[1] have shown that the changes in microporosity which accompany this irreversible expansion during graphitization occurs because of the sudden formation and rapid evolution of hydrogen sulfide gas. Letizia[2] studied the puffing of several cokes with and without puffing inhibitor and found that puffing of non-inhibited cokes was proportional to the sulfur content.

The special puffing test used in this evaluation consists of heating 1"øx1" long cylinders, cut from 4" diameter moldings, at a controlled uniform upheat rate. Changes in sample length perpendicular to the axis of molding are measured by means of a calibrated graphite dilatometer. The accuracy of this test is such that total puffing is measured to ±0.25%. Figure I illustrates puffing curves of two types. Curve A is typical of an inhibited formulation of coke C while curve B represents that of uninhibited coke C stock. Total puffing values, defined as %ΔL from minimum length to maximum length are designated as $\%\Delta L_1$ and $\%\Delta L_0$ for inhibited (curve A type) and uninhibited (curve B type) stock, respectively. As shown in Figure I, the two values $\%\Delta L_1$ and $\%\Delta L_0$ are defined differently. Only primary puffing, which usually occurs in the 1500-2300°C region, is included in $\%\Delta L_1$. Total puffing occurring between 1200-2900°C is the $\%\Delta L_0$ value.

Puffing was almost nil regardless of upheat rate among the four rates studied on baked electrode stock made with low-sulfur coke A, and containing 1 pph Fe_2O_3 inhibitor (Fig. II & III). Even in baked coke A electrode stock with no puffing inhibitor, puffing is nil at the two slower upheat rates and low to moderate at the faster upheat rates (Fig. II). In contrast, puffing is pronounced in baked electrode stock fabricated with coke D, a high sulfur coke. With coke D, puffing increases appreciably with increasing upheat rate. At the fastest upheat rates, 1 pph Fe_2O_3 does little to inhibit high sulfur coke D as puffing severity of the inhibited stock is almost equivalent to that of uninhibited stock.

Coke B baked electrode stock exhibits puffing characteristics similar to coke A stock but total puffing levels of the former are about 3-5 times that of the latter depending upon upheat rate. This is true for both inhibited and uninhibited stock. Puffing characteristics of coke C stock are similar in trend to those of coke D stock discussed above, but total puffing is about 25-50% lower at a given upheat rate for the former.

Figures IV and V graphically illustrate the relationships of coke-sulfur level and puffing behavior for the electrode stock during graphitization. Similarities of cokes A and B on one hand and cokes C and D on the other hand are clearly depicted in the figures. Total puffing levels of the two highest puffing, high-sulfur cokes rise sharply with increasing upheat rates while upheat rate has much less impact on the low-sulfur cokes.

Coefficient of linear thermal expansion (CTE) and apparent density were measured on the 1"øx1" long graphitized plugs after the puffing experiments. A good correlation exists between coke-sulfur content and apparent density of the graphitized plug at fast heating rates (Fig. VI). Correlations are poorer at slow heating rates. Also, moderate to good correlation exists between CTE and heating rate among the puffing cokes. Figure VII illustrates this relationship.

In summary, magnitudes of both $\%\Delta L_0$ and $\%\Delta L_1$ of electrode stock are related to the sulfur level of the coke from which it was prepared. Low sulfur coke is easily inhibited to almost zero puffing with low to moderate levels of Fe_2O_3 inhibitor. Graphitization rates have a significant effect on total puffing ($\%\Delta L_0$ or $\%\Delta L_1$) of electrode stock. This effect is greatest in stock formulated with high-sulfur cokes.

A good correlation exists between coke-sulfur level and density of graphitized plugs at fast heating rates. Also, a moderate to good correlation exists between CTE of

graphitized plugs and heating rate for puffing (high-sulfur) coke stock.

References

1. M.P. Whittaker and L.I. Grindstaff, Carbon, 7, pp. 615-21 (1969)
2. I.Letizia, Abstracts of the Tenth Biennial Conference on Carbon, July, 1971.

****

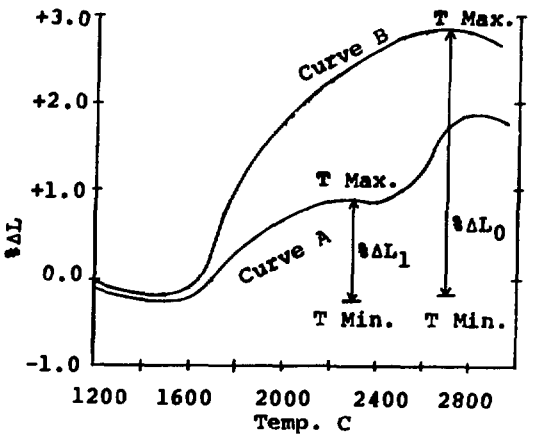


Fig. I. Puffing Curves for Coke C stock with (A) and without (B) Inhibitor

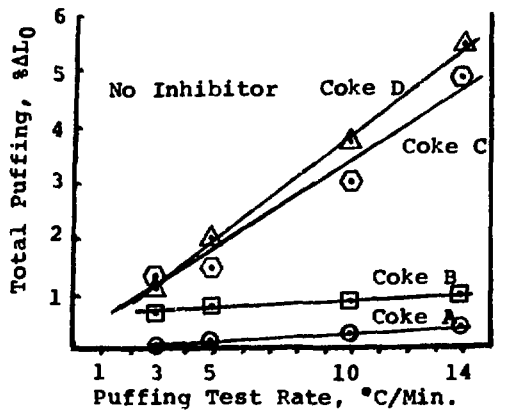


Fig. II. Upheat Rate Vs. Puffing

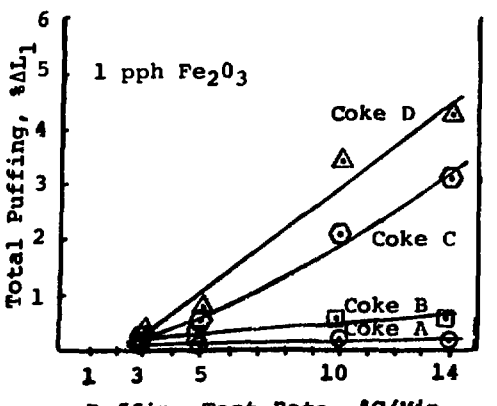


Fig. III. Upheat Rate Vs. Puffing

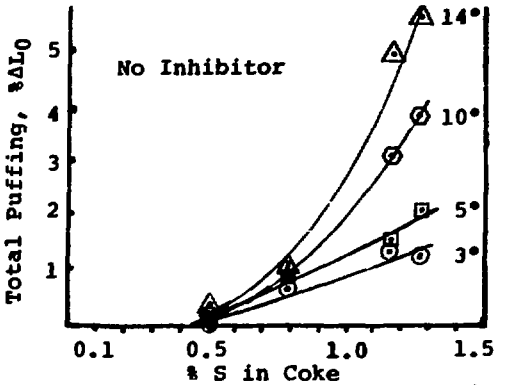


Fig. IV. Coke Sulfur Vs. Total Puffing

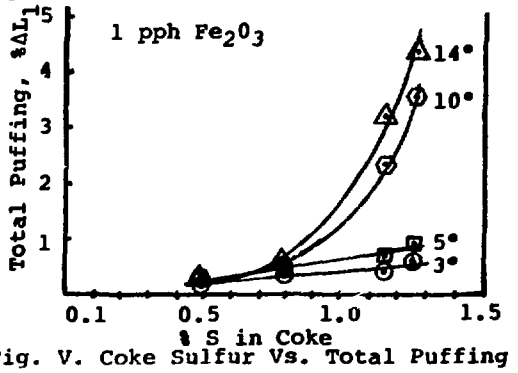


Fig. V. Coke Sulfur Vs. Total Puffing

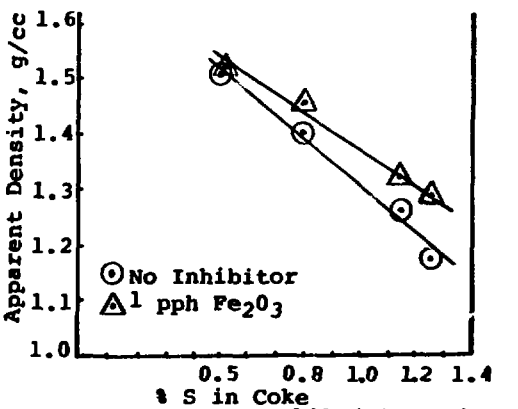


Fig. VI. AD Vs. %S at 14°C/Min. Upheat

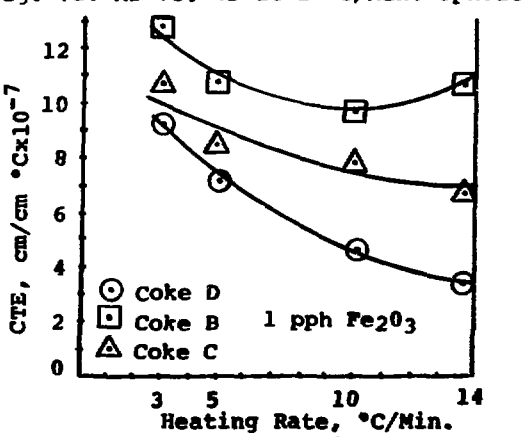


Fig. VII. CTE Vs. Heating Rate

EFFECT OF COKE-SIZING ON PUFFING CHARACTERISTICS OF BAKED STOCK

L. D. Loch, K. W. Tucker, L. A. Joo'
Great Lakes Research Corporation, Elizabethton, Tennessee 37643

Puffing characteristics determined by a dynamic puffing test were utilized to evaluate coke sizing-puffing relationships. Four types of baked stock, ranging from all-flour mixes to coarse particle electrode type mixes were formulated with both high puffing coke C* (sulfur content 1.2%) and low-puffing coke B (sulfur content 0.8%). Each mix type with each coke type was evaluated without inhibitor and with 1 pph Fe_2O_3 between 1200° and 2900°C. Puffing tests at both 5°C/min. and 14°C/min. were conducted on each of the samples. The puffing test procedure, and sample puffing curves are described briefly in the reference cited below*.

The following is a general description of the four mix types evaluated in this study:

Mix #1 stock - all flour (largest particle size <0.21mm)
Mix #2 stock - medium fine-grain, largest particle size 1.6mm
Mix #3 stock - medium-grain, largest particle size 6.7mm
Mix #4 stock - medium coarse-grain, largest particle size 12.7mm

Table I summarizes the results of this study. Total puffing values, defined as $\%\Delta L$ from minimum length to maximum length, are designated as $\%\Delta L_1$ or $\%\Delta L_0$ for inhibited and uninhibited stock, respectively. Results are much as expected with degree of puffing, in general, increasing with both increasing upheat rate and increasing mix coarseness. Puffing in low-puffing and non-puffing coke stock is less affected by mix type and upheat rate than in puffing coke stock but both follow the same general trends in their puffing behavior.

Uninhibited mix #2 baked stock made with coke B (low puffer) puffs 0.24% and 0.62% at 5°C/min. and 14°C/min. upheat, respectively, while mix #4 baked stock made from the same coke, also uninhibited, puffs 1.27% and 2.07% under the same graphitization conditions.

Uninhibited mix #2 baked stock formulated with high puffing coke C puffs 0.69% and 2.01% at 5°C/min. and 14°C/min. upheat rates, respectively, while uninhibited mix #4 baked stock made from the same coke puffs 2.09% and 5.28% under the same graphitization conditions.

The same trends noted in the above examples, except at lower total puffing levels, are followed by baked stock inhibited with 1 pph Fe_2O_3. Baked stock intermediate in particle sizing between mixes #2 and #4 have intermediate total puffing levels.

It is apparent from the examples cited above that fine-grain stock is more easily inhibited than coarse-grain stock fabricated from the same coke. Figures I and II depict the relationships among mix type, total puffing and puffing inhibition (1 pph Fe_2O_3 vs. none) for baked stock prepared from cokes B and C, respectively. Placement of the mix type on the graph's horizontal axis was assigned on the basis of the size in mm of the largest coke particles within that mix. Good correlations exist between total puffing and mix coarseness as discussed in the above examples.

In addition to determining puffing characteristics on all the baked stock shown in Table I, apparent densities and coefficients of linear thermal expansion (CTE) were obtained on the 1"ø x 1" long puffing plugs after the puffing test. All of these plugs were well-graphitized since all were tested to 2900°C.

In some instances densities show the expected decrease with increased total puffing, particularly at high heating rates. Processing conditions and the small sample size tend to "wash out" correlations when slow heating rates are involved. Considering the small sample size of the puffing plugs a fair correlation exists between CTE and total puffing. Figure III illustrates this relationship.

In summary, the degree of puffing ($\%\Delta L_0$ or $\%\Delta L_1$) increases significantly with increasing mix coarseness. Also, puffing increases as the heating rate is increased. Stock formulated with cokes C and B follow generally the same trends although coke C is obviously a higher puffer.

As puffing increases due to larger particle size in the stock, density of the stock tends to decrease. CTE's follow an inverse correlation with $\%\Delta L_0$ or $\%\Delta L_1$.

*For coke description see abstract "Puffing of Electrode Stock As Influenced by Sulfur Content and Heating Rate" by K. W. Tucker, et. al., 13th Biennial Carbon Conference

Table I
Effect of Coke Sizing on Puffing of Baked Stock

Coke	Mix Type	Inh.	Total Puffing (%ΔL_0 or %ΔL_1) at Heating Rate (°C/Min.) 5°	14°	A.D. After Graph. Heating Rate (°C/Min.) 5°	14°	CTE (cm/cm °Cx10^{-7}) After Graph. Heating Rate (°C/Min.) 5°	14°
B	1	No	0.11	0.23	1.41	1.42	19.1	15.4
B	2	No	0.24	0.62	1.41	1.45	8.2	12.9
B	3	No	0.80	1.06	1.46	1.40	8.1	9.5
B	4	No	1.27	2.07	1.44	1.39	11.0	11.0
B	1	1F	0.05	0.05	1.42	-	14.7	-
B	2	1F	0.07	0.26	1.54	1.48	14.7	15.4
B	3	1F	0.26	0.49	1.49	1.46	10.8	10.8
B	4	1F	0.50	1.30	1.50	1.41	9.9	6.8
C	1	No	1.33	2.24	1.28	1.21	10.2	10.8
C	2	No	1.29	3.01	1.48	1.35	13.9	7.9
C	3	No	1.52	4.92	1.46	1.26	7.0	7.0
C	4	No	2.09	5.28	1.37	1.25	7.2	3.3
C	1	1F	0.03	0.16	1.40	1.41	14.7	12.7
C	2	1F	0.14	1.32	1.51	1.44	14.9	11.8
C	3	1F	0.59	3.13	1.49	1.32	8.5	6.8
C	4	1F	0.92	4.39	1.52	1.24	-	3.3

1F = 1 pph Fe_2O_3

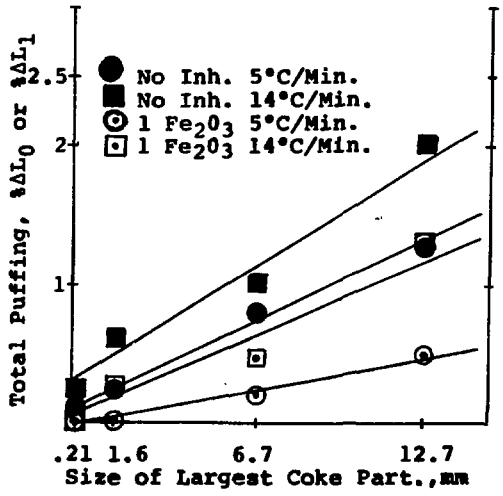


Fig. I. Puffing Vs. Mix Type-Coke B

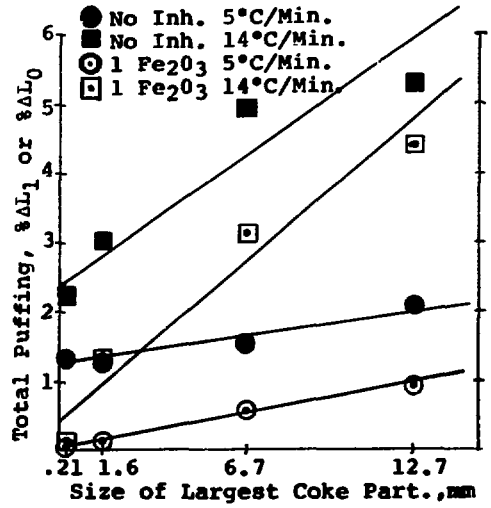


Fig. II. Puffing Vs. Mix Type-Coke C

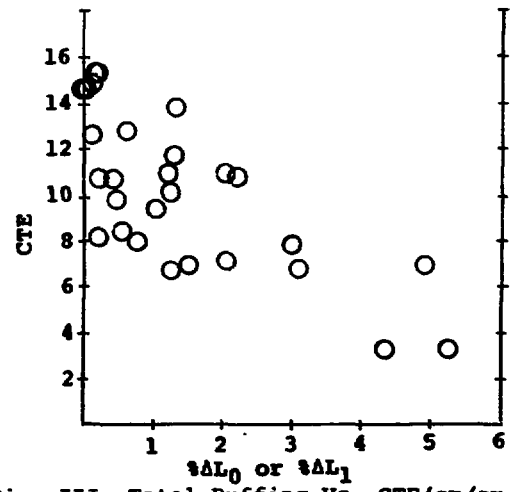


Fig. III. Total Puffing Vs. CTE(cm/cm °Cx10^{-7}

The Use of Sulfur to Control Physical Properties in Graphite*

C. R. Kennedy
Metals and Ceramics Division, Oak Ridge National Laboratory†

It is fairly well known[1-3] that the irreversible expansion during the final heat treatment to graphitization temperatures is related to the sulfur content in filler cokes. While this expansion, commonly called *puffing*, is well known and carefully monitored in industry, very little has been published concerning the reaction. The major concern has been in eliminating or inhibiting the reaction with stable sulfide-forming additives. Rarely is the sulfur reaction related to fabrication or physical properties. It is the purpose of this investigation to isolate the effects of sulfur as a single variable and to describe those properties dependent upon the sulfur content in the filler coke.

The filler cokes in this study were all derived from A-240 petroleum pitch using a small 4 kg laboratory coker. The sulfur content of the A-240 pitch varied from 0.3 to 3.25 wt %, yielding green cokes with 0.25 to 2.70% sulfur. Iron oxide was studied as an inhibitor by additions to a 3% sulfur A-240 pitch before coking. The filler cokes were made by two procedures, one to produce the typical acicular coke yielding a highly anisotropic graphite; the second, using a modified process to randomize the coke structure to yield more isotropic graphites. The latter procedure accomplished the isotropy while retaining the inherently high crystallinity of the cokes made from the A-240 petroleum pitch. The filler cokes were all coked to 500°C, ground and screened such that 100% -88 μm.

The graphites were all made using an ORNL process to plasticize the outer surfaces of the green filler coke.[4] This was done to achieve highly efficient bindering and uniform packing of moldings with the different fillers. Coal tar pitch 30M was used as the plasticizer and A-240 pitch as the final binder. The green as-molded bulk density was a common 1.31 to 1.33 g/cm^3 in all cases. Several moldings of each mix were made and baked under restraint. In each case, one molding was graphitized without impregnation, a second molding was given a single A-240 pitch impregnation, and in most cases a third molding was rebaked and given a second pitch impregnation. The final graphites were evaluated by obtaining the 1000°C mean coefficient of thermal expansion (CTE), electrical resistivity, sonic velocities, and bend test properties.

The generally accepted concept of the irreversible expansion or *puffing* reaction is related to the sudden release of sulfur. This release creates adequate internal strains to cause a significant increase in micropores less than 0.1 μm in diameter.[1] This increase in volume by the microporosity results in lower final bulk densities and alterations in both the thermal and mechanical properties of the graphite. The decrease in final bulk density with increased sulfur content is shown in Fig. 1. It is also clearly demonstrated that the volume expansion is independent of impregnation. Obviously, this would be expected if the porosity generated occurs after the impregnation and not before.

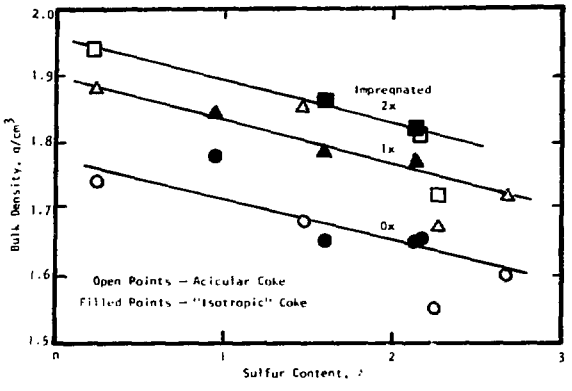


Fig. 1. Sulfur Content in the Filler Coke Decreases the Final Graphite Density.

The always less-than-theoretical coefficient of thermal expansion is a result of the material expanding into the defect structure. To be effective, the defects must be preferentially aligned normal to the c axis. The volumetric CTE (2× with-grain CTE + against-grain CTE) used to cancel anisotropy differences is shown in Fig. 2 to be significantly reduced by increased sulfur content. This suggests a preferential alignment of porosity which may well result from the internal pressure splitting the lower strength interlayer bonds. The effect of Fe_2O_3 to

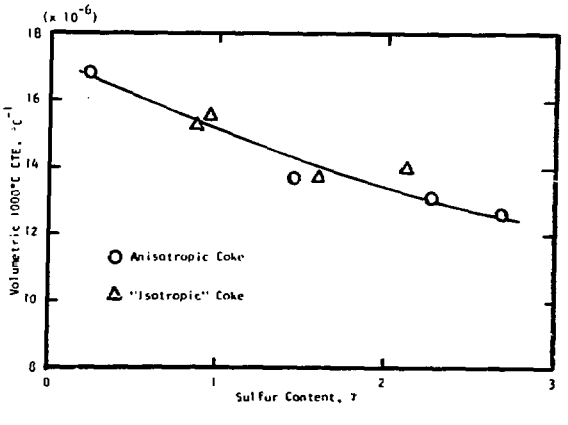


Fig. 2. Sulfur Content in the Filler Coke Decreases the Coefficient of Thermal Expansion.

*This work was funded by the Naval Surface Weapons Center under Contract No. N-60921.

†Operated by Union Carbide Corporation for the Energy Research and Development Administration.

inhibit the reaction increases the CTE, as shown in Fig. 3, suggesting an elimination of the microporosity.

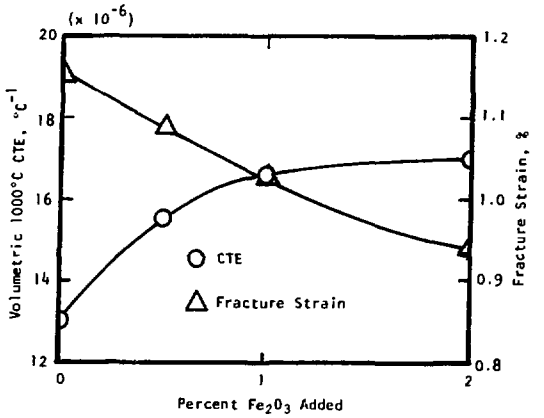


Fig. 3. Fe_2O_3 Additions Decrease the Thermal Stress Resistance of Graphite.

The ability of graphite to significantly microfracture without rapid crack propagation to failure distinguishes brittle graphites from those with significant toughness. The microcracking is actually a stress relief system to homogenize the stress, reducing the potential for crack propagation. It was observed that while the actual fracture strength-total porosity relationships are essentially independent of the sulfur content, the fracture strain is significantly improved by increased sulfur content. The effect of Fe_2O_3 inhibitors is again to reduce the fracture strain with little effect on fracture strength. The elastic properties, evaluated by sonic velocity measurements,[5] demonstrated the singular dependence of the bulk compressibility to total porosity. However, Poisson's ratio decreased, as shown in Fig. 4, with increased sulfur content. The implication is that, with higher sulfur content and higher microporosity, a significant portion of the strain is a result of void opening or closure. The fineness of the structure allows for greater fracture strains without a decrease in strength.

In summary, the effect of increased sulfur content in a soft coke, as derived from Ashland A-240 petroleum pitch, is to first reduce the potential

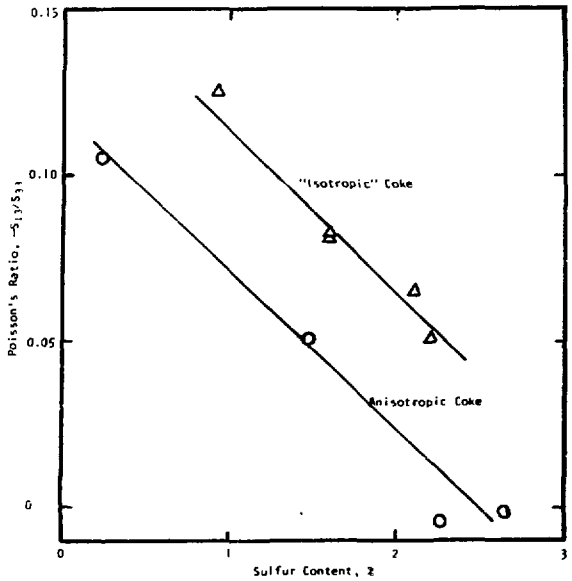


Fig. 4. Sulfur Content Decreases Poisson's Ratio.

bulk density of the final graphite by an irreversible volume expansion. The microporosity produced by the sulfurous-gas evolution effectively reduces the CTE and increases the strain to fracture without a loss in strength. The implication of these results, with the reduced Poisson's ratio, is that the porosity is very fine, evenly distributed, and oriented normal to the c axis. In effect, increased sulfur content offers a fine solution to obtaining graphites with extraordinary thermal stress resistance and toughness.

References

(1) M. P. Whittaker and L. I. Grindstaff, *Carbon*, 7(5), 615 (1969).

(2) E. Fitzer, K. J. Huttinger, and A. Megalopoulos, *11th Biennial Conference on Carbon*, p. 67, 1975.

(3) E. Fitzer and S. Weisenburger, *11th Biennial Conference on Carbon*, p. 245, 1975.

(4) C. R. Kennedy, *11th Biennial Conference on Carbon*, p. 304, 1973.

(5) C. R. Kennedy, *Elastic Constants of Graphite*, this conference.

OCCUPATIONAL EXPOSURE TO FUGITIVE EMISSIONS FROM A GRAPHITE PRODUCTION OPERATION*

W. H. Griest and H. Kubota, Analytical Chemistry Division
and
W. P. Eatherly, Metals and Ceramics Division
Oak Ridge National Laboratory, Oak Ridge, Tennessee

In recent years, an increased awareness has arisen of the polynuclear aromatic hydrocarbon content of emissions from sources such as coke ovens, coal tar heaters, or internal combustion engines. However, the fugitive emissions generated during the production of graphite have received relatively little, if any, attention. The purpose of this interdivisional study is to characterize potential PAH-containing fugitive emissions associated with the in-house production of graphite from a petroleum pitch distillate. The processes used in this production of graphite have been described in previous Carbon Conferences,[1,2] and the work operations of concern in this study involved the chopping, grinding, and sieving of pitch, coke, or pitch-modified coke as well as certain autoclave loading and unloading operations with pitch-infused coke. Emissions from baking ovens also were monitored.

In the first phase of the study, organic fugitive emissions associated with specific work operations were characterized by a prioritized system of analysis of air sample particulates collected on air filter pads in a survey examination of the operations. The particulates collected on the air filter pads were spiked with ^{14}C labeled benzo(a)pyrene (BaP), extracted with benzene, and the fluorescence spectra of the crude extracts were recorded. The extracts were prioritized for specific BaP analysis by a ranking according to their fluorescence intensity at a BaP emission wavelength and their particulate weight. Prioritized extracts were subjected to adsorption column chromatography and final BaP measurement by fluorescence or gas chromatography (GC). Recoveries were determined by liquid scintillation counting. The grinding of coke or pitch-coated coke produced total particulate air concentrations from ~0.2 to 25 mg/m^3, with BaP air concentrations from 0.23 to 0.63 mcg/m^3. The chopping of pitch yielded somewhat lower emissions, with 0.92 mg/m^3 of particulates and 0.12 mcg/m^3 of BaP. This result may arise from the sticky, cohesive nature of the raw pitch and a lesser tendency of the agglomerated particles to become airborne. Furnace emissions appeared to be relatively low. On a 72-hr heating cycle, a bake oven produced 0.06 mg/m^3 total particulates and 0.075 mcg/m^3 BaP calculated as 72-hr averages. The instantaneous concentrations at any point in the heating cycle, however, could have been higher.

The single work operation associated with the highest emissions was the removal of pitch-impregnated coke blocks from an autoclave bucket. On one occasion when considerable difficulty was experienced in dislodging the blocks, the total particulate air concentration reached 9.31 mg/m^3 and BaP was 2.70 mcg/m^3. The residue from the infusing pitch in the bucket probably was the major source of BaP in these emissions. On a separate occasion when the autoclaved blocks were removed from the bucket with relatively little difficulty, the total particulate and BaP levels were 0.20 mg/m^3 and 0.19 mcg/m^3, respectively. These data suggest that considerable variability is possible in the measured emissions associated with a given work operation. Factors contributing to such variability would include differences in how the operations were carried out as well as the usual uncertainties in reproducing an air sample collection.

Since most of these work operations were carried out in a single workroom, the greatest single source of potential worker exposure appeared to be generally restricted to that room. Hence, in the second phase of this study, emissions generated in that room during the course of a typical work shift were characterized in greater detail to estimate an overall potential exposure resulting from the various work operations carried out in a shift.

Stationary high-volume air samples were positioned at three locations within the workroom to monitor emissions which might be offered to a worker at those three sites. Air filter cassettes were changed hourly to allow an hour-by-hour measurement of emissions. The worker carried a breathing zone personal monitor to estimate actual hourly exposure. The samples were analyzed by the same prioritized system as before.

In relatively full periods of emissions corresponding to unloading and reloading of a coking furnace, and the loading of an autoclave bucket, high-volume air samplers located at three workroom positions indicated hourly air concentrations of total particulates ranging from ~0.07 to 0.6 mg/m^3. In time intervals of peak emissions resulting from grinding operations and cleaning the floor and grinding equipment with a vacuum, total particulates increased to as high as 1.75 mg/m^3 and BaP air concentrations reached 0.72 mcg/m^3 in one location. Comparison of the data for the three samplers showed the generation and spread of emissions across the room. In one time interval, an air sampler across the room from the site of the grinding operations indicated emissions equal in concentration, but delayed somewhat in time, with those monitored by the sampler next to the grinding operation. This result suggests that the building air conditioning moved the emission cloud directly past the second sampler and that the core of the emissions cloud was undiminished in concentration. Hence, dilution of emissions may not always be assumed and worker exposure at a location somewhat removed from the actual site of emission generation potentially may be as high as at the actual generation site.

Significantly, the emissions indicated by a breathing zone personal monitor carried by a worker

*Research sponsored by the Energy Research and Development Administration under contract with the Union Carbide Corporation.

were three to five times greater in concentration than those monitored by the stationary high-volume air samplers. During full periods of emissions, total particulate breathing zone air concentrations were ~0.1 mg/m^3, but during periods of peak emissions total particulates increased to as much as 5.6 mg/m^3, and BaP air concentrations reached about 1.3 mcg/m^3. These higher emission concentrations indicated by the personal monitor must reflect at least two factors. First, the personal monitor is closer than the high-volume air samplers to the source of emissions (*i.e.*, the production operation being carried out by the worker). Second, the worker is constantly moving and shifting about, and may come into and out of contact with localized, possibly stagnant and highly concentrated plumes or clouds of emissions inaccessible to the stationary high-volume samplers.

However, PAHs other than BaP might be present in the particulates and their presence was investigated by subjecting a 24-hr air sample to a gas chromatographic multicomponent PAH analytical procedure.[3] Thirty identifiable (co-chromatography and/or mass spectroscopy) PAH ranging in ring size from 9-methylfluorene to 1,12-benzoperylene were tentatively identified. Four-ring PAHs were present in greatest concentrations. Chrysene was the most abundant PAH, with an air concentration of 1.91 mcg/m^3 (24-hr average) and a concentration in the particulates of 6.45 mcg/mg. Two C_1-chrysene/benzanthracene/triphenylene (isomer indeterminate by MS) totaled 2.23 mcg/m^3. A benzofluoroanthene, a five-ring PAH, was present at 0.79 mcg/m^3. BaP was roughly estimated (because of interferences) at ~0.25 mcg/m^3. Some unassigned isomers of benzofluoroanthene, methylchrysene, and/or methylbenzanthacene possess carcinogenic activity, but isomer assignments, for the species in the air sample, have not yet been carried out. The remaining PAH ranged in concentrations from 0.4 to 0.01 mcg/m^3. The total GC-volatile PAHs were estimated to correspond to an air concentration in the range of 8 to 17 mcg/m^3 (24-hr average), and to constitute 3 to 5% by weight of the particulates. Thus, BaP made up only a small part of the total PAH in the air particulate sample, although it is the PAH of greatest popular interest.

To assess the potential inhalability of the workroom emissions, a particle size analysis was carried out on several breathing zone total particulate samples. Particulate air concentrations were found to range from 0.1 to 2 × 10^5 particles/l with a mass median diameter of 7.5 μm, depending upon the particular grinding operation. About 70% by weight of the particles were <10 μm in diameter; hence a significant portion were within a respirable range of particle sizes. However, only about 1% were within the 0.8 to 1.6 μm diameters corresponding to maximum particle deposition in the fine bronchioles and alveoli.[4]

An overall consideration of the results from this study suggests that graphite production from petroleum pitch can release highly localized (in both time and space), respirable, PAH-containing particulate fugitive emissions. Worker protection equipment is in use in our workrooms, and emission-containment devices are being designed. Similar measures are suggested for other laboratories producing graphite from petroleum or coal-tar pitches.

References

(1) C. R. Kennedy and W. P. Eatherly, *18th Biennial Conference on Carbon*, p. 241 (held at Pittsburgh, Pa., July 28–August 1, 1975).

(2) O. J. Horne and C. R. Kennedy, *Ibid.*, p. 255.

(3) H. Kubota *et al.*, pp. 281–289 in *Trace Substances in Environmental Health-IX*, D. D. Hemphill, ed., University of Missouri, Columbia, 1975.

(4) H. L. Green and W. R. Lane, pp. 349–350 in *Particulate Clouds: Dusts, Smokes, and Mists*, Van Nostrand Co., Inc., New Jersey, 1964.

MAGNETIC ORIENTATION STUDIES OF SYNTHETIC MESOPHASE PITCHES

C. A. Kovac and I. C. Lewis
Union Carbide Corporation, Carbon Products Division
Parma Technical Center, Parma, Ohio 44130

I. Introduction

Previous work by Singer and Lewis[1] has shown that carbonaceous mesophase spherules with the familiar Brooks-and-Taylor structure align in a magnetic field with their c-axes (optical axes) perpendicular to the magnetic field direction. Mesophase spheres with unusual optical properties have been reported by Honda, et al.[2], for pitches to which carbon black has been added. These authors proposed a very different structure from that described by Brooks and Taylor[3].

We have also observed unusual optical effects in spheres contained in mesophase pitches made from model compounds with anhydrous aluminum chloride. To further investigate these effects, we have studied these materials using polarized light and sensitive tint optical microscopy and magnetic field orientation.

II. Experimental

The synthetic pitches which were studied were made from the pure compounds naphthalene and anthracene by reaction with anhydrous aluminum chloride at temperatures from 160-300°C. Residual inorganic material remaining in the pitches after reaction was removed by acid hydrolysis. These pitches were then examined by conventional polarized light microscopy techniques.

Magnetic orientation of these materials was done using the apparatus and sample preparation techniques described previously by Singer and Lewis[1]. A magnetic field of 10 Kgauss was used. Samples were heated in the magnet gap to temperatures between 300°C and 400°C and were held in the field at these temperatures for 1/2 hour. Experiments were done with each material both with and without rotation of the sample tubes around an axis perpendicular to the field.

After cooling to room temperature in the field, the oriented samples were sectioned for microscopy to give both transverse and longitudinal views. Transverse views contained a plane of section parallel to the magnetic field and, for rotated samples, perpendicular to the rotation axis. Longitudinal views contained a plane of section perpendicular to the magnetic field. Optical evaluation of the samples was done using polarized light and sensitive tint microscopy.

III. Results and Discussion

The pitches prepared using $AlCl_3$ contained from 10-60% mesophase. Microscopy of the unoriented samples showed the mesophase to be present in the form of spheres as well as large coalesced regions. Spheres which exhibited rotating cross extinction patterns appeared quite similar to typical Brooks-and-Taylor spheres in polarized light. However, in sensitive tint, the quadrants showed exactly opposite color configurations to those which were observed for "normal" spheres. To further investigate this apparent anomalous behavior, magnetic orientation experiments were performed.

As Singer et al.[4] have demonstrated, mesophase from plate-like aromatic molecules will orient in a magnetic field with the optic axis perpendicular to the field direction, whereas conventional liquid crystals from rod-like molecules will orient with the optic axis parallel to the field direction. Examination by polarized light microscopy of the longitudinal views of the samples not rotated in the field showed spheres having no apparent orientation with respect to one another. However, the transverse views of the magnetically oriented, rotated samples showed spheres that were all of uniform darkness (complete extinction), which did not change upon stage rotation. This result implies that the direction of view is parallel to the optic axis of the oriented mesophase, i.e., the optic axis is aligned parallel to the rotation axis and perpendicular to the field. These observations are consistent with the conclusion that the mesophase in these unusual spheres consists of flat, disc-like molecules not rod- or lath-like molecules, and that the optical sign of the mesophase is negative, as is observed in other carbonaceous mesophase systems.

Examination of the longitudinal sections of the rotated samples showed that the spheres present were all well-oriented by the field. In polarized light observation, these spheres appear to have extinction patterns similar to those observed for spheres with Brooks-and-Taylor type structure. As is observed with Brooks-and-Taylor spheres, the magnetic field also orients the spheres internally and curvature can be observed only in a thin shell near the sphere surface. On examination with a sensitive tint plate, the regions of curvature in the outer shell showed an opposite color configuration from that observed for "normal" spheres. That is, the areas which would appear blue in a "normal" sphere, appear yellow, and vice versa. Also, it was observed that while the extinction brushes in the Maltese cross of a normal sphere emanate from the poles, in these unusual spheres the brushes emanate from the equator.

These results suggest the new structure (II) for these spheres which is shown in Figure 1 together with the standard Brooks-and-Taylor structure (I). The three-dimensional structures of the spheres are given by a body of rotation around the perpendicular axis shown. The internal orientation of the spheres is lamellar, just as in the Brooks-and-Taylor sphere. However, near the surface, the layers orient themselves parallel to the sphere surface and not perpendicular as is observed for a Brooks-and-Taylor sphere. The new structure has a

belt-like singularity around the equator rather than the two single poles that occur in a "normal" sphere.

In conclusion, the mesophase spheres observed in pitches made from model compounds with $AlCl_3$ show a difference in structure from that of spheres produced in normal pitch materials. This structural difference is believed to arise from interactions at the interface of the mesophase and isotropic phase, which give rise to a change in orientation at the surfaces of spheres. Such unique surface effects may be tied to chemical differences in the mesophase from these model systems.

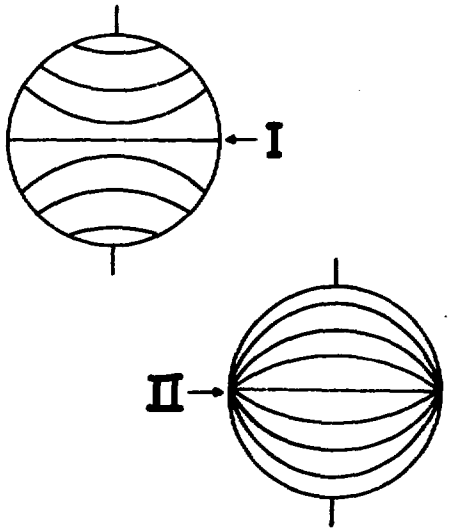


Figure 1. Mesophase Sphere Structures: (I) Standard Brooks-and-Taylor Structure, (II) Proposed Structure for Mesophase Spherules in Synthetic Model Pitches.

References

1. L. S. Singer and R. T. Lewis, Summary of Papers, Eleventh Biennial Conference on Carbon, Gatlinburg, Tenn. June 4-8, 1973, paper CT-27, p. 207.

2. H. Honda, et al, ibid, paper CG-32, p. 219.

3. J. D. Brooks and G. H. Taylor, Chemistry and Physics of Carbon, Volume 4, Edited by P. L. Walker, Jr., Marcel Dekker Inc., New York, N.Y., 1968, pp. 243-286.

4. L. S. Singer, R. T. Lewis, A. T. Lauria, and S. L. Strong, Fifth Internation Liquid Crystal Conference, June 17-21, 1974, Stockholm, Sweden, and private communication.

Acknowledgments

We wish to acknowledge assistance and helpful discussions provided by L. S. Singer, R. T. Lewis, and A. Saupe, and to thank L. S. Singer for assistance with the magnetic orientation experiments.

INFLUENCE OF A MAGNETIC FIELD ON THE MOLECULAR ARRANGEMENT OF MESOPHASE SPHERULES

S. MATSUMOTO, S. OI, T. IMAMURA, N. NAKAMIZO, Y. YAMADA, H. HONDA
National Industrial Research Institute of Kyushu
Tosu-shi, Saga, 841, Japan

Introduction

Brooks and Taylor[1] studied the structure and molecular arrangement of carbonaceous mesophase spherules which were formed in pitches during heat treatment at 350-450°C by the use of polarized-light microscopy and electron diffraction method.

On the other hand, new type mesophase spherules having a molecular arrangement different from that proposed by Brooks and Taylor have been found[2] when pitches are heat treated with a small amount of carbon black (APF or GPF). Fig.1 shows the molecular arrangement of these spherules.

The behavior of Brooks-Taylor type spherules in a magnetic field was reported[3-4] and it was proved that these spherules were aligned with their polar diameter perpendicular to the magnetic field direction. In above report, molecular arrangement of Brooks-Taylor type spherules remained unchanged in a magnetic field up to 10K gauss.

We have studied the behavior of the new type mesophase spherules in various magnetic field strengths and it was found that the molecular arrangement of the new type spherules formed by addition of APF could be transformed into that of the Brooks-Taylor type spherules when a magnetic field of over 3K gauss was applied during heat treatment. The mechanism of this phenomenon was investigated.

Experimental

About 5wt% of carbon black (APF or GPF) was added into quinoline-soluble coal tar pitch and mixed homogeneously at 430°C under stirring. The mixture thus obtained was heat treated at 430°C for a certain period at various magnetic field strengths with sample rotation (also cooled in the field). The mesophase in pitch was examined in both parallel and perpendicular directions to the magnetic field direction using a reflected polarized-light microscopy with crossed polarizers and a gypsum plate.

Results and Discussion

When the pitch is mixed with GPF and heat treated in 8K gauss magnetic field, the new type mesophase formed with their polar diameter parallel to the direction of the magnetic field. Above phenomenon is proved by the polarized-light microscope observation that there are many spherules which have same extinction contour and pleochroism with stage rotation especially on the face parallel to the magnetic direction as shown in Fig.2. And the molecular arrangement of the spherules remains that of the new type ones in a magnetic field up to 12K gauss.

When APF is used, the new type mesophase spherules are also formed in the pitch at a field strength less than 2K gauss, but the Brooks-Taylor type spherules are also found when the field strength is increased above 3K gauss, as shown in Table 1.

As mentioned above, the addition of GPF to the pitch loads to the formation of the new type mesophase spherules irrespective of the field strength applied, while APF produces in the pitch both the Brooks-Taylor type and new type spherules depending on the field strengtn. Among several attempts using carbon blacks, the new type spherules are found only when APF and GPF are employed. Those carbon blacks are always attached to the surface of mesophase spherules regardless of the magnetic field strength. Carbon blacks other than APF and GPF are not attached to the surface of mesophase spherules and do not produce the new type spherules. There is no appreciable difference between APF and GPF with respect to particle size, manufacturing procedure, properties and microstructure. However, those carbon blacks have different influence on the formation process of mesophase spherules in the magnetic field, as is evident in Table 1. It can be considered that carbon blacks such as APF and GPF give a strong effect on the molecular arrangement of mesophase spherules especially by the fine crystal face existing on exterior of these carbon blacks.

It is of paticular interest to know at what stage of mesophase formation the magnetic field influences on the molecular arrangement of mesophase spherules. After new type spherules were formed in the pitch containing APF under the influence of the magnetic field of 2K gauss at 430°C and cooled down to room temperature. The pitch containing the new type spherules were heat treated again in the magnetic field of 8K gauss at 430°C for 30 min. The mesophase spherules obtained by this treatment were also the new type ones. From this fact, the new type mesophase spherules formed once in the pitch cannot be transformed into the Brooks-Taylor type spherules even though the

magnetic field strength [illegible] 3K gauss, this indicates that the field strength is not enough to transform the new type spherules into the Brooks-Taylor type one and that the interaction between APF and mesophase constituent molecules is extremely strong. It can be considered that the molecules in the pitch matrix are aligned parallel to the magnetic field direction when the magnetic field is applied. In this case the magnetic field prevents the molecules surrounding the APF carbon black from being oriented parallel to the APF surface. Therefore the interaction between APF and those molecules is weakened in the presence of the magnetic field and then the Brooks-Taylor type spherules which are more stable than the new type ones are formed.

References

[1] J. D. Brooks and G. H. Taylor, Carbon, 3, 185 (1965)
[2] H. Honda, Y. Yamada, S. Oi and K. Fukuda, 11th Carbon Conference, Extended Abstracts, CG-27 (1973)
[3] Y. Sanada, T. Furuta, H. Kimura and H. Honda, Carbon, 10, 644 (1972)
[4] L. S. Singer and R. T. Lewis, 11th Carbon Conference, Extended Abstracts, CG-33 (1973)

Table 1. Influence of a magnetic field on the molecular arrangement of mesophase spherules.

Strength of magnetic field (K gauss)	APF added	GPF added
0	N.T.	N.T.
1	N.T.	N.T.
2	N.T.	N.T.
3	B-T.T.	N.T.
4	B-T.T.	—
6	B-T.T.	—
8	B-T.T.	N.T
10	—	N.T.
12	—	N.T.

N.T.; New type mesophase spherules
B-T.T.; Brooks-Taylor type mesophase spherules

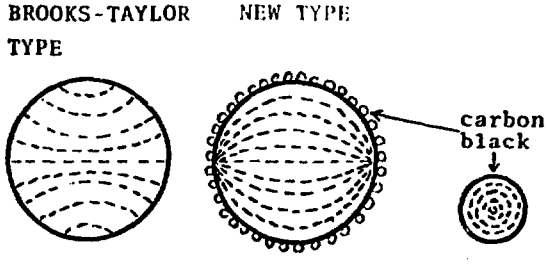


Fig.1. Molecular arrangement of the Brooks-Taylor type mesophase spherules and the new type one

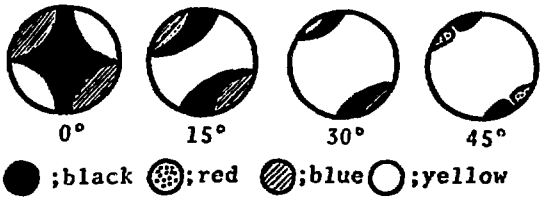


Fig.2. Extinction contour and pleochroism of the new type mesophase spherules with stage rotation (crossed polarizers with a gypsum plate).

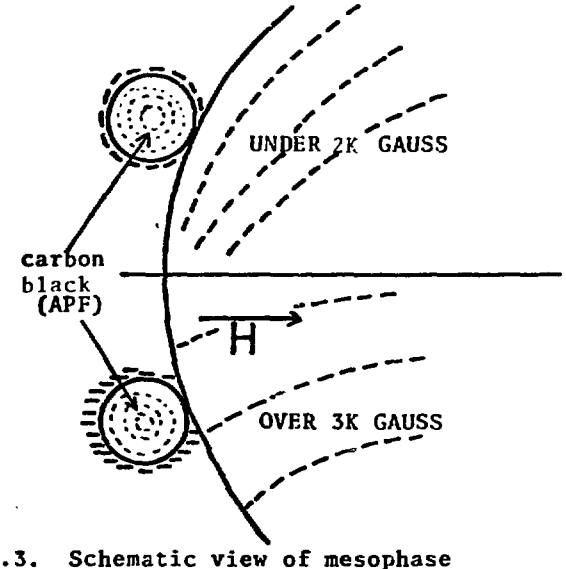


Fig.3. Schematic view of mesophase spherules with carbon blacks(APF) in various magnetic field strengths.

DISCLINATION STRUCTURES IN COKE AND GRAPHITE

J. L. White and J. E. Zimmer
The Ivan A. Getting Laboratories
The Aerospace Corporation
P. O. Box 92957, Los Angeles, California 90009

Introduction

The crystal defects known as rotational disclinations are rare in metals and ceramics because the strong curvatures of a disclinated crystal involve intolerable lattice strains [1, 2]. However, disclinations are common in liquid crystals because the absence of crystalline registry between adjacent parallel molecules allows local displacement and ample relaxation in lattice strain [2]. Disclination structures are prominent features of coke and graphite because a lamellar liquid crystal, the carbonaceous mesophase, forms in the final stages of liquid-phase carbonization [3, 4].

Some basic aspects of disclinations in the carbonaceous mesophase were discussed at the Baden-Baden Conference [5]. The distinctive feature of carbonaceous mesophase is the plate-like aromatic molecule, which serves as the basic building block of the lamellar liquid crystal in contrast to the rod-like molecules of nematic liquid crystals. Four types of line wedge disclinations commonly found in the mesophase as well as coke and graphite are sketched schematically in Fig. 1. The disclinations are topological discontinuities that result from the stacking of layer-molecules to form lamellae which retain some freedom to bend and twist as they trace out a lamelliform or Möbius morphology.

The Formation of Disclination Structures

In the pyrolysis of a graphitizable precursor, the mesophase appears initially as spherules with the morphology first defined by Brooks and Taylor [6]. See Fig. 2. The mesophase layers define doubly curved surfaces (except for the equatorial plane) which intersect the spherical phase boundary at or

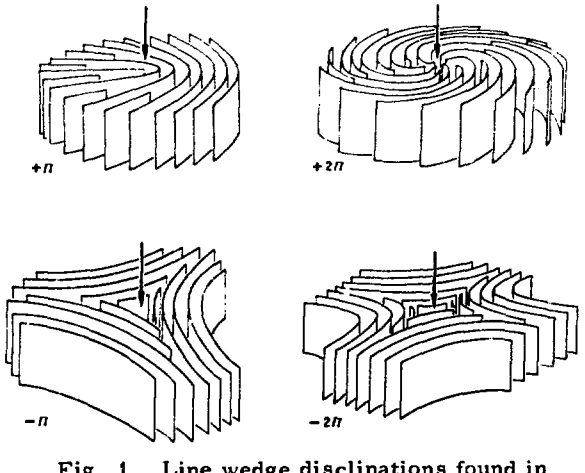


Fig. 1. Line wedge disclinations found in coke and graphite [3, 5]

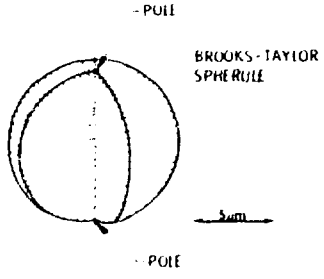


Fig. 2. Layer orientation in mesophase spherule

near 90°. As pyrolysis proceeds, these spherules grow and coalesce to form bulk mesophase with its characteristic lamelliform morphology. The disclinations found in fresh undeformed mesophase are thus complex three-dimensional structures that result from the repeated formation of multiple connections between coalescing spherules.

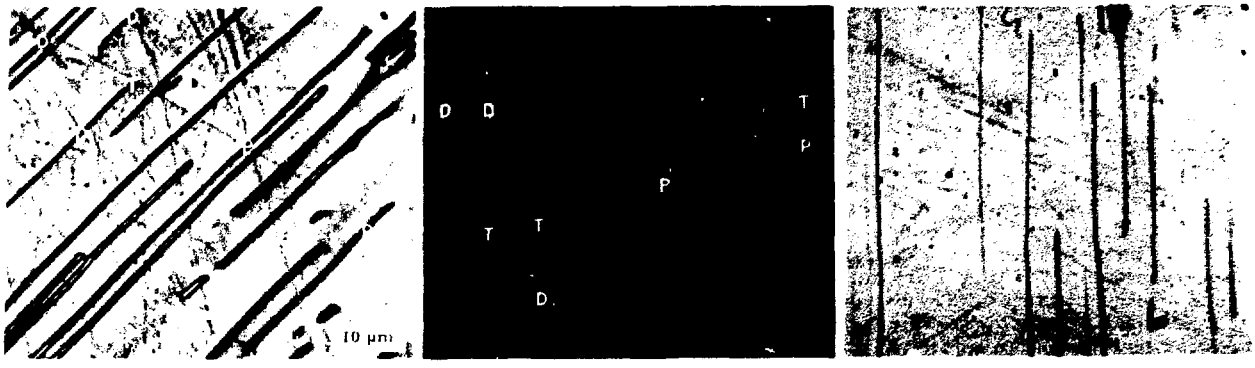
Many mesophases are sufficiently fluid, at least in the early stages after precipitation and coalescence, to be readily deformed by the percolation of gas bubbles or by mechanical deformation [7]. Such deformations produce the fine fibrous or lamellar microconstituents which are the hallmark of the needle cokes. These microconstituents offer good subjects for detailed study of disclination structures because knowledge of the preferred orientation of mesophase lamellae relative to a selected cross-section can markedly simplify interpretation of the polarized-light response on the polished section.

Disclinations in the Lamellar Microconstituent

The disclination structures in the deformed microconstituents generally occur at a scale just resolvable by polarized-light microscopy. The carbonaceous mesophase as well as its heat-treated fossils, coke and graphite, are uniaxial negative crystals demonstrating maximum reflectivities when the line of polarization is parallel to the lamellae and minimum reflectivities when this line is perpendicular to the lamellae [8]. By varying the polarizing conditions, information can be obtained on the details of disclination structure.

The fine lamellar morphology [7] occurs in the walls of bubbles formed by the escape of volatile gases. The lamellar microconstituent in such a bubble wall is illustrated in Fig. 3 for three conditions of polarization: (a) crossed polars, with the lamellae at 45° relative to the line of polarization to obtain maximum contrast; (b) polarizer only, with the line of polarization perpendicular to the lamellae; and (c) polarizer only, with the line of polarization

*This work was supported by the U. S. Air Force under Contract No. F04701-76-C-0077.



(a) Crossed polars (b) Polarizer horizontal (c) Polarizer vertical

Fig. 3. Lamellar microconstituent of a bubble wall in a decant oil pyrolyzed to 500°C

parallel to the lamellae. Inspection of these micrographs will show that some lines of Fig. 3b, marked D, disappear when the polarizer is rotated by 90° and that most of the remaining non-disappearing lines can be resolved as doublets by crossed polarizers.

These observations are consistent with the structure sketched in Fig. 4. Each line of Fig. 3b corresponds to a fold. If the plane of section is nearly parallel with the top of the fold, the line will disappear when the polarizer is parallel to the fold and the line observed by crossed polars will not be resolvable to a doublet. In this case, the fold terminates in a twist disclination (indicated by T in Fig. 3); the disclination core is sketched as a ribbon rather than a line to account for the apparent radii of most folds (of the order of 0.5 micron). If the plane of section intersects the fold at a higher angle, the line will not disappear upon rotation of the polarizer and can usually be resolved to a doublet under crossed polars. In this case, the line is terminated by line wedge disclinations of strength $\pm\pi$ (cf. Fig. 1), and the specific type of wedge disclination can be resolved by noting the direction of movement of an extinction contour when the line of polarization is rotated.

It may be noted that two lines, marked P, of Fig. 3 are partially disappearing, i.e., one segment disappears when the polarizer is rotated while the remaining segments can be resolved to doublets under crossed polars. This response implies that the rotation vector of the fold varies, i.e., the edge of the fold is not straight but curved with only a limited segment running nearly parallel to the plane of section. Thus the double curvature of mesophase layers, which may be regarded as normal for coarse undeformed mesophase, can be retained to some degree in highly deformed microconstituents. From the viewpoint of graphitizability, the process of dewrinkling such doubly curved layers to attain graphitic interlayer registry must necessarily involve mass transfer by diffusion within the layers.

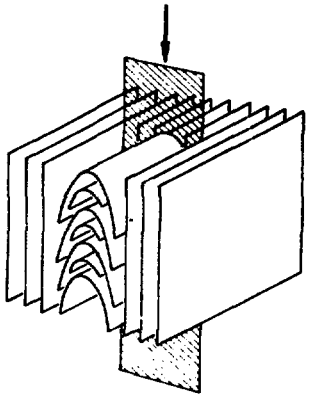


Fig. 4. Twist disclination of rotation π normal to disclination line

Acknowledgments

The authors thank M. Buechler and F. J. Turnbow for their experimental work and acknowledge the assistance of Ashland Oil, Inc., and the Union Oil Company of California in supplying precursor materials.

References

[1] W. F. Harris, Surface and Defect Props. of Solids, 3, 57 (1974).

[2] F. R. N. Nabarro, Theory of Crystal Dislocations, Clarendon Press, Oxford, 120-7 (1967).

[3] J. L. White and J. E. Zimmer, Surface and Defect Props. of Solids, 5, 16 (1976).

[4] J. L. White, Prog. Solid State Chem., 9, 59 (1975).

[5] J. L. White and J. E. Zimmer, CARBON '76 Preprints, 197 (1976).

[6] J. D. Brooks and G. H. Taylor, Carbon, 3, 185 (1965).

[7] J. L. White, in Petroleum-Derived Carbons, Eds. T. M. O'Grady and M. I. Deviney, Am. Chem. Soc. 282 (1976).

[8] C. Cornford and H. Marsh, CARBON '76 Preprints, 223 (1976).

STRUCTURAL CHARACTERIZATION OF FINE MORPHOLOGY IN CARBON USING HIGH RESOLUTION ELECTRON MICROSCOPY

H. Marsh and D. Crawford
Northern Carbon Research Laboratories, School of Chemistry,
University of Newcastle upon Tyne, Newcastle upon Tyne NE1 7RU, U.K.

Introduction

In 1973, the above Laboratories were offered financial support from the Science Research Council to advance our theoretical and practical experience in the use of phase contrast, high resolution electron microscopy in which the constituent lamellar molecules of carbon are projected as lines or fringes on to the screen of the microscope, a technique which owes much to Ban (Ref. 1). When studying graphitic materials, there appears to be less of a problem with interpretation as parallel fringes, extending over considerable distances, can be focussed onto the screen. It is with isotropic carbons and anisotropic carbons of HTT ~1500 K, that problems of interpretation arise. The detail of the relative positions of short, non-linear fringes appears to be (at least) a function of focal position adopted during imaging, of specimen thickness and of extent of exposure of the carbon specimen to the electron beam. This investigation is now complete and consists of an appraisal of semi-theoretical aspects and several structural analyses of carbonizations and graphitisation which form part of the overall studies of the Laboratories. The following is a summary of the essential findings.

The Technique of Phase-Contrast Electron Microscopy

The potential benefits of defocus phase-contrast electron microscopy in terms of elucidation of structural detail are such that no other technique can seriously be considered. However, the attendant contrast-transfer difficulties inherent in this type of work appear to be prohibitive in terms of the extraction of realistic information (Ref. 2, 3). Hence, the major problem is whether or not it is possible to arrive at a working compromise of using an optimum contrast transfer window which does not exclude relevant information. The approach to the problem is one of establishing an acceptable experimental basis for microscopy as distinct to the complementary theoretical analyses (Ref. 3).

For phase objects, purely geometrical considerations alone, in demanding a minimal phase difference between waves scattered from the top and bottom of the specimen (Ref. 4) give a thickness limitation requiring $t \ll 25$ nm for a resolution of d=0.3 nm. More exacting requirements are evident in the weak-phase approximation. Values of $t < 15$ nm for disordered carbons and $t < 7.5$ nm for crystalline carbons probably represent upper limits. For disordered carbons, a complicated super-imposition of image detail could well prove the ultimate limitation to specimen thickness. Generally, for carbons, the sample should preferably be as thin as is consistent with the probable microstructure.

For the JEOL 100C TEM, a specification of the spherical aberration constant of 1.4 mm, i.e. C_s (this parameter defines the contrast transfer properties of the microscope and hence the efficiency of imaging) is inadequate for the range of lattice spacings in the range 0.30 to 1.0 nm of importance in disordered carbons.

Hence, because detail within this range cannot be imaged in a consistent manner an optical working situation requires the choice of the most suitable defocus position. This can only be done by observing an image on the microscope viewing screen and hence decisions based on the visibility of detail would seem to be reasonable. It is considered that at a defocus position (Δf) of -90 nm the range of reasonable imaging is for lattice spacings (d) of 0.34 to 1.5 nm. A dip in intensity occurs at d = 0.46 nm. At a defocus position of -130 nm the range of imaging is for lattice spacings of 0.3 to 0.56 nm which covers the graphite basal-plane spacing of 0.335 nm. However, there is an information gap in the range d = 0.56 to 0.72 nm and information in the range d = 0.31 to 0.56 nm is presented with reversed (negative) contrast. It is concluded that the near-Scherzer optimum underfocus of Δf = -90 nm should be used wherever possible for all carbon imaging when a disordered component is apparent. It is considered that at Δf = -90 nm typical images of large carbon crystallites, small carbon crystallites and systems of defective graphitic sheets indicate that a sensible direct interpretation (in terms of a projected charge-density distribution) is possible for thin samples of carbon. With a Δf of -130 nm, fringe-contrast is reversed within crystallites so presenting difficulties in measuring the crystallite width for microcrystalline carbon. Also for disordered carbons the transfer gap operating at this level of defocus induces loss of information vital to the characterization of microstructure and overestimates of the degree of crystallinity.

The Elucidation of Structure in Carbon

Catalytic Graphitization of Carbons: Chemical catalysis of graphitization carried out under vacuum in an Fe-doped polyfurfuryl alcohol carbon results in the formation of relatively well-developed turbostratic-graphite sheets at unusually low temperatures (873 K). Without catalysis, temperatures in excess of 2000 K would normally be required to initiate the ordering necessary in the production of similarly 'developed' material (Ref. 5).

Voids in Carbons and Graphites: It is concluded that optimum-defocus images represent the only means of obtaining information concerning void character-

istics in disordered carbons . The voids, as observed, can be classified in terms of structural classifications. Primary voids are formed by deviations from a favoured interlayer or intermolecular spacing. Secondary voids are formed by morphological aspects of crystallites and associations of crystallites. For example, sharp-edged space can be created bounded by intact graphitic sheets. Needle-shaped primary voids, 0.4 nm width and 1 to 3 nm in length often occur with non-twinned tilt boundaries, twist boundaries etc. relieving induced crystallographic stress. In three-dimensions the void is more likely to be "penny-shaped". Other types of void which have been imaged include tapered, isometric, constricted, inter-connecting, bottle-shaped, closed-ended, slit and wedge shapes. Essentially, the void character is closely dependent upon the crystallographic structure of the carbon or graphite.

Heat-treatment of Graphitizing Carbons: Changes have been examined in anisotropic carbon from its formation following coalescence of the mesophase (HTT 750 K) to anisotropic cokes (HTT 1148 K) Orgreave lean coal-tar forms mesophase, at 750 K, composed of stacked lamellar molecules about 1.2 nm in length but with smaller molecules present between the orientated molecules and misorientated with respect to the major axis of preferred orientation. At HTT 945 K these smaller molecules interlink with the larger ones causing disruptions within locally pre-orientated material. A strained structure is created within the semi-coke which now contains micro-inclusions of inhomogeneous material, 2.0 nm in size, and also grains about 20 nm in diameter. Further heat-treatment initiates the annealing of the strain so increasing molecular size, planarity and local preferred orientation. (Ref. 6).

In a study of a graphitizing carbon from polyvinyl chloride the preferred stacking of basal planes (HTT 923 K) confirms the model of equatorial stacking of molecules predicted from optical microscopy and electron diffraction. Secondary structure of crystallites from the lamellar molecules developed at an HTT of 1373 K being completed at 1573 K. An ordering into strips or sheets of material is initiated at 1773 K and develops continuously to 2273 K when they can be 20 nm in width and may extend for distances greater than 400 nm in the L_a direction. They are composed of closely-linked micro-crystallites. Three-dimensional ordering appears at 2273 K and at 2673 K the micro-crystallites have now formed a single large crystallite with dimensions of the strips. These strips are linked by narrow, long crystals of carbon or by a disordered, three-dimensional array of basal planes. This linking matrix re-crystallizes at temperatures of about 2673 K. Voids appear between the crystallites.

Beam Sensitivity of Graphitizable Carbons: Samples of low HTT (<1000 K) are sensitive to the electron beam. The (002) diffraction peak loses form and becomesdiffuse as a result of thermal and irradiation damage. This is marked for a sample of coke (HTT 750 K), the damage being less critical in cokes of HTT 945 K. Damage can be reduced by using lower magnifications for as long as possible, and prefocussing the objective lens so reducing exposure times to less than 10 seconds.

Heat-treatment of Non-graphitizing Carbons: Polyvinylidene chloride carbon (HTT 1073 K) is characterized by a mean apparent layer length of 1.1 nm and an apparent spacing of 0.68 nm. In the temperature range 1073 to 1973 K a growth of deformed inter-twining graphitic layers occurs to establish a ribbon model. The growth of turbostratic crystallites at $H^2T \geq 1973$ K and the progression to a thin-walled, isotropic three-dimensional closed foam-structure is now postulated. These structural changes explain the complexity of the mechanism of loss of porosity and surface area (>1000 m^2g^{-1}) in these PVDC carbons, by heat treatment (Ref. 7, 8, 9).

References

1. Ban L.L., "Surface and Defect Properties of Solids", Chem. Soc. London, 1, pp. 54-94 (1972).
2. Millward G.R. and Thomas J.M., Proc. 4th Conf. Ind. Carbon and Graphites S.C.I. London, pp. 492-497 (1976)
3. Jefferson D.A., Millward G.R. and Thomas J.M., Act. Cryst. A32, pp. 823-828 (1976).
4. Hanszen K.J., Advances in Optical and Electron Microscopy 4, 1 (1971).
5. Crawford D., Marsh H. and Taylor D.W., Carbon '76, Deutsche Keramische Gesellschaft, pp. 243-6 (1976).
6. Crawford D. and Marsh H., Carbon '76, Deutsche Keramische Gesellschaft, pp. 231-4 (1976).
7. Ban L.L., Crawford D. and Marsh H., J. Appl. Cryst. 8, 415 (1975).
8. Oberlin A., et al., Tanso, No. 80, p. 29 (1975).
9. Marsh H. and Wynne-Jones W.F.K., Carbon, 1, 269 (1964).

Acknowledgements

We express our appreciation to the Science Research Council for financial support.

A PHASE-CONTRAST ELECTRON MICROSCOPE AND OPTICAL MICROSCOPE STUDY OF ANISOTROPIC CARBONS OF DIFFERENT OPTICAL TEXTURE

R.A. Forrest, Maggi French, H. Marsh, J.A. Griffiths and J.L. White*
Northern Carbon Research Laboratories, School of Chemistry,
University of Newcastle upon Tyne, Newcastle upon Tyne NE1 7RU, U.K.
*The Aerospace Corporation, P.O. Box 92957, Los Angeles, California.

Introduction

It is an interesting aspect of formation of synthetic graphites that their structure is closely dependent upon the chemical composition of the parent pitch substance and the conditions of carbonization. Graphites with a wide range of physical properties can thus be fabricated, possessing optical textures ranging from large domains of needle-cokes to the small fine mozaics (<5 μm) of the so-called isotropic graphites. Metallurgical and foundry cokes contain anisotropic components, usually mozaic (<1 μm) and some flow-type (Ref. 1). Those differences, chemical, structural or physical, in the formation of nematic liquid crystals and the properties of subsequent mesophase, which influence the size and coalescence behaviour of mesophase require further investigation. Once the mesophase is recognizable it is not susceptible to chemical analysis (being an aromatic polymeric substance) and structural analyses may be more rewarding. Two experimental approaches have therefore been adopted, i.e. quantitative reflectance microscopy and phase-contrast electron microscopy to image molecular constituents.

The Experimental Approach

Carbons have been prepared from A200 Ashland petroleum pitch, DIJ2 coal-extract, Orgreave coal-tar pitch, Gilsonite pitch and polyvinyl chloride by carbonizing at 5 K min^{-1} to 1100 K under nitrogen, and then under argon to 1300, 1500, 1700, 2000 and 2300 K. Resultant carbons were mounted in resin and polished surfaces prepared. Carbons from the petroleum and coal-tar pitch possessed optical textures of isochromatic domains, with the carbons from the DIJ2 coal-extract possessing large mozaics (10 μm) and from the Gilsonite pitch small mozaics (<5 μm). There was, accordingly, available a series of carbons, of increasing size of optical texture, prepared by identical methods.

Quantitative reflectance microscopy: The percentage of light (of given wavelength) reflected from polished surfaces of carbon is a function of the refractive index 'n', density, and the orientation, size and perfection of the constituent anisotropic units or molecules. Cornford and Marsh (Ref. 2) discuss the use of quantitative reflection measurements from surfaces of carbons. This method may therefore be capable of distinguishing aspects of lamellar molecular composition and perfection of stacking within the carbons of different optical textures.

High-resolution electron microscopy: This technique is capable of resolving the lamellar structure of these carbons by fringe-imaging. The magnification involved are so high and the sample examined so small that a criticism of the method is that a non-representative portion of the sample may have been examined. To overcome this criticism, use is made of a micro-manipulator whereby a micro-cutting tool is operated in conjunction with an optical microscope and carbon from a characterized region of the optical texture is removed for microscopic investigation, using a JEOL 100C electron microscope.

Objectives

The overall purpose of this study is to further our understanding of these factors which influence the viscosity of the mesophase. This is because viscosity influences the ability of the mesophase to coalesce (formation of disclinations) or to form small mozaics without coalescence (unless restricted to boundary situations), the mozaics being fused growth units of mesophase. In the carbons of higher HTT it may be possible to image some of the disclinations predicted by White and Zimmer (Ref. 3) from analyses of optical micrographs.

Differences in viscosity may be associated with chemical bonding between (across) the lamellar molecules, or to non-lamellar molecules. Direct imaging of the molecules and a reflectance analysis should give relevant information. An analysis of X-ray diffraction studies of Mochida et al. (Ref. 4) indicates no close correlation of $C_o(002)$, $L_c(002)$ with size of optical texture.

Discussion

In quantitative reflectivity studies, interest is with maximum and minimum reflectivities from selected areas of the surface. Using both air and oil objectives one is then in a position to calculate other optical parameters such as bireflectance and absorptive index. To obtain the maximum reflectivities one has to scan the specimen diligently. Maximum reflectivities occur either from basal plane surfaces (these are essentially isotropic, exhibiting no minimum on rotation of the specimen stage of the microscope) or when the polarized light is parallel to the basal planes (rotation through 90° will then reveal the minimum reflectivity).

It is found that maximum reflectivites in air continue to rise with increasing HTT to about 1500 K. The reflectivity from the A200 Ashland petroleum cokes appears to level off with HTT at about 30-31%. The reflectivity of cokes from DIJ2 coal-extract is still rising at 33.5% (HTT 2000 K), with the Gilsonite cokes showing reflectivities which fall from about 33% (HTT 1500 K) to about 28% (HTT 2000 K). The reflectivities of carbons from polyvinylchloride (PVC) also show this maximum. This maximum may have several origins. It could be due to the development of micro-fizzures whereby the amount of carbon under the spot of light of the reflectance

microscope diminishes as the micro-cracks widen. A second explanation is that, at a certain stage of the graphitization process, the lamellar constituent molecules become strained and deformed by cross-linkage and bond-shortening mechanisms. This zig-zag structure of molecules has actually been recognized in phase-contrast fringe-imaging in the electron microscope (Ref. 5). A third explanation is that an adsorption edge is moving into the cokes of increasing HTT and reflectivities will be modified by significant changes in electronic absorption processes within the lattice of the graphite. A fourth explanation is essentially an experimental artefact , namely that some form of preferential alignment is occurring in the resin blocks so that true maximum values are not being located.

However, on the evidence so far available it would appear that reflectivities from polished surfaces of carbons are not closely dependent upon the optical texture. This implies that optical texture is essentially a macro phenomenon and that the structure of individual constituent lamellar molecules is a function of the chemistry of pyrolysis and growth of the lamellae with its inclusion of heteroatoms, single and multiple vacancies etc.

The high-resolution electron micrographs show the transition from the small lamellae, approximately in parallel stacking and characteristic perhaps of structure in mesophase, to the graphitic crystallites of the samples of highest HTT. The detail can best be assessed by inspection of the many available micrographs which will be available at the Conference.

References

1. Patrick J.W., Reynolds M.J. and Shaw F.H., Fuel, London, 52, 198 (1973).
2. Cornford C. and Marsh H., Carbon '76. Deutsche Keramische Gesellschaft, pp. 298-301 (1976).
3. White J.L. and Zimmer J.E., "Surface and Defect Properties of Solids," Chem. Soc. London, 5, pp. 16-35 (1976).
4. Mochida et al., Fuel, London, 56, pp. 49-56 (1977).
5. Marsh H. and Crawford D. Unpublished results.

Acknowledgement

We express our appreciation to the European Coal and Steel Community for financial support.

STRUCTURE OF COKE FORMED DURING THERMAL HYDROCRACKING OF ATHABASCA BITUMEN

B.N. Nandi, K. Belinko and J.M. Denis
Energy Research Laboratories, Dept. of Energy, Mines and Resources
555 Booth Street, Ottawa, Canada, K1A 0G1

Introduction

Coke formation during thermal hydrocracking of bitumen from the tar sands reduces the yield of useable distillate fuels and is one of the principal causes of fouling of the reactor during the cracking process (1). The chemical complexity of the feed stocks has made difficult any attempts to relate the physical character of the coke to the various classes of compounds present.

The use of working definitions of coke, such as benzene-insolubles (2), tend to be somewhat misleading. A significant portion of the benzene-insoluble residue produced during thermal hydrocracking of Athabasca bitumen has been found to be soluble in a stronger solvent such as quinoline (3). The implication is that this "coke" may perhaps be more accurately termed a coke precursor.

This paper offers microscopic evidence to support the formation of at least two distinctly different coke structures during thermal hydrocracking of bitumen. These cokes will be shown to form independently of each other and to correspond to specific fractions of the bitumen.

Experimental

Athabasca bitumen used in these studies was supplied by Great Canadian Oil Sands of Fort McMurray Alberta. Deasphalting of the heavy oil product obtained from thermal hydrocracking of the bitumen was carried out according to the ASTM method (forty volumes of pentane to one volume of oil (4)). The deasphalted heavy oil was subsequently distilled under vacuum (40 mm Hg) at 260°C.

Carbonization of asphaltenes and deasphalted heavy oils was carried out under a controlled rate of heating. The sample was placed in a horizontal quartz tube (15 mm dia. and 50 cm length) in a Kanthal-wound tube furnace which was heated at 10°C/min. The tube was initially evacuated and then filled with argon at atmospheric pressure.

Carbonization experiments involving deasphalted heavy oils with addition of sulphur were carried out in a vertical tube furnace. The mixture of DHO and sulphur was poured into a platinum crucible and inserted in the furnace at 400°C. The temperature in the furnace was then gradually raised to 550°C at 10° C/min. This procedure was adopted to minimize loss of sulphur during heating.

Samples for petrographic examination were prepared by embedding the cokes in lucite plastic and polishing the surface. A Leitz reflected light microscope was used to examine the optical structures of the coke.

Results and Discussion

Typical examples of the structure of the coke formed during thermal hydrocracking of Athabasca bitumen are shown in Figures 1 and 2. This coke was collected from the outer surface of the thermocouple sheath in the reactor subsequent to a 21-day run carried out at 460°C and 13.89 MPa (5). Two distinctly different coke structures are discernable in these photographs; a grain mosaic type and a flow type. The presence of spherical agglomerates of a grain type coke within the matrix of the flow type coke is observed in Figure 2.

In order to identify the origin of these cokes, asphaltenes and deasphalted heavy oils (DHO) from hydrocracked Athabasca bitumen were individually carbonized under conditions described in the Experimental section. The residue from carbonization of the vacuum distillation bottoms of the deasphalted heavy oils showed a characteristic flow-type anisotropic coke structure (6), Figure 3. On the other hand, carbonization of the asphaltenes at 350°C resulted in a fine-medium grain-mosaic coke structure, Figure 4. On further heating to 450°C a gradual transition to a coarse grain mosaic structure occurred, Figure 5. Carbonization experiments at higher temperatures (up to 1000°C) failed to alter the coarse mosaic structure of the "asphaltene coke" to a flow-type structure.

Based on these findings, it is evident from Figure 1 that the formation of "asphaltene-coke" on the thermocouple wall preceeded the deposition of coke formed from the heavy oil. This observation is consistent with the fact that the asphaltenes polymerize more readily than the oil fractions, and tend to precipitate out of the bitumen first because of the increase in molecular weight.

In a recent publication (7) it was reported that laminar stacking of asphaltenes occurred on inert particles present in the feed stock (e.g., coal) within the liquid phase of the reactor. It is possible that these spherical agglomerates are incorporated into the matrix of the coke formed on the surface of the thermocouple sheath as shown in Figure 2.

To explain the differences in coke structure resulting from carbonization of asphaltenes and deasphalted heavy oils, a series of experiments using elemental sulphur was carried out. The presence of sulphur is expected to induce cross-linkage between the heavy oil molecules (8,9) and may therefore alter the flow-type coke structure obtained from carbonization of the heavy aromatic oils.

Various quantities of sulphur were mixed with the DHO and the mixtures heated with stirring for several minutes to ensure proper homogeneity. The mixtures were then carbonized under conditions described in the Experimental section. The resulting coke structures are shown in Figures 6-9 for 5%, 7.5%, 10.2% and 20.5% sulphur, respectively. A progression from flow-type (Figure 6) to coarse-grain (Figures 7 and 8) and finally to fine-grain (Figure 9)

was apparent with increasing sulphur content in the DHO. The presence of sulphur would appear to have therefore induced cross-linkage in the heavy oil fraction during carbonization.

The addition of sulphur to samples of asphaltenes and subsequent carbonization at about 500°C resulted in a fine grain mosaic-coke structure, Figure 10. Comparing this micrograph with Figure 3 suggests that the presence of sulphur increased the extent of cross-linkage in the "asphaltene-coke".

The implication of these findings is that the difference in structure between the "asphaltene-coke" and "heavy oil-coke" arises primarily from the extent of cross-linkage between molecules during the carbonization stage. It seems likely from the results reported that the asphaltenes contain certain functional groups and aromatic structures which result in cross-linkages during carbonization, whereas the heavy oils contain fewer such groups.

Speight (10) investigated the oxygen functional groups in bitumen by infrared spectroscopy and concluded that the majority of the oxygen in the asphaltene fraction existed as hydroxyl groups (mainly phenolic), while the majority of the oxygen within the heavy oils occurred as carbonyl groups (primarily as esters (11)). The pyrolysis of phenolic compounds has been shown to induce cross-linkage (12-14). Carbonyl functional groups may, on the other hand, tend to split off as carbon monoxide or carbon dioxide under hydrocracking conditions, thereby leaving a free radical that is quickly stabilized by reaction with hydrogen before a cross-link can be formed.

Conclusions

The differences in the coking properties of the asphaltenes and the heavy aromatic oils of hydrocracked bitumen may be attributed to the extent of cross-linkage formed during carbonization. Asphaltenes give a fine mosaic grain structure on coking which transforms to a coarse grain structure as the coking temperature is increased. Deasphalted heavy oils on the other hand, give a flow-type structure on carbonization. The flow-type structure obtained from the deasphalted heavy oils could be transformed to a grain-type structure by inducing cross-linkages by addition of sulphur prior to carbonization.

References

1. Pruden, B.B., Logie, R.B., Denis, J.M. and Merrill, W.H. Research report ERP/ERL 76-73 (OP), Fuels Research Laboratory, Dept. of Energy, Mines and Resources, Canada; 1976.
2. Speight, J.G. Fuel 49, 134; 1970.
3. Belinko, K. and Nandi, B.N. (unpublished results).
4. American Society for Testing Material, Part 15, D-20 42; 1975.
5. CANMET (Canada Centre for Mineral and Energy Tech.) Process Engineering Section, Dept. of Energy, Mines and Resources, Ottawa, Canada. (Run No. 71-1-2)
6. Patrick, J.W., Reynolds, M.J. and Shaw, F.H. Fuel 52, 198; 1973.
7. Nandi, B.N., Belinko, K. and Denis, J.M. The distribution of coke precursors in the reactor during thermal hydrocracking of bitumen; to be presented at the Canada/Venezeula Oil Sands Symposium, Edmonton, Alberta, May 1977.
8. Kipling, J.J., Sherwood, J.N., Shooter, P.V. and Thomson, N.R. Carbon 1, 315; 1964.
9. Kipling, J.J. and Shooter, P.V. Carbon 4, 1; 1966
10. Moschopedis, S.E., Fryer, J.F. and Speight, J.G. Fuel 55, 184; 1976.
11. Moschopedis, S.E. and Speight, J.G. Fuel 55, 187; 1976.
12. Cypres, R. and Bettens, B. Tetrahedron 30, 1253; 1974.
13. Cypres, R. and Bettens, B. Tetrahedron 31, 359; 1975.
14. Ouchi, K. Carbon 4, 59; 1966.

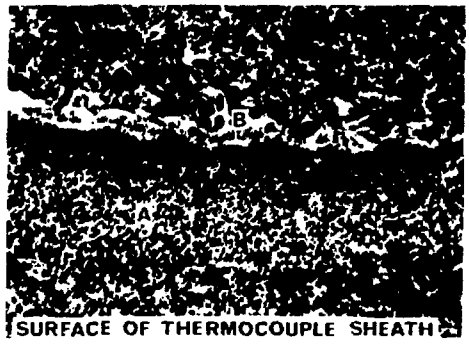


FIGURE 1 - Coke collected from the thermal hydrocracker; A-grain-mosaic; B-flow-type



FIGURE 2 - Same as Figure 1; continuation of upper part (B) of previous figure



FIGURE 3 - Coke formed from DHO carbonized at 500°C

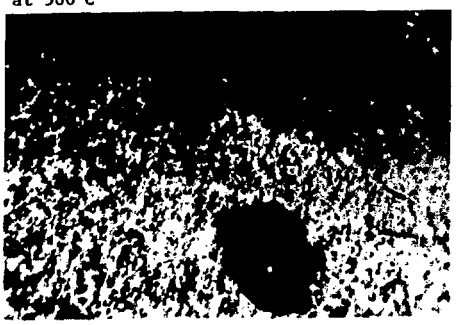


FIGURE 4 - Initial stages of coke formation from asphaltenes at 350°C; upper part-fine grain; lower part-medium grain

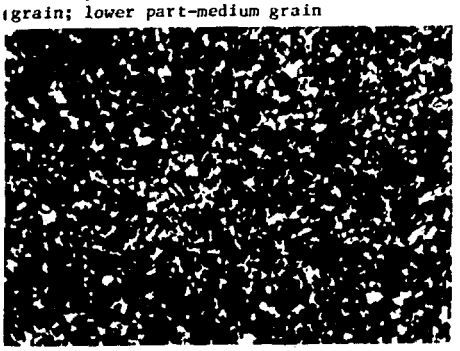


FIGURE 5 - Coke formed from asphaltenes carbonized at 450°C; coarse-grain

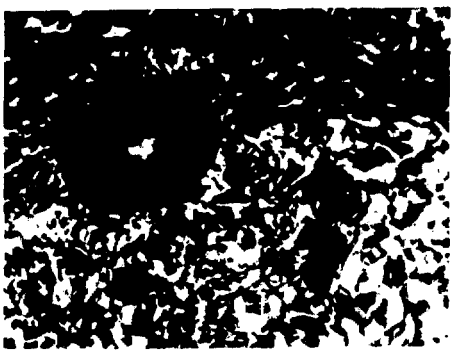


FIGURE 6 - Coke formed from DHO and 5.0% sulphur

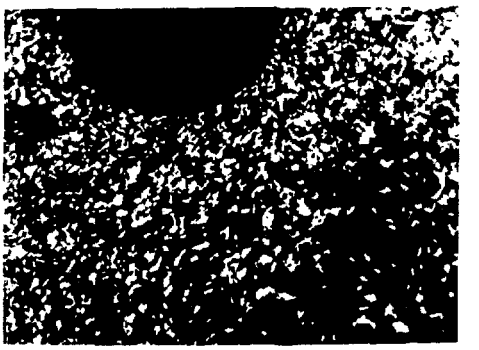


FIGURE 7 - Coke formed from DHO and 7.5% sulphur

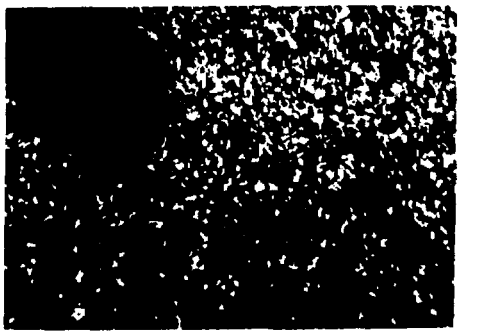


FIGURE 8 - Coke formed from DHO and 10.2% sulphur

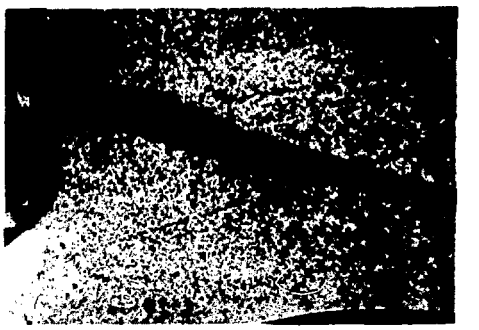


FIGURE 9 - Coke formed from DHO and 20.5% sulphur



FIGURE 10 - Coke formed from asphaltenes at 5% sulphur; fine-grain structure

CARBON MICROSTRUCTURAL DEVELOPMENT AT HIGH PRESSURES

W. Chard and H. Keck*
Battelle Columbus Laboratories

* Maj. Keck was formerly associated with the Air Force at AFML

Introduction

In recent years there has been a continually increasing interest in the effect of pressure on the chemistry and kinetics of various organic compounds during pyrolysis and carbonization (1,2,3). Corresponding interest in the development and formation of mesophase carbon from various organic compounds has also been reported(4,5,6). The formation of mesophase has been shown to be a key process in the transformation or organic liquids to graphitizeable carbon. The importance of heating rate, composition, and pressure in the development of mesophase has been demonstrated but a real understanding of methods for controlling and maintaining this phase have not yet been developed. Pressure has been shown to have a pronounced effect on carbonization mechaniams but the lack of control or lack of understanding of how to control the mesophase development under pressure has lead to only small scale laboratory experiments relating to these effects.

Experiments to-date have not emphasized the relationship between carbonization effects and pressure methods. These techniques have included conventional hot pressing in heated dies, low pressure (less than 1000 psi) standard gas autoclaving and high pressures gas processing (greater than 10,000 psi). The behavior of any organic compound during carbonization will be dependent on the method in which pressure is applied. The carbon yield will be effected by the specific technique used but more importantly, the microstructural development of the carbon during decomposition of the organic compound will be significantly affected. The extent of mesophase coalescence and gas-phase bubble perculation and related carbon mosphology are dependent on the specific pressurization method and not merely the pressure at which carbonization has been performed.

Pressure Processing Description

Within the past ten years the hot isostatic pressing (HIP) process has been developed into an efficient fabrication technique for producing unique powder metallurgy components and more recently in densifying high performance 3D carbon-carbon composites for strategic missile nose tip and rocket nozzle throat applications(7,8). The process developed to densify and carbonize porous woven carbon fiber preforms has been identified as high pressure impregnation/carbonization (HiPIC). The process essentially involves the carbonization of liquid pitch impregnated preforms at temperature of 650 C and pressures of 15,000 psi in sealed steel containers. The typical carbonization cycle is illustrated in Figure 1. Performing the pyrolysis and carbonization in vacuum sealed metal cans significantly retards the buble nucleation characteristics of the gaseous decomposition products and reduces the coalescing tendencies of the mesophase. The solubility of gaseous decomposition products is significantly increased and the kinetics of carbonization are retarded. The microstructural development of the carbon solid is therefore directly related to the sequences which occur within the processing containers and the ability of the container to remain sealed.

Experiments at Battelle Columbus Laboratories identified that a significant increase in temperature occurs within 15-inch diameter by 20-inch long processing containers when the cans fail to remain sealed during carbonization(9). Temperatures within these pitch-filled containers raised from approximately 520 C to over 800 C in several minutes time while carbonizing at 15,000 psi. This "exotherm" effect is apparently due to either increased heats of reaction within the pitch liquid after the container failed due to pressure build-up from decomposition gases or to an actual exoterm which occurred as the result of carbonization which caused a large gaseous decomposition effect which in turn caused the container to fail. It is proposed that the "exotherm" was caused by the failure of the container which in turn increased the decomposition and carbonization reactions in the pressurized pitch. The microstructural development of the carbon solid from the liquid pitch will be dependent on the type of processing container, open or sealed can, and the pressure and temperature parameters during carbonization in the 400 to 600 C range.

The carbonization of pitch impregnants while at pressures of 15,000 psi has produced a high density, fine porosity carbon not attainable by conventional techniques. Other advantages include (1) over 90 weight percent carbon (coke) yields from coal tar pitch, (2) short processing cycle times in attaining high density carbon (graphite) materials, and (3) refined microstructured carbons (graphites). The process is still being developed and little fundamental research work has been performed in udnerstanding the chemistry and kinetics which are occurring.

Discussions of Results

The microstructure, and properties, of carbon-carbon composites and bulk graphites are dependent on the specific methods used in carbonizing organic precursors. The ability of a process to control and reduce mesophase coalescence is dependent upon reducing bubble nucleation and gaseous decomposition products in a liquid organic during carbonization. Not only can a unique fine-grained isotropic carbon (graphite) be produced if this condition is controlled but a fine pore structure, homogeneous bulk solid is produced. Process economicc or processing time may alao be significantly improved. Numerous

unique microstructural carbons (graphites) have been observed during the development of the HIPIC process.

Highly graphitizeable carbons have been produced utilizing HIPIC processing of coal tar pitch materials. Coke yields always exceed 90 weight percent and the microstructural character of the carbon (graphite) solid is dependent on certain conditions during processing such as when can failure time, impregnant composition, carbonization pressure and the presence of substrate surfaces. The characteristics of the excess coke (carbon) surrounding the C/C materials is different than the microstructure of the carbon within the fiber preform at the pore interstices. The fiber surfaces appear to modify the nucleating characteristics of the carbon but the extent to which this can be controlled is not known. The microstructural characteristics of carbon formed outside of the fiber preforms is illustrated in Figure 2. Although both the fine-grained and coarser structures possess the same bulk porosity, the inherent microstructure is considerably different. The difference in microstructure is caused by the time at which the container fails and thermal fluctions within the cane. Some of the most interesting microstructures have been observed in large pores within the coke mass surrounding the preforms. suspended mesophase concentrations have been observed along one side of numerous pores, as illustrated in Figures 3 and 4, while adjacent areas show mesophase coalescing into a solid surface structure. The use of higher carbonization pressures may develop a more stable mesophase microstructure by eliminating or retarding can failure and maintaining mesophase stability without coalescence through the liquid/solid carbonization range. The hot isostatic carbonization of organic precursors does allow for unique control of carbon microstructures and products in large production size capabilities. Further development of this process is expected to produce unique carbon-bar materials of unusual quality.

References

(1) Wang, P. W., High Temperature-High Pressures, 6, (1974), pp 127-136

(2) Marsh, H., Carbon, 9, (1971), pp 159-177.

(3) Fitzer, E. and Teswiesch, B., Carbon 11, (1973), pp 570-574.

(4) Huttinger, K. and Rosenblatt, V., 4B London Conf. Carbon, (1974).

(5) White, J. and Price, R., Carbon 12, (1974), pp 321-334.

(6) Restor, D., 12th Carbon Conf., (1975).

(7) Stover, F., AFML-TR-69-67, Vol. III, (1970).

(8) Chard, W. and Levin, A., 12th Carbon Conf., (1975).

(9) Chard, W., First High-Pressure Carbonization Workshop, (1975).

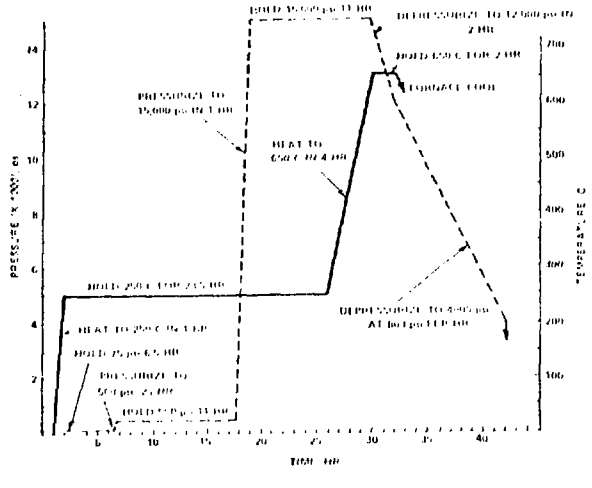


FIG. 1. HIPIC PROCESSING CYCLE

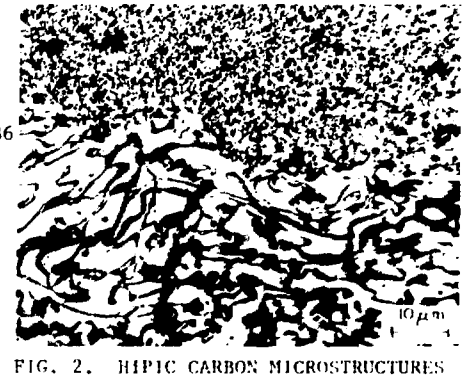


FIG. 2. HIPIC CARBON MICROSTRUCTURES

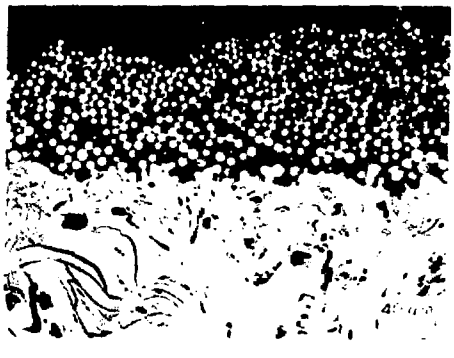


FIG. 3. HIPIC MESOPHASE DEVELOPMENT

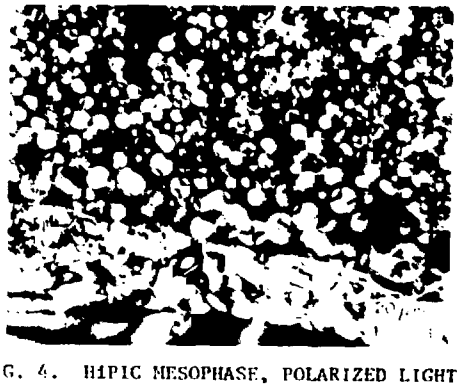


FIG. 4. HIPIC MESOPHASE, POLARIZED LIGHT

THERMAL AND ELECTRICAL PROPERTIES OF PETROLEUM COKES

E. G. Morris and J. M. Faircloth
Great Lakes Research Corporation
Elizabethton, Tennessee 37643

The overall coefficient of heat transfer of several fractions of sized petroleum coke particles was measured at different temperatures under a static pressure of 3.0 PSI. The temperature gradient across 2.5 cm of material was measured during a steady state thermal equilibrium condition. A radial-out-flow device, 9.5 cm ID by 12.0 cm OD, with an electrical resistance heat source was used, and the coefficient of thermal conductivity (k) of the samples was calculated from heat flow measurements using the log-mean temperature difference. Heat balance was maintained axially so that a radial heat flow could be approximated. The resulting calculations ignore convective and radiation losses through the granular matrix. However, for reasonably small temperature gradients at low sample temperatures the k-value provides a quick and quite realistic measurement of the conductive heat loss through a sized granular, insulation barrier. Comparison of these coefficient values between cokes with varying degrees of heat treatment and for different sizes of coke particles allows the proper choice of material for thermal insulation of graphite or other high temperatures furnaces.

The k-values of sized petroleum coke particles in Tyler screen size fractions of -10/20 mesh, -20/35 mesh and -35/60 mesh were studied on a normal calcined coke which was later graphitized to 2500°C. Figure #1 shows the k-values for the calcined coke for average temperatures from 100°C to 600°C. The k-values for the three particle size fractions were remarkably similar. The overall difference was less than 20%.

Figure #2 shows the k-values for the same size fractions after the coke was graphitized to 2500°C. The k-values for the graphitized coke were two to five times higher than for the calcined material. The k-value for any specific particle sizing generally increased from 20% to 50% as the average sample temperature increased from 100°C to 600°C. Since the thermal conductivity of graphite decreases with temperature the measured increase of k-value with temperature is due to the increased significance of convection and radiation modes of heat transfer. The particle sizing had a much greater effect on the k-value of the graphitized coke than the temperature. The similarity of k-values between the different sizes of calcined coke does not exist for the graphitized particles and coarser size fractions have higher k-values.

While the thermal conductivity of an insulation coke material is an important design parameter for high temperature work, the electrical resistivity (ER) is also important due to the current losses through the conductive coke medium when using electrical resistance heating as is currently practiced by manufacturers of carbon and graphite products particularly when processing electrodes in Acheson graphite furnaces. Since the thermal conductivity and ER of a particle matrix are a function of pressure and particle sizing as well as temperature, a study was made of the ER properties of both a calcined and graphitized petroleum coke for 5 closely sized particle fractions from -10/20 mesh to -200 mesh. These measurements were made on a cylindrical column of coke particles at room temperature under static pressure loads from 1 to 10 psi. These tests differ from traditional ER measurements on coke particles in that the particle sizing was coarser and the packing density was altered only by the small applied pressure. These ER values include both the particle resistivity and contact resistances between the particles and, therefore, provide a useful approximation to the actual operating resistance which would be encountered in a high temperature electrical furnace.

Figure #3 shows the change in ER with increasing pressure for both a calcined and graphitized petroleum coke sized to -10/20 mesh particles. The plots are shown as log-log graphs due to the exponential decrease in ER with increasing pressure caused by the rapid decrease in particle contact resistance. The difference in ER between the calcined and the graphitized material is one order of magnitude. This was an expected result since the graphite structure of the coke particles would substantially reduce the ER of the material.

Figure #4 shows the ER at a static pressure of 5 psi for petroleum coke in size fractions of -10/20 mesh, -20/35 mesh, -35/65 mesh, -100/200 mesh and -200 mesh for both calcined and graphitized particles. The horizontal scale is based on the log of the average particle diameter within each size fraction. For both the calcined and graphitized material, the ER of closely sized particle fractions increased as the average particle size decreased. This is due to the inverse relationship between particle size and the number of contact resistances per unit volume of material. Due to the changes, in ER for various particle sizings and

heat treatment temperatures, any particular coke material could be tailored to fit a required ER value by judicious selection of particle sizings and degree of heat treatment. Combining these data with the previously discussed thermal conductivity data will allow the most profitable selection of coke for furnace packing.

References

1. McAdams, Heat Transmission, McGraw-Hill, 1942.

2. Pinnick, Proceedings of the 1st and 2nd Carbon Conferences, University of Buffalo, 1953.

COEFFICIENT OF THERMAL CONDUCTIVITY VS. AVERAGE TEMPERATURE

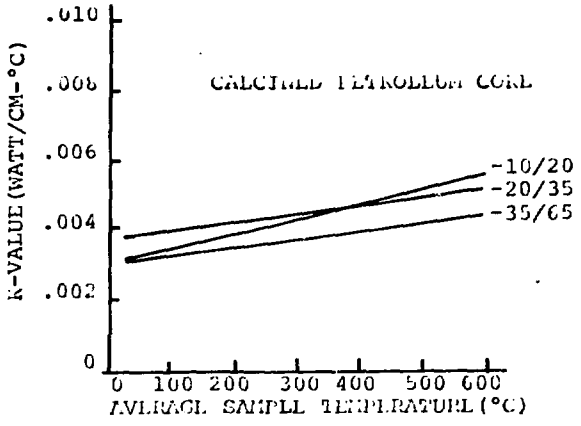


FIGURE 1

COEFFICIENT OF THERMAL CONDUCTIVITY VS. AVERAGE TEMPERATURE

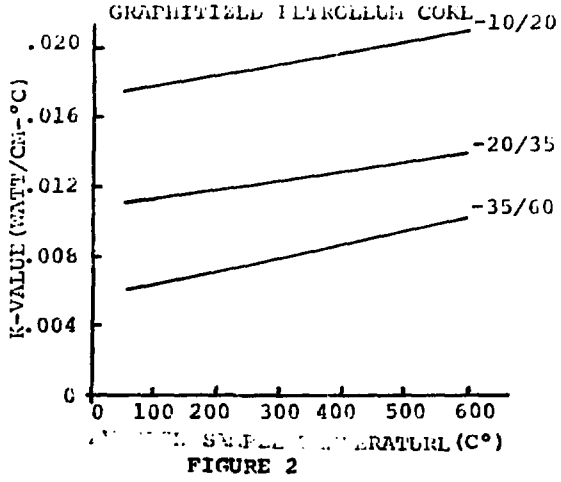


FIGURE 2

ELECTRICAL RESISTIVITY VS. APPLIED PRESSURE

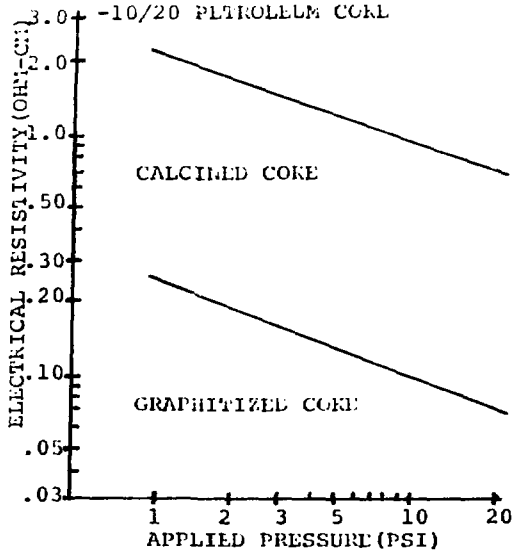


FIGURE 3

ELECTRICAL RESISTIVITY VS. PARTICLE SIZING

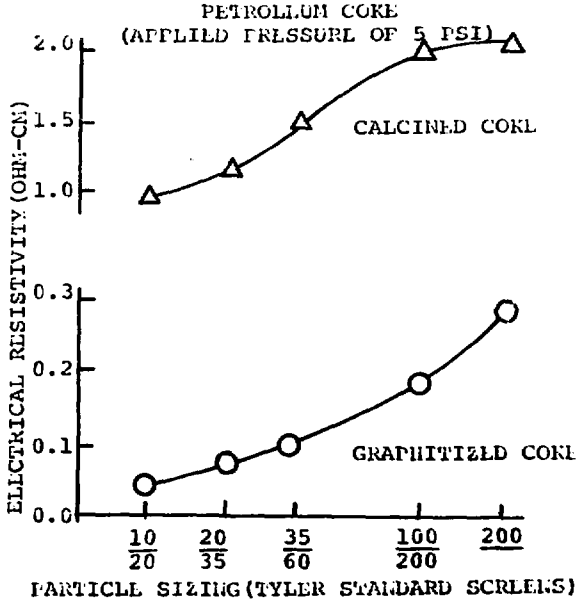


FIGURE 4

L.T.I. CARBON PERMUCOSAL DENTAL IMPLANTS

A. Norman Cranin, D.D.S., Director
Michael F. Rabkin, D.D.S., Asst. Prosthodontist and Implantologist
Howard Silverbrand, D.D.S., Fellow, Implantology
Samuel Unger, D.D.S., Asst. Prosthodontist and Implantologist
Department of Dental and Oral Surgery
The Brookdale Hospital Medical Center
Brooklyn, New York 11212

Jack E. Armitage, D.D.S. Assoc. Professor of Oral Pathology
Michael Meenaghan, D.D.S. Assoc. Professor of Oral Pathology
and University of Buffalo
School of Dentistry
Buffalo, New York 14214

The specific objectives of this research were the:

1. Evaluation of L.T.I. carbon implant-tissue interface at the osseous and gingival levels as a function of time.

2. Evaluation of clinical, radiographic and histologic aspects of implant-host site environment.

A. Methods and Materials

Pyrolytic isotropic carbon were used as the material of choice. It was applied to cores of graphite by alloying vapor deposited carbon with silicon over a steady state fluidized bed [1]

The design of the implants were that of a basic blade of approximately 2.0 mm bucco-lingual width, two infrastructural fenestrations, a grossly matte finished surface with a highly polished 2.0 mm cervical band and a permucosal abutment suitable for the application of a fixed retainer.

B. Implantation

One porous carbon coated blade implant was placed in each dog hemimandible so that permucosal sites for later evaluation resulted. Pericervical permucosal portions of the implant were highly polished to offer surrounding gingiva a hygienic environment. Seventeen hemimandibles were used for implantation and a schedule for edentulation-implantation and sacrifice was closely followed.

Evaluation

A. Clinical Evaluation

A schedule for both clinical and radiographic observation were followed. The animals were observed on a bi-monthly basis and lateral as well as occlusal radiographs taken of each hemimandible.

Radiographic changes such as crestal bone resorption, pericervical saucerization, architectural alterations and increase in peri-implant radiolucency (capsule thickness) were noted monthly.

B. Microscopic Evaluation

After sacrifice and perfusion of each animal with 10% formalin, mandibular block osteotomies yielded specimens of the implant-bone soft tissue complexes. These were studied in both hard tissue and decalcified forms.

Surgical Technique

Using a surgical air turbine under sterile coolant, an osteotomy was cut to the width of a #701 L surgical bur and sufficiently deep to accept the implant passively to the depth of the polished cervix.

Results

Clinical Findings

A major difference was noted between the large and small dogs. The animals in the under 10 kg. weight group had implants which showed varying levels of mobility with marked pocket formation, gingival hemorrhage and some hyperplasia. One implant was so mobile that its removal was warranted.

In the larger group, firmness of the implants was a constant characteristic. Pocket formation was minimal to moderate and healthy, non hemorrhagic gingiva was the rule. Whether or not fixed prostheses were applied, the clinical observations did not vary.

Radiographic Findings

Some saucerization (up to 2 mm) was noted in the small animals but little or none was found in the mandibles of the larger dogs. In most the larger animals, a clear-cut lamina dura was identifiable surrounding the implants.

Histology

A variety of histologic techniques were employed by groups at Tulane University [2] and the University of Buffalo. [3]

Two major groups were recognized - the large dogs which presented generally good to excellent findings and the small ones which met with universally unsatisfactory results.

The latter group offered evidence of epithelial downgrowth, acute inflammatory response, widened connective tissue capsules with fibers in parallel configurations to the implants.

The group of large animals on the other hand, for the most part presented from slight to moderate epithelial downgrowth. The coronal-most connective tissue fibers were often attached to or adherent to the implant and were sometimes oriented in a horizontal to oblique direction. Little or no inflammation was seen and consistent areas of osseous bridging offered evidence of viable bone. Connective tissue capsules present when bone was found not to be butting directly against carbon offered evidence of osteoid or new bone formation within them and in one instance periosteal like tissues and an osteoblast were found at the tissue-implant interface. There was not a trend toward catabalic change directly related to implant time in-situ.

Summary and Conclusion

1. Small dogs, having small mandibles, did not fare as well as their heavier counterparts.

2. Because of the natural radiolucence of silicon alloyed L. T. I. carbon implants on graphite matrices, customarily accepted radiographic interpretations were not as profound as with classically radiopaque implant materials.

3. By comparison to metallic implants of similar times in place [4] the amount of epithelial proliferation, pocket formation and hyperplasia surrounding L. T. I. carbon implants was surprisingly little. After 14 months of implant study with bridges no significant difference was noted as compared to those without bridges.

4. L. T. I. carbon appears to have osteogenetic potential when placed in bone..

5. Because of the polished cervix of pyrolite endosteal implants, a high level of gingival health is promoted.

6. The irregular surface of these implants at the infrastructural level appears to be responsible for an intimate relationship of oblique or horizontal connective tissue fibers and on occasion even direct bone opposition. L. T. I. carbons modulous of elasticity, so close to that of bone, is probably responsible for minimal osseous host-site change.

This report describes the use of low temperature isotropic carbon dental implants, finds them to be more successful than metallic implants studied under comparable conditions and indicates promise for them as abutments for [illegible].

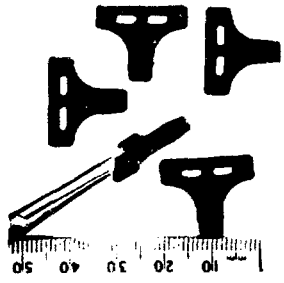
References

1. Bokros, J. C. in Chemistry and Physics of Carbon, Vol. [illegible] P. L. Walker, ed. Dekker, New York, 1969, Chapter 1.

2. Klawitter, J. J. Research techniques for evaluating tissue growth within porous materials. Paper presented at a Symposium-Workshop in Research Techniques in Biomaterials Evaluation, Clemson University, Clemson, S. C. 1971

3. Armitage, J. and Meenahan, M. Personal Communication re: the use of the Jung-Model K power driven microtome and histologic techniques for implant evaluation, Feb. 1977.

4. Schnitman, P. Thesis for masters degree - Dental Implants in Beagle Dogs - In preparation, 1971-1972.



L. T. I. Carbon Dental Implants



Soft Tissue - Implant Interface



Bone - Implant Interface

CARBON MATERIALS FOR ORAL IMPLANTATION: A PRELIMINARY REPORT

D. Leake, S. Michieli, S. Freeman, Harbor General Hospital, Torrance, California
J. Bokros and A. Haubold, General Atomic Company, San Diego, California

The purpose of this study is to evaluate in laboratory animals and in man, vacuum vapor deposited carbon as a coating for cast metallic implants fabricated for subperiosteal dental implantation and mandibular condyle replacements. Subperiosteal implants are used in edentulous mandibles or maxillae to provide stability for specially constructed dentures for patients who cannot otherwise satisfactorily wear a dental prosthesis. Conventional dentures may be unsatisfactory because of atrophy of the alveolar ridge or because of high muscular attachments on the alveolar ridge. Subperiosteal implants have been used successfully, particularly in the mandible, for over 25 years [1-3]. The success rate, however, has been compromised because the implant must function in a chronic load bearing, through-the-mucosa setting. Thus, they are exposed into the mouth and interface with both bone and soft tissues. The material generally used is cast Vitallium. While design plays a critical role, equally important is the material used to fabricate the subperiosteal implant. Design considerations have been well evaluated, but an entirely satisfactory material has yet to be clinically accepted. Carbons of various sorts appear to have great potential for usefulness in these applications. They have excellent chemical biocompatibility. An advantage of the vacuum vapor deposited carbon is that it can be used to form a thin impermeable barrier that will confer this biocompatibility of carbon on otherwise less compatible materials such as metals [4].

The subperiosteal implants were fabricated according to the classical principles for subperiosteal design and fabrication and then coated with ORALPLATE TM carbon (General Atomic Company, San Diego, California.

The subperiosteal implants have four posts that traverse the mucosa in order to support the dental prosthesis (figure 1). These posts have a tendency to irritate the mucosa resulting in inflammation which, if unchecked, progresses to exposure of the implant and possibly frank infection. It was hypothesized that by coating the implant with carbon, the mucosa around the posts would be less irritated.

Clinical Experience

Two patients with severely atrophic mandibles, for whom subperiosteal implants were entirely appropriate, were chosen as candidate patients. Benefits versus risks were discussed with the patients.

Surgical Technique

A subperiosteal flap was turned, exposing the bare mandibular bone. Custom impression trays were used to prepare appropriate models of the mandibular bone. Using these models, subperiosteal dental implants were cast by a commercial dental laboratory. The cast Vitallium subperiosteal implant was plated with carbon. Two weeks later the patients returned for implantation. The flap was turned again, exposing the alveolar bone subperiosteally and the implant inserted. The mucosa was closed with multiple interrupted 3-0 non-absorbable monofilament sutures (Nylon or Tedvek). Sutures were removed at 10 days to 2 weeks. Dentures were fabricated subsequently. The patients have been seen at 6 weekly intervals in order to evaluate the oral hygiene and the health of the mucosa. Radiographs have been taken at 3 monthly intervals. The mucosal response has been excellent. There has been no evidence of inflammation or of erosion or ulceration. Radiographically there have been no discernible changes in the alveolar bone adjacent to the implant. The implant has remained stable and provides a solid functioning support for the dental prosthesis.

Mandibular Condyle Replacement

Compared to the subperiosteal dental implant, there is no general agreement on what optimum design considerations may include for mandibular condyle replacement. The design usually is based on empirical observations. An x-ray of the patient's mandible is used as the guide [5]. Indications for condylar replacement include severe ankylosis, traumatic avulsion or agenesis.

Studies in Dogs

Vapor deposited carbon coated Vitallium implants for mandibular condylar head replacement were evaluated in 5 dogs. The condylar heads were designed in 3 configurations to evaluate their performance in a laboratory animal. The head of the mandibular condyle was removed unilaterally in each dog, using an air driven bur. The various condylar replacements were placed subperiosteally and affixed with 5 mm carbon coated Vitallium screws and the wound closed in layers. The condylar replacements were cast in Vitallium as overlays for the lateral aspect of the mandible: 1) with 4 holes for screw placement, 2) with 4 holes for screw placement and a pin to countersink into the posterior border of the ramus of the mandible, 3) with 4 holes for screw placement and with 3 pins to be countersunk into the lateral aspect of the ramus of the mandible. Based on visual inspection of the animals, it appears that the condyles with pins countersunk into the lateral aspect are quite stable while the other 2 models were somewhat mobile. Sacrifice of the animal with the condyle replacement with a posterior border pin confirmed that there was some loosening of the screws and that the implant was slightly mobile. The success of the lateral pin models and the need for condylar excision and replacement in a patient encouraged us

to evaluate a similar style replacement in man.

In the patient presented here, ankylosis of long standing had resulted in an opening of the mandible of less than 5 mm interincisal distance (normal 35 - 45 mm).

Surgical Procedure

An incision was made at the posterior border and angle of the mandible exposing the area of the mandibular condyle. A bony carapace extended inferiorly from the zygomatic arch covering the condylar head. This was removed along with a dense fibrous connective tissue band holding the condylar head in the fossa and the enlarged, roughened condylar head was removed with an air driven bur. The prosthesis was fitted into place by countersinking holes in the lateral aspect of the ramus of the mandible to accept the pins prepared in the condylar replacement. Four holes were countersunk through the lattice work of the implant and 7 mm carbon coated Vitallium screws were inserted (figure 2). An opening of nearly 30 mm was achieved on the operating room table without opening the contralateral side. The patient has been able to eat solid foods and continues, after 6 months, to function in a nearly normal way with an unassisted opening of 25 mm.

Summary and Conclusions

Vacuum vapor deposited carbon as a coating for implant materials confers a high degree of inertness. The observations reported here, although preliminary in nature, tentatively confirm the usefulness of carbon coating for subperiosteal implants by imparting greater tissue tolerance to transmucosal posts. The observations on condylar replacement implants have also encouraged us to investigate further, both in the laboratory and in man, these provocative clinical problems.

[1] T.C. LEE, J. Calif. Dent. Assoc., 47, 36, (1971).

[2] R.L. BODINE et R.L. KOCH, J Prosthetic Dent., 4, 396, (1954).

[3] R.L. BODINE, J. Prosthetic Dent., 32, 188, (1974).

[4] A. HAUBOLD, Annals of the New York Academy of Sciences, 283, 383, (1977).

[5] J.N. KENTet W.E. Lavelle et K.D. DOLAN, Oral Surg., Oral Med., Oral Path., 37, 489, (1974).

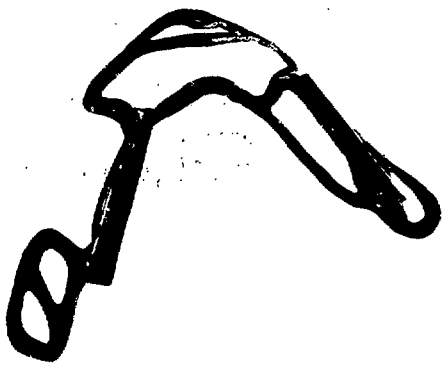


Fig. 1 : Cast Vitallium subperiosteal dental implant coated with vacuum vapor deposited carbon (ORALPLATE TM). The four small posts traverse the mucosa and are topped by a lintel to support the denture.

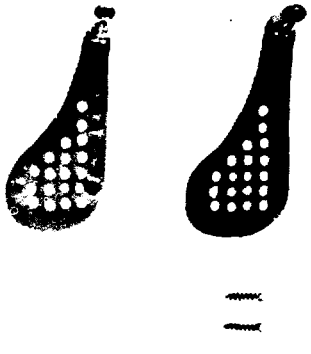


Fig. 2: **Prototype human mandibular condyle replacements, Leake and Freeman design. Left, cast Vitallium; right, vapor deposited carbon (ORTHOPLATE TM) coated Vitallium condyle. 7 mm Vitallium screws are also coated with vapor deposited carbon.**

VAPOR DEPOSITED CARBON COATED TOOTH ROOT REPLICAS

S. Michieli, D. Leake, S. Freeman,[1] J. Bokros, A. Haubold,[2] and A. Pizzoferrato[3]
1. UCLA Campus at Harbor General Hospital, Torrance, California,
2. General Atomic Co., San Diego, California, 3. Fizzoli Institute, Bologna, Italy

Successful dental implants are dependent on both design and materials considerations. The aim is to achieve long term stability and retention with the implant in function. In the work reported here, tooth root replicas were made of cast vitallium and coated with a thin impermeable layer of vacuum vapor deposited carbon. The design advantage of a tooth root replica is that masticatory loads are distributed through the supporting alveolar bone of the jaw much as they are in normal dentition. One of several common causes for the failure of various implant designs is excessive loading of a small alveolar area, *i.e.*, stresses are not distributed adequately [1, 2]. The materials used have extensive implant histories and their biocompatibilities are well known. The principal advantage of the carbon coating is the enhancement of the permucosal surface where the tooth, its root seated in bone, must penetrate the mucosa into the mouth. This area generally contributes to implant failure because of lack of a seal between implant and mucosa. Inflammation of the mucosa, the collection of debris on the tooth cervix, or neck, and bacterial invasion disrupt the integrity of the implant and host.

Materials and Methods

Sixteen carbon coated implants were cast in vitallium, coated with carbon and implanted in 5 dogs. The implants were replicas of premolars for 10 teeth and of molars for 6 teeth. The design, shown in figure 1, incorporates the tapered root normally found in these teeth, and a large hole in the root to allow bony ingrowth from the surrounding alveolar tooth socket. The tooth cingulum was smaller than in normal teeth to decrease the length of the gingival carbon junction, yet big enough to support masticatory forces [3]. The cingulum should be smooth at the gingivocarbon junction to promote good hygiene. The implant shoulders should be of appropriate size to allow them to be located below the alveolar bone surface (figure 1).



Fig. 1: TOOTH ROOT REPLICAS for human (L) and dog (R).

For comparison, two alumina oxide (Al_2O_3) coated titanium implants were placed in the opposite side of the jaw to evaluate the permucosal acceptance of the two different coatings. The Al_2O_3 was applied by Plasma-jet to form a chemical bond between ceramic and metal.

Additionally, four LTI-Si carbon endosteal blades were placed in the mandibles of two dogs, adjacent to carbon replicas in one animal, and on the opposite side in the other. This was to evaluate the bone-carbon interface of the two different implant designs.

The tooth root replicas were prepared in two ways. Initially, the replicas were made from impressions taken of tooth extraction sites and the implants were placed in the animals about 2 weeks after extraction. Later, the implants were replicated from impressions of corresponding mandibular teeth from other dogs of similar size and were implanted in the study animal immediately after extraction.

Metallic splints were cemented over the remaining teeth and over the implant tooth crown and circummandibular wires were placed to provide additional stabilization. Unfortunately, the circummandibular wires were intermittently loose requiring tightening or replacing. The animals were given antibiotics for 1 week following surgery. During the first 2 weeks after surgery tissues surrounding the implant posts were checked every 2 or 3 days and basic oral hygiene therapy around the implant region was performed. Thereafter each animal was evaluated every 2 weeks by radiographic examinations in order to evaluate mandibular bony behavior, and hygiene was performed. The dogs' diet was exclusively soft food, usually for the first week only. No infections developed because of implants or transmucosal or circummandibular wires as indicated by both clinical and radiographic examinations. Results: Four of the five animals were sacrificed about three months after implantation. I.V. alizarine was given one month pre-sacrifice for intravital staining. On removing the metallic splint, the implant mobility was evaluated and rated according to the lateral displacement of the implant. The gingival sulcus was also probed and the pocket depth reported in millimeters (Table I). After sacrifice, radiographs were taken of the entire mandible as well as each alveolar section containing the implants. Histological specimens were taken of the mucosa around the implant's cervix, and alveolar sections of the mandibles containing one implant per specimen. These latter have been embedded in methylmethacrylate resin and cut in sections of about 60 to 80 u. for microradiographic and histologic examinations. The results of these preliminary data, the radiographic examinations, visual observations with probing and the histology, suggest that the combination of design and materials is worthy of further study.

Conclusions

1) The mechanical stability of tooth root replicas was found to be higher than endosteal blades. Seven out of the 16 implants had no mobility and were completely firm (Table II). However, it has been shown that the blade design used for this study was less than ideal and the General Atomic Company has modified the design for the LTI-Si blade study in animals [4]. It should be noted that the looseness of the splint was a detriment to the implant. Others have now reported that it is advantageous to implant blades without splints [5]. 2) Histological sections were compatible with satisfactory biological acceptance for both carbon and alumina tooth root replicas. 3) When both carbon and alumina sprayed implants had the same degree of stability (less than .5mm of mobility) the permucosal response was comparable. There was a moderately hyperplastic epithelium with macrophages present in the perivascular connective tissue, the number present increasing with pocket depth.

It has been observed that porous tooth roots are lost with time because, as the microporous structure becomes invaded by bacteria, there is progressive resorption of the bony socket [6]. However, the shortness of the study reported here, three months, precludes us from substantiating this observation. It was clear, none the less, that the stability of tooth root replicas and the permucosal response to carbon coated implants give promise of great usefulness for this combination of design and material in dental implantology.

[1] D. SMITH. J. Dent. Res., 54, Spec. Issue B, B146, (1975.

[2] S. HULBERT et J.T. BENNETT = J. Dent. Res., 54, Spec. Issue B (1975).

[3] S. MEER, Proc. of 6th Intl. Biomat. Symp., Clemson Uni.., S. Carolina, (1974).

[4] S.F. HULBERT et J.C. BOKROS. Personal Comm.

[5] A.N CRANIN. Personal Communication

[6] L.J. PETERSON et J.J. KLAWITTER et al. Proc. of 8th Ann. Intl. Biomat. Symp., Apr. P13, Phil., (1976).

COMPARISON OF TOOTH IMPLANTS IN DOGS

Dogs	Sacrificed after Implant No. of Days	Wt. in kg	Time Between Extraction and Implantation	Tooth Replaced and Implant Type*	CLINICAL RESULTS: Lateral Mobility (mm) Right Mandible	Gingival Sulcus (mm) Right Mandible	Lateral Mobility (mm) Left Mandible	Gingival Sulcus (mm) Left Mandible	Tooth Replaced and Implant Type
1 (1312)	96	27	12 days	V 3rd p.m. V 1st mol.	2 1.5	3-4 3	1.5 .5	3-4 2-2.5	V 3rd p.m. T 1st mol.
2 (1209)	96	38	16 days	V 3rd p.m. V 4th p.m. B 1st mol.	1.5 1.5 1.5	1.5-2 2.5 2-3	1.5 0	2.5 2.5-3	B 3, 4th p.m. V 1st mol.
3 (1368)	82	28	0	V 3rd p.m. T 1st mol.	1.5 0	1-3 1-1.5	0 0	1-2 1	V 3rd p.m. V 1st mol.
4 (1376)	88	27	0	V 4th p.m. V 1st mol.	1 0	1.5 1	.5 .5	1-3 0.5-2	V 4th p.m. V 4th p.m.
5 (970)	Alive, Splint removed 102 days	17	0	B 3, 4 p.m. B 1st mol.	1 2	5-6 >5	.5 0 0	2.3 3 1.5-3	V 3rd p.m. V 4th p.m. V 1st mol.

* key: V = vacuum vapor deposited carbon root replicas (16); T = Titanium root replicas coated with Al_2O_3 (2); B = LTI-Si carbon blades (4)

TABLE I

COMPARATIVE CLINICAL RESULTS IN DOGS

IMPLANTS COMPOSITION	TOOTH ROOT REPLICAS: Vacuum Vapor Deposited Carbon Coated Vitallium		Al_2O_3 Sprayed Titanium	ENDOSTEAL BLADES: LTI - Si Carbon
	Premolars	Molars	Molars Only	
No. of Implants	10	6	2	4
LATERAL MOBILITY < .5mm	40%	83%	100%	0%
SULCUS DEPTH < 2mm	30%	66%	50%	0%

TABLE II

VARIOUS APPLICATIONS OF PYROLYTIC CARBON IN ALVEOLAR BONE TO RETARD RESORPTION AND STIMULATE OSTEOGENIC ACTIVITY.

A Preliminary Report

Jack Warrens, D.M.D.
1370 Rosecrans St.
San Diego, Calif. 92106

In the oral cavity, when a tooth is extracted or a bone defect has occurred as a result of a pathologic process, the bone repairs itself through the osteogenetic activity of the osteobast cells that infiltrate the ensuing blood clot in the socket of the defect site. The filling in of the defect is an ongoing regenerative sequence, but the resulting healed bone volume is reduced and a contraction or resorption of the lateral and crestal alveolar bone results. This causes a weakening of the adjacent teeth and/or reduces the gross area of ridge which may be called upon to support a dental prosthesis. Our need has been to have a biomaterial in a bulk configuration that could be placed into the defect thereby increasing the rate of regeneration as less bone volume would be required, therefore the collapse of the ridge would be reduced and the original volume could be more normally maintained. Further, in pathologic disease of alveolar bone such as is found in periodontal disease around natural teeth roots, we sought a configuration of a biomaterial that could be packed into these defects to aid in stabilization and support of weakened dentition while healing was taking place after surgical intervention.

DISCUSSION

Investigation in animals and humans of implants inserted into fresh extraction sites is showing that such carbon implants are capable of inhibiting alveolar bone loss.[1] The results suggest that the carbon surface may be osteogenic in nature which could have substantial impact in other modalities. These early observations have led to the use of small carbon particles in boney defects to aid in the regeneration of bone around periodontal diseased teeth.[2] In previous work with vitreous carbon endosseous dental implants, we found it had two distinct disadvantages. One, it is radiolucent, and two, it is brittle, which required bulk or metal reinforcing for strength. The radiolucency factor has hindered radiographic studies in that we "lose the implant" in the films thereby making it impossible to track accurately or follow its position in relation to its supporting bone. Further, we could never adequately delineate the apposition of the new bone growth in relation to the surface of the implant. Studies have shown the bio-compatibility of pyrolytic carbon (LTI carbon) in the environment of the bone found in the oral cavity.[3] The LTI carbon overcomes these two disadvantages, hence our interest centered on this material as the one of choice for our current studies in animals and humans. A third application of carbon we found was it is capable of being coated to metals such as vitallium or titanium with a strong surface bond where this modality was desired.

TECHNIQUE:

Four configurations of these endosseous implants have been utilized to date. Cones or cylinders, segmented sections, granular particles and blades are available. We will discuss here the first three configurations wherein the carbon is to be (fig. 1) completely buried and encapsulated with new bone growth. The cones or cylinders are placed as immediate root replacements at the time of extraction of the natural tooth. These are utilized where the defects are large. The segment configuration is used in smaller defects and the granular particles are packed into infraboney pockets found adjacent to natural roots for support of same. Any combination of the above sizes can be utilized in the same defect to afford the best "fill" but keeping in mind not to overfill the defect as the unincorporated pieces beyond the direct influence of the blood clot will enfoliate. (fig. 2) In fact, we found it is best to keep the level of the fill 2mm. below the level of the lowest point of crestal bone support so that an adequate cover of new bone growth will bridge over the implants to submerge completely all carbon. An advantage of the segment and particle sizes is that if extrusion or exfoliation develops, the total "fill" is not lost, only the topmost portion.

RESEARCH:

Our current studies also include buried cones and cylinders that are re-exposed surgically subsequent to healing and a super structure, with a female extension, is cemented into the root to simulate a tooth replacement. The advantage of this technique is that the new bone growth encapsulates the carbon root in a completely physiologic environment to afford the maximum stabilization of the implant prior to loading with occlusal forces.

Histologic studies of buried biomaterials all in the same host, are also currently underway to compare their respective interfaces. (fig. 3) By placing one of each of the following materials in the same animals (dogs), we hope to determine if they are equally biocompatible or if, in fact, carbon is superior as preliminary reports seem to indicate. Vitallium, LTI carbon, titanium, titanium coated acrylic, and surgical stainless are the five being utilized in this study; the conclusions will be reported elsewhere.



Fig. 1, carbon cones, cylinders, segmented spheres and particles



Fig. 2, radiographs of segments encapsulated with new bone

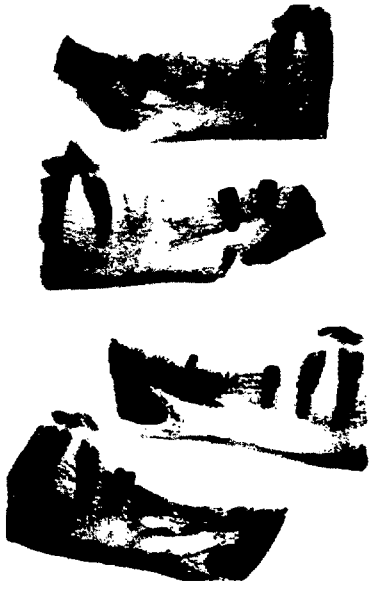


Fig. 3, sections of dog mandibles showing implants prior to sectioning

SUMMARY:

Animal and clinical results to date have been significantly encouraging to indicate that this modality appears to stimulate osteogenic activity which hastens the repair of boney defects and, in turn, retards the rate and quantity of alveolar bone resorption in animals and humans.

BIBLIOGRAPHY

1. Stallard, R.E., Geneidy, A.K., Skerman, H.J., "Vitreous Carbon Implants--An Aid to Alveolar Bone Maintenance." Oral Implantology, Vol. VI - No. 2 - 1975.

2. Meffert, Roland M., "Periodontal Aspects of Implants." Implantology Review, Vol. 6 - No. 4 - 1977.

3. Hamner, J.E., III, Reed, O.M., "Pyrolite Carbon Dental Implants in Baboons," Medical Primatology 1972. Proc. 3rd Conf. exp. Med. Surg. Primates, Lyon 1972, part II, pp. 177-181 (Karger, Basel 1972).

EXPERIENCE WITH BIOCOMPATIBLE CARBON AT RANCHO LOS AMIGOS HOSPITAL

J. Reswick, Sc.D., V. Mooney, M.D., D. McNeal, Ph.D. and M. Quigley, C.P.O.

Biocompatible carbon, both in the form of vitreous carbon (VC) and as low temperature isotropic (LTI) (Pyrolytic) carbon vapor deposited on a graphite substrate, have been used with human subjects and patients at Rancho Los Amigos Hospital for five years. Two general configurations have been employed; viz, percutaneous electrodes in a form similar to collar buttons and as collars for direct skeletal attachments at the point of exposure through the skin.

Percutaneous Electrodes

Since December 1972, 127 percutaneous electrodes have been placed in volunteers and patients in the Contracture Prevention, Chronic Pain Relief and Sensory Feedback programs. Three materials have been evaluated; viz; vitreous carbon (VC), low temperature isotropic carbon (LTI) and titanium (TI). Clinical results have been nearly the same with all three materials. Electrical impedance is remarkably stable following insertion and is generally between 200-400 ohms, depending upon the spacing between electrodes. Little polarization is seen with the carbon electrodes, so the impedance is almost purely resistive.

Of the 127 electrodes used, 40 (38%) had to be removed because of infection or excessive skin irritation around the electrode and surrounding tissue. It has been anticipated that mechanical trauma will be reduced considerably, with a corresponding decrease in the failure rate, with the introduction of the magnetic connector shown in Figure 1. Twenty-three buttons with magnetic connectors have been used. Only two of these failed.

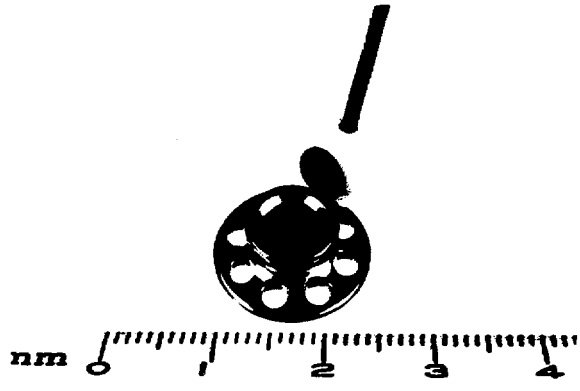


Fig. 1 Percutaneous Electrode with Connector

Intraneural electrodes which exit the skin through carbon buttons (Figure 2) have been fabricated for use in the Sensory Feedback Prosthesis program. In this case the carbon is insulated from the wire and the magnetic connector, and it is used only to provide percutaneous passage. The indifferent electrode (also shown in Figure 2) is identical except that a small carbon tip is attached to the coiled wire. The carbon tip is placed outside the nerve, but in close proximity to it.

Clinical experience at Rancho Los Amigos Hospital through 1976 is summarized in Tables I and II. Table I shows 127 buttons organized by type of material, and Table II shows these same buttons organized by category of application. An

Table I

Material	Number Successful	Avg. Mos. Successful	Longest Success	Number Unsuccessful	Avg. Mos. Until Failure	Success Rate
Titanium	21	8.4	20	16	8.5	57%
LTI	24	8.3	24.5	17	8.9	59%
VC	33	5.9	35	16	6.8	67%

Table II

Category	Number Successful	Avg. Mos. Successful	Longest Success	Number Unsuccessful	Avg. Mos. Until Failure	Success Rate
Volunteer	17	2.9	8	7	4.6	71%
Pain Relief	17	12.6	35	19	7.2	47%
Contracture Correction	38	6.9	24.5	20	10.2	66%
Sensory Feedback	6	7.0	9	3	8.0	67%

application is considered "successful" if an implanted button does not have to be removed for reasons other than the termination of the patient's treatment.

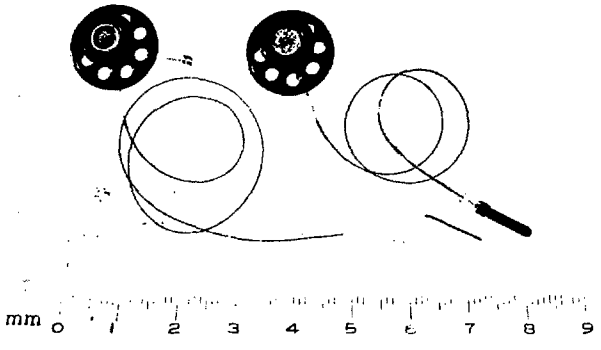


Fig. 2 Intraneural Electrode

Skeletal Attachment of Prosthesis

Through a unique collaboration among Rancho Los Amigos Hospital Rehabilitation Engineering Center, Kennedy Space Center of NASA, and General Atomic Company in San Diego, California, a system for directly attaching a limb prosthesis to the bone of the amputated limb of the stump of the amputee has been developed (Figure 3). A hollow metal intramedullary pin is cemented with methylmetacrylate into the amputee's bone. The metal unit is provided with a collar coated with low-temperature isotropic carbon. The skin closes around the carbon collar, creating a bacteriological seal and leaving the internal bore of the metal unit exposed to the outside. A quick-disconnect rod derived from Space applications is built into the prosthesis so that it can be inserted into the bore of the intramedullary unit for attaching the prosthesis. A normal stump socket on the prosthesis is used to absorb most of the limb load and to provide torsional stability.

This unit was implanted in one patient, who tolerated the implant for over a year. The skin around the carbon collar finally pulled away and became infected due to the mechanical forces exerted by the prosthesis necessitating removal of the device.

A new design (yet to be implanted) using a flexible element between the carbon and the intramedullary rod has been fabricated. It is hoped that this device will reduce the stresses between the skin and the carbon. It will be used on an upper extremity where skin stresses are expected to be less than on a lower extremity.

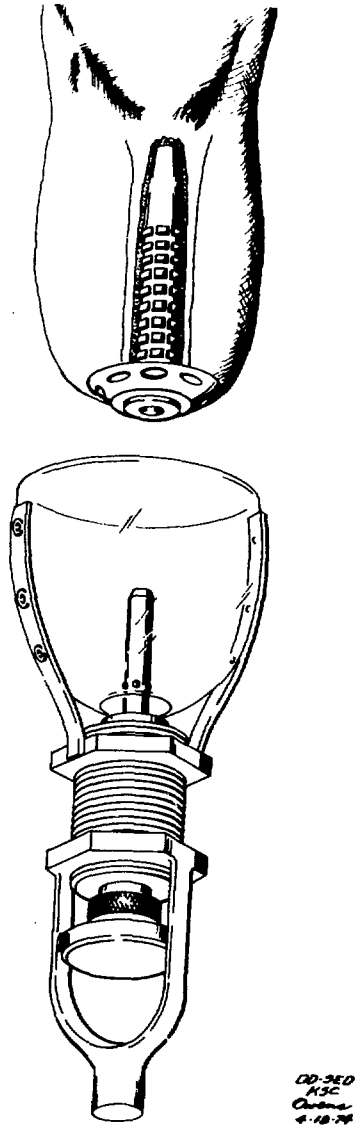


Fig. 3 B-K Prosthesis Attachment

THE LOW CURRENT CARBON ARC AND THE PROPERTIES OF GRAPHITE NEAR THE SUBLIMATION TEMPERATURE

W. W. Lozier* and M. R. Null*
Union Carbide Corporation, Carbon Products Division
Parma Technical Center, Parma, Ohio 44130

Old and new data on the crater radiation from the low current carbon arc have been examined on the basis of two different hypothetical interpretations: (a) the radiation orginates from the crater surface, or (b) the radiation originates from the crater surface and from particles in the adjacent arc stream.

Radiation Originates from Surface

Data from the low current carbon arc[1-3] provides strong evidence that the radiation from the crater can be characterized by a surface temperature close to 3800K. The measured values of spectral radiance are in excellent agreement with those values expected from the Planck radiation formula and the measured values of spectral reflectance (and emittance) over a range of wavelengths from below 0.3 to above 1.7μm. Other data[4,5] agree acceptably with those of References 1-3 regarding the spectral radiance, but they differ greatly in the values for the spectral reflectance and the temperature at the crater surface.

Euler's values of the spectral reflectance[4] are 10 to 15 times too large, but they can be rationalized by taking into account the irradiation-produced increase in temperature of the crater surface. The use of the Null-Lozier[2] and Schurer[3] values of reflectance with values of irradiance[6] appropriate for Euler's experiment leads to the calculation of an irradiation-produced temperature increase of 27K in his experiment and shows that only 5 to 10 percent of this increase in radiance resulted from reflected radiation. An approximate energy balance in Table I for the arc-produced energy fluxes conducted into the electrode and radiated from the crater surface and the assumption that Euler's 120 $W(cm)^{-2}$ irradiation flux absorbed at the crater surface divides in the same ratio as the arc-imposed energy flux leads to calculated temperature increases of 24 and 33K, respectively, for the graphite grade SPK and the lampblack grade L113SP electrodes.

Schurer[3] has shown that Magdeburg's[5] value of crater reflectance is greatly in error because of an incorrect value for the reflectance of the "cold" crater surface.

Schurer[3] found that the crater surface temperatures of ten different grades of high purity electrodes from three manufacturers spread over a range of 50K, indicating that the temperature of the crater surface may depend to a small extent upon the materials and origin of manufacture and, perhaps, upon the conditions of operation of the arc.

The temperature of the crater surface after interrupting the arc (Figure 1) shows initial rapid cooling that fits almost equally well a square root or a linear time dependence over the first 0.05 ms interval for both lamp black and graphite electrode materials. No acceptable interpretation has been found using a linear time dependence for the cooling. The results are satisfactorily interpreted on the basis of radiation from the surface and one-dimensional thermal conduction in a semi-infinite body according to the relation[2]

$$(\Delta T_c)t^{-\frac{1}{2}} = 2(R_o + F_o)(\pi k c \rho)^{-\frac{1}{2}} \qquad \text{Eq. (1)}$$

where F_o and R_o are the heat fluxes at time t = 0, respectively, conducted into the body and radiated from the surface; and k, c, and ρ are, respectively, the thermal conductivity, specific heat, and bulk density of the material. The value of thermal conductivity 8.8×10^{-3} $W(cmK)^{-1}$ is calculated from Eq. (1) as shown in Table I. This value of conductivity is 25 to 50 times smaller than that measured for the bulk electrode materials, and it is the same order of magnitude as the values measured by Euler[7] and by Rasor and McClelland[8]. The cooling (extended to longer times) in Figure 1, shows a transition to much slower "square-root-of-time" cooling rates after a temperature decrease and cooling time, respectively, approximately 300K and 100μs for the SPK electrode and 500K and 360μs for the L113SP one. An approximate value for the thickness, ℓ, of the low conductivity layer is obtained from the dimensional relation $\ell^2 = (kt)/c\rho$ giving $\ell = 4.65 \times 10^{-4}$cm and 10.3×10^{-4}cm, respectively for the SPK and L113SP materials.

The values for the thermal conductivity and the transition time obtained above explain satisfactorily three hitherto puzzling features observed in the intermittent irradiation experiment of Null and Lozier[2]: (a) the instantaneous nature of the temperature changes, (b) the linear dependence of the temperature change upon the value of the irradiance, and (c) the more than two-fold greater temperature change for the lampblack electrode than for the graphite one. In addition, the magnitude of the temperature change is predicted approximately (within 30 to 55 percent).

Radiation Originates from Surface and Particles

A novel interpretation of the radiation from the crater assumes that particles emitted from the crater seriously distort the observations of crater radiance. Our analysis differs from that of Abrahamson[9] in the size and role of the particles. The size of the particles and their fractional surface coverage were determined from the magnitude and spectral characteristics of the reflectance of the "hot" and the "cold" crater surface compared with the known attenuation effects of small particles upon radiation. Our model, consisting of a cloud of graphite particles (radius 0.08μm) and the crater surface at temperatures, respectively, above and below the value

*Retired

3800K, gives a promising explanation of he observed radiance of the graphite-based electrode but not the lampblack-based one. It may also explain the changes in radiance of the graphite-based electrode caused by irradiation of the crater and those occuring after extinction of the arc, without requiring anomalous reduction of the spectral reflectance and the thermal conductivity near 3800K temperature. However, the irradiation-produced increase of crater radiance is wrongly predicted to be greater for the graphite-based electrode than for the lampblack-based one.

Choice Between the Two Hypotheses

Heat balance and heat transfer modes in the arc stream and at the crater surface have been considered, and they indicate that the spatial distribution of the expended arc power is greatly different with the two interpretations. The "surface" model indicates a larger heat flux conducted from the crater surface to the electrode than the "surface-plus-particles" one, the difference between the values of the conducted heat flux for the two models being expended in the arc space. The "surface" model calls for a large reduction in thermal conductivity when the electrode material approaches the crater surface. The failure of the "surface-plus particles" model to account for the effect of different electrode materials as contrasted with the near-total success of the "surface" model tips the balance of evidence strongly toward the validity of the latter model.

References

1. Null, M. R. and Lozier, W. W., J. Opt. Soc. Am. 52, 1156 (1962).
2. Null, M. R. and Lozier, W. W., WADD Technical Report 61-72, Vol. 21, Carbon Arc Image Furnace Studies of Graphite, July (1963).
3. Schurer, K., Appl. Opt. 7, 461 (1968).
4. Euler, J., Ann. Physic 11, 203 (1953).
5. Magdeburg, H. and Schley, U., Z. Angew. Phys. 20, 465 (1966).
6. Null, M. R., and Lozier, W. W., J. Soc. Mot. Pict. and TV Engineers 68, 80 (1959).
7. Euler, J., Ann. Physik 18, 345 (1956).
8. Rasor, N. S. and McClelland, J. D., J. Phys. Chem. Solids 15, 17 (1960).
9. Abrahamson, J., Carbon 12, 111 (1974).

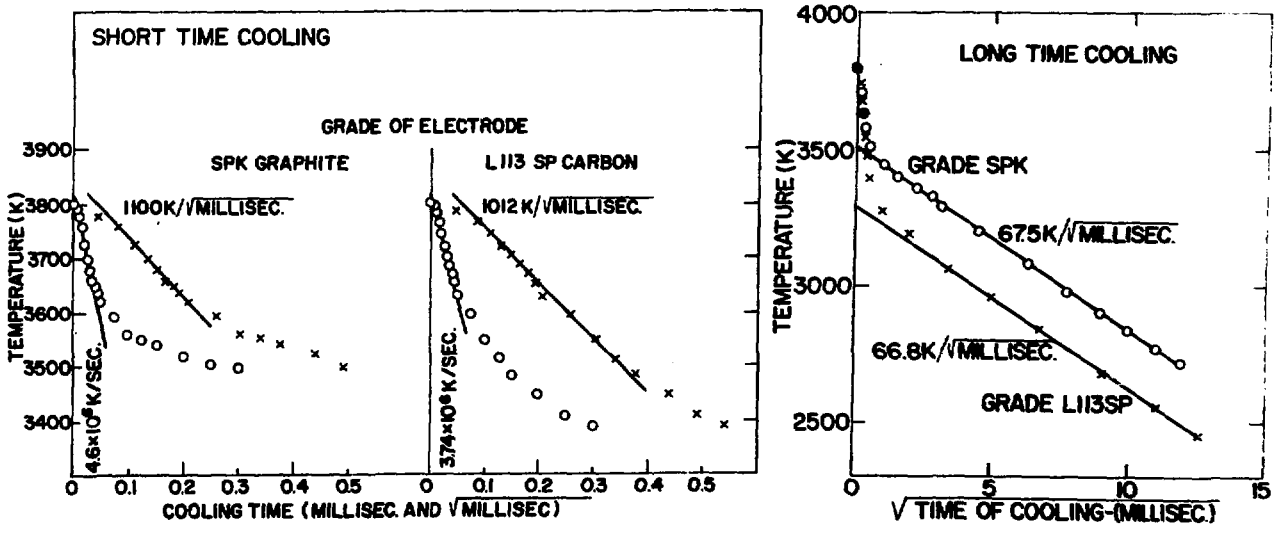


Figure 1. Cooling curves of crater surface temperature after arc extinction for graphite and lampblack electrodes.

PERPENDICULAR ELECTRIC FIELD EFFECT ON THE ELECTRIC RESISTIVITY OF THIN GRAPHITE CRYSTALS

Yoshiko Fujibayashi Onashi and Sanchi Mizushima

School of Engineering, Keio University

From the analysis of the magnetic field dependence of the Hall coefficient and the transverse magnetoresistance of thin graphite crystals using McClure's method(1), it was found that thin crystals of graphite have larger number densities of holes and electrons as well as smaller mobilities than bulk crystals(2). This size effect of graphite crystals seems to arise from the surface layer.

In this study, the electric resistivity of thin graphite crystals was measured with application of electric field perpendicular to the basal planes of the crystal surface up to 7.0×10^5V/cm at liquid helium temperature.

The method to prepare specimens was the same as that described in the previous paper(3). Current flow through the specimen was kept at around 10^3A/cm^2.

The resistivity of graphite crystals of various thickness less than 1μm was found to change with the electric field E applied perpendicularly to the surface, examples of which are illustrated in Fig.1. Here, E>0 means that the sample is charged negative.

The resistivity of crystals of any thickness monotonically decreases with increasing electric field (E>0), while for E<0 it increases with increasing field, except for the specimen of 460A thickness. The magnitude of this effect is of the order of several per cent at the highest field in this study. This tendency becomes conspicuous for thinner crystals, and for the thinnest crystal $\Delta\rho/\rho$ at first increases, reaches a maximum, and then monotonically decreases. The oscillations in the curves of $\Delta\rho/\rho$ vs. E did not appear unlike in the case of bismuth films studied by Yu.F.Ogrin et al.(4), which was explained by the quantum size effect(5).

The authors wish to thank Professor Y. Hishiyama of Musashi Institute of Technology and Dr. H. Nagashima of Toshiba Ceramics Co. Ltd. for kindly supplying graphite flakes. The work was partly supported by the Kurata Research Grant from the Kurata Foundation.

REFERENCES

1. McClure J. W., Phys. Rev. 112, 715(1958).
2. Fujibayashi Y., J. Phys. Soc. Japan 34, 989(1973).
3. Mizushima S., Fujibayashi Y. and Shiiki K., J. Phys. Soc. Japan 30, 299(1971).
4. Ogrin Yu. F., Lutskii V. N. and Elinson M. I., Soviet Phys. Solid State 9 2547 (1968).
5. Sandmirskii V. B., Soviet Phys. JETP 25 101(1967).

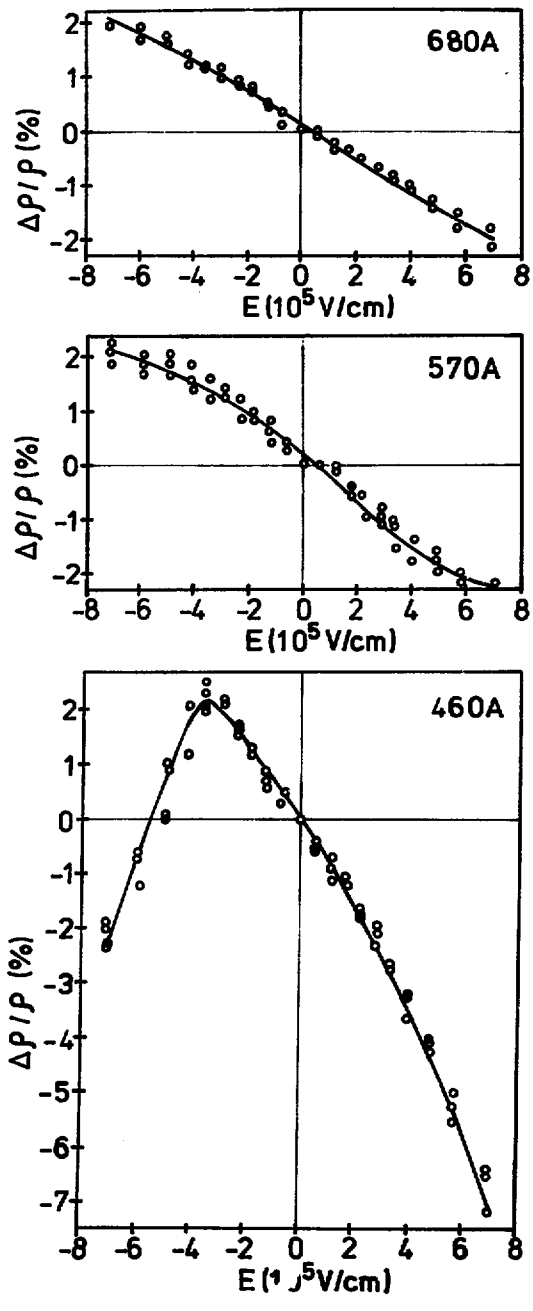


Fig.1. Resistivity as a function of electric field applied perpendicularly to the surface for various crystal thickness at 4.2K.

ESAKI KINK EFFECT IN GRAPHITE

Sanchi Mizushima and Yoshiko Fujibayashi
School of Engineering, Keio University, Yokohama, Japan

Introduction

The Esaki kink effect is a phenomenon discovered by L. Esaki[1] on bismuth; the current vs. voltage relation shows a sharp kink at a certain voltage when the specimen is subjected to a transverse magnetic field at low temperatures. The cause of this effect is explained as follows. As shown in Fig. 1, the

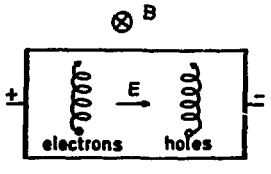


Fig.1 Transverse drift of carriers

electrons and holes drift in the transverse direction if the electric and magnetic fields are applied perpendicularly, as long as the scattering can be neglected. When the drift velocity reaches the velocity of phonons, stimulated emission of phonons begins, hindering the further rise of the velocity of carriers in the transverse direction, thus increasing the current in the direction of the electric field.

In this study we looked for the same effect in graphite, and could clarify a peculiar feature of this material in this effect[2].

Experimental

Since the Esaki effect is a high field phenomenon and the electric conductivity of graphite is rather high, prevention of the temperature rise during the current pulse is important. It was necessary to make the specimen very thin and expose its surface directly to the coolant.

Specimens were prepared from single crystals by cleaving along the basal plane to below one thousand angstroms, cementing to a tip of glass slide and cutting into a four terminal structure under a microscope.

The current-voltage curve was obtained by applying square current pulse of different value to the specimen, and observing the voltage and current on an oscilloscope at a determined time after the start of the pulse. The kink effect needs a finite build-up time; each experimental curve is thus a function of the pulse length.

All experiments were done by dipping the specimen in liquid nitrogen or air, in other words, at about 80 K.

Results

It was found after many runs of experiment that the behavior of the kink effect changes drastically with the carrier mobility.

Fig. 2 shows a typical result of low mobility specimens. Here, the mobility is 1.0×10^4 cm^2/V·s. In this figure, the two

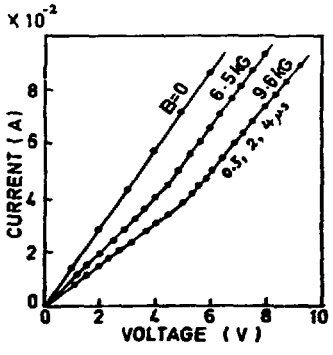


Fig.2 Kinks of a low mobility specimen

curves under the magnetic field have only one kink each, becoming parallel to each other at voltages above the kink, just in the same way as in bismuth.

It is also seen that the curves remain unchanged from 0.5 to 4 μs. This means that the build-up time is quite short, below 0.5 μs.

The velocity of phonons, s, that cause the kink can be calculated as equal to the transverse component of the drift velocity of carriers at the kink as,

$$s = (E/B)/[1 + (\omega_c \tau)^{-2}]$$

where E is the electric field, B the magnetic field, ω_c the cyclotron frequency and τ is the relaxation time of carriers. $\omega_c \tau$ may be determined from the magnetoresistance.

The kink appearing in our low mobility specimens gives on the average 8 km/s as the transverse drift velocity of carriers. This value corresponds roughly to the propagation velocity of transverse lattice vibrations, which is actually 12 km/s in the long wavelength region.

From this result we can say that in low mobility specimens, that is, in defective material, drifting carriers interact strongly with transverse phonons.

Nextly, Fig. 3 represents the results of measurement done on specimens of intermediate mobility. Here, the curves show somewhat complicated behavior.

For a short pulse, 0.5 μs in the figure, there appears a weak kink or the low field kink at first in the course of voltage increase, written as K for the curve of 9.6 kG; then the curves approach straight lines. The point of intersection of the initial ohmic curve and the high field straight line gives the second kink, shown as K' in case of 9.6 kG, which may be called high field kink.

On the other hand, when the pulse is suf-

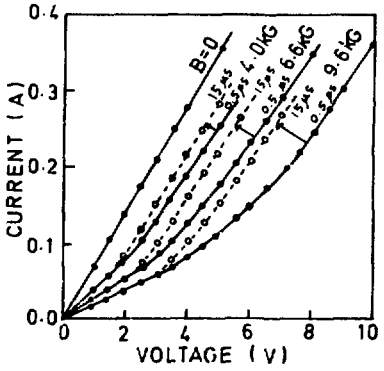


Fig.3 Kinks of an intermediate mobility specimen

ficiently long, 15 μs in the figure, the curves become another set of straight lines starting from the low field kink.

The low field kink in the figure corresponds to the kink in Fig. 2, because the calculated drift velocity has the same value of about 8 km/s, and moreover after a long pulse every curve approaches a fully-developed Esaki curve with a single kink. Therefore, this kink is due to the interaction of carriers with transverse phonons. But the long build-up time indicates that in this material the interaction is weak.

The high field kink, which had to be determined by extrapolation in the above figure, is considered to correspond to the interaction between carriers and longitudinal lattice vibrations; the velocity of relevant phonons was calculated as 17 km/s.

It is to be noted here that the interaction with longitudinal phonons is so strong, that even 0.5 μs pulse is long enough for the full developement of the "high field" kink effect.

Experiments were made then on specimens of highest mobility. Somehow, these specimens broke down easily when the electric field exceeded the high field kink. Anyway, an example is given in Fig. 4. The mobility of this specimen is 2.2 X 10^4 cm^2/V s. As seen in the figure, the low field kink is now very weak. The high field kink could not be studied enough, but lies at around 5.5 V.

It was found incidentally that at electric fields slightly higher than the high field kink in Fig. 4 the change of voltage with time observed on the oscilloscope shows a kind of two-step relaxation as sketched in the same figure.

The hump N appears only in a very limited range of applied current; it moves quickly from right to left with a slight increase of current, disappearing into the initial ringing region. It is apparent that the initial relaxation of voltage is caused by the high field effect, while the second one by the low field effect. The relaxation time or the build-up time of the former effect is judged to be extremely short except in the neighborhood of the high field kink.

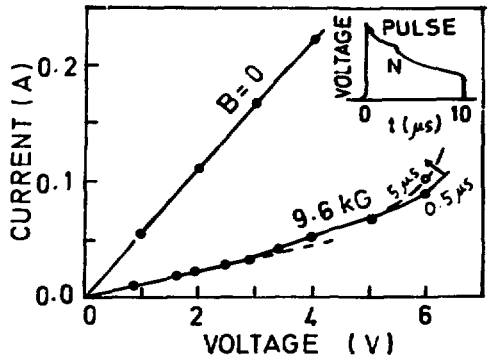


Fig.4 Kinks of a high mobility specimen

Discussion and conclusion

As shown above, in specimens of low carrier mobility, or defective material, the kink effect appears with a short build-up time when the drift velocity of carriers in the transverse direction becomes about 8 km/s. This value agrees roughly with the velocity of transverse lattice vibrations. On the other hand, in crystals of high mobility the above kink or the low field kink becomes weak and needs a long build-up time, while at higher electric fields the other kink comes out with a very short build-up time when the drift velocity reaches about 17km/s, corresponding to the longitudinal lattice vibrations in the basal plane.

Drift velocities of carriers at the kink field are a little smaller than expectation; one reason might be the distribution of the carrier mobility, while another the samllness of the applied magnetic field.

It is concluded that carriers have a strong interaction with longitudinal lattice waves, but if the crystal is defective the interaction with transverse waves becomes also important.

References

1. Esaki L., Phys. Rev. Letters 8,4(1962)
2. Mizushima S. and Fujibayashi Y., J. Phys. Soc. Japan 38,1027(1975)

TWO TYPES OF BROADENING OF THE ESR LINE IN THE TRANSITION REGION, EFFECTS OF OXYDIZING ATMOSPHERE

S. Mrozowski
Department of Physics and Astronomy, Ball State University
Muncie, Indiana 47306

The nature of the broadening of the ESR line in carbons occurring in the heattreatment range of 900-1500°C was investigated. It is shown that the broadening upon reheat (Hennig-Smaller effect) is due to impurities; also how this and the silicon broadening can be eliminated. On the other hand, a strong broadening is found to occur upon original heattreatment or anneal of neutron irradiated material which is connected with some internal structural changes in the carbon material itself. The influence of the chlorine, oxygen and water, as well as of a reheat upon this type of broadening, was studied.

RELATIONSHIP BETWEEN PREFERRED ORIENTATION, THERMAL EXPANSION, AND COKE PREPARATION TEMPERATURE OF SOME EXPERIMENTAL GRAPHITES*

O. J. Horne+ and C. R. Kennedy
Oak Ridge National Laboratory#
Oak Ridge, Tennessee 32830

Introduction

Efforts to improve the overall thermal stress resistance of specialty graphites have centered upon increasing the isotropy of the graphite structure. In order to effectively determine the effect of these various methods of isotropy improvement, objective quantitative methods of anisotropy measurements are necessary and are the secondary topic of both this and the succeeding paper.

It should be understood that graphite has both a crystallographic and a defect anisotropy which affect physical properties. These are generally inter-related and are strongly influenced by the fabrication procedure. While the effects of crystallographic anisotropy are reasonably understood[1,2,3], the effects of defect anisotropy on the physical properties are vague. These defects will strongly affect both the thermal expansion as well as the mechanical properties, thus having a strong effect on the overall thermal resistance.

In the present study, CTE's of a series of graphites were found to vary regularly with coke preparation temperature. These graphites have been examined to determine whether the CTE differences were due to orientation or structural differences resulting from the modifications in the fabrication procedures.

Orientation effects were determined by use of an X-ray diffraction technique conceived by Jetter and Borie[4] and applied to graphite by Cavin[5]. This technique directly yields the crystallite orientation processing variables. Values of the preferred orientation parameter R were also calculated from both CTE and electrical resistivity data. Thus, direct comparisons were made between the actual crystallographic preferred orientation, the CTE anisotropy with a c-axis accommodation type of defect structure and the resistivity anisotropy with a defect structure that hinders conductivity in the a-axis.

Experimental

A. Sample Preparation

The H1 graphites were fabricated from experimental green cokes prepared from A-240 petroleum pitch obtained from Ashland Oil Company. The green cokes were prepared by fusing approximately 1800 g of A-240 pitch in carbon boats for 1 hour at 575, 600, 650, or 675 C under an inert atmosphere. After firing, the cokes were ground and dry-mixed with appropriate amounts of A-240 pitch binder and subsequently slurry-blended with benzene until reasonably dry. After grinding to -120 mesh, the mix was warm molded at approximately 95 C at a pressure of 2000 psi. The 1.6-inch-diameter blocks were cooled under pressure and placed in restraining holders. After heat treatment to 1000 C on a controlled 3-day cycle, the carbonized blocks were removed from the restraining holders and heated to 2800 C on a 1-day cycle. The graphitized bodies were then machined for physical and orientation property measurement specimens.

B. Property Measurements

The CTE's (room temperature to 1000 C) were calculated using data obtained from a TemPres TD-710 dilatometer.

X-ray diffraction data, obtained from spherical samples machined on one end of a cylindrical stem, were determined by use of a North American Phillips X-ray diffraction unit. Readings of intensity of the diffracted beam at various orientations of the anisotropic sphere and of the background radiation were made by the ORTEC Model 432A Digital Rate Meter and recorded on teletype tape.

Orientation parameters were subsequently calculated from (1) X-ray diffraction data[5], (2) from CTE measurements[4] using

$$\frac{1}{R_{\parallel}} = 0.5 \frac{CTE_{\parallel}}{CTE_{\perp}} + 1.0$$

and (3) from electrical resistivity (ρ) values[4] using

$$\frac{1}{R_{\parallel}} = \frac{\rho_{\parallel}}{\rho_{\perp}} + 0.5.$$

Accommodation factors were calculated using[2]

$$\sigma_{oz} = R_{oz}\sigma_{oz} + (1-R_{oz})\,\gamma_{oz}\sigma_{c} .$$

Results and Discussion

Properties of the experimental graphites are listed in Table 1.

As indicated in Figure 1, the binder content did not noticeably affect the CTE measurements. But a significant decrease in the CTE parallel with the molding direction, accompanied by an equivalent change in the perpendicular direction, occurred with increasing heat treatment temperature. As shown in Figure 2, no change in crystallite orientation was revealed by X-ray analysis. As illustrated in Figure 3, the accommodation factor showed a significant decrease with increasing heat-treatment temperature.

Thus, the CTE differences were due to structural differences resulting from the heat-treatment temperature variation in that the development of an internal microcrack defect structure increased with increasing coking temperature.

* This work was funded by the U.S. Naval Surface Weapons Laboratory under the REVMAT Program.
+ Present address: Battelle Columbus Laboratories
505 King Avenue
Columbus, Ohio 43201
Operated for the Energy Research and Development Administration by Union Carbide Corporation.

References

1. G. E. Bacon, J. Appl. Chem. 6, 477 (1956).
2. R. J. Price and J. C. Bokros, Carbon 6, 18-97 (1964)
3. W. N. Reynolds, Carbon 6, 277 (1968).
4. L. K. Jetter and B. S. Borie, Jr., J. Appl. Phys. 24, 532 (1953).
5. O. B. Cavin, Preferred Orientation and its Effect on Radiation Stability, paper presented at the EURATOM meeting, "The Effects of Fast Neutron Irradiation at Temperatures above 600°C on the Physical and Mechanical Properties of Graphite and Pyrocarbons," Brussels, Belgium, May 5-6, 1969.

TABLE 1. EFFECT OF HEAT TREATMENT TEMPERATURE ON PHYSICAL PROPERTIES OF GRAPHITE

Sample Number	A-240 Binder Content (pph)	Molding Pressure (psi)	Heat Treatment Temperature[d] (C)	Orientation Parameter $R_{\parallel}$[a] (from X-ray Measurements)	Measured CTE (C^{-1}, x 10^6) $\parallel$	Measured CTE (C^{-1}, x 10^6) $\perp$	$R_{\parallel}$ (from CTE Values)	Accommodation Factor $\gamma_{\parallel}$	Measured Electrical Resistivity (ρ, $\mu\Omega$-cm)		$R_{\parallel}$ Calculated (from Electrical Resistivity)
H1-78B	10	2000	575	0.5717	7.0	5.1	0.5930	0.53	1730	1110	0.4658
H1-78C	12	2000	575	0.5645	8.2	5.0	0.5495	0.62	1690	920	0.4279
H1-78D	14	2000	575	0.5980	7.4	4.8	0.5647	0.60	1550	830	0.4224
H1-85A	12	2000	600	0.5735	6.9	4.0	0.5369	0.53	2360	1740	0.4733
H1-85B	14	2000	600	0.5650	6.6	4.2	0.5600	0.49	1620	1080	0.5000
H1-86C	16	2000	600	0.5903	6.8	4.2	0.5526	0.54	1750	1030	0.4547
H1-82A	12	2000	650	0.5597	5.8	3.7	0.5606	0.43	2970	1370	0.3600
H1-82B	14	2000	650	0.5894	5.8	3.7	0.5606	0.46	2650	1550	0.4526
H1-82C	16	2000	650	0.5790	5.8	3.7	0.5606	0.45	2080	1293	0.4134
H1-84C	12	2000	675	0.5755	5.2	3.2	0.5517	0.39	3110	--	--
H1-84D	14	2000	675	0.5851	5.2	3.2	0.5517	0.40	2020	1560	0.4588

[a] From x-ray diffraction data.

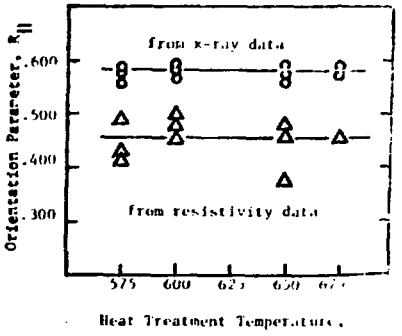


Fig. 2. Orientation Parameter as a Function of Heat-Treatment Temperature.

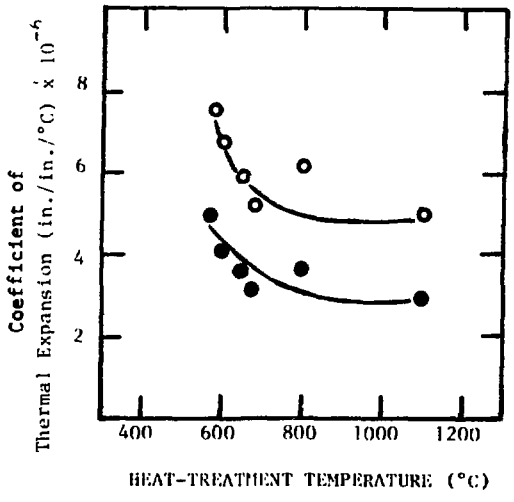


Fig. 1. The Effect of A-240 Pitch Heat-Treatment Temperature on the Coefficient of Thermal Expansion of Graphites Fabricated from A-240-Derived Cokes.

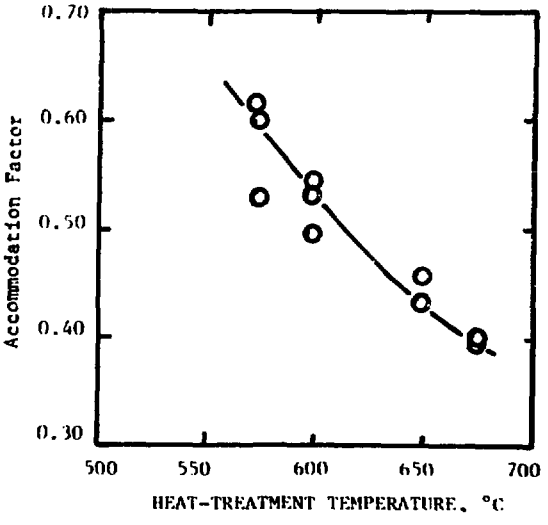


Fig. 3. Accommodation as a Function of Heat-Treatment Temperature.

RELATIONSHIP BETWEEN PREFERRED ORIENTATION, THERMAL EXPANSION, AND MOLDING PRESSURE OF SOME EXPERIMENTAL GRAPHITES*

O. J. Horne+ and C. R. Kennedy
Oak Ridge National Laboratory#
Oak Ridge, Tennessee 37830

Introduction

Efforts to improve the overall thermal stress resistance of specialty graphites have centered upon increasing the isotropy of the graphite structure. In order to effectively determine the effect of these various methods of isotropy improvements, objective quantitative methods of anisotropy measurements are necessary and are the secondary topic of both this and the succeeding paper.

It should be understood that graphite has both a crystallographic and a defect anisotropy which affect physical properties. These are generally inter-related and are strongly influenced by the fabrication procedure. While the effects of crystallographic anisotropy are reasonably understood[1,2,3], the effects of defect anisotropy on the physical properties are vague. These defects will strongly affect both the thermal expansion as well as the mechanical properties, thus having a strong effect on the overall thermal resistance.

In the present study, CTE's of a series of graphites were found to vary regularly with molding pressure. These graphites have been examined to determine whether the CTE differences were due to orientation or structural differences resulting from the modifications in the fabrication procedures.

Orientation effects were determined by use of an X-ray diffraction technique conceived by Jetter and Borie[4] and applied to graphite by Cavin[5]. This technique directly yields the crystallite orientation processing variables. Values of the preferred orientation parameter R were also calculated from both CTE and electrical resistivity data. Thus, direct comparisons were made between the actual crystallographic preferred orientation, the CTE anisotropy with a c-axis accommodation type of defect structure and the resistivity anisotropy with a defect structure that hinders conductivity in the a-axis.

Experimental

A. Sample Preparation

The H2 graphites were fabricated from high quality acicular green coke supplied by Great Lakes Carbon Corporation. After addition of 20. pph of 30-m pitch obtained from Allied Chemical Corporation, the mixture was slurried in benzene, stirred until dry and then mikropulverized. After firing for 1 hour at 325-350 C, the modified coke was again mikropulverized. Appropriate quantities of A-240 binder pitch (obtained from Ashland Oil Company) were dry mixed with the modified filler and subsequently slurry blended using benzene until reasonably dry. After grinding to -120 mesh, the mix was warm molded at approximately 95 C and at pressures of 1000, 1500, 2000, and 3000 psi. The 1.6-in.-diameter blocks were placed into restraining holders. After carbonization to 1000 C on a controlled 3-day cycle, the carbonized blocks were removed from the restraining holders and heated to 2800 C on a 1-day cycle. The graphitized bodies were then machined to obtain samples for the physical and orientation property measurements.

B. Property Measurements

The CTE's (room temperature to 1000 C) were calculated using data obtained from a TemPres TD-710 dilatometer.

X-ray diffraction data, obtained from spherical samples machined on one end of a cylindrical stem, were determined by use of a North American Phillips X-ray diffraction unit. Readings of intensity of the diffracted beam at various orientations of the anisotropic sphere and of the background radiation were made by the ORTEC Model 432A Digital Rate Meter and recorded on teletype tape.

Orientation parameters were subsequently calculated from (1) X-ray diffraction data[5], (2) from CTE measurements[4] using

$$\frac{1}{R_{\parallel}} = 0.5\,\frac{CTE_{\parallel}}{CTE_{\perp}} + 1.0$$

and (3) from electrical resistivity (ρ) values[4] using

$$\frac{1}{R_{\parallel}} = \frac{\rho_{\parallel}}{\rho_{\perp}} + 0.5 \quad .$$

Accommodation factors were calculated using[2]

$$\alpha_{oz} = R_{oz}\,\alpha_{oz} + (1-R_{oz})\,f_{oz}\,\alpha_{c} \quad .$$

Results and Discussion

Properties of the experimental graphites are listed in Table 1.

As indicated in the Table and in Figure 1, the binder content did not noticeably affect the CTE measurements of the graphites. However, the with-grain CTE shows a constant value with increasing mold pressure while the across-grain CTE increases with molding pressure. Thus, the degree of CTE anisotropy is directly proportional to mold pressure. The direct dependence of anisotropy on molding pressure was a reflection of a corresponding increase in the degree of preferred orientation with mold pressure. This would indicate a decrease in the orientation parameter R measured in the direction of molding. However, when the samples were analyzed by X-ray diffraction, no change in R in either direction was observed to occur with varying molding pressure (Figure 2). A change in CTE with no change in crystallite orientation must be attributed to a change in the degree of accommodation. Thus, as shown in Figure 3, $\gamma_{\parallel}$ increases and the degree of formation of microcracks which accommodate thermal expansion in the parallel direction decreases with increasing molding pressure.

* This work was funded by the U.S. Naval Surface Weapons Laboratory under the REVMAT Program.

+ Present Address: Battelle Columbus Laboratories, 505 King Avenue, Columbus, Ohio 43201

Operated for the Energy Research & Development Administration by Union Carbide Corporation.

References

1. G. E. Bacon, J. Appl. Chem. 6, 477 (1956).
2. R. J. Price and J. C. Bokros, Carbon 6, 18-97 (1964).
3. W. N. Reynolds, Carbon 6, 277 (1968).
4. L. K. Jetter and B. S. Borie, Jr., J. Appl. Phys. 24, 532 (1953).
5. O. B. Cavin, Preferred Orientation and its Effect on Radiation Stability, paper presented at the EURATOM meeting, "The Effects of Fast Neutron Irradiation at Temperatures above 600°C on the Physical and Mechanical Properties of Graphite and Pyrocarbons," Brussels, Belgium, May 5-6, 1969.

TABLE 1. EFFECT OF MOLD PRESSURE ON PHYSICAL PROPERTIES OF GRAPHITE

Sample Number	A-240 Binder Content (pph)	Molding Pressure (psi)	Heat Treatment Temperature[a] (C)	Orientation Parameter $R_{\parallel}$[b] (from X-ray Measurements)	Measured CTE (C^{-1}, x 10^6) ∥	Measured CTE (C^{-1}, x 10^6) ⊥	$R_{\parallel}$ (from CTE Values)	Accommodation Factor $\gamma_{\parallel}$	Measured Electrical Resistivity (ρ $\mu\Omega$-cm)		$R_{\parallel}$ Calculated (from Electrical Resistivity)
H2-8E2	9	1000	-	0.5764	7.30	5.13	0.5843	0.563	1320	800	0.4431
H2-10A2	10.5	1000	-	0.5819	7.30	5.13	0.5843	0.570	1240	800	0.4876
H2-12A2	12	1000	-	0.5876	6.88	4.97	0.5910	0.543	1180	770	0.4920
H2-8F1	9	1500	-	0.5869	7.04	5.13	0.5931	0.556	1230	740	0.4625
H2-10B1	10.5	1500	-	0.5824	7.04	5.13	0.5931	0.550	1170	780	0.5000
H2-12B2	12	1500	-	0.5974	6.92	5.26	0.6032	0.560	1160	760	0.4935
H2-8C1	9	2000	-	0.5637	7.30	4.93	0.5746	0.547	1260	730	0.4492
H2-10C1	10.5	2000	-	0.5783	7.53	5.01	0.5709	0.584	1190	710	0.4595
H2-12C2	12	2000	-	0.5219	7.45	5.00	0.5721	0.511	1170	680	0.4503
H2-8D4	9	3000	-	0.5777	7.67	5.04	0.5679	0.594	1310	770	0.4543
H2-10D4	10.5	3000	-	0.5941	7.54	4.92	0.5910	0.607	1180	770	0.4970
H2-12D2	12	3000	-	0.5656	8.06	5.17	0.5620	0.609	1380	830	0.4624

[a] As-received coke was fired at 500°C for 1 hr (H2 series).

[b] From x-ray diffraction data.

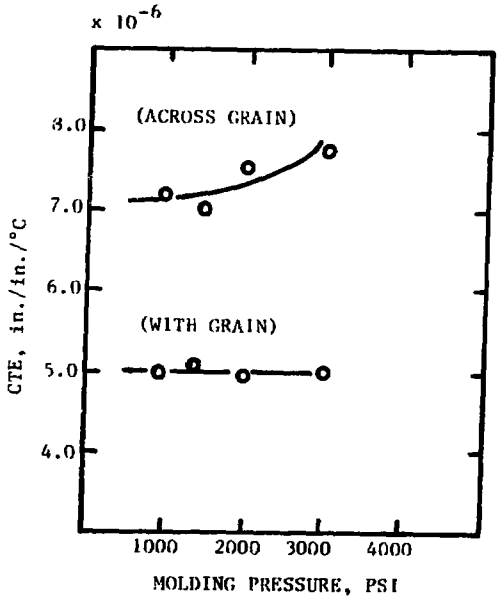


Fig. 1. The Effect of Mold Pressure on the CTE of Experimental Graphites.

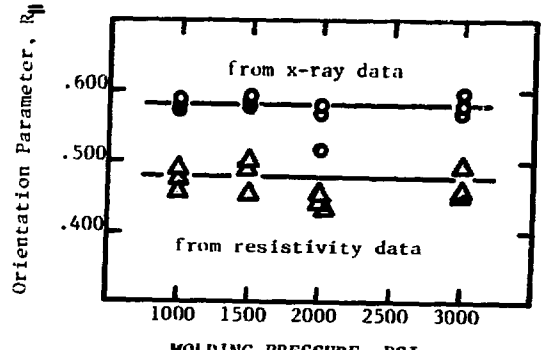


Fig. 2. Effect of Molding Pressure on the Orientation Paramter $R_{\parallel}$

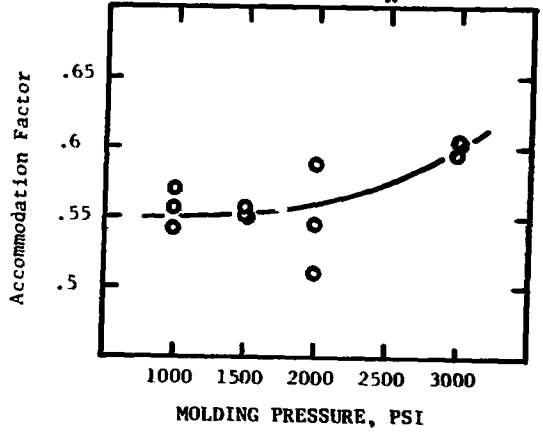


Fig. 3. The Effect of Mold Pressure upon the Accommodation Factor.

NUCLEAR GRAPHITES BASED ON COAL TAR PITCH
BEHAVIOUR UNDER NEUTRON IRRADIATION BETWEEN 400 AND 1400°C

P.MOTTET, A.FILLATRE, P.CHILL, G.MICAUD
Commissariat à l'Energie Atomique, CEN Saclay (France)

J.LORE, P.COPINAULT
Groupe Péchiney Ugine Kuhlmann, PARIS (France)

1. INTRODUCTION

Two semi-isotropic graphites based on coaltar pitch coke have been developed for use as a moderator in HTGRs. This paper summarizes the dimensional changes and the evolution of the physical and mechanical properties of P_3JHAN and P_3JHA_2N graphites under the effect of neutron irradiation.

2. MATERIALS

P_3JHAN and P_3JHA_2N graphites based on coal tar pitch coke are manufactured by extrusion according to a classical process. Their physical and mechanical properties are described in table I. The anisotropy factor of these graphites falls between 1.3 and 1.4, with coefficients of thermal expansion (CTE) between those of anisotropic petroleum coke graphites and gilsocoke graphites. If the thermal conductivity is slightly lower than that of petroleum coke graphites, the density and mechanical characteristics are improved due to the excellent compatibility between the filler and the binder /1/.

3. BEHAVIOUR UNDER NEUTRON IRRADIATION

More than 1200 samples of P_3JHAN, taken from both the axial and radial directions, have been irradiated in the Osiris (Saclay), HFR (Petten), and ORR (Oak Ridge) reactors. The maximum fluence thus far reached is 12×10^{21} n.cm^{-2} ϕFG* in the case of P_3JHAN and 4×10^{21}n.cm^{-2} for P_3JHA_2N. Irradiation temperatures for both graphites have ranged from 400°C to 1400°C.

3.1. Dimensional changes

The dimensional behaviour of P_3JHAN and P_3JHA_2N graphites is shown in figures 1 and 2. No significant effect of the impregnation has been observed between the two graphites.

The maximum axial shrinkage is 4,5% at 1350°C with a turnaround near 7.10^{21}n.cm^{-2} ϕFG. At lower temperatures, between 500 and 1100°C, shrinkage continues up to 10^{22}n.cm^{-2} ϕFG.

In the radial direction, the maximum shrinkage is about 2.2% at 1350°C and 5×10^{21}n.cm^{-2}. The turnaround occurs at higher fluences when the irradiation temperature is decreased. Expansions are observed above approximately 10^{22}n.cm^{-2} ϕFG as new porosity is generated /2/.

3.2. Evolution of physical properties

The CTEs measured between 25 and 425°C, increase slowly with fluence at low temperatures and decrease at temperatures higher than 700°C. The variation does not exceed 10%.

Figures 3 and 4 show the degradation of the thermal conductivity of P_3JHAN graphite in the axial and radial directions, respectively. A saturation appears at approximately 2×10^{21} n.cm^{-2} ϕFG, although the decrease in conductivity is smaller at increased irradiation temperatures.

3.3. Variation of mechanical properties

The fraction
versus fluence for P_3JHAN graphite is shown in figure 5. The increase in the modulus of elasticity is greater when the irradiation temperature is lower.

Stress-strain curves have been drawn from irradiated specimens. We observed two different types of behaviour depending on the irradiation temperature. Between 500 and 900°C the graphite strains with a constant energy /3/, while above 900°C the energy changes without strain variation /4/.

4. CONCLUSION

The pitch coke graphites studied are less stable than petroleum coke graphites of comparable CTE and anisotropy. This seems to indicate that the fibrous structure of the coke has a preponderant effect under neutron irradiation. This study of characterization before and after irradiation has allowed to specifiey the conditions under which these graphites may be used in HTGRs.

* graphite damage fluence =
1.25 fluence E > 0.18 MeV =1.85 EDN fluence

Bibliography

/1/ J.P. AUBERT, J.IANAYE, A.BUGAILLON
Mouillabilité des cokes par le brai
Carbon Conf. Baden-Baden
preprints p 375, 1972

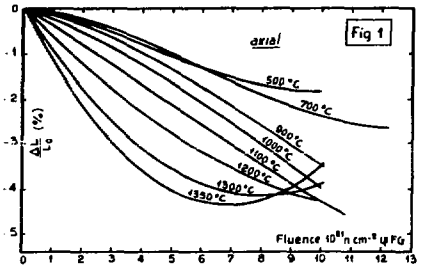
/2/ G.R.INGLE, J.C.HOKKOS
10th Biennial Conf. on Carbon
Bethlehem, Penn., 1971

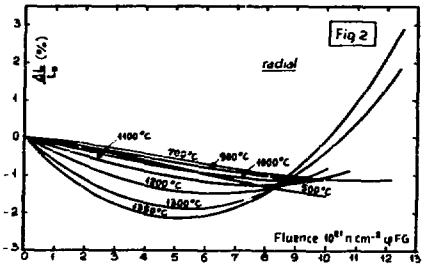
/3/ J.S.OCHARD, H.H.W.LOTTY
Proc. fifth Carbon Conf.
Vol 1, p 519, 1962

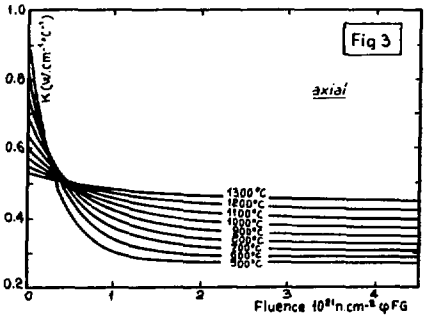
/4/ M.R.E.EVERETT, F.RIDEALGH
Carbon Conf. Baden-Baden
preprints p 191, 1972

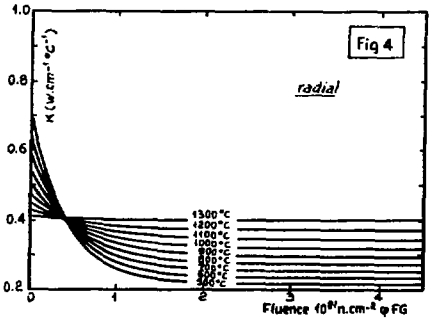
Physical and mechanical properties
of the PyHWN and PyHWyN graphite

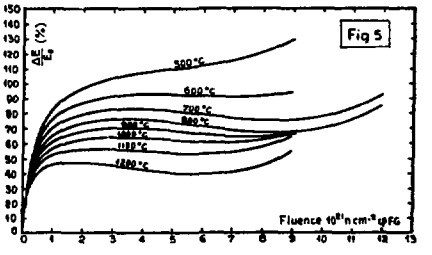
Graphite	PyHWN		PyHWyN	
Direction	axial	radial	axial	radial
Bulk density $g.cm^{-3}$	1.73	1.73	1.71	1.71
Thermal expansion $\bar{\alpha}$ 525°C / 25°C $10^{-6}\ °C^{-1}$	3.05	4.21	3.08	4.23
Thermal conductivity W $cm^{-1}\ °C^{-1}$	1.54	1.18	1.70	1.29
Young Modulus daN mm^{-2}	1005	709	1143	772
Tensile strength daN mm^{-2}	1.12	0.76	1.44	0.98











ISOTROPIC NUCLEAR GRAPHITE. THE EFFECT OF NEUTRON IRRADIATION

J.DEE, A.BELLAMY
Groupe Méchinay Ugine Kuhlmann, Paris (France)

P.MOTTET, G.MOYNE
Commissariat à l'Energie Atomique, CEN Saclay (France)

1. INTRODUCTION

The search for nuclear graphites having a behaviour that is sufficiently stable and isotropic under neutron irradiation has led manufacturers to use isotropic cokes or to carry out isostatic pressing of a fine grain coke/pitch mixture. In the former case there is a difficulty in supplying coke while in the second case the manufacturing cost is rather high.

COMBAULT et al /1/ have shown that the macroscopic properties of electro-graphites depend mainly on the nature of the coke used, characterized by its apparent dilatability α_a (axial expansion of a cylindrical specimen made under special conditions /2/ /3/ starting with finely crushed coke).

The principal industrial forming processes (extrusion or pressing), intended for the manufacture of graphite from carbonaceous mixtures, can be considered as uniaxial because they tend to orient the grains of coke in the same direction. There exist, however, multiaxial forming processes which cause the grains to be randomly oriented so that no preferred direction is apparent. Among the different multidirectional processes one can number isostatic pressing, extrusion with alternative pressing, and pre-extrusion after multiple crushings of a fine-grained cured product. It is thus possible to prepare macroscopically isotropic graphites from any coke and in particular, from cokes as anisotropic as needle cokes. An additional advantage of these isotropic graphites is that they have low coefficients of thermal expansion (CTE) which lead to lower thermal stresses.

2. EXPERIMENTAL PROCEDURES

Isotropic graphites made from several types of cokes (pitch and petroleum cokes) with an apparent dilatability ranging from 1.20 and 3.60 have been prepared by using multidirectional forming processes. All of these graphites have been fabricated from a mixture composed of typical coal tar pitch (KS = 92°C) and crushed coke. The maximum grain size of the coke is 1.6 mm except for the grade PZ 130 of which the maximum grain size is 0.4 mm. All of these products were cured at 1000°C and have been impregnated once or twice with pitch before graphitization at 2700°C and purification.

3. PHYSICAL AND MECHANICAL PROPERTIES OF THE PRODUCTS

The main characteristics of these products are shown on Table I. One may note that all the graphites are isotropic with respect to thermal expansion. They have lower CTE than graphites prepared from isotropic cokes like gilsocoke (CTE about 5 to 6.10^{-6} °C^{-1}). P_2HAN and P_2HA$_2$N graphites, prepared from pitch coke by normal extrusion, are less isotropic. Pitch impregnation carried out before graphitization enable one to obtain high densities and mechanical characteristics comparable to those of conventional graphites.

4. BEHAVIOUR UNDER NEUTRON IRRADIATION

The irradiation of these graphites have been carried out in the fast neutron reactor Rapsodie (Cadarache), between 800°C and 1400°C and at fluences up to $1.7\ 10^{22}$ n.cm^{-2} ϕIC*. In addition to the graphites noted above, two fine grain isotropic graphites (ref. 5.1134 and 5.1135) manufactured by Le Carbone Lorraine Co (Gennevilliers) have been irradiated.

The dimensional changes as a function of fluence are shown on Figures 1 and 2 and lead to the following remarks :

- the product PZ 130, which is distinguished from PZ 140 by the grain size, exhibits pre-isotropy and larger axial dimensional changes.
- the non impregnated products PZ 140, PZ 138, PZ 141 undergo isotropic changes : they expand at lower fluences and at higher rates for simply or doubly impregnated products.
- the graphite PZ 140 based on an isotropic petroleum coke has a more stable behaviour than PZ 143 graphite made from more isotropic pitch coke.
- the products 5.1134 and 5.1135, in spite of their fine textures, exhibit dimensional changes equivalent to the above graphites. However, their behaviour is not as good as other fine-grained graphites /4/. One will note the low dimensional stability of the petroleum coke graphite in spite of its lower CTE.
- in general, these isotropic graphites are less stable than P_2HAN and P_2HA$_2$N except for the non impregnated products.

The CTE of the impregnated graphites do not change greatly in contrast to those of non impregnated graphites which undergo large variations.

The thermal conductivity of the impregnated graphites drops very rapidly as a function of fluence and then saturates at a level varying according to the state of initial graphitization. At fluences greater than $1.2\ 10^{22}$ n.cm^{-2} ϕIC, the thermal conductivity undergoes a second degradation which occurs at higher fluences if the graphite has a better stability.

* graphite damage fluence = 1.25 fluence E > 0.18 MeV = 1.85 EDN fluence

5. CONCLUSION

The use of multidirectional forming processes enables one to obtain isotropic graphites from anisotropic cokes. Under neutron irradiation these graphite exhibit isotropic behaviour. Their dimensional stability is **lower** than that of graphites based on isotropic cokes or made by isostatic pressing of fine grained coke/pitch mixtures.

Bibliography

/1/ P.CONNAULT, P.LUCHAIRIAN, M.VOUTE
Classement des cokes suivant leur dilatabilité apparente
Carbon Conf. Baden-Baden
preprints p. 371, 1972

/2/ P.CONNAULT, J.LAHC, J.PAILLISSON, M.VIAL, P.MOTTET
Changes in the properties of Nuclear Graphites obtained from a mixture of cokes
10th Biennial Conf. on Carbon
Bethlehem, Penn., 1971

/3/ C.F.COUT, M.JANEL, J.A.HIBL
Technical Documentary Report
WAPD TR 61.7, p. XXXVI, p. 1-, Oct. 19

/4/ P.MOTTET, G.HICAUD
Graphite obtenu par pressage isostatique
Comportement sous irradiation neutronique
CEA-N 1[illegible], Sept. 19

Table I - Physical and mechanical properties of isotropic graphites

Ref. graph.	Coke nature	α_d (1)	Forming Process (2)	Pitch Impreg.	Density g.cm^{-3}	CTE $\bar{\alpha}_{25}^{526}$ 10^{-6}°C^{-1} axial	CTE radial	Anisotropy α_t/α_a	Resistivity (μΩ cm) axial	Resistivity (μΩ cm) radial	Tensile Strength daN.cm^{-2} (3) axial	Tensile Strength daN.cm^{-2} (3) radial
P$_3$JHAN	Pitch coke	3.0	U	1	1.74	3.05	4.71	1.55	900	1165	15[illegible]	9[illegible]
P$_3$JHA$_2$N	Pitch coke	3.0	U	2	1.79	3.08	4.23	1.35	860	1066	175	110
PZ 130	Regular Petroleum coke	2.15	M	1	1.74	3.06	3.80	1.24	995	1076	205	150
PZ 135	Premium Petr. needle coke	1.20	M	0	1.61	2.40	2.65	1.10	1220	1140	-	9[illegible]
PZ 138	Regular Petr.	2.15	U	0	1.57	3.20	2.99	0.90	1340	1140	-	100
PZ 143	Regular Petr.	2.15	M	2	1.75	3.25	2.96	0.91	875	780	150	110
PZ 140	Pitch coke	3.6	M	0	1.59	4.15	4.15	1	1650	1520	-	105
PZ 145	Pitch coke	3.6	M	2	1.81	4.96	4.65	0.95	1100	1040	165	150
S.1139	Petr. coke	-	S	1	1.65	3.12	3.12	1	1500	1500	-	-
S.1365	Pitch coke	-	S	1	1.79	5.06	5.28	1.04	1560	1550	-	-

(1) apparent dilatability of coke
(2) U = uniaxial forming process, M = multiaxial forming process, S = special forming process
(3) measured on "diabolo" specimens

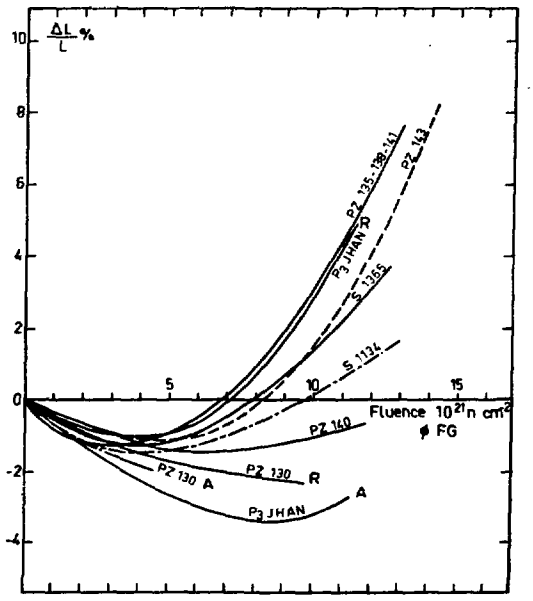


Fig 1. Dimensional changes at 1000°C

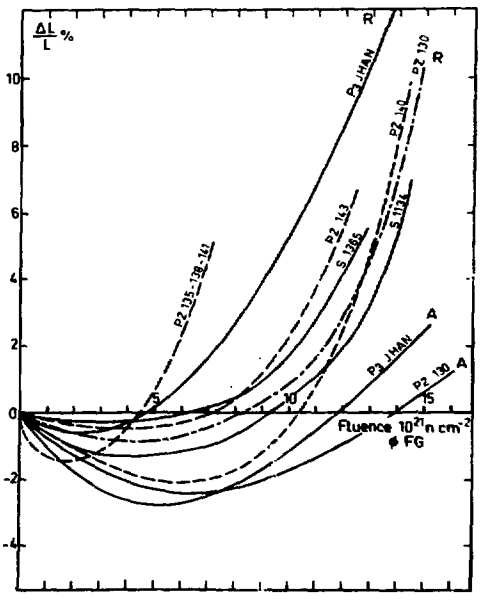


Fig 2. Dimensional changes at 1300°C

PROPERTIES AND BEHAVIOUR UNDER IRRADIATION OF ISOTROPIC FINE GRAINED GRAPHITES

J. MAIRE J. FOURRE A. PERNOLLET

LE CARBONE LORRAINE
37/41 rue Jean Jaurès
92230 Gennevilliers France

Le Carbone Lorraine (LCL) has manufactured for a long time fine grained graphites with high properties. On the 1st table one notes the values of the properties of grades 3780, 2239, 5890 wich are commercial products.

To answer Nuclear Energy requirements LCL has prepared a fine grained isotropic material grade 7477 by isostatic molding. It's possible to obtain prismatic blocks useful for HTR and graphite elements for MSBR. In the last case, the fluence taken by the graphite can reach 4.10^{22} n/cm2 EDN* instead of 5.10^{21} for the HTR. Consequently, it was interesting to prepare finer grained graphites than the classical nuclear products. The table 2 give the values of the properties of these graphites.

Grade 7477 is perfectly adequate for HTR. If we look at the irradiation properties of US materials and if we compare the properties before irradiation of the US materials and French very fine grained grades S270 and S 1260, we can conclude that these two grades could be adequate for the MSBR.

IRRADIATION BEHAVIOUR

1 - HTR - The grades 3780 WEG, 5890 and 7477 were tested after irradiation by kernforschungsanlage Jülich (1), Japan Atomic Energy Research Institute (2) and the French Atomic Energy Commission (3) at temperatures between 600°C and 1300°C with fluence riching 5.10^{21} n/cm2 EDN. Grade 7477 is the best : its dimensional change is generally < 1 % at temperatures between 600°C and 1100°C. The other grades are less interesting : contraction riching 1 % to 2 %.

The three figures (3, 4, 5) show the results obtained by the three laboratories and figure 6, all results compared with the same neutron unit ØFG :
$ØFG \approx 1{,}85\ EDN \approx 1{,}25\ n > 0{,}18$ MeV. It's important to note the sharp evolution of dimensional changes above 1100°C.

On the other side, KFA has studied the dimensional changes, versus doses and graphitization temperature of grade 2239 (fig. 7). (The temperature is given by the value of magneto-resistivity). The minimum dimensional change is given by the highest temperature of graphitization.

Finally Jaeri made corrosion's studies with water vapor and hydrogen at high temperatures. It showed that with H_2 the corrosion was very small with grade 7477.

2 - MSBR - Various grades of very fine grained graphite were irradiated in the French Reactor Osiris at temperatures of 800°C and 1300°C, with doses up to 2.10^{22} n/cm2 EDN. The results of irradiation are not get known, but we hope to have some of them for the conference.

With the aim of improving graphite's density and of reducing their porosity especially to have pore dimensions sufficiently low to have no penetration of fused salts, these graphites have been several times impregnated with a mixture of pitch and resin.

After impregnation, carbonisation and graphitization, the densities, porosities and largest pore dimensions have the values given on table 8.

These impregnated materials have also been irradiated in the same way.

COMMENTS

Grade 7477 is difficult to obtain in large pieces. Consequently, we developped a graphite with double texture.(4) The term "double texture" means a product obtained by molding aggregates of fine grained coke. This material is easier to bake and to graphitize than 7177 itself.

In the range of ultra fine grained graphite, it's necessary to note that it would be impossible to manufacture large pieces (like HTR blocks) but it's possible to make blocks or bars with at least one dimension less than two inches.

In that way, we, at LCL, continue to improve density and mechanical properties of graphites.

The better materials recently obtained in this way ; ultra fine grain, high mechanical properties and high density are shown in table 9. These better grades could be irradiated in 1978.

On the other hand, to improve density and to reduce porosity and pore dimensions, the study of impregnation continues on various grades of graphite with resins, pitch and chemical vapor deposition of carbon with vacuum and pressure technique.

As a conclusion Le Carbone Lorraine present materials which could be used for HTR and MSBR. Le Carbone Lorraine goes on developping this range of materials which corresponds better to it's capabilities than that of graphites used in gaz-graphite reactors.

Moreover, in cooperation with SERS, LCL hopes to make less expensive products at prices convenient for HTR. This is especially the case for the "double texture" graphite.

ACKNOWLEDGMENT

We thank greatfully KFA, JAERI and CEA for the communication of the results obtained on our products after irradiation.

* 2.10^{22} turn around

(1) "Carbon 76" BADEN-BADEN - July 1976

(2) Private communication

(3) Note CEA-N-1903 - September 1976
P.MOTTET and G. MICAUD
"Graphite obtenu par pressage isostatique"
"Comportement sous irradiation neutronique"

(4) French patent n° EN 75-19678 - June 1975
J. FOURRE - J.P. GERVAIS - J. MAIRE
"Graphite à double texture"

Characteristics \ grades	Unités	Tableau 1			Tableau 2		
		3780	2239	5890	7477	S1260	8270
Density		1,60	1,80	1,82	1,75	1,65	1,76
Flexural strength RF	daN.cm^{-2}	235	500	600	350	450	650
Thermal expansion 25 to 525°	10^{-6}°C^{-1}	3	4	4,2	4,7	6,1	5
Porosity	%	24	10	8	12	25	13,8
Highest pore radius r	µ					0,3	0,8
Mean pore radius	µ					< 0,2	0,5

Characteristics \ grades	Unités	Tableau 8			Tableau 9		
		7477 3H	8270 1H	S1260 1H	S1346	S1410	S1410 1H
Density		1,88	1,84	1,76	1,90	1,79	1,87
Flexural strength RF	daN.cm^{-2}	690	650	590	800	750	800
Thermal expansion 25 to 525°	10^{-6}°C^{-1}	3,9	4,6	5,9	5,3	5,1	
Porosity	%	3,9	8,5	10,9	8,4	14,5	6,8
Highest pore radius r	µ	0,8	0,4	0,5	1,2	0,3	0,1
Mean pore radius	µ				1	0,2	0,06

1, 2, 3H means number of impregnations.

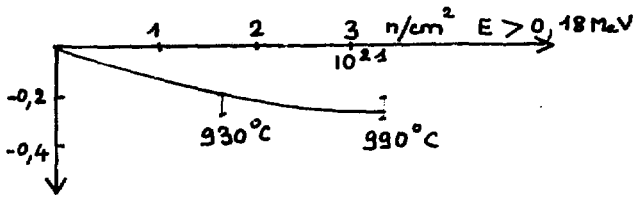


Fig. 3 - Dimensionals changes 7477 - JAERI

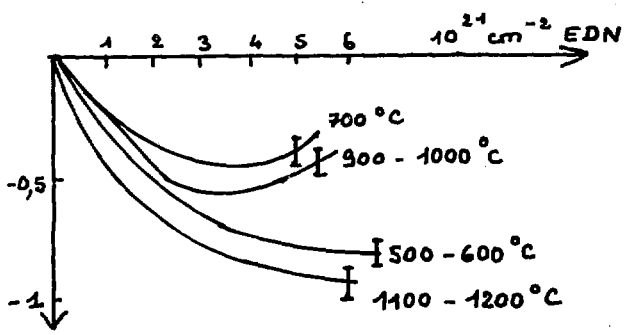


Fig. 4 - Dimensionals changes 7477 - KFA

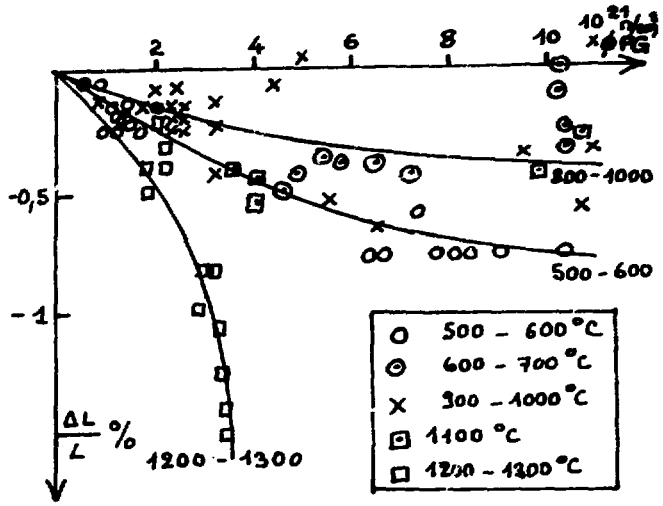


Fig. 5 - Dimensionals changes 7477 - CEA

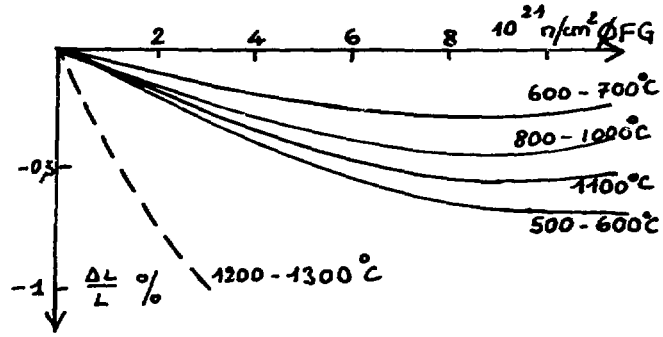


Fig. 6 - Dimensionals changes 7477

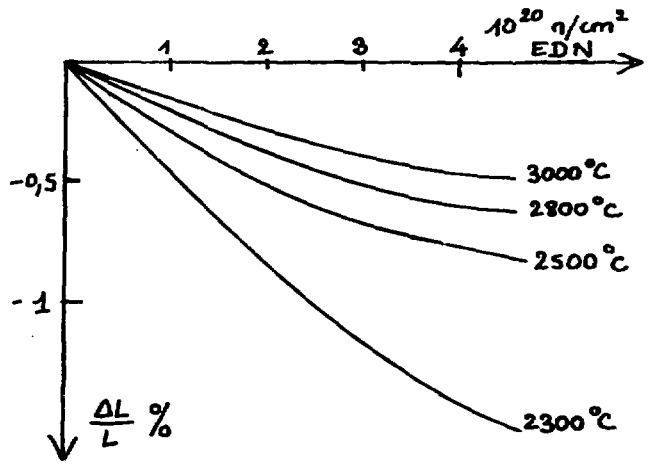


Fig. 7 - Dimensionals changes 2239
f(temperature of graphitization) KFA

TENSILE PROPERTIES OF NEUTRON-IRRADIATED GRAPHITES

R.J. Price, General Atomic Company, Box 81608, San Diego, CA 92138

Introduction

The mechanical design of graphite components for high temperature gas-cooled nuclear reactors (HTGRs) requires measurements of the changes in Young's modulus and tensile strength of the structural graphite as functions of neutron fluence and irradiation temperature. This paper summarizes the results from several hundred tensile tests on fuel block graphites irradiated under HTGR conditions.

Materials

Three grades of nuclear graphite were tested. H-327 (Great Lakes Carbon Company) is an extruded needle coke graphite used for the fuel and replaceable reflector blocks of the 330 MW(e) Fort St. Vrain reactor. Grades H-451 (Great Lakes Carbon Company) and TS-1240 (Union Carbide Corporation) are extruded near-isotropic petroleum coke-based graphites which are candidates for future large HTGR's. Specimens from three different extrusion lots of H-451 were included.

Experimental

The specimens were cylinders measuring 6.3 mm diameter × 23 mm long which were cemented between metal end-pieces and tested at ambient temperature, using precision chains to apply the load and a crosshead speed of 2 μm/s. The strain was measured with a 12.7 mm gauge-length extensometer. The specimens were first loaded to 7 MPa, unloaded to 0.7 MPa, and reloaded to failure. Young's modulus was measured from the 0.7 MPa to 7 MPa portion of the reloading curve.

Irradiation took place in a series of three fully instrumented, controlled temperature capsules which were irradiated in the C-3 position of the Oak Ridge Reactor. Each capsule contained ten graphite crucibles operating at temperatures ranging from 870 to 1630 K. Some specimens were transferred from capsule to capsule to increase the neutron fluence. The maximum fluence was 9×10^{25} n/m^2 (E > 29 fJ).

Results

Data for H-451 graphite are shown in Figures 1 and 2. The percent increase in Young's modulus or tensile strength is plotted against the fast neutron fluence, with the data grouped into three temperature regions. Each point shows the mean of about ten specimens, and the error bars indicate plus or minus one standard deviation. Young's modulus undergoes an almost immediate increase, followed by a plateau, and then a second rise which increases the modulus to about three times its original value after a fluence of 9×10^{25} n/m^2 (E > 29 fJ) at 1110-1250 K. The tensile strength follows a similar trend, but the percent increase is lower than for Young's modulus, amounting to about 100% at the highest fluence.

Figures 1 and 2 include data for both axial and radial orientations, midlength-center and midlength-edge locations in the parent log, and three different extrusion lots. The percent increases in modulus and strength for all specimens fall into the same bands, despite considerable variations in the preirradiation properties. Average preirradiation strengths ranged from 10.8 to 18.6 MPa in the axial direction and from 8.5 to 16.6 MPa in the radial direction, depending on the lot and the location of the specimens in the parent log.

TS-1240 graphite showed similar property changes to H-451 graphite. However, needle coke-based H-327 graphite did not show the secondary increase in modulus and strength at a temperature of 1110-1250 K evident in Figures 1 and 2.

The statistical spread in strength values is an important factor in the mechanical design of graphite structures. Irradiation increased the standard deviation of the strengths, but the coefficient of variation (standard deviation divided by the mean) showed no clear trend with irradiation, with the possible exception of the most highly irradiated axial H-327 specimens whose coefficient of variation apparently increased.

The irradiation-induced increase in strength (S) can be related to the irradiation-induced increase in Young's modulus (E) thus:

$$S/S_o = (E/E_o)^k$$

The exponent, k, was evaluated for each graphite grade and orientation, with the following results:

H-451, axial and radial:	k = 0.64
TS-1240, axial and radial:	k = 0.48
H-327, axial:	k = 0.67
H-327, radial:	k = 0.40

Discussion

The trend in Young's modulus as a function of neutron fluence is similar to the reported increase in sonic modulus,[1] except that the initial increase in Young's modulus found in the present work was higher. This probably results from the fact that the sonic modulus of unirradiated graphite is typically 20% higher than the static Young's modulus, whereas the two determinations would be expected to agree after irradiation because of the removal of anelastic effects. The initial rise to a plateau may be attributed to pinning of basal dislocations by point defect clusters, which increases the effective C_{44} shear modulus of individual crystallites. The second rise may be explained by the progressive tightening of the structure as microcracks close and intercrystalline restraints increase.

The irradiation-induced strength increase was roughly proportional to the square root of the increase in Young's modulus, as would be expected from the Griffiths fracture model if neither the surface energy nor the critical flaw size is influenced by irradiation. The same relationship has been observed after low temperature irradiations,[2] whereas work at higher temperatures[3] has suggested a linear relationship between strength and sonic

modulus. The apparent discrepancy is again largely attributable to the difference between sonic and static determinations of Young's modulus in unirradiated graphites.

Acknowledgements

This work was supported by the U.S. Energy Research and Development Administration under Contract EY-76-C-03-0167, Project Agreement No. 17.

References

(1) M.R. Everett, et al., Dragon Project Report DP 877 (1974).

(2) P.T. Nettley, et al., Proc. Symp. on Advanced and High Temperature Gas Cooled Reactors, p. 603, (IAEA, Vienna, 1969).

(3) M.R. Everett and F. Ridealgh, High Temperatures - High Pressures, 4, 329 (1972).

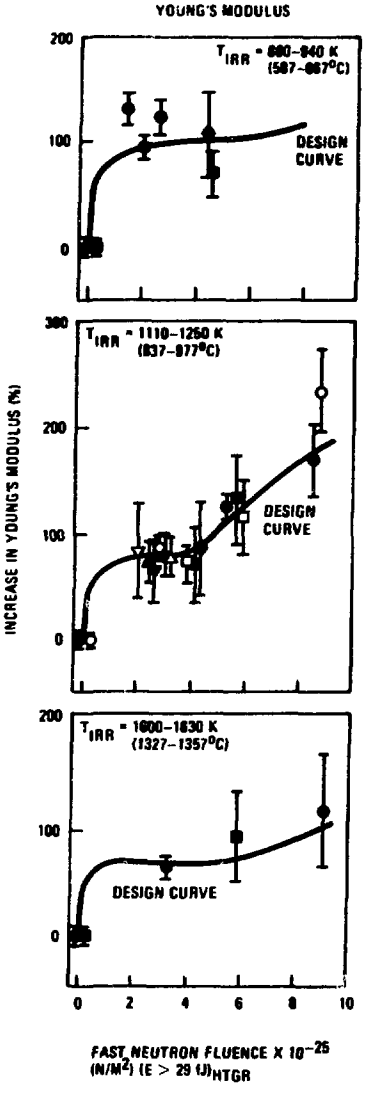


Figure 1. Change in Young's Modulus of H-451 Graphite as a Function of Fast Neutron Fluence

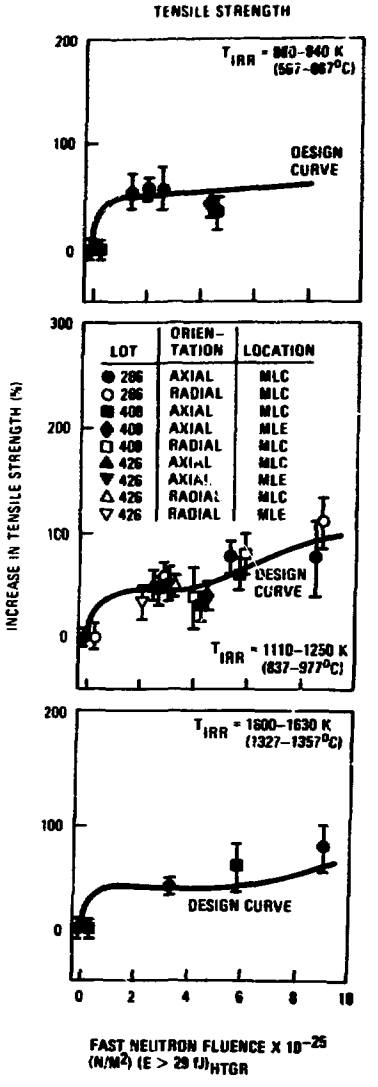


Figure 2. Change in Tensile Strength of H-451 Graphite as a Function of Fast Neutron Fluence

FATIGUE OF NEAR-ISOTROPIC GRAPHITE: INFLUENCE OF STRESS CYCLE

R.J. Price, General Atomic Company, Box 81608, San Diego, CA. 92138

Introduction

Graphite components in high temperature gas-cooled reactors (HTGRs) are subject to cyclic stresses from power cycling and possibly from seismic vibrations. Design of these components requires a knowledge of the fatigue behavior of the graphite under loading cycles which may differ in stress ratio, i.e., the ratio of the *minimum* stress during a cycle to the maximum stress during a cycle.

Fatigue data on extruded near-isotropic *H-451* graphite (Great Lakes Carbon Company), which is a candidate for fuel and replaceable reflector blocks in large HTGRs, have been reported for a stress ratio of 0 (tension-zero stress cycle).[1] The *present work consisted of uniaxial fatigue* tests at ambient temperature on H-451 graphite and on a large diameter molded graphite, grade PGX (Union Carbide Corporation), under stress ratios ranging from -1 (tension-compression cycle) to +0.5 (tension-tension cycle). Grade PGX is used for core support blocks in HTGRs.

Experimental

H-451 specimens were taken in the axial orientation a quarter of the way along the *parent log* and between 25 and 100 mm from the edge. PGX specimens taken in both axial and radial orientations between 50 and 150 mm from the end of the log and one-third of the radius out from the log centerline. Specimens for a particular test series were spread uniformly over the sampling zone. The specimens were right cylinders 12.7 mm diameter by 25.4 mm long and were cemented between steel end-pieces using V-block jigs for alignment. The tests were run in air at ambient temperature in a modified Fatigue Dynamics fatigue machine equipped with a load cell and a special test cage in which two opposed loading rams move in coaxial linear bearings to ensure uniaxial loading in both tension and compression. Tests were run at 400 cycles/minute until the specimen fractured or 100,000 cycles were reached without fracture.

Results and Analysis

For each material and orientation, the first test series consisted of 30-35 control tensile tests on standard fatigue specimens to establish the mean tensile strength. Mean strengths were 18.9 MPa for H-451 (axial); 7.6 MPa for PGX (axial); and 9.5 MPa for PGX (radial). Fatigue tests were then run, using stress ratios of -1, -0.5, 0 and +0.5 for H-451 graphite and -1 and 0 for PGX graphite. During each series of tests, between 7 and 10 specimens were run at each of five maximum stress levels which ranged from 0.6 to 1.0 times the mean tensile strength. The stress levels were selected to avoid an excessive number of run-outs beyond 100,000 cycles.

Figure 1 is a typical S-N curve in which the logarithm of the maximum stress, S, is plotted against the logarithm of the number of cycles at failure, N. The stresses have been normalized by dividing the mean tensile strength. The tensile data and first-cycle failures are plotted at N = 0.25, and run-outs are shown as open circles at N = 100,000.

The S-N curves resemble those of metals, except that the scatter band is wider. The scatter makes unsuitable the methods of statistical analysis usually applied to fatigue measurements on metals, in which the fatigue lives for each stress setting are treated as a separate population with a log-normal or Weibull distribution. Instead the following statistical model was used:

$$\log(S) = \alpha + \beta \log (N) + \varepsilon$$

where α and β are constants and ε is a random variable distributed normally with a mean of zero. The data in the S-N curves were analyzed according to this model, counting the tensile test data but excluding run-outs. The least-squares straight line and the x/y lower tolerance limits (representing the limits above which at least x% of all observations will fall, with y% confidence) were calculated and are shown in Figure 1.

The *downward* slope of the S-N curves become steeper as the stress ratio decreased, i.e., as the stress became compressive during a part of the cycle. For axial specimens of H-451 graphite, the endurance limit for 50% survival to 100,000 cycles fell from 80% of the mean tensile strength at a stress ratio of 0.5 to 60% of the mean tensile strength at a stress ratio of -1. The corresponding 99/95 lower tolerance limits were 60% and 44% of the mean tensile strength. For engineering design it is convenient to plot the results on a constant life fatigue diagram (Goodman diagram), which relates the fatigue life to the following interdependent loading cycle parameters: maximum stress, minimum stress, stress amplitude, and mean stress. Figure 2 shows a Goodman diagram for axial specimens of H-451 graphite.

When normalized by dividing by the mean tensile strength, the endurance limits for PGX graphite were somewhat higher than for H-451 graphite under similar conditions. For a stress ratio of -1, the PGX endurance limit for 50% survival to 100,000 cycles was 66% of the mean tensile strength in the axial orientation and 74% in the radial orientation. Corresponding 99/95 lower tolerance limits were 52% and 56%.

Acknowledgements

This work was supported by the U.S. Energy Research and Development Administration under Contract EY-76-C-03-0167, Project Agreement No. 17.

Reference

(1) R.E. Bullock, Extended Abstracts of the 12th Biennial Conference on Carbon, p. 141 (American Carbon Society, 1975).

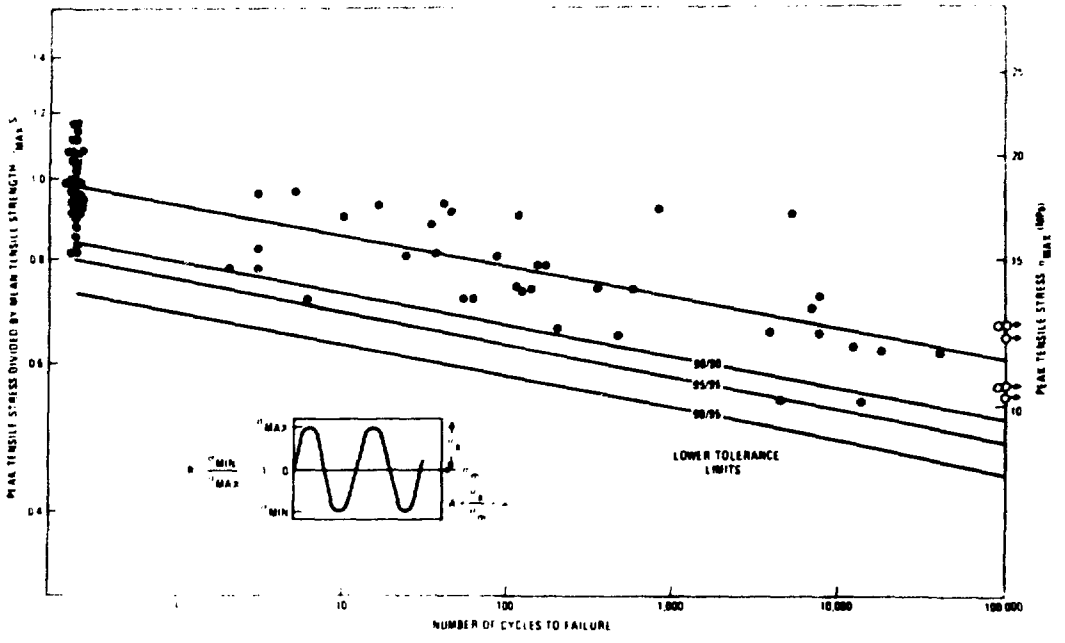


Figure 1. Log-log plot of normalized maximum stress versus number of cycles to failure. H-451 graphite, axial orientation, stress ratio, R, = -1. Lower x/y tolerance limits represent the limits above which at least x% of the points will fall, with y% confidence.

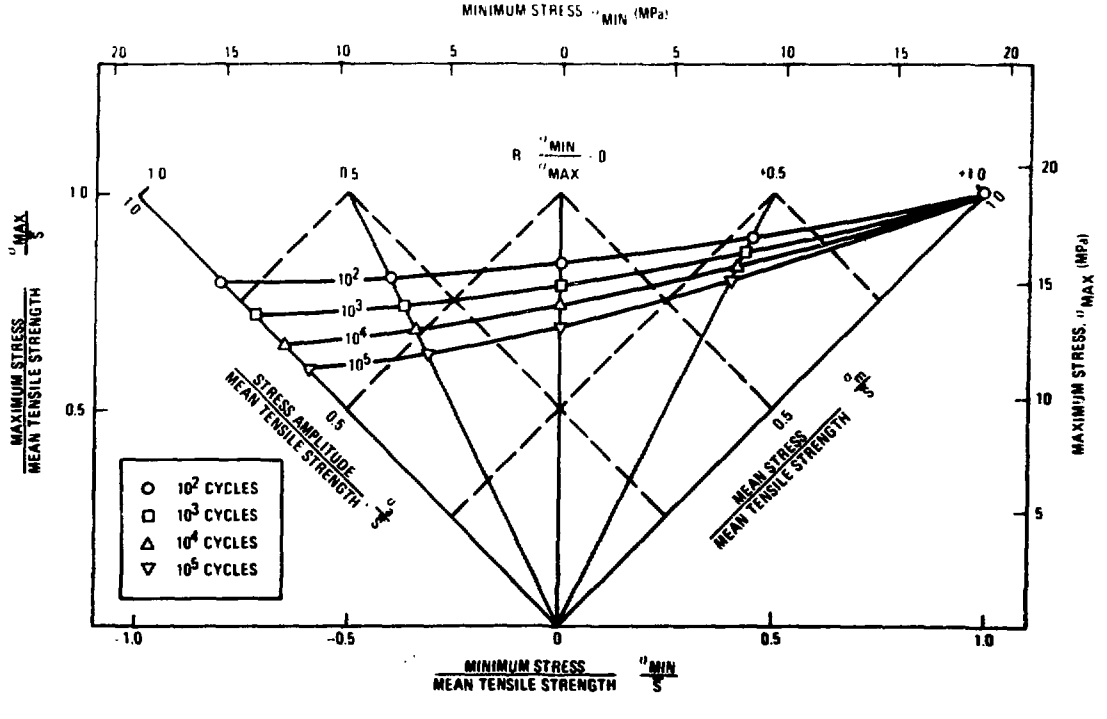


Figure 2. Constant life fatigue diagram (Goodman diagram) for H-451 graphite, axial orientation, tested in air at ambient temperature. Curves correspond to 50% survival probability.

NEGATIVE MAGNETORESISTANCE AND ELECTRICAL CONDUCTION IN GLASSY CARBON

S. Ho, P. Saxena and R. H. Bragg

Molecular and Materials Research Division, Lawrence Berkeley Laboratory
and Department of Materials Science and Mineral Engineering, College of Engineering, University of California, Berkeley, California 94720

The electrical properties of glassy carbon (GC) have been the subject of a few investigations, but the understanding is far from complete. It continues to be a matter of debate and considerably more work in this area is needed to delineate the electrical properties. We have studied the temperature dependence of the electrical conductivity (σ) of GC heat treated at different temperatures in the range 1000-2800°C. We have also measured the magnetic field and temperature dependence of the magnetoresistance of GC heat treated at different temperatures. Our measurements were taken inside a dewar with a 50KG superconducting magnet in the temperature range 10 to 300°K.

The conductivity was found to increase with temperature (T) indicating semiconductor behavior for all the samples. The conductivity exhibits two different behaviors with HTT separated at HTT 2000°C. For HTT > 2000°C, σ saturates at low temperatures, whereas for HTT < 2000°C there is a sharp decrease as T is reduced as shown in Fig. 1. For the higher HTT range two contributions to σ were found. A temperature independent σ_o due to boundary scattering, and a temperature dependent contribution of the form $\exp(-BT^{-n})$ where $n = 1/4$. This temperature dependent part of σ is believed (see fig. 2) to be due to the hopping conduction of the localized spins.

For the lower HTT range a similar separation is valid except at the lowest temperatures. Subtracting out the hopping contribution the remainder exhibits a logarithmic temperature dependence which saturates into σ_o by 100°K. This lnT dependence is characteristic of the Kondo behavior of the localized spins in the lower HTT range.

GC has negative magnetoresistance ($\Delta\rho/\rho$) for all HTT. The magnitude of this negative magnetoresistance was found to increase as the magnetic field (H) increases up to H = 50KG, and as the measurement temperature is lowered the sample's HTT increases. For HTT below 2000°C the analysis used above was not successful. The behavior of $\Delta\rho/\rho$ becomes more complex, although the general trend remains the same.

We believe that negative $\Delta\rho/\rho$ arises from field dependent scattering from localized spins.[2] For this mechanism it is well known that $\Delta\rho/\rho \propto -m^2$ where m is the effective magnetic moment per spin. Analyzing the behavior $|\Delta\rho/\rho|^{1/2}$ a unique dependence was discovered in the higher HTT range. The negative $\Delta\rho/\rho$ is found to be a single valued function of the parameter $H/T^{1/2}$ as shown in fig. 3.

Whereas the experimental behavior of σ and $\Delta\rho/\rho$ have been established, the understanding is still not complete. Measurements at lower temperatures are planned to extend the range of our investigation of the electrical properties. Also a coherent picture can emerge only when correlations with other electronic properties of GC are made, and additional experiments are planned for the future. Theoretical work is also needed to completely explain some of our experimental observations such as the $f(H/T^{1/2})$ dependence of $\Delta\rho/\rho$.

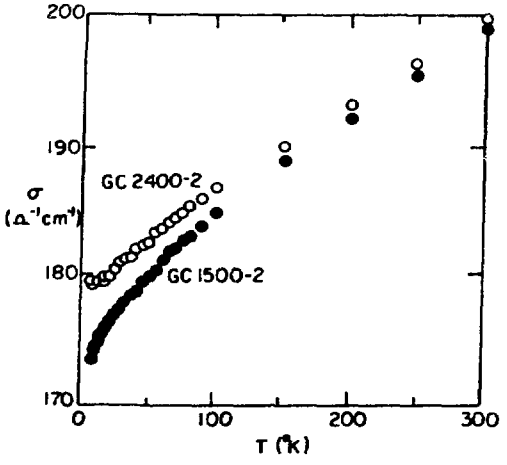


Figure 1

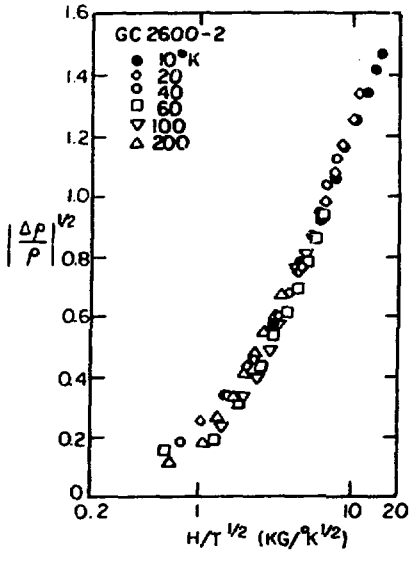


Figure 3

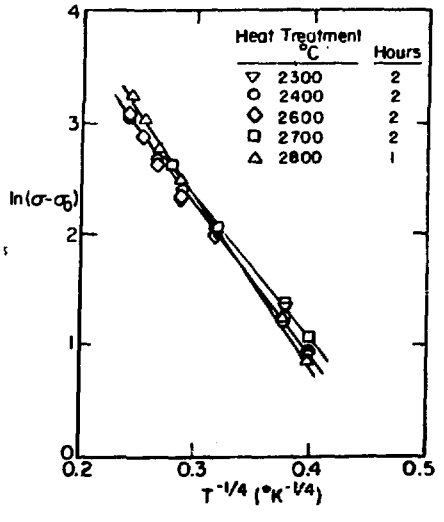


Figure 2

MAGNETORESISTANCE OF DISORDERED CARBONS AT LOW TEMPERATURE

Y. Hishiyama, Y. Kaburagi and A. Ono
Musashi Institute of Technology
1-chome, Tamazutsumi, Setagaya-ku, Tokyo 158, Japan

Introduction

Several years ago, the transverse magnetoresistance was measured in soft carbon heat treated between 1000°C and 3200°C for temperatures at 1.7K and 4.2K[1,2]. One unusual behavior for the magnetoresistance was a positive magnetoresistance for disordered samples of low heat-treatments. This was also measured in anthrathene char heat treated between 800°C and 1200°C for temperature at 4.2K [3]. From the analysis of the temperature dependence of the electrical conductivity σ, the positive magnetoresistance was associated with the variable range of hopping conduction between localized states in amorphous material described by Mott[4] for which $\sigma \propto \exp[-(T_0/T)^{1/4}]$, T_0 being a constant. For more complete experimental understanding, a systematic study of the changes in the positive magnetoresistance at low heat-treatments has been undertaken for temperatures between 1.4K and 4.2K in the work presented in this paper.

Experimental

Samples were prepared from a bamboo char and raw petroleum cokes (samples B and C). Heat-treatment of the samples was carried out at temperatures between 900°C and 1500°C for three hours. The magnetoresistance has been measured by dc method up to 60 kG. The temperature dependence of the electrical resistance has also been studied for temperatures between 1.4 K and 4.2 K.

Results and Discussion

Electrical resistivity of the samples heat treated at 900°C exhibits the $T^{-1/4}$ dependence, which is evidence for the existence of localized states in these samples. Logarithms of the relative resistance $R_T/R_{4.2}$ are plotted against $T^{-1/4}$ in Fig. 1. The results of the magnetoresistance on these samples are shown for measuring temperature of 4.2K in Fig. 2. These results confirm those obtained previously.

The magnetoresistance of the bamboo char heat treated at 900°C is positive at all fields and at all temperatures investigated. No variation of the magnetoresistance against magnetic field direction is observed. The magnetoresistance increases with increasing magnetic field and with decreasing temperature. Log-log plots of the magnetoresistance value vs. magnetic field show that the magnetoresistance varies approximately as H^2 with decrease of exponent at high field. Decrease of exponent becomes appreciably with decreasing temperature.

The magnetoresistance of the cokes heat treated at 900°C shows complicated variations on both magnetic field and temperature. The magnetoresistance is positive at all fields, and varies weakly against magnetic field direction. The results of the sample B are shown in Fig. 3, where $(\Delta\rho/\rho)_{max}$ and $(\Delta\rho/\rho)_{min}$ are the maximum transverse magnetoresistance and the minimum at the same magnetic field. In this and other samples, maxima in the mean transverse magnetoresistance vs. temperature at constant magnetic field are observed. The mean transverse magnetoresistance is defined by the mean value of the maximum transverse magnetoresistance and the minimum. Temperature at the maximum is about 2K. This behavior is associated with the onset of the anisotropic negative component which is stronger at higher magnetic fields and lower temperatures

The anisotropic negative magnetoresistance can be attributed to characteristic of the growing graphitic crystallite, the region of the pseudo-metallic conductivity. Therefore, the results of the samples of cokes heat treated at 900°C suggests a structural model of these samples involving regions of the pseudo-metallic conductivity connected by the variable range of hopping conduction, as the model proposed by Hamilton, Cross and Adkins for amorphous carbon films[5].

The pseudo-metallic conduction becomes dominant with increasing heat-treatment temperature. The $T^{-1/4}$ dependence of $\ln[R_T/R_{4.2}]$ is no longer observed for the samples of the cokes heat treated above 1100°C. The negative component of the magnetoresistance becomes remarkable with increasing heat-treatment temperature, which can be illustrated in Fig. 3 with the results obtained for the sample B heat treated at 1100°C.

For the samples of the cokes heat treated at 1500°C, the magnetoresistance is negative at all fields and at all temperatures. With increasing magnetic field, the mean transverse magnetoresistance decreases at first and then tends to saturate at constant temperature. It decreases with decreasing temperature at lower fields, while it increases at higher fields. This implies that the positive component due to hopping conduction superposes on the negative magnetoresistance of the graphitic layer plane. Therefore, amorphous regions still remain in these samples.

References

1. Komatsu Y., Carbon 7, 177 (1969).
2. Hishiyama Y., Carbon 8, 259 (1970).
3. Carmona F., Delhaes P., Keryer G. and Manceau J. P., Solid State Comm. 14, 1183 (1974).
4. Mott N. F., Phil. Mag., 19, 835 (1969).
5. Hamilton E. M., Cross J. A. and Adkins C. J., P Proc. 5th inter. Conf. on Amorphous and Liquid

Semi-conductors, Vol. 2, 1225 (Garmisch-Partenkirchen 1973).

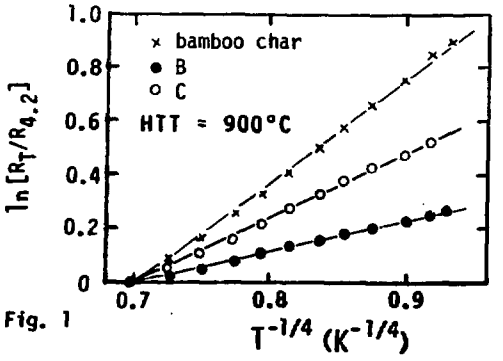


Fig. 1

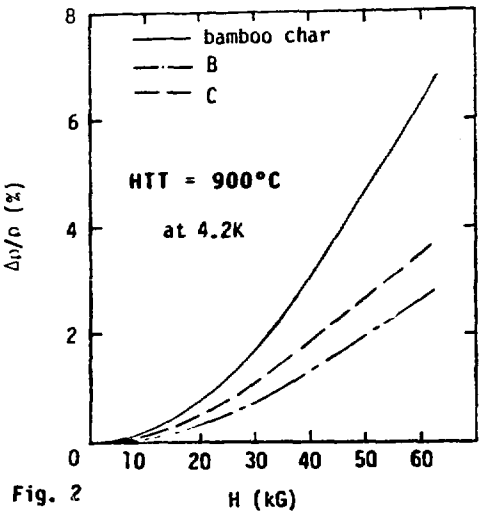


Fig. 2

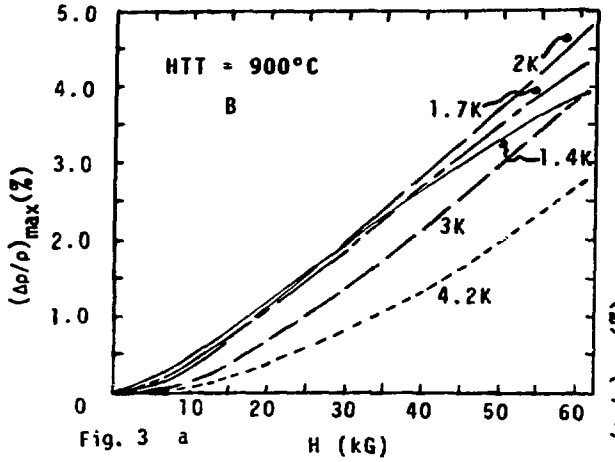


Fig. 3 a

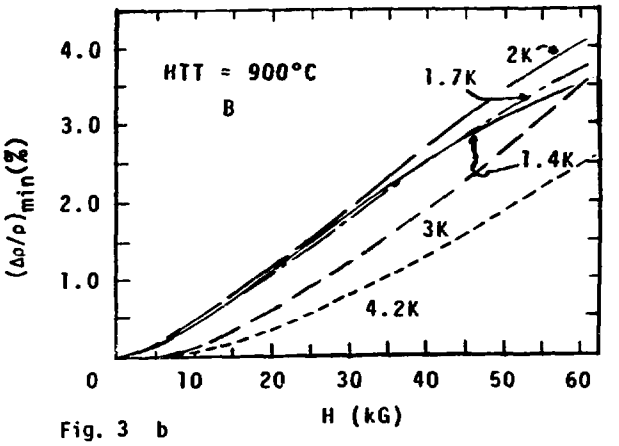


Fig. 3 b

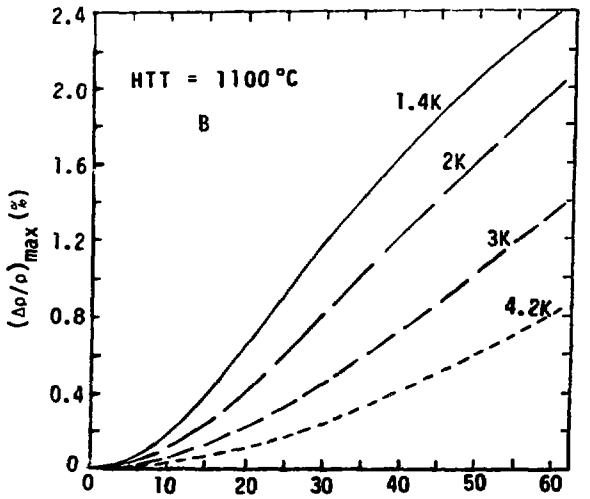


Fig. 4 a

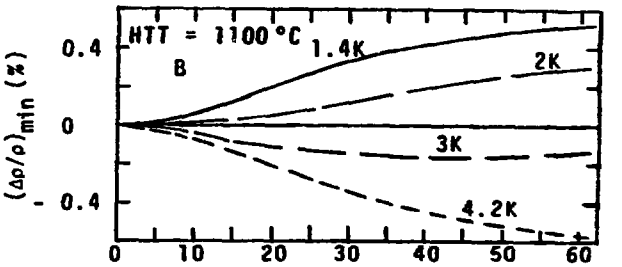


Fig. 4 b

BAND THEORY OF PYROCARBONS AND COKES

by Oscar GONZALEZ* and Alphonse CHARLIER

Laboratoire de Physique du Solide, Université de Metz (France)

I. Introduction.

We present a two dimensional model which gives good agreement with observed experimental results [1] on pyrocarbons and cokes near the graphitization zone.

It is based on Wallace's [2] calculations, supplementary terms are provided by including overlapping integral between nearest neighbouring atoms and exchange integral between second neighbouring atoms in the layer.

II. Energy.

By linear combination of Bloch atomic orbitals we construct the following secular determinant

$$0 = \begin{vmatrix} E_0 - \gamma_0' f(k) - E & F(k)(E_0 S_{AB} - \gamma_0 - E S_{AB}) \\ (E_0 S_{AB} - \gamma_0 - E S_{AB}) F^*(k) & E_0 - \gamma_0' f(k) - E \end{vmatrix}$$

The energy values obtained by determinantal resolution, the energy E_c and the dispersion formula near the corner of the first Brillouin zone are respectively :

$$E(k) = E_0 \pm \frac{\gamma_0 |F(k)| \mp \gamma_0' f(k)}{1 \mp S_{AB} |F(k)|}$$

$$E_c = E_0 + 3\gamma_0'$$

$$|E - E_c| = \pm \frac{(9\gamma_0' S + \gamma_0)\sqrt{3}\pi a |k - k_c|}{1 - 3a\sqrt{3}\pi S |k - k_c|}$$

III. State's density.

The number of electronic states in the energy interval d E is

$$N(E) = \frac{4Am}{27\pi a^2 S^2} \left(\frac{|E - E_c|}{\frac{1}{m} + |E - E_c|} \right)$$

$$m = \frac{3S}{9\gamma_0' S + \gamma_0}$$

this seems to be a reasonable curve intermediate between the Wallace's theoretical linear form and the Coulson more experimental one.

IV. Electrical conductivity

In order to estimate the electrical conductivity parallel to the graphitic layer, the general current density

$$\vec{j} = 2e \int \vec{v} f(\vec{k}) \, d^3k$$

and the Fermi-Dirac distribution function :

$$f(\vec{k}) = f_0 + g(\vec{k})$$

f_0 undisturbed function

$$g(\vec{k}) = -\frac{e\tau}{\hbar c} \vec{\mathcal{E}} \cdot \vec{V}_k f_0$$ supplementar

term due to applied electrical field, are used and lead us to

$$\vec{j} = -\frac{4e^2\tau}{\hbar^2 c} \int \frac{\partial f_0}{\partial E} \left[\int (\vec{V}_k E)(\vec{\mathcal{E}} \cdot \vec{V}_k E) \, c$$

After integral evaluations we obtain

$$\sigma_{//} = \frac{16\pi e^2 \tau KT}{\hbar^2 c} \left[\log 2 - m\pi KT \right.$$

This result may be regarded as the sum of two terms : Wallace's one and a supplementary correction $\Delta\sigma_{//}$ with

$$\Delta\sigma_{//} = -\frac{48\pi^2 e^2 \tau (KT)^2 S}{\hbar^2 c (9\gamma_0' S + \gamma_0)}$$

A theory of the mean free path has been given Mott and Gurney [3] ; according to this calculation

$$\tau = \frac{l}{v} \qquad l = C \left(\frac{T}{\Theta}\right)^{1/2} \left(e^{\frac{\Theta}{T}} - 1\right)$$

Θ is the Debye temperature of the sample.

The agreement with experimental measuremen is good if we assume a dependance between high temperature treatment and the Debye temperatur

V. Diamagnetic susceptibility.

The value of the diamagnetic susceptibility is obtained by a similar procedure as that used by Mc Clure.

$$\chi = \chi_{\text{Mac Clure}} \left(1 + \frac{9\gamma_0' S}{\gamma_0}\right)^2$$

$$\chi_{\text{Mac Clure}} = -\frac{0{,}010}{T} \operatorname{sech}^2 \frac{\xi}{2KT}$$

The comparaison with Ganguli and Krisnnan's (4) experimental results permits the evaluation of the parameter γ_0' ; the numerical value is 0,02 eV.

VI. Conclusion.

This rough theoritical model may be completed with better calculation of the relaxation time and its dependance with graphitization.

VI. References.

(1) FLEIT C.A, J. of App. Phys. 33,11, (1962)
SHARMA S.R., SEN GUPTA. S.K, J. Sci. Industr. Res. Vol 20 D, 247-251 (1961)

(2) WALLACE P.R., Phys. Rev. 71, 9, 622-634 (1947)

(3) MOTT & GURNEY Electronic Processes in Jonic Crystals, 107, University Press

(4) MAC CLURE J.W, Phys. Rev 104, 656-671 (1956)

* Present adress "Universidad de Oriente", Physics Department CUMANA (Sucre) VENEZUELA

LOW TEMPERATURE MAGNETIC AND THERMAL PROPERTIES OF AN AMORPHOUS CARBON

F. CARMONA and P. DELHAES

Centre de Recherche Paul Pascal, Université Bordeaux I, 33405 TALENCE (FRANCE)

and

J.L. THOLENCE and J.C. LASJAUNIAS

Centre de Recherche sur les très basses températures

CNRS, CEDEX 166, 38000 GRENOBLE (FRANCE)

Introduction

The physical properties of a series of anthracen chars heattreated at temperatures (HTT) lower than 1500°C have been extensively studied and reported in other publications [1] [2] [3]. A non-metal transition was evidenced and interpreted by the existence of density fluctuations [3]

We shall report further measurements of the magnetization between 0.1 and 2K, the magnetocaloric effect and the specific heat under 2K of the sample heattreated at 700°C which lays on the non-metallic side of the pseudo transition.

Magnetization measurements

The magnetization M of the sample was measured over the temperature range 0.1-4.2K under various magnetic fields H increasing from 0.8 to 70 kOe. We have reported in the insert of figure 1 the reverse low field susceptibility versus temperature : there is evidence of a CURIE-WEISS law :

$$\chi_p = \frac{C}{T-\theta}$$

with $\theta = 0.8$ and $C = 38\ 10^{-6}$ uem cgs g^{-1} K.

Defining the reduced variable x as :

$$x = \frac{\mu H}{k(T-\theta)}$$

where μ is the BOHR magneton and k the BOLTZMAN constant, we have reported the experimental values of M versus x for the low and high values of x on figure 1 and figure 2 respectively. Figure 1 shows the expected linear x dependence of M.

We have drawn on figure 2 the line calculated with the LANGEVIN relation of the magnetization of N dipoles of spin 1/2

$$M = N\mu \text{ th } x \qquad [1]$$

Magnetocaloric effect

A (small) magnetic field change ΔH acting on a perfect paramagnetic material at temperature T under adiabatic conditions results in a temperature change ΔT such as :

$$\Delta T = -\frac{T}{C_{p,H}} \left(\frac{\partial M}{\partial T}\right)_{P,H} \Delta H$$

where $\left(\frac{\Delta M}{\Delta T}\right)_H$ is the derivative of the magnetization o the sample at constant pressure and field by respect to temperature, and $C_{p,H}$ the specific heat at consta pressure and field. $C_{p,H}$ being known [1] for the thre magnetic field strenghts 20,30 and 40 kOe, we have determined $\left(\frac{\partial M}{\partial T}\right)_{P,H}$ for the same values of H.

We have reported on figure 3 the values of :

$$\left(\frac{\partial M}{\partial x}\right)_{P,H} = -\frac{\mu H}{kx^2} \left(\frac{\partial M}{\partial T}\right)_{P,H} \quad \text{versus x}$$

From relation [1] we can deduce :

$$\left(\frac{\partial M}{\partial x}\right) = N\mu \left(\frac{2}{e^{x} + e^{-x}}\right)^2 \qquad [2]$$

which gives the theoretical curve drawn on figure 3.

Specific heat under 2K

The specific heat results between 0.15 and 2K are given in log-log coordinates on figure 4. The previous results [1] above 1.5K are recalled. The present measurements agree with a temperature dependence of the form :

$$C_p \sim T^n$$

with $n \sim 0.6$ significantly less than 1. Reporting the results in a C_p/T versus T^2 plot (insert of figure 4) the experimental values diverge as T decreases. Such a behaviour has been already reported in low HTT soft carbons [4] with a quite similar characteristic. But,

there is no evidence of a true peak for 3 K as reported on other amorphous carbons [4].

Discussion

The first striking feature which emerges from these results is the magnetization and the magnetocaloric effect do not depend simply on the reduced variable x at very low temperature and strong fields. The other interesting fact is the non-linear temperature dependence of the very low temperature specific heat, which contradicts the linear dependence found at higher temperatures [1]. Such a non-integer exponent was already found in other disordered solids [6] but appears here as a puzzling result . It seems to us that at very low temperatures we have a magnetic interaction between localized centers with an energy spectrum due to a very short range order [5]. This clar therefore behaves as a kind of spin glass. A definite model has to be proposed to explain this behaviour.

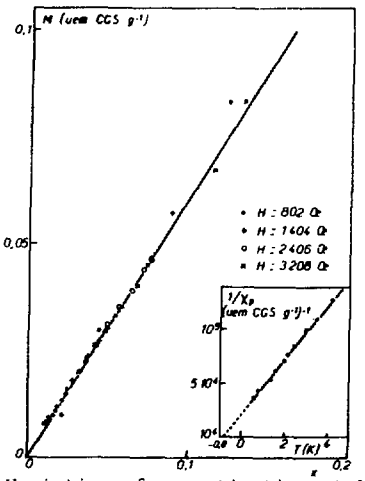


Figure 1 : Variation of magnetization at low fields and Curie-Weiss law (see insert)

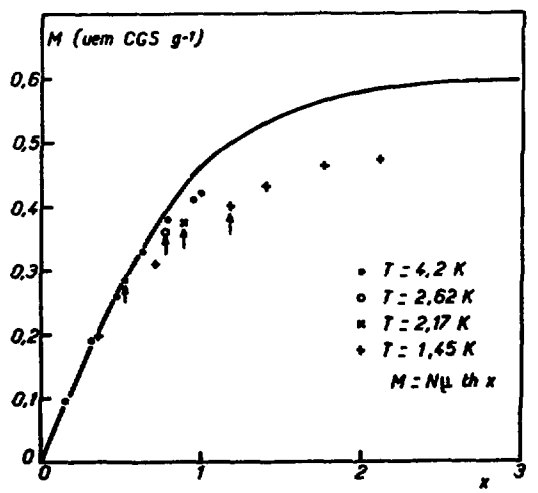


Figure 2 : Variation of magnetization at high fields

1-G. DLONDET-GONTE, P. DELHAES and M. DAUREL, Sol. St Comm. 10, 819 (1972)

2-F. CARMONA, P. DELHAES, G. KERYER and J.P. MANCEAU, Sol. St Comm. 14, 1183 (1974)

3-F. CARMONA and P. DELHAES to be published

4-K. KAMIYA, S. MROZOWSKI and A.S. VAGH, Carbon 10, 267 (1972)

5-S. MROZOWSKI and A.S. VAGH, Carbon 14, 211 (1976)

6-J.C. LASJAUNIAS, P. MAYNARD and D. THOULOUZE, Sol St Comm 10, 215 (1972)

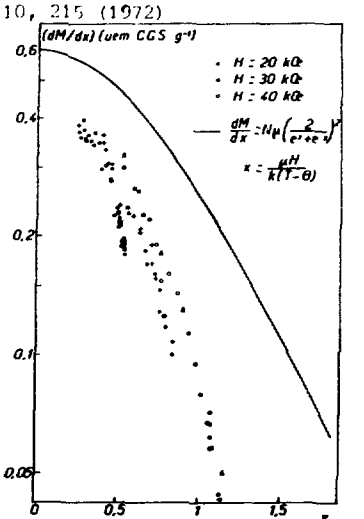


Figure 3 : Magnetocaloric results in reduced coordinates.

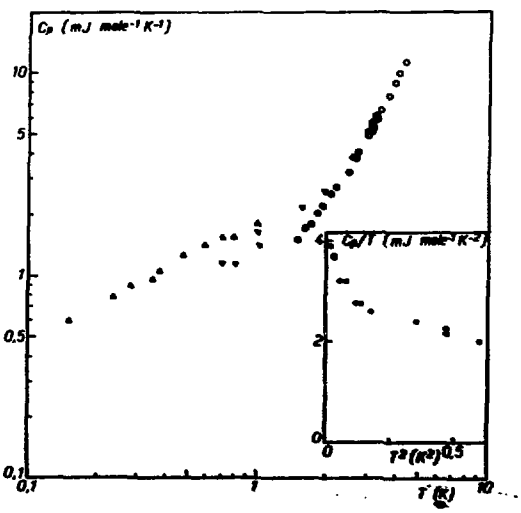


Figure 4 : Thermal variation of the specific heat Cp in logarithmic coordinates and C_p/T versus T^2 (see insert)

LATTICE DEFECTS AND LOW TEMPERATURE SPECIFIC HEAT PEAKS IN SOFT CARBON AND POLYCRYSTALLINE GRAPHITE

S. Mrozowski and A. S. Vagh
Department of Physics and Astronomy, Ball State University
Muncie, Indiana 47306

The specific heat of a soft carbon and a polycrystalline graphite was investigated using a dilution refrigerator at the NASA Lewis Center in Cleveland, down to 75 millidegrees. The variation in height of the two specific heat peaks and of the linear effect with heattreatment, neutron irradiation dose and thermal anneal, support the contention that the peaks are due to formation of antiferromagnetic islands throughout the randomly distributed localized electronic spin system.

*) Supported in part by the National Science Foundation.

MAGNETIC FIELD DEPENDENCE OF SPECIFIC HEAT PEAKS IN NEUTRON IRRADIATED POLYCRYSTALLINE GRAPHITE

A. S. Vagh and S. Mrozowski
Department of Physics and Astronomy, Ball State University
Muncie, Indiana 47306

The specific heat of a sample of neutron irradiated polycrystalline graphite was investigated using a dilution refrigerator at the NASA Lewis Center in Cleveland in a magnetic field. Whereas the presence of magnetic field raises the higher temperature peak at 0.74°K, it lowers the peak at 0.265°K. The meaning of this result will be discussed in relation to other information concerning the origin of these peaks.

SPECIFIC HEAT OF NEUTRON IRRADIATED GLASSY CARBON (GC 30) IN THE INTERMEDIATE RANGE OF TEMPERATURES 3-78°K

E. Michael, B. Myers and S. Mrozowski
Department of Physics and Astronomy, Ball State University
Muncie, Indiana 47306

The low temperature apparatus was modified for specific heat measurements throughout the intermediate range of temperature and matching electronic circuits built for that purpose. Samples of GC 30 irradiated to various doses were investigated, one of them also after anneal to 3000°C. The way the different curves tend toward a common value at 78° will be presented and the meaning of the results discussed.

SARAN CARBON--A SUPERIOR ADSORBENT FOR VOLATILE COMPOUNDS

Donald D. Schmidt, Richard G. Melcher
Dow Chemical U.S.A.
Midland, Michigan 48640

Introduction

Saran carbon has been described in the literature for more than 25 years. It is a pure, high surface area carbon made by pyrolysis of poly(vinylidene chloride) or vinylidene chloride copolymers (Sarans). Saran degrades and crosslinks by evolving hydrochloric acid at temperatures well below its melting point. Crosslinked polymer can then be heated above the original melting point without fusion. Since the Saran never melts, the Saran carbon produced has the same shape as the Saran starting material.

Potential commercial applications of Saran carbon as an adsorbent have been explored at The Dow Chemical Company, the sole producer of Saran polymers in the United States. Saran carbon beads as large as 10 mesh and as small as 150 mesh have been made and studied on the laboratory scale. These beads have been labeled Dow Developmental Adsorbent with experimental designation number XF-4175L for sampling purposes.

Saran suspension beads were made by modification of the polymerization technique described by Meeks.[1] These Saran beads were then carbonized by pyrolysis methods similar to those described by Dacey and Thomas[2] and many others.

Physical Properties

The Saran carbon beads are very hard and non-dusting. They will not mark paper. They are easy to handle in analytical applications in which quantitative transfer is important. The measured Moh hardness of Saran carbon is about 4.5. Its CWS hardness number is 97. No measureable attrition was observed in a Saran carbon fluidized bed after 200 hours.

Saran polymer as the starting material for carbon affords processing options that coal or coconut shells cannot give. Control of granule shape is the prime example. In addition to beads, Saran carbon can be made into pellets or tablets by compacting Saran into these shapes. The crosslinking of the polymer during carbonization acts as a strong carbon binder. Therefore, the Saran carbon granules do not lose their strength or integrity in acidic and basic media.

The macroporosity of Saran carbon can also be controlled. Saran suspension beads have a porosity of 25-30%, with about one micron pores throughout the beads. This macroporosity is retained upon carbonization. Mercury intrusion curves show that Saran carbon has much more interconnected pore volume in the macropore range (greater than 300 Angstroms) than coconut shell carbon. These macropores are important for access of fluids to the micropores where nearly all the adsorption takes place. The macropore volume of Saran beads (and, consequently, of Saran carbon) can be increased by adding organic solvents such as methylene chloride or heptane to vinylidene chloride before suspension polymerization.

The molecular sieve properties of Saran carbon have been widely discussed in the literature.[2-5] The amount of adsorption of molecules of different molecular cross-sections has established the size of micropores. They have been described at various times as 5 to 12 Angstroms in diameter, depending on the initial Saran polymer composition and heat treatment temperatures.

Air Sampling Tubes

Saran carbon has been evaluated as an adsorbent in our laboratory under dynamic flow through packed beds. These are the types of adsorption conditions encountered industrially. Its use in air sampling tubes for industrial hygiene samples was studied because of its ease of handling. Saran carbon beads packed in 4 mm i.d. tubes were found to give longer than normal breakthrough times with volatile compounds such as vinyl chloride, methyl chloride, methylene chloride, and acrylonitrile. For example, with one gram samples of Saran carbon and Pittsburgh Activated Carbon PCB (coconut shell carbon) packed in tubes, methyl chloride broke through the Saran carbon tube three times longer than the coconut shell carbon tube. Air contaminated with 50 ppm methyl chloride flowed through the tubes at 50 ml/min. One percent breakthrough of methyl chloride occurred in 2.5 minutes with the coconut carbon tube and 7.5 minutes with the Saran carbon tube.

Volatile adsorbents on Saran carbon gave in nearly every case 100% recovery factors when desorbed in carbon disulfide or when desorbed by heating to 200°C in nitrogen. Thus, the Saran carbon not only adsorbs and retains volatile organic compounds much better than the best commercial carbon for this use, but also desorbs quantitatively. For example, Saran carbon in air sampling tubes was used to adsorb vinyl chloride, methyl chloride, dimethyl ether, ethyl chloride, and vinylidene chloride from air downwind of a chemical plant. The compounds concentrated in this way were desorbed thermally directly in a gas chromatograph. Concentrations in the 1 to 100 parts per billion range were obtained. The thermal desorption was quantitative so the Saran carbon air sampling tubes were re-used several times.

Gas Mask Canisters

These unexpectedly long breakthrough times with volatile compounds were also found for Saran carbon in gas mask cartridges. Ten ppm vinyl chloride in 85% relative humidity air was pumped through twin chemical cartridge respirators at 64 liters per minute. The concentration of vinyl chloride in the effluent stream was analyzed as a function of time. The Saran carbon cartridges broke through to 1 ppm vinyl chloride after two hours. The cartridges packed with coconut shell carbon broke through in less than 15 minutes.

In addition to prolonged breakthrough times, Saran carbon in gas masks might allow simpler canister design. Saran carbon beads pack well without channeling and are not dusty. Thus, it might be possible to remove some of the partitions, screens, and filters from present canister design.

Economic Considerations

Saran as a raw material for carbon is both more expensive and more corrosive upon carbonization than coconut shells or coal. Consequently, Saran carbon will be several times more expensive. Specialty adsorption uses that can afford a higher carbon cost have to be found for Saran carbon if it is to become a commercial adsorbent.

References

1. Meeks M.R., Macromolecular Synthesis 4, 137 (1972).
2. Dacey J.R. and Thomas D.G., Trans. Faraday Soc. 50, 740 (1954).
3. Lamond T.G., Metcalf J.E. III, and Walker P.L., Jr., Carbon 3, 59 (1965).
4. Walker P.L., Jr., Mineral Industries 35, 1 (1966).
5. Barton S.S., et.al., J. Colloid Interfac. Sci. 44, 50 (1973).

CHARCOALS AS CATALYST SUPPORTS IN THE TRAPPING OF METHYLRADIOIODIDE(131)

Victor R. Deitz
Naval Research Laboratory
Washington, D. C. 20375

INTRODUCTION

Commercial solid adsorbents are used in the nuclear industry as final back-up beds to conventional chemical processes for waste disposal and as a solid sink for the permanent retention of nuclides. Several important features are novel to the nuclear applications. First, the waste products are present in extremely low magnitudes; the concentration unit of ppb is considered to be high. It is well known that many adsorption isotherms measured for different charcoals in the conventional concentration ranges actually cross over when the data are extended to lower values. Such behavior has complicated the selection of the adsorbent when it is based only on conventional testing procedures.

A second factor is the design of an installation for operating periods of one to three years without adsorbent replacement. Thus, a qualification acceptance test of a new material must be supplemented by some knowledge of satisfactory performance after a year or more service. The adsorption process must operate in polluted environments that may be local to nuclear power sites; the process is thus vulnerable to the vagaries of air pollution.

This paper is restricted to the use of a base charcoal as a catalyst support in the trapping of methylradioiodide. While the base charcoal alone may be adequate for removing elementary iodine, the trapping of organic iodides in air flows of high humidity require impregnated materials. Several new impregnations have been examined and some of the results are presented. The evaluation was made with methylradioiodide(131) as the test gas in specified air flows having a contact time of 0.25 seconds and a test bed of 2-inch diameter and 2-inch height. The prehumidification was 16 hours at 96 RH (1).

Charcoal Impregnations

A charcoal and the impregnation must combine to realize the following objectives: (a) the efficiency in trapping organic iodides must be above 99% in air flows at high relative humidity, (b) the product must have good thermal stability in order to minimize the desorption of any iodine product, (c) the impregnated charcoals must possess particle integrity in specified particle ranges against excessive dust formation, (d) the charcoal must be compatible with a high pH of the impregnating solutions, and (e) the product must retain efficiency in the presence of local air pollutants.

Iodine in its various chemical compounds can have oxidation states I^-, I^0, I^{+1}, I^{+5}, and I^{+7}. When alkaline solutions of these salts (for example KI and KIO_3) are mixed, the solution then contains intermediate oxidation states due to several well known disproportionation reactions (2). A number of such solution mixtures have been impregnated on charcoals (3) and the total iodine content varied from 1 to 3 wt.% of the dry charcoal. A second component, a high flash point amine, such as hexamethylenetetraamine (HMTA), was added after the oxyiodine salts. Solution concentrations were adjusted so that the charcoal retained a dry appearance after the 2-stage impregnation.

Results

A few of the many values obtained in independent runs for the penetration of methyliodide are given in Table 1. When paired with suitable base charcoals, excellent trapping can be obtained. The coal base charcoals appear to be better than coconut and wood charcoals for the designated impregnations.

Table 1: Penetration of Methyl Iodide Using Impregnations of Oxyiodine Salts

	Source	Impregnation	Penetration(%)
207A	Coal	KI, KIO_3, HMTA	0.21,0.21,0.38 0.35,0.22,0.25
MBV	Coal	I_2,KI,KOH, HMTA	0.51,0.30,0.43 0.30,0.29,0.29
CHR-76108	Coal	KI,KIO_3, HMTA	0.56,0.74,0.32 0.51,0.37,0.71
337	Pet.Coke	KI_x	0.73,0.44,1.10 2.08,1.09,0.72
G-210	Coconut	KI,KIO_3, HMTA	3.92,3.27,4.21 1.56,2.06,3.0
GX-202	Wood base	KI,KIO_3, HMTA	1.62,1.18,1.04 1.38,2.34,1.5
G-212	Coconut	I_2,KOH, HMTA	4.9,4.0,5.0 4.6,2.4,4.7

Thermal Stability

Thermal analyses of several impregnated charcoals have been made in a temperature gradient of 5°/min and the CO, CO_2, I_2 and organic iodides have been monitored. The results indicate rather complex chemical reactions that release both elementary iodine and volatile organic iodides at temperatures well below the ignition of the charcoals. The spontaneous ignition of the impregnated charcoals appears to be of secondary importance in the nuclear applications.

The iodine emission varies with both charcoal and the impregnation formulation. This behavior may best be seen when base charcoals are impregnated with only elementary iodine (0.5%). The rate of emission of iodine was first followed using a heating rate of 5°/min. by sampling the air flow (5 L/min) directly into the micro-coulombmeter and then in a repeat determination the rate was determined by sampling the air flow after it had passed through a quartz tube held at 700°C. Some typical results (Table 2) for three charcoals show the variation with both charcoal and temperature. Note that the iodine emission is a small fraction of the total iodine added to the charcoal, but, nevertheless, this is in the concentration range pertinent to a nuclear application.

Table 2: Rate of Iodine Emission (nanomoles/minute)

Charcoal	I_2 Added	Temp.	I_2	Organic Iodide
177	25.6 mg	180°C	0.2	2.1
BPL 10X16	29.5	"	0.9	0.5
GX 32	17.2	"	5.7	2.5
177	25.6	200°C	0.4	4.6
BPL 10X16	29.5	"	3.7	1.5
GX 32	17.2	"	13.8	2.0

Trapping Mechanism

A reaction mechanism for CH_3I retention was devised as a guide to further research. The many combinations of the salts of iodine oxyacids used as impregnating solutions in the present study have one thing in common: in basic solutions it is possible to form the hyperiodite species. The formation is thermodynamically possible from calculated heats of formation. Postulating a small but finite concentration of OI^- in the boundary surface of a charcoal, the following trapping mechanism may occur:

$$CH_3I^{131}(g) + K^+ OI^-(c) \rightarrow CH_3OI(g) + KI^{131}(c) \quad (1)$$

$$CH_3OI(g) + K^+OH^-(c) \rightarrow CH_3OH(g) + K^+ OI^-(c) \quad (2)$$

The free energy change for the sum of these two reactions is -17.45 Kcal. A CH_3I molecule in approaching the OI^- species on the surface (Figure 1) is oriented with CH_3 towards the ion and I directed away. By means of a Waldon Inversion a transition state I is formed which readily is transformed into products II as indicated. A neighboring mobile OH^- surface group then rapidly forms the transition state II which results in the formation of III, CH_3OH and the original reactive OI^- species. A chain reaction is thus established with the following features:

1. The chain involves the regeneration of the active species OI^- and furnishes a stable sink for radioiodine, namely KI^{131}.

2. The free energy change is favorable.

3. The charcoal support serves as a sink for the CH_3OH produced.

4. The mechanism accounts for high efficiency when the pH is high and a low efficiency observed when the pH is reduced.

5. The observed axial location of I(131) in the charcoal bed follows catalytic kinetics.(4)

6. Economical quantities of impregnants are employed.

One test for the reaction mechanism is the detection of methyl alcohol as a reaction product. Obviously, excess methyl alcohol will serve as a "poison" in the proposed mechanism.

The complete reaction mechanism is doubtlessly very complex. In some cases the adsorption process appears to dominate the trapping kinetics. However, in most cases, efficient trapping appears to occur via a catalytic process.

References

1. RDT Standard M16-1T, October, 1973, Division of Reactor Res. & Dev., Tech.Inf.Ctr.,Oak Ridge,Tenn.

2. Downs, A.J. and Adams, C.J., "The Chemistry of Chlorine, Bromine, Iodine and Astatine", Pergamon Texts in Inorganic Chemistry, Vol. 7 (1975).

3. Deitz, V.R. and Blachly, C.H., Proc. 14th ERDA Air Cleaning Conf. (1976).

4. Deitz, V.R., Blachly, D.H. and Jonas, L.A., Proc. 14th ERDA Air Cleaning Conf. (1976).

Acknowledgement

The sponsorship of the Division of Nuclear Fuel Cycles and Production, John C. Dempsey, Contract Manager, is gratefully acknowledged.

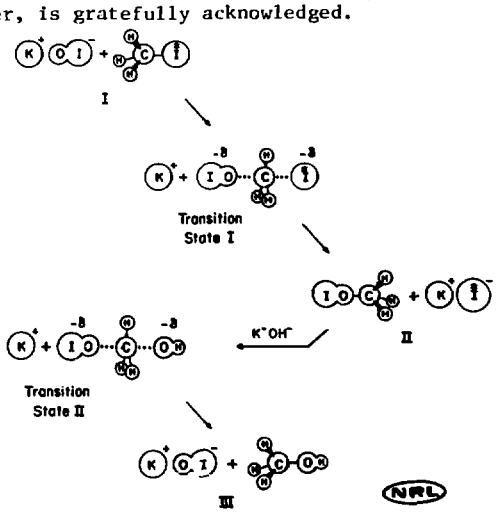


Fig. 1: A Mechanism for the Trapping of Methyl Iodide

CORRELATION OF STRENGTH WITH PHYSICAL PROPERTIES*

W. C. Morgan and F. L. Becker
Battelle, Pacific Northwest Laboratories
Richland, Washington

Introduction

Most investigators have assumed that fracture of graphite occurs either at constant strain (S^2 E) or at constant strain-energy (S^2 E), as per the Griffith equations (1-3). But both concepts assume that the material is brittle, isotropic, and without voids. To the contrary, manufactured graphites are deformable, extremely anisotropic on a microscopic scale, and seldom approach theoretical density.

Porosity of brittle solids can be treated "idealistically" in two ways: 1) The material may be visualized as a continuous solid, containing discrete pores (bubbles), or 2) It may be visualized as being a continuous void, containing particles which are bonded together at their points of contact.

Theory

MacKenzie (4) has derived the effect of porosity on elastic properties for the continuous-solid model, and Kerner (5) has treated the continuous-pore model. Both models yield a very large dependence of elastic properties on porosity, with the continuous-pore model predicting the larger effect.

Most brittle materials exhibit a dependency which is intermediate between the predictions of the two models. Euler (6) has shown how the two models can be combined to yield a better fit to experimental data.

Unfortunately, except for the treatment by Mrozowski (7), the dependency of strength on porosity has not received similar (or, at least, successful) attention. Although the model developed by Mrozowski leads to a considerable dependency of both strength and elastic moduli on porosity (as is observed), some of the finer details, such as relative dependence of the two properties (8), are not in agreement with theory. Considerable data has, however, been accumulated and empirical relationships have been developed for porous ceramics (9-11), as well as for graphites. In general, these relationships indicate that a 10% change in porosity will produce about 50% change in strength; this is the same "rule-of-thumb" which emanated from the pioneering work of Griggs (12) on the loss of strength during oxidation of graphite.

Assuming the empirical correlation: $(S/S_0) = (\rho/\rho_0)^{\alpha}$, where S = compressive strength, ρ = density, and the subscripted "o" indicates a reference state; the "rule-of-thumb" yields $\alpha = 6.58$. Assuming a similar relationship for elastic moduli: $(E/E_0) = (\rho/\rho_0)^{\beta}$, $(S/S_0) = (E/E_0)^{\gamma}$, where $\gamma = \alpha/\beta$. Euler's model gives a calculated change of ~40% in elastic moduli between 80% (ρ = 1.81 Mg/m^3) and 70% (ρ = 1.58 Mg/m^3) of theoretical density; the exact calculations yield $\beta = 3.78$ and $\gamma = 1.74$.

Results With Unoxidized Samples

Six 3-inch diameter by 6-inch long samples were machined from different sections of a log of a high-density, high-strength graphite**. Density and elastic moduli [calculated from ultrasonic velocities, measured by the "pitch-catch" method (13)] were obtained and the samples were tested for compressive strength in accordance with ASTM Standard C-695 (14). The best "physically reasonable" correlations, with the Young's moduli (E_e) and shear moduli (E_s) measured parallel to the axis of the samples, are:

$$S = 0.3424\ \rho^{1.84} E_e^{1.87}, \text{ and}$$

$$S = 1.338\ \rho^{2.41} E_s^{1.74}, \text{ with}$$

S in megapascals, ρ in megagrams per cubic meter, and E in gigapascals.

For the moduli measured diametrically, the best correlations are:

$$S = 0.6109\ E_e^{1.69\nu - 0.412}, \text{ and}$$

$$S = 3.875\ E_s^{1.67\nu - 0.198}, \text{ where}$$

ν = Poisson's ratio.

The exponents for E are in excellent agreement with value, $\gamma = 1.74$, which was derived above. Moreover, the maximum difference between calculated and measured strength is 1.9% of measured strength (for the correlation of strength with density and shear modulus); the maximum difference for the other three correlations is 1.4%.

Results With Oxidized Samples

Nine samples, 3-inches in diameter and 8-inches long, were oxidized at varying rates in an atmosphere of 80% CO_2, 20% CO, to between 5 and 10% weight loss; oxidation profiles ranged from mostly surface to nearly homogeneous. After oxidation, 1 inch was removed from each end of the samples; density, ultrasonic velocity, and compressive strength were then measured. Original strengths were calculated, using the correlations determined for the unoxidized samples; change in strength was then correlated with change in ultrasonic velocity: $(S/S_0) = (v/v_0)^{\lambda}$, where v is the ultrasonic velocity (either of the shear wave or of the longitudinal wave), and $\lambda \geq 2.3$.

The maximum difference between calculated and measured strength is 6.4% of measured strength (for the correlation of strength with Young's modulus and Poisson's ratio); the correlation of strength with density and Young's modulus yields a maximum difference of only 3.3%.

* This paper covers work performed by Battelle-Northwest under Energy Research and Development Administration Contract No. EY-76-6-06-1830.

** Stackpole Carbon Company, Grade 2020, log No. 89970 B-F880 #219; $\rho \geq 1.8$ Mg/m^3, $S_0 \geq 86$ MPa for 1 inch-diameter samples (1 MPa = 145.04 psi).

Conclusions

- Relationships have been developed between strength and changes in ultrasonic velocity; which can be used to accurately and non-destructively determine the compressive strength of Stackpole Grade 2020 graphite.
- There is reason to believe that the general relationship between strength and elastic moduli may be applicable to other graphites and to porous ceramics.
- This is a promising area for both experimental and theoretical work.

References

1. A. A. Griffith, Phil. Trans. Royal Soc. (London), A221, 163 (1920).
2. A. A. Griffith, Proc. First International Congress for Applied Mechanics, Delft, p. 55 (1924).
3. G. C. Sih and H. Liebowitz, Int. J. Solids and Structures, 3, 1 (1967).
4. J. K. Mackenzie, Proc. Phys. Soc. (London), 63B, 2 (1950).
5. E. H. Kerner, Proc. Phys. Soc. (London), 69B, 808 (1956).
6. F. Euler, J. Appl. Phys., 28, 1342 (1957).
7. S. Mrozowski, Proc. First and Second Conference on Carbon, Univ. of Buffalo, p. 195 (1956).
8. J. Okada and Y. Takeuchi, Proc. Fourth Conference on Carbon, Pergamon Press, p. 657 (1960).
9. E. Ryschkewitsch, J. Am. Ceram. Soc., 36, 65 (1953).
10. W. J. Duckworth, J. Am. Ceram. Soc., 36, 68 (1953).
11. R. L. Coble and W. D. Kingery, J. Am. Ceram. Soc., 39, 377 (1956).
12. B. Griggs, US-ERDA Report HW-42498 (April 1956).
13. J. W. Faircloth, Jr. and I. W. Gazda, Twelfth Biennial Conference on Carbon, Univ. of Pittsburgh, p. 125 (1975).
14. "Method of Test for Compressive (Crushing) Strength of Graphite," Annual Book of ASTM Standards, Parts 17 and 45.

EFFECTS OF OXIDATION ON THE MECHANICAL PROPERTIES OF CARBON/GRAPHITE*

T.C. Peng
McDonnell Douglas Research Laboratories
McDonnell Douglas Corporation
St. Louis, Missouri 63166

The mechanical properties of carbon/graphite are degraded by oxidation via mass removal and microstructural deterioration. Karcher et al. [1] showed that a 1% mass loss reduced the tensile strength by 15% and increased the pore density and the average pore diameter.

We investigated the mechanical properties of polycrystalline graphite (ATJS) and vitreous carbon [2] as functions of temperature, oxygen flow, and oxidation time. The reductions in ultimate tensile strength as a function of temperature are shown in Fig. 1. The effects of oxygen mass flow are shown in Fig. 2. Oxidation effects below threshold temperatures (~ 850 K for ATJS and ~ 1050 K for vitreous carbon) were within experimental error. These threshold temperatures for oxidation agree with those obtained from thermogravimetric analysis in air (~ 900 K for ATJS and ~ 1000 K for vitreous carbon). [3] The higher threshold temperature for vitreous carbon corroborates its higher oxidation resistance. [2, 4] Consequently, the strength reduction near oxidation threshold is caused by loss of mass.

At higher temperatures the reduction in strength of graphite/vitreous carbon is not compatible with mass loss alone (< 30% mass loss reduced tensile strength by 60% for ATJS and 76% for vitreous carbon). Optical and scanning electron microscopy show large-scale erosion; thus, pore enlargement and graphite component debonding are responsible for the enhanced loss in ultimate tensile strength at high temperatures. Presently, the relative contributions of mass loss and microstructure deterioration to changes in strength are undefined. However, the temperature at which the ultimate tensile strength starts to decline rapidly (~ 950 K for ATJS and ~ 1200 K for vitreous carbon) can serve as an indicator of the increased contribution from microstructure deterioration.

The oxidation effects on microstructure were investigated by scanning electron microscopy. The unoxidized ATJS graphite has a relatively smooth surface caused by the fine grain binder. The oxidized ATJS shows a rough surface with large protruding filler particles (~ 50 μm) having the appearance of being weakly bonded; the individual pores become large holes (~ 25 μm) interconnected with broad channels ~ 5 μm wide.

This difference of surface structure between the oxidized and unoxidized ATJS supports the hypothesis that the binder oxidizes at a faster rate than the filler and that during oxidation a partially oxidized filler particle can be removed from the surface as a particulate. [5]

The unoxidized vitreous carbon has an extremely smooth surface; grain structure and pore size appear as small dark pits at 1600X. The initial effects of oxidation cause a rapid increase in pore density as well as pore size. When oxidation becomes significant, the surface is filled with large circular depressions plus distinguishable grains (~ 2 μm). The high homogeneity in vitreous carbon produces a highly uniform oxidation effect on

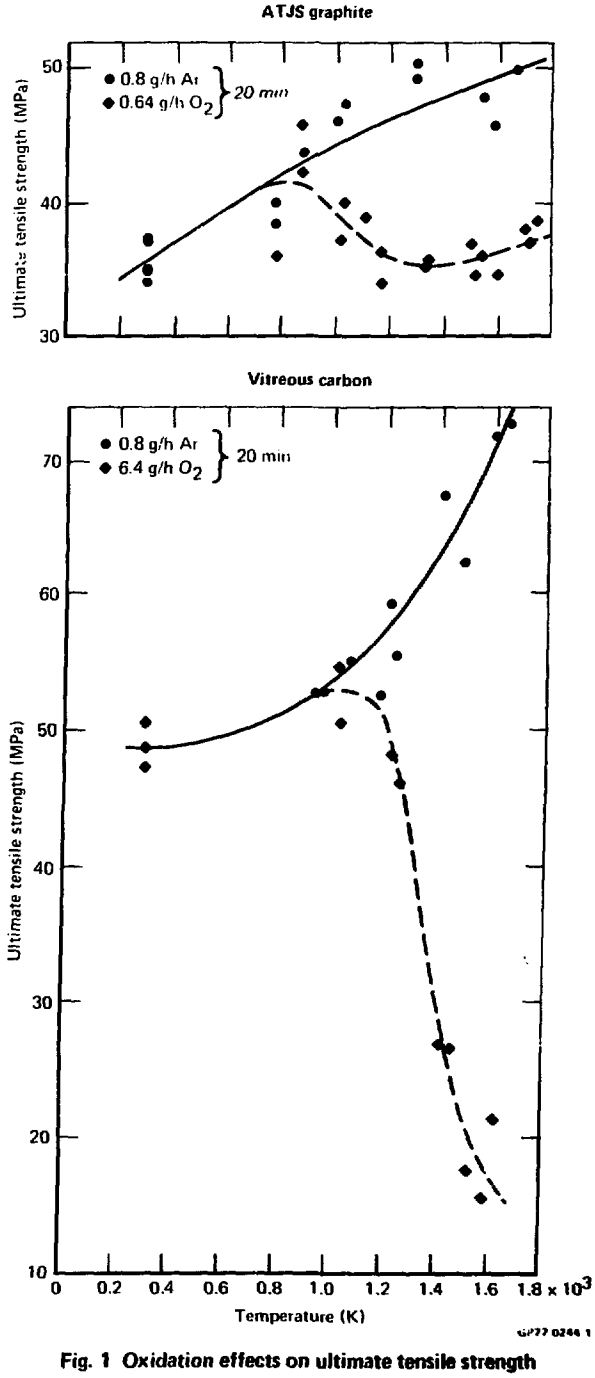


Fig. 1 Oxidation effects on ultimate tensile strength

*This research was conducted under the McDonnell Douglas Independent Research and Development Program.

the surface with little evidence for particulate removal. Fine grain structures and homogeneous erosion provide two major reasons for the high oxidation resistance of vitreous carbon.[4]

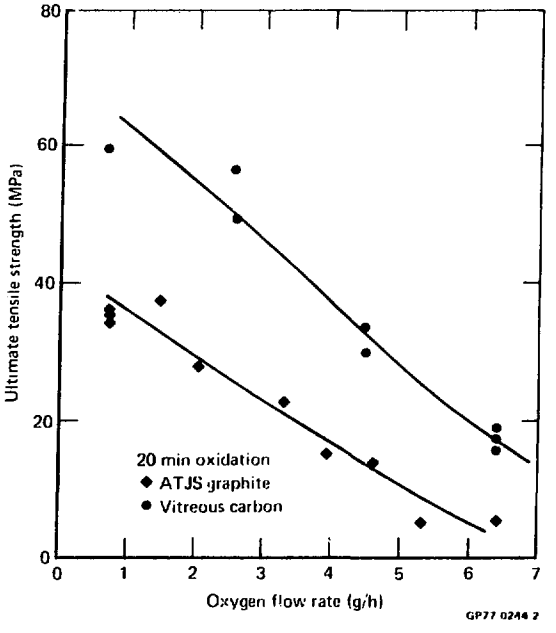


Fig. 2 Oxygen flow rate effects on ultimate tensile strength

REFERENCES

(1) W. Karcher, R. Krefeld, and P. Glaude, "The Effect of Thermal Oxidation by Water Vapor on the Mechanical Strength of Nuclear Graphite," 9th Biennial Conference on Carbon, Chestnut Hill, MS (1969).

(2) F.C. Cowlard and J.C. Lewis, "Vitreous Carbon A New Form of Carbon," J. Mater. Sci. 2, 507 (1967).

(3) I. Shaipro, "Oxidative Characterization of Carbon Fibers and Graphite," 10th Biennial Conference on Carbon, Bethlehem, PA (1971).

(4) J.C. Lewis, "Comparative Study of the Gaseous Oxidation of Vitreous Carbon and Various Graphite," 2nd Conference on Industrial Carbon and Graphite, London, England (1965).

(5) H.G. Maahs and D.R. Schryer, "Particle Removal in the Ablation of Artificial Graphite," AIAA J. 7, 2178 (1969).

THE EFFECT OF OXIDATION ON THE COMPRESSIVE STRENGTH OF GRAPHITE*

P. A. THROWER, J. C. BOGNET

Department of Material Sciences
The Pennsylvania State University
University Park, PA 16802

Introduction

The use of graphite for load bearing members in a nuclear reactor with a slightly corrosive environment calls for an understanding of those factors which influence the degradation of mechanical properties by gasification processes. The work reported here is solely concerned with the way in which oxidation in air influences the compressive strength and strain-to-failure of two different graphites, viz., Stackpole 2020 and Great Lakes H440 grades. It is expected to have data on gasification by CO_2, and possibly H_2, available for presentation at the conference.

Experimental

Samples of both graphites in the form of right cylinders 0.25" diameter (ϕ) x 0.50" long (ℓ) and 0.75"ϕ x 1.50"ℓ were compressed to fracture in an Instron testing machine. It was found that thin pieces of Teflon tape at the ends of the sample minimized frictional effects. The compressive strengths and strains-to-failure were found to have the same mean values for both sample sizes in each case.

Strain rate was varied between 0.1"/min and 0.002"/min and again no effect was found on either the fracture stress or strain-to-failure. It was therefore decided to use a strain rate of 0.01"/min and samples of 0.25"ϕ x 0.50"ℓ.

The data presented here were obtained by oxidizing samples in air in an open ended tube furnace at temperatures between 500°C and 800°C. The graphite cylinders were held in Pyrex tongs during the oxidation which protected the end faces from reaction and thus allowed the samples to be used in subsequent compression tests without their failing due to these faces crumbling.

Results

A comparison of compressive strength and strain-to-failure as measured on unoxidized samples and the corresponding values given by the manufacturers is given in Table 1. The measured strains-to-failure are approximately double those anticipated.

The effect of oxidation on the compressive strength (σ_c) of the two graphites is shown in Figure 1. It can be seen that even though oxidation temperatures varied between 500°C and 800°C, there is apparently no effect of temperature on the relationship between strength and burn-off. For both graphites, a burn-off of 8-9% is sufficient to produce a 50% loss in strength.

Table 1

Graphite	Fracture Stress (psi)		Strain-to-Failure (%)	
	Given	Expt.	Given	Expt.
H440	7,800	8,100	~2	4.4
2020	13,000	11,000	1.9	4.3

While it was impossible to accurately measure the diameter of oxidized specimens due to their friable surface, it was somewhat surprising that even up to 50% burn-off there was no appreciable change in external sample dimensions.

Examination of sections of oxidized samples using the scanning electron microscope reveals no boundary between oxidized and unoxidized areas and oxidation appears to be reasonably uniform throughout the sample. Figure 2 shows regions of a sample of H440 graphite oxidized to 15% burn-off. While there is no significant difference between photographs from different regions of the sample, it is obvious that the binder is oxidized much more rapidly than the filler. Whereas oxidation of filler particles occurs mainly at their edges, oxidation of binder occurs at sites throughout its volume. The larger number of active sites in the binder is responsible for its rapidly being transformed into a spongy material while surrounding filler particles are relatively untouched. A higher magnification view of binder material (Fig. 2c) clearly shows that the binder has a rather crude layer structure and that oxidation has occurred at points within layers as well as at layer edges.

Discussion

The production of a 50% loss in compressive strength by a 8-9% burn-off irrespective of oxidation temperature is in agreement with the results of Board and Squires [1] on the effect of CO_2 oxidation on British PGA graphite. It was assumed that such a large strength reduction was due to loss of binder which holds filler particles together. Fig. 2 does in fact show greater reactivity of binder over filler and hence the hypothesis is probably valid.

A plot of $\log_{10} \sigma_c$ against burn-off is shown in Figure 3. For the 2020 graphite, the relationship appears to fall on two parallel lines with a jog at about 28% burn-off. On the other hand, all data for H440 seems to fall on one straight line. The importance of the apparent discontinuity in the 2020 data is not yet clear but there is a discontinuity in the strain-to-failure vs burn-off plot for the same graphite (Figure 4). Both Board and Squires[1] and Rounthwaite et al.,[2] indicate that strain-to-failure for tensile fracture is approximately constant with respect to burn-off and this is true here for H440 but only up to ~28% burn-off for 2020 after which it increases rapidly.

A tentative model of the observed behavior might therefore include the following features

a) more rapid gasification of binder than filler
b) load-bearing properties mainly due to filler
c) total binder removal in 2020 at ~28% burn-off (n.b., this does not correspond to a 28% binder content)
d) loss of specimen ridgidity and a rapid strength decrease on removal of binder
d) a higher binder concentration in H440 (the weaker material) than in 2020.

References

1. J. A. Board and R. L. Squires, Proc. 2nd Conf. on Ind. Carbon and Graphite, Soc. for Chem. Ind., London, 1966, p. 289.
2. C. Rounthwaite, G. A. Lyons and R. A. Snowdon, ibid., p. 299.

*Sponsored by the U.S. ERDA under Contract No. EY-76-S-02-2712.*000

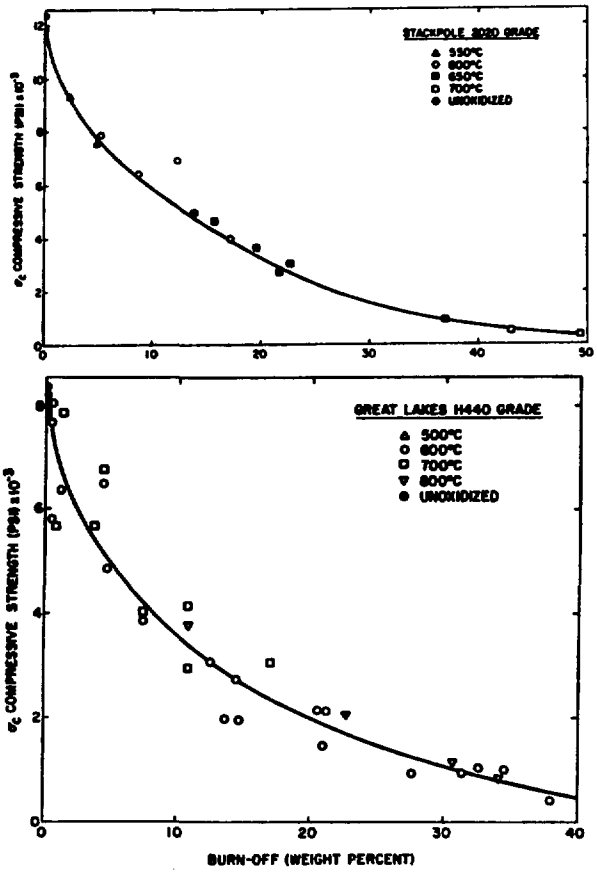
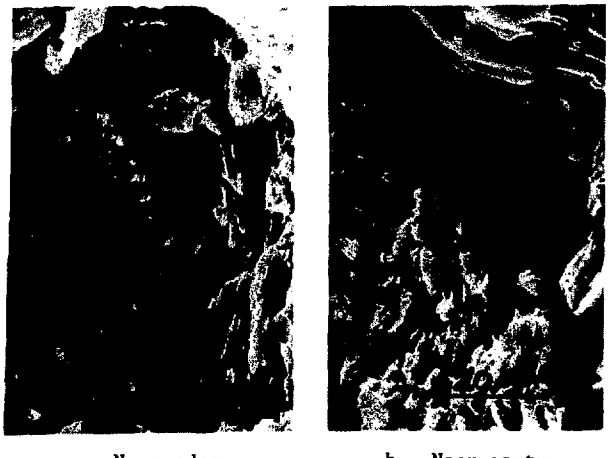


Fig. 1



a. Near edge b. Near centre

Fig. 2

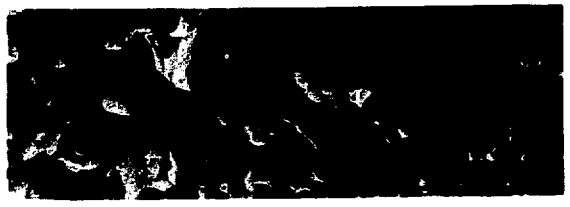


Fig. 2c

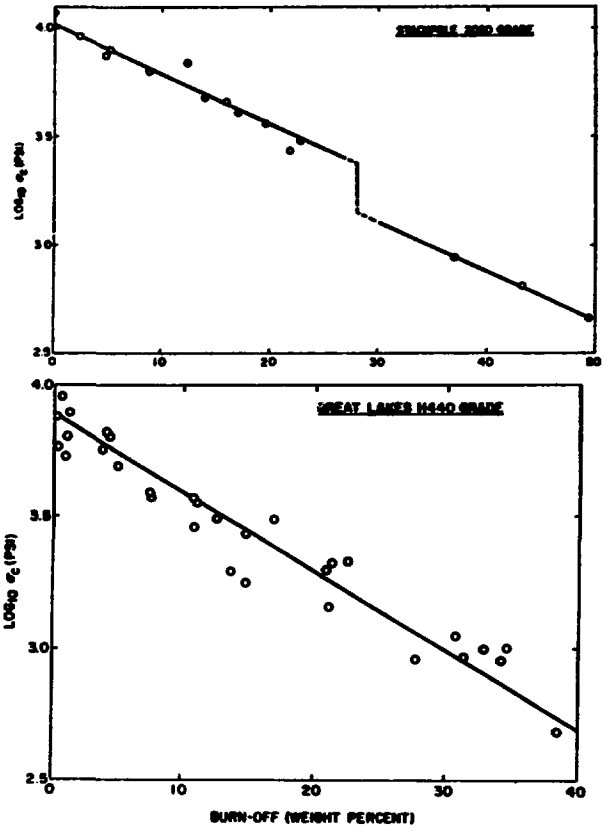


Fig. 3

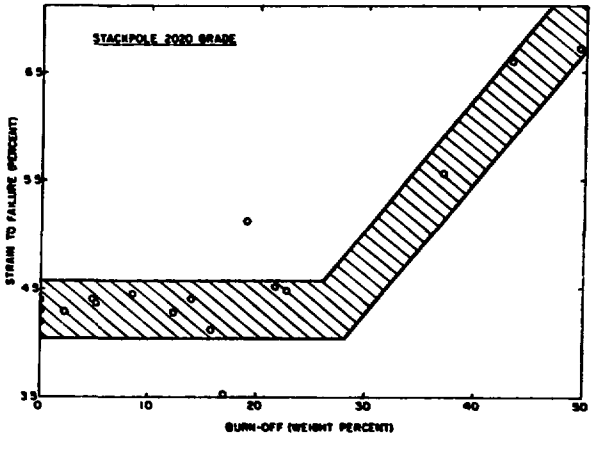


Fig. 4

APPLICATION OF X-RAY MEASUREMENTS FOR CHARACTERIZATION OF ARTIFICAL CARBONS

E. FITZER, K.-H. KÖCHLING, G. SCHWARZ

Institut für Chemische Technik
Universität Karlsruhe, W.Germany

Introduction

The paper is concerned with characterization of commercially important carbon materials by X-ray diffraction analysis. As well-known there exist careful investigations on the effects of microstructure of homogeneous carbons on their diffraction behaviour, although the objective valuation of the different structural models used for interpretation of experimental average diffraction data is still difficult. Additional problems arise from the heterogeneity of carbon and graphite samples as far as the degree of order of the different parts within the specimen is concerned. This problem of questionary significance of experimental data for characterization of heterogeneous samples is hardly studied systematically until now, and no international agreement exists about guidelines for practical application. The present work should contribute to the efforts of IUPAC commission on "Characterization of Carbon".

Under the same experimental conditions integral intensity of diffraction lines of ordered and disordered carbon can vary within orders of magnitude. As in carbon technology mostly heterogeneous mixtures of various carbons must be characterized, for example filler and binder carbons within one sample, the superficial interpretation of sharp diffraction lines as representative average can be misleading and can simulate a higher degree of graphitization even in case of minor contents of well graphitized particles.

Literature

Already 1960 it was tried to analyse mixtures of non graphitizing carbon with natural graphite by the intensity ratio of (001 - lines, at various angles (H.BEUTELL et al, 1973). Although this method is suitable in particular cases (W.WEISWEILER et al.1971), principal limitations arise from the use of a non graphitizing matrix in such reference material. Therefore the present experiments are based on graphitizable coke with varied heat treatments as main constituent of the sample.

Experimental

Sample material was prepared by mixing pre-heattreated powder of coal tar pitch coke with additions of 0 (0.1) 2 (1) 10 (5) 50 wt.-% of natural graphite flakes (Ceylon), $\bar{c}/2 = 3.354$ Å, polycristalline graphite, $\bar{c}/2 = 3.359$ Å, and microcristalline graphite (Kaisersberg), $c/2 = 3.357$ Å, as listed in tab.1. Ni-filtered Cu-K_α-radiation with BRAGG-BRENTANO-arrangement and planar samples were used for the diffraction measurements. Sample thickness was optimized by experiments (50 mg/cm^2, corresponding to a sample thickness of 0,25 mm), because numerical correction of the absorption effect is too difficult in case of heterogeneous targets.

The effect of sample heterogeneity on (001)-diffraction lines

In order to describe the effect of the two different carbon types within the various samples we will distinguish between three limiting cases as shown in fig. 1.

Case A: The appearance of two clearly separated diffraction lines.
Case B: Superposition of both lines with the possibility of easy separation for evaluation of the single diffraction profiles
Case C: Superposition of both lines without the possibility of visual separation

The experimental results are compiled in fig. 2. The added amount of well graphitic component is indicated as abscissa. No difference in diffraction lines between mixtures with natural graphite flakes and well-graphitized artificial carbon was found as far as samples with additions up to 10 wt.-% are considered.

In the case of glass-like carbon small additions of graphitized samples (about 0,1%) can be detected already. In the case of tar and pitch coke as main constituents of samples the lower limit for semi-quantitative estimation of well graphitized parts is found to be in the order of 0,2%.

The upper limit of the addition causing separate lines according case A is found to be 10% approx. for the (002)-interference. The limits for the second order of the (001)-interference are indicated by dotted lines being between 0,3 and 12-15%.
The ordinate of fig.2 indicates maximum heat treatment temperatures of the pitch coke component of the samples. In all cases a heat treatment time of one hour was used. Already heat treatment at 1700°C causes superposition of the diffraction lines according to case B at every percentage of the addition. Easy separation is still possible in samples with graphitic additions between 0.2 and 10%. With increasing heat treatment temperature the composition suitable for easy analysis by (001)-lines is shifted to higher contents of additive, i.e. for 1900°C heat treatment temperature between 1 and 20 wt.-%. The same effect is valid for the analysis of the (004)-lines.
If heat treatment temperatures above 2200°C were applied, complete superposition of both lines was found in all cases according to case C, however, with the possibility to estimate the content of well graphitized

additions by the asymmetry of the base-line if additions between 3 and 2o% are considered. If higher contents of well graphitized parts are present there exists no possibility for estimation by analysis of the base-line.

Effect of sample heterogeneity on (hkl)-diffraction lines:

As known modulation of two-dimensional reflections of non graphitized carbons is caused by heat treatment above 2000°C. This is valid for (10)- and (11)-reflexions. (10) two-dimensional reflexions are strong enough to be found in nearly all types of samples, whereas (11)-lines can hardly be seen in non graphitized carbons. Therefore (110)- and (112)-lines were selected for indication of graphitized parts because no superposition by (11)-lines is to be expected. Three-dimensional (110)- and (112)-lines can be seen in case of non heat treated matrix material if additions of at least 10 wt.-% are used. Below this limit no quantitative evaluation is possible. According to our experimental results quantitative estimation of at least 5o% well-graphitized carbon is possible by calibrating the intensity of three-dimensional interference against the intensity of the base-lines with an accuracy in the order of ± 5%. As can be seen from fig. 2 the evaluation of these (110)- and (112)-lines can be regarded as a supplement to the results from analysis of the base-lines.

With increasing heat treatment temperature the quantitative evaluation of the three-dimensional diffraction lines becomes more difficult and is completely impossible if heat treatment temperatures above 1900°C were applied because of the graphitization effect of the pitch coke and the resulting modulation of (11)-lines of the main part of the samples (see range II in fig.2).

The area III in fig.2 covers compositions of samples in which the content of added well graphitized part is too low to enable a distinction between the addition and the effect of matrix graphitization.

Conclusions

The applicability of the methods described above for characterization of heterogeneous carbon and graphite samples will be discussed in detail. Industrial samples with varied types of filler and binder carbons, or filler carbons of original high sulfur content after heat treatment above puffing temperatures, non graphitized carbon with stress graphitized binder contents and finally the effect of catalytic graphitization in various sample materials will be described in more detail.

References:

M. BEUTELL, E.FITZER, R.GAIN, O.VOHLER (1963) Proceedings of the 5th Carbon Conference, Vol. II, pp. 319 - 333

W. WEISWEILER, W. BRAUN (1971); Carbon Vol.9, pp. 457 - 465

HTT of the coal tar pitch coke	used diffraction lines
1500°C, $\bar{c}/2$ = 3,450 Å	002, 004
1650°C, $\bar{c}/2$ = 3,435 Å	002, 004
1900°C, $\bar{c}/2$ = 3,405 Å	002, 004
2200°C, $\bar{c}/2$ = 3,390 Å	002, 004, 110, 112

Tab. 1: Compilation of coke-HTT and X-ray interferences

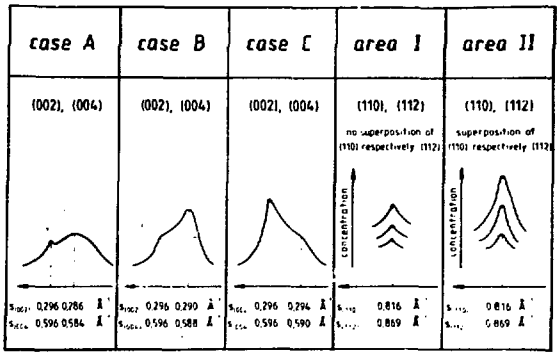


Fig.1: Position and shape of X-ray interferences as function of the graphite content and HTT of the samples (see fig.2)

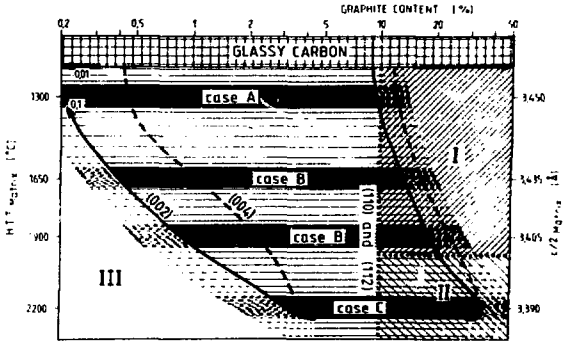


Fig.2: Applicability of the different X-ray interferences (see fig.1) on characterization of heterogeneous carbons

RAMAN SPECTRUM OF GROUND NATURAL GRAPHITE

M. Nakamizo*, M. Inagaki**, H. Kakiyama* and H. Honda*

* National Industrial Research Institute of Kyushu, Tosu, Saga 841, Japan
** Faculty of Engineering, Nagoya University, Chikusa-ku, Nagoya 464, Japan

Introduction

Carbons and polycrystalline graphites show two Raman lines at 1580 cm^{-1} and 1360 cm^{-1} which originate from the in-plane vibrational motion of carbon atoms within graphite layer planes[1]. The 1360 cm^{-1} Raman line disappears in natural graphite and stress-annealed pyrolytic graphites which possess a perfect hexagonal lattice belonging to the space group D_{6h}^4. However, the 1360 cm^{-1} vibrational mode becomes Raman active when defective structures are present in the layer planes, i.e., a defect-induced Raman mode. Therefore, it can be considered that the intensity of the 1360 cm^{-1} line is structure-sensitive and proportional to the amount of structural defects in the hexagonal layer planes.

Inagaki has reported from his X-ray works that the effective Debye parameter B_{eff} is sensitive to a small amount of deformation of crystal structure and can be used as a measure of imperfection of the layer planes for polycrystalline graphites[2]. The parameter B_{eff} represents the displacement of carbon atoms from the ideal positions of hexagonal lattice along the direction of the c-axis which may result from lattice defects.

The present study has been made to find the behavior of the 1360 cm^{-1} Raman line when structural defects are introduced into Ceylon natural graphite by grinding and to compare Raman results with the effective Debye parameter B_{eff} obtained on the same sample.

Experimental

Ceylon natural graphite was purified in a flowing halogen gas at 2700°C. About 2 grams of the graphite sample was ground in an agate mortar in air at room temperature for various times extending over 200 hr. Raman spectra of the ground samples of graphite were recorded on a JEOL Raman spectrophotometer JRS-S1 equipted with a photon-counting detector and a Coherent Radiation argon-ion laser CR-2. Most of the measurements were carried out on pressed powder pellets using the 488 nm argon line providing 400 mW at the sample. The intensity of the 1360 cm^{-1} line was measured with its line height relative to that of the 1580 cm^{-1} line and is expressed by R.

The effective Debye parameter B_{eff} was determined from the observed slope of the plots of X-ray diffraction intensities of (00L) lines against $\sin^2\theta/\lambda^2$[3]. The C_o spacing and specific surface area of the ground graphite were measured according to the ordinary procedures.

Results and Discussion

Fig. 1 shows Raman spectra of the ground samples of Ceylon natural graphite for various times up to 200 hr. The original sample exhibits an intense graphite line at 1580 cm^{-1}. The 1360 cm^{-1} Raman line also appears very weakly in this sample, suggesting the existence of structural defects which may have been introduced in the course of sample preparation. When the natural graphite is ground for several tens of hours, the 1360 cm^{-1} line increases gradually its intensity and becomes much stronger than the 1580 cm^{-1} line at 200-hr grinding. This indicates that defective structures increase in the graphite samples as grinding time is increased and that the crystal lattice of graphite is remarkably destroyed by grinding. As is obvious in Fig. 1, another Raman line appears around 1620 cm^{-1} which is clearly seen in the sample ground for 200 hr. The exact nature of this Raman line can not be explained at present but may be associated with the existence of finely ground particles of graphite containing extremely defective structures. However, all the spectral lines of the sample ground for long time are still sharp compared to Raman lines of various carbons obtained at heat treatment temperatures below 2000°C [4,5]. One of the possible expanations is to assign the 1620 cm^{-1} Raman line to the stretching vibration of conjugated carbonyl groups attaching to the edge carbon atoms of the graphite layer planes, because fine grinding leads to an increase in surface area of the graphite particles and oxygen in air is easily chemisorbed on the free valence bonds of the edge carbon atoms [6].

Fig. 2 shows changes of the relative intensity ratio R for two Raman lines, effective Debye parameter B_{eff}, C_o spacing and specific surface area of the ground graphites with grinding time. All but C_o spacing increases gradually with increasing grinding time up to 30 hr. For grinding times more than 30 hr, all the values of these parameters increase very rapidly. The C_o spacing of the ground samples remains constant (6.708 A) up to 30-hr grinding. From the analysis of the X-ray diffraction profiles, the first 30-hr grinding leads to a transformation of the hexagonal form of the graphite lattice to the rhombohedral form, and the amount of the latter form reaches about 30 wt% of the ground graphite [7]. During this transformation process in which C_o spacing remains unchanged, the values of both R and B_{eff} increase gradually, suggesting a partial destruction of the graphite lattice within the layer planes by grinding. This indicates that the parameter, C_o spacing is less sensitive than R and B_{eff} to a small structural change in the graphite lattice.

As mentioned in the first section, both the parameters R and B_{eff} are associated with structural defects and increase in proportion to their amounts present in the graphite layer planes. It is, therefore, expected that there exists a certain relationship between R and B_{eff}. Plots of R and C_o against B_{eff} for the ground graphite are shown in Fig. 3 where for comparison the same plots are also included for various graphitized cokes [8]. As is evident from the figure, a linear relationship exists between the parameters R and B_{eff} for both the ground graphite and the graphitized cokes. The difference in the slope between two curves indicates that structural defects introduced into the natural graphite in the grinding process are different from those which are present originally in the cokes and can be gradually removed

in the graphitization process. A similar difference between both the processes is seen for the plots of C_o spacing against B_{eff}, showing a rapid decrease in the C_o spacing of the cokes and a gradual increase in the C_o spacing of the ground graphite as each process proceeds along the direction indicated by arrow. In other wards, the C_o spacing of the cokes decreases very rapidly as the structural defects are removed by graphitization, while that of the ground graphite increases gradually as the defects are introduced by grinding.

For the same value of B_{eff}, different values of R and C_o are obtained between the grinding and graphitization processes. This indicates that both the parameters R and B_{eff} can be used along with C_o spacing to characterize graphite and carbon materials. Various types of structural defects need to be investigated further for the structural characterization of those materials.

References

[1] F. Tuinstra et al., J. Chem. Phys., 53,1126(1970)
[2] M. Inagaki, Carbon 13, 307(1975)
[3] M. Inagaki et al., J. Mat. Sci., 8, 312(1973)
[4] M. Nakamizo et al., Carbon, 12, 259(1974)
[5] T. G. Miller et al., 12th Bienn. Conf. on Carbon, p.105
[6] P. L. Walker, Jr., et al., Proc. of 1957 Conf. on Carbon, p481
[7] M. Inagaki et al., Tanso, No.74, 76(1973)
[8] Presented at 13th Bienn. Conf. on Carbon(1977)

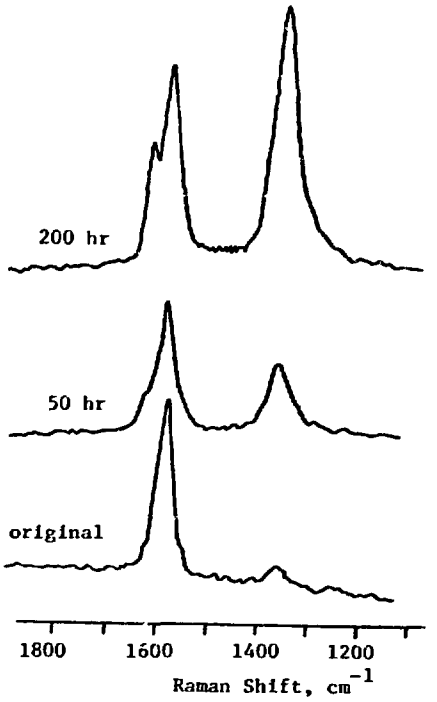


Fig. 1 Raman spectra of the ground graphites

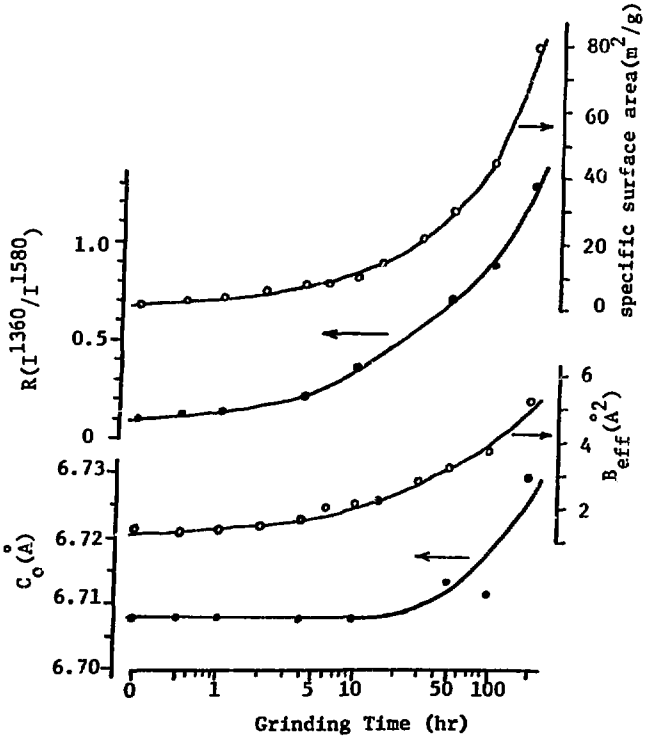


Fig. 2 Plots of R, C_o, B_{eff} and specific surface area against grinding time

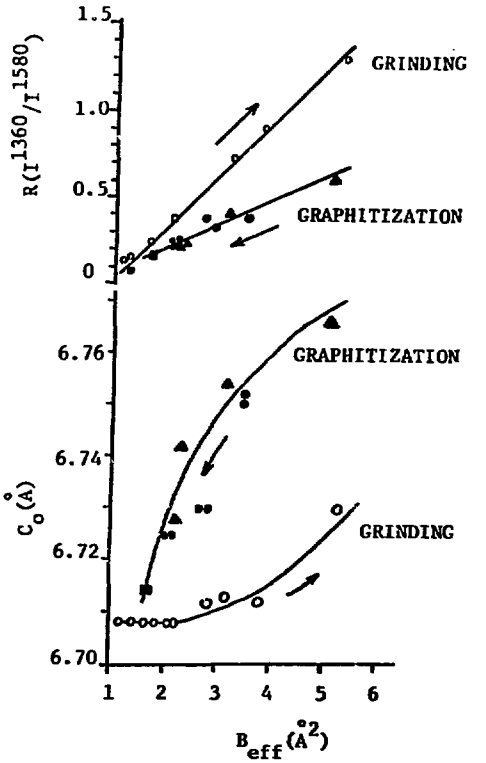


Fig. 3 Plots of R and C_o against B_{eff} for the grinding and graphitization processes

RAMAN SPECTRA OF CARBONS AND THEIR INTERCALATION RESIDUE COMPOUNDS

André Marchand and Chantal Garrigou-LaGrange
Centre de Recherche
Paul Pascal
Domaine Universitaire
University of Bordeaux
33405 Talence France

New lines have been observed in the Raman spectrum of carbons and their intercalation compounds. A detailed study of their polarization has been conducted and assignments of these new frequencies are suggested. Of particular interest is the resonance Raman spectrum of bromine in its residue compounds.

RAMAN SPECTRA AND CHARACTERIZATION OF CARBON MATERIALS

R. Vidano and D.B. Fischbach
Department of Mining, Metallurgical & Ceramic Engineering, University of Washington FB-10
Seattle, Wash. 98195

The Raman spectra of carbon materials have been thought to comprise just two lines, at 1580 and 1360 cm^{-1} (1-6); but recent studies (7,8) have revealed several additional lines for both crystalline graphite and disordered carbons. Some results of an ongoing investigation for the behavior of these lines and of the characterization of various carbon material types are described here.

Spectra were excited with 488 (sometimes 514.5) nm radiation from a CRL 52 Ar^+/Kr^+ laser and scanned with a Spex 1401 double monochromator/photomultiplier detector with a spectral slit width setting of 8 cm^{-1}. Many materials were studied including natural graphite single crystals (NGSC); compression-annealed pyrolytic carbon (CAPC); "massive" (MPC) and fluidized-bed (FBPC) pyrocarbons; glassy carbons (GC); and carbon fibers from PAN, rayon, and pitch. Virgin or fracture surfaces were used; but also the effects of mechanical polishing, ion-bombardment etching, reactor irradiation, and oxidation were observed for some materials. The FBPCs and GCs were heat treated over the range 1000-3000°C. Spectra were analyzed in terms of line position, integrated intensity I, and full width at half height W using an analogue type curve synthesizer and Gaussian line shapes.

The positions and some characteristics of the lines observed are summarized in Table I. Polarization studies still in progress suggest that G_1', G_2', G", and perhaps D and D' are polarized but that G is not. The studies also suggest that all lines (except perhaps G") result from in-plane vibrational modes. The previously reported G and D lines have been ascribed to E_{2g} and A_{1g} vib. modes respectively (1). D' is responsible for the blue-shift of the apparent G line to ~1600 cm^{-1} in very disordered carbons. In such carbons both G and D appear as broad peaks on very broad pedestals. The G' band appears to be the first overtone of D. D is silent in crystalline graphite, while G' is absent or attenuated in very disordered carbons and damaged graphites where D is strong, though the two co-exist in annealed carbons. This suggests that the mode(s) involved exhibit electro-optic anharmonicities (9). It also seems significant that only one line (1370 cm^{-1}) is observed in hexagonal BN.

The structure-sensitivity of the spectral features makes Raman spectroscopy a useful technique for carbon materials characterization. Representative spectra are shown in Fig. 1. The CAPC cleavage spectrum is typical of crystalline graphites, comprising a sharp G, weak G", and strong G_1', G_2'. Damage by ion etching attenuates G' and generates D & D'; similar effects result from polishing layer edges. For GC (1000°C); D, D', and G overlap and G' is absent; but it develops as a symmetrical band with increasing HTT. MPCs exhibit G', D', G, and D but I and W depend on deposition temperature (1600-2500°C).

The development with HTT of the widths W_G, W_D and the relative integrated intensities I_D/I_G, $I_{G'}/I_G$ for several carbons are compared in Fig. 2. The GCs were obtained from Beckwith and Sigri; the FBPCs were deposited from propylene. The graphitizability of C-13 (1150°C) was fairly high while that of C-4 (1350°C) was medium according to diamagnetic, density, and X-ray diffraction data (10). The HTT for G' appearance depends on carbon type and corresponds to $W_D \leq 90$ cm^{-1}. Initial widths increase with graphitizability; final widths for the FBPCs are lower than that for GC. The major spectral evolution occurs for HTT < 2400°C, while the carbons are still disordered, and the influence of layer stacking order appears to be negligible.

The spectral characteristics of fiber carbons are sensitive to precursor/processing differences, correlate well with mechanical properties, and depend systematically on surface "orientation". In Fig. 3, I_D/I_G for lateral surfaces is plotted against that for fractured cross sections for a large number of fiber types. Disorder decreases with increasing thermo-mechanical processing, but in all cases $I_D > G$ as expected. A pronounced trend, increasing with modulus E, for the surface to be more ordered than the interior (cross section) is evident (2). This supports other evidence for a developing sheath/core duplex structure. The strong influences of precursor and processing are clear in an I_D/I_G plot, Fig. 4. The sharp peak in PAN fibers correlates with fracture parameter behavior (11) and may be related to the influences of residual stresses and nitrogen. The high disorder in anisotropic (mesophase) pitch fibers is attributable to low processing temperatures (<2000°C). The effects of HTT ($E \leq 100$ GN/m²) and hot-stretching ($E > 100$) are qualitatively similar for fibers from rayon and isotropic pitch.

The Raman activity of carbons originates from in-plane lattice vibrational modes, and is responsive primarily to defects and distortion affecting the symmetry and perfection of the layer structure. As the detailed origins of the lines become better understood, Raman spectroscopy promises to evolve from a useful empirical characterization method to a sensitive probe into the nature of the structural disorder.

Research supported by the National Aeronautics and Space Administration as part of Grant #NGL 48-002-004

1. Tuinstra F. & Koenig J.L., J. Chem. Phys. 53 (3) 1126 (1970)
2. Tuinstra F. & Koenig J.L., J. Compos. Mat. 4 (10) 492-9 (1970)
3. Brillson L.J., Burstein E., Maradudin A.A. & Stark T., J.Phys.Chem.Sol.Suppl. 32 187-93 (1971)
4. Nakamizo M., Kammereck R., & Walker P.L.,Jr., Carbon 12 (3) 259-67 (1974)
5. Nathan M.I., Smith J.E., & Tu K.N., J. Appl. Phys. 45 (5) 2370 (1974)
6. Miller T.G., Fischbach D.B., & Macklin J.M., 12th Carbon Conf. Extended Abs. (Pittsburgh), 1975 Miller T.G., M.S. Thesis, Univ. of Washington, 1975
7. Vidano R. & Fischbach D.B., submitted to J. Amer. Ceram. Soc. (1977)
8. Nakamizo M., private communication; and this conf.
9. Herzberg, G., Infrared and Raman Spectra, D. van Nostrand, New York, 1945
10. Reatty R.L. & Fischbach D.B., Carbon '72 Preprints (Baden-Baden), 1972; 11th Carbon Conf. Extended Abs. (Gatlinburg), 1973; Beattie R.L., Ph.D. Thesis Univ. of Washington, 1974 (also ORNL-TM-4504, 1975)
11. Tokarsky E.W. & Diefendorf R.J., 12th Carbon Conf. Extended Abs. (Pittsburgh) 1975

TABLE I

PEAK	POSITION(cm^{-1})	WIDTH(cm^{-1})	OCCURENCE	I/I_G
G	1580	$\leq$20	All carbons & graphites	1.0
G"	1560	$\leq$20	Crystalline graphite	$\leq$0.1
G_1'	2695	$\leq$40	Crystalline graphite	$\leq$0.5
G_2'	2735	$\leq$40		$\leq$0.5
G'	2700-2720	$\leq$75	Annealed carbons	$\leq$1.0
D	1360	$\geq$40	Disordered carbons	$\leq$3.0
D'	1620	$\leq$45	Disordered carbons	$\leq$0.4

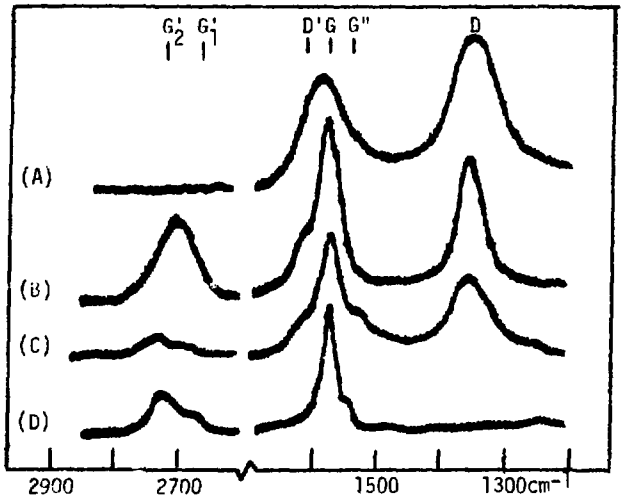


Fig. 1; Raman Spectra of: (A) GC-1000°C; (B) MPC-1800°C; (C) CAPC-ion etched; (D) CAPC-cleaved.

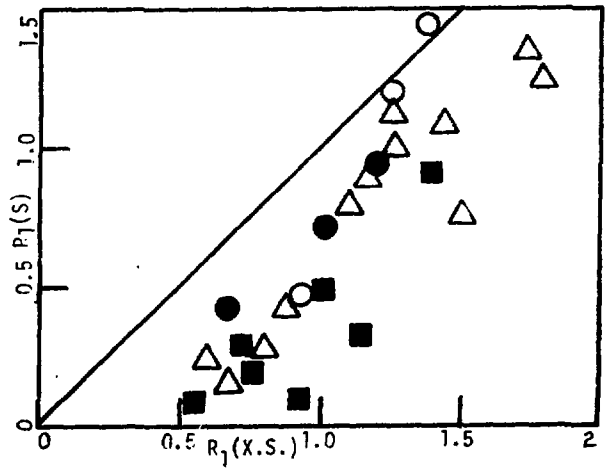


Fig. 3; $R_1=I_D/I_G$(SURFACE) vs $R_1=I_D/I_G$(CROSS SECTION) for carbon fibers.

Fig. 4; $R_1=I_D/I_G$(SURFACE) vs modulus for carbon fibers. →

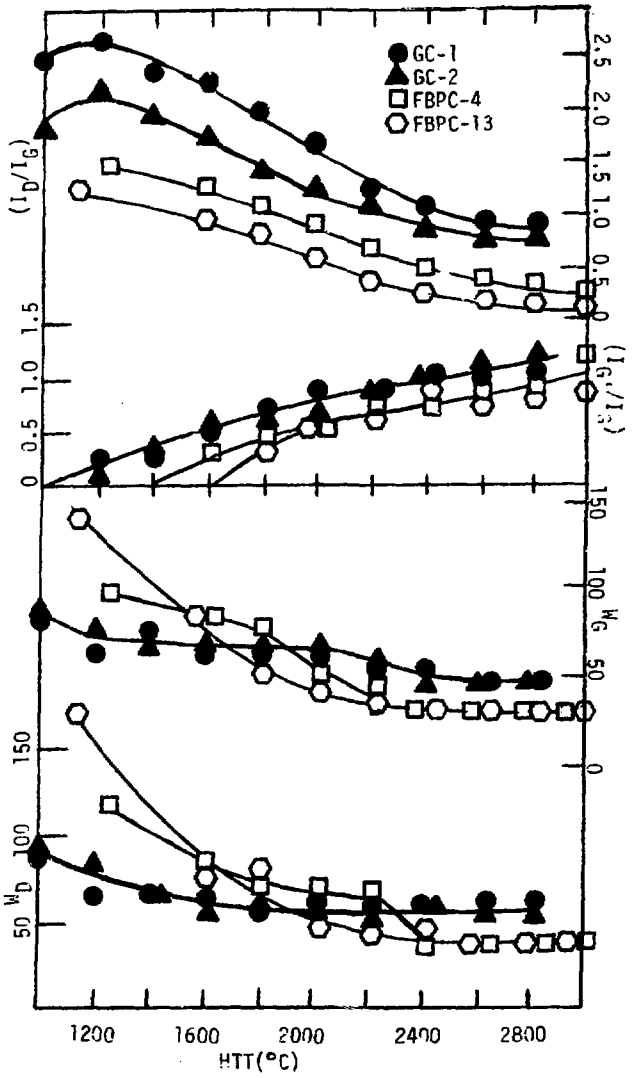
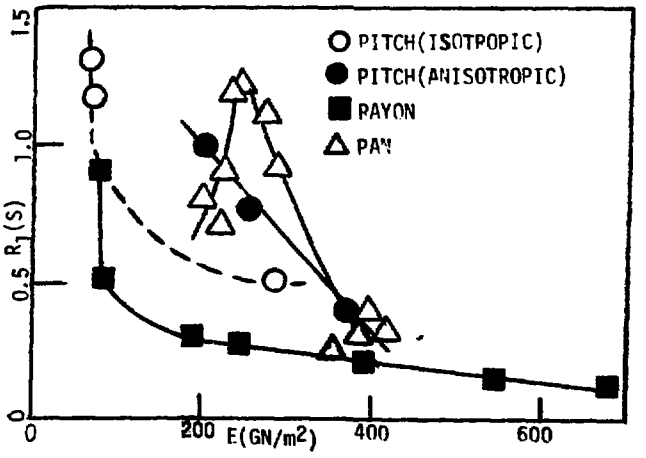


Fig. 2; I_D/I_G & $I_{G'}/I_G$ vs HTT and W_G & W_D vs HTT for GC and FBPC.



RAMAN SPECTRA, EFFECTIVE DEBYE PARAMETER AND MAGNETORESISTANCE

M. Nakamizo,[*1] M. Inagaki[*2] and Y. Hishiyama[*3]
*1 Nat. Ind. Res. Inst. Kyushu, Tosu 841
*2 Nagoya Univ. Chikusa-ku, Nagoya 464
*3 Musashi Inst. Tech., Setagaya-ku, Tokyo 158

Introduction

Carbon shows an Raman line at about 1360 cm^{-1} in addition to the line at 1575 cm^{-1} which is expected theoretically[1]. This additional line at 1360 cm^{-1} decreases its intensity as well as width with increasing HTT[1,2]. The ratio in intensity, R= I(1360)/I(1575), may be used as a measure of the lattice defects in graphite structure.

The effective Debye parameter B_{eff} has been measured on various well-graphitized carbons and graphites. It was found to decrease with the increase in HTT[3] and to increase with mechanical grinding and neutron irradiation[4]. So, B_{eff} may also be used as a measure of graphitization.

The transverse magnetoresistance $(\Delta\rho/\rho)$ of the soft carbons increases with increasing HTT[5] and approaches to the large value which is observed in graphite.

In the present work, we measured the Raman intensity ratio R, the effective Debye parameter B_{eff} and the maximum transverse magnetoresistance $(\Delta\rho/\rho)_{max}$ on the same graphitized cokes.

Experimental

Cokes from different sources were heat-treated at HTT ranging from 2500° to 3000°C in nitrogen flow, as shown in Table 1. A part of each coke was crushed in an agate mortar for X-ray diffraction and Raman studies. Grinding time was kept as short as possible (less than 1 min.). From the remaining part of the coke, the specimen for magnetoresistance measurement was cut into rectangular prism, size being 1.2×4.4×0.7mm.

Raman spetra were obtained by laser Raman spectrometer with an argon ior laser providing 400 mW of 4800 Å radiation on the sample compressed into pellet with or without KBr. The angle between the laser beam and the sample surface was ca. 20° and the scattered light was observed under 90° from the laser beam.

The effective Debye parameter B_{eff} was determined from the slope of linear relation between diffraction intensities of 00ℓ lines (ℓ =2,4,6 and 8, if possible) and $\sin^2\theta/\lambda^2$.

Magnetoresistance was measured at liquid temperature and the magnetic field of 10 kG by d. c. amplification technique by rotating the field in two modes. By taking account of the preferred orientation of crystallites the maximum transverse magnetoresistance $(\Delta\rho/\rho)_{max}$ was determined.

Results

In Figs. 1 and 2, R and $(\Delta\rho/\rho)_{max}$ are plotted against B_{eff}, respectively. These three parameters are closely related with each other; R increases linearly with increasing B_{eff}, and $(\Delta\rho/\rho)_{max}$ decreases rapidly at first and then gradually but almost linearly with increasing B_{eff}.

Discussion

Both Raman lines at 1575 and 1360 cm^{-1} are assigned to in-plane motion of carbon atoms in graphite lattice [1] and the latter is allowed to appear if there exist parts where the hexagonal symmetry of graphite is no longer maintained. On the other hand, large value of B_{eff} is due to out-of-plane displacement of carbon atoms which is associated with defects in the layer plane. The linear relation observed between R and B_{eff} may suggest that both are related to respective component along a- and c-axes of the same displacement of atoms due to lattice defects.

Magnetoresistance decreases with the increase in the concentration of trapped electrons which are accompanied by lattice defects. At low value of B_{eff} (<0.25), in other words, at the region of less defective structure, $(\Delta\rho/\rho)_{max}$ decreases rapidly with increasing B_{eff}.

Three parameters R, B_{eff} and $(\Delta\rho/\rho)_{max}$ depend on the concentration of lattice defects through in-plane motion, out-of-plane displacement and concentration of trapped electrons. They can be used as parameters for the characterization of graphitized carbons.

References

1) F. Tuinstra & J. L. Koenig, J. Chem. Phys. 53, 1126 (1970)
2) M. Nakamizo et al., Carbon 12, 259 (1974)
3) M. Inagaki, Carbon 13, 307 (1975)
4) M. Inagaki et al., TANSO 1973 [No. 74] 76 (1973)
5) Y. Hishiyama, Carbon 8, 259 (1970)

Table 1 Samples and HTT

Cokes	HTT (°C)	Symbol
QS	3000	⊕
PVC	3000	○
Petro	2800	■
Conoco No.1	2800	●
Texas	3000	×
Wilmington	2800	▲
Kendal	2540 ~ 3000	△
Gilsonite	2800	⊗

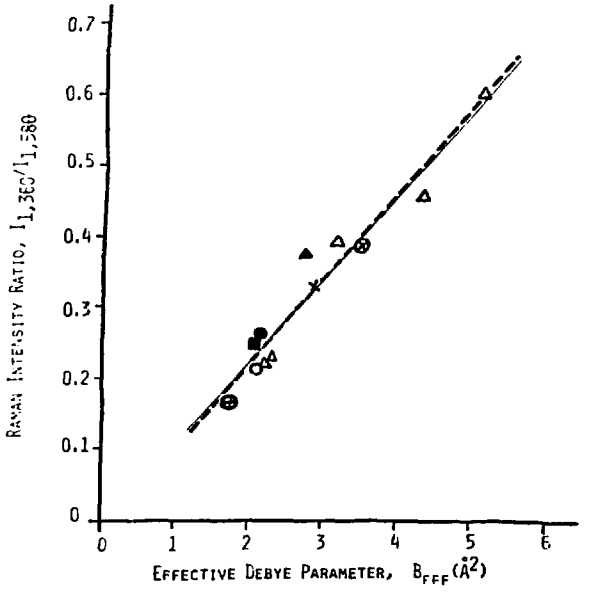


Fig. 1 Relation between B and B_{eff}.

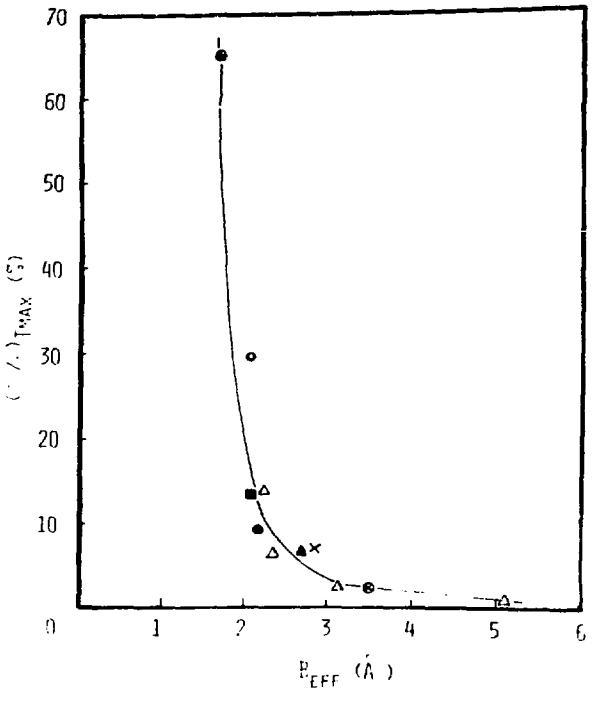


Fig. 2 Relation between $(\Delta\rho/\rho)_{max}$ and B_{eff}.

FORCE CONSTANTS FOR THE GRAPHITE LATTICE

A.P.P. Nicholson and D.J. Bacon
Department of Metallurgy and Materials Science,
The University, P.O. Box 147, Liverpool, U.K.

1. Introduction

Early force-constant models of graphite [1,2] assumed that lattice vibrations parallel and perpendicular to the basal plane are independent, and, although such decoupling is computationally convenient for the calculation of some crystal properties, these models have only a limited application. They describe a lattice which is unstable, since the shear modulus C_{44} is zero, and are inappropriate for defect-structure calculations for example. Thus, in an earlier study [3,4] which used the method of lattice statics to obtain the atomic displacements around a vacancy, we were restricted to a two-dimensional model of a layer.

The purpose of the present work was to develop a stable, three-dimensional model so that further defect calculations can be made. We required the model to predict the experimental elastic constants and give a good fit to the available phonon-dispersion data [5]. In earlier developments of three-dimensional models to fit this data, Nicklow et al. [5] and Mani and Ramani [6] determined force constants based on pair-wise interactions and valence constants respectively. In both sets, a non-zero value of C_{44} was assigned, but, for these models, this has the consequence of requiring an external pressure to be imposed to maintain equilibrium, and thus C_{44} would become zero under the application of stress-free equilibrium. The model used here avoids this difficulty.

2. The Model and Force Constants

A full discussion of the problems involved in fitting the constants involved in interactions between up to third neighbours in a plane and up to second neighbours on adjacent planes is the subject of a forthcoming paper [7]. We give there the relations which must be obeyed for stress-free equilibrium, and, in addition, it is noted that since the Cauchy relation $C_{13}=C_{44}$ is not satisfied by the elastic constants, at least one three-body interaction between adjacent layers is required. The available experimental data are insufficient to enable the constants of the most-general model to be determined, and it is necessary to set some constants to zero and to limit by physical reasoning the range of values of others. Full details are given in [7], and it is sufficient to merely present here values for the model which was finally found to best meet the requirements outlined in section 1.

Some constants were those which can be considered to arise from a pair-wise, interatomic potential function V(r), and others were of the valence type. The former give rise to forces on atoms which are either parallel or perpendicular to the line joining two atom centres, and are given by

$$R_n = d^2V/dr^2 \text{ and } T_n = r^{-1}\, dV/dr \text{ (at } r = r_n)$$

respectively, where r_n is the perfect-lattice spacing between nth nearest neighbours. For the model considered here, n = 1,2,3,4,5, as shown schematically in Fig.1, where the atoms neighbouring the atom at the origin (atom O) are labelled 1 to 5. We have assumed that the 5th-neighbour interaction between, say, atoms O and 5 is the same as that between atoms 1 and 5. In addition to these 10 parameters, three valence constants were used. They are (a) an interplanar constant λ giving energy changes due to changes in angle ϕ shown in Fig.1 as $\frac{1}{2}\lambda r_1^2 \sin^4\phi\,(\Delta\phi)^2$; (b) an in-plane, adjacent-bond-angle constant u, as used in earlier, simple models [1,2]; and (c) an in-plane, adjacent-bond-length constant v, equivalent to k_{rr} used in [6].

The values found for these various parameters are given in Table 1 in units of Nm^{-1}. As discussed in [7], they can be expressed in terms of the more conventional force-constant matrix for interactions between nth neighbours, which has the form (referred to $\hat{x}_1$, $\hat{x}_2$, $\hat{x}_3$):

$$\begin{pmatrix} A_n & D_n & E_n \\ -D_n & B_n & 0 \\ F_n & 0 & C_n \end{pmatrix}$$

where $B_4 = A_4$; D_n is non-zero only for n=2; E_n and F_n are non-zero only for n=5 (interaction O-5, for example) and n=5' (interaction 1-5, for example); and $F_5' = E_5'$.

The numerical values (in Nm^{-1}) of the remaining constants are given in Table 2, as are those calculated from the constants given by Nicklow et al. [5] and Mani and Ramani [6].

3. Discussion

The elastic constants (in $10^{10}Nm^{-2}$) given by the new model are compared with experimental values and those obtained in [5] and [6] in Table 3. The predicted dispersion curves along the Γ-A and Γ-M axes of the zone are shown in Fig.2. It can be seen that the new model gives an excellent fit to the experimental data, and, furthermore, it describes a lattice in stress-free equilibrium. The latter condition was not met in the models of Nicklow et al. [5] and Mani and Ramani [6]. (Additional inconsistencies in the latter work are discussed in [7].)

The present model uses a combination of pair-wise and valence potentials, and this has a distinct advantage for defect-structure calculations. The forces required to simulate defects can be derived very easily from the force constants; these forces are zero in a pure valence-potential model, and would have to be obtained from an independent calculation [4]. For a single vacancy in the present model,

for example, the force acting on the nth nearest-neighbour atom in an unrelaxed position is simply $-r_n T_n$. For n=1, this equals -20 eV/Å. The application of this model to the structure of vacancy clusters is in progress.

Acknowledgements

The work was supported by the UKAEA, Harwell. Useful discussions with Dr.J.W. Martin and Mr. J.H.W. Simmons are acknowledged.

References

1. A.Yoshimori and Y.Kitano, J.Phys.Soc. Japan, 11, 352 (1956).
2. J.A.Young and J.U.Koppel, J.Chem.Phys., 42, 357 (1965).
3. A.P.P.Nicholson and D.J.Bacon, Phys.Stat.Sol.(a), 28, 613 (1975).
4. A.P.P.Nicholson and D.J.Bacon, Carbon, 13, 275 (1975).
5. R.Nicklow, N.Wakabayashi and H.G.Smith, Phys. Rev., B5, 4951 (1972).
6. K.R.Mani and R.Ramani, Phys.Stat.Sol. (b), 61, 659 (1974).
7. A.P.P.Nicholson and D.J.Bacon, J.Phys.C: Sol. St., in the press.
8. E.J.Seldin and C.W.Nezbeda, J.Appl.Phys., 41, 3389 (1970).
9. O.L.Blakslee, D.G.Proctor, E.J.Seldin, G.B.Spence and T.Weng, J.Appl.Phys., 41, 3373 (1970).

Table 2

Force Constant	New Model	Ref. 5 +	Ref. 6 +
A_1	323.362	362.00	4.977
B_1	279.950	199.00	625.941
C_1	231.950	199.00	46.863
A_2	-23.533	-52.00	48.933
B_2	91.440	133.00	60.260
C_2	-38.533	-52.00	7.423
D_2	22.517	0	31.758
A_3	-18.830	- 3.70	-22.779
B_3	0	28.80	-22.779
C_3	0	28.80	0
A_4	0.529	0.77	0.626
C_4	0.997	5.80	5.724
A_5	0.433	0	0
$B_5 = B_5'$	- 0.250	0	0
C_5	0.362	0	0
E_5	- 0.259	0	0
F_5	- 1.612	0	0
A_5'	- 0.053	0	0
C_5'	0.848	0	0
E_5'	0.465	0	0

+ Finite Pressure values

Table 1

T_1	231.950	R_1	241.746	α	-0.486
T_2	-38.533	R_2	122.440	β	8.000
T_3	0	R_3	-18.830	γ	-4.400
T_4	0.250				
T_5	- 0.250				

Table 3

	New Model	Expt. 8,9	Ref. 5	Ref. 6
C_{11}	106*	106	144	43
C_{66}	44*	44	46*	91
C_{33}	3.65*	3.65	3.71	3.65*
C_{13}	1.50*	1.50	$=C_{44}$	$=C_{44}$
C_{44}	0.40*	0.40	0.46	0.40*

* Experimental value used to fit force constants.

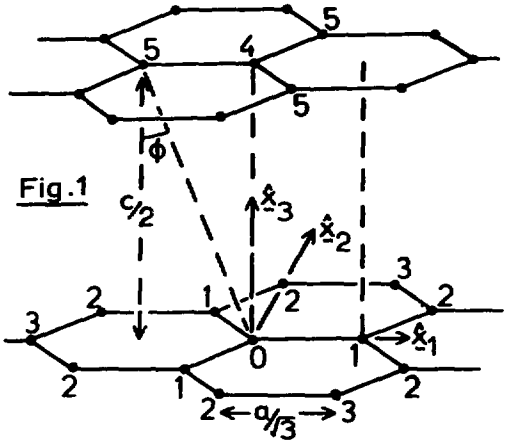


Fig.1

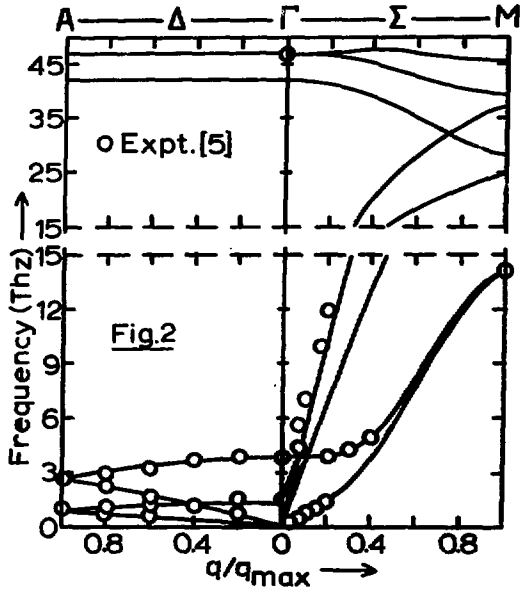


Fig.2

THE ADSORPTION OF ALCOHOLS ON SEVERAL GRAPHITE OXIDES

J. de D. López-González, A. Martín-Rodríguez, A. Martín-Pozuelo and F. Rodríguez Reinoso.

Departamento de Química Inorgánica. Facultad de Ciencias. Universidad de Granada. (Spain).

INTRODUCTION

During the process of formation of graphite oxide from any graphite, there is an alteration of the graphite structure, leading to a separation of the graphite lamellae, the original basal spacing in graphite (3,35 Å) changing to about 6,3 Å in graphite oxide. The basal spacing in graphite oxide will depend on the degree of oxidation of the original graphite and on the amount of water retained between the lamellae. The mechanism of graphite oxide formation leads to the fact that graphite oxide develops most of its surface area in internal regions of its structure. From the adsorption point of view, the interlamellae regions play the role of submicropores (1) as it happens with many other adsorbents (2). These internal regions of graphite oxide are not accesible to non-polar molecules adsorbed at very low temperatures (3), since the interlamellae spacing must increase in order to facilitate the adsorption of these molecules. However this increase in the basal spacing may take place when retaining polar molecules (4).

In this work, the adsorbates used have been ethylene-glycol, methanol and ethanol, and the adsorption temperature 25ºC. The graphite oxides (prepared by the Staudenmaier method (5)), have been obtained from different graphites: natural based graphite (N), artificial graphite (A) and pyrolytic graphite (P).

RESULTS

1. Adsorption of ethylene-glycol

The adsorption of ethylene-glycol has been studied in a conventional gravimetric system using silica springs balances. The samples studied have been graphite oxides from the different kinds of graphite mentioned above, attacked from 1 to 5 days.

The adsorption of ethylene-glycol by the different samples has been studied first at relative pressure $p/p_o = 1$, followed by the desorption at 10^{-3} torr. The adsorption and desorption runs have been repeated several times, and it has been found that both processes are not reproducible although the differences are small in the samples from graphites N and A (both polycrystallines), as it can be seen in Fig. 1 for the oxide from natural based graphite. However, the differences are very large for those graphite oxides from pyrolitic graphite.

On the other hand, the irreversibility is much larger for the adsorption runs of a given graphite oxide, than for the corresponding desorption runs as it can be deduced from Fig. 2, in the case of graphite oxide from pyrolytic graphite.

From the experimental results of adsorption of ethylene-glycol, and considering 22 $Å^2$ (4) as the cross-sectional area of the adsorbate in this case, the interlaminar surface areas of the graphite oxides have been calculated giving values from 1500 to 1550 $m^2 \cdot g^{-1}$, which are of the same order of the theoretical interlaminar surface area of graphite oxide obtained following different experimental methods (4).

In any case, and according to the interlaminar surface area determined by the retention of ethylene-glycol on samples attacked during 5 days, the order of such area is A > P > N.

2. Adsorption of methanol and ethanol

The adsorption of these alcohols has been followed in a gravimetric system with mercury cutt-offs and using silica spring balances. In this case samples of graphite oxide studied are those resulting from a 5 days attack on the different kinds of graphites. The adsorption isotherms of methanol on the three graphite oxides can be seen in Figure 3 in which, for simplicity, desorption isotherms are not shown. The adsorption of ethanol follows the same pattern as methanol.

The adsorption of methanol and ethanol shows also the same pattern as the adsorption of ethylene-glycol in the sense that the order of adsorption is A > P > N. In all cases the calculated monolayer of methanol or ethanol adsorbed ranges from 20 to 30 $mg \cdot g^{-1}$.

The desorption after saturation of methanol and ethanol leads, in all cases, to hysteresis loops indicating that the desorption process is taking place in a different way to the adsorption of the adsorbate. The oxide from pyrolytic graphites gives a large hysteresis loop but those from artificial and natural based graphites are small. This indicates that in the former oxides there is a large retention of adsorbate after desorption.

At the present moment the electron diffraction of the different oxides and the X-ray diffraction study of the graphite oxide-adsorbate complexes are been carried out

and the data will be given at the moment of presentation of this paper.

REFERENCES

(1) FRIPIAT, J.; CLAUSSIDON, J. and JELLY, A.; "Chimie Physique des Phenomenes de Surface". Masson & Cia. Paris (1971).

(2) GREGG, S.J.; "Surface Chemistry of Solids". Chapman and Hall, London (1965).

(3) LOPEZ-GONZALEZ, J.D.; BAÑARES MUÑOZ, M.A. AND RAMIREZ SAENZ, A.; Química e Industria, 17, 4 (1971).

(4) MARTIN RODRIGUEZ, A.; LOPEZ-GONZALEZ, J. D. and DOMINGUEZ VEGA,F.; Anales de Química, 69, 909 (1973).

(5) STAUDENMAIER, L.; Ber., 31, 1481 (1898); 37, 1394 (1899).

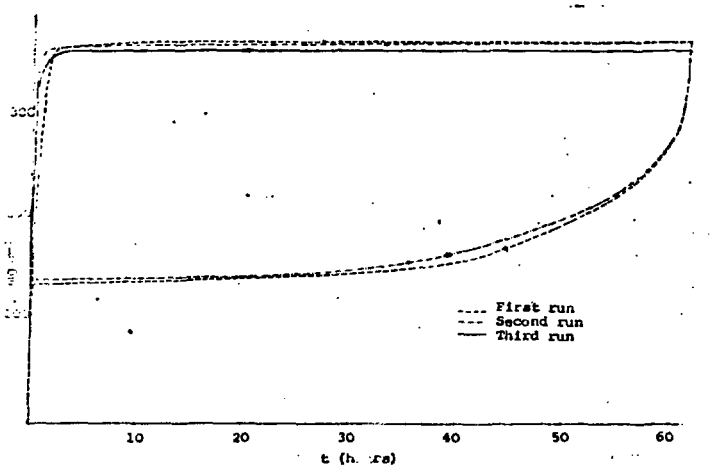


Fig. 1

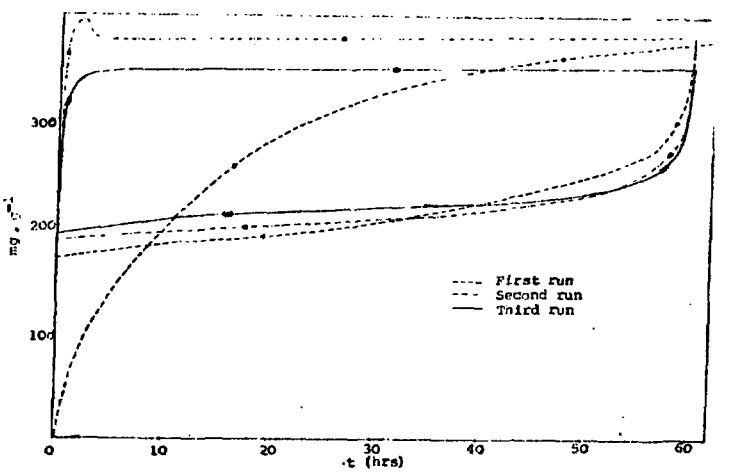


Fig. 2

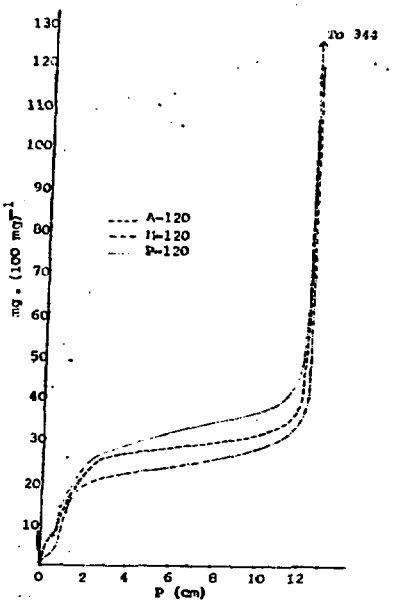


Fig. 3

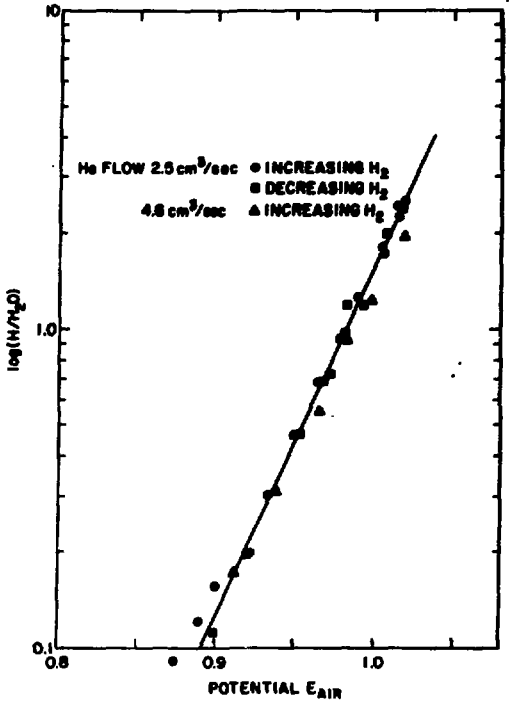
THE KINETIC DEPENDENCE OF IRON CATALYZED GRAPHITE OXIDATION ON OXYGEN POTENTIAL*

H. S. Isaacs
Brookhaven National Laboratory
Upton, N. Y. 11973

The influence of gaseous components on the rate of oxidation of pure graphite is relatively well understood and has been presented analytically.(1) With impure graphites, the dependence is more complex. Some impurities catalyze the oxidation but give the same dependence on gaseous concentrations,(1) and others, e.g., iron which causes marked rate changes with small changes in gas composition,(2) but no quantitative information was available as to how rapidly these rates changed with gas composition. This work describes measurements of rates as a function of the oxygen activity or potential.

The apparatus consisted of an electrobalance to measure the weight of graphite suspended in a furnace. The iron impregnated graphite was prepared from high purity nuclear graphite. Helium was used with controlled hydrogen to water concentration ratios. After passing over the specimen, the oxygen potential of the gas was measured using an electrochemical oxygen meter at 650°C with air as a reference. The calibration of the meter in terms of the H_2/H_2O ratio is shown as a functional potential in Figure 1. This logarithmic curve was in excellent agreement with that calculated from thermodynamic data.

(1) M. B. Peroomian, et al, Report No. GA-A12493, January 1974.
(2) P. L. Walker, Jr., et al, Chem. & Phys. of Carbon, Vol. 4, 287 (1968).

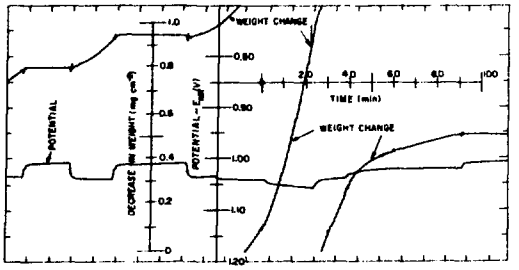


RELATIONSHIP BETWEEN POTENTIAL AND H_2/H_2O RATIO

The effect of changes in gas composition on the weight and oxygen potential are shown in Figure 2 for a high (15%) burnoff sample. Rapid potential changes followed changes in the helium composition but measurements showed a potential of -1.02 volts was critical. When the potential was less negative, no oxidation was evident, while when more negative, the graphite began oxidizing. The oxidation could, therefore, be turned off and on as the gas composition was changed. This potential is close to the oxygen potential at which iron and

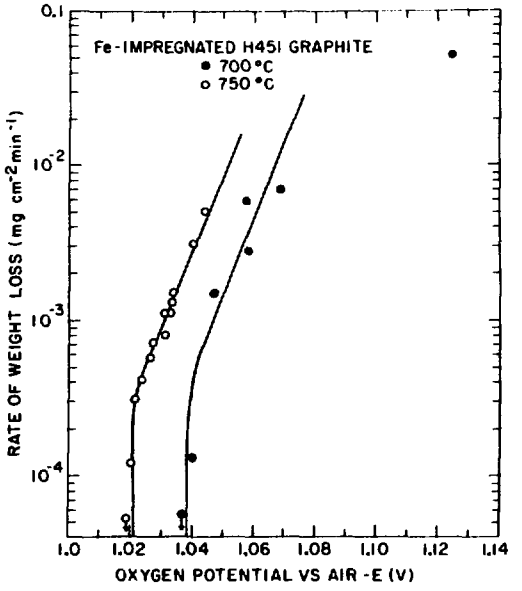
*This work was performed under the auspices of the United States Nuclear Regulatory Commission.

wustite are in equilibrium, and significantly less than that corresponding to magnetite and wustite equilibrium. The results are, hence, in agreement with a model where the oxidation is catalyzed by iron but not by wustite.



POTENTIAL AND WEIGHT CHANGE WITH TIME FOR 15% BURNOFF IRON IMPREGNATED GRAPHITE

Figure 2 also showed that when the potential decreased progressively below -1.02, the rate of oxidation continued to increase. This behavior was found to be reproducible both qualitatively and quantitatively and can be seen in Figure 2. The results in Figure 3 show the relationship between potential and oxidation rate for 750°C. At potentials just below the critical value, the rate of oxidation changed rapidly and then increases logarithmically with potential. A similar behavior was observed at 700°C for ∿15% burnoff samples. As the relationship between the rate and the potential is logarithmic, it can simply be shown that the rate of oxidation is related to the oxygen activity or H_2/H_2O ratio. The slopes for the respective logarithmic relationships indicated that the rate of oxidation of the iron containing graphite increases approximately with the square of the H_2/H_2O ratio or with the reciprocal of the oxygen activity to the fourth power. With high purity graphite, the rate of oxidation by water vapor is inhibited by the presence of hydrogen in contrast to the observations presented here, indicating in the presence of iron, hydrogen acts as a strong stimulant for the oxidation process.



EFFECT OF POTENTIAL ON OXIDATION RATE

The same rapid response to changes in the oxygen potential with iron impregnated graphite with low burnoff and on impure graphites containing iron, was not observed. The fine pore structure in the low burnoff sample prevented rapid exchange between the gases within and external to the specimen, and rates could not be controlled. The impurities, other than iron, catalyzed the oxidation and gave a background of hydrogen as well as a continued rate of oxidation at all oxygen activities tested. These results were, nevertheless, in agreement with those presented for the high burnoff specimen but were complicated by the gas composition changes with depth in the graphite.

THE BEHAVIOUR OF HYDROGEN AND CARBON MONOXIDE WITH GRAPHITE FERRIC CHLORIDE

S. Parkash and S. K. Chakrabartty
Fuel Sciences Division, Alberta Research Council, Edmonton, Alberta, Canada
and
J. G. Hooley
Chemistry Department, University of British Columbia, Vancouver, British Columbia, Canada

Intercalation in graphite appears to modify the chemical or catalytic activity of certain substances. The modification, however, may result from one or more possibilities. Thus the new activity may be caused by some substance produced by a side reaction that is concurrent with intercalation. For instance, it has been claimed that intercalating CrO_3 in graphite modifies its ability to oxidize an alcohol (1). However, this ability is caused by the production, during intercalation, of lower oxides of chromium (2). A second possibility is that the electron density on the two basal planes of each graphite flake has been changed because of the charge transfer that accompanies intercalation. This possibility has been used to explain the catalytic formation of HBr from its elements in the presence of graphite-metal chloride compounds (3). A third possibility is that catalysis or oxidation, etc., occurs within the layer plane system and, therefore, in a different fashion than with graphite or with the pure substance before intercalation. In this case the reacting species must diffuse between the layer planes and the products must diffuse out. This has often been assumed to occur but whether it does or does not occur has, in our opinion, yet to be demonstrated. We have studied this possibility by determining the composition pressure isotherms of a gaseous reactant on graphite and on graphite-ferric chloride. If diffusion does occur between the intercalated layers then the isotherms for the graphite-ferric chloride should show a much higher reactant composition at one or more pressures. Because the recent energy crisis has redirected attention to the catalytic synthesis of hydrocarbons via the Fischer Tropsch route (4-6) we chose to study the isotherms of H_2, of CO and of their mixture (1:1) on graphite, on graphite-ferric chloride and on a mixture of graphite and ferric chloride. The data should tell us whether all three of the above possibilities should be considered in explaining any catalytic activity or only the first two.

To further the scope of our investigations, the catalytic formation of hydrocarbons from H_2 and CO on graphite-ferric chloride and on a mixture of graphite and ferric chloride was also investigated.

Graphite (G_0) was of Madagascar origin, acid purified and sieved to -40 + 45 mesh. Graphite-ferric chloride of stoichiometry C_8FeCl_3 (G_I) was prepared from G_0 and anhydrous $FeCl_3$ by the two temperature tube method (7) and then washed free of $FeCl_3$. Mixture of graphite and $FeCl_3$ (G_M) was prepared by standard incipient wetness technique (4) where G_0 was impregnated with $FeCl_3$ solution of concentration equivalent to C_8FeCl_3 followed by overnight drying at 110°C. There was no intercalation, whatsoever, in this case.

Before proceeding with the adsorption measurements, the surface of the graphite was cleaned by outgassing the previously 110°C oven dried samples for a period of ∿16 hr in high vacuum (10^{-6} Torr) at room temperature. High temperature evacuation was not appropriate because of thermal unstability of G_I.

The specific surface area (using BET equation) and pore-size distribution (using Kelvin's equation) in the range 20-400 A° diameter were determined from the N_2 adsorption isotherms at 77°K using Micromeritic surface area and pore volume analyzer. The same gas adsorption apparatus was used for H_2 and CO isotherms determined at 25°C and up to 700 Torr initial pressure. Equilibrium period of 90 min was allowed for every point of isotherm.

For adsorption isotherms from H_2 and CO mixture (1:1) a sample flask having a side arm (∿3 cm) fitted with a septum using stainless steel fittings was used. After 90 min equilibrium period, gas mixture was analyzed on a Fisher Gas Partitioner using molecular sieve column. From the analysis, the amounts of H_2 and CO adsorbed individually from their mixture was computed.

Catalytic formation of hydrocarbons over G_I and G_M, previously activated in a rapid flow of H_2 (1ℓ/min) in situ at 375°C for 48 hr, using a mixture of H_2 and CO (2:1) was studied in a fixed bed laboratory reactor at 325°C and 90 psi pressure. For product analysis, a Hewlett-Packard 7620A gas chromotograph with silica gel column was used in conjunction with an electronic Hewlett-Packard 3380A integrator.

Results and Discussion

N_2-BET surface area of G_0 upon intercalation with $FeCl_3$ (G_I) remained unchanged (0.3 m^2/g) whereas simple impregnation of $FeCl_3$ (G_M) showed a slight increase. The percentage of pore volume composed of pores less than 40 A° in radius was ∿47 which reduced to ∿33 for G_I and ∿26 for G_M.

Adsorption isotherms of H_2, CO from pure gases and from their mixture (1:1) are shown in Fig. 1. The amounts of H_2 as well as of CO uptake for G_0 and G_I were almost identical at any pressure up to one atmosphere while for G_M the uptake of both H_2 and CO was ∿5 times greater. Similarly the concurrent sorption of H_2 and CO from their mixture was almost of the same magnitude (although ∿70% higher compared to sorption from pure components) for G_0 and G_I while for G_M it was far greater. This observation, repeated several times, that upon intercalation of G_0 with $FeCl_3$ there was no increased uptake of either H_2 or CO, was of significant consequence. It rules out the possibility that the modified

chemical or catalytic activity of metal intercalated graphite is the result of diffusion of reacting species between the layer planes; because, if this had been the case, then the isotherm for G_I would have shown a much higher uptake at one or more pressures. Experimental evidence of this fact, probably for the first time, is apparent from our studies.

In comparison to H_2 and CO adsorbed individually, the adsorption of both the gases is enhanced invariably, especially for G_I and G_M, when adsorbed simultaneously from their 1:1 mixture. This behaviour is akin to several metal catalyst systems reported in the literature (8). Mutual enhancements for the adsorption of both H_2 and CO during simultaneous course of adsorption are attributed partly due to complex formation between the adsorbed species and partly due to 'cooperative work functions'. Tamaru (9) and Tsuchiya and Shiba (10) are of the opinion that the oppositely oriented chemisorbed dipoles of $H^{\delta+}$ and $CO^{\delta-}$ alter the work function of the metal in opposite manner; the increase caused by one is partly offset by the other and finally enhances the limiting adsorption of H_2 and CO. Enhancement is more pronounced for G_M than G_I.

The catalytic activity for hydrocarbon synthesis is observed when G_I or G_M is heated above 300°C. We believe that the activity develops by the thermal decomposition of $FeCl_3$ to $FeCl_2 + Cl_2$ and is caused only by that fraction that diffuses out of the graphite. For G_I, this product has been shown (11) to have a Mossbauer spectrum isomer shift which is the same for heating in H_2 or N_2 or a vacuum. However, above 350°C in H_2 it is known that some metallic iron is produced. Now, the $FeCl_2$ and any Fe may behave differently when adsorbed on graphite that had been intercalated (G_I) than on graphite that had not been intercalated (G_M). Any difference could be caused by the charge transfer to the basal planes from intercalated material in G_I and the fact that some of this intercalated material remains in the structure after heat treatment.

References

1. Lanlancette, J.M., Rollin G. and Dumas, P., Can. J. Chem. 50, 3058 (1972).
2. Hooley, J.G. and Reimer, M., Carbon 13, 401 (1975).
3. Rudorff, W., Stumpp, E., Spreissler, W. and Siecke, F.W., Angew. Chem. 2, 67 (1963).
4. Vannice, M.A., J. Catalysis 37, 449, 462 (1975).
5. Dalla Betta, R.A., Piken, A.G. and Shelej, M., J. Catalysis 40, 173 (1975).
6. Shah, Y.T. and Perrotta, A.J., Ind. Eng. Chem., Prod. Res. Dev. 15, 123 (1976).
7. Hooley, J.G., Carbon 11, 225 (1973).
8. Sastri, M.V.C., Gupta, R.B. and Viswanathan, B., J. Catalysis 32, 325 (1974).
9. Tamaru, K., Trans. Faraday Soc. 59, 979 (1963).
10. Tsuchiya, T. and Shiba, T., Bull. Chem. Soc. Japan 38, 1726 (1965).
11. Hooley, J.G., Bartlett, M.S., Liengme, B.V. and Sams, J.R., Carbon 6, 681 (1968).

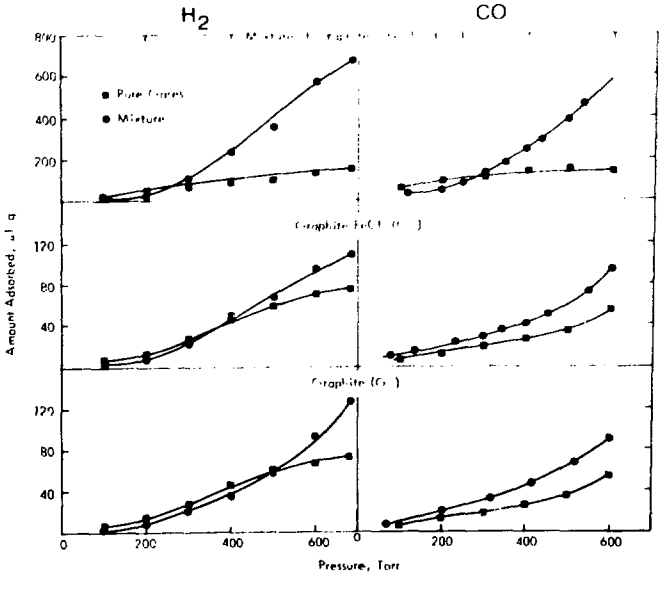


Fig. 1 H_2 and CO adsorption isotherms from pure gases and their 1:1 mixture

ADSORPTION OF BENZENE ON EXFOLIATED GRAPHITE BETWEEN - 70°C AND - 5°C

M. Coulon, Y. Khatir and L. Bonnetain

Laboratoire d'Adsorption et Réaction de Gaz sur Solides

Ecole Nationale Supérieure d'Electrochimie et d'Electrométallurgie

Domaine Universitaire - BP 44 - 38401 - Saint Martin d'Hères - France

General outlook of the isotherms.

A network of adsorption isotherms of benzene on exfoliated graphite has been determined between -70°C and -5°C by mean of a classical volumetric apparatus equiped with a Mc Leod gauge.

Down to the lowest studied temperature - i.e. well under the expected two dimensional critical temperature estimated from the three dimensional one - the isotherms still do not exhibit any change of curvature at low temperature and degree of covering (Fig. 1)

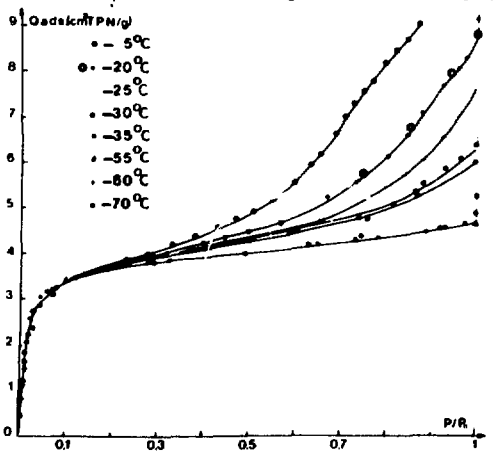


Fig. 1 : Adsorption isotherms of benzene on exfoliated graphite (✪ desorption at - 20°C)

We confirm a quite unuasual characteristic of these isotherms which intersect in the vicinity of the point B (1-2). Beyond the point B and at constant relative pressure the adsorbed amount increases with temperature.

Above -35°C, the formation of a second layer can be distinguished.

Isosteric heats and differential entropies.

In the studied temperature range neither the isoster nor the log P vs 1/T plot determined from the benzene sublimation equilibrium can be represented by a single straight line. As a first approximation they can be each represented by two sets of straight lines intersecting at about -35°C, -40°C. Thus they define two temperature ranges we will call further on the low and high temperature range.

The isosteric heat and differential entropies derived from the slopes and the intercepts on the ordinate axis for 1/T = 0 of the straight line portions of the isosteres are plotted on figures 2 and 3 versus the adsorbed amount.

In the low temperature range (Fig. 2), the isosteric heat decreases linearly with the adsorbed amount whereas the differential entropy increases from zero covering to adsorbed amounts corresponding to rela-

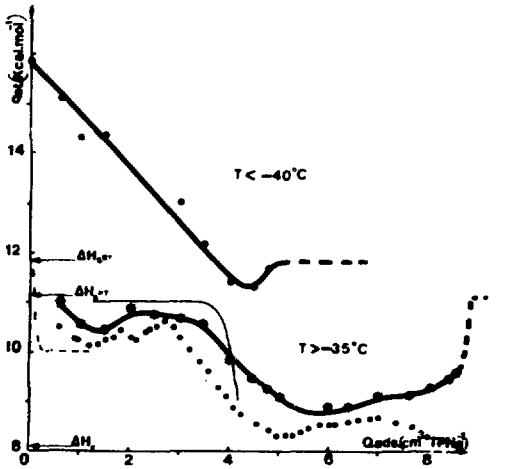


Figure 2 : Variation of the isosteric heat.
- ✱ low temperature range (T < - 40°C)
- ✱ high temperature range (T > - 35°C)
- PIERCE and EWING (2) (-10°C < T < -20°C)
- ● PIEROTTI and SMALLWOOD (3) (0°C < T < 50°C)
- DOLLIMORE, HEAL and MARTIN (4)(80°C < T < 97°C)

ΔH_s BT enthalpy of sublimation (in the low temperature range.

ΔH_s HT enthalpy of sublimation (in the high temperature range.

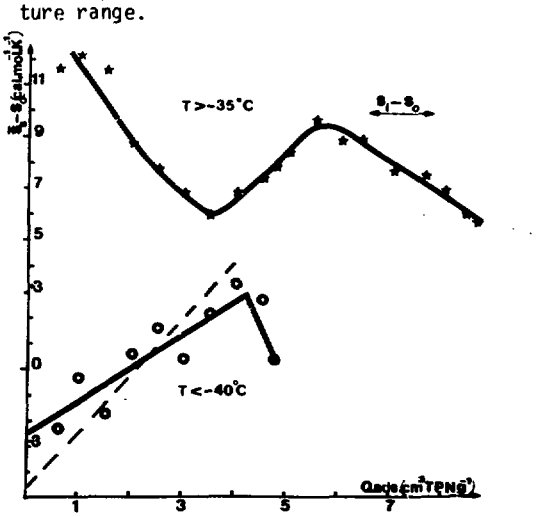


Fig. 3 : Variation of the differential entropy
- ★ high temperature range
- ✪ low temperature range
- —— estimation of the variation of the thermic entropy

$S_\ell - S_o$ molar entropy of fusion of benzene at -50°C

tive pressures close to unity (Fig. 3).

In the high temperature range, the isosteric heat is more or less constant up to point B then, decreases and increases again during the formation of the second layer. This is quite consistent with the results of PIERCE and EWING (2) and those PIEROTTI and SMALLWOOD (3) and DOLLIMORE, HEAL and MARTIN (4) obtained above the three dimensional triple point temperature (Fig. 2). The variation of the differential entropy with covering can be rather straightforwardly interpreted as a first decrease caused by a compression of the first layer, a further increase caused by the beginning of the formation a second layer and a last decrease caused by the compression during the completion of the second layer (Fig. 3).

Determination of benzene cross-section and degree of covering.

Since the early work of KISELEV (5) most of the previous authors (3, 4) have supposed the benzene molecule cross-section to be equal to 40 Å^2. This value is consistent with a hexagonal close-packed arrangement of molecules laying flat on the graphite surface. Monolayer capacity had been computed either on the assumption of monolayer completion at the point B (1) or by mean of BET equation (3). We found that BET isotherm linearization gives a rather poor fitting and capacity values 85 to 90 % smaller than the point B.

Systematic graphite surface controls have been performed by krypton adsorption at liquid nitrogen temperature. From the value of the adsorbed amount at the point B and on the assumption that krypton atom cross-section is equal to 14,3 Å^2 (6), benzene cross-section can be computed using the following equation:

$$\sigma_{C_6H_6} = \frac{q_m\,(Kr)}{q_{C_6H_6}}\,\sigma_{Kr}$$

$q_m(Kr)$ = 9,5 cm^3 NTP g^{-1} (point B of Kr isotherm)

σ_{Kr} = 14,3 Å^2

$q_{C_6H_6}$ = adsorbed amount of benzene (cm^3 NTP g^{-1})

On Table I the cross-section computed from various points of the isotherms are compared with the cross-section of the benzene molecule in the low-Miller-index surfaces of the three dimensional benzene crystal at - 50°C (7).

The BET capacity yields a cross-section consistent with an arrangement of close packed molecules parallel to the surface and the point B yields a somewhat smaller value. However it is to be emphasized that the values derived from adsorbed amounts in the vicinity of unit relative pressure in the low temperature range are much smaller and very near to the cross-section in the benzene crystal planes of high density (in this temperature range the shape of isotherm, the variation of isosteric heat and differential entropy give strong evidences that there is a single adsorbed layer up to the saturation vapor pressure).

The high density of molecules in (010) (100) (111) planes is accounted by the fact that the molecules are tilted with respect to one another in order that every molecule presents a maximum interaction with its neighbours.

TABLE I

Basis of cross-section determination	(Å)	q(cm^3 NTP g^{-1})
BET equation	41,2	3,3
Point B	38,8	3,5
$q_{C_6H_6}$ near $P/P_0 = 1$		
- at - 70°C	30,2	4,5
- at - 40°C	27,2	5,0
(001) benzene crystal plane	35,7	
(010) -	25,8	
(100) -	33,5	
(111) -	27,6	

Since the van der Waals mutual interaction of benzene molecules is very similar to benzene-graphite interaction-(this is attested by a heat of adsorption close to the heat of sublimation) - a possible tilting of adsorbed molecules at high coverage due to lateral interaction can well be considered that would explain the small cross-section calculated.

Discussion.

The experimental values of differential entropy has been compared with theoritically computed values based upon the different modes of molecular motion available to the adsorbed molecule.

In the low temperature range, the experimental values are in accord with a model of localized molecules adsorbed flat on the graphite surface at low coverage. Increasing coverage induces a progressive tilting of the molecules caused by lateral interactions and allows the progressive release of two degrees of rotational freedom. Hence the monolayer capacity will increase with temperature.

In the high temperature range the adsorbed phase seems to be in the same state described by earlier workers (8, 3, 4) for temperature ranges above the 3D. melting point (i.e. mobile layer with two degrees of rotational freedom ruled by a 2D. VOLMER equation of state).

These results implies that it exists a second order phase transition in the first layer about - 40°C, quite insensitive to the pressure, between a localized and a mobile hypercritical phase.

References.

1. B.W. DAVIS and C. PIERCE J. Phys. Chem., 70, 1051 (1966)
2. C. PIERCE, B. EWING J. Phys. Chem., 71, 11, 3048 (1967)
3. R.A. PIEROTTI, R.E. SMALLWOOD J. Coll. Int. Sci., 22, 469, (1966)
4. D. DOLLIMORE, G.R. HEAL, D.R. MARTIN J.C.S. Farad I, 68, 832 (1972)
5. A.A. ISIRIKYAN, A.V. KISELEV J. Phys. Chem. 65, 601 (1961)
6. A. THOMY, REGNIER, MENAUCOURT J. of Crystal Growth 13-14, 159 (1972)
7. E.G. COX Rev. Mod. Phys. 30, 159, (1958)
8. A.V. KISELEV, D.P. POSHKUS Trans. Far. Soc. 59, 428 (1963).

ADSORPTION OF LONG CHAIN ELECTROLYTES ON CARBONS

R.C. Bansal

(Department of Chemistry Panjab University, Chandigarh-160014, India)

Until recently little work has been done on the adsorption of long chain electrolytes such as surfactants on carbon surfaces (1-6). Since these compounds are invariably present in the industrial waste water, the problem has assumed considerable importance from the point of view of water pollution control. The present work describes some of the adsorption isotherms of surfactants on different types of carbons and attempts to explain the mechanism of adsorption of cationic and anionic surfactants.

The adsorption isotherms of cetyl trimethyl ammonium bromide (CTAB), a cationic surfactant, sodium dodecyl benzene sulphonate and sodium di-(2 ethyl hexyl) sulpho succinate (SDS), both anionic surfactants from their aqueous solutions on a series of sugar charcoals and several commercial grade carbon blacks were determined at 30°C in the concentration range 5×10^{-5} to 25×10^{-3}M. The results for CTAB and SDS on charcoals in the concentration range upto 2.5×10^{-3}M are shown in Figs 1 and 2. The adsorption tends to reach a limiting value after this concentration and therefore has been omitted in the figures. The distinctive feature of these isotherms is the existence of a pronounced maxima at a concentration of about 1.5×10^{-3}M for CTAB and 1.8×10^{-3} M for SDS.

The shape of the isotherm is independent of the nature of the carbon surface although the magnitude of adsorption is different for different carbons at each concentration. The adsorption of the anionic surfactant, SDS, increases with increase in the temperature of outgassing while that of CTAB decreases with increase in the temperature of outgass ing upto 800°C and increases thereafter. It appears that whereas the adsorption of an anionic surfactant onto a carbon surface is related inversely to the amount of associated oxygen, the adsorption of a cationic surfactant is related directly to the amount of associated oxygen.

Broadly speaking the isotherms could be split up into three parts: a gradual increase in adsorption with increasing concentration upto 1×10^{-3}M for CTAB and 1.25×10^{-3}M for SDS; a steep almost linear rise in adsorption with increasing concentration in the range $1 \times 10^{-3} - 1.8 \times 10^{-3}$M; and a symptotic fall at higher concentrations ultimately ending up towards a limiting value. The discontinuities in the curves and the occurrence of the maximum were verified by repeating the adsorption experiments. The duplicate values were found to be in good agreement indicating that these breakes are real.

It is interesting to correlate the adsorption isotherms with the formation of aggregates in solution i.e., with the critical miscelle concentration (cmc). The cmc was determined by the conductance measurements of the solutions of surfactants (7). The conductance - concentration curve shows a break at cmc.

It is seen that the break in the adsorption curve for all the surfactants agree very closely with the cmc. However, the maxima in the adsorption curve in each case occur at considerably higher concentrations. It is also evident that the characteristic break in the adsorption curve occurs almost at the same concentration irrespective of the nature of the carbon surface. This shows that the cause for it lies in the solution and not in the nature of the adsorbent surface.

Rates of Adsorption: The rates of adsorption were studied for time intervals varying between 30 minutes and 24 hrs. on several samples and several concentrations. The adsorption was rapid in the first few hours and was atleast 50 per cent complete within first 2 hrs. By the end of 12 hrs. the adsorption was almost complete. The rate of adsorption increased with increase in temperature.

Heats of Adsorption: The isosteric heats of adsorption for the adsorption of CTAB was determined from the adsorption isotherms at 30 and 40°C on a sample of carbon black. The shape of the isotherm was similar at the two temperatures. The heat of adsorption was of the order of 900 cals per mole indicating physical nature of the adsorption.

Influence of pH on adsorption: A few

experiments were carried out by controlling the pH of the surfactant solution by the addition of equal amounts of solutions of HCl or NaCl or NaOH of known strengths. Though the pH of the mixed solutions did not remain strictly constant over the whole ra range of concentrations for one experiment, the change was slight (0.1 - 0.4 pH units). It was found that the adsorption of CTAB decreases on increasing the pH of the solution.

References :

1. Tamamushi, B. and Tamaki, K., Trans. Faraday Soc., 55 1013 (1959).
2. Vold, R.D. and Sivaramakrishnan, M.M., J. Phys. Chem., 62 984 (1958).
3. Kettlemoyer, A.C., Okewis, J.D. and Chessick, J.J., J. Am. Oil Chemists Soc., 39 280 (1962).
4. Okewis, J.D. and Kettlemoyer, A.C., Proc. 3rd Intern. Confr. Surface Activity Cologue, 1960 Vol. II p.401.
5. Day, R.A., Greenwood, F.G. and Parfitt, G.D., Chem. Phys. Appl. Surface Active Subst. Proc. Intern. Congr. 4th (1964).
6. Goroduov, V.D., Izv. Vyssh. Uchet. Zaved, Neft Gaz 14 33 (1971).
7. Neil, J.M. and Stirton, A. J., J. Phys. Chem., 60 899 (1956).

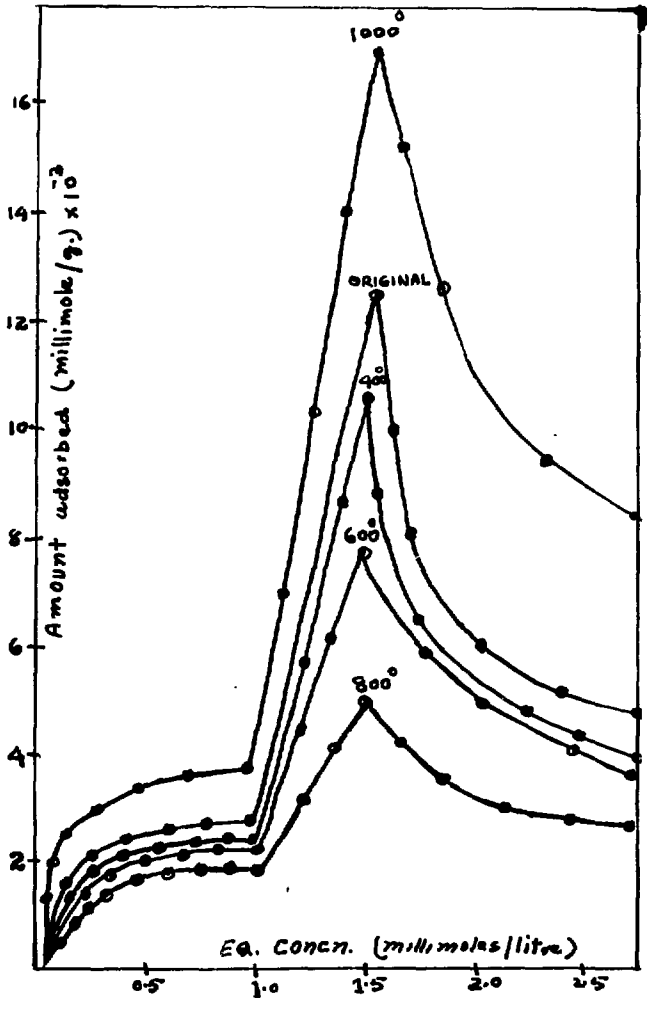


Fig. 1 Adsorption isotherms of CTAB on sugar charcoals outgassed at different temperatures.

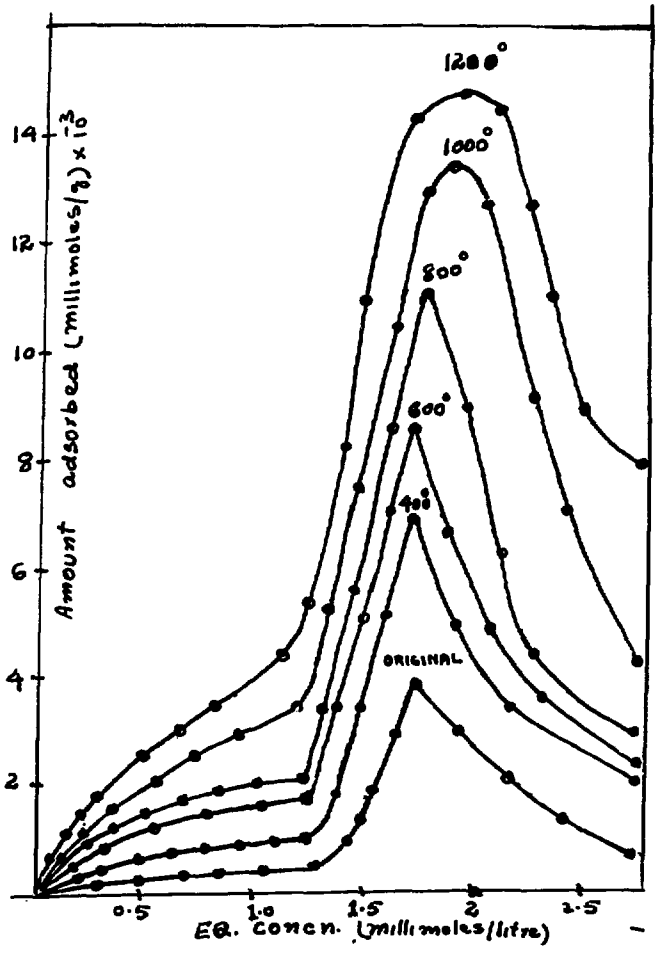


Fig.2 Adsorption isotherms of SDS on sugar charcoals outgassed at different temperatures.

SURFACE STUDY OF CARBON FIBRES WITH AUGER ELECTRON SPECTROSCOPY

F Hopfgarten

National Defence Research Institute, Department 2, S-104 50 STOCKHOLM 80, Sweden

Introduction

The commercial exploitation of carbon fibres rests on the discovery of effective methods of increasing the interfacial shear strength between the surface of the cylindrical fibre and the compatible material with which they are combined to form a composite material.

Since the structural characteristics of carbon/epoxy composites are usually evaluated by measuring the short beam shear strength (a measure of interlaminar shear strength), it is important to correlate the shear with the bonding between the fibres and the matrix material.

Knowledge of the atomic structure of the surfaces of carbon fibres is therefore essential and the surface structure has recently been studied by mass spectrometry and low temperature adsorption of H_2 and Ar by Møller and Fort, Jr (1). The atomic composition of the external surface of carbon fibres has also been investigated by the application of high energy photoelectron spectroscopy (ESCA) by Barber, Swift, Evans and Thomas (2) and with Auger electron spectroscopy by Connell (3).

Experimental

Six types of polyacrylonitrile-based fibres were examined viz. Torayca T300A, Torayca M40A, Torayca T200A, Courtaulds HM-S, Courtaulds A-S, Courtaulds HT-S. They can be divided in three groups, named Type 1, Type 2 and Type 3 depending on their mechanical properties. Type 1 are the high modulus carbon fibres Courtaulds HM-S and Torayca M40A. Type 2 are the high tensile strength carbon fibres Courtaulds HT-S and Torayca T300A. Type 3 are the high strain carbon fibres Courtaulds A-S and Torayca T200A. A tow of carbon fibres consists of 2000, Torayca, and 10000, Courtaulds, individual parallel filaments each only 8-9 µm.

A hemicylindrical mirror analyzer (Vacuum Generators 850 CMA) fitted with a microfocus electron gun (LEG 32) was used for Auger studies. In order to minimize possible intensity variations of the Auger-signals due to the geometrical extensions of the carbon fibres, the electron beam (Ø 5 µm) was allowed to scan with high velocity across a large area. Thus all Auger spectra shown, are average results from a surface area equal to 2x2 mm. Concentration gradients were studied by simultaneous ion-etching of the samples. For this purpose an argon-ion beam was used with an ion current density of 20 $\mu A/cm^2$ and an acceleration voltage of 2 keV ($3.2 \cdot 10^{-16}$ J). The profile studies were made to a depth of 30 nm (300 Å). All measurements were performed at a pressure of 10^{-7} Pa. This pressure was attained without any bake-out of the vacuum chamber.

Results and Discussion

The Auger spectroscopy examination gave the concentration gradients for oxygen, sulfur and chlorine to a depth of 30 nm (300 Å) for the six carbon fibres. The concentration gradients for oxygen in the six carbon fibres are present in fig 1a for sulfur in fig 1b and for chlorine in fig 1c. It may be noted that the oxygen content of Torayca type 1 and type 2 carbon fibres increases with the depth in the carbon fibres. Type 3 fibres have a high oxygen concentration on the fibre surface and the concentration decreases with depth to a depth of 5 nm (50 Å) in the fibre. This might be because these fibres have large surface roughness. They are not so well crystallized and so they have a larger surface area than the other four carbon fibres. The concentration of chlorine in the six fibres is nearly constant. The chlorine comes probably from oxidation of the fibres with hypochlorite. It is of interest that sulfur is present in all the carbon fibres. On the surfaces there is no sulfur except for the Torayca type 3 fibre. In all the other carbon fibres the sulfur concentration increases with depth in the fibres to about 10 nm (100 Å) and is then constant. Sulfur has been found in PAN-based carbon fibres earlier by Kalnin (4) 0.2-0.5 %, Liberman and Boles (5) found about 0.05-0.1 % in three different types of PAN-based carbon fibres. Sodiumthiocyanat-solution is used as solvent for the polymerisation of the acrylonitrile. It seems likely that the use of this solvent results in some residual sulfur in the carbonised fibres. Such a hypothesis would also suggest a constant sulfur concentration within the fibre. The present Auger examination confirms this as is demonstrated by fig 1b. The low sulfur concentration at the surface of the fibres especially for Type 1 and Type 2 probably arises from their heat treatments during manufacture. Removal of sulfur and chlorine is difficult if the sulfur and chlorine atoms are situated between the graphite basal planes and not in cavities. The distances between graphitic basal planes in carbon fibres are between 0.341 to

0.342 nm (6,7) compared with 0.335 nm in graphite. C-S bond distances are between 0.155 and 0.181 nm and C-Cl bond distances between 0.1635 and 0.1767 nm. Thus there could be a carbon-sulfur-carbon cross-link between the alyers perpendicular to the axis of the microfibrils.

References

1. P.J. Møller and Fort, Jr. T. Colloid and Polymer Sci. 253 (1975) 98.
2. M. Barber, P. Swift, E. L. Evans and J. M. Thomas, Nature 227 (1970) 1131.
3. G. L. Conell, Nature 230 (1971) 377.
4. I. L. Kalnin, 12th Biennial Conference on Carbon, Pittsburgh, Summary of Papers AI-12, (1975).
5. M.L. Lieberman and G.T. Holes, J. Mater. Sci. 7 (1972) 654.
6. D. F. Harling, JEOL News 9c (1971) 22.
7. S. Goldfein, Report 01901-23 PMMR, Project No. 1T162105AH84 (1975), Laboratory 4000, US Army Mobility Equipment, Research Development Center, Fort Belvoir, Virginia 22060.

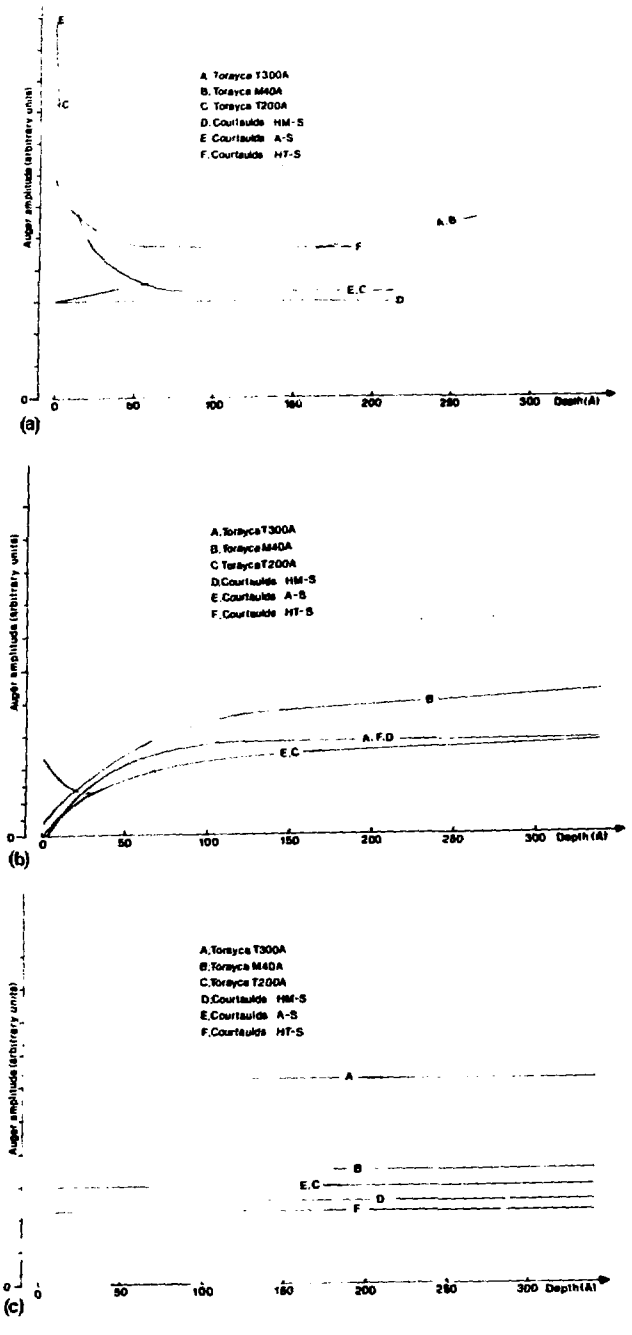


Fig. 1. The concentration gradient for (a) oxygen, (b) sulfur, (c) chlorine in carbon fibres deduced from Auger electron spectroscopy examination.

SURFACE CHARACTERISTICS OF PAN BASED CARBON FIBRES

B. Rand and R. Robinson
Department of Ceramics, Glasses and Polymers, University of Sheffield, Sheffield S10 2TZ, UK

Introduction

Although the surface properties of high performance carbon fibres are of technological importance, many aspects are still not fully understood (1), particularly the mechanism whereby the interlaminar shear strength (ILSS) of fibre/resin composites is enhanced by oxidative surface treatments (2,3). In an attempt to further elucidate the surface characteristics of PAN based fibres and their interactions with the type of functional groups which may be present in resin systems the investigations reported here were undertaken.

Experimental

High modulus (HM), high strength (HT) and type A carbon fibres both untreated (u) and surface treated (s) by the manufacturer were investigated along with a series of HM fibres oxidised in 68% fuming nitric acid for periods of 9,12,25 and 50 hours followed by rigorous extraction in water.

Nitrogen adsorption measurements were carried out gravimetrically using a Beckman RIIC LM600 VM microbalance, buoyancy effects being reduced to a minimum. Adsorption-desorption measurements were made in the range 0.01-1.0 p/p_o at 78K after degassing to $< 10^{-5}$ torr at temperatures up to 950°C.

Oxygen chemisorption was also performed gravimetrically at 340°C following the 950°C degassing. N_2 was gradually admitted to 90 torr and after equilibration O_2 was added to bring the total pressure to 110 torr. There was a rapid establishment of the buoyancy effect (previously assessed during the N_2 admissions) followed by a slower weight increase due to complex formation. Under these conditions weight increases of ±1.2 µg could be measured reproducibly.

The Microscal flow calorimeter was used to follow the adsorption of organic solutes; its mode of operation has been described in detail previously (4). Heat effects produced by adsorption of components from a carrier fluid which flows over a bed of adsorbent are detected by thermistors and displayed as peaks on a potentiometric recorder. Equal quantities of chopped fibres were carefully inserted into the calorimeter and compacted as nearly as possible to the same degree prior to measurement. Solvent was then flowed over the fibres at a precisely controlled rate and small quantities (usually 20 µl) of a solution of known concentration were injected into the stream. The areas of the exothermic and endothermic peaks produced by adsorption and desorption of species at the interface were measured by planimetry. n-butanol, n-butylamine, n-butyric acid and 1-2-epoxypropane dissolved in n-heptane (0.037 M) were the major adsorbates investigated.

Results and Discussion

Degassing in vacuum at elevated temperatures brought about appreciable weight losses of all fibres, the amount increasing with increasing temperature. The vapours emitted were consistent with the removal of trapped carbonization products as suggested previously (5). Nitrogen isotherms on these fibres were of type II, and were displaced to higher amounts adsorbed and exhibited sharper 'knees' after degassing at elevated temperatures. Figure 1 shows the amount adsorbed on the HM-u fibres degassed at various temperatures, plotted against the amounts adsorbed on the room temperature degassed sample at the same relative pressure (de Boer (6) type of analysis). The intercepts indicate the development of microporosity during heating. Similar results were obtained with all types of fibres and the microporosity created by heating at 950°C increased after surface oxidation.

Comparing the isotherms of the HM fibres oxidised in nitric acid with the untreated fibre in the same way, shows that oxidation produces no microporosity but increases the external surface area. The comparative plots show a decrease in slope at high amounts adsorbed suggesting some mesoporosity, but no hysteresis was apparent in the adsorption isotherms. The commercial surface treatments produced no significant change in the surface areas of all types of fibres. The active surface areas of the untreated fibres increased in the direction

type A > type HT > type HM ,

were markedly increased by the manufacturer's surface treatment and to a much greater extent by nitric acid oxidation (HM fibres). It will be demonstrated that the fraction of the surface which is 'edge' surface also increases during this type of surface treatment. In this respect the effect resembles the change in active surface area of graphon during air oxidation observed by Walker and Janov (7).

Figure 2(a) shows a model trace obtained from the calorimeter following the injection of a reversibly adsorbed species into the solvent stream. The adsorption and desorption peaks are of equal area. Injections of n-butanol and 1-2-epoxypropane solutions into the n-heptane solvent stream produced effects approximating to this model, but with fibres of low active surface area the adsorption peak area was sometimes smaller than that of the desorption peak as a result of the endothermic heat of dilution becoming appreciable in comparison with the heat of adsorption. Adsorption of n-butyric acid could not be detected on any fibres, whilst n-butylamine was adsorbed very strongly and in part irreversibly. The trace obtained with this latter species was as shown in Figure 2(b); a large exothermic peak was followed by a tiny desorption peak. The second and subsequent adsorption peaks were smaller than the first, these being of reproducible area after the third injection. Injecting n-butanol after the n-butylamine adsorptions resulted in no change in the peak area, indicating that the irreversibly held butylamine is on different sites from those on which the alcohol adsorbs reversibly. However, when the n-butanol was injected into a flowing stream of n-butylamine solution no adsorption could be detected. This suggests the reversibly adsorbed amine and alcohol adsorb on the same sites, the amine being preferentially held there.

Whilst there is evidence of a very small increase in the n-butanol peak areas as the external areas of the HM nitric acid oxidised fibres increase, the areas of the first and the subsequent reversible exothermic butylamine peaks are magnified greatly by this treatment, Figure 3. There may also be a marginal decrease in the epoxypropane peak areas. On the commercially surface treated fibres the n-butylamine peak areas are also increased markedly but, as observed earlier, the external area is unaffected. In all cases the n-butylamine peak areas could be correlated with the active surface area measurements, a different relationship applying to each type of oxidation series.

n-Butylamine adsorption has previously been correlated with the amount of acidic surface complex on carbon surfaces (8) and it seems reasonable to assume that these are the sites for adsorption of this species. If this is so the results suggest that the fraction of the active surface which is covered by the acidic type of complex increases with oxidation time in nitric acid (HM-fibres) and is also greater for fibres treated by this method than those surface treated by the supplier.

The relevance of these results to the mechanism of enhancement of the ILSS of composites by surface treatment processes will be commented on at the meeting.

References

1. McKee, D.W. and Mimeault, V.J., "Chem. & Phys. Carbon", Vol.8, 151-245, (1973).

2. Herrick, J.W., 23rd Am. Tech. Conf. SPI Reinforced Plastics/Composites div., sect. 16-A, (1968).

3. Scola, D.A. and Brooks, C.S., 25th Soc. Plastics Ind. Meeting, Washington D.C., February 1970.

4. Grozcek, A.J., Lubric. Sci. Tech., 9, 67, (1966).

5. Mimeault, V.J. and McKee, D.W., Nature, 224, 793 (1969).

6. Lippens, B.C., Linsen, B.G. and de Boer, J.H., J. Catal., 3, 32 (1964).

7. Walker, P.L. Jr., and Janov, J., J. Colloid Interface Sci., 28, 449 (1968).

8. Puri, B.R., "Chem. Phys. Carbon", Vol.6, 191-282 (1970).

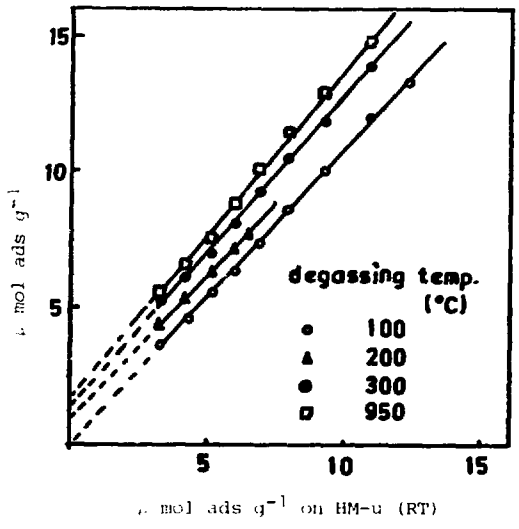


Fig.1 N_2 adsorption on HM-u fibres

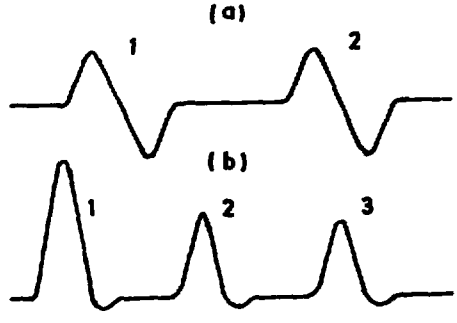


Fig.2 Typical calorimeter peak shapes - successive injections of adsorbate

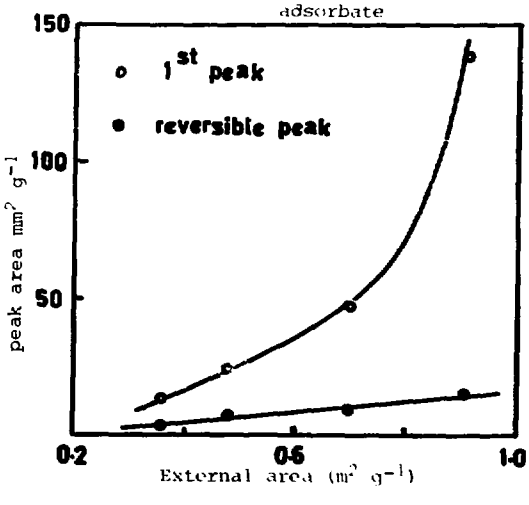


Fig.3 n-Butylamine peak areas for HM fibres oxidised in nitric acid

FIBER DENSITY ANALYSIS BY DENSITY GRADIENT TECHNIQUE

P. C. Pinoli, A. Ambrosio
Department of Materials Sciences
Lockheed Palo Alto Research Laboratory
3251 Hanover St., Palo Alto, Calif. 94304

1. Introduction

Currently many diverse fluid displacement procedures are employed to measure carbon/graphite fiber density. Cross referencing of available fiber density data is difficult due to the use of different test fluids and the low precision associated with some techniques. Precise fiber density values are required for aerospace applications to insure final part density uniformity and to determine composite void fractions. The density gradient procedure described in this paper was developed at the Lockheed Palo Alto Research Laboratory (LPARL) in 1975 and subsequently transferred to the Hitco Corporation in Gardena, Calif. as a standard test procedure for carbon fabric CCA3-1641B. The procedure follows the general outline of ASTM-1505 with specific techniques employed to make it directly amenable to carbon/graphite fiber analysis. All of the precision and accuracy data presented was generated on experimental carbon fabric. The commercial fabric is used extensively throughout the aerospace industry with phenolic resin to produce ablative composite hardware.

2. Experimental

Specific equipment and procedures not specified in the ASTM-1505 procedure are presented.

Column Preparation, Ref. Figure 1

Benzene, ρ = 0.8794 gms/cc and 1,1,2,2, Tetrabromoethane (TBE), ρ = 2.9638 gms/cc are the fluids used to produce a gradient column with the appropriate density range. Specific materials employed are as follows:

- o Pyrex tube, heavy wall with closed end, 160 cm high x 2.54 cm I.D.
- o Basket, cylindrical shape 2 cm high, fabricated from $\approx$ 40 mesh copper screen, soft soldered.
- o Chain, 1/8" round bead stainless steel, $\approx$ 7 cm diameter x 15 cm long drum attached.
- o Motor speed control, Minarik model SL-14.
- o Glass density floats, SGA D-1190 from SGA Scientific Inc., 737 Broad St., Bloomfield, N. J.
- o Meter tape, 150 cm long purchased from any yardage store, double back taped to column exterior.

Aluminum components must be avoided due to chemical attack by TBE. A cork is used to seal off the column when not in use and a slotted cork used during test operations to reduce fluid evaporation. The continuous siphon procedure, per ASTM Method B, is used to "build the column". Liquid flowing into the column is directed to flow down the bead chain at a rate of 1 cm column rise per minute. A disc of #1 filter paper is placed in the basket to reduce splashing. The basket is continuously raised to maintain its level consistent with the rising fluid height. The column is filled to within 5 cm of the top and 2 cm of pure benzene is introduced to "cap off" the column. The column is mounted in a fume hood to prevent excessive exposure to the benzene vapor. No temperature control is provided; as the laboratory temperature changes the calibration float beads adjust accordingly.

Specimen Preparation

Care is exercised at all times to insure against fiber bundle break up. Carbon fabric is sampled at specific locations with a 1/2" or 5/8" cork borer tool. Location identity is maintained by removing cord segments from the disc side or sides. All cord cuts follow the warp or fill direction to prevent frayed edges. Yarn samples are about 10 cm long. Sizing is removed from the specimens by exposure to hot MEK for epoxy compatible sizing and water for PVA. Residual moisture and solvent is removed by oven drying for a minimum of 2 hours at 105°C. All specimens must be dried prior to testing. Some carbon fibers with type 1 isotherm pores may require a longer drying time at temperature and under vacuum to remove all of the residual moisture. After drying, specimens are introduced directly into a beaker with pure benzene and subjected to a 5 minute ultrasonic agitation. The conditioned specimens are introduced directly into the column without allowing the benzene to dry out. Fabric discs are simply dropped in and for yarn samples 3-2 cm lengths of sample yarn are cut above the column and allowed to drop into the column. A timer is initiated at introduction and 5 minute interval density values are measured until equilibrium is approached.

3. Discussion

The development of fast and precise data by this technique requires insight into 3 factors which greatly influence fiber response. These factors are surface debris, residual moisture and the internal pore fill rate. Surface debris is occasionally present on low fired carbon fiber and is primarily residual inorganic compounds driven out of the fiber during pyrolysis. This material is removed by the 5 minute benzene ultrasonic operation. Residual moisture is always present in carbon or graphite fibers and values, up to 4% by weight, have been measured on as received carbon fabric. The water molecule is very small approx. 3.5Å diameter, and has a propensity for penetrating deep into the pore

fiber structure. If the moisture is not removed prior to testing the water molecules will supplant normal air void areas which cannot be penetrated by the benzene molecule, which is about 5.9Å in diameter. Since water is insoluble in benzene it is also possible that residual water molecules will be pushed into smaller void areas by the penetrating benzene. Residual fiber moisture will induce higher fiber density values. Using the experimental procedure outlined and a 30 minute test time, 16 specimens of varied experimental carbon fabric were tested at LPARL and the Hitco Corporation to determine the test procedure precision. The standard deviation of difference between laboratories was 0.00208 gms/cc with the observation error standard deviation of 0.00147 gms/cc. This relates to a 68% confidence level to ± 0.00147 gms/cc and essentially 100% confidence at ± .00441 gms/cc.

The measured fiber density accuracy was determined by fabricating phenolic matrix composite hardware from the same experimental fabric. Figure 2 presents the measured fiber density versus final composite density with a theoretical line based on a 37½ weight % matrix. The theoretical composite densities were calculated from the following volume balance equation:

$$g_{c\rho c}^{-1} = g_{r\rho r}^{-1} + g_{f\rho f}^{-1}$$

where g = weight % of c-composite, r-resin and f-fiber
ρ = density gms/cc respectively.

Some scatter of fabricated composite density data can be expected due to inprocess variables which will alter the matrix volume fraction. Phenolic resin staging prior to cure, degree of debulking, bleeder cloth application and other small variables can induce slight changes in the final part matrix volume fraction. The theoretical calculations however assume a constant matrix/fiber fraction with no void content. The relationship demonstrated in Figure 2.appears to indicate two significant results; the measured fiber density data is accurate and the inprocess variables which can alter the matrix volume fraction are minimal.

4. Conclusions

The density gradient technique has demonstrated excellent precision and accuracy for measuring carbon fabric density. The test appears amenable to the entire range of carbon/graphite fabric and yarns which are currently being produced. The simplicity and precision demonstrated by this technique indicate it should be considered as the bases for an industry wide test procedure.

5. Acknowledgements

The authors would like to recognize the valuable support of Pete Barry, Bob Shaffer and Gene Rubin at Hitco.

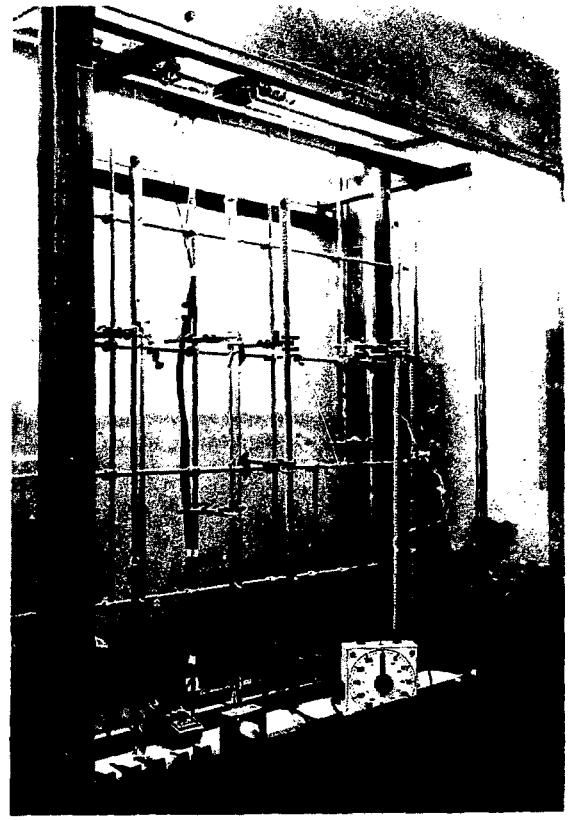


Figure 1

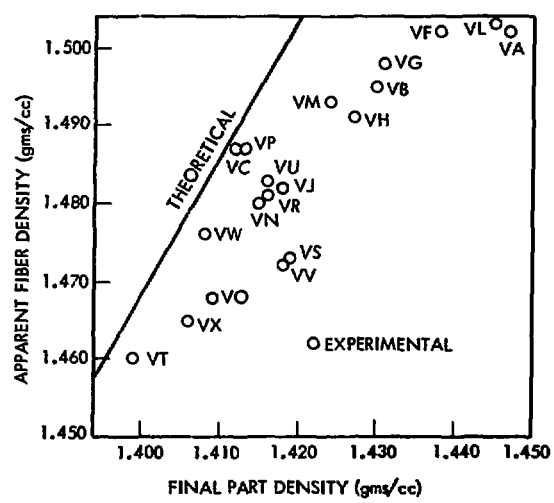


Figure 2

PORE ANALYSIS OF CARBON FABRIC BY DENSITY GRADIENT TECHNIQUE

P. C. Pinoli, A. C. Johnson
Lockheed Palo Alto Research Laboratory
3251 Hanover Street
Palo Alto, California 94304

1. Introduction

All polymeric carbon fibers have an internal pore structure. The size, shape and open or closed nature of these pores are instrumental factors which determine the effective fiber density within a composite. Since composite thermoset resins can penetrate into these pores the technique of measuring effective fiber density must utilize an excellent penetrating test fluid and be capable of providing very precise density values. A density gradient technique, which utilizes benzene as the penetrating fluid, was developed to meet these requirements [1]. If the carbons atom spatial arrangement of all polymeric carbon fibers is similar, the measurement of fiber density is in reality a study of the internal pore structure [2]. Commercial carbon fabric CCA3-1641B, produced by the Hitco Corporation, Gardena, California was used to study the relationship of the pore structure and fiber density. This paper analyzes the effect of fabric oxidation and residual moisture on fiber density values as determined by the density gradient technique.

2. Experimental

Oxidation and absorption specimens were 2" squares placed into tared aluminum dishes for handling. All specimens were pre-dried for 16 hours at 105°C under vacuum to remove residual fiber moisture. The specimens were quickly removed from the oven and weighed to obtain the initial specimen weight. After weighing, the specimens were returned directly to the vacuum oven. Oxidation specimens were moved directly from the vacuum oven to a large muffle furnace previously stabilized at 450°C. At 5 minute intervals the specimens were removed from furnace, weighed immediately and returned to the vacuum oven. A test chamber for moisture absorption study was prepared by filling a descicator jar, to within 2 cm of the base plate, with distilled water. Specimens were moved directly into the descicator from the vacuum oven and were left in this approx. 100% R.H. environment for 25 hours. Each specimen was removed individually from the descicator and placed on the balance pan. The specimen was allowed to desorb by evaporation until the desired pre-determined absorption value was reached. At this point disc specimens were introduced into a beaker of pure benzene. The beaker was then exposed to 5 minutes ultrasonic agitation and the specimens introduced directly into the density gradient column.

3. Discussion

The objective of this study was to determine factors which could induce carbon fabric density variability and subsequently effect the final product composite density. A BET surface area and pore size study by E. B. Stuart, and T. Ising of of the University of Pittsburgh indicated the presence of type 1 isotherm micropores which are constricted or capillary connected voids [3,4]. The open or closed nature of these voids to a penetrating composite resin could significantly affect the composite structure density. To analyse the nature of the internal pore structure, specimens were oxidized up to 4% and fiber density measurements made by the density gradient technique. Figure 1 presents the fiber oxidation effect on density. The density values presented are all based on 30 minute exposure time in the gradient column. The initial portion of the "S" curve is interpretated as a closed pore skin layer which is removed by about 0.88% oxidation at point "A". This relates to the removal of 300Å of skin carbon structure. After removal of this "skin" the internal pore structure is penetrated by the intruding fluid and the apparent fiber density increases accordingly. The density effect of oxidation, in excess of point "B" is much less than the A to B rate and appears to be asymtotical. The dramatic oxidation effect in fiber density demonstrates the importance of oxygen free HTHT. Our fiber density acceptance limit is 1.490 gms/cc. This can be exceeded by 0.7% oxidation and would require 0.3 to 0.6 ft.^{3} air per yard of fabric depending upon the fabric weight and CO or CO_2 reaction.

The effect of residual moisture on fiber density was determined by pre-filling the internal pore structure with measured weight % water and measuring the apparent fiber density. The technique employed ensures the residual fiber moisture is not surface moisture but molecules of water trapped within the constricted internal pore structures. The experimental data is compared to theoretical calculations in Figure 2. The theoretical line is based on a wt.% addition to the initial fiber density i.e. the apparent fiber density with 1% by wt. water is 1.458 + 0.015 = 1.473 gms/cc. This assumes no net volume change associated with the 1% wt. addition. The small slope variance of experimental and theoretical data can be associated with a slight fiber swelling effect which would increase pore penetration or experimental error. The slope change of experimental data at 4% residual moisture indicates pore saturation.

The rayon based carbon fiber we have studied has received sufficient HTHT to partially close the pyrolysis pore structure. Jenkins and Kawamura have recently speculated that all carbon fibers are related to glassy carbon in structure and pore development [2]. Our study on cellulose based fiber is in agreement, however the temperature range of pore closure for cellulose carbon occurs in the 1,200°C to 1,700°C range as compared to 700°C to 1,200°C range for conventional glassy carbon [5].

4. Conclusions

The carbon fibers tested have a semi-permeable skin about 300Å thick and porous interior core. The skin pore structure is permeable to the small water molecules and impermeable to the much larger molecules of benzene or thermoset resin.

5. References

1. P. C. Pinoli, A. Ambrosia, Fiber Density Analysis by Density Gradient Technique, 3 Biennial Conf. on Carbon, Irvine, Calif.
2. G. M. Jenkins, K. Kawamura, Polymeric Carbons-Carbon Fibre, Glass and Char, Cambridge University Press, 1976.
3. E. B. Stuart, Surface Area and Pore Size of Carbon Fibers, SETEC-CH-76-018, University of Pittsburgh, 1976.
4. S. J. Gregg, K. S. W. Sing, Adsorption, Surface Area and Porosity, Academic Press, 1967.
5. H. W. Davidson, H. H. Losty, Impermeable Cellulose Carbon, General Electric Journal, Vol. 30, No. 1, 1963.

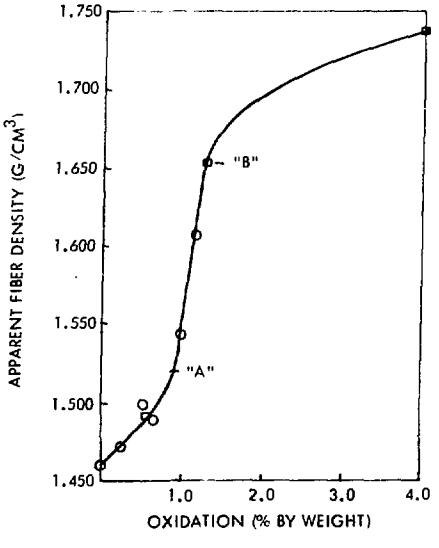


Figure 1

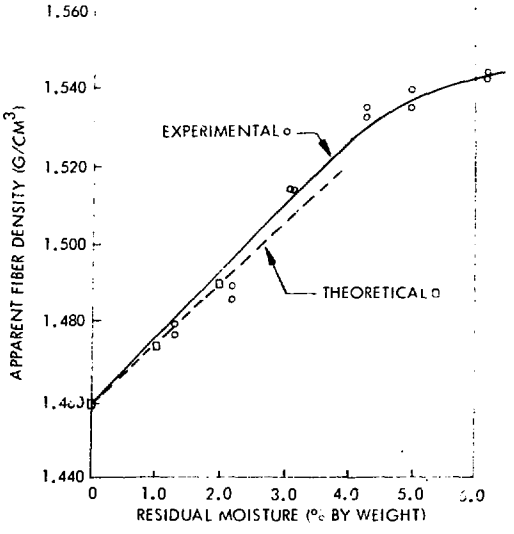


Figure 2

CURRENT CONDUCTION EXPERIMENTS WITH SINGLE CARBON FIBERS

I. R. McNab
Westinghouse Research and Development Center
Pittsburgh, Pennsylvania 15235

Introduction

The electric current conducted by single horizontal carbon fibers, either plain or coated with thin layers of various metals (Au, Ag, Cu, Ni), has been measured in air, Ar, and He at fiber temperatures up to 1500°C. The observed resistance variations have been correlated with theory showing that gaseous conduction is the limiting factor in this case, even though convective cooling is the dominant loss mechanism. Current densities in coated fibers in excess of 1.2 MA/cm^2 have been achieved.

Apparatus

The measurements were made in a 38 cm high, 25 cm diameter domed glass bell jar which could be evacuated and filled through a 1.9 cm hole in the base plate. The fiber to be tested was placed horizontally between two clamps, 44.5 mm apart, and kept in slight tension by a light spring. Electrical current was provided by a 500 mA, 500 V dc supply and monitored by standard digital meters.

Theory

The heat balance for a horizontal, current-carrying fiber is obtained by equating the electrical heating with the losses arising from convective, conductive, and radiative cooling. In the present case, some valid approximations permit this general equation to be simplified.

Thus, because the fibers have a large length-to-diameter ratio (> 5000) in the present geometry, axial heat conduction along the fiber has a negligible influence on the fiber temperature over most of the fiber length.

Fiber temperatures in these experiments have been below 500°C in air, 1400°C in Ar, and 1500°C in helium. Under these circumstances, radiation can be shown to contribute a relatively small amount to the total cooling. Specifically, for the quoted temperatures, the radiative-to-convective cooling ratio is < 0.02 for air and He, and < 0.13 for Ar, showing that radiation may be neglected in most cases.

This is caused by the extremely high heat transfer coefficient for small fibers. For small diameters (d), the convective heat transfer coefficient (h_c) reduces to the simple expression

$$h_c = 0.45\ k_f/d \qquad (1)$$

where k_f is the thermal conductivity of the fluid. That is, h_c is dominated by conduction of heat from the fiber to the surrounding atmosphere.

To a good approximation, the heat balance for the fibers investigated here can, therefore, be represented by

$$I^2R/\ell = \pi\ d\ h_c\ (T - T_a) = 0.45\ \pi\ k_f\ (T - T_a) \qquad (2)$$

where I^2R/ℓ is the ohmic heating per unit length, and T_a the atmosphere temperature.

Experiments

Several different fiber/coating/atmosphere combinations have been tested, including: Thornel 300 in air, Ar, He; Modmor Type 2 in He; Ni and Ag-coated Modmor Type 2 in He; Au, Ni, and Cu-coated Thornel 300 in He. Thornel is manufactured by Union Carbide and Modmor by Morganite Inc.; both are based on a polyacrylicnitrile precursor.

Carbon Fibers

At 20°C, the measured resistance of the clamped Thornel fibers was from 19.4 to 24 kΩ. Scanning Electron Microscopy (SEM) photographs of typical fibers indicated a mean diameter of 6.3 μm, corresponding to a mean fiber resistivity of 1520 μΩ cm. Modmor Type 2 fiber exhibited a lower resistance (8 kΩ) and larger diameter (8.44 μm), corresponding to a resistivity of 1000 μΩ cm.

For comparison, manufacturers' data for Modmor Type 1 and Type 2 fiber gives 775 μΩ cm and 1500 μΩ cm, respectively, with fiber diameter variations of at least ± 5%.

Application of increasing voltages resulted in increasing currents and fiber temperatures, until burn-out occurred. For Thornel 300 this occurred at 7.4 to 8.2 μA in air, up to 30 μA in Ar, and 47 μA in He. Modmor Type 2 fibers carried currents of up to 86 μA in He at pyrometrically estimated fiber temperatures up to 1500°C.

In air, the fiber resistance increased slightly just before burn-out occurred, presumably because partial oxidation reduced the fiber diameter. In argon and helium, consistent results were obtained up to at least 800°C, but a time-dependent "run-away" effect occurred above about 1000°C. This effect, in which the fiber resistance decreased as the temperature increased, became particularly rapid above about 1400°C. Graphitization of the carbon is the likely cause, but oxidation may have also been involved, since noticeable thinning of the fiber was observed prior to burn-out.

Metal-Coated Fibers

Coating the fibers with metal substantially changed the observed behavior, with fiber resistances at ambient temperatures being as low as 12 Ω/cm.

Using coating thicknesses estimated from SEM photographs, some discrepancies between the derived and expected resistivities were found. Thus, measured coating resistivities were 2, 4.8, and 5.5 times the usual bulk values for Ag, Ni, and Au, respectively. Data for copper was uncertain, with some values being above and others below, the bulk values. These resistivity differences are likely to be caused by the non-uniformity and/or the strained nature of the coatings.

Relatively large currents were conducted with these coated fibers. For these particular specimens, Ag-coated fibers showed the highest mean value (161 mA in He), followed by Cu (106 mA), Ni (45 mA), and Au (33 mA). Maximum currents > 750 mA were conducted by single Ag-coated fibers, corresponding to coating current densities > 1.2 MA/cm^2.

As expected from heat transfer considerations, the highest currents were conducted in He, followed by air and Ar.

In the case of uncoated fibers, small visible hot spots developed at certain currents and presaged the subsequent breaking of the fiber at higher currents. With coated fibers, in contrast, most breaks occurred at lower temperatures (150 to 300°C), even in inert atmospheres and for no visible reason. This may have been caused by either chemical or mechanical weakness introduced during the coating process, or by an interaction between the coating and the underlying fiber.

Comparison of Theory and Experiment

Because k_f is a function of temperature, and the fiber temperature (T) was not easily measured, it is not simple to determine whether Equation (2) correctly describes the observed behavior. An alternative procedure has, therefore, been evolved. In this, the appropriate gaseous thermal conductivity variation is inserted into Equation (2) to give

$$I^2R/\ell = f\ (T) \qquad (3)$$

which describes how the heat dissipation varies with temperature. Using the measured current and voltage, Equation (3) enables the fiber temperature and resistance to be estimated simultaneously. Referencing the fiber resistance to the value at 20°C then permits the resistance ratio to be compared with independent values for the temperature coefficient of resistivity.

Typical results for uncoated Thornel and Modmor fibers in helium are shown in Fig. 1. The horizontal bars indicate measurements for which time-dependent effects occurred. The asterisk represents an extrapolation of manufacturers' data for Modmor Type 2 fiber for the temperature range up to 200°C (R_o is the resistance at ambient temperature).

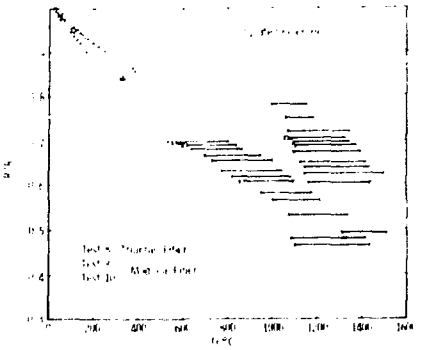


Fig. 1 - Resistance ratio for unplated fibers in helium.

The procedure denoted by Equation (3) was followed for coated fibers. Fig. 2 shows data for tests with silver-coated Modmor fibers in He.

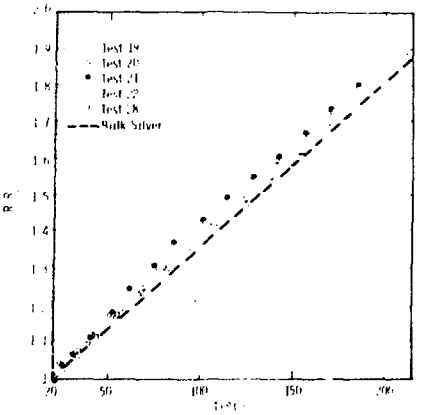


Fig. 2 - Resistance ratio for silver-plated fibers in helium.

Satisfactory agreement with independent temperature coefficient of resistivity values was only achieved when the constant in h_c was assumed to be about 20% higher than given in Equation (1). Since SEM photographs show the surface of coated fibers to be uneven, a possible explanation for this difference may be that the increased surface area causes an increase in h_c. Alternatively, the temperature coefficient of the thin coated layer may differ from that of bulk material, either because of structural or temperature inhomogeneities.

Acknowledgments

The careful work undertaken by P. A. Ciarelli in handling these single fibers and making the electrical measurements is gratefully acknowledged, as is the development of fiber plating techniques by H. E. Ricks and W. R. Gass.

PIEZORESISTANCE OF CARBON FIBERS

D.B. Fischbach & Y. Komaki
Department of Mining, Metallurgical & Ceramic Engineering FB-10, University of Washington, Seattle, Wash. 98195

A few studies on the change of electrical resistance R of carbon fibers with applied stress have been reported (1-3) for fibers from PAN, using resistance bridge techniques. Resistivities ρ were confirmed to be high and found to be noisey; R increased with tensile strain, except for the highest modulus fibers where it decreased; changes were largely reversible; and the results were explained in terms of contact resistances within the substructure, with emphasis on ρ increases (2). The piezoresistance characteristics are being further investigated as part of a study, by both electrical and dynamic mechanical (torsion pendulum) techniques, of the micromechanical behavior of carbon fibers. Preliminary results of an initial survey of the behavior of fibers from rayon and anisotropic (mesophase) pitch as well as PAN are described.

Individual fibers, ~5 cm long, were attached with glue and silver paint to a micrometer head/calibrated flexure spring tensile stressing device. The resistance was measured with a precision potentiometer and high impedance null detector/amplifier feeding a recorder. Initially, the current thru the fiber was kept very low, ≤ 0.5 μA, to minimize possible localized heating effects. Tests still in progress indicate that Ohm's law is obeyed for currents up to 15-20 μA (current densities to ~40 A/cm^2) for both stressed and unstressed fibers; but noise levels tend to increase greatly above ~15 A/cm^2, and there is increasing risk of irreversible R changes at higher levels. Measurements have been made on PAN-based fibers (Hercules A-S, HT-S, HM-S) and fibers from rayon (T-11 thru T-100) and anisotropic pitch (AP-27 - AP-53) from Union Carbide. SEM cross section area measurements on fibers from the same batch, and batch elastic modulus values E from the suppliers were used to compute nominal tensile strains ϵ from the measured loads.

The results are shown in Fig. 1 where the percent change in resistance is plotted against tensile strain and the numbers by the curves are E in Mpsi. The low-strain behavior is qualitatively similar for the three fiber types, and consistent with that reported for fibers ex-PAN (1-3): The slope S is positive for fibers with low E (and HTT), decreases with increasing graphitization and becomes negative for the most graphitic high E fibers. However, for fibers ex- hot stretched rayon, and anisotropic pitch, with $E \gtrsim 50$ Mpsi $dS/d\epsilon > 0$ and $S > 0$ for $\epsilon > 0.2\%$. The strain gage equa., $S = d/d\epsilon(\Delta R/R_0) = (1 + 2\nu) + d/d\epsilon(\Delta\rho/\rho_0)$, relates the piezoresistance to separate geometrical (elongation plus Poisson contraction) and resistivity terms. Poisson ratio values in the range $0.15 \leq \nu \leq 0.4$ have been reported for fibers (4,5). Then at low strains $\Delta\rho < 0$ for $S < 1.3$ to 1.8 depending on fiber type. In Fig. 1, $S \simeq 1.3$ for the ex-rayon 50 Mpsi fiber and $\simeq 1.8$ for the 35 Mpsi ex-PAN fiber. However, in the more graphitic fibers $\Delta\rho$ reverses sign with increasing ϵ and can develop high plus values at high strain levels.

Resistivity changes thus appear to dominate the piezoresistance behavior, and their origins must be sought primarily in the fibrillar substructure of the fibers. Tensile straightening of stacked layer-ribbon microfibrils may contribute directly to the resistivity decrease; but the influence of strain-sensitive internal contact resistances in a fibrillar series/parallel network seems more important (2). Dynamic torsional stiffness increases with tensile stress in graphitized fibers (6), suggesting increased coupling between adjacent fibrils due to straightening and Poisson contraction. This would also reduce parallel contact resistances, decreasing ρ. However, high tensile stresses will tend to open series contacts between fibril ends and may account for the resistivity increase at higher strains. Shorter continuous fibril lengths might be expected for fibers from anisotropic pitch and hot-stretched rayon than for ex-PAN fibers.

This research was supported by the U.S. Army Office of Research under grant DAAG-29-76-G-0169.

1. Connor P.C. & Owston C.N., Nature 223 1146 (1969)
2. Owston C.N., J.Phys.D(Appl.Phys) 3 (11) 1615 (1970)
3. Berg C.A., Cumpston H. & Rimsky A., Textile Res. J. 42 486 (1972)
4. Reynolds W.N., Chem. & Phys. Carbon, Walker & Thrower, edit., Dekker, New York, Vol. 11, 1973, pp 1-67
5. Smith P.E., J. Appl. Phys. 43 2555 (1972)
6. Henrichsen P.E. & Fischbach D.B., 12th Carbon Conf. Ext. Abs., Univ. Pittsburgh, July 1975, p.135; Henrichsen, Ph.D. thesis, U. Washington, May 1976

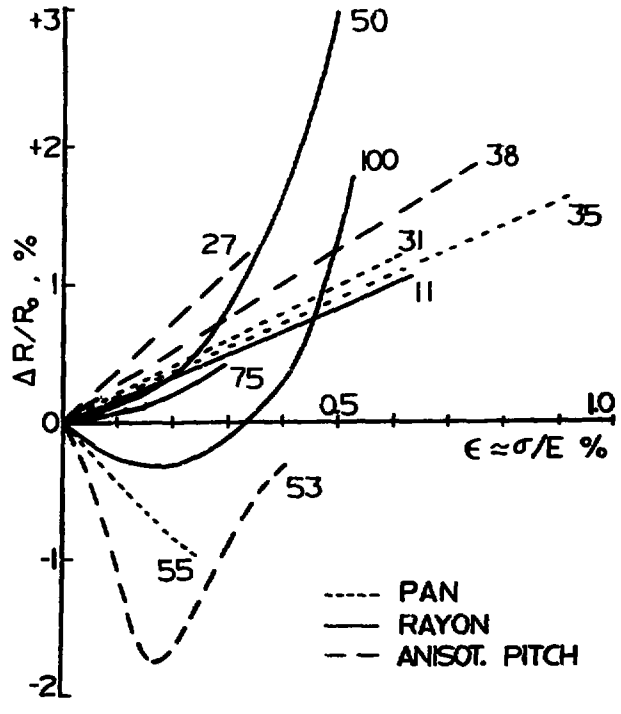


Fig. 1. Resistance change as a function of tensile strain for some representative carbon fibers.

[illegible]

[illegible] intercalation compounds are related to high electrical conductivity. The intercalation compounds of cellulose pre-oriented carbon fiber with potassium (1) and nitric acid (2) have been reported. After intercalation with potassium, the electrical conductivity of the fiber was increased by a factor of about 20, but the temperature dependence of the conductivity between room and liquid helium temperatures was the same as the starting fiber's one, even after saturation with potassium, viz., they showed negative temperature coefficient of resistivity. The absorption of the agent did not destroy the fiber structure. By nitration of the fiber the conductivity also increased, and the mechanical properties were changed.
The carbon fibers obtained by pyrolysing benzene have been indicated to be one of the most graphitizable carbon (3) - (6).
The present paper deals with the preparation and electrical properties of graphite fiber nitrate, being so-called as a residue compound, by using the carbon fibers through benzene decomposition. They have high electrical conductivity and do not show any lowering of mechanical strength.

The original graphite fibers were prepared by heat treatment of carbon fibers at 3000°C, which were grown on a substrate at 1100°C by pyrolysing benzene diluted with hydrogen. The graphite fibers consisted of concentric graphite layers around the fiber axis like the annual rings of a tree. These fibers were cut into 1 - 3 cm length, and had a constant diameter of 10 - 30 μm. The fiber samples were immersed in fuming nitric acid kept at 20°C. After 24 hrs. of immersion they were taken out into the air and kept in the container with sodium carbonate for more than 24 hrs. By these procedures the intercalated fibers, so-called as a residue compound, were formed (hereafter denoted as GFN).

The electrical resistivity is decreased rapidly to 7% of starting value after 10 min. of immersion in nitric acid, indicating the formation of an intercalation compound. Subsequently the resistivity decreases much gradually and remains almost unchanged after 24 hrs. of nitration. The fiber thus formed seems to be a stage II intercalation compound. It could indicate that nitrate diffuses into fiber through the surface. When the fiber is taken out into the air and kept in the container, the resistivity increases gradually. After several hours it becomes stable, at which the value is about 15% of the starting fiber's one. The resistivity changes that occured during the procedure are shown in Table 1. The fiber nitrate (GFN) thus obtained showed no appreciable resistivity change in the air over long periods of time (Fig.1).

Though the fiber's diameter increases slightly after nitration, the fiber structure is not destroyed. The cross-section morphology of the annual ring structure is still retained in GFN.

In Fig.2, the electrical resistivity of GFN is [illegible] operation with original graphite fiber. The fiber [illegible] characteristic, which [illegible] the [illegible] of the [illegible] temperature [illegible] phonons. The temperature [illegible] of the resistivity is about [illegible] at 30°. The variation in resistivity is almost [illegible] at temperatures below 30°, this trend being [illegible] in different samples, and might be the result of impurities and defective lattice. When the ambient temperature is increased to the rate slower than 3°/hr, an anomaly in resistivity is observed, which may correspond to the order-disorder transition of graphite-nitrate (7). At temperatures above 100°, the resistivity increases significantly because of the decomposition of the compound.

Magnetoresistance effect, measured by applying the magnetic field perpendicular to the fiber axis, is shown in Fig.3. They show a positive effect throughout the temperatures examined.
The magnetoresistance anisotropy, measured by changing the angle between the fiber axis and the magnetic field, is also retained. These results suggest the existence of the graphitic layers unaffected by nitrate.

The variation of thermoelectric power with temperature is shown in Fig.4, in comparison with original graphite fiber. The thermoelectric power changes to a positive sign after nitration, and increases monotonically with increasing the temperature. The phonon-drag effect observed in graphite fiber disappears, presumably because of a disturbance of the crystal lattice and shortening of the mean free path of carriers.

In summary, by nitration the fibers with metallic p-conductivity are obtained from the graphite fibers. Their mechanical strength is almost the same as the original fiber's one. They could afford promise of being used as electrical conductor.

Table 1. The electrical resistivity of fiber sample at room temperature

Original graphite fiber	8×10^{-5} (Ω·cm)
Nitrated fiber (in nitric acid)	0.6×10^{-5}
Nitrated fiber (in the air, GFN)	1.2×10^{-5}

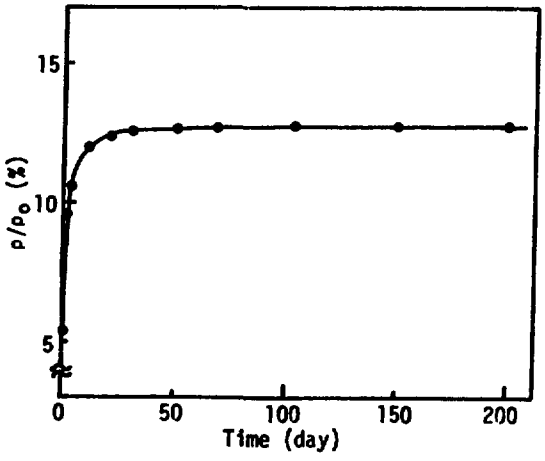


Fig. 1. Change of electrical resistivity with time at room temperature.

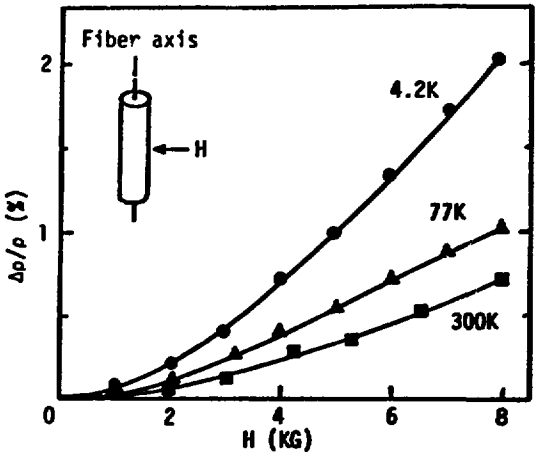


Fig. 3. Magnetoresistance effect of graphite fiber nitrate.

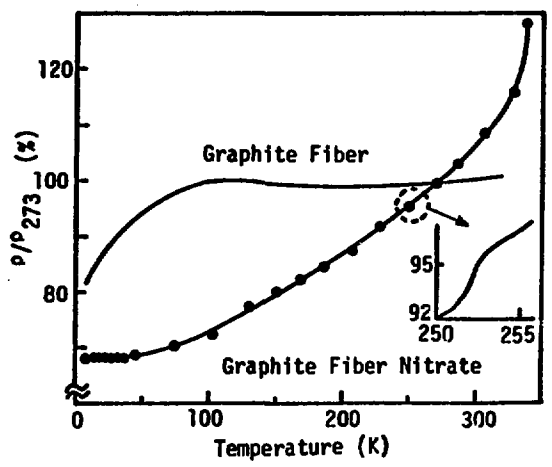


Fig. 2. Temperature dependence of electrical resistivity.

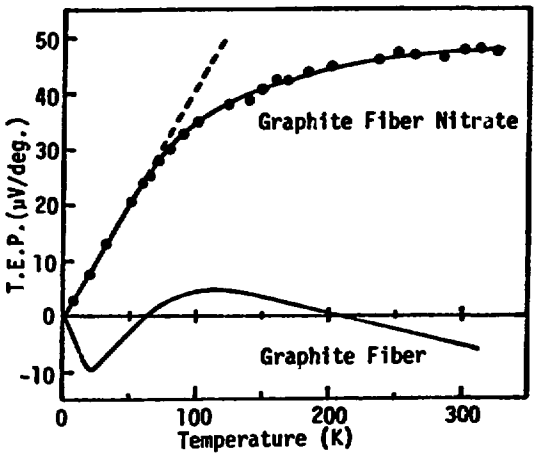


Fig. 4. Thermoelectric power of graphite fiber nitrate.

References

1. C.Herinckx, R.Perret and W.Ruland, Nature 220, 63 (1968).
2. F.L.Vogel, Carbon 14, 176 (1976).
3. T.Koyama, M.Endo and Y.Hishiyama, Japan. J. appl. Phys. 13, 1933 (1974).
4. A.Oberlin, M.Endo and T.Koyama, J. cryst. Growth 32, 335 (1976).
5. A.Oberlin, M.Endo and T.Koyama, Carbon 14, 133 (1976).
6. M.Endo, T.Koyama and Y.Hishiyama, Japan. J. appl. Phys. 15, 2073 (1976).
7. A.R.Ubbelohde, Proc. Roy. Soc. A. 304, 25 (1968).

THE MECHANISM OF THE ADDITION AND REMOVAL OF Br_2 IN A CARBON FIBER

J. G. Hooley*
The University of British Columbia
Vancouver, B.C. V6T 1W5, Canada

Victor R. Deitz
Naval Research Laboratory
Washington, D. C. 20375

Introduction

In general, the behavior of carbon fibers depends on the source material, the pyrolysis program (temperature, time, and environment), and on special chemical post-treatments. For example, a commercial fiber can be designated as a low temperature (1200-1500°C), a medium (2000-2500°C), or a high temperature (above 3000°C) product. This paper is concerned with the interaction of bromine with some carbon fibers and the results are compared with those reported for the intercalation of bromine by crystalline graphites.

Materials

The fibers were selected from commercial sources using both PAN and pitch as precursors. F-5 is a Courtauld HM PAN fiber. F-46 is a Union Carbide carbon fiber, Type P, on which the finish, normally present, was removed by heating at 500°C in a helium flow. F-44 and F-54 are pitch-base fibers (Union Carbide) which had been heated above 3000°C. P-35 and P-36 were obtained as the residues from an air-bromine treatment of F-54 (45 hours at 20°C). Spec C SP-1 were flakes of purified natural graphite (100 μm) from National Carbon Co.

Experimental

The bromine adsorption and desorption isotherms (20°C, P_o = 177 torr) were determined on 100 mg samples in an all glass, recording vacuum balance (1). The x-ray diffraction results were determined by Carl Vold of the NRL Material Sciences Division using a Phillips Vertical Diffractometer (Cu source). The emission of bromine with temperature programming was determined by J. B. Romans of the NRL Surface Chemistry Branch using a modified microcoulombmeter (Mast Instrument Co.). The calibration was made with dry air saturated with a halogen of known vapor pressure.

Results

The bromine isotherms in Figure 1 for F-54 were first taken to saturation and back to zero pressure (points X for I and O for II). After the return to zero pressures, isotherm III (points +) and isotherm IV (points ⊕) were obtained without the pronounced threshold pressures of isotherms I and II. The three bromine isotherms in Figure 2 were not taken to saturation, but were returned to zero pressure from different positions of adsorption. No intercalation of Br_2 was found in F-46, even at saturation; also no emission of Br_2 was observed in the thermal cycling to 550°C of this fiber.

The 002 separations of an original fiber and the same fiber after bromine treatments are given in Table 1. The values are also given for the average dimension of the diffracting domain, the interpretation of which is given in Discussion.

The emission of bromine from P-36 is shown in Figure 3 for two complete heating cycles to 530°C using the same sample. The bromine contents of the fibers were determined by an activation analysis based on irradiation in a Linac Reactor using 40 MeV. Similar behavior was reported earlier for crystalline graphite(2).

Discussion

It is instructive to compare the 20°C isotherms of Br_2 on natural graphite, Spec C SP-1 (3) and on the highly graphitized F-54 carbon fiber.

1. Threshold Pressure, P_t

In the 100 μm flakes of natural graphite P_t is 15-20 torr. In F-54, diameter 18 μm, the value of P_t is 60 torr for the initial exposure to Br_2, but this drops to 10 torr after one cycle of saturation and back to zero pressure, Figure 1. This resembles the behavior of a 2200°C pyrolytic graphite PG1 (4) where P_t was initially 95 torr for a 7 mm thick sample. After one cycle to saturation and back to zero, the sample had split into thin flakes for which P_t was 60 torr. In the case of the fiber F-54, this same behavior would be expected if the graphite domains in the original fiber were interlocked or imbedded in a matrix. The resultant stress raises P_t to 60 torr above which intercalation and expansion occur.

The x-ray diffraction results in Table 1 agree with a model of interlocking crystallites.

* With financial assistance from the National Research Council of Canada.

Table 1: (002) Separation Before and After Bromine

	(002)	Diameter Diffracting Domain
F-44	3.371	670 Å
P-35	3.392	730
F-54	3.375	790
P-35	3.396	840
P-35 (500°C)	3.389	820

The average dimension of the diffracting domain is 770Å and in the cross-section of the fiber (18 μm diameter) there are 5×10^4 domains. Thus, each carbon fiber can be viewed as a carbon composite. The intercalation of Br_2 and expansion of each domain cracks the matrix in a great variety of places along and around the fiber and to different degrees. Because the carbon layers are mostly parallel to the fiber length, the cracks should also be parallel to the length. In fact, this can be seen in the SEM for PAN fibers (F-5) intercalated with $AlCl_3$. It was noted that the crack was longitudinal and not all the way through the fiber. Now, when the pressure of Br_2 in F-54 is lowered to zero, most of the Br_2 leaves the graphitized regions which collapse and allow the cracks to close so that the fiber approaches its original cross-sectional shape. When the Br_2 pressure is now raised again, the graphitized regions are again intercalated but at a lower P_t (10 torr) because the fiber is now under much less stress than the original fiber. This change is also shown by the rates of intercalation. Thus, in the initial exposure, the rate is very slow in the first 10 torr above P_t; beyond that and during the second intercalation, the rate is much faster.

Saunders, Ubbelohde and Young (5) showed that the application of pressure decreased the amount of Br_2 intercalated in graphite. The relief of an internal stress should behave in the reverse manner.

Finally, it is of interest that for the fiber F-46 the P_t was so high that even in saturated Br_2 vapor at 20°C there was almost no weight increase. This fiber had not been heat treated at as high a temperature as F-54, and it has been shown before that this will raise P_t for an electron accepting reactant such as Br_2. The intercalation pressure for the F-46 fiber may be above saturation pressure.

2. Composition near Saturation

The composition is best considered just below saturation so that condensation in the inter-fiber or inter-flake regions is not a factor (1). At 20°C, saturation pressure is 175 torr so that 160 torr is suitable. For the natural flakes in Spec C - SP1 the amount is

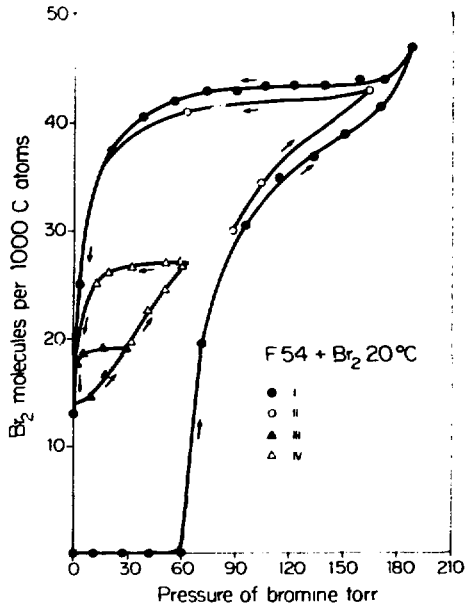


Figure 1: Intercalation adsorption and desorption isotherms (I, II original; III, IV after pumping).

$10^3 Br_2/C = 60$ or $C_{17}Br_2$. For the F-54 fiber it is 48 or $C_{21}Br_2$. This lower Br_2 content could well be the result of the presence of non-graphitized regions - the matrix referred to above - in which the intercalation of Br_2 does not take place.

3. Residue "Compound"

In the carbon fiber F-54, the residual Br_2 at zero pressure amounts to 14 moles per 1000 moles carbon. This is about three times the amount left in the 100 μm flakes of Spec C - SP1. Since the graphite crystallites in F-54 are about 7.7 nm across, one would expect a much smaller amount of residual Br_2 in such small crystals. One possible explanation is that when the fiber first cracked open, some of the internal porosity became exposed to Br_2 and filled with liquid as the pressure increased. On pressure reduction this region emptied at lower pressures than for filling and not completely because the closing of the cracks sealed them off. Specifically, the total volume of these pores for a fiber of density 1.6 gm cm^{-3} might be 0.6 cm^3 gm^{-1} and, if filled with liquid Br_2 would contribute 43 moles of Br_2 per 1000 moles carbon. This is the observed total amount near saturation. Much of this must be intercalated to account for the cracking of the fiber. An unknown, remaining amount is in the available pores and,

when the pressure is lowered, will leave. If the pores are about 0.8 nm in diameter (6) and are open ended cylinders they would empty at 20 torr pressure. This pressure is close to the sudden decrease in Br_2 content in the desorption curves of Figures 1 and 2. There will of course be a range of pore diameters and therefore of pressure drops in desorption. This could well account for the fact that the desorption curve is asymptotic to the P = 0 axis whereas for natural flakes it is asymptotic to the P = 10 torr line almost down to the residue composition (1).

The large residue noted for the fiber at zero pressure might have been caused by the closing of the cracks as the intercalated Br_2 departed, thus preventing the loss of all the Br_2. However, on heating the residue to 530°C and cooling (Figure 3), there is a total emission of 1.1% of the Br_2 on heating to 530°C and about 7% on cooling to about 100°C. This retention of most of the Br_2 at 530°C is difficult to explain. The amount of Br_2 in the matrix between crystallites should reach a pressure that would open the cracks and allow the Br_2 to escape. The intercalated Br_2 should also escape. One possible explanation is that most of the residual Br_2 is strongly held in what are loosely called defects in the graphitized domains. On heating to 450°C some of this may defect to the porous matrix but not leave the fiber until it cools to 200°C. At this temperature the stresses set up by the anisotropy of the temperature coefficients of expansion cause either further cracking or a partial opening of the original system of cracks. The two coefficients are:

(1) Parallel to axis: -1.2 to -1.3×10^{-6} per °C

(2) Perpendicular: $+5.5$ to 8.4×10^{-6} per °C

Repeated cycling from 20° to 530°C causes further loss of Br_2, but to a diminished extent. The total loss in cycle 1 was 8.1 wt.% and in cycle 2, the loss was only 2.7 wt.%. Thus, a substantial bromine residue remained in the fiber after heating twice to 530°C.

A second explanation for the strong retention of bromine is the pinning of some edge atoms which severely reduces the emission of bromine. However, the composition near saturation does not seem to be much influenced in repeated cycles of adsorption and desorption.

References

1. Hooley, J. G., Can. J. Chem. 37, 899 (1959).

2. Deitz, V. R. and Bitner, J. L., 11th Biennial Conf. on Carbon Extended Abstracts Paper 1C4, 199-200 (1973).

3. Hooley, J. G., Can. J. Chem. 40, 745 (1962).

4. Hooley, J. G., Garby, W. P. and Valentin, J., Carbon 3, 7-16 (1965).

5. Saunders, G. A., Ubbelohde, A. R. and Young, D. A., Proc. Roy. Soc. London A271, 512 (1963).

6. Arons, G. N., MacNair, R. N., Coffin, L.G. and Hogan, H. D., Textile Research J. 44, 874-883 (1974).

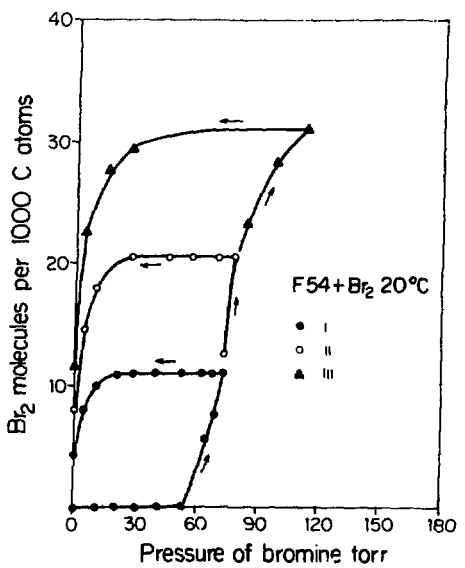


Figure 2: Intercalation isotherms desorbed from different levels.

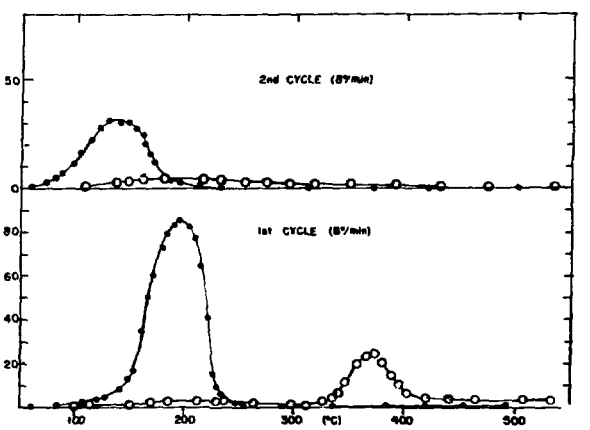


Figure 3: Bromine emission (ordinate micrograms) at constant rate of heating (open circles) and cooling (closed circles).

ASPECTS OF FORMATION OF GRAPHITIZABLE CARBONS FROM BLENDS OF PITCH-LIKE SUBSTANCES

H. Marsh, I. Macefield and Janet Smith
Northern Carbon Research Laboratories, School of Chemistry,
University of Newcastle upon Tyne, Newcastle upon Tyne NE1 7RU, U.K.

Introduction

The establishment of the preferential, parallel stacking of lamellar molecules in anisotropic carbons, as distinct from quite random arrangements within isotropic carbons, is now accepted as being via the nematic liquid crystals and the mesophase (see references listed in Ref. 1 and 2). The origins of nematic liquid crystals, their nucleation, growth and stabilization, are still imperfectly understood. One aspect of growth concerns the chemical heterogeneity of pitch substances, and the almost dominant role of certain molecular constituents. Considering the wide range of molecular size, shape, weight and constitution of parent substances, it is somewhat of an enigma to understand how the mesophase can grow and yet contain such a high element of crystallographic order. This paper discusses the dominant role of certain molecular constituents.

Origins of Nematic Liquid Crystals

As the pitch parent material is subject to increasing carbonization temperatures then inter- and intra-molecular re-arrangements produce an increasing concentration of large, lamellar constituent molecules. In all liquids there exist statistical associations of molecules and no doubt this association also occurs in fluid pitch. When a critical condition of temperature, molecular weight and molecular concentration is established, these nucleation associations (homogeneous), instead of rapidly dissociating, continue to grow to establish a new phase, as seen in optical microscopy (Ref. 3). The formation of the nematic liquid-crystal probably is assisted by the high enthalpies of physical adsorption which are possible when two large lamellar molecules 'come together' flat surface to flat surface.

It is considered that the development of these liquid crystals is insensitive to the detail of chemical composition of molecular constituents, but is very sensitive to the size and shape of these constituent molecules. But once having been formed by an essentially physical process, then chemical processes within the liquid crystals immediately become dominant and dictate subsequent events. Extents of 'cross-linkage' between the lamellar constituent molecules influence the viscosity of the liquid crystal and mesophase and ultimately the optical texture of resultant anisotropic carbons.

As discussed by Marsh (Ref. 4) it is a known property of documented nematic liquid crystal systems that they can accommodate material which itself would not form nematic liquid crystals. This process probably occurs during the growth of liquid crystals from pitch systems. In fact, Crawford and Marsh (Ref. 5), using phase-contrast, high resolution electron microscopy, were able to identify molecules contained (trapped) within the lamellar stacks. It is this aspect of the growth of mesophase which is reported here, using methods of extraction from single pitch-like substances and by blending pitches followed by the carbonization of the blends.

The Experimental Approach

An anthracene-oil coal extract (D112) was extracted with a range of solvents and the soluble and insoluble fractions carbonized. Resultant carbons were examined by optical microscopy. Also, in attempts to produce carbons with a range of optical texture, blends (binary) made up of A200 Ashland petroleum pitch, D112 coal-extract, Gilsonite pitch, asphaltenes and Orgreave coal-tar pitch, in varying ratios, were carbonized and resultant carbons examined by optical microscopy.

Discussion

The general conclusion of the study of carbonizations of pitch blends is that it is not possible to modify systematically and progressively, the size of optical texture (i.e. size of isochromatic areas as seen in polished sections) by co-carbonizing, in increasing percentage content, two pitches one of which would give large domains (e.g. A200 petroleum pitch), the second giving small mozaics (e.g. Gilsonite pitch). Small additions (<15%) of the A200 pitch to a pitch giving small mozaics had little effect upon the formation of the mozaics, but then over a further small increase in concentration the behaviour of the A200 pitch became dominant and large domains resulted (see Figure 1). It was as though the molecules of the Gilsonite pitch became trapped within the liquid crystals of the A200 pitch and it was the latter which controlled final properties. Separation (dilution) of the Gilsonite system may have prevented cross-linkage between the molecules of the Gilsonite pitch so preventing enhanced viscosity which produces the characteristic small mozaic structures.

Similarly, extraction by solvents of components of the pitch is capable of preventing the formation of nematic liquid crystal systems in the insoluble residues. These results into blending and solvent extraction are broadly in agreement with the recent findings of Mochida et al. (Ref. 5). These authors separated four SRC pitches with benzene into solvent-solubie: solvent-insoluble fractions and subsequently carbonized blends of soluble-insoluble fractions from different pitches. Two of the original pitches formed anisotropic flow structures, and two formed mozaic structures. All the insoluble fractions formed isotropic carbon; however, the anisotropic structures formed on blending were not predictable.

A thorough elemental, ^{1}H nmr and ^{13}C nmr analysis proved unrewarding.

It would appear as though the correlation of anisotropic structure (optical texture) with blend composition is of the form of Figure 1. The position of line AB may vary with the origins of pitch P_1 and P_2. The analysis of Mochida et al. may be unrewarding because what is of major importance is not the chemistry of the pitch as obtained but its chemistry immediately prior to formation of the nematic liquid crystal systems. The complexity of pyrolysis chemistry is such that predictions from parent molecular systems in multi-component mixtures cannot be contemplated. What could be looked for is the development of large, lamellar aromatic molecules in sufficient concentration to act as the dominant partner and establish anisotropic flow structures.

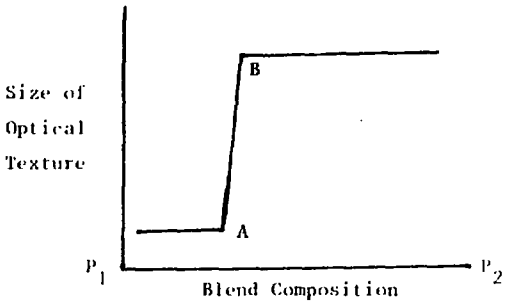


Figure 1.

References

1. Marsh H., Proc. 4th Conf. on Industrial Carbon and Graphites, S.C.I. London, pp. 2-38 (1976).
2. White J.L. and Zimmer J.E., "Surface and Defect Properties of Solids", Chem. Soc. London, 5, pp. 16-35 (1976).
3. Lewis R.T. Abstracts, 12th Conf. on Carbon, p. 215 (1975).
4. Marsh H., Fuel, London, 52, pp, 205-12 (1973).
5. Crawford D. and Marsh H., Carbon '76. Deutsche Keramische Gesellschaft, pp. 231-234 (1976).
6. Mochida I., et al., Fuel, London, 56, pp. 49-56 (1977).

Acknowledgement

We express our appreciation to the National Coal Board for financial support.

Compatibility of Pitch Fractions in their Cocarbonization Process

Isao Mochida, Kazuma Amamoto, Keiko Maeda, and Kenjiro Takeshita
Research Institute of Industrial Sience, Kyushu University 86, Fukuoka, Japan 812.

The carbonization process giving a graphitizable needle coke consists of the condensation reaction and rearrangement of condensed molecules into layer structure. Then, fusibility and suitable reactivity which may lead to low viscosity of the carbonization matrix are required for the carbonizing materials to be the source of needle cokes[1]. Such requirements must reflect the total features of a pitch because a pitch is composed of many components, one of which may sometimes play a role of a solvent to keep the system fusible, and the other of which can initiate the condensation, accelerating the carbonization. Although it is difficult to define the components of a pitch precisely, benzene soluble(BS) or insolble(BI) is a practical fractionation because fusible BS can often work as a solvent during the carbonization and dissolved BI accelerates the carbonization. Thus, the concept of compatibility was introduced to describe the cocarbonization properties of the mixtures of BS and BI. In the present paper, the concept of compatibility is reviewed from the viewpoints of its qualitative representation and its modification, referring the structural argument of the pitch.

Material: Two kinds of SRC(Solvent Refined Coal) pitch named No.1 and No.2 were used in the present study. The BS fractions of coal-tar pitch(Nittetsu Chemical Co.), ethylene-tar pitch(ET) (by-product at the thermal cracking of naphtha(Koa Oil Co.), and Kureha pitch(KP-BS) (by-product at the thermal cracking of crude oil. Kureha Chemcal Industry) were also used.
Carbonization: Carbonization was carried out in a pyrex tube(30 mmϕ x 300 mm) under a nitrogen gas flow. The rate of temperature increase was 150°C/hr. The holding time at a fixed temperature was 2 hr. The mixed pitch consists of 60% BS and 40% SRC-BI in every case.

Cocarbonization of SRC-BI fractions with the BS fractions of other pitch sources clearly suggested the concept of compatibility. Although all BS fractions used in the present study gave needle cokes in their single carbonization, some of their mixtures with the SRC-BI gave needle cokes and other did mosaic ones, that is, KP-BS and No.1-BS gave needle cokes in cocarbonization with both SRC-BI fractions, but ET and No.2-BS did mosaic one with both SRC-BI. The CP-BS formed a needle coke with No.1-BI but did a mosaic one with No.2-BI.

The cocarbonization compatibility could be qualitatively described by observing a series of the cokes which were produced by varying the mixing ratio of BS and BI.

The cocarbonization properties were tried to be correlated with the molecular weight, H/C ratio and fa value[2] of BS, however no relation was observable. Nevertheless, the poor compatibility of ET which produced fine mosaic cokes with SRC-BI is presumable to come from its small molecular weight. Based on above assumption, modification of ET to be compatible with SRC-BI was carried out by the thermal and acid-catalyzed reactions. The reactions can be classified into three categories. The first one is the catalytic reaction with aluminum chloride which is a typical Lewis acid of non-transition metal ion, the second one is the catalytic one with ferric chloride which is a typical Lewis acid of transition metal ion, and the third one is the thermal reaction without catalyst. Microphotographs of carbons obtained from SRC-BI and ET or BS fraction of modified ET(M-ET-BS) are shown in Fig. 1. Although original ET gave fine mosaic cokes with SRC-BI regardless of No.1 and No.2. Modification with aluminum chloride(I: refer to Table 1) converted ET compatible with both SRC-BI to give needle cokes, however modification with ferric chloride(II: refer to Table 1) produced still fine mosaic cokes with both SRC-BI similarly as the original ET did. Thermal treatment(III: refer to Table 1) gave a needle coke with No.1-BI but failed with No.2-BI.

Some properties of original ET and M-ET-BS were summarized in Table 1. Although all reactions increased the molecular weight by 110-180, they brought about slight change in the values of H/C and fa. The most significant difference is observed in the values of Ho/H and Hγ/H, which are calculated from NMR analysis. The pitch modified with aluminum chloride had the higher values to giving the excellent needle cokes with SRC-BI. In a previous paper[3], the values of Ho/H of the carbonization intermediates were reported high when aluminum chloride was used as the catalyst giving needle cokes, whereas they were low when alkali metals or transition metal chlorides were used to give isotropic or mosaic cokes. Such observation could be explained in terms of lowered melting point and suitable reactivity of the partially hydrogenated ring which were preferable for the carbonizing system to maintain the liquid phase.

The same explanation may be applicable for the better compatibility, and suggests a possibility that further hydrogenation may improve the compatibility of M-ET-II-BS. The results are shown in Fig.2, indicating that the above explanation is valid.

Thus, the concept of compatibility is quite useful to describe the carbonization properties of the pitches and provides directions for their modification.

References
1) I. Mochida, K. Kudo, N. Fukuda, and K. Takeshita, Carbon, 1975, 13, 135.
2) J.K. Brown, and W.R. Lodner, Fuel, Lond., 1960, 39, 87.
3) I. Mochida, E. Nakamura, K. Maeda, and K. Takeshita, Carbon, 1976, 13, 489, ibid., 1976, 14, 123.

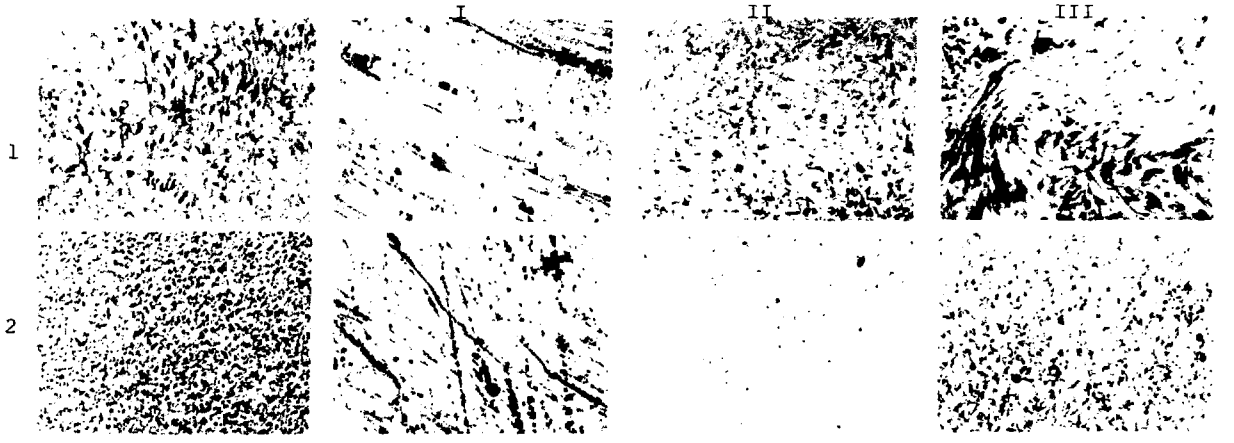


Fig.1 Microphotographs of cokes obtained from the mixture of ET or MET-BS and SRC-BI under crossed nicols (X 200). Carbonization; 600°C-2hr (1) No.1-BI (2) No.2-BI (Orig.) ET original, (I) MET-I-BS, (II) MET-II-BS, (III) MET-III-BS

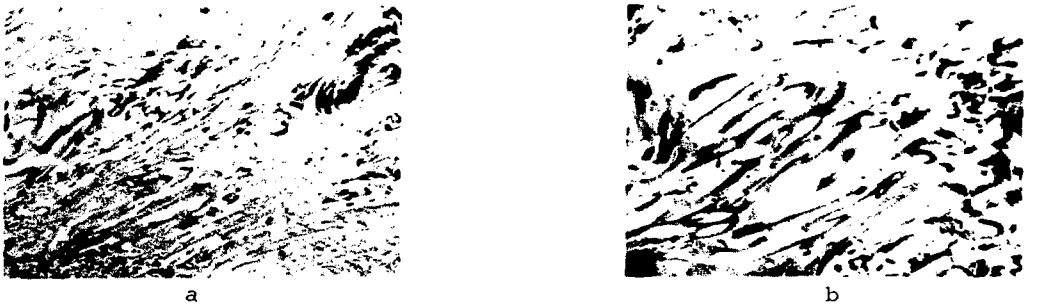


Fig.2 Microphotographs of cokes obtained from the mixture of hydrogenated MET-II-BS and SRC-BI under crossed nicols (X 200). Carbonization; 600°C-2hr
(a) cocarbonization with No.1-BI
(b) cocarbonization with No.2-BI

Table 1. Some properties of ET and MET-BS

	Modification Conditions	Y.[1] (%)	BS[2] (%)	H/C	Ha/H[3]	H^1-NMR Hα/H[3]	Ho/H[3]	Hγ/H[3]	fa	C^{13}-fa	MW
Orig.	ET-Original		100	0.95	50.0	35.9	12.2	1.9	0.76	0.76	230
MET-I	1.0 mol $AlCl_3$ 260°C-4 hr	97	71	0.90	33.7	35.8	24.2	6.3	0.70	0.63	410
MET-II	1.0 mol $FeCl_3$ 400°C-0 hr	85	74	0.90	47.6	34.5	15.0	2.9	0.76	0.72	340
MET-III	None catalyst 400°C-0.5 hr	50	99	0.83	48.5	33.3	15.8	2.4	0.79	-	350

1) $Y.(\%) = \frac{\text{MET after modification}}{\text{ET before modification}}$ 2) $BS(\%) = \frac{\text{BS in MET}}{\text{MET after modification}}$ 3) %

RELATIONSHIPS BETWEEN THE CHARACTERISTICS OF PETROLEUM FEEDSTOCKS AND THE GRAPHITIZABILITY OF THEIR PETROLEUM COKES

M. Kakuta*, T. Kooriki*, Y. Sanada**

* Osaka Research Laboratory, Koa Oil Company, Takaishi-shi, Osaka 592, Japan
** Faculty of Engineering, Hokkaido University, Sapporo 060, Japan

INTRODUCTION

Many investigators have found that the physical properties of petroleum coke are very much dependent upon the composition and characteristics of the feed stocks used to make the coke.

In order to determine the relationships between the characteristics of the raw materials and the physical properties of petroleum cokes derived therefrom, investigations were undertaken to study the carbonization and graphitization processes for various petroleum fractions.

EXPERIMENTAL

Sumatran Light vacuum residue (S/L VR), Sumatran Light vacuum distillate (S/L VD) and Decant Oil from a catalytic cracking process were used as samples. S/L VR was fractionated into saturates, aromatics, resins and asphaltenes by the alumina adsorption method. S/L VD and Decant Oil were separated into saturates and aromatics by the solvent extraction method. Each fraction was subjected to determine the data of density, Conradson carbon, elementary analysis, molecular weight and Nuclear Magnetic Resonance (NMR) measurement. And then, the chemical structural parameters were computed.

Each fraction was carbonized in an autoclave under a pressure of 20 kg/cm^2 (gauge) at increasing temperatures. The fluidity of each fraction during the mesophase transformation was monitored by a Gieseler-type plastometer. The coke products were examined by a scanning electron microscope and a polarized light microscope.

The coke product from each sample was graphitized by heat-treating at 2,600°C for 30 minutes under a nitrogen atmosphere. The graphitized coke was characterized by X-ray diffractometry. The peak intensity I(002) was determined from (002) diffraction peak, which was normalized by the internal standard method.

RESULTS AND DISCUSSION

The composition and properties of petroleum vacuum residue, vacuum distillate, decant oil and their fractions are shown in Table 1.
The hydrogen distributions determined from NMR data and structural parameters are summarized in Table 2 (procedure based upon Yamada et al (1)). As can be seen from Table 2, there were considerable differences in chemical structural parameters for the various fractions.

From microscopic observations, the coke derived from saturate fraction showed a generally fibrous texture. On the other hand, coke derived from resin and asphaltene fractions primarily exhibited a mosaic texture, sometimes with pores.

The fluidity curves for S/L VR fractions during carbonization are shown in Fig. 1. The saturate fraction solidified at about 538°C, the aromatic fraction at 535°C, the resin fraction at 514°C, and the asphaltene fraction at 507°C. For saturates, the liquid state was maintained sufficiently long during the stage of mesophase transformation such that a needle-like coke was formed, as observed microscopically.

With regard to asphaltenes and resins, on the other hand, owing to the relatively low solidification temperature, the growth of mesophase would be suppressed and consequently a mosaic-like texture would be observed. White and Price (2) proposed that it would be convenient to interpret the mesophase transformation reaction by dividing it into fast-reacting and slow-reacting components. That is to say, the former may correspond to asphaltenes and resins, while the latter would be attributed to saturates.

The saturate fraction from S/L VR was heat-treated in an autoclave under a pressure of 20 kg/cm^2 (gauge) at 450°C, at various residence times from 15 to 75 minutes. The saturates heat-treated for 15 minutes were in an isotropic liquid phase until the appearance of spherical bodies. From the component analysis the fa value increased from 0.12 to 0.54 and the molecular weight decreased from 880 to 490. The nucleation and growth of spherical bodies occurred progressively with increasing residence time from 45 minutes to 75 minutes. On the basis of these observations it would be postulated that the mesophase system was converted into a needle-like coke by further heat-treating.

Figure 2 shows the relationships between the X-ray peak intensity I(002) for each graphitized coke and the C/H atomic ratio of the feed materials. This figure shows that the degree of graphitizability of the fractions correlates with the C/H ratios; that is, in decreasing order of graphitizability, saturates > parent residue > aromatics > resins > asphaltenes. This tendency is similar to that of the fluidity behavior previously shown in Fig. 1.

To further clarify the relationships between raw material characteristics and coke quality, trials were conducted to relate the chemical structural parameters shown in Table 2 and X-ray peak intensity I(002). It was generally found that the smaller the value of R (the number of aromatic rings) or the smaller the value of CAL (the number of alkyl side chains), the higher the value of I(002). From these results, it is hypothesized that, if an aromatic ring has too many alkyl side chains, during condensation polymerization the product becomes crosslinked rather than stacked, thereby causing the degree of orientation of the crystallite to be poor.

Reference

1) Yamada Y., Furuta T., Sanada Y., Anal. Chem., **48** (11), 1637 (1976).

2) White J. L., Price R. J., Carbon **12**, 321 (1974).

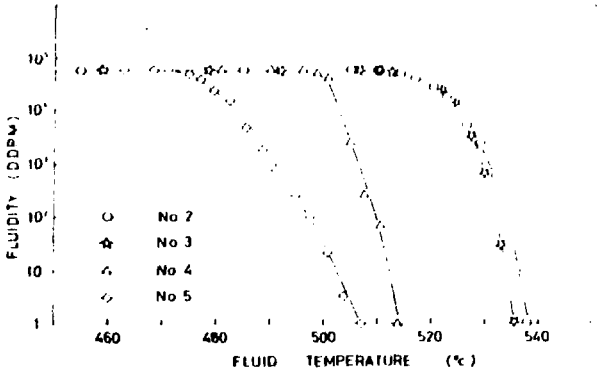
Table 1 Properties of sample used

Petroleum feedstocks	Sample Type	No.	Yields (wt.%)	Spec. Gr. (15°/15°)	M.R. (wt.%)	Visc. at 100°C (cSt)	Elemental analysis (wt.%) C	H	Atomic H/C Ratio	Fa (n.R)
S/L VR	Original Oils	1	100.0	0.9[illegible]	30.5	450	86.2	12.4	0.[illegible]	0.19
	Saturates	2	37.5	0.861	0.55	30	85.8	13.2	0.[illegible]	0.12
	Aromatics	3	26.0	1.015	23.4	3050	88.5	10.[illegible]	0.[illegible]	0.53
	Resins	4	31.0	1.019	45.1	1515	85.[illegible]	[illegible].6	0.[illegible]	0.40
	Asphaltenes	5	1.4	1.050	500.	12.0	81.[illegible]	8.2	1.01	0.56
S/L VD	Original Oils	6	100	0.955	2.0	370	86.[illegible]	12.8	0.[illegible]	0.1
	Saturates	7	[illegible]	0.[illegible]60	0.0	370	85.6	14.2	0.61	0.0
	Aromatics	8	12	1.032	1.4	270	9[illegible]	[illegible].5	0.11	0.53
Decant Oil	Original Oils	9	100	1.[illegible]41	2.9	2[illegible]	87.5	11.1	0.[illegible]	0.37
	Saturates	10	5[illegible]	0.[illegible]27	0.[illegible]	3[illegible]	85.[illegible]	14.1	0.[illegible]	0.0
	Aromatics	11	45	1.1[illegible]	7.9	250	91.[illegible]	7.4	1.01	0.[illegible]

Table 2 Results of hydrocarbon distribution and structural parameters of the fractions from petroleum feedstocks

Sample No.	Hydrocarbon distribution (%) f_A	f_{A_N}	f_B	f_N	σ	DPT	IPT	CA	CAL	CBL	CL
1	1.7	14.6	0.6	19.7	[illegible]	25	14	[illegible]	[illegible]	41	[illegible]
2	7.7	21.0	61.5	[illegible].3	9	26	[illegible]	23	10	7[illegible]	[illegible]
3	13.5	22.7	53.7	[illegible].0	14	22	[illegible]	27	[illegible]	[illegible]	3
4	15.4	[illegible].[illegible]	41.[illegible]	10.7	5[illegible]	[illegible]	5	[illegible]	[illegible]		[illegible]
[illegible]	16.[illegible]	[illegible].[illegible]	43.3	14.3	[illegible]	10	[illegible]	10	[illegible]	[illegible]	[illegible]
9	11.	1[illegible].	65.[illegible]	12.0	[illegible]	[illegible]	[illegible]	[illegible]	[illegible]	[illegible]	[illegible]
11	71.[illegible]	41.	14.0	[illegible].[illegible]	[illegible]	11	[illegible]	14	[illegible]	[illegible]	1

R : Average number of total rings per molecule.
σ : Number of peripheral carbon in a condensed aromatic sheet.
IPT : Number of internal carbon in a condensed aromatic sheet.
CA : Total aromatic carbon atoms per molecule.
CAL : Number of aromatic carbon atoms alkyl substituted condensed aromatic sheet.
CBL : Number of carbon atoms other than CAL, CL to a condensed aromatic sheet.
CL : Number of aliphatic carbon atoms gamma or further to a condensed aromatic sheet.



No. 2 Saturates
No. 3 Aromatics
No. 4 Resins
No. 5 Asphaltenes

Fig. 1 Fluidity curve for resonance formed in sample no. 2, 3, 4, 5 (from S/L VR)

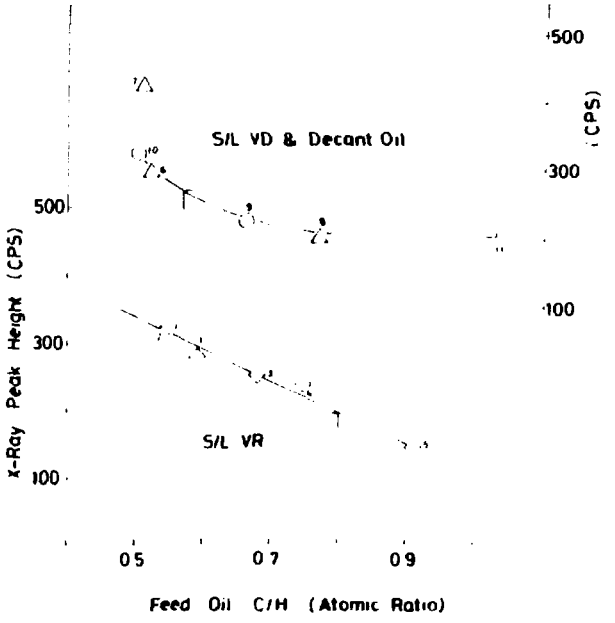


Fig. 2 X-ray peak height of coke after 500°C treatment

INFLUENCE OF SULFUR AND METALS ON MESOPHOSE FORMATION

S. Oi, T. Imamura, M. Komatsu, Y. Yamada, M. Nakamizo, H. Honda
National Industrual Research Institute of Kyushu
Tosu-shi, Saga, 841, Japan

Introduction

When petroleum residue containing the large amounts of sulfur is heat-treated, mesophase formed in this residue shows the fine mosaic texture. By addition of inorganic sulfur to the pitch which showed the fibrous texture, the texture of mesophase turns the fine mosaic. Marsh et al(1) reported that the size of the mesophase spheres formed in anthracene was about 25μm, and the size of the mesophase spheres formed in anthracene and 10wt% of ferrocene was 10μm. It is considered that the mesophase texture formed in the petroleum residue is the fine mosaic because sulfur and metals in the petroleum residue prevent twc precesses of the mesophase spheres growth and of smoothly proceeded molecular rearrangement in the coalesced mesophase. This report describes the influence of sulfur and metals containing the pitch on the mesophase texture.

Experimental

Cracked oil used is thermal cracked oil which is obtained from Khafji asphalt heat-treated at 420°C for 70 min, contains about 3 wt% sulfur and is free from metals. This oil is mixed with vanadium acetylacetonate, nickelocene, ferrocene and copper phtalocyanine, and the mixtures are heat-treated at 430°C for a certain period and were observed by using a polarized-light microscope.

Results and Discussion

Khafji asphalt, cracked oil and the mixtures of cracked oil and organometallic compounds are heat-treated at 430°C for 180 min. The sulfur and metal contents in those samples are shown in Table 1. The sulfur content is about 6wt% for all the samples. The metal contents are 420 ppm for Khafji asphalt, 32 ppm for cracked oil and from 802 to 2849 ppm for the mixtures. Micrographs of those samples are shown in Fig.1. Mesophase formed in Khafji asphalt shows the fine mosaic texture and that in cracked oil shows the fibrous texture in spite of 6wt% sulfur content (Fig.1-a). Mesophase shows the fibrous texture for the mixture of cracked oil with Cu, the coarse mosaic texture for cracked oil with Fe and the fine mosaic texture for cracked oil with Ni and V (Fig.1-b). Thus, the mesophase textures are different with kinds of metal added in cracked oil and influence of metals on the growth process of the mesophase spheres is stronger than sulfur.

It is clear that the texture of mesophase do not be influenced by existence of organic sulfur compounds in cracked oil. The mesophase texture in coal-tar pitch free from sulfur with 1wt% Fe (Ferricene) (2) showed the coarse mosaic and turned to the fine mosaic with increase of Fe. Amount of Fe in cracked oil, which cause transformation from the fibrous texture to the coarse mosaic texture, correspond to about 0.1 times amount of Fe in coal-tar pitch. Therefore, the change of the mesophase texture occures easily with coexistence together sulfur and metals.

On the other hand. Fig.2 shows amounts of quinoline-insolubles in cracked oil heat-treated at 430°C as a function of residence time. Amounts of quinoline insolubles correspond to the amounts of mesophase transformation. The amounts of mesophase transformation increased in order of Fe, Ni and V in cracked oil for a definit time. This result indicates that the mesophase transformation is accelerated by organic sulfur compounds and Ni, V in cracked oil during heat treatment. In other words, Ni and V in cracked oil function as the catalyst which accelerate mesophase.

Also, from comparsion of Fig.1 and 2, it is considered that the mesophase texture is related to the increase rate of the mesophase transformation, that is, in the case of the mixture of cracked oil with Ni or V, those mesophase spheres coalesce with each other after growth up little and the coalesed mesophase shows the fine mosaic texture because the large amounts of mesophase in the cracked oil are formed at the same time by the catalytic action of Ni or V.

Dickie et al (3) reported that the asphalten containing petrolum residue form the micelle structure, and these micelles are containing organic sulfur compounds and metal compounds. When the asphalten in petroleum residue was heat-treated, mesophase formed in the asphalten showed the fine mosaic texture. Therefore, it is suggested that organic sulfur compounds and Ni, V in cracked oil change into molecules constructing mesophase with the thermal decomposition and polymerization, form the micelle structure and the formed micelles nucleate the fine mosaic texture of mesophase.

References

(1) Marsh, H., Foster, J. M., Hermon, G. and Hey, M., Fuel, Lond. 52, 234 (1973)
(2) Oi, S., Yamada, Y. and Honda, H., Tanso No. 85, 47 (1976)
(3) Dickie, J. P. and Yen, T. F., Anal. Chem., 39, (14), 1847 (1967)

Table1 Metal contents and sulfur content

Sample	Metals (ppm) V	Ni	Fe	Cu	S (%)
Cracked oil	10	12	8	0	6.0
Cracked oil+V	802	-	-	-	-
Cracked oil+Ni	-	1200	-	-	6.0
Cracked oil+Fe	-	-	913	-	5.3
Cracked oil+Cu	-	-		-2840	5.4

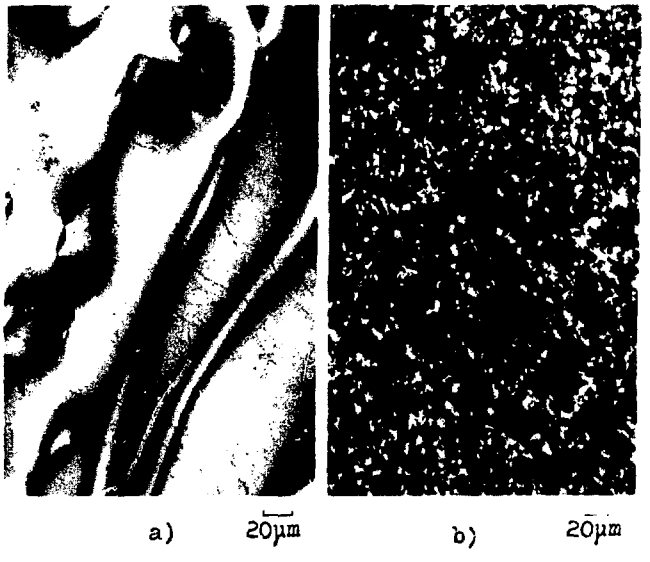


Fig.1 Mesophase formed in cracked oil heat-treated at 430°C for 180 min.
a) cracked oil b) cracked oil added V

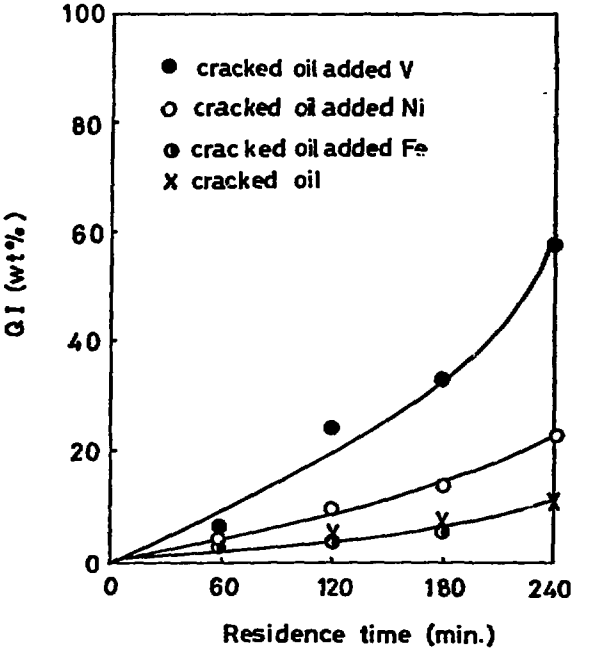


Fig.2 Relation between amounts of quinoline insolubles and residence time

ISOTROPIC COKE BASED ON REACTIVE TAR FROM COAL PRESSURE VAPORISATION

H. Tillmetz and G. Pietzka (Sigri Elektrographit GmbH, D-6229 Frankfurt 61, Germany)

Introduction

Isotropic cokes are of special interest for the manufacture of isotropic carbon and graphite shapes used in nuclear reactors. At the Carbon Conference at Baden-Baden 1976 it was shown that isotropic cokes can be obtained from pitch precursors to which α-resins (QI) have been added. These cokes cover a wide range of CTE (1). This method requires the separation of both the primary and the secondary α-resins from selected pitches. It is also known that materials like natural bitumina and thermal-setting resins are suited for the manufacture of isotropic cokes. The presupposition for the formation of isotropic coke from pitch is a high reactivity resulting in a three-dimensional crosslinking during the carbonisation. An interesting material with the presupposed properties and which is available on the market is the tar formed in the coal pressure vaporisation process.

Experimental

The experiments were performed with tars formed in the coal pressure vaporisation process (CPV). To reduce the content of insoluble matter especially minerals the tars were filtered. The softening point of the tar was increased by distillation. The properties of the resulting pitch are listed in Table 1.

The tars were additionally examined by gas and high pressure liquid chromatography and NMR-spectroscopy. The gas chromatography was performed in the well known technique with a column filled with siliconrubber on Chromosorb. The high pressure liquid chromatography (gel permeation technique) was performed with a column filled with Styragel of 3000 Å, 1000 Å, 500 Å and 100 Å exclusion pore size, a pressure of 51 bar and quinoline as eluation liquid. A UV-spectrometer at 370 nm was used as detector. The special technique of gel permeation chromatography for tars and pitches is described in detail in (2). The NMR-spectroscopy was used to characterize the molecular composition of the tars especially to measure the content of the aromatic and aliphatic bonded hydrogen.

The CPV-pitch has been carbonized in laboratory using a heating rate of 25°C/h and in a baking furnace using a heating rate of about 2,5 °C/h in the temperature range of between 350 - 450°C. The final temperatures varied between 950 and 1000°C. The resulting cokes were examined by measuring the coefficient of thermal expansion of the coke grains (calcined at 1300°C) as described elsewhere (3). For detailed information on the isotropic behaviour the relation of the three linear coefficients of thermal expansion of coke cubes were used.

Results

The gas chromatographic examination of the pyridine soluble constituents of the CPV-pitch shows that this matter has only a small content of aromatic compounds having a low molecular weight, like naphthalene or anthracene. The broad underground peak is an evidence of the asphaltenic character of the matter similar to petro-bitumina. The gel permeation chromatography demonstrates that the average molecular weight of the soluble matter is much higher for the CPV-pitch than for a coaltar pitch with a comparable softening point. The good solubility of about 93 % of the CPV-pitch in toluene is caused by its different molecular structure. These differences can be explained by the results of the NMR-spectroscopy proving a larger content of reactive aliphatic and naphthenic molecular groups in the CVP. These reactive groups explain the tendency of this tars to form preferably isotropic coke structures during the carbonisation process.

The coke data (given in Table 2) show that a slow carbonisation rate results in more anisotropic coke structures. By decreasing the heating rate (25°C/h to 2,5°C/h) in the critical temperature range of the coke formation between 350 and 450°C the CTE (volume) is decreased from 13,5 and 11,3 • 10^{-6}/K to 7,3 and 7,6 • 10^{-6}/K respectively and the anisotropy ratio is increased from 1,21 and 1,28 to 1,64 and 1,39 respectively. Obviously a low heating rate enables a better orientation of the pitch constituents during the carbonisation process. Furthermore it can be shown that a low heating rate causes a higher scattering of the measured CTE values.

Literatur :

1) H. Lehmann, H. Hahl and G. Pietzka,
Carbon Conf. 1984, p. 144, 1984 - Bad

2) H. Tillmann, W. Kramer and G. Pietzka,
Carbon Conf. 1984, p. 146, Bad-Honnef

3) G. Pietzka, J. Wilhelm and H. Hahl,
Carbon Conf. 1982, p. 422, Bad-Honnef

Table 1: Properties of filtered CPV-pitch

		sample 1	sample 2
Softening point (KS)	°C	85	104
Coke yield Din 51720	%	58,7	63,5
Coke yield baking furnace	%	64,7	69,2
Quinoline insoluble	%	0,1	0,1
Toluene insoluble	%	0,8	7,2
Pyridine insoluble	%	25,6	26,9

Table 2: Coke from CVP

	sample 1	sample 2
Laboratory (25°C/h; 350-450°C)		
CTE (volume) · 10^{-6}/K	13,5	11,3
Anisotropy ratio	1,71	1,28
Baking furnace (2,5 °C/h; 350-450°C)		
CTE (volume) · 10^{-6}/K	7,3	7,6
Anisotropy ratio	1,64	1,39

COKE FORMATION MECHANISMS IN SELECTED SLURRY OILS

H.C. Fritz, H.L. Hsu, L.I. Grindstaff, Great Lakes Research Corporation, P.O. Box 1031, Elizabethton, TN 37643 and
M.P. Whittaker, Great Lakes Carbon Corporation, 299 Park Avenue, New York, NY 10017

Introduction

Results of mesophase formation studies conducted on a variety of hydrocarbon liquids including coal tar pitch, certain fractions of coal tar pitch and various petroleum residues have been reported. (1-8) Only a few investigators have reported on coke formation mechanisms in actual delayed coker feedstocks. White and Price (7) described mesophase microstructures in a number of coker feedstocks ranging from Gilsonite to a decant oil. Whittaker and Grindstaff (6) compared mesophase formations observed in several reduced crudes which are the usual feedstocks for the production of "regular" petroleum (sponge) cokes.

One of the principal feedstocks for the production of premium or needle cokes is clarified slurry oil from fluid catalytic cracking operations. Due to an increasing demand for premium cokes, efforts are being made to provide additional quantities of feedstocks by upgrading certain slurry oils presently unsuited for the production of high quality needle cokes. (9) Some slurry oils contain small amounts of micron-size catalyst fines which remain in suspension despite conventional separation techniques designed to remove them. These catalyst fines, because of their extreme fineness, have a pronounced effect on mesophase formation and thus the resultant needle coke structure. This paper describes mesophase formations and coke structures observed in selected slurry oils before and after removal of catalyst fines by filtration techniques.

Experimental

Materials.

Two slurry oils identified as "A" and "B" were evaluated. Except where indicated, the slurry oils were used as received from the refinery. Pertinent properties of the two feedstocks are summarized below.

	A	B
API @ 60°F	- 2.1	4.6
Viscosity, cps @ 210°F	27	15
Conradson Carbon, Wt. %	10.9	5.2
Carbon, Wt. %	90.30	90.05
Hydrogen, Wt. %	7.22	8.12
Sulfur, Wt. %	1.31	1.15
Aromaticity (NMR)	0.67	0.60

Laboratory Cokings.

Laboratory cokings were made in a 4 liter glass flask equipped with a distilling head and thermocouple well. The materials were heated slowly to a predetermined setting temperature and allowed to remain at this temperature for a time sufficient to harden the coke. To adjust the volatile content of the raw coke to the desired level, final heating was made at a relatively slow rate of temperature increase to a maximum of 550°C.

Smaller samples were conveniently prepared by simulating the above coking operation on a test tube scale in a fluidized sandbath. The maximum operating temperature of the bath was 600°C. Appropriate controls for the fluidizing air and temperature were employed to achieve the desired reproducibility and minimize thermal gradients (±3°C) within the bath at the normal operating temperature of 440-450°C.

Microscopic Studies.

After the desired treatment, the glass test tubes were carefully removed and the residue recovered intact for preparation of polished sections by conventional techniques. The polished sections were microscopically examined with reflected polarized light. Longitudinal cross-sections of the residues were used to observe the effect of time on mesophase formation. To relate pertinent structural characteristics to ash constituents, various polished samples were examined with an Acton Laboratories Model MS64 electron microprobe.

Ultrafiltration.

Filtration was conducted under vacuum at about 120°C in a Buchner funnel using Reeve Angel 984H filter paper which is capable of retaining solids in the range of approximately 0.1 micron diameter. To ensure a perfect seal, a thin layer of high vacuum grease was applied around the edges of the filter paper.

Results and Discussion

A most convenient and rapid means of assessing the potential of a slurry oil as a needle coke feedstock is to observe the mesophase during the early stages of coke formation. During recent evaluation experiments, slurry oil "A" was found to contain micron-size solids, believed to be catalyst fines, which interfered with the orderly growth and coalescence of mesophase spherulites. Solids removed by filtration and analyzed by X-ray fluorescence (XRF) were found to be composed principally of silicon and aluminum which confirmed the

presence of catalyst fines. Size analysis by Coulter Counter indicated the fines to be 63% less than 2 microns.

Coke formation in slurry oil "A" is characterized by the following structural variations:

1. a fine disordered structure (i.e. non-coalesced mesophase) during the initial stage.
2. a coarser disordered structure with increasing tendency for coalescence of the irregular spherulites.
3. normal spherulite formation, growth and coalescence.

Slurry oil "B", a known precursor of high quality needle coke, is characterized during the entire coke formation process with no inhibition of normal spherulite formation, growth and coalescence. Removal of the solids from slurry oil "A" resulted in mesophase formation which was essentially equivalent to slurry oil "B".

Certain anomalous structures observed by polarized light microscopy were examined by electron microprobe to determine the nature of the interfering solids. These structures were scanned to detect the presence of aluminum and silicon. The disordered structures which were predominant during the early stages of coke formation were shown to contain concentrations of approximately 5-10% of aluminum and silicon. Areas of high concentrations of catalyst fines which were randomly dispersed throughout the disordered mesophase structure yielded aluminum and silicon contents as high as 15%.

Laboratory cokes were prepared from
1. slurry oils "A" and "B" as received from the refinery;
2. slurry oil "A" after removal of fines by filtration;
3. slurry oil "B" after the addition of small amounts of micron-size alumina.

Evaluation of the laboratory cokes indicated that interference of mesophase formation by catalyst fines or by deliberate additions of finely divided alumina resulted in a more isotropic structure than is desired in high quality needle cokes. Removal of the fines from slurry oil "A" resulted in a suitable needle coke feedstock.

References

1. Brooks, J.D. and Taylor, G.H., Carbon 3, 185 (1965).

2. Kipling, J.J. and Shooter, P.V., Carbon 4, 1 (1966).

3. Brooks, J.D. and Taylor, G.H., "Chemistry and Physics of Carbon", Ed. P.L. Walker, Jr., 4 243 (1968).

4. Dubois, J., Agace, C., and White, J.L., Metallography 3, 337 (1970).

5. Honda, H., Kimura, M., Sanada, Y., Sugawara, S., and Furuta, T. Carbon 8, 181, (1970).

6. Whittaker, M. P. and Grindstaff, L.I., Carbon 10, 165 (1972).

7. White, J.L. and Price, R.J., Carbon 12, 321 (1974).

8. Yamada, Y., Oi, S., Tsutsui, H., Kitajima, E., Tsuchitani, M., Kakiyama, H. and Honda, H., 12th Biennial Conf. on Carbon, Extended Abstracts (1975) 271.

9. Scovill, W.E. and Day, D.R., U.S. Patent 3,704,224 (1972).

GRAPHITISING CARBONS FROM COAL VIA SOLVENT EXTRACTION: EFFECTS OF PROCESSING CONDITIONS ON PRODUCT QUALITY

G.M. KIMBER
Coal Research Establishment, Cheltenham, GL52 4RZ, UK

Introduction

The National Coal Board's basic process for the production of high purity coke from coal via solvent extraction has been described previously[1,2]. This paper outlines how the properties of coal extract cokes are dependent on the original coal and the manner in which it is processed. The ways in which the growth and coalescence of mesophase during coking influences the thermal expansion of graphite rods made from these extract cokes are described.

Experimental

A range of U.K. coals were digested in anthracene oil (a coal tar distillate boiling nominally 250-400°C) at 360-420°C for up to 5 hours. Either a 50 Kg batch rig or a 100 Kg h^{-1} continuous process development unit was used at pressures of up to 1 Nmm^{-2}. After filtration at 200-250°C the resulting coal solutions were coked either in 15 kg batches to a final temperature of 500°C or in a 120 kg hr^{-1} delayed coking facility with its associated rapid preheating system. Amongst the characterisation techniques applied to the cokes were measurements on 15 mm dia. extruded rods made from the coke after the appropriate calcining, forming, baking and graphitising. It should be noted that in strict contrast to Jasienko[3] no hydrogen is added.

Results and Discussion

The low temperature (0-100°C) longitudinal coefficient of thermal expansion of graphite rods (CTE) has long been used as a measure of the degree of needle likeness and quality of petroleum cokes. Coal extract cokes have been found to obey a similar relationship in that the larger the extent of anisotropy visible microscopically the lower the CTE. However, it is not yet established whether the same absolute relationship between CTE and quality applies to both types of cokes particularly when trying to correlate with the overall performance of a graphite electrode in an arc furnace. For example coal extract coke graphites exhibit a greater resistance to thermal shock than might be expected.

It appeared from initial tests that extract coke properties were very dependent on the parent coal. This aspect was studied first using fixed extraction and coking conditions; Fig. 1 shows the effect of coal rank on CTE for these conditions, with the higher rank coals generally giving the lower CTE's. However, there is an appreciable scatter about the mean line and this is due in part to differences in petrological composition of coals.

In the series of experiments when only the digestion time and temperature were varied, Fig. 2, it was found that short times and low temperatures gave small mesophase growth when the filtrate was eventually coked. Thus CTE reduced as residence time was increased. One of the mechanisms contributing to this is the depolymerisation of the coal which continues during prolonged digestion causing atoms and groups, that could sterically hinder alignment into graphite precursors, to be evolved.

The separation of the undissolved coal particles (mainly mineral matter and fusinite) from a coal digest is an

expensive operation and it is thus important economically to determine the effects of any deviations from highest efficiency that can technically be achieved. The results of experiments where a portion of the digest was made to bypass the filter are shown in Fig.3, where the ash in the coke is taken as a measure of the total solids passing the filter. The solids that pollute the filtrate inhibit mesophase growth and coalescence during coking thus giving a higher CTE. However, in the CRE process, after digestion under a certain range of conditions, the residue particles build up into a filter cake which is efficient both in retaining sub-micron particles and in giving a high filtering rate.

The series of experiments in which the preheat temperature (i.e. that at the inlet to the delayed coker) was altered shows that even having started with a good coal, and having digested and filtered it properly it is possible by incorrect coking, to produce isotropic rather than anisotropic coke. Fig.4 shows that unless a certain threshold temperature is achieved a high CTE graphite will eventually result. The macrostructure of the coke is dependent on how the polymerising feed (with the changing viscosity) is affected by the disturbances caused by gas and vapour, both in the preheater where there is a high degree of turbulence and in the coke bed itself. In some of these respects coal extract solutions are different to the feeds used to make petroleum cokes.

Acknowledgements

The author thanks the Coal Board for permission to publish this paper; any views expressed are his and not necessarily those of the Board.

References

1. J. Owen, 12th Conf. Carbon 1975.
2. USP 3,966,585 1976.
3. S. Jasienko, 12th Conf. Carbon 1975.

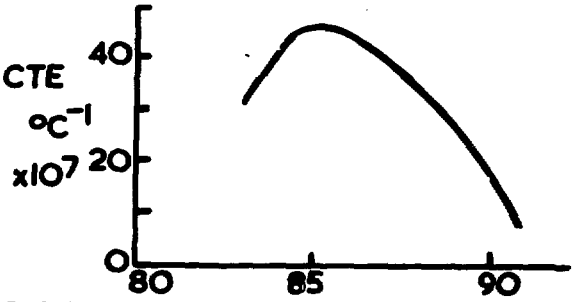


FIG.1.

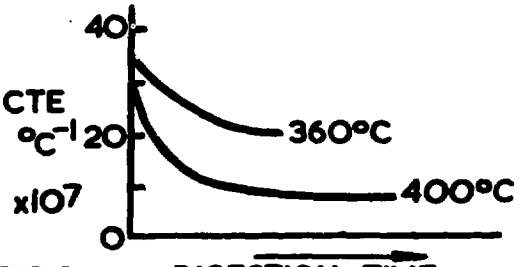


FIG.2

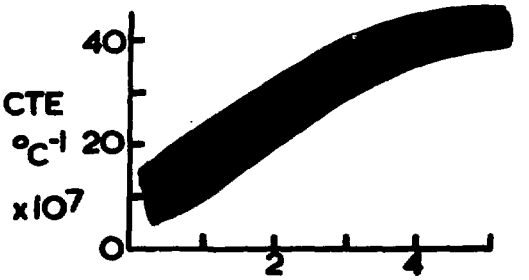


FIG.3

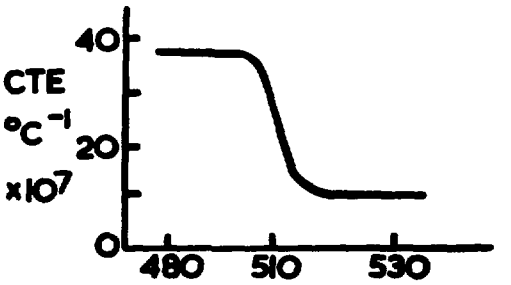


FIG.4

THERMAL EXPANSION OF MICROCONSTITUENTS OF COKE

J. E. Zimmer and J. L. White
The Ivan A. Getting Laboratories
The Aerospace Corporation
P.O. Box 92957, Los Angeles, California 90009

Introduction

Polycrystalline graphites for electric-arc-furnace electrodes and aerospace applications should have low coefficients of thermal expansion to be thermally shock-resistant. The type of filler coke directly influences the thermal expansion of bulk graphite; measurements of the thermal expansion of graphites fabricated from a variety of cokes have shown the dependence of thermal expansion on the filler coke [1]. The low volumetric thermal expansion of polycrystalline graphites and cokes, in all cases lower than the volumetric thermal expansion of single crystal graphite, has been attributed to the degree of preferred orientation of the crystallites [2] and to accommodation of the crystallite c-axis expansion by intercrystalline voids [3]. The preferred orientation depends on the structure of the filler coke particles and on the fabrication process. It has become apparent that accommodation appears to relate to the development of shrinkage cracks upon the initial heat treatment of semi-cokes [4].

As a class, graphites fabricated with needle cokes have the lowest coefficients of thermal expansion. Previous work on the thermal expansion of needle cokes [4, 5] has shown that the fine fibrous microconstituent, which constitutes only a portion of a typical delayed needle coke [6], is anisotropic in its thermal expansion. The fine fibrous structure, consisting of folded, corrugated arrays of graphitic layers that are straight and parallel along the needle axis, has a low thermal expansion parallel to this axis that is a function only of the crystallite a-axis expansion. In the transverse direction, the thermal expansion is slightly higher, but less than the thermal expansion of the complex, three-dimensional morphology of a fine isotropic coke. It was also shown that the thermal expansion in the transverse direction of green needle coke had a very high thermal expansion and that the thermal expansion was reduced significantly with heat treatment to only 700-800°C [4, 7].

Understanding the mechanism of accommodation of thermal expansion of an individual coke microconstituent involves relating the coke morphology and microcrack structure to heat-treatment temperature and the intrinsic thermal expansion of the coke itself. Thus, the objectives of this work were to measure the thermal expansion of the fine fibrous microconstituent of needle coke and the fine isotropic microconstituent of an isotropic coke as a function of heat treatment temperature and to observe the changes in microstructure with heat treatment.

Experimental

Thermal expansion specimens 4mm square by 10mm long were cut from larger pieces of Marathon and Carborundum premium needle cokes that had a distinctive needle shape and appearance. The long dimension was normal to the needle axis. Specimens of a fine isotropic (Robinson) coke and an isotropic coke prepared from an Edgington asphalt pyrolyzed to 425°C were also prepared. The thermal expansion was measured with a Leitz quartz dilatometer to 400°C after each heat treatment. In some cases, the same specimens were successively heat treated to higher temperatures and measured.

Results

The effect of heat treatment on the thermal expansion in the transverse direction of the fine fibrous microconstituent and on the thermal expansion of the fine isotropic microconstituent is shown in Fig. 1, along with similar measurements by Mochida [5]. For both microconstituents, a significant reduction in thermal expansion occurred upon heat treatment to only 700°C. This reduction in expansion is related to the development of shrinkage cracks associated with the densification of the green coke. The real density of green coke increases from 1.4 g/cc near 600°C to about 2.2 g/cc at 1400°C [8], producing these shrinkage cracks. Little reduction in thermal expansion occurred upon heat treatment to graphitizing temperatures.

Micrographic evidence of the formation of shrinkage cracks upon heat treatment of the green cokes is given in Figs. 2 and 3. For the fine fibrous microconstituent, a significant increase in the number of shrinkage cracks occurred between 550 and 600°C. On heating to 1100°C, the shrinkage cracks widened, but did not noticeably increase in number. At 600°C, shrinkage cracks also occurred in the fine isotropic microconstituent (Fig. 3), whereas they were not present at 425°C. The shrinkage cracks in the fine fibrous microconstituent tend to be large compared to its folded, corrugated morphology as characterized by polarized-light extinction contour spacings of 1 to 10 microns. The cracks which run parallel to the layers along the needle axis, can extend fairly easily in the transverse direction. In contrast, the shrinkage cracks in the isotropic microconstituent are quite small as the cracks are confined by the doubly-curved layers of its complex, three-dimensional morphology.

The thermal expansion of green mesophase coke is higher than that for crystalline graphite. This may be explained by the fact that at this stage extensive polymerization has not begun and the individual molecules are bonded by van der Waals forces both perpendicular and parallel to the plane of the molecule. The low density of green coke implies that the free volume of a typical mesophase molecule is 60% greater than a region of a graphitic basal plane with a similar mass. This free volume would allow greater thermal motion and thus a high thermal expansion in both directions.

This work has shown that the two coke microconstituents, fine fibrous and fine isotropic, which result from different precursors [8], have different thermal expansions and that for both the shrinkage cracks introduced by heat treatment to only 700°C act as accommodation sites. However, within a typical needle coke produced from a deformable mesophase precursor, there are several distinct

microconstituents of which the fine fibrous structure is just one. Relating the thermal expansion of these other microconstituents to their morphology and shrinkage crack structure may thus lead to the identification of a coke morphology, and a coking process, that would have an even lower thermal expansion than the fine fibrous microconstituent.

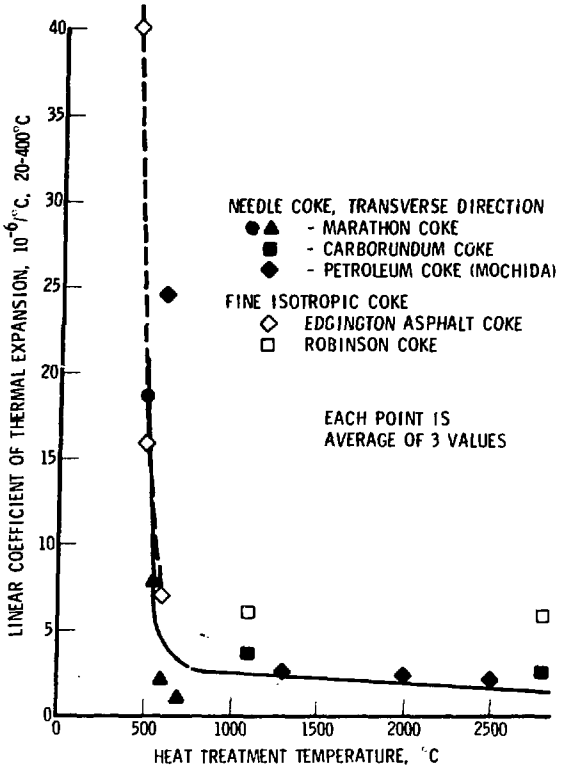


Fig. 1. Effect of heat treatment on thermal expansion of fine fibrous and isotropic microconstituents. The data by Mochida [5] are for temperature range of 350-450°C.

Acknowledgment

The authors thank F. J. Turnbow for his valuable assistance in these experiments. This work was supported by the U.S. Air Force under Contract No. F04701-76-C-0077.

References

[1] G. B. Engle, Carbon 12 (1974) 291.

[2] G. E. Bacon, J. Appl. Chem. 6 (1956) 477.

[3] S. Mrozowski, Proc. First and Second Conf. Carbon, Waverly Press (1953) 31.

[4] J. E. Zimmer and J. L. White, Carbon '76 (1976) 309.

[5] I. Mochida, M. Ogawa and K. Takeshita, Bull. Chem. Soc. Japan 49 (1976) 514.

[6] J. E. Zimmer and J. L. White, 12th Conf. Carbon, Extended Abstracts (1975) 22.

[7] F. M. Collins, Proc. Third Conf. Carbon, Pergamon Press (1957) 659.

[8] J. L. White, Progr. Solid State Chem. 9 (1975) 59.

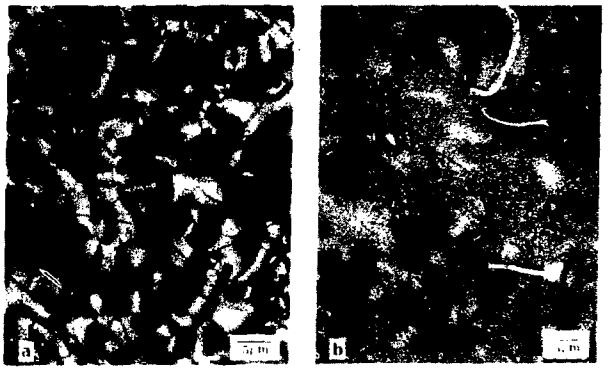


Fig. 3. Shrinkage cracks in fine isotropic microconstituent heat treated to 600°C; (a) cross polarizers, (b) bright field.



550 C 600C 1100C

Fig. 2. Shrinkage cracks in transverse cross section of fine fibrous microconstituent, polarized light.

THERMOGRAVIMETRIC INVESTIGATION OF THE CARBONIZATION OF SOME PITCHES

G.W. Collett and B. Rand
Department of Ceramics, Glasses and Polymers, University of Sheffield, Sheffield S10 2TZ, UK

Introduction and method of analysis

The technique of non-isothermal thermogravimetry is a standard method of assessing the pyrolysis range of organic materials and can, in favourable circumstances, be used to obtain kinetic parameters. However, in this latter application it should be used with caution since differences in kinetic parameters can arise where methods of interpretation vary (1). These methods have been critically reviewed by Sharp (1) and Doyle (2) and the application to the pyrolysis of pitches and similar materials is briefly discussed here before being applied to a thermogravimetric study of selected samples.

The kinetics of isothermal decomposition reactions are described by the general rate equation,

$$\frac{d\alpha}{dt} = A.f(\alpha).\ \exp(-\frac{E}{RT}) \qquad .....[1]$$

where α is the fractional weight loss, $f(\alpha)$ takes a form dependent on the mechanism of the reaction and the other terms have their usual meanings. Under dynamic conditions [1] becomes

$$\frac{d\alpha}{dT} = \frac{A}{\beta}.f(\alpha).\ \exp(-\frac{E}{RT}) \qquad .....[2]$$

where β is the constant heating rate. Equation [2] can be used either in its differential or integrated form and there are a diversity of methods of evaluating the integral. In pyrolysis reactions of concern here $f(\alpha)$ has usually been assumed to take the form

$$f(\alpha) = (1-\alpha)^n \qquad .....[3]$$

where n is supposedly an 'order' of reaction (3), (5) often having a value between 1 and 2. However, as Sharp (1) points out only certain values of n have any physical significance for heterogeneous reactions. Moreover, the $f(\alpha)$ may not be the same over the whole pyrolysis range especially in the case of pitches which are extremely fluid when volatilization commences but become semi-cokes as α tends to unity.

Wallouch, Marty and Heintz (4) combined equations [2] and [3] and evaluated the temperature coefficients of pyrolysis of a variety of pitches, which varied from 40-100 kJ mole^{-1}. Huttinger (5) used [2] and [3] in integral form, evaluating the integral by van Krevelen's referent method (3) and also obtained apparent activation energies in the above range. However, much higher values (250-350 kJ mole^{-1}) were measured by Lapina et al (6) for precursors which yield graphitizable products. These results can be compared with van Krevelen's (1) own studies of coals and related materials which yield values of about 200 kJ mole^{-1}.

Since van Krevelen's studies other approximations to the integral form of equation [2] have been proposed (2) and a particularly useful expression is

$$\log g(\alpha) = \log(\frac{AE}{\beta R}) - a - \frac{bE}{RT} \qquad .....[4]$$

where $g(\alpha)$ is the integral of $f(\alpha)$ and a and b are empirical constants which are tabulated by Doyle (2) and can be used to evaluate E from a suitable plot of the thermogravimetric data. Ozawa (7) has suggested a very simple method of determining kinetic parameters based on equation [4] in which the thermogravimetric data is determined at a number of constant heating rates and E is determined from

$$\left(\frac{d \log \beta}{d(\frac{1}{T})}\right)_\alpha = -\frac{bE}{R} \qquad .....[5]$$

since $\log g(\alpha)$ is constant at constant values of α. This method has advantages for reactions such as pitch pyrolyses since no assumption need be made about the kinetic mechanism and the activation energy can be determined at different values of α regardless of whether the same $f(\alpha)$ applies at all stages of the process. However, it is assumed that the $f(\alpha)$ does not change with temperature at a fixed value of α. Friedman (8) has suggested a similar method based on equation [2] in which

$$\ln\left(\beta.\frac{d\alpha}{dt}\right)_\alpha = \ln A + \ln f(\alpha) - \frac{E}{RT} \qquad .....[6]$$

although this method should be less accurate since it involves differentiation of the thermogravimetry curve.

In this study these two methods have been applied to the pyrolysis of selected pitches.

Experimental

100 mg samples of pitch were suspended in open silica crucibles from one arm of a CI Electronics Mark 2B microbalance and heated at a constant rate in a continuous flow of dry nitrogen at a flow rate of 50 ml$_N$ min^{-1}. The furnace was controlled by a Stanton Redcroft linear programmer capable of rates between 0.5 and 10°C min^{-1}. The temperature was monitored immediately below the sample crucible and displayed continuously along with the weight change on an Oxford 2000 2-pen chart recorder.

The materials investigated were an Orgreave coal tar binder pitch (softening point, 101°C, Ring and Ball), an Orgreave coal tar impregnation pitch (softening point, 83°C, Ring and Ball); Gilsonite pitch and an Ashland petroleum pitch (200).

Results and Discussion

The normalised α-temperature curves are shown in Fig.1 for the Orgreave binder pitch and the applications of Ozawa and Friedman's methods of analysis are illustrated in Figs 2 and 3. The slopes in both these cases increase with increasing values of α indicating that the activation energy changes with the fractional weight loss. A similar effect occurs with the other materials and the activation energies are given in Table 1.

Table 1

Activation Energies

Sample	Ozawa method (kJ mole^{-1})	Friedman method (kJ mole^{-1})
Orgreave binder pitch	78-140	78-165
Orgreave impregnation pitch	66-110	70-110
Ashland 200	135-160	150-160
Gilsonite	115-160	-

The two methods of analysis give remarkably similar results although Ozawa's method is much the simpler to apply and is therefore to be preferred. The range of activation energies for each sample increases with the softening point consistent with the observations of Wallouch et al (4). These authors also observed that mixing two pitches of different softening points resulted in an activation energy for pyrolysis intermediate between those of the two starting materials. In view of the results in this study their activation energies should perhaps be considered to represent average values over the pyrolysis range. However, they serve to emphasise that pitches are mixtures of complex organic molecules with varying molecular weight distributions. During pyrolysis, polymerisation processes and distillation of low molecular weight fragments shift the distribution towards higher molecular weights and the carbonaceous mesophase separates out eventually as a separate phase. Hence,in view of the dependence of the activation energy on softening point, which is also related to the molecular weight distribution, it is perhaps not too surprising to find that the activation energy for pyrolysis increases with fractional weight loss.

References

1. Sharp, J.H., "Kinetics and Other Theory", Chapter 8 in "Thermogravimetry", ed. Redfern, J.P. and Keatch, C.J., Butterworth, London, in the press.

2. Doyle, C.D., "Techniques and Methods of Polymer Education", Vol.1, Chapter 4, 113-216, E. Arnold, London (1966).

3. van Krevelen, D.W., Van Hearden, C. and Huntjens, F.J., Fuel, 30, 253 (1951).

4. Wallouch, R.W., Murty, H.N. and Heintz, E.A., Carbon, 10, 729 (1972).

5. Huttinger, K.J., 3rd Conference on Industrial Carbons and Graphite SCI, London, 136 (1971).

6. Lapina, N.A., Ostrovskii, V.S. and Syskov, K.I., Carbon, 14, 39 (1976).

7. Ozawa, T., Bull, Chem. Soc. Japan, 38, 1881 (1965).

8. Friedman, H.L., J. Polym. Sci., B., 7, 41 (1969).

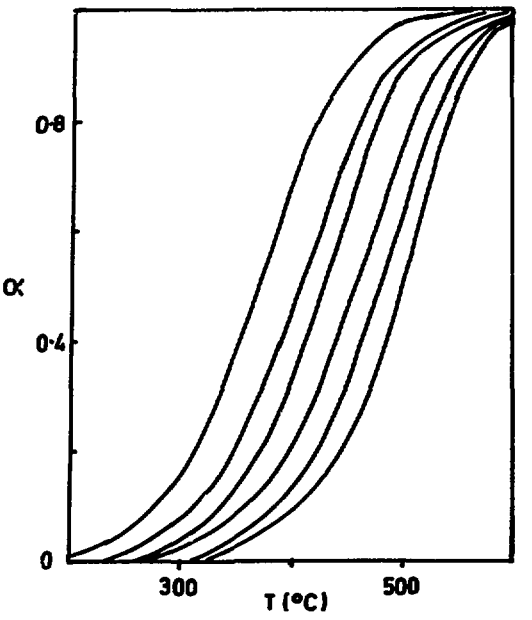


Fig.1 TG curves for binder pitch at different heating rates

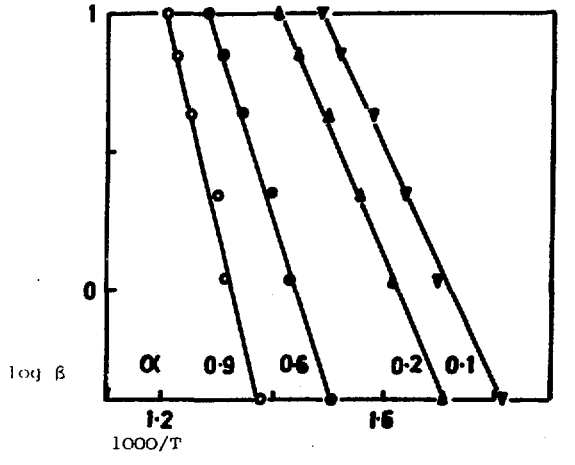


Fig.2 Ozawa plot of data in Fig.1

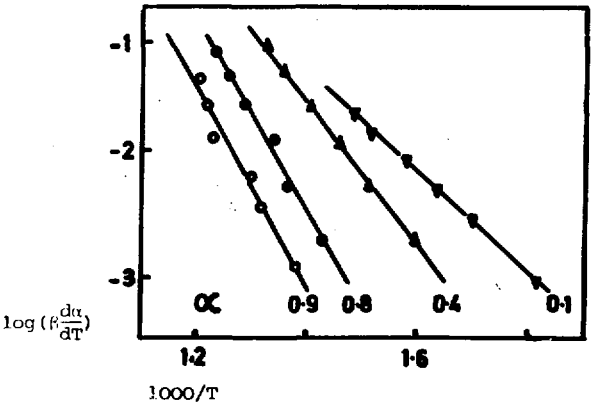


Fig.3 Friedman plot of data in Fig.1 →

STRUCTURAL ASPECTS OF MESOPHASE MATERIALS FROM PETROLEUM, COAL AND OIL SHALE

T. F. Yen

University of Southern California
Los Angeles, California 90007

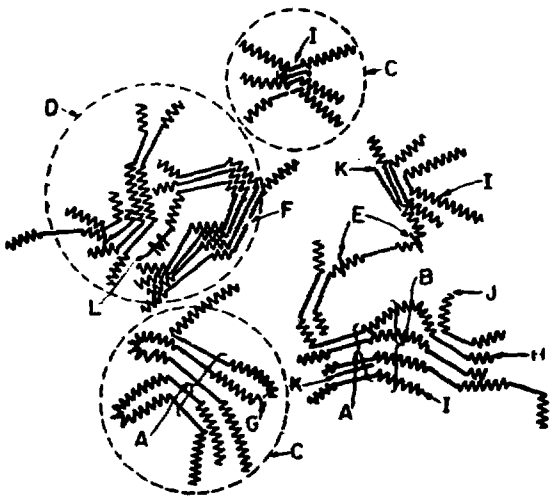
Petroleum pitch and semicoke have been used in the specialty graphite area as high quality carbon precursors for graphites and carbon fibers. The performance of these finished materials depends on the characteristics of their starting feedback supply. However, in recent years the impact due to the shortage of petroleum, as well as the improvement of refining technology, forces one to look for other alternative energy sources, such as coal and oil shales. These materials will become important in the next decade as they are inevitably to be developed as substitutions for petroleum during the interim period until ultimate energy sources, such as solar energy and fusion are technologically demonstrated.

Coal and oil shale, as well as petroleum, are all fossil fuels. The pathways of their diagenesis and source materials are entirely different. Therefore, it is expected that there be differences in the structures of their asphaltic (carboneceous) bitumens. These bitumens are important in that they are the precursors leading to the mesophase formation under carbonization. Within the macrostructure of bitumens, sufficient embryonic nematic crystals may be the nucleus to control the mesophase.

Macrostructure of Asphaltic Bitumen

Naturally-occurring bitumen is not entirely isotropic in its structure. It is a mesomorphic liquid, i.e., many individually-oriented clusters are suspended and randomly distributed within their lower molecular weight homologs. The individually oriented clusters consist of a number of planar aromatic molecules stacked vertically in layers due to the π-π association. The side substituents of these aromatic systems are zig-zag chains due to the requirement of succession of the tetrahedronally-linked carbon atoms. These chains act as a "shock absorber" in a sea of floating "islands."

Fig. 1 depicts the general macrostructure of asphaltic bitumen (1). The association of the π-systems actually gives interlayer distance of ca. 3.5 A which yields (002) peak under x-ray diffraction. This type of association is equivalent to the layered structure of graphite which is termed crystallite (A). The zig-zag chain can orient in a bundle-like fashion (B) depending on the torsional angle when propagation of SP^3-bonded orbital takes place. These island-like stacks are termed particles (C). Usually particles can further associate into micelles (D), the periferal groups are polar. There are a number of weak links (E) along the chain configuration, some of these are ether, thioether or even hydrogen bonds, which can undertake cleavage. There are imperfections in the aromatic systems with di- or trivalent heteroatoms such as nitrogen, sulfur or oxygen. Clusters may



Macrostructure of Asphaltics

A. Crystallite	B. Chain Bundle
C. Particle	D. Micelle
E. Weak Link	F. Gap and Hole
G. Intracluster	H. Intercluster
I. Resin	J. Single Layer
K. Petroporphyrin	L. Metal

also be linked either by folding the chains--intracluster (G); or by bridging through weak links--intercluster (H). The resin (I) is a small homolog of asphaltene which is larger and the molecular weight is higher. Simple layer (J) of the stacked clusters can be formed by disassociation, provided that conditions do not favor the reassociation. Petroporphyrins (K) is a single layer containing extended conjugation of pyrroles. The metal (L) can be a center of coordination for several clusters.

The schematic illustration is useful for the structural change during heat treatment. In general, aromaticity increases upon the application of heat. The conversion of asphaltenes into carbenes and carbenes into carboids is such an example. The average number of effective layers (Me) increases from a value of 5 to a larger value of 15. For petroleum coke the value can raise up to 35 (2). Under heat, more hydroaromatic structures can become aromatic. Hence the increase is not only along the z-axis, but also an anticipated growth in the x, y-plane, that is, an increase in layer diameter.

Prediction of Coal and Shale Oil as Mesophase Sources

The development of the oriented areas of mozaics and domains under carbonization is important. The growth of such anisotropy during graphitization

is also important. What will be discussed here is the constituents of different bitumens for this type of study. The stacking defects will be caused by the extent of heteroatoms as well as metals. Table I is a brief summary of the constituents in petroleum-, coal-, and shale-derived asphaltenes. The predominant type of heteroatoms is different in various asphaltenes, e.g., in each molecule of petroleum-derived asphaltene, there are 2 or 3 sulfur atoms; in each of the oil shale-derived asphaltene, there are 2 or 3 nitrogen atoms; and in each of the coal-derived asphaltene, there are about 2 or 3 oxygen atoms.

Table I. Composition of Different Asphaltenes

	Petroleum	Shale	Coal
Metals	V, Ni	Fe, Ni	Ge, Mo
Major Hetero-atoms(N, O, S)	S	N	O
Aromatics	peri	kata or link	kata

Table II. Structural Parameter of Various Asphaltenes

	Petroleum	Shale	Coal
f_a	0.2-0.5	0.4	0.6-0.7
L_a (A)	10-15	7-12	7-14
L_c (A)	20	15	10
σ	0.5-0.7	0.5-0.6	0.5-0.5
H_I/C_A	0.3-0.5	0.8-0.9	0.6-0.8
n	4-6	2-3	1-2

Table II lists different parameters as measured by NMR and X-ray diffraction. The higher aromaticity (f_a) of coal and coal-derived products may be important for the graphitization process, but the drawback may be that coal is kata-condensed systems. The fact that coal-derived asphaltene has shorter substitution (n) and lower extent of substitution (σ) may not be the most desirable parent substance. The longer chain and the excessive amount of substitution may have the "buttressing" effect for aromatization. Another consideration is that in trace metals, e.g., alkali metal may catalyze polycondensation. In this manner, the prediction of the application of shale-derived asphaltene to mesophase formation is in between that of petroleum-derived product and that of the coal-derived product.

Finally, the spin correlation studies indicate that both singlet-triplet transitions and doublet states exist with the bituminous aromatic sheets (3). The thermal excitation is attributed to the propagation of Wannier excitons. As graphitization occurs, the Wannier spins act as independent mobile or delocalized excitons. The odd electrons eventually become charge carriers and can be degenerated to certain extent as in a metal. All those depend on the J-value (singlet-triplet energy) and $\Delta\epsilon$ (conduction energy gap) of the mesophase source material. To summarize, it is not only the chemical composition of parent substances that determines mesophase growth, but the macrostructure of the parent source material also plays an important role.

References

(1). J.D. Dickie, and T.F. Yen, "Macrostructures of the Asphaltic Fractions by Various Instrumental Methods," Anal. Chem., 39, 1847-1852 (1967).

(2). T.F. Yen, "Chemistry of Asphaltene in Coal Chemistry," Preprints, Workshop on Coal Chemistry, Stanford Research Institute, pp. 144-164 (1976).

(3). T.F. Yen, and D.K. Young, "Spin Excitation of Bitumen," Carbon 11, 33-41 (1973).

EFFECT OF BORON CARBIDE ADDITION ON SOME PROPERTIES OF HOT-PRESSED POLYCRYSTALLINE GRAPHITE MADE FROM COKE POWDER

K.MIYAZAKI, T.HAGIO, K.KOBAYASHI, H.HONDA
National Industrial Research Institute of Kyushu
Tosu-shi, Saga, 841, Japan

Introduction

Recently K. Kobayashi et al[1] have reported that graphitized high density carbon could be fabricated from coke powder by hot-press method without the use of a pitch binder phase only with the addition of a small amount of boron oxide as a accelerating agent for sintering and graphitization of carbon particles.

From this results it was thought that boron carbide addition might also influence on sintering and graphitization of carbon particles as well as boron oxide. The purpose of this experiment is to clarify some properties of the sintered bodies made from coke powder with boron carbide addition (0-50wt%) and to know the effect of boron carbide on both sintering and graphitization.

Experimental

Calcined pitch coke powder under 149 micron size and boron carbide powder of 1-2 micron size were pulverized and mixed by tungsten carbide motar with different boron carbide addition from 0 to 50wt%. Then each of the mixed powder of 20g with different mixing ratio was set between graphite die and punch, and heated at various temperature from 1400°C to 2200°C and held at the temperature for 60 min under a pressure of 200kg/cm^2 by hot-press apparatus. Rate of heating was 40 min from room temperature to 1800°C, 60 min to 2000°C and 80 min to 2200°C. The compacts obtained after hot-pressing were examined to clarify the effect of boron carbide addition and that of hot-pressing temperature on some properties such as texture, density, mechanical strength, electric resistivity and graphitization degree of coke.

Results and discussion

Disk-shaped compacts of 30mm in diameter and about 12-21mm in height were obtained after hot-pressing of the mixed powder of coke and boron carbide.

Some properties of the compacts were remarkable different with the amount of previous addition of boron carbide and the hot-pressing temperature.

Fig.1 gives the relative density of the compacts after hot-pressing at the temperature of 1800, 2000 and 2200°C with different boron carbide content in originals.

The relative density generally increase with increase of boron carbide content and hot-pressing temperature. The rate of increase is particularly remarkable within 10% addition and maximum density of 96% was obtained in the case that hot-pressing temperature was 2200°C and the boron carbide content was more than 30%.

Fig.2 gives change of the bending strength of the compacts after hot-pressing with increase of boron carbide content in originals. The strength increase with increase of boron carbide content and hot-pressing temperature. The behaviour of increase is particularly outstanding at 2200°C, that is, the value shows a rapid rate of increase in the range less than 30% and reaches to about 1500kg/cm^2 at about 30% addition, then the rate becomes slow with increase of boron carbide content. In either case from the samples with no boron carbide addition or at the hot-pressing temperature below 1800°C, strong compacts could not be obtained. It is known from these data that hot-pressing temperature of at least 2000°C is necessary in order to obtain a dense and strong compact.

Fig.3 gives change of the electric resistivity of the compacts after hot-pressing with increase of boron carbide content in originals. The electric resistivity once decreases with increase of amount of boron carbide addition, and shows minimum value at 10-20wt% addition. The minimum value decrease with increase of hot-pressing temperature. In the case of 2200°C minimum value of $0.9\times10^{-3}\Omega$-cm was obtained at 10wt% addition.

The resistivity has a tendency to increase again in the range above 20wt% addition. This tendency is more outstanding in the case of 1800°C treatment, while the increase rate is very slow or almost constant in that of 2200°C.

Fig.4 gives change of d(002) spacing of coke of the compacts with increase of boron carbide content in originals after hot-pressing at different temperature.

It is known from this result that the effect of boron carbide addition is particularly remarkable at 2000 and 2200°C than at 1800°C. At 1800°C, d(002) decrease continuously with increase of boron carbide addition, but the change is very small. At 2000°C, d(002) decreases rapidly from 3.420 Å at 0% to 3.370Å at 10wt% addition and then it keeps almost constant at about 3.370Å in spite of the increase of the amount of boron carbide. At 2200°C, d(002) decrease more remarkably from 3.388Å at 0% to the minimum value of 3.360Å at 5wt% and then it increases again gradually to about 3.370 Å at 50wt% addition.

In the case of 2200°C apparent crystallite size, La(110) increased rapidly from 400Å at 0% to maximum value of 1200Å at 5wt% addition. At 2000°C, La showed also

maximum value of about 700Å at 5-20wt% addition, while at 1800°C change of La value is not so remarkable with increase of boron carbide addition.

Development of (112) reflection peak was also accelerated at 2000 and 2200°C by boron carbide addition. Lc(112) showed maximum value of about 30Å at 5wt% addition in the samples treated at 2200°C.

It is clear from these X-ray data that boron carbide addition has an effect to accelerate graphitization of coke. Particularly it was most effective in the range near 5wt% addition at 2200°C.

It has already well known by many investigators[2-7] that boron solid-soluted into graphite structure above about 2000°C and give some influence its X-ray parameter. In this experiment boron atom comes from boron carbide also considered to be solid-soluted into coke structure and promote the formation of graphitic structure. Furthermore under the condition of hot-pressing coke particles began to sinter each other with diffusion of boron atom into substitutinal or interlayer position, and the compacts was densified and strengthened above the temperature of 2000°C. From chemical analysis and X-ray analysis solid-soluted boron content was assumed about 1%. In the samples with higher borom carbide content, supply of boron atom into coke particle is thought to be more uniformaly to promote sintering and further linkage between boron carbide and carbon grain might give some effect to raise the compact strength.

References (1) K.Kobayashi et al, Abstract for the 12th Carbon Conf. (1975); (2) F. Tombrel, Rev. Hautes Temper. et Réfract, t, 3, 79 (1966); (3) J.A.Turnbull et al, Carbon, 3, 387 (1966); (4) W.V.Kotlensky, Carbon, 5, 409 (1967); (5) C.E.Lowell, J. Amer. Ceram. Soc., 50, No.3, 142 (1967); (6) S.Marinković et al, Carbon, 7, 185 (1969); (7) Jean-Pierre Rouchy et Jucques Méring, C. R. Acad. Sc. Paris, 277, série C, 533 (1973)

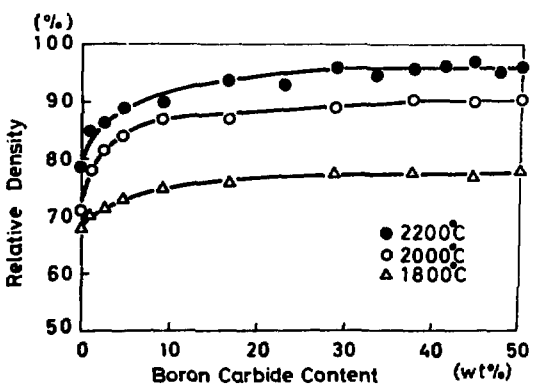


Fig.1 Change of relative density of the compacts after hot-pressing with boron carbide content in originals.

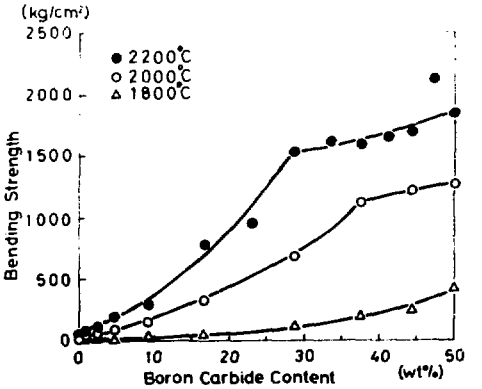


Fig.2 Change of bending strength of the compacts after hot-pressing with boron carbide content in originals.

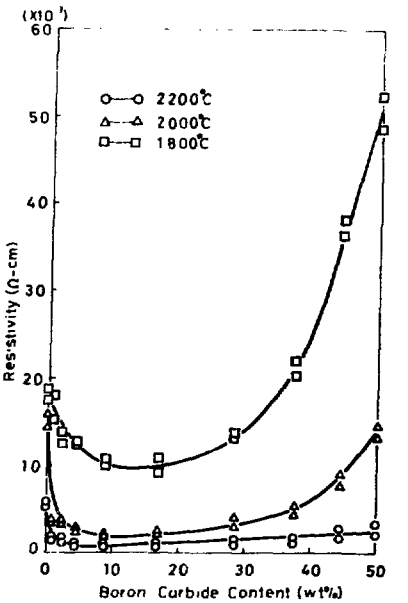


Fig.3 Change of electric resistivity the compacts after hot-pressing with boron carbide content in originals.

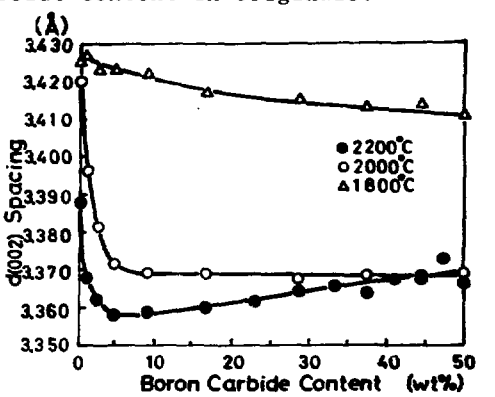


Fig.4 Change of d(002) spacing of coke after hot-pressing with boron carbide content in originals.

EFFECT OF HOT-PRESSING TEMPERATURE ON SINTERED POLYCRYSTALLINE GRAPHITE MADE FROM PITCH COKE WITH B_2O_3 ADDITION

T.HAGIO, Y.MATSUSHITA, K.KOBAYASHI, H.HONDA

National Industrial Research Institute of Kyushu
Tosu-shi, Saga, 841 Japan

Introduction

K. Kobayashi et al[1] have reported that high dense and strong polycrystalline graphite was fabricated by hot-pressing method from calcined pitch coke powder with B_2O_3 addition. In that case about 10% B_2O_3 addition was found to be most effective for sintering and graphitization of coke powder.

This paper describs on effect of hot-pressing temperature influenced on some properties of polycrystalline coke compacts made from calcined pitch coke powder with 10% B_2O_3 addition at various temperatures from 1200 to 2200°C under a pressure of 200kg/cm^2 comparing the compacts made from same powder with no addition under same condition.

Experimental

Both calcined pitch coke powder with 10wt% B_2O_3 added as aqueous solution and the powder with no addition were used as the starting materials. After drying the samples in a drying oven each 15g was set in a graphite die of 30mm in diameter and hot-pressed at various temperature from 1200 to 2200°C under a pressure of 200kg/cm^2. The holding time at the desired temperature was set for 30 min and after cutting off the heating the sample was kept within a die for 15 min under the pressure.

After hot-pressing the compacts of 30mm in diameter and 10-14mm in height were obtained. In order to know the effect of hot-pressing temperature, density, mechanical strength, graphitization degree, boron and boron carbide content of the compacts were examined.

Results and discussion

Fig.1 gives change of bulk density of the compacts with hot-pressing temperature. The compacts from the powder with B_2O_3 addition shows almost constant value of 1.6g/cm^3 in the range from 1200 to 1800°C and then the value increase to about 2.0 g/cm^3 at 2200°C. While the compacts from the powder with no addition shows continuous increase with increase of hot-pressing temperature, but the values are all lower than those from the powder with B_2O_3 addition.

Fig.2 gives change of bending strength and compressive strength of the compacts with increase of hot-pressing temperature. The strength once decrease with increase of the temperature, shows minimum value at 1600-1800°C and raise again above 2000°C in the case of the compacts from the powder with B_2O_3 addition. While strength of the compacts from the powder with no addition increase slightly with rise of the temperature, but the value is very small even at 2200°C. It is interesting to notice that both kinds of compacts have almost same strength at 1600-1800°C range.

Fig.3 gives change of d(002) spacing of coke with hot-pressing temperature. From 1200 to 1800°C both compacts from B_2O_3 addition and no addition show same values at the temperature range from 1200 to 1800°C, but at 2000 and 2200°C d(002) spacing of the compacts from the powder with B_2O_3 addition is considerably lower than those from no addition. The value of 3.356A at 2200°C is nearly equal to that of natural graphite. Apparent crystallite size, Lc(002), increased remarkably above 2000°C comparing that of coke powder with no addition as shown in Fig.4. (112) reflection peak of the compact from the powder with B_2O_3 addition was also observed to develop above 2000°C. From these X-ray data it is known that graphitization is accelerated by B_2O_3 addition above 2000°C.

Fig.5 gives change of total boron content and content of boron forming as boron carbide structure with increase of hot-pressing temperature in the compacts made from the powder with B_2O_3 addition. Total boron content is almost constant about at 2.5wt%. Boron carbide is formed at 1600°C and the content decrease with increase of the temperature. In the range from 1200 to 1400°C boron exists as a form of boron oxide and in the range from 1600 to 1800°C most of boron exite as a form of boron carbide structure. Above 2000°C a part of boron is considered to solid-soluted into coke structure and promote sintering and graphitization of coke.

It is concluded that the hot-pressed compacts made from coke powder with 10wt% B_2O_3 addition could be classified into three types. The first is the one made below 1400°C in which coke particles adhered each other with B_2O_3 glass phase, the second is the one made between 1600 and 1800°C which consist of the mixture of independent coke particles and small amount of boron carbide, and the last is the one made above 2000°C of which boron is considered to give strong influence for sintering and graphitization of coke by its diffusion into coke structure.

Therefore in this experiment hot-pressing temperature above 2000°C is found to be necessary for obtaining dense and strong polycrystalline graphite.

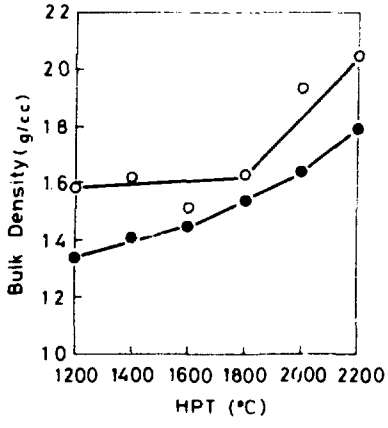
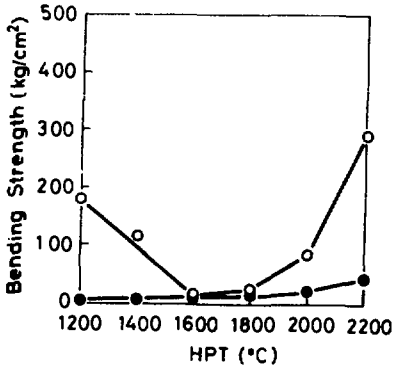


Fig.1 Change of bulk density of the compacts with hot-pressing temperature.
○: coke with 10% B_2O_3 addition
●: coke with no addition



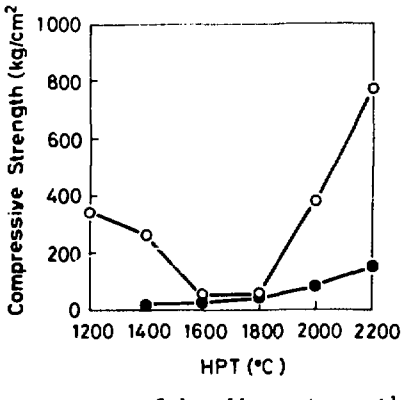


Fig.2 Change of bending strength and compressive strength of the compacts with hot-pressing temperature.
○: coke with 10% B_2O_3 addition
●: coke with no addition

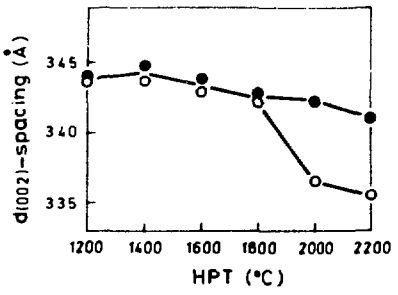


Fig.3 Change of d(002) spacing of coke with hot-pressing temperature.
○: coke with 10% B_2O_3 addition
●: coke with no addition

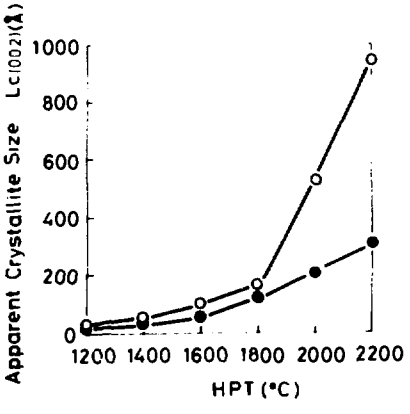


Fig.4 Change of apparent crystallite size, Lc(002), of coke with hot-pressing temperature.
○: coke with 10% B_2O_3 addition
●: coke with no addition

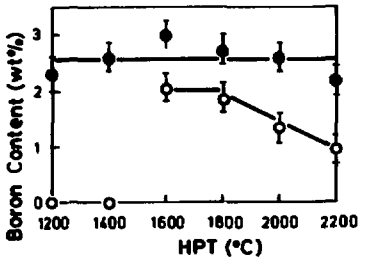


Fig.5 Change of boron content in the compacts with hot-pressing temperature.
●: total boron content by chemical analysis
○: content of boron forming B_4C estimated by X-ray analysis

Reference

(1) K. Kobayashi et al, Abstract for the 12th Carbon Conf. (1975)

EFFECT OF B_2O_3 ADDITION ON SINTERING AND GRAPHITIZATION OF CARBON MATERIALS

K.KOBAYASHI, T.HAGIO, K.MIYAZAKI, Y.MATSUSHITA, S.KONDO, K.IWATA, H.HONDA

National Industrial Research Institute of Kyushu
Tosu-shi, Saga, 841, Japan

Introduction

Most graphite products are generally fabricated with the use of pitch binder phase, as pitch binder phase is necessary to cement carbon particles for compaction of carbon materials.

K.Kobayashi et al[1] have reported that dense and strong polycrystalline graphite was made by hot-pressing method from calcined pitch coke powder with B_2O_3 addition.

It has been already well known by many investigators[2-6] that boron dissolves substitutionally in graphite structure with a maximum solubility of 2.35% at 2350°C[2]. In the solid solution, the in plane lattice parameter a-spacing increases and d(002) spacing decreases with boron content. There is also evidence that boron in excess of the solubility limit may occupy an interlayer position increasing d(002) spacing.

We have found in addition to these facts that boron derived from boron oxide is effective to sinter coke particles under hot-pressing. This paper describes on some properties of the products made from various kind of carbon materials with B_2O_3 addition and necessary experimental condition for obtaining dense and strong polycrystalline graphite. And the effect of B_2O_3 addition on both sintering and graphitization was also investigated.

Experimental

Pitch coke, petroleum coke, aceton-furfural resing carbon, pyrolytic carbon and carbon fiber were used as starting materials. Except for carbon fiber the raw materials pulverized into fine powders and B_2O_3 added as an aqueous solution. After drying the powder was set in a graphite die of 30mm and heated at various temperature up to 2200°C under a pressure of 200kg/cm^2. In the case of the carbon fiber the fiber dipped in B_2O_3 aqueous solution and after drying it set along one direction in a graphite die, and then hot-pressed under the same condition. After hot-pressing some properties such as, density, mechanical strength, graphitization degree, boron and boron carbide content of the compacts were examined and factors affecting the properties were investigated.

Results and discussion

(1) Effect of Pressure and Temperature

Some pressure during heat-treatment, was known to be necessary for obtaining dense and strong compacts, Without pressure strong compacts could not be obtained. Fig.1 gives behaviour of typical shrinkage couve of the sample with increase of temperature under pressure of 200kg/cm^2. From this curve initial rapid densification occured in the range from room temperature to about 400°C is considered to be due to that B_2O_3 changes to liquid phase and coke particle are rearranged to closer packing within the glass matrix under pressure. Second rapid densification is observed above 2000°C. Hagio et al[7] report in the experiment on hot-pressing of pitch coke with B_2O_3 addition that above 2000°C d(002) decrease, Lc(112) increase and mechanical strength of the compacts increased. Other carbon materials showed same tendency with temperature. From these facts rapid densification above 2000°C is also known to be caused by sintering and graphitization of carbon particles under a pressure with diffusion of boron into graphite structure. In this experiment upper limit of pressure was set at 200kg/cm^2 because of considering safety limit of graphite die and punch. However, it is thought if higher pressure is applied, hot-pressing temperature could be lowered for obtaining same properties of the compacts, or the properties could be improved even at same temperature.

(2) Effect of Content of B_2O_3 Addition

Most suitable content of B_2O_3 addition was a little different on sample to sample. For graphitizing-type carbon such as pitch coke, petroleum coke and pyrolytic carbon 8-12wt% addition was generally found to be most effective for sintering and graphitization to obtain dense and strong polycrystalline graphite. Table 1 gives some examples of the hot-pressed compact at 2200°C made from the powder with 10wt% B_2O_3 addition and with no addition. And Fig.2(a) gives typical examrle on change of some properties of graphitizing-type carbon such as pitch coke with increase addition of B_2O_3 at 2200°C.

For non-graphitizing-type carbon such as aceton-furfural resin carbon or carbon fiber, suitalbe content of B_2O_3 addition showed some difference on sample to sample. Fig.2(b) gives change of some properties of aceton-furfural resin carbon with increase addition of B_2O_3. In the case of carbon fiber the denser and stronger compacts was obtained at the higher content of B_2O_3 addition. This difference is considered to be due to some difference in shape, texture and structure between raw materials. All these non-graphitizing-type carbon with B_2O_3 addition showed composit (002) reflection profile like similar pattern obserbed on non-graphitizing-type carbon at usual heat-treatment.

(3) Some Properties of the Hot-pressed Products at Suitable Experimental Condition.

In addition to these factors above described, powder size distribution and calcining temperature of raw material, method of B_2O_3 addition give some influence of the properties of the hot-pressed compacts. Table 2 gives some properties of hot-pressed products made from various carbon materials with B_2O_3 addition under the suitable condition.

Ref. 1) K.Kobayashi et al, Abstracts 12th Conf. on Carbon, 247 (1975); 2) C.E.Lowell, J. Amer. Soc., 50, 142 (1967) ; 3) J.A. Turnbull et al, Carbon, 3, 387 (1966) ; 4) S.Marinkovic et al, Carbon, 7, 185 (1969) 5) H.Gasparoux et al, Carbon, 3, 65 (1965); 6) W.V.Kotlensky, Carbon, 5, 409 (1967); 7) Hagio et al, in this abstract, 13 Carbon Conf. (1977)

B_2O_3	addition(10wt%)			no addition		
	ρ (g/cc)	S (kg/cm²)	Co (Å)	ρ (g/cc)	S (kg/cm²)	Co (Å)
Pitch coke	2.01	600	6.722	1.77	50	6.823
Petroleum coke	2.03	250*	6.720	1.75	60	6.818
Pyrolytic carbon	2.07	432	6.712	1.57	43	6.839

* Bending

↑Table 1. Some properties of hot-pressed products from the powder with 10wt% B_2O_3 addition and no addition at 2200°C.

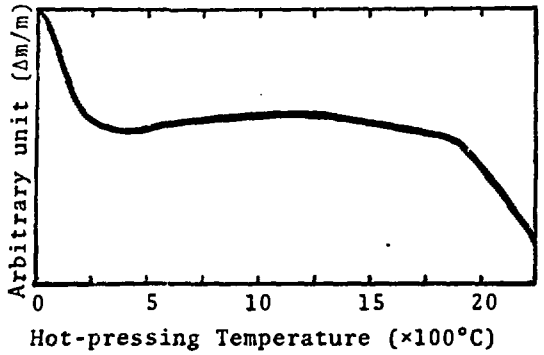
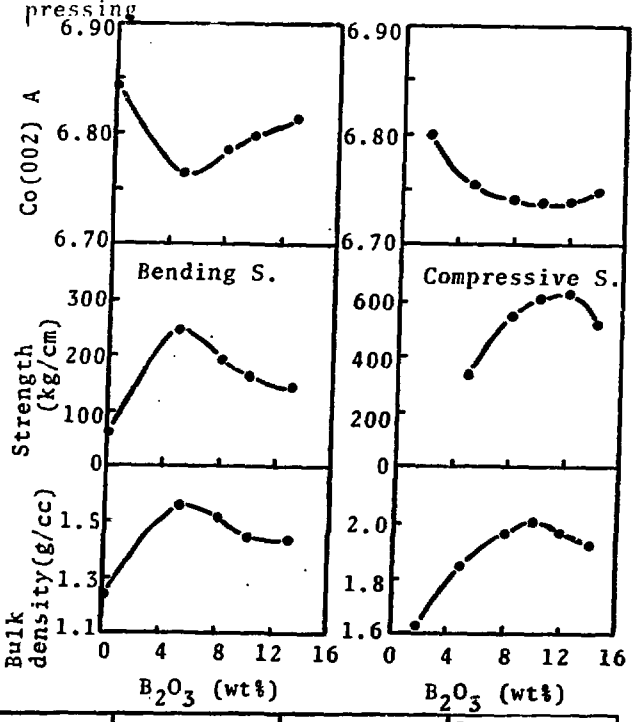


Fig.1 Typical shrinkage curve during hot-pressing



→Fig.2. Some prerties of hot-pressed products (a) pitch coke and (b) aceton furfural resin carbon with content of B_2O_3 addition at 2200°C.

	Pitch coke	Petroleum coke	Aceton-furfural resin carbon	Carbon fiber	Pyrolytic carbon	Conventional artificial graphite
Bulk density(g/cc)	2.0-2.1	2.0-2.1	1.6-1.7	1.8-1.9	2.0-2.15	1.6-1.8
d(002) (Å)	3.36-3.37	3.355-3.365	3.37-3.38	3.37-3.38	3.355-3.360	3.36-3.37
Lc(002) (Å)	>600	>1000	300-400	400-500	>1000	>500
Compressive strength (kg/cm²)	1000	800	1000-1200	—	600-700	500-600
Bending strength (kg/cm²)	600	400	600-700	2000	300-400	200-300
Electric resistivity (μΩcm)	700-1000	500-1000	—	—	—	1000

Table 2. Some properties of hot-pressed products under suitable condition.

VARIOUS VIBRATION METHODS FOR THE FORMING OF CARBON PRODUCTS

S. Wilkening, Leichtmetall-Forschungsinstitut der
Vereinigte Aluminium-Werke AG, 5300 Bonn, Germany

1. Introduction:

In many industrial fields the vibration or shaking principle is a well-known technique for compacting granular materials. The vibration methods differ widely. Vibratory compaction can be very effectively applied to shape green carbon mixtures. During the last two decades a fascinating development took place in the area of vibration forming of carbon products. For sake of its own manufacture of large anode and cathode blocks for aluminium reduction cells and also other electrodes the Vereinigte Aluminium-Werke AG has been strongly engaged in the development and application of vibrating machines.

2. Principle of a vibratory compacting machine:

The fundamental parts commonly used for the construction of a vibratory moulding apparatus for green carbon mixtures are illustrated diagrammatically in Fig. 1. The arrangement and connection of the moulding parts (designated as 2, 3 and 4 in Fig. 1) on the vibrating table (1) plays a significant role for the efficiency and uniformity of compaction. Viscous carbon mixes containing pitch-coated coke particles do not behave like dry granular materials. They exhibit a high damping factor. During vibration the heavy top weight acts as a counter-mass and exerts compressing impacts on the carbon mixture. One variable clearly defined in the vibrating system is the exciting force and its frequency.

It is however very difficult to describe the mechanism of the whole vibrating machine by useful mathematical equations. Furthermore there are compaction parameters of the carbon mixtures like binder viscosity, kind of filler material and plasticity.

3. Types of vibratory compacting machines:

On the basis of the construction elements in Fig. 1 a series of forming modifications were investigated in our laboratory ten years ago. Some models are shown as simplified drawings in Fig. 2 to 6. Generally it could be stated that excellent compaction is attained if the main parts of the moulding equipment are allowed to vibrate independently. Relative motions should occur between bottom plate, shell and top weight. It was observed that even good compactness could be reached when transferring vertical vibratory motions from the shell surface to the green carbon mixture by friction forces. The arrangement according to type V (Fig. 3) has become our standard shaping procedure in our laboratory to develop product formulations. The assembly according to type IV (Fig. 2) is applied for most of the industrial vibration units, because it has obviously less engineering problems.

Additional measures may be taken to intensify compaction by a variable speed drive to adjust the frequency to an optimum, by hydraulic or pneumatic pressures upon the top weight to induce a slight continuous flow in the viscous medium (see Fig. 4), or by application of vacuum to remove the detrimental air from the carbon mix (see Fig. 5). The pronounced advantages of vacuum vibration forming are increased apparent densities of the carbon products by 0.05 to 0.1 g/cm^3, an improved shape stability of large blocks and a better homogeneity and structure. An example of a vibration mould for special shapes is depicted in Fig. 6.

4. Plant vibratory machines:

Most modern vibratory compacting machines are characterized by maximum exciting forces of about 1000 kN at 1450 r.p.m. and combined application of variable rotation speed, vacuum and additional hydraulic pressure to the top weight. These machines are capable of moulding carbon blocks up to a weight of about 3.3 metric tons and a length of 3.7 m (12 feet).

5. Development of continuous vibrating methods:

A continuous compacting and shaping method might be desirable when a great number of identical pieces has to be produced. The vibrator has not to be started and stopped for each carbon body formed. The passage of critical vibration regions is avoided and time is saved for "working" of the green carbon mixture.

The vertical section of an experimental strand vibratory compactor is shown in Fig. 7. It represents a first attempt in the direction in making electrodes without interruption. The mixture is filled into a vertically vibrating tube and sinks down into a funnel-shaped compacting chamber, where it is compressed from a larger to a smaller diameter by horizontally vibrating wall-segments. The wedge-shaped space is alternately narrowed and widened. So far promising results have been obtained.

Another concept for a continuous vibratory moulding procedure is outlined in Fig. 8. The carbon mixture is moved on a conveyor belt with L-shaped mould sections between a vibrating table and a top weight carrying a sloping bottom plate. The side walls (not shown in Fig. 8) are fixed to the vibrating table and form a lane through which the L-shaped sections travel.

The above-mentioned methods exemplify the great versatility of the vibration principle for forming carbon bodies.

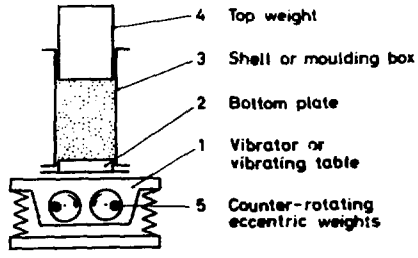


Fig. 1 Main parts of a vibratory compacting machine

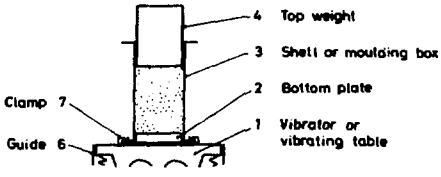


Fig.2 Vibratory compactor Type IV
Parts 1, 2 and 3 are connected

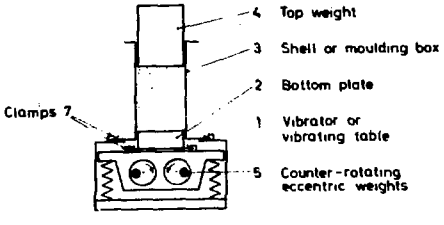


Fig.3 Vibratory compactor Type V
Parts 1 and 2 are connected, part 3 is connected to the frame

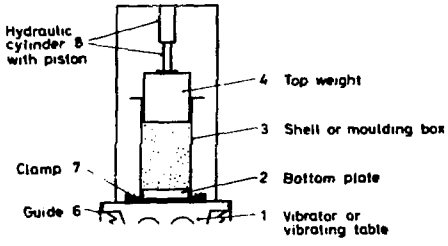


Fig.4 Vibratory compactor Type VIII
Parts are connected as in type IV.
Additional hydraulic pressure upon top weight

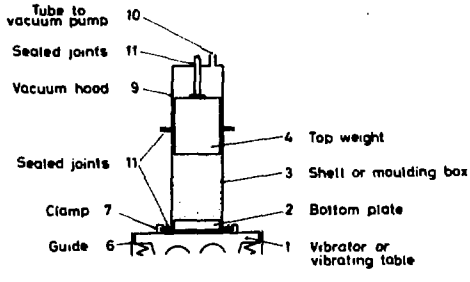


Fig.5 Vibratory compactor Type IX
Parts are connected as in type IV.
Additional application of vacuum

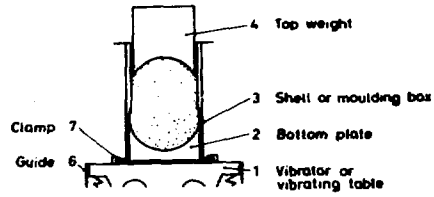


Fig.6 Vibratory compactor Type X
Horizontal forming of cylinders.
Parts are connected as in type IV

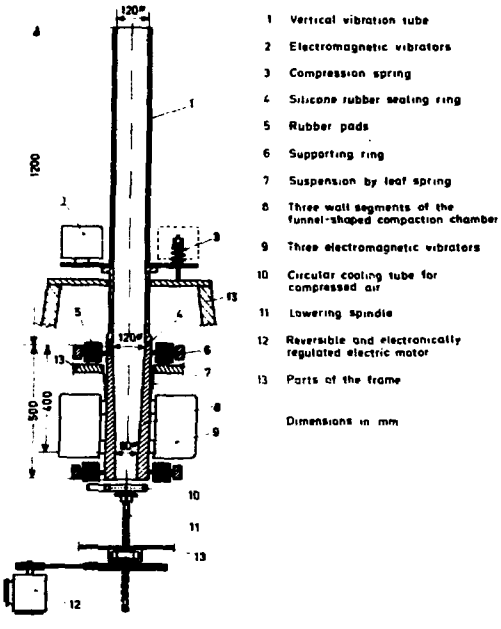


Fig.7 Diagrammatic view of our laboratory strand vibration compactor

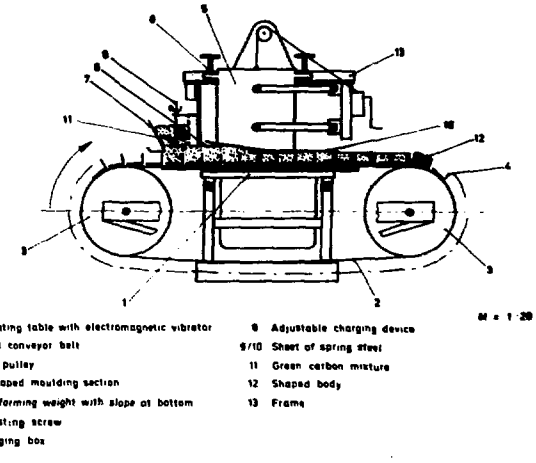


Fig.8 Diagrammatic side view of a conveyor belt vibration compactor

THE INFLUENCE OF QUINOLINE INSOLUBLE PITCH CONSTITUENTS ON THE IMPREGNATION BEHAVIOUR

H. Tillmanns and G. Pietzka (Sigri Elektrographit GmbH, D-6230 Frankfurt 83, Germany)

Introduction

The continual increase in both the electrical and mechanical duties imposed in the electrodes used in arc furnaces has to be matched by improvements in both the raw materials and in the graphite technology. Particularly the mechanical and electrical properties of electrodes can be increased by impregnation of the carbon or graphite artifacts.

The tendency of using binders with higher softening points results in the increase of the bulk density and the decrease of the porosity. Any second impregnation step is rendered difficult by the decreased porosity. In order to improve the efficiency parameters of the impregnation have been studied.

The influence of the impregnation on both the pitch composition and the electrode properties was studied by G.W. Plewin et al. (1). In this work it could be shown that the infiltration of medium and low molecular weight compounds of pitch is favored. The negative influence of the quinoline insolubles has been pointed out but studies on the influence of the quinoline insoluble pitch constituents on the infiltration velocity has not been made.

This paper is concerned with this question and will show that the content of quinoline insolubles is one of the important factors for the selection of pitches.

Experimental

To understand the mechanism of the impregnation behaviour of carbon and graphite three questions have to be answered:

1. Are the quinoline insoluble pitch constituents infiltrated into the artifacts?
2. If the quinoline insoluble pitch constituents can not be infiltrated, which is the influence of the filter cake formed onto the surface on the infiltration velocity of the other pitch constituents?
3. How is the overall impregnation behaviour of pitch in respect to temperature, pressure and especially to QI-content?

The first question can not be answered by the knowledge of the pore size distribution of baked carbon artifacts and of the grain size distribution of the QI. Both the pore size distribution and grain size distribution are within the same range of size, but the pore diameter is normally smaller than the grain diameter. This explains the well known difficulties in the impregnation of carbon artifacts with very small pores using commercial soft pitches the QI of which is larger than 3 %. To study the infiltration behaviour of quinoline insoluble constituents of selected high and low temperature tars and of a special impregnation pitch an filtration experiment was performed with an 5 mm thick disc cut from a carbon electrode. The applied pressure difference was 1 bar.

The influence of a filter cake formed by segregated quinoline insoluble pitch constituents was examined with a porcelain filter disc on which a layer of these constituents of different thickness (0,26 - 2,6 mm) was sedimented. Anthracene oil was used as a model liquid as its viscosity at room temperature is nearly the same as the viscosity of pitch at about 200°C. Furthermore the molecular structure of the anthracene oil is comparable with the structure of the pitch constituents.

The pressure difference was varied between 0,3, 0,6 and 1 bar. The influence of the thickness of quinoline insoluble layers on the porcelain filter disc were measured as the relative filtration rate related to the filtration rate of anthracene oil measured with the clean filter disc.

The overall impregnation behaviour of commercial pitches in respect of temperature, pressure and QI-content was measured with a filter disc made from carbon having a thickness of 5 mm. The filtration pressure could be increased up to the limit given by the mechanical strength of the carbon disc. The examinated temperature range was 180 - 230°C.

Results

The results of the infiltration tests constituents are summarized in Table 1. These results show that especially in a low temperature tar the quinoline insoluble constituents must have a very small grain size. About one third of the QI penetrates the carbon disc, whereas two thirds of the QI are retained at the surface as a filter cake. On the other hand the grain sizes of the QI's of the high temperature tar and the impregnation pitch must be larger than the average pore diameter of the carbon disc. The QI's are almost completely retained. Furthermore the filtration rate is decreased from 13,4 to 7,0 g/h by increasing the QI content from 0,6 to 13 %. The low filtration rate of the impregnation

pitch is mainly caused by the larger viscosity of about 100 k Pa s.

To determine the influence of the filter cake containing the quinoline insoluble constituents the filtration rate was measured in a second experiment. The tests showed that the filtration rate of anthracene oil decreases with increasing filtration time. The reason for this strange behaviour is a swelling of the filter cake whereby the quinoline insoluble constituents are forming a kind of colloidal skin (Table 2).

The following experiments were performed with swelled and sedimented quinoline insoluble constituents only. The influence of pressure difference and thickness of the filter cake on the relative filtration rate are shown in Table 3. An increasing pressure difference causes a degressive decrease of the relative filtration rate. An increasing layer thickness results in a nearly linear increase of the relative filtration time at low pressure differences of 0,33 bar, whereas at a pressure difference of 1 bar the relative filtration time is hardly changed if the layer thickness is doubled from 1,3 to 2,6 mm. This means that the filter cake containing QI is compressible. The low relative filtration time at a layer thickness of 0,26 mm can only be explained by an incomplete layer of QI on the disc. It can be calculated that a filter cake of QI up to 2 mm thickness will be formed in an industrial impregnation process using an impregnation pitch with a QI content of 2 - 3 %. The strong influence of the QI content of the impregnation pitches on the filtration rate was confirmed by experiments using different pressures and temperatures.

Table 2: Unswelled and swelled QI-layers of 1,3 mm thickness. Filtration time of 5 ml anthracene oil.

Filtration cycle	1	2	3	4
Filtration time (min, sec.) of unswelled QI	2'55"	2'40"	3'50"	4'15"
Filtration time (min, sec.) of swelled QI	17'53"	17'30"	17'32"	17'28"

Table 3: Influence of pressure difference and thickness of the QI filter cake on the relative filtration time

Thickness of the filter cake (mm)	0	0,26	0,78	1,3	2,6
Pressure difference (bar)					
0,33	1	6	28	41	87
0,66	1	3	18	25	37
1,00	1	1,5	14	18	20

Reference

1) G.W. Plewin et al., Chimija twerogo topliwa, 6, 95 (1972)

Table 1: Infiltration behaviour of the quinoline insoluble constutuents of a low temperature and a high temperature tar and of a commercial impregnation pitch

	low temperature tar	high temperature tar	impregnation pitch
Softening point (KS) °C	20	20	61
QI content, %	0,6	13	3,5
Temperature °C	120	140	160
Filtration rate g/h	13,4	7,0	2,1
QI content of the filtrate, %	0,25	0,01	0,6
Percentage of penetrated QI, %	30	0	2

WETTABILITY OF CARBON AND GRAPHITE BY METAL MELTS

B. GOETZE, U. ROSENBLATT

INTRODUCTION

This investigation was induced by problems with graphite-dies in continous die-casting machines. The effect of chemical reaction between graphite and metal-melt on the wear rate of the graphite die should be established.

An indicator for the chemical reaction is the wettability which can be described quantitatively by the wetting angle when using the sessile drop method.

According to the initial problem technically relevant metals as cast-iron, copper and copper alloys have been investigated. As substrate carbon and graphite of different porosity have been used.

EXPERIMENTAL

The sample of metal (0,3 g each) was positioned on the graphite substrate, the surface of which was polished and cleaned by ultra sonic erosion.

Sample and substrate were placed in a high temperature furnace so that the molten metal drop could be observed and photographed and temperature measurement could be carried out by a registrating pyrometer.

Before heating the whole system was evacuated to 10^{-5} bar and then filled with argon of purest quality to atmospheric pressure. After heating to definite temperature and reaching equal temperature in the whole system the molten drop was photographed. Accurate adjustment of the camera was assured.

From the photographs the wetting angle was taken as shown in Fig. 1. The wetting angle of the molten drop on the graphite substrate was considered as measure for the grade of reactivity.

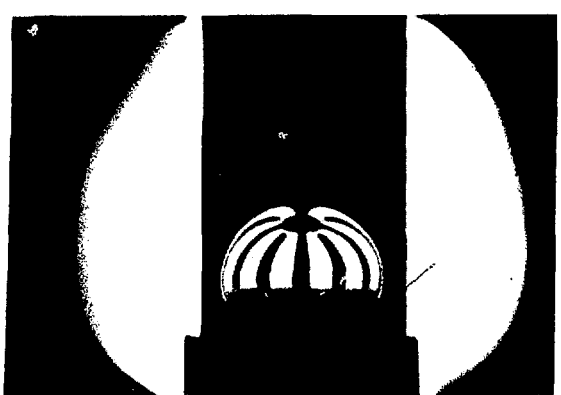


Fig. 1. Wetting angle of the molten drop

RESULTS

1. Cast iron

The wetting angle of the cast iron samples as function of the temperature is shown in Fig. 2. As expected a strong effect of the temperature on the reactivity between cast iron and graphite is observed. In the range of 1500 °C the drop begins to 'creep' ($\theta \sim 90$ °).

Practically no differences between graphite grades can be observed.

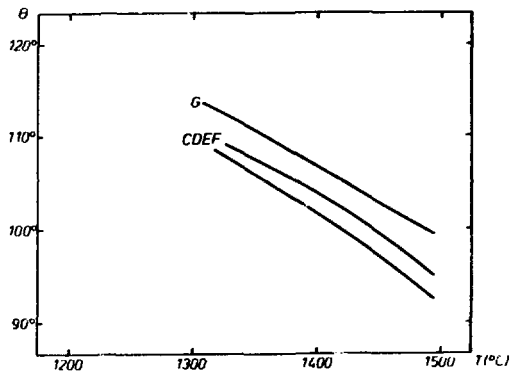


Fig. 2. Effect of temperature on the reactivity of cast iron

2. Copper

The effect of temperature on the wetting angle of the copper samples is shown in Fig. 3. As expected copper as a nonwetting metal shows practically no reactivity with graphite even at high temperatures. Graphite grade "G" has the lowest porosity and shows the lowest reactivity.

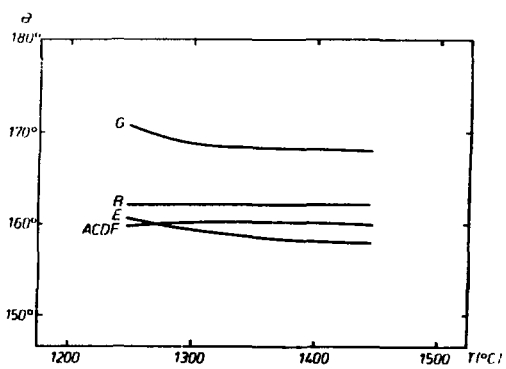


Fig. 3. Effect of temperature on the reactivity of copper

3. Copper-alloy (CuZnNi12)

The results are shown in Fig. 4. Clearly the dependance of the reactivity from the graphite grade appears. The grade with the highest porosity shows the strongest reactivity. With decreasing porosity reactivity decreases too.
The effect of temperature on the reactivity is of second order.

Surprising is that the lowest reactivity is shown by grade "A", a carbon grade. This fact led to a study on the effect of the degree of graphitisation on the reactivity.

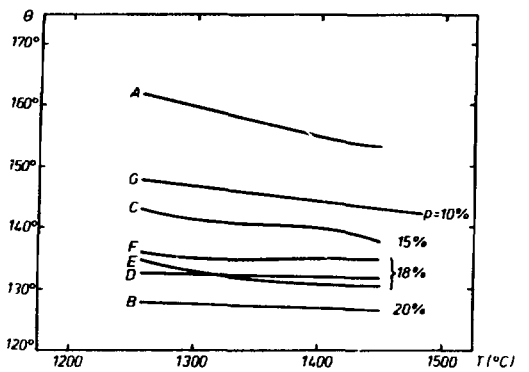


Fig. 4. The effect of porosity on the reactivity of CuZnNi12)

4. Effect of high temperature treatment

Carbon grade "A" changes with increasing high temperature treatment (HTT) into grade "B". The variation in the wetting behavior by CuZnNi12 with increasing HTT of grade "A" is shown in Fig. 5. The wetting measurements have been carried out at 1200 °C.

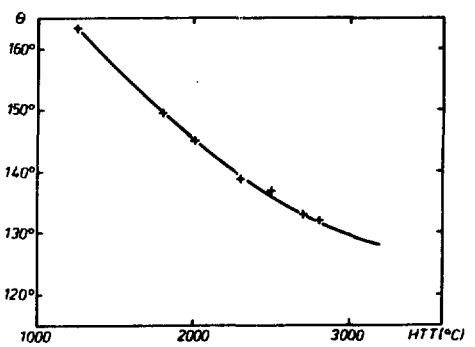


Fig. 5. Effect of degree of graphitisation on the reactivity of CuZnNi12

DISCUSSION

The results of the measurements led to the following conclusions:

- the reaction between a wetting metal and graphite is a function of the temperature, not of the grade of graphite
- the reaction between a nonwetting metal and graphite can not be induced by temperature
- the reaction between an alloy consisting of wetting and nonwetting metals and graphite is a function of the porosity. The reaction is a function of the degree of graphitisation too.

LITERATURE

W. Patterson, D. Amman, S. Engler
Giesserei Tech. Wiss. Metallk. Nr. 20
(1958) 1037/47

CALCULATION OF STEADY STATE TEMPERATURES IN GRAPHITE ELECTRODES IN AN ELECTRIC ARC STEEL FURNACE

Tu-Lung Weng and E. J. Seldin
Union Carbide Corporation, Carbon Products Division
Parma Technical Center, Parma, Ohio 44130

I. Introduction

The temperature distribution in a graphite electrode conducting an electric current in an electric arc steel furnace will change in the course of a steel melting cycle. Near the end of the cycle, when the steel bath is molten and the furnace wall is hottest, the temperature distribution within the electrode approaches or attains what is called the "steady state" temperature distribution, which represents the highest temperatures which may be attained within the electrode in the process of melting steel. Prior to this work, Yavorsky and Elliot[1] have calculated both transient and steady state temperature distributions in an electrode in an electric arc steel furnace; their calculations of steady state temperatures were performed by using an analytical solution of the heat conduction equation[2], where the radiation boundary condition was approximated by Newton's law of cooling in which the heat transfer is proportional to the temperature difference between the electrode surface and the furnace wall. Our approach has been to use an iterative computer method and a radiation condition at the surface of the electrode involving the fourth power of the temperatures to obtain what we believe to be a more accurate solution of the problem.

II. Method of Calculations

Three computer programs were written to obtain the steady state temperatures in electrodes. The programs treat (a) the temperature as a function of radius only for a uniform diameter electrode in a region away from the tip and far enough away from the holder so that there is no axial heat flow, (b) the temperature as a function of radial and axial position for an electrode with uniform diameter and flat tip in the region from the tip to a distance three or four times the radius away from the tip, and (c) the temperature as a function of radial and axial position for a tapered electrode with a flat tip. In all cases, we consider a region of the electrode which does not include a joint.

In each program, the electric current density is assumed to be uniform. The furnace wall is assumed to be at a constant temperature, and heat flow between the electrode surface and the furnace wall is by radiation only. The electrical resistivity and thermal conductivity are both allowed to vary with temperature and radial position. In programs (b) and (c), the steel bath is considered to be at a constant temperature and heat flow between the electrode tip and the steel bath is assumed to be by radiation only. We also assume circular symmetry in the electrode and ignore the proximity of neighboring electrodes. Provisions were made in program (a) to account for skin effect and convective cooling at the electrode surface, and both conditions made only minor changes in the final results.

In program (a), we consider a sectional volume of the electrode, as shown in Figure 1, which is bounded by two radii, and we schematically divide the sectional volume into a matrix of elements by uniformly spaced concentric cylindrical interfaces. The average temperature of an element is represented by the temperature at its nodal point, which is the point at the center of the element. Using the finite difference method, a heat residue equation, which gives the heat flow (or heat residue) into or out of each element, is obtained for each element of the matrix. The first step in calculating the steady state temperatures is to assign "guess" temperatures to the nodal points of the elements. The steady state temperatures are obtained by adjusting the temperature values in the elements by an iterative relaxation method[3] so as to reduce the absolute value of all of the heat residues to some acceptable small value. The steady state temperature distribution is, by definition, that set of temperature values for the elements which gives a zero heat residue for each element in the matrix. In program (b) for the electrode with uniform diameter and flat tip, the matrix is extended from one to two dimensions so that heat can flow axially as well as radially; the interfaces between elements are uniformly spaced planes parallel to the electrode tip. In program (c) for the tapered electrode, the matrix is more complex and contains more elements than the matrix for program (b), but the method is the same.

III. Results

Figure 2 shows the temperatures obtained with program (a) for a 24 in. diam. graphite electrode for several values of current. Typical properties of electrode graphite have been used in the calculations. The results indicate that a current of 100 Kamp or more would cause the temperature at the center of the electrode to be approximately 2500°C or higher; since creep begins to be appreciable and strength decreases in that higher temperature range, these curves show the practical current carrying ability of an electrode of the given diameter. The family of curves also shows that the surface temperature of the electrode increases only slightly as the current is increased; a measurement of surface temperature, therefore, gives very little indication of the temperature at the center of the electrode.

Figure 3 shows the temperature as a function of normalized radius for electrodes of different diameters, all of which carry the same current of 70 Kamp. This type of plot is helpful in selecting the size of an electrode for a given current carrying capacity.

Figure 4 shows the temperature profiles at several axial positions in a 24 in. diam. electrode carrying a current of 60 Kamp as obtained with program (b).

The assumed steel bath temperature was 2700°C.* This temperature, which is one of the variable parameters in the calculations, is intermediate between the melting temperature of pure iron, 1535°C, and its boiling point of 3000°C. The temperature distribution at a distance of 36 in. from the electrode tip is the same as that obtained with program (a). The curves show that the temperature at the tip is very close to the assumed steel bath temperature and the axial temperature gradients are greatest near the tip. There is a large gradient at the outer edge of the electrode tip because the calculations assume the somewhat unnatural condition that the corner element of the matrix radiates to one temperature on the side facing the steel bath and to a very different temperature on the side facing the wall of the furnace.

The programs which have been developed make several simplifying assumptions in the electrode geometry and in the furnace temperatures which are necessary in order to make the problem mathematically tractable. The programs are essentially mathematical tools, which may be modified and refined as desired, and which can be used for calculating the steady state temperatures for electrodes with different physical properties and with varying furnace temperatures.

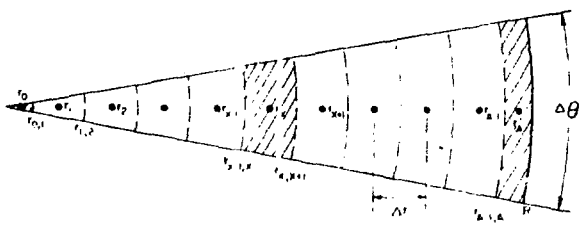


Figure 1. Matrix of elements for program (a), showing element nodal points and interfaces.

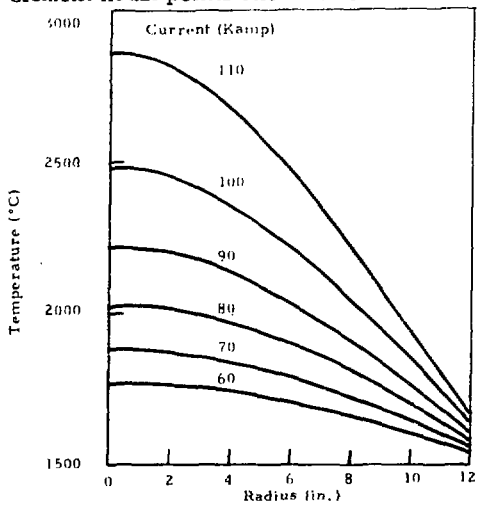


Figure 2. Temperature vs. radius for a 24 in. diameter graphite electrode conducting different currents. Furnace wall temperature = 1500°C.

References

1. Yavorsky, P. J. and Elliot, J. F., Proc. of the 29th Electric Furnace Conference, AIME, December, 1971, pp. 195-202.
2. Carslaw, H. S. and Jaeger, J. C., Conduction of Heat in Solids, Oxford Univ. Press, 1959.
3. Schneider, P. J., Conduction Heat Transfer, Addison Wesley Publishing Co., 1955.

*The "steel bath temperature" is an effective localized temperature directly under the electrode tip which includes the heating effect of the moving plasma of the arc.

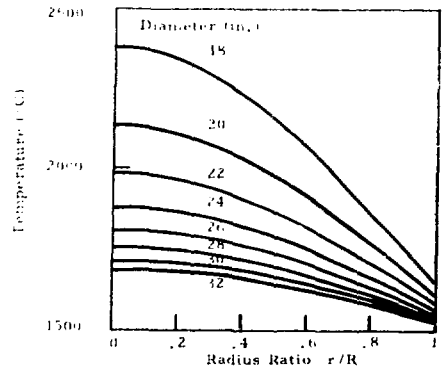


Figure 3. Temperature vs. normalized radius for graphite electrodes of different diameters. Furnace wall temperature = 1500°C. Current = 70 Kamp.

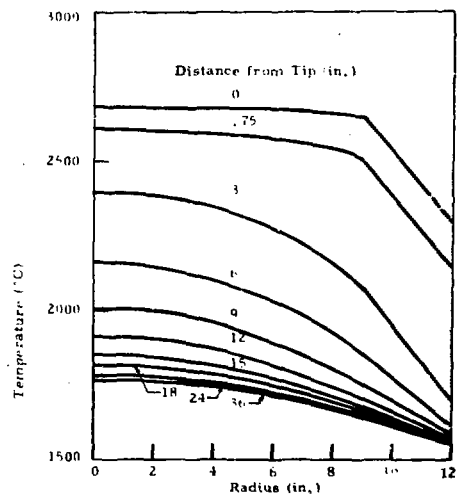


Figure 4. Temperature vs. radius at different distances from tip for a 24 in. diameter graphite electrode. Furnace wall temperature = 1500°C. Effective steel bath temperature = 2700°C. Current = 60 Kamp.

ADHESION CHARACTERISTICS OF THIN VACUUM DEPOSITED CARBON FILMS

N.K. Agarwal, H.Z. Shim and A.D. Haubold
General Atomic Company
P.O. Box 81608
San Diego, California 92138

I. INTRODUCTION

In recent years, highly favorable results have been obtained using low temperature isotropic (LTI) pyrolytic carbons in prosthetic devices requiring a high degree of thromboresistance.[1] The development of vacuum-deposited carbon films was undertaken to extend the application of carbon to geometries and configurations that can not reasonably be fabricated from LTI carbon. The structural, physical and compositional characteristics of vacuum deposited carbon films have been found to be similar to LTI carbon.[2,3]

Thin carbon films have been produced on complex shaped metallic and polymeric bio-implant devices. To be truly useful, however, these films must bond well to the substrate and show good adhesion in service. The bond strength, interfacial characteristics and fracture mechanisms are, therefore, important considerations for successful applications of these films.

Thin film adhesion can be divided into several types: (a) interfacial or monolayer adhesion in which the film and the substrate meet at a well defined boundary is characterized by an abrupt change from the film material to the substrate material in distance on the order of a monolayer thickness; (b) interdiffusion adhesion in which there is a gradual change in composition across the interfacial region which may be several hundred angstroms thick provided there is some solubility of the film and substrate and there is sufficient driving energy to promote diffusion; (c) intermediate layer adhesion due to compound formation at the interface and (d) mechanical adhesion due to interlocking of the film and substrate due to surface roughness. In most cases, the actual adhesion is a result of several of the above types. The most desirable type of interface, from the standpoint of adhesion, is one in which stresses in the interfacial region are distributed over an appreciable volume. This can best be done by grading the composition of the interface from that of the substrate material to that of the coating material. The purpose of this study was to examine the interfacial characteristics of as-deposited carbon films on two different metallic substrates and to determine the obtainable bond strength of carbon films on metallic and polymeric materials.

II. EXPERIMENTAL

Vacuum deposition was used to deposit thin carbon films (~ 4000Å) on metallic and polymeric substrates. The coating apparatus and deposition technique have been described previously.[2] The substrates were sputter-cleaned by inert gas ion bombardment before film deposition and ion bombardment was continued during deposition. The substrate voltage was varied from 1.8 to 4.0 KV, while the argon pressure and deposition rate were kept constant 5×10^{-3} torr and 10A/sec, respectively. The metallic substrates (stainless steel and titanium) consisted of highly polished discs 0.25 inch in diameter and 0.005 inch thick. The polymeric substrate (Vespel-a polyimide) consisted of small cylinders 0.25 inch in a diameter and 0.5 inch long.

Epoxy resin was used to cement the metallic test specimen carefully between identical stainless rods and cured for 48 hrs. The rods were grooved near the ends to promote film debonding somewhere inside the film and not at the edge, so that a true bond strength and not a tearing or peeling strength could be measured. A precision fixture and ball joints used to assure a tensile force normal to the film and along the axes of the rods. Tests were conducted on a standard Instron with a crosshead speed of 0.02 in/min. In the case of polymer test specimens, one end was threaded to provide a good grip while other end was polished before film deposition.

An Auger electron spectroscopy system[4] that employs an in-site ion beam sputtering gun was used for composition depth profiling through the film and for probing the interface. Peak-to-peak heights for carbon and substrate elements were multiplexed and recorded as a function of sputtering time. A complete spectrum was periodically obtained through the film and interfacial region.

III RESULTS AND DISCUSSION

Table I lists the experimental conditions and average bond strengths measured from at least six identical specimens of different substrate materials. Considerable effort was spend in maximizing the adhesive strength of different cements available but nevertheless, in several cases, debonding occured not at the film-substrate interface but at the cement/substrate interface.

Bond strength greater than 5100 psi were achieved for both carbon/stainless steel and carbon/titanium systems. All substrates were sputter cleaned under identical plasma conditions and substrate bias voltage was adjusted to different values during film formation. Excellent adhesion obtained on stainless steel substrate under all conditions indicates ease of thin carbide layer formation at the interface at temperatures as low as 100°C. At higher bias conditions and therefore higher substrates temperatures (>400°C), larger thermal stresses may have contributed to somewhat reduced bond strength. The formation of carbide layer was confirmed by Auger spectroscopy (Fig. 2) and is probably due to effective ion-bombardment cleaning of the substrate which is exposed to highly reactive (partially ionized) carbon vapor during film deposition.

In case of titanium substrates, bond strength increased with higher bias voltage and substrate temperature. These substrates showed higher oxygen concentration at the interface and therefore required somewhat larger activation (higher substrate temperature) for the formation of a carbide layer at the interface. Auger Spectra confirmed the formation of titanium carbide layer at the interface.[5] The thickness of interfacial region in both stainless steel and titanium substrates was estimated to be of the order of a few hundred Angstroms (~ 200-300 A).

TABLE I
BOND STRENGTH OF THIN CARBON FILMS OF STAINLESS STEEL, TITANIUM AND VESPEL SUBSTRATES

Substrate Type	Bias Voltage (KV)	Bond Strength (psi)[a]	Debonded Interface
Vespel	1.6	≈2860 ± 383	Film/Substrate
Stainless	1.8	4957 ± 550	Cement/Substrate
Titanium	1.8	≈1569 ± 203	Film/Substrate
Vespel	1.8	≈3399 ± 587	Film/Substrate
Vespel	2.0	≈3718 ± 1069	Film/Substrate
Vespel	2.2	(b)	(b)
Vespel	2.4	(b)	(b)
Stainless	2.5	4237 ± 390	Cement/Substrate
Titanium	2.5	≈3952 ± 383	Film/Substrate
Stainless	3.0	4563 ± 305	Cement/Substrate
Titanium	3.0	≈5174 ± 331	Cement/Substrate
Stainless	3.5	≈5113 ± 462	Film/Substrate
Titanium	3.5	4258 ± 253	Cement/Substrate
Stainless	4.0	≈5297 ± 469	Film/Substrate
Titanium	4.0	≈4157 ± 420	Film/Substrate

(a) Average of six tests or more (± standard deviation)
(b) Failure occured in the bulk polymer.

The polymer substrate were treated in a weak plasma before film deposition at several substrate bias voltages. Averages bond strengths of more than 3000 psi were measured on most specimens except where the failure occured in the bulk polymer itself. The nature of interfacial region in polymer-carbon system was not examined but is speculated that C - C type bonding may have been established between carbon film and substrate.

CONCLUSIONS

(a) Vacuum deposited thin carbon films adhere strongly to metallic (stainless and titanium) and polymer (Vespel) substrates. The bond strengths are comparable to those achievable with the best available structural adhesives.[6]

(b) Interfacial examination reveals a thin compound layer formation which should ensure good adhesion of carbon films on metallic implant devices.

Supported in part by NIH contract NO1-HV-4-2928.

References

1. J.C. Bokros, et.al., in Chemistry and Physics of Carbon, Vol. 9 (Dekker, New York, 1972) p. 103.

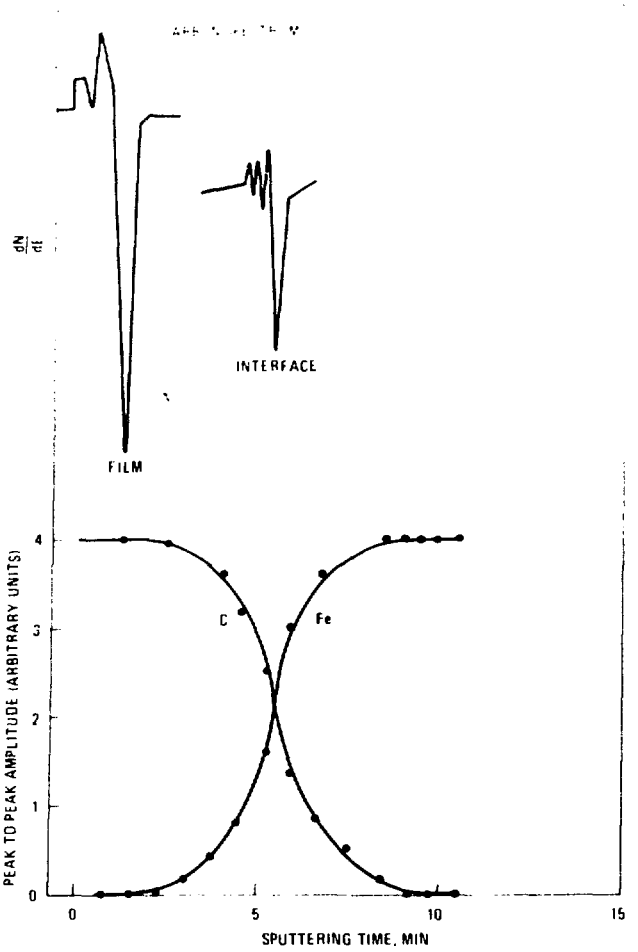


Fig. 1 - Auger depth profile of carbon/stainless steel interface. The change in the shape of carbon spectrum shown at the top is indicative of carbide formation at the interface.

2. N.K. Agarwal, et.al., Thin Solid Films, 37 (1977)

3. H.S. Shim, et.al., Proceedings of 13th Carbon Conference, Irvine, USA (1977).

4. Physical Electronics Industries, Scanning Auger Microprobe Model - 541.

5. H.S. Shim, et.al., Jour. Bioengineering 1 45, 1976.

6. N.J. Delollis, Adhesive for Metals, (pp. 63-64) Industrial Press, New York (1970).

DESIGN AND OPERATION OF A GRAPHITE CREEP IRRADIATION EXPERIMENT*

P. L. Sena, W. H. Cook, J. A. Conlin, and W. J. Lackey
Oak Ridge National Laboratory, Oak Ridge, Tenn. 37830

A series of irradiation tests has been planned to determine the creep characteristics of various graphites of interest to nuclear reactor designers. The graphites selected for testing in the first experiment of this series included grades H-327, H-451, and AFX-5QBG. A constant stress compressive test was selected as the basis for our design.

The primary and secondary creep coefficients will be determined as functions of fluence, temperature, stress, and Young's moduli of elasticity. These data will be obtained with a series of irradiation capsules that are alternately irradiated at 900, 600, and 1250°C in fluence increments of approximately 1, 1, 2, and 4 × 10^{21} neutrons/cm² until each set of test specimens for each test temperature has accumulated a fluence in excess of 8 × 10^{21} neutrons/cm². The compressive stresses at each temperature will be 13.8 MPa (2000 psi) and 20.7 MPa (3000 psi). Each graphite specimen will be characterized before neutron irradiation and subsequently after each accumulated increment of fluence. Each capsule will contain a set of unstressed control specimens that match the stress specimens. Basically, the total creep strains are determined by the dimensional differences between stressed specimens and their matching control specimens after each irradiation. The primary creep strain has been found to be recoverable under irradiation if the stress is removed.[1] Therefore, selected stress-tested specimens will be irradiated again at their test temperature to recover and thereby determine their primary creep strains.

The capsules for these experiments are being irradiated in the E-5 core facility, a flux-trapped position, of the 30-MW Oak Ridge Research Reactor (ORR).

Capsule OC-1, the first experiment in this series, was designed to irradiate twenty-eight 15.24-mm (0.600 in.) dia by 25.4-mm (1.00 in.) long compressively stressed graphite test specimens at 900°C to the first planned exposure level of 1 × 10^{21} neutrons/cm². A compressive stress of 13.8 MPa (2000 psi) was applied to 20 of the specimens in the test by precalibrated metal bellows expanded by gas pressure against the specimen columns. Eight of the specimens in the two columns had reduced diameters so as to increase the stress to 20.7 MPa (3000 psi). The capsule also included 28 unstressed control specimens made of the same types of graphite as were the stressed specimens.

A cross sectional view showing the two stressed specimen columns in the in-core portion of the capsule is shown in Fig. 1. The specimens have shallow holes in each end to accommodate the graphite pins and spacers which serve as centering guides for the specimen column. The force from each bellows at the top of the specimen column was transmitted through a graphite push-rod. At the end of each column, the force was sensed by an LVDT type load cell. Since monitoring of the pressure in the bellows was the primary measure of the load being applied to the specimens, the LVDT-type load cell was intended to provide backup information during the early stage of the irradiation and ensure that the force was indeed transmitted through all of the specimen column.

The unstressed control specimens were stacked and centered in a manner similar to the stressed specimens, except that a longitudinal hole was provided to serve as a guide for the 3.2-mm (1/8 in.) dia stainless-steel sheathed Chromel-Alumel movable thermocouple that was installed in each column. These thermocouples could be moved through a 0.39 m (15 in.) stroke, thus providing temperature traverses from the midplane of the uppermost specimen to the midplane of the lowest specimen in each column.

The capsule was designed to operate on gamma heat alone approximately 100°C below design temperature. A gas gap was provided between the specimen holder sleeve (see Fig. 1) and the water-cooled capsule vessel so that the thermal conductance could be controlled by gas gap size and inert gas composition. Design operating temperature and control were achieved by twenty 1.6-mm (1/16 in.) dia stainless-steel-sheathed MgO-insulated Nichrome V heaters wrapped around the specimen holder as shown in Fig. 1, and retained there by the graphite sleeve that is slipped over the holder.

Because of the need to maintain a precise temperature control along the specimen column, a computer was acquired to control the experiment temperatures automatically and to record the data. Algorithms were developed which related the thermocouple temperatures to the specimen temperatures which the computer used to adjust the heaters to the required operating levels.

Irradiation of capsule OC-1 was conducted from April 1 to May 22, 1976. The capsule was operated at a nominal specimen temperature of 900°C in the ORR E-5 core position for about 34,170 MWhr with the reactor operating at 30 MW for a total peak fluence of about 1.3 × 10^{21} neutrons/cm² (E > 0.18 MeV).

We had difficulty in maintaining the 900 ± 10°C uniform temperature along the length of the specimen columns. Temperatures of the specimens were high and off-design in the upper 16% of the specimen column. In order to maintain the lower part of the specimen column at or near the design temperature, the specimens in the upper 100 mm were permitted to operate at up to about 930°C. Also, the temperature profile along the length of the specimen columns had a small dip approximately one-third of the way down from the tops of the specimen columns throughout the irradiation period. The two movable thermocouples provided direct monitoring of the temperatures along the length

*Research sponsored by the U.S. Energy Research and Development Administration under contract with the Union Carbide Corporation.

[illegible] the graphite [illegible] at the [illegible] as shown in Fig. [illegible].

Power control and data acquisition by the computer worked very well during the [illegible] experiment. The average temperature recorded by two type-S thermocouples located in the graphite specimen holder in each zone was controlled by the computer to within [illegible] from the requested set point as long as adequate heater power was available to the corresponding zones to permit the computer to maintain the requested temperature if the gamma heat profile changed.

Operation of the two LVDT load cell transducers was disappointing. Attempts to calibrate the devices [illegible] before irradiation were largely unsatisfactory. They did respond to specimen loading bellows pressure changes, but large hysteresis effects in the load cell responses were noted as the bellows pressures were changed. This was particularly evident in the West specimen column, and may have been an indication that the bellows specimen stack was becoming wedged, and a ratchetting may have occurred during increases to full reactor power and design operating temperatures. This binding would cause excessive compressive stresses on the specimens due to thermal expansion. Postirradiation examinations of the test specimens indicate that this probably occurred during the irradiation. Results from the creep measurements and other parameters being monitored in this series of tests are being presented by Kennedy [illegible] at this conference.

[illegible] a differential clearance between the specimen centering [illegible] and the ID of the hole in the specimen holder to prevent possible friction forces that may be caused by interference due to thermal expansion and graphite creep of the guides. A pneumatic electromechanical device, designated a PEM cell, has been developed to replace the LVDT type load cell used in capsule OC-1. The new load cell uses metal bellows similar to those used to load the specimen columns. When the load is applied to the specimens, an insulated contact button located inside the PEM cell bellows is in electrical contact with the top flange of the bellows. The PEM cell bellows is then pressurized with helium to a high enough pressure to overcome the load on the specimens and open the electrical contact. By measuring the pressure required and detecting the resistance between the contact button and the grounded bellows (infinite when open), a determination of the load being applied to the specimen column can be made, thus ensuring that the load is indeed being applied to the column. By virtue of its all-metal construction, except for the alumina insulator, we expect the PEM cell to be relatively insensitive to damage from high temperature and radiation.

References

(1) R. J. Price, GA M2352 (November 1, 1972).

(2) C. R. Kennedy [illegible], this conference.

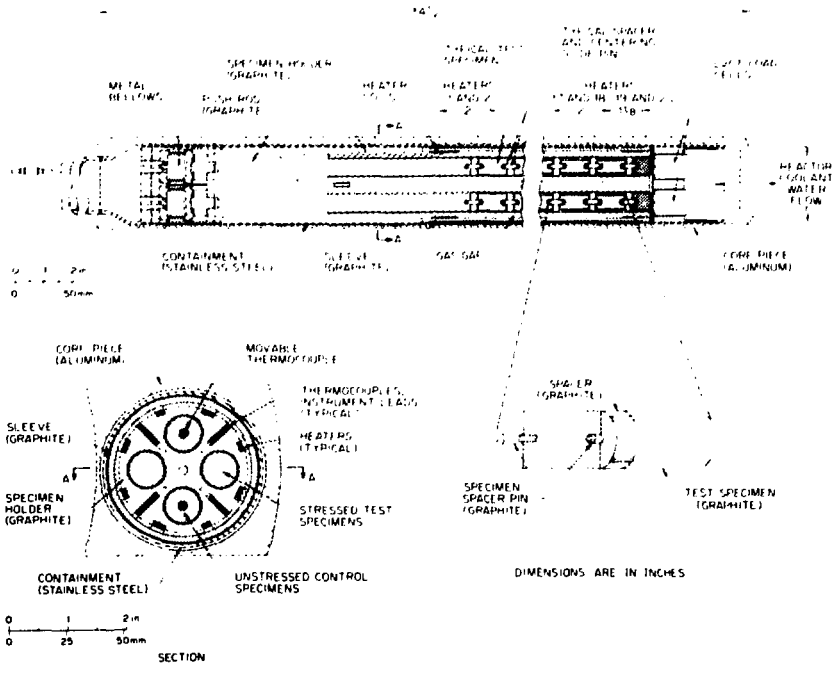
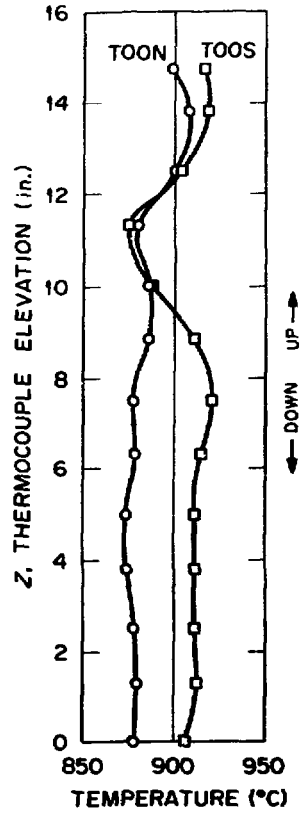


Fig. 1 (Left) Cross-Sectional View of In-Core Portion of Graphite Creep Capsule OC-1. Fig. 2 (Right) ORR Capsule OC-1. Results from Typical Movable Thermocouple Traverse.



RESULTS OF IRRADIATION CREEP TESTING GRAPHITE AT 900°C*

C. R. Kennedy, W. H. Cook, and W. P. Eatherly
Metals and Ceramics Division, Oak Ridge National Laboratory

The displacement damage of graphite under neutron irradiation causes graphite to change dimensions. The dimensional instability requires careful attention when graphite is used as the moderator and reflector structure in nuclear devices. The neutron flux and temperature gradients in the graphite blocks result in time-varying differential growth with resulting stresses similar to thermal stresses with an ever-increasing temperature gradient. Graphite fortunately has the ability to creep under irradiation, allowing the stress intensity to relax below critical levels for fracture. The creep strain also serves to average the radiation-induced strains, thus contributing to the dimensional stability of the core.

Several experimental programs have been undertaken to study radiation-induced creep, but always with the emphasis on creep strain and induced stresses.[1–3] Of secondary interest has been the study of the potentially, equally important dependence of other physical properties upon the creep deformation.[1] It is the purpose of this study to describe the results of the first of a series of creep experiments run in the Oak Ridge Research Reactor (ORR). The details of the elaborate irradiation experiment are described by Senn *et al.*[4] The graphite specimens were compression creep tested in two identical columns at 900°C under design stresses of 13.8 and 20.7 MPa. The grades tested were H-327, H-451, and AXF-5QBG. All of the specimens were stressed in the extrusion direction except for one radial specimen of both grades H-451 and H-327. The AXF-5QBG specimen has been previously compression creep tested by Gray[2] at 800°C, 10.4 MPa, to a fluence of 1×10^{18} (n/m^2). Dimensional changes, electrical resistivities, sonic velocities, and the coefficient of thermal expansion (CTE) to 800°C were measured on each stressed and control specimen in the experiment.

The dimensional measurements of the specimens clearly indicated ratchetting by the load cell readout during the experiment. It appears that each time the reactor shut down, the specimen column shrank, the loading system followed the shrinkage, and jammed solid. Upon startup, the column expanded against the jammed load system to fairly high stresses which then relaxed due to the irradiation creep. Thus, we have three sets of specimens, one set of controls under zero stress, one set of specimens under a constant 13.8 MPa and 20.7 MPa, and one set experiencing creep relaxation of thermal stresses. The latter is an exaggerated condition similar to actual service requirements. The specimens subjected to the ratchetting exhibited deformation several times greater than those under constant stress.

The creep coefficients calculated from the constant stress specimens are given in Fig. 1. These values include corrections for elastic modulus and CTE changes and assumes the primary creep equal to the initial elastic strain. These corrections are confirmed by the H-451 axial data with a wide spread in fluence levels to allow an extrapolation back to the "0" intercept. These results, shown in Fig. 1, are obviously in good agreement with the creep coefficient decreasing linearly with increasing modulus of elasticity. The value of the creep coefficients is also in good agreement with values given by Veringa and Blackstone[3] considering the flux level effect. The uncertainty in the load cell output by irradiation damage precludes accurate calculations of the creep coefficient by the relaxation behavior. However, the total strain introduced into the specimens indicates a creep coefficient of a similar value to the constant stress specimens.

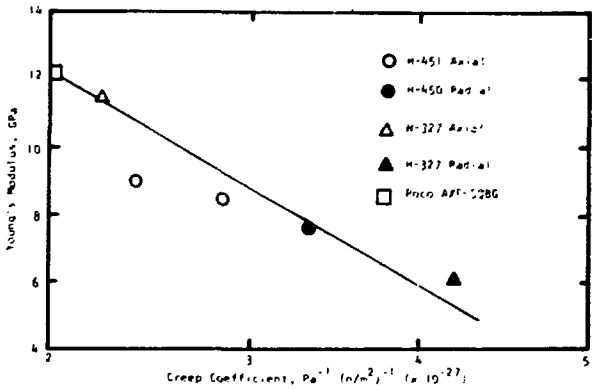


Fig. 1. The Creep Coefficient at 900°C under Compression.

Diameter measurements of the stressed specimens indicate a significant reduction in volume by the compressive stresses. The ratio of the increase in diameter to the axial compressive strain varied from −0.1 to −0.2, significantly less than −0.5 required for no volume change. The decrease in volume was close to 2% for several of the higher strained specimens.

The effect of compressive creep deformation did increase the CTE in a manner similar to the results of Brocklehurst and Brown.[1] The increase in the CTE appears to be linear with the creep deformation as shown in Fig. 2. The values of A and B in the figure are the constants of the equation

$$\text{mean CTE} = A + BT \qquad (1)$$

The values of B are generally similar for all graphites relatively independent of grade, method of fabrication, and preferred orientation. As seen in Fig. 2, the value of B retains this independence of grade and orientation, but increases sharply with deformation. The value of A, of course, is a function of grade and preferred orientation. Therefore, the ratio A/A_0 is used for comparison rather than the actual value as for B. As seen in Fig. 2, the values of A do not increase with deformation as significantly as the value of B.

*Research sponsored by the U.S. Energy Research and Development Administration under contract with the Union Carbide Corporation.

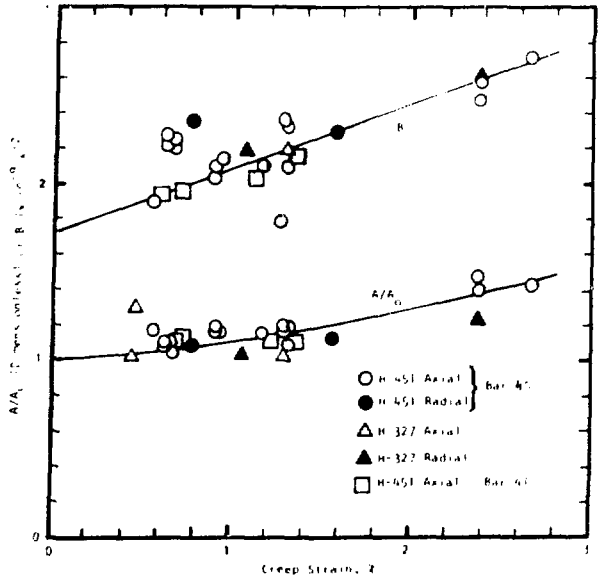


Fig. 2. Compressive Strain at 900°C Increases the Mean Coefficient of Thermal Expansion ($\bar{\alpha}$=A+BT).

The decrease in Young's modulus from the unstressed irradiated control samples by compressive deformation is given in Fig. 3. Apparently, like the CTE, the alteration is independent of the fluence and dependent only upon the total deformation. Poisson's ratio, while virtually unchanged by irradiation without stress, is dramatically reduced to essentially zero by the compressive deformation. This is shown in Fig. 4 for grade H-451.

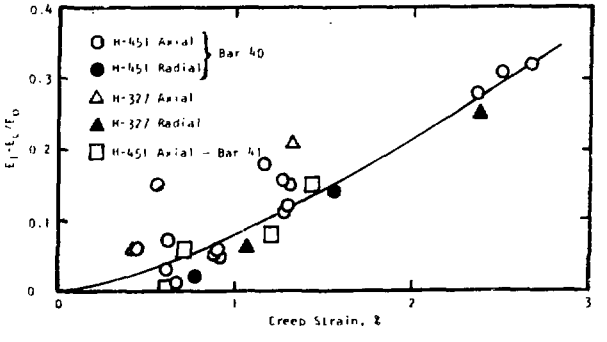


Fig. 3. The Reduction of Young's Modulus by Creep Strain.

The ability of the graphite to sustain compressive strains up to 2.5% have been demonstrated at 900°C. The mechanism of the deformation is at least uncertain; however, it is clear from the physical property measurements that the initial structure has been altered. The reduction in Young's modulus can result from two causes. The first is a flattening of the void volume to reduce the overall spring constants, and the second is a reorientation to increase the anisotropy of the graphite. Both of these events

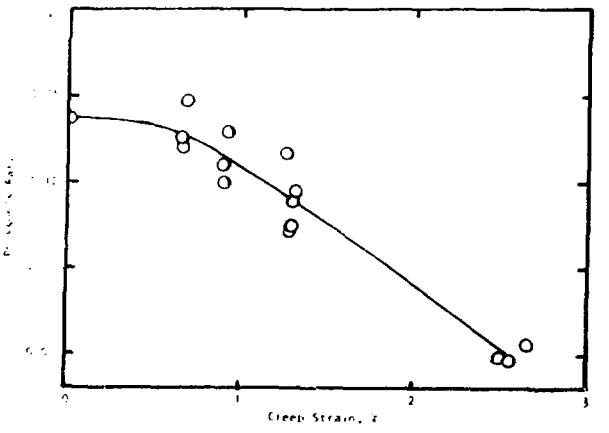


Fig. 4. The Reduction of Poisson's Ratio of Grade H-451 by Creep Strain.

will also increase the CTE as observed. However, the effect of deformation was to slightly and uniformly increase A with a significant increase in the value of B of Eq. (1). This implies that void flattening is the dominant feature in reducing the CTE. This does not infer a healing of the voids, but, to the contrary, the reduction in Poisson's ratio describes an actual decrease in the continuity of the structure. The major implications of these results are:

1. Compressive strains increase the CTE and tensile strains decrease the CTE. The actual magnitudes are larger than reported in the literature in that the creep deformation has a greater influence upon B than A in Eq. (1).
2. The effect of pore collapse and/or reorientation by compressive strains decreases the elastic moduli and very likely the tensile strength of the graphite. This will be of importance in withstanding the reverse thermal stresses during shut-down operations.

References

(1) J. E. Brocklehurst and R. G. Brown, *Carbon* 7, 487 (1969).

(2) W. J. Gray, *Carbon* 11, 383 (1973).

(3) H. J. Veringa and R. Blackstone, *Carbon* 14, 279 (1976).

(4) R. L. Senn, J. A. Conlin, W. H. Cook, and W. P. Eatherly, this conference.

I IRRADIATION CREEP AND ITS FLUX DEPENDENCE ON NEAR ISOTROPIC GRAPHITE AT 850°C

H. Veringa, E.C.N. Petten, Netherlands
M.R. Cundy, Euratom Petten, Netherlands

1. Introduction

An irradiation creep experiment has been performed on a sample of near isotropic H 451 graphite in the HFR at Petten. The irradiation was performed under tension in the axial direction at 850°C up to a fast fluence of $2,8 \times 10^{21}$ ncm^{-2}DNE and resulted in a final creep strain of 0,35%. This paper summarises the irradiation experience and analyses the results.
The purpose of the experiment was to investigate the dependence of the steady state creep rate on the applied stress and on the fast flux density. To achieve this, a single sample of the material was irradiated successively in two positions of the reactor having different flux levels. Clear evidence of a flux effect was observed in that the creep rate, defined as the strain per unit of stress and fluence, showed a strong decrease with increasing flux density.

2. Irradiation Device

Creep is measured continuously during the irradiation using a differential technique /1/. A single cylindrical sample is maintained under a tensile load by a pneumatic bellows system and the resulting dimensional change is compared with that of unstressed graphite reference shells (Fig.1). A sensor is moved alternately between the stressed and unstressed samples. This movement is induced by pneumatic bellows and is detected by a pair of linear displacement transducers. The in-core section of the machine comprises the irradiation samples and flux monitors in a graphite drum. The measuring system bellows and transducers are located out of core in the upper section of the machine. Out-of-pile equipment automatically records creep, sample load, and temperature.

3. Irradiation History

The irradiation was performed in both a low and a high flux position of the reactor. The stress was initially set at 4.56 MPa but after 1170 hrs it was increased to 5,98 MPa. The temperature was controlled in the range 820°C to 850°C throughout the irradiation. At 2700 hrs the measuring system became unreliable due to debris becoming trapped between the sensor and the sample.

4. Results

The irradiation device was well suited to perform elasticity tests both before and during irradiation. The results are shown in Fig.1. It can be seen that during irradiation the Young's Modulus undergoes an increase which is equal to or higher than increments measured on irradiated but unstressed samples of the same graphite Fig.2. This accords well with the dislocation model, and previous results /2/ indicating that creep causes no decrease in the Young's Modulus as long as no accelerated or tertiairy creep is taking place.

The creep strain and temperature are plotted as a function of neutron fluence and time in Fig.3. The transient creep at the start of the irradiation was low in comparison with other published results /3/ and the saturation dose was also low. However, it should be noted that in order to decrease the risk of failure during irradiation, a tensile test was performed before irradiation up to 80% of the quoted ultimate tensile stress /4/. A reasonably large permanent set, resulting in a high back stress, may have been introduced in the graphite /5/ which during the first step of irradiation had to be recovered and thus considerably reduced the transient creep. The transient creep contribution after the stress increase was in better agreement with that expected /3/. In the successive irradiation periods, reasonably accurate values for the steady state creep coefficient could be established Fig. 3.
It can be seen that on the one hand an increase in stress of approximately 30% has nearly no influence on the creep coefficient but on the other hand, it decreases with an increase in the neutron flux density. Both observations can be explained by the theoretical models for irradiation creep in graphite /6/ /7/, particularly the flux density dependence which was also demonstrated in the restrained shrinkage experiments /6/.

5. Conclusions

- The steady state creep rate is nearly independent of the applied stress
- The creep rate increases with decreasing neutron flux density (at least in the range $(1.2 \times 10^{14}$ ncm^{-2}s^{-1})
- Transient and steady state creep has not caused mechanical deterioration of the graphite at fluences lower than 2.10^{21} ncm^{-2}.

6. References

1. Hausen H,Lölgen R, Cundy M, Journal Nuc.Mat. Vol. 65 (1977) p 148
2. Veringa H,Blackstone R,Lölgen R, Proc. 2nd International Carbon Conf. p 361 Baden-Baden 1976
3. Kleist G, Leushacke D, Schuster H, Proc. 2nd International Carbon Conf. p 345
4. Engle G, Price R, Johnson W, Beaven L, General Atomic Report GA-A12944 UC7
5. Jenkins, Brit.Journal Appl.Phys. 1962 Vol 13, p30
6. Veringa H, Proc. 2nd International Carbon Conf. p 322
7. Kelly B, Foreman A, Carbon 12. 151 (1974)
8. Veringa H, Blackstone R, Carbon 14, 279 (1976)

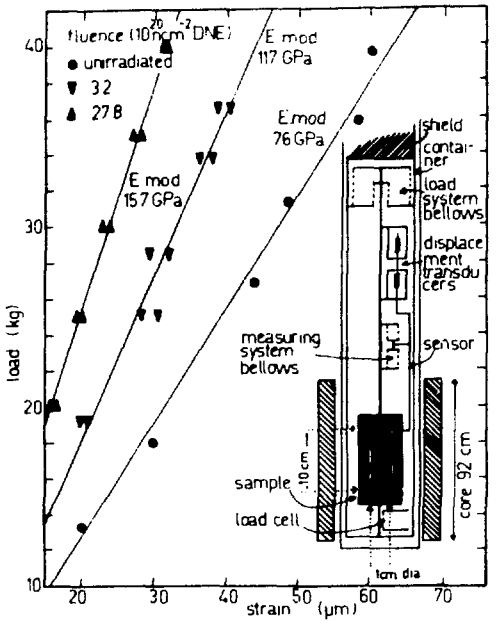


Fig.1 Load-deflection measurements before, during and after irradiation and schematic of strain registration system

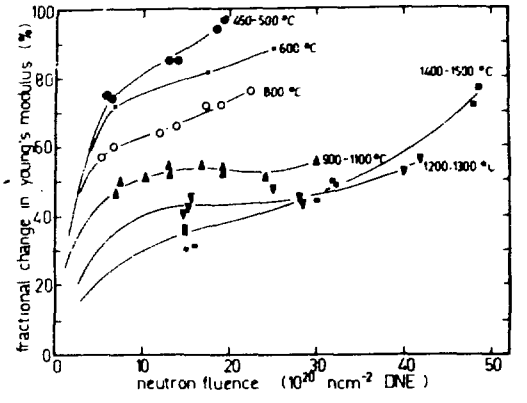


Fig.2 Change in Youngs Modulus of H451 graphite for both head directions

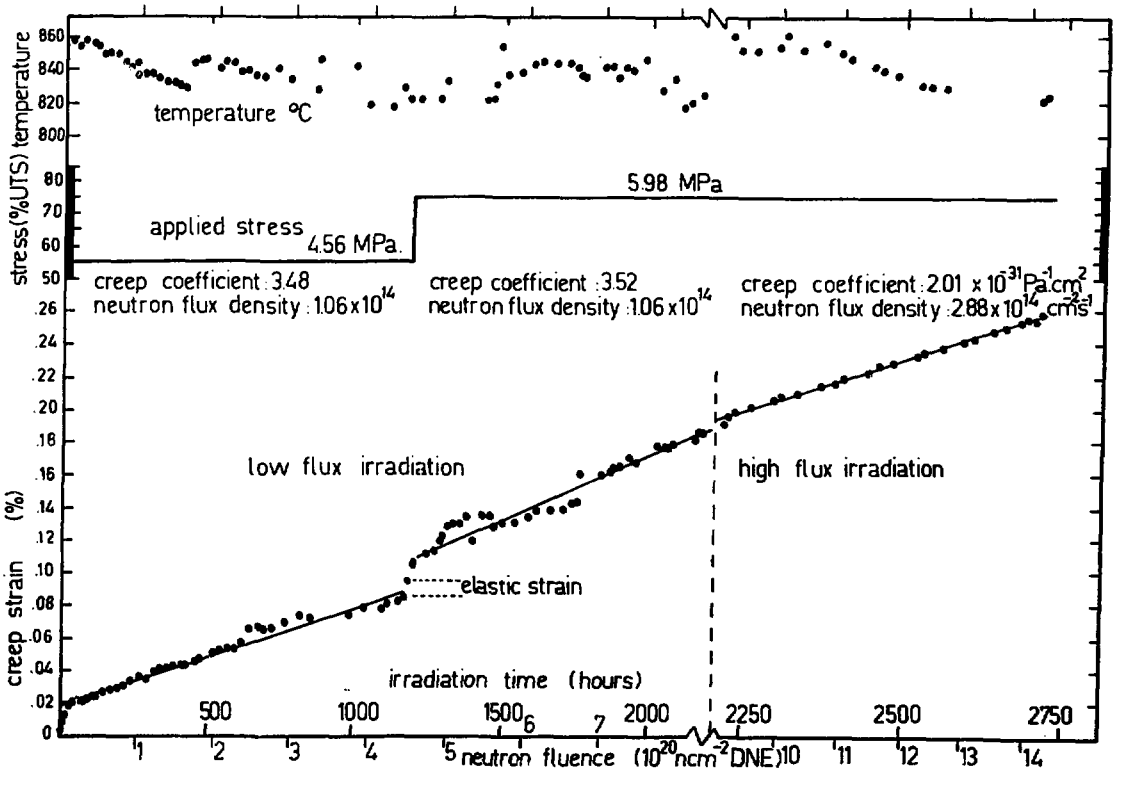


Fig.3 Irradiation History

NONDESTRUCTIVE TESTING I:
CORRELATION OF DETECTABLE FLAW SIZE WITH GRAIN STRUCTURE BY ULTRASONIC TECHNIQUES IN GRAPHITE

J. F. Rosendahl, J. T. Gill, L. D. Fiel
POCO Graphite, Inc.
Decatur, Texas 76234

Ultrasonics is a branch of acoustics dealing with periodic waves of frequencies above the audible range (greater than approximately 20,000 Hertz). The maximum usable ultrasonic frequency is about 10^{10} Hz, corresponding to a wavelength in air of about 3.4×10^{-6} cm and in water of 1.5×10^{-5} cm. Because of their short wavelength, ultrasonic waves travel through a medium in much sharper beams and can form sharper shadows than can audible or low frequency sound waves. Hence, they can be used to detect small flaws, voids, or inclusions in a given material.

The standard ultrasonic sources are piezoelectric and magnetostrictive ocsillators. Both of these are electroacoustic transducers, whose flexibility depends on the design and limitations of the oscillating electrical circuits. Since ultrasonic waves of sufficiently high frequency and intensity can be made to travel in a beam with little spreading, such a beam can explore a physical medium and detect nonhomogeneities in it by reflection. This is the principle of the Ultrasonic Reflectoscope, invented by F. A. Firestone, in which an ultrasonic beam or pulse penetrating a material produces an echo when it strikes a flaw or discontinuity that has different acoustical properties from the surrounding material. This echo can be detected by the same transducer that emits the original pulse.

An important factor in ultrasonic flaw detection is the particular material being inspected. Certain characteristics of the material determine the size of the smallest detectable defects. One of these is called back scattering. A certain amount of the energy from the incident ultrasonic beam will be scattered back to the transducer because of tiny individual reflections from the grains or characteristic voids in the material in which it is propagating. This residual acoustic "noise" will set a limit on the size of a defect than can be detected. Graphite is a material which is particularly susceptible to this problem. Another factor limiting the size of detectable flaws is overall attenuation of the ultrasonic beam. As the beam travels through the material, its strength continually decreases, due to beam spreading, back scattering, etc. Thus, the minimum detectable defect is a function of its depth in the material and of the scattering and other attenuative properties of the material being inspected.

Another factor affecting response is the nature of the defect (voids or inclusions). The strength of the reflection from a defect depends on the relative acoustic impedances between the medium and the defect; therefore, more energy would be reflected from a void of a given size than from an inclusion of the same size because only a portion of the energy is reflected from the inclusion (the remaining energy travels into and past the inclusion).

The ultimate criterion for defect resolution is its size relative to the wavelength of the ultrasonic pulse. As a rule-of-thumb, a flaw is considered to be potentially detectable if its relative dimensions are no smaller than one-half the wavelength of the ultrasonic wave passing through the graphite.

The wavelength of an ultrasonic pulse traveling through a material can be expressed as:

$$L = \frac{1}{f}\sqrt{\frac{E\,(1-\mu)}{\rho\,(1+\mu)\,(1-2\mu)}} \qquad (1)$$

where L = wavelength
f = frequency
E = Young's modulus
ρ = density
μ = Poisson's ratio

The velocity of the ultrasonic wave can be expressed as:

$$c = Lf \qquad (2)$$

$$c = \sqrt{\frac{E\,(1-\mu)}{\rho\,(1+\mu)\,(1-2\mu)}} \qquad (3)$$

Obviously, the higher the frequency of the ultrasonic wave, the smaller the flaw that can be detected. However, as previously mentioned, graphite is a highly attenuative material for ultrasonic waves. The attenuation is strongly dependent on the frequency; the higher the frequency, the more attenuative graphite becomes. These attenuation properties of graphite limit the upper frequency which can be used for adequate penetration; thus, limiting the minimum detectable flaw size.

An experiment was devised in order to determine if any correlation exists between the grain structure (size) and the resolution of detectable flaws in graphite using ultrasonic techniques. Six grades of graphite were selected for this experiment. The grain structure ranged from moderately coarse to fine-grain. Each grade of graphite was machined into a 1" x 2" x 6" test block, and a series of seven calibration holes were drilled on one end and one side of each test block. The holes ranged from 0.0135 inches in diameter to 0.2010 inches, and were approximately one-half inch deep.

These calibrated test blocks were

subsequently tested using ultrasonic techniques. The materials with coarser grain structure exhibited more back scatter and "noise", limiting the resolution of the smallest detectable flaw size. The finer grain materials showed less back scatter, were less attenuative to ultrasonic waves, and smaller defects could be dectected.

References

1. Frederick, Julian R.: Ultrasonic Engineering, John Wiley & Sons, Inc., 1965.

2. Babikov, O. I.: Ultrasonics and Its Industrial Applications, Consultants Bureau, 1960.

3. Carlin, Benson: Ultrasonics, McGraw-Hill Book Company, Inc., 1960.

4. Goldman, Richard: Ultrasonic Technology, Reinhold Publishing Corp., 1962.

5. Brown, Basil: High-Intensity Ultrasonics, London Iliffe Book Ltd., 1965.

6. Hueter, T. E.: Sonics, John Wiley & Sons, Inc., 1962.

7. Baker, R. A., et al: Ultrasonic Characterization and Computerized Analysis of Graphite Billets, Sandia Laboratories Report No. SC-DR-70-763, December 1970.

8. Baker, R. A.: Ultrasonic Evaluation of Carbon-Carbon Composite Materials, Sandia Laboratories Report No. SC-R-70-4389, October 1970.

9. Serabian, Steven: Influence of Attenuation Upon the Frequency Content of a Stress Wave Pocket in Graphite, the Journal of Acoustical Society of America, Vol. 42, No. 5, 1052-1059, November 1967.

10. Cook, J. L.: Correlation of Nondestructive and Mechanical Testing of Graphite, McDonnell Douglas Astronautics Company, Report No. DAC-62118, February 1969.

11. Stinebring, R. C.: Application of Nondestructive Testing Techniques for Evaluating and Characterizing Graphite and Ceramic Materials, AVCO Corporation, Report No. AFML,TR-69-163, June 1969.

NONDESTRUCTIVE TESTING: II.
X-RAY IMAGING OF GRAPHITE AND GRAPHITE PRECURSORS

J. T. Gill, J. F. Rosendahl, L. D. Fiel
POCO Graphite, Inc.
Decatur, Texas 76234

The purity and structural uniformity of specialty grade graphite must be very high, and many applications of these high quality materials require that each individual piece be tested. Purity tests can be made from statistical approaches. However, structural uniformity quality control must be performed on each end use piece, and these quality control tests cannot be destructive ones. Therefore non-destructive test methods must be used, and these methods must 1) identify any structural defects which would adversely affect performance of the material in a particular application, and 2) permit indentification of these defects at significant resolutions.

X-ray imaging is one technique of quickly finding, classifying and analyzing structural defects both in graphite precursors and in final graphite products.

The apparatus which was used in these studies is a 250 KV X-Ray unit manufactured by Diano Corporation.

Standard graphite blocks made from coarse grain and fine grain graphites were used as reference materials. To determine the resolution of the instrument on these materials, holes of various sizes were drilled into these graphite blocks. The blocks were then X-rayed, and instrument settings were noted which allowed the resolution of void-type defects in size ranges set by the sizes of the drilled holes. The holes were then filled with ungraphitized carbon dust, with ungraphitized carbon rods, and with graphite rods which had been graphitized to different temperatures, and the instrument settings for resolution of impurity-type defects in graphites were noted. Resolution of defects in these graphite structures is related to grain size in the base graphite materials. Therefore photomicrographs of the graphite structures were made, and graphite particle size as measured from these photomicrographs is related to resolutions which are possible in coarse and fine grain graphite.

A non-destructive test method such as X-ray imaging can be very useful in determining the uniformity of a cabon or graphite material prior to impregnating it with some non-carbonaceous material, particulary metals. Standard carbon blocks with various size holes drilled in them were used to correlate instrument resolution with void-type discontinuous areas in these blocks, enabling these discontinuous areas to be detected prior to incorporation of metals throughout the billet.

In order to study the utility of X-ray imaging on graphite/metal composites, graphite blocks which had been impregnated with metals and had various size holes drilled in them were used. Again, resolution limits on these materials were found by noting instrument settings at which the holes, which would correspond to unimpregnated or discontinuous areas, could be seen.

THE EFFECT OF ALIGNED MATRIX MATERIAL ON THE MECHANICS OF CRACKED FIBERS

E. L. Stanton

Prototype Development Associates, Inc.
Santa Ana, California 92705

Introduction

The present study examines computationally a crack problem with finite geometry and two orthotropic phases intended to represent a cracked graphite fiber surrounded by an aligned matrix phase or sheath. The scope of the study is strictly heuristic and is not intended as a replica modeling of any particular fiber-matrix system although representative elastic constants are used. Recent studies of an isotropic finite dimensional bar with a penny shaped crack [1] are used as a control problem to verify the computational model.

The Model

The control problem was modeled using symmetry with two isoparametric finite elements, Figure 1, with their parametrization adjusted to give singular strains in any direction emanating from the edge of the crack. This model produced good agreement with the earlier results of Gykenyesi and Mendelson for crack opening displacements and stresses in the neighborhood of the crack. The same geometric model was used for the fiber-matrix problem with properties as follows:

$E_T = 2$ msi , $E_L = 57$ msi (Fiber)

$E_T = 2$ msi , $E_L = 80$ msi (Aligned matrix)

$G_T = 0.5$ msi , $G_{TL} = 1$ msi (Both)

$\nu_T = 0$, $\nu_{TL} = 0.05$ (Both)

Note that high E/G ratios tend to reduce the accuracy of a model but should not change the character of the solution. Several boundary conditions were analyzed that produce uniform stress, uniform strain and uniform displacement respectively in the axial direction. The uniform strain condition was simulated by applying a uniform axial stress to each phase in proportion to its axial stiffness and is most representative of conditions in a long fiber. In all cases the total force applied to the model was constant and equal to that in the control problem. The high axial modulus of the aligned matrix simulates conditions thought to occur during processing. Note that this alignment of the basal planes is opposite to that of the sheath phase associated with densification by chemical vapor deposition (CVD).

Results

The crack opening displacements shown in Figure 2 for the isotropic case have nearly damped out at the loaded surface. Significantly larger crack opening displacements occur in the graphite fiber for both uniform stress and uniform strain boundary conditions as a result of the low shear modulus. They are respectively 1.25E-4, 2.50E-4, and 1.77E-4 inches for the isotropic uniform stress, orthotropic uniform stress and orthotropic uniform strain conditions. The appearance of the deformations in the uniform strain case is nearly identical to that in Figure 2 when normalized to the same scale. However, the uniform stress case resulted in clearly visible axial displacements at the loaded surface when displayed to the same scale. The uniform displacement boundary conditions produced an unusual result that may be more a mathematical curiosity than fiber-matrix mechanics. In this case the center of the crack surface displaced very little producing a shape like the beam function associated with a unit rotation at the edge of the crack.

The axial stress in the plane of the crack as a function of the parametric coordinate, $\xi = \sqrt{r/0.77}$, is shown in Figure 3 for the control problem and the orthotropic uniform strain case. Stresses proportional to the square root of the radius appear as linear functions of this coordinate. The finite element stresses are recovered at the Gaussian points and extrapolated to the boundary which accounts for their finite amplitude. Note that the axial stress in the orthotropic matrix material is higher and a more nonlinear function of the parametric coordinate indicating the strength of the singularity has increased. This one parameter, however, does not adequately describe the mechanics of the cracked fiber-matrix system. A contour plot of the ϵ_{13} shear strain over the Z_1 , Z_3 face of the two element model, Figure 4, shows this strain propagates strongly all along the fiber-matrix interface. As a result of this behavior, the crack would be more likely to result in disbonding of the two phases than fracture of the matrix phase in the plane of the crack. The driving force for this behavior can be explained in terms of the equilibrium equations

$$\sigma_{11,1} + \sigma_{12,2} + \sigma_{13,3} = 0$$

$$\sigma_{31,1} + \sigma_{32,2} + \sigma_{33,3} = 0 \qquad (1)$$

in which the terms $\sigma_{12,2}$ and $\sigma_{32,2}$ are zero by virtue of axial symmetry. The sharp gradient in the radial stress in the radial direction, $\sigma_{11,1}$ is accentuated by the bimaterial interface as is evident from the ϵ_{11} strain contours shown in Figure 5. It is also evident from these contours that greater modeling detail would be required to obtain high resolution of the stress response. Nevertheless these figures provide an insight into the mechanics of the problem comparable to photoelastic analyses.

Conclusions

The results presented indicate that a cracked fiber with an aligned matrix phase is likely to disbond at the fiber-matrix interface under uniform axial strain conditions. Computational mechanics in this case provided an insight into material behavior comparable to photoelastic studies in isotropic models. This is a particularly useful approach in the study of load redistribution in highly anisotropic carbon composites damaged during processing.

References

1. Gyekenyesi, J. P. and Mendelson, A., "Three-Dimensional Elastic Stress and Displacement Analysis of Finite Geometry Solids Containing Cracks," NASA TM-X-71467, 1974.

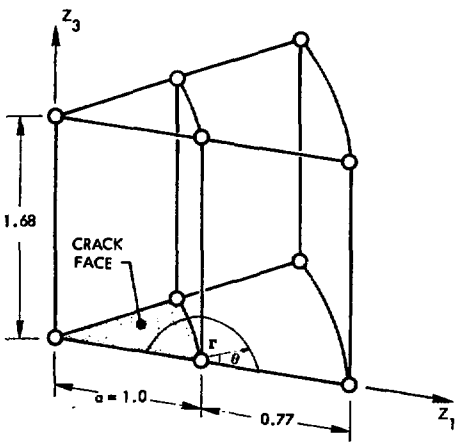


Figure 1. PATCHES-III model of cracked fiber

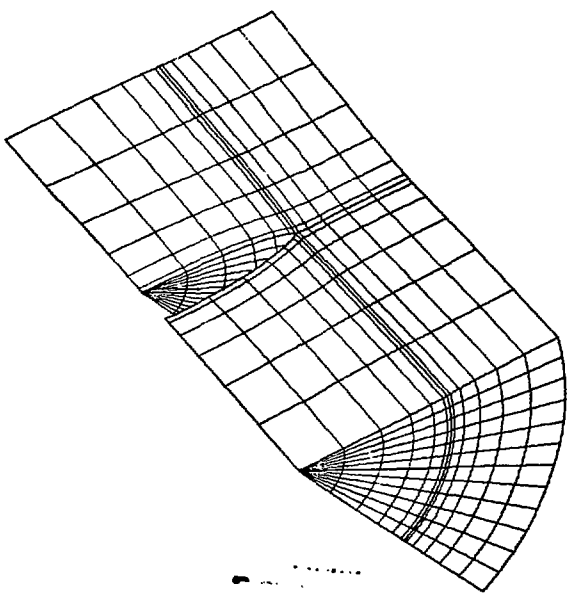


Figure 2. Cracked fiber elastic deformations

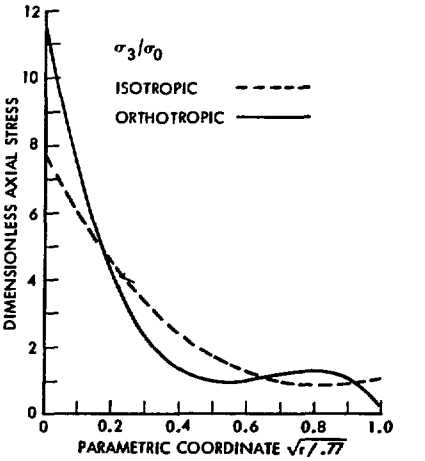


Figure 3. Axial stress comparisons

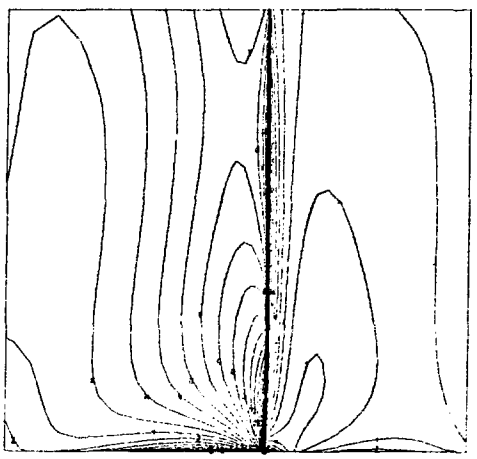


Figure 4. Shear strain contours ϵ_{13}

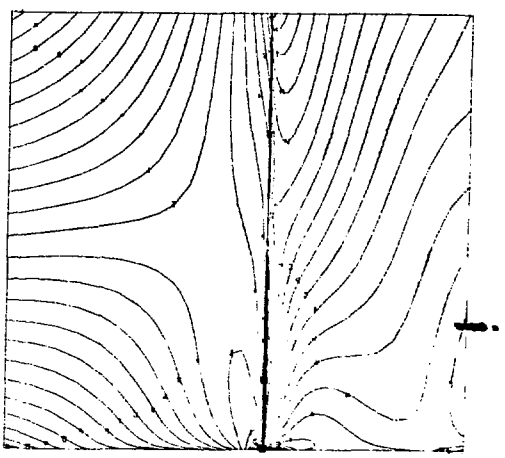


Figure 5. Radial strain contours ϵ_{11}

A PHYSICALLY BASED ANALYTICAL TENSILE MODEL FOR CARBON-CARBON COMPOSITES

J. S. Evangelides
The Ivan A. Getting Laboratories
The Aerospace Corporation
P. O. Box 92957, Los Angeles, California 90009

The unique thermostructural properties of carbon-carbon composites has afforded an opportunity to achieve significant improvements in reentry vehicle and rocket nozzle performance. The increasing use of carbon-carbon composites has created the need for an analytical model to predict composite properties. Such a model, if it is to be of use to the processor as well as the designer, must be physically based using identified microstructural characteristics with micromechanical principles to predict composite stress-strain behavior. The objective of this effort was directed towards developing an analytical model for composite tensile behavior. The development of such a model combined with experimental verification can provide a means of predicting optimum microstructural features, effect of defects, and failure criteria. Therefore, the model can provide guidance for materials research and development as well as inputs to structural analyses.

The analysis and modeling of carbon-carbon composites requires an understanding of the influence of many composite microstructural variables: filaments,matrices, filament-matrix interactions, construction parameters and processing procedures. Consequently, the initial steps in this study were to identify the microstructural characteristics and to determine the mode and sequence of constituent failures. The microstructural characteristics of interest, filament and matrix orientation and microcracking, have been described in Reference 1. The crack propagation studies were conducted in the scanning electron microscope to identify the microstructural parameters that control crack initiation and propagation (Ref. 2). Previous work on carbon-carbon composites have shown that the crack path was controlled by the highly oriented lamina in the matrix and that fracturing occured not at the fiber-matrix interface but within the matrix (Ref. 3). Model input parameters were obtained from these experimental measurements or observations in order to eliminate the necessity for estimating parameters.

Th ability to predict the uniaxial tensile properties of a multidirectional composite by a physically based analytical model reguires the input of unit cell properties. This in turn requires the development of longitudinal and transverse unidirectional property models. A longitudinal model has been developed and reported previously (Ref. 4). This model could predict the experimental stress-strain behavior of carbon-carbon composites manufactured by high and low pressure procedures. In addition, the significant effect of bent filaments on strength was first predicted by the model and then confirmed by crack propagation tests in the SEM.

Through the longitudinal modeling efforts and microstructural analyses, the exceptionally high and difficult-to-explain modulus of composites fabricated by low pressure procedures was attributed to the highly aligned graphitic planes laying parallel to the filaments. A similar problem exists in attempting to explain the extremely low transverse modulus of such unidirectional composites. One mechanism proposed to explain the experimental data was that the majority of the filaments are not bonded to the matrix (Ref. 5). However, analyses of the fracture faces of transverse tension specimens indicated that the majority of the filaments had matrix bonded to them. Consequently, other mechanisms must be sought. One, following along similar lines, is that circumferential microcracks exist in the sheath surrounding the filaments. Another mechanism to be discussed deals with modeling the composite based on the microstructural features of the matrix phase.

The transverse model consists of filament, sheath and bulk matrix containing porosity arranged in series with equal stress in each. On the basis of the photomicrograph and sketch of a transverse view of a unidirectional composite in Figure 1, it is suggested that the sheath can be taken as well aligned graphite planes containing 90-deg kinks across the entire composite cross section. This description, which is idealized in Figure 2, is completely consistent with the longitudinal model already developed.

The sheath modulus was calculated using the equation for a kink along 100% of the sheath length:

$$E_{ts} = E_t \left\{ \frac{3\pi}{4} \left(\frac{R}{K} + 1 + \frac{E_t}{2G_t} \right) \right\}^{-1}$$

where R = kink radius
E_t = single crystal Young's modulus
G_t = single crystal shear modulus
$K = R - T_s/\ln((R + T_s/2)/(R - T_s/2))$
T_s = Sheath thickness

For a Thornel 50 filament with a 6 μm diameter and sheath thickness of 0.5 μm, the calculated modulus was 0.10×10^6 psi . The transverse modulus of a Thornel 50 fiber has been measured at 0.65×10^6 psi (Ref. 5).

A number of approaches exist for calculating the modulus of the bulk matrix which was assumed to be a porous isotropic material. An approach by Greszczuk calculates the average stress and strain in an isotropic elastic body containing a square array of cylindrical pores (Ref. 7). A second approach, by Mackenzie, calculates the shear modulus by applying a homogeneous shear to a large sphere containing a pore (Ref. 8).

Wagner, O'Rourke, Armstrong measured the tensile and shear moduli and Poisson's ratio of an isotropic bulk graphite with a 15 to 31% range in porosity (Ref. 9). The results of this study were compared to Greszczuk and Mackenzie assuming Poisson's ration independent (ν) and dependent ($\nu = Fn(V_p)$) on porosity (Fig. 3). The tensile modulus of a coal tar pitch bulk matrix was obtained from the experimental data of Eitman, Greszczuk, and Jortner (Ref. 5). The tensile modulus of the pitch with 40% porosity was 0.52 x 10^6 psi. Using Mackenzie's equation and assuming a Poisson's ratio of .24, E_o was calculated to be 2.48 x 10^6 psi.

The effective composite transverse modulus (E_c) for representative Thornel 50-pitch composites is shown in Table 1. Porosity was found to have a smaller effect than anticipated. Decreasing the porosity by one-half resulted in only a 13% increase in modulus. These calculated moduli compared favorably to the experimentally measured valves of 0.15 to 0.30 x 10^6 psi. (Ref. 5).

Another mechanism must account for the lower range of these experimentally measured moduli. Micrographs and x-ray radiographs of these composites indicated that extensive macro/microcracking was present. Therefore, the displacements due to the presence of cracks must also be considered. Based upon the work of Tada, Paris, and Irwin (Ref. 10), the displacements associated with a crack of length 2a in a body of width 2b and height 2h was calculated. Assuming the composite is uniform body with average properties, the effective transverse composite modulus was calculated for a composite specimen (0.70 x 0.25 x 0.25 inch) with various a/b ratios (Ref. 11). It is seen from Table 1 that the scatter in the experimental measurements can be predicted by these analyses.

The combination of microstructural analyses to characterize composite structure and crack propagation modes, and micromechanical principles can be used to develop a physically based composite model. The transverse model being developed can predict the experimental modulus of unidirectional composites only when the matrix is taken as a highly aligned sheath containing kinks.

Acknowledgments

This work was supported by the Naval Surface Weapons Center under Air Force Contract No. F04701-76-C-0077.

References

(1) J. S. Evangelides, 13th Conference on Carbon Extended Abstracts, (1977)
(2) J. S. Evangelides, 12th Conference on Carbon Extended Abstracts, p. 93 (1975)
(3) J. S. Evangelides, et. al., TOR-0076(6726-01)-1 The Aerospace Corporation (September, 1976)
(4) J. S. Evangelides, Army Symposium on Solid Mechanics, (September 1976)
(5) D. Eitman, et. al., MDC G4730, McDonnell Douglas Astronautics Company (July 1973)
(6) D. L. Lowe, DIN 76SDR 2329, General Electric Company, (July 1976)
(7) L. G. Greszczuk, NASC Contract N00019-72-0221, (May 1973)
(8) J. K. Mackenzie, Proc. Phys. Soc. A. 65, 349 (1955)
(9) P. Wagner, et. al., J. Am Germ. Soc. 55, 214 (April 1972)
(10) H. Tada, et. al., Stress Analysis of Cracks Handbook, Del Research Corp., (1973)
(11) J. S. Evangelides, et. al., TOR-0077(2726-05)-1 The Aerospace Corporation (March 1977)

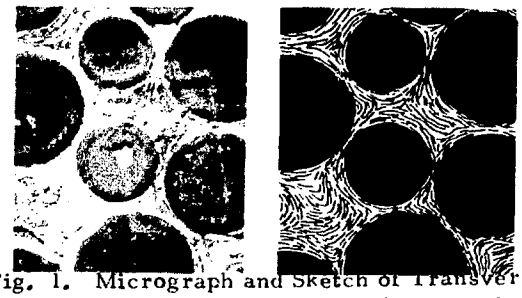


Fig. 1. Micrograph and Sketch of Transverse Section of Unidirectional Composite

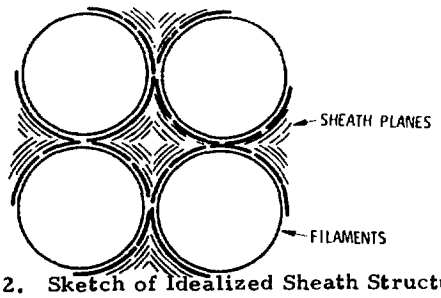


Fig. 2. Sketch of Idealized Sheath Structure

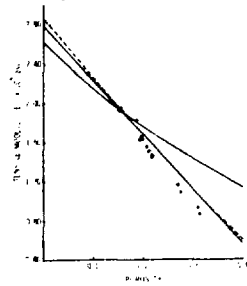


Fig. 3. Effect of Porosity on Tensile Modulus

Table 1. Predicted Transverse Moduli

Porosity	Matrix Modulus (10^6 psi)	Fracture (%)	a/b	Composite Modulus (10^6 psi)
15	1.77	1	0	0.20
10	1.99	8	0	0.23
			0.20	0.21
			0.50	0.18
			0.75	0.15
5	2.24	13	0	0.26

Filament Modulus = 0.65 x 10^6 psi
Sheath Modulus = 0.10 x 10^6 psi
Filament Fraction = 60%
Sheath Fracture = 22%

APPLICATION OF FRACTURE MECHANICS FOR C/C-COMPOSITES

E. FITZER, K. KARLISCH

Institut für Chemische Technik
Universität Karlsruhe,W.-Germany

C/C-Composites are known to be a carbon material with high strength and high stiffness. As described by TERWIESCH,1972, HILL et al., 1974, and FITZER et al.,1976 the properties of the reinforcing fibres can be utilized up to 100% in unidirectionally reinforced C/C-composites. All C/C-composites however show brittle fracture behaviour with a maximum strain to failure of about 1% only. Our studies are based on C/C-composites prepared with pitch as carbon matrix precursor. All samples have been carbonized up to 1400°C preceded by an autoclave baking under elevated gas pressure up to 550°C, and densified by repeated impregnation/recarbonization cycles. The resulting carbon/carbon-composites have typical bulk densities of about 1,7 g/cm^3 and maximum flexural strengths up to 1200 MN/m^2 in the case of unidirectional reinforcement with 5o vol.% of the fibre. C/C-composites with similar properties can be prepared by CVD impregnation of preformed carbon fibre frameworks with pyrocarbon.

In modern fracture mechanics critical stress intensity factors are widely used for characterization of fracture behaviour of common engineering materials. Also for fibre reinforced composites critical stress intensity factors were published by McGARRY et al.,1972, GAGGAR,1975,but only for glass-and carbon-fibre reinforced composites with epoxy matrix. The authors pointed out that meaningful results can only be obtained if the crack is growing in direction of a notch, which is parallel to the reinforcing fibre-or fabric-direction. Because of limitations in the size of the available sample material, it was necessary to modify the ASTM Norm STP 463 for our own measurements. The geometry of the samples is shown in Fig.1. The sample size was varied with maximum values of B=10mm, 2 H=4 mm, and w=36 mm . As far as primary notches are concerned notch lengths between o,4 and 5 mm were tested. In the case of notches parallel to the fibre direction no infinitesimal curvature at the tip of the notch is necessary, as has been proved for ceramic material by PABST, 1973.

There might exist principal doubts whether stress intensity factors of C/C-composites can be meaningful, especially if the limited sample size is taken into consideration. The present study should indicate, whether reproducible measurements can be performed and useful fracture mechanical data can be obtained.

Systematic studies of the effect of geometrical sample dimensions on the stress intensity factor were performed with C/C-compsoites containing 35 vol.% of stacked graphitized fabrics, type SIGRATEX GDS 8-30. The layers of fabric were oriented perpendicular to the tensile direction, the notch being applied parallel to the warp direction of the fabric.

Typical diagrams showing the dependence of crack mouth opening as function of the applied tensile force can be recognized in Fig.2. The analytical calculation of stress intensity factors from the experimental data was performed using the following equation 1 which is valid for a compact tension specimen:

$$K_Q = \frac{P \cdot \sqrt{a}}{B \cdot w} \left[o,295 - 1,855\left(\frac{a}{w}\right) + 6,557\left(\frac{a}{w}\right)^2 - 10,17\left(\frac{a}{w}\right) + 6,389\left(\frac{a}{w}\right)^4 \right] \cdot 10^2$$

It has been found that neither the width of the crack nor the specimen thickness have an influence on the resulting stress intensity factor K_Q. The influence of normalized distance H/w on the values of the stress intensity factor is shown in Fig.3. It can be recognized that the K_Q-value is independent on H/w if the H/w-ratio exceeds values of o,2. It was also confirmed experimentally (Fig.4) that the K_Q-value is independent on the normalized depth of the notch a/w.

Results concerning the stress intensity factor calculated with the compliance method (Fig.5), and with the analytical method (equation 1) are compared in Table 1. It can be seen, that there is a good agreement of the calculated K_Q-values at 15,1 N·mm$^{-3/2}$. Therefore only the upper value, which is given in Fig.3, can describe the critical stress intensity at the tip of the notch for this material, sample configuration and test method described above.

The experimental data seem to be reproducible provided that the samples are reproducibly prepared and have homogeneous structures.

References

E. FITZER, M. HEYM, 1976, Werkstofftechnik, 7, 264

S.K. GAGGAR, L.J.BROUTMAN, 1975, Proc. 3oth Annual Technical Conference, Reinforced Plastics/Composites Institute, Section 9-E

J. HILL, C.R.THOMAS, E.J.WALKER, 1974, International Conference on Carbon Fibres, London, Paper No. 19

F.J.McGARRY, J.F.MANDELL, 1972, Proc.27th Annual Technical Conference, Reinforced Plastics/Composites Institute,Inc.,Sect.9-A,p.1

R.F.PABST, 1973, Fracture Mechanics of Ceram. Vol.2, Ed.R.C.Bradt et al., Plenum Press

B. TERWIESCH, 1972, Diss. am Inst.f.Chem. Technik der Universität Karlsruhe

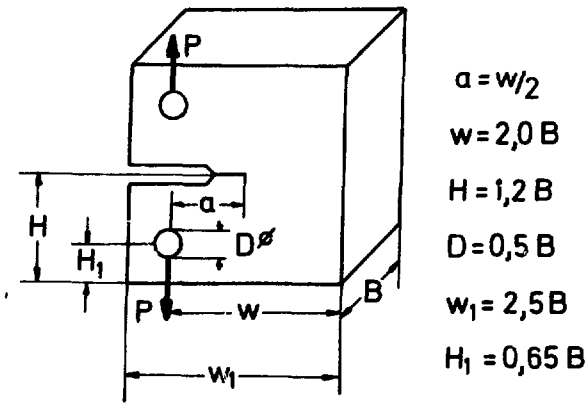


Fig.1: Sample geometry

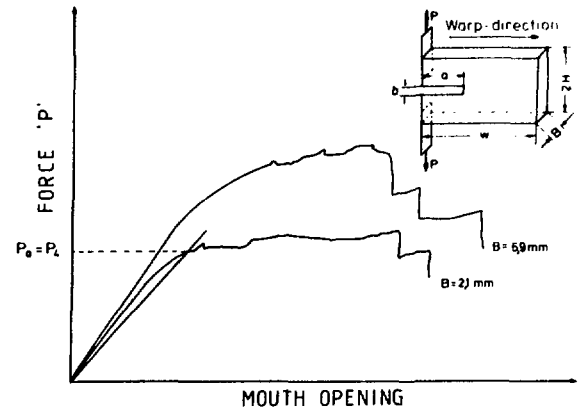


Fig.2: Crack mouth opening as function of the applied tensile force for composites with fabric reinforcement

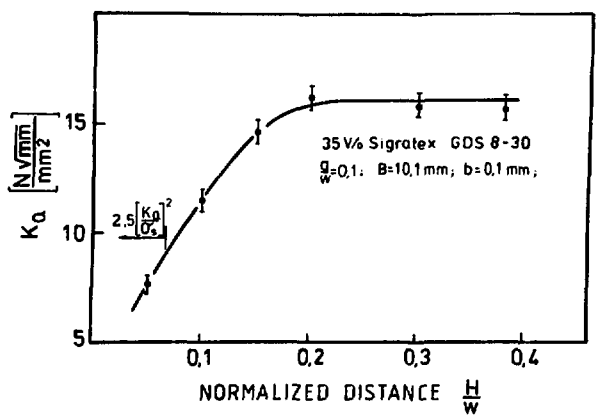


Fig.3: Dependence of the stress intensity factor on H/w (see fig.1)

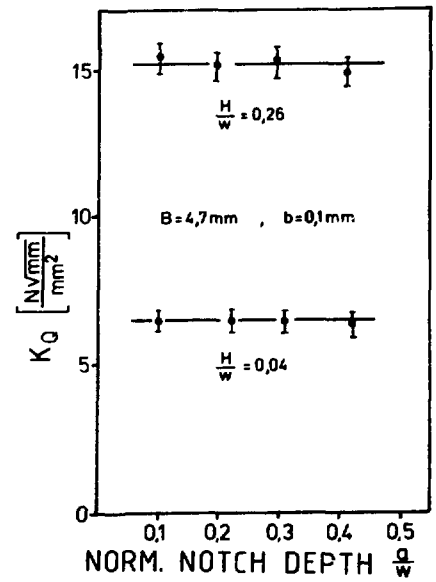


Fig.4: Stress intensity factor as function of a/w (see fig.1)

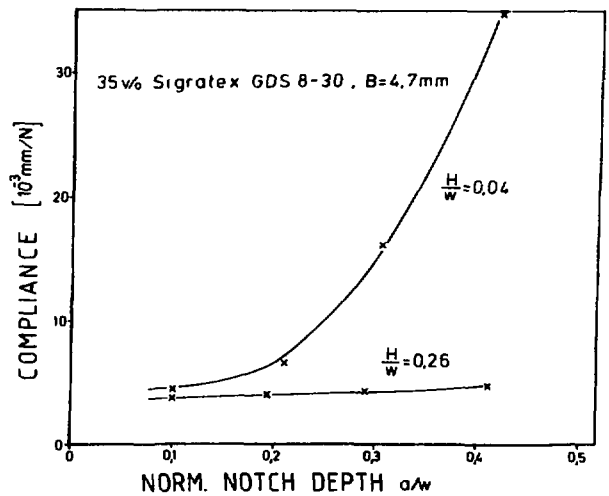


Fig.5: Compliance as function of dimension ratios

H/w	a/w	G_c N mm/mm^2	$K_{c\,ber.}$ N mm$^{-3/2}$	K_Q N mm$^{-3/2}$	Differenz %
0,04	0,1	0,0108	10,8	6,5	+ 66
0,04	0,22	0,1375	12,4	6,5	+ 91
0,04	0,31	0,1702	13,6	6,5	+109
0,04	0,42	0,1950	14,5	6,4	+127
0,26	0,1	0,0325	18,8	15,5	+ 21
0,26	0,19	0,0253	15,5	15,1	+ 3
0,26	0,29	0,0201	14,8	15,3	- 3
0,26	0,41	0,0269	15,8	14,9	+ 6

Tab.1: Comparison of stress intensity factors determined by the compliance and the analytical method

CORRELATION OF A PHYSICALLY BASED STATISTICAL THEORY OF FRACTURE WITH FULL SCALE GROUND TESTS OF REENTRY NOSETIPS

J. D. Buch, J. G. Crose, R. L. Holman, T. E. Mack
Prototype Development Associates, Inc.
Santa Ana, California 92705

Introduction

Ballistic reentry environments impose a severe thermostructural requirement on graphite nosetips. Analytical methods are needed to define the material property-reentry performance relationships through a failure criterion. Deliberate conservatism in the definition of allowable strains is not an acceptable approach because of the resulting artificial limitations on reentry capabilities. Consequently, the need exists for an accurate representation of graphite behavior in thermostructural analytical techniques.

Background

Molded graphite is a transversely isotropic material with highly variable fracture stresses and strains. The statistics themselves exhibit anisotropy with lesser fracture variability in across grain than in the with grain direction. The deformation is nonlinear, temperature dependent, different in tension and compression and anisotropic. The nonlinearity cannot be described by plastic slip concepts as evidenced by its unique measured biaxial response (Ref. 1). The accurate representation of graphite response therefore requires appropriate fracture and deformation theories.

A physically based, anisotropic, statistical and polyaxial failure strength theory was previously described and correlated with all reported ATJS laboratory failure data (Ref. 2). The physical basis for this model is the preferred orientation and strength distributions for flaws which persist through molding and graphitization. A nonlinear multiaxial stress-strain behavior model of graphite which reflects the above unique behavior has been developed by Jones and Nelson (Ref. 3) and reduced to practice for ATJS graphite (Ref. 4). These procedures constitute the basis for an accurate description of graphite thermostructural failure response.

Thermostructural problems are driven by thermal expansion strain compatability and consequently the thermally induced mechanical strains are relatively insensitive to the nonlinear mechanical behavior as shown in Reference 5. The predicted stresses, however, will be considerably in error if nonlinearity is incorrectly taken into account. A post processor (Ref. 4) was established to transform predicted thermomechanical strains into representative stresses, via the Jones and Nelson stress-strain model (Ref. 3). Then, the failure probabilities are found by the anisotropic statistical failure theory (Ref. 2). The material constants and their temperature dependence were obtained from the extensive experimental programs conducted by Southern Research Institute. The remainder of this paper describes the application of this methodology to full scale ground tests of ATJS nosetips.

Ground Test Experiments

The hyperthermal environments of rocket nozzle exhausts (Ref. 6) and arc plasma jets (Ref. 7) have been used to provide controlled studies on fracture of full scale ATJS nosetips. The "plug" and "shell" configurations studied are indicated in Figure 1, as well as the locations and states of stress which promote fracture.

In the 21 rocket nozzle tests (Ref. 6), the transition from nosetip survival to failure for plug nosetips was experimentally determined by selecting varying levels of severity of thermal exposure and subjecting several nosetips to each level of severity. Post test observation and sectioning established the pass/fail ranking.

For a given test condition, the failure probability was defined by the ratio of failures to total number of tips tested in that condition (N_f/N). Error bounds were estimated by assuming that the outcome of a hypothetical additional test would be completely random.

State-of-the-art nosetip heating codes were used to define the time dependent temperature distributions. These were input to the thermostructural analysis code to define the strain distributions which were subsequently post processed to determine failure probability.

The predictions and experimental data are shown in Figure 2. The correlation is good with a slight trend to conservatism (5 to 7 percent). Statistical analysis indicates that the confidence in meeting or exceeding the predictions is approximately 90 percent. Adjustment of material parameters to eliminate the apparent conservatism and "improve the fit" could be performed, but would reduce the confidence in meeting or exceeding predictions. The ground tests therefore indicate that high reliability without excess conservatism is a characteristic of the methodology.

Similar agreement with the arc heated shell tip experiments was obtained (Fig. 3). However, because only one tip per test condition was studied, statistical confidence cannot be specified.

Attempts to correlate these ground tests with stresses predicted by elastic-plastic modeling resulted in large conservatism and poor correlation with data. In effect, predicted stresses are too large as they do not account for the increased compliance (biaxial softening)

directly observed in laboratory studies (Ref. 1). The correct nonlinear multiaxial response must be taken into account to predict accurate stress distributions.

Conclusions

Careful attention to accurate representation of the unique deformation and failure characteristics of graphite has resulted in a proven analytical methodology for reliable thermostructural predictions with minimal conservatism. The methodology constructed is consistent with all known laboratory observations on deformation and fracture and with full scale nosetip studies. The approach to thermostructural response developed herein has application to other graphites as well.

References

1. Jortner, J., AFML-TR-73-170, October 1973.
2. Crose, J. G., Buch, J. D., and Robinson, E. Y., Proc. 12th Conf. on Carbon, 1975, p. 131.
3. Jones, R. M. and Nelson, D., J. Composite Mater., Vol. 9, 1975.
4. Holman, R. L., Crose, J. G., and Buch, J. D., Proc. 13th Conf. on Carbon, 1977.
5. Mack, T. E. and Crose, J. G., Proc. 13th Conf. on Carbon, 1977.
6. Groener, L. S. and Kochendorfer, P. K., Philco-Ford Aeroneutronic Division, Newport Beach, CA, Publication U-4969, October 1971.
7. Baker, D. L., Starrett, H. S., and Budde, C. L., AFML-TR-76-26, April 1976.

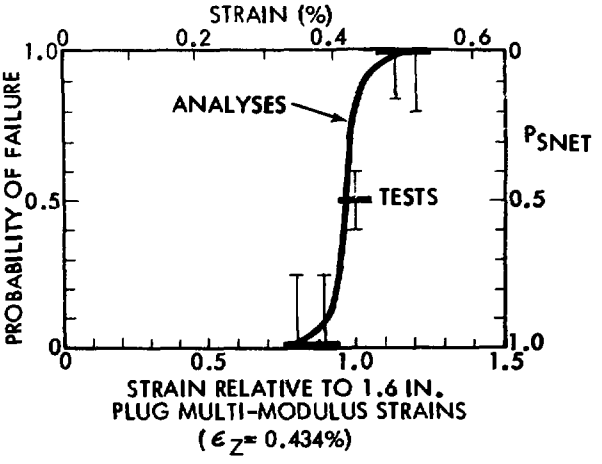


Figure 2. Failure Probability Vs. Peak Axial Strain for LORN ATJS Plug Nosetips (Ref. 6)

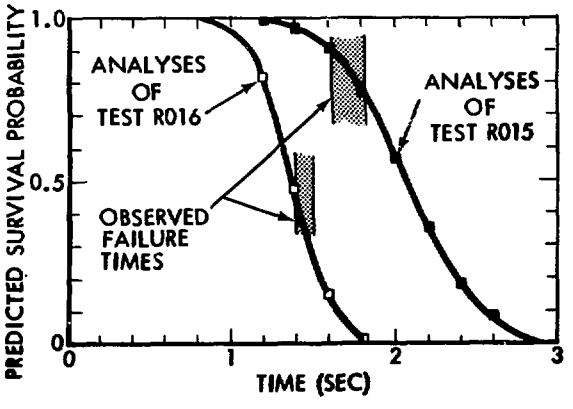


Figure 3. Survival Probability Vs. Time for 50 MW ATJS(WS) Graphite Shell Nosetips (Ref. 7)

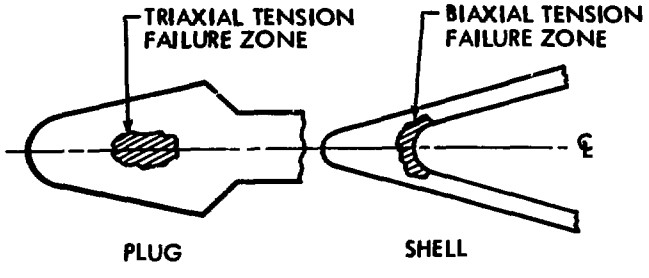


Figure 1. Typical Nosetip Geometries and Potential Fracture Sites

COMPARED ADSORPTIVE PROPERTIES OF ACTIVE CARBONS FROM OLIVE STONES AND ALMOND SHELLS

C. Berenguer, J. de D. López-González, F. Martínez Vilchez and F. Rodríguez Reinoso.

Departamento de Química Inorgánica. Facultad de Ciencias. Universidad de Granada. (Spain).

INTRODUCTION

There is no doubt about the growing needs of active carbons with a low producing cost and having adequate adsorptive properties and other specific properties. This paper reports some basic information on the adsorptive properties of active carbons prepared from olive stones, a waste-product from the manufacture of olive oil in mediterranean countries, and from almond shells. Both raw materials are rather abundant and low priced, and have adequate botanical structures (1) to give hard active carbons allowing re-cycling in adsorption processes.

EXPERIMENTAL

Olive stones and almond shells were crushed and washed in diluted sulphuric acid followed by refluxing in water to total acid removal. The raw materials were then carbonized under nitrogen with a heating rate of 5ºC min^{-1} at 850ºC with a soaking time of 1 hour, the yield being about 27% for olive stones and 23 % for almond shells. The carbonized products were activated in carbon dioxide at 825ºC for different periods of time to give a wide range of burn-off.

The adsorption of N_2 at 77 K and CO_2 at 195 and 273 K has been carried out using conventional McBain silica spring balances (2). The volumes of meso- and macroporosities were determined using a mercury porosimeter manufactured by Carlo Erba. Chemical analyses of the raw materials and carbonised products are given in Table 1.

Table 1

	C%	H%	N%	S%	Ash%
olive stones	48.2	5.7	0.0	0.0	0.03
carbonized olive stones	94.6	1.0	0.0	0.0	0.21
almond shells ...	47.8	6.0	0.4	0.4	0.10
carbonized almond shells	94.6	0.7	0.4	0.4	0.29

RESULTS

Examples of adsorption isotherms of nitrogen at 77K on active carbons from olive stones (samples named O-time of activation) and from almond shells (samples named A-time of activation) are contained in Fig. 1. The adsorption isotherms of CO_2 at 273 K on the same samples are included in Fig. 2. The adsorption isotherms of the carbonized and not activated products are included in Fig. 1 and Fig. 2 as O-C and A-C, respectively.

As it can be deduced from Fig. 1 and Fig. 2, activated olive stones adsorb in a greater extent than those from almond shells. The surface areas of all samples are included in Table 2.

Table 2

Surface area of carbons (m^2 g^{-1})

	N_2 (77K)	CO_2(195K)	CO_2(273K)
O-C	74	584	532
O-2	959	864	715
O-8	1342	1241	984
O-16	1889	1692	1340
A-C	115	531	550
A-2	673	523	-
A-8	954	888	710
A-16	1446	1360	869

The as-carbonized materials exhibits some restriction of nitrogen adsorption at 77K and this is characteristic of diffusional resctrictive processes in ultramicroporous carbons (3), restriction which is eliminated with activation.

The variation of surface area with time of activation is shown in Fig. 3 (from carbon dioxide adsorption at 273K) where there is a linear increase in surface area with the time of activation in both kinds of active carbons, but the increase is faster for the activated olive stones.

The mercury porosimetry measurements show the development of porosity on activation; there is a development of mesoporosity in the activated carbon from olive stones in a higher extent than in those from almond shells, but in the later active carbons there is a greater develppment of macroporosity. In both cases the more activated samples have about 0.3 cm^3 g^{-1} of pore volume in pores of 200 nm to 200 μm diameter in the case of carbons from almond shells and about 0.6 cm^3 g^{-1} in the case of carbons from olive stones.

Since according to Dubinin (4) the gradient D of the equation of Dubinin-Radushkevich is a measure of the diameter of the microporosity of the adsorbent, the variation of the gradient D from isotherms of adsorption of carbon dioxide at 273 K with extent of activation is in Fig. 4. As it can be seen, the diameter of microporosity is larger in active carbons from olive stones and increases faster with activation.

Consequently with the above considerations, it can be deduced that olive stones and

almond shells, both very abundant in Mediterranean countries can yield active carbons with large effective surface areas, relatively high hardness and the specially important characteristics of very low ash content and low sulphur content.

REFERENCES

(1) ILEY Margaret, MARSH H. and RODRÍGUEZ-REINOSO, F., Vol. 11, p.633-638, Carbon (1973).

(2) Mc BAIN J.W. and BAKR, A.A; J. Am. Chem. Soc., 48, 690 (1926).

(3) MARSH H. and RAUD, B.; J. Coll. Interface Sci. 33, 101 (1970).

(4) DUBININ, M. N.; Chemistry and Physics of Carbon (Edited by P.L. Walker, Jr.), Vol. 2, p. 51. Edward Arnold, London, (1966).

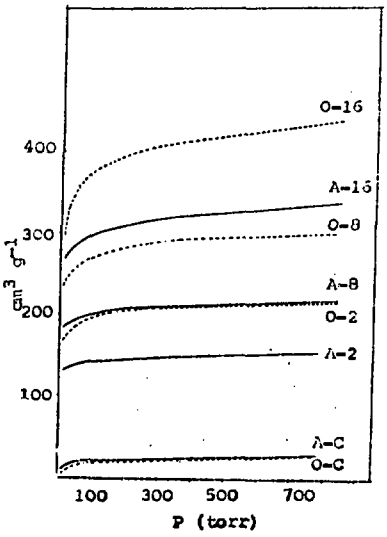


Fig. 1

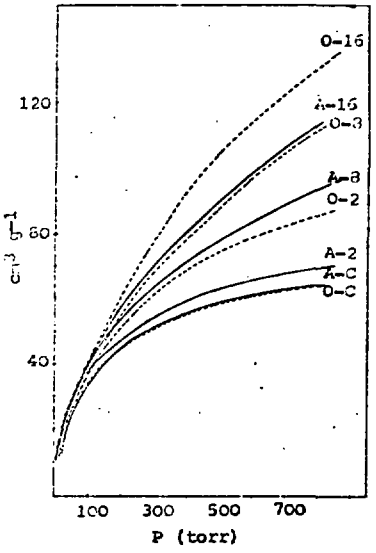


Fig. 2

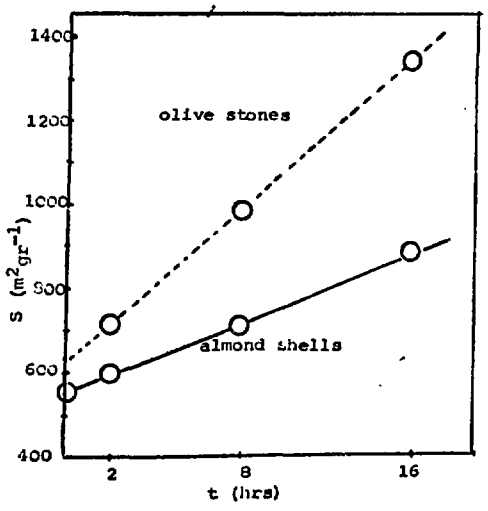


Fig. 3

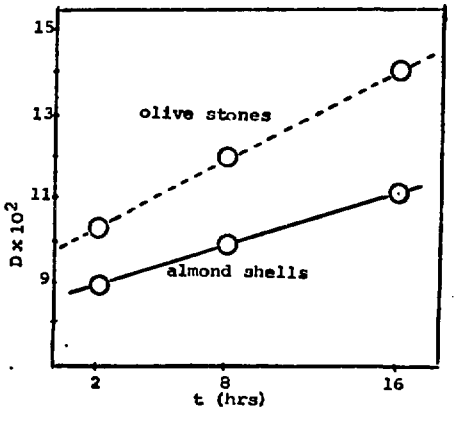


Fig. 4

RETENTION OF 2,4-DICHLOROPHENOXIACETIC ACID BY AN ACTIVATED CARBON

A. Jiménez-López, J. de D. López-González and C. Valenzuela-Calahorro.

Departamento de Química Inorgánica. Facultad de Ciencias. Universidad de Granada (Spain).

According to some workers (1) there are some functional groups in active carbons which are very similar to those existing in the organic components of soil; as it is well known these organic components are in some way related to the degradation of many herbicides (2). Taking in account the above considerations we have studied the retention of 2,4-Dichlorofenoxiacetic acid (2,4-D) in aqueous solution by a granular activated carbon (supplied by Merck) with a particle size of 1,5 mm. We have studied the kinetics of the retention process and at the same time, the adsorption isotherms of such herbicide. The active carbon used has been characterized by determining its oxygen content, surface area (by N_2 adsorption at 77K) and pore size distribution.

The kinetic study has been carried out at 10, 20, 30, 40 and 50ºC using solutions of different initial concentrations of 2,4D and a constant amount of adsorbent for each temperature. From the plots $-\frac{dc}{dt} = f(t)$ (Fig. 1) the initial velocities of retention have been calculated, and the order of the retention process and the specific velocities have been calculated from the plots of $\log(-\frac{dc}{dt}) = f(\log c)$ (Fig. 2). According to Eyring (3) the changes in enthalpy and entropy for the formation of the activated species have been calculated from the plot of $\log \frac{k}{T} = f(\frac{1}{T})$ (Fig. 3) giving values of $\Delta H^{\ddagger} = 6.7$ Kcal mol^{-1} and $\Delta S^{\ddagger} = 45.5$ cal/ºmol. The change in free energy and the equilibrium constant have been calculated from the above values at each temperature.

The retention isotherms of 2,4-D at 20 and 50ºC (Fig. 4) have been obtained; they are of the L-3 type of Giles's clasification (4). For C/C_o values greater than 0.5 the retention is taking place in multilayer. On the other hand, the isotherms follow the Langmuir equation (Fig. 5) up to $C < 8 \times 10^{-4}$ M (equivalent to $C/C_o < 0.50$). From these plots, the values of Xm and b have been calculated. The values of Xm are:

$$Xm_{(20ºC)} = 2.69 \times 10^{-3} \text{ mole } g^{-1}$$

$$Xm_{(50ºC)} = 2.19 \times 10^{-3} \text{ mole } g^{-1}$$

The surface accesible to 2.4-D has been calculated from these data, assuming that the molecule is retained perpendicularly to the solid surface. Since in these conditions the cross-sectional area of the molecule is 30 $Å^2$, the values of the surfaces are

$$S_{(20ºC)} = 486 \text{ m}^2 \text{ g}^{-1}$$

$$S_{(50ºC)} = 396 \text{ m}^2 \text{ g}^{-1}$$

The values of the constant b are:

$$b_{(20ºC)} = 6.45 \times 10^{3} \text{ l x mole}^{-1}$$

$$b_{(50ºC)} = 6.65 \times 10^{3} \text{ l x mole}^{-1}$$

and they indicate that although the retention process is almost enterely physical, there is some contribution of chemisorption.

Finally, the differential heats and entropies of retention have also been calculated (Fig. 6 and Fig. 7). The $\Delta \bar{H}$ values range from 0 to 3 Kcal $mole^{-1}$ and this seems to confirm that the retention is a physical process.

REFERENCES

(1) HASSLER, J.W.; "Activated Carbon", Chamical Publ. Co., Inc. New York (1963).

(2) SHEETS, T.J., CRAFTS, A.S. and DREVER, H. R.; J. Agr. Food Chem.; 10, 458-462 (1962).

(3) ANDER, P. and SONNESSA, A.J.; "Principles of Chemistry". The Macmillan Co. New York (1965).

(4) GILES, C.H., Mac EVANS, T.H., NAKHWA, S.N. and SMITH, D.; J. Chem. Soc. 3973 (1960).

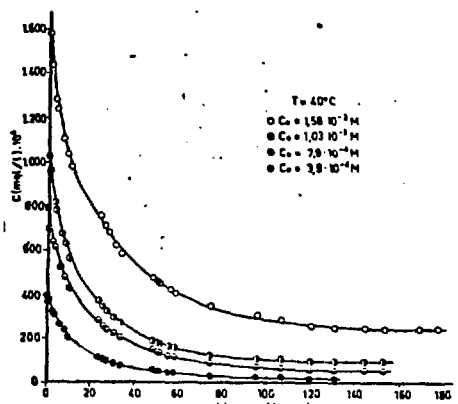


Fig. 1

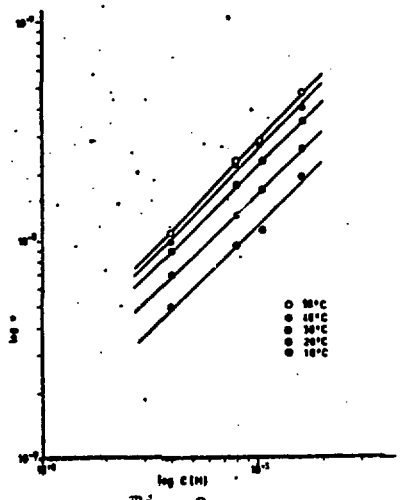


Fig. 2

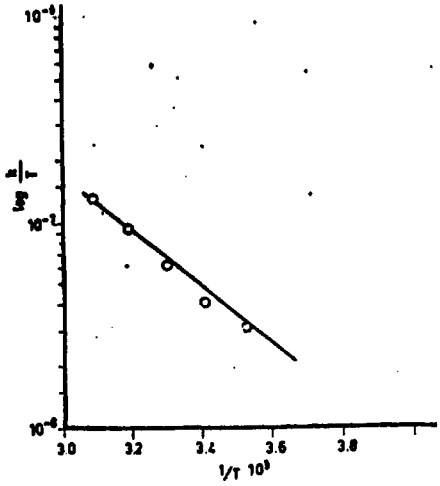


Fig. 3

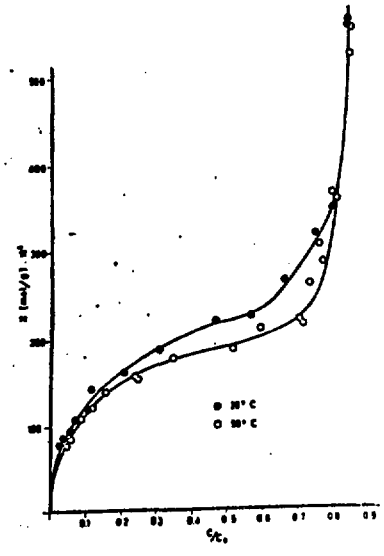


Fig. 4

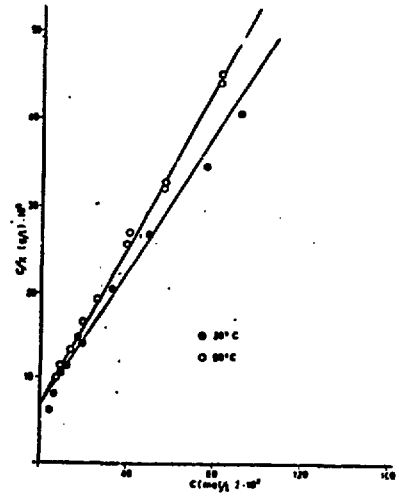


Fig. 5

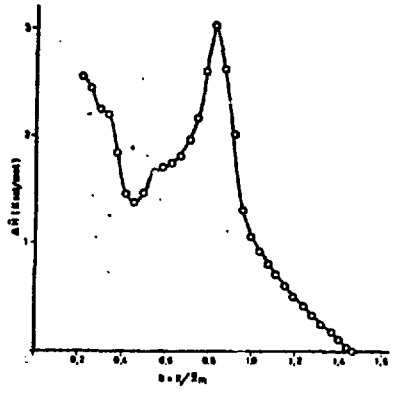


Fig. 6

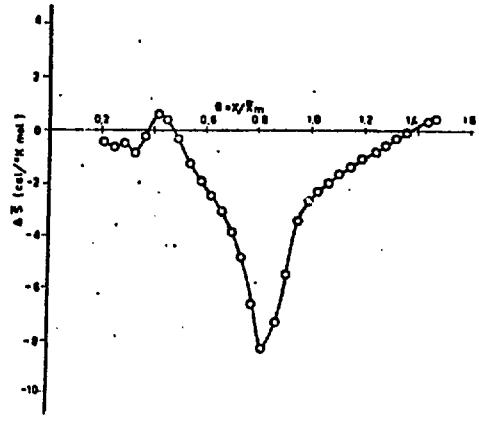


Fig. 7

ADSORPTION OF HCN AND H_2O VAPOR MIXTURES BY ACTIVATED AND IMPREGNATED CARBONS

G. A. Freeman, P. J. Reucroft and C. T. Chiou
Department of Metallurgical Engineering and Materials Science
University of Kentucky
Lexington, Kentucky 40506

Introduction

Isotherms for HCN on BPL activated and ASC whetlerite carbons[1] and for H_2O on the same carbons[2] have been measured and characteristic parameters for these adsorbate-adsorbent combinations have been noted. Under non-laboratory conditions, adsorption usually takes place in the presence of water vapor. It is therefore of interest to investigate the adsorption properties of the BPL activated and ASC whetlerite carbons with respect to HCN in the presence of water vapor at about 80% humidity. The data from the single vapor isotherms are used as a basis for interpreting the results of a binary mixture adsorption study.

Experimental

The experimental technique employed for single vapor isotherm measurement and the carbons investigated have been described previously.[3] Binary vapor isotherms were measured by three different procedures: 1) the carbon sample was allowed to equilibrate with H_2O vapor and then an HCN isotherm was measured while maintaining the initial amount of H_2O in the system; 2) the carbon sample was allowed to equilibrate with HCN vapor and then an H_2O isotherm was measured while maintaining the initial amount of HCN in the system; 3) a mixed gas consisting of H_2O and HCN was introduced into the system. In the first procedure, two gas storage flasks were used; one to store pure HCN gas and the other for cold trapping the binary mixture. After allowing the carbon sample to equilibrate with H_2O vapor, a valve (V6) isolated the adsorption chamber from both gas storage flasks. A liquid nitrogen cold trap was employed to trap the H_2O vapor not in equilibrium with the carbon behind a second valve (V7), which was then closed. HCN was next allowed to enter the system in a region between valves V6 and V7. V7 was opened after the H_2O had evaporated, and the two vapors were allowed to mix and reach room temperature before V6 was opened to the adsorption chamber. This procedure kept the partial pressure of H_2O constant and allowed the HCN partial pressure to be increased in controlled steps. The sample mass was allowed to stabilize as in the single gas isotherm determinations and the data recorded. Subsequent amounts of HCN were introduced in the same manner by cold trapping the H_2O/HCN mixture after V6 had been again closed to prevent the adsorbate pressure from changing in the adsorption chamber. The second procedure was similar with the roles of H_2O and HCN reversed.

In the third procedure, a carbon sample was first allowed to come into equilibrium with a particular pressure of H_2O vapor and then the water vapor was collected in one of the gas storage flasks and allowed to mix with a controlled amount of HCN. The mixture was then treated in the same manner as a single vapor to determine an isotherm.

Care was taken to have each isotherm pass through a point where the partial pressure of water was ~0.8 of its saturation vapor pressure and the partial pressure of HCN was ~0.15 of its saturation vapor pressure.

After every isotherm, the carbon sample was heated to 400°C (BPL activated) or 150°C (ASC Whetlerite) for several hours at ~10^{-6} torr and the sample mass was recorded. Any increase over the initial dry sample mass was ascribed to chemisorption of the adsorbates.

Results and Discussion

Figure 1 is a conventional isotherm showing the volume of HCN adsorbed per gram of BPL activated carbon as a function of relative pressure (P/P_0) of the HCN adsorbate. P is the equilibrium isotherm pressure and P_0 the saturated vapor pressure of adsorbate. This data may also be plotted according to the Dubinin-Polanyi adsorption isotherm equation:[4] $\log W = \log W_0 - k\varepsilon^2$, where W is the volume of adsorbate, W_0 is the volume of adsorbate at saturation, k is a parameter which characterizes the adsorbate-adsorbent interaction, and ε, the adsorption potential, is equal to $RT\ln(P_0/P)$, where R is the gas constant and T the absolute temperature. W_0 and k values of 0.42 c.c./gm and 14.9×10^{-8} cal.$^{-2}$mole.^{2} were obtained for the BPL carbon and a W_0 value of 0.35 c.c./gm. was obtained for ASC Whetlerite. After exposure to HCN the BPL samples could be completely regenerated and did not, within our accuracy, show any significant chemisorption effects. The ASC Whetlerite did chemisorb > 0.04 c.c./gm., which lowered the adsorptive capacity of those samples for future isotherm measurements.[1]

Figure 2 is a conventional isotherm showing the volume of H_2O adsorbed per gram of BPL activated carbon as a function of relative pressure of the H_2O adsorbate. Plotting this data according to the Dubinin-Polanyi adsorption isotherm equation yielded W_0 values of 0.40 c.c./gm. and 0.36 c.c./gm. for the BPL activated and the ASC impregnated carbons respectively. No chemisorption effects were observed. As shown in Fig. 2, there is a great deal of hysteresis exhibited, which persists at all relative pressures between 0.002 and 1.[2]

Figure 3 shows conventional isotherms for the three modes of binary vapor adsorption. The adsorption is expressed as mass adsorbed per gram of adsorbent in all three cases. The top curve shows the adsorption of HCN as a function of HCN relative partial pressure for a BPL carbon sample in equilibrium with H_2O at a relative partial pressure of 0.84 and an initial adsorption equal to 0.374 gm. of H_2O per gm. of carbon. Additional adsorption of HCN occurs which, with the H_2O already adsorbed, exceeds the amount of HCN or the amount of H_2O absorbed in a single vapor isotherm run. The HCN adsorption

considered alone, however, is only about half that observed for HCN in a single vapor isotherm.

The middle curve shows the adsorption of H_2O as a function of H_2O relative partial pressure for a BPL carbon sample in equilibrium with HCN at a relative pressure of 0.19 and an initial adsorption equal to 0.301 gm. of HCN per gm. of carbon. There is very little additional adsorption of water (~0.003 gm. of H_2O per gm. of BPL carbon) in the presence of HCN even up to relative water vapor pressures 1.

The lowest curve is the adsorption of an H_2O/HCN mixture as a function of the ratio of the total pressure of the H_2O/HCN mixture to the sum of their saturation vapor pressures. The adsorption noted in this phase of the experiment was substantially less than that observed in the other two modes of adsorption.

It is instructive to note that each of the isotherms shown contain points which reflect HCN relative pressures up to 0.2 and H_2O relative pressures up to 0.8.

It would appear that the HCN gas is soluble in water and goes into solution with the adsorbed (liquid) phase present on the carbon which has been pre-exposed to water vapor relative pressures of about 0.8. This adsorption probably does not reflect the adsorptivity of the carbon, but rather the affinity of the H_2O adsorbed (liquid) phase for HCN.

When the carbon is pre-exposed to HCN and then to H_2O, the total absorption seems to be almost entirely due to HCN with only a very small adsorption of H_2O. This implies that while HCN is soluble in water, under the conditions of adsorption, the reverse is not true.

The adsorption of the mixture, without any pre-exposure, results in less adsorption than would be expected for either vapor separately. This may be interpreted as a competitive process which is not conducive to mutual adsorption.

In all cases, the BPL activated carbon samples showed very small chemisorption effects entirely consistent with the limits of experimental precision. The ASC Whetlerite carbons showed chemisorption effects similar to those exhibited in the adsorption of HCN alone.

Acknowledgments

This research was supported by the Department of the Army through Edgewood Arsenal Contract No. DAAA15-74-C-0163.

References

1. P. J. Reucroft and C. T. Chiou, Seventh Quarterly Report, October 1975-January 1976, Edgewood Arsenal Contract DAAA-74-C-0163.

2. P. J. Reucroft and C. B. Freeman, Tenth Quarterly Report, October 1976-January 1977, Edgewood Arsenal Contract DAAA-74-C-0163.

3. C. T. Chiou and P. J. Reucroft, to be published in Carbon.

4. P. J. Reucroft, W. H. Simpson, and L. A. Jonas, J. Phys. Chem., 75, 3526 (1971).

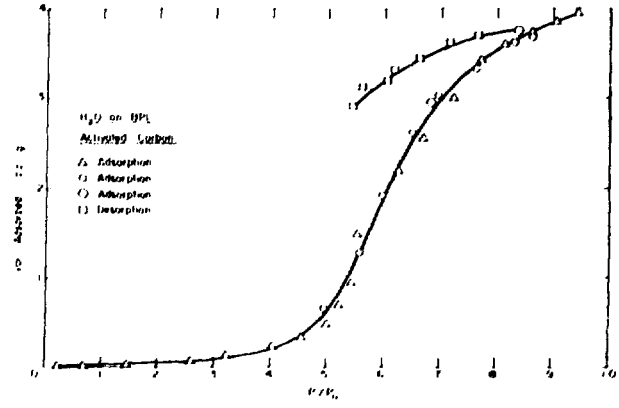


Figure 2. H_2O on BPL Activated Carbon

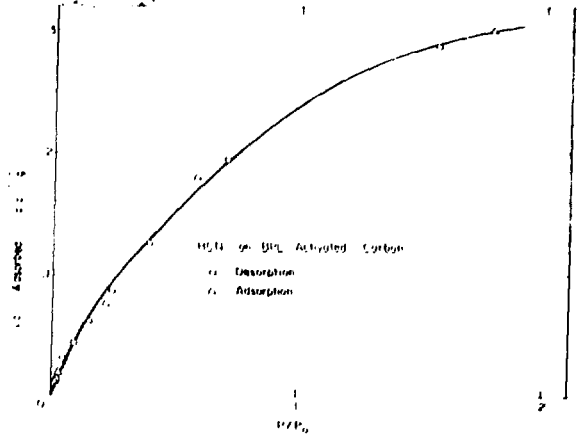


Figure 1. HCN on BPL Activated Carbon

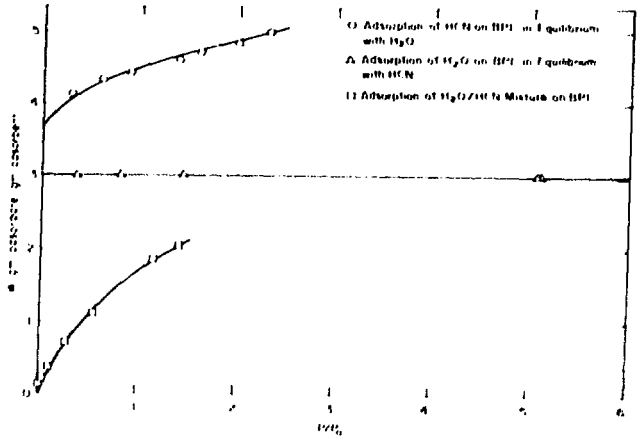


Figure 3. Mixed Vapor Isotherms on BPL Activated Carbon

INTERACTION OF OZONISED OXYGEN WITH MICROCRYSTALLINE CARBONS

B.R. PURI, V.M. ARORA
Department of Chemistry, Panjab University, Chandigarh, India.

Interactions of charcoals, carbon blacks and activated carbons with ozone, mixed in oxygen upto 2.5 per cent, in aqueous and nonaqueous media as well as in dry state at ambient temperature, have been investigated amongst others by Deitz and Bitner (1,2), Donnet and coworkers (3,4,5) and Puri et al (6). The reactions involve, amongst other things, gasification of the carbon, chemisorption of oxygen and formation of degradation products if water is used as the medium (4,5,6). The intensity of interaction is less if a nonaqueous liquid is used as the medium. Suitable mechaniams have been proposed (1,2,4,5). Nitrogen adsorption (77.4°K) on charcoal after the interaction showed a significant fall (2). The data on carbon blacks indicated development of microporosity in the products (3). The present paper relates to the study of the nature of the surface oxygen complexes formed and alterations in surface unsaturation and surface area produced on the interaction of a few microcrystalline carbons with ozonised oxygen (~2.5 per cent ozone) at 30°C.

Materials and Methods

Two samples of ash-free charcoal, prepared by the carbonisation of cane sugar and coconut shells and outgassed at 750° and 1000°C(7), nine samples of carbon blacks and a sample of commercial steam-activated carbon were used. Carbon (5g) was taken in a porcelain tube (dia ≈ 5-in or 12.5 cm) which was kept in a thermostat (30°C±0.1°) and connected on one side to an ozoniser (Gallenkamp,GE-150) and to a series of conical flasks, containing known volumes of standard (0.2N) baryta solution (for estimating carbon dioxide formed), on the other . Ozonised oxygen (~2.5 per cent ozone) was passed at the rate of 2l/hr over the carbon bed, kept rotating at 18-20 revolutions per min, for 24 hr. The carbon was then withdrawn, stored under nitrogen and examined for (i) oxygen content by evacuating 1g material at 1000°C and analysing the gases (CO_2,CO and H_2O) evolved (8); (ii) barium hydroxide values as a measure of surface acidity(9); (iii) bromine value as a measure of surface unsaturation (7); and (iv) surface area by determining adsorption isotherms of carbon dioxide at 0°C and applying Dubinin equation(10).

Results and Discussion

The amount of carbon 'burnt' as carbon dioxide during the reaction extended for 24 hr and that of oxygen chemisorbed and recovered as CO_2,CO & H_2O on high temperature-evacuation are given in Table 1. The gasification is seen to be maximum in the case of activated carbon and to be comparatively more in charcoals than in carbon blacks. It is significant to note that nearly 7 per cent of oxygen by weight could be added to each charcoal as well as to the activated carbon on treatment in ozonised oxygen at 30°C. The amount added to carbon blacks, however, is less and varies from 2 to 3 per cent by weight. The chemisorbed oxygen is seen to give rise to both CO- and CO_2-surface complexes. In the case of carbon blacks the interaction also involves partial conversion of CO- into CO_2-surface complex. The elimination of a part of the oxygen as water vapour appears to be due to fixation of oxygen at sites containing residual hydrogen in the carbons. The amount of carbon 'burnt' and that of oxygen chemisorbed in a given material is comparatively less than the value obtained when the interaction at the same temperature was studied in aqueous medium (6).

The CO_2-complex formed in each case was found to be partly acidic and partly nonacidic (11). The non-acidic (or neutral) complex is considered to arise from fixation of oxygen at certain unsaturated sites, measured by bromine value,and, therefore, to cause a corresponding fall in the bromine value (11). In the present case, however, the amount of the nonacidic complex formed is much more than the fall in bromine value observed. It appears probable that the treatment in ozone results in creating more unsaturated sites. This was checked by outgassing the charcoals at 750° so as to eliminate the entire CO_2-complex. The bromine values were redetermined and found to be appreciably higher (by over 35 % in most cases) than the initial values. The role of unsaturated sites in improving catalytic performance of carbons has been emphasised in previous publications (12).

The interaction is seen to cause a considerable rise in surface area,by about 50 per cent in carbon blacks and 90-100 per cent in 700° and 1000°- sugar charcoals; the value for the activated carbon,however, shows a fall by about 40 per cent(cf.Table 1). The interaction in the case of sugar charcoals was then continued for longer periods. The values showed a rise upto 48 hours treatment and then became 1178 and 1136 m^2/g respectively. Beyond that there was a decline & the values decreased to 965 and 878 m^2/g after 80 hours of the

Table I

Effect of interaction of carbons with ozonised oxygen at 30°C on gasification of carbon, chemisorption of oxygen & surface area of products.

Sample	Amount of carbon gasified (g/100g)		Oxygen content(g/100g)evolved as CO_2	CO	H_2O	Total	Surface area (m^2/g)
SC-750°C	3.05	(a)	nil	1.92	nil	1.92	550
		(b)	2.66	3.02	1.67	7.35	1040
SC-1000°C	3.92	(a)	nil	nil	nil	nil	323
		(b)	2.60	1.92	1.52	6.04	720
CC-750°C	2.20	(a)	nil	2.14	nil	2.14	562
		(b)	3.20	2.75	2.76	8.71	851
CC-1000°C	5.88	(a)	nil	nil	nil	nil	537
		(b)	2.86	1.68	2.33	6.87	885
Active Carbon	9.33	(a)	1.04	1.47	2.84	5.35	1005
		(b)	5.57	1.36	6.32	13.25	608
Philblack-A	1.21	(a)	0.19	0.33	0.13	0.65	46
		(b)	1.73	nil	2.11	3.84	76
Philblack-E	1.36	(a)	0.40	0.41	0.44	1.25	132
		(b)	1.80	0.30	2.17	4.27	182
Philblack-I	1.56	(a)	0.35	0.63	0.36	1.34	103
		(b)	1.73	0.30	2.63	4.66	160
Spheron-4	2.00	(a)	0.54	2.83	0.70	4.07	224
		(b)	3.36	1.45	2.51	7.32	291
Spheron-6	2.25	(a)	0.50	2.12	0.46	3.08	138
		(b)	2.07	1.30	2.39	5.76	229
Spheron-9	2.60	(a)	0.54	1.93	0.71	3.18	151
		(b)	2.75	1.16	2.68	6.59	221
Spheron-C	1.85	(a)	0.58	2.00	2.60	3.18	288
		(b)	3.95	1.57	2.71	8.23	361
Mogul	1.31	(a)	2.21	4.18	1.44	7.83	324
		(b)	3.95	2.86	3.71	10.52	410
Elf-0	1.43	(a)	1.18	2.17	0.71	4.06	209
		(b)	3.26	1.40	2.97	7.63	300

SC = Sugar charcoal; CC = Coconut shell charcoal; (a) = Before interaction; (b) = After interaction.

treatment. It appears that if oxidation in steam around 800° or in ozone at 30° enhances surface area by the creation of more kinks, corners, edges etc., these very structures get 'burnt' on continued exposure to oxidising atmosphere.

References

1. Deitz,V.R.&Bitner,J.L.,Carbon,10,145,1972.
2. Deitz,V.R.&Bitner,J.L.,Carbon,11,393,1973.
3. Papirer,E.,Donnet,J.B. & Schutz,A., Carbon, 5, 113, 1967.
4. Donnet,J.B.,Ehrburger,P. & Vost,A., Carbon,10, 773, 1972.
5. Donnet,J.B. &Ehrberger,P.,Carbon, 8, 697, 1970.
6. Puri,B.R.,Bansal,R.C.,Aggarwal,V.K. & Bhardwaj,S.S.Indian J.Chem.11,1020,1973.
7. Puri,B.R.,Sandle,N.K. & Mahajan,O.P., J.Chem.Soc., 932, 4880, 1963.
8. Puri,B.R. & Bansal,R.C.,Carbon,1, 451, 1964.
9. Puri,B.R. & Bansal, R.C.,Carbon, 1, 457 (1964).
10. Dubinin,M.M. in Chemistry & Physics of Carbon, edited by P.L. Walker,Jr., Vol. 2 (Marcel Dekker, Inc.,New York) 1966, p. 51.
11. Puri,B.R. & Sharma, S.K.,Indian J. Chem. 8,1119, 1970.
12. Puri,B.R. and Kalra,K.C.,Indian J.Chem. 5, 638 (1967).

AN EXAMINATION OF FIVE PREFERRED ORIENTATION FUNCTIONS

William S. Horton
Institute for Materials Research
National Bureau of Standards
Washington, D.C. 20234

Introduction

Beginning with Bacon [1] there have been attempts to describe the preferred orientation of graphitic materials. The use of the m-th power of the cosine of the orientation angle, ϕ, has been attributed to him. Although in many cases a rough approximation to the degree of preferred orientation is sufficient to distinguish among specimens, at other times it is desirable to have a more accurate measure. It has been suggested [2] that numerical integration is the safest procedure to evaluate data for the intensity-orientation angle relation. On the other hand, if a theory of formation mechanism for pyrolytic graphite is available, it should suggest the form of the orientation function and agreement would provide some evidence for its correctness. Previously evaluation of suggested functions have not completely considered the problems of measurement. For these reasons five functions were examined analytically and empirically using eleven sets of data. The aim was to see if for this limited set a choice of function was evident.

Bragg and Packer [3] proposed the Gaussian distribution for the angle, ϕ, that the crystallite c-axes make with the reference plane. Ruland [4] suggested a function equivalent to that proposed by Ergun and Schehl [5], $1/(1 + b' \sin^2\phi)$. Later Ergun [6] preferred a modified Bragg distribution with the angle replaced by its sine. In the following examination the Lorentz function, $1/(1 + c\phi^2)$, is also included.

General Characteristics of the Functions

All five of the intensity expressions are bell-shaped, but only the Bacon function is identically zero at $\phi = \pi/2$. This has been suggested [2] as a reason for discarding it because direct observation has shown some crystallites at this orientation. Another probable requirement is that the first derivative of the function should be zero at $\phi = \pi/2$. This is not satisfied by the Bragg or Lorentz functions. Further distinctions among these and the other functions depend upon the degree of preferred orientation of the material, as indicated by the half-intensity angle, $\phi_{1/2}$. Depending on the value of $\phi_{1/2}$, the functions may or may not be distinguishable, (Figs. 1-4).

Fitting Experimental Data

Data used include those obtained by the author in 1971, those reported by Ergun [5], and the original data of Hishiyama *et al* [7] kindly supplied by Professor Inagaki [8]. The Horton data were taken on cylindrical specimens from an as-deposited pyrolytic graphite previously reported [2,9].

It was decided to fit the curves to the data using a least squares technique with the possibility that the quality of the fit would be an indication of the best function to choose. Allowance was made for the possibility that a "background" may have been inadequately compensated and that the setting of the specimen for maximum diffraction may have been inexact. In the equations the parameters to be estimated enter non-linearly and the usual least squares method will not suffice. The Gauss-Newton method although obtaining sufficiently accurate initial estimates was not always trivial. The Horton data consisted of five sets; the Ergun data consisted of two; and the Inagaki data consisted of four. With five functions this meant 55 fittings, plus any extras used for obtaining initial estimates or for fitting functions with fewer constants

Results

For 50 of the 55 fits the "background" parameter was found to be statistically significant; 23 of the "ϕ-max" parameters were significant.

In a large number of cases, the residuals showed trends rather than a random scatter. This suggests in some cases that the correct function has not been chosen. In other cases, another explanation may be possible.

Attempting to choose among the functions was approached by examining the estimates of the standard deviation of the residuals. The smallest value is likely to result from the best fit. This does not provide a perfect method but appears to be the best available, as long as one doesn't use it too arbitrarily. To allow somewhat for the difficulty of deciding between two reasonably close values, the number of times a function had either the smallest or next-to-smallest value was counted. The following table resulted.

Table 1. Number of Best or Next Best Fits

Bacon	3
Bragg	9
Ergun	6
Lorentz	2
Ruland	2
Total	22

Discussion

It appears that the Bragg distribution is the most likely one governing the angles of layer poles in oriented graphite-like materials. However, for the data presented, the Ergun function cannot be completely ruled out because it came in a reasonably close second. Furthermore, it satisfies the slope requirement at $\pi/2$.

The often found need for a constant term in the function may be an indication of inadequate treatment of the base-line effects, or it may be an indication that a fraction of the poles are uninfluenced by forces causing orientation. Then there will be two orientation constants to describe a material, the unoriented fraction and the orientation parameter. Furthermore, it will be possible to have two materials with orientation functions that intersect. This possibility has been described as probably necessary [2].

References

[1] Bacon, G. E., J. Appl. Chem., 6, 477-81 (1956).

[2] Thrower, P. A., Nagle, D. C., and Horton, W. S., J. Appl. Cryst., 6, 347-51 (1973).

[3] Bragg, R. H., and Packer, C. M., Nature, Lond., 195, 1080-2 (1962).

[4] Ruland, W., J. Appl. Phys., 38, 3585-6 (1967).

[5] Ergun, S., and Schehl, R. R., J. Appl. Cryst., 5, 409-11 (1972).

[6] Ergun, S., Carbon, 14, 139-50 (1976).

[7] Hishiyama, Y., Kaburagi, Y., Inagaki, M., Imamura, T., and Honda, H., Carbon, 13, 540-2 (1975).

[8] Inagaki, personal communication.

[9] Horton, W. S., J. Res. NBS, 74A, 325-30 (1970).

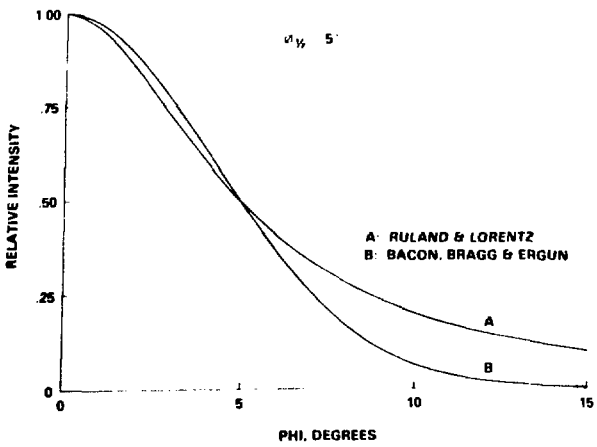


Figure 1

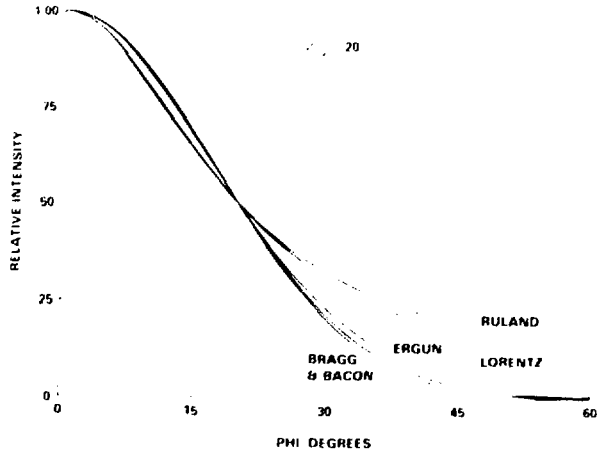


Figure 2

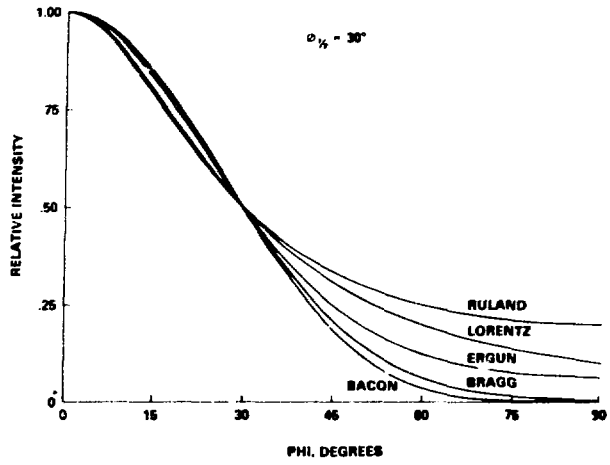


Figure 3

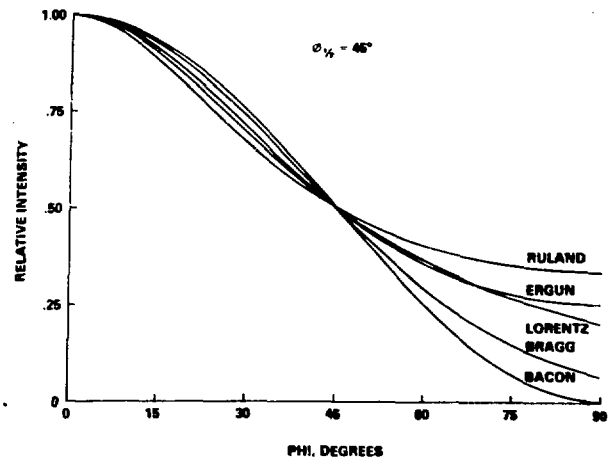


Figure 4

A COMPARISON OF OPTICAL METHODS FOR DETERMINING PREFERRED ORIENTATION IN NEARLY ISOTROPIC PYROCARBON

D. M. Stevens
General Atomic Company
San Diego, California 92138

Introduction

Nearly isotropic pyrocarbon deposited in fluidized beds has found important application as a coating on fuel particles for high-temperature gas-cooled reactors [1]. It has been known for more than a decade that the dimensional stability of these coatings during fast neutron irradiation requires an initially low preferred crystallite orientation [2]. Only recently has it been quantitatively shown by Kaae et. al. [3] that the required preferred orientation is indeed very low. The difficulty of making accurate x-ray measurements of low preferred orientation is largely responsible for the long time lapse between these developments. The use of optical reflectivity methods has alleviated this problem somewhat [4].

A highly sensitive optical method has been under development at General Atomic Co. [5,6]. This approach involves the use of a reflecting microscope with both a polarizer and an analyzer (i.e. a micropolarimeter). Recently this method was modified which resulted in a more practical and more powerful micropolarimeter [7]. This device is operated in a manner analogous to synchronously rotating the polarizer and the analyzer, and is referred to as a synchronous micropolarimeter (SMP). At the same time, General Atomic has been operating a device which is essentially a duplicate of the instrument described in Ref. 4. This microscope is used to measure reflected intensities as a function of the polarization direction of normally incident light, and is referred to as a polarizing microreflectometer (PMR). The subject of this report is a comparison of preferred orientation measurements obtained from the SMP and the PMR.

Experimental

The methods used to deposit pyrocarbon in fluidized beds have been described previously [8]. The carbons were deposited onto small graphite discs which were incorporated into the fluidized bed. The source gas was propylene, and the deposition temperature ranged from 1300° to 1500°C. (Although deposition temperature remained essentially constant throughout each individual coating run.) Deposition conditions were controlled so that several deposits were produced at widely different coating rates, but with essentially constant densities. Sample series of this nature were prepared at six different densities (see results below). The deposits were removed from the graphite substrates and mounted in polyvinylchloride. They were then sectioned perpendicular to the plane of the substrate and mechanically polished. Final polishing was done using 0.05μm alumina on an automatic polishing machine.

The SMP employs a He-Ne laser for a light source and the test region on the sample surface was 21μm in diameter. The PMR uses a white light source and the test region was 24μm in diameter. The sample surface was in immersion oil in both instruments. Local inclinations of the sample surface are corrected in the SMP by tilting the sample. This capability is not available in the PMR. Each test region was identified with fiducial marks. Using these marks, measurements in the two instruments were obtained from essentially the same test regions. Optical anisotropy measurements from each instrument are transformed to preferred orientation in terms of the Bacon Anisotropy factor (BAF). BAF is unity for uniformly distributed crystallites and increases without limit as the crystallites approach parallel alignment.

Results and Discussion

Measurements were made at six test regions on each of 33 disc samples. The results from the SMP are shown in Fig. 1. At a given density, BAF falls off rapidly with increasing coating rate initially, and changes very slowly at high coating rates. For constant coating rate, BAF increases with increasing density, and appears to be comparatively sensitive to density at high density values.

The results from the PMR fell in about the same range and exhibited a similar dependence upon coating rate, but a clear systematic variation with density could not be resolved. This comparative characteristic of the two instruments apparently arises from the improved sensitivity of the SMP. The higher sensitivity of the SMP is demonstrated in the two optical micrographs in Fig. 2. These are micrographs of the same pyrocarbon coated fuel particle. A polished metallographic section through the midpoint of the particle is viewed in reflection using horizontally polarized light at normal incidence. Without an analyzer, a slightly higher reflected intensity is observed at the top and bottom positions on the coating (i.e. 12:00 o'clock and 6:00 o'clock positions) as compared to the intensities at the right-most and left-most positions (i.e. 3:00 o'clock and 9:00 o'clock positions). This variation which corresponds to the signal detected by the PMR, is very subtle and difficult to resolve even though the preferred orientation of this pyrocarbon is more than an order of magnitude beyond the range of interest.

However when an analyzer is inserted into the reflected light with verticle transmission axis, a pronounced variation in intensity is observed at different positions along the circumference of the coating. If reflection from the sample surface does not cause the plane of polarization to shift from its original horizontal direction, then the analyzer will absorb the light. This condition occurs at four positions on the pyrocarbon coating, causing dark bands at the 12:00 o'clock position and at 90 degree intervals from that position. At intermediate positions, a rotation of the polarization direction allows a component of the reflected light to be transmitted by the analyzer. This rotation is directly related to the variation in reflected intensity observed with only a polarizer [9], and the net effect is that the analyzer has provided a pronounced improvement in sensitivity.

BAF measurements from the two instruments were correlated using three "least-squares" criteria. The line $Y=a+bX$ was fit to the data X_i, Y_i, where X_i is the value of (BAF-1) from the SMP, and Y_i is the value of (BAF-1) from the PRM, each from the ith test region. The parameters "a" and "b" were chosen so as to minimize Σd_i^2 where d_i is the distance between the ith data point (X_i, Y_i) and the line fit to the data. The path over which d_i was obtained was determined by the least-squares criterion: for criterion 1, the

path was parallel to the Y-axis, for criterion 2, the path was parallel to the X-axis, and for criterion 3, the path was perpendicular to the line being fit to the data (i.e. for criterion 3, d_i was the shortest distance between the point and the line). The results are shown in Table 1. In each criterion the correlation coefficient was 0.87 ± 0.02, but the variation in the parameters "a" and "b" according to the criterion might be a better indication of how well the relationship is known.

Criteria for choosing between the three lines are not completely clear. When X is well known and scatter is attributed only to Y, then criterion 1 is chosen, (vise versa, then criterion 2 is accpeted). But when scatter is equally attributable to X and Y, then criterion 3 should be chosen. Very little statistical information is available for making a choice. However, there is a physical basis for expecting $BAF_{PMR} \simeq BAF_{SMP}$, and since the third criterion yields nearly unit slope, it is the recommended choice.

References

1. Goeddel W. V., Nucl. Appl. 3, 599 (1967)
2. Bokros J. C., and Price R. J., Carbon 4, 441 (1966).
3. Kaae J. L., Bullock R. E., Scott C. B. and Harmon D. P., E.R.D.A. report GA-A14052, July 1976, to be published in Nucl. Tech.
4. Koss P. and Wallisch K., International Carbon Conference, Baden-Baden, Germany, June 1972.
5. Stevens D. W., Eleventh Biennial Conference on Carbon, Gatlinburg, Tenn., June 1973.
6. Stevens D. W., Twelfth Biennial Conference on Carbon, Pittsburgh, Pa., July 1975.
7. Stevens D. W., Proceedings of the International Materials Symposium, University of California, Berkeley, August 1976.
8. Bokros J. C., Carbon 3, 17 (1965).
9. Stevens D. W., General Atomic Report GA-A13307, January 1975.

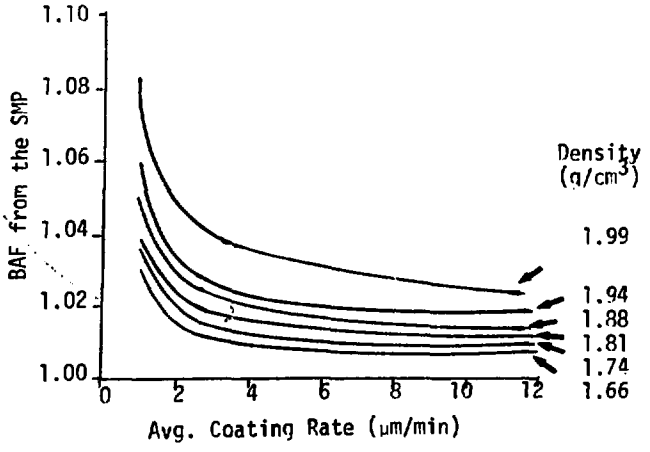


Fig. 1. Influence of Coating Rate and Density on BAF from the SMP

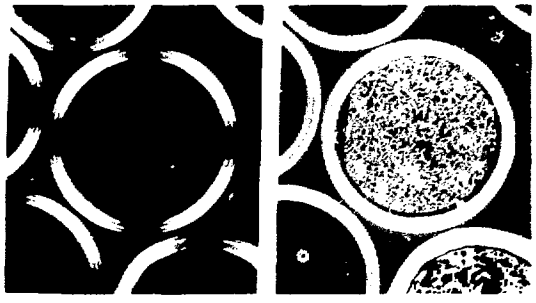


Fig. 2. Micrograph of an anisotropic pyrocarbon coating on a fuel particle, showing the effect of an analyzer on the optical signal.

TABLE 1
Least Squares Parameters for Correlation Between Preferred Orientation Data from the SMP and the PMR

Criterion	a	b	σ_x (†)	σ_y (‡)
1	0.014	0.90	0.0116	0.0104
2	0.005	1.18	0.0102	0.0119
3	0.010	1.03	0.0105	0.0108

† σ_x is the standard deviation from the line in the direction parallel to the x-axis.

‡ σ_y is the standard deviation from the line in the direction parallel to the y-axis.

X-RAY STUDIES OF GRAPHITIZATION OF GLASSY CARBON

S. Bose, R. Saxena and R. H. Bragg

Department of Materials Science and Minerals Engineering
University of California Berkeley, and the Materials and Molecular Research Division of
the Lawrence Berkeley Laboratory, Berkeley, California 94720

The structure of glassy carbon (GC) can be characterized by the interlayer spacing d_{002}, the crystallite sizes, L_a in the layer planes, L_c normal to the layer planes and the size parameters of the voids enclosed by the graphite like ribbons of the structure. Wide angle x-ray diffraction patterns have been used to determine d_{002}, L_a and L_c while small angle x-ray scattering (SAXS) was used to determine the void parameters. The x-ray diffraction pattern of GC consists of broad peaks near the graphite 00ℓ and hko reflexions. The background intensity is relatively high[1]. In addition there is intense SAXS from the voids.[2] The tail of the SAXS considerably modifies the line profile of (002) reflexion. To determine the structural parameters the background, assumed to be incoherent scattering, was subtracted first. Next, the tail end of the small angle portion which followed a trend $I(2\theta) \propto (\sin\theta)^{-n}$ was subtracted after determining n from small angle region only. Then the Lorentz and polarization corrections were made. Since the interference peaks were broad, a correction for the variation of atomic scattering factor across the peak was also made.

The xray parameters were determined to follow the kinetics of "graphitization" of GC heat treated for various times at temperatures between 1000°C and 2800°C. SAXS data were collected to understand the kinetics of 'void growth'.[2]

The variations of d_{002}, L_c and L_a for isochronal heat treatment are shown in Fig. 1. Three regions can be identified in the variations. Below 1500°C, d_{002} decreases. From 1500°C to 2100°C it remains approximately constant at 3.44A°. Beyond 2100°C, however, d_{002} decreases. L_a, L_c increase within the range of heat treatment.

To determine the activation energy of graphitization, the method of superposition[3] was tried. Fig. 2 shows the variation of L_c as a function of heat treatment time (HTt) at various temperatures (HTT). Fig. 3 shows the composite curve obtained by superposition after translation along the lnt axis. The curves for 1700°C and 2000°C are mutually superposable but do not overlap the curves for other HTT. This suggests that upto 2000°C there is a slower kinetics. The activation energy derived from curves above 2000°C comes out to be 225 ± 30 K. cal/mole. Attempts to superpose L_a and d_{002} were partially successful.

The kinetics of 'void growth' is represented in Fig. 4. Radius of gyration of the voids determined from SAXS is plotted against HTt for different HTT. It is clear that there is a distinct 'kinetics' associated with the growth of the voids.

REFERENCES

1. R. H. Bragg and M. L. Hammond, Abstracts, Seventh Biennial Conference on Carbon (Cleveland, June 1965); *also* Carbon 3, 340.

2. Madan Biswal and Robert H. Bragg, Twelfth Biennial Conference on Carbon (Pittsburgh, July 1975), p. 151-3.

3. Fischbach, D. B., Technical Report 32-532, Jet Propulsion Lab., Cal Tech, 1966.

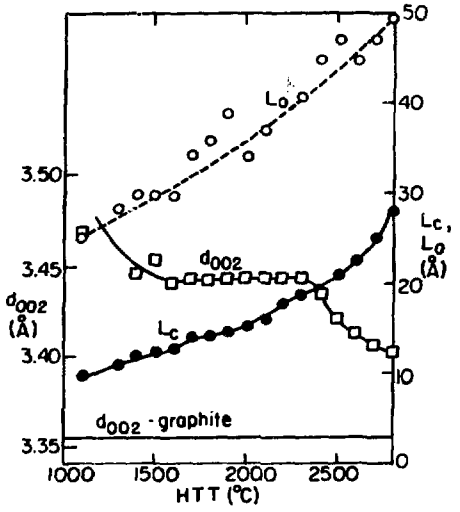


Figure 1

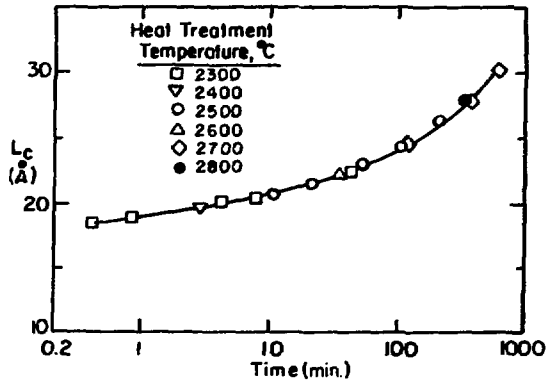


Figure 3

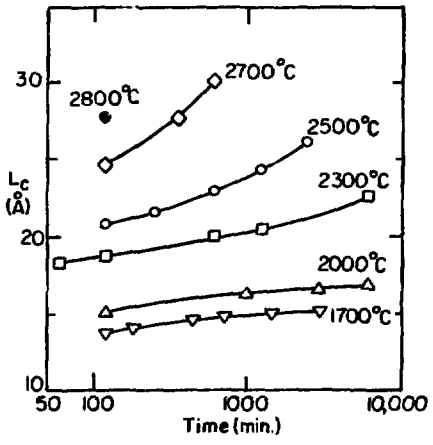


Figure 2

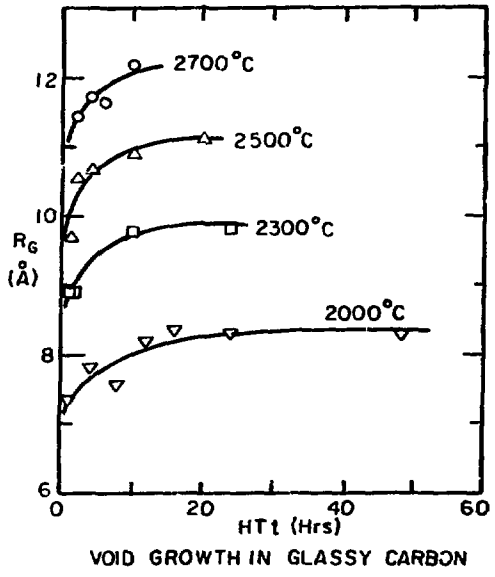


Figure 4

HIGH RESOLUTION DARK - FIELD E M APPLIED TO CARBON CHARACTERIZATION PAN FIBER MICROTEXTURE

A. OBERLIN *, F. MOLLEYRE **, M. BASTICK **

* Laboratoire Marcel Mathieu (ER 131 du CNRS) Université d'Orléans, 45045 Orléans, France

** Laboratoire de Physico-Chimie Industrielle ENSIC, 1 rue Grandville, 54042 Nancy, France

Carbon fibers are made of carbon layers more or less parallel to the fiber axis but their a axis is distributed at random. The azimutal disorder of the a axis generates hk cylinders corresponding to the rotation of each set of hk reciprocal lines. These cylinders then rotate around the fiber axis. The SAD pattern thus obtained is schematically represented in fig. 1b or 2b. Two different models of texture (1,2) fit equally well with these patterns since scattering which averages the results forbids any choice. Fig. 1a represents the fibrillar model while 2a represents a part of the lamellar one, i.e a distorted turbostratic carbon layer stack. Lattice-imaging cannot separate between the two models for two reasons. First too many details are superimposed so that no valuable restoration of the real texture can be deduced. The second reason derives from the fact that the 00.2 fringes approximate carbon layers seen edge-on. The kind of artefact which may occur is illustrated in fig. 3 which compares an object (fig. 3a) to its restoration (fig. 3c) obtained from 00.2 lattice imaging (fig. 3b). In longitudinal thin-sections or in ground materials, fibrils or folded parts of distorted lamellae look the same. In the same way, in transverse sections, the continuity of 00.2 fringes can be due either to a real curvature of the layers or to a superimposition of details situated at different levels in the fiber.

To overcome these difficulties dark field has necessarily to be used ; 00.2 DF leads to the same results than 00.2 fringes and may be used to measure the N number of parallel layers (3). Only a careful comparison of both 10 and 11 DF can separate between the fibrillar and the lamellar models. Let first consider the fibrillar model (fig. 1). If the aperture is set on 10 position the ribbons imaged as regions containing bright moiré fringes (fig. 1c) have one of their a axis approximately parallel to the fiber axis (misorientation depending on the aperture opening) and also are more or less tilted, which depends on the aperture opening. If the aperture corresponds to the 11 position more ribbons should light on since the allowed amount of tilting is then practically ± 90°. This no longer depends on the aperture opening but on the diameter of the 11 reciprocal line. Both 10 and 11 DF images show ribbon-like bright domains, variable in width, representing the prjection of the fibrils on the observation plane. On the contrary, for the lamellar model (fig. 2) ribbon-like domains should appear only in 10 DF and 11 should be quite different. Characteristic features to be noticed are the following : first more isometric domains appear which contain bright moiré fringes, then bands without contrast occur at the very location where bright domains were used to appear in 00.2 DF, finally diffuse bright lines (corresponding to moiré fringes seen obliquely) edge these bands. (Similar reasoning may be applied to the a axis of the turbostratic stack lying perpendicular to the fiber axis ; if so, 10 has to be inverted with 11). It can also be deduced from fig. 2 that, if the ρ curvature radius of the stack increases and tends to produce flat isometric lamellar particles, 10 and 11 positions should give identical images.

Such considerations have been applied in the present work to commercial PAN fibers heat-treated at 2500° C (AG 25 produced by SEROFIM, France). The fibers were prepared for EM by thin sectioning (transverse and longitudinal sections) and by wet-grinding. SAD patterns show a turbostratic material containing a small amount of partially graphitized regions (4,5). Therefore fiber texture has been found homogeneous and entirely lamellar.

The validity of the lamellar model established by high resolution DF has to be confirmed by other experiments. First the occurence of lamellae instead of ribbons, then the homogeneity of the fiber have to be proven. The occurence of lamellae is emphasized by fiber exfoliation. A lamellar compound was made by treating the fibers by a mixture of H_2SO_4 and $K_2Cr_2O_7$ during one hour ; the fibers were then exfoliated by H_2O_2. Very stable water suspensions were thus obtained including mainly small isometric lamellae besides fragments of intact fibers (the suspensions were shown to be graphite oxide free by SAD control). Krypton adsorption isotherms were performed on fiber surface at 77 K(6). They show that the surface is homogeneous and the steps produced at low p/p_o values are typical of adsorption localized on basal planes of graphite layers and not on their edges. The amount of chemical groups distributed on the surface is also evaluated to be low, which fits well with the lack of reactive carbons i.e edge-carbons. All the experiments agree quite well with the fact that both surface and core of the fibers are lamellar. Homogeneity of the fiber has been tested and confirmed by oxidation kinetic studies using O_2 and CO_2. Oxidation rate was followed by DTG and gas analysis. The curves are all monotonous, sample reactivity does not change when oxidation gets deeper and deeper.

In conclusion it must be kept in mind that lattice-fringes represent only a part of the reciprocal space which can be possibly analysed by imaging. It is absolutely necessary to achieve the exploration of the whole available reciprocal space in using DF techniques especially in using as many reflections as possible.

(1) R. Bacon. In Chemistry and Physics of Carbon 9, 1 (1973) P.L. Walker, P.A. Thrower ed. Dekker N.Y.

(2) W.N. Reynolds. In Chemistry and Physics of Carbon 11 1 (1973) P.L. Walker, P.A. Thrower ed. Dekker N.Y.

(3) S.C. Bennett, D.J. Johnson and R. Murray, Carbon 14, 117 (1976)

(4) D. Crawford and D.J. Johnson, J. Microsc. 94,51 (1971)

(5) D.J. Johnson, D. Crawford and B.F. Jones, J. Mater. Sc. 8, 286 (1973)

(6) A. Thomy, M. Matecki et X. Duval, Carbon 9, 587 (1971)

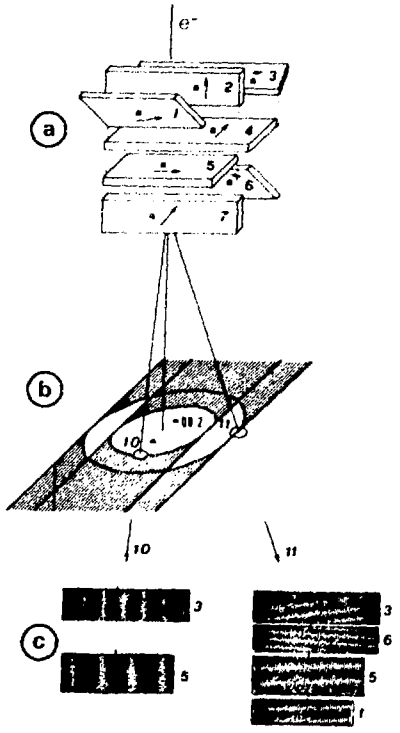


Figure 1

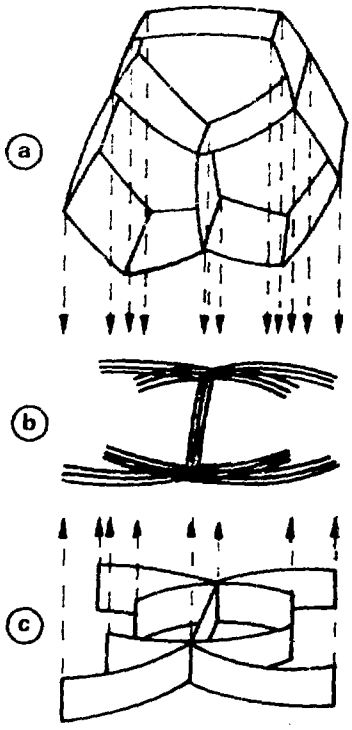


Figure 3

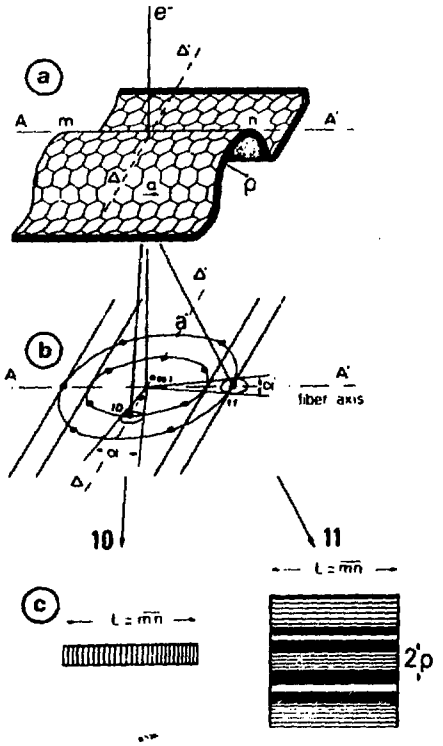


Figure 2

EFFECTS OF FIBER CHOICE AND WEAVE GEOMETRY UPON CYLINDRICAL WEAVE CARBON/CARBON

John J. Kibler
Materials Sciences Corporation, Blue Bell, PA

Summary

A material synthesis study is described herein, which has had the goal of providing guidance to the experimental carbon/carbon materials development programs for cylindrical weave integral throat and entrance section carbon/carbon nozzles.

A wide range of weave geometries and fiber choices were evaluated to determine both the thermomechanical properties and processing- and service-induced stress levels for cylindrical weave materials. The results of this study indicate that weave geometries which favor reduced axial and radial fiber content and increased hoop fiber content result in a reduction of hoop fiber stress levels.

For many weaves, the billet I.D./O.D. ratio has been shown to have a significant effect upon the processing stresses. Radial fiber pullout due to free surface effects has been shown to significantly increase the predicted hoop fiber stresses over cases where the radial fibers are assumed to act to their fullest capability.

Discussion

This study has been restricted to cylindrical weave materials. For cylindrical weaves, it can be shown that the thermal stress states developed in the hoop fibers during processing are the critical ones. It can also be shown that the thermal stresses in service, for the kinds of geometries being considered, are relatively of secondary importance. However, a screening for service-induced thermal stresses was made on the basis of a very simple temperature gradient to be sure that no serious discrepancies among the behavior of the various materials were being overlooked. A true evaluation of service performance requires consideration of at least two-dimensional stress states, rather than the one-dimensional ones considered herein, so that the shear stresses can be included. The shear stresses are a possible source of weakness of these materials during service.

The analytical screening required first determining the available fiber properties for the ten fibers to be considered. The unavailable properties were estimated and the range of geometries and loading conditions were defined. Next, the composite properties were computed and combined with the loading conditions and nozzle geometry to define the fiber stress levels. Composite strengths were predicted, and the resulting stress ratios (fiber strength/fiber stress) for each loading condition were determined. The materials with the least chance of experiencing damage during processing and the best chance of surviving firing gradients could thus be defined and identified as the best candidates for future evaluation.

Fiber Properties

The fibers which were considered for nozzle application included several commercially available fibers, T50, T300, HM1000, Pitch fiber (VS0022), along with several experimental fibers. At the time of the analysis, some preliminary test data on the axial properties of all of these fibers were available, and those properties were used in the analyses.

The available property data for most of the fibers considered included axial moduli and dry yarn strength versus length at room temperature, modulus and strength at several elevated temperatures, and axial thermal expansion of the yarns. Various estimating procedures were utilized to obtain the required fiber properties for those cases where the absence of good test methods or test data or both resulted in fiber properties being unavailable.

Test results provided "as received" yarn strength versus length data such that the room temperature Weibull strength parameters could be defined. For the fibers where no strength data at elevated temperatures existed, the moduli and strengths were assumed constant with temperature. This assumption is reasonable for most graphite fibers for temperatures up to near 4000F. For fibers where some elevated temperature properties were available, the elevated temperature moduli and strengths were utilized.

Weave Geometries

With all multidimensional composites, significant variations in properties can be obtained through variations in weave geometries. With cylindrical weaves, the manufacturers have a reasonable degree of latitude in weaving the preforms. Therefore, a study of the weave geometry effects was undertaken to define the factors which are most desirable for a cylindrical weave relative to processing- and service-induced thermal stress levels.

Fiber packing within the fiber bundles was assumed to be 58%. Axial prism volume fractions were considered from 25 to 45%. Radial prism volume fractions were considered from 5 to 35%, while the hoop prism volume fraction was varied between 15 and 45%. Thus a wide range of weave geometries were considered to identify the trends apparent due to weave configuration.

Loading Conditions

Two basic loading conditions were considered: processing-induced stresses due to the graphitization cycle and service-induced stresses due to temperature gradients within the nozzle.

Prior to the last graphitization cycle during processing, it is assumed that a high pressure pitch impregnation cycle has resulted in filling all of the cracks and voids within the unit cell. Thus, no cracks exist at the start of graphitization. As the temperature is increased to 1000F, the pitch will carbonize, resulting in some cracking. The amount of cracking at 1000F is assumed to be small, such that assuming an uncracked unit cell at 4000F is slightly conservative.

A nozzle billet subjected to a uniform temperature rise develops thermal stresses due to property mismatches at several levels: between the fiber and matrix within the fiber bundle, between the subcell regions within the unit cell, and due to the cylindrical anisotropy of the nozzle billet.

The service-induced stresses occur on a processed material. Hence, subcell cracking will exist and it is appropriate to use post-processing properties. Service stresses arise from temperature gradients, cylindrical anisotropy, nozzle geometry, and internal nozzle pressures. For screening purposes, a slice of the nozzle was analyzed. Internal pressures were not applied. A linear temperature gradient was assumed.

Results

The variables addressed during this study have been aimed at determining the best potential fibers and weave configurations for a cylindrical weave rocket nozzle material. Each of the major areas considered is discussed below.

Changing radial and circumferential volume fractions while holding the axial prism volume fraction at 25% was found to result in increasing stress ratios with increasing hoop fiber content.

The effects of geometry changes and the differences between processing-induced stresses and a linear temperature gradient were investigated for the T50 PAN fiber system. The hoop fiber stresses decrease with decreasing axial fiber content and increasing hoop fiber content. In all cases, the stress ratios resulting from a temperature gradient on a fully processed material are higher than the processing-induced stress ratios. This indicates that processing induces the most severe thermal environment for a cylindrical weave. The limiting case is an all hoop wrap material. However, an all hoop wrap material may not be desirable due to low resistance to cracking between hoop fibers and possible poor recession performance. In other words, failure modes other than hoop fiber failure will dominate if the geometry is varied to an extreme. The limits to which one might change the geometry without involving other detrimental effects were not fully explored in this study.

If one assumes that the radial fibers are intact and carrying their full load in the composite, then very large radial fiber stresses are predicted. Since the radial fibers are short and intersect two free surfaces, the fiber bundles can crack away from the surrounding composite. If the radial fiber bundles crack away from the composite at the surface, then some finite distance along the fiber bundle is required before the fiber bundle stresses can be built up to their full level. It is this phenomenon which is believed to prevent large numbers of yarns being fractured during graphitization of a 3-D cartesian billet. In cylindrical weaves, radial fiber unbonding results in a significant increase in the radial expansion coefficient of the billet and a very large increase (40-70%) in the hoop fiber stress levels.

The effect of changing billet geometry on processing stress levels is of concern since the goal of the material development is to apply carbon/carbon to larger diameter nozzles. As an initial step in evaluating the effects of billet geometry upon processing-induced stress levels, several T50 PAN materials were modeled in billets with a fixed 10" O.D. and a variable I.D. The effect of billet geometry (R/t) upon the hoop fiber stresses depends upon the cylindrical anisotropy of the material. If the weave is balanced, such that radial and hoop moduli and thermal expansions are equal, then there are no macroscopic stresses developed for a uniform temperature rise and the billet R/t will not affect the hoop fiber stress levels during processing. If, however, the weave is not balanced or if radial fibers pull out, then increasing billet R/t results in increasing hoop fiber stress levels.

NONLINEAR FINITE ELEMENT ANALYSES OF REENTRY VEHICLE GRAPHITE NOSETIPS

T. E. Mack and J. G. Crose
Prototype Development Associates, Inc.
Santa Ana, California 92705

Introduction

Reentry vehicle graphite nosetips must be designed to withstand the extreme aerodynamic heating, pressure, and shape change associated with reentry environments. Expense and difficulty in obtaining sufficient instrumented flight test data, combined with requirements for increasing vehicle probability of survival, dictates the need for accurate material characterization and test proven analytical methods. The development of such analytical methods, however, is complicated by the unusual behavior of graphite under load and limited availability of multiaxial mechanical property data.

Molded graphite, a transversely isotropic material, exhibits different nonlinear stress-strain behavior in tension and compression and its strain response tends to be greater in biaxial tension than uniaxial tension ("biaxial softening" phenomenon, Ref. 1). Also, the material's inelastic strain behavior is not isovolumetric ("plastic" volume change) which indicates that classical theories of plasticity are not applicable.

A finite element analysis method which incorporates an appropriate nonlinear anisotropic stress-strain law has been developed (Ref. 2). The method, in conjunction with a physically based statistical failure theory (Ref. 3, 4), was applied to the prediction of thermostructural failure of graphite nosetips tested in a rocket nozzle environment. The method closely correlated with test results and provided evidence of the importance of accounting for inelastic volume change in the nonlinear stress-strain model.

Analytical Method

The nonlinear analysis method is an iterative solution technique which independently varies the material properties for each subsequent solution cycle based on the magnitude (nonlinearity) and sense (tension or compression) of the previous solution cycle's stress state. The method uses a temperature dependent material model developed by Jones and Nelson (Ref. 2). The strain energy

$$U = (\sigma_r \varepsilon_r + \sigma_z \varepsilon_z + \sigma_\theta \varepsilon_\theta + \tau_{rz} \gamma_{rz})/2$$

is used to scale the degree of nonlinear response by relating material properties to multiaxial stress strains in accordance with the following empirical material property equation,

$$\text{Material Property} = A[1-B(U/U_o)^C]$$

where A, B, and C are constants determined from uniaxial stress-strain and strain-strain test data. The model accommodates unequal tension and compression nonlinear stress-strain curves of varying shape and variable Poisson's ratios. Use of the method implies that volume change can occur as a result of material tearing and microcracking ("biaxial softening").

The probability of failure theory (Refs. 3, 4) uses a stressed based, anisotropic, weakest link statistical approach. The method correlates well with uniaxial and biaxial experimental failure data.

Test and Analysis Correlations

Eight (8) graphite plug nosetips were tested in a shrouded rocket nozzle environment (Ref. 5). The specimen failure times were determined by ultrasonic measurements. Experimental probability of failure for this test series was 75 percent (six (6) specimens failed).

The new material model and associated iterative solution logic were updated into the SAAS III computer program (Ref. 6) and used to analyze the tested nosetip. Fig. 1 shows the test results and analysis predictions illustrating the excellent correlation obtained. One specimen failed without sonic detection. The upper and lower estimates of the test scatter (Fig. 1) were obtained by assuming that this specimen could have failed at any time up to and including 10.6 seconds, when it was first detected (by camera) to have failed.

To further evaluate the nonlinear analysis method, SAAS III linear solutions were completed. The stresses were substantially greater than those computed by the nonlinear method. The strains, however, were relatively insensitive to the method of analysis, as illustrated in Fig. 2. The linear strains were transformed into approximated nonlinear stresses, using a modified version of the Jones and Nelson model (Ref. 7). Fig. 1 also compares the linear analysis predicted failure curve with the test data. The results were somewhat conservative (consistent with other ground test analyses). The nonlinear results clearly removed the linear analysis conservatism.

Conclusions

Nonlinear analyses showed excellent agreement with test results. The Jones/Nelson nonlinear material model represents a reasonable approach to more accurately model the stress-strain behavior of graphite. The demonstrated availability of numerical techniques which accurately simulate the actual response of graphite represents a significant advance in thermostructural technology.

References

1. J. Jortner, "Multiaxial Response of ATJ-S Graphite," AFML-TR-73-170, October 1973.
2. R. M. Jones and D. A. R. Nelson, "A New Material Model for the Nonlinear Biaxial Behavior of ATJ-S Graphite," J. Composite Materials, Vol. 9, January 1975.
3. J. D. Buch, J. G. Crose, and E. Y. Robinson, "Failure Criteria in Graphite," AFML Final Report, PDA 1023-00-26, Prototype Development Associates, Inc., January 1977.
4. J. G. Crose, J. D. Buch, and E. Y. Robinson, "A Fracture Criterion for Anisotropic Graphites in Polyaxial Stress States," Proc. 12th Conf. on Carbon, 1975.
5. M. J. Rebholz and R. D. Teter, LMSC-D436937, Lockheed Missiles and Space Co., Sunnyvale, CA, June 1976.
6. J. G. Crose and R. M. Jones, "SAAS III, Finite Element Stress Analysis of Axisymmetric and Plane Solids with Different Orthotropic, Temperature-Dependent Material Properties in Tension and Compression," TR-0059 (S6816-53)-1, The Aerospace Corporation, San Bernardino, California, June 1971.
7. R. L. Holman, J. G. Crose, and J. D. Buch, "Application of the Jones/Nelson Non-Linear Stress-Strain Law to Reentry Survival Predictions," 13th Conf. on Carbon, July 1977.

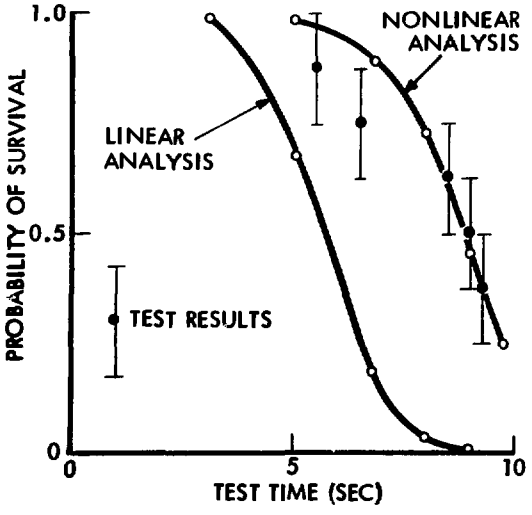


Figure 1. Probabilities of Survival Versus Test Time

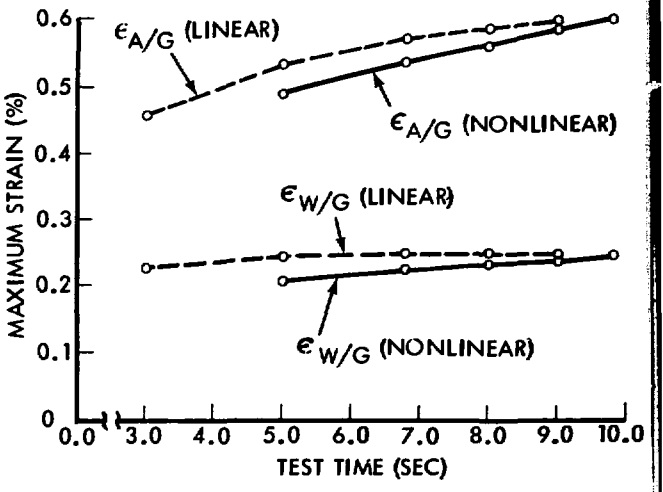


Figure 2. Maximum Across Grain and With Grain Strains Versus Test Time

ANALYTICAL RELATIONSHIPS BETWEEN BULK DENSITY AND PORE SIZE IN 3D CARBON-CARBON COMPOSITES

Julius Jortner
McDonnell Douglas Astronautics Company
Huntington Beach, California 92647

Achieving high density of 3D carbon-carbon composites requires repeated impregnations of the weave (with pitch, resin, and/or pyrolytic carbon), pyrolyses, and graphitizations [1][2][3]. The bulk density of graphitized 3D composites is limited by the opening of cracks on cooling from the graphitization temperature [4], the "freezing-in" of pyrolysis-gas bubbles in pitch-precursor carbon, and the formation of voids or cracks as the solidified matrix shrinks during pyrolysis and graphitization. Thus, even if the apparent density of the matrix and fibers were to be that of perfect graphite (about 2.26 g/cm^3), the attainable bulk density of the composite would be measurably lower. The bulk density of near-isotropic polycrystalline graphites is similarly limited to about 2.1 g/cm^3 [5] [6]. Another limitation is the dimensional growth of carbon-carbon billets, in the later stages of processing, which sometimes results in reduced density in spite of mass gains [1].

Crack Volume

The volume of crack space V_c formed in a unit volume of composite on cooldown to room temperature T_R from the crack-opening temperature T_c may be estimated:

$$\frac{V_c}{T_c - T_R} = 2\alpha_{Y_t}[1-\xi(1-\xi)] + 3\alpha_M \xi(1-\xi) - \alpha_{Y_a}[2+\xi(1-\xi)] \quad (1)$$

where the α's are the thermal expansion coefficients of the yarn bundles (α_{Y_t} is transverse and α_{Y_a} is parallel to the axis of the fibers) and the matrix (α_M), and ξ is the ratio of x_z to x (Figure 1) for weaves in which $x = y$ and $x_z = y_z$. Equation (1) assumes cracks, of the type sketched in Figure 1, completely relieve the internal tensile stresses that would act during cooldown as a result of $\alpha_{Y_t} > \alpha_M > \alpha_{Y_a}$.

Calculations made using equation (1) imply three to five percent of the volume is occupied by the crack space. Representative values for thermal expansivities were used: yarn-bundle expansivities (α_{Y_t} = 7 to 13 x 10^{-6}/°C, α_{Y_a} = 1 to 1.8 x 10^{-6}/°C) were based on data for unidirectional carbon-carbons made with high-modulus fibers [7][8] and on in-situ measurements using elevated-temperature microscopy of 3D composites [9]; α_M was taken as 5 x 10^{-6}/°C, equal approximately to that of ATJS graphite. The crack-opening temperature was taken as ranging from about 2000°C to 2800°C [9]. Sensitivity of crack volume to weave geometry, as represented by ξ, appears to be a second-order effect.

Pore Size

3D carbon-carbons, densified with pitch at pyrolysis pressures p below a threshold value p*, tend to contain one pore in each matrix pocket. The threshold pressure may be viewed as the pressure at which the pyrolysis gas occupies the same volume as is made available by the shrinking liquid pitch; that is, at p* there is no need for liquid pitch to be ejected from the composite during the initial stages of pyrolysis. At $p < p^*$, outflow of pitch promotes coalescence of gas into one large bubble in each matrix pocket. Composites pyrolyzed at (or above?) p* will tend to retain a number of separate small pores in each matrix pocket. Judging from microstructural views of finished composites[10], p* is in the vicinity of 900 atmospheres; probably p* is quite sensitive to the grade of pitch and to the thermal and barometric histories of the pyrolysis.

These speculations lead to the concept of a "mechanical" carbon-yield factor Y' (which is pressure dependent) in addition to the coke-yield factor Y (which appears insensitive to pressure above about 50 atm [2][11]). Thus, the volume fraction c of graphite (of apparent density ρ_G) retained within a matrix pocket after impregnation with a unit volume of liquid pitch (having an initial density ρ_L) is:

$$c = Y Y' \rho_L / \rho_G \quad (2)$$

Values of Y' above one might occur at $p > p^*$.

The bulk density of the 3D carbon-carbon may be given as:

$$\rho_B = \rho_{AY}(V_Y - V_{YP}) + \rho_{AM}(V_M - V_P) \quad (3)$$

where the volume fractions add up to unity:

$$V_Y + V_M + V_{YP} + V_P + V_C = 1 \quad (4)$$

and ρ_{AY} = apparent density of yarn bundle
ρ_{AM} = " " " matrix in pockets
V_Y = volume fraction of yarn bundles
V_M = " " " matrix pocket
V_P = " " " matrix-pocket pores
V_{YP} = " " " yarn bundle voids
V_C = " " " crack space

For illustrative purposes, we assume a balanced weave ($x = y = z$, $x_z = y_z = z_m = 0.5x$, $V_M = 0.5$, see Fig. 1). If N pores of dimension x_P reside in each matrix pocket:

$$V_P \cong N\left(\frac{x_P}{x_M}\right)^3 V_M \quad (5)$$

Combining equations (3),(4) and (5), one can derive the relations between average pore size and bulk density shown in Figure 2. Additional assumptions behind Figure 2 are $\rho_{AY} = \rho_{AM}$, $V_C = 0.04$, and that V_{YP} is either zero or included in V_C. The assumption implicit in this treatment, that the yarn bundles are essentially fully densified and do not gain in density while the matrix pores are diminished during the last several process cycles, receives support from process histories of unidirectional and 3D composites densified in the same batch [12].

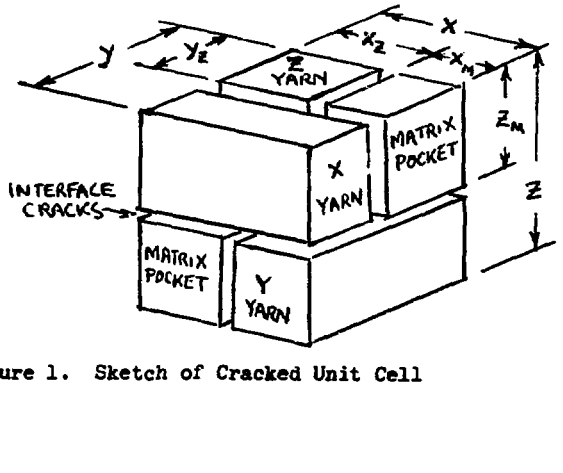


Figure 1. Sketch of Cracked Unit Cell

Billet Growth

Each additional impregnation/pyrolysis/graphitization cycle contributes to the fractional mass gain and the fractional volume growth of the billet:

$$\frac{\Delta m}{m} = \frac{\rho_A}{\rho_B}\left[C_c V_c + C_p V_p\right] \qquad (6)$$

$$\frac{\Delta V}{V} \doteq \frac{4}{3} C_c G V_c \quad \left(\text{for balanced weaves}\right) \qquad (7)$$

where C_c = volumetric yield of graphite in cracks
C_p = " " " " " in pockets
G = factor to account for other effects on the creep strain of yarn bundles during graphitization
ρ_A = apparent density of the composite

A decrease in bulk density can occur with added processing if the fractional volume growth exceeds the fractional mass gain. Combining equations (3),(4),(5) (6) and (7), gives the following estimate for the maximum attainable bulk density ρ_B^* :

$$\frac{\rho_B^*}{\rho_A} = \frac{C_p + V_c\left(C_c - C_p\right)}{\frac{4}{3} C_c G V_c + C_p} \qquad (8)$$

The volumetric yields may be estimated from equation (2) using reasonable estimates of the various factors: Y = about 0.8 [2]; Y' = 1.0 for the crack space and for pores densified at $p > p^*$, and Y' = about 0.3 for pores densified at $p \ll p^*$; $\rho_t/\rho_G = 0.67$ [13]. Based on these preliminary estimates, and taking the creep factor G as unity, maximum density is predicted to range between $0.92\rho_A$ and $0.95\rho_A$, for an assumed crack volume $V_c = 0.04$. The growth limits to bulk density are schematically shown in Figure 3.

Concluding Remarks

The bulk density of graphitized 3D carbon-carbons appears limited to about 92 to 95 percent of the apparent density of the constituents. Principal factors contributing to this limitation are the crack space that forms during graphitization and the billet growth phenomenon. The variation of pore size with bulk density is greatest as the maximum bulk density is approached; at high bulk densities, pore size is also quite sensitive to variations in apparent density. In composites densified with pitch, pore-size sensitivity will be reduced if pressures higher than a threshold value are applied during pyrolysis while the pitch is still fluid.

These conclusions are derived from the simplified illustrative calculations offered above. The issues deserve more detailed treatments as to the influences of weave geometry, yarn-bundle porosity, and differences between the apparent densities of the yarn bundles and the matrix pockets, among other factors. Study of the process parameters that control apparent density and the in-situ volumetric yields of graphite appears worthwhile, as does study of the creep behavior of yarn bundles at high temperatures.

Acknowledgement

This work was sponsored by the McDonnell Douglas Corporation under an Independent Research and Development program.

References

1) Seibold R.W., at this conference (1977)
2) Burns R.L. and Cook J.L., Petroleum-Derived Carbons, ACS Symposium Series 21, 139-154 (1976)
3) Chard W. et al, Ibid., 155-171 (1976)
4) Jortner J., Proc Army Symp Solid Mech, 81-97, AMMRC MS 76-2 (Sep 1976)
5) Mrozowski S., Proc 1st & 2nd Conf on Carbon (1956)
6) Hodgson E.W.Jr, Cornell Aero Lab DM 2270 E6 (1972)
7) Perry J.L. and Adams D., J Mat Sci 9,1764-74(1974)
8) Wilson R., U.S.Navy NSWC/WOL/TR76-47 (Feb 1976)
9) Jortner J., paper to 29th Pacific Regional Mtg, Am Ceram Soc, San Francisco (Nov 1976)
10) Eitman D.A. amd Binder J.D., Science Applic, Inc, SAI-061-76-09-002, Santa Ana, Calif (Sep 1976)
11) Fitzer E. and Terwiesch B., Carbon 11,570-74(1973)
12) Eitman D.A. et al, McDonnell Douglas report to US Navy (NSWC/REVMAT) MDC G5423 (July 1974)
13) White J.L., Aerospace Corp report to US Air Force, SAMSO-TR-74-93 (Apr 1974)

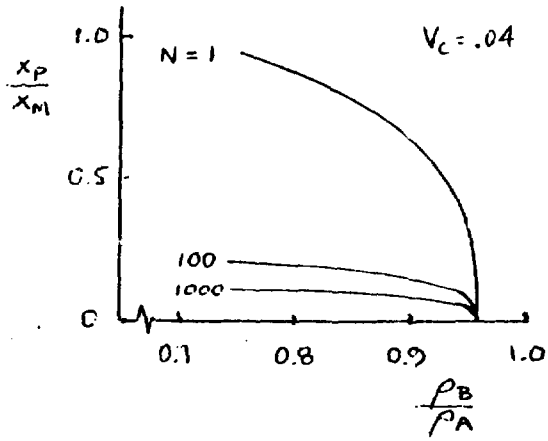


Figure 2. Pore Size vs. Density (No Growth)

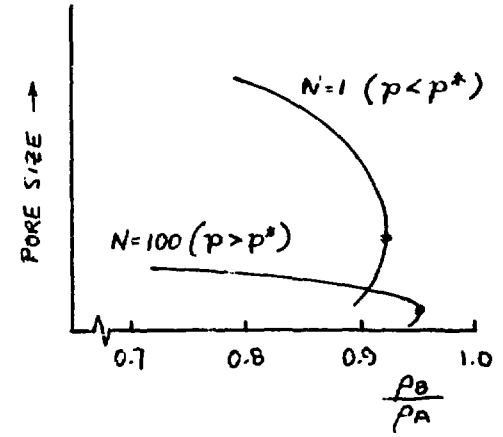


Figure 3. Growth Limits to Density (Schematic)

APPLICATION OF THE JONES/NELSON NONLINEAR STRESS-STRAIN LAW TO REENTRY GRAPHITE SURVIVAL PREDICTIONS

R. L. Holman, J. G. Crose, J. D. Buch
Prototype Development Associates, Inc.
Santa Ana, California 92705

Introduction

Reentry vehicle graphite nosetips encounter a severe thermostructural loading condition. Accurate prediction of material deformation response requires a set of constitutive relationships to account for the unique mechanical response of aerospace graphites demonstrated in laboratory studies by Jortner (Ref. 1).

This behavior, termed "biaxial softening," is the observation of increased strain and compliance in biaxial stress states over that accounted for by classical elastic-plastic deformation theories (Fig. 1). The data indicates the need for a new material model that can account for coupling between multiaxial stresses other than, and in fact opposite to, normal Poisson effects.

Jones and Nelson (Ref. 2) have developed a material model based on a strain energy scalar as the state variable controlling the constitutive equations of material response. The adaptation of this model for practical application and its use with a previously developed statistical failure model for prediction of graphite failure is the subject of this paper.

Modeling Approach

The method developed by Jones and Nelson uses the strain energy density function

$$U = (\sigma_r\varepsilon_r + \sigma_z\varepsilon_z + \sigma_\theta\varepsilon_\theta + \tau_{rz}\gamma_{rz})/2$$

normalized to a reference value U_o as a scalar quantity to vary the material properties as a function of stress state. The equation selected by Jones and Nelson is

$$\text{Material Property} = A[1-B(U/U_o)^C]$$

where the constants A, B, and C are determined from test data. In theory, the above equations are used in an iterative scheme to determine the secant moduli and Poisson ratios which simultaneously satisfy the individual stress-strain relationships, as well as the total strain energy to stress state dependence. Figure 2 shows the functional relationship of the variables for a uniaxial stress state. An inherent problem with the Jones/Nelson equation is that it does not extrapolate well beyond the data to which it was fit. A typical fit of the model to graphite data gives a stress-strain curve that rolls over and becomes asymptotic to zero stress at large strains. While this causes no problems for uniaxial strains within the failure limits of graphite, the total strain energy for a multiaxial stress state can be great enough to operate on the extrapolated stress-strain curve well beyond the failure point. The net result is a solution which is difficult or impossible to converge upon, as well as being a poor representation of material behavior.

A solution to this problem has been developed in which a two part stress-strain curve is used. The Jones/Nelson equation is used to describe the uniaxial stress-strain relation up to the failure threshold and a linear equation of the form

$$\sigma = \sigma_o + E_\infty\varepsilon$$

is used thereafter. The constants σ_o and E_∞ are determined so that the line passes through the mean failure stress and strain point and the 95 percent survival stress and strain values from available uniaxial test data. The Jones/Nelson curve is constrained to intersect and be tangent to the linear portion at the 95 percent survival level. This technique correlates the stress and strain failure statistics, as well as accurately modeling observed stress-strain curves.

The resulting stress-strain model is shown in Figure 3. The linear relationship was reformulated so that the secant modulus is calculated by

$$E_{sec} = 8UE_\infty^2/\left(-\sigma_o+\sqrt{\sigma_o^2+8UE_\infty}\right)^2$$

which is compatible with the strain energy formulation used by the Jones/Nelson equation.

The amount of data available for the dependence of Poisson ratios on strain energy was considered insufficient to develop a valid model, so constant values are assumed. It was also found that interpolating values of the constants A, B, and C between temperatures gave erratic results. This was remedied by interpolating the values of the calculated secant moduli.

Results

Material models using the modified Jones/Nelson formulation have been developed for several aerospace grade graphites. They have been used in conjunction with a stress based statistical failure criterion (Ref. 3) and comparisons with laboratory test data for uniaxial and biaxial failure strains are presented in Figures 4 and 5. Additional correlation with predicted strains for full scale ground tests of ATJS nosetips (Ref. 4) provides further verification of the method.

Conclusion

An analysis method for thermostructural evaluation of graphites has been developed which accounts for the deformation and fracture behavior particular to graphitic materials. The practical application of the model has

been demonstrated and its predictions are consistent with all known laboratory failure data.

References

1. J. Jortner, "Multiaxial Response of ATJS Graphite," McDonnell Douglas Astronautics Co., AFML-TR-73-170, October 1973.
2. R. M. Jones, D. A. R. Nelson, Jr., "A New Material Model for the Nonlinear Biaxial Behavior of ATJ-S Graphite," J. Composite Materials, Vol. 9, January 1975.
3. J. G. Crose, J. D. Buch, E. Y. Robinson, "A Fracture Criterion for Anisotropic Graphites in Polyaxial Stress States," Proc. 12th Conf. on Carbon, 1975.
4. J. D. Buch, J. G. Crose, R. L. Holman, T. E. Mack, "Correlation of a Physically Based Statistical Theory of Fracture...," Proc. 13th Conf. on Carbon, 1977.

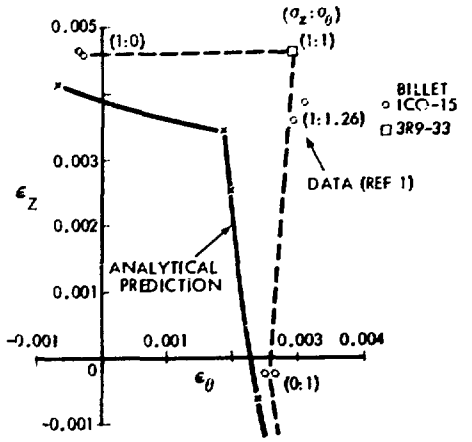


Fig. 1. ATJS Biaxial Stress Response at 70°F for 3550 psi Maximum Principal Stress Elastic-Plastic Theory Prediction and Data

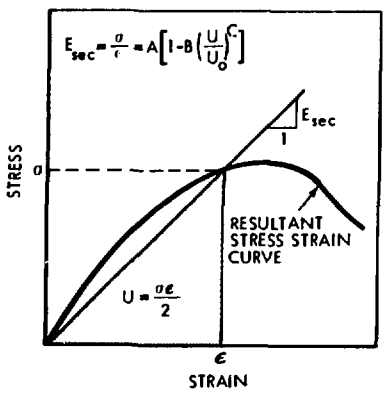


Fig. 2. Jones/Nelson Model of Uniaxial Stress-Strain Behavior

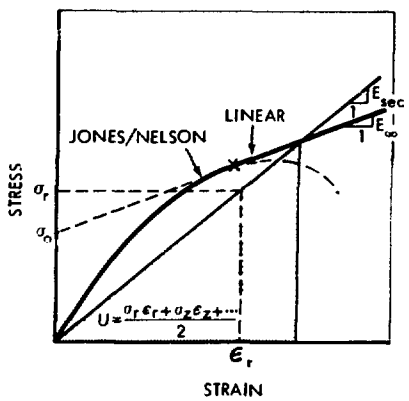


Fig. 3. Modified Jones/Nelson Model of Multiaxial Stress-Strain Behavior

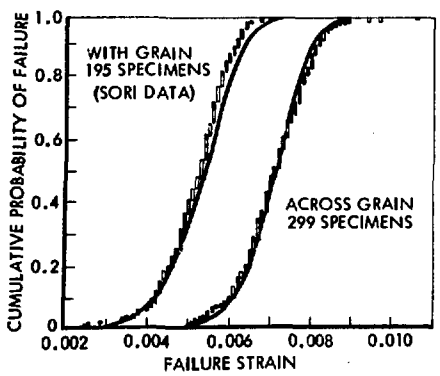


Fig. 4. 994-2 Graphite Failure Strain at 2000°F, Predictions and Data

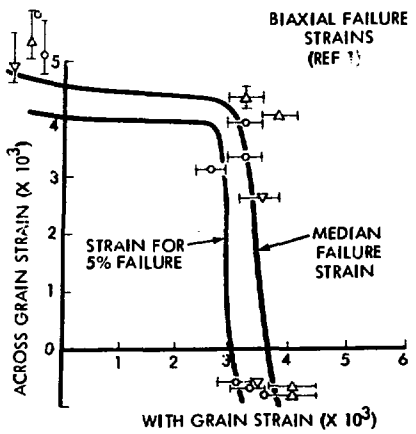


Fig. 5. ATJS Biaxial Failure Strains at 2000°F, Predictions and Data

CHARACTERIZATION OF CARBON CARBON COMPOSITES

R. J. Diefendorf
Rensselaer Polytechnic Institute
Materials Engineering Department
Troy, New York 12181

Ideally, composite properties should be predictable from a knowledge of constituent properties and composite geometrical parameters. In conventional resin matrix composites, some of the more important constituent properties can be directly measured on the constituents, while the remainder can be derived from composite measurements.

Carbon/carbon composites present a more complex case as the available evidence indicates that matrix and fiber properties undergo significant mechanical property changes during fabrication. Furthermore, the fiber and matrix are interacting, such that identical processing of the constituents will produce different mechanical properties from those derived from the composite. The interaction is a maximum for high preferred orientation constituents, as a small variation in preferred orientation will produce large property change. For high modulus fibers and graphitizable matrices, constituent properties in the final composite cannot be inferred from independent constituent tests, but usually must be derived from preferred orientations, and microstructures, as well as composite tests. Relationships between X-ray preferred orientation and modulus[1,2] or coefficient of thermal expansion[3] have been made, but are not convenient to use for carbon/carbon composites. Similar relationships should exist for optical preferred orientation. Quantitative reflected polarized light microscopy has been used in the past to obtain a number which describes the average orientation. While accurate if only a single orientation is present in the field of view, it provides a biased result if a distribution exists. The problem can be solved by measuring light intensity distributions. Although theoretical problems remain, preliminary studies indicate that optical measurements provide a method to quantitatively determine preferred orientation distributions which can be related to modulus, and coefficient of thermal expansion.

References

1. Ruland, W., "The Relationship Between Preferred Orientation and Young's Modulus of Carbon Fibers", Poly. Preprints Vol.9 #2, 1968.

2. Diefendorf, R. J., Fitzer, E. and Heym, M., "Verstarkungsfasern für Verbundwerkstoffe", Chemie Ingenieur Technik 48 #9, 765 (1976).

3. Butler, B. L. and Duliere, S. F., Relation of Carbon Fiber Axial Thermal Expansions to Their Microstructures", Sandia Laboratories SLA-73-0485, 1973.

GLASSY CARBON AS A CATALYST SUPPORT

P. L. Walker, Jr., A. Oya and O. P. Mahajan
Department of Material Sciences
The Pennsylvania State University
University Park, PA 16802

Introduction

Noble metal catalysts supported on activated carbons are used in several industrial chemical processes. However, these carbons are invariably associated with mineral impurities which may act in some cases as dissociating centers for reactant molecules and/or may act as catalyst poisons. Further, activated carbons usually have a polymodal distribution of pores whose diameters vary from a few angstroms to several thousand angstroms. Depending upon the sizes of the reactant and product molecules involved in catalytic reactions, a part of the area contained in smaller pores and, hence, the catalyst contained in such pores may not be accessible for the reactions. There is thus interest in the production of relatively pure carbons with desired shape (configuration), porosity, pore size distribution and surface area. We believe that such carbons can be prepared by judiciously choosing and/or modifying the experimental conditions and procedures outlined by Hucke (1) for the preparation of glassy carbons. The present study describes the results of such an attempt.

Experimental

The basic ingredients for preparing glassy carbons with controlled porosity are: a carbon-yielding binder, a liquid pore former, a dispersing agent and a consolidating agent (1). The pore forming liquid helps escape of gases during pyrolysis of the binder. The function of the dispersing agent is to produce a uniform distribution of the various ingredients. The consolidating agent promotes catalytic polymerization of the binder. In the present study we have used furfuryl alcohol (FA) as the binder, diethylene glycol (DEG) as the pore former, Triton X-100 (iso-octyl phenoxy polyethoxy ethanol) as the dispersing agent and p-toluene sulfonic acid (PTSA) as the consolidating agent. We have also used polyethylene glycol (PEG) both as a pore former and as a dispersing agent.

The following procedure was used to prepare carbons. The consolidating agent was added to the mixture of the dispersing agent and pore former at about 75-95°C. After cooling the resultant solution to about 15°C, the binder was added in small amounts with constant stirring; the temperature during the addition was kept between 20 and 25°C. The mix was then allowed to polymerize at 20-25°C for 2.5 hr, after which it was put into molds (glass tubing, 6mm O.D. and 25cm long). For thermal setting, the following cycle was generally used: 24 hr in cooling water at 15-20°C, 24 hr at room temperature (20-25°C), 24 hr at 45°C, 2 days at 70°C (after 12 hr at 70°C, samples were removed from the molds) and 3 days at 95°C. The polymerized sample 'rod' was cut into pellets of about 2cm in length. The pellets were then pyrolyzed in a N_2 flow using the following heating cycle: 100-300°C at 4°C/hr, 300-325°C at 2°C/hr, 325-425°C at 5-6°C/hr and 425-700°C at 10°C/min. Soak time at 700°C was 2 hr. Two samples were further heated in an Ar flow to different temperatures, up to a maximum of 1500°C, using a heating rate of 10°C/min. Soak time at each selected maximum heat treatment temperature (HTT) was 2 hr.

Surface areas of carbons were determined from N_2 adsorption at 77°K using the BET equation and from CO_2 adsorption at 298°K using the Polanyi-Dubinin[2] equation. Pellet density was determined by mercury displacement. Pore size distribution was determined from mercury porosimetry data obtained up to a maximum pressure of 30,000 psi. For a given carbon, the cumulative volume of mercury intrusion (up to 30,000 psi) has been referred to as its pore volume in the text.

Results and Discussion

Recipes for the production of samples are given in Table 1. Surface areas, pellet densities and pore volumes of various carbons heat treated at 700°C are given in Table 2. The volumes of mercury intrusion into pores as a function of pressure for different samples are plotted in Figure 1. Pore diameters corresponding to maxima in pore size distribution curves are referred to as D_m in the text and are listed in Table 2. For each sample, the CO_2 area is significantly higher than the N_2 area. [2]This indicates the presence of micropores in which adsorption of N_2 at 77°K is restricted due to activated diffusion. [2]For various samples, pore volumes vary from 0.022 to 0.493 cm^3/g, pellet densities vary from 0.840 to 1.375 g/cm^3 and D_m values vary from ~ 60 to 50,000A.

Samples 1 and 2 differ markedly in their properties, particularly N_2 areas, pore volumes and D_m values. The two samples differ only in the proportion of the dispersing agent in the starting mix used for their preparation. Thus, by varying the proportion of the dispersing agent in the starting mix it should be possible to prepare carbons with different properties.

Four additional carbon samples were prepared from the same starting mix as was used for preparing sample 3, but the heat treatment conditions between the polymerization and carbonization steps were different in each case. It was found that with the exception of N_2 areas, thermal history used has some effect on other properties studied.

The results obtained with samples 5 and 6 are very significant. For preparing sample 5, PEG is used both as a pore former and as a dispersing agent. If instead of PEG, a 1:1 mixture of PEG and Triton X-100 is used, marked changes in properties of the carbon produced (sample 6) are observed. For instance, D_m values for samples 5 and 6 are 50,000 and 210A, respectively. These results

suggest that by varying the proportion of PEG and Triton X-100 in the starting mix it should be possible to prepare carbons having D_m values over a wide range of pore diameters.

It is well known that the structure of porous carbons can be modified by suitable heat treatment. Effect of HTT in the 700-1500°C range on the properties of samples 3 and 4 is shown in Table 3. Pore volumes and D_m values (not shown) are essentially independent of HTT. Pellet densities show some variation upon heating. Both the N_2 and CO_2 areas decrease sharply above 1000°C. For HTT ≥ 1400°C, the N_2 and CO_2 areas are about the same.

In conclusion, results of the present investigation strongly suggest the possibility of preparing glassy carbons with desired porosity, pore size distribution and surface area as catalyst supports.

References

1. Hucke, E. E., U.S. Patent 3,859,421, Jan. 7, 1975.

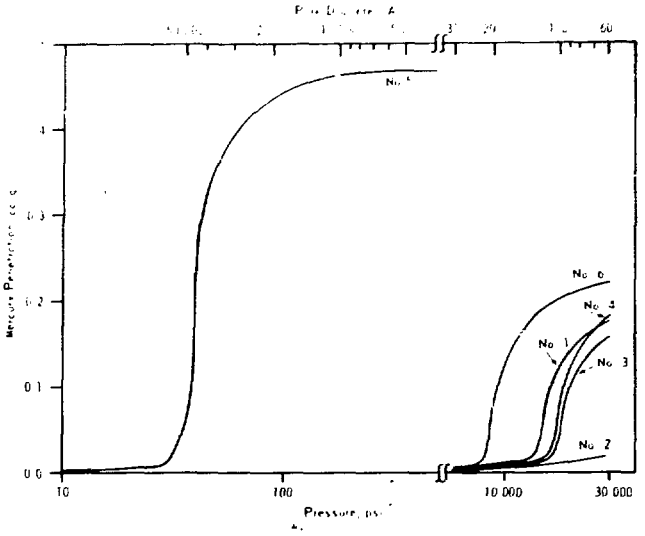


Figure 1. Pore Size Distributions in Carbon Pellets

TABLE 1

RECIPES FOR PRODUCTION OF SAMPLES

Sample	FA	DEG/PEG	Triton X-100	PTSA
1	100 cm^3	57 cm^3 DEG	50 cm^3	11.3 g
2	100	57	100	11.3
3	100	25	75	11.3
4	100	15	85	11.3
5	100	100 PEG	0	17
6	100	50	50	17

TABLE 2

PROPERTIES OF CARBONS

	Surface area, m^2/g		Pellet density	D_m	Pore Volume
Sample	CO_2	N_2	(g/cm^3)	(A)	(cm^3/g)
1	712	442	1.114	108	0.173
2	932	39	1.375	60	0.022
3	830	420	1.185	103	0.159
4	781	454	1.125	103	0.181
5	856	520	0.840	50,000	0.493
6	872	470	1.091	210	0.221

TABLE 3

EFFECT OF HEAT TREATMENT ON PROPERTIES OF CARBONS

	Surface area, m^2/g		Pellet Density	Pore Volume
HTT, °C	CO_2	N_2	(g/cm^3)	(cm^3/g)
		Sample 3		
700	830	420	1.185	0.159
900	994	282	1.192	0.162
1000	972	126	-	-
1100	513	92	1.217	0.161
1300	154	81	1.211	0.164
1400	72	72	-	-
1500	52	67	1.206	0.163
		Sample 4		
700	781	454	1.125	0.181
900	846	384	1.178	0.181
1100	377	97	1.183	0.179
1300	156	87	1.171	0.180
1500	72	90	1.154	0.180

VISCOSE CARBONS: MODIFICATION OF THERMAL DECOMPOSITION OF VISCOSE BY INORGANIC ADDITIVES

A. Capon and F.A.P. Maggs
Chemical Defence Establishment, Porton Down, Salisbury, Wiltshire, UK

Introduction

The yield of carbon char from cellulosic precursors may be augmented by treatment of the cellulose with inorganic additives prior to carbonisation. The effect on the thermal decomposition and on the char yield of impregnating viscose rayon with inorganic chlorides has been studied using DTA and TGA techniques.

Experimental

Rayon cloth samples were impregnated by immersion in salt solutions by a reproducible technique. Analysis showed that the uptake of salt during preparation could be calculated from the equation, weight of salt (mg/g) = solution strength (mg/ml) x volume occluded (ml/g). (By the technique used 1.4 ± 0.1 ml/g of solution were occluded). Samples were carbonised in flowing nitrogen (5 ml/min) at 5°C/min using Stanton Redcroft TGA and DTA apparatus. Char yields were recorded at 450°C and on occasions at 850°C. Samples were not dried prior to use.

Char Yield

The char yield of unimpregnated viscose was 22% at 450°C and 13% at 850°C (dry basis). In all cases examined prior treatment with a 5% w/w solution augmented the char yield. Yields obtained with different metal chlorides at 450°C varied as follows.

20 - 30% Au
30 - 40% Na, K, Ni, Al, Sn, Hg, NH_4
40 - 50% Li, Mg, Ca, Sr, Ti, Cr, Mn, Cu, Zn, Cd

For six salts the effect of strength of the impregnation solution on char yield at 850°C was examined. The results (Fig.1) show that small amounts (10 - 20 mg/g) of impregnant have a marked effect on yield and that the rate of yield increase diminishes with increasing impregnation.

Thermal Decomposition

The DTA and TGA curves obtained exhibited a wide variety of behaviour. All salts with the exception of Na and K caused a lowering of the decomposition temperature, and in general chlorides within each periodic grouping gave rise to reaction in the same temperature zone. (Li was an exception, causing a substantial lowering of the decomposition temperature). The results may be superficially grouped according to the number of reaction zones observed (cf. Fig.2). In one group a single temperature zone of reaction (zone B, ~ 200 - 330°C) at or near the zone shown by untreated viscose, was observed. Other impregnants gave rise to two zones of reaction, one in the 100 - 200°C region (zone A), the second in zone B. In a few cases (e.g. $HgCl_2$) more complex behaviour was observed. In all cases a maximum in the rate of weight loss coincided with a peak in the DTA curve.

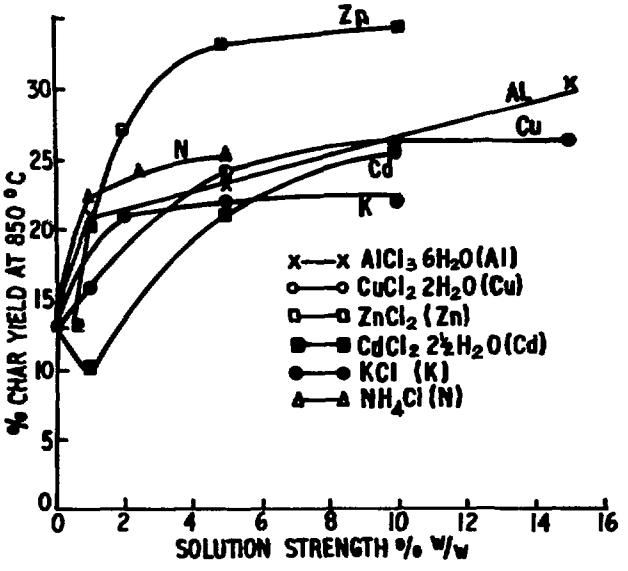


Figure 1. Variation of Char yield with impregnation solution strength.

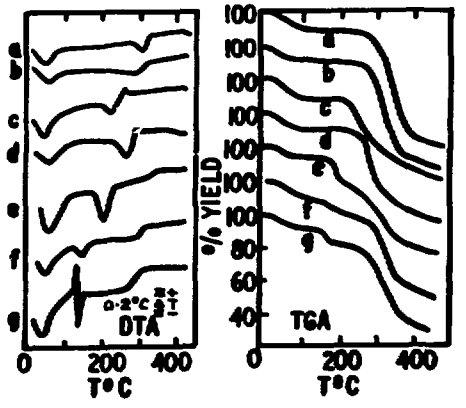


Figure 2. DTA and TGA curves for (a) Untreated viscose and treated with 5% w/w solns. of (b) KCl, (c) $ZnCl_2$, (d) $CdCl_2$, (e) NH_4Cl, (f) $AlCl_3$, (g) $CuCl_2$. N_2 Atmosphere: 5°C/min.

Further distinctions were disclosed by varying the quantity of impregnant (1). For KCl the zone B temperature remained unchanged, but the extent of the energy changes diminished with increasing impregnation.

For $ZnCl_2$ and $CdCl_2$ the zone B temperature was reduced, the temperature of decomposition being lower the greater the amount of impregnation. For NH_4Cl, $CuCl_2$ and $AlCl_3$, increasing the extent of impregnation increased the extent of the zone A reaction and reduced the extent of the zone B reaction, the reaction temperature of both zones being essentially unaltered.

Several reaction mechanisms have so far been distinguished: (i) Reaction of impregnant in zone B with thermally unstable viscose (e.g. KCl, NaCl); (ii) Catalytic enhancement of the initial dehydration reaction at the expense of a depolymerisation process in zone B (e.g. $ZnCl_2$, $CdCl_2$); (iii) Decomposition of the salt to yield HCl, partial reaction of the viscose in the released HCl, followed by completion of the decomposition at higher temperatures (e.g. NH_4Cl, $AlCl_3$); (iv) Formation of a viscose/salt complex followed by breakdown of the complex and further decomposition at higher temperatures (e.g. $CuCl_2$).

Mixed Impregnants

Experiments have also been carried out with mixed salt impregnations. In general the DTA and TGA results showed peaks attributable to the individual components of the reaction mixture. This is illustrated in Figure 3 where the reactions of $ZnCl_2$ and $CuCl_2$ are clearly visible in the DTA and TGA traces of the mixed impregnant sample. Decompositions at higher temperatures tend to be diminished, however, in the presence of salts reacting at lower temperatures.

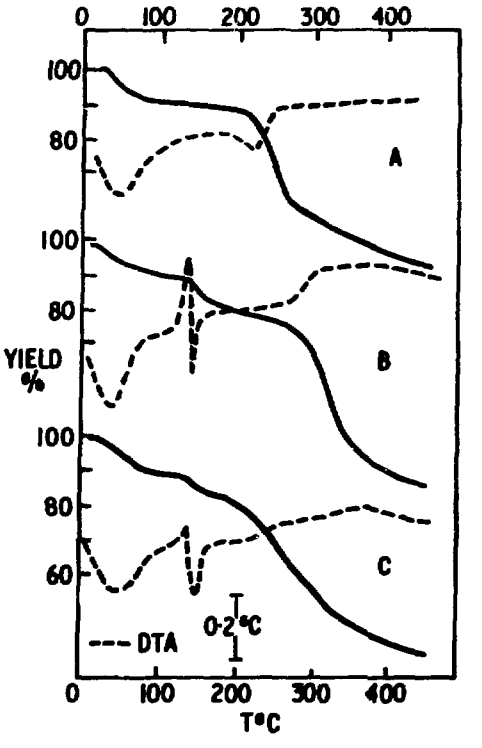


Figure 3. DTA and TGA curves for viscose rayon impregnated with 5% w/w solns. of (A) $ZnCl_2$, (B) $CuCl_2$ and (C) 2.5% w/w each of $ZnCl_2$ and $CuCl_2$.

Reference

(1) Capon A. and Maggs F.A.P., *Proc. Int. ICTA, Salford, UK, Sep 1976*, p.176. D. Dollimore (Editor), Heyden (1976).

ACTIVATION OF FIBROUS CHARS

F.A.P. Maggs, A. Capon, and M.E. Smith
Chemical Defence Establishment, Porton Down, Salisbury, Wiltshire, UK

Summary

The rates of activation by carbon dioxide of chars prepared from viscose rayon precursors treated with inorganic chlorides have been studied. The rates of reaction, activation energies and Arrhenius factors are discussed in terms of a Compensation Effect.

Experimental and Results

Strips of viscose rayon cloth were treated reproducibly by dipping in solutions containing 5% w/w of a metal chloride plus 2.5% NH_4Cl, and drying, they were then carbonised (6^oC/min, 4 l/min N_2) to the desired activation temperature (700 - 900^oC). The resulting chars were activated by flowing CO_2 (4 l/min) for varying periods of time. Weights were recorded. In one series, CO_2 formed both the carbonising and activating gas; in two series the N_2 flow was replaced by CO_2 at 600^oC. The object of the variations was to prepare chars of varying reactivity towards CO_2.

Rates of reaction (D) were calculated from the linear loss of weight with time of activation in terms of the initial weight of char (w_o); thus $D = -dw/dt.w_o$. True rates of reaction ($-dw/dt.w$) thus rose with increasing reaction. D therefore represents the initial rate of reaction (at zero activation). The results are presented in Table 1. The Arrhenius plots showed little deviation from linearity: activation energies (AE) and Arrhenius factors (A) have been derived from these plots.

Discussion

A considerable range of char reactivity has been achieved by the variations in the method of char preparation. In the temperature range studied the order of increasing rates of reaction of the chars is: $ZnCl_2/N_2$, $AlCl_3/CO_2$, $ZnCl_2/CO_2$, $BaCl_2/N_2$, untreated rayon/N_2, $CaCl_2/N_2$ (the gases indicating the carbonisation atmosphere. AE and A also increase in the same order.

The presence of CO_2 at temperatures above 600^oC leads to an increase in activation rate in comparison with samples prepared in N_2. Assessment of the accessible surface area by heat of wetting measurements using benzene and silicone fluid showed that the presence of CO_2 above 600^oC prevents the pore closure which otherwise occurs in an inert atmosphere. The more open char structure then shows a higher reactivity. The linearity of the Arrhenius plots implies that a single reaction - controlling mechanism persists over the temperature range studied, probably chemical rather than diffusional.

Inspection of the Arrhenius plots suggests the existence of an isokinetic temperature (T') near 600^oC, at which the rate of reaction D' is the same for all the solids.
Thus, for a given char (activation energy AE_1) $\ln D/D' = AE_1/R\,[1/T' - 1/T]$. Alternatively, for a given series of related chars, at a given temperature T_1, $\ln D$ will vary linearly with AE according to the equation
$\ln D/D' = AE/R\,[1/T' - 1/T_1]$. If now the equation is recast in the usual Arrhenius form
$\ln D = -/E/RT + [AE/RT' + \ln D']$, then
$\ln A = AE/RT' + \ln D'$. We may thus expect that for a series of related solid/gas reactions $\ln A$ will vary linearly with AE. This relation, the Compensation Effect (1), thus stems directly from the occurrence of an isokinetic temperature.

The present data have been tested for this phenomena by plotting $\ln D$ versus AE for the six solids at each of the temperatures 1023, 1073, 1123^oK (Figure 1), the intercept at AE = 0 giving $\ln D'$. The plot of $\ln A$ versus AE (Figure 2) also allows $\ln D'$ to be found. In both cases, linear graphs are obtained; values $D' = 6.10^{-4}$ g/g/min and $T' = 890^oK$ have been calculated.

The compensation effect can only occur when the reactants are closely related; in the present case the chars were all prepared from a common source, viscose rayon. The limitation on the range of rayon chars for ag a common system is a matter for further work.

Reference

(1) Exner O., *Coll.Czech.Chem.Comm.* 37, 1425 (1970).

TABLE 1. Rates of Activation by CO_2

Impregnation/ Carbonisation Atmosphere	Activation Temperature ^{O}C	Activation Rate (D) mg/g/min	Activation Energy (ΔE) Kjoule/mol	Arrhenius Factor (A) g/g/min
$ZnCl_2/N_2$	800 850 900	2.5 4.4 8.0	125	10^3
$ZnCl_2/CO_2$	750 800 875	2.6 5.7 22	160	10^5
$ZnCl_2/N_2:CO_2$ - 600°C	750 800 850	2.7 6.6 15	170	10^6
$AlCl_3/N_2:CO_2$ - 600°C	800 850 900	2.5 4.2 17	165	10^5
$BaCl_2/N_2$	750 850 900	2.0 20 48	220	10^9
$CaCl_2/N_2$	725 750 775 800 825	5.2 27 31 81 160	110	10^{15}
No impregnation/N_2	750 800 850	1.5 9.2 29	220	10^9

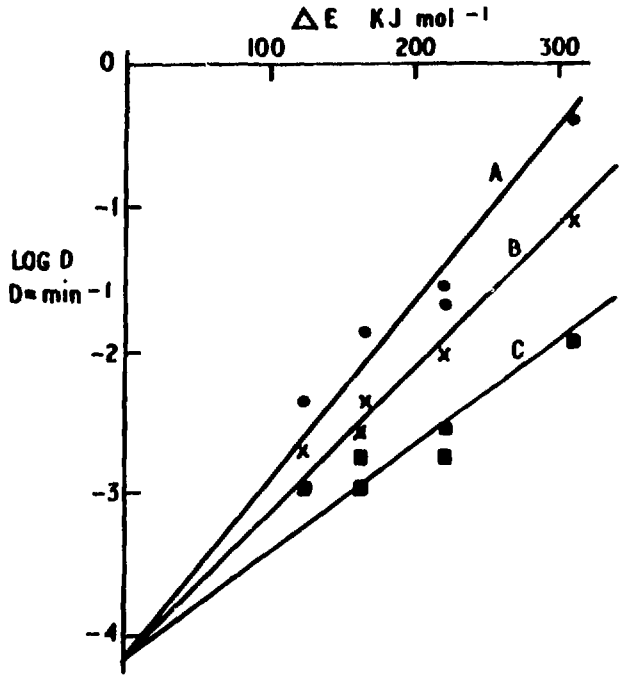


Figure 1. Variation of Log D with ΔE, constant temperature (A) 1123°K, (B) 1073°K, (C) 1023°K.

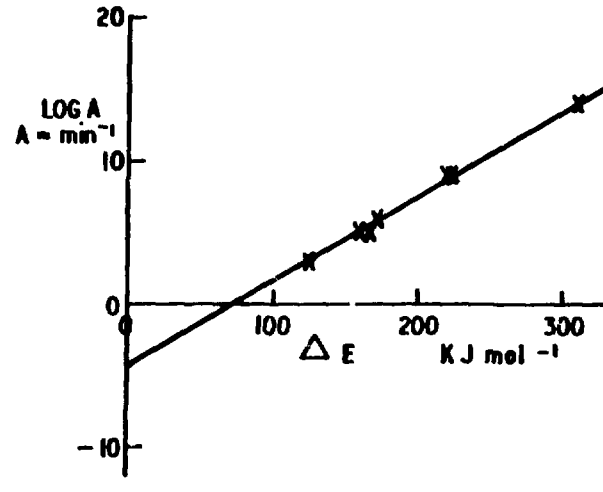


Figure 2. Variation of Log A with ΔE.

Towards Density Determination of Pyrolytic Carbon Layers Deposited on Nuclear Fuel Microspheres

W. Delle, K. Koizlik, H. Nickel, E. Wallura
Institut für Reaktorwerkstoffe der Kernforschungsanlage Jülich GmbH, Fed. Rep. Germany

In High-Temperature Gas-Cooled Reactors (HTGR), the fuel is applied in the form of small spherical kernels, some 100 µm in diameter depending upon the fuel cycle concept. The fuel kernel is coated by a sequence of pyrolytic carbon layers. The inner layer adjacent to the kernel is always highly porous to provide the particle with a free volume for the fuel kernel swelling and the gaseous fission product reception. The outer high density layers form a pressure vessel and fission product barrier. It is obvious that because of the importance of the particular layers the apparent, bulk or geometric density has to be controlled carefully.

The APPARENT, BULK OR GEOMETRIC DENSITY is the mass per unit volume. It is assumed that the volume is homogeneously filled with mass. It includes the volumes of the substance, displacements, micro and macro pores - open and closed - and of the internal voids.

The geometric density is measured by determining the increase in volume and mass after the deposition of the particular pyrolytic carbon layer. The diameter can be determined by use of microscopic measurements or x-ray micrographs.

For statistical considerations and on-line quality control an automatic optical particle analyzer developed by OSGAE Seibersdorf/Austria is used (1). A quantity of coated particles is moved along a constant light source and a very small measuring gap with intervals of approximately 20 particles per second. The gap area shadowed by a particle is measured by means of a photodiode and is a measure for the diameter. The apparatus is controlled and the data are evaluated by an on-line process computer. This technique is suitable for diameters of 150 to 1500 µm. After weighing the investigated portion of particles, the apparent density can be calculated.

As far as the porous buffer layer is concerned, it is not sufficient to determine the density directly after its deposition. During the deposition of high dense pyrolytic carbon on the buffer layer it may occur that at least the outer zone is infiltrated by carbon and thus densified. Therefore it is necessary to measure the densities of both the inner and outer layers once more after fuel production by applying the SINK-FLOAT method.

The purpose of this method is to determine the density of layers by suspension in a density gradient column. The gradient column consists of isobutanol and bromoform chemicals mixed continuously in varying proportions so as to cover a range of densities from 0.8 $g \cdot cm^{-3}$ to 2.8 $g \cdot cm^{-3}$. Pyrolytic carbon fragments cracked from coated particles are suspended into the column. The density is defined at the point in the column where the test specimen of pyrolytic carbon has reached the same density as the liquid in which it is suspended (fig. 1) and thus floating in the column.

The geometric and sink-float densities of a sample are equal, provided the substrate is impermeable. The permeation depends on the pore size as well as surface tension, but not on the viscosity of the liquids used. The densities mentioned above are not equal in the case of low density carbon, because the liquid in the column penetrates the pores with an open entrance greater than 10nm. Therefore the volume measured is too small, so that the reading of the sink-float density is too high (fig. 2). PECHIN et al. have proposed an equation to correct these influences (2).

In KFA this problem has been solved experimentally. Studies have been carried out to prove the combination of two measuring procedures to yield true values for the apparent or geometric density of the buffer layer even after the deposition of the high dense layer:

- sink-float method
- quantitative image analysis.

The quantitative image analysis measures macropores with diameters greater than 200 nm. For this procedure, the pyrocarbon coatings are applied in the form of ceramographic sections of the coated fuel particles.

The measurement is carried out by an electronic, automatic image analyser. Working mode is the classification of the coating to be inspected on the basis of the gray value contrast between pores (dark) and carbon (bright).
From the sink-float density, d_s, one can calculate a porosity, P_s, which is too small because the closed pores only are considered

$$P_s = 1 - \frac{d_s}{d_x} \qquad (1)$$

with d_x as X-ray density. By the quantitative image analysis the total macro porosity, P_M, is measured. For buffer layers the total porosity, P, results in

$$P = P_s + P_M \qquad (2)$$

This equation is valid for pyrolytic carbon with closed pores smaller than 200 nm.
The apparent, bulk or geometric density, d, of the porous pyrolytic carbon can be calculated by applying the equation

$$d = d_x(1 - P) \qquad (3)$$

The results obtained have shown, that density values from mass and volume measurements and from the application of the combined methods described above agree well for porous buffer layers (3).

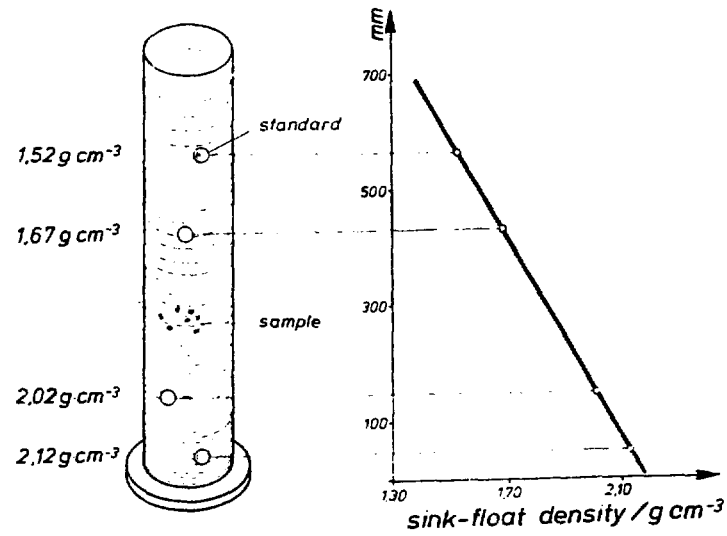


Fig. 1: Gradient column for the measurement of sink-float density

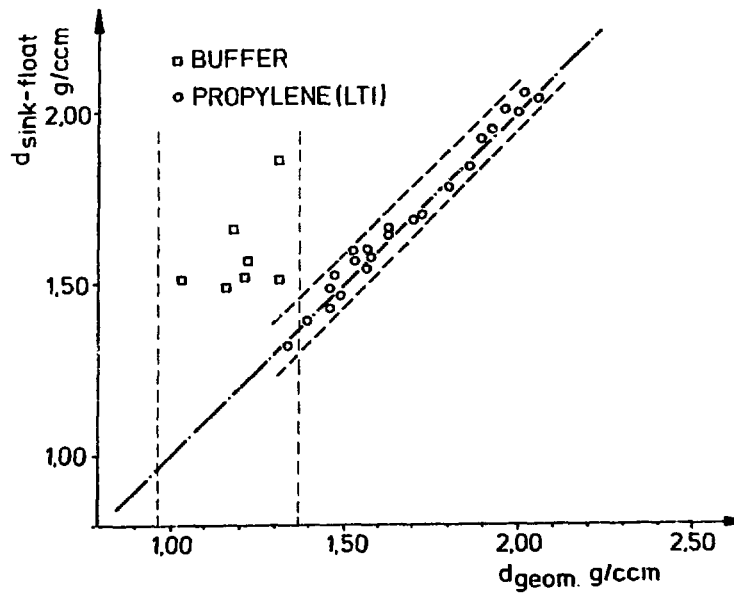


Fig. 2: Interrelation between sink-float and geometric density

References

(1) Wallisch, K. Koss, P.: Automatic size analysis of coated fuel particles, USGAE Report 2342 (1974)

(2) Pechin, W.H., Lackey, W.J., Sease, J.D., Eatherly, W.P.: Quality control tests for High-Temperature Gas-Cooled Reactor recycle fuel, Nuclear Fuel Quality Assurance, IAEA Vienna (1976)

(3) Uhlenbruck, H., Koizlik, K., Hoven, H., Wallura, E., Nickel, H.: Meßgrößen und Fehler der quantitativen Bildanalyse - Definition und quantitative Beschreibung, KFA Report Jül-1411, (1977)

STRUCTURE OF PYROCARBON COATINGS FOR NUCLEAR FUEL AND IMPLICATIONS FOR QUALITY ASSURANCE

By M S T PRICE
(United Kingdom Atomic Energy Authority, AEE, Winfrith, United Kingdom)

The High Temperature Gas-Cooled Reactor (HTR) is a second generation nuclear reactor with the ability to stretch uranium resources(1,2) and unique potential to achieve high efficiency in converting fission energy into useable forms (up to 90% for a combined electricity and district heating plant(3,4)). It depends for its success, inter alia, on several areas of carbon technology. In particular the basic unit of fuel is the coated particle which consists of a spheroidal ceramic kernel (such as uranium oxide) surrounded by a series of coatings. The coatings may be composed wholly of pyrolytic carbon (termed BISO), include an interlayer of silicon carbide (termed TRISO) or the pyrolytic carbon and silicon carbide may be co-deposited. They must in combination constitute a barrier to the escape of actinides and fission products.

From the several deposition processes (eg fluidisation, tumbling bed, vibrating bed) considered in the early 1960's, high temperature fluidised bed coating has emerged as the standard manufacturing process and batch sizes up to 35kg have been coated. The problems of coating these small nuclear fuel particles (200-800 μm diameter plus $\sim$200 μm total coating thickness) have first been solved empirically. The result has been a strong linkage between small-scale manufacture and irradiation performance.

Initially coatings were laid down at high temperature (typically $>$ 1600°C) using methane as the source gas. As irradiations proceeded, it emerged that the outer pyrocarbon layer on large TRISO particles was failing at fast neutron doses of about 3.10^{21}n.cm^{-2} Dido Nickel Equivalent. More recently it was observed that pyrolytic carbons deposited at lower temperatures ($<$1500°C) were able to withstand much higher fast neutron doses. During this phase the irradiation effects were generally assessed by measuring the change in properties of small strips of carbon deposited on discs coated at the same time as the particles. The validity of measuring the properties of deposits on discs was always in doubt because of the different hydrodynamic behaviour of particles and discs, as well as strong interactions between layers in service.

Using a material which is as structurally sensitive as pyrolytic carbon in an application where the consequences of poor performance are financially serious it is important to establish the loop manufacture - quality - performance so that an adequate Quality Assurance (QA) programme can be defined. With commercialisation imminent it was considered to be the time to launch a concerted effort to try to improve the understanding of the factors controlling the process of coating with pyrolytic carbon. It was also hoped that this might help provide a basis for a QA programme. An important step was the formulation by Lefevre (5) of a process model which postulates that the structure of pyrocarbon is made up of spherical growth features (SGF's). The model has the merit that it predicts the relative size of the SGF's as a function of various input parameters such as carbon : hydrogen atom ratio in the coating gas and can therefore be used to design experiments. An approximate check of the model was made by asking 30 operators to classify photomicrographs of ceramographic sections of 24 different coatings according to the coarseness of the deposits. The average ranking which resulted is compared with prediction in Figure 1.

These encouraging results led to a systematic programme but this first required standardisation of input parameters (eg the method of obtaining the same deposition temperature irrespective of gas composition, specific heat and heat of decomposition (6)). A series of 15 coating runs was then undertaken to check the model and details are given in (7). Only the structure of the outer pyrocarbon layers of TRISO particles was varied and the morphology of these layers was examined by scanning electron microscopy of a fracture surface or by optical microscopy after electrochemical oxidation of a polished section. The photomicrographs were first measured by 3 operators and a good correlation obtained (8) but detailed examination of the data showed that it was obviously necessary to standardise the method of measurement. The structure was therefore quantified for both the size distribution of agglomerates and the number per unit area by the use of a simple linen gauge consisting of a magnifying glass and graticule. The test method was proven using an Analysis of Variance technique (9). Nine of the previous 15 batches chosen to be representative of the spread of results, were then remeasured by 2 previously validated operators. The results obtained from Polaroid photographs of SEM images (mag. x13000) and wet oxidation photomicrographs (mag. x1000) are compared with predictions in Figure 2. A strong correlation is indicated with an identical slope for the two test methods but a different Y-intercept. The presence of SGF's has also been confirmed qualitatively by transmission electron microscopy.

The 15 coating batches have been irradiated in the Colibri HTR 5 experiment but post-irradiation examination results are not yet available. The opportunity has therefore been taken to apply the linen gauge measurement method to SEM fractographs of 5 coating batches from the immediately previous irradiation experiment (HTR 4). The results obtained are plotted against survival of the outer pyrocarbon layer in Figure 3.

It is concluded therefore that low temperature isotropic pyrocarbons consist essentially of spherical growth features whose relative size can be predicted from the Lefevre model and controlled by appropriate input parameters. The method of measurement of SGF is somewhat tedious but is at present the only validated method of measuring pyrocarbon structure. At a later stage an

automatic image analyser or automatic optical anisotropy measurement may be more suited to routine quality control. But the former has not been developed and there is considerable debate about the validity of the latter. Workers disagree as to the importance or not of the polishing method for the preparation of specimens prior to measurement of optical anisotropy and there has been little benefit from attempts to provide inter-laboratory comparisons and standards. Since the size of packed spheres controls the size of the cusps between the spheres, porosity measurement could also be considered as a control method.

Turning to the question of QA for pyrocarbon it is useful to take advantage of the approach taken by Delle et al (10) to deduce test methods by working backwards through the coated particle failure modes, the parameters affecting reliability and the testing parameters. Such a technique leads to the hypothesis that adequate QA for pyrocarbon coatings on nuclear fuel particles can be achieved with only -

i a validated automically controlled coating process;

ii a weighing balance;

iii a validated optical particle size analyser;

iv a validated method of measuring structure.

The work outlined here has shown that structure (expressed as the size of spherical growth features), is a controllable parameter related to particle endurance but more work is necessary to achieve an automatic measuring method.

REFERENCES

1. L R Shepherd, 'What Role for Fission?'. Nature 265, 394, 3 February 1977.
2. P R Kasten et al, 'Assessment of the Thorium Fuel Cycle in Power Reactors', ORNL/TM-5565. Jan. 1977.
3. K Bammert, 'The Oberhausen Heat-and-Power Station with Helium Turbine', address at inauguration of EVO Plant, Oberhausen-Sterkrade. 19 December '74.
4. L R Shepherd, 'The Future of the High Temperature Reactor', Paper to BNES, 18 Nov. 1976; to be published in Journal of British Nuclear Energy Society.
5. R L R Lefevre. Carbon '76, Baden-Baden, 27 June /2 July 1976, preprints p. 531.
6. R L R Lefevre & M S T Price to be published in Nuclear Technology.
7. J Guilleray, R L R Lefevre, M S T Price and J-P Thomas, Proc. 5th Interna. Conf. on Chemical Vapor Deposition, Stoke Poges, 22-26 September 1975 (Electrochemical Society, Princeton 1975), p. 727.
8. J Guilleray, R Zeyen, J-P Audebeau and M S T Price. Paper presented at Deutsches Atomforum Reaktortagung, Dusseldorf, 30 Mar/2 Apr. '76, p. 367.
9. J Guilleray, R Zeyen, J-P Audebeau & M S T Price, Carbon '76, Baden-Baden, 27 June/2 July '76. Preprints, p. 529.
10. W Delle, K Kolzlik, H Luhleich, J-P Audebeau & M S T Price, ibid. p. 547.

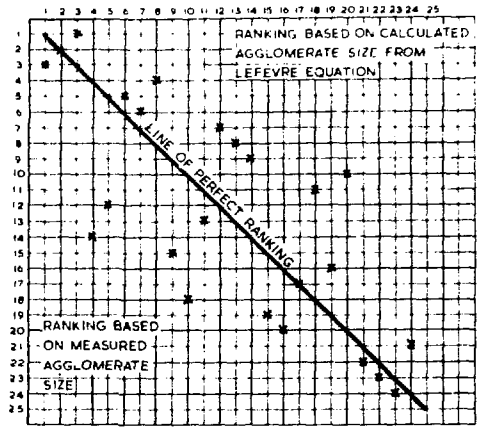


Fig. 1 - Comparison of Ranking Between Calculated SGF Size and Observed Coarseness of Structure in a Photomicrograph of a Polished Section.

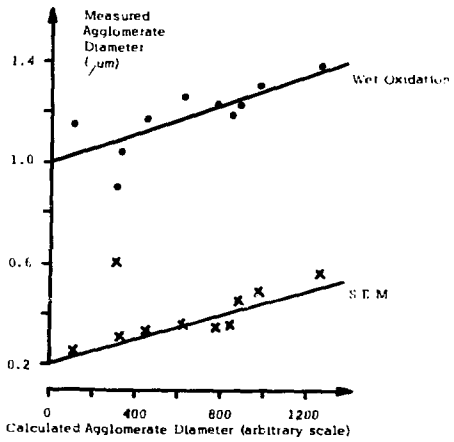


Fig. 2 - Regression of the Mean SGF Size Measured on 'Wet Oxidation' and SEM Photomicrographs on the Predicted Values.

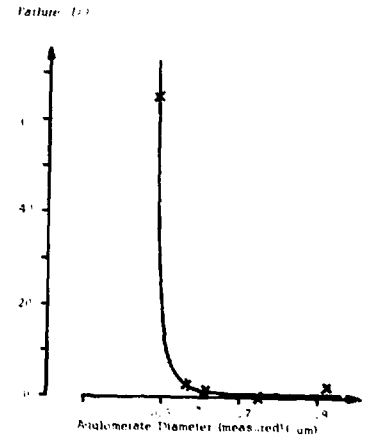


Fig. 3 Particle Failure in HTR 4 Experiment Versus Measured SGF Diameter.

IMPROVED GRAPHITE MATRIX FOR COATED PARTICLE FUEL*

D. Schell, K. Davidson, C. Hollabaugh, R. Reiswig, P. Wagner,
Los Alamos Scientific Laboratory, Los Alamos, New Mexico 87545

Introduction

High temperature gas cooled reactor (HTGR) fuel elements consist of hexagonal prismatic graphite blocks containing numerous longitudinal cylindrical holes. Some of the holes are used for He coolant passages while others contain fuel rods. The fuel rods, around 1.57-cm diam, consist of short, ~ 5-cm-long segments which are made by a molding process. In making the segments a tube is filled with a mixture of spherical particles consisting of coated fissile particles and coated fertile particles to give the desired U and Th loading and carbon shim particles to fill the remaining segment volume. The void between the particles is infiltrated with pitch or a mixture of pitch and a fine graphite flour. The fuel rod segments are heat treated and placed in a fuel channel in the graphite fuel element. The fuel rod matrix is relatively low in density and thus has poor thermal conductivity.

A program was started at the Los Alamos Scientific Laboratory (LASL) in 1973 to develop a fuel rod having high temperature capabilities for possible use in a gas-cooled nuclear process heat reactor. There were two parts to the program; one to develop an improved coated fuel particle which would increase the temperature capability of the fuel, and the other to incorporate these particles in a dense graphite matrix using an extrusion process. This paper will discuss only the second part of the program, that of incorporating coated particles in an extruded graphite matrix.

An extruded fuel rod could be made in one piece, long enough to fill the fuel channel in an HTGR fuel element; around 75 cm. The fissile and fertile loadings in HTGR fuel rods vary considerably depending on the positions in the reactor. An average fuel rod would contain 41 vol% coated particles and this was selected as the nominal loading in our extrusion experiments. The 41 vol% was the total of 6 vol% fissile particles (~ 550 μm diam) and 35 vol% fertile particles (~ 800 μm diam). Although an actual extruded fuel rod would not contain carbon shim particles, only graphite filler particles, our development extrusions, which were made primarily for irradiation tests in the High Flux Isotope Reactor (HFIR), contained carbon shim particles to keep the loading of 41 vol% particles constant. This was done to simplify the evaluation of experimental variables although loadings as high as 55 vol% particles were made.

Increasing the conductivity of the fuel matrix would allow higher reactor coolant temperatures without increasing the temperature of the fuel particles. Thermal conductivity measurements indicated a factor of 10 improvement of an extruded matrix over a conventional fuel segment.

Experimental Procedure

Extrusions made early in the program contained suitably sized spherical glass beads. These were used until spherical carbon particles and coated particles became available. The extrusions were useful in working out extrusion mix composition, investigating various graphite filler flours and measuring relative matrix densities. Also, some indications of suitable die design, extrusion pressures and relative extrusion strengths were obtained. A partially polymerized furfuryl alcohol, Varcum 8251, used extensively in making extruded graphitic fuels and shapes for the Rover (Nuclear Propulsion Reactor) program,[1] was used as the binder for practically all particle-loaded extrusions. Varcum is a thermosetting resin having a carbon residue, upon heat treatment, of 45 . It is desirable to use a thermosetting resin as the extrusion binder in that upon polymerization the extrusions are easily handled and dimensional stability is maintained.

Several different reactor grade graphite flours were used in these extrusion experiments. They varied both in particle size and shape. Thermax, up to 15 pph, was added to many extrusion mixes.

It became evident very early in this program that there was a serious problem with macrocracks in the matrix created during the heat treatment of the extrusions. The matrix shrinks when heat treated but is restrained by the relatively large unforgiving beads, thus cracking occurs. The finer the graphite the greater was the tendency for cracking. For this reason much of our extrusion work used a relatively coarse, -60 mesh, reactor grade 1008 graphite flour from Great Lakes Carbon Corporation.

The first coated particles which were available to us were made by General Atomics for the Fort St. Vrain HTGR. These were TRISO fertile particles having ThC_2 cores and two pyrolytic carbon coats with a SiC coat in between.

We could not extrude these particles without indications of particle failure. When the ThC_2 cores of the particles were exposed to air (moisture), the carbide hydrolyzed and the volume change caused a spall on the surface of the extrusion. This problem was evident to some degree on all extrusions, even those made at very low extrusion pressures. The load required to crush a particle was rather low, averaging 1.8 kg.

Although we apparently needed a stronger particle for a successful extrusion program, these particles proved to be very useful in investigating mix and extrusion variables. We found that we could readily extrude 12.5-mm-diam rods a meter long with little taper or dimensional variation.

Extrusion pressures varying by a factor of 3 were used with an estimated pressure on the extrusion mix of 2 MPa considered optimum. This pressure provided adequately strong extrusions but minimized particle damage.

A few different die designs were investigated, giving the impression that die design had little or no effect on the quality of the extrusions. This was probably due to the low extrusion pressures.

Heat treating cycles were established to cure and carbonize the thermosetting binder. The final heat treatment was to 2075 K in an Ar atmosphere using a graphite resistance furnace. No deleterious effects were noted on the extrusion or particles due to this heat treating temperature.

*Supported by the Division of Nuclear Research and Application, U.S. Energy Research and Development Administration.

Early extrusion mixes were simply made by hand mixing the appropriate amounts of the various ingredients and particles together. Satisfactory extrusion mixes were also made by solvent mixing or through the use of a Patterson-Kelley twin-shell blender. Intensive mixing could not be used because of particle damage. We found that if the graphite matrix flour and the Varcum binder were intensively mixed together before the particles were added to the mix the matrix density increased a few percent. The intensive mixing was done through a series of grinding operations, using a commercial meat chopper, and extrusions. The coated particles and shim particles, which were previously blended together, were then hand blended into this mix. The mix was usually extruded three or four times with hand mixing between extrusions. A vacuum system on the extrusion press evacuated the extrusion die, chamber and extrusion mix prior to and during extrusion. There were no indications that particle damage was associated with the number of times a mix was extruded. Multiple extrusion did increase the matrix density. Experiments also indicated that the uniformity of the distribution of coated particles in the extrusion mix did not change with multiple extrusions.

Further development work continued using stronger coated particles which had crushing loads averaging 2.8 kg. Particle damage during extrusion and heat treatment did not appear to be a serious problem. Samples of extrusions leached at 1225 K for 8 h in a mixture of Cl_2 and CO showed no weight loss.

It has been reported that coated particles may be damaged by interaction between the outer pyrolytic carbon coat on the particle and the matrix. If the matrix sticks to the coating, the coating may be damaged when the matrix shrinks during thermal treatment or volume changes that occur during irradiation. We found that we could at least partially isolate the particles from the matrix by coating the particles with a fugitive coating prior to extrusion. The coating was applied to the particles using a solvent. Carnauba wax was the preferred coating material in that it gave the most consistent results. In work at LASL we have observed no indications of interaction between the particles and matrix whether the particles had a fugitive coating or not. This includes a few irradiated samples.

Irradiation Specimens

Over a period of about a year, extrusions containing both fissile and fertile coated particles were made for three tests in the HFIR reactor at Oak Ridge. This represented ten separate extrusion batches.

Several extrusions were similar in nature but contained different developmental coated particles. Two extrusions used graphite flours which originated from graphites developed for making HTGR fuel elements. Other extrusions used different heat treating cycles with four of the extrusions being heat treated to 2375 K.

Matrix carbon densities were around 1.63 g/cm^3.

Some problems did occur in making the irradiation specimens. Macrocracks in the matrix appeared when the graphite flour contained an excess of fines. There was no problem, however, with the specimens being adequately strong. The cracks did not change in appearance or affect the irradiation performance of the specimens during full term fluence and temperature conditions.

One problem peculiar to making irradiation specimens was that the diametrical tolerance was tight and it was inadvisable to machine the diameter because of particle damage. This meant that the extrusion die size and shrinkage of the extrusion during heat treatment determined the diameter. The ends of the specimens were machined so it was necessary to leach the specimens prior to irradiation to remove exposed U and Th. Metallography on duplicate specimens did not reveal any damage to the coated particles due to the extrusion or heat treating operations.

Another problem was in obtaining samples for analyses which were representative of the irradiation specimens. The specimens were very small, containing only 1.2 to 1.6 cm^3. Chemically analyzing a portion of a specimen, which was customary, gave erratic results. Analyzing complete duplicate specimens gave much more uniform results. However, the final solution to the problem was to gamma count each specimen for both U and Th. Similar specimens were then selected for chemical analyses and irradiation.

Conclusions

A process was developed to extrude coated particle loaded graphite having high particle loadings, > 45 vol%, good dimensional stability, high matrix density, > 1.6 g/cm^3, and thermal conductivity much improved over impregnated fuel sticks. It was demonstrated that the metal loading and volume percent particles in an extruded fuel could be closely controlled and that particle damage was minimal.

References

(1) D. H. Schell, J. M. Taub and J. W. Taylor, "The Fabrication of Uranium-Loaded Graphite," LAMS-2587 (1961).

PROPERTIES OF EXTRUDED FUEL RODS FOR HTGR APPLICATIONS*

R. L. Hamner, J. M. Robbins, and W. P. Eatherly

Oak Ridge National Laboratory, Oak Ridge Tennessee 37830

Until recently, a small program existed at ORNL and at LASL investigating extrusion as a process for fabricating fuel rods or elements for High Temperature Gas-Cooled Reactors. This work was undertaken because of the relative simplicity of the extrusion process over injection molding techniques. Also, in looking ahead to process heat reactors where the outlet gas temperatures of 1000°C or greater are desirable, the fuel would operate at temperatures no higher than steam-cycle reactors if in direct contact with the helium coolant. Hollow extruded rods with a strong continuous matrix offer such a configuration.

Fabrication of extruded elements has been discussed at a previous Carbon Conference[1], and is based on NERVA technology. The principle differences are that the curing and carbonizing times were decreased from a 40-hr cycle to five hours, and extrusion rates were increased to ten feet per minute. At this rate, the small table-top extrusion press utilized at ORNL could easily fabricate fuel rods for three to four reactor cores per year. Matrix densities of greater than 1.4 Mg/m^3 could easily be maintained and varied only about 6% from no fuel particle loading up to a maximum of 40 volume-% particle loading. Above 45 volume-% mechanical degradation of the matrix became obvious due to shrinkage relative to the particles.

The two obvious advantages of extrusion are its simplicity and its ability to yield high thermal conductivities even after irradiation damage. These conductivity measurements are reported elsewhere in this conference[2]; the importance of high matrix conductivity is to reduce the thermal gradient across particles by about a factor of three, thus significantly reducing the uranium migration due to oxygen transport or thermal diffusion.

The most significant disadvantage of extruded elements is the limitation on fuel particle volume loading. The injection-molded elements have a maximum loading of about 59 volume-% whereas extruded rods can probably attain only 45–50 volume-%. The higher loadings become increasingly important as one attempts to reach conversion factors above 0.66 in the General Atomic prismatic core design. Hence extruded rods would be impractical in the GA core configuration without significant redesign.

A number of other questions have been raised as to the practicality of fabrication by extrusion, and the purpose of this paper is to dispose of these insofar as possible. It must be pointed out most of the data on extrusion quoted here arise from a single semi-production run of 630 lineal feet of nominal 0.5-inch diameter fuel rods at 30 volume-% loading with very little attempt to optimize the system.

Ojection: Diameters will very significantly more than for molded rods. Standard deviation on diameters from rod-to-rod and within-a-rod were

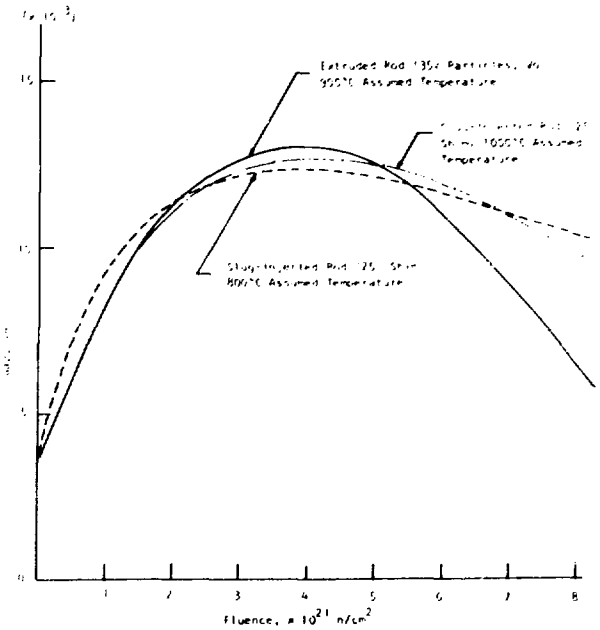


Fig. 1. Gap Thickness as a Function of Fluence Between Injected Molded Rods and Extruded Rods and the Graphite Block Making Up the Entire Fuel Element.

0.0007 inches (0.12%). Batch-to-batch variations were statistically insignificant. The total range in diameter was 0.0023 inches. These numbers are comparable to those observed for molded rods.

Radiation damage will induce increased shrinkage of the continuous matrix leading to an increased temperature drop across the gas gap between fuel rod and graphite block. All available data on dimensional changes in typical injection molded and extruded rods under comparable conditions has been smoothed and is given in the accompanying figure. During at least the early part of the fuel rod life when uranium is still present in significant quantities, there are no differences in the gas gap between the two types of rods.

Densities of the matrix will vary considerably making weight a poor means of determining fuel homogeneity. Matrix density for these rods was calculated at 1.75 Mg/m^3. The lineal rod densities within the batch examined determined to be 2.763 g/cm with a standard deviation of 0.0026 g/cm (0.09%) and a total range of 0.0071 g/cm (0.26%). These are quite within the range required for accountability. A random sample of 80 of the 30-inch rods were weighed and a variance analysis performed. The within-a-batch standard deviation was 0.0177 g/cm (0.7%) but includes errors in length and broken edges on end cutting. The batch-to-batch variation was quite large (approximately 2.1%), but this was

*Research sponsored by the U.S. Energy Research and Development Administration under Contract with Union Carbide Corporation.

traced to the variability of the coated particle densities. The particles were reject BISO-coated thorium carbide and not only exhibited poor coatings, but were cracked as well. Finally, one rod was cut into samples 1.90 cm long and alternate samples oxidized and the residue weighed. The oxide mean value was 39.99 wt-% with a standard deviation of 0.79%. This is statistically consistent with a 0.09% deviation from rod-to-rod. In all, we conclude rod weight is acceptable as both a process control and accountability measure.

X-radiography can only be used as a qualitative tool since the rods are essentially opaque to x-rays along the centerline three-fourths of the rod volume.

The 30-inch rods will bow and be difficult to insert into the graphite fuel block. Only a single Fort St. Vrain fuel block was filled from this rod run, representing about 130 randomly selected rods. All inserted easily, with only one having to be pushed gently into the block. Clearance between rod and hole diameters was approximately 0.010 inch on the average. These rods were extruded into and heat-treated on graphite pallets containing 3/4-inch face-to-face hexagonal grooves rather than nominal 1/2-inch diameter semi-circular grooves, and hence bowing could be expected to be larger than normal. To determine the point at which a rod would break, a single surplus rod was supported on a 27-inch span and broken in flexure. The mid-point tranverse distortion was 0.435 inches. Hence there should be no difficulty in inserting 30-inch rods into a block.

In summary, it is our considered opinion extrusion offers a very viable alternative form of fuel rod fabrication in core designs less restrictive than the General Atomic prismatic block configuration. Although not investigated here, continuous auger extrustion, hollow shaped cylindrical shapes, and concentric coextrusion of several types of material are accepted techniques in graphite technology.

(1) R. L. Hamner, J M Robbins, J. H. Coobs, *Development of Continuous-Matrix Fuel Rods for Advanced High Temperature Gas-Cooled Reactors*, Paper NF-11, 11th Biennial Conference on Carbon, June 1973.

(2) J. P. Moore, R. S. Graves, W. P. Eatherly, ***Thermal Conductivity and Electrical Resistivity*** *of Simulated Fuel Elements*, this conference.

Thermal Conductivity and Electrical Resistivity of Simulated Fuel Elements*

J. P. Moore, R. S. Graves, and W. P. Eatherly
Metals and Ceramics Division, Oak Ridge National Laboratory

It is well-known that important changes may occur in the physical properties of bonded fuel rods during their lifetime within a reactor. These changes are caused by the high temperatures, environment, and lastly (and probably most importantly) by the high neutron fluxes. Neutrons have a strong effect in reducing the thermal conductivity, λ, by introducing defects such as vacancies and dislocations into the basal planes of graphitic material.[1] The reduction of λ raises the operating temperature which lowers the lifetime of the graphite. Although the quantitative effects of neutron irradiation on the λ of polycrystalline graphites have been extensively studied,[2-4] they have not been studied for carbonaceous material nor for carbonaceous material containing various quantities of spherical fuel particles which are envisioned for use in a high-temperature gas-cooled reactor (HTGR). The primary purpose of this experiment, therefore, was to measure the thermal conductivity of simulated fuel elements consisting of inert particles suspended in a carbonaceous matrix as a function of temperature, T, volume percent particle loading, and neutron fluence. The electrical resistivity, ρ, Seebeck coefficient, S, and coefficient of thermal expansion, CTE, were also measured as functions of the same parameters. The CTE and S, however, will not be discussed here.

Specimen Description and Measurement Technique

This experiment included extruded specimens with nominal simulated-fuel particle contents of 0, 13, 23, and 35 vol % with matrix densities of 1.75, 1.70, 1.65, and 1.60 Mg/m^3, respectively. These four were formed by extrusion with a matrix of 75.7 wt % graphite, 24.3 wt % thermax, and prepolymerized furfuryl alcohol. A series of slug-injected specimens, all with about 58 vol % inert particles, were fabricated with a matrix of 28.5 wt % graphite filler in pitch. The matrix densities of the latter specimens were about 0.60 Mg/m^3. Since measurements of λ after irradiation were done outside a hot cell, inert carbon particles were used as surrogates for fuel particles to minimize postirradiation radioactivity. After fabrication, all specimens were heat treated at 2070 K for 1.8 Ks in argon. The specimens were irradiated in the High Flux Isotope Reactor at Oak Ridge National Laboratory at nominal temperatures of 1220 K.

Steady-state longitudinal techniques[5] were used for most of the λ, ρ, and S measurements. The ρ was measured using a standard four-probe reversible-dc technique with the thermocouple elements serving as potential probes. Measurement uncertainties were about ±0.4%, ±5%, and ±0.1 μV/K for the ρ, λ, and S, respectively.

Results

Unirradiated Material — Thermal conductivity results obtained on the unirradiated specimens are shown in Fig. 1 as a function of T. The λ decreases smoothly with increasing particle content and λ decreases with increasing T. The two curves below 400 K were generated with a low-temperature technique on specimens from a previous experiment, and these are in relative agreement with the present results.

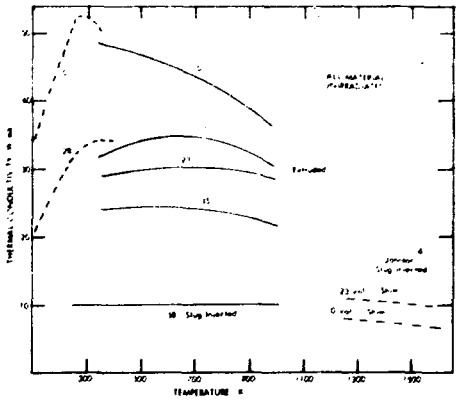


Fig. 1. The λ of Unirradiated Simulated-Fuel Elements versus T. The two low T curves were obtained on extruded elements with a different matrix.

The λ of unirradiated material at 400 K and the electrical conductivity, $\sigma = \rho^{-1}$, at 300 K are shown in Fig. 2 versus volume percent particle loading. The λ decreases smoothly with particle loading, and this curvature is mirrored by σ. This similitude

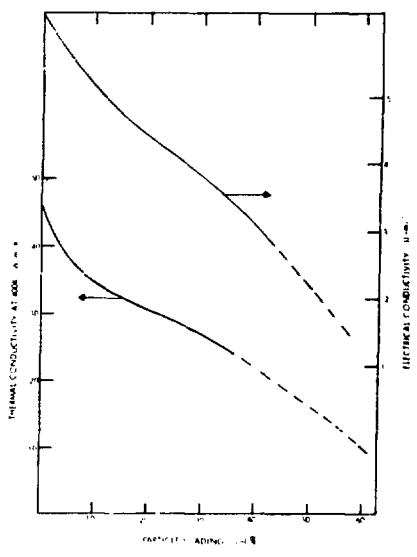


Fig. 2. The λ (400 K) and σ (300 K) of Unirradiated Simulated-Fuel Elements Versus Volume Percent Loading.

*Research sponsored by the Energy Research and Development Administration under contract with the Union Carbide Corporation.

indicates that, to a first approximation, λ and ρ are dependent on the same variables within the composites.

Irradiated Material – After irradiation, the electrical resistivities of all surviving specimens were measured near 300 K. The ρ versus fluence is shown in Fig. 3. The ρ of the slug-injected materials is much greater than that of the extruded materials and increases steadily with increasing fluence. The ρ of the extruded specimens increases with fluence initially, saturates above about 4 to 6 $\times 10^{25}$ n/m^2, and then begins to increase again above 6 to 9 $\times 10^{25}$ n/m^2.

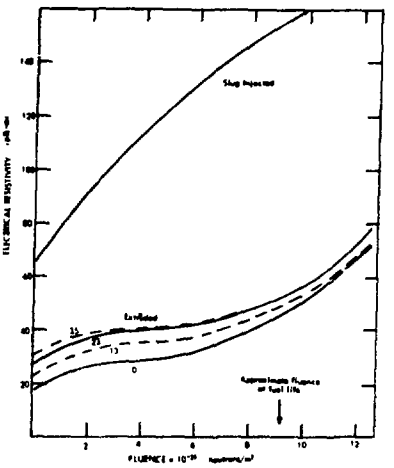


Fig. 3. The Room Temperature ρ of Extruded and Slug-Injected Fuel Elements Versus Neutron Fluence.

The smoothed λ results are given in Table I. Over the entire temperature range, the matrix material for the extruded specimens (*i.e.*, the specimen with 0 vol % particles) has a steadily reducing λ with increasing neutron fluence. The λ of the 13 and 23 vol % specimens remains essentially constant with increasing fluence until the fluence goes above 5 $\times 10^{25}$ n/m^2. The λ of the 35 vol % specimen actually increases with fluence initially and remains quite high beyond 5 or 6 $\times 10^{25}$ n/m^2. The λ of the extruded specimens remains high over the fluence range where ρ of each material approaches a constant value. The unirradiated slug-injected specimen and the one irradiated to 2.34 $\times 10^{25}$ n/m^2 contained 58 vol % fuel particles, whereas actual fuel normally contains a lower percentage fuel with the difference being composed of graphite particles. For example, the last specimen listed in Table I consisted of 36.5 vol % simulated-fuel particles and 20.2 vol % shim. The λ of this specimen near 400 K was only 5 W/mK. Thus the λ of the 35 vol % extruded specimen after 9.0 $\times 10^{25}$ n/m^2 was a factor of 2.6 greater than a slug-injected specimen with similar simulated-fuel particle loading and fluence.

Discussion of Results

The λ and ρ results are primarily controlled by the carbonaceous matrix material and the effect of neutrons on different components of this matrix. The matrix density of all extruded specimens is a factor of 2.6 greater than the matrix density of the slug-injected specimens. At all irradiation stages this density difference has a dominant effect on the properties.

Table I. Smoothed Values for the Thermal Conductivity of Simulated Fuel Elements Versus Temperature, Neutron Fluence, and Particle Loading

V[a]	η[b]	Thermal Conductivity, W/mK						
		400 K	500	600	700	800	900	1000
0	0	47.5	47.2	46.2	44.6	42.1	39.0	35.3
0	2.0	40.4	42.3	43.3	43.3	42.4	40.6	38.0
0	8.1	20.0	21.2	21.9	22.0	21.7	21.0	--
0	12.1	9.6	10.1	10.5	10.6	10.6	10.6	10.5
13	0	33.0	34.6	35.2	34.9	34.0	32.2	30.6
13	2.0	32.8	34.1	34.5	34.2	33.6	32.3	30.4
13	4.0	29.0	29.6	29.9	29.7	29.4	28.8	28.0
13	8.1	18.8	19.8	20.5	21.0	21.0	20.6	19.7
13	12.1	11.2	12.0	12.5	12.7	12.5	12.0	11.0
23	0	29.5	30.0	30.2	30.4	30.2	29.6	29.2
23	2.3	28.6	30.0	30.8	30.5	29.6	28.1	26.0
23	4.5	28.1	28.7	28.8	28.6	28.0	27.1	26.0
23	9.0	18.0	18.8	19.2	19.2	18.9	18.3	17.6
35	0	24.2	24.6	24.7	24.2	23.2	22.0	--
35	2.3	27.6	29.0	30.0	30.2	29.6	28.0	26.0
35	4.5	22.2	24.0	25.6	26.7	27.8	28.5	28.5
35	9.0	12.5	13.4	14.2	14.4	14.0	13.0	11.5
58[c]	0	10.2	10.8	11.2	11.3	11.2	10.8	10.4
58[c]	2.3	11.8	12.0					
58[d]	8.6	15.0						

[a] Volume percent simulated-fuel particle loading.

[b] Neutron fluence $\times 10^{-25}$ n/m^2

[c] All particles were simulated fuel.

[d] 36.5% simulated-fuel particles and 20.2% shim.

The most interesting aspect of the data is the initial increase of λ in the 35 vol % extruded specimen with neutron irradiation. The λ of this material, as well as λ of the 13 and 23 vol % specimens, remains high beyond a fluence of 5 or 6 $\times 10^{25}$ n/m^2. This initial increase of λ in the 35 vol % specimen is caused by the partial ordering of the carbonaceous material surrounding the graphite filler particles under the influence of the neutron flux and strain. This effect has been observed previously in similar structures where the heat treatment was at such a low temperature (2070 K) and the neutron irradiation occurred at such a high temperature (1220 K).[7]

References

(1) B. T. Kelley, *Chemistry and Physics of Carbon*, Vol. 5, p. 119, P. L. Walker, ed., Marcel Dekker, Inc., New York, 1969.

(2) W. J. Gray and A. L. Pitner, *Carbon*, 9, 699–716 (1971).

(3) J. P. Moore *et al.*, *Nucl. Technol.* 22, 88 (1974).

(4) H. Matsuo, *J. Nucl. Mater.* 42, 105 (1972).

(5) J. P. Moore, D. L. McElroy, and R. S. Graves, ORNL-4986 (September 1974).

(6) W. R. Johnson, GA-A12910 (GA-Ltr.-9), UC-77; March 1974.

(7) W. Delle, GERHTR-131 (April 1974).

FABRICATION OF GRAPHITE MATRIX FUEL FOR PULSED REACTORS*

K. V. Davidson, D. H. Schell, Los Alamos Scientific Laboratory, Los Alamos, N.M. 87545
C. H. Karnes, R. H. Marion, Sandia Laboratories, Albuquerque, N.M. 87115

Introduction

A program was initiated by Sandia Laboratories (SLA) to increase the total fluence in the experimental cavity of the Annular-Core Pulsed Reactor (ACPR) for fast reactor fuel element transient and safety testing. The ACPR, described by D. J. Sasmor et al.,[1] is a TRIGA-type reactor with a 23-cm dry central cavity serving as the primary experiment irradiation test region. The ACPR is fueled with a $UZrH_{1.6}$ alloy arranged in a hexagonal "annulus" to provide an experimental region 23 cm diam x 30 cm long. The present ACPR capabilities are steady-state operation to 300 kW [$\phi \approx 10^{13}$ n/(cm^2 sec)], and pulsing mode operation with an initial period as short as 1.3 msec, a pulse width (FWHM) of 4.5 msec, and a total fluence of 3 x 10^{15} n/cm^2 for a maximum pulse.

The large central irradiation cavity and the short initial periods have created interest in using the ACPR to simulate the conditions required for LMFBR fuel element and transient safety testing. A total cavity fluence of 8 x 10^{15} n/(cm^2 sec) for a maximum pulse and to ~ 2 MW for the steady-state power level are the goals for the reactor performance.

A two region core was proposed consisting of an outer driver region of the hydride fuel and an inner region of fuel with higher temperature and enthalpy capabilities. This would permit a higher pulse fluence capability and maintain the operating temperature limitations of the hydride fuel. The safety aspects of a strong prompt negative temperature coefficient would be provided by the hydride fuel region.

Several candidate fuels have been considered for the high-temperature regions of the core. One of these is the (U,Zr)C-graphite composite fuel developed by the Los Alamos Scientific Laboratory (LASL) during the Rover (Space Nuclear Propulsion Reactor) Program.[2,3] This experience has also recently been used to fabricate carbide-graphite composite fuel rods for the TREAT converter studies[4] being performed by Argonne National Laboratories (ANL).

Materials

Developmental fuel extrusions were made by extruding either a mixture of graphite flour-Thermax, ZrC, and UO_2 or graphite flour-Thermax and (U,Zr)C solid solution powder. All extrusions were bonded with Varcum 8251, a partially polymerized furfuryl alcohol. If a pore former was added to the mix it was either wood flour or tapioca starch.

Thermax (carbon black) was added to the extrusion mixes in amounts varying from 5 to 15 pph of the graphite flour.

The reactor grade ZrC and the 93% enriched $^{235}UO_2$ powders had an average particle size of 3.5 μm and 5.0 μm respectively.

The solid solution (U,Zr)C powder was made by reacting a mixture of ZrO_2, UO_2 and carbon to 2550 K. Several powders with varying U contents, having high density particles, all -325 mesh, were made.

Two high purity graphite flours having different particle sizes and having different coefficients of thermal expansion (CTE) were used for both the extrusion and hot pressing work. The flours were -200 mesh, -325 mesh and < 10 μm.

All hot pressings were made with combinations of solid solution (U,Zr)C and graphite flours including special smaller fraction sizes other than -325 mesh. Camphor was used as a fugitive binder to prevent segregation of the powders.

Fabrication Procedures

All extrusion batches were mixed in a Patterson-Kelley twin-shell blender equipped with an intensifier bar and liquid addition apparatus. The dry ingredients and 88% of the required Varcum binder were mixed in the blender. The remaining Varcum binder was added step-wise during the extrusion operation.

The mix was successively passed through a commercial meat chopper and extruded a number of times to thoroughly homogenize all ingredients. The 150-ton extrusion press is equipped with a vacuum system for evacuation of the extrusion die, chamber and mix before each extrusion. The final extrusion was made into graphite fixtures used to contain the extrusion during the first stage of heat treatment. Extrusions were heat treated slowly over a period of 9 days to the final desired temperature, usually ~ 2900 K.

Hot pressing mixes were made by blending the required dry ingredients with camphor and chlorothene in a Patterson-Kelley blender.[5] The camphor acts as a fugitive binder to condition the surface of the particle to prevent the segregation of the powders, which have widely different densities, during die loading operations. Chlorothene is used to dissolve the camphor to ensure thorough mixing but is evaporated from the mix prior to loading the hot pressing dies.

The graphite hot pressing dies are 32 mm inside diameter. The hot pressings were usually about 75 mm long. Hot pressing conditions varied but good pressings were made at pressures of 24 MPa (3500 psi) and temperatures around 2800 K.

Nondestructive Testing

The as-fabricated extrusions and hot pressings were radiographed for defects such as cracks, voids and inclusions. Density variations in the hot pressings were also detected. The fuels were gamma scanned in 1-cm increments to determine the ^{235}U distribution uniformity.

Discussions

Fuel materials for the ACPR must be able to withstand high thermal stresses. Important mechanical properties contributing to thermal stress resistance are low coefficient of thermal expansion (CTE), low modulus and high fracture strength. A fuel having high thermal diffusivity and heat capacity is also desirable. Because of the short heating time, rapid dissipation of the heat from the fuel particles to the entire fuel is necessary. Although other proposed fuels for the ACPR have higher heat capacities than the (U,Zr)C-graphite, the high potential enthalpy and thermal stress resistance of the graphite fuel makes it a good candidate.

*Work supported by the U.S. Nuclear Regulatory Commission (Project No. A1032) and the U.S. Energy Research and Development Administration under Contract AT(29-1)-789.

The first developmental fuel extrusions, 35.5 mm diam, contained ZrC, UO_2 and carbonaceous materials. During heat treatment the UO_2 converted to the carbide and entered into solid solution with the ZrC. In converting the oxide to carbide, carbon is lost lowering the graphite matrix density. When the solid solution is formed, a continuous carbide network results. Thus the heat treated extrusion consists of intertwined continuous networks of graphite and carbide. The carbide phase, 35 vol% of the fuel, has a high CTE so a high CTE graphite was used to reduce the mismatch in thermal expansion. Although this material was strong, the high CTE, 6.7 x 10^{-6}/K, tended to reduce its thermal stress resistance.

Hot pressings, which had high (35 vol%) carbide contents, tended to have isolated carbide particles although there was agglomeration of the carbide. The CTE was > 7 x 10^{-6}/K.

Ideally, graphitic fuels would consist of small, < 20 μm, isolated fuel particles surrounded by a high density graphite matrix. Several changes were made to achieve this structure. The carbide content was reduced as was the size of the graphite flour which had a lower CTE than used previously. The combination of these changes should result in improved thermal stress resistance. Also, in the case of the extrusions, the carbide phase was added to the extrusion mix as (U,Zr)C solid solution powder rather than ZrC and UO_2. The CTE was reduced to ~ 4.4 x 10^{-6}/K and the matrix density increased from ~ 1.5 to 1.6 g/cm^3. A high matrix density is required to increase the enthalpy of the system thus tending to reduce the maximum temperature the fuel would experience when pulsed.

Hot pressings made with the above changes still had high CTEs, ~ 8 x 10^{-6}/K. The graphite matrix densities were as high as 2.0 g/cm^3.

Experimental Results

Extrusions made with ZrC plus UO_2 which had relatively high porosities and a continuous carbide (35-vol%) structure could be readily fractured when pulsed in the ACPR.

Two extrusions, one in the shape of an annulus and the other a core to fit inside the annulus, were used and the carbide phase was added as (U,Zr)C solid solution powder. The annulus contained 20 vol% carbide (CTE of 4.3 x 10^{-6}/K) while the core, having a higher U loading, contained 30 vol% carbide and a CTE of 5.8 x 10^{-6}/K). This fuel was subjected to multiple reactor pulses producing the most severe temperature distribution and thermal stresses possible in the ACPR. No fractures, cracks or fragments were detected. Peak temperatures were approximately 2400 K.

An extrusion containing 17 vol% (U,Zr)C, also made with low CTE graphite and solid solution powder, was extruded in the shape of a solid 35.5-mm-diam cylinder. Samples of this extrusion were pulsed 6 times at full power to peak temperatures of 2350 K without failure. The CTE of this material was 4.4 x 10^{-6}/K with a room temperature modulus of 18 GPa (2.6 x 10^6 psi) and fracture strength of 34 MPa (4900 psi).

Hot pressed fuels containing 35 vol% (U,Zr)C solid solution were made with "high" and "low" porosity, 20% and 11% respectively. The high porosity material failed at modest energy depositions but the material with a lower pore volume performed very well in the ACPR tests. One set of samples withstood 55 maximum pulses without fracturing or chipping. The peak temperature was approximately 2300 K.

Further hot pressings having lower carbide contents (17 to 32 vol%) made with low CTE graphite flour all showed excellent thermal stress resistance. Fuel pellets survived numerous full power pulses without damage. The high matrix density of the hot pressings increased the enthalpy of the fuel so that for a given power input the peak temperature would be about 10% less than for a similar extruded fuel. A typical hot pressing had a CTE of 7.7 x 10^{-6}/K, room temperature modulus of 17 KPa (2.4 x 10^6 psi) and fracture strength of 38 MPa (5500 psi).

Other properties measured on many samples, both extrusions and hot pressings, were heat capacity, thermal diffusivity, enthalpy, fracture strain and peak to minimum radial energy profile.

Conclusions

Extrusion and hot pressing techniques have been developed for fabricating developmental fuel for the ACPR. Both methods produced fuel materials which have been shown to survive more severe thermal stress environments than will be present in the upgraded version of the ACPR. An extensive data base exists for this type of fuel and the manufacturing procedures are considered state-of-the-art.

References

(1) D. J. Sasmor, J. A. Reuscher, P. S. Pickard, J. B. Rivard, J. S. Philbin and R. L. Coats, "Fuel Selection Considerations for the Annular-Core Pulsed Reactor Performance Improvement," Transactions American Nuclear Society 19, 129 (1974).

(2) K. V. Davidson, W. W. Martin, D. H. Schell, J. M. Taub and J. W. Taylor, "Development of Carbide-Carbon Composite Fuel Elements for Rover Reactors," LA-5005 (1972).

(3) L. L. Lyon, "Performance of (U,Zr)C-Graphite (Composite) and (U,Zr)C (Carbide) Fuel Elements in the Nuclear Furnace I Test Reactor," LA-5398-MS (1973).

(4) K. V. Davidson, "U,(Zr)C-Graphite Fuel for TREAT Converter Studies," Nuclear Technology 28 23-30 (1976).

(5) K. V. Davidson, R. E. Riley, and J. M. Taub, "Carbide-Graphite Composites," LA-3569-MS (1966).

THERMAL TREATMENT OF HTGR FUEL*

G. W. Weber† and R. L. Beatty
Oak Ridge National Laboratory, Oak Ridge, Tennessee 37830

Introduction

The reference fuel kernel in high-temperature gas-cooled reactors (HTGRs) is UO_2 and UC_2 finely dispersed in microspheres of porous carbon derived from weak-acid ion-exchange resins (WAR).[1,2] These resins are available commercially as sized and shaped microspheres derived from acrylic acid-divinylbenzene. Amberlite IRC-72 (manufactured by Rohm & Haas) and Duolite C-464 (manufactured by Diamond Shamrock) were used in this study.

After drying, carbonization to 900°C completes the H_2O evolution and thermally decomposes the resin, producing finely dispersed UO_2 in a porous carbon matrix. Typical properties are carbon-to-uranium ratios of from 4 to 6 with a density of 2.4 to 3.7 Mg/m^3 and 67 to 75 wt % U.

Carbothermic reduction of the UO_2 (conversion) produces UC_2 and $UC_{1-x}O_x$ with the evolution of CO. The percent oxygen removed is defined as the percent conversion (UO_2 = 0%, UC_2 = 100%). Final weight percent uranium ranges from 72 to 86% with corresponding densities from 2.4 to 6 Mg/m^3.

This work determined the effect of heating rate during carbonization on the bulk physical and chemical properties, the variation during processing of significant material properties, and the effect of conversion conditions on the thermodynamic predictions.

Experimental Procedure

Processing occurs in vertical graphite resistance furnaces containing cylindrical graphite fluidization tubes having conical bottoms. Chamber diameters are nominally 2.54 to 6.35 cm (1.00 to 2.5 in.). Temperature measurement is accomplished with sheathed Chromel-P–Alumel bed thermocouples to 700°C and optical pyrometry for higher temperatures. Fluidizing (argon) gases are supplied through calibrated flowmeters.

Thermogravimetric (TGA) and differential thermal analysis (DTA) were conducted with a Mettler recording vacuum thermoanalyzer 300. To establish the effect of heating rate during carbonization on bulk properties, Amberlite IRC-72 and Duolite C-464 were heated at controlled rates to 500°C followed by rapid heating to 1200°C.

Property variation during processing was investigated by heating both resins at 2°C/min to 500°C and then at 20°C/min to a selected temperature. Mercury density and porosimetry, BET surface area, carbon-to-uranium ratio, particle size, and bulk physical properties were determined.

Comparisons of observed and predicted conversion levels for different gas flows, resin types, temperatures and batch sizes were made in 35 experiments with gas flows from 0.295 to 7.37 , of argon per gram of uranium from 1500 to 1690°C at conversion levels from 15 to 93%. Batch sizes varied from 28 to 486 g in furnace tubes from 35 to 108 mm in diameter.

Results

The Amberlite IRC-72 TGA analysis showed a gradual weight loss to 270°C for 2°C/min, a large weight loss from 360 to 440°C, and little subsequent weight loss to 1000°C. Faster heating rates increased the weight loss.

The Duolite material shows little weight loss until 210°C where a gradual loss occurred. Faster weight losses occur with lower heating rates to approximately 315°C, above which the weight loss accelerates. Above 480°C, little weight loss occurs to 1000°C. The Duolite resin requires higher temperatures for equivalent decomposition than does the Amberlite material, which is attributed to the higher degree of polymer cross-linking resulting from the higher uranium concentration. The predominance of the reaction rate in the 350 to 460°C region is apparent throughout.

The DTA results show three broad endotherms for both resins. Comparison with the TGA results indicates that the peaks correspond to the weight losses. The relative peak sizes correspond to the relative weight losses. The similar thermal behavior indicates that similar processes may be occurring in both resins above 270°C.

The effect of heating rate on Amberlite IRC-72 from 200 to 500°C, the predominant TGA region, on the weight loss, volume loss, and carbon-to-uranium ratio shows a strong linear dependence on the log of the heating rate. As carbothermic reduction to UC_2 requires a carbon-to-uranium ratio of 4, any technically feasible heating rate will be satisfactory. Duolite C-464 shows a stronger correlation with higher carbon-to-uranium ratios.

Comparisons of the carbon-to-uranium ratio are significant as a higher ratio reduces the agglomeration tendency during conversion. Both resins show reduced agglomeration tendencies with slower heating rate through the critical range. Conversion runs under comparative conditions indicate Duolite resin to be superior in resisting agglomeration.

The changes in weight loss, volume loss, and tap density are shown for Amberlite in Fig. 1. Tap density is obtained from the bulk volume occupied by the particles. The weight loss curve follows the TGA behavior. The behavior of Duolite C-464 is similar. Particle size, carbon-to-uranium ratio, and mercury density closely replicate the TGA and shrinkage curves. Mercury porosimetry shows that carbonized Duolite C-464 has 0.05-μm pores, significantly

*Research sponsored by the U.S. Energy Research and Development Administration under Contract with the Union Carbide Corporation.

†Now with the Oak Ridge Y-12 Plant.

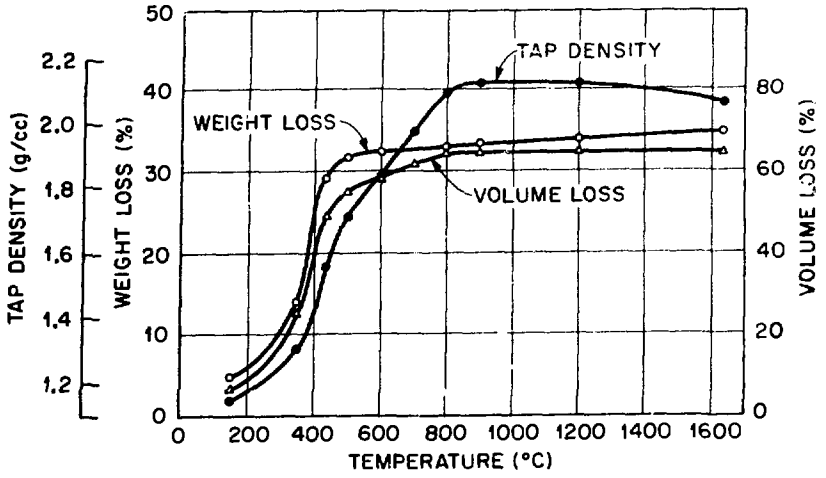


Fig. 1. Weight Loss, Volume Loss and Tap Density Variation from 150 to 1625°C for Uranium-Loaded Amberlite (IRC-72) Weak-Acid Resins.

larger than the 0.015 μm Amberlite IRC-72. Both resins showed similar variations from 150 to 1625°C. Smaller pores open from 150 to 440°C while thermal decomposition proceeds. From 500 to 1200°C, the pores coalesce and increase in size.

The changes in volume, weight, and density with conversion levels at 1625°C (after carbonization at 2°C/min) are shown in Fig. 2 for Amberlite IRC-72. Duolite C-464 had a similar behavior. Particle size and mercury density variation with conversion level correspond to the bulk property variation.

The conversion behavior of various batches at different gas flows is shown in Fig. 3. The gas flow is in liters of argon per gram of uranium per percent conversion obtained. The dashed-regression-line fit for $y = ax^b$ and the conversion reaction curve are shown. The two resins were not significantly different.

The strong dependence of conversion on gas flow agrees with the model described by Lindemer[2] and Beatty.[3] If sufficient porosity is available so that carbon monoxide removal is not diffusion-rate limited, conversion can be predicted from the equilibrium partial pressure of carbon monoxide.

Conclusions

1. Chemical and bulk physical properties closely reflect the TGA behavior and are sensitive to heating rate through a critical temperature range from about 350 to 460°C during the carbonization process. The carbonization process is near optimal at a rate of approximately 2°C/min through the critical range and the maximum practicable rate outside this range.

2. The carbothermic reduction of UO_2 can be accomplished at 1500 to 1750°C in a controlled manner by the rate of CO removal by the inert sweep gas and temperature as predicted by thermodynamic calculations.

References

(1) C. B. Pollock, J. L. Scott, and J. M. Leitnaker, *High-Temperature Nuclear Reactor Fuel*, U.S. Patent No. 3,856,622 (To U.S. Atomic Energy Commission) (December 24, 1974).

(2) R. L. Beatty, *Carbonization and Coating of Fueled Resin Microspheres*, Am. Ceram. Soc. Bull. 53 (4), 363 (1974).

(3) T. B. Lindemer, *Nucl. Appl. Technol.* 9 (November 1970).

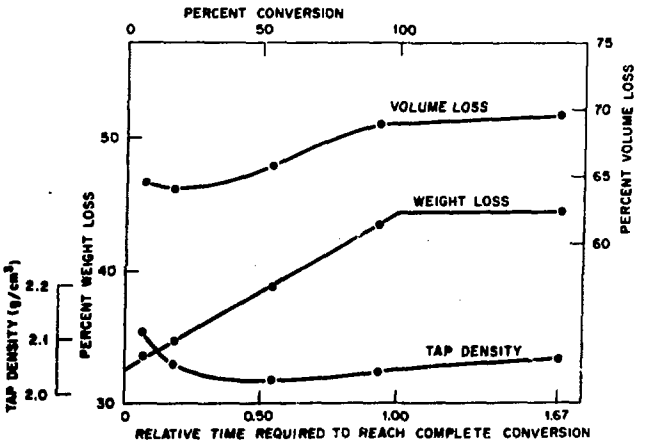


Fig. 2 (Left) Weight Loss, Volume Loss, and Tap Density Variation as a Function of Conversion Level at 1625°C for Uranium-Loaded Amberlite (IRC-72) Weak-Acid Resin.

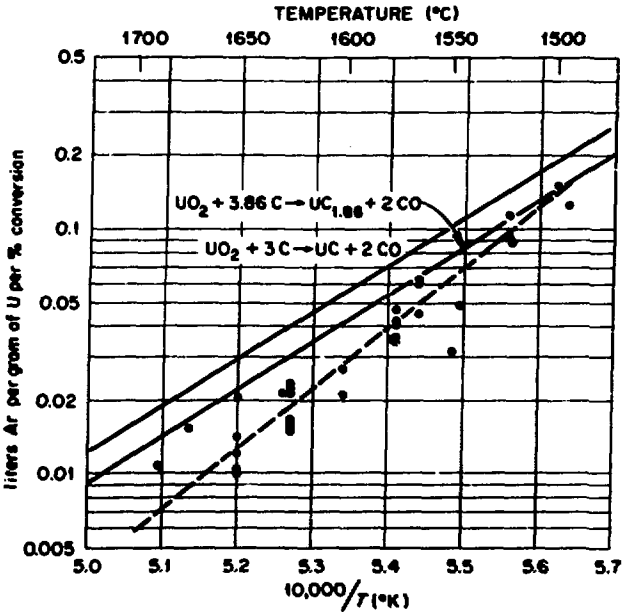


Fig. 3 (Right) Conversion Behavior of Weak-Acid Resin-Derived Fuel.

[illegible] OF CARBON-CARBON COMPOSITES

E J Walker, L F Irwin and [illegible]
Aldermaston, Reading, RG7 4PR, England

Introduction

We have previously described investigations of carbon-carbon composites exposed to fast neutrons in the DIDO, light water moderated reactor (1,2). The property improvements obtained, the structural modifications and the potential use of these materials in nuclear energy generation and aerospace warranted further work.

Experimental

Carbon-carbon composites of thickness varying from 1 mm to 10 mm were prepared using PAN based HT and HM fibres and rayon based cloth. The composite structures were unidirectionally reinforced (UNI), 0^0-90^0 cross-plied and all cloth. Densification was by chemical vapour deposition (CVD) or resin re-impregnation (RIP). Using two different fibres, two structures and two densification routes yielded eight different composites under evaluation plus one woven cloth composite. The properties measured are dimensional stability, longitudinal and transverse flexural strength, modulus, shear strength and impact strength after exposure to fast neutron doses varying from 10^{17} to 10^{20} n cm^{-2}.

Experiments have been done to study the effects of exposure in air and in inert atmosphere. The effect of temperature is also being studied. So far only moderate temperatures have been used eg 50C and 250^{0}C but these cover a range where interesting effects are observed using other graphites.

One of the problems in this work is the activation of impurities by thermal and epi-thermal neutrons causing handling difficulties during post exposure evaluation. A rig is under design which will incorporate boron carbide and cadmium shielding to reduce the residual activity. The use of boron carbide to provide γ-heating and helium flow for cooling also assists in achieving different exposure temperatures. Observations using HT fibre exposed to 10^{19} n cm^{-2} with and without shielding, showed that for boron carbide the activity after 100 days removal from the reactor was reduced from 3.8×10^{-6} to 4.5×10^{-7} curies/g/10^{19} n cm^{-2} and for cadmium was reduced from 7.7×10^{-7} to 1.6×10^{-7} curies/g/10^{19} n cm^{-2}, reductions of 8.4 : 1 and 4.8 : 1 respectively.

Results

Figure 1 shows the effect of exposure in air at 150^0-250^{0}C to fast neutron doses up to 1.5×10^{20} n cm^{-2} on the flexural strength and modulus of UNI-HT-CVD composites. Both properties increased steadily up to approximately 5×10^{19} n cm^{-2} then both fell abruptly such that at 1.5×10^{20} n cm^{-2} their values were less than the unirradiated values. Figure 2 shows some structural data obtained by neutron diffraction on the same material after similar exposures. The apparent d_{002} increased steadily and the apparent L_c decreased up to 5×10^{19} n cm^{-2}, then the rate of change increased sharply. Under the conditions of this experiment an exposure of approximately 10^{20} n cm^{-2} seems to be a threshold for the UNI-HT-CVD material, below which property improvements occur and above which the high concentration of interstitial clusters disrupt the structure bringing severe reduction in mechanical properties.

Table 1 gives the dimensional changes with exposure for the nine composites under evaluation. In almost every case where change occurred it was a shrinkage. The one small length increase is thought to be due to measurement error. Measurements were made to an accuracy of 0.0005 in. but changes of 0.001 in. or less have been recorded as zero. The shrinkage in length of UNI composites, in length and breadth of cross-plied composites and no change in depth suggest that the fibres are changed in length but not in diameter. The structural evidence in Figure 2 indicated that at exposures around 10^{20} n cm^{-2}, there was large expansion in the c-axis direction which would be expected to manifest itself as an increase in diameter. The absence of dimensional change perpendicular to the fibres suggests that the c-axis expansion may be accommodated in cylindrical pores or [illegible] cracks in the fibres themselves or within the cylindrical matrix sheaths surrounding the fibres. The former effect would lead to changes in fibre properties, the latter to changes in composite properties and may account for the increased shear strength and reduced impact strength previously reported.

The HT fibre length appears to shrink more that the HM fibre length; at an exposure of 10^{20} n cm^{-2} almost twice as much. Whereas the UNI-HM and 0^0-90^0-HT composites appear not to shrink at 10^{19} n cm^{-2}, the 0^0-90^0-HM and low modulus cloth composites shrink slightly. This may be due to the lower shear strength of the cross-plied HM and woven cloth composites or increased crystallinity.

Table 1 also shows that the RIP composites shrink slightly less than the CVD composites. There are two possible reasons for this; the first is that the pyrocarbon deposited by the CVD process has been shown to be oriented preferentially with its a-axis parallel to the fibres and may be shrinking in a similar manner. The glassy carbon from the resin is not well oriented. The second reason is that the RIP composites are generally of slightly higher density (1.6 cf 1.5 g cm^{-3}) than the CVD composites and also have higher shear strengths (30 cf 20 MN m^{-2}). Thus they resist the tendency for the fibres to shrink.

Further details of the mechanical properties of the composites after exposure will be given at the Conference.

References

(1) E J Walker, L F Pain and P B Roscoe, 12th Bienn Conf on Carbon, Pittsburgh, 1975- Paper CE-1.

(2) E J Walker, L F Pain and P B Roscoe, 2nd Int Carbon Conf, Baden-Baden, 1976 - Paper P5.2

TABLE 1

Dimensional Changes

Material	Exposure ($n\ cm^{-2}$)	% Change in: Length	Breadth	Depth
UNI-HT-RIP	10^{18}	0	0	0
	10^{19}	-0.11	0	0
	10^{20}	-0.68	0	0
UNI-HT-CVD	10^{18}	-0.10	0	0
	10^{19}	-0.28	0	0
	10^{20}	-0.55	0	0
UNI-HM-RIP	10^{18}	0	0	0
	10^{19}	+0.11	0	0
	10^{20}	-0.27	0	0
UNI-HM-CVD	10^{18}	0	0	0
	10^{19}	-0.12	0	0
	10^{20}	-0.40	0	0
0/90-HT-RIP	10^{18}	0	0	0
	10^{19}	-0.26	0	0
	10^{20}	-0.68	-1.01	0
0/90-HT-CVD	10^{18}	0	0	0
	10^{19}	-0.20	0	0
	10^{20}	-0.79	-0.81	0
0/90-HM-RIP	10^{18}	-0.13	-0.18	0
	10^{19}	-0.14	-0.27	0
	10^{20}	-0.40	-0.54	0
0/90-HM-CVD	10^{18}	-0.17	-0.18	0
	10^{19}	-0.15	-0.18	0
	10^{20}	-0.49	-0.68	0
Low modulus graphite cloth - CVD	10^{18}	-0.14	-	0
	10^{19}	-0.19	-	0
	10^{20}	-0.53	-	0

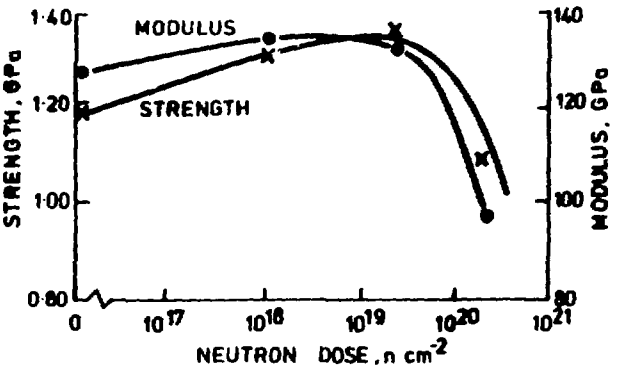


Figure 1 Flexural Strength and Modulus vs. Exposure. UNI-HT-CVD

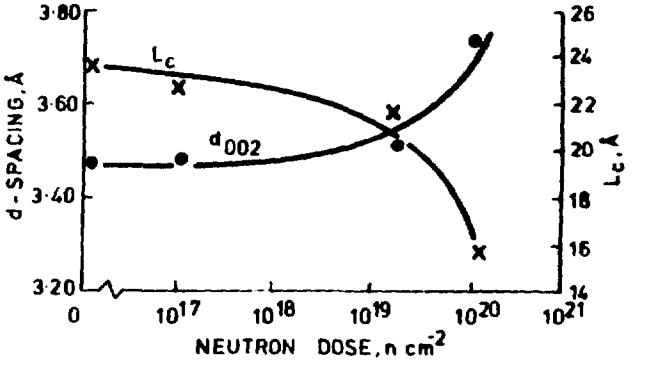


Figure 2 Apparent d-spacing and crystallite size vs. Exposure. UNI-HT-CVD

EFFECTS OF MATRIX AND PROCESS VARIATIONS ON PROPERTIES OF 3-D CARBON-CARBON COMPOSITES

R. W. Seibold
McDonnell Douglas Astronautics Company
Huntington Beach, California 92647

Introduction

Considerable latitude exists for designing carbon-carbon composites with prespecified performance attributes suitable for reentry vehicle components, including nose tips, heat shields, and rocket nozzles. This can be done via selection of fibrous reinforcement properties and construction and by choice of matrix precursor materials and processing conditions. Under this program, three-dimensionally woven graphite yarn preforms were densified to yield carbon-carbon composites, using various matrix precursor materials and processing conditions. Effects of process modifications on process efficiency (density gain per cycle) and volume increase of the composites and on the final bulk density, open porosity, and permeability were assessed.

Experimental and Results

Sixteen carbon-carbon composites (Table 1) were processed from 3-D fibrous preforms woven by Fiber Materials, Inc., from Thornel 50 yarns in an orthogonal 2-2-3 construction (shown in Ref. 1). The dimensions of billets 697 and 676 were approximately 4 x 4 x 8 in., and the other 14 billets were approximately 2 to 16% of this volume. The baseline process was multiple cycles of (1) coal tar pitch impregnation, (2) pyrolysis at 1,000 psig (300 psig for the first three cycles), and (3) graphitization in argon to 2,800°C. The pyrolysis temperature was 675°C for the initial pitch cycle and 1,000°C for all other cycles. The matrix was Allied Chemical CP275-Grade 15V coal tar pitch. The pitch was pre-heat-treated for all impregnation cycles except the initial one, to increase char yield.

Modifications included carbon vapor deposition (CVD) steps, resin densification steps, pyrolysis and graphitization temperature variations, and extra densification (impregnation plus pyrolysis) and graphitization cycles. For CVD, methane at 1,100°C was employed either at the beginning of processing (initial CVD) or following the second pitch densification step (intermediate CVD). For intermediate resin processing, two ENF resin densification steps were conducted after the second pitch densification step, or if an intermediate CVD step was employed in the same billet, two steps after the CVD step. For final resin processing, the final three densification steps were with ENF resin. ENF is 50-50 mixture of Dow Chemical DEN 438 epoxy novolac resin and Quaker Oaks furfuryl resin precursor. The 2,400°C, 2,800°C, or 3,100°C heat treatments in argon were conducted after each densification step except the initial one or the first of two intermediate resin cycles. The time above 2,500°C was 3 and 6 hours for each 2,800°C and 3,100°C cycle, respectively. For graduated increases in pyrolysis temperature, the temperatures for the second and third pitch cycles were 775°C and 875°C, respectively, and the first 2,800°C graphitization cycle followed the fourth pitch densification cycle.

Table 2 summarizes process efficiency, degree of "overprocessing" past maximum composite density, volume increase, and selected physical properties of the 16 materials. The viscous permeability coefficient was determined from measurements of nitrogen flow through the composite in the 3-D weave Z direction. Figure 1 depicts typical in-process property changes for material BB-2. In addition, detailed microstructural examination and mechanical, thermophysical, and ablative testing was done. Some results of these latter evaluations are being reported by J. Jortner at this conference and will be referred to in the discussion.

Discussion

The composites increased in volume during processing, particularly during later process steps when the density was high. The linear growth tended to be larger in the X and Y directions than in the Z direction, a consequence of the unbalance of the 2-2-3 weave. Analyses of the growth mechanisms have been reported in Ref. 1 and by L. B. Greszczuk at the present conference. The magnitude of the growth appears to be dependent on processing details and varied between nearly zero and 13% volume change. The growth can limit or decrease the ultimate density of the composite as the volumetric increase can equal or exceed the mass increase in the last process cycles (Figure 1). Potential devices for limiting growth are intermediate resin processing, high-temperature graphitization, and reduced maximum temperatures for early process cycles.

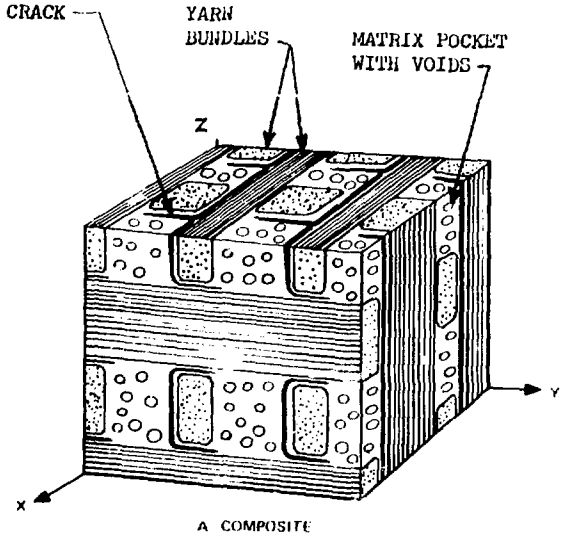
Graphitization to 3,100°C appeared to improve process efficiency. Within the three groups of no CVD, intermediate CVD, and initial CVD, the 3,100°C variations all had relatively high bulk densities, high thermal diffusivities, decreased room-temperature strength, and improved ablation performance. The 2,400°C heat treatment resulted in poor process efficiency and decreased mechanical properties (excepting shear strength). Multiple final graphitization cycles resulted in increased cracking and decreased ablative performance.

Intermediate resin cycles produced increased process efficiency, decreased apparent density, decreased macropore size, and improved off-axis strength. Microscopy revealed that the resin tends to produce a carbon matrix that occupies the interior area of weave pockets or large pores rather than coat the outer edges (as pitch processed at 1,000 psig does), thus increasing the composite internal surface area available for further pitch deposition and resulting in

This work was sponsored by the Naval Surface Weapons Center, Silver Spring, Maryland, under Contract N60921-74-C-0241.

Closure of the cracks upon heating the composite may therefore be expected to drastically reduce the permeability at temperatures near the graphitization temperature. Development of methods to measure permeability at elevated temperatures should be encouraged as some applications of 3D carbon-carbons (e.g. rocket nozzle liners and reentry-vehicle nosetips) involve exposure to hot high-pressure gas.

The data presented suggest there may be a basis for estimating the permeability of similar composites from porosimetry and/or microscopy, when permeability data is lacking. It should be noted that all the composites studied here were of the same weave and yarn; other weaves may give quantitatively different trends, although the same qualitative relationships are expected.



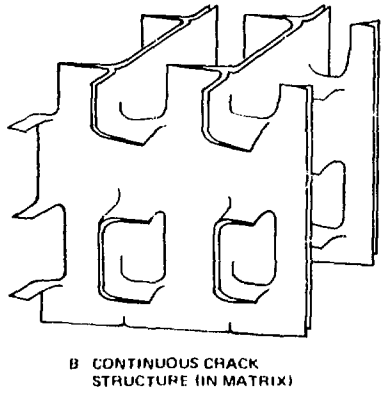


Figure 1. Microstructural Features.

References

1) McAllister L.E. and Taverna A.R., 10th Biennial Conf. on Carbon, Summary of Papers, p66(1971)
2) Stover E.R. and Latva J.D., 11th Biennial Conf. on Carbon, Extended Abstracts, p277(1973)
3) Seibold R.W., at this Conference(1977)
4) Jortner J., Proc. Army Symposium on Solid Mech., pp 81-97, AMMRC MS 76-2 (Sep 1976)
5) Greszczuk L.B., at this Conference(1977)
6) Perry J.L. and Adams D.F., Carbon 14, 61 (1976)
7) Jortner J., paper to 29th Pacific Regional Mtg Am. Ceram. Soc., San Francisco (Nov 1976)
8) Green L. Jr, and Duwez P., J. Appl. Mech., pp 39-45 (Mar 1951)

Acknowledgement

The sponsorship of the U. S. Naval Surface Weapons Center, Silver Spring, Maryland is gratefully acknowledged.

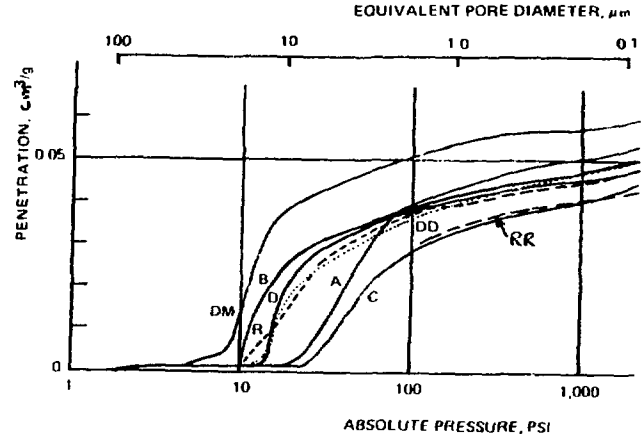


Figure 2. Representative Porosimetry Data.

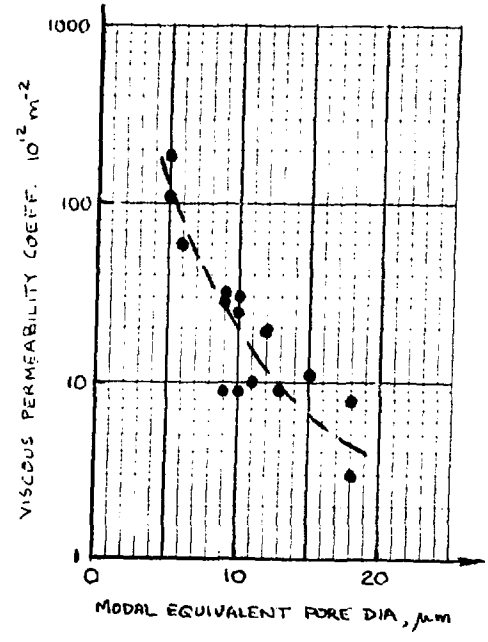


Figure 3. Trend of Data.

MICROSTRUCTURAL FEATURES WHICH INFLUENCE THE ABLATION PERFORMANCE OF CARBON-CARBON COMPOSITES†

D.A. Eitman
Science Applications, Inc.
Santa Ana, California

Introduction

The response of graphitic materials to high temperature thermochemical erosion may be approached by considering the interaction of microconstituents to the environment. These microconstituents in the carbon-carbon materials examined may be generally grouped into reinforcement type, matrix form immediately adjacent to the reinforcement, matrix form in areas without reinforcement and the pore structure of the material. This paper presents key observations made on a wide variety of carbon-carbon composite post-test ablation models as a precursor to modeling efforts. By using this type of information in the modeling effort rather than a more empirical approach, the sensitivity of performance to microstructure may be examined analytically. Results may then be used to indicate directions for microstructural improvement through alternate construction and processing options.

The approach in using microstructural information for modeling thermochemical ablation response has already been demonstrated for bulk graphites [1, 2]. In these works, several different bulk graphites were characterized and relationships were found between pore structure and surface roughness which could be applied in improving thermochemical performance. Preliminary application of this approach has also been attempted with limited success—for advanced carbon-carbon materials [3, 4]. However, the greater heterogeneity of carbon-carbon composites (as compared to bulk graphites) requires an extension of the existing approach.

Experimental Approach

In order to insure that the microstructure of the material examined was representative of that subjected to a controlled thermochemical environment, samples for observation were excised from a tested ablation model. A typical schematic of the sectioning plan for a tested ablation model is shown in Figure 1. Photomicrographs, typical of those

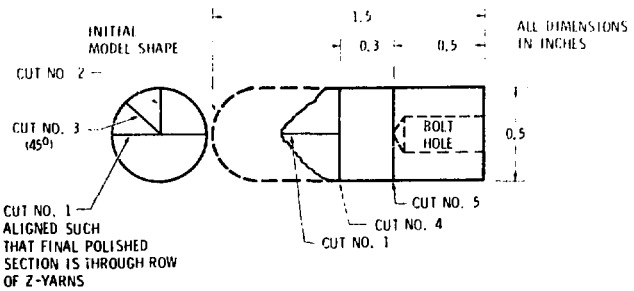


Figure 1. Ablation Model Cutting Plan

shown in Figures 2 and 3 were taken at various magnifications. The lower magnification photomicrographs were used for measuring the large features of the composite such as yarn spacing and large pore diameters. At higher magnifications, the interaction of the microconstituents of the composite with the thermochemical environment may be observed. In addition, by using polarized light microscopy (Figure 3), it was possible to determine the relative crystallographic orientation of the reinforcement and matrices.



Figure 2. Ablation Model Section — Low Magnification

Additional microstructural features were measured quantitatively by using density as measured by helium displacement. Interconnecting pore size and total porosity were measured using mercury intrusion at pressures to 60,000 psi. Available internal surface area was measured using standard gas adsorption methods [5]. Finally, the availability of this internal surface area was measured using a gas permeability test.

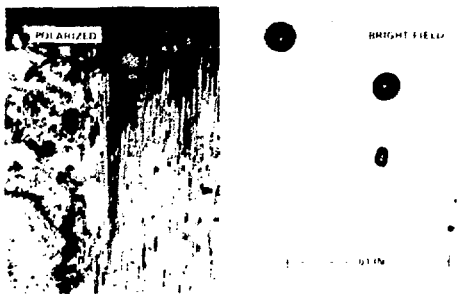


Figure 3. Section of a Yarn Normal to Ablating Surface

From these tests a description of the total pore structure, shown in Figure 4, was obtained. This information can now be related to composite fabrication details for establishing relationships between processing and microstructure and, for exploring relationships between thermochemical erosion mechanisms and material microstructural features.

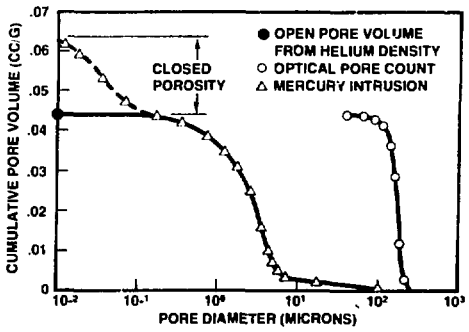


Figure 4. Pore Charaterization of a 3D Carbon-Carbon

†This work was performed under the sponsorship of the Air Force Materials Laboratory, Contract F33615-76-C-5153.

increased pitch pickup. Initial CVD processing resulted in decreased bulk and apparent composite densities, increased closed porosity in the yarn bundles, decreased composite stiffness, and higher ablative recession rates. Intermediate CVD processing had only marginal effect on the composite properties.

Most of the comparative density and porosity improvement of material 676 relative to material D occurred near the end of processing, possibly indicating an improved ability of liquid pitch to remain in larger composites during the late carbonization cycles when the paths for penetration are narrow. The baseline low-pressure pitch process provides reasonably high process efficiencies until the composite porosity is reduced to approximately 15%. Thereafter, either increased process pressures (e.g., 15,000 psig) or modifications such as intermediate resin cycles are needed to achieve high efficiencies.

Acknowledgements

The contributions of C. R. Rowe of the Naval Surface Weapons Center and D. A. Eitman and J. Jortner are acknowledged.

Reference

1. Jortner, J. Cracking in 3D Carbon-Carbon Composites During Processing and Effects on Performance. Army Symposium on Solid Mechanics, Cape Cod, Mass, 14-16 Sept 1976.

Table 1

Code	Process Variations	ND†	NG†
697*	Baseline Pitch, Large Block	13	12
676	Baseline Pitch, Large Block	15	14
D	Baseline Pitch, Small Block	15	14
A	Graduated Increases in Pyrolysis Temperature	18	14
DD	Three Added Cycles (Relative to D)	18	17
R	Intermediate Resin Impregnation	16	14
RR	Intermediate and Final Resin Impregnation	13	11
B	Low-Temperature Heat Treatment (2,400°C)	18	17
C	High-Temperature Graphitization (3,100°C)	16	15
DM	Three Graphitization Cycles at Completion of Processing	15	16
BB-1	Intermediate CVD	16	15
BB-2	Intermediate CVD and Intermediate Resin	16	14
BB-3	Intermediate CVD and High-Temp Graph (3,100°C)	15	14
BC-1	Initial CVD	14	14
BC-2	Initial CVD and Intermediate Resin	14	13
BC-3	Initial CVD and High-Temp Graphitization (3,100°C)	13	13

†ND - Total number of densifications. NG - total number of graphitizations.
*Billet 697 was processed separately from the other materials during early process cycles.

Table 2

Code	Densifications to 1.87 g/cm³ Bulk Density	Densifications/ Graphitizations Past Maximum Density	Volume Increase %†	Block Data‡ ρ_B g/cm³	Block Data‡ ρ_A g/cm³	Block Data‡ P %	Specimen Data‡ ρ_B g/cm³	Specimen Data‡ ρ_A g/cm³	Specimen Data‡ P %	Viscous Permeability Coefficient 10^{10} in⁻²
697	10	0/0	4	1.92	2.07	7.5	-	-	-	0.7
676	12	0/0	8	1.94	2.09	7.3	-	-	-	-
D	13	0/0	3-9	1.91	2.10	8.9	1.91	2.12	10.0	1.6
A	14	2/2	2	1.90	2.07	8.4	1.90	2.11	10.1	3.8
DD	13	2/2	13	1.92	2.08	8.2	1.91	2.12	10.0	0.7
R	11	0/0	2-7	1.91	2.07	8.2	1.91	2.10	9.3	1.2
RR	11	0/0	0-3	1.90	2.06	7.4	1.91	2.08	8.3	7.1
B	15	2/2	7	1.88	2.06	8.7	1.87	2.10	11.0	0.7
C	10	0/0	4	1.94	2.09	7.3	1.94	2.12	8.6	11.2
DM	13	0/2	10	1.88	2.11	11.2	1.88	2.12	11.5	0.2
BB-1	13	2/2	5	1.88	2.06	8.9	1.89	2.11	10.1	2.0
BB-2	11	1 or 2/1 or 2	4	1.90	2.05	7.3	1.91	2.06	7.3	0.6
BB-3	10	0/0	8	1.92	2.07	7.6	1.93	2.11	8.5	2.0
BC-1	-	2/2	6	1.83	2.04	10.0	1.83	2.05	11.7	0.5
BC-2	11	2/2	N. D.	1.87	2.02	7.3	1.88	2.07	9.2	0.6
BC-3	10	2/2	N. D.	1.87	2.06	8.1	1.89	2.08	10.1	0.6

† Approximate volume increase from before first graphitization to end of processing.
‡ ρ_B - Bulk density. ρ_A - Apparent density (ASTM C-20 water immersion for blocks; helium pycnometry for specimens). P - open porosity calculated from bulk and apparent densities.

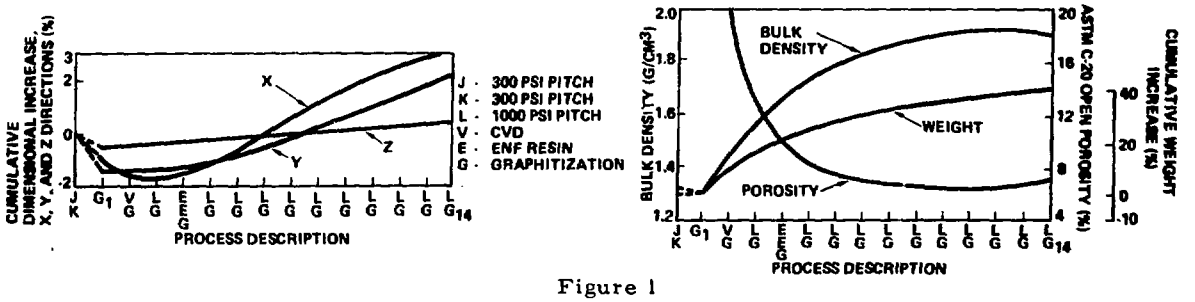


Figure 1

PERMEABILITY, POROSIMETRY, AND MICROSTRUCTURE OF 3D CARBON-CARBON COMPOSITES

Julius Jortner
McDonnell Douglas Astronautics Company
Huntington Beach, California 92647

Making low-porosity carbon-carbon composites, reinforced with graphite fibers in three orthogonal directions (3D weave), includes repeated impregnations (with pitch, resin and/or CVD), pyrolyses, and graphitizations [1][2][3]. The microstructure of composites containing Thornel-50 yarns, graphitized to about 2700°C, includes cracks between yarn bundles forming a continuous network, shown schematically in Figure 1 [4]. These cracks are believed to result from thermal stresses induced by the anisotropic contractions of yarn bundles during cooling from the peak graphitization temperature [4]. The width of the cracks is a partial measure of the creep extension of the yarn bundles during heating to the peak graphitization temperature. This view of microcrack formation is supported by high yarn-bundle stresses estimated to occur during the graphitization cycle [5], and by photomicrographs of 3D composites before and after graphitization [6].

A consequence of the postulated mechanism of crack formation is the closure of the cracks upon reheating the composite. Observations of samples heated to 1600°C in a scanning electron microscope corroborate this prediction and show reheating such composites to the graphitization temperature can reduce porosity to less than half the value measured at room temperature [7]. That is, the cracks at room temperature account for more than half the void volume of low-porosity composites.

Consideration of the crack network, as it appears at room temperature, suggests:

a) the cracks are the major path contributing to permeability of these materials to fluids,
b) the cracks are the main passages by which mercury penetrates the pores of the composite in porosimetry tests, and
c) a relation should therefore exist between gas permeability and the equivalent pore entrance size inferred from mercury porosimetry.

Experiments

The composites described by Seibold [3], and one other, were studied. Variations in the densification and graphitization process details produced samples exhibiting a range of permeability and porosimetry data (Table 1).

Permeability was measured at room temperature by passing nitrogen through disks 0.8 cm thick. The disk axis was parallel to one set of yarns. Pressures up to 20 atmospheres were applied to one face of the disk in a gasketed fixture while the other face was maintained at one atm. Both the viscous and inertial permeability coefficients (α and β, respectively) were estimated by fitting to the data the equation of Green and Duwez [8]:

$$\frac{p_i^2 - p_o^2}{(2\mu RTL)\dot{m}} = \alpha + \beta\left(\frac{\dot{m}}{\mu}\right)$$

where R, μ, T are the gas constant, viscosity, and temperature, L is the disk thickness, $\dot{m}$ is the mass flow of gas, and p_i and p_o are the inlet and outlet gas pressures.

Mercury intrusion tests were conducted by standard means. Some of the results are shown in Figure 2. The point of steepest rise in the curve of penetration vs. pressure was taken as the measure of the most representative pore-entrance size. This modal value of the equivalent pore diameter ranged between 5 and 20 microns. The typical crack widths observed on photomicrographs are also in this range.

Figure 3 shows the empirical trend between permeability (as represented inversely by the viscous coefficient) and modal equivalent pore size. It may be noted that attempts to relate permeability to bulk density, open porosity, or internal surface area (by BET) did not show as good a trend.

Table 1

Material *	Viscous Permeability Coefficient 10^{12} per m^2	Inertial Permeability Coefficient 10^9 per m	Modal Equivalent Pore Dia. μm
D	24	1.0	10
A	59	1.9	6
DD	10	0.05	11
R	19	0.8	12
RR	110	5.0	5
B	11	0.4	15
C	190	4.4	5
DM	3	0.04	18
BB1	31	1.6	9
BB2	9	0.3	9
BB3	30	1.2	10
BC1	8	0.2	18
BC2	9	0.2	10
BC3	9	0.2	13
GE223*	30	0.5	9

*All materials used Thornel-50 yarn in a "223" weave; spacing of parallel yarn bundles was about 0.8 mm. GE223 (core of Billet 331) was processed with CVD plus five pitch cycles (1000 atm pyrolyses) and 2700°C graphitizations. Other materials had pyrolyses at 68 atm; for their descriptions see Seibold [3].

Conclusions

The reasonably good correlation of Figure 3, between permeability and porosimetry data, and the similarity of microscopically-observed crack widths to the modal pore sizes inferred from porosimetry, offer indirect support to two commonsense notions:

a) the observed crack network is the major pathway for both viscous gas flow and capillary liquid penetration into 3D carbon-carbon composites
b) the permeability of the composite will depend to a large extent on the width of the cracks.

Carbon-Carbon Composite Variables

Eleven different carbon-carbon composite types are being characterized on this program. The reinforcement types used in the various composites include Thornel 50, HMS Pan, Thornel 300 and Union Carbide's pitch precursor yarn. Constructions using 3D orthogonal geometry and fine weave pierced fabric geometries are being evaluated. Weave spacing variations in the class of 3D orthogonal materials are also being evaluated.

Most of the materials have been subjected to processing with coal tar pitch at 15,000 psi. A major variable in processing, however, is whether or not CVD was used prior to the 15,000 psi densification. Several composites utilizing lower pressures and/or combinations of both low and high pressure processing are also included. Table I is a list showing the variables involved for all composites being characterized on the program.

TABLE 1 COMPOSITE VARIABLES

REINFORCEMENT TYPE	MATRIX PRECURSORS	PROCESSING VARIABLES PRESSURE	MATRIX COMBINATIONS
THORNEL 50	COAL TAR PITCH	– 1000 PSI	EPOXY PHENOLIC + PITCH
THORNEL 300	PETROLEUM PITCH	– 5000 PSI	CVD + PITCH
HMS 1000-3000	EPOXY PHENOLIC	– 10000 PSI	LOW + HIGH PRESSURE
VSA (PITCH)	CVD CARBON	– 15000 PSI	

Discussion

In considering the effect of microstructure on the thermochemical ablation performance of carbon-carbon composites, it is convenient to divide the material into two zones. The first zone concerns the surface of the material at the material-thermochemical environment interface. The second zone is that material immediately beneath the surface which, if available to enter into the reaction, is preconditioned and will, at some later time affect the interface between the material and the environment.

The relative rates of thermochemical erosion of the composite constituents at the specimen surface can be readily observed on photomicrographs. These constituents consist of the yarns normal surface (or nearly so), yarns transverse to the surface and pockets in the reinforcement structure filled with matrix material. Differential rates of erosion of the constituents lead to a roughened surface which interacts with the ablation environment and results in enhanced heat transfer.

In some environments, the boundary layer is relatively insensitive to the behavior of the large, isolated discontinuities and is primarily dependent on the roughness developed within the individual constituents to provide numerous roughness elements. The most significant consideration in this regard is the axial yarn bundles which have differential erosion rates between the filaments oriented normal to the surface of the specimen and the matrix material between these filaments. The type, orientation and density of this matrix material affects its performance. In addition, differential thermal expansion between the filament and the matrices may lead to an open interface which is readily attacked. Roughness developing in this manner can then induce turbulent flow and thus enhance heat transfer rates.

The response of a graphitic material in-depth is dependent on the internal surface available for reacting with the thermochemical environment. This is controlled by both the permeability of the material and the surface associated with the pore structure. Also, the primary thermochemical erosion mechanism (i.e. either sublimation or oxidation/reduction reactions) are important. If an extensive amount of internal surface is available then a significant portion of the mass loss of the material may be from below the surface. This material is then preconditioned and may affect the total mass loss in two ways. First, existing discontinuities in the material may become enlarged and, when they reach the surface, will result in higher surface roughness. This higher roughness, in turn, interacts with the environment to produce higher heat transfer rates and therefore higher total mass loss for the same external conditions. The other effect, which is more important in bulk graphites than in carbon-carbon composites, is that the internal material may be pre-weakened and upon reaching the surface, may fail mechanically. A photomicrograph showing fairly extensive in-depth erosion is presented in Figure 5.

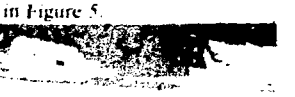




Figure 5. In-Depth Material Erosion at an Ablating Surface

By having the sensitivity of permeability and surface area defined by a model which quantitatively predicts performance in a given environment, it is then possible to make material improvements through process alterations and subsequent microstructure alterations thus tailoring the material for a special environment.

Summary

Microstructural characterization is being conducted on a number of carbon-carbon composites to provide information for use in quantitative models to predict performance in a thermochemical ablation environment. Heat transfer considerations as influenced by the roughness of the material in the environment may be used by including measured geometric discontinuities as determined using photomicrographs. The role of reactions occurring below the surface may also be considered by including measured permeability and specific internal surface area in the modeling effort. The developed model can then be used to show the sensitivity of various microstructural elements to performance and direction may be given for fabrication changes leading to materials with enhanced performance.

References

1. Kratsch, K.M., Meyer, P.A. and Dirling, Jr., R.B., "Erosion Mechanisms and Improvement of Graphite Materials, Vol. I, Graphite Selection and Characterization", AFML-TR-70-307, Vol. I, January 1971.

2. Kratsch, K.M., Dirling, Jr., R.B. and Swain, C.E., "Erosion Mechanisms and Improvement of Graphite Materials, Vol. IV, Summary", AFML-TR-70-307, Vol. IV, May 1973.

3. Dirling, Jr., R.B., "Exploratory Development for Ablation Modeling of Advanced Carbon-Carbon Composites", Fourth Quarterly Report, McDonnell Douglas Astronautics Company Report MDC G 4B12, September 1973.

4. Dirling, Jr., R.B., et.al., "Ablation/Erosion Evaluation of Reentry Vehicle Materials, Vol. I, Nosetip Materials", AFML-TR-76-21, Vol. I, February 1976.

5. Brunauer, S., Emmett, P.H. and Teller, E., "BET Method", J. Amer. Chem. Soc., 60, 309, 1938.

INFLUENCE OF CARBON POLYMORPHS ON ABLATION OF GRAPHITIC MATERIALS*

A. G. Whittaker and J. S. Evangelides
The Ivan A. Getting Laboratories
The Aerospace Corporation
El Segundo, California

Three nose tip models that were tested in the Air Force Flight Dynamics Laboratory 50 MW ablation test facility were studied with respect to their microstructure and for evidence of transformation of graphitic carbon to linear carbon forms. Two were 994 graphite and one was a GE 223 multidirectional carbon-carbon composite.

The sectioned nose tips were metallographically polished and ion-etched with xenon specifically for examination in the scanning electron microscope. A low-magnification overview of the cross-sectioned nose tip indicates that microstructural changes occurred near the ablated surface. The light areas in the micrographs indicate higher secondary electron emission and the presence of linear carbon polymorphs. These light areas occurred not only in bands across the top (ablated surface) of the specimen but also in depth. Higher magnification clearly shows the significant microstructural differences that existed for material 200 to 300 μm below the top surface. There is an absence of large pores and an indication of columnar structure, but this region still had the etched structure indicative of graphite basal alignment. Affected material occurring in bands to a depth of 500 μm had microstructural characteristics similar to that occurring at the surface.

The different carbon forms (e.g., graphite, diamond, lonsdaleite, and chaoite) have characteristic carbon negative ion spectra, as observed in the Ion Microprobe Mass Analyzer (IMMA), and the signal intensity ratio for C_2^-/C_6^- is the most diagnostic feature for the carbon forms [1]. The symbol C_x^- refers to a molecule for x carbon atoms with a single negative charge. The absolute C_6^- intensity for all the linear forms is at least three orders of magnitude greater than the C_6^- signal from graphite or graphite material. By means of the C_2^- and C_6^- signals, profiles can be obtained that show the distribution of the linear forms. Complete negative ion spectra can be obtained at particular points to obtain a rough measure of the extent of transformation, and in some cases, to identify the linear carbon form.

A general IMMA search over the nose tip sections revealed that some of the graphitic material transformed to the linear carbon forms and were in a thin layer at the top. Profiles of C_2^- and C_6^-, starting at the surface and extending axially down the section, indicate that the layer of extensive transformation was approximately 300 μm thick and that the concentration of the linear forms died away very rapidly beyond this depth, except for isolated regions at depths of about 400 to 500 μm. These profiles correspond to the micrographic result of banded microstructural regions. Complete negative ion spectra taken at selected points along the profile confirmed the results indicated by the C_2^-/C_6^- ratio. The profiles obtained on the 994 graphite and the GE carbon-carbon composite were essentially indistinguishable with regard to both distribution and identity of polymorphs. Also, the carbon-carbon composite fiber orientation had no effect on the transformation, and the matrix behaved the same way as the fibers.

A very limited electron diffraction study of samples taken from the nose tip showed that carbon XII was formed at the ablating surface, carbon VII and XI formed in the first 50-μm thick layer, and chaoite was formed ~200 μm below the surface. However, the nose tip was not quench-cooled; therefore, these may not be the carbon forms that existed while the nose tip was under test conditions.

Studies on the effect of quench-cooling carbon that was heated to ~3800 K by laser heating on carbon showed that, when a sample was allowed to cool by just turning off the laser, there existed a layer of linear polymorphs about 280 to 300-μm thick, similar to that found on the nose-tip sections. The average cooling rate involved here was ~2000°C/sec. If the sample was quenched (cooling rate ~30,000°C/sec), the linear forms were found to a depth of about 2400 μm, and there was evidence that the transformation was more extensive when the sample was at 3800 K. Since the nose tips showed normal behavior with regard to linear polymorph formation, there is good reason to believe that perhaps 1.5 to 2.4 mm of the nose tip could be transformed under reentry conditions. The exact amount would, of course, depend on the temperature gradient in the nose tip.

There is some evidence that the rate of transformation is not the same for all forms of graphitic carbon. In a two-phase carbon, the filler appears to transform faster than the binder. Consequently, an analysis of the final slow-cooled nose tip gives very little insight into the course of events that occur in the carbon during the heating and cooling phases during reentry.

Reference

1. Stuckey, W. K. and Whittaker, A. G., "Identification of Carbon Allotropes by Ion Microprobe Mass Analysis," TP176, 10th Biennial Conference on Carbon, LeHigh University, 27 June - 2 July 1971.

* This work was supported by the U.S. Air Force under Contract No. F04701-76-C-0077.

ABLATIVE RECESSION OF 3D CARBON-CARBON COMPOSITES

J. Jortner, F. I. Clayton, R. W. Seibold
McDonnell Douglas Astronautics Company
Huntington Beach, California 92647

R. R. Williams
McDonnell Douglas Research Laboratories
St. Louis, Missouri 63166

C. R. Rowe
Naval Surface Weapons Center
Silver Spring, Maryland 20910

The excellent resistance of graphite to ablative recession in hypersonic environments has long been recognized [1][2]. Carbon-carbon composites appear to provide similar ablative performance with better resistance to brittle fracture [3][4]. This paper describes an experimental study of ablation in turbulent flow of several 3D carbon-carbons all made with the same reinforcement but differing in process details.

Experiments

Materials tested included ATJS graphite and fifteen carbon-carbons all based on the same "223" 3D weave. Fourteen of the composites, densified with pitch, resin, and/or CVD at maximum pyrolysis pressure of 68 atmospheres, have been described by Seibold [5]. One other composite tested (GE223) had been processed with CVD plus five cycles of pitch densification involving pyrolyses at 1000 atmospheres and graphitizations at 2700°C.

Ablation tests were conducted in the MDC-200 plasma-arc heater[6] at MDRL's HIP facility, St. Louis. This Huels-type arc heater uses two hollow cylindrical electrodes. Filtered air, injected tangentially between electrodes, is heated by the arc, flows through the front electrode, and exits via a water-cooled nozzle of 0.375-inch throat diameter, 0.45-inch exit diameter, and an exit Mach number of 1.7. A special cooling technique reduces electrode erosion [7]; no particle impact was observed on any of the models.

The models were 57°-half-angle cones with 0.3-inch diameter afterbodies (Figure 1). The tip was 0.05 inch from the nozzle exit plane and was kept at that fixed position in the stream by a laser-activated recession compensator system [8]. The arc heater was adjusted to give a stagnation pressure of 100 atm at the model. Each model was kept in the stream until 0.25-inch recession occurred. Based on movie films, the cone half-angle stayed fairly constant (between 53° and 67°) during the tests. Model surface temperatures, measured using Thermogage pyrometers (0.9 μm wavelength) aimed about midway between the centerline and the cone circumference, ranged between 3200°C and 4000°C. Typical data is shown in Figure 2.

Run-to-run variations were observed in the bulk enthalpy of the plasma-heated air (between 2200 and 2400 Btu/lb). To place the data on a common basis, recession rate was assumed proportional to the centerline enthalpy of the air stream. As in [2], the centerline enthalpy was estimated higher than the bulk enthalpy by a factor sufficient to account for the discrepancy observed between heat flux measured with calorimeters during facility calibrations and the theoretical heat flux predicted for uniform enthalpy using the theory of Fay and Riddell [9].

Table of Data

Material	HIP Run No.	Bulk Density g/cm³	Measured Recession in/sec	Normalized Recession in/sec
D	1027	1.91	0.177	0.177
A	1027	1.90	0.179	0.179
DD	1027	1.91	0.167	0.167
R	1027	1.91	0.176	0.176
RR	1028	1.91	0.151	0.151
B	1028	1.87	0.208	0.208
C	1028	1.94	0.153	0.153
DM	1029	1.88	0.246	0.214
BB1	1027	1.88*	0.176	0.176
BB2	1028	1.91*	0.243	0.243
	1029	1.91	0.197	0.171
BB3	1029	1.93*	0.183	0.160
	1028	1.93	0.175	0.175
BC1	1027	1.83*	0.250	0.250
BC2	1028	1.85*	0.215	0.215
	1029	1.88	0.213	0.185
BC3	1029	1.89*	0.206	0.180
	1029	1.89	0.207	0.180
GE223	1027	1.90	0.145	0.145
	1028	1.90	0.141	0.141
ATJS	1025	1.83	0.160	0.150
	1026	1.83	0.167	0.156

1) 7 models per run, all at 100 atm stagnation press.
2) Bulk enthalpies (Btu/lb) were 2200 for runs 1027 and 1028, 2300 for runs 1025 and 1026, and 2400 for run 1029.
3) Bulk density is for representative billets of each material, except * denotes density of ablation model.

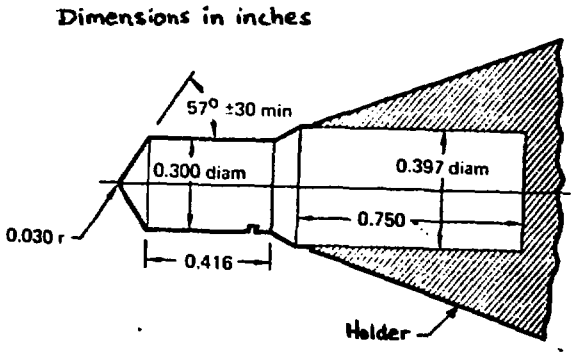


Figure 1. Ablation Test Model

Discussion

Normalized recession rates are shown vs bulk density in Figure 3; where two models of a material were tested, the average is plotted. Two lines are drawn: the solid line is the trend for thirteen of the composites; the dashed line is the expected variation of recession rate with density, assuming mass loss rate is constant for the given environment. The discrepancy between the two trends may result from differences in the heat transfer rate to each model, or from non-thermochemical effects such as mechanical erosion.

Heat transfer augmentation in turbulent flow depends on surface roughness [10]. While the relationship of roughness to microstructure and processing in carbon-carbons is incompletely understood, intuition and available evidence suggest pore size to be of major influence [11]. Matrix pockets of 3D composites densified with pitch at low pressure (68 atm) usually contain one relatively-large pore. The pore size, and therefore the roughness, may be expected to vary with the attained bulk density [12]. For composites densified with pitch at 1000 atm, the matrix pockets contain a dispersion of small pores, similar to the porosity observed in ATJS. In such materials, increases in density might affect the number of pores without necessarily reducing the maximum pore size. Thus the GE223, the ATJS graphite, and the most dense of the low-pressure-processed materials, all lie close to the same dashed trend line in Figure 3. The only other low-pressure-processed material to lie near that line is "RR" which also has small pores by virtue of the impregnations with resin [5].

Conclusions

Plasma-arc testing of 3D carbon-carbons shows recession rate in turbulent ablation to be a strong function of bulk density for materials processed with pitch at low pyrolysis pressures. This suggests that surface roughness developed during ablation is strongly affected by density in such materials. The dependence of roughness on density can probably be reduced by the use of high (1000 atm) pyrolysis pressures, or by the use of thermosetting resin as an impregnant.

Quantitative characterization of the microstructure and the roughness of the models tested would be necessary to substantiate these inferences. The role of aeromechanical erosion should be also investigated as an alternate (or supplementary) hypothesis.

Acknowledgements

The work described was sponsored by the U. S. Naval Surface Weapons Center, Silver Spring, Maryland. The contributions of D. A. Eitman (selection and process development of the low-pressure-processed composites) and J. W. Stultz (ablation testing) are gratefully acknowledged.

References

1) Bishop W.M. and DiCristina V., AIAA J, 6 (Jan 1968)
2) Kratsch K.M., Martinez M.R., Clayton F.I., Greene R.B. and Wuerer J.E., AIAA paper 68-1153 (1968)
3) Kratsch K.M., Schutzler J.C. and Eitman D.A., AIAA paper 72-365 (1972)
4) Schmidt D.L., SAMPE J, pp 9-19 (May/June 1972)
5) Seibold R.W., at this conference (1977)
6) Painter J.H. and Ehmsen R.J., AIAA paper 71-259 (March 1971)
7) Painter J.H., AIAA paper 75-705 (May 1975)
8) Williamson R.A.,Rinehart W.A. and Williams R.R., AIAA paper 73-380 (March 1973)
9) Fay J.A. and Riddell F.R., J Aerosci, 25 (Feb 1958)
10) Dirling R.B.Jr, AIAA paper 73-763 (July 1973)
11) Jortner J. and Clayton F.I., McDonnell Douglas Report MDC G6390 (April 1976)
12) Jortner J., at this conference (1977)

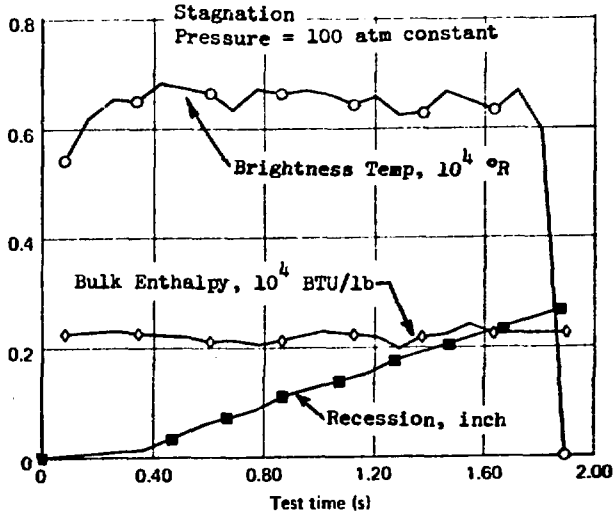


Figure 2. Typical test data

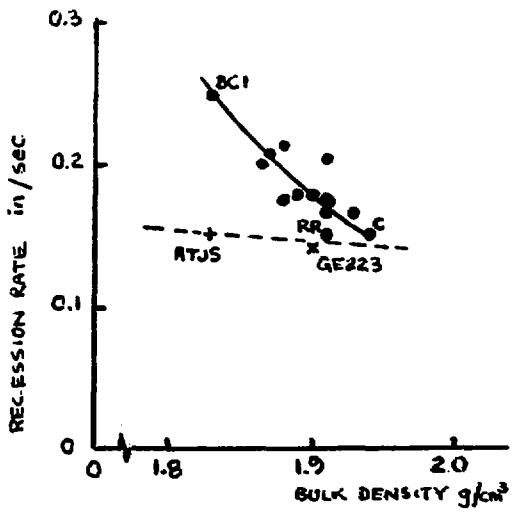


Figure 3. Data Trends

A KINETIC STUDY OF THE TRANSFORMATION GRAPHITE ⇌ LINEAR CARBON FORMS BY X-RAY DIFFRACTION*

A. G. Whittaker
The Ivan A. Getting Laboratories
The Aerospace Corporation
El Segundo, California

This paper is a progress report on one of the aspects of the continuing research at Aerospace on the carbon phase diagram and the linear carbon forms. Our work and the results of other investigators suggest that the carbon phase diagram has the general form shown in Figure 1. This figure is intended to be more illustrative than quantitative since certain features have been exaggerated to make them easier to discuss. The dashed line designated JANAF represents the vapor pressure graphite would have if it were the stable form up to the melting point. Because the linear forms are the stable forms, their vapor pressure lies below the JANAF curve everywhere. Since the difference between the vapor pressure of the linear forms and the JANAF curve is small, it is one of the features that has been exaggerated.

The research reported here concerns the transformations graphite ⇌ linear form No. 1 and linear form No. 1 ⇌ linear form No. 2 along the solid-vapor boundary. The graphite ⇌ linear form No. 1 transformation occurs near 2600 K, linear form No. 1 ⇌ linear form No. 2 occurs near 2800 K, and the third transformation occurs at ~3050 K. It has been known for several years that a number of observations suggested that the transformation rates for rising temperature are much lower than the rates of the reverse transformations. Recently, it was found that these transformations could be followed by x-ray diffraction; this made it possible to acquire quantitative data on the rate constants.

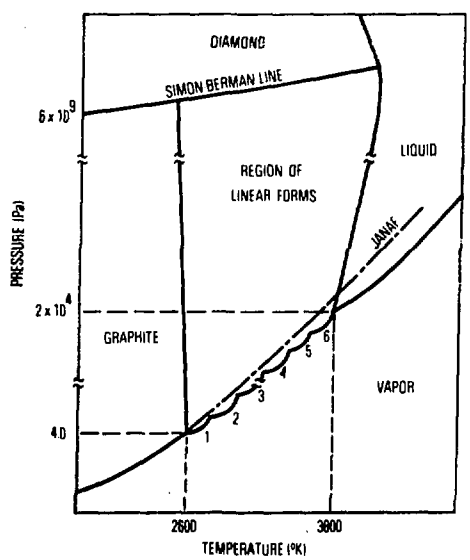


Figure 1. Carbon Phase Diagram

The apparatus used for this work was a General Electric XRD-5 diffractometer equipped with a fixture for heating pyrolytic graphite (PG) samples resistively in an argon atmosphere so that the x-ray reflection could be measured while the sample was hot. The PG was oriented such that the x-ray reflection was from the basal plane edges. Intensity of the reflection from the (010) planes was followed as a function of time for several hours. At the end of this period, the diffractometer was set to the graphite (002) reflection and then the heating current was turned off. No (002) reflection was detectable at the end of the heating period. However, several minutes after turning off the heating current, the (002) reflection started to increase as the linear forms transformed back to graphite. As a first approximation, it was assumed that the rate of intensity decrease of the (010) reflection was proportional to the rate of transformation of graphite to linear form and that the transformation was a first-order reaction. Rate constants calculated on this basis are given in Table 1. The linear form to graphite transformation gave a typical first-order decay curve and it was analyzed by the established methods for such cases. Although the accuracy of these data in Table 1 are probably good only to order of magnitude, they quantitatively confirm the previous qualitative observations on relative transformation rates.

Identification of the linear forms is not complete but is expected to be ready for the July presentation. Also, as more experiments are carried out, the transition temperatures will be more accurately located.

Table 1. Rate Constants for Carbon Transformations

Transformation	Temperature (°K)	Rate Constant (1/sec)
Graphite/linear form No. 1	2680	2.2×10^{-5}
Graphite/linear form No. 2	2840	5.1×10^{-5}
Linear form No. 2/graphite	~300	2.6×10^{-2}
Linear form No. 1/graphite	~300	1.9×10^{-3}

*This work was supported by the U.S. Air Force under Contract No. F04701-76-C-0077.

THE EFFECT OF MICROPOROSITY ON GRAPHITIZABILITY OF GLASSY CARBON

By J. L. Kaae, General Atomic Company, San Diego, Calif.

Introduction

The glassy carbons obtained by pyrolysis of thermosetting resins are well known for their resistance to crystallite growth during high-temperature exposure. Phase-contrast observations with transmission electron microscopy have shown that these carbons are composed of interweaved crystallites in a tangled geometrical arrangement (1). It has been suggested that the resistance to crystallite growth is due to this tangled microstructure (2). That considerable microporosity is present in the glassy-carbon microstructure is obvious from the relatively low density of this material. The role which the microporosity plays in the resistance to crystallite growth is the subject of this paper.

It is known from studies of isotropic pyrolytic carbons with microstructures similar to those of glassy carbons that high-temperature fast-neutron irradiation causes considerable densification of the tangled microstructure, obviously resulting in removal of much of the microporosity (3). The mechanism of this densification is thought to result from the expansion of individual carbon crystallites perpendicular to the layer planes and the shrinkage of the crystallites parallel to the layer planes. Thus, high-temperature irradiation of a glassy carbon should produce the tangled microstructure with greatly reduced microporosity and annealing of irradiated and unirradiated material should allow a study of the effect of the microporosity on crystallite growth.

Experimental

The carbon investigated was obtained from the Beckwith Carbon Company and was designated 1300 Grade indicating heat treatment to 1800°C. Small pieces of this material were irradiated in a series of capsules used primarily to study the behavior of graphites during irradiation, a program supported by the U.S. Energy Research and Development Administration (Contract E(04-3)-167, Proj. Agrmt. 17). Following irradiation, specimens were heated to either 1200°C, 1900°C or 2200°C and held for one hour at these temperatures in a graphite-resistance furnace.

Measurements of the apparent crystallite size, L_c, were obtained from x-ray diffractometer traces of the (002) reflection using copper Kα radiation. L_c was calculated from the formula: $L_c = 0.89\lambda/\beta \cos\theta$. where λ is the wave length of the radiation, β is the half-heigh peak width, and θ is the Bragg angle.

Specimens were also examined with transmission electron microscopy. To prepare specimens for this examination, they were first mechanically polished to a thickness of about 50μm and then were thinned by sputtering with 6 Kev argon ions until they were sufficiently thin for transmission with 100 Kev electrons.

Results and Conclusions

The variation of density with fast-neutron exposure at 1100°C is shown in Fig. 1. As expected, fast-neutron irradiation did cause densification of the material. The specimen selected for subsequent examination was one exposed to a fast-neutron fluence of 10.3×10^{21} n/cm^2, E>0.18 Mev. As can be seen from the figure, this specimen had a density of 2.04g/cm^3.

The apparent crystallite size calculated from broadening of the (002) x-ray diffraction peak is shown in Fig. 2 as a function of the annealing temperature. Because of the very broad nature of the diffraction peak and because lattice strains also can contribute to broadening, these values should not be taken literally as a crystallite size, but they can be considered as a measure of the crystalline perfection.

Irradiation produced some increase in the apparent crystallite size, but on subsequent annealing there was very little increase up to the maximum temperature employed (2200°C). On the other hand, the unirradiated material showed significant increases in the apparent crystallite size when it was annealed at temperatures above 1900°C. Thus, it seems that removal of the microporosity from glassy carbon produces a material which is more stable on subsequent annealing than the carbon with microporosity.

A transmission electron micrograph of the unirradiated carbon after annealing at 2200°C is shown in Fig. 3. The magnification is not sufficiently high that layer planes can be resolved, but if the magnification was increased, planes could be resolved in each of the small bands in the micrograph. Several of these bands indicated by arrows. Thus, these bands are images of regions within the specimen where curved and/or twisted ribbons or sheets of parallel layer planes are perpendicular to the specimen surface. These microstructural observations are consistent with those made previously on fragmented specimens(1).

A similar micrograph of the irradiated specimen after annealing at 2200°C is shown in Fig. 4. Not surprisingly, it does not appear the same as the unirradiated material. Bands are no longer visible. However, very small diffraction-contrast fringes are now present. Several are marked by arrows. Although slightly smaller, these fringes appear identical to those observed in isotropic pyrolytic carbons where it was shown that the fringes always appeared in regions where the layer planes were perpendicular to the surface of the foil and that the fringes were perpendicular to the layer planes (4,5). Assuming this to be the case in Fig. 4, the orientations of the diffraction-contrast fringes suggest that the tangled microstructure is still present since the fringes frequently fall in a series which apparently defines a band similar to those of the unirradiated material. (See the fringes marked by arrows in Fig. 4.) Also, within small regions fringes are oriented in many different directions. Thus, irradiation apparently did not destroy the tangled microstructure.

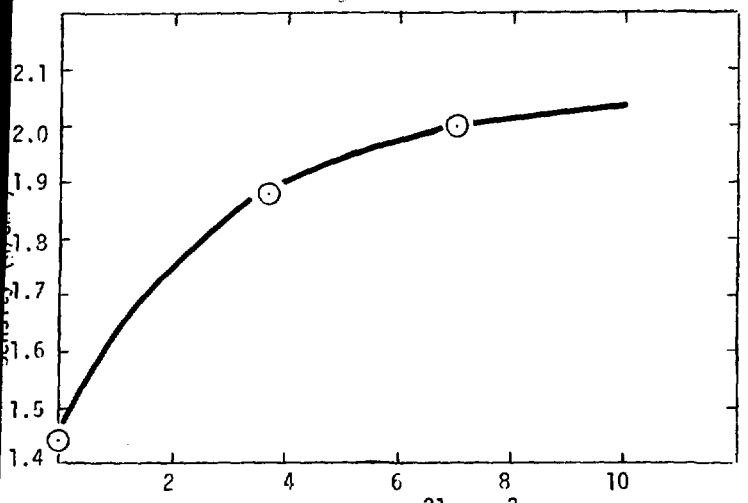
These results indicate that the microporosity in the tangled microstructure of glassy carbon is not the structural feature responsible for its resistance to crystallite growth during annealing. Rather they show that removal of the microporosity enhances the stability of the material. The high resistance to crystallite growth in glassy carbon probably lies in the tangled nature of the microstructure. Since increases in the average crystallite size most probably occur through growth of one crystallite at the expense of others and since interstitial mobility in the crystallites is high in directions parallel to the layer planes (6), easy transfer of atoms to one crystallite would require that adjoining crystallites have nearly the same orientation. This is not the situation in glassy carbon. Densification of the structure through irradiation apparently does not change this arrangement, but "tightening up" of the structure would accentuate the

misalignment of neighboring crystallites and thereby make crystallite growth more difficult.

References

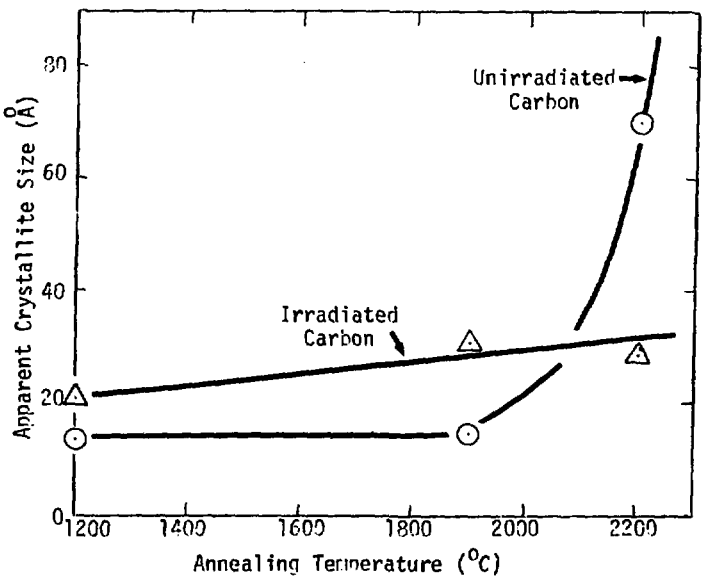
1. L. L. Ban and W. M. Hess, Abstracts Tenth Biennial Conference on Carbon, June, 1971.
2. L. L. Ban, D. Crawford and H. Marsh, Abstracts Twelth Biennial Conference on Carbon, July, 1975.
3. J. L. Kaae, Journal of Nuclear Materials, 57, 82 (1975).
4. J. L. Kaae, Carbon, 10, 701 (1972).
5. J. J. Kaae, Carbon, 13, 55 (1975).
6. P. A. Thrower, Chemistry and Physics of Carbon, V5, P217.

Figure 1



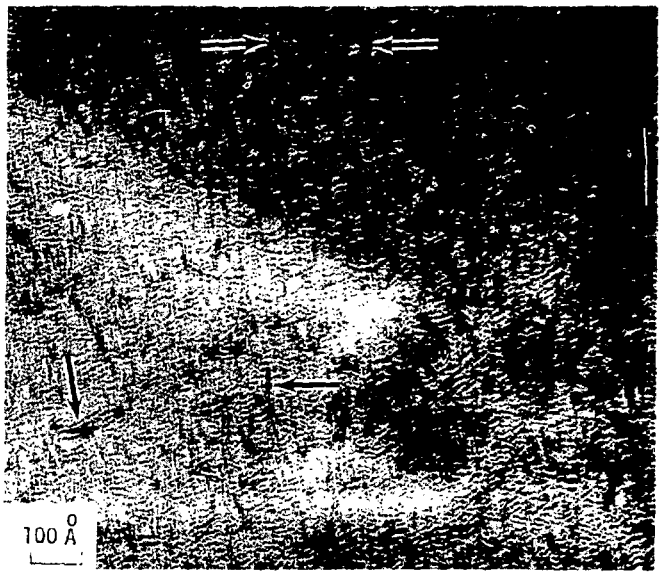
Variation of density during irradiation at 1100°C.

Figure 2



Apparent crystallite size (L_c) as a function of annealing temperature.

Figure 3



Microstructure of unirradiated carbon after annealing at 2200°C. Arrows indicate bands which are images of crystallites whose layer lanes are perpendicular to the surface of the specimen.

Figure 4



Microstructure of irradiated carbon after annealing at 2200°C. Arrows indicate diffraction contrast fringes similar to those observed in isotropic pyrocarbons.

RELATION BETWEEN SULFUR CONTENT AND X-RAY PROFILE OF COKE

Y. YAMADA, S. OI, M. TSUCHITANI, M. HONDA, K. SHIBATA, M. NAKAMIZO, H. HONDA

National Industrial Research Institute of Kyushu

and M. INAGAKI

Faculty of Engineering, Nagoya University

Introduction

It have been reported already that carbon materials containing sulfur and nitrogen form partially graphitized part at relative low temperatures below 2000°C. Recently, Fitzer et al(1) described that the catalytic effect of sulfur on graphitization of cokes with 0.4-0.7wt% sulfur causes the reduction of the activation energy for graphitization from 7-10eV to about 3-4eV between 1400°C and 2000°C.

This paper reports on the results of X-ray measurements and observation by high-electron microscope of high sulfur content petroleum cokes heat-treated between 1100°C and 1300°C in order to clarify the origin of partial graphitization within the sulfur containing cokes.

Experimental

Khafji and Gachsaran vacuum residues were heat-treated at 450°C for 15 hr. Meso-carbon microbeads were mesophase spherules formed in Khafji vacuum residue heat-treated at 420°C, and mesophase spherules were separated from the heated residue as quinoline-insolubles. These microbeads were heat-treated at 450°C for 15 hr. The sulfur contents in sample cokes are shown in Table 1.

Table 1. Sulfur content in the samples

Sample	Sulfur (wt%)
Khafji coke	6.7
Gachsaran coke	3.4
Microbeads	8.3

Those samples were heated at HTT above 1000°C, and were examined by X-ray measurement and high-resolution microscopy.

Results and Discussion

Khafji and Gachsaran cokes were heat-treated at 1000-1700°C for 0.5 hr. (002) X-ray diffraction profiles of the cokes consist of two components corresponding to ordinary soft carbon phase (26° component) and graphitized phase (26.5° component) for Khafji coke heat-treated above 1300°C and for Gachsaran coke heat-treated above 1400 °C. Representative (002) diffraction profiles are shown in Fig.1 for both the coke heat-treated at 1100, 1200 and 1300°C for various times in the range of 0.5 hr to 30 hr. At HTT 1200°C, the observed intensity of the 26.5° component for Khafji coke with the initial sulfur content of 6.7wt% increases with an increase of residence time, and the 26° component exists as a shoulder on the 26.5° component for Khafji coke heated for 30 hr (Fig.1-a). In the case of Gachsaran coke, the two components of 26° and 26.5° components appear when the coke is heat-treated with times longer than the case of Khafji coke (Fig.1-c). The (002) diffraction profile of Khafji cokes heated at 1100°C for 30 hr is similar to that of the cokes heated at 1200 and 1300°C (Fig.1-b). Gachsaran coke heated at 1100°C for 30 hr exists the 26° component only (Fig.1-d).

For Khafji coke obtained at 1200°C for 30 hr, (112) diffraction apprats slightly, indicating a three dimentional order within the coke.

Fig.2 shows high-resolution micrograghs of Khafji cokes heat-treated at 1200°C for 0.5 hr and 30 hr. A lot of small layer plane segments can be seen in the coke heat-treated for 0.5 hr. There is no prefered orientation. The coke treated for 30 hr shows the existence of well-ordered layer planes. This well-ordered regions are present in quantity in the coke and are considered to correspond to the 26.5° component.

In Fig.3 are shown plots of sulfur content in the cokes as a function of HTT. Sulfur release in the cokes during heat-treatment occurs at a definite temperature for each coke, i.e., 1300°C for the Khafji coke and 1400°C for the Gachsaran coke. The temperatures at which sulfur release occurs suddenly, correspond to the temperatures at which the 26.5° component appears in the (002) diffraction profile. Therefore, the appearance of the 26.5° component may be related to the sudden release of sulfur in the cokes. A similar phenomenon was observed for the coke from a mixture of naphthalene and inorganic sulfur compound. In this case, the 26.5° component becomes predominant as the sulfur content decreases.

On the other hand, the meso-carbon microbeads were heat-treated at 1000-1500°C for 0.5 hr. The heated microbeads gave the (002) diffraction profiles of the 26° component only at all the temperature range of 1000°C to 1500°C. The sulfur contents in the heated microbeads, as shown in Fig.4

decrease gradually with the raising temperature from 450°C to 1300°C and decrease in fairly large quantities at the temperature between 1300°C and 1400°C. This sulfur release in the heated microbeads is different behavior from that in the Khafji and the Gachsaran cokes. (see Fig.3)

There is no appearance of the 26.5° component in the case of the heated microbeads. This indicates that the sulfur release which occurs gradually at the temperature below 1300°C reduces the catalytic effect of sulfur for the formation of the graphitized phase to be caused by the sulfur release, even if the sulfur content decreases in fairly large quantities at the temperature 1300°C and 1400°C.

Reference

(1) E. Fitzer and S. Weisenburger, Carbon, 14, 195 (1976)

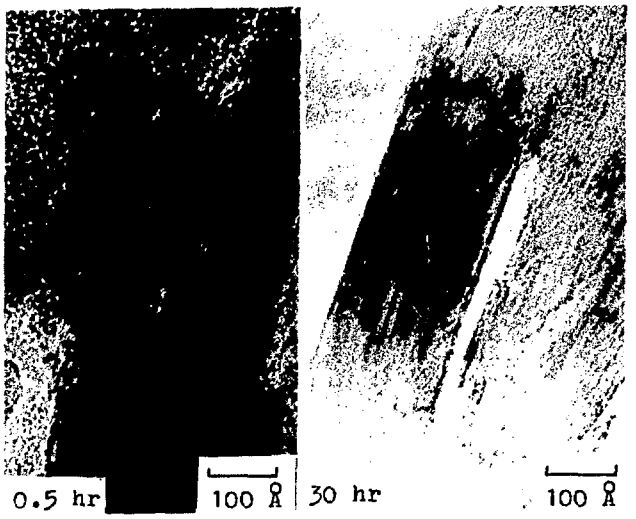


Fig. 2 High-resolution electron micrographs of Khafji cokes

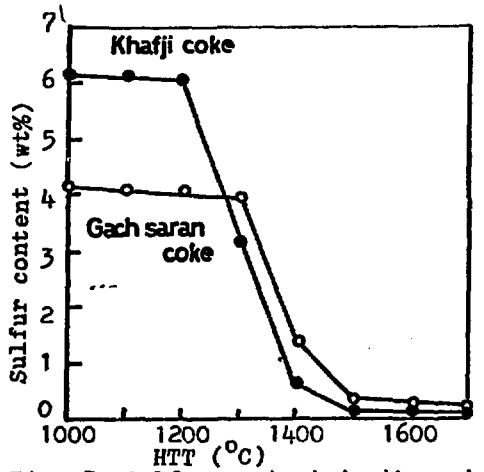


Fig. 3 Sulfur content in the cokes

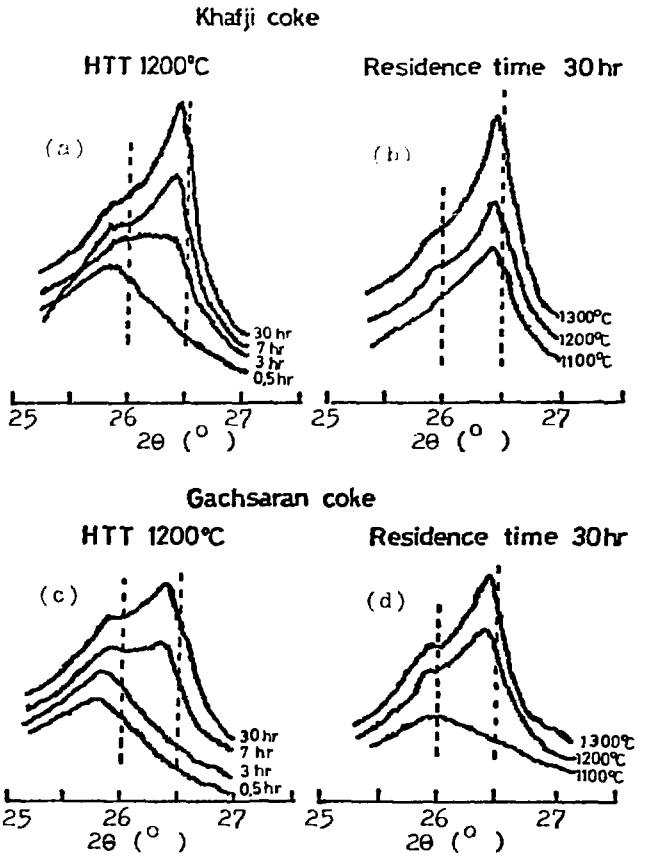


Fig. 1 (002) diffraction profiles

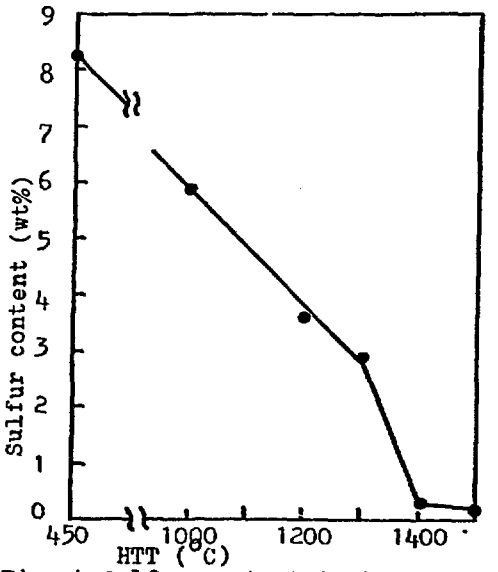


Fig. 4 Sulfur content in the heated microbeads

GRAPHITIZABILITY OF CARBONS UNDER 5 KBARS PRESSURE

M. Inagaki and S. Naka
Faculty of Engineering, Nagoya University
Chikusa-ku, Nagoya 464, Japan

Introduction

Most of carbons have been classified into either graphitizing or non-graphitizing carbons. This classification of carbons is rather rough, but very convenient to explain and understand the graphitization behaviour of carbons at high temperatures under normal pressure.

We have heat-treated different kinds of carbons under a pressure of 5 kbars. The non-graphitizing carbons, phenol resin char [1], glassy carbon[2] and carbon beads[3,4], are graphitized completely under 5 kbars at the relatively low temperature as 1600°C. On the graphitizing carbons, however, the different results are obtained ; on the poly vinylchloride coke carbonized up to 700°C the complete graphitization through heterogeneous process is observed[5,6], but on the same coke heat-treated at high temperature the graphitization retards remarkably[7].

Here, we will show the graphitizability of carbons under high pressure quite different from that under normal pressure: the carbons non-graphitizing under normal pressure are graphitizing under high pressure.

Experimental

Different carbons were used as the starting materials. These carbons were heat-treated under a solid pressure of 5 kbars at various temperatures for 1 hour. The piston cylinder type apparatus was used. The temperature of heat treatment was determined from electric power input by using the relation between temperature and power input which was established beforehand with the aid of a chromel-alumel thermocouple.

On the specimen heat-treated, the X-ray diffraction profiles were measured by using Ni-filtered Cu Kα radiation and a recording goniometer. The average interlayer spacing d_{002} was determined from 002 and 004 profiles referring to an inner standard of silicon.

Results

In Figs. 1 a) and b), the changes of 004 diffraction profile with HTT under 5 kbars are shown on two different petroleum cokes calcined up to 1400°C. The formaer is graphitized completely, as has been observed on the polyvinylchloride coke [5]. The latter, however, shows only partial graphitization even after the heat treatment at 1900°C under 5 kbars. It appears to consist of two component profiles, the component at high angle side having the d_{002}-spacing of 3.36 A (graphitic component). We found a similar partial graphitization on various petroleum cokes calcined, the amount of the graphitic component depending on the coke.

In Figs. 2 a) and b), the changes of 004 diffraction profile are also shown on the mesophase spherules which have been separated from an asphalt by quinoline. The as-separated spherules show partial graphitization, but on the same spherules pre-heated at 2200°C no graphitic component detected. The retardation effect of pre-heat-treatment on graphitization under 5 kbars was observed on other kinds of mesophase spherules[8]. A similar retardation of graphitization under 5 kbars was observed on the fluid coke [9] and gilsonite coke[10].

In Figs. 3 a) and b), the change of 002 diffraction profile are shown on the carbon beads. They are made from pitches and are non-graphitizing under normal pressure. The carbon beads carbonized up to 1000°C are graphitized abruptly at about 1600°C. The same abrupt graphitization was observed on the phenol resin char[1] and glassy carbon spheres[2]. The retardation effect of pre-heat-treatment is again observed on the carbon beads. In this case, however, it is not so remarkable as the cases described above. Large amount of graphitic component seems to be formed after the heat treatment at 1800°C under 5 kbars.

Discussion

From this series of experiments, we understand the importance of the microstructure of the starting materials on the graphitization under 5 kbars. The isotropic random microstructure is favorable for graphitization under pressure, though it does not give graphite structure under normal pressure. Therefore, we would say that the non-graphitizing carbons are graphitizing under high pressure. The carbons with anisotropic microstructure show a wide range of graphitizability, from complete graphitization to almost no graphitization at 1900°C under 5 kbars. According to the detailed observations by high resolution electron microscopy[11], the sizes of the elemental domaine of carbon layers are 10 - 30 Å for both graphitizing and non-graphitizing carbons. These carbons are graphitized under 5 kbars. By the heat treatment under normal pressure, elemental domaines grow remarkably in graphitizing carbons, but only little in non-graphitizing carbons. The sizes of the domaine, in other words, the sizes of graphite-like layers, are probably responsible for retardation effect of pre-heat-treatment on graphitization under 5 kbars, for graphitizing carbons the effect being remarkable and for non-graphitizing carbons not so remarkable.

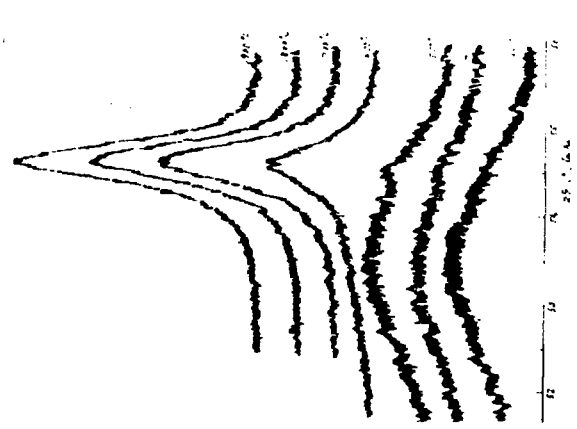


Fig. 1 a) Petroleum coke

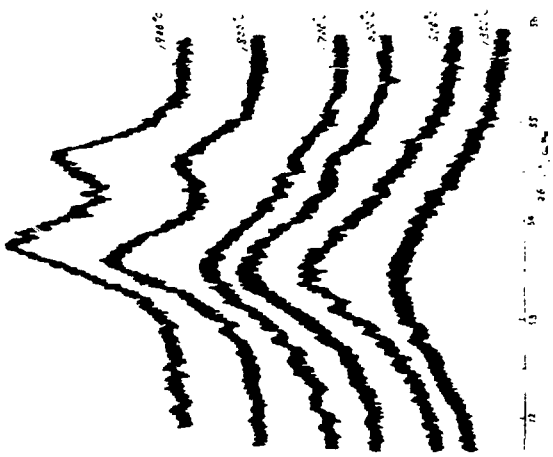


Fig. 1 b) Petroleum coke

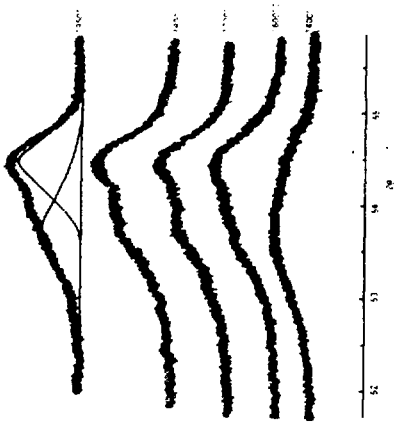


Fig. 2a) Mesophase spherules as-separated

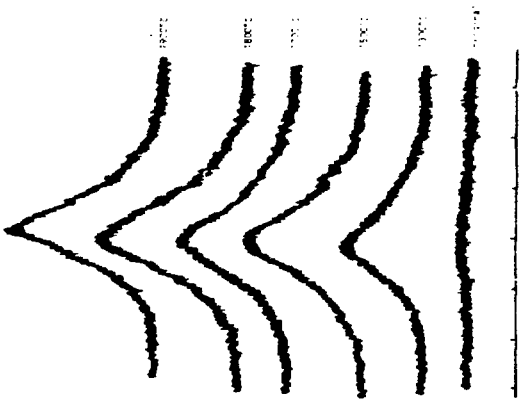


Fig. 2b) Mesophase spherules 2200°C-pre-heated

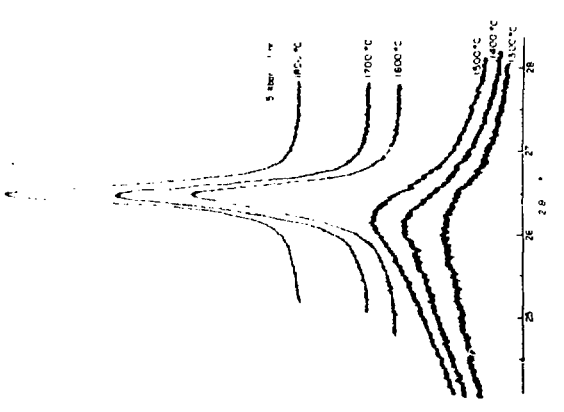


Fig. 3a) Carbon beads

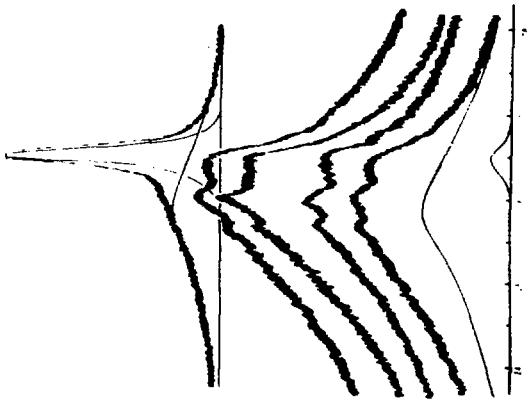


Fig. 3b) Carbon beads 2760°C-pre-heated

References

1. K. Kamiya, M. Inagaki, M. Mizutani & T. Noda, Bull. Chem. Soc. Japan 41, 2169 (1968)
2. M. Inagaki & S. Naka, J. Mat. Sci. 10, 814 (1975)
3. M. Inagaki, Y. Tamai, S. Naka & K. Kamiya, Ceram. Bull. 52, 856 (1973)
4. M. Inagaki, K. Horii & S. Naka, Carbon 13, 97 (1975)
5. T. Noda, K. Kamiya & M. Inagaki, Bull. Chem. Soc. Japan 41, 485 (1968)
6. K. Kamiya, M. Inagaki & T. Noda, High Temp.-High Press. 5, 331 (1973)
7. K. Kamiya, M. Inagaki & T. Noda Bull. Chem. Soc. Japan 43, 926 (1970)
8. M. Inagaki, Y. Tamai, S. Naka, Y. Yamada & H. Honda, Carbon 14, 203 (1976)
9. M. Inagaki, Y. Tamai, S. Naka & K. Kamiya, Carbon 12, 639 (1974)
10. M. Inagaki, Y. Tamai & S. Naka, Tanso 1973 [No. 75], 118 (1973)
11. A. Oberlin, G. Terriere & J. L. Boulmier, Tanso 1975 [No. 80], 29 (1975)

APPARENT CATALYSIS OF GRAPHITIZATION. IV. EFFECT OF TITANIUM

H. N. Murty,* D. L. Biederman** and E. A. Heintz***
Technical Department
Airco Speer Carbon-Graphite
P. O. Box 828
Niagara Falls, New York 14302

*Present Address: The Carborundum Co., Niagara Falls, N.Y.
**Present Address: Stauffer Chemical Co., Mt. Pleasant, Tenn.
***To whom all correspondence should be addressed.

Additions of titanium at the 5% (wgt.) level enhance the graphitization process to such an extent that a 2500°C heat treated catalyzed coke has a degree of graphitization equivalent to a 2700°C heat treated uncatalyzed coke.

Titanium appears to react with the less organized carbons by a reactive wetting process[1] in which some recrystallization of graphite is observed alongside of the titanium carbide formed during the heating process. In all cases, it is apparent that the catalyst reacts with the less-organized carbons[2] which tend to enhance their mobility and that of the catalyst[3,4] to enhance the graphitization process.

The cokes used in this study were typical of the graphite industry. Coke A was a premium rotary calcined petroleum coke; Coke B was a well-aligned vertically calcined petroleum coke while Coke C was a rotary calcined isotropic coke prepared from the mineral Gilsonite. All prior heat treatments, sizing of the cokes and x-ray diffraction data were performed as described previously.[5,6]

The titanium metal used was obtained from Alfa Products Division of Ventron Corporation as a -325 mesh powder with a minimum purity of 99% (wgt.). The desired amount of metal was added to the coke sample and intimately blended to ensure uniformity. To avoid segregation effects due to storage, each coke-metal sample was prepared and blended immediately prior to the heat treatment. Analysis of the one-hour, 2700°C heat treated samples before and after the heat treatment showed that no detectable amount of the titanium was lost during the heat treatment. In all cases, a level of 5% (wgt.) titanium powder was added to the cokes. Unadulterated samples were calcined in separate compartments at the same time in order to ensure constancy of heat treatment. Duplicate runs were performed at each temperature and the x-ray data, reported in Table I, for these runs never differed by more than 0.0006Å; averages are presented in Table I for Cokes A and B. Coke C behaves similarly.

TABLE I
Interlayer Spacing of Catalyzed and Uncatalyzed Cokes

Temperature (°C)	Interlayer Spacing ($c_t/2$, Å) Coke A		Coke B	
	Uncatalyzed	Catalyzed	Uncatalyzed	Catalyzed
1600	3.4331	3.4357	3.4266	3.4305
1700	3.4253	--	3.4227	--
1800	3.4279	3.4243	3.4214	3.4253
1900	3.4240	3.4231	3.4214	3.4249
2000	3.4219	3.4208	3.4225	3.4208
2200	3.4090	3.4037	3.4101	3.4037
2300	3.3880	3.3851	3.3886	3.3851
2400	3.3815	--	3.3833	--
2500	3.3724	3.3650	3.3730	3.3656
2600	3.3700	--	3.3698	--
2700	3.3656	3.3582	3.3667	3.3599

The Mering and Maire[7] degree of graphitization for the same materials were calculated and showed that there is little, if any, catalysis of graphitization up to 2000°C, confirming the report of Whittaker and Fritz.[8] Above 2200°C there is a rapid decrease in interlayer spacing and rapid increase in the degree of graphitization for the titanium doped coke samples. Generally, the degree of graphitization for the catalyzed cokes at 2500°C is equivalent to the

degree of graphitization of the uncatalyzed cokes at 2700°C. It is interesting to note that the catalytic effect appears to proceed as Coke A > Coke B > Coke C, that is in the order of decreasing anisotropy. In other words the presence of titanium had the greatest catalytic effect on the most anisotropic coke.

Some recent work by Matthews and Jenkins[1] has shown that titanium metal shows definite signs of wetting graphite in the process of being heated to 2700°C. Once the graphite and titanium react, however, cubic particles of titanium carbide are visible on the surface as detected by stereoscan microscopy. Some re-crystallization of the graphite near the titanium carbide particles appears evident. One could tacitly assume that the (liquid) titanium metal reacts with those groups of carbon atoms which were not as highly developed as some of their neighbors. These could be considered to be analogous to those specific atoms which are thought to decelerate the graphitization process.[2] Since there is evidence for some recrystallization of graphite alongside the titanium carbide particles,[1] the conclusion could be made that the wetting by the titanium assisted in their further development. This view is quite consistent with the observation of others concerning the mobility and preferential removal of selected carbon atoms in the catalysis of graphitization.[2,3,4]

Marsh and Warburton have also recently reported the catalytic influence of titanium additions of up to 20% (wgt.) on three cokes of varying anisotropy.[9] They measured crystallite-height and -diameter and found some catalytic activity at temperatures as low as 1600°C but considerable enhancement of graphitization at 2700°C, especially for the most isotropic coke. They concluded that the most probable mechanism of catalysis involves dissolution with subsequent precipitation of graphite at increasing temperatures. Unfortunately, no interlayer spacing data is presented so no direct comparison of the increased degree of graphitization can be made with this work. Nonetheless, the importance of carbide formation and the structure of the initial carbon is stressed in the work of Marsh and Warburton[9] and confirmed by Matthews and Jenkins.[1]

In the present study, the useful liquid phase is very small, from 1675°C (melting point of titanium) to ca. 1900°C (formation of carbide). Reference to both the interlayer spacing and degree of graphitization data, as a function of heat treatment temperature, show that little, if any, catalysis occurs by titanium below 2000°C. However, at temperatures in excess of 2200°C considerable catalysis occurs, again suggesting that the carbon atoms used in the formation of the carbide were those decelerating the graphitization process in the uncatalyzed cokes. Of significant practical interest in the manufacture of graphite, is the fact that if the carbides decompose (to the metal vapour and graphite), apparent graphitization occurs at a lower temperature than when the carbide exhibits high thermal stability.

Using the method reported earlier,[5,6] apparent activation energies (E_a) of the titanium catalyzed systems may be calculated. Using the parameter, g_o, defined previously as a kinetic function, the apparent activation energies may be calculated and are presented in Table II. The similarity of the catalyzed and uncatalyzed E_a values indicates that the mechanism of the graphitization process is, at least, similar in both cases, but the rate has certainly been increased as shown by the displacement of the lattice constant values listed in Table I.

TABLE II
Activation Energies (E_a) for the Catalyzed and Uncatalyzed Systems

Coke	E_a, Kcal/mole	
	Uncatalyzed[5]	Catalyzed With 5% (wgt.) TI
A	231	242
B	226	264
C	219	220

Literature Cited

1. R. B. Matthews and G. M. Jenkins, J. Materials, Sci., 10 (11), 1976 (1975).
2. J. Gillot, B. Lux, P. Cornuault and F. W. Chaffaut, Paper CP-17, 9th Biennial Conference on Carbon, Boston College, Chestnut Hill, Mass., June 1969.
3. M. L. Pearce and E. A. Heintz, J. Phys. Chem., 70, 1935 (1966).
4. T. Noda, M. Inagaki and T. Sekiyat, Carbon, 3, 175 (1965).
5. H. N. Murty, D. L. Biederman and E. A. Heintz, Carbon, 7 (6), 667 (1969).
6. ibid., 683 (1969).
7. J. Maire and J. Mering, Proc. Ind. Carbon Conf., London 2, 204 (1957).
8. M. P. Whittaker and H. C. Fritz, Paper SS-81, 10th Biennial Conference on Carbon, Lehigh University, Bethlehem, Pa., June 1971.
9. H. Marsh and A. P. Warburton, Carbon 14 (1), 47 (1976).

GRAPHITIZATION OF THIN CARBON FILMS

M. OBERLIN, J. OMA, A. OBERLIN

Laboratoire Marcel Mathieu (ER 131 du CNRS)
Université d'Orléans, 45045 Orléans, France

The results obtained by heat-treatment of thin carbon films are somewhat confusing (1) since it cannot be clearly demonstrated if these films are graphitizable or not. The following data were obtained by high resolution electron microscopy (EM) study. The thin carbon films were deposited under vacuum upon a NaCl cleavage. They were then removed from NaCl and laid on carbon supporting grids (these grids are made by heating a cellulose tissue at 3000°C). They were then progressively heat-treated from 1000°C up to 3000°C in a covered crucible in an argon flow. Carbon films deposited at room temperature are amorphous and correspond to a random network model (2). On the contrary, when heat-treated, they become turbostratic carbons.

SAD patterns show that the thin carbon films are progressively graphitizable. Above 2000°C the hk.l maxima appear and get sharper and sharper as HTT increases, in a way similar to any other soft carbon (fig. 4). L_a crystallite diameter has been measured by using both 10 and 11 dark field images. The N number of parallel layers has been measured, close to the carbon film breaks, since these breakages cause folding and thus 00.2 scattered beams to appear. N has been deduced from 00.2 DF images, SAD patterns and 00.2 lattice fringes.

At 1000°C all the EM techniques show the film to be formed by stacks 2 to 3 layers thick and smaller than 10 Å in diameter (3). Lattice imaging and SAD pattern as well, show a high degree of preferred orientation, therefore, each elementary carbon layer stack is tilted and twisted at random towards its neighbour. Only very small changes occur before 1250°C. Between 1250° and 1850° N increases very quickly and this growth is only limited by the thickness of the film. 00.2 DF images show that the small bright dots less than 10 Å (fig. 1) which are located on the folds are progressively replaced by bands of equal thickness rich in intense Bragg fringes (fig. 2). Over 1850°C whatever the HTT, the 00.2 DF images always show such single or multiple bands (single fold or rolled film). The bands which apparently look single but in fact include many folds are very common. This phenomenon can be easily explained in considering SAD patterns. At 2490°C for instance (fig. 4), as at any other high HTT, the free surfaces which limit both faces of the folds lead to observe in SAD patterns many subsidiary maxima (fig. 5) on both sides of the main 00.2 reflection (or 00.4). Their period allows the measurement of the diffracting domain thickness ; this thickness can also be evaluated in considering the 00.2 reflection width. In fig. 5 it is approximately 80 Å. The arrows in fig. 2 indicate a region where the measured thickness is 40 Å in A and 80 Å in B. If compared to fig. 3 (lattice fringes), the N number of fringes is 12 (≈ 40 Å) or 24 (80 Å). The real thickness of the carbon film is thus 40 Å but the two parts of the fold are parallel enough to induce interferences between the scattered beams of two crystallites (spatial coherence), thus leading to double the values. Noticeably, in the B region of fig. 3, nothing indicates where in the fringes the boundary between the two films can be. Between two experiments the real film thickness varies from 25 to 50 Å at the most, N_{max} thus varies from 7 to 15 at or above 1850°C.

11 DF images (fig. 6), if HTT < 2400°C, show hexagonal domains containing **moiré** fringes. This obviously shows that 2 or 3 crystallites at least are superimposed inside the film. The real L_c thickness cannot thus be related to the N number of parallel planes (equal to the film thickness) and is smaller. It is only at 2490° and above (fig. 6) that domains without any moiré fringes become more and more numerous and look homogeneously bright or out of contrast. At 3000°C all of them are bright or out of contrast. And thus L_c = N = film thickness. These DF images also lead to the measurement of the L_a crystallite diameter, plotted in fig. 7 versus HTT.

SAD patterns show that thin films are graphitizable. L_a values can be precisely measured in highly heat-treated thin films (or thin particles) owing to DF images when other diffraction techniques cannot succeed. Thin films L_a reach 3000-5000 Å. The N number of parallel layers is precisely measured by SAD, DF and lattice fringes and can be related both to film (or particle) thickness and to L_c value. In thin carbon films, N_{max} is equal to the film thickness and L_c remains smaller below 3000°C. At this temperature a unique crystallite extends over the whole film thickness (25-50 A) which is demonstrated by the lack of moiré fringes. The g graphitization value is thus one.

(1) I.S. Mc Lintock and J.C. Orr. In Chemistry and Physics of Carbon 11, 243 (1973), P.L. Walker, P.A. Thrower ed. Dekker N.Y.

(2) A. Oberlin, M. Oberlin and M. Maubois, Phil. Mag. 32, 833 (1975).

(3) A. Oberlin, G. Terrière and J.L. Boulmier, Tanso (Japan) 80, 29 and 83, 153 (1975).

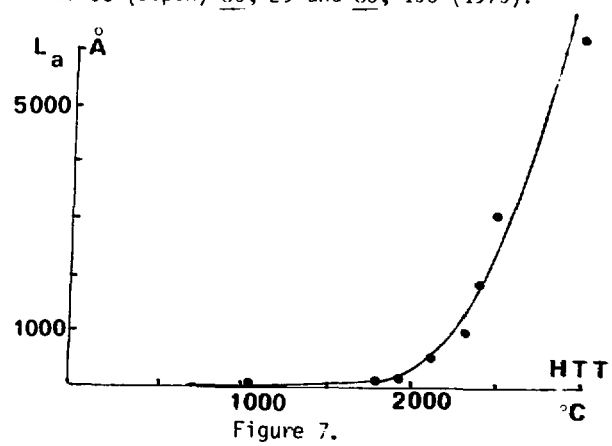


Figure 7.

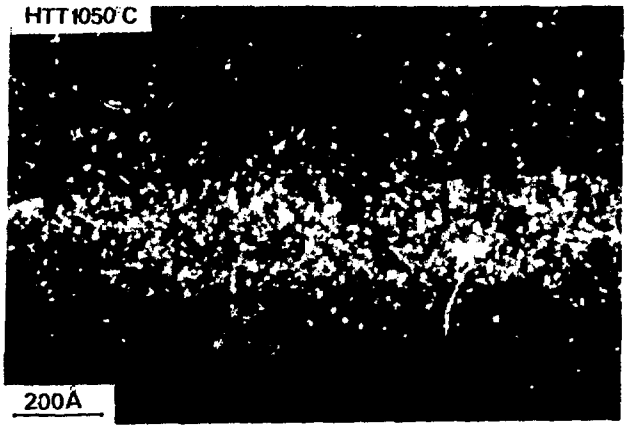


Figure 1

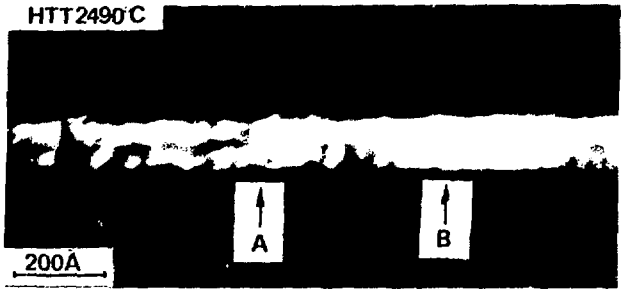


Figure 2

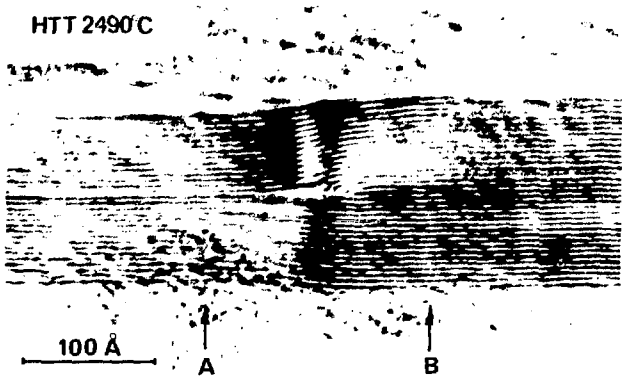


Figure 3

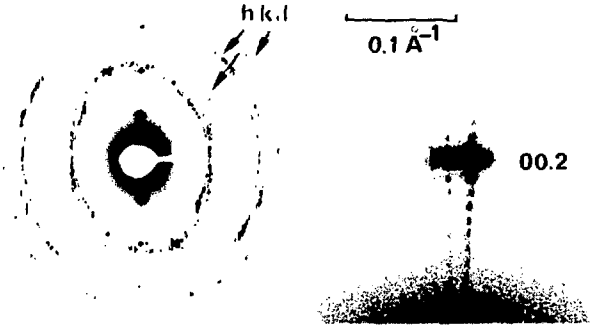
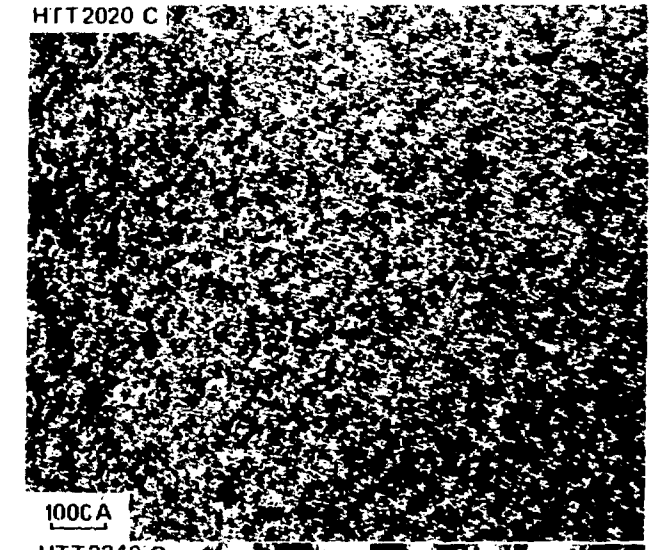


Figure 4

Figure 5



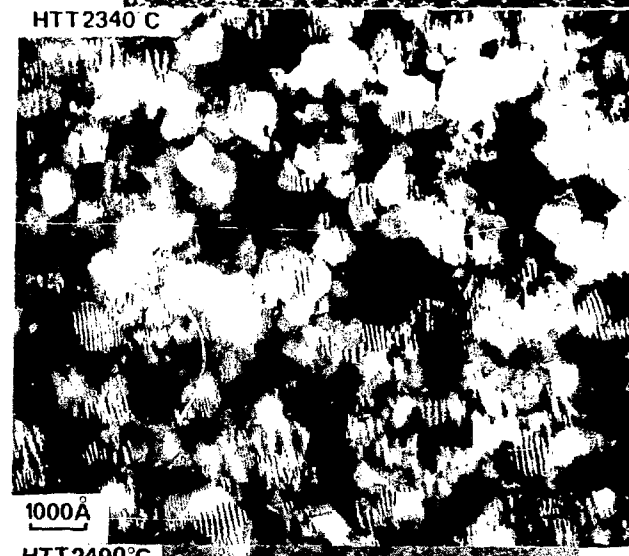




Figure 6

CERAPHITE, A HARD AND HIGH STRENGTH NEW CARBON MATERIAL

C. Nakayama, M. Okawa, H. Nagashima
Research Laboratory of Toshiba Ceramics Co., Ltd.
30 Soya, Hatano City, Kanagawa Prefecture, Japan

Introduction

There are a number of different raw materials and methods used in the manufacture of carbon materials (carbon and graphite products) to achieve desired characteristics. For most carbon materials, however, the properties are determined by two factors, the raw materials used and the manufacturing techniques applied. Up to this time considerable research concerning relation between the properties and the said factors has been made by many researchers enabling us to state that properties of a carbon material can be controlled by careful selection of raw materials and establishment of a suitable manufacturing process.

CERAPHITE, the subject of our presentation, is a new type carbon material possessing the characteristics common to glassy carbon materials, such as excellent hardness, high strength and high corrosion resistance, etc., as described below, and it originated from a new conception using a new manufacturing process. CERAPHITE has been developed using as its raw material the carbon made and supplied by Kureha Chemical Industry Co., Ltd., and is ready to be offered to the market.

Manufacturing process

Most carbon materials are made from mixtures of carbon filler and binder pitch. The behaviors of these two in the baking process are quite different from each other and hence difficulties arise. In the baking of a body shaped from the mixture, the binder pitch which is a green material softens, melts, emits gas, foams and contracts while the carbon filler which is not a green material does not act in the same ways, but expands. As a result of this difference in their behaviors when heated, the structure of processed materials usually becomes porous and is weak. This makes it difficult to produce a strong and dense carbon material.

To cope with this difficulty, we tried to develop a homogeneous raw material 1) eliminating binder pitch. The raw material for CERAPHITE was prepared from petroleum pitch through thermal and chemical treatments. It was then crushed, pressure-molded and the shaped bodies were baked in a furnace. In the baking, the carbon does not melt but its particles cohere together. In this heat treatment, the thermal and atmospheric conditions are made uniform for every part of the shaped body. Also adjustments are made both in the preparation of the raw material of CERAPHITE and in the manufacturing process to make the cohesion of particles tight, to expel pores from between the particles and to minimize pores and cracks which may have existed in the particles themselves.

In the case of products made of glassy carbon materials, it is generally thought that a thickness more than several millimeters is difficult to achieve whereas there is no such restriction on the thickness of products made with CERAPHITE. Larger shapes can be manufactured, the size of a large piece presently being 180mm in thickness, 250mm in diameter and 1000mm in length, and the weight of a piece can reach 30kgs. CERAPHITE coming out of a baking furnace is in the shape of blocks, columns, cylinders or crucibles etc., which can be further diversified into desired shapes by machining. To date CERAPHITE has been made into a variety of shapes without causing either a notable difference in the homogeneity and the other properties, nor with increases in size has the homogeneity and quality deteriorated, although deterioration normally tends to arise as a product increases in size.

Properties and Characteristics

As shown in Table 1, CERAPHITE is a hard and strong carbon material with a low open porosity and a high electric resistivity. CERAPHITE is isotropic and the ratio of electric resistivities is as low as max. 1.03.

The graph of X ray Diffraction Parameters of CERAPHITE is shown in Fig. 1. CERAPHITE is a typical non-readily graphitizable carbon, high in the parameter of Co(002) and low in the parameters of Lc(002) and La(110). The changes in its X ray parameters are not remarkable in the range of 2000-2500°CHTT, but in the area exceeding about 2600°CHTT, crystallization becomes apparent and the properties of CERAPHITE change correspondingly.

The microscopic structure of CERAPHITE shows the homogeneity of very fine particles with extremely tight particle-to-particle cohesion. The pores remaining between particles are very small, less than 1μm, and the major part of them are closed pores, as shown in Fig. 2.

CERAPHITE is characterized by its high resistivity to acids. Very little corrosion takes place in the boiling acids -

nitric acid, sulfuric acid and their mixture. Also it resists to molten metals such as aluminum and silicon, etc.

Applications

By virtue of its strength, CERAPHITE is excellent as a material for making hot press molds for manufacture of ceramic products. When used as boats, crucibles and susceptors for production of semiconductor materials, CERAPHITE sufiers very litile from corrosion in the chemical etching. Owing to its wear resistance, CERAPHITE is considered as a material for bearings and vanes in machinery and also for bioengineering use.

Table 1. Typical Properties of CERAPHITE

Bulk Density	1.60
Flexural Strength (kg/cm^2)	800
Compressive Strength (kg/cm^2)	2700
Tensile Strength (kg/cm^2)	550
Young's Modulus ($10^5 kg/cm^2$)	1.7
Scleroscope Hardness	110
Coefficient of Thermal Expansion ($10^{-6}/°C$)	3.0
Thermal Conductivity (cal/cm·sec·°C) (at 93.5°C)	0.037
Open Porosity (%)	4.7
Electrical Resistivity (10^{-3}Ohm·cm)	3.9
Anisotropy (Ratic of Electric Resistivities)	max. 1.03
Ash Content (%)	max. 0.1

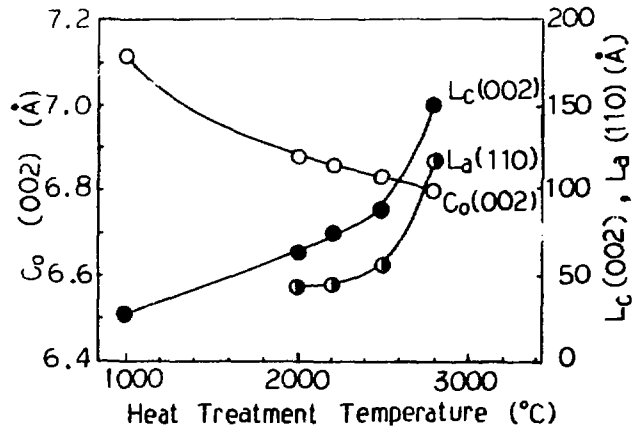


Fig.1 X ray Diffraction Parameters

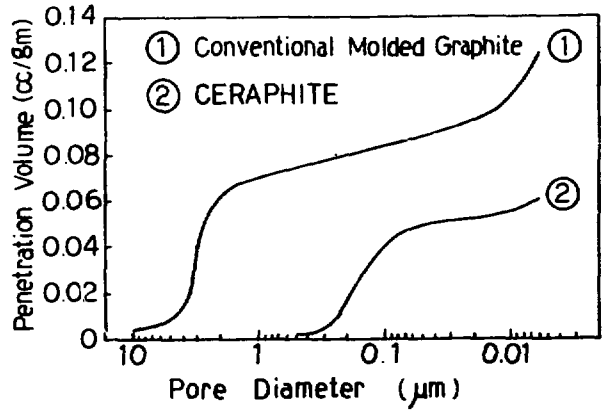


Fig.2 Cumulative Pore Size Curves

Reference

1) S. Ōtani et al., Tanso No.52, 13, (1968)

PRODUCTION SCALE UP OF THE GRAPHNOL N PROCESS

P. G. Ruopp, L. D. Loch and L. A. Joo'
Great Lakes Research Corporation, Elizabethton, TN

A raw petroleum coke base, fine grain graphite, Graphnol N3, is one of several developed on a laboratory scale by Oak Ridge National Laboratory for the U.S. Navy. The unique Graphnol materials exhibit high thermal shock resistance and very high strain-to-failure (elasticity) characteristics. Therefore, these graphites are particularly well-qualified for aerospace nosecone and leading edge applications. At Great Lakes Research Corporation (GLRC) the Graphnol N3 process has been modified and scaled-up under sponsorship of the Naval Surface Weapons Command.[1] The scale-up to 5øx9 inch production-size billets represented a volume increase of some eight times that of laboratory billets. This necessitated a corresponding increase in batch size and equipment capacities.

The distinctive process, as indicated in the accompanying flow chart, involved preliminary coke homogenization through blending and uniform heat treatment followed by close preliminary sizing of the raw petroleum coke filler with a maximum particle size of 120 mesh (125μ). Approximately twenty five percent of the minus 400 mesh (37μ) material is removed for graphitizing at 2500°C.

The graphitized fines are reblended with the original coke and combined with 30 medium (S.P. ca. 103°C) pitch in a solvent slurry operation. This "mix" then is heat treated to 325°C for one hour. All heat-treated material is remilled and combined with A-240 petroleum pitch and a plasticizing agent in a second solvent slurry operation. This "mix" is allowed to air dry before final milling and molding.

The material is molded at 100°C and 2000 psi and then allowed to cool under pressure to room temperature, before ejection.

Each green billet is loaded into a graphite-lined steel restraint. The billets are baked to 820°C in six days followed by pitch impregnation and rebake before graphitization to 3200°C.

During the scale-up of this process the following parameters were found to be critical: 1) the furnace oxygen level during heat treatment of the coke-pitch mixtures; 2) the particle size distribution at each milling step; 3) green density during molding; 4) the bake cycle to achieve desired baked density; 5) percent pitch pick-up as an indicator of both billet uniformity and proper baking off-fire temperature.

The ability to protect larger batches from oxidation during heat treatment of the coke-pitch mixes became an obvious first requirement to achieve the required green density. An oxygen level of less than 100 ppm is required during the heating of the mixes. Higher levels cause enough embrittlement of the pitch coating to greatly reduce compaction during molding. Mixes heat-treated within the control limit for oxygen produced densities of 1.41±.01 g/cc while oxidized mixes yielded green densities of 1.25 g/cc. Billets of marginal green density could be processed successfully through graphite only to exhibit high resistivity, indicative of previous oxidation. Modifications of the furnace design and of the techniques for oxygen analysis proved to be very successful in this regard.

Mix agglomeration, which had plagued previous scale-up attempts, occurs while preheating the mix for molding. A main objective during this contract was to eliminate the agglomeration in order to guarantee structural integrity and consistent within-billet properties. This has been accomplished by means of a cold mix-screening and precompacting step. The resulting cold compacts, although low density (1.10 g/cc), are easily handled and subsequently uniformly heated prior to final molding.

In order to maintain geometric uniformity and maximize baked density, each billet is baked in a separate graphite-lined steel restraint. The original, internally-threaded design was altered to include a set of external bolts which provided ease in assembly and disassembly of the units and prolonged the life of the shrink-fitted liners.

Studies of bake cycle parameters led to adoption of an eight day schedule employing heating rates of 10° per hour to 200°C, 4° per hour to 600°C and 6° per hour to an 820°C off-fire temperature. Cooldown rates of 50-70°C per hour, as obtained by cutting the furnace power at off-fire temperature, developed hoop stresses in the 5øx9 inch billets and caused linear splits on the surface. A controlled 6° per hour cooldown to 500°C followed by natural cooling at 20° per hour to 200°C yielded excellent billets. After the adoption of this cycle, no defects in the billets could be attributed to the baking step.

Large-scale graphitization at 3200°C of up to twelve 5øx9 inch billets per load was successfully accomplished with a 31 hour heating schedule. The off-fire temperature has not been finalized due to the fact that the slower rate and larger loads used in the scaled-up equipment led to longer cooldown periods and may provide conditions for overgraphitization. This over-graphitization could cause degradation of some properties.

****

Table I

Non-Destructive Physical Test Results of Graphnol N3: 3øx3 and 5øx9 Inch Billets

Pc	Density g/cc	Resistivity ohm-cmx10^{-5} WG	Resistivity ohm-cmx10^{-5} AG	MOE psi x 10^{-6}
3øx3-1	1.785	710	960	0.97
-2	1.782	715	1015	0.96
-3	1.811	750	1060	1.09
-4	1.806	670	885	1.06
-5	1.776	640	885	0.96
-6	1.787	645	900	1.04
5øx9-1	1.774	620	900	0.90
-2	1.773	660	850	0.93
-3	1.790	620	890	0.96
-4	1.777	640	940	0.96
-5	1.773	660	900	1.00
-6	1.787	615	940	0.95

FLOW SHEET A
COKE PREPARATION

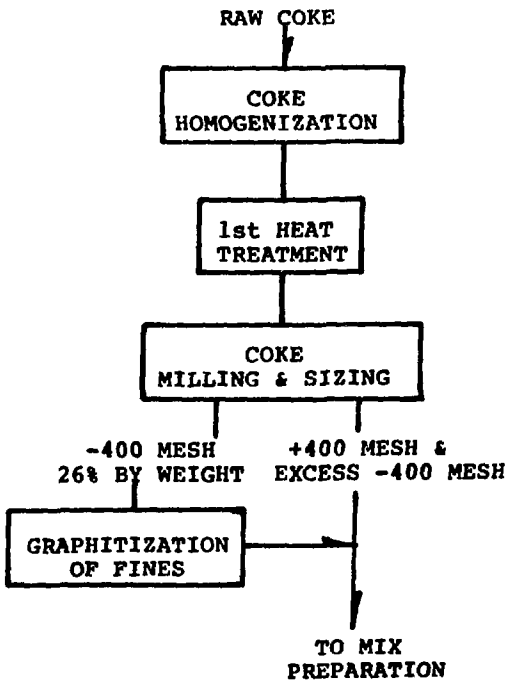


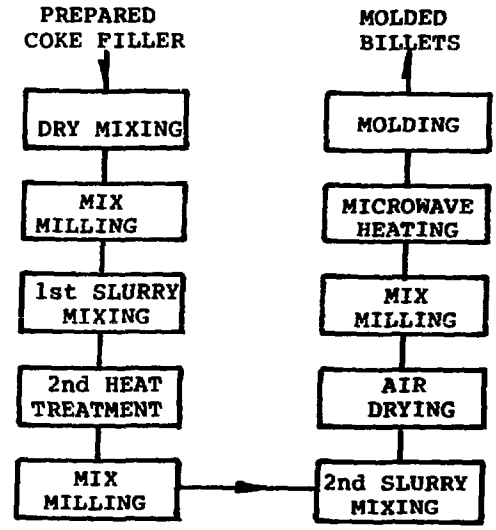
Table 1 shows initial non-destructive test comparisons between the 3øx3 and the 5øx9 inch billets produced at GLRC.

Further production work at the scaled-up level will allow for the optimization of process flow as well as for finalization of the specifications for the various process check points.

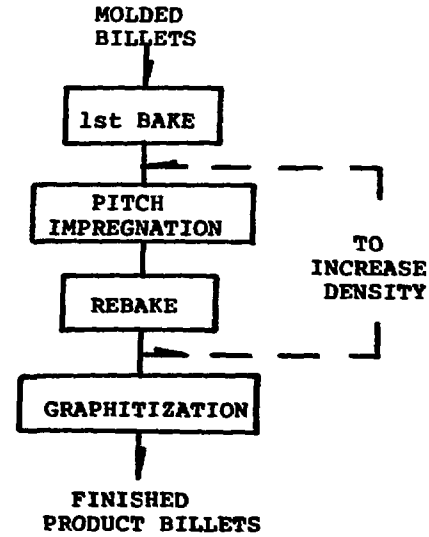
****

[1]Contract No. N-00197-76-C-0088

FLOW SHEET B
MIX PREPARATION AND MOLDING



FLOW SHEET C
HIGH TEMPERATURE PROCESSING



THE MICROSTRUCTURE OF VAPOR DEPOSITED CARBON FILMS

H.S. SHIM, N.K. AGARWAL, A.D. HAUBOLD
General Atomic Company
P.O. Box 81608
San Diego, California 92138

The carbon film thickness ranging from 500 to 1250Å were deposited onto cellulose acetate at constant pressure (3×10^{-2} torr) with bias power ranging from 100 to 500W. Free standing carbon films suitable for transmission electron microscopy including electron diffraction were obtained by dissolving the cellulose acetate away.

The electron diffraction pattern of all carbon films studied revealed the weak and broad diffraction peaks super-imposed on a strong background. Broad peaks indicate that the constituent crystallites are extremely small. Strong background is indicative of the presence of a noncrystalline substance that did not contribute to the diffraction peaks. The positions of the peaks were determined by using an optical densitometer and a polycrystalline aluminum standard specimen. The first band was roughly in the (002) angular position of graphite, the second (100), the third (004), the fourth (110), and the fifth (210). Since there were no (h, k, l) type reflection, it is concluded that the observed bands correspond to (002), (10), and (11) reflection of a turbostratic form of carbon (Table I).

TABLE I

Vapor Deposited Carbon Observed Lines	(b) S_o	Graphite (a) (h,k,l)	(b) S_o
No. 1	1.84	002	1.84
No. 2	2.97	100	2.96
No. 3	3.80	004	3.67
No. 4	5.30	110	5.12
		200	5.91
No. 5	7.60	210	7.81

(a) From Ref. 1,
(b) $S_o = (4\pi \sin\theta)/\lambda$; $\lambda = 0.037$Å

The preferred orientation of the crystallites was studied by observing the change in diffraction pattern as specimen tilted in the microscope. The tilt angle, which is the angle between incident electron beam and specimen normal, was varied from 0 to 75 deg. The basic patterns of the carbon films remained unchanged, indicating that the crystallites in the bulk of the films were randomly oriented and thus satisfying Bragg law for a given reflection over the range of tilt angles. If there were a preferred orientation, segmented ring would have been observed instead of continuous rings. The carbon films are therefore isotropic.

In order to estimate the size of crystallites, the background intensity which decreases with increasing diffraction angle was substracted from the observed (002) peak intensity of one of the specimen so that the reconstructed peak was symmetrical. From the broadening of (002) peak, the crystallite size in the C-direction was calculated to be about 8 to 10Å.

Transmission electron micrographs of a typical carbon film revealed a homogeneous structure with no distinctive growth features. The structural homogeneity, as well as the measured density of about only 1.7 to 1.8 g/cc and the strong background in the diffraction pattern, indicates that the carbon films consist of somewhat loosely packed components, probably misaligned, single-layered carbons.

The modulation of peaks of carbon films deposited at low and high bias powers, respectively, was weak and about the same with each other, but it was stronger in carbon films deposited at intermediate bias powers. This is not understood at the present time, because of the complex nature of the deposition process. It is however an indication that the structure (e.g., crystallite size) of vapor deposited carbon can be controlled by a suitable choice of deposition parameters.

In conclusion, the vapor deposited carbons can be formed that is similar to LTI pyrolytic carbons available under the trade name of Pyrolite^{R}.* The LTI carbons are used in medical devices requiring a high degree of thromboresistance[2,3]. Since the important structural parameters of the vapor deposited carbons are comparable to those of LTI carbons, it is felt that these carbon films will exhibit the same biocompatibility.

This work was supported in part by NHLI (S.D. Bruck, Program Manager).

* General Atomic Company, San Diego, California.

(1) Kakinoki, J., et.al., Acta Cryst. 13, 171(1960)

(2) Bokros, J.C., LaGrange, L.D., Schoen, F.J., in Chemistry and Physics of Carbon, Vol. 9, 103, Dekker, New York (1972).

(3) Bokros, J.C., and Akins, R.J., in Proceedings of 4th Buhl International Conference on Materials, p. 243, Carnegie Press, Pittsburgh (1971).

STUDIES OF THE RATE OF OXIDATION OF ATJ GRAPHITE BY STEAM

R. D. Burnette, C. Velasquez, G. Hightower and K. Koyama
General Atomic Company

INTRODUCTION

The thermally induced oxidation of nuclear grade graphites by steam at temperatures around 1000°C is controlled by both mass transport and reaction kinetics. This complication has given rise to a number of theoretical treatments (1, 2, 3, 4) which describe simultaneous diffusion and chemical reaction in the porous media. This paper utilizes a model advanced by Dodson[4] and compares it to experimental results for ATJ nuclear graphite. In this study the parameters surface-to-volume ratio, temperature, concentration and in-pore diffusion were considered.

THEORY

It is generally concluded that thermally induced oxidation of graphite proceeds by the following steps: (1) in-pore gas phase diffusion of reactant to active sites, (2) chemisorption, (3) chemical reaction and (4) desorption and diffusion of products out of the porous media. The present theoretical treatment neglects the final step in this process, assuming that reactant diffusion, chemisorption and chemical reaction are rate controlling. The equation of Dodson describing simultaneous diffusion and chemical reaction in a porous media was re-defined to give a general solution for total rate of oxidation: i.e.,

$$R_T = S/V\ L\ F_i\ R_s \qquad (1)$$

where: R_T is the total reaction rate of the sample, s^{-1}, S/V is the surface-to-volume ratio of the graphite specimen, cm^{-1}, L is the "diffusion length" given by $(D_{eff}/K_V)^{\frac{1}{2}}$ where D_{eff} is the effective diffusion coefficient for water vapor in the porous media given by $D_{eff} = mD_{1,2}$ where $D_{1,2}$ is the diffusion coefficient of H_2O in He and m is a constant characteristic of the porosity and tortuosity of the graphite. K_V is the volumetric reaction rate constant, s^{-1}, defined as: $K_V = R_s \rho RT/12\ P_{H_2O}$. F_i is a geometrical effectiveness factor. For the cylindrical samples used in this study:

$$F_i = \frac{I_1(R_o,L)}{I_o(r_o/L)} \qquad (2)$$

where I_1 I_o are modified bessel functions first kind, first and zero order, respectively, r_o is the radius of the cylinder. R_s is the chemical surface reaction rate in the absence of mass transport control, frac/sec. R_s in this study is shown to be described adequately by a Langmuir type equation as given in the results section. A useful result of these formulae is the relation

$$\frac{C}{C_o} = \frac{I_o}{I_o}\frac{(r/L)}{(r_o/L)} \qquad (3)$$

where C_o is the water vapor concentration at the surface of the sample or r_o and C is the concentration at radius = r.

EXPERIMENTAL

Samples were trepanned from ATJ production graphite blocks as supplied by Union Carbide. They were machined to the desired geometry, then ultrasonically cleaned in acetone to remove residual graphite dust, organic or other impurities, dried in an oven at 100°C and weighed. Oxidation rate measurements were performed with use of automatic recording microbalances. Reaction rates were calculated from weight loss versus time data. Test samples were suspended from the balance beam by means of a platinum wire, inside a gas tight quartz hangdown tube positioned inside a resistively heated SCR controlled furnace. Helium was passed over the samples at flow rates ranging from 100 to 1000 cc/min (linear velocities of 0.4 to 4 cm/sec. Above 300 cc/min the increase in rate of oxidation approached zero order with respect to flow, thus rate studies were conducted at 300 to 500 cc/min. Various moisture levels from 200 to 30,000 μatm were obtained by blending dry helium with water saturated helium via the use of calibrated flowmeters. Moisture concentrations were monitored with either a MEECO electrolytic type (range 1-1000 ppmv) or an EG&G Model 880 dewpoint type (range 1000-30,000 ppmv) moisture monitor. Hydrogen concentrations from 500 to 10,000 μatm were obtained by the use of premixed cylinders. ATJ test samples were right circular cylinders 3.8 cm long having diameters of 0.64, 1.3, 1.9, 2.5, and 3.2 cm, and having S/V of 6.8, 3.6, 2.6, 2.1 and 1.8 cm^{-1} respectively. In addition thin slabs were used, 0.32x2.5x 5.0 cm, S/V = 7.5 cm^{-1}. The thin slabs and small cylinders were used to determine R_s or K_V. The larger cylinders were used to determine the mass transport parameter m.

RESULTS AND DISCUSSION

It was found that the local isothermal chemical reactivity of thin slabs or cylinders of ATJ graphite was generally described by:

$$R_s = \frac{F_b K_1 P_{H_2O}^{0.9}}{1+K_2 P_{H_2}} \qquad (sec^{-1}) \qquad (4)$$

where F_b = a factor to normalize burnoff

$$K_1 = \frac{3.65\times10^{11}}{T}\exp(-68000/RT)\ \ (sec^{-1}\ atm^{-0.9})$$

$$K_2 = \frac{4.51\times10^{3}}{T}\exp(14500/RT)$$

The thermally dependent constants K_1 and K_2 determined at 1% burnoff are similar to those obtained by Everett et al., (Ref. 3) in studies of G-5 nuclear grade graphite. A plot of R_s vs 1/T is given in Fig. 1 where the experimental data points are compared with the rate expression, equation (4).

By plotting the overall reaction rates obtained at 980°C expressed as a surface oriented process, mg/cm^2 sec vs S/V, it was determined that for S/V below 3.6 cm^{-1}, (Dia.>1.3 cm) the reaction rate per cm^2 was relatively constant, indicating that F_i in Eq. 1 was essentially 1. The diffusion parameter m was determined by substituting into Eq. 1 values of K_V obtained from the experiments using the thin slabs and cylinders. The values of m for all the ATJ graphite samples ranged from 0.002 to 0.003.

A plot of log P_{H_2O} vs. log rate is shown in Fig. 2 for the largest specimen used, 3.2 cm dia. The solid lines, were calculated from the theoretical Eq. 1 using the reaction rate data and m factors previously determined. Figure 3 is a plot of log H_2 concentration vs log rate showing the excellent correlation with calculated lines.

A long term proof test was performed in which a 2.5 cm dia. ATJ cylinder was oxidized to 16% weight loss at conditions designed to give a non-uniform oxidation profile. The burnoff profile of the oxidized sample was determined with the use of a lathe technique and compared to the predicted profile calculated using a modified form of Eq. 3. The results of this comparison shown in Fig. 4, and indicate remarkable agreement between the calculated and experimental results.

CONCLUSIONS

The steam oxidation characteristics of ATJ graphite has been shown to correlate well with a simple general relation describing simultaneous diffusion and chemical reaction. It was found that the reaction kinetics were adequately described by a Langmuir type equation. Reactant transport in the porous media is shown to be correlated by a semi-empirical factor, m, applied to the ordinary gas phase diffusion coefficient.

REFERENCES

1. Walker, P.L., Rusinko, F. and Austin, L. G., "Gas Reactions of Carbon", Adv. in Cat., Vol. 11
2. Hewitt, G.F., "Gaseous Mass Transport Within Graphite", Chem. and Phys. of Carbon, Vol. 1, Marcel Dekker, Inc., N.Y. (1965).
3. Everett, M.R., Kinsey, D.V. and Romberg, E., "Carbon Transport Studies", Chem. and Phys. of Carbon, Vol. 3, Marcel Dekker, Inc., N.Y.(1968).
4. Dodson, M.H., "The Depth of Oxidation of Graphite: A Theoretical Approach", DEG Report 148 (CA) (UKAEA), 1960.

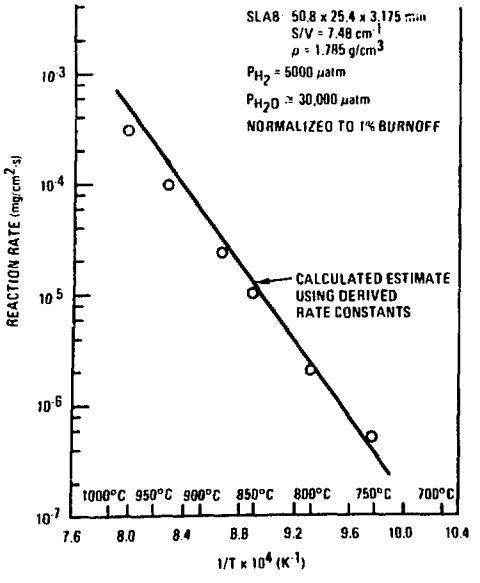


Fig. 1

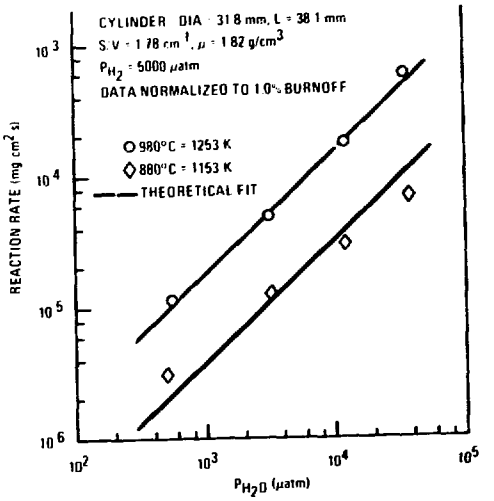


Fig. 2

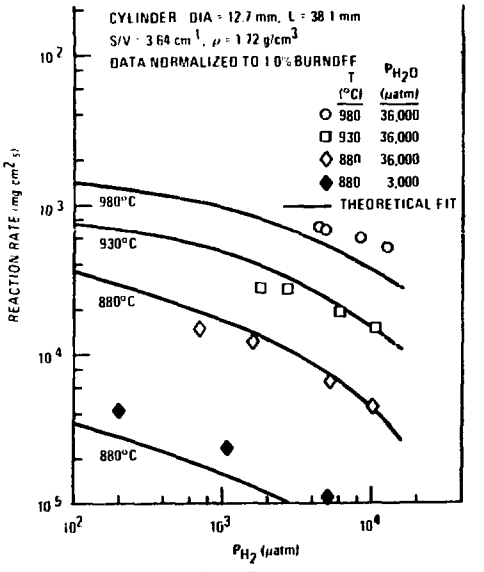


Fig. 3

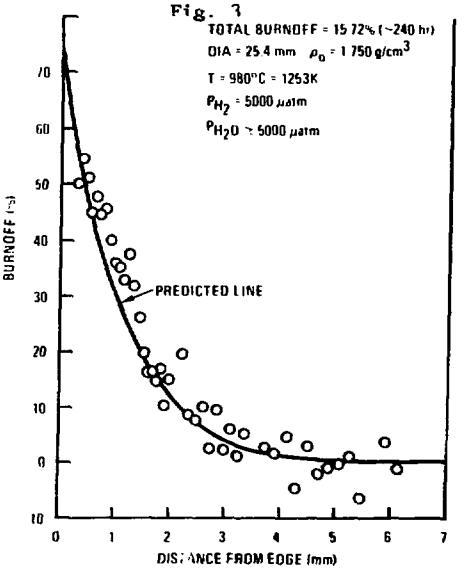


Fig. 4

THE KINETICS OF THE CARBON-OXYGEN REACTION IN PYROLYTIC GRAPHITES AND ITS RELATION TO THE DEGREE OF ORIENTATION

J. de D. López-González, M. Rodríguez-Gallego, F.Rodríguez-Reinoso and L. Zurita-Herrera.

Departamento de Química Inorgánica. Facultad de Ciencias. Universidad de Granada. (Spain).

The carbon-oxygen reaction has been studied for many years, but the results found in the literature vary greatly deppending on the materials used and the experimental conditions. The use of highly oriented pyrolytic graphite seems to be a good solution to this problem as it has been shown in previous papers (1,2), but even in this case there can be variations in experimental data according to the degree of orientation, grain size, and other characteristics of the pyrolytic graphite used. In order to find the influence that these variables may have on the kinetics of the carbon-oxygen reaction we are carrying out the study of the carbon-oxygen reaction on different highly oriented pyrolytic graphites kindly supplied by Dr. A. Moore, of The Union Carbide Corporation, Cleveland, Ohio.

Samples of about 15 x 10 x 1mm. were cut from the original specimens and the carbon-oxygen reaction was followed in a Cahn RG Electrobalance using an oxygen pressure of 50 Torr. The temperature range of the reactivity runs was from 650ºC to 800ºC, where the reaction rate was chemically controlled. In all cases the reaction presents a high initial reaction rate which gradually drops to a steady state value. There is not a great difference between the steady state values found at a given temperatures for the several graphites used, but the difference is large for the initial values of the reaction rates. The high initial reaction rates are not due to the attack on the basal planes of the graphites as it has been shown by reacting the samples again after cleavage of the basal surfaces of the previously oxidized samples; in this case the oxidation rate is practically constant and equal to the steady state rate of the first reaction. Consequently, the high initial reaction rate is due basically to the oxidation of the edge surfaces of the samples and the differences between the rates for the different samples of graphite studied must be attributed to differences in the reactivity of the edges of the materials.

The reactivity data have been used to determine the kinetics of the carbon-oxygen reaction in each kind of graphite. The Arrhenius plots of the oxidation rate (the steady state value) at the different temperatures for 50 Torr oxygen pressure, allows the calculation of the activation energy. The order of the reaction was determined by using samples of identical dimensions at 750ºC and in the oxygen pressure range from 20 to 120 Torr. The activation energy obtained for the different samples of graphite used ranges from 65 to 46 Kcal $mole^{-1}$ and the order of the reaction gave always values from 0.6 to 0.7, near the ideal value of 0.5 corresponding to the attack of two neighbouring carbon atoms by an oxygen atom .

In order to find a relationship between the experimental values for the activation energy and the crystalline perfection of the graphite used, we have carried out a qualitative determination of the degree of orientation (3) of the different graphites and the determination of their grain size (4). In the first case, the samples of graphite, prior to the reaction run, were positioned in an X-ray diffractometer with the layer plane surface normal to the plane of the incident beam ; an automatic drive motor rotates the sample and the proportional counter records the variations of diffraction intensity at different angles. Once the diffractograms were obtained, the samples were oxidized with 50 Torr O_2 at 800ºC for 8 hours and the diffraction experiment repeated, in order to see the variation in reflectance of the samples due to the oxidation.

The grain size of the graphites was determined by etching the graphite basal surfaces in molecular oxygen (50 Torr O_2 at 750ºC for several short periods of time). Subsequent examination of the etched specimens under the optical microscope gave an estimate of the crystallite size. The sample of pyrolytic graphite with lower reflectance and larger crystallite size gave the lower value for the activation energy and, at the same time , this graphite shows the larger increase in reflectance after oxidation (it increases up to more than four times the original reflectance). On the other hand, the graphite with larger original reflectance and larger crystallite size gave the higher value for the activation energy, and very low increase in reflectance after oxidation.

The samples studied have been seven and we have found that for the intermediate samples there is not a so clear relationship between the values of activation energy and reflectance and crystallite size. This is the reason why at this moment a quantitative determination of the degree of orientation is being carried out, by

calculating the mosaic spread of the different graphites and oxidized samples.

It is hoped that a quantitative relationship may be given at the moment of the presentation of this paper.

REFERENCES

(1) RODRIGUEZ-REINOSO, F., THROWER, P.A. and WALKER, P.L.Jr.; Carbon, 12, 63 (1974).

(2) LOPEZ-GONZALEZ, J. de D., RODRIGUEZ-REINOSO, F. and ZURITA-HERRERA, L.; Anales de Química. In press.

(3) NAGLE, D.C.; Ph. D. Thesis. The Pennsylvania State University (1973).

(4) RODRIGUEZ-REINOSO, F. and THROWER, P.A.; Carbon, 12, 269 (1974).

THE RATE OF OXIDATION OF CARBON FIBERS IN AIR

Bernard H. Eckstein
Union Carbide Corporation, Carbon Products Division
Parma Technical Center, Parma, Ohio 44130

Introduction

Most earlier work on the oxidation of carbon fibers was aimed at modifying the fibers' surfaces to improve interfacial bonding. There are also TGAs and oxidation studies at temperatures where carbon fibers are oxidized fairly rapidly. This paper provides information on the long term isothermal oxidation of carbon fibers based on polyacrylonitrile, rayon, and mesophase pitch between 230 and 315°C.

Materials and Methods

The yarns and cloths studied, all products of Union Carbide, are shown in Table I. The first three items are derived from PAN, items 4-10 are based on rayon; the rest are made from mesophase pitch. Analyses were made because it was expected that the rate of oxidation would be affected by the carbon content of the samples, and because alkali and alkaline earth metals are oxidation catalysts for carbon materials, especially at low temperatures. The densities were obtained in a density gradient column. The metallic elements were determined by atomic absorption.

For the oxidation measurements, duplicate 3 gram samples of each test item were suspended in a Freas Oven with an air flow of about 3 cfm. The nominal temperatures of 230, 290, and 315°C were maintained to ±2°C. The samples were weighed on a 1 mg balance except for the 230°C items where a balance with 0.1 mg sensitivity was used. The samples were weighed initially as received, after 4 hrs. at temperature, after 24 and 72 hrs. at temperature, and approximately at 3 or 4 day intervals thereafter until 1000 hrs. of exposure had been exceeded. The results are summarized in Table II and some typical curves are shown in Figure 1.

The materials used contain different amounts of finishes, have different surface areas, and may, therefore, sorb different amounts of atmospheric gases, etc. To eliminate these variables and obtain a measure of the weight loss due to the isothermal oxidation of the carbon, a weight loss vs. time curve was plotted for each sample. Usually, there was a rapid initial weight loss, then a levelling off. The more nearly level portion of this curve was extrapolated back to time 0, and the intercept was used as the starting weight. Table II lists an initial (4 hrs.) weight loss, and then weight losses to 100, 300, and 1000 hrs. These latter three are calculated from the intercepts; to obtain the actual weight loss at those times, the initial weight loss needs to be added.

Another element of arbitrariness: It was assumed, considering the low weights and heat capacities of the samples, that they would reach the oven temperature in 10 minutes, and that they would cool to room temperature in 5 minutes. Hence, the samples were allowed to sit in the room air for about 5 minutes before being weighed. They gradually gained weight at room temperature due to the resorption of atmospheric gases, but this weight increase was almost negligible in this short time.

Discussion of Results

The first item in Table II is commercial "Thornel"*-300; the second item is the same, finish free. The materials are of comparable purity and show no substantial differences in their oxidation behavior except for the higher initial weight loss for item 1, due to loss of the finish. Neither yarn survived 1000 hrs. at 315°C. However, the third item, a higher modulus version derived from the same precursor, shows a higher carbon content, greater purity, and a weight loss of well under 1% after 1000 hrs. at 315°C.

Among the rayon-based carbon fibers, there is one anomaly: WYB yarn, produced by carbonization under stress-free conditions, showed no weight loss except at 315°C. Both samples behaved similarly, and this behavior is being investigated further. The WCA cloth, also produced in a stress-free condition, showed only very low weight losses, less than .25%. The remaining yarns in this group, which achieve their strengths and elastic moduli (25, 50, and 75 Mpsi, resp.) by hot stretching, seem to show increasing sensitivity to oxidation with increasing orientation, but the numbers are too close to be considered conclusive.

The pitch-based carbon fibers exhibit oxidation rates comparable to the rayon-based fibers of comparable moduli. They have much better oxidation resistance than the PAN-based fibers. Grade VSA-11, a commercial material with modulus of 55 Mpsi, shows good oxidation resistance, but not as good as the experimental grade VS-0031, with a modulus of only about 35 Mpsi and again, presumably, a smaller degree of crystallite orientation. Among the cloths, grade VC-0150 is similar to the VS-0031 in filament properties and shows similar oxidation behavior. The VC-0149 has lower modulus, but is also somewhat less pure and oxidized more rapidly.

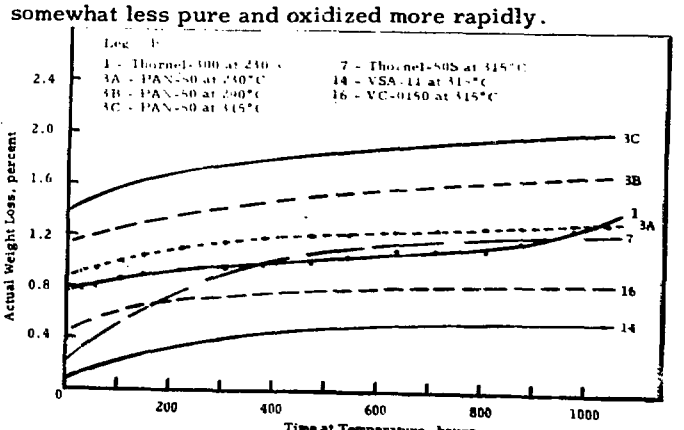


Figure 1. Typical Actual Weight Loss Curves

*"Thornel" is a registered trademark of Union Carbide Corporation.

Table I

Description of the Carbon Fibers Studied

Item	Material	Density Mg/m^3	Nominal Filament Diameter µm	Analyses: Carbon %	Hydrogen %	Ash %	Li, ppm	Na, ppm	K ppm	Mg, ppm	Ca, ppm	Ba, ppm
1	Thornel 300, WYP, UC-309	1.76	6.9	93.3	0.38	0.566	0.27	2020.0	49.8	3.1	7.0	1.1
2	Thornel 300, WYP, No finish	1.76	6.9	93.4	0.41	0.638	0.27	2160.0	52.0	5.7	5.8	0.3
3	PAN-50, WYR, UC-309	1.82	6.6	99.6	0.20	0.025	0.20	58.9	5.0	8.3	28.1	0.6
4	WYB	1.31	8.9	99.9	----	0.075	0.003	43.2	14.1	0.3	23.7	1.7
5	Thornel-25, WYD, UC-304	1.42	7.4	99.9	----	0.147	0.01	104.0	12.1	11.3	87.4	0.9
6	Thornel-50, WYG, UC-304	1.66	6.6	99.9	----	0.026	0.01	32.2	4.1	0.5	5.3	0.4
7	Thornel-50S, WYH, UC-307	1.66	6.6	99.9	----	0.074	0.003	37.3	18.2	7.2	44.4	1.6
8	Thornel-50S, WYH, No finish	1.68	6.6	99.9	----	0.009	negligible	0.8	0.5	0.3	0.5	0.3
9	Thornel-75, WYJ, UC-307	1.80	6.0	99.9	----	0.014	0.002	4.0	2.3	0.3	0.5	0.3
10	WCA Carbon Cloth	1.40	8.1	99.9	----	0.002	0.002	6.7	1.6	0.8	1.8	0.2
11	VS-0031, No shear treatment	1.91	13.0	98.8	----	0.236	0.10	13.5	15.3	26.4	7.2	11.0
12	VS-0031, Shear treated	1.91	13.0	98.8	----	0.141	0.09	14.4	9.0	23.2	15.4	6.8
13	VSA-11, UC-304	2.02	13.0	99.0	----	0.009	0.002	12.3	1.9	0.8	4.1	2.3
14	VSA-11, No finish	2.06	13.0	99.0	----	0.017	0.009	14.0	1.4	0.4	17.2	3.3
15	VC-0149 cloth	1.84	13.0	98.6	----	0.167	0.14	230.0	10.2	4.1	74.7	5.8
16	VC-0150 cloth	2.06	13.0	99.0	----	0.134	0.009	5.3	0.7	0.7	61.7	4.0

Table II

Percent Weight Loss of Carbon Fibers in Air

Item	Fiber	At 230°C: Initial 4 hrs.*	100 hrs.	300 hrs.	1000 hrs.	At 290°C: Initial 4 hrs.*	100 hrs.	300 hrs.	1000 hrs.	At 315°C: Initial 4 hrs.*	100 hrs.	300 hrs.	1000 hrs.
1	Thornel 300, WYP, UC-309	.76	.07	.20	.69	.88	.10	1.80	21.1	1.08	3.66	18.5	
2	Thornel 300, WYP, No finish	.04	0.00	.03	.20	.04	.08	2.76	19.9	0.04	4.81	21.30	
3	PAN-50, WYR	.88	.10	.24	.44	1.13	.09	.28	.55	1.38	.21	.40	.64
4	WYB	0.00	0.00	0.00	0.00	0.00	0.00	0.00	0.00	0.00	0.00	.68	6.30
5	Thornel-25, WYD	.32	.03	.06	.14	.07	0.00	.18	.42	.36	.37	.66	.69
6	Thornel-50, WYG	.47	.05	.13	.07	0.00	.05	.15	.53	.33	.35	.78	1.27
7	Thornel-50S, WYH	.28	.03	.08	.24	.40	0.00	.12	.40	.22	.31	.71	.89
8	Thornel-50S, WYH, No finish	.20	.32	.49	.56	.18	.35	.45	.45	.36	.40	.66	1.20
9	Thornel-75, WYJ, UC-307	.32	.13	.26	.44	.32	.04	.14	.96	.30	.20	.57	1.12
10	WCA Carbon Cloth	.02	0.00	.02	.23	.04	0.00	.03	.05	.08	.04	.12	.20
11	VS-0031, No shear treatment	0.00	0.00	0.00	0.00	.12	.08	.16	.22	.25	.07	.15	.36
12	VS-0031, Shear treated	.03	0.00	.01	.04	0.00	0.00	0.00	.18	.04	.06	.14	.19
13	VSA-11, UC-304	.80	.15	.40	.80	1.76	.19	.43	.59	1.00	.40	.95	1.90
14	VSA-11, No finish	.01	.02	.05	.14	.10	.18	.15	.22	.08	.13	.32	.46
15	VC-0149 cloth	.07	.11	.41	1.55	.04	.19	.53	1.42	.39	.90	1.84	6.00
16	VC-0150 cloth	.04	.02	.04	.08	.05	.15	.37	1.21	.42	.19	.29	.39

* To obtain the true weight loss at 100, 300, or 1000 hours, add the "initial" weight loss to the reading given (see text).
** 92% total weight loss at 875 hours.
*** 88% total weight loss at 875 hours.

TENSILE PROPERTIES OF AXF-5Q GRAPHITE

L. D. Fiel, J. T. Gill, J. F. Rosendahl
POCO Graphite, Inc.
1601 S. State Street
Decatur, Texas 76234

R. A. McCormack, H. S. Starrett
Southern Research Institute
2000 South Ninth Avenue
Birmingham, Alabama 35205

The tensile properties of AXF-5Q Graphite have been determined at 70°F, 2000°F and 3000°F. The specimens used in tensile property evaluation were taken from two manufactured parts, two inch thick plates and aeroshells (eight inch diameter cylinders). The bulk of the data presented here was obtained from specimens removed from plates.

The tensile measurements were made in a Southern Research Institute (SoRI) gas bearing facility. Two types of specimens, shown in Figure 1, were used in plate tensile property evaluations. Thickness, or "c", direction specimens were 1.70 inches in length and were used for strength determination at room temperature, only Three inch specimens taken in the "a" or "b" directions, were used to determine stress-strain behavior at 70°F, 2000°F and 3000°F.

Nondestructive characterization, consisting of measurements of bulk density and sonic velocity for each specimen, was performed prior to testing. In addition, the three inch specimens were X-rayed.

After mechanical testing, fracture faces of all specimens were inspected in order to check for material anomalies, such as voids, cracks or pore clusters. Where these were found, both their size and location were recorded.

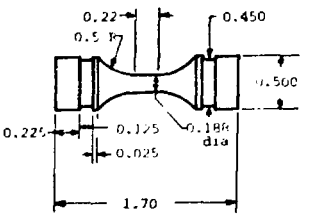
Figures 2, 3 and 4 are composite plots of stress-strain curves obtained in tensile evaluations of the three inch specimen from 70°F, 2000°F and 3000°F, respectively. These show the variability encountered in the stress-strain response of the plate material.

Figure 5 shows the probability of failure at a given stress level for both "a" and "c" direction specimens at 70°F and for "a" direction specimens only at 2000°F. The similarity of the two 70°F populations indicates that results obtained are essentially the same for both of "a" and "c" direction specimens. The fact that no volume effect is observed was expected since the gage volume of the two specimen types differs by only about a factor of four. The figure supports the conclusion that strength data obtained using the smaller specimen are valid. That the material is isotropic for strength is also inferred by the results shown on this figure.

The curve shown for 2000°F tensile evaluations of "a" direction specimen reveals the expected strength increase at the higher temperature.

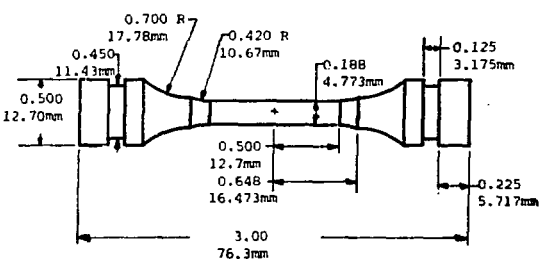
Figures 6 and 7 are plots of ultimate tensile strength at 70°F versus density and sonic velocity, respectively. The correlation between both density and sonic velocity and the ultimate strength indicate the suitability of these two monitors for possible use in quality control.

Figure 8 is a plot of ultimate tensile strength versus fracture face anomaly size. Anomalies greater than seven or eight mils in major diameter act as strength reducers. This result sets the required level of sensitivity for any nondestructive test which would be used to inspect the materials prior to use in hardware. For example, use of NDT to detect flaws of the type observed in Specimen BS-83-T-2 could be used to increase design allowables or reliability. This specimen has the low strength value shown in Figure 5.



"c" Direction Tensior Specimen

Note: Unless otherwise indicated all dimensions are in inches



"a" or "b" Direction Tensile Specimen

Figure 1. Specimens Used in Plate Tensile Property Evaluations

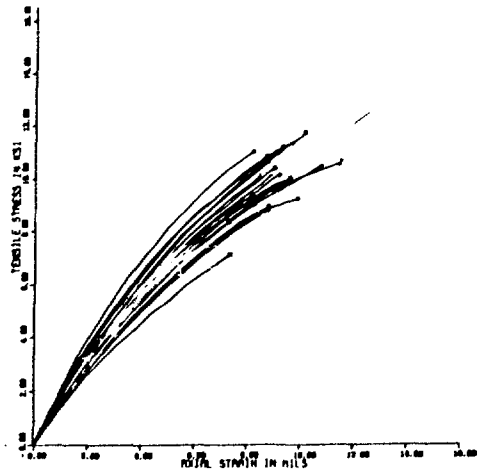


FIG. 2. COMPOSITE PLOT OF STRESS-STRAIN CURVES FOR 70 DEG F TENSILE EVALUATIONS OF VARIOUS POCO PLATE MATERIALS

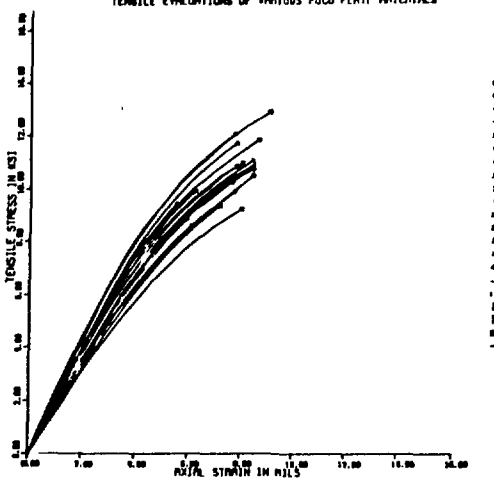


FIG. 3. COMPOSITE PLOT OF STRESS-STRAIN CURVES FOR 3000 DEG F TENSILE EVALUATIONS OF VARIOUS POCO PLATE MATERIALS

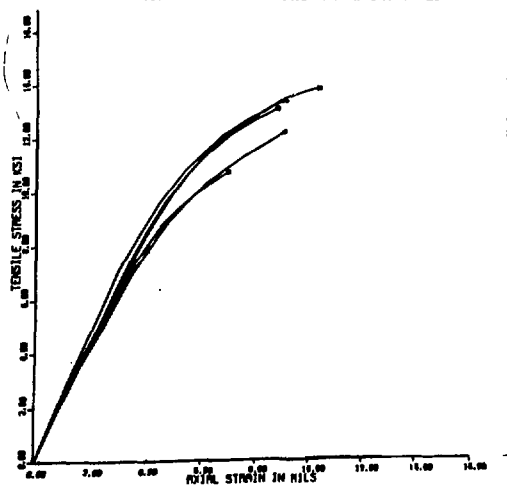


FIG. 4. COMPOSITE PLOT OF STRESS-STRAIN CURVES FOR 3000 DEG F TENSILE EVALUATIONS OF VARIOUS POCO PLATE MATERIALS

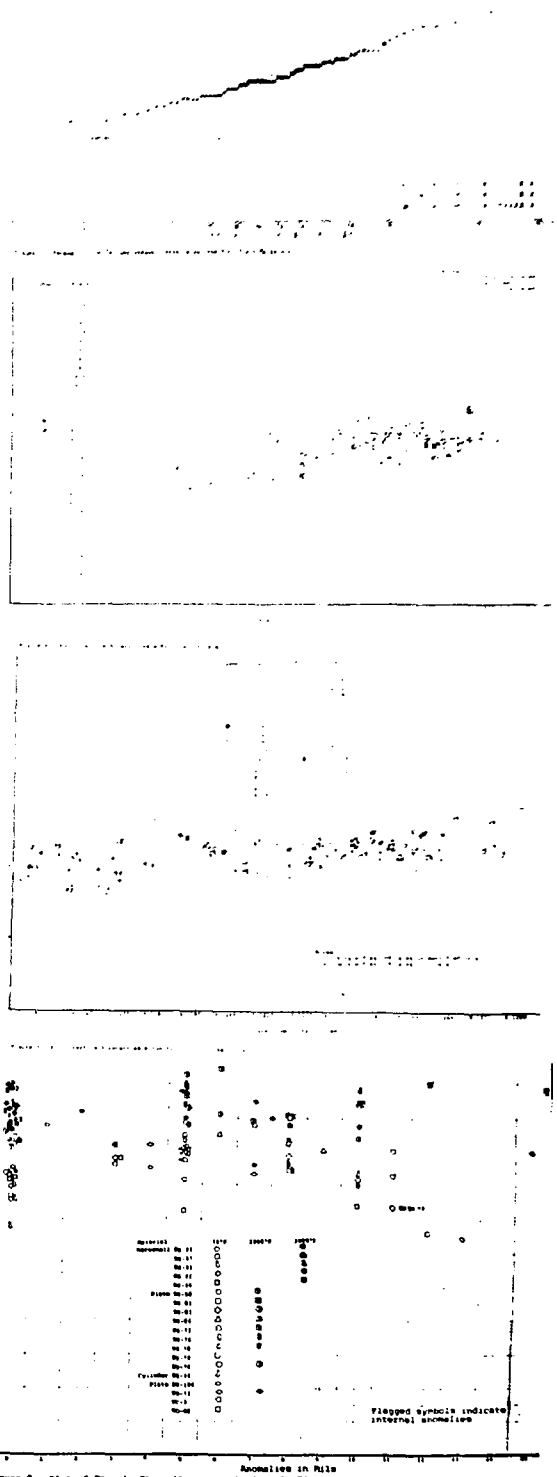


Figure 8. Plot of Tensile Strength versus the Anomaly Size

ELASTIC CONSTANTS OF GRAPHITE*

C. R. Kennedy
Metals and Ceramics Division, Oak Ridge National Laboratory†

The elastic constants can be obtained by direct mechanical measurements, resonant methods, or from sonic velocity measurements. Generally, it is a project requiring careful planning, sensitive equipment, skilled testing and knowledgable evaluation to derive the elastic constants for an anisotropic material such as graphite. The purpose of this paper is to describe a fairly simple procedure to easily and accurately obtain the elastic constants of graphite using sonic velocity measurements. This is accomplished by noting an additional degree of symmetry in both molded and extruded textures.

Sonic velocity measurements directly yield the stiffness values, C_{ij}'s; but the compliances, S_{ij}'s, must be calculated. Using different transmitting crystals, both the longitudinal and the two shear wave mode velocities can easily be measured. The general method is to measure the velocities in the z direction, the axis of symmetry, and one of the normal directions, x or y. This will directly yield four of the five elastic constants used to describe elastic deformation of a body with hexagonal symmetry with one isotropic plane. In the past, it was considered necessary to determine the velocities in one intermediate direction to evaluate the fifth constant (C_{13}); however, it will be shown and demonstrated that only the two normal directions are required. This was found possible by observing that the shear wave velocity associated with the C_{44} did not vary with the angle of measurement.

When plane waves are propagated through a solid, the Cristoffel velocity equations for the three transmitted modes in an orthogonal coordinate system are as follows:[1]

$$\begin{vmatrix} \Gamma_{11} - \rho v^2 & \Gamma_{12} & \Gamma_{13} \\ \Gamma_{12} & \Gamma_{22} - \rho v^2 & \Gamma_{23} \\ \Gamma_{13} & \Gamma_{23} & \Gamma_{33} - \rho v^2 \end{vmatrix} = 0 \qquad (1)$$

where ρ = density of the solid, v = velocity of the wave propagation, and the Γ_{ij} are the Cristoffel stiffnesses. For a wave propagating in a direction whose cosines are ℓ, m, n with reference to a Cartesian coordinate system, the Γ_{ij} take on the following form for a crystal of hexagonal (D_{6h}) symmetry:

$$\Gamma_{11} = \ell^2 c_{11} + m^2 c_{66} + n^2 c_{55}$$

$$\Gamma_{12} = \ell m \, (c_{12} + c_{66})$$

$$\Gamma_{13} = n\ell \, (c_{13} + c_{55})$$

$$\Gamma_{23} = mn \, (c_{13} + c_{44})$$

$$\Gamma_{22} = \Gamma_{11}$$

$$\Gamma_{33} = m^2 c_{44} + n^2 c_{33}$$

with $c_{55} = c_{44}$ and $c_{66} = 1/2(c_{11} - c_{12})$.

Equations (1) diagonalize when the wave propagates in the z-axis direction or in the x-y plane. For the first case, $n = 1$, $m = \ell = 0$, and

$$\begin{vmatrix} c_{44} - \rho v_{z_1}^2 & 0 & 0 \\ 0 & c_{44} - \rho v_{z_2}^2 & 0 \\ 0 & 0 & c_{33} - \rho v_{z_3}^2 \end{vmatrix} = 0$$

with the obvious solutions

$$\rho (v_{z_1}^{z_1})^2 = c_{44} \; ; \quad \rho (v_{z_2}^{z_2})^2 = c_{44} \; ; \quad \rho (v_{z_3}^{z_3})^2 = c_{33} \qquad (2)$$

where $v_{z_1}^{z_1}$ is a plane wave traveling in the z direction and polarized in the z direction (i.e., longitudinally), and $v_{z_2}^{z_2}$ is traveling in the z direction but polarized transversely (i.e., shear wave).

In the second case, in which the wave velocity is in the x-y plane, because of cylindrical symmetry, we may take $n = m = 0$ and obtain

$$\begin{vmatrix} c_{11} - \rho v_{x_1}^2 & 0 & 0 \\ 0 & c_{66} - \rho v_{x_2}^2 & 0 \\ 0 & 0 & c_{44} - \rho v_{x_3}^2 \end{vmatrix} = 0$$

with the obvious solutions

$$\rho (v_{x_1}^{x_1})^2 = c_{11} \; ; \quad \rho (v_{x_2}^{x_2})^2 = c_{44} \; ;$$
$$\rho (v_{x_3}^{x_3})^2 = c_{66} = \tfrac{1}{2}(c_{11} - c_{12}) \qquad (3)$$

with the same notation as before.

Equations (2) and (3) therefore yield the stiffness constants c_{11}, c_{33}, c_{44}, and c_{12} from the relevant velocity measurements. It remains to determine c_{13}.

Consider a wave propagating in the direction r not lying in the x-y plane. Then m may be taken as zero and the secular determinant becomes

$$\begin{vmatrix} \ell^2 c_{11} + n^2 c_{44} - \rho v_r^2 & 0 & n\ell(c_{13} + c_{44}) \\ 0 & \ell^2 c_{66} + n^2 c_{44} - \rho v_r^2 & 0 \\ n\ell(c_{13} + c_{44}) & 0 & \ell^2 c_{44} + n^2 c_{33} - \rho v_r^2 \end{vmatrix}$$

One solution factors out:

$$\rho \left(v_r^{xy}\right)^2 = \ell^2 c_{66} + n^2 c_{44} \qquad (4)$$

representing a shear wave. The remaining two solutions are a shear wave v_r^{rz} and a longitudinal wave v_r^r obtained from the quadratic

*This work was funded by the Naval Surface Weapons Center under Contract No. N-60921.
†Operated by Union Carbide Corporation for the Energy Research and Development Administration.

$$\ldots c_{\ldots} + n\,c_{\ldots} \ldots \quad \ldots + \ldots c_{\ldots} + n\,c_{\ldots} = \ldots v_{\ldots}^{2}$$

$$n + \ldots c_{\ldots} + c_{\ldots} \quad (5)$$

In general these solutions will depend upon the directional cosines ℓ and n. In the present case (see Fig. 1), the shear wave $v_{\ldots}^{\ldots}$ is found empirically not to depend on the cosines. For the special cases $\ell = 0$, $v_{\ldots}^{\ldots}$ becomes $v_{\ldots}^{\ldots}$, and for the case $n = 0$, $v_{\ldots}^{\ldots}$ becomes $v_{\ldots}^{\ldots}$, both of which satisfy

$$\ldots \left(v_{\ldots}^{\ldots}\right)^{2} = \ldots v_{\ldots}^{\ldots 2} = c_{44}$$

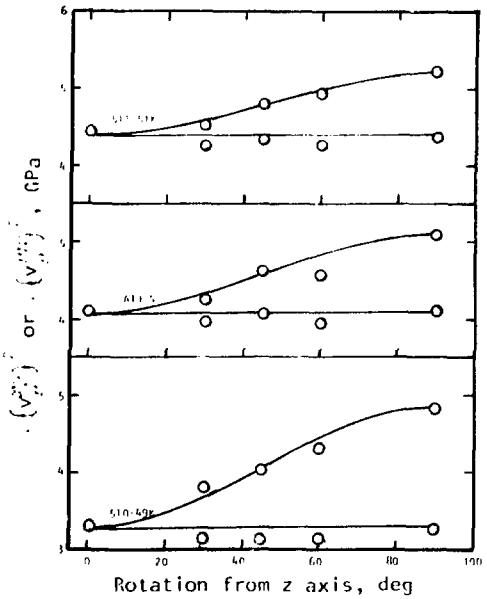


Fig. 1. Shear Velocity Measurements as a Function of the Angle of Rotation.

Therefore we may conclude on the basis of the data for any ℓ and n

$$\ldots \left(v_{\mu}^{\ldots}\right)^{2} = c_{44} \quad (6)$$

and the associated longitudinal wave becomes

$$\rho\left(v_{\mu}^{\ldots}\right)^{2} = (c_{11} - c_{33})\ell^{2} + c_{33} \quad (7)$$

which depends quadratically on the directional cosine ℓ.

Substituting Eq. (6) into Eq. (5) and using $n^2 + \ell^2 = 1$, we obtain

$$c_{13} = \left(c_{11} - c_{44}\right)^{1/2}\left(c_{33} - c_{44}\right)^{1/2} - c_{44}$$

Thus, the value of c_{13} can be calculated from the values of c_{11}, c_{33}, and c_{44}. And all five elastic constants can be obtained from measurements only in the axial and one transverse direction. This is further confirmed by comparing the calculated values of $\ldots v_{\ldots}^{\ldots}$ to the measured values in Fig. 2. Additional confirmation is also shown by a comparison of sonically derived constants to values obtained by the strain gage techniques in Table I.

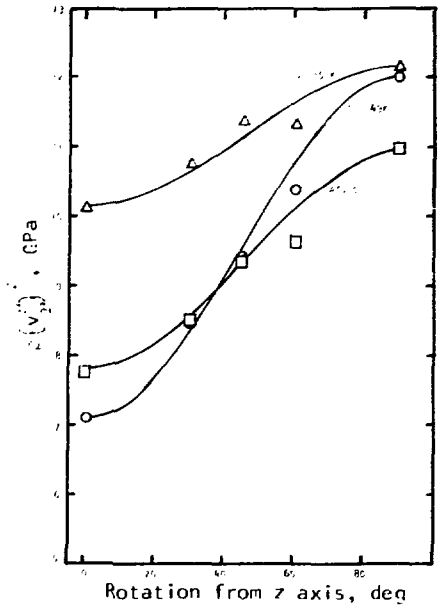


Fig. 2. Longitudinal Velocity Measurements as a Function of the Angle of Rotation.

Table I. A Comparison of Elastic Constants

	Graphite Grade					
	ATJ-S		H-451		AGOT	
	M[a]	S	M[b]	S	M[c]	S
$1/S_{11}$, MPa	11.44	10.76	7.86	8.55	11.95	12.07
$1/S_{\ldots}$, MPa	8.00	7.67	7.17	7.54	5.05	5.17
$-S_{12}/S_{11}$	0.11	0.06	0.11	0.14	0.05	0.04
$-S_{13}/S_{11}$	0.13	0.13	0.11	0.12	0.11	0.12
$-S_{13}/S_{33}$	0.09	0.09	0.13	0.14	0.08	0.07

M – by direct mechanical test

[a]Southern Research Institute

[b]General Atomic Company

[c]Oak Ridge National Laboratory

S – by sonic techniques, Oak Ridge National Laboratory.

Reference

(1) R.F.S. Hearmon, p. 68 in *An Introduction to Applied Anisotropic Elasticity*, Oxford University Press, London, 1961.

THE ROOM-TEMPERATURE MECHANICAL PROPERTIES OF BORON-DOPED GRAPHITE

Marion Eslick and D.J. Bacon
Department of Metallurgy and Materials Science, The University,
P.O. Box 147, Liverpool L69 3BX, U.K.

1. Introduction

From earlier studies on boron-doping, it is well-known that boron can have a significant effect on the physical properties of graphite. For example, Soule and Nezbeda [1] showed that the dynamic basal-shear modulus C_{44} increases at room temperature from 0.45 GN/m^2 to 4.5 GN/m^2 as the boron level in natural single crystals increases from 7 to 1500 ppm. This 10-fold increase was attributed to dislocation pinning by boron atoms. Wagner and Dickinson [2] investigated the influence of boron on physical properties such as interplanar spacing, electrical resistivity, thermal conductivity and dynamic Young's modulus for polycrystalline graphite. All showed important changes for boron concentrations up to 0.8 wt %, but the room-temperature modulus only showed a 19% increase from 16.4 GN/m^2 to 19.5 GN/m^2; this, again, was attributed to dislocation pinning. The boron in the polycrystalline case was added to the green mix during the manufacturing process. In the light of their own and earlier evidence, Wagner and Dickinson concluded that up to about 0.16 wt %, boron enters the graphite lattice substitutionally, and between this level and 0.8 wt %, some occupies interstitial sites but without carbide formation.

The aim of the present work is to investigate the effect of boron addition on mechanical properties such as the dynamic modulus and the form of the stress-strain curve of an isotropic, polycrystalline graphite. This note presents preliminary results on the room-temperature properties.

2. Material and doping procedure

The material used was a Gilso carbon, nuclear-grade graphite supplied by the UKAEA, Springfields Laboratory. The density was 1.75 gms/cc. Specimens for compression testing were machined in the form of cylinders 10 mm long and 4 mm diameter, and specimens for the dynamic modulus determination were 20 mm long and 4 mm diameter. The compression tests were carried out on an Instron machine at a cross-head speed of 0.2 mm/min. They included tests to fracture and load-unload tests to measure hysteresis loss below the fracture stress. The dynamic modulus was measured by the resonance technique.

Boron was diffused into the specimens by heating them in the presence of boron powder in an argon atmosphere at 2900°C for one hour. The boron content of some specimens was subsequently determined by chemical analysis at Springfields. A good indication of the presence of boron in the graphite lattice is the effect it has on the thermal conductivity [2]. The variation of the conductivity with boron concentration in the material used here is shown in Fig.1. The change is quite consistent with that reported by Wagner and Dickinson [2] and is evidence of the success of the diffusion technique employed.

In order to ensure that any changes in properties due to further graphitization of the specimens at 2900°C would not influence conclusions on the effects of boron, a group of 'control' specimens were given the same heat treatment in the absence of boron, and changes in properties can therefore be measured relative to these specimens. The effect of heat treatment on the thermal conductivity was negligible, as indicated by the filled circle in Fig.1.

3. Results

The dynamic Young's modulus of all specimens was measured before (E_o) and after (E) the heat treatment and addition of boron, and the change ($E-E_o$) produced is shown as a function of boron concentration in Fig.2. Each data point is the mean of eight values. and the bars indicate the standard deviation. The mean values for the control specimens before and after heat treatment were 10.19 and 9.23 GN/m^2 respectively.

The effect of boron on the static modulus measured in the compression tests is shown in Fig.3. Six specimens were tested at each boron level, but the scatter in the data is much larger than for the dynamic case since the modulus was not measured before the diffusion treatment. Nevertheless, the trends clearly follow those observed in Fig.2. The variations of fracture stress and strain to fracture with boron concentration are shown in Fig.4. It can be seen that the trends in these data are similar to that of the modulus. No systematic change in hysteretic energy loss at a given amplitude with boron level was observed.

4. Discussion

Perhaps the most surprising feature of the data given in the preceding section is that the changes in the mechanical properties are so small. For example, the changes in the dynamic modulus E, which are similar to those reported by Wagner and Dickinson [2], are two orders of magnitude smaller in percentage terms than those produced in the single-crystal modulus C_{44}. The latter are very much in line with those found by Seldin and Nezbeda [3] in single-crystal and pyrolytic samples after neutron irradiation. Since the changes in C_{44} are almost certainly due to dislocation pinning, the small changes reported here could be considered to throw doubt on the role dislocations play in determining the elastic and yielding mechanisms of polycrystalline graphite. However, it is more likely that the fact that E does change by approximately 10% is an indication of the contribution C_{44}, and hence dislocations, make to the polycrystalline properties. For example, it is well-known (see [4] for review) that the elastic properties of a polycrystal fall

between the two extremes of the uniform-strain model of Voigt and the uniform-stress model of Reuss. If it is assumed that C_{44} is the only single-crystal constant significantly affected by addition of boron, then a 10-fold increase in C_{44} would make an insignificant change to the Voigt modulus and an almost 10-fold change to the Reuss modulus. The present results suggest that the true modulus is more heavily weighted to the Reuss form than is, say, the arithmetic mean of the two extremes.

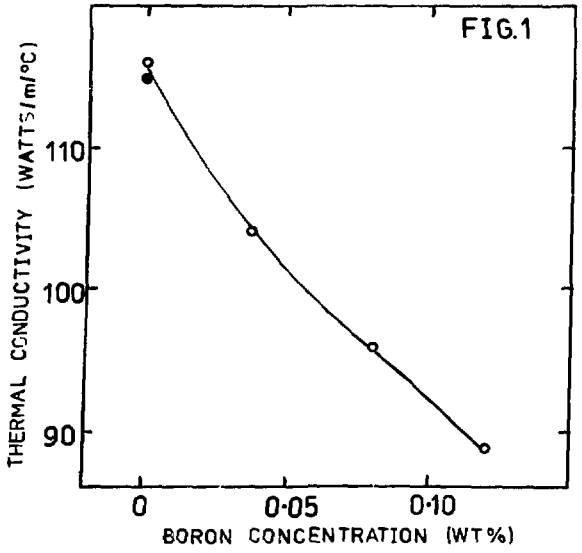
The assumption that C_{44} is the only constant changed by boron doping has not yet been tested by experiment. It is the only constant changed significantly by neutron irradiation [3], and we are currently repeating the mechanical property measurements on neutron-irradiated specimens. The results of this investigation and further analysis and work on the boron doping will be reported at a later date.

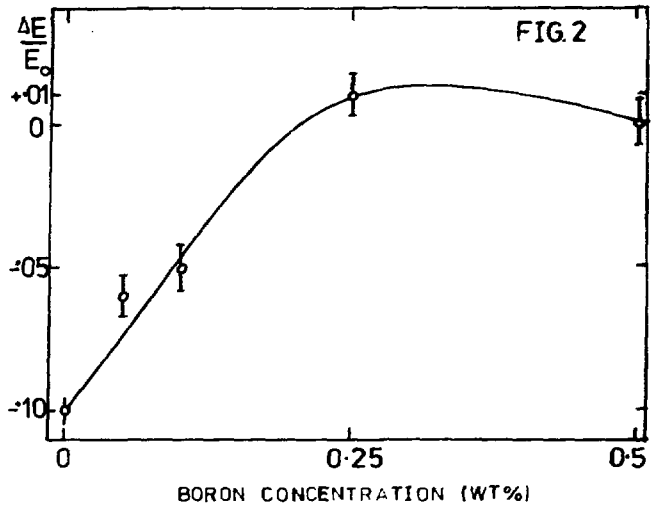
Acknowledgments

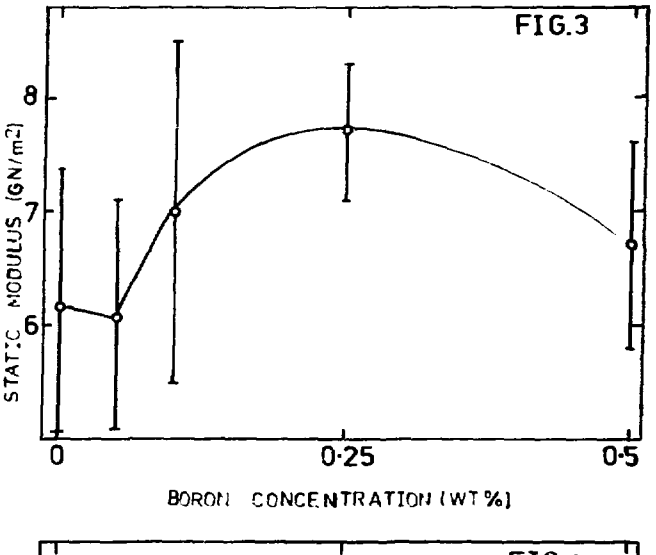
This work was supported by the UKAEA and the award by the SRC of a CASE studentship to M.E. The authors acknowledge helpful advice and encouragement from Mr. B.T. Kelly, and assistance with boron doping and conductivity and modulus measurements from members of the Harwell and Springfields Laboratories.

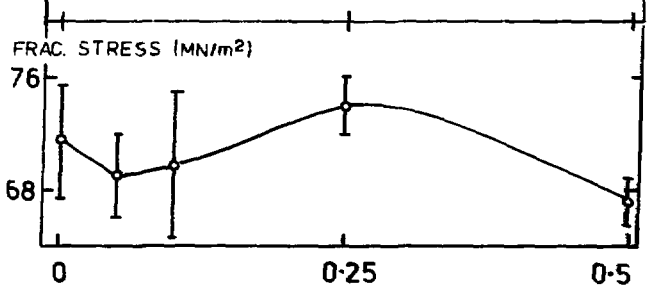
References

1. D.E.Soule and C.W.Nezbeda, J. Appl. Phys., 39, 5122 (1968).
2. P.Wagner and J.M.Dickinson, Carbon, 8, 313 (1970).
3. E.J.Seldin and C.W.Nezbeda, J. Appl. Phys., 41, 3389 (1970).
4. G.M.Jenkins, in Chem. Phys. Carbon, vol. 11, p.189, Marcel Decker, N.Y. (1973).









PHYSICAL PROPERTIES OF CDE CHARCOAL CLOTH

By F.A.P. Maggs, G.A. Robins, and M.E. Smith

Chemical Defence Establishment, Porton Down, Salisbury, Wiltshire, UK

Introduction

In another paper to this Conference (1) the adsorptive properties of CDE charcoal cloth have been described. In the present paper the ranges of tensile strength, flexibility, electrical resistivity and other physical properties measured on samples taken from an experimental plant producing charcoal cloth in 60 cm wide, 50 m long rolls are given. The variation of some of these properties with extent of activation is also recorded.

Cloth Structure

The cloth is a woven material composed entirely of charcoal, and although several weave forms have been made, the major production has been in square form linen weave having 13 double threads per cm; the properties recorded in this paper refer to this form only. The diameter of the filaments forming the thread is ca. 20 μm (scanning electron micrographs).

The surface density, w (weight per unit area) lies in the range 9 to 16 mg/cm^2. The bulk density, measured by compressing a pile of discs until further compression has little effect is 0.25 - 0.3 g/ml. The cloth thickness is in the range 0.04 to 0.05 cm.

Cross-Sectional Area

This may be estimated as $\frac{2wk}{d}$, assuming weave isotropy, and a thread crimping factor k; d is the envelope density of the filaments and has been estimated as 1.8 g/ml for unactivated material. It has also been observed (2) from electron micrographs that activation proceeds internally, the filament diameters showing only small changes during the process. From these observations the cross-sectional area of the linen weave cloth has been estimated as 4 x 10^{-3}cm^2 per cm.

Breaking and Tensile Strength

The breaking strength of samples of cloth taken from experimental production falls in the range 2.5 to 3.5 kg/cm width. The tensile strength thus falls in the range 6.3 to 8.8 x 10^5g/cm^2 (60 to 80 MN/m^2) (a quarter of the tensile strength of a single carbon fibre derived from rayon).

Flexural Rigidity

This was measured by the method of BSS 3356: 1961. Values range from 100 to 400 mg cm. [Such values are found for dress linens; a light canvas gives ca. 4500 mg cm]. The material thus has a cloth-like, flexible "handle", and may be utilised as a conventional fabric.

Air Flow Resistance

From measurements of the pressure drop (ΔP) across a number of multi-layer pads of charcoal cloth at a series of air velocities (6 to 60 cm/s) it was calculated that in the equation $\Delta P = KnL$, K varied from 11 10^{-3} to 18 10^{-3} cm water gauge (11 to 18 N/m^2) where n is the number of layers in the pad and L the linear air velocity (cm/s).

Electrical Resistance

For a material having two-dimensional isotropy, the resistance may be expressed as Ohms per square of material (independent of the size of the square). The resistance is a function of production parameters such as temperature and extent of activation: values ranging from 10 to 300 ohms per square have been recorded. By use of the cross-sectional area derived earlier, specific resistances in the range 0.04 to 1.2 ohm/cm^3 are calculated.

Variation of Properties with Activation

Strips of unactivated material were activated in CO_2 for different periods, the weight loss being recorded. Surface density is found to decrease linearly with increasing activation, and thus may be used to assess the extent of activation. Strength, electrical resistance and flexural rigidity were measured with the results shown in Figure 1 where fractional changes (in terms of unactivated material) are plotted against the activation yield. Flexibility is improved by activation; loss of breaking strength through loss of material is unimportant until activation beyond 60% yield is reached. It is noted that loss of electrical conductivity is greater than that calculated merely from loss of conducting carbon from the cross-sectional area.

References

(1) Adsorptive Properties of CDE Charcoal Cloth, Maggs F.A.P., Robins G.A., and Smith M.E. This Conference.

(2) Robins G.A. M.Sc. Thesis, Bath University, U.K. September 1974.

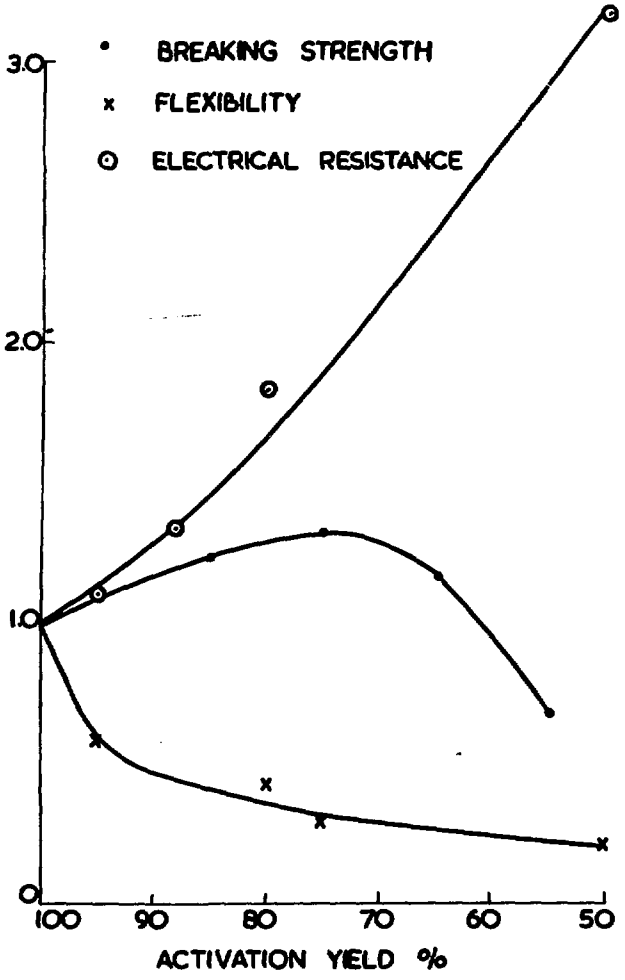


Figure 1. Variation of physical properties with activation

SHEAR DEFORMATION OF 3D CARBON-CARBON COMPOSITES

Julius Jortner
McDonnell Douglas Astronautics Company
Huntington Beach, California 92647

The strength and stiffness of graphitized 3D carbon-carbon composites, when loaded mechanically along a direction parallel to a set of yarns, appear to be dominated by the properties of that set of yarn bundles because the continuity of load through transversely-oriented yarn bundles and matrix material is interrupted by the open crack pattern (described in [1] [2]). Thus, it is not surprising that good linear correlations have been observed between tensile strength (and stiffness) and the fiber area-fraction in the direction of loading. Shear behavior however, depends upon the transfer of force from one set of yarns to another. Given the crack pattern, two orthogonal sets of yarns communicate mechanically only through load paths that are of limited area and somewhat tortuous. As the temperature is raised, and the cracks close to the extent that frictional load transfer can take place across them, the shear stiffness of the composite should increase. That such an effect does take place is illustrated by measurements of shear modulus at several temperatures up to 2500°C [1].

Shear behavior is closely related to tensile or compressive behavior in directions other than the principal yarn directions. Such "off-axis" tensile or compressive tests can be used to rigorously derive the shear modulus and to infer a good approximation to the shear stress-strain behavior [3] [4]. For example, uniaxial compression in the 45-degree off-axis direction (bisecting the 90° angle between two yarn sets) may be resolved into "on-axis" shear plus biaxial compression (Figure 1). As the shear deformations in typical orthogonal carbon-carbons will be large relative to the compressional strains, such tests offer a convenient way of studying shear behavior. Figure 2 shows schematically some of the essential features of the stress-strain response of 3D carbon-carbons tested in 45-degree off-axis compression at room temperature:

a) the strains attained are much higher than strains-to-failure in on-axis tests;

b) the stress-strain curves are smoothly non-linear and much of the non-linear strain is recovered on unloading. (Non-linearity frequently occurs in on-axis tests, but is usually accompanied by jogs in the curve that are attributed to progressive cracking of filaments, and other irreversible effects).

A technique has been developed to obtain replicas of specimen surfaces while the specimens are under load in a mechanical-test machine. Replicas were made from a 45° off-axis compression specimen of one of the materials (D) described by Seibold [5]. These replicas were then processed for viewing in the electron microscope, and photographs were taken in a scanning electron microscope. The replica is essentially a "negative" of the specimen surfaces; thus cracks and pores appear as protrusions in the photos. Figure 3 shows the development of a crack within a yarn bundle at strains of about 5 percent. No other type of damage is readily apparent at this magnification. On a much finer scale, at about 5000X magnification, there appears to be an opening of very fine cracks in the matrix between filaments within a yarn bundle. The high strains measured in such specimens appear to be accommodated by distortions of existing cracks, extension of cracks surrounding yarn bundles, and formation of new cracks within the yarn bundles. None of these processes appear to involve breakage of filaments.

These are preliminary results. Encouragement may be derived from the success of the observational technique: there appears to be much more information to be gleaned from more detailed photography and from taking replicas at other load conditions (including zero load after unloading).

The smooth non-linear loading/unloading stress-strain curve in off-axis compression is qualitatively similar in essential features to the stress-strain response of bulk graphite in uniaxial compression. In studies of prooftesting graphite [6] [7], it was found that annealing after loading would restore the original dimensions of the specimen (erase the residual strain) and also restore the virgin stress-strain response. The mechanisms underlying this phenomenon are not well understood. Some controversy surrounds the question whether polycrystalline graphite deforms non-linearly by means of classical dislocation-motion plasticity or by means of crack opening or by both mechanisms. It would be of interest to discover whether the carbon-carbon system also responds to annealing in the same way as does graphite.

References

1) Jortner, J., Proc. Army Symposium on Solid Mech., pp 81-97, AMMRC MS 76-2 (Sep. 1976).
2) Jortner, J., at this conference (1977).
3) Greszczuk, L. B., Douglas Aircraft Company Paper No. 3670 (Sep. 1966).
4) Petit, P. H., ASTM STP 460, pp 83-93 (1969).
5) Seibold, R. W., at this conference (1977).
6) Seldin, E. H., Carbon 4, 177-191, (1966).
7) Jortner, J., Proc. Conference on Continuum Aspects of Graphite Design, pp 641-651, USAEC CONF-701105 (Feb. 1972).

Acknowledgements

The work was sponsored by the McDonnell Douglas Corporation under an Independent Research and Development program. The author thanks J. A. Zelik for devising the concept and technique of replicating specimens while under load, V. Kerlins for implementation of the replication and microscopy, and J. C. Peck for stimulating discussions of the results.

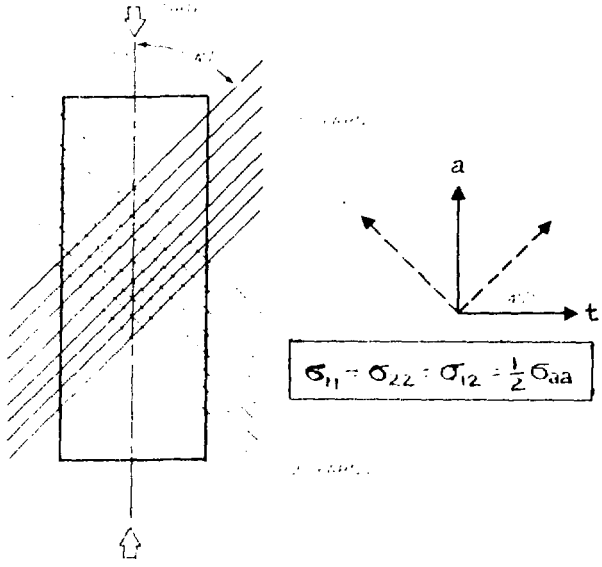


Figure 1. Off-axis compression test of 3D carbon-carbon composite.

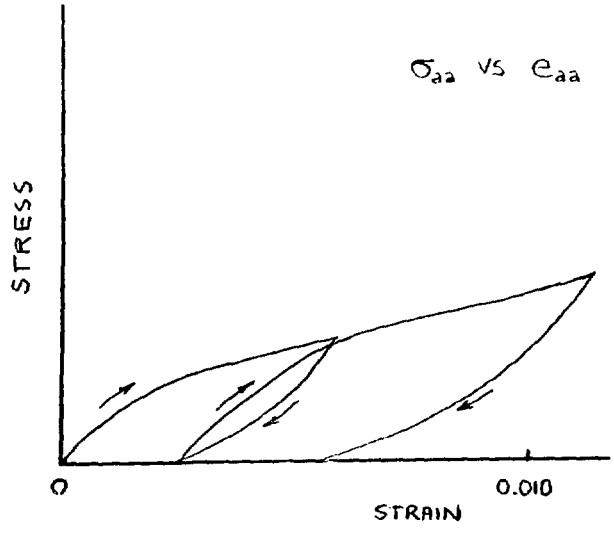


Figure 2. Typical stress-strain response.



Figure 3. Replicas of the same region at two loads during an off-axis compression test of a 3D carbon-carbon (Material D):

Top: at zero load

Bottom: at 5500 psi stress and approx. 5 percent strain

Note extension of cracks around yarn bundle at center of photo and occurrence of new crack through the bundle.

A STUDY OF THE DEPENDENCE OF [illegible] ON [illegible]

F. P. Kennedy, Vanderbilt University, Nashville, Tennessee

and

C. E. Kennedy, Metals and Ceramics Division, Oak Ridge National Laboratory

The relationships of strength to porosity and grain size for many polycrystalline ceramic materials have been examined extensively in numerous investigations.[1-4] These studies, through the careful preparation of fabricated ceramics and glasses, have produced several empirical formulas, generally rationalized by fracture mechanics. Extending these concepts to the applications of graphite, Knibbs, Andersson, Buch, Zimmer, and Meyer[5-8] have proposed similar relationships of strength to porosity and grain size. However, experimental verification of these proposals was obtained from testing poorly defined, commercially available materials. Buch, Zimmer, and Meyer emphasize the need for a clear definition of the structural morphology to define the critical defect. The purpose of this study is to furnish unambiguous experimental information to compare the various empirical strength-particle size relationships. This is accomplished by testing graphites fabricated using a green isotropic filler of carefully controlled particle sizes. The graphites were made to achieve the same final 1.5 g/cm³ bulk density. By controlling the fabrication and density, particle size is the single variable. This investigation also considers the particle size effect on other physical properties; the coefficient of thermal expansion (CTE), electrical resistivity, fracture strain, and Young's modulus.

Isotropy is obtained by using green Robinson filler coke to fabricate the experimental graphites. This coke, made from an air blown petroleum residuum, has a very solid, fine, randomized optical domain structure. The graphites were made using an ORNL process[9] to plasticize the outer surfaces of the green filler coke. This is done to obtain highly efficient bindering with uniform packing of moldings with fillers of a very narrow size range. Coal tar pitch 50M was used as a plasticizer and A-240 petroleum pitch was used as the final binder. The plasticized filler particles were carefully screened to obtain the particle size ranges given in Table I.

Four 10 mm-dia moldings were made and baked under restraint. One molding was graphitized without impregnation and a second molding impregnated with petroleum pitch before graphitization to 3000°C. This was to assure that the final graphite densities or porosities were over a common range. This was very successful, as shown in Table I, except for the two larger particle size ranges. The 450-μm material was improved significantly by a second impregnation; however, the larger 725-μm material was very resistant to densification. As shown in Table I (third column), the shrinkage of the initial filler size in processing is calculated and given.

The graphites were evaluated by testing a minimum of three brittle ring samples, 18-mm-OD, 10-mm-ID, and 6.4 mm thickness, from each block to yield the bend strength, Young's modulus, and fracture strain. Two 6.4 mm-dia samples, across-grain and with-grain, were made to determine the electrical resistivity and the 1000°C mean coefficient of thermal expansion (CTE). The porosity-dependent properties were either interpolated or extrapolated for each particle size range for comparisons to be made at a common 1.85 g/cm³ density. The properties measured are given in Table II.

Table I. Particle Size Range and Final Bulk Density of Fabricated Graphite

Particle size Range (μm)	Mean Particle Size Screened (μm)	Shrinkage (%)	Bulk Density, g/cc Impregnation	
			Without	With one Pitch
105-125	115	9.0	1.84	1.91
125-149	137	11.0	1.86	1.89
149-177	163	13.0	1.85	1.90
177-210	194	13.5	1.86	1.87
210-250	230	18.0	1.89	1.90
105-149	127	10.0	1.84	1.87
125-177	151	11.0	1.84	1.86
149-210	180	14.0	1.85	1.90
177-250	211	15.0	1.84	1.84
300-590	345	15.0	1.75	1.78[1.86][a]
590-1000	690	22.5	1.69	1.71[1.83][a]

[a]Impregnated twice.

Several attempts have been made to define the relationships between the strength of brittle polycrystalline solids to porosity and grain size. We found that the particle size data may be described by the Petch relationship; however, for these data the asymptotic (σ_o) stress was not equal to zero, as indicated in other studies for graphite. Therefore, the more convenient Knudsen relationship for particle size combined with the Ryshkewitch-

The generally accepted model for fracture of polycrystalline graphite is that a crack propagates from pore to pore normal to the stress axis, following paths of least resistance. This may be along optical domain boundaries or around the boundaries of misaligned particles. There actually exists microcracking well below the failure stress which increases in number with increasing applied stress. The microcracking is associated in magnitude to the nonlinear component of the stress-strain behavior of graphite. The ability of a graphite to achieve large strains to failure is limited by the ability of the structure to accommodate homogeneous microcracking without resulting in rapid crack propagation to failure. The microcracking is actually a stress-relief system which differentiates graphite from classically brittle ceramic materials.

*This work was funded by the Naval Surface Weapons Center under Contract No. N-60921.

†Operated by Union Carbide Corporation for the Energy Research and Development Administration.

Table II. Properties of 1.85 g/cm³ Graphites

Particle Size (μm)	Fracture Strength (MPa)	Fracture Strain (%)	Modulus of Elasticity (GPa)	Resistivity (μΩ-cm)	1000°C CTE (C^{-1} · 10^{-6})
725	46.2	0.68	10.3	850	6.35
430	52.1	0.71	11.3	880	6.50
180	68.3	0.75	12.3	1000	6.55
170	71.0	0.80	13.0	970	6.76
155	75.8	0.81	13.3	955	6.71
140	79.3	0.84	13.1	970	6.79
130	77.9	0.86	13.0	960	6.87
120	80.0	0.86	13.1	990	6.86
110	81.4	0.88	13.1	960	6.91
100	84.1	0.89	13.7	1000	6.93
90	86.9	0.91	13.1	950	6.95

Duckworth expression for porosity is used:

$$\sigma_f = \sigma_0 \, e^{-\alpha p} \, D^{-m} \qquad (1)$$

where σ_f = fracture strength (MPa), σ_0 = zero porosity strength (644 MPa), p = fractional porosity, α,m = constants (α = 3.47, m = 0.312), D = particle size (μm). The independence of porosity and particle size is assumed; however, while the particle size-strength relationship is demonstrated over a log cycle, the strength-porosity data were only available from 15 to 22% for the 430-μm material.

These graphites made using a filler with uniform 3-4 μm optical domains compared to a minimum 70 μm particle size emphasize the interparticle pore as the possible weak link controlling fracture. However, it must be realized that the pore size is controlled by the filler particle size. The value of m = 0.312 (less than 0.5) suggests that the critical size or pore size does not decrease proportionately with decreasing particle size. This can be shown to be associated with the known tendency for agglomeration with decreased particle size increasing the effective length of the pores.

Young's modulus was found to have a similar exponential function of porosity; however, the generally assumed independence of particle size was not observed. We found the following expression necessary to describe the decreasing modulus with increasing particle size:

$$E = E_0 \, e^{-\beta p} \, D^{-n} \qquad (2)$$

where E = Young's modulus (GPa), E_0 = zero porosity modulus (31.6 GPa), β,n = constants (β = 2.2, n = 0.11), p = fractional porosity, D = particle diameter (μm). This implies that a rationalization of the modulus of elasticity must include the effects of nonspherical porosity and defective particles which reduce the inherent spring constants within the structure.

The total strain (ε_T) to fracture can be separated into two components, the elastic strain (ε_e) and a nonlinear component (ε_c) resulting from crack extension.

$$\varepsilon_T = \varepsilon_e + \varepsilon_c \qquad (3)$$

The elastic strain can be represented by

$$\varepsilon_e = \sigma_f/E = \sigma_0/E_0 \, e^{(\beta-\alpha)p} \, D^{n-m} \qquad (4)$$

from Eqs. (1) and (2). Subtracting the elastic strain from the total strain to failure, we found that the nonlinear strain was constant and independent of particle size. However, the fracture strain did increase with decreasing porosity, as expected.

$$\varepsilon_c = 3.2 \cdot 10^{-3} \, e^{-1.5 \cdot p} \qquad (5)$$

and

$$\varepsilon_T = \sigma_0/E_0 \, e^{(\beta-\alpha)p} \, D^{n-m} + 3.2 \cdot 10^{-3} \, e^{-1.5 \cdot p} \qquad (6)$$

This suggests that there exists, for each structural morphology, a strain component due to microcracking that is independent of particle size.

The less-than-theoretical value of CTE is a result of the material expanding into the defect structure. Therefore, as the particle size is reduced by breaking the particles through the defects, the defect concentration is reduced. The CTE is shown to increase with reduced particle size as

$$(1000°C) \; CTE = 8.57 \, D^{-0.0[illegible]} \qquad (7)$$

No apparent effect of porosity was observed. The very small defect structure in these particles is obvious by the very large CTEs shown in Table II for this material and the fairly small increase due to reduced particle size.

Finally, it is noted that while electrical resistivity (ρ) has a strong dependence upon porosity, it is thought to be independent of particle size. We found, again like the modulus, that a logarithmic function represents the 1.85 g/cm³ data fairly well.

$$\rho = 1500 \, D^{-0.0[illegible]} \; \mu\Omega\text{-cm} \qquad (8)$$

In summary, this study has yielded experimental data which describes the dependence of physical properties upon particle size. These data emphasize the need to describe the structural morphology in detail, particularly in defining the microstructural defect-controlling fracture. These results clearly describe a defect which is not equal to nor linearly related to the particle size; however, as suggested by Knudsen, it is logarithmically related to the particle size. It is also shown that while the total fracture strain increases with reduced particle size, the nonlinear or crack strain is constant for constant porosity. While not expected, both the modulus of elasticity and the electrical resistivity increased with decreasing particle size. The coefficient of thermal expansion also increased with decreasing particle size, but was less than expected.

References

(1) E. Orowan, *[illegible]*. 12, 186–232 (1948).
(2) H. J. Petch, *J. Iron [illegible]*, (London), 174 [1], 25–28 (1953).
(3) F. P. Knudsen, *J. Am. [illegible]*, 42[8], 376–387 (1959).
(4) S. C. Corniglia, *J. Am. [illegible]*, 55[12], 610–618 (1972).
(5) R. H. Knibbs, *J. [illegible]*, 24, 174 (1967).
(6) C. A. Andersson and E. I. Salkovitz, *[illegible]*, p. 275, 1973.
(7) J. D. Buch, ASTM-STP-605, pp. 124–141, 1976.
(8) J. E. Zimmer and R. A. Meyer, *[illegible]*, p. 95, 1975.
(9) C. R. Kennedy, *11th Biennial Conference on Carbon*, p. 304, 1973.

THE TEMPERATURE DEPENDENCE OF ELASTIC CONSTANTS OF POLYCRYSTALLINE GRAPHITE

J. D. Buch
Prototype Development Associates, Inc.
Santa Ana, California 92705

Introduction

The graphite crystal structure exhibits extremely high anisotropy in bonding, as evidenced in the thermal conductivity, thermal expansion, and elastic constants. The anisotropy of these bulk properties appears well correlated to the preferred orientation of the crystalline phases. The elastic constants of bulk graphite exhibit a temperature dependence which is not representative of direct crystalline properties (i.e., a maximum near the final fabrication temperature). This behavior is not typical of the behavior of polycrystalline forms of less anisotropic elements.

The anisotropy of the crystalline elastic constants is related to the first derivative of the interatomic force versus distance relationship; i.e., the harmonic bonding approximation. The anisotropy of the thermal expansion coefficients depends upon the second derivative of the interatomic force relationships; i.e., the anharmonic aspects of the various bonds. The temperature dependence of the elastic constants in the classical regime is rooted, in part, in the anharmonic aspects of the various bonds.

The purpose of this note is to explore the relationships between free thermal strains, restrained cool-down strains in bulk graphites, and their interaction through the anharmonic aspects of the bonding between basal planes.

Theoretical Aspects

The simplifying notion that the final graphitization temperagure, T_g, approximates a stress free state will be used. During cool-down, the "c" directions of the crystal will undergo very large free contractions, while the "a" directions will contract considerably less. If there is good particle to particle bonding, this will give rise to constraint of the "c" direction contraction and the development of tensile strains and stresses in the "c" directions. Compressive strains and stresses will also be developed in the "a" directions.

Because of the large differences in stiffness between the "a" and "c" directions, most of the differential contraction will be taken up by developing large "c" direction strains. The magnitude of these strains, ϵ^*_{33} will be a function of the microstructure, including factors such as the relative particle to particle orientations, the general degree of preferred orientation, the location of pores and cracks, and the convolution of basal planes within the coke particle. For the present purposes, their magnitude at temperature, T, will be estimated as

$$\epsilon^*_{33} \simeq 1/3(\alpha_c - \alpha_a)(T_g - T) \qquad (1)$$

where α_c and α_a are the crystalline thermal expansion coefficients.

Mrozowski (Ref. 1) has argued that these strains give rise to microcracks and a resulting decrease of elastic modulus. The microcrack closing and unspecified "healing" which occurs upon reheating is taken to be the physical basis of the modulus dependence. While microcrack formation associated with this mechanism does occur, not all of the differential microstrains are relieved and it is difficult to accept chemical or other means of restoring the stress carrying ability of basal plane cracks at relatively low temperatures.

Seldin (Ref. 2) and others, have observed that the only crystal elastic constants which are of the same order of magnitude as bulk elastic constants are those of basal plane extension and shear (C_{33} and C_{44}). Based upon this, the bulk elastic behavior appears to be dominated by crystalline shear. Therefore, factors which reduce the basal plane elastic constants will result in reduction of bulk elastic stiffnesses.

Green and Spain (Ref. 3) have recently reported experimental determinations of the anharmonic elastic constants of the basal plane

$$\frac{1}{C_{33}}\frac{\partial C_{33}}{\partial \epsilon_{33}} \sim -15 \quad \text{and} \quad \frac{1}{C_{44}}\frac{\partial C_{44}}{\partial \epsilon_{33}} \sim -10 \qquad (2)$$

These are in good agreement with values deduced by Kelley (Ref. 4) from theoretical studies of the thermal expansion coefficients and elastic moduli. Very strong sensitivity of elastic constants to layer spacing is implied. The tie between anharmonic basal plane bonding, thermal expansion, and bulk elastic response is through Eqs. (1) and (2) and an appropriate particulate composite relationship; e.g., Price (Ref. 4) or Smith (Ref. 5).

Results

Combinations of Eqs. (1) and (2) provides the following approximations for the effective in situ elastic crystal constants.

$$C^*_{44} = C_{44}\{1-1/3(10)(\alpha_c-\alpha_a)(T_g-T)\} \qquad (3)$$

$$C^*_{33} = C_{33}\{1-1/3(15)(\alpha_c-\alpha_a)(T_g-T)\} \qquad (4)$$

Specifically, for $T_g - T = 2400^oC$, and $\alpha_c - \alpha_a = 35 \times 10^{-6}/C^o$ the approximate in situ elastic constants are

$$C^{*}_{11} \quad 0.72\, C_{11} \quad \text{and} \quad C^{*}_{33} \quad 0.58\, C_{33} \; . \qquad (5)$$

These imply a 28 to 42 percent decrease in room temperature bulk stiffness as a result of cooldown from graphitization.

Discussion

The present rationalization of temperature dependence of elastic properties is unique to highly anisotropic crystal structures, and would not occur in highly symmetric crystal structures. The rationalization of the influences of differential thermal contraction, bond anharmonicity, and bulk properties is schematically summarized in Fig. 1, where the departure from behavior of ordinary solids is emphasized.

Actual mesophase coke microstructures need explicit attention. High degrees of preferred orientation as occur in some pyrolytic graphites and fibers would result in far less average differential contraction and, by implication, less peaking of modulus versus temperature. Modulus versus temperature trends for pyrolytic graphite, T50 fiber and ATJS bulk graphite in Fig. 2 support this hypothesis. More normal modulus behavior occurs in the absence of large differential cooldown strains (Fig. 3).

The concept of altered in situ crystalline elastic coefficients (and possibly thermal expansion coefficients by a similar approach) as a function of layer plane spacing could provide an important step in developing quantitative structure-property relationships for various carbon forms. An important contribution to neutron irradiation induced increases in elastic constants of reactor graphites may be through the relief of cooldown micro stresses accompanying point defect formation and/or migration. Also, the role of the anharmonic bonding terms would imply that for bulk graphites, elastic linearity is only an approximation at any strain level and therefore unequal mechanical stiffnesses in tension and compression could logically follow. The differential crystalline stresses are also often considered the source of the observed strength increases with temperature.

Conclusion

The rational use of in situ crystal constants differing from the free crystal constants has potential for contributing to the understanding of the complex structure properties relations known to exist in carbon forms.

References

1. Mrozowski, S., Proc. 1st and 2nd Carbon Conference (1956).
2. Seldin, E. J., Carbon, 4, 177 (1966).
3. Green, J. F., et al., J. Phys. Chem. Solids, 34, 1927 (1973).
4. Kelly, B. T., Carbon, 10, 435 (1972).
5. Price, R. J., Phil. Mag., 12, 561 (1965).
6. Smith, R. E., et al., Carbon, 14, 185 (1976).

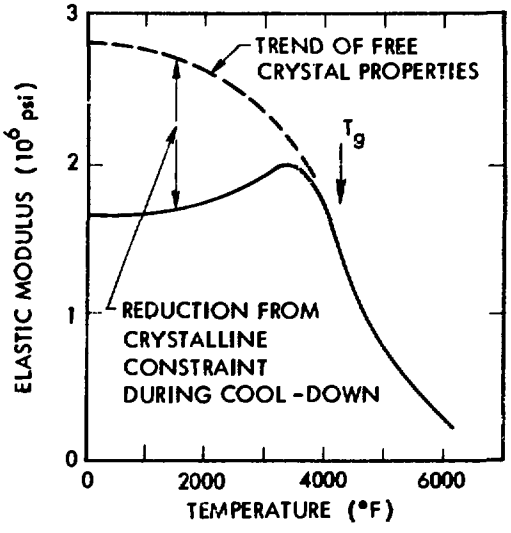


Fig. 1. Crystalline and Bulk Modulus Vs. Temperature

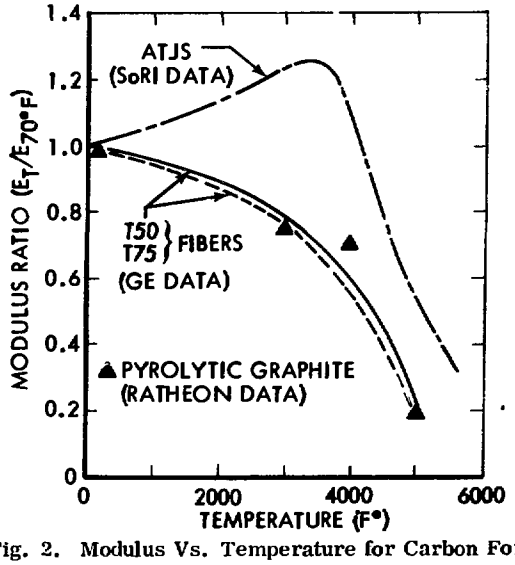


Fig. 2. Modulus Vs. Temperature for Carbon Forms

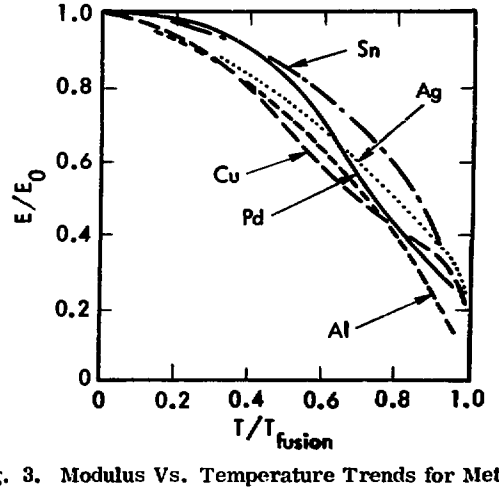


Fig. 3. Modulus Vs. Temperature Trends for Metals

OXIDATION MECHANISMS OF CARBON-CARBON COMPOSITES

H. W. CHANG AND R. M. RUSNAK

Bendix Research Laboratories
Southfield, Michigan 48076

Introduction

The performance of carbon composites as aircraft friction materials is dependent on the oxidation resistance of the composite. In order to improve this oxidation resistance, the mechanisms by which oxidation occurs over the range of temperatures encountered in aircraft braking should be understood. Therefore this investigation was undertaken to determine the rate controlling mechanisms as a function of oxidizing temperature. In particular attempts were made to differentiate between chemisorption, diffusion through pores, and diffusion through a stagnant gas film.

Experimental Procedure

The composite used in this study was made out of 25% binder A, 15% binder B, 40% carbon fiber and 20% filler. Two forms of composites were studied. One was in bulk form having dimensions of 1.250 x 1.000 x 0.250 in. (henceforth called bulk composite). The other was in ground form with submicron particle sizes (henceforth called ground composite). Three different kinds of test samples were investigated: They were heat-treated at different temperatures ranging between 1000 and 2400°C. The heat treatment was done with an induction furnace under a 99.998% pure argon atmosphere.

The oxidation rates of ground composite were measured by thermogravimetric analysis on a DuPont 950 analyzer, using 5 mg samples. A 100 cc/min flow of air was used as the oxidizing gas. The oxidation rates of bulk composites were measured using a quartz tube furnace. A periodic weight measuring procedure was used. The reaction rates were calculated from plots of weight against reaction time between 5 and 10% sample burn-off.

Results and Discussion

The oxidation rates of both ground and bulk composite were found to follow the Arrhenius type equation:

$$\text{rate} = A \cdot \exp(-E_a/RT)$$

Table I summarizes the activation energies for ground and bulk composites heat-treated at different tempratures. The range of activation energy for bulk composites is 10.5 to 29.5 kcal/mole while ground composites have a range of activation energies between 35 and 43.3 kcal/mole. The fact that the activation energy of the ground composite is greater than that of the bulk composite (Table I) from 450 to 650°C indicates that the bulk composite oxidation is occurring by diffusion through pores in this temperature range. The grinding reduces the diffusion path length of the pores such that it is no longer limiting and chemisorption which has a higher activation energy than diffusion through pores becomes the rate controlling oxidation mechanism. If no change in activation energy has occurred with grinding, then it would be concluded that chemisorption was the rate controlling mechanism for bulk composite oxidation. In fact, the bulk composite activation energies are about one half of those of the ground composite as shown in Table I. This is in agreement with Wheeler's discussion (1) which indicates that if the rate controlling step of oxidation is diffusion of oxygen into the pores, the activation energy will be one half of the value one would obtain under a strictly chemically controlled case. Therefore, in the temperature range from 450 to 650°C for bulk composite, the diffusion through pores is the controlling oxidation mechanism. Although the activation energies for ground composites are greater than those for the bulk, its values (35.0 - 43.3 kcal/mole) are still somewhat lower than those for pure carbon or graphite (2) (50-58 kcal/mole). This may be attributable to impurities in the material which are known to lower the activation energy (3).

As the reaction temperature increases, Wicke points out (4) that the rate controlling step becomes the diffusion of oxygen through the stagnant film to the exterior of the carbon sample. Under such a case, Walker (2) shows that the oxidation rate is proportional to the square root of the reactant flow rate, i.e.

$$\frac{\text{Rate (1)}}{\text{Rate (2)}} = \left(\frac{\text{flow (1)}}{\text{flow (2)}}\right)^{1/2}$$

In order to define the temperature at which the diffusion through a stagnant gaseous surface layers becomes the rate controlling step, the oxidation rates of bulk composites were measured at higher temperatures than the preceding experiments at different flow rates. Table II summarizes the results. At 750°C, the relation between rate ratio and flow ratio holds very well, indicating that the predominant oxidation mechanism at this temperature is diffusion of oxygen through the stagnant gas film. However, at 650°C the above equation

does not hold, confirming that the pore diffusion mechanism is dominant at this temperature.

In conclusion the rate controlling mechanisms in carbon composite oxidation is diffusion through pores in the temperature range from 450 to 650°C, while between 650 and 750°C the rate controlling mechanism shifts to diffusion through a stagnant film.

References

1. Wheeler, A., Adv. in Catalysis 3 249 (1951).

2. Walker, Jr., P. L., Rusinko, Jr., F., and Auston, L. G., Adv. in Catalysis II 133 (1959).

3. Rakszawski, J. E. and Parker, W. E. Carbon 2 53 (1964).

4. Wicke, E., Proceedings of Fifth Symposium on Combustion p 245 Reinhold, New York 1955.

TABLE I COMPARISON OF ACTIVATION ENERGY (KCAL/MOLE) (REACTION TEMPERATURE 450-650°C)

SAMPLE	GROUND	BULK	RATIO (BULK/GROUND)
A	35.0	10.5	0.30
B	39.1	19.8	0.51
C	43.3	29.5	0.68

TABLE II RATIOS OF OXIDATION RATES AND FLOW RATES (BULK COMPOSITE)

Flow (cc/min)	$\left(\frac{\text{Flow}}{\text{Flow} = 100}\right)^{\frac{1}{2}}$	650°C		750°C	
		Rate (% Loss/Min)	$\frac{\text{Rate}}{\text{Rate } (F = 100)}$	Rate (% Loss/Min)	$\frac{\text{Rate}}{\text{Rate } (F = 100)}$
100	1.00	0.11	1.0	0.29	1.0
500	2.24	0.13	1.2	0.71	2.4
1000	3.16	0.15	1.4	0.97	3.3
1500	3.87	0.16	1.5	1.03	3.6

ACTIVATED CARBON TEXTILES

RICHARD N. MACNAIR
US Army Natick Research and Development Command, Natick, Massachusetts

Introduction

Activated carbon can be incorporated in various forms into permeable materials for use in protective clothing. Garments made of these materials are sorptive to chemical vapors and aerosols and could be used to prevent contact of chemicals with skin of personnel in areas where chemicals are manufactured or used. Such garments would thus reduce or eliminate real and potential hazards to chemical plant or laboratory workers who may be exposed to harmful chemicals which can be absorbed through the skin. Garments of this type are generally more comfortable than nonpermeable protective gear because they are air and moisture permeable.

Sorptive textile materials having potential for use in garments can be made in various ways. These include surface coatings with activated carbon powder, impregnation with activated carbon powder, and carbonization and activation of a suitable yarn or fabric precursor.

Surface Coatings

Surface coatings can be applied by dusting the powder onto a fiber, fabric, or porous film but the amount of activated carbon deposited in this manner is severely limited by surface area of the material and low adhering forces. Fabric, of course, holds more of the carbon powder than film or fiber because of particle entrapment between fibers or yarns, but it does not adhere well. One potential solution to this problem is to use a suitable binder with the carbon. Evaluation at the US Army Natick Research and Development Command, Natick, of a carbon/binder mixture applied to a solid monofilament of nylon has indicated that considerable additional research would be required to prevent rupture and flaking of the coatings when the filament bends, and rubs against another. Similar problems were anticipated with film and fabric so this method was abandoned in favor of other approaches.

Impregnation

Impregnation of various materials with an activated carbon powder slurry containing an acrylic latex binder has met with more success than filament coating. Treatments of this type have been applied to woven fabric, non-woven fabric and foam. Each of these types of treated material was prepared from an aqueous slurry of the carbon by immersion of the material in the slurry, squeezing out the excess between two rolls and drying the product. Sometimes more than one immersion is necessary to obtain a desired add-on of the slurry. By varying the amount of carbon in the slurry and the number of immersions it is possible to obtain maximum sorptivity consistent with fabric capacity. A tightly woven fabric has less capacity or void space for such a slurry than does a loosely woven or loosely constructed non-woven fabric. An open celled foam has the largest capacity. Fabrics which have been investigated at Natick for such impregnations are cotton sateen, reinforced nylon non-woven fabric and reinforced polyurethane foam.

Another useful way to impregnate material is to incorporate the activated carbon powder into the base material before the textile material is made. Porous film, porous sheet, filament or yarn containing activated carbon is thus obtainable. Using this method of impregnation polypropylene filament as well as Teflon composite sheets containing high carbon loadings have been prepared by Natick and W. L. Gore and Associates, respectively. The latter material is related to Gore-Tex* fibrillated or expanded Teflon film. Activated carbon has also been mixed with viscose dope and the mixture spun and coagulated into monofilament fibers. As high as 80% carbon has been incorporated into viscose monofilament by this method. Sorptivity of all these materials varies with the amount of carbon which can be incorporated and with the amount of pore blockage. Viscose yarn and fabric and the Teflon porous sheet material containing activated carbon were highly sorptive while polypropylene filament was less sorptive due to an increased diffusion barrier and substantially less carbon content.

Yet another way of incorporating activated carbon in materials is to insert the carbon in the core of a hollow tube or filament. This has been done successfully at Natick on an experimental scale using polyethylene and polypropylene and the resulting filaments have shown a degree of sorptivity in spite of the film barrier between the source of vapor and the carbon.

Carbonization and Activation

A more direct method of obtaining activated carbon textile materials is to carbonize and activate a suitable fabric or yarn precursor such as viscose, phenolic, acrylic, or other material. Activated carbon fabric in a plain weave has been prepared at Natick. The British material may soon be available commercially. Activated felt was prepared by Barnebey Cheney and Carborundum. Roving was prepared by Carborundum. Monofilament yarn was, or is being, prepared from viscose yarn by Union Carbide, 3M Company, and Georgia Institute of Technology under contract with the US Army Natick R&D Command. All of these materials can be made with high surface area, i.e., above 800m^2/g and are highly sorptive but they do not have sufficient textile properties to be used for clothing by themselves. Thus, they must be combined with other textile materials. For this purpose, activated carbon yarns have been incorporated into knitted and woven fabrics and activated carbon fabrics have been attached to other fabrics by stitching or laminating. Some of these composites were described at the 12th Biennial Carbon Conference.

*Trademark of W. L. Gore and Associates, Elkon, MD

EVALUATION OF GASIFICATION REACTIVITIES OF COALS BY DIFFERENTIAL THERMAL ANALYSIS[a]

C. Chow, H.M. Hawthorne[b], E. Peters and I.H. Warren
Centre for Materials Research, University of British Columbia
Vancouver, Canada

Introduction

Thermal analysis of coals is inherently difficult because of the heterogeneity of the material, the complexity of the chemical reactions and the physical changes which occur during coal pyrolysis. However it has been shown that with careful experimentation D.T.A. can be useful both in differentiating between coals of differing rank and in characterizing some of the processes taking place throughout pyrolysis and carbonization [1]. D.T.A. has not been used significantly for assessing the reactivities of various coals towards gasification, even though most of the technologically important gasification reactions are either strongly exothermic or endothermic. We report here the results of some preliminary D.T.A. experiments made on several Western Canadian coals in an attempt to use the technique to assess their gasification reactivities.

Experimental

D.T.A. experiments were carried out using a DuPont-900 instrument in the normal manner except that a one-way (upward) gas flow was maintained in the combustion tube. Thermograms were recorded in dry air, N_2, CO, CO_2 and H_2 and steam atmospheres at various heating and gas flow rates. T.G.A. tests were run under similar conditions in air and N_2 to aid interpretation of the thermograms. Coals ranging in rank from semi-anthracite to lignite were tested.

Results and Discussions

Highly reproducible thermograms were obtained for all coals tested once optimum heating and gas-flow rates, sample packing and base-line compensation conditions etc. were established. In nitrogen atmosphere, D.T.A. thermograms reveal information about the internal processes occurring as coals are heated. Three distinct activities are present: (1) Dehydration of moisture at low temperatures (endothermic); (2) distillation and polymerization of volatiles in the range 300°C-500°C (exothermic) and (3) carbonization which continues to high temperatures (endothermic). D.T.A. in carbon dioxide does not differ from that in N_2 up to 800°C, but above this a strong endothermic peak occurs, due to reduction of CO_2. The inflection temperature of the endothermic peak, T_m, occurs in the range 900°C-1400°C depending on sample reactivity and heating rate. Typical thermograms for a lignite sample are shown in figure 1.

In CO atmosphere, there is no evidence for major additional activity, thermograms resembling closely those in nitrogen, although some methanation could have occurred (exothermic). In H_2 environment D.T.A. thermograms are even less informative, due primarily to high thermal conductivity of H_2 gas, which lowers the sensitivity of the system.

Reactivity towards the water gas reaction is found to vary not only with the heating rate, but also the 'soak period' of the coal in the steam prior to reduction of H_2O. The following have been observed: (1) a strong endothermic peak, at 950°C-1050°C depending on heating rate, which is due to the reduction of H_2O to CO and H_2; (2) broad exothermic peaks in the range 700°-800°C appear if steam is introduced at this stage or earlier, and the intensity increases with "soak period"; (3) a fast heating rate results in complete reduction to ash, while the slower the heating rate, the lower the extent of reaction at the same temperature. These observations confirm the fact that steam has an activating effect on coal towards hydrogenation and methanation, especially prior to the plastic zone. However the coal cannot be reactivated if it has undergone substantial carbonization.

Kinetic parameters can be obtained from the variation of endothermic peak inflection temperatures with heating rate [2,3]. Figure 2 shows plots of $\ln [(T_m^2)/\alpha]$ versus $1/T_m$ (α = heating rate) for present results and approximate activation energy and frequency factor values obtained from slopes and intercepts of these plots are listed in table 1. We note that deviation from linearity of such plots, as in the lignite (Hat Creek) coal, is frequently observed in diffusion-controlled processes [4].

The use of non-isothermal kinetic methods (eg. D.T.A.) to study reactivities of coal has many advantages over isothermal methods (e.g. T.G.A.), although the kinetic analysis is more complex since reaction rates are changing with temperature [5]. The reactivity of coal towards a gasification reaction at a certain temperature has meaning only if the detailed history of prior thermal treatment is included. Fortunately the use of the D.T.A. method monitors all changes taking place up to the temperature where reaction occurs. In the case of an isothermal method such as study of weight loss with time at a fixed temperature this important information is not obtained.

(a) Financially supported by Canada Centre for Mineral & Energy Technology (CANMET), Ottawa.

(b) Present address - National Research Council of Canada, Mechanical Engineering Division (Western Laboratory), Vancouver, Canada.

References

1. G.J. Lawson, Chapter 25 (SOLID FUELS) in "Differential Thermal Analysis" (Ed. Mackenzie), Academic Press, 1970.
2. G.F.J. Garlick and A.F. Gibson, Proceedings of the Physical Society, 60 (1948), 574.
3. W. Hoogenstraaten, Philips Research Reports, 13 (1958), 533.
4. A.C.D. Chaklader and R.C. Cook, J. Amer. Ceramic Soc., 47 (1968), 712.
5. "The Historical Development of Applied Non-isothermal Kinetics" by Joseph H. Flynn in "Thermal Analysis" Vol. 2, P. 1111, Edited by R.F. Schwenker, Jr. and P.D. Garn, Academic Press (1969).

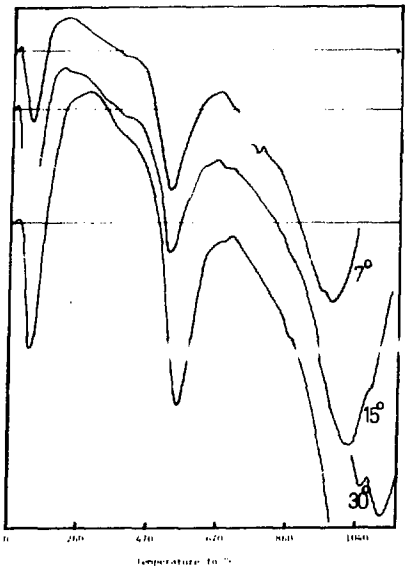


Fig.I. DTA endotherms of a Hat Creek coal(lignite) in I atmosphere of N_2 at 3 heating rates.

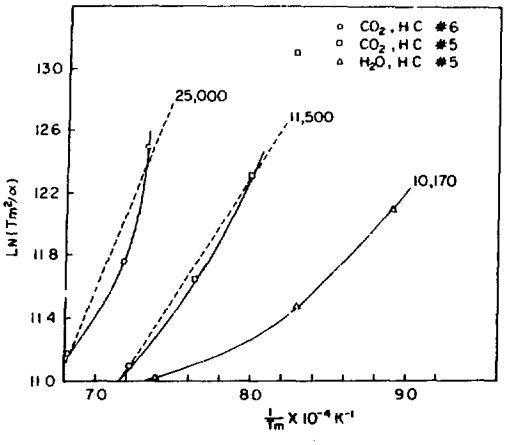


Fig. 2. Kinetic plots for Hat Creek coals in CO_2 and steam reactions.

Sample	E/R(K°)	K_o(Min^{-1})
HC#5 (CO_2)	11500	2.5 x 10^5
HC#6 (CO_2)	25000	50 "
Kaiser(Washed)	26315	207 "
HC#5 (H_2O)	10170	2.37 x 10^5

Table I. Kinetic parameters for gasification reactions with reacting gases given in parenthesis.

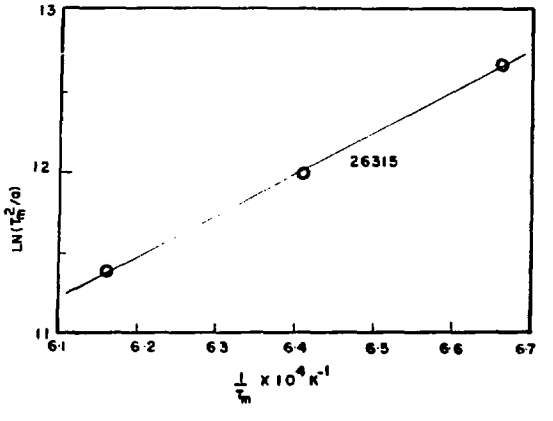


Fig.3. Similar plot for a Kaiser coal(semi-anthracite) where good linearity is observed,due to the absence of diffusion process.

INTERCALATION PROPERTIES OF THE CARBON LINERS OF ALUMINUM REDUCTION CELLS

J.G. Hooley
Department of Chemistry,
University of British Columbia, Vancouver, Canada
P.T. Hough
Arvida Research Centre
Aluminum Co. of Canada Ltd.

Introduction

The carbon lining of Al reduction cells does swell during its life as a cathode. This is believed to be caused by penetration of the carbon layer planes by the sodium produced by the action of Al on NaF. The nature of the solid solutions of Na in various carbons has been studied by Dewing(1) using an electrolytic technique. He found an activity coefficient which increased by a factor of 10^7 over the range of 1200° to 1800°C for the heat treatment of the carbon. He noted that the Fermi level also rises with temperature of treatment and, because Na intercalation involves a transfer of electron charge to the carbon layer planes, he concluded that intercalation would be favored by a low Fermi level and therefore a low temperature of heat treatment. Indeed, he found maximum swelling in the presence of Na for the carbon treated at 1200°C. This influence of temperature on the extent of Na intercalation has been confirmed by Metrot and Herold(2) and by Pflugmacker and Boehm(3). The latter found a surprisingly small increase in average interlayer spacing - only 0.045 nm for the maximum composition of C_{12} Na and less for carbon blacks treated above 1200°C. They concluded that the Na was intercalated in an irregular fashion with preference for those parts of the structure where the distance between layers is wider than the X ray average. This is again in agreement with the work of Dewing(1) who found no steps and therefore no stages of composition in his system.

It is noteworthy that the early work of Fredenhagen(4) showed that K, Rb and Cs all gave C_8 M with not only natural graphite but also with charcoal and lampblack. This has recently been confirmed by Salzano(5) for Cs in graphitized and non graphitized carbon blacks. The lack of an effect of graphitization and therefore of Fermi level on composition could be accounted for by the fact that the ionization potential of these three metals is lower than for Na.

It occurred to us that carbons could also be characterized by noting the uptake of an electron accepting intercalator. In this case, the content should be higher for carbons with the higher Fermi level that comes from a higher temperature of treatment. This has indeed been noted for Br_2. However, the amount of Br_2 intercalated by low temperature carbons is negligible. We therefore chose an electron acceptor which, in natural graphite, has a much lower threshold pressure for intercalation than has Br_2. This is $AlCl_3$ for which the threshold is $<10^{-6}$ relative to saturation as compared with 0.1 for Br_2. It will indeed intercalate pot liner carbon and has the added advantage that the amount intercalated can be differentiated from the amount adsorbed on a surface. This is because, in the absence of Cl_2, no uptake occurs in natural graphite of low surface area even in saturated $AlCl_3$(g) at the BP of 180°C(6). The inclusion, however, of ~20 torr Cl_2 allows rapid intercalation to give $C_{\sim 8}$ $AlCl_3$ 0.25 Cl_2(6). Hence, in carbons of higher surface area, one run is made on each of 3 samples, all at 180°C. One in $AlCl_3$(g) just below saturation, a second in pure Cl_2 at 500 torr and a third in $AlCl_3$(g) just below saturation + 500 torr of Cl_2. The sum of the first two is assumed to be adsorption and is subtracted from the third one to give the amount intercalated. This has been applied to carbon blacks and fibers(7) and is here applied to cell linings and associated materials.

Experimental

The original liner, the liner used for 3000 days and the electrically calcined anthracite (ECA) were ground, sieved and treated with boiling 6M HCl to constant weight. This required 30 hr. for the used liner, less for the others. The raw anthracite, pitch and tar were heated in a slow stream of N_2 to 500°C for a few hrs, then to 1000°C for 5 hrs. They were then ground and acid treated to constant weight. The % weight losses are shown in Table I and appear to be independent of sieve size for the original and used liner carbons. Duplicate samples were also reproduced.

The procedure for the intercalation runs on 0.3 gm samples has been published(7). In each case, any weight increase was treated as if it were $AlCl_3$ in calculating the molar ratios in Table 2. Again, reproducibility and independancy on mesh size were apparent. The expansion that should accompany intercalation was obvious. Thus, both the original and used cell material was, after intercalation, of much greater bulk volume - about a factor of two for the used material. It was also more porous and was blacker than before intercalation.

Discussion

The results for liner carbon are in accord with those of Dewing(1). Just as the electron donor Na was more intercalated by a carbon of low temperature of heat treatment and therefore of low Fermi level, so the electron acceptor $AlCl_3$ is less intercalated. Thus, raw anthracite treated for 5 hr. at 1000°C would not intercalate $AlCl_3$ but after electrical calcining (ECA) at 1700-1900°C would intercalate 19 units on the scale of Table 2. Similarly, whereas the original liner material intercalated 20 units, "use" for 3000 days at an average temperature of 900-950°C (maximum 1000-1050°C, minimum 850°C) raised this to 100 units. In fact the amount intercalated by this used liner carbon was about 80% of the amount intercalated by the highly ordered natural graphite. This is surprising, in view of the relatively low temperature of the liner during its life time. Since the graphitization has been found to occur in these lining materials in a very short period of time(8), it is postulated that free Na is a

prerequisite to such rapid structural changes. Holding anthracite at 1000°C for a short period of time (5 hr) did not produce any evidence of graphitization, and indeed there is no reason to believe that very long periods of time at this temperature would produce any graphitization.

The pitch and tar are interesting in that considerable intercalation of $AlCl_3$ does occur in samples heated for only a few hours at 1000°C. This is presumably because they initially contain a variety of large, flat, aromatic molecules which are able to align themselves in parallel sheets during the liquid phase of the heat treatment. Anthracites also contain large flat aromatic molecules but do not pass through a liquid phase on treatment of 1000°C. In the absence of the high mobility of a liquid phase, one must either extend the period of heat treatment, as with used liner carbon, or go to a higher temperature than 1000°C as with ECA.

It is of interest that both the original liner and the ECA intercalated 20 units of $AlCl_3$. The liner contains 15% pitch and tar and 85% ECA and on a simple composition basis would be expected to intercalate 24 units of $AlCl_3$. The difference however, could be caused by the fact that the heating cycle for the pitch and tar in the liner carbon was not the 5 hr at 500°C + 5 hrs at 1000°C used in this laboratory.

Table 1

	500°C	1000°C	6MHCl
Liner, original			
20-40 mesh			0.8
100-170 mesh			1.9
Liner, used			
20-40 mesh			40
100-170 mesh			41
ECA			0.5
Anthracite	4	3	0.6
Pitch	49	7	0.1
Tar	72	5	0.3

Percent weight decrease in N_2 stream or in boiling acid.

Conclusion

Intercalation of disordered carbons by $AlCl_3$ is favoured by higher calcination temperatures. It is also enhanced by the prior reordering of the structure by intercalating sodium which occurs in all aluminum reduction cells during electrolysis. It is also favored by a liquid phase during the heat treatment of a pitch or tar. These are all factors that increase both the degree of graphitization and the Fermi level so that intercalation by an electron acceptor is favored. Dewing(1) has shown that such factors would decrease the intercalation of an electron donor such as Na. He therefore finds that a melt of Na_3AlF_6 and and Al causes less swelling and hence less Na intercalation, in a carbon that had been heated to a higher temperature. Hence the measurement of $AlCl_3$ intercalation described in this paper might be of value in characterizing carbons for use as lining materials in Al reduction cells.

References

1. Dewing E.W. Trans. Met. Soc. AIME 227 1328 (1963).
2. Metrot A. and Herold A. J. Chim. Phys., Physico Chim. Biol. 71, 73 (1969).
3. Pflugmacher I. and Boehm H.P. Proc. 3rd Conf. Ind. Carbon and Graphite, London (1970), 62.
4. Fredenhagen K. and Cadenbach G. Z. anorg. allg. chem. 158, 249 (1926).
5. Salzano F. and Aronson S. J. Inorg. Nucl. Chem. 30, 2317 (1968).
6. Hooley J.G. Carbon 11, 225 (1973).
7. Hooley J.G. Carbon 13, 469 (1975).
8. Waddington, J. Extractive Metallurgy of Aluminum Vol. 2 ed. G. Gerard Interscience 1963 pg. 435.

Table 2

Acid treated "Carbon"	1 $AlCl_3$	2 Cl_2	3 $AlCl_3$+Cl_2	3-2-1 Intercalated
Natural graphite	0.0	0.0	120	120
Liner, original				
20-40 mesh	0.7	0.2	21.2	20
20-40 mesh	1.3	0	20.8	19
100-170 mesh	0.9	0.2	21.6	20
Liner, used				
20-40 mesh	2.8	0.1	102	99
3000 days				
20-40 mesh	5.5	0.0	106	100
100-170 mesh	3.0	0.1	96	93
ECA 1800C				
20-40 mesh	1	0	19.6	19
Anthracite 1000C				
20-40 mesh	0	0	0.5	0.5
Pitch 1000C				
20-40 mesh	1	0.3	50.8	49
Tar 1000C				
20-40 mesh	1	0.5	61.2	60

Weight increase as moles $AlCl_3$ per 1000 moles carbon.

KINETICS OF PYROLYTIC CARBON DEPOSITION AT HIGH TEMPERATURES AND LOW PRESSURES

A. Wehrer, P. Wehrer and X. Duval
Centre de Cinétique Physique et Chimique du CNRS
B. P. 104
54600 VILLERS les NANCY - France

The kinetics of carbon deposition by heterogeneous decomposition of carbon containing gases on carbon surfaces has been studied at temperatures between 1000 and 2000°C. The possibility of gas phase reactions has been eliminated by the use of sufficiently low gas pressures. Experiments have been carried out with a molecular flow of gas passing over an electrically heated carbon filament, the reaction products being continuously analyzed with a mass spectrometer. Different reactants have been used for comparison, including hydrocarbons (methane, ethane, ethylene, acetylene, allene, diacetylene, benzene, naphthalene, anthracene) and CH_3Cl and C_6H_5Cl (carbon-halogen compounds decompose without carbon deposition). Decomposition of hydrocarbons evolves almost exclusively hydrogen.

Methane and ethane decompose very slowly and a carbon deposit can barely be detected. Rates of decomposition of other hydrocarbons are about a thousand times faster, and surprisingly are not very different: at 1400°C, the collision yields, i.e., the ratios of number of reacting molecules to number of impinging molecules on the surface, range between 10^{-4} and 10^{-5}. The effect of temperature on reaction rates is remarkably similar for all these carbon deposition reactions: the rate increases with temperature up to a maximum at about 1400°C, and then decreases from this temperature to about 1900°C. The occurrence of a maximum in reaction rate followed by a negative temperature coefficient is of course quite unusual for chemical reactions. Surface area determinations by means of physical adsorption have shown that it is not due to a change in the roughness factor of the surface of deposited carbon, which remains approximately constant at a value of about 4.5. It is not due either to a variation of the accommodation coefficient of reactant molecules, which also remains approximately constant.

This unusual change of reaction rate with temperature is however akin to that observed previously in all carbon gasification reactions under comparable temperature and pressure conditions. It had then been shown that upon temperature changes, stationary reaction rates were not obtained immediately, but through transient rates, decreasing or increasing, following respectively an increase or decrease of temperature. A detailed experimental investigation of these transient effects (which are also observed upon pressure changes) has led to the conclusion that the (small) reactive part of the surface is increased *by gasification of the solid, but the new reactive sites* so created can be destroyed by thermal healing; this latter effect predominates at higher temperatures and is responsible for the negative temperature coefficient.

It is remarkable and significant that qualitatively similar transient effects are observed in carbon deposition reactions. The question which arounce immediately is: are the reaction sites reactive in gasification reactions also active in decomposition reactions with carbon deposition? There is effectively a good correlation between the reactivities of a carbon surface with respect to both gasification and deposition. A surface enriched with reactive sites by a gasifying reactant under proper conditions, will temporarily show an enhanced activity with respect to deposition reactions. Even more significant is the following experiment: if two reactants (at different partial pressures), one gasifying and the other depositing carbon, are made to react simultaneously with a carbon surface, the faster reaction rate will determine the stationary concentration of reactive sites and impose the rate of the other reaction.

THE INFLUENCE OF THE TYPE OF QUINOLINE INSOLUBLES ON THE QUALITY OF COAL TAR BINDER PITCH

D. R. Ball
Union Carbide Corporation, Carbon Products Division
Parma Technical Center, Parma, Ohio 44130

The Coal Tar Research Association, now amalgamated with the British Carbonization Research Association, has been running a cooperative series of tests on coal tar pitch binders with aluminum producers. Some of the tests have already been reported in the literature[1]. A more recent series[2], concerned with the importance of the nature of the quinoline insolubles, QI, also has relevance to the graphite electrode producer. The seven pitches involved have been evaluated as binders by measuring the flexural strength of 19 mm diameter graphite electrodes. The evaluation was carried out at British Acheson Electrodes Limited (Union Carbide Corporation).

The pitches were produced from a single tar. The tar was centrifuged into QI rich and QI lean fractions by the British Steel Corporation. The Pitch A produced from the QI rich tar is a typical graphite electrode binder pitch. The seven pitches denoted A through G were produced by CTRA. It will be appreciated from the table that the pitches differ principally in the type, or origin, of the QI, viz "natural", carbon black, and mesophase. Two pitches were produced by straight run distillation: these contain the so called "natural" QI. A third, natural QI, pitch was made by mixing low QI pitch with QI concentrate. The QI content of the low QI pitch was also increased both by the addition of a carbon black in attempt to simulate natural QI, and by the addition of mesophase through heat treatment.

A conventional processing scheme, an all flour petroleum coke, and a common binder level (25% w/w pitch), were adopted. No effort was made to optimize the process to each binder. The 19 mm rods were all baked, and graphitized, together as a group.

There are two conclusions to be drawn from the results summarized in the table:

(a) The typical electrode pitch (QI rich pitch A) is superior.

(b) The addition to the QI lean material of QI as natural QI concentrate, carbon black, and mesophase through heat treatment, did not upgrade the lean material.

References

1. Mason, C. R., Fuel 1970, 49, 165.

2. Betts, W. and Sharp, J., private communications.

PITCH						GRAPHITE PROPERTIES			
	Properties								
Description	SP, °C Mettler	MCC %	BI %	QI %	QI type	Density Mg/m³	Flexural Strength MN/m²	σ	n
Pitch A, produced from QI rich fraction by distillation.	108	58.2	36	13	natural	1.54	16.1	1.2	8
Pitch E, produced from QI lean fraction by distillation	112	55.4	28	1	natural	1.50	14.4	0.5	7
Pitch D is pitch E enriched with natural QI concentrate.	111	58.8	36	13	natural	1.53	14.1	0.7	6
Pitch B, produced from QI lean tar heat soaked at 410°C.	113	58.1	36	14	4% natural 10% mesophase	1.49	11.4	0.9	6
Pitch G, produced from QI lean tar heat soaked at 380°C in presence of 1,8 dinitronaphthalene.	114	58.1	36	15	4% natural 11% mesophase	1.52	12.1	0.7	7
Pitch C, produced from QI lean tar distilled after addition of carbon black.	110	56.7	31	13	4% natural 9% black	1.51	14.5	0.8	6
Pitch F is pitch E with added carbon black.	112	57.1	33	12	4 natural 8 black	1.52	13.8	0.7	6

(a) The mesophase content (as QI) was calculated by difference.
Notes (a) SP - Softening Point MCC - Modified Conradson Carbon n - number of rods processed.
(b) The carbon black used was Philblack G, ASTM No. N660, a furnace black of particle size 460 Å.

USE OF PETROLEUM RESIDUES AS BINDER PITCHES - - RELATION OF FIXED CARBON AND SOFTENING POINT OF PITCH WITH COMPONENT PROPERTIES AND CORRELATION OF BINDING POWER WITH FIXED CARBON OF ITS COMPONENTS

H. Tanaka, T. Tano, E. Kitajima,* Y. Yamada and H. Honda**
*Osaka Research Laboratory, Koa Oil Company, Takaishi-shi, Osaka 592, Japan
**National Industrial Research Institute of Kyushu, Tosu-shi, Saga 841, Japan

1. INTRODUCTION

The purpose of this experimental program was three-fold:-

(a) to determine the relationship between the fixed carbon (FC) content of a pitch with the FC of its component parts.
(b) to determine the relationship between the softening point (SP) of a pitch and the SP of its component parts.
(c) to determine if a relationship exists between the binding strength of a pitch, when used as an electrode binder, and the FC properties of its component parts.

2. EXPERIMENTAL

Four petroleum products were selected to be used to make pitches which were used as the basis for the test program. These basic products were vacuum residue from Gach Saran Crude (G), vacuum residue from Arabian Light Crude (L), Decant Oil from a fluid catalytic cracker (F), ethylene plant tar from a naphtha cracking plant (N). And a commercial binder pitch made from coal tar (T) was also included for comparison.

Each of these feeds were heat-treated at 420 -440°C from 10 to 240 minutes to make pitches which were solvent fractionated into the following three fractions shown as Figure 1:

(i) Benzene insolubles (A fraction)
(ii) Benzene soluble but n-heptane insolubles (B fraction)
(iii) n-heptane solubles (C fraction)

The fixed carbon (FC) and softening point (SP) of each whole pitch and each fraction were tested. These test results are shown in Table 1 along with the weight percent of each fraction. FC was measured by Japan Industrial Standard JIS K 2425 which is similar to ASTM method No. D 2416. In this test the quantity of residual or fixed carbon is determined after the sample has been heated at 800°C for 30 minutes. SP was measured using a micro melting point procedure as developed by National Industrial Research Institute of Kyushu.

Afterwards each pitch was blended with electrode grade coke and heated to 1,000°C to make a electrode test piece for strength testing. The compressive strength of each test piece made with the various pitches is also included on Table 1.

3 RESULTS AND DISCUSSION

An attempt was made to determine what was the relationship between the FC of the whole pitch and the weighted average FC of its three fractions. Figure 2 shows plot of the sum of the weighted averages of the fraction FC vs. the FC of the whole pitch. It can be seen that it is necessary to add a correction factor, α, to the weighted average sum of the products FC to make it equivalent to the FC of the whole pitch. As seen from Figure 2, the value of α calculated is approximately 7.2 such that the following relationship can be written:

$$FC_{Pitch} = (FC_A)(A) + (FC_B)(B) + (FC_C)(C) + \alpha \quad \ldots\ldots (1)$$

where,

(1) FC_{Pitch}, FC_A, FC_B and FC_C are the test values of fixed carbon of the pitch and its three fractions, and,
(2) α is the correction factor. (approx. 7.2)

The need for α is probably due to the effect of mutual interaction between each fraction during carbonization of pitches.

As a second experiment, an attempt was made to develop a relationship between the SP of the whole pitch and its three fractions. However, the SP of the A fraction was too high to measure, being above 400°C. Therefore, the following regression equation was used for a trial test with a pseudo SP (SP ps.) for the A fraction:

$$SP_{Pitch} = (SP\ ps.)(A) + (SP_B)(B) + (SP_C)(C) + \beta \quad \ldots\ldots (2)$$

where SP_B and SP_C are the values of the SP of the B & C fractions, respectively, and β is a constant.

Regression results based on the above formula show $SP_{ps.}$ to be 413 and β to be -96. A plot of observed SP_{Pitch} values vs. calculated values using the above formula is shown in Figure 3. This relationship shows a good correlation factor of 0.94. As with α in the FC relationship, the need for β as a correction factor is considered to be the effect of chemical and/or physical interaction between each fraction.

As a final goal an attempt was made to develope a relationship which would predict pitch binding capability, when used as an electrode binder, with component FC property. Basis a regression analysis it was found that the following three factors have a strong statistical relationship with the binding strength of pitch:

(i) The average FC of fractions A and B
(ii) The difference between FC_A and FC_B
(iii) B, the wt. fraction of benzene solubles/n-heptane insolubles

As such, the following equation was found to give the best estimate of pitch binding strength, which is defined as, F-value:

$$F = \left[\frac{FC_A + FC_B}{2} + (FC_A - FC_B)\right] \times (B) \quad \ldots\ldots\ldots (3)$$

Values of F calculated from the above formula for the pitches tested have been listed in Table 1 next to the compressive strength of the electrode using this pitch as a binder. The relationship between F-value and electrode strength has been plotted in Figure 4. This correlation seems to be reasonably predictive, having a correlation factor of 0.87.

Table 1 Properties of pitches and its fractions

Symbol	Heat treatment condition (°C)	(min.)	Pitch C/H Ratio Atom.	Pitch FC (wt%)	Pitch SP (°C)	Fractions Yield (wt.%) A	B	C	Fractions FC(wt.%) A	B	C	Fractions SP (°C) B	C	Binding power Comp.1) Strength	F-2) value (x 10)
G	430	60	1.09	58.8	132	33.6	21.8	44.6	71.5	71.4	28.1	225	30	530	156
La	420	120	1.15	59.6	107	34.0	20.3	45.7	71.6	71.8	27.8	300	30	370	145
Lb	430	60	1.16	59.4	129	32.5	27.1	40.4	69.0	73.0	29.8	300	42	690	182
Lc	440	34	1.26	63.8	141	36.9	23.7	39.4	69.3	75.4	33.9	300	52	500	157
Ld	430	80	1.40	71.1	208	53.5	17.8	28.7	75.5	64.1	35.7	300	48	75	144
Na	420	15	1.29	59.9	132	24.4	35.1	40.5	78.2	68.7	27.8	300	37	860	291
Nb	430	10	1.34	59.7	129	20.6	39.8	39.6	72.5	70.5	28.1	300	60	960	293
Nc	430	60	1.50	69.1	164	47.4	23.0	29.6	72.1	68.1	27.9	300	50	410	170
Fa	430	150	1.45	49.4	57	25.6	28.7	45.7	66.3	59.1	17.3	125	30	380	201
Fb	430	210	1.53	53.6	74	30.2	28.8	41.0	72.0	60.3	17.1	115	30	720	224
Fc	440	120	1.57	55.3	82	32.8	29.4	37.8	74.6	57.0	17.5	110	30	950	245
T	-	-	1.79	60.9	99	30.5	43.6	25.9	78.3	57.4	16.6	120	30	910	387

1) Compressive strength of baked carbon block (kg/cm^2), 2) Calculated by equation (3)

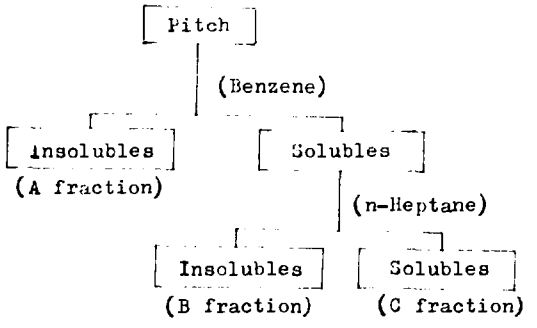


Fig. 1 Fractionation scheme

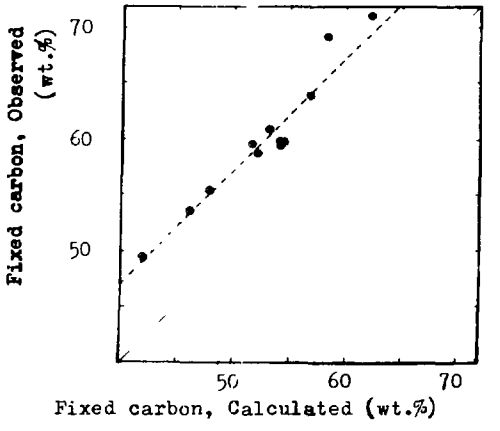


Fig. 2 Relation of FC, Actual and Calculated

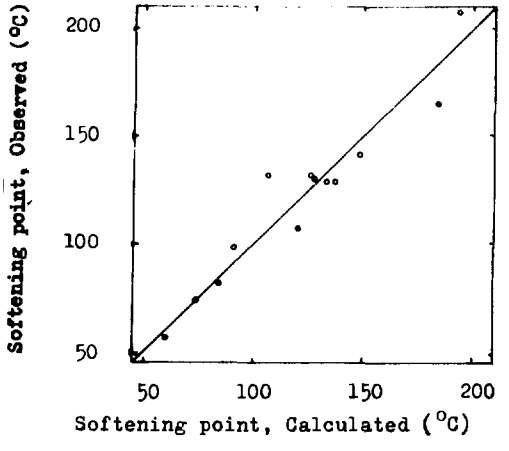


Fig. 3 Relation of SP, Actual and Calculated

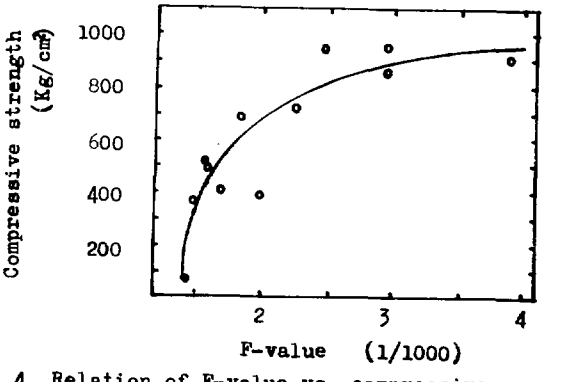


Fig. 4 Relation of F-value vs. compressive strength

CHEMICAL CHANGES DURING THE MILD AIR OXIDATION OF PITCH

J. Barr and I. C. Lewis
Union Carbide Corporation, Carbon Products Division
Parma Technical Center, Parma, Ohio 44130

Introduction

Oxidation and air blowing is an important step in processing of certain carbonaceous materials. Air oxidation has been used in the manufacture of asphalts[1], preparation of binder pitches[2], and in thermosetting pitch fibers[3]. Extensive oxidation is known to introduce cross-linking and lead to disordered carbon structures.[3,4] Chemical mechanism[5] and mesophase formation[6] studies on the effects of oxidation on carbonaceous materials have also been reported.

This paper presents the results of an investigation of the effect of mild air oxidation on well-graphitizing pitches derived from coal tar and petroleum. Various techniques have been used to monitor the chemical changes which occur during the oxidation process and to relate the results to subsequent graphite development.

Experimental

A. Materials

The coal tar and petroleum pitches were commercially available materials. The Mettler softening point of the coal tar pitch was 110°C, whereas the petroleum pitch exhibited a Mettler softening point of 122°C.

B. Air Blowing

The apparatus used in the air blowing experiments consisted of a heated resin flask fitted with a stirrer, condenser, and fritted glass inlet tube for the air. The temperature of the pitch was monitored by using a thermocouple immersed in the liquid pitch. The samples (650 grams) were heated rapidly to their softening points, and then at a rate of 38°C/hr. to 250°C. Air flow was maintained at 1 to 1.5 liters/minute. Air blowing was continued at 250°C for 6 to 8 hours to achieve softening points of 175° to 180°C.

C. Distillation

The distillation was performed at a pressure of about one micron using standard laboratory glassware.

Experimental Results

A. Pitch Properties

Pitches with softening points of 175±5°C were prepared by air blowing and by vacuum distillation of the coal tar and petroleum pitches. The products were characterized by solubility in benzene and quinoline and by elementary analysis. These data, along with the product yields, are given in Table I. The results show that the air oxidation of both materials leads to a greater increase in the benzene insolubles content than is found for the distilled pitches. This effect is greatest for the petroleum pitch. The solubility in quinoline was essentially unaffected by the air blowing.

Both distillation and air blowing lead to an increase in atomic carbon-hydrogen ratio. Furthermore, the carbon-hydrogen ratios were equal after distillation and air blowing of each pitch. Only the petroleum pitch showed a small increase in oxygen content as a result of air blowing.

B. Infrared Analysis

The infrared spectra of the air-blown coal tar and petroleum pitch did not show absorptions which could be attributed to oxygen containing functional groups. The oxidized petroleum pitch showed a slight decrease in aliphatic hydrogen absorptions.

Table I

Summary of Properties of Distilled and Air Blown Pitches

	Coal Tar Pitch		
Property	As Rec'd	Distilled	Air Blown
Softening Point, °C	110	173	174
Yield of Distilled/Air Blown, %	---	80	93
Benzene Insoluble, %	32.7	42.7	49.0
Quinoline Insoluble, %	13.2	16.1	16.7
Carbon, %	93.2	94.3	94.0
Hydrogen, %	4.24	4.00	4.01
Oxygen, %	1.4	1.2	1.6
Atomic C/H Ratio	1.83	1.96	1.95

	Petroleum Pitch		
Property	As Rec'd	Distilled	Air Blown
Softening Point, °C	122	178	181
Yield of Distilled/Air Blown, %	---	75	93
Benzene Insoluble, %	8.6	13.1	29.4
Quinoline Insoluble, %	0.3	0.1	0.1
Carbon, %	93.6	94.1	93.4
Hydrogen, %	5.58	5.34	5.26
Oxygen, %	0.39	0.50	1.2
Atomic C/H Ratio	1.40	1.47	1.48

C. NMR Analysis

High resolution proton NMR spectra were obtained for the pitches before and after oxidation. The petroleum pitch was much more aliphatic than the coal tar pitch and contained numerous alkyl side chains. The aromatic

hydrogen contents for the two starting materials were 57% and 91% respectively. After oxidation, the soluble portion of the petroleum pitch showed a slight increase in aromaticity while the NMR spectrum of the coal tar pitch was relatively unchanged.

D. Gel Permeation Chromatography (GPC)

Molecular weight data for toluene soluble portions of the pitches by GPC were obtained by procedures described previously[7]. The results are listed in Table II.

Table II

Molecular Weight Analysis (GPC) for Treated Pitches

Pitch	Toluene Sol.%	$\overline{Mw}$	$\overline{Mn}$	D
Untreated Petroleum	85	606	564	1.075
Distilled Petroleum	78	654	595	1.099
Oxidized Petroleum	59	635	579	1.098
Untreated Coal Tar	58	521	507	1.029
Distilled Coal Tar	45	519	504	1.030
Oxidized Coal Tar	43	518	503	1.029

The data show a decrease in solubility and an increase in molecular weight with air oxidation of the petroleum pitch. There was essentially no difference in the GPC data for the distilled and air blown coal tar pitches.

E. Mesophase Development

Samples of the distilled and air oxidized pitches were heat treated further in an inert atmosphere to produce mesophase. There was little difference in the nature and amount of mesophase produced by the subsequent heat treatments, although the air oxidized pitch contained a large amount of nonmesophase pyridine insolubles.

F. Graphite Structure

The pitches were heat treated to 3000°C and x-ray analyses were obtained for the graphitized samples. The x-ray interlayer spacing data are given in Table III.

Table III

X-ray Interlayer Spacings for Graphitized Pitches (3000°C)

Pitch	$C_o/2$, Å*
Untreated Coal Tar	3.363
Distilled Coal Tar	3.363
Oxidized Coal Tar	3.362
Untreated Petroleum	3.360
Distilled Petroleum	3.355
Oxidized Petroleum	3.357

*Average of (004), (006), and (008) spacings.

Discussion

Our results show that the effects of mild oxidation on well-graphitizing pitches lead mainly to an increase in molecular weight without necessarily introducing oxygen into the product. This reaction appears more facile with the less aromatic petroleum pitch. Both mesophase formation studies and x-ray analysis of the derived graphites show that the oxidative treatments have little effect on the ultimate graphitization process. These conclusions are consistent with an oxidative mechanism involving a dehydrogenative condensation of the relatively high molecular weight aromatic components in the pitches.

References

1. E. J. Barth, Asphalt Science and Technology - Gordon and Breach Science Publishers, New York (1962), p. 386.

2. H. Abraham, Asphalts and Allied Substances, Volume II, D. Van Nostrand & Co., New York (1961), p. 98.

3. S. Otani, Carbon, 3, 31 (1965).

4. J. S. Kipling, J. N. Sherwood, P. V. Shooter, and N. R. Thompson, Carbon, 1, 315 (1964).

5. I. C. Lewis and L. S. Singer, Summary of Papers presented at the American Carbon Society Ninth Biennial Conference on Carbon, Boston College, June 16-20 (1969).

6. F. Gootarzi, G. Hermon, M. Iley, and H. Marsh, Fuel, 54, 105 (1975).

7. I.C. Lewis and B.A. Petro, J. Poly. Sci., 14, 1975 (1976).

PYROLYSIS MECHANISM AS STUDIED BY ELECTRON MICROSCOPY, DTA, IR AND ESR

A. OBERLIN[+], M. VILLEY[+], A. COMBAZ[++], P. ROUYHET[+++] and P. SETTON[++++]

[+]Lab. Marcel Mathieu (ER 131 du CNRS) Université d'Orléans 45045 Orléans,France

[++]Compagnie Française des Pétroles 39, quai A. Citroën 75739 Paris 15,France

[+++]Lab. de Physico-chimie Université de Louvain 1348 Louvain la Neuve Belgique

[++++]Lab. d'Etudes Physico-chimiques Université d'Orléans 45045 Orléans,France

Carbon ability to graphitize first depends on its precursor chemical composition (hydrogen or oxygen rich) then on experimental pyrolysis conditions : reticulation by air, for instance, which changes carbon properties, is technologically important. The present work considers controlled pyrolysis of two materials : A material is relatively hydrogen rich and oxygen poor (sporopollenin H/C 1,56 O/C 0,34), B material is hydrogen poor and oxygen rich (lignite H/C 1,12 O/C 0,44). For both samples 140 mg have been packed in a covered graphite crucible and heat-treated in a N_2 flow at 4 /mn. Differential thermal analysis (DTA) was performed during heat-treatment. Samples corresponding to various representative points of the DTA curve were subjected to rapid quenching under inert gas out of the furnace. They have been used for weight loss measurements (WL), chemical analysis, infra red spectrometry (IR) electron-spin resonance (ESR) and electron microscopy (EM) studies. Carbonization paths of A (dashed line) and B (full line) materials are represented in the Van Krevelen patterns of fig. 1 (H/C atomic ratio is plotted versus O/C atomic ratio). The corresponding weight losses (WL) and rates of WL (DWL) as well as DTA curves are respectively represented in fig. 2, 3 and 4.

Visual observation as well as optical and scanning microscopy studies show that sporopollenin (A material) melts at 436 C (point n 3) while B material (lignite) remains powdered. The large diffuse exothermic peak in the DTA curve of A followed by an exothermic plateau and the two diffuse peaks of B correspond to tar departure. For B they are shifted toward the lower HTT and the first maximum in DTA coincide with the maximum rate of tar departure (peak in DWL curve). On the contrary for A it is the beginning of the DTA plateau which coincides with DWL curve peak (after melting). Maximum WL for A material is much higher than for B (80 as compared to 60).

Numbered samples on DTA curve were studied in dark-field (DF) high resolution EM. The incident beam is progressively tilted relatively to a small objective aperture set paraxial (diameter 0,18 A^{-1}, Airy disc diameter $\simeq$ 7 Å) and the optical image is observed during tilting (1,2). Bright dots appear on a dark-field whenever a hkl scattered beam passes through the aperture. In all samples, bright dots less than 10 Å in size appear only when 00.2, 10 and 11 beams of turbostratic carbons are approximately paraxial and thus pass through the aperture. These dots have been verified to be real objects in using through-focus series and various apertures (3). Stacks of aromatic molecules containing 2 or 3 layers and less than 10 aromatic rings thus become obvious.

If the 00.2 beam is only used for DF imaging, the carbon layer stacks which appear as bright dots are those situated edge-on on the supporting film. For A material all samples heat-treated below 460 C (numbered from 1 to 5 on DTA curve) show bright dots homogeneously distributed in the particles. Since they are distributed as such, the stacks are thus at random in the material. In the n 6 sample corresponding to the DTA plateau at 460 C the bright dots gather in clusters about 1.000 Å in size (fig. 5). For producing clusters, carbon layers of neighbouring stacks have to lay parallel. A molecular orientation has thus been developed in regions about 1.000 Å in size. Misorientation of the carbon layer stacks can be described by evaluating first their azimutal disorder (twist), then their deviation from the Bragg angle (tilt). Twist is approximated to the 00.2 ring portion intersected by the aperture ie 40 . Tilt is evaluated by using a goniometer stage ie $\pm$ 30 . For HTT higher than 460 C size of the stacks and extent of the molecular orientation remain constant. Therefore bright dot cluster contrast increases. Since neither twist nor tilt changes the contrast improvement should be due to a decrease in layer distorsions. It is probably related to the progressive disappearance of non aromatic molecules linked to the layers. For B material all the samples can be considered as containing aromatic layer stacks distributed at random (it is only above 1.000 C, that very small clusters of bright dots occur, the molecular orientation extent is in this case smaller than 50 Å).

The A material (sporopollenin) has been treated 5h at 200 C in air (reticulation). The curves in dotted line in fig. 1 to 4 respectively represent its carbonization path, WL, DWL and DTA. It is noticeable that reticulated A sample is then absolutely comparable to B : carbonization path is slightly lower and weight loss as well. The two diffuse DTA peaks are reduced to one and it is shifted toward the low HTT. Molecular orientation characteristic of A sample (1000 Å in size) disappears and the material does not melt.

A material is extremely sensitive to experimental conditions. For instance, if a very small amount of sporopollenin (< 10 mg) is heated in an open crucible (4) under a nitrogen gas flow the material does not melt and the molecular orientation almost disappear (< 50 Å in extent).

These data can be correlated to IR spectra (5) obtained on all the samples indicated by a representative point on WL curves (fig. 2). For A material heated in a covered crucible (dashed line DTA curve) molecular orientation occurence coincides with the extremum of aromatic CH groups, after OH, carbonyl

and carboxyl groups have practically disappeared and when aliphatic CH groups have reached a low value. This occurs slightly before the maximum spin concentration as measured by ESR (6,7).B material is quite different from A : OH groups are more numerous in B and their number decreases very slowly during heat-treatment. Aliphatic CH groups are less numerous and their number decreases faster while aromatic CH are both much less numerous and more stable when heat-treated. New groups C-O-C not present in A material occur in B and remain remarkably stable for a HTT as high as 600°C. Reticulation of A material or even heat-treatment of A in an open crucible changes the amount of various groups so as to increase OH groups and to decrease aliphatic CH groups and aromatic CH groups.

Chars issued from A or B materials may be considered as built-up of a few aromatic rings molecules (4-10 rings) piled up by 2 or 3. They are connected by non aromatic structures. If the latter are mainly aliphatic tar yield is large. First melting then occurence of a local molecular orientation are favoured. They are also favoured by all the factors which lead to tar retention. Molecular orientation occurs after melting when the rate of tar departure is maximum producing a maximum of mobility of the aromatic molecule stacks. Molecular orientation is reduced or inhibited when oxygen content increases and when tar percentage decreases which corresponds to a linkage between stacks of aromatic molecules. This can be related to the C-O-C groups which appear in B material. Finally reticulation mechanism should be first related to a combination of oxygen and aliphatic carbon groups (8) which produce water and is responsible for OH increase and aliphatic CH decrease in IR spectra. Then melting and consequently molecular orientation should be inhibited by linkage due to C-O-C bonding developing in A material after reticulation.

(1) A. Oberlin, J.L. Boulmier and B. Durand, Geochim. & Cosmochim. Acta, 38, 647 (1974).

(2) A. Oberlin, G. Terrière and J.L. Boulmier, Tanso (Japan), 80, 29 and 83, 153 (1975).

(3) A. Oberlin, M. Oberlin and M. Maubois, Phil. Mag. 32, 833 (1975).

(4) M. Villey, A. Oberlin and A. Combaz, C.R. Acad. Sc., 282 D, 1657 (1976).

(5) P. Rouxhet, unpublished data.

(6) R. Setton, personal communication.

(7) J. Sallé, Thèse Orléans (1977).

(8) D.W. Van Krevelen, Coal, XXVI, 463 (1961). Elsevier ed.

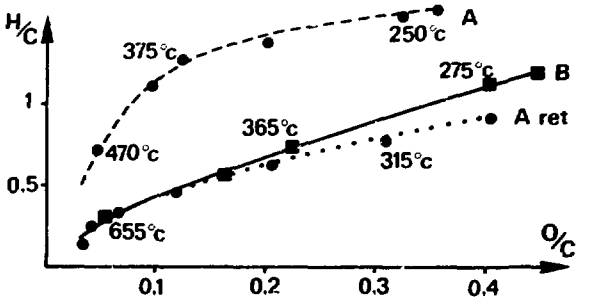


Figure 1

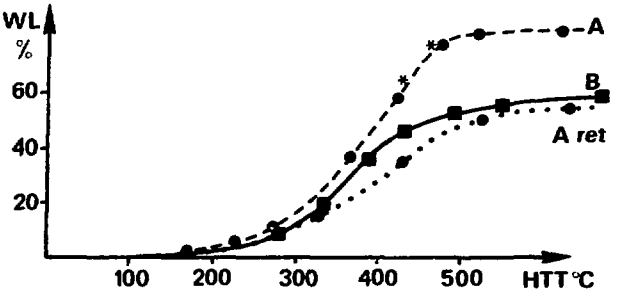


Figure 2

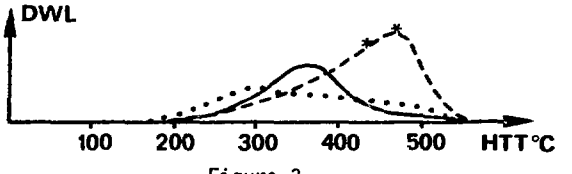


Figure 3

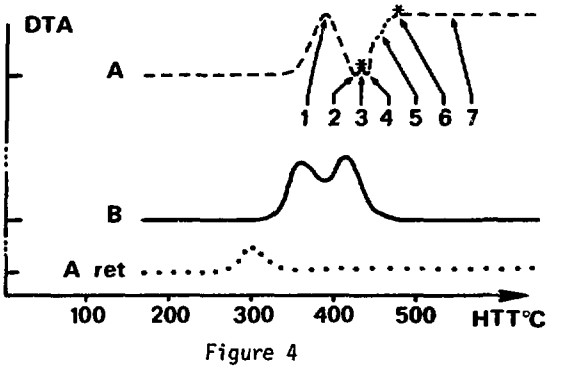


Figure 4

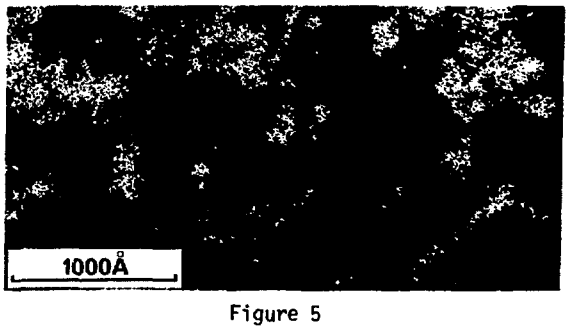


Figure 5

THE PROCESS OF CARBONIZATION AND GRAPHITIZATION OF PETROGRAPHIC COMPONENTS OF HARD COALS
PART I. PROPERTIES AND STRUCTURE AND THE COKING PROCESS OF PETROGRAPHIC COMPONENTS OF HARD COALS

S.JASIEŃKO, H.KIDAWA
Politechnika Wrocławska, Wrocław, ul. Gdańska 7/9, Poland

The basic petrographic components of hard coals-vitrinites, exinites, micrinites, fusinites, differ considerably in their properties and structure even within particular ranks of coals [1-12].

Despite numerous investigations on the behaviour of coals on heat treatment there is missing a full discernment in the literature even on the coking process of petrographic components separated from coals of a full coalification scale and no investigations were carried out on their process of graphitization.

In the paper the results of investigations on the separation, properties and structure of petrographic components from coals of the Polish Coal Basins /The Upper and Lower Silesian Coal Basin/, with a peculiar regard to their behaviour on heat treatment are presented.

Separation of petrographic components

The basic petrographic components - vitrinite, exinite, micrinite and fusinite - were separated from coals of various ranks: flame coal /79,%C/, gas-coking coal /83,3%C/, orthocoking coal /89,3%C/, meta/semicoking coal /87,2%C/ and anthracite /91,7%C/.The separation of the petrographic components was carried out by the organic heavy liquids method /carbon tetrachloride and toluene/.All the petrographic components: vitrinite, exinite, micrinite and fusinite could be isolated in case of flame and gas-coking coal.From the remaining coals only vitrinite and fusinite were isolated.In the most pure form, the vitrinites /97,2-99,2%/ and fusinites /93,8 - 98,4%/ were isolated, the lower degree of purity of the obtained exinites /90,4 and 93,8%/ is caused by appearance of a strong fusion of exinite with other components. The isolated micrinites are the concentrates containing 50% of the pure component.

Properties and structure of petrographic components

The petrographic components within all ranks of coals, show that there are differences which appear in the physico-chemical and technological properties and in the structure.Most visibly they are marked in the coals of lower rank.

The content of volatile matters decreases towards: exinites-vitrinites-micrinites -fusinites.The content of C element is the lowest in the vitrinite, higher in exinite and micrinite, and the highest in the fusinite.The content of hydrogen falls towards:exinite-vitrinite-micrinite-fusinite The highest content of oxygen have the vitrinites and micrinites, the lowest fusinites.Most of aliphatic and alicyclic compounds /2930,2860,1450,1380 cm^{-1}/ appear in exinites, considerably less in vitrinites, not much in micrinites.The vitrinites and the exinites in comparison with correspondent micrinites contain higher quantities of aromatic hydrogen /910 - 750 cm^{-1}/.The aromatic groups of the hydrogen in case of vitrinites are the best developed in gas-coking and orthocoking coals.A great part oxygen functional groups in exinites and vitrinites are the hydroxyl groups of phenolic type /3700 - 3100 cm^{-1}/, which in micrinites and fusinites appear in very small quantites. The content of functional groups changes in a characteristic way with coalification.In exinites, vitrinites and micrinites with the rise of their coalification degree the content of aliphatic and alicyclic compounds as well as of the oxygen groups decreases.

The fusinites show an insignificant content of the functional groups.During the coalification process the fusinites do not undergo essential changes.

Exinite compared with other components shows in all coals the lowest degree of coalification.Exinite is distinguished by the highest content of volatile matters, hydrogen, non aromatic hydrocarbon groups and by a high content of aromatic CHgroups

The participation of non aromatic configurations in petrographic components decreases towards:exinite-vitrinite-micrinite-fusinite and with the rank of coal.

The intensity of interference bands appearing on the X-Ray diagrams of vitrinites and the calculated values of structure parameters, show that there is a process of ordering of the vitrinite structure in coalification process.Particularly strong increase of structure packing degree is observed when passing from the vitrinite of the gas-coking to the orthocoking coal.

The appearance of weakly shaped 002, 100 band and of visible γ band on X-Ray diagrams shows that the structure of exinites is weakly ordered.

The micrinites are distiguished by the best packing of their structure /the smallest interplanar spacings d_{002}/.

Fusinites show higher dimensions of layers in comparison with the remaining petrographic components, these layers, however are weakly packed.The degree of ordering of fusinites structure depends in small degree on the rank of coal.The differences which appear in the distances of interplanar spacing and the dimensions of crys-

tallites between the investigated fusinites, may be explained by the petrographic heterogeneity of fusinites.

The differenes appearing in the chemical composition and in the structure between the petrographic components are the cause of their different behaviour in the coking process.The thermal resistance increases towards:exinite-vitrinite-micrinite-fusinite.The exinite behave as fluido-plastic substances.Among the investigated vitrinites, plasticity, caking and coking properties and expansion pressure on coking show only the vitrinites which occupy the mediumposition in the coalification scale, the gas-coking coal ,orthocoking and meta/semicoking coals.The best coking properties show the vitrinite from orthocoking coal/RI-o7,FSI=9,b=140%,d_{max}=2620 ‰/min/.The vitrinites from coals which occupy the extreme positions in the coalification series those from flame coal and from anthracite do not soften during the heating.The micrinites in principle should be numbered among the inert components.The fusinites remain completely inert in the coking process.

Properties and structure of cokes obtained from petrographic components

The petrographic components were coked in Gray-King apparatus in a temperature of 1000°C.In the obtained carbonization products chemical properties and structure were tested by applying the ultimate and proximate analysis and the structural microscopic and X-Ray examinations.

As results of an intense thermal decomposition of less resistant structural configurations, the content of volatile matters decreases /1,1-3,3%/ and also of hydrogen /0,4-1,0%/, while the content of C element increases /95,4-98,3%/.

In the coking process, essential changes of optical properties in the products of carbonization appear.The petrographic components may remain optically isotropic,or they may form areas which show an optical anisotropy of different range and intensity.In case of coking of vitrinites and exinites the type of developing anisotropic texture is strictly connected with rank of coal.

The cokes of vitrinites from flame and gas-coking coals are optically isotropic. The cokes of vitrinites from orthocoking, meta/semicoking coal and anthracite are optically anisotropic.

The coke of vitrinite from orthocoking coal is distinguished by a very large variety of anisotropic forms which are formed during coking.Areas of structure showing a fine-grained,coarse-grained, shell, fibrous and band anisotropy with predominant shell and fibrous anisotropy are formed passing into the band anisotropy.In the cokes of vitrinites from meta/semicoking coals and anthracite,mainly the areas showing a lump anisotropy and a small number of areas with band anisotropy appear.

The coke of exinite from the flame coal contains very small areas showing an optical anisotropy, in form of a fine grained anisotropy of a low intensity.The coke of exinite from gas-coking coal consists of areas showing a strong anisotropy in form of small and middle sized shells.The cokes of micrinites and fusinites are optically isotropic.

The structural X-Ray examinations have shown that largest dimensions of crystallites and the best packing of layers show the cokes obtained from vitrinites of ortho and meta/semicoking coals and the coke from exinite of a gas-coking coal/Fig.1/.

The smallest heights of crystallites and the weakest packing of layers show the cokes from vitrinites of lower coalificated coals as well as the cokes obtained from fusinites and micrinites.The cokes obtained from inertinites show relatively high dimensions of crystallites diameters.

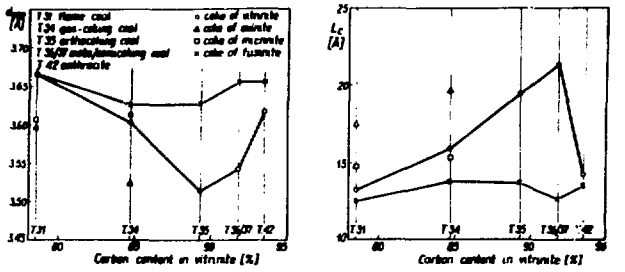


Fig.1 Structure parameters of cokes from petrographic components of hard coals

References

[1] Kröger C.,Brennstoff-Chemie,37,182 /1956/; 38 , 33 /1957/.

[2] Kröger C., Forschungsberichte des Landes Nordrhein-Westfalen,Nr 727,Westdeutscher Verlag/Köln und Opladen /1959/.

[3] Kröger C.,Mues G.,Brennstoff-Chemie,42, 33/1961/.

[4] Van Krevelen D.W.,Coal,Elsevier Publishing Company, Amsterdam, 1961.

[5] Ergun S.,Mc Cartney T.,Mentser M., Economic Geology, 54, 1068 /1959/.

[6] Ziółkowski J.,Prace GIG, Kom.Nr 229 /1959/; Kom. Nr 253 /1960/.

[7] Given P.H.,Peover M.E.,Wyss W.F., Fuel, 39, 323 /1960/; 44,425 /1965/.

[8] Oelert H.H., Brennstoff-Chemie, 48 , 331 /1967/.

[9] Ghosh T.K.,Fuel, 50, 218 /1971/; 51, 90 /1972/.

[10] Jasieńko S.,Zeszyty Naukowe Politechniki Wrocławskiej,Chemia 11, Nr 102 /1965/

[11] Jasieńko S.,Kidawa H.,Kowalik H., Chemia Stosowana, 13, 263 /1964/.

[12] Jasieńko S.,Kidawa H., Prace Naukowe IChiTNiW Politechniki Wrocławskiej, Nr 11,149 /1972/.

THE PROCESS OF CARBONIZATION AND GRAPHITIZATION OF PETROGRAPHIC COMPONENTS OF HARD COALS
PART II. THE CHANGES OF PROPERTIES AND STRUCTURE OF COKES FROM PETROGRAPHIC COMPONENTS IN THE PROCESS OF GRAPHITIZATION

T.JAKUBIEC, H.LIDAWA
Politechnika Wrocławska, Wrocław, ul. Gdańska 7/9, Poland

The papers of Franklin [1], Blayden, Riley and Wilson [2], Jasienko and co-workes [3, 4, 5] have shown that the cokes obtained from hard coals may be divided into three groups of substances: non-graphitizing -cokes from low rank; graphitizing-cokes from coking coals; graphitizing at very high temperature-cokes from anthracites.

In the literature no investigations on the graphitization processes of cokes obtained from petrographic components were found.

The cokes obtained from petrographic components: exinites, micrinites and fusinites separated from hard coals of different rank /Part 1/ have been subjected at 1500, 2000, 2500°C to the process of graphitization. The chemical properties and the structure of carbonization and graphitization products was examined.

Changes of chemical composition of the cokes in the process of graphitization

The mentioned changes takes place at different rates and their intensity and range depend on the kind of coke.

On high temperature treatment of cokes generally may distinguish the following stages: 1000-1400°C changes in the elemental composition leading to the formation of new structural elements, but with weak increase of their ordering; 1400-2000°C - ordering of structural elements within the planes, the formation of turbostratic structure; 2000-2500°C spacial ordering of the structure.

In the process of graphitization of the cokes of all the studied petrographic components, the changes of chemical nature have a very similar course. The highest intensity of these changes take place up to 1500°C. In the graphitization products obtained at 1500°C the content of the C element is above 99,2/99,0-99,4%/, the content of hydrogen ~0,2%. The sulphur components show a higher thermal resistance than those of carbon and hydrogen; their decomposition takes place with a variable intensity within particular temperature ranges up to 2500°C. In the products of graphitization obtained at 2000°C of cokes from fusinites and from exinites as well as from vitrinites of flame coal there is about the same content of sulphur /0,1 /. Sulphur components of higher thermal resistance appear cokes from vitrinites of orthocoking coal, also meta/semicoking coal and anthracite.

The decompsition of mineral substance proceeds the easiest in the process of graphitization of cokes from fusinites, the slowliest in the cokes from exinites.

Changes of structure of cokes in the process of graphitization

Microscopic Examinations. The cokes of vitrinites from flame and gas-coking coals remain optically isotropic; the structure of coke of vitrinite from orthocoking coal in principle does not change; the cokes of vitrinite from meta/semicoking coal and vitrinite from anthracite show a strong increase of intensity optical anisotropy, mainly at 2000-2500°C.

In cokes of exinites an insignificant increase of the range and of intensity of the optical anisotropy appears.

In the process of graphitization of optically isotropic cokes-micrinites, and fusinites a small quantity of anisotropic phase appears at 2000-2500°C. In all the types of the studied coals the fusinites with a well preserved cellular structure remains entirely optically isotropic in the process of graphitization up to 2500°C.

X-Ray Examinations. The cokes from petrographic components differ essentially by their susceptibility to ordering the structure in the process of graphitization /Fig. 1-4/. In case of cokes from vitrinites and exinites a strong dependance of the quantity of structural changes on the degree of coalification of the original petrographic components appear.

The cokes of vitrinites from flame and gas-coking coals behave as the non-graphitizing substance, they give products of a very stable ordering of the structure, taking place only in two dimensional system. The process of graphitization of the coke of vitrinite from the orthocoking coal leads to a gradual development of the graphitoidal structure /at 2500°C G=0,17/. The coke of vitrinite from meta/semicoking coal shows only an insignificant susceptibility to graphitization, /at 2500°C G=0,16/. The coke of vitrinite from anthracite within the temperature up to 2000°C behaves as the non-graphitizing substances. An intense ordering of its structure appears however above 2000°C temperature, after destruction of the cross linking bonds. The product of graphitization obtained in 2500°C achieves a better formed graphitoidal structure than the analogous graphitization products of cokes of other examined petrographic components.

The cokes of exinites from flame and gas coking coals are charactered by a considerably higher ability to ordering of their structure than the cokes of corresponding vitrinites.

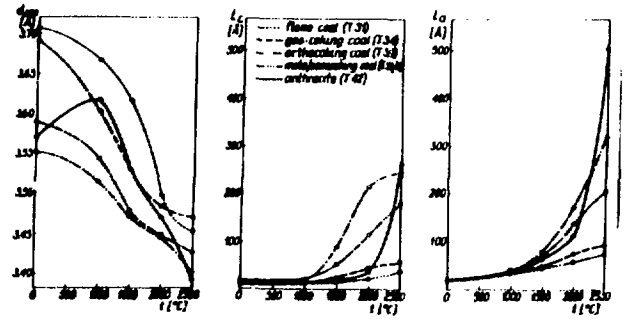


Fig. 1 Changes of structure parameters of cokes from vitrinites on the graphitization.

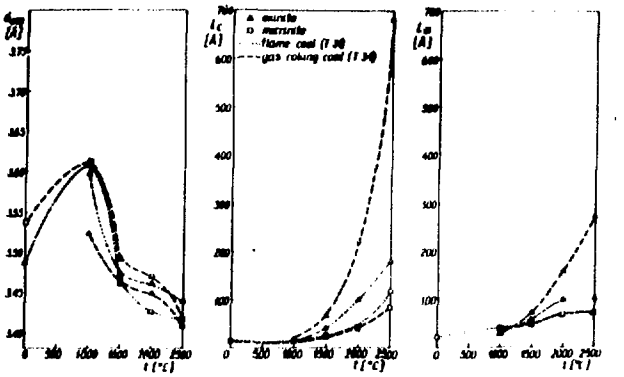


Fig. 2 Changes of structure parameters of cokes from exinites and micrinites on the graphitization.

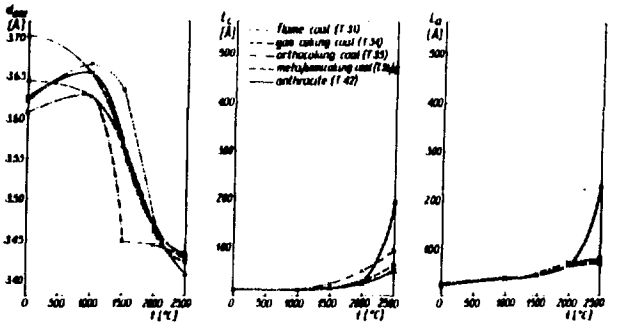


Fig. 3 Changes of structure parameters of cokes from fusinites on the graphitization

To a higher of coalification of the exinite corresponds the higher intensity of structural changes appearing in the process of graphitization.The product of graphitization obtained at 2500°C of the coke of exinite of the flame coal shows only the turbostratic-structure.An analogous graphitization product of exinite from gas-coking coal has features of a graphitoidal structure.In the process of graphitization of cokes from of exinites the tendency to a parallel arrangement of layers decidedly dominates over the increase of layer planes.

The cokes of micrinites have a limited susceptibility to ordering of the structure in the process of graphitization.In the products of graphitization of cokes from micrinites there is strong packing of layers, considerably better than in corresponding products of graphitization of cokes from non-graphitizing petrographic components.The three dimensional ordering of the structure does not appear.

The cokes of fusinites from all the investigated coals, characterized by a very low susceptibility to ordering of the structure belong to the groups of non-graphitizing substance.The cokes of fusinite behave very like, except the coke of fusinite from anthracite.An exception found in the case of the cokes from fusinite from anthracite where a distinct increase of the degree of structure ordering at 2000-2500°C is observed, might result from a considerable quantity of vitrinite inclusions as well as of the presence of intermediate forms between vitrinite-semifusinite appearing in the orginal fusinite.

Conclusions

The behaviour of cokes from petrographic components on high temperature heat treatment /graphitizing or non-graphitizing/ is a logical consequence of their structure.

The cokes of exinite from gas-coking coal and of vitrinite from orthocoking coal behave as graphitizing substances; the cokes of vitrinite of flame coal, the cokes of micrinites and fusinites separated from coals of different degree of coalification, belong to non-graphitizing substances; the cokes from anthracite undergo the process of graphitization not below 2000°C.

The obtained results give also essential information about the possibility to use the hard coals as row material, to obtain carbon and graphite materials.It seems that the cokes from vitrinites of flame coals may by useful to obtain materials like "glassy carbon".The cokes from orthocoking coal may be a row material for electrode industry.From coals and anthracite,which will be used as a row materials for the production of carbon and graphite materials macerals of inertinite group should be removed.

References

[1] Franklin R.E.,Proc.Roy Soc. A 209, 196 /1951/.

[2] Blayden H.E.,Gibson J.,Riley H.L., Proc. Conf. Ultra-fine Structure of Coals and Cokes, BCURA, London, 1944 p.176.

[3] Jasieńko S.,Preprints,II Sympozjum Przemysłu Elektrodowego, Opole,1966 p.348.

[4] Swietlik U.,Dissertation,Politechnika Wrocławska, 1974.

[5] Jasieńko S.,Kidawa H., Preprints, 2nd International Carbon Conference, Baden-Baden 1976, p.394.

AUTHOR INDEX

	Paper Number	Page Number
Agarwal, N. K.	MF-2(2)	140
	I-3(8)	338
	I-4(3)	428
Aisenberg, S.	B-1(5)	87
Alexander, W. K.	N-1(6)	113
Amamoto, K.	MG-3(2)	306
Ambrosia, A.	F-4(3)	292
Andrade, J. D.	B-1(7)	91
Armitage, J. E.	B-4(1)	216
Arora, V. M.	AC-3(4)	363
Atkins, J. H.	CR-2(2)	43
Ayache, C.	E-1(1)	52
	E-1(5)	60
Ayasse, J. B.	E-2(2)	145
Bacon, D. J.	N-1(3)	107
	CC-1(6)	276
	MF-4(3)	439
Ball, D. R.	MG-5(1)	457
Bansal, R. C.	CR-4(5)	286
Barr, J. B.	F-1(2)	96
	MG-5(3)	460
Bastick, M.	CC-3(4)	371
Baswell, I. L.	B-1(6)	89
Beatty, R. L.	N-4(7)	400
Becker, F. L.	MF-3(1)	261
Belinko, K.	MG-2(6)	209
Berenguer, C.	AC-3(1)	357
Biederman, D. L.	MG-4(5)	420
Bognet, J. C.	MF-3(3)	265
Bokros, J. C.	B-1(1)	79
	B-2(3)	157
	B-2(4)	159
	B-2(5)	161
	B-4(2)	218
	B-4(3)	220
Bolinger, P. N.	Ia-1(3)	17
	F-3(2)	166
Bonjour, E.	E-2(2)	145
Bonnetain, L.	CR-4(4)	284
Bose, S.	CC-3(3)	369
Bradshaw, W. G.	F-1(3)	98
	F-2(1)	126
Bragg, R. H.	E-4(1)	246
	CC-3(3)	369
Bright, A. A.	F-1(4)	100
Bruck, S. D.	B-1(2)	81
Bruckmann, H.	B-3(4)	182
Buch, J. D.	MM-1(4)	355
	MM-2(4)	379
	MF-4(7)	447
Buchanan, R. A.	B-1(6)	89
Bullock, R. E.	MF-2(3)	141
Burnette, R. D.	CR-6(1)	429
Buscailhon, A.	N-2(2)	238
Capon, A.	CR-5(2)	384
	CR-5(3)	386
Carmona, F.	E-4(4)	252
Carr, R.	B-2(4)	159
Chakrabartty, S. K.	CR-4(3)	282
Chang, H. W.	CR-7(1)	449
Chard, W. C.	MG-2(7)	212
Charlier, A.	E-4(3)	250
Chatterji, D.	CR-2(5)	48
Chiou, C. T.	AC-3(3)	361
Chiu, T. H.	CR-1(2)	9
	B-1(3)	83
	B-1(4)	85
Chow, C.	CR-7(3)	452
Chwastiak, S.	F-1(2)	96
Clayton, F. I.	Ia-3(5)	411
Collett, G. W.	MG-1(5)	27
	MG-3(9)	320

	Paper Number	Page Number
Combaz, A.	MG-5(4)	462
Conlin, J. A.	N-3(1)	340
Cook, W. H.	N-3(1)	340
	N-3(2)	342
Cormault, P.	N-2(1)	236
Coulon, M.	CR-4(4)	284
Courtney, A. L.	MF-1(1)	1
Cranin, A. N.	B-4(1)	216
Crawford, D.	MG-2(4)	205
Creasey, N. H.	B-1(8)	93
Crose, J. G.	MM-1(4)	355
	MM-2(2)	375
	MM-2(4)	379
Cundy, M. R.	N-3(3)	344
Curci, T. J.	La-2(1)	68
Dahle, D.	La-2(4)	74
Davidson, K. V.	N-4(3)	392
	N-4(6)	398
D'Andrea, J. F.	F-3(2)	166
de Combarieu, A.	E-1(5)	60
Delhaes, P.	F-3(1)	164
	E-4(4)	252
Delle, W. W.	N-4(1)	388
Denis, J. M.	MG-2(6)	209
Didchenko, R.	F-1(2)	96
Diefendorf, R. J.	MM-2(5)	381
Deitz, V. R.	AC-2(2)	259
	F-4(8)	301
Dillon, R. O.	E-1(2)	54
	E-2(1)	143
Donnet, J. B.	I-1(5)	37
Dowell, M. B.	CR-1(3)	11
	CR-3(3)	136
Driggers, G. W.	La-2(6)	78
Duval, X.	CR-7(5)	456

	Paper Number	Page Number
Eatherly, W. P.	N-1(5)	111
	I-2(7)	197
	N-3(1)	340
	N-3(2)	342
	N-4(4)	394
	N-4(5)	396
Eckstein, B. H.	CR-6(3)	433
Ehrburger, P.	I-1(5)	37
Eicher, H.	I-1(4)	35
Eilman, D. A.	La-3(3)	408
Emori, T.	E-2(4)	149
Endo, M.	F-4(7)	299
Ealick, M.	MF-4(3)	439
Evangelinden, J. G.	La-2(5)	76
	MM-1(2)	351
	La-3(4)	410
Fairclath, J. M.	MG-2(8)	214
Farrell, D. C.	B-2(3)	157
	B-2(4)	159
	B-2(5)	161
Feingold, R.	B-2(1)	155
Fiel, L. D.	CC-2(1)	346
	CC-2(2)	348
	MF-4(1)	435
Fillatre, A.	N-2(1)	236
Finchbach D. B.	F-2(3)	130
	CC-1(4)	272
	F-4(6)	298
Fitzer, E.	F-2(2)	128
	F-3(3)	168
	B-3(3)	180
	CC-1(1)	267
	MM-1(3)	353
Forrest, R. A.	MG-2(5)	207
Foreman, W. C.	E-2(5)	151
	E-2(6)	153
Fourre, J.	N-2(3)	240
Freeman, G. B.	AC-3(4)	361
Freeman, S.	B-4(2)	218
	B-4(3)	220

	Paper Number	Page Number
French, M.	CR-3(2)	134
	MG-2(5)	207
Fritz, H. C.	MG-3(6)	314
Fry, M. J.	F-3(6)	174
Fujibayashi, Y.	E-3(3)	229
Garrigou-LaGrange, C.	CC-1(3)	271
Gebhardt, J. J.	F-3(2)	166
Geigl, E.-H.	F-3(3)	168
Gettleman, L.	B-2(1)	156
Gill, J. T.	CC-2(1)	346
	CC-2(2)	348
	MF-4(1)	435
Gintinger, G.	I-1(3)	33
Goetze, B.	I-3(6)	334
Goldman, A. E.	N-1(6)	113
Gouna, J.	MG-4(6)	422
Goupin, J. M.	I-1(1)	31
Graves, R. S.	N-4(5)	396
Greatorex, C. L.	I-1(2)	32
Grenzeczuk, L. B.	La-2(2)	70
Griest, W. H.	I-2(7)	197
Griffiths, J. A.	MG-2(5)	207
Grindstaff, L. I.	MG-3(6)	314
Hagio, T.	I-3(1)	324
	I-3(2)	326
	I-3(3)	328
Hahn, R.	CR-2(3)	44
Hammer, R. L.	N-4(4)	394
Haubold, A. D.	B-1(7)	91
	B-4(2)	218
	MF-2(2)	140
	B-4(3)	220
	I-3(8)	338
	I-4(3)	428
Hawthorne, H. M.	CR-7(3)	452
Heintz, E. A.	I-2(1)	186
	MG-4(5)	420
Heym, M.	F-2(2)	128
	F-3(3)	168
Hightower, G.	CR-6(1)	429
Hishyama, Y.	E-4(2)	248
	CC-1(5)	274
Ho, S.	E-4(1)	246
Hochegger, G.	I-1(3)	33
Hoffman, W. P.	AC-1(4)	121
Hollabaugh, C. M.	N-4(3)	392
Holman, R. L.	MM-1(4)	355
	MM-2(4)	379
Hommy, C. A.	B-3(5)	184
Honda, H.	MG-2(2)	201
	CC-1(2)	269
	MG-3(4)	310
	I-3(1)	324
	I-3(2)	326
	I-3(3)	328
	MG-4(3)	416
	MG-5(2)	458
Honda, M.	MG-4(3)	416
Hooley, J. G.	CR-4(3)	282
	F-4(8)	301
	CR-7(4)	454
Hooton, H. A.	MF-1(1)	1
Hopfgarten, F.	F-4(1)	288
Horne, O. J.	E-3(5)	232
	E-3(6)	234
Horton, W. S.	CC-3(1)	365
Hough, P. T.	CR-7(4)	454
Hsu, H. L.	MG-3(6)	314
Huffstutler, M. C., Jr.	B-3(1)	176
Hulbert, S. F.	B-1(1)	79
	B-2(3)	157
	B-2(4)	159
	B-2(5)	161
Hüttinger, E. J.	CR-2(3)	44
	B-3(4)	182
Huttner, W.	B-3(3)	180
Imamura, T.	MG-2(2)	201
	MG-3(4)	310
Inagaki, M.	CC-1(2)	269
	CC-1(5)	274
	F-4(7)	299
	MG-4(4)	418

	Paper Number	Page Number
Irwin, J. L.	Ia-1(2)	15
Isaacs, H. S.	CR-4(2)	280
Iwata, K.	I-3(1)	324
James, R. A.	B-2(2)	156
	B-2(6)	163
Jasienko, H. S.	MG-5(5)	464
	MG-5(6)	466
Jenkins, D. H. R.	B-3(2)	178
Jimenez-Lopez, A.	AC-3(2)	359
Johnson, A. C.	F-1(3)	98
	F-4(4)	294
Jonas, L. A.	AC-1(1)	115
	AC-1(2)	117
Joo', L. A.	I-2(4)	191
	I-2(5)	193
	I-4(2)	426
Jortner, J.	MM-2(3)	377
	Ia-3(2)	406
	Ia-3(5)	411
	MF-4(5)	443
Juhola, A. J.	AC-1(3)	119
Kaae, J. L.	MF-2(3)	141
	MG-4(2)	414
Kaburagi, Y.	E-2(4)	248
Kakiyama, H.	CC-1(2)	269
Kakuta, M.	MG-3(3)	308
Kalis, P.	B-2(1)	155
Kappler, P.	I-1(5)	37
Karlak, R. F.	F-2(1)	126
Karlisch, K.	MM-1(3)	353
Karnes, C. H.	N-4(6)	398
Kawamura, K.	E-1(7)	64
	E-2(4)	149
Keck, H.	MG-2(7)	212
Kelly, B. T.	N-1(1)	104
	N-1(2)	105
Kennedy, C. R.	I-2(6)	195
	E-3(5)	232
	E-3(6)	234
	N-3(2)	342
	MF-4(2)	437
	MF-4(6)	445
Kennedy, E. P.	MF-4(6)	445
Kent, J. N.	B-2(3)	157
	B-2(4)	159
	B-2(5)	161
	B-3(5)	184
Khatir, Y.	CR-4(4)	284
Kibler, J. J.	MM-2(1)	373
Kidawa, H.	MG-5(5)	464
	MG-5(6)	466
Kimber, G. M.	MG-3(7)	316
Kimura, S.	F-3(5)	172
Kimura, T.	E-2(3)	147
King, R.	B-1(7)	91
Kitajima, E.	MG-5(2)	458
Klawitter, J. J.	B-2(4)	159
	B-2(5)	161
Kobayashi, K.	I-3(1)	324
	I-3(2)	326
	I-3(3)	328
Köchling, K.-H.	CC-1(1)	267
Koizlik, K.	N-4(1)	388
Komaki, K.	F-4(6)	298
Komatsu, M.	MG-3(4)	310
Kondo, S.	I-3(1)	324
Kooriki, M.	MG-3(3)	308
Kovac, C. A.	MG-1(3)	23
	MG-2(1)	199
Koyama, K.	F-4(7)	299
	CR-6(1)	429
Kreps, L. W.	E-1(6)	62
Kubota, H.	I-2(7)	197
LaCava, A.	MG-1(6)	29
Lahaye, J.	I-1(5)	37
Lamere, G.	Ia-2(4)	74
Lander, L. L.	Ia-2(3)	72
Laramee, R. C.	Ia-2(4)	74
Lasjaunias, J. C.	E-4(4)	252
Leake, D.	B-4(2)	218
	B-4(3)	220

	Paper Number	Page Number
Lemons, J. E.	B-1(6)	89
Lewis, I. C.	MG-1(1)	19
	MG-1(3)	23
	MG-2(1)	199
	MG-5(3)	460
Loch, L. D.	I-2(4)	191
	I-2(5)	193
	I-4(2)	426
Loll, P.	F-3(1)	164
López-González, J. de D.	CR-4(1)	278
	AC-3(1)	357
	AC-3(2)	359
	CR-6(2)	431
Lore, J. G.	N-2(1)	236
	N-2(2)	238
Lowe, D. L.	F-3(4)	170
Lowrey, W. H.	E-1(4)	58
Lozier, W. W.	E-3(1)	226
Ludwig, F. A.	I-1(6)	39
Macefield, I.	MG-3(1)	304
Mack, T. E.	MM-1(4)	355
	MM-2(2)	375
MacNair, R. N.	CR-7(2)	451
Maeda, K.	MG-3(2)	306
Maggs, F.A.P.	MF-1(2)	3
	B-1(8)	93
	CR-5(2)	384
	CR-5(3)	386
	MF-4(4)	441
Mahajan, O. P.	AC-1(5)	123
	CR-5(1)	382
Maire, J.	N-2(3)	240
Marchand, A.	CC-1(3)	271
Marion, R. H.	N-4(6)	398
Marsh, H.	CR-2(4)	46
	CR-3(1)	132
	CR-3(2)	134
	MG-2(4)	205
	MG-2(5)	207
	MG-3(1)	304
Martín-Pozuelo, A.	CR-4(1)	278
Martín-Rodríquez, A.	CR-4(1)	278
Marx, D. R.	CR-2(1)	41
Matsumoto, S.	MG-2(2)	201
Matsushita, Y.	I-3(1)	324
	I-3(2)	326
McClure, J. W.	E-2(1)	143
McCormack, R. A.	MF-4(1)	435
McKee, D. W.	CR-2(5)	48
McNab, I. R.	F-4(5)	296
McNeal, D.	B-4(5)	224
Meenaghan, M.	B-4(1)	216
Melcher, R. G.	AC-2(1)	257
Micale, F. J.	CR-1(2)	9
Micaud, G.	N-2(1)	236
	N-2(2)	238
Michael, E.	E-4(7)	256
Michieli, S.	B-4(2)	218
	B-4(3)	220
Mitchell, R.	Ia-2(4)	74
Miyazaki, K.	I-3(1)	324
	I-3(3)	326
Mizushima, S.	E-3(2)	228
	E-3(3)	229
Mochida, I.	MG-3(2)	306
Molleyre, F.	CC-4(4)	371
Mooney, V.	B-4(5)	224
Moore, J. P.	N-4(5)	396
Morelli, G. W.	I-2(3)	189
Morgan, C. S.	N-1(5)	111
Morgan, W. C.	MF-3(1)	261
Morris, E. G.	MG-2(8)	214
Mottet, P. S.	N-2(1)	236
	N-2(2)	238
Mrozowski, S.	I-2(2)	188
	E-3(4)	231
	E-4(5)	254
	E-4(6)	255
	E-4(7)	256
Murty, H. N.	I-2(1)	186
	MG-4(5)	420
Myers, B.	E-4(7)	256

	Paper Number	Page Number
Nagashima, H.	I-4(1)	424
Nakamizo, M.	MG-2(2)	201
	CC-1(2)	269
	CC-1(5)	274
	MG-3(4)	310
	MG-4(3)	416
Nakayama, C.	I-4(1)	424
Nandi, B. N.	MG-2(6)	209
Nicholson, A. P. P.	CC-1(6)	276
Nickel, H.	N-4(1)	388
Nieβ, R.	CR-1(1)	7
Null, M. R.	E-3(1)	226
Nyilas, E.	CR-1(2)	9
	B-1(3)	83
	B-1(4)	85
Oberlin, A.	CC-3(4)	371
	MG-4(6)	422
Oberlin, M.	MG-4(6)	422
	MG-5(4)	462
Ohashi, Y. F.	E-3(2)	228
Ohshima, H.	E-1(7)	64
	E-1(8)	66
Ohuchi, Y.	E-1(8)	66
Oi, S.	MG-2(2)	201
	MG-3(2)	310
	MG-4(3)	416
Okawa, M.	I-4(1)	424
Ono, A.	E-4(2)	248
Otto, K.	CR-2(6)	50
Ouchi, K.	MG-1(2)	21
	MG-1(4)	25
Oya, A.	CR-5(1)	382
Pacault, A.	F-3(1)	164
Pain, L. F.	F-1(5)	102
	N-4(8)	402
Parkash, S.	CR-4(3)	282
Peng, T. C.	MF-3(2)	263
Pernollet, A.	N-2(3)	240
Peters, E.	CR-7(3)	452
Pickering, R. S.	MF-1(3)	5
Pietzka, G.	MG-3(5)	312
	I-3(5)	332
Pinoli, P. C.	F-2(1)	126
	F-4(4)	294
	F-4(3)	292
Pizzoferrato, A.	B-4(3)	220
Powell, G. L.	N-1(5)	111
Prescott, B.	Ia-2(4)	74
Price, M. S. T.	N-4(2)	390
Price, R. J.	N-2(4)	242
	N-2(5)	244
Puri, B. R.	AC-3(4)	363
Quigley, M.	B-4(5)	224
Rabkin, M. F.	B-4(1)	216
Rakszawski, J. F.	I-2(3)	189
Rand, B.	MG-1(5)	27
	F-4(2)	290
	MG-3(9)	320
Rao, A. S.	N-1(3)	107
Rehrmann, J. A.	AC-1(1)	115
Reiswig, R. D.	N-4(3)	392
Reswick, J. B.	B-4(5)	224
Reucroft, P. J.	AC-3(3)	361
Rivin, D.	CR-2(2)	43
Robbins, J. M.	N-4(4)	394
Robins, G. A.	MF-1(2)	3
	MF-4(4)	441
Robinson, R.	F-4(2)	290
Rodríguez-Reinoso, F.	CR-4(1)	278
	AC-3(1)	357
	CR-6(2)	431
Rodríguez-Gallego, M.	CR-6(2)	431
Roetling, J. A.	Ia-1(1)	13
Romey, I.	F-1(1)	94
[illegible]coe, P. B.	F-1(5)	102
	N-4(8)	402

	Paper Number	Page Number
Rosenblatt, U.	B-3(4)	182
	I-3(6)	334
Rosendahl, J. F.	CC-2(1)	346
	CC-2(2)	348
	MF-4(1)	435
Rouxhet, P.	MG-5(4)	462
Rowe, C. R.	Ia-2(3)	72
	F-3(4)	170
Ruopp, P. G.	I-4(2)	426
Rusnak, R. M.	CR-7(1)	449
Samida, M.	B-2(2)	156
Sanada, Y.	MG-1(4)	25
	MG-3(3)	308
Saxena, R.	E-4(1)	246
	CC-3(3)	369
Schell, D. H.	N-4(3)	392
	N-4(6)	398
Schill, R.	N-2(1)	236
Schlesselman, H. D.	N-1(6)	113
Schmidt, D. D.	AC-2(1)	257
Schmitt, C. R.	I-1(1)	31
Schnitman, P.	B-2(1)	155
Schreyer, J. M.	I-1(1)	31
Schultz, R. L.	B-2(2)	156
	B-2(6)	163
Schwarz, G.	CC-1(1)	267
Seibold, R. W.	Ia-3(1)	404
	Ia-3(5)	411
Seldin, E. J.	I-3(7)	336
Senn, R. L.	N-3(1)	340
Setton, R.	MG-5(4)	462
Shelef, M.	CR-2(6)	50
Shibata, K.	MG-4(3)	416
Shim, H. S.	B-1(7)	91
	MF-2(2)	140
	I-3(8)	338
	I-4(3)	428
Shulman, L. B.	B-2(1)	155
Silverbrand, H.	B-4(1)	216
Singer, L. S.	MG-1(1)	19
	F-1(4)	100
Sinha, R. K.	AC-1(6)	125
Smith, J.	CR-3(2)	134
	MG-3(1)	304
Smith, M. E.	MF-1(2)	3
	CR-5(3)	386
	MF-4(4)	441
Sohma, J.	MG-1(4)	25
Sottosanti, P.	Ia-2(4)	74
Spain, I. L.	E-1(2)	54
	E-1(4)	58
	E-2(1)	143
Stanton, E. L.	MM-1(1)	349
Starrett, H. S.	Ia-2(6)	78
	MF-4(1)	435
Stecker, G.	I-2(4)	191
Stevens, D. W.	CC-3(2)	367
Stover, E. R.	Ia-1(1)	13
	F-3(2)	166
Stumpp, E.	CR-1(1)	7
Sugihara, K.	E-1(3)	56
	E-1(7)	64
Takeshita, K.	MG-3(2)	306
Tanaka, H.	F-3(5)	172
	MG-5(2)	458
Tano, T.	MG-5(2)	458
Tatarzycki, E. M.	MF-2(1)	138
Taylor, A. J.	Ia-2(1)	68
Taylor, D. W.	CR-2(4)	46
	CR-3(1)	132
Tholence, J. L.	E-4(4)	252
Thompson, N. G.	B-1(6)	89
Thrower, P. A.	CR-2(1)	41
	MF-3(3)	265
Tillmanns, H.	MG-3(5)	312
	I-3(5)	332
Trimm, D. L.	MG-1(6)	29
Tsuchitani, M.	MG-4(3)	416

	Paper Number	Page Number
Tsuzuku, T.	E-1(7)	64
	E-1(8)	66
	E-2(4)	149
Tucker, K. W.	I-2(4)	191
	I-2(5)	193
Unger, S.	B-4(1)	216
Uptegrove, D. R.	F-2(3)	130
Vagh, A. S.	E-4(5)	254
	E-4(6)	255
Valenzuela-Calahorro, C.	AC-3(2)	359
Vastola, F. J.	AC-1(4)	121
Velchez, F. M.	AC-3(1)	357
Velasquez, C.	CR-6(1)	429
Veringa, H.	N-3(3)	344
Vidano, R.	CC-1(4)	272
Villey, M.	MG-5(4)	462
Vogel, F. L.	E-2(5)	151
Wagner, N. J.	AC-1(6)	125
Wagner, P.	N-4(3)	392
Walker, E. J.	N-4(8)	402
Walker, P. L., Jr.	AC-1(4)	121
	AC-1(5)	123
	CR-5(1)	382
Wallouch, R. W.	I-2(1)	186
Wallura, E.	N-4(1)	388
Warren, I. H.	CR-7(3)	452
Warrens, J.	B-4(4)	222
Weber, G. W.	Ia-2(1)	68
	N-4(7)	400
Wehrer, A.	CR-7(5)	456
Wehrer, P.	CR-7(5)	456
Weng, T. L.	I-3(7)	336
White, J. L.	CR-3(2)	134
	MG-2(3)	203
	MG-2(5)	207
	MG-3(8)	318
Whitehead, H. D.	I-1(1)	31
Whittaker, A. G.	Ia-3(4)	410
	MG-4(1)	413
Whittaker, J. M.	B-2(2)	156
	B-2(6)	163
Whittaker, M. P.	MG-3(6)	314
Wilkening, I. S.	I-3(4)	330
Williams, P. T.	N-1(4)	109
Winkler, E.	I-1(4)	35
Wolter, D.	B-3(3)	180
Woolfson, M.	B-2(1)	155
Woollam, J. A.	E-1(6)	62
Yamada, Y.	MG-1(4)	25
	MG-2(2)	201
	MG-3(4)	310
	MG-4(3)	416
	MG-5(2)	458
Yamashita, Y.	MG-1(2)	21
Yasuda, E.	F-3(5)	172
Yazawa, K.	E-2(3)	147
Yen, T. F.	MG-3(10)	322
Young, K. R.	Ia-2(1)	68
Youssef, A.	AC-1(5)	123
Zeller, C.	E-2(5)	151
Zimmer, J. E.	MG-2(3)	203
	MG-3(8)	318
Zumwalt, L. R.	N-1(4)	109
Zurita-Herrera, L.	CR-6(2)	431